ASTES

Advances in Science, Technology & Engineering Systems Journal

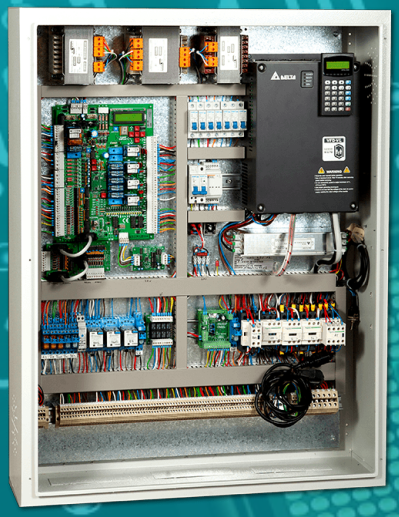

VOLUME 3-ISSUE 4|JUL-AUG 2018

www.astesj.com
ISSN: 2415-6698

Editorial

Advances in Science, Technology and Engineering Systems Journal (ASTESJ) is an online-only journal dedicated to publishing significant advances covering all aspects of technology relevant to the physical science and engineering communities. The journal regularly publishes articles covering specific topics of interest.

Current Issue features key papers related to multidisciplinary domains involving complex system stemming from numerous disciplines; this is exactly how this journal differs from other interdisciplinary and multidisciplinary engineering journals. This issue contains 38 accepted papers in Electrical and Electronics domains.

Editor-in-chief
Prof. Passerini Kazmersk

ADVANCES IN SCIENCE, TECHNOLOGY AND ENGINEERING SYSTEMS JOURNAL

Volume 3 Issue 4 **July-August 2018**

CONTENTS

ASTES

Advances in Science, Technology and Engineering Systems Journal Vol. 3, No. 4, 01-07 (2018)

www.astesj.com

ASTESJ

ISSN: 2415-6698

Performance Enhancement of MIMO-OFDM Using Redundant Residue Number System

Mohamed Abd Elghany Khalifa*, Amr Elsayed Emam, Mohamed Ibrahim Youssef

Al-Azhar university, Electrical Engineering Department, Faculty of Engineering, Cairo, Egypt

ARTICLE INFO

Article history:
Received: 24 May, 2018
Accepted: 27 June, 2018
Online: 02 July, 2018

Keywords:
Conventional Codes
Equalizers
Error Detection and Correction
Redundant Residue Number System
Wireless Communication

ABSTRACT

The data transmitted over wireless communication systems are affected by various elements as noise, interference or distortion, and to be able to combat these factors the paper propose the utilization of Redundant Residue Number System (RR NS) coding as a Forward Error Correction (FEC) technique to enhance the performance of MIMO-OFDM communication system compared to other conventional coding and equalization techniques.
The system Bit Error Rate (BER) and Peak-to-Average Power Ratio (PAPR) were measured through a MATLAB programs for different simulated channel conditions, including the effect of signal amplitude reduction and multipath delay spreading. The simulation results had shown that RRNS coding scheme provides an enhancement BER performance and reduced PAPR in comparison to conventional error detection and correction schemes through using the distinct features of Residue Number System (RNS).

1. Introduction

The wireless communication systems defined in IEEE standards (802.11n WLAN and 802.16 WMAN), are based on Multiple-Input-Multiple-Output (MIMO) antenna along with Orthogonal Frequency Division Multiplexing (OFDM) technology, which are referred to as MIMO-OFDM system.

The MIMO-OFDM system, provide an attractive wireless communication system that fits future wireless networks through providing high-data-rate wireless access at high Quality of Service (QoS) taking into accounts that the spectrum is a rare resource element and propagation conditions are difficult due to existence of fading and interference from other signals. [1]

The MIMO antenna technology from its side provides efficient frequency spectrum usage through spatial multiplexing gain, and enhanced communication link reliability because of the transmit system diversity gain [2]. On the other hand, the OFDM block distribute data over multiple numbers of closely spaced orthogonal carriers providing higher spectral efficiency by spacing the channels closer together without fearing from harmful effect of inter-carrier interference as carriers are orthogonal to each other.

Still, the wireless digital networks are prone to bit errors during transmission, thus error detection and correction techniques are implemented to reduce bit-error effects and ensure receiver eventually is able to restore the correct packet of information.

A new coding scheme for error detection and correction in MIMO-OFDM communication systems is provided in the paper using a Redundant Residue Number System (RRNS) instead of the current error control codes, where the RRNS had showed an enhanced system performance over conventional error correction techniques.

The paper starts with a short description on the Forward Error Correction (FEC) Methodology as seen in section 2, then in section 3 the Residue Number System and redundancy features and applications are given, followed in section 4 by illustration for RRNS error detection and correction implementation. In section 5, the overall system architecture is provided, and in section 6 methods of system evaluation are given. In section 7 simulation results are provided for the analysis of the communication system performance and finally in section 8 a conclusion was drawn.

2. Forward Error Correction Methodology

The Forward Error Corrections are methods which are used to enhance the channel capacity through adding redundant data to the message in a way that it can be restored at the receiving side even if there are a errors present during the transmission process. This redundant data allow receiver to detect and correct errors

*Mohamed Abd ElGhany KHALIFA, Al-Azhar University, Egypt, +2 01223944375, mohamedgheth@yahoo.com

without needing to retransmit the message again and without requiring a handshaking process between Transmit/Receive systems. [3]

The advantage of FEC schemes is shown in noisy channels where a large number of retransmissions would be required - in case of its absence - before a packet is received free of errors. Also, it is used in cases where no feedback exists between the receiver and the transmitter.

The encoded message could be systematic coded if portion of the output is directly resembling the input or non-systematic coded if the output is a modified form of the original information through shuffling original message symbols across several code using an inter-leaver to improve the performance of FEC codes, and thus the errors would have a more uniform distribution form.[4]

The coding techniques used as FEC schemes in previous literature [5, 6], could be categorized as block error correction codes, and convolutional error correction codes. The first ones are as Hamming, BCH, Reed-Solomon, and turbo codes, while the second ones are as Viterbi, and Low-Density Parity Check Code (LDPC).

3. Residue Number System Review

The RNS provides an efficient and effective arithmetic computation through transformation of large integers into smaller sets of digits.

The Residue numbers has unique features, as it is a carry-free arithmetic, which implies its ability to perform the operations related to the individual residue digits of different moduli independently. Also, the residue representations carry no weight-information which prevents the propagation of error in other digit-positions [7].

The RNS defined through selecting v positive pair-wise relative primes m_i ($i = 1, 2, 3 \dots v$) referred to as moduli, such that any integer N, describing a message, is given by the sequence (r_1, r_2 ..r_v) in the range $0<N<M_I$ in a unique matter;

$$r_i = N \pmod{m_i}; \quad (1)$$

Where;

r_i is remainder that is least positive when N is divided by modulus m_i

$$M_I = \prod m_i; \quad (2)$$

Where;

M_I is the dynamic range of information symbols'.

Then; to restore the symbols, two approaches are available; a parallel implementation scheme through using the Chinese Reminder Theorem (CRT) or a sequential approach that use the Mixed Radix Conversion (MRC) algorithm. In the coming subsection a description of the two methods are provided.

3.1 Chinese Remainder Theorem Method

The method relies on a mathematical idea that was given in the 4th century AD in china [8 – 10]; where for any v-tuple (r_1, r_2 ….r_v) such that $0 \le r_i < m_i$; there is only one integer N where $0 \le N < M_i$ and $r_i = N \pmod{m_i}$ which allows to recover the message. The numerical value of N is calculated based on equation (3):

$$N = \sum r_i \, T_i \, M_i \pmod{M}; \quad \text{for i: 1 to n} \quad (3)$$

Where;

$$i = 1 \text{ to } v;$$

$$M_i = M/m_i; \text{ M is dynamic range}$$

$$T_i = M_i^{-1} = \text{inverse value of } M_i; \quad (4)$$

Where;

$$| M_i \times M_i^{-1} |_{mi} = 1$$

3.2 Mixed Radix Conversion Method

For a of pair-wise relatively prime moduli set $\{m_1, m_2, \dots, m_n\}$ and a residue state $\{r_1, r_2, \dots r_n\}$ of a number X, that number can be uniquely represented in mixed-radix form as given in equation (5) and (6): [11]

$$X = \{z_1, z_2, \dots, z_n\} \quad (5)$$

And;

$$X = z_1 + z_2 m_1 + z_3 m_2 m_1 + \dots + z_n m_{n-1} m_{n-2} \dots m_1 ; \quad 0 \le z_i \le r_i \quad (6)$$

So, all what is required is to obtain the value of z_i to determine X. Where each value of z is represented as function of the moduli and residue representations as seen in table (1);

Table (1): Representation of z_i

Parameter	Representation
z_1	$= r_1$
z_2	$= \|\|m_1^{-1}\|_{m2} \ (r_2 - z_1)\|_{m2}$
z_3	$= \|\|(m_2 m_1)^{-1}\|_{m3} \ (r_3 - (z_2 m_1 + z_1)\|_{m3}$
z_n	$= \|\|(m_{n \dots \dots} m_2 m_1)^{-1}\|_{mn} \ (r_n - r_{n-1} \ m_{n-2} \ \dots \ z_2 m_1 + z_1)\|_{mn}$

And as seen in table (1), the Mixed Radix Conversion (MRC) is considered a sequential process, where obtaining z_i requires generating z_{i-1} first.

4. Proposed Error Detection and Correction Algorithm

The provided error detection and correction scheme use a set of RNS moduli's as an information symbols and additional RNS moduli's as a redundant symbol, all are which addressed as Redundant Residue Number System (RRNS). Through the use of RRNS it gives the designer, advantages both in terms of error detection and correction capabilities and in terms of maximum operating frequency. In fact, the operations on each residue digit are independent and so the mathematical operations as addition, subtraction, and multiplication on the full dynamic range are split in various channels and executed in

a parallel way on each of the moduli over a smaller dynamic range.

In this scheme the redundant moduli's' are selected to be greater than any of the other chosen moduli set and are not used in determining the dynamic range of the system. So, the RRNS is obtained by inserting an additional $(u - v)$ number of moduli $m_{v+1}; m_{v+2}; \ldots..; m_u$, where $m_{v+j} \geq max\{m_1; m_2; \ldots\ldots; m_v\}$ as a redundant modulus, to the previously introduced RNS, to form an RRNS of u positive, pairwise relative prime moduli. [12, 13]

So, an integer N in the range $[0; M_I]$ is represented as a u-tuple residue sequence, $(r_1; r_2; \ldots\ldots; r_u)$ with respect to the u moduli. The properties of the RNS indicated in the previous section; especially the independence of digits allows recovering the integer N by any v out of u residue digits using their related moduli, which would enable the redundant residue number to be used for self-checking, error-detection and correction in digital processors as seen in Figure (1). In addition, the RRNS technique is the only one that is capable of using the same arithmetic module for generating both the original information part and the parity part of a RRNS code-word [7].

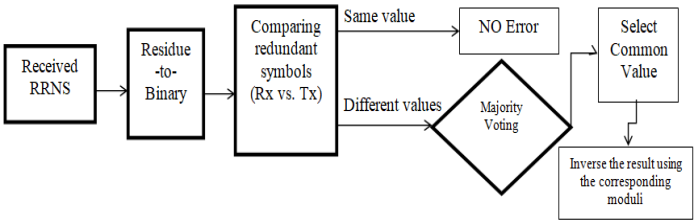

Figure 1. Error detection and correction algorithm

From Figure (1) seen above; the received redundant symbols are converted back to binary system and compared to the expected ones, and through this comparison the system would detect the occurrence of an error in the transmitted message.

Then, for error correction it is required to identify the modulus that generated the error either in m_3, or m_2 or m_1. Using the MRC method [11], a test on each of the information moduli with the two redundant moduli is performed and through this test it was able to identify and correct the bit which generated the error [14]. Thus, through the detection and correction algorithm, the error would be detected and corrected without the need to re-transmit again the information.

5. System Model

The communication system, as shown in Figure (2) is initialized with a binary data random source, that is converted to residue numbers and protected from errors by adding parity residue symbols using the RRNS encoding algorithm provided in section 4 instead of using LDPC encoder currently used in DVB-S2 communication systems, then the packet is modulated, coded through the Space-Time Block Coding (STBC) encoder that configure the way information are routed on multiple antenna system using algorithms as alamouti scheme [15], passed to a Serial-To-Parallel (S/P) converter for parallel transmission and then through an Inverse Fast Fourier Transform (IFFT) block where both act as an OFDM transmitter, and again converted back to serial sequence through Parallel-To-Serial (P/S) converter to the transmission antenna array system.

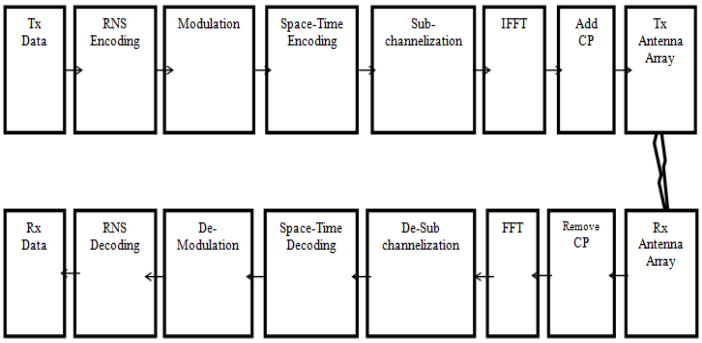

Figure 2. MIMO-OFDM System model

Before transmission a Cyclic prefix (CP) is inserted to combat the effect of Inter Symbol Interference (ISI) and Inter Carrier Interference (ICI) that would be caused by the multipath channel [16]. This CP is an image of the last section of the OFDM symbol that is inserted in the front of transmitted OFDM symbol.

To represent the satellite channel in the model shown in Figure (2), several channel fading are given; starting with Additive White Gaussian Noise (AWGN) channel, and then adding multipath fading factors through using Rice-Log-Normal distribution (RLN) distribution fading model [17].

The receiver blocks are the reverse blocks of the transmitter; where the CP is removed from the received stream, Serial-To-Parallel (S/P) converter for parallel transformation then passed to a Fast Fourier Transform (FFT) that is used to demodulate the signals for each residue sub-channel, and then converted back again to serial sequence through Parallel-To-Serial (P/S) converter. Then, the signal is decoded using the STBC, demodulated and recovered after R/B (Residue-to-Binary conversion).

6. Evaluation Methods

The RRNS-based MIMO-OFDM system performance is evaluated through the parameters defined and presented in this section.

6.1 Bit Error Rate (BER) measurements

The error probability for M-PSK modulated transmission in AWGN is given by:

$$P_{ERR} = \gamma \sum_{k=1}^{\min(2,\lceil \frac{M}{4} \rceil)} Q\left(\sqrt{2\sigma x}\sin\left(\frac{(2k-1)\pi}{M}\right)\right) \quad (7)$$

$$\gamma = \frac{2}{\max(log2\, M, 2)} \quad (8)$$

Where;

M is the constellation size,

ρ is the SNR per symbol.

x is a chi-square distributed random variable.

6.2 PAPR Evaluation Method

The performance is evaluated by measuring the Peak-to-Average Power Ratio (PAPR) of the signal *x(t)* [18], as seen in equation (9);

$$PAPR = 10 \log (\max|x_k|^2 / E[|x_k|^2]), \text{ in dB.} \quad (9)$$

Where;

E = Expectation operator

6.3 Channel Capacity

A way to characterize the channel performance of the system is through the Shannon channel capacity metric. Shannon in [19] defined the capacity as the maximum information rate a channel can support at a low error probability. The capacity of MIMO system is given in equation (10) as;

$$C = \log_2 [\det(I_n + \frac{\rho}{N}\mathbf{H}\,\mathbf{H}^H)] \quad (10)$$

Where;

I_n : n × n identity matrix

N: The number of transmit antennas

H^H: Conjugate transpose of H

7. Simulation Results

The proposed system performance was investigated using MATLAB tool, which involves the transmission of data streams through a FEC coding scheme whose integrity depends on OFDM with 512-ary QAM and Cyclic Prefix (CP):1/8, over different fading channels.

The examination was focused on the utilization of either equalizers or coding schemes as an error correction techniques, and analyzing the system performance of such techniques with that using RNS with redundant moduli's as an error detection and correction algorithm.

The MIMO-OFDM system performance was studied through measuring the BER and PAPR over AWGN, Rayleigh and Rician Lognormal (RLN) fading channel conditions.

7.1 Using Equalizers as Error correction scheme

The BER performance as seen in Figure (3), takes into account the simulation of several types of equalizers that are utilized for error correction.

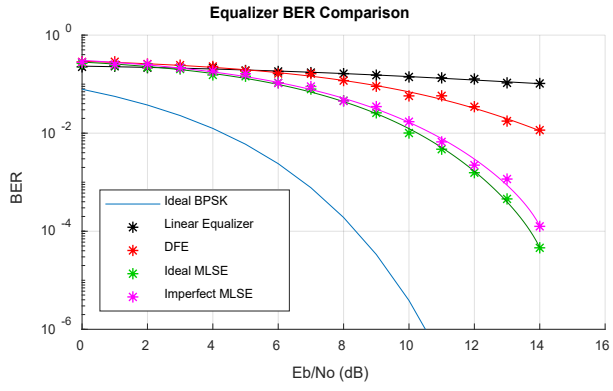

Figure 3. BER w.r.t E_b/N_o for various Equalization techniques

From figure (3), it is seen the enhanced performance of MLSE over DFE and linear equalizer, and thus next simulations focus on analyzing the performance of MIMO-OFDM with RNS coding system with and without MLSE equalizer over the RLN + AWGN channel, as seen in Figure (4).

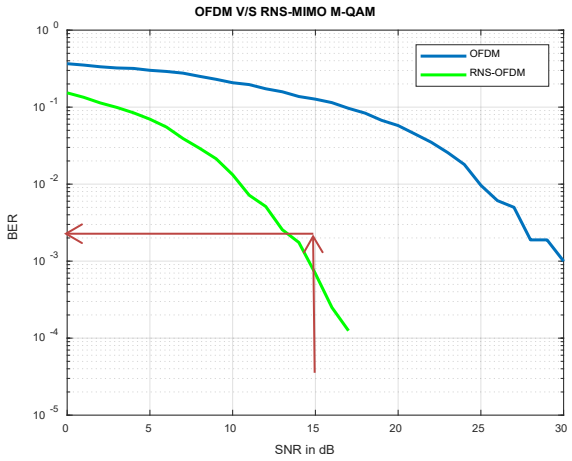

Figure 4.a. MIMO-OFDM RNS system with Equalizer

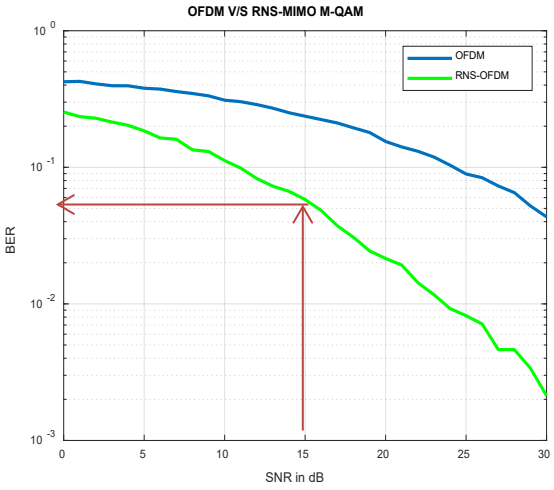

Figure 4.b. MIMO-OFDM RNS system without Equalizer

From Figure (4), for a SNR = 15, the BER for the communication system with error correction is $1*10^{-3}$ while it reaches $5*10^{-2}$ for the system without error correction.

7.2 BER performance with Current Coding Correction Schemes

The performance over AWGN channels for current error correction schemes that utilize coding approach as seen in Figure (5), shows that Golay code (which is a Block Error correction type) provides the best error correction code compared to other cods.

The current generation of linear block codes uses LDPC coders which utilize high multiplexing capacity and are differentiated from Golay codes through decoding approach; whereas binary Golay codes are decoded through algebraic methods, the LDPC codes are decoded in an iterative approach. In the next subsections analysis will be focused on LDPC coders as it is the one that is currently used in DVB-S2 systems.

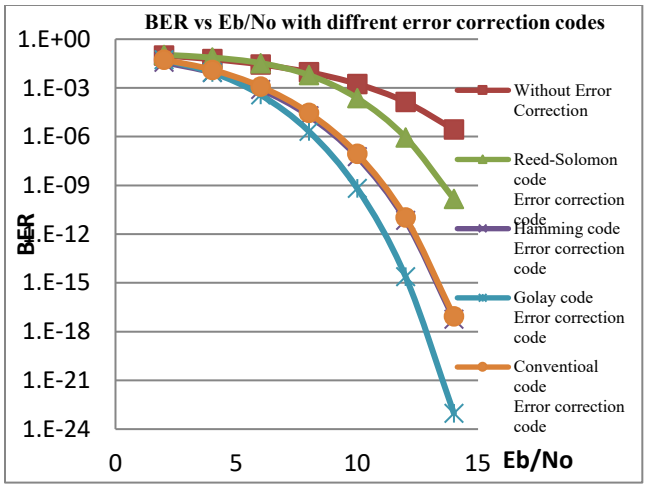

Figure 5. BER vs. E_b/N_o for current correction codes

7.3 Using Coding Techniques as Error correction scheme

Implementing an MIMO-OFDM communication system and comparing the system when converting the transmitted bits to residue coding (RNS-OFDM), and again when using LDPC algorithm as FEC Scheme (FEC-RNS-OFDM).

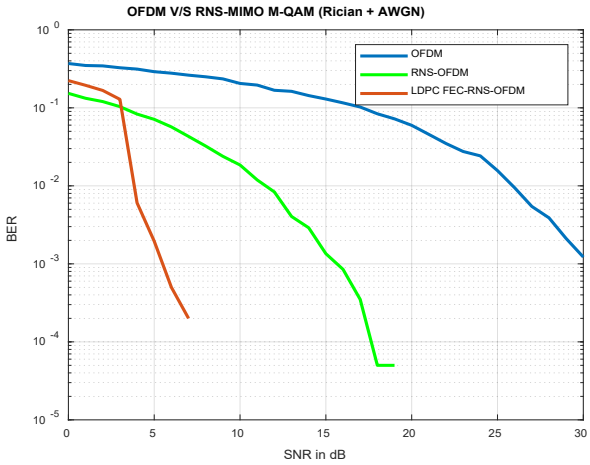

Figure 6.a. MIMO-OFDM RNS system with FEC coding (Rician Channel)

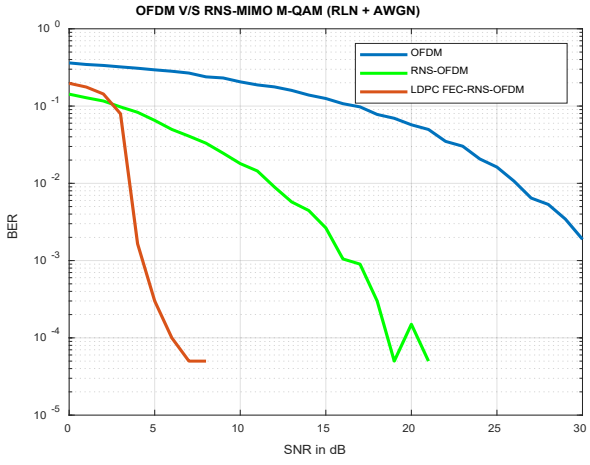

Figure 6.b. MIMO-OFDM RNS system with FEC coding (RLN Channel)

Where; Figure (6.a) and (6.b) shows the performance, enhancement done going from OFDM to RNS-OFDM then implementing an FEC-LDPC scheme. Also, the effect over different channels (small and deep fading) has been analyzed.

7.4 Comparison between different Error correction techniques

After analyzing in previous subsections, the utilization of equalizers and coding techniques as an error correction schemes; both techniques are compared over RLN + AWGN channel as seen in Figure (7).

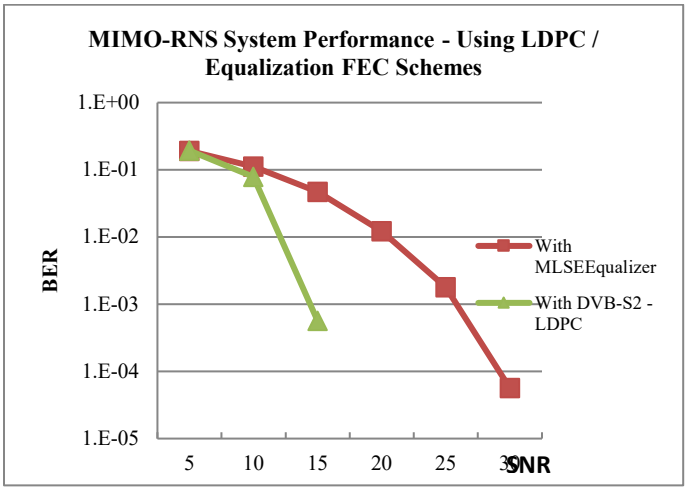

Figure 7. MIMO-OFDM RNS system with FEC schemes

In Figure (7) above, the LDPC coding provide enhanced performance over MLSE equalizer as an error correction scheme especially for higher SNR.

7.5 BER Performance for RRNS as FEC scheme

The system performance is evaluated with respect to the proposed scheme that utilize RNS coding with redundant moduli's for MIMO-OFDM system as an alternative error correction method. A redundant error correction using RNS is used were RNS moduli's are {3, 5, 7}, and redundant set is {11}.

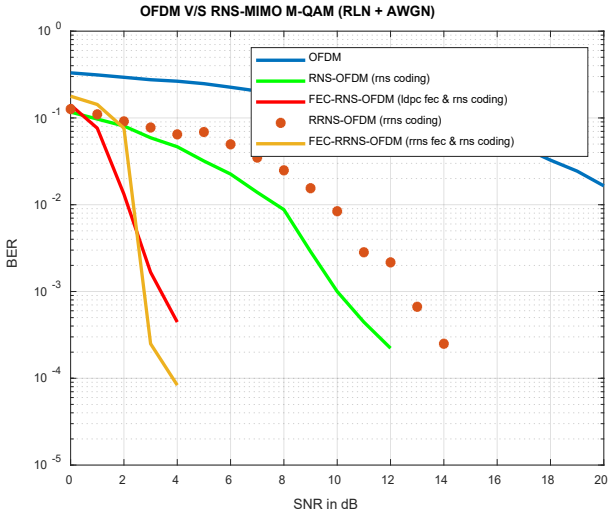

Figure 8. MIMO-OFDM system performance

From Fig (8) seen above, the error correction scheme with redundant RNS provide a comparable performance with that using LDPC scheme that is currently used in DVB-S2 systems.

7.6 BER for RNS vs. RRNS schemes in MIMO-OFDM System

Using RNS moduli's {3, 5, 7, 11}, and redundant set initially with moduli {13} then with redundant moduli's {13, 17}, evaluating the system performance with and without redundant moduli's as seen in Figure (9).

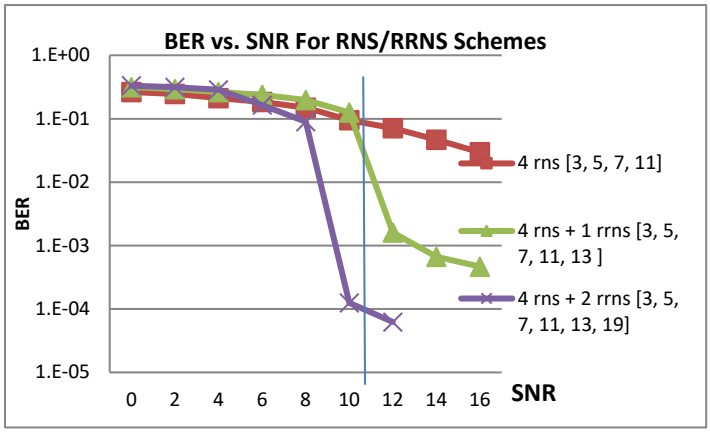

Figure 9. RRNS vs. RNS Performance comparison

From the above Figure (9), it is shown that for a SNR = 11db, an enhancement of the BER by 1 dB is seen when using one redundant moduli, and 3 dB when using two redundant moduli's in-comparison to the system without redundant moduli's.

7.7 PAPR performance for MIMO-OFDM with RRNS as FEC

For a MIMO-OFDM system over an ITU LOS + AWGN fading model channel, the PAPR for the transmitted signal is as shown in Figure (10).

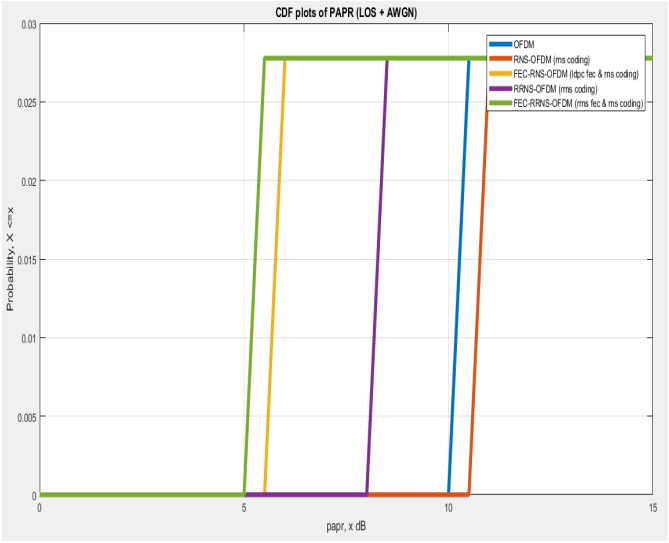

Figure 10. PAPR measurement for MIMO-OFDM system

From the above Figure (10), it is shown that the system with RRNS has the minimum signal amplitude by about 20% compared with LDPC FEC scheme (FEC-RNS-OFDM) and better than the systems that don't use FEC schemes.

7.8 Effect of Increasing RNS moduli on channel capacity

In Figure (11) a MIMO-OFDM system is analyzed over a RLN + AWGN channel for various RNS moduli sets.

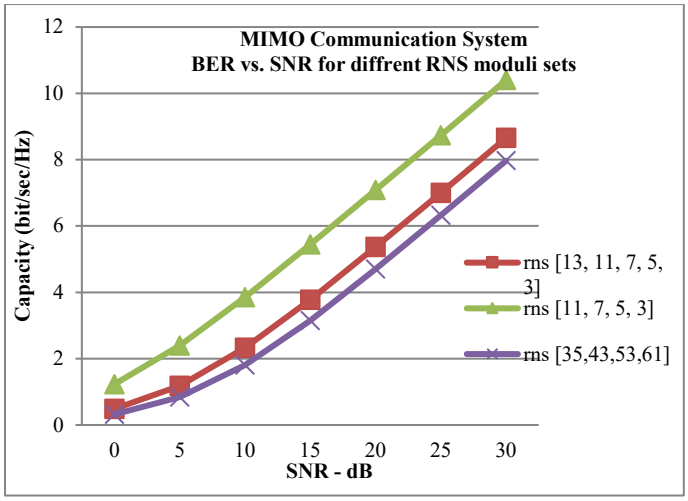

Figure 11. Channel Capacity for various RNS moduli sets

Where, in Figure (11) it is shown that the increase of number of RNS moduli value leads to a decrease in channel capacity due to the increased amplitude representation, and thus it is better to select some low order moduli set to be able to enhance the system performance.

8. Conclusion

The usage of RNS coding with its ability for parallel distributed arithmetic and independence between different arithmetic blocks, would simplify the overall system design and reduces the complexity of the individual building blocks.

The paper provides a method to detect and correct signal errors using RRNS. Where a four and then a six-length moduli set have been proposed; in the first time three out of the four were information moduli and one was redundant moduli, and in the second the first four moduli set is the information moduli and the last two is the redundant moduli respectively. Thus, a one and again two redundant moduli were used for error detection and correction.

Through the performed simulations it was proven that this system provide less receiving system complexity and the straight forward error detection algorithm due to the absence of carry propagation between the arithmetic blocks, reduced dynamic power by about 20% due to using small arithmetic units, and finally enhanced error detection and correction features, which improves as the redundant moduli increase taking benefit from the independent transmission feature; where an error in one sub-channel in RNS is not propagated into the other sub-channels and thus isolating the faulty residuals and as a consequence allow for fault tolerance and facilitate error detection and correction, but on the other hand this comes on the expense of reducing the available communication system channel capacity.

Conflict of Interest

I would like to declare that there is no conflict of interest.

References

[1] H. Bolcskei, "MIMO-OFDM wireless systems: basics, perspectives, and challenges," in IEEE Wireless Communications, vol. 13, no. 4, pp. 31-37, Aug. 2006. doi: 10.1109/MWC.2006.1678163

[2] A. J. Paulraj, R. U. Nabar, and D. A. Gore, Introduction to Space-Time Wireless Communications, Cambridge, UK: Cambridge Univ. Press, 2003.

[3] Jatinder Singh, Jaget Singh. "A Comparative study of Error Detection And Correction Coding Techniques", 2012 Second International Conference on Advanced Computing & Communication Technologies.

[4] B. Vucetic; J. Yuan (2000). Turbo codes: principles and applications. Springer Verlag. ISBN 978-0-7923-7868-6.

[5] DVB-S. EN 300 421 V1.1.2 (08/97). Digital Video Broadcasting; Framing structure, channel coding and modulation for 11/12 GHz satellite services. ETSI, 1997.

[6] DVB-S2. EN 302 307 V1.1.2 (06/06). Digital Video Broadcasting; Second generation framing structure, channel coding and modulation systems for Broadcasting, Interactive Services, News Gathering and other broadband satellite applications. ETS, 2006.

[7] M. Roshanzadeh, A. Ghaffari and S. Saqaeeyan, Using Residue Number Systems for Improving QoS and Error Detection & Correction in Wireless Sensor Networks, Communication Software and Networks (ICCSN), May 2011 IEEE 3rd International Conference on Page: 1-5

[8] K. W. Watson, "Self-checking computations using residue arithmetic," Proc. IEEE, vol. 54, pp. 1920–1931, Dec. 1966.

[9] Hao-Yung Lo, Ting-Wei Lin, 2013. "Parallel Algorithms for Residue Scaling and Error Correction in Residue Arithmetic". published by Wireless Engineering and Technology, Vol.4 No.4.

[10] A. Omondi, Residue number systems: theory and implementation. Imperial College Press, 2007.

[11] Pallab Maji, June 2011. Application of Residue Arithmetic in Communication and Signal Processing. Master of Science. NATIONAL INSTITUTE OF TECHNOLOGY, Rourkela, Orissa-769008, India

[12] Aingel James, Ameenudeen Pe, Jilu James, Minny George, "Multiple error correction using non-binary Redundant Residue Number System", *India Conference (INDICON) 2015*, 2015, ISSN 2325-9418.

[13] Hari Krisna, Kuo-Yu Lin, and Jenn-Dong Sun, A coding Theory Approach to Error Control in Redundant Residue Number Systems- Part I: Theory and Single Error Correction, IEEE Transactions on Circuits and Systems II: Analog and Digital Signal Processing Vol 39 issue 1 pp 8-17 Jan 1992

[14] Salifu Abdul-Mumin1, Kazeem Alagbe Gbolagade, "An Improved Redundant Residue Number System Based Error Detection and Correction Scheme for the Moduli Set". Advances in Wireless Communications and Networks journal, 2016; 2(1): 11-14.

[15] Devlal, Y. (2015). MIMO Performance analysis with Alamouti STBC Code and V-BLAST Detection Scheme. International Journal of Science, Engineering and Technology Research (IJSETR), 4(1), 199-204. Retrieved from ijsetr.org/wp-content/uploads/2015/01/IJSETR-VOL-4-ISSUE-1-199-204.pdf.

[16] Sandeep Kaur, Gurpreet Bharti, "Orthogonal Frequency Division Multiplexing in Wireless Communication Systems: A Review". International Journal of Advanced Research in Computer Engineering & Technology Vol. 1, Issue 3, May 2012

[17] Vatalaro, Francesco & Mazzenga, F & De Maio, G & Forcella, A. (2002). The generalized Rice lognormal channel model—first and second order statistical characterization and simulation. International Journal of Satellite Communications. 20. 29 - 45. 10.1002/sat.700.

[18] Paredes, M. (2015). Reduction of peak-to-average power ratio in OFDM systems. doi:10.14711/thesis-b650985

[19] Ramoni Adeogun, "Capacity and Error Rate Analysis of MIMO Satellite Communication Systems in Fading Scenarios", International Journal of Electrical and Computer Engineering (IJECE) Vol. 4, August 2014.

ASTES

Advances in Science, Technology and Engineering Systems Journal Vol. 3, No. 4, 08-20 (2018)

www.astesj.com

Special Issue on Multidisciplinary Sciences and Engineering

ASTESJ

ISSN: 2415-6698

Simulation Strategy to Enhance Oxygen Uptake and Reaction Forces at Leg Joints and Vertebral Bodies During Ergometer Exercise Under Altered Gravity

Yoshihiko Tagawa*, Masayuki Omoto, Hiroo Matsuse, Naoto Shiba

School of Medicine, Orthopaedics, Kurume University, 830-0011, Japan

A R T I C L E I N F O

Article history:
Received: 05 June, 2018
Accepted: 22 June, 2018
Online: 02 July, 2018

Keywords:
Space exploration
Disuse atrophy
Astronaut
Elderly
Ergometer exercise
Hybrid training
Electrical stimulation

A B S T R A C T

Moderate exercise has been implemented in spaceflight programs to prevent muscle and joint damage under extreme circumstances such as microgravity. Although the physical effects of exercise have been investigated experimentally, advanced modeling and simulation techniques are powerful tools that could provide insight into the physical limitations, optimal conditions, and mechanisms that might lead to muscle and joint damage. Ergometers are safe for patients and elderly individuals because exercise intensity can be easily regulated. Moreover, ergometer exercise that removes the load imposed by body weight on leg joints would better reflect training conditions in locations such as the International Space Station or on the surfaces of the Moon and Mars, where the force of gravity is lower than that on the Earth. A hybrid training system (HTS) that combines the electrical stimulation of antagonist muscles and volitional contraction of agonist muscles is an effective training method. Co-contractile motions in the HTS can counteract the reduced effect of gravitational force on leg joints during ergometer exercise. The present study aimed to validate the ability of an ergometer exercise model to measure oxygen uptake and joint reaction forces by comparison with experimental results and create strategies for electrically stimulating leg joint muscles for modulation under altered gravity. The simulation results suggested that the HTS could easily control the magnitude of oxygen uptake and joint reaction forces. Optimal cycling conditions to achieve desirable values for oxygen uptake and joint reaction forces would help to maintain the health of astronauts and appropriate exercise programs could be implemented in constrained space facilities.

1. Introduction

Space exploration and aging induce physical deconditioning. Space exploration has been limited so far to a low Earth orbit and short visits to the Moon, but deconditioning will become more serious after lengthy exposure to microgravity and hypogravity in manned spaceflights to Mars and bases there and on the Moon. Effective and efficient countermeasures within limited spaces such as those in spaceships are indispensable for maintaining human health. This report extends the work that was originally presented at IEEE EMBC 2017 [1].

A method of creating countermeasures against microgravity and hypogravity must be established to safely generate effective outcomes. Ergometer exercise reduces the load imposed by gravitational force on leg joints and the metabolic cost is comparable to that of walking on a level surface [2]. This type of exercise is beneficial for persons with knee osteoarthritis and elderly individuals seeking to engage in cardiovascular training. However, such exercise is ineffective for maintaining musculoskeletal function during spaceflight because the mechanical load provided by aerobic exercise is too low to prevent muscle atrophy at 0 g [3]. Preventing bone loss requires a compressive load along the bone axis similar to the repetitive forces at work during routine activities on the Earth. Astronauts are instructed to execute resistance and endurance exercises for about two hours and day for six days a week in a combination of countermeasures against the effects of microgravity. The conflicting requirements of safe aerobic training with less intensive loads on leg joints must be satisfied under lengthy exposure to microgravity. Creating appropriate experimental approaches on the Earth and under microgravity and hypogravity is very challenging.

*Yoshihiko Tagawa, Email: tagawa.yoshihiko877@mail.kyutech.jp

Although the effects of exercise on the human body have been investigated using mostly experimental approaches, advanced modeling and simulation techniques could be powerful tools for gaining insight into issues such as human physical limitations, forces at joints and forces generated by contracting muscles and the optimal conditions for training or exercise. Such techniques will help to quantitatively and qualitatively predict the effects of exercise under conditions of altered gravity. The present study used ergometer exercise models with the AnyBody Modeling System (AMS) ver. 6.0.6 (AnyBody Technology A/S, Aalborg, Denmark).

Oxygen uptake and loading on leg joints during ergometer exercise have only been examined experimentally. The present study aimed to validate an ergometer exercise model over a wide range of conditions to estimate oxygen uptake and reaction forces at leg joints and vertebral bodies by comparing the outcomes with experimental results, to develop a strategy for electrically stimulating antagonist muscles of joint motion to modulate oxygen uptake and joint loading under altered gravity, and to determine optimal conditions to satisfy conflicting requirements. A hybrid training system (HTS) that combines the electrical stimulation and volitional contraction of antagonist and agonist muscles, respectively, is an effective type of training [4] even for upper limbs under microgravity [5]. Co-contractile motions in the HTS can counteract the reduced effect of the gravitational force on leg joints during ergometer exercise.

2. Simulation Models for Ergometer Exercise

The musculoskeletal model in the AMS replicates a 50th percentile European male with a mass of 75 kg and a height of 1.76 m, respectively [6]. We modified the muscle activity function and muscle strength of "BikeModel" [7] in the AnyBody Managed Model Repository (AMMR ver.1.6.3) to construct a conventional ergometer (CER) exercise model with the HTS and reduced muscle strength. A seated model was constructed from the "StandingModel" based on the "BikeModel" and "LegPressMachine" in the AMMR ver.1.6.3 for recumbent ergometer (RER) exercise. Figure 1 shows both models that can simulate cycling with electrical stimulation of muscles around the leg joints based on the HTS concept and reduced muscle strength to represent weakened muscles. External forces and moments were applied to the thorax to maintain upper body posture while cycling on the CER model, even though the model lacks arms. In the RER model, a constant force of 56 N was applied to both anterior superior iliac spines to fix the pelvis on the seat of the ergometer. Friction forces (static friction coefficient of 0.6) between the surfaces of the backrest and the thoracic region, and between the gluteus region and the seat were also assumed instead of external forces and moments at the thorax. Thus, a person using the RER could exercise even at a gravitational acceleration < 1 g (9.81 m/s^2) on the Earth. The relative positions of the hip joint and crank axis of the RER were determined to mimic that of the CER. The ankle plantar angle on the RER was obtained experimentally from our recumbent ergometer cycling with a position mimicking that of CER exercise at a pedal rate of 60 rpm and a mechanical load of 60 W. The leg joint angles of both models became similar (Figure 2). A crank torque on the pedal of the RER has a phase shift of quarter cycle of a crank torque on that of the CER.

The amount of oxygen uptake during exercise on the models can be derived from the caloric equivalent of oxygen [8] required for muscle power. The simulation results included oxygen uptake of 3.5 ml/kg/min at rest only when compared with the experimental results that were plotted with reference to regression equations derived from the literature.

Recruitment patterns in a redundant muscle system such as the human body are produced based on optimal methods to minimize an objective function and they consist of the ratio of muscle force to maximal muscle force; that is, muscle activity. The AnyBody system offers min/max criteria for muscle recruitment [9]: the largest endurance for a task or identical activation of all muscles contributes positively to balancing external force, thus minimizing maximal muscle activity as much as possible when muscles work together. This would be a physiological criterion for minimal fatigue [10]. We combined the quadratic term of muscle activity with the objective function. A Hill-type muscle model [11] was adopted for the leg of the exercise model.

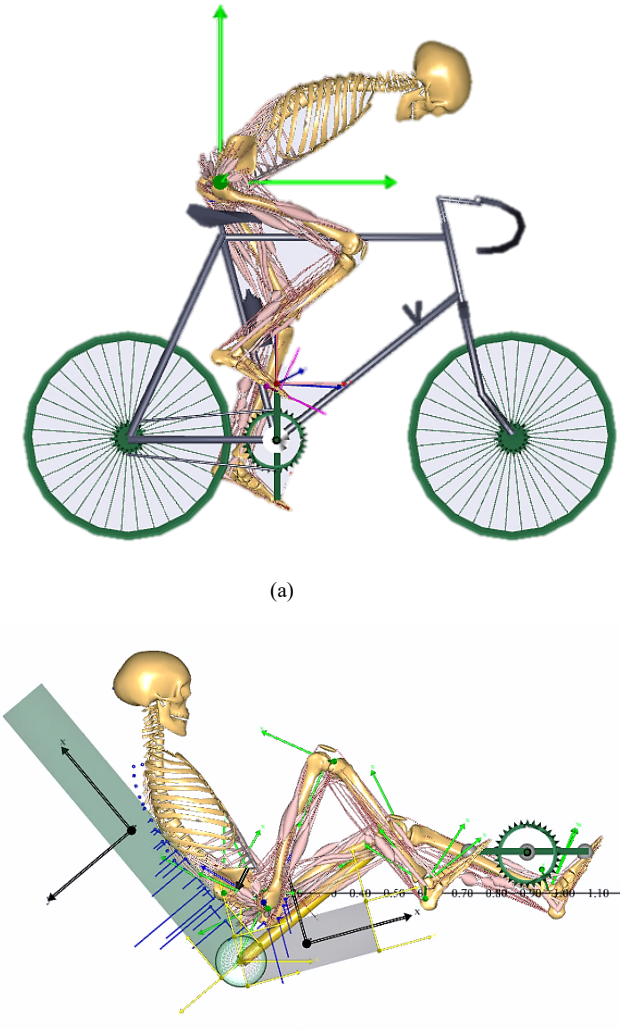

(a)

(b)

Figure 1. Simulation models for ergometer cycling with hybrid training system (HTS) and reduced muscle strength. (a) Conventional ergometer (CER) from "BikeModel" in the AnyBody Managed Model Repository (AMMR ver.1.6.3). (b) Recumbent ergometer (RER) constructed from CER with backrest angle of 130° and seat tilt of 15°.

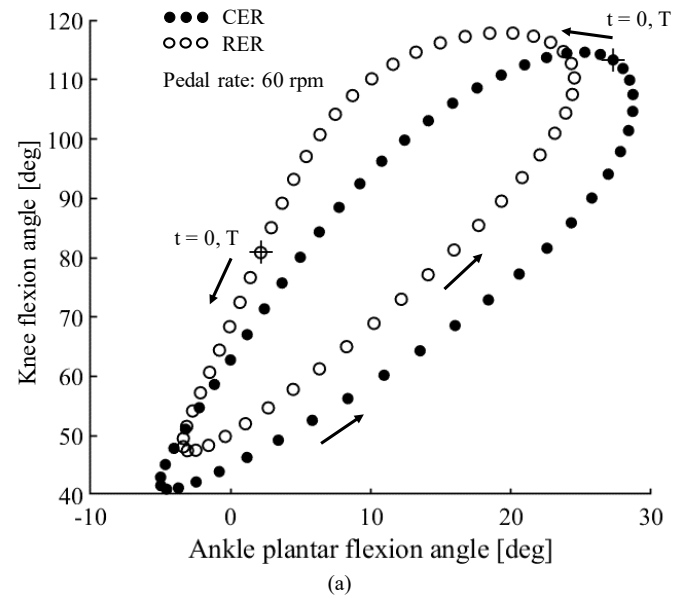

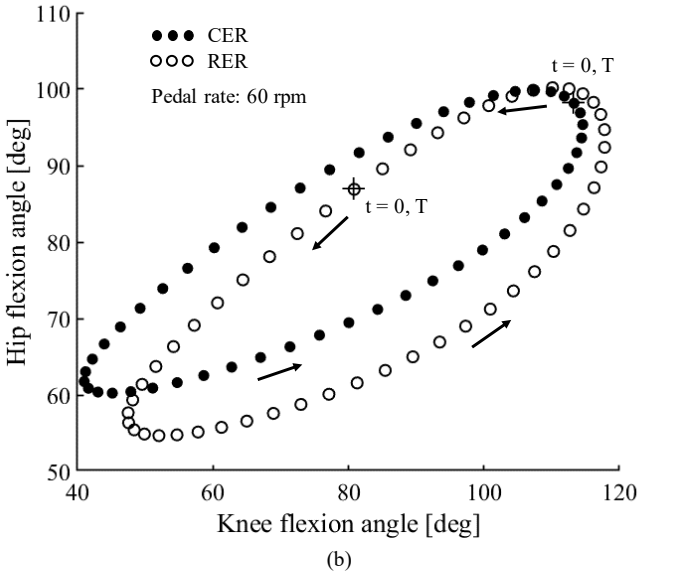

Figure 2. Comparisons of leg joint angles between conventional ergometer (CER) and recumbent ergometer (RER) exercise at pedal rate of 60 rpm. (a) Ankle plantar flexion vs. knee flexion. (b) Knee flexion vs. hip flexion. T, pedaling duration. At time 0, the right foot is located at highest point.

3. Validation of Ergometer Exercise Models

Volitional CER (VCER) and volitional RER (VRER) exercise models were validated based on comparisons with experimental results on the Earth. The saddle height and position were set to 0.78 m superior and 0.17 m posterior from the crank axis on the VCER. The center of the hip joint was positioned 0.77 m posterior and 0.15 m inferior from the crank axis on the VRER. The length of both cranks was 0.17 m. The effect of the HTS combined with the CER (HCER) was also investigated.

3.1. VCER Exercise at 1 g

The pedal rate and mechanical load of the VCER exercise model were varied with expanded experimental ranges. Figure 3 and 4 show oxygen uptake (ml/kg/min) at a pedal rate of 60 rpm under variable mechanical loads, and at defined mechanical loads of 81.7 and 0 W under different pedal rates, respectively. The simulation results shown in Figure 3 closely agreed with the experimental results [12] and increased linearly as mechanical load increased. The simulation results shown in Figure 4 were also similar to the experimental results [13,14] and increased

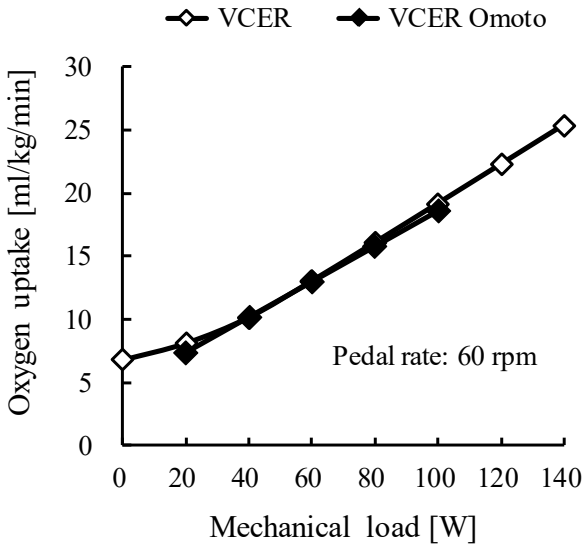

Figure 3. Oxygen uptake during volitional conventional ergometer (VCER) exercise at a pedal rate of 60 rpm under various mechanical loads. Unfilled and filled symbols indicate simulated and experimental results, respectively. Omoto, oxygen uptake data from [12].

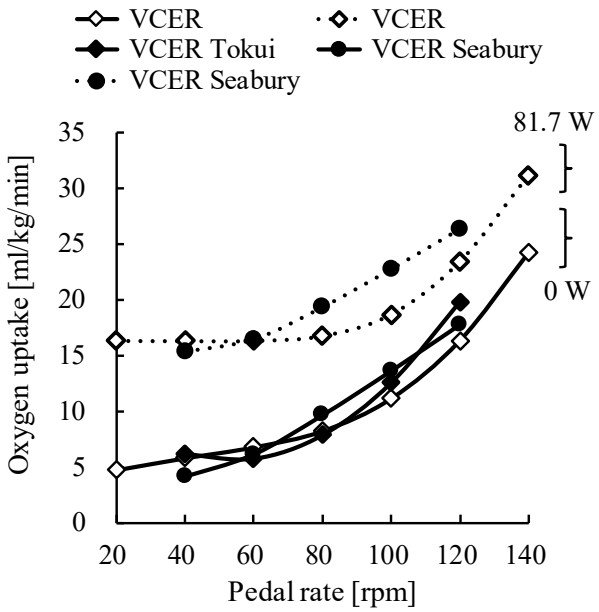

Figure 4. Oxygen uptake during volitional conventional ergometer (VCER) exercise under various mechanical loads (0 and 81.7 W) and pedal rates. Unfilled and filled symbols indicate simulated and experimental results, respectively. Tokui and Seabury, oxygen uptake data from [13] and [14].

nonlinearly, showing quadratic curves as the pedal rate increased. Oxygen uptake will consistently increase beyond the upper limit of the experimental range.

The maximum magnitude of resultant forces at the knee joint during cycling has been measured using instrumented knee implants in elderly individuals who were free of pain and physically active after total knee replacement (TKR) [2]. We

assumed 25% less muscle strength in the leg of the VCER exercise model with the muscle recruitment criterion of combined min/max and quadratic forms of muscle activity for comparisons with measured results. The simulated magnitude of the reaction force was reduced by approximately 10% of that using 100% muscle strength in the model. Moreover, the saddle height was set to 0.815 m, which mimicked the experimental conditions [2]. The simulated knee joint force closely agreed with the experimental findings of elderly individuals who engaged in ergometer exercise with an increasing mechanical load (Figure 5). The slow pedal rate resulted in a larger knee joint force. The increase in knee joint reaction force might be consistent with that above the experimental range.

The similar findings of these comparisons supported the validity and reliability of the ergometer exercise model except when values were beyond the lower limit of the experimental range. Little is known about ergometer exercise experiments at lower mechanical loads and pedal rates.

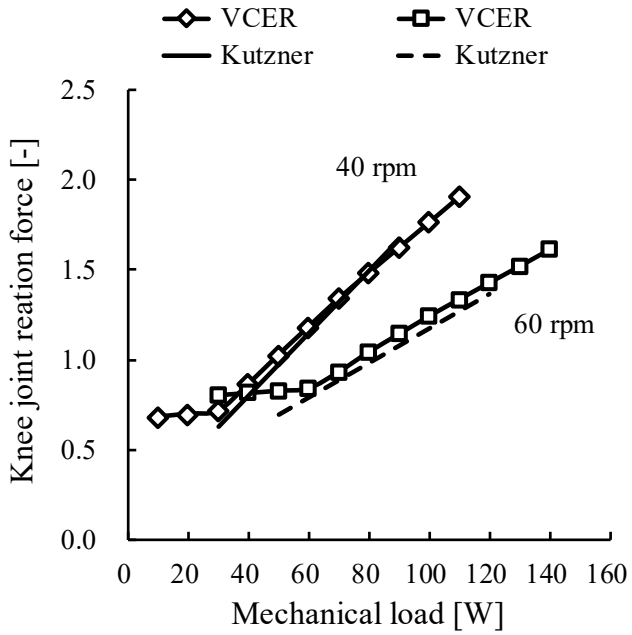

Figure 5. Comparison of experimental and simulated results of knee joint reaction force during volitional conventional ergometer (VCER) exercise under various mechanical loads and pedal rates of 40 and 60 rpm. Reaction force is maximum magnitude of force normalized by body weight. Saddle height in simulation was set to 0.815 m to mimic experimental condition. Kutzner, joint reaction force data from [2].

3.2. VRER Exercise at 1 g

Although both models had similar angles of leg joints, the upper body in the CER was dropped forwards and the body in the RER was inclined backwards (recumbent). Mean oxygen uptake at a pedal rate of 75 rpm in both positions was essentially identical at the same mechanical load [15]. Consumption tended to increase at higher loads in the recumbent position [15]. Simulated oxygen uptake in the VCER and VRER models was compared from the perspective of different mechanical loads and pedal rates (Figure 6.)

The difference in oxygen uptake between the two types of exercise rapidly increased as pedal rates increased, with oxygen uptake being higher for VRER, than VCER exercise. Further investigation is needed to validate the effect of RER exercise on the body.

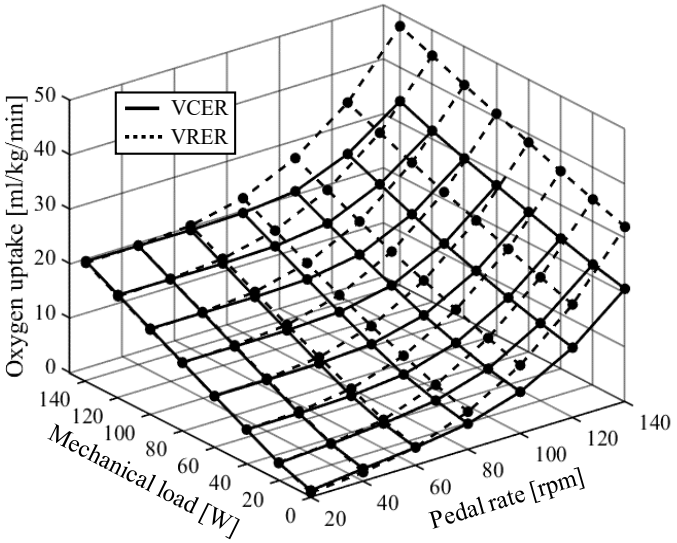

Figure 6. Comparison of simulated oxygen uptake during volitional conventional (VCER) and recumbent (VRER) ergometer exercise under different mechanical loads and pedal rates. Solid and dotted lines indicate VCER and VRER exercise, respectively. More oxygen was consumed during VRER than VCER exercise. Both results increased linearly according to increasing mechanical load and nonlinearly according to increasing pedal rate.

3.3. HCER Exercise at 1 g

The HTS was applied to the leg joints during ergometer exercise using the same leg motion as that used for volitional cycling. Stimulation intensities on the quadriceps femoris and hamstrings of the simulation model were determined at 1% and 5% of the maximum muscle activity, respectively, using the lower boundary of the muscle activity function in AnyBody. Stimulation that can fully activate assigned antagonist muscles at a specific intensity is ideal, unlike the actual situation during surface electrical stimulation (SES) [16-19]. The results of the simulation with low-intensity HTS closely agreed with the experimental findings of high-intensity SES (Figure 7). Additional effects of stimulation at intensities of 10%, 2% and 10% to the gastrocnemius, soleus, and tibialis anterior, respectively, were simulated to induce more oxygen uptake. At a pedal rate of 60 rpm (1-s cycle time), the antagonist muscles of the right knee during extension and flexion at the knee joint were stimulated for specific durations when knee angular velocities were > 2.0 and < –2.0 rad/s, respectively. These durations corresponded to 34% of the cycle time. The threshold of angular velocity of the plantar flexion angle of the right ankle was set to 1.0 rad/s, the corresponding duration of which was 26% of the cycle duration. The onset of stimulation on the left knee and ankle joints shifted half a cycle. The stimulus durations at all pedal rates were kept constant by adjusting the angular velocity setpoint according to the rate.

The increased oxygen uptake in the HCER was caused mainly by muscle co-contraction at the knee and ankle joints. The HCER linearly increased oxygen uptake, and the additional stimulation of muscles at the ankle joint similarly increased oxygen uptake.

The increase in oxygen uptake with the HTS shows that the HCER can achieve the same exercise intensity as the VCER at higher mechanical loads.

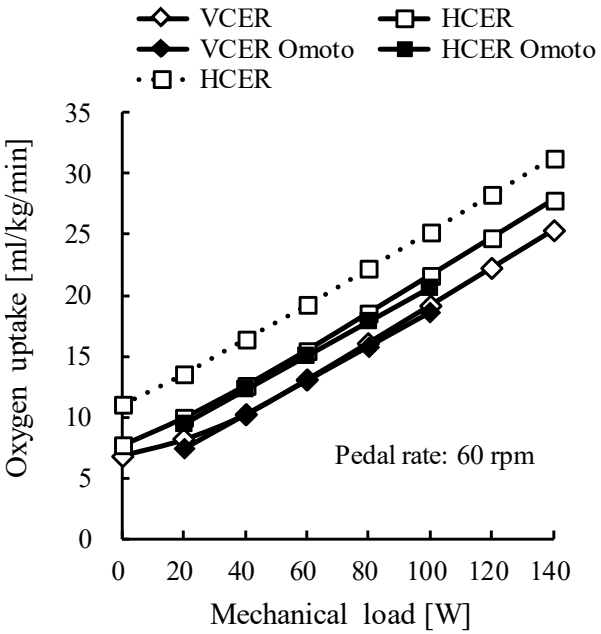

Figure 7. Comparison of simulated and experimental results of oxygen uptake during volitional conventional ergometer (VCER) exercise and hybrid training system (HTS) combined with conventional ergometer (HCER) exercise under different mechanical loads at pedal rate of 60 rpm. Solid line, HTS acting on knee joint; dotted line, HTS acting on ankle and knee joints. Unfilled and filled symbols indicate simulated and experimental results, respectively. Omoto, oxygen uptake data from [12].

4. Prediction Under Altered Gravity

The simulation and experimental results at the acceleration of gravity on the Earth closely agreed. The effects of different accelerations of gravity, such as microgravity in spaceships and hypogravity on the surfaces of Mars and the Moon, on the human body must be considered for safe space exploration, maintaining health under altered gravity, and returning smoothly to activities of daily life (ADL) on the Earth. Good agreement will support various predictions under altered gravity.

4.1. Oxygen Uptake During VCER and VRER Exercise Under Altered Gravity

The amounts of oxygen uptake at 0 g under mechanical loads of 60 and 120 W were essentially identical for each exercise. As gravity increased, oxygen consumption assumed a concave form during VCER exercise and a moderately concave form at both loads during VRER exercise. Although oxygen uptake varied, but the difference remained the same independently of gravity [20]. The lower oxygen uptake for the VCER and VRER ranged from 0.7 to 1.2 g and was dependent to some degree on mechanical load (Figure 8). The range of moderate gravity seemed to play assistive and resistive roles in the opposite leg for efficient oxygen consumption. Oxygen uptake during VCER exercise under varying gravitational acceleration became more concave than that while on the VRER. This might have been due to the different structure between the VCER and VRER; namely, the coordination of muscle activities of both legs is enhanced to maintain the pelvis position and steady cycling on the VCER under hypo- and hypergravity, respectively. In contrast, the backrest of the RER seat supports a reaction against the forward pushing force on the pedal of the VRER and restrained activities of lower limb muscles at hypergravity.

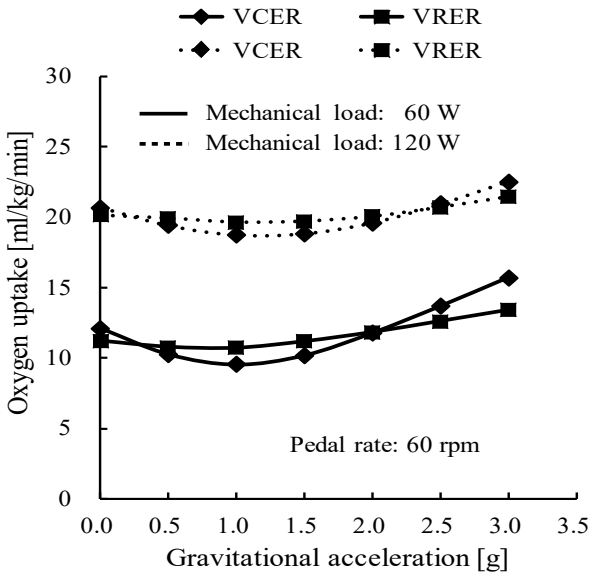

Figure 8. Simulated oxygen uptake under mechanical loads of 60 and 120 W and altered gravitational acceleration during volitional conventional ergometer (VCER) exercise and volitional recumbent ergometer (VRER) exercise. g, acceleration of gravity on the Earth; 1 g = 9.81 m/s^2. Pedal rate, 60 rpm.

4.2. Oxygen Uptake and Joint Reaction Force During VCER and VRER Exercise at 0 g

Oxygen uptake and the maximum magnitude of leg joint reaction forces that were normalized by body weight in the model, increased linearly with increasing mechanical load during VCER (Figure 9) and VRER exercise (Figure 10). Oxygen uptake and joint reaction forces at the knee and hip joints during VCER exercise were larger overall at 0 g (dotted lines) compared with those at 1 g (solid lines). Knee reaction force during VRER exercise was larger overall at 0 g than at 1 g, and oxygen uptake slightly increased with moderate variations under altered gravity.

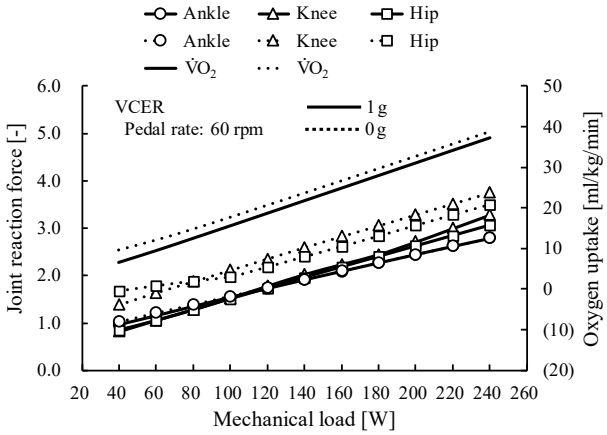

Figure 9. Comparison of joint reaction forces and oxygen uptake between 1 g (solid line) and 0 g (dotted line) during volitional conventional ergometer (VCER) exercise at pedal rate of 60 rpm. Joint reaction force is maximum magnitude of force normalized by body weight. $\dot{V}O_2$, oxygen uptake.

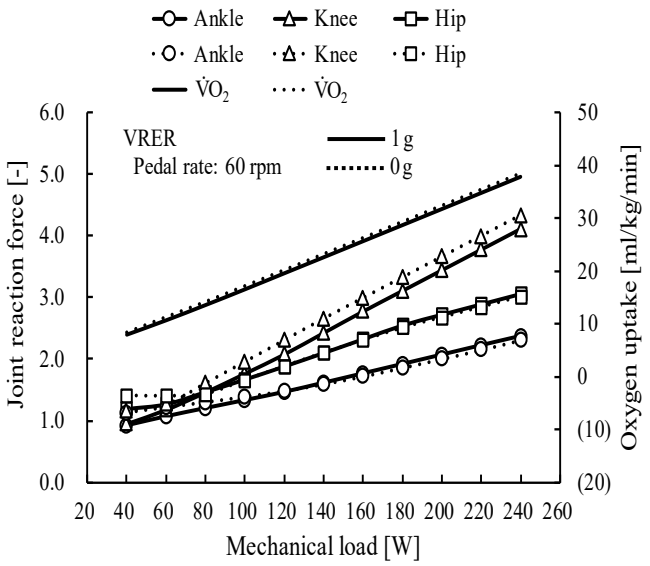

Figure 10. Comparison of joint reaction forces and oxygen uptake between 1 g (solid line) and 0 g (dotted line) during volitional recumbent ergometer (VRER) exercise at pedal rate of 60 rpm. Joint reaction force is maximum magnitude of force normalized by body weight. $\dot{V}O_2$, oxygen uptake.

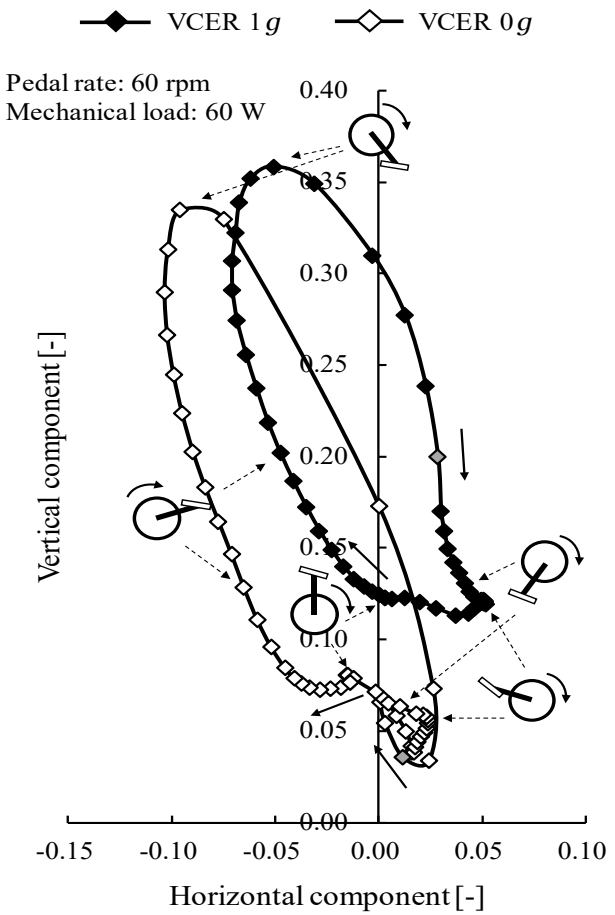

Figure 11. Comparison of pedal reaction forces between 1 g (filled symbols) and 0 g (unfilled symbols) during volitional conventional ergometer (VCER) exercise at a pedal rate of 60 rpm and mechanical load of 60 W. Pedal reaction force is shown in horizontal and vertical components, normalized by body weight. Gray symbol, lowest point of pedal.

4.3. Compensatory Actions During VCER Exercise at 0 g

The vertical component of the pedal reaction force became reduced and the horizontal component increased at 0 g (Figure 11), and the resultant pedal reaction force was lower than that at 1 g. The simulated force perpendicular to the crank (effective force) in the sagittal plane during VCER exercise was lower at 0 g with a pedal rate of 60 rpm and a mechanical load of 60 W than that at 1 g (Figure 12).

Muscles in the leg are activated to compensate for gravitational loss (Figure 13). Muscle force and joint reaction forces increase at 0 g and the increase in oxygen uptake was enhanced. The compensatory actions were smaller in the VRER than in the VCER, but the trends were similar.

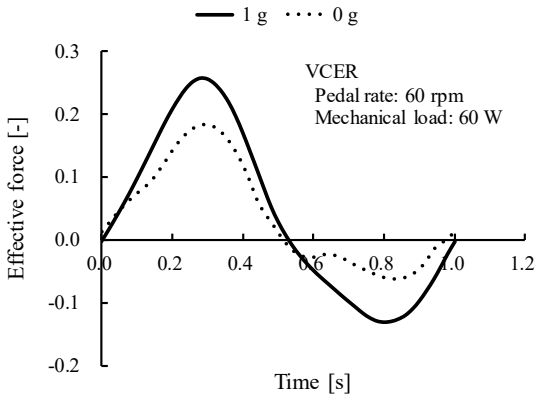

Figure 12. Comparison of effective force between 1 g (solid line) and 0 g (dotted line) during volitional recumbent ergometer (VCER) exercise at pedal rate of 60 rpm and mechanical load of 60 W. Effective force perpendicular to crank, normalized by body weight.

4.4. Effect of HTS on Ergometer Exercise at 0 g

Figure 14 shows the simulation results of oxygen uptake and knee joint reaction force during HCER exercise at 0 g with a mechanical load and two pedal rates corresponding to the experiment shown in Figure 5 at 1 g. The stimulation intensity was 10% and 20% of the maximum muscle activity of the quadriceps femoris and hamstrings, respectively. The oxygen uptake during VCER at 0 g varied linearly and increased at a pedal rate of 60 rpm.

Oxygen uptake under HTS will vary linearly with the same increment at mechanical loads that exceed the upper limit of the experimental range (similar to what is shown in Figure 9 for the VCER). The maximum magnitude of knee joint reaction forces during HCER exercise was over 3-fold body weight, which was much larger than the experimental and simulation results within the range of the mechanical load shown in Figure 15.

We confirmed the effects of the HTS on the reaction forces at leg joints over the mechanical load range of the experiment (Figure 15). The quadriceps femoris and hamstrings were stimulated at the same intensity as that shown in Figure 14. The maximum magnitude of resultant reaction forces induced at the knee and hip joints were ≥ 3-fold body weight and equivalent at least to the maximum at a mechanical load of 200 W during VCER exercise at 0 g (Figure 9). The maximum reaction forces at the leg joints at 40 rpm were essentially larger than those at 60 rpm.

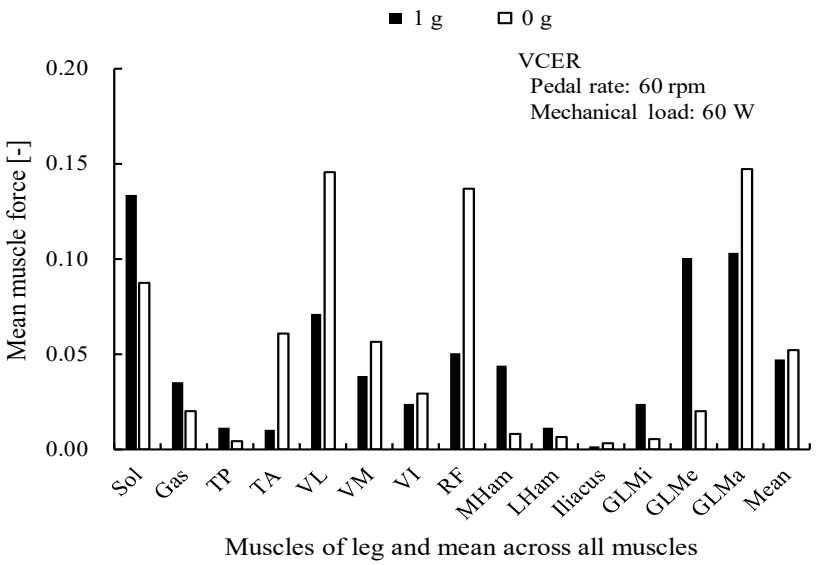

Figure 13. Comparison of mean forces of leg muscles between 1 g (filled bars) and 0 g (unfilled bars) during volitional conventional ergometer (VCER) exercise at pedal rate of 60 rpm and mechanical load of 60 W. Force is averaged during one cycle, normalized by body weight. Mean, average of mean muscle force of leg at 0 g and became larger than that at 1 g. Abbreviations: Gas, gastrocnemius; GLMa, gluteus medius; GLMe, gluteus medius; GLMi, gluteus minimus; LHam, lateral hamstrings; MHam, medial hamstrings; RF, rectus femoris; Sol, soleus; TA, tibialis anterior; TP, tibialis posterior; VI, vastus intermedius; VL, vastus lateralis; VM, vastus medialis.

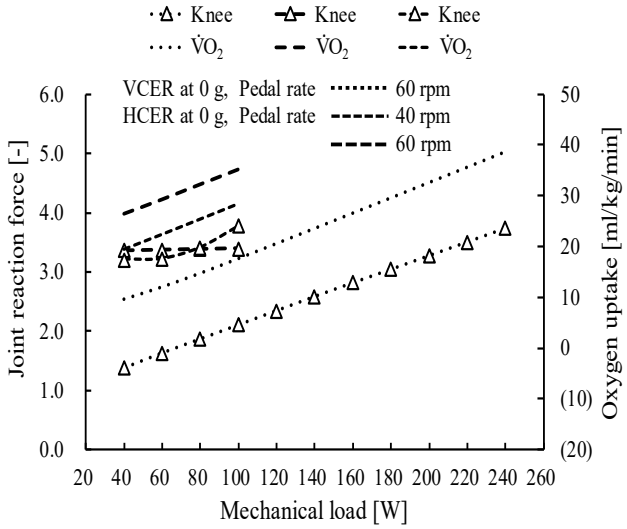

Figure 14. Comparison of knee joint reaction force and oxygen uptake at 0 g during volitional conventional ergometer (VCER) exercise and hybrid training system (HTS) combined with conventional ergometer (HCER) exercise under various mechanical loads and pedal rates of 40 and 60 rpm. Joint reaction force is maximum magnitude of force normalized by body weight. $\dot{V}O_2$, oxygen uptake.

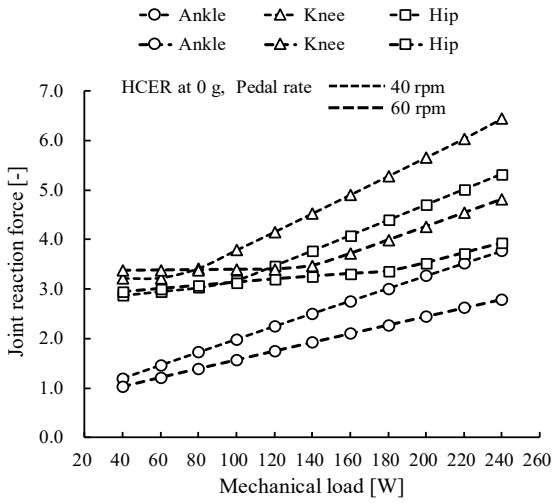

Figure 15. Comparison of joint reaction forces at 0 g during hybrid training system (HTS) combined with conventional ergometer (HCER) exercise under different mechanical loads and pedal rates of 40 and 60 rpm. Joint reaction force is maximum magnitude of force normalized by body weight.

The HTS increased the amount of oxygen uptake and knee joint reaction forces. The simulated results of oxygen uptake and knee joint reaction force during VCER and HCER exercise at 0 g were comprehensively compared under various mechanical loads and pedal rates (Figures 16 and 17, respectively). The amount of variation in the incremental pedal rate was contradictory. The quadriceps femoris and hamstrings of the HCER model were stimulated at intensities of 10% and 20% of the maximum muscle activity, respectively.

The optimal cycling conditions of mechanical load and pedal rate required to achieve a specific intensity and knee joint reaction force can be determined by minimizing the objective function, f (1). Table 1 shows the calculated optimal values for VCER and HCER exercise at 0 g. The reaction force was normalized by the body weight of the model.

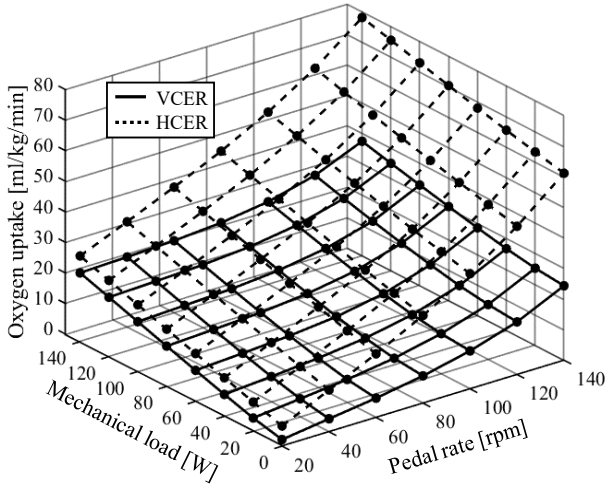

Figure 16. Simulated results of oxygen uptake at 0 g during volitional conventional ergometer (VCER) exercise and the hybrid training system (HTS) combined with conventional ergometer (HCER) exercise under various mechanical loads and pedal rates. Solid and dotted lines, VCER and HCER exercise, respectively. More oxygen was consumed during HCER than VCER exercise.

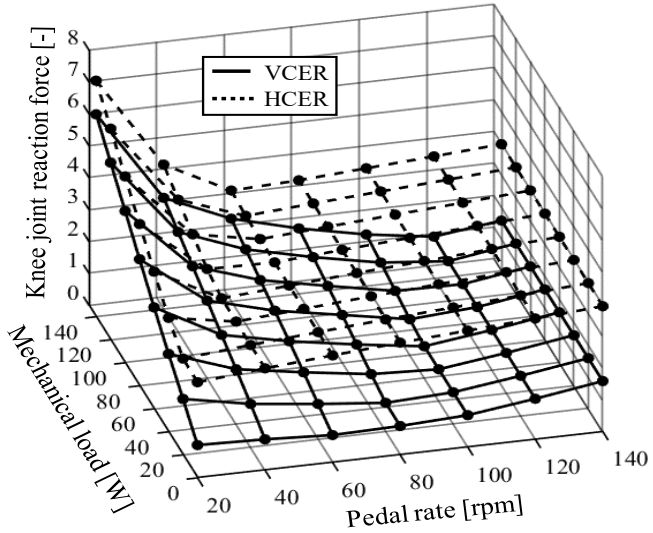

Figure 17. Simulated results of knee joint reaction at 0 g during volitional conventional ergometer (VCER) exercise and the hybrid training system (HTS) combined with conventional ergometer (HCER) exercise under various mechanical loads and pedal rates. Solid and dotted lines, VCER and HCER exercise, respectively. Knee joint reaction force is greater at lower pedal rate and greater mechanical load in both exercises. Joint reaction force is maximum magnitude of force normalized by body weight.

$$f = w_1\left(\dot{V}O_{2,m} - \dot{V}O_{2,d}\right)^2 + w_2\left(F_{Kj,m} - F_{Kj,d}\right)^2 \quad (1)$$

$\dot{V}O_{2,*}$: oxygen uptake, $F_{Kj,*}$: reaction force at knee joint normalized by the body weight of the model, *: m, model; d, desired value, w_1, w_2: weight coefficients

Table 1. Optimal cycling conditions for VCER and HCER at 0 *g*

Model	Optimal cycling conditions		Desired / realized values	
	Mechanical load [W]	***Pedal rate*** [rpm]	***Oxygen uptake*** [ml/kg/min]	***Reaction force at knee joint*** [-]
VCER	120	42.5	20/20	3.0/3.0
HCER	54.9	35.2	20/20	3.0/3.2
VCER	182	61.7	30/30	3.0/3.0
HCER	92.7	48.0	30/30	3.0/3.3
VCER	243	77.7	40/40	3.0/3.0
HCER	133	59.6	40/40	3.0/3.4

HCER, hybrid training system combined with conventional ergometer; VCER, volitional conventional ergometer

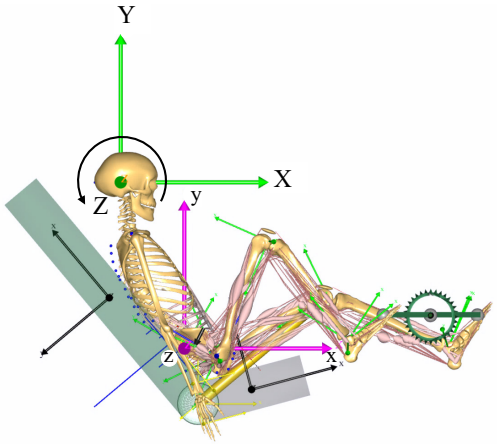

Figure 18. Human-ergometer system. System rotates about the Z axis of O-XYZ. O-XYZ, inertial frame; o-xyz, frame of human-ergometer system with origin at pelvis.

Oxygen uptake and joint reaction forces were simulated by altering the rotational velocity of the RER model at 0 g, a pedal rate of 60 rpm and a mechanical load of 60 W (Figure 18). We assumed that the upper limb in this model reflected the force of artificial gravity at a fixed shoulder joint. The rotational axis Z was set to pass close to both ears. The RER rotated at a constant angular velocity at increments of 90 deg/s from 0 to 450 deg/s. The centrifugal acceleration of the origin of the human ergometer frame at each velocity (o-xyz), was 0, 0.16, 0.65, 1.45, 2.59, and 4.04 g. The HTS was introduced at the knee and ankle joints to increase oxygen uptake and joint reaction forces at the ankle, knee, and hip joints.

Figure 19 shows the maximum magnitude of resultant forces between adjacent vertebral bodies located below the 12th thoracic vertebra. The resultant forces were greater during the HTS combined with the RER (HRER) than VRER exercise at angular velocities of 0 and 90 deg/s. Both results increased quadratically with increases in the angular velocity of the human ergometer system, in which the respective artificial gravity of which was quadratically proportional to the angular velocity. The resultant forces between adjacent vertebral bodies remarkably increased with increasing artificial gravity to > 360 deg/s that generated a centrifugal acceleration of 2.59 g, and were close to the resultant forces that are generated when walking on a level surface [21].

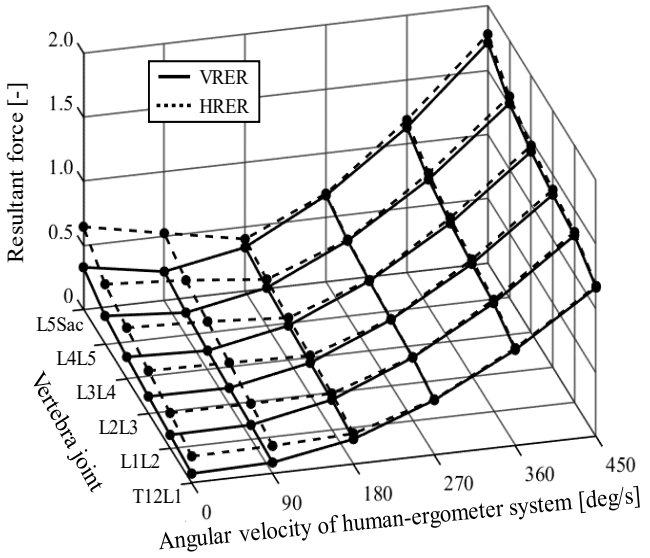

Figure 19. Comparison of peak resultant forces between adjacent vertebral bodies during volitional recumbent ergometer (VRER) exercise and the hybrid training system combined with recumbent ergometer (HRER) exercise at 0 g, a pedal rate of 60 rpm and mechanical load of 60 W. Solid and dotted lines, VRER and HRER exercise, respectively. Reaction force is the maximum magnitude of the force, normalized by body weight. Stimulation intensity, 10%, 20%, 20%, 4% and 20% at quadriceps, hamstrings, gastrocnemius, soleus and tibialis anterior, respectively. L5Sac, between 5th lumbar spine and sacrum; LiLi+1, between ith and (i+1)th lumber vertebrae (i = 2,3,4); T12L1, between 12th thoracic and 1st lumbar vertebrae.

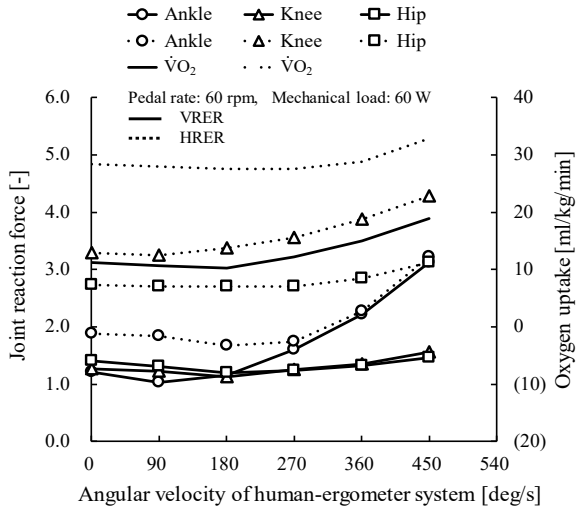

Figure 20. Comparison of peak joint reaction forces and oxygen uptake during volitional recumbent ergometer (VRER) exercise and the hybrid training system combined with recumbent ergometer (HRER) exercise at 0 g, pedal rate of 60 rpm and mechanical load of 60 W. Solid and dotted lines, VRER and HRER exercise, respectively. Mean, average of mean leg muscle forces. Stimulation intensity, 10%, 20%, 20%, 4% and 20% at quadriceps, hamstrings, gastrocnemius, soleus and tibialis anterior, respectively. Joint reaction force is maximum magnitude of force, normalized by body weight.

5. Discussion

Human in an environment with microgravity will experience disuse atrophy, resulting in the loss of mass and strength in muscles and bones. Exercise under such extreme circumstances has been examined and moderate exercise intensity has been implemented in spaceflight programs. Conventional ergometer cycling is a safe type of exercise that is easily implemented, because the exercise intensity can be controlled. Advanced modeling and simulation techniques are powerful tools that can provide insight into the physical limitations, optimal conditions, and mechanisms that might lead to muscle and joint damage instead of experimental approaches under extreme environments. Few studies have applied mathematical modeling and experimental approaches to determine joint reaction forces while walking [22] and oxygen uptake during ergometer exercise [20]

The cycling exercise model was constructed by modifying a commercially available bicycle model to simulate oxygen uptake during HTS cycling at 1 g and 0 g. The simulated oxygen uptake during VCER and HCER exercise at 1 g closely agreed with the experimental results described in [12] (Figure 7). Mean oxygen uptake at a pedal rate of 75 rpm in dropped forward and recumbent positions is essentially identical at the same mechanical load, but slightly increased at higher loads in the recumbent position [15]. Since we confirmed the same tendency in the VRER (Figure 6), several features of RER exercise predicted by simulation seemed acceptable. Oxygen uptake in hypergravity was lower during VRER than VCER exercise. This might have been due to the coordination of muscle activities in both legs being enhanced to maintain the steady crank rotation during VCER exercise, whereas reaction force generated from the back rest contributes to adjust the moment at the leg joints in the VRER. Consequently, the mean muscle forces of the legs in the VRER at hypergravity of 3 g became moderate and averaged far less than those in the VCER (Figure 21). Large muscle forces of the soleus (one-joint muscle across the ankle) were generated to balance the large pedal reaction forces at high gravitational and centrifugal acceleration.

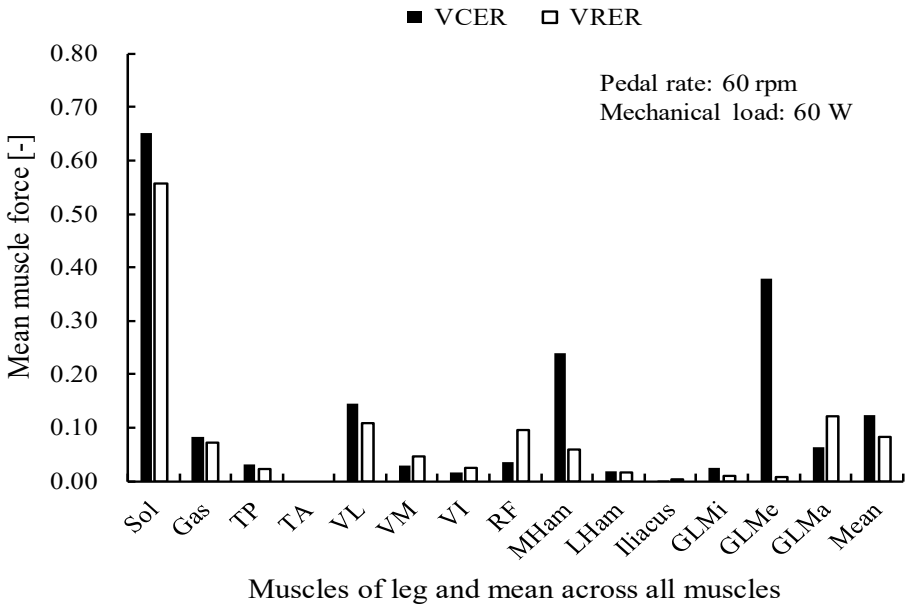

Figure 21. Comparison of mean leg muscle forces during volitional conventional (VCER, filled bars) and volitional recumbent (VRER, unfilled bars) ergometer exercise at 3 g, a pedal rate of 60 rpm and mechanical load of 60 W. Force was averaged during one cycle, normalized by body weight. Abbreviations: Gas, gastrocnemius; GLMa, gluteus medius; GLMe, gluteus medius; GLMi, gluteus minimus; LHam, lateral hamstrings; MHam, medial hamstrings; RF, rectus femoris; Sol, soleus; TA, tibialis anterior; TP, tibialis posterior; VI, vastus intermedius; VL, vastus lateralis; VM, vastus medialis.

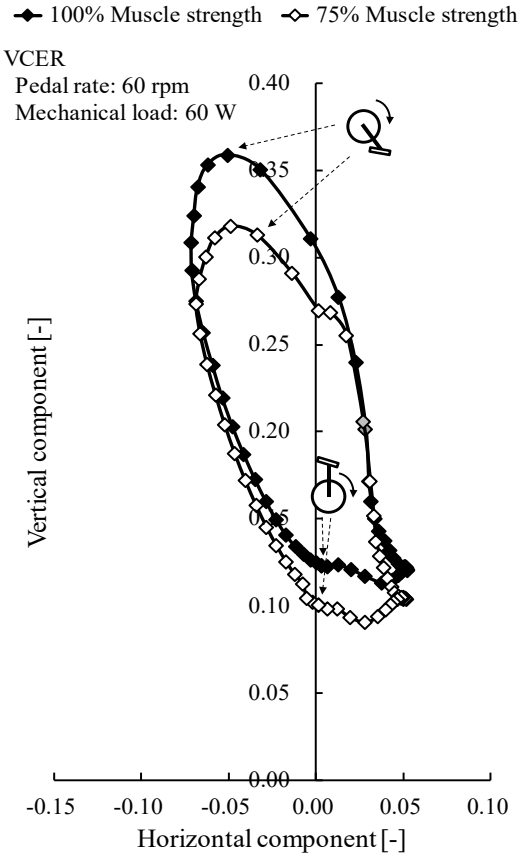

Figure 22. Comparison of pedal reaction forces between 100% muscle strength (filled symbols) and 75% muscle strength (unfilled symbols) of volitional conventional ergometer (VCER) exercise at 1 g, a pedal rate of 60 rpm and mechanical load of 60 W. Joint reaction force is shown in horizontal and vertical components, normalized by body weight. Gray symbol, lowest pedal position.

The resultant pedal reaction force at 0 g was lower than that at 1 g (Figure 11). The effective force during VCER exercise with a pedal rate of 60 rpm and a mechanical load of 60 W was less at 0 g than at 1 g (Figure 12). The effective and resultant forces at 0 g will be decreased by compensatory actions of the loss of function due to zero gravity to maintain a specific pedal rate against an external mechanical load. Activated muscles in the leg at 0 g (Figure 13) are associated with such compensation. Effective and resultant forces decreased when elderly persons pedaled on the ground at 1 g compared with younger persons under the same cycling conditions [24]. Knee joint reaction

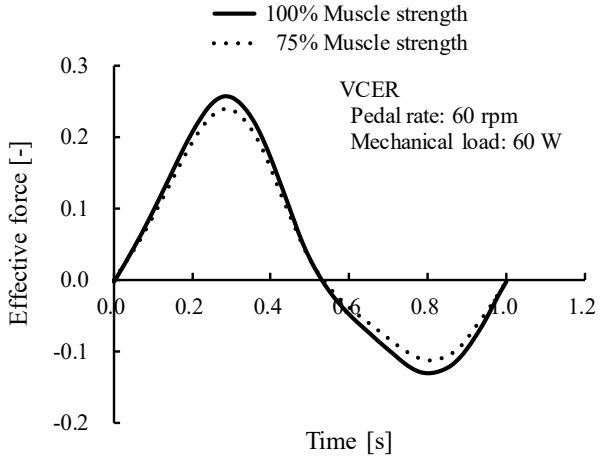

Figure 23. Comparison of effective force between 100% muscle strength (solid line) and 75% muscle strength (dotted line) of volitional conventional ergometer (VCER) exercise at 1 g, a pedal rate of 60 rpm and mechanical load of 60 W. Joint reaction force normalized by body weight is shown in horizontal and vertical components.

forces in elderly individuals (n = 9; age, 62–76 years) during ergometer cycling 15 months after TKR were measured [2]. Simulated VCER exercise at 1 g with leg muscles weakened to mimic elderly persons after TKR agreed with their experimental findings (Figure 5). Moreover, we confirmed the same decreasing trend in the kinetics of pedal reaction force in VCER exercise at 1 g with weakened muscles of the leg (Figures 22 and 23). Comparisons between experimental and simulation results can indicate different compensatory actions between VCER with full muscle strength at 0 g and reduced muscle strength at 1 g.

From the perspective of physical adaptation, it is interesting that decreases in the magnitude of effective and resultant forces showed an identical trend during ergometer cycling by elderly persons at 1 g and healthy persons at 0 g. A loss of function in external factors such as a weightless environment should be compensated to realize the same motion on the Earth. The internal factor of weakened muscles will require elderly persons to choose different compensation methods, such as muscle coactivation [25].

A compressive load along the bone axis coupled with some high-force impulsive loading is generally required to maintain bone health. The following effects of repetitions per day for six weeks using an identical load on the ulna of mature turkeys were indicated [26]: a minimal number of repetitions is required to prevent bone loss, a greater number of repetitions is required to gradually increase bone formation, and even with an increase in the number of repetitions, there is a specific number of repetitions that shows no significant difference in bone formation. From a response relationship between peak strain magnitude and changes in ulnar bone mass in mature turkeys, the minimal effective strain to prevent bone loss was identified [27]. The effects of disuse, adaptation, mild overload and pathological overload on the strength of load-bearing bones were associated with the magnitude of strain [28]. The effects of both the number of repetitions and of the magnitude of joint reaction forces caused by muscle contraction force, external force, and virtual gravity on body elements must be considered under microgravity and hypogravity.

Astronauts are at high risk for bone fracture, especially during exposure to the stresses of re-entry into the atmosphere of the Earth after a long period of weightlessness [3]. Ergometer exercise can reduce the load imposed by gravitational force on the leg joints with a metabolic cost comparable to that of walking on the Earth [2]. This type of exercise is beneficial for persons with knee osteoarthritis and elderly individuals planning to engage in cardiovascular training but not for persons who are exposed to long periods of weightlessness. Fortunately, the HTS is compact, and should become a useful countermeasure to induce coactivated muscle activity during ergometer exercise. It allows repeated high loading on bones during long-term weightlessness (Figures 15, 17 and 20), which will elicit adaptive bone remodeling.

The great trochanter becomes highly deconditioned during long space flights [29]. Young males have undergone unilateral lower leg suspension (ULLS) for four weeks in a model of a weightless environment [30,31]. We conducted a ULLS experiment that included a healthy man with one foot completely weight-free, and a ULLS+HTS experiment involving four healthy men. The HTS electrical stimulation was applied to the quadriceps and hamstrings for 16 min three times a week while seated. Deconditioning of the hip at the femoral neck and greater trochanter was prevented. We confirmed the activities of the abductor, gluteus medius and minimus muscles attached to the greater trochanter using electromyography. Muscle activities of the gluteus medius and minimus muscles were simulated at 0 g and 1 g during VCER exercise (Figure 13), which elicited more activity of the vastus lateralis and rectus femoris of the knee extensor at 0 g than at 1 g, whereas the activity of the hip abductor at 0 g considerably decreased. Applying HTS stimulation to the quadriceps and the hamstring at intensities of 10% and 20%, respectively, recovered mean muscle forces induced by the gluteus minimus and medius 4.5- and 2.5-fold, respectively, compared with the absence of HTS stimulation at 0 g. Much larger loading will improve the reduced mineral density of the greater trochanter at 0 g.

Centrifugal acceleration is a physical phenomenon that might serve as an alternative to gravitational acceleration, and it is referred to as artificial gravity. Because the primary factor affecting physical deconditioning during spaceflight is the loss of gravitational loading and stimulation, the most effective physical countermeasure would be to introduce gravity [3]. Thus, artificial gravity generated by centrifugal acceleration has been studied. However, joint reaction forces in a rotating human-ergometer have not been analyzed from the viewpoint of preventing bone loss and reduced muscle strength. We examined oxygen uptake and joint reaction forces with altered rotational motion of the RER model while cycling at a pedal rate of 60 rpm and a mechanical load of 60 W (Figure 18). The resultant force on each vertebral body (Figure 19) at a rotating velocity > 360 deg/s was close to the results of walking on a level surface at 1 g [21], independently of the effects of HTS stimulation of the leg muscle. The eccentric force of the soleus at higher artificial gravity far exceeded the lower boundary force of the soleus induced by the HTS. The HTS affected the level of reaction forces at all leg joints whereas artificial gravity did not affect those at the knee and hip joints (Figure 20). Stimulation of the ankle joint increased oxygen uptake during HCER exercise at 1 g (Figure 7) as well as reaction force on the ankle joint (Figure 20). Intensive contractions of the gastrocnemius and the soleus muscles induced by the HTS will prevent the loss of bone density in the calcaneus.

An optimal method enabled the determination from conflicting characteristics, of the pedal rate and mechanical load during ergometer cycling that generates exercise intensity and loads on leg joints equivalent to those extant during daily physical activities on the Earth. Optimal cycling conditions were simulated to generate specific values for oxygen uptake and knee joint reaction force at 0 g under the constraints of using specific values for oxygen uptake as an index of aerobic and resistive exercise intensity, and of the knee-joint reaction force required to maintain bone mass and strength. The validity of the cycling exercise model with the HTS for oxygen uptake at 1 g was shown by comparisons between simulated and experimental results (Figure 7). The simulated optimal cycling conditions showed that muscle co-contraction during the HTS cycling under microgravity, which decreases both the pedal rate and mechanical load on the ergometer pedal (Table 1), can offer a strategy to decide the most effective training conditions derived from various combinations. This is an advantage for the operational demands of space vehicles

or isolated bases located far from the Earth to maintain human health with time constraints and minimal environmental disruption.

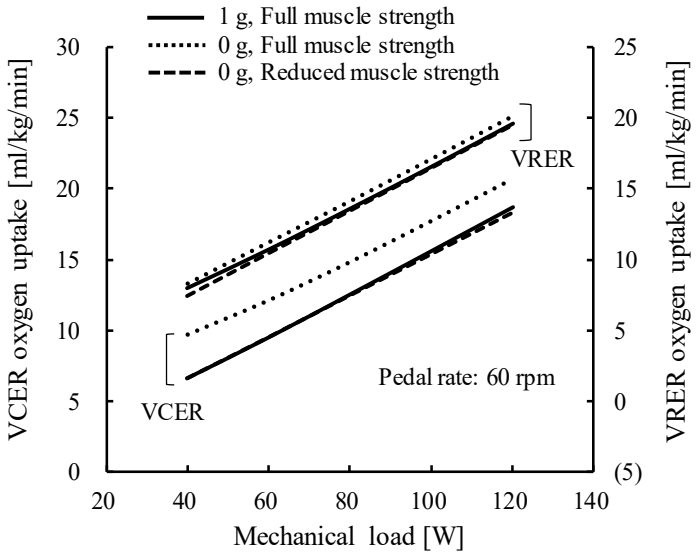

Figure 24. Comparison of oxygen uptake at 1 g and 0 g between volitional conventional ergometer (VCER) and volitional recumbent ergometer (VRER) exercise at full and reduced muscle strengths under different mechanical loads. Representative deconditioning in simulation with reduced muscle strength was assumed for muscles opposing gravity effects, and the muscle recruitment criterion was changed for the decrease in oxygen uptake. Pedal rate, 60 rpm.

Less oxygen is uptaken under experimental microgravity than on the Earth [20], which reflects lower metabolic internal power. The experiment was repeated during a 180-day flight aboard the Mir station. Long-term exposure to weightlessness resulted in physiological deconditioning, and crews underwent repeated measurements under deconditioning. The oxygen uptake in Figure 9 was simulated under a healthy physical condition. To compare with the experiment under long-term exposure to microgravity, weakened muscle was assumed in the VCER and VRER models as follows.

An oxygen uptake of 40 ml/kg/min in the simulation is approximately 84% of the mean maximal oxygen uptake in healthy adult males (age, 20-31 years) during ergometer exercise at 1 g [33]. Having 3-fold body weight in the simulated and desired reaction forces at the knee joint and the simulated reaction forces at the hip joint approximates the measured maximum magnitude of resultant forces at the knee joint during level walking in vivo at 1 g [34,35] and at the hip joint [35,36], respectively.

6. Conclusions

The validity of the ergometer exercise models was proven by comparisons with experimental findings. Model analysis provided perspectives even with widely varying parameters and altered exercise conditions. The HTS principle with exercise predicted an effective countermeasure to prevent deconditioning during lengthy exposure to microgravity. This approach will support future travel to Mars and will offer a benefit against hypogravity on the surfaces of the Moon and Mars. An optimal method could provide a better alternative to prevent deconditioning considering exercise intensity and loads on joints induced by daily activities at 1 g and operational demands in isolated equipment and facilities located far from the Earth.

This simulation was limited by the fixed leg angles and oxygen uptake, even under altered conditions of cycling and gravity. Leg angles during closed kinematic exercise such as cycling on an ergometer change according to age [24] and pedal rate [37]. The entire body including the cardiovascular and pulmonary systems undergoes deconditioning in microgravity [3], which alters the muscle fiber component ratio [38]. Open kinematic exercise such as knee and ankle joint flexion and extension does not require an ergometer or coordination between both legs during cycling. This exercise combined with the HTS will be simulated to confirm the amount of oxygen uptake and joint reaction forces. Changes in the ratio of the number of fast- to slow-twitch muscle fibers that are associated with oxygen uptake ability will be confirmed using the AMS, because these ratios increase under microgravity [38].

Conflict of Interest

The authors declare no conflict of interest.

Acknowledgments

This work was supported by JSPS KAKENHI Grant Numbers JP26506014, JP265006025.

References

[1] Y. Tagawa, N. Yamamoto, M. Omoto, H. Matsuse, and N. Shiba, "Simulation of Oxygen Uptake and Leg Joint Reaction Force During Ergometer Exercise Under Altered Gravity," in 39th Annual International Conference of IEEE EMBC, Jeju Island, Korea, 2017. DOI: 10.1109/EMBC.2017.8037219.

[2] I. Kutzner, B. Heinlein, F. Graichen, A. Rohlmann, A.M.Halder, A. Beier, and G. Gergmann, "Loading of the knee joint during ergometer cycling: telemetric in vivo data," J. Orthop. Sports Phys. Ther., **42**(12), 1032-1038, 2012. DOI: 10.2519/jospt.2012.4001

[3] G. Clement and A. Bukley (Editors), Artificial Gravity, Microcosm Press and Springer, 2007.

[4] T. Yanagi, N. Shiba, T. Maeda, K. Iwasa, Y. Umezu, Y. Tagawa, S. Matsuo, T. Yamamoto, K. Nagata, and J.R. Basford, "Agonist contractions against electrically stimulated antagonists," Arch. Phys. Med. Rehabil., **84**(6), 843-848, 2003. DOI: 10.1016/S0003-9993(02)04948-1

[5] N. Shiba, H. Matsuse, Y. Takano, K. Yoshimitsu, M. Omoto, R. Hashida, Y. Tagawa, T. Inada, S. Yamada, and H. Ohshima, "Electrically stimulated antagonist muscle contraction increased muscle mass and bone mineral density of one astronaut - Initial verification on the International Space Station," PLoS One, **10**(8), 14 pages, 2015. DOI: 10.1371/journal.pone.0134736

[6] T. Weber, A.A. Al-Munajjed, G.J. Verkerke, S. Dendorfer, and T. Renkawitz, "Influence of minimally invasive total hip replacement on hip reaction forces and their orientations," J. Orthop. Res., **32**(12), 1680-1687, 2014. DOI: 10.1002/jor.22710

[7] Under Interface Features, Lesson 2-4, The AnyBody Modeling System version 6.0.6, AnyBody Tutorials, 2016.

[8] E.T. Howley and B.D. Franks, Health Fitness Instructor's Handbook, Human Kinetics, 1997.

[9] J. Rasmussen, M. Damsgaard, and M. Voight, "Muscle recruitment by the min/max criterion –a comparative numerical study," J. Biomech., 34(3), 409-415, 2001. DOI: 10.1016/S0021-9290(00)00191-3

[10] M. Damsgaard, J. Rasmussen, S. T. Christensen, E. Surma, and M. de Zee, "Analysis of musculosketetal systems in the AnyBody Modeling System," Simul. Model Pract. Th., **14**(8), 1100-1111, 2006. DOI: 10.1016/j.simpat.2006.09.001

[11] M.L. Ohlsson and M. Gulliksson, "Least squares approach to inverse problems in musculoskeletal biomechanics," Technical report, Mid Sweden University, 10 pages, 2009.

[12] M. Omoto, H. Matsuse, Y. Takano, S. Yamada, H. Ohshima, Y. Tagawa, and N. Shiba, "Oxygen uptake during aerobic cycling exercise simultaneously combined with neuromuscular electrical stimulation of antagonist," J. Nov. Physiother., **3**(6), 185-191, 2013. DOI: 10.4172/2165-7025.1000185

[13] M. Tokui, "Analysis of the muscular mechanical efficiency focused on internal and external power," Ph.D Thesis, Kyushu Institute of Technology, 2008, (in Japanese).

[14] J.J. Seabury, A.C. Adams, and M.R. Ramey, "Influence of pedaling rate and power output on energy expenditure during bicycle ergometry," Ergonomics, **20**(5), 491-498, 1977. DOI: 10.1080/00140137708931658

[15] H.I. Griffiths, "Comparison of energy expenditure among three different cycling positions," Graduate Student These, Dissertations, & Professional Papers, University of Montana, 1989.

[16] Y. Tagawa and N. Yamamoto, "For improvement of motor function by surface electrical stimulation," Special Issue, J. Inst. Elect. Engnr. Jpn., **136** (19), 666-669, 2016, (in Japanese).

[17] T. Watanabe, Y. Tagawa, E. Nagasue, and N. Shiba, "Surface electrical stimulation to realize task oriented hand motion," in 31st Annual International Conference of the IEEE EMBS, Minneapolis, Minnesota, USA, 2009. DOI: 10.1109/IEMBS.2009.5333812

[18] T. Watanabe, Y. Tagawa, and N. Shiba, "Mapping method using a super multi-electrical stimulation device," in 15th IFESS Annual Conference, Vienna, Austria, 2010.

[19] M. Gobbo, N.A. Maffiuletti, C. Orizio, and M.A. Minetto, "Muscle motor point identification is essential for optimizing neuromuscular electrical stimulation use," J. NeuroEng. Rehabili., **11**(6), 6 pages, 2014. DOI: 10.1186/1743-0003-11-17

[20] M. Girardis, D. Linnarsson, C. Moia, D.R. Pendergast, and G. Ferretti, "Oxygen cost of dynamic leg exercise on a cycle ergometer: effects of gravity acceleration," Acta Physiol. Scand., **166**(3), 239-246, 1999. DOI: 10.1046/j.1365-201x.1999.00564.x

[21] A. Rohlmann, M. Dreischarf, T. Zandr, F. Graichen, and G. Bergmann, "Loads on a vertebral body replacement during locomotion measured in vivo," Gait & Posture, **39**(2), 750-755, 2014. DOI: 10.1016/j.gaitpost.2013.10.010

[22] S. Dendorfer and S. Torholm, "Harness – walking in microgravity," Final Report on Feasibility Study, Report no: 21385/08/NL/PA, AnyBody Technology A/S, 20-24, 2008.

[23] G.A. Dudley, P.A. Tesch, B.J. Miller, and P. Buchanan, "Importance of eccentric actions in performance adaptations to resistance training," Aviat. Space Environ. Med., **62**(6), 543-550, 1991.

[24] J.W. Seo, D.H. Kim, S.T. Yang, D.W. Kang, J.S. Choh, and G.R. Tack, "Comparison of joint kinematics and pedaling force in the young and the elderly," J. Phys. Ther. Sci., **28**(8), 2245-2248, 2016. DOI: 10.1589/jpts.28.2245

[25] Y. Tagawa, Y. Ogata, and N. Yamamoto, "Simulation of muscle activity during cycling with full and reduced muscle strengths of the leg," in 39th Annual International Conference of IEEE EMBC, Poster, Jeju Island, Korea, 2017.

[26] C.T. Rubin and L.E. Lanyon, "Regulation of bone formation by applied dynamic loads," J. Bone Joint Surg., **66-A**(3), 397-402, 1984.

[27] C.T. Rubin and L.E. Lanyon, "Regulation of bone mass by mechanical strain magnitude," Calcif. Tissue Int., **37**(4), 411-417, 1985.

[28] H.M. Frost, "A 2003 update of bone physiology and wolff's law for clinicians," Angle Orthod., **74**(1), pp.3-15, 2004. DOI: 10.1043/0003-3219(2004)074<0003:AUOBPA>2.0.CO;2

[29] M.R. Barratt and S.L. Pool (Editors), Principle of Clinical Medicine for Space Flight, Springer, 2008.

[30] T. Ito, Y. Tagawa, S. Tanaka, N. Shiba, Y. Umezu, T. Yamamoto, and J.R. Basford, "Development of practical and effective hybrid exercise for use in weightless environment," in 26th Annual International Conference of the IEEE EMBS, San Francisco, USA, 2004. DOI: 10.1109/IEMBS.2004.1404185

[31] R. Takeuchi, Y. Tagawa, T. Inada, K. Suetsugu, K. Mimura, and N. Shiba, "A countermeasure for preventing atrophy of musculoskeletal system under microgravity," in SICE-ICCAS 2006 SICE-ICASE International Joint Conference, Busan, Korea, 2006. DOI: 10.1109/SICE.2006.315451

[32] M. Praagman, E.K.J. Chawick, F.C.T. van der Helm, and H.E.J. Veeger, "The relationship between two different mechanical cost functions and muscle oxygen consumption," J. Biomech., **39**(4), 758-765, 2006. DOI: 10.1016/j.jbiomech.2004.11.034

[33] T. Matsuo, K. Ohkawara, S. Seino, N. Shimojo, S. Yamada, H. Ohshima, K. Tanaka, and C. Mukai, "An exercise protocol designed to control energy expenditure for long-term space missions," Aviat. Space Environ. Med., **83**(8), 783-789, 2012. DOI: 10.3357/ASEM.3298.2012

[34] I. Kutzner, B. Heinlein, F. Graichen, A. Bender, A. Rohlmann, A. Halder, A. Beier, and G. Bergmann, "Loading of the knee joint during activities of daily measured in vivo in five subjects," J. Biomech., 43(11), 2164-2173, 2010. DOI: 10.1016/j.jbiomech.2010.03.046

[35] P. Damm, I. Kutzner, G. Bergmann, A. Rohlmann, and H. Schmidt, "Comparison of in vivo measured loads in knee, hip and spinal implants during level walking," J. Biomech., **51**, 128-132, 2017. DOI: 10.1016/j.jbiomech.2016.11.060

[36] G. Bergmann, A. Bender, J. Dymke, G. Duda, and P. Damm, "Standardized loads acting in hip implants," PloS One, **11**(5), 23 pages, 2016. DOI: 10.1371/journal.pone.0155612

[37] R.R. Bini, M. Rossato, F. Diefenthaeler, F.P. Carpes, D.C. dos Reis, and A.R.P. Moro, "Pedaling cadence effects on joint mechanical work during cycling," Isokinet. Exerc. Sci., **18**(1), 7-13, 2010. DOI: 10.3233/IES-2010-0361

[38] V.R. Edgerton, M.Y. Zhou, Y. Ohira, H. Klitgaard, B. Jiang, G. Bell, B. Harris, B. Saltin, P.D. Gollnick, R.R. Roy, M.K. Day, and M. Greenisen, "Human fiber size and enzymatic properties after 5 and 11 days of spaceflight," J. Appl. Physiol., **78**(5), 1733-1739, 1995. DOI: 10.1152/jappl.1995.78.5.1733

ASTES

Advances in Science, Technology and Engineering Systems Journal Vol. 3, No. 4, 21-25 (2018)

www.astesj.com

Special Issue on Multidisciplinary Sciences and Engineering

ASTESJ

ISSN: 2415-6698

Scientific Principles behind 2017 World Universiade of Safety Lantern and Torch

Wei Long Chen, Fang Lin Chao*

Department of Industrial Design Chaoyang University of Technology,436, Taiwan R.O.C

ARTICLE INFO

Article history:
Received: 11 May, 2018
Accepted: 12 June, 2018
Online: 02 July, 2018

Keywords:
Scientific principles
Safety lantern
Torch
Convection

ABSTRACT

The torch relay for the 2017 Taipei Summer Universiade started June. The innovative torch design was altered and tested, follow-up production successfully. For preventing weather effect, the head of the torch embedded with a unique airflow structure that allowed the sacred flame to pass the wind and rain tests. The safety lantern displays a 3D spiral flash. Safety lantern uses biofuel so that the mother flame can transport by air. The scientific principles are Stack effect, Coanda effect, Bernoulli's principle, and Capillary phenomenon. Product design refers to principles and a series of work from the specifications to determine the product structure. Cross-discipline collaboration is needed to increase the integrity.

1. Introduction

The torch relay for the 2017 Taipei Summer Universiade started June 20 in the Italian city of Turin [1], "with a vision to shape the leaders of tomorrow through their experiences of international student sport." It was then passed by Professor Gianmaria Ajani, the rector of the University of Turin, to Matytsin. He then transferred the flame to the Taipei 2017 Torch, which was held by Ko Wen-je, the Mayor of Taipei (Figure 1). The domestic leg of the Torch Relay took the flame and visited 22 cities and counties.

The unique design developed by cooperation of both designers and engineers. The torch design included Taiwan's essential design elements and craft skills. With the collaboration of scientist and designer, the concept was revised and tested, follow-up production successfully [2]. For preventing weather's affection, the head of the torch embedded with a unique airflow structure that allowed the sacred flame to pass the wind and rain tests. The safety lantern displays a single three-dimensional spiral flash (Figure 2).

Safety lantern have several vertical vanes, each vane has a section encircled by the concealing member defining a flow accelerating zone. External air flows into the flow diverting mechanism through the air intake ports, circumferentially conceals with the wall.

Figure 2 also shows the concept of torch design comes from Confucian's article "Gentlemanly fair play." The Master said, "Supportive, encouraging, congenial – such a man may be called a gentleman." Fair play induces supportive and encouraging with a player, congenial with friends.

The torch is made of metal, on which there are an array of ventilating holes. The lower holding portion made of weaving bamboo comes from eastern civilization.

The safety lantern keeps the mother flame continuously so that the fire can pass through the different location. The design includes a safety feature to avoid accidental burning if the fuel leaks out. There is no CO generated during combustion, so the safety lantern can transport using commercial air traffic.

Figure 1. Torch used in 2017 Taipei Summer Universiade [2]

*Corresponding Author: Fang Lin CHAO, Email: flin@cyut.edu.tw

Figure 2. The concept of torch design comes from Confucian [2], design team: H.L Chang of Ui-D Taiwan. The safety lantern keeps the mother flame continuously, the torch table presenting the flash at the main venue of the sports competition, and the relay torch. The height of safety lantern and torch are 50 cm and 70cm.

2. Scientific Principles

The spiral frame of safety lantern is distinct and has a stable shape and an elongated height (Figure 2). Air driven by buoyancy goes upward and draws in fresh air through the passages which make air flowing therein rotate and go upward.

For the torch, after gas and air mixing process and is being ignited by the igniting needle, combustion flame flowing out from the top cap and fresh air drawn from the side holes for mixing. Gas and air mixture undergoes the mixing processes and flows out of the plurality of exit.

2.1. Stack effect

The safety lantern has a concentrated hot zone around and above the combustion head due to combustion flame and spiral flow around. Heated air with lower density in the heated region flows upward and creates low pressure to draw fresh air from intake port into the transparent shield, thereby increasing the height of flame in the torch. This phenomenon is known as stack effect or chimney effect.

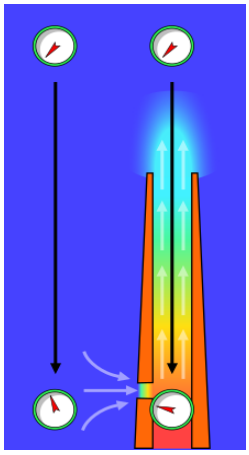

Figure 3. The safety lantern: stack effect [3] (gauges represent absolute air pressure, airflow indicates with grey arrows)

2.2. Coanda effect and centrifugal force effect

The passages direct fresh air toward the inner surface of a transparent shield at a specific angle to create a spiral air flow pattern and tangent to the inner surface of the shield. This feature dramatically helps to stabilize swirling air flow pattern due to Coanda effect and centrifugal force.

Coanda effect [4] related to the tendency of a fluid jet to stay attached to a convex surface. The pressure difference across the jet causes the jet to deviate towards the nearby surface Figure 4, and then to adhere to it. The separation angle is a function of the Reynolds number of the fluid.

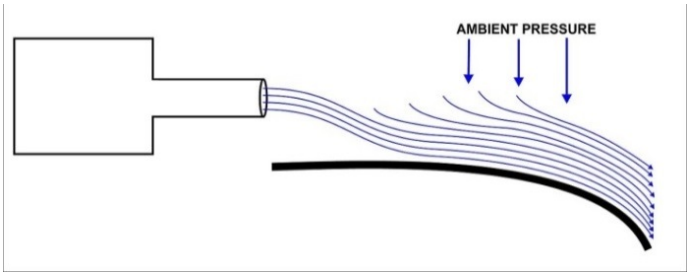

Figure 4. The jet will cling to the surface because any molecules of ambient air that move into the space between the jet and swept away, adhere to the surface even if it is curved [4].

The fluid stream attaches a contour when the flow is directed at a tangent to that surface. This spiral motion of air flow also induces centrifugal force. The safety lantern takes advantages of stack effect and Coanda effect which help to create a stable spiral and elongated flame. The centrifugal force is an inertial force directed away from the axis of rotation that appears to act on objects when viewed in a rotating reference axis [5]. In a rotating reference frame, objects appear to be under the influence of a radially outward force that is proportional to their mass, to the distance from the axis, and to the square of the angular velocity [4]. The detail of structure in the safety lantern shows in Figure 5.

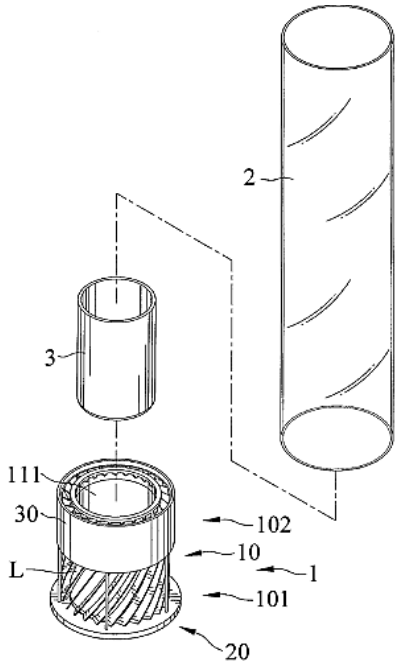

Figure 5. The safety lantern [7]: a perspective view of the flame device, where 1: assembly, 2: glass tube, 3: container, 20: basement, 30: cover guider, 10: passages, 101: inlet end, and 102: acceleration zone.

The safety lantern produces a swirling flame, and a stable fluid creates within the guided shield channels. Heated air in the shield creates buoyancy due to a difference in air density. The perspective view (Figure 5) showing the flame device producing a stable and prolonged flame in a steady fluid field. Undergoes convection directs air through the transparent glass shield (#2). Centrifugal forces also keep air moving spirally and drive air into the safety lantern.

2.3. Capillary phenomenon

The capillary phenomenon is the ability of a liquid to flow in narrow spaces in opposition to gravity [6]. The effect can find in the drawing up of water between the hairs of a paint-brush. If the diameter of the tube is sufficiently small, then the combination of surface tension and adhesive forces dominate. The thinner the space in which the liquid can travel, the further up it goes. In torch design, we choose liquid transparency "biofuel" as fuel.

The capillary phenomenon presents while the biofuel's viscosity is low. This property allows the fuel transport from the fuel tank to the upper ignition area. When fuel is filled into the body below the wick, the wick can volatilize fuel for combustion. The cord placed in the holding space and the two jaws can hold the wick so that the wick's head end located in the burn area [7]. The user can turn to adjust the elastic, change the clamping gap when clamping the cord will be compressed. Adjust the speed at which the wick draws fuel, thus controlling the size of the combustion flame. The Use of metal mash wick also removes the disadvantage of waste and burn out of traditional cotton thread core.

2.4. Bernoulli's principle

Bernoulli's principle states that an increase in the speed of fluid co-occurs with a decrease in pressure. Bernoulli's equation is sometimes valid for the flow of gases: provided that there is no transfer of kinetic or potential energy from the gas flow to the compression or expansion of the gas. Bernoulli equation applies to incompressible fluids, and steady compressible fluids up to approximately Mach number 0.3 [8]. There are many applications in surrounding life, such as an injector on a steam locomotive. The pitot tube is used to determine the airspeed. The flow speed of fluid can also be measured using the Venturi meter [9]. The pressure in the reduced diameter region decreases and display in the meter by liquid height difference.

The main body of the torch is an aluminum metal rod. The hollow metal tube contains the gas supply lines. The high-pressure gas is conveyed upward by a metal pipe from a fuel tank in below. The upper section has an enlarged gas mixing zone. At the top of the gas mixing zone is the metal flame exit cover. The high-pressure gas gradually spreads to the top metal cover of the torch. As shown in Figure 6, the central hole on the metal cover is the exit of the main flame. There are four big holes next to it, which is the side flame exit. When the gas in the torch ejectes at high speed, the pressure in the central area becomes smaller; therefore, the external air will flow from the side of the leaf-shaped opening into the mixed gas area (Figure 7). When the outside air enters the mixed gas zone, it can also cool the aluminum rod; it avoids the chance of being exposed to the outside of the torch.

The surrounding metal shell wrapped on the outside of the aluminum metal tube. The hand grip is under the metal shell, and the grip is a structure woven with bamboo. Burning the flame increases the temperature of the aluminum metal tube. There is an air layer between them (Figure 7), the thermal conductivity of the air is very low which reduced the amount of heat transfer between internal pipe and the periphery. When cold air enters from the intake holes, it also cools the metal pipes at the same time.

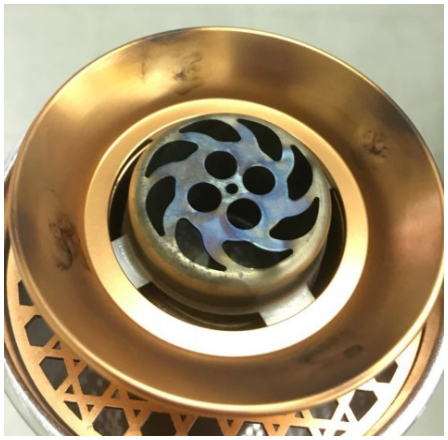

Figure 6. The metal cover on top of the torch: The central hole is the exit of the main flame. There is four side flame exit. The outer leaf-shaped opening is air inlet of the mixing zone.

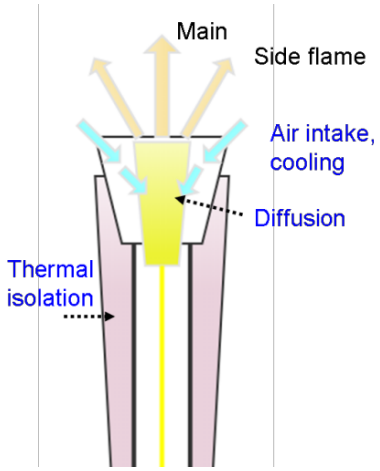

Figure 7. Torch: External airflow driven by Bernoulli's principle, where the gas ejects and spreads (diffusion). The low pressure in the central area causes the external air enters the air intake holes into the mixing zone. The air between the aluminum rod and surrounding metal decoration also provide thermal isolation.

3. Experimental Evaluation

In the previous chapter, we discussed the scientific principles behind the design of the torch. In this chapter, we utilize two prototypes and perform functional tests. The purpose of the experiment is verifying the benefits of the above scientific principles in design. The prototype of the product is one-to-one scale and tested according to the conditions of use. In addition to the shape of the flame, we also care about the safety of the user, and we hope to appropriately lower the temperature of the product in areas that may be in contact with user's body.

3.1. Safety Lantern

Figure 8 indicates the evaluation of the experimental prototype. We observed safety lantern with spiral shape and an elongated height. As the air is heated, it rises along the guide channel, and the airflow is a steady laminar flow. Because of the Coanda effect, the airflow is attached to the inner wall of the glass and rotates upwards. As the stack effect and centrifugal force continue to rise

upward, a stable flash formed in the lower half zone. After passing through the middle area, transition and turbulent zone take place, and the shape of the flame is irregular.

The combination of the mentioned effects can substantially elongate the height of flame and change the swirling speed of flash according to flame visualization required. If the flame guiding member is absent, it is difficult to control a smooth flow. The flame guiding member allowed controlling natural convection and drawn fresh air from outside the chamber. The flame guiding member of 44-degree skew angle shows a reasonable display quality (Figure 8). When cold air is introduced, it also cools the metal and glass tube. The temperature measurement of aluminum castings and iron plate indicated the contact temperature is not higher than 60 degrees C.

Figure 8. Evaluation of experimental prototype. There are three flame zones; laminar zone (lower), transition zone (middle), and turbulent zone (upper).

3.2. Torch

There are five flame outlets above the fire exit, which scatter at different angles respectively to show the flame shown in Figure 9 and 1. The runner at the fuel outlet must be balanced so that the flame maintains a similar height in all directions. It successfully demonstrated the five lights which symbolizing the Olympic Games.

Figure 9. The flow diverting mechanism design of the torch

At the previous trial, the torch flame that burns on mixing gas from first mixing process undergoes convection directly with air, thereby creating a more significant portion of colorless and transparent flame, causing a less visible swirling pattern and shorter in flame height. We will expand the gas mixing area at the gas outlet, let the gas mix and send it out from the top hole. After gas and air mixed in the chamber, the torch shows a reasonable display quality.

4. Cross-discipline Collaboration

Although scientific principles are well known, designer seldom can integrate. Product design refers to a series of work from the specifications to determine the product structure. The designer must take into account the form, technology, and regulations, through the appropriate product form to reveal differentiated value.

4.1. Integration

We experienced cross-discipline collaboration is vital to torch design. It covers material, combustion, fluid dynamics, heat transfer, usability, and aesthetics. One of successful field practice project is EU-IDES-EDU: "Master and Post-Graduate education and training in multi-disciplinary teams." In [10], describes the necessity of more integrated and cross-disciplinary approaches to building design. The challenges encountered during implementation of the design education across different professions were discussed. The Integrated Design Process (IDP) was developed to streamline the design process of solar integrated low-energy buildings. The involvement of engineers in early stage improved design significantly.

We also experienced idea jumping iteratively through the stimulus of CAE simulation and prototype experiment during torch design. In [11] authors present "speculative design as a means to technological fluency." Speculate means form a theory or conjecture about a subject without firm evidence. Creativity's natural imply explore and discover a new connection between facts or knowledge. Firm evidence is only a stepping stone to problem-solving. Technological fluency is a term used to describe a level of expertise: the capability to understand, use, and assess technology beyond its rote application. By using a Speculative Design approach to extend the idea of technological fluency in new directions, broadening understandings of the development of technology and adding a dimension of criticality [12].

Design often plays a central role in technology fluency programs. The design process typically derived from engineering approach in which functional requirements drive the process toward the solution. Speculative design project involves the construction of prototypes. The education of the designer's technological imagination consists in learning how to use tools, expression, techniques for rapid prototyping, processes of iterative experimentation, and skills in social negotiation and integration [12].

Cross-disciplinary and integrative are significant attributes of technological fluency in speculative design projects. Pressures internal and external to engineering courses for the adoption of multidisciplinary team-based work are discussed. Some key factors arising from the survey are addressed [13].

4.2. The design process and CAE

The critical elements of renovation in torch design are related to cross-discipline and knowledge. As shown in Figure 10, the design guide help prevent mistake arrangements. CAD/ CAE are used to realize the idea quickly.

There are many engineering issues in torch design; such as heat transfer, fluid dynamic, mechanical stress and other physical principles. The flow field simulation enables fine tune of geometric design. Functional test proof and confirm the product features, through a series of measurements such as thermal energy, flame height, contact temperature (glass and metal). After that, the checklist and regulations were reviewed to enable the modified concepts.

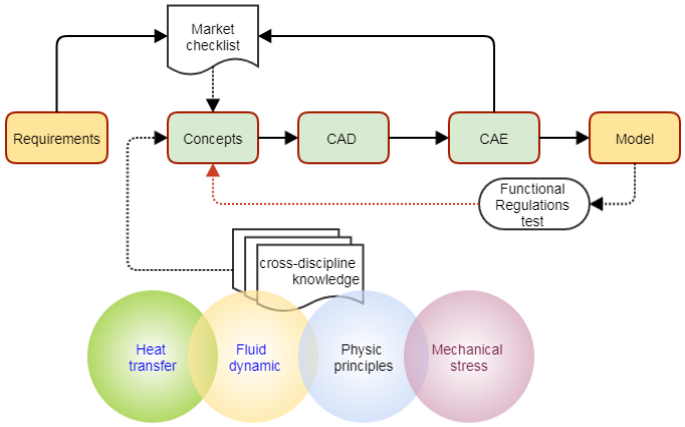

Figure 10. Design process

We built the digital model with CATIA. As shown in Figure 10, the prototype model can utilize for measuring actual physical parameters. Comparing the measured data and simulation results, we refine the CAE models. When the settings are confirmed, the designer can use the digital model to obtain design parameters. After that, a functional test proof and validate the product features. The cross-discipline knowledge help prevent contradiction design. The CAE is used to verify the idea quickly and shortens development cycle time.

The role of a designer is changing according to the evolutional technology and society. From the torch project, product renovation needs to cooperate with others expertise closely. Understanding the relevant principles in the product can lead to support through cross-domain collaboration.

5. Conclusions

In this article, we discussed the scientific principles within the torch and safety lantern with spiral shape and an elongated height; namely Stack effect, Coanda effect, Bernoulli's principle, and Capillary phenomenon. After gas and air mixing process and is being ignited, combustion flame flowing out from the grooves and fresh air drawn from the passages mix. Air in the shield driven by buoyancy goes upward and brings in fresh air through the passages which make air flowing therein rotate and go uphill.

The process of design also provided. We employee qualitative and CAE design process to fulfills its primary and auxiliary functions. Design process helps understand combustion phenomenon and trend. Through the model test, designer and engineers can select proper parameters. Cross-discipline collaboration is needed to increase the integrity of the concept. Designers should experience the scientific principles to collaborate with other team members in cross-domain development.

Acknowledgments

We wish to thank design effort of Ui-D, and students in CAE Lab in Chaoyang University of Technology for supplying the testing and measurement. This research partially supported by the Pro-Iroda company with prototyping.

References

[1] https://www.insidethegames.biz/articles/1051799/taipei-2017-torch-relay-begins-in-turin

[2] https://udn.com/news/story/11406/2671767

[3] https://en.wikipedia.org/wiki/Stack_effect

[4] https://en.wikipedia.org/wiki/Coand%C4%83_effect

[5] https://en.wikipedia.org/wiki/Centrifugal_force

[6] https://en.wikipedia.org/wiki/Capillary_action#Phenomena_and_physics_of_capillary_action

[7] Chen, Wei-Long, and Jan-Nan Chen. "Device for producing stable and augmented flame." U.S. Patent 8,641,413, issued February 4, 2014. https://patents.google.com/patent/US8641413B2/en

[8] White, Frank M. Fluid Mechanics, 6th ed. McGraw-Hill International Edition. p. 602, 2017.

[9] Kamela, M., "Thinking about Bernoulli," The Physics Teacher, **45**(6), 379-381, 2007. https://doi.org/10.1119/1.2768700

[10] C., Brunsgaard, P. Dvořáková, A. Wyckmans, M. Laskari, "Integrated energy design–Education and training in cross-disciplinary teams implementing energy performance of buildings directive (EPBD)", Building and Environment, **72**, 1-14, 2014. https://doi.org/10.1016/j.buildenv.2013.10.011

[11] Lukens, Jonathan, and Carl DiSalvo. "Speculative design and technological fluency." International Journal of Learning and Media, **3**(4), 23-40, 2011. doi:10.1162/IJLM_a_00080

[12] Burdick, Anne, and Holly Willis. "Digital learning, digital scholarship and design thinking." Design Studies, **32**(6), 546-556, 2011. https://doi.org/10.1016/j.destud.2011.07.005

[13] Denton, H. G. (1997). Multidisciplinary team-based project work: planning factors. Design Studies, **18**(2), 155-170, 1997. https://doi.org/10.1016/S0142-694X(97)85458-0

ASTES

Advances in Science, Technology and Engineering Systems Journal
Vol. 3, No. 4, 26-32 (2018)
www.astesj.com
Special Issue on Multidisciplinary Sciences and Engineering

ASTES Journal
ISSN: 2415-6698

Stream Cipher by Reed-Solomon Codes

Tao Wu*[1,2], Ruomei Wang[1]

[1] *School of Data and Computer Science, Sun Yat-Sen University, Guangzhou 510006, P.R. China*

[2] *Shenzhen Research Institute of Sun Yat-Sen University, Shenzhen 518057, P.R. China*

ARTICLEINFO

Article history:
Received: 04 May, 2018
Accepted: 07 July, 2018
Online: 14 July, 2018

Keywords:
Stream cipher
Reed-Solomon code
Public-key cryptography

ABSTRACT

Stream cipher can be used in constrained environments to provide information security and reduce energy expense at data transmission. In this paper, it is shown that Reed-Solomon (RS) code can be used to implement stream cipher, which is widely used for error corrections of data in transmission and storages. The proposed stream cipher combine the keys with the messages, and conceals the cipher within the erroneous RS code. Then at the receiving part the cipher can be checked out by RS decoding, leaving the information unchanged. There are several advantages with this scheme: First, compared with the usual stream cipher including two engines, only one engine is required, making the synchronization of the stream cipher and messages easily. In the situation, the stream cipher and the messages are held as a whole while the alignment of stream cipher is not needed. Thus the usual power consumptions for synchronization and key generation at the receiving part can be saved. Second, the stream cipher increases the security level by adding the difficulty of decoding a random linear RS code, which stores the key streams like public key cryptography. Since the RS encoding and decoding modules are already included in many computer systems or devices, the new scheme may be implemented by reconfiguration rather than extra hardware units. Compared with generalized RS code for code-based public-key cryptography like McEliece system, it uses systematic encoding instead of nonsystematic encoding, which decreases the power overhead. Unlike the encryption by public keys and decryption by private keys of McEliece system, it encrypts messages by private keys from stream cipher and decrypts texts by public keys implemented in the RS decoder.

1 Introduction

Stream cipher by Reed-Solomon (RS) code this work intends to implement encryption by encoding if necessary [1]. As the encoding-encryption paradigm has been used in the standard for mobile telephony GSM [2, 3], it has received much attention so far. RS code has been widely used in communications and storage systems to correct errors, which can also be used together with BCH code to ensure data integrity [4]. The idea of using RS code as a carriage for stream cipher comes from the observation of RS code for code-based cryptography, where it is found that the errors are intentionally inserted and recovered with much computation and energy [5, 6]. In fact, the code-based peudo random generator and its security can be considered to achieve stream cipher [7]. In [8], the generalized RS code is used to reduces the density of a transform matrix and improves weakly secure data exchange.

Stream cipher belongs to symmetric cryptography and can be built by many devices, such as linear and nonlinear feedback shift registers. For example, the Rakaposhi stream cipher consists of a 128-bit nonlinear feedback shift register, a 192-bit dynamic linear feedback shift register, and a nonlinear filter function [9]. Ubiquitous environments demands security, speed and power consciousness in processing huge amount of multimedia data [10], in which stream cipher can be used. Stream cipher is an engine that generates bit streams to mix the message. At the sending part, the

*Tao Wu, Shenzhen Institute of Industry-University-Research, Sun Yat-Sen University, email: nstrch@outlook.com

https://dx.doi.org/10.25046/aj030404

plain text is confused with one bit stream, while at the receiving part, the cipher text is processed with the same bit stream again to recover the message. The stream cipher is like a determined peudo-random discrete function, of which the security can be analyzed by the generating mechanism of the cipher. A stream cipher can be marked by a key stream (K) and the initialization vector (IV), while the adversary may recover all the secret bits of K after observing many related (K, IV) pairs [9].

Usually, an one-way function and multiple steps are devised to safeguard the key generations or initialization processes, let bit XOR as the only operation to encrypt the message. By contrast, people also seek approaches to implement more secure code by public key cryptography. Code based cryptography [11] with Goppa codes [12] or MDPC codes [13], for example, can be applied to realize McEliece system . Meanwhile, generalized RS code can also be used to implement asymmetric cryptography [6], which brings out short keys compared with that obtained by Goppa code.

In this work, a stream cipher with RS code is proposed, in which the messages are encoded as RS codewords. This idea comes from its similarity to the configured logic with a DSP unit in FPGA. At the receiving part, the plaintexts and cipher are recovered from RS codes. The contributions of this paper include:

- a mechanism to include stream cipher in RS encoding and decoding, which is able to cover the message in a simple way.
- a review of related work about stream cipher of different schemes.
- a hardware implementation of stream cipher along by RS code.

The remaining parts of this paper is organized as follows: Sect. 2 is a review of RS encoding and decoding; Sect. 3 briefly introduces the related work with stream cipher and code-based cryptography; Sect. 4 discusses the stream cipher along with RS code; then the hardware implementation and comparison of the stream cipher are given in Sect. 5; the last section concludes this paper.

2 RS Code

RS code is widely used for error corrections. The encoding can be either implemented by polynomial division with shift registers, or it can be performed by multiplying the generating matrix [14]. Suppose the RS code is defined over $GF(2^m)$ with n code bits and k information bits. Message sequence $(u_{k-1}, \ldots, u_1, u_0)$ is equivalent to

$$u(X) = u_0 \cdot X^{k-1} + u_1 \cdot X^{k-2} + \cdots + u_{k-1}. \quad (1)$$

Let the parity check code be $(v_0, v_1, \ldots, v_{n-k-1})$, with $v(X) = X^{n-k}u(X) \mod g(X)$, then the code polynomial yields

$$c(X) = X^{n-k}u(X) + v_0 \cdot X^{n-k-1} + v_1 \cdot X^{n-k-2} + \cdots + v_{n-k-1}, \quad (2)$$

where $u(X) = \sum_{i=0}^{k-1} u_i \cdot X^{k-1-i}$, $n-k = 2t$, and t is the maximum number of error corrections. Then the encoded symbols will read $(v_{n-k-1}, \ldots, v_0, u_{k-1}, \ldots, u_0)$, with v_i and u_i being symbols in $GF(2^m)$.

Suppose the code generator is expressed as $g(X) = \prod_{i=1}^{2t}(X - \alpha^i) = g_0 + g_1 X + \cdots + g_{2t-1}X^{2t-1} + X^{2t}$. Then $g_0 = \prod_{i=1}^{2t} \alpha^i$, $g_1 = -\sum_{i=1}^{2t} \prod_{j \neq i}^{1 \leqslant j \leqslant 2t} \alpha^j$. For $2 \leqslant i \leqslant 2t-1$, the generator polynomial can be computed in Galois field recursively. In Matlab, the generator polynomial can be computed directly by function `rsgenpoly`.

Once the generator is calculated, the generator matrix can be obtained. Take $n = 255$, $k = 223$, $t = 16$, and $m = 8$, then the generating matrix can be computed in Matlab as follows:

```
n= 255;
k= 223;
t= 16;
m= 8;
tvc= zeros(1, 33);
tvc= [ 45  216  239  24  253  104  27 ...
       40  107  50  163  210  227  134 ...
       224  158  119  13  158  1  238 ...
       164  82  43  15  232  246  142 ...
       50  189  29  232  1];
gvc= gf(tvc, m);
dv= gf(zeros(k, n- k));
qv= gf(0, m);
gpc= fliplr(gvc);
 for i= 0: 1: k-1
     tmpv= gf([1, zeros(1, n- k+ i)], m);
     [Q, R]= deconv(tmpv, gpc);
     length1= length(R );
     indx= find(R~=gf(0, m), 1, 'first');
     dv(i+1, n- k- length1+ indx: n- k)
     = R(indx: length1);
 end
gtx= gf(zeros(k, n), m);
% gtx is the generating matrix
gtx(:, 1: n-k)= fliplr(dv);
gtx(:, n- k+ 1: n)= gf(eye(k, k), m);
```

The encoding of RS code can be computed as modular division in the polynomial field [14]. Let $b(X) = X^{n-k}u(X) \mod g(X)$, then $b(X) + X^{n-k}u(X)$ can be divided by $g(X)$ and become a RS code polynomial. The symbol u_0 with the lowest index is usually processed as the symbol with the highest weight for convenience.

The RS decoding is divided into four steps, i.e., syndrome computation, solution of error location polynomial, Chien search, and determination of the error values by Forney's algorithm. RS code is defined in the extension field $GF(2^{m \cdot s})$, and syndromes can be

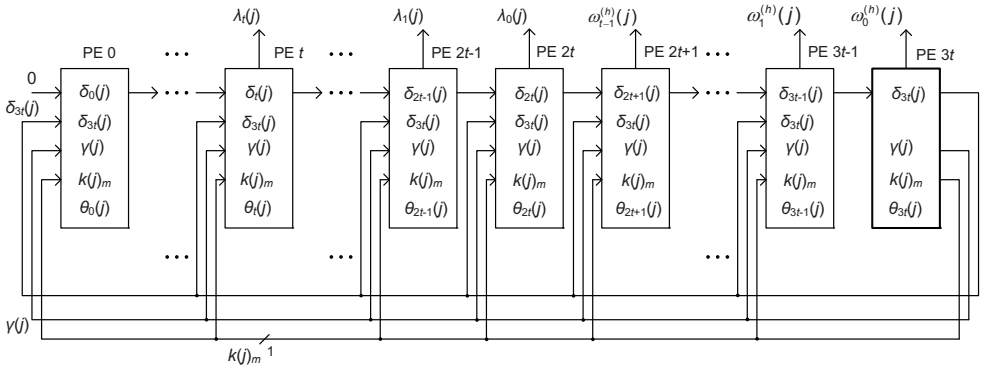

Figure 1: System architecture to solve error location polynomial [16, 1].

computed according to [15]:

$$S_i = r(\alpha^i) = \sum_{j=0}^{n-1} r_j \cdot \alpha^{i \cdot j}, \tag{3}$$

where $r_j \in GF(2^m)$, $1 \leqslant i \leqslant 2t$.

The error polynomial can be obtained by the improved inversion-less Berlekamp-Massey algorithm [16]. The resulting error polynomial reads

$$\sigma(X) = \sum_{i=0}^{e} \lambda_i X^i, \tag{4}$$

where $v \leqslant t$. λ_i is used to calculate the error locations. The error values are

$$\begin{aligned} Y_i &= \frac{z^{2t}\Omega^{(h)}(z)}{\sigma'(z)}\Big|_{z=X_i^{-1}}, \\ &= \frac{z^{2t} \cdot \sum_{i=0}^{e-1} \omega_i^{(h)} \cdot z^i}{\sum_{i=2k-1}^{k=1,\ldots,\lceil \frac{e}{2} \rceil} \lambda_i \cdot z^{i-1}}\Big|_{z=X_i^{-1}}, \end{aligned} \tag{5}$$

where $\Omega^{(h)}(z) = \sum_{i=0}^{e-1} \omega_i^{(h)}(z) \cdot z^i$, the symbol h denotes the higher partial products from z^{2t} to z^{2t+e-1}, and e is the number of error locations.

The system architecture of RS decoding [16, 1] is shown in Fig. 2. First, the original passages through processing elements are replaced by direct connections of signals. Second, the control logics are totaly integrated into the last processing element for simplicity. The signal $k(j)_m$ is the sign bit of the integer $k(j)$, where m denotes the m-th bit. The coefficients from λ_t to λ_0 come out of from PE t to PE $2t$, while the coefficients from $\omega_{t-1}^{(h)}$ to $\omega_0^{(h)}$ are produced from PE $2t+1$ to PE $3t$.

Among the processing elements, there exists matrix products. Typically, the matrix multiplication $[\alpha^m, \alpha^{m+1}, \ldots, \alpha^{2m-2}]^T = Q \cdot [1, \alpha, \ldots, \alpha^{m-1}]^T$, the $GF(2^m)$ can be computed according to $C = A \cdot B = (L + Q^T \cdot U) \cdot B$ proposed in [17]. In Matlab, the matrix Q in $GF(2^8)$ can be obtained in the following:

```
Tx= zeros(m-1, m);
Ty1= zeros(m, m);
vf0= [1, 0, 1, 1, 1, 0, 0, 0];
Ty(:, 1: m-1)= [zeros(1, m-1); eye(m-1)];
Ty(:, m)= vf0.';
Ty1= Ty^m;
Ty1= mod(Ty1, 2);
Tx= Ty1(:, 1: m-1).';
Q= Tx;
```

The Chien search circuit is composed of t multipliers in $GF(2^m)$ and a few adders. It is used to find out the error locations by a full search if $\lambda_i \neq 0$.

3 Related Work

The popular stream cipher consists of two key stream generators, as is shown in Fig. 2 [18, 19]. The plaintexts are masked by the keys on the left, and then decrypted by the same stream on the right. The symbol 'IV' denotes initialization vector.

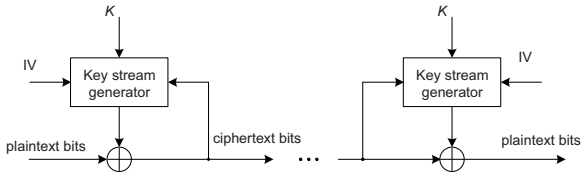

Figure 2: Traditional stream cipher by two key generators.

A random number generator (RNG) can be implemented by the linear feedback shift register (LFSR)[20] that generates peudo-random numbers for stream cipher, as is shown in Fig. 3. In practise the RNG can also be constructed by other digital or analog circuits.

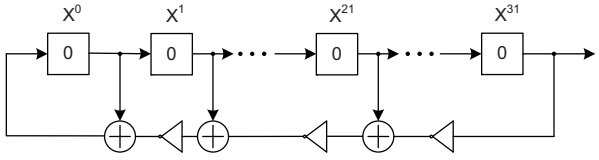

Figure 3: Linear feedback shift registers by XNOR gates[21].

A light-weight and energy-friendly stream cipher is proposed for wireless sensor network (WSN) in [18]. The paper suggests use the linear combination of pervious packets to generate the peudo-random key bits in a stream cipher, where a mixed protocol is advanced and public key is used to achieve data privacy [18].

Joint encoding and encryption by LDPC codes and RS codes for public key cryptography is a tradeoff between security and reliable communication [5, 22, 6]. New scrambling and permutating matrices for McEliece system with RS codes are proposed in [6] to enhance security. In [2] the wire-tap encoding and the error correction encoding are concatenated to enhance security. And in [3], a generator matrix, an invertible matrix, and gamma generator are used to produce the ciphertexts.

A provable secure stream cipher based syndrome decoding problem is presented in [7], which uses regular words to speed the system up and quasi-cyclic codes to reduce memory requirements. The results seem to be based on quasi-cyclic BCH codes.

4 Proposed Approach

Now suppose the message piece is r and the random numbers s are combined or XORed, then one can encode $(r \oplus \alpha \cdot s)$, where α is the multiple of s or a $u \times v$ matrix with $u = s/w$, $v = r/w$ and w is the width of a symbol. Next, one piece of the symbols s is inserted by addition modulo 2^m, and the new message reads $r' = M + s$. At the other terminal, by RS decoding one can recover s as well as $(r + \alpha s)$. Finally, the $r = (r + \alpha s) - \alpha s$ can be restored. The whole process is shown in Fig. 4. Especially, the insertion of errors avoids zero bytes by changing them as nonzero bytes within random numbers.

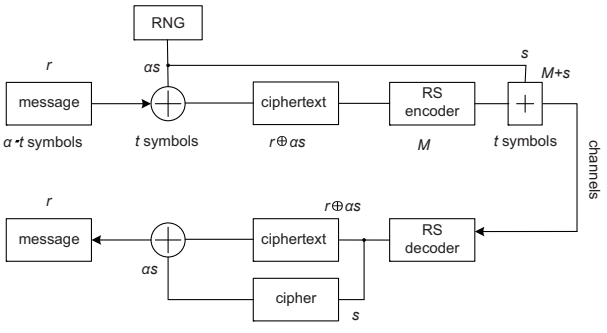

Figure 4: Stream cipher by RS code.

First, the security of a code-based system can be seemed as a public-key security problem, while the usual stream cipher is a symmetric cryptosystem. The proposed mechanism embeds the stream cipher along Reed-Solomon codes looking like a public-key cryptography: considering the key streams as private keys for encoding, and looking at the RS code parameters as the public key to decrypt the ciphertexts.

The security of the proposed scheme may also be improved by the application of shortened codes. In this way, the n-symbol codewords are replaced by a $(n - \delta)$-symbol codewords. Take the wireless communication for example, the sender and receiver share the same hardware units, i.e., stream engines, encoders and decoders. Then, the stream cipher with the sender can be seen as private keys to encrypt the messages. The choices of (1) whether a subfield subcode is chosen (2) whether a shortened code is chosen (3) whether the same decoder exists can be used as the public keys. If the decoder exists and the other two parameters are rightly chosen, then the stream cipher can be separated from the message bits by RS decoding.

In detail, one can use subcode or shortened code to decrease the error rate or improve the security of the system, as is shown in Fig. 5. The subfield subcode over $GF(p^s)$ have the same length n but is smaller than its parent code [23] with the word width, which is compressed from $\lceil sm \log_2 p \rceil$ to $\lceil s \log_2 p \rceil$. In fact, the length n of a subfield subcode may be larger than the size of a subfield, but is constrained its parent field size. Notice that the parity check symbols keep about double word size of other code symbols in Fig. 5.

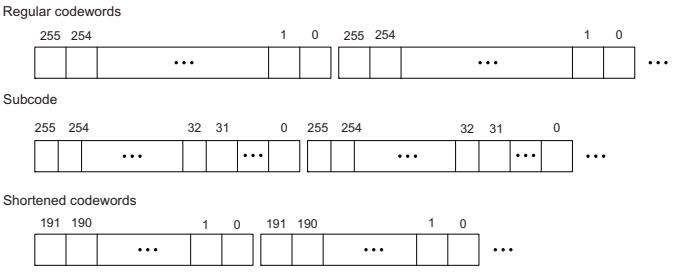

Figure 5: Stream cipher by subcode or shortened RS codes.

Secondly, the proposed scheme reduce the hardware cost and complexity by reusing the encoder for encryption and recovering the key streams by the decoder. Therefore, the task of aligning the stream engines to time sequence becomes unnecessary. As the number of stream cipher engines decreases from 2 to 1, it reduces the continuous power consumption much. On the one hand, it reduces the hardware units by a half; on the other hand, the renewal frequency of the stream cipher engine can be lowered down. Also, it is not easy to align the messages to real time, but it is feasible to align the messages at code sequence. The oscillator frequency may vary from time to time, while the stream cipher engines requires accurate alignments. The existence of time delay in mobile phones proves the validity of code alignment.

Furthermore, if the function of RS decoding and encoding is occasionally used, then the encryption can be used as an auxiliary function. Otherwise, if the error correction through the transmission path is requirable, then the first few code symbols can be designated as masks of key streams while the next words can be corrected by the remained error correction capability. Since error correction logic and stream cipher are basic units in wireless communications, this scheme

secret data as stream cipher

```
00000000h: 31 30 38 3D 33 5E 33 2A 32 5E 32 0D 0A 0D 0A  ; 108=3^3*2^2...
```

message

```
00000000h: 54 48 65 20 57 61 74 65 72 20 4D 61 72 67 69 6E ; THe Water Margin
00000010h: 20 74 65 6C 6C 73 20 74 68 65 20 73 74 6F 72 79 ;  tells the story
00000020h: 20 6F 66 20 72 65 62 65 6C 6C 69 6F 6E 20 61 6E ;  of rebellion an
00000030h: 64 20 73 74 72 75 67 67 6C 65 20 6F 66 20 73 6B ; d struggle of sk
00000040h: 69 6C 6C 65 64 2C 20 62 72 75 74 65 2C 20 6F 72 ; illed, brute, or
00000050h: 20 62 72 61 76 65 20 6D 65 6E 20 69 6E 20 61 63 ;  brave men in ac
00000060h: 69 65 6E 74 20 43 68 69 6E 61 2E 20 54 68 65 79 ; ient China. They
00000070h: 20 61 72 65 20 6E 61 6D 65 64 20 4A 69 61 6E 67 ;  are named Jiang
00000080h: 20 53 6F 6E 67 2C 20 4A 75 6E 79 69 20 4C 75 2C ;  Song, Junyi Lu,
00000090h: 20 53 68 65 6E 67 20 47 6F 6E 67 73 75 6E 2E 2E ;  Sheng Gongsun..
000000a0h: 2E 0D 0A 0D 0A 0D 0A                           ; .......
```

message encrypted by stream cipher

```
00000000h: 65 78 5d 1d 64 3f 47 4f 40 7e 7f 6c 78 6a 63 6e ; ex]d?GO@~lxjcn
00000010h: 11 44 5d 51 5f 2d 13 5e 5a 3b 12 7e 7e 62 78 79 ; □D]Q_-□^Z;□~~bxy
… …
```

Figure 6: Hiding information as stream cipher in RS codes.

Table 1: Advantages of Proposed Stream Cipher Compared to Other Schemes

Reference	Function	Implement	Topology	ENC/DEC Symmetry	Reuse for ECC	No. of RNG	Randomness	Code
This work	Stream data	Hardware	1-to-N	Not full	Yes	1	Not strictly	RS
[10]	Stream data	Hardware	1-to-1	Symmetric	No	2	Required	No
[7]	Stream data	Software	1-to-1	Symmetric	No	2	Required	Quasi-cyclic
[8]	Exchange data	Software	N-to-N	Not	No	0	-	GRS

combines their functions.

Thirdly, it may be applicable to transmit extra data through the key streams and therefore increase the throughput of inserted codewords. For example, the $(255, 223, 16)$ RS code has 223 information symbols. If the encoder are used for stream cipher, then 16 symbols of information can be added to the codeword secretly. The information rate is increased from $223/255 = 0.87$ to $239/255 = 0.94$. As is shown in Fig. 6, it is able to mix information with secret data in the proposed codes.

5 Comparison

The comparisons of this work compared with peer works are shown in Tab. 1. It should be noticed that the proposed scheme is not full symmetric, for which the cipher is decoded through the public-key. The architecture is implemented in a topology of 1-to-N, with N being any natural numbers including 1. If $N = 1$, then there are two parties to communicate with each other; or else it can be used in a network. By contrast, the stream cipher is usually supposed to follow 1-to-1 topology. While the encoding and decoding architectures in our work are non-symmetric, the whole stream cipher engine can be made nearly symmetric by integrating an encoder and decoder together. Moreover, this work needs only 1 random number generator while other stream ciphers requires 2 to N random number generators, since the key stream is embedded in the data stream in this work.

The weakly secure data exchange problem with generalized Reed-Solomon code is discussed in [8], in which data exchange between multiple parts rather than two parts are considered.

Also, in the proposal the random number generator is not that strictly required and pseudo random numbers can be used, while other works pay much attention to the random number generator itself, owing to different mechanism for stream ciphers. While traditional stream cipher uses continuous random bits, this work applies data structures of codewords to separate data. The references [8, 7] also uses GRS codes and quasi-cyclic codes to encode data and bring out randomness.

The architecture and hardware implementation results with [10] is demonstrated in Tab. 1 and Tab. 2. It uses a hardware common key cryptography named RAC for stream cipher, where the random numbers are used as addresses to relocate the data bits. The random numbers are generated by the recipient as addresses to resort the received ciphertext. Assuming the stream cipher engine in [10] works in a pipeline, then it is able to encrypt and decrypt 1 byte every clock cycle with throughput up to 3.2 Gps. Nevertheless, considering that the data from the sender or to the recipient should be stored in a RAM for reorganization, so the real decryption throughput may be only a half, let alone the time for fetching instructions.

Finally, the power consciousness of this design is

demonstrated by the application of RS code, whereas McEliece systems usually use nonsystematic encoding with an increase of computational efforts by $n/(n-k)$ times. In addition, if there are demands of error corrections for channels, the hardware units may be reconfigured and reused at different times.

Table 2: Hardware Implementation of Stream Cipher Engine by Reed-Solomon Code.

Design	Platform	LUTs	f_{max} (MHz)	Throughput (Gps)
Enc	XC5VLX85-2	318	480	3.79
Dec	XC5VLX85-2	5253	270	0.289
Enc/Dec	XC5VLX85-2	5905	270	1.82/0.289
[10]	0.18 μm CMOS	1.38 mm^2	400	1.6∼ 3.2

The stream cipher with encoding and decoding by RS codes is described by Matlab for test at first, then it is described by Verilog HDL for hardware implementation. As is shown in Tab. 2, the stream cipher engine is simulated by Modelsim 6.2, synthesized by Synopsys Synplify Pro 2014, and placed and rooted in Xilinx ISE 14.7. The code parameters are chosen as usual in [24], i.e.,
$m = 8$: number of bits per symbol,
$n = 255$: number of symbols per codeword,
$k = 223$: number of message symbols in a codeword,
$t = 16$: number of corrected errors by symbols.

According to the theory and results in [7], the security level of the cipher in the above table is about *80* bits of keys with symmetric cryptography.

In Tab. 2, the RS code supports correcting 16 symbols of errors along with 223 symbols of messages. It takes about 3.78 μs to correct 2 errors of symbols, and 7.06 μs to correct 16 errors of symbols. Its information throughput without parity check bits are 1.59/0.253 Gbit/s respectively for encoding and decoding.

6 Conclusion

Stream cipher is often used for mobile communications between two parties. In general, this paper proposes an easy scheme to implement stream cipher along with the popular RS code, which relies on RS encoding and decoding to cover and uncover the key streams. It is beneficial to easily evaluate the complexity and enhance the security of communication systems. The proposed cipher is based on the NP-complete problem of decoding a random linear code, which simply conforms to many solved code-based security issues. The cipher also decreases one key generator and reduces unnecessary power consumption for the synchronization between parties.

Acknowledgment

The author would like to appreciate the editor and reviewers for their kind help. This work is supported by Shenzhen postdoctoral base for innovation and practice and partly by Shenzhen basic research program (No. JCYJ20170307141601162).

References

[1] T. Wu and R. Wang, "Stream cipher by Reed-Solomon code," in *International Conference on Information and Communication Technology Convergence (ICTC)*, 2017, pp. 422–427.

[2] F. E. Oggier and M. J. Mihaljevic, "An information-theoretic analysis of the security of communication systems employing the encoding-encryption paradigm," arXiv, 2018. [Online]. Available: http://arxiv.org/abs/1008.0968

[3] A. N. Alekseychuk and S. V. Gryshakov, "Secure and practical randomized stream ciphers based on ReedSolomon codes," *Cybernetics and Systems Analysis*, vol. 53, no. 2, pp. 262–268, 2017.

[4] S. Lin and J. Daniel J. Costello, *Error Control Coding*. Upper Saddle River, New Jersey: Pearson Education, Inc., 2004.

[5] M. Baldi, *QC-LDPC Code-Based Cryptography*, ser. Briefs in Electrical and Computer Engineering. Springer, 2014.

[6] M. Baldi, F. Chiaraluce, M. Bianchi, and J. R. D. Schipani, "Enhanced public key security for the McEliece cryptosystem," *Journal of Cryptology*, vol. 29, no. 1, p. 127, January 2016.

[7] P. Gaborit, C. Lauradoux, and N. Sendrier, "SYND: a fast code-based stream cipher with a security reduction," in *IEEE International Symposium on Information Theory*, 2007, pp. 186–190.

[8] M. Yan, A. Sprintson, and I. Zelenkoy, "Weakly secure data exchange with generalized reed solomon codes," in *IEEE International Symposium on Information Theory*, 2014, pp. 1366–1370.

[9] M. Orumiehchiha, J. Pieprzyk, E. Shakour, and R. Steinfeld, "Security evaluation of Rakaposhi stream cipher," in *International Conference on Information Security Practice and Experience (ISPEC 2013)*, ser. Lecture Notes in Computer Science, R. Deng and T. Feng, Eds., vol. 7863. Berlin, Heidelberg: Springer, 2013, pp. 361–371.

[10] M. Fukase, H. Takeda, R. Tenma, K. Noda, Y. Sato, R. Sato, and T. Satot, "Development of a multimedia stream cipher engine," in *International Symposium on Intelligent Signal Processing and Communication Systems (ISPACS2006)*, Tottori, Japan, 2006, pp. 562–565.

[11] H. C. van Tilborg, *Fundamentals of cryptology: A Professional Reference and Interactive Tutorial*. Boston/Dordrecht/London: Kluwer Academic Publishers, 1999.

[12] T. Eisenbarth, T. Guneysu, S. Heyse, and C. Paar, "Microeliece: Mceliece for embedded devices," in *CHES*, ser. LNCS, vol. 5747, 2009, p. 4964.

[13] S. Heyse, I. von Maurich, and T. Güneysu, "Smaller keys for code-based cryptography: QC-MDPC McEliece implementations on embedded devices," in *CHES*, ser. LNCS, vol. 8086, 2013, pp. 273–292.

[14] S. Lin and J. Daniel J. Costello, *Error Control Coding- Fundamentals and Applications*. New Jersey: Prentice Hall, 1983.

[15] B. Sklar, "Reed-solomon codes," 2001. [Online]. Available: http://ptgmedia.pearsoncmg.com/images/art_sklar7_reed-solomon/elementLinks/art_sklar7_reed-solomon.pdf

[16] D. V. Sarwate and N. R. Shanbhag, "High-speed architectures for reedsolomon decoders," *IEEE Transactions on VLSI Systems*, vol. 9, no. 5, pp. 641–655, October 2001.

[17] A. Reyhani-Masoleh and M. A. Hasan, "Low complexity bit parallel architectures for polynomial basis multiplication over $GF(2^m)$," *IEEE Transactions on Computers*, pp. 945–959, 2004.

[18] H. Lin, A. J. A., D. Bai, and Y. Liu, "A light-weight stream cipher for wireless sensor networks," in *Future Wireless Networks and Information Systems*, ser. Lecture Notes in Electrical Engineering, Y. Zhang, Ed., vol. 143. Berlin, Heidelberg: Springer, 2012, pp. 627–638.

[19] B. Sklar, *Digital Communications Fundamentals and Applications*. Beijing: Publishing House of Electronics Industry, 2015, in Chinese.

[20] A. Canteaut, "Linear feedback shift register," pp. 726–729, 2011, reference Work Entry.

[21] "Linear feedback shift registers in virtex devices," 1996. [Online]. Available: http://www.xilinx.com/support/documentation/application_notes/xapp052.pdf

[22] M. Esmaeili and T. A. Gulliver, "Joint channel coding-cryptography based on random insertions and deletions in quasi-cyclic-low-density parity check codes," *IET Communications*, vol. 9, no. 12, pp. 1555–1560, 2015.

[23] J. I. Hall, http://users.math.msu.edu/users/jhall/classes/codenotes/Subfields.pdf, Michigan State University, pp. 89–99, 2012, codes over Subfields.

[24] Z. Liang and W. Zhang, "Efficient Berlekamp-Massey algorithm and architecture for Reed-Solomon decoder," *Journal of Signal Processing Systems*, vol. 86, p. 5165, 2017.

ASTES

Advances in Science, Technology and Engineering Systems Journal Vol. 3, No. 4, 33-44 (2018)

www.astesj.com

Special Issue on Multidisciplinary Sciences and Engineering

ASTESJ

ISSN: 2415-6698

Direct Torque Control of Multiphase Doubly Converter-fed Asynchronous Machines Incorporating the Harmonic Torques

Javier Martínez-Román*[1], Luis Serrano-Iribarnegaray[1], Juan Carlos del Pino-López [2], Pedro Cruz-Romero[2]

[1]*Department of Electrical Engineering, Universitat Politècnica de València, Camino de Vera s/n, 46022, Valencia,Spain*

[2]*Department of Electrical Engineering, Universidad de Sevilla, Camino de los Descubrimientos s/n, 41092 Sevilla, Spain*

A R T I C L E I N F O

Article history:
Received: 05 June, 2018
Accepted: 22 June, 2018
Online: 11 July, 2018

Keywords:
Harmonic torques
Asynchronous machines
Space phasors
Direct Torque Control
Multiphase machines
GAFTOC principle

A B S T R A C T

Doubly fed asynchronous machines have an outstanding property: they can be operated up to twice rated speed delivering full rated torque. This paper presents, for the first time in the literature, a control system for multiphase asynchronous machines fed by Voltage Source Inverters (VSIs) both in stator and rotor that incorporates the harmonic torques. The system has three main and distinctive features: the independent control of the fundamental and harmonic torques, a very fast dynamic response for each one of these torques and a powerful method for selecting the best suited inverter state to achieve the evolution of the fundamental and harmonics flux linkage space phasors prescribed by the external control loops. The first feature is achieved through the decoupling of the multiphase machine provided by the Space Phasor Theory (SPhTh). The second one comes from the application of the General Approach for a very Fast TOrque Control (GAFTOC) principle. The third feature relies on using for multi-phase VSIs a simple but powerful switching-table based mode of operation that overcomes the limitations of the switching-table based modes of operation developed up to now, that only enable for the inverter to feed machines with no harmonic torques contribution.

1. Introduction

Multiphase machines are receiving increasing attention in the last two decades. This is due to several important advantages over their three-phase counterparts [1] like greater fault tolerance, reduced ratings of the electronic converters components, and the ability to make use of certain field harmonics (the greater the phase number, the higher the number of harmonics) in order to increase the total machine torque. This last possibility is only feasible for machines with relatively large winding factors for the low order harmonics (concentrated or nearly concentrated windings). The multiphase machines control development has been mainly directed so far to Induction Machines (IM) and to Permanent Magnet Synchronous Machines (PMSM). Multiphase Doubly Converter-Fed Asynchronous Machines (DCFAM) have not been dealt with in the technical literature so far. Yet, these machines show the great advantage over IM and PMSM of having an extended operating range to twice the rated speed while keeping the ability to provide full rated torque, thus effectively doubling the machine rated power. This outstanding property has only been considered so far in the case of three-phase DCFAM [2-4].

To extend the already developed Direct Torque Control (DTC) solutions for three-phase DCFAM to multiphase DCFAM with harmonic torques, Fig. 1, one must solve first three main problems:

a) decoupling the fundamental and harmonic torques for their independent control,

b) achieving a very fast dynamic response for each one of these torques, and

c) developing a switching table based operation strategy for multiphase VSIs feeding machines with harmonic torques contribution.

The first problem is easily addressed though the multiphase machine decomposition and decoupling carried out in the SPTh, as presented in [5].

Once the muti-phase machine decoupling has been achieved, solving the second problem boils down to simply apply to each one of the independent machines the GAFTOC principle [6], *in which the stator and rotor flux linkages space phasors, Ψ, play the fundamental role*. In this regard, it should be underlined that, from a conceptual viewpoint, Field Oriented Control (FOC) and DTC, the two well-stablished high performance electric drives control

*Corresponding Author: Javier Martinez-Roman, Email: jmroman@die.upv.es

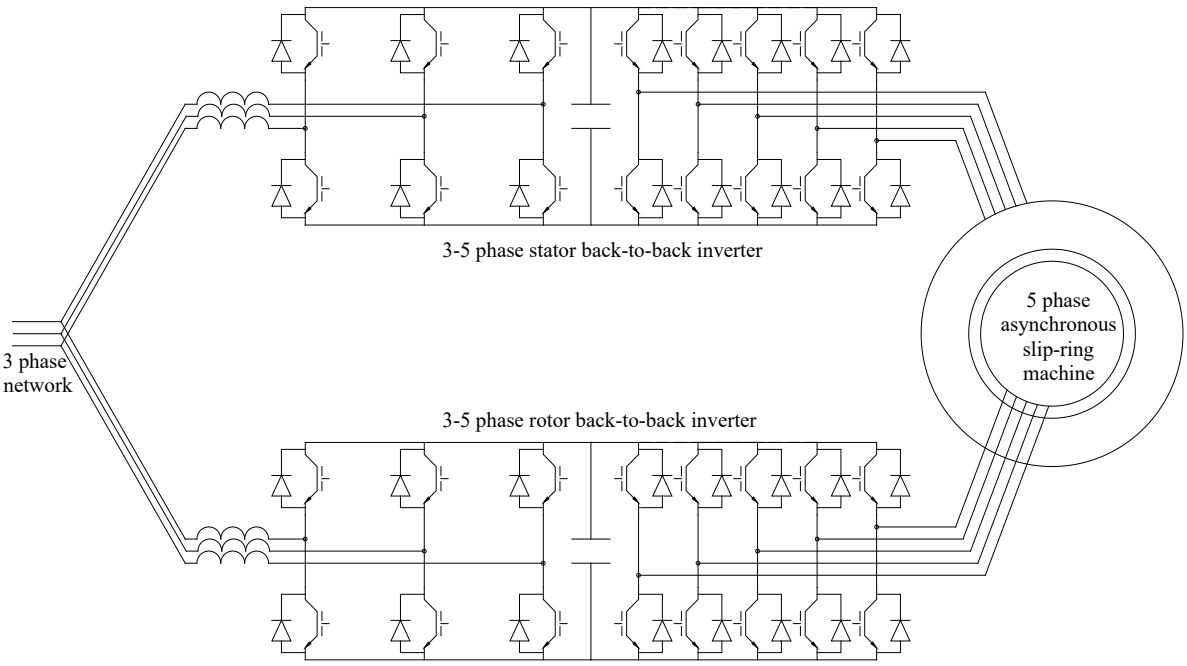

Figure 1. Doubly-converter-fed 5 phase asynchronous machine with 3-5 phase stator and rotor back-to-back inverters

methods, are two equivalent variants of the same and general GAFTOC principle, as explained in detail in section 7 of [6].

In this regard, for multiphase IM control, both FOC and DTC methods have been used. In the first case control schemes that allowed torque increases by incorporating harmonic torques were early developed [7]. Regarding the DTC method (which is the field of main interest of this paper) it has been also applied to multiphase IM, especially in the last years [8–10]. Yet in all of these cases, in clear contrast to some FOC implementations, there has never been torque improvement by space harmonics. As to muti-phase PMSM, they are, from the mathematical viewpoint and the control complexity, much simpler (no rotor windings) than IM. However, even in these cases, the DTC of the machine, to the best of the authors' knowledge, has also always been developed (with the exception of the results claimed in [11]), making use only of the fundamental torque [12-16]. As to the DTC of multiphase DCFAM, it has not been dealt with yet in the technical literature, not even in the simpler case of only fundamental wave operation.

With regard to the third problem, that is, with regard to the multiphase VSI operation, the first attempts at using a Space Vector Pulse Width Modulator (SVPWM) [17], were only able to control the fundamental voltage space phasor. Later on, [18] introduced a solution for the multiphase SVPWM with separated d-q spaces that allows the independent control of the d1q1-d3q3 voltage space phasors, but only with several constraints between their arguments and frequencies. These drawbacks were over-come in [19]. Still different improvements to the SVPWM operation of multiphase VSIs have been developed [20, 21]. In the case of multilevel converters, the choice of available inverter switching states increases considerably. In this respect [22] introduced a new multilevel multiphase SVPWM algorithm and [23] a generic digital Very High speed integrated circuit hardware Description Language (VHDL) module to implement it. All these strategies for selecting the inverter switching state require complex and time-consuming calculations, imply the use of Pulse Width Modulator (PWM) signal generators and assume, explicitly or implicitly, that the inverter can be modelled as an ideal controllable voltage source (which is not, since it has only a restricted a discrete number of switching states). Moreover, making use of an inverter operated this way for the machine control (usually in the FOC version) requires coordinate transformations (and thus a previous accurate determination of the angle between the involved reference frames). A switching-table based inverter operation strategy, initially introduced for three phase inverters [24], overcomes these drawbacks. In the case of multi-phase VSIs, this strategy has been first developed for inverters feeding 5-phase machines [8, 12, 13, 25]) and dual-three-phase machines [14, 16]. In a later and valuable paper [26], the switching-table based inverter operation strategy was extended to multiphase VSIs with an arbitrary odd number of phases, resorting to the so called virtual vectors definition methodology. In all of these cases, an ideal sinusoidal winding distribution has been assumed. Obviously, under this ideal assumption, only the fundamental space waves produce torque. Therefore, all of the methods developed until now are oriented to generate only fundamental voltage phasor precluding at the same time the presence of harmonic voltage phasors at the inverter output (suppression harmonics schemes). Indeed, these low order harmonic voltage phasors would drive large stator harmonic currents since the impedance (stator resistance plus leakage reactance) associated to these currents, which do not produce torque, is very small.

However, it seems neither logical nor the best option to disregard in all cases the possibility and advantages of *torque enhancement through harmonics contribution in the case of the DTC of multiphase machines*. In fact, these advantages have often been exploited in the case of FOC.

In view of the three aforementioned problems, this paper presents a switching-table based inverter operation strategy capable of simultaneously adjusting the fundamental and harmonics voltage space phasors, thus overcoming the limitations of the switching-table based modes of operation developed up to now (that only enable for the inverter to feed machines with no

harmonic torques contribution). Then, once this tool is available, the paper develops a DTC of a multiphase DCFAM, with voltage source inverters both in stator and rotor, Fig.1, with fundamental and also harmonic torques that, moreover, are controlled in an independent and very fast manner. This system keeps the main advantages of both three phase DCFAM (feasible operation up to twice the machine rated power and a balanced power share between the stator and rotor inverters) and multiphase configuration (greater fault tolerance, reduced ratings of the electronic converters components and torque enhancement through harmonics contribution).

The structure of this paper is as follows: first, section 2 describes by means of space phasors the fundamentals to split the actual multiphase machine into a set of much simpler machines, with only one effective flux linkage space phasor in stator, $\boldsymbol{\Psi}_{str}$, and another one in the rotor, $\boldsymbol{\Psi}_{rot}$ These fictitious machines are mechanically coupled, but electrically independent. Then, section 3 presents the new switching-table based operation strategy for multiphase VSIs feeding machines with useful harmonic torques. For the sake of simplicity, the strategy is explained on a five-phase machine. This strategy is computationally very light and can be easily extended to inverters with more than five phases and/or to multilevel inverters. Afterwards, section 4 develops in detail the scheme for the very fast and decoupled harmonic torques control which relies on the simultaneous and independent stator and rotor flux linkage space phasors control in each fictitious machine. The whole system has been checked in a five phase machine through an extensive set of simulations under different operating conditions, including step response to torque and speed references as well as speed reversals. Several of these simulations are displayed and commented in section 5. Finally, the main conclusions are summarized in section 6.

2. Multiphase Machines Decoupling Through the SPhTh

The approach overwhelmingly used for machines transient analysis is the so called magnetic coupling circuit approach (MCCA). Put it simply: the MCCA regards the machine as a network made up of resistances and inductances, many of which vary with the rotor position. This network is dealt with by means of complex matrix transformations.

The SPhTh for cylindrical or salient pole symmetrical machines with arbitrary number of phases and space harmonics has been presented in [5]. By contrast to the MCCA (machine as a network with rotor position dependent parameters), the SPhTh states that a machine can also be regarded as an electromechanical device that produces electromagnetic (field) waves with a restricted propagation capacity, namely they are forced to turn inside its air gap. These space waves, especially the scalar electric potential difference, the vector magnetic potential difference and the linear current sheet waves:

- can easily be characterized by dynamic space phasors: the voltage, flux linkage and current sheet space phasors, respectively
- can easily be correlated with the time phase quantities.

Notice that the SPhTh fully rejects space phasors to be mere mathematical entities without any physical meaning. In fact quite the opposite is true.

Another fundamental concept in the SPhTh is the dynamic m–phase system (DmPhS) of sequence *g*. By definition, the *m* quantities (*m* currents, *m* voltages, etc.) of an *m*-phase symmetrical winding are said to constitute a DmPhS of sequence "*g*", if they meet the following equations:

$$\begin{aligned} x_1(t) &= x(t)\cos[\varepsilon(t) - g\cdot 0\cdot\frac{2\pi}{m}] \\ x_2(t) &= x(t)\cos\left[\varepsilon(t) - g\cdot 1\cdot\frac{2\pi}{m}\right] \\ &\cdots\cdots\cdots\cdots\cdots\cdots\cdots\cdots\cdots\cdots\cdots\cdots \\ x_m(t) &= x(t)\cos\left[\varepsilon(t) - g\cdot(m-1)\cdot\frac{2\pi}{m}\right] \end{aligned} \tag{1}$$

where x(t) and ε(t) can be arbitrary time functions.

A DmPhS of sequence *g* only has two independent variables, *x(t)* and *ε(t)*. Thus, it can be fully characterized by a mathematical tool called the dynamic time phasor of the DmPhS of sequence *g:*

$$\left[\vec{X}\right]_g = \left[x(t)\ e^{j\,\boldsymbol{\varepsilon}(t)}\right]_g \tag{2}$$

Variables *x(t)* and *ε(t)* correspond with the instantaneous amplitude and position of the dynamic time phasor in its complex plane. Dynamic time phasors of the same sequence can be added up graphically and vectorially in an analogous manner as the classical Kapp's phasors do. If the *m* phases of the winding are numbered 1,2 ,….,*y*, ….. (*m*-1), *m*, the quantity of the general phase *y* of system (1) is obtained by simply projecting the phasor onto the phase axis in the complex plane of sequence *g*. That is ($\Re e$ stands for "real part of"):

$$x_y(t) = \Re e\left[x(t)e^{j\varepsilon(t)}e^{-jg(y-1)2\pi/m}\right] \tag{3}$$

Obviously, if amplitude and speed of the dynamic time phasor are constant, the DmPhS in (1) becomes a sinusoidal polyphase system of sequence *g*.

Sequences *g* and (*m* – *g*) are called complementary sequences. Any DmPhS of sequence *g* can always be converted into a DmPhS of sequence (*m* – *g*) in accordance with the equation (symbol * stands for conjugate complex):

$$\left[\vec{X}\right]_g = \left[\vec{X}^*\right]_{m-g} = \left[x(t)\ e^{-j\,\boldsymbol{\varepsilon}(t)}\right]_{m-g} \tag{4}$$

By definition, the complementary DmPhS of the one in (4) is:

$$\begin{aligned} &Complementary\ \left\{\left[\vec{X}\right]_g\right\} = \\ &= \left[\vec{X}\right]_{m-g} = \left[x(t)\ e^{j\,\boldsymbol{\varepsilon}(t)}\right]_{m-g} \end{aligned} \tag{5}$$

Comparing (4) and (5) it follows that the dynamic time phasors of two complementary DmPhSs are exactly equal except that their instantaneous arguments are opposite.

Let it be a seven-phase (*m*=7) stator symmetrical winding of a salient pole machine and consider the numerous stator electric potential difference space waves which appear at the stator surface with arbitrary changes in their amplitudes and speeds. It has been proven [5] that each of these waves with *p*, *8p*, *15p*, etc. pole pairs

(that is, each of the harmonic waves of relative order $h = 7q + 1$ with $q = 0, 1, 2, 3$, etc.) produces in the winding a voltage DmPhS of sequence 1. Likewise, each of the waves of order $h = 7q + 2$; $h = 7q + 3$, etc. produces a voltage DmPhS of sequence 2, 3, etc, respectively. Therefore, for a 7-phase stator winding all of the electric potential difference waves in axial direction at the stator surface can be classified into seven families. The instantaneous amplitudes and positions of the different waves belonging to the same family are, in the general case, quite different from one another. However, all of them originate DmPhSs of the same sequence which can be added up to give a resultant DmPhS of this same sequence. Thus, the combined action of all of the waves of one family on the phase voltages can be characterized by just one equivalent or effective voltage space phasor. Or alternatively: the resultant voltage DmPhS produced by a whole family of waves can be imagined to be produced by one only effective or equivalent space wave, the phasor of which is just the effective space phasor of the waves family.

Moreover, the two effective voltage DmPhSs produced by the families with $h = 7q + 1$ and $h = 7q + 6$ are DmPhSs of complementary sequence. Therefore, they can be added up so that just one space phasor suffices to characterize the combined action of both families (which form a group of space waves with $h = 7q \pm 1$). The same statement applies to the families with $h = 7q \pm 2$ as well as to the families with $h = 7q \pm 3$. Thus, the combined effect of all of the electric potential difference waves on the voltages of the seven phases in any dynamic state is fully characterized by just four effective voltage space phasors (one of which being the homopolar phasor). These conclusions apply too to the magnetic vector potential difference space waves (space phasors $\boldsymbol{\Psi}$), and can be extended to a symmetrical winding with an arbitrary number of phases, m.

Similarly, a current DmPhS of sequence g flowing through the stator symmetrical m-phase winding of a salient pole machine produces only current sheet space waves of relative order $h = mq \pm g$. Its complementary current DmPhS produces exactly the same space waves group, except that the instantaneous speed of any wave in this second case is opposite to that of the first case.

In summary, each one of the different $\boldsymbol{u}$, $\boldsymbol{\Psi}$ *and* $\boldsymbol{i}$ *effective dynamic space phasors existing in the multiphase machine is related to one specific and independent group of space harmonics*. This physical reality has been analyzed in detail in [5] and constitutes the true base that enables to "untangle" rather easily the structure of a constant air gap multiphase machine (either PMSM, IM or DCFAM) and to split it into an equivalent set of much simpler machines, *mechanically coupled but electrically independent*. Each one of these machines is associated to each one of the independent group of space harmonics mentioned above. As already pointed out in [5], it should be indicated here too that the authors in [27] had already dealt with the particular case of PMSM (no rotor winding and constant rotor magnetic field influence into the stator windings) following an approach completely different from the SPhTh. Resorting to different analysis tools (endomorphism, orthonormal base of eigenvectors, etc) they arrived at decoupling laws for PMSM mathematically fully equivalent to the general results presented in [5].

On the other hand, it is well known that only the interaction of stator and rotor space waves with the same pole number can produce torque. Assume again a symmetrical asynchronous machine with seven phases in stator and rotor. If one applies, exclusively, e.g., a current DmPhS of sequence $g = 5$ (or g=2) to the stator and another one to the rotor, the space waves (and their associated torques) of the two complementary families $h = 7q \pm 2$ can be controlled in any dynamic state *without modifying the space waves of the remaining families. This is just the physical base underlying the decoupled control of the multiphase machine*.

Moreover, by contrast to mains-connected machines, in multiphase converter-fed machines it is not necessary to take into account all the members of each wave family for determining the torque because in this case only the head members of their groups (that is, the harmonics with the lowest pole number) are able to provide a non-negligible instantaneous torque contribution. Notice, e.g. that in all control schemes of converter-fed three phase induction machines presented in the technical literature only the fundamental waves (that is, the head members of the stator and rotor waves families) are considered as to the torque production. The impact on the machine torque of the harmonic waves is considered negligible [30]. Therefore, in what follows, only the head members of each group of two complementary waves families will be considered (e.g., for a seven phase winding without homopolar components these head members are the fundamental, the third and the fifth harmonic space waves).

A three phase doubly converter-fed asynchronous machine without homopolar components only has one voltage and one flux linkage effective space phasor in the stator, and the same applies to the rotor. Its phasorial stator electric equation reads:

$$\overrightarrow{u_{str}} = R_{str}\overrightarrow{i_{str}} + \frac{d\overrightarrow{\Psi_{str}}}{dt} \tag{6}$$

In the DTC technique, since stator emf and voltage are almost equal quantities (if the resistive voltage drop is neglected), stator voltage space phasor guides the stator flux linkage phasor forcing it to approach a circular trajectory, so that this way only rotational emfs are induced, Figure 2.

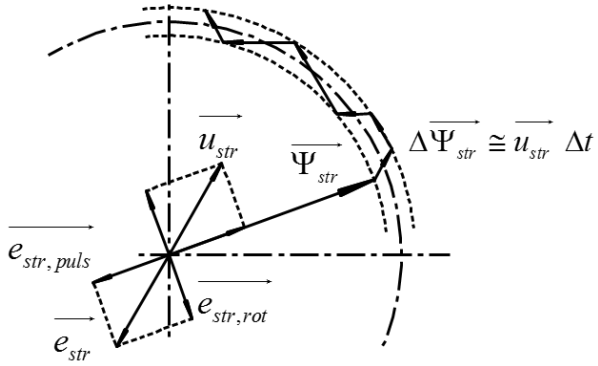

Figure 2. Stator flux linkage phasor changes in a modulation step and stator pulsational and rotational EMFs space phasors

Indeed, if $\overrightarrow{u_{str}} \cong -\overrightarrow{e_{str}}$, then according to (6):

$$\overrightarrow{u_{str}} \cong \frac{d\overrightarrow{\Psi_{str}}}{dt} \quad \Rightarrow \quad \overrightarrow{\Delta\Psi_{str}} \cong \overrightarrow{u_{str}} \cdot \Delta t \tag{7}$$

that is, during any converter control cycle the variation of the $\boldsymbol{\Psi}_{str}$ phasor takes place very closely in the direction of the voltage space phasor selected during the interval, Figure 2. In other words, the amplitude of $\boldsymbol{\Psi}_{str}$ is controlled by using radial voltage phasor components (that is, pulsational emf, which only affects the flux linkage module), whereas the torque is adjusted by applying tangential voltage components, that is, rotational emf, directly related to the torque generation, as explained in detail in [6], and which only affects the flux linkage phasor speed, producing a "tangential pull" on it.

Just as in three phase machines without homopolar components, the decoupled machines obtained from the actual multiphase machine also have only one effective voltage and one effective flux linkage space phasor in stator and rotor. Thus, as explained in [5], the electric polyphase winding (stator or rotor) equation of any of these independent machines reads:

$$\overrightarrow{u_{wind,x}} = R_{wind,x}\overrightarrow{i_{wind,x}} + \frac{d\overrightarrow{\Psi_{wind,x}}}{dt} \Rightarrow$$
$$\Rightarrow \overrightarrow{\Delta\Psi_{wind,x}} \cong \overrightarrow{u_{wind,x}} \cdot \Delta t \tag{8}$$

where x stands for stator or rotor. For more details on this subject, refer to [5].

3. Switching-Table Based Operation Strategy for Multiphase VSIs Feeding Machines with Useful Harmonic Torques

Single phase PWM presents a single degree of freedom: the ratio of t_{on} to t_{off}. Three phase PWM present three degrees of freedom, although only two of them are effective in terms of the load voltage space phasor due to the usual three wire connection. In DTC these two degrees of freedom result in the ability to obtain the most suitable load voltage space phasor out of the only 2^3=8 possible switching state combinations to modify the magnitude and angle of the stator flux linkage phasor prescribed by the external control loop. It is apparent that for every additional converter phase a new degree of freedom is available. Then the problem arises of finding a suitable connection between the control variables in a multiphase load and the corresponding VSI switching state selection.

In a 5-phase two level converter there are 2^5=32 switching states available (two of them resulting in the same null voltage space phasor). Therefore, they produce 31 different voltage space phasors of the first and of the third harmonic space waves. Let us consider a 5-phase machine, whose phase 1 is set at the real axis, fed by a converter with V_{bus} dc bus voltage. The status of each of the 5 inverter legs is defined by a set of five Boolean variables, $[sw]_x$, for which 1 means that phase x is connected to the dc bus positive terminal in Figure 1, and 0 that it is connected to the negative terminal. Each one of the 32 inverter switching states is then defined by the 5 bits of the following switching state index, sw:

$$sw = [sw]_5 \times 2^4 + [sw]_4 \times 2^3 + [sw]_3 \times 2^2 + [sw]_2 \times 2^1 + [sw]_1 \times 2^0 \tag{9}$$

Likewise, the voltage of any x-phase measured to the dc bus mid-point is given by

$$u_{x-phase,sw} = V_{bus}\left([sw]_x - \frac{1}{2}\right) \tag{10}$$

The fundamental and 3rd harmonic voltage space phasors are calculated from the phase terminal voltage according to:

$$\overrightarrow{u_{1,sw}} = \sum_{x=1}^{5} u_{phase-x,sw} e^{j(x-1)\frac{2\pi}{5}}$$
$$\overrightarrow{u_{3,sw}} = \sum_{x=1}^{5} u_{phase-x,sw} e^{j3(x-1)\frac{2\pi}{5}} \tag{11}$$

The 31 circles in Figure 3 mark the affixes of the 31 different voltage space phasors of the fundamental wave in its phasorial domain. Analogous information provide the 31 circles in Figure 4 with regard to the third harmonic. These voltage space phasors for the 32 switching states are then organized as column vectors:

$$\vec{u}_1 = \begin{bmatrix} \overrightarrow{u_{1,1}} \\ \dots \\ \overrightarrow{u_{1,32}} \end{bmatrix} ; \vec{u}_3 = \begin{bmatrix} \overrightarrow{u_{3,1}} \\ \dots \\ \overrightarrow{u_{3,32}} \end{bmatrix} \tag{12}$$

Notice that the index or number of each row in (12) expressed in binary system coincides with the switching state index, sw, that originates the voltage space phasor corresponding to the mentioned row.

The first step into the selection of the adequate switching state is to evaluate every state in terms of its ability to change magnitude and angle of the two flux linkage space phasors, $\boldsymbol{\Psi}_1$ and $\boldsymbol{\Psi}_3$. To do so the complex phasorial plane of each space harmonic is divided into 20 equal sectors (The reason to divide each one of the two phasorial domains into 20 sectors is to assure that while each flux linkage space phasor remains within a given sector, the real and imaginary parts of all 30 non null voltage space phasors, calculated in a reference frame aligned with the flux linkage space phasor, do not change their signs). Then the real and imaginary parts of the voltage space phasors of the first and third harmonics corresponding to each switching state combination are calculated in a reference frame in which the real axis is directed along the middle of the sector, Figure 3 and Figure 4.

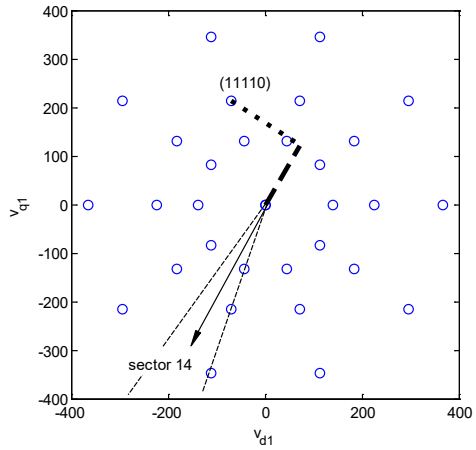

Figure 3. Real (thick dashed) and imaginary (thick dotted) parts of the fundamental *voltage* space phasor when the fundamental *flux linkage* space phasor lies in sector 14. The inverter switching state considered is 11110.

According to the winding equation (8) and section 2, Figure 2, *it is just these real and imaginary parts that quantify how well suited each switching combination is to quickly modify the corresponding flux linkage space phasor magnitude and angle respectively*. For example, the higher and positive the real part of the voltage phasor the better suited to increase flux linkage phasor magnitude, while the higher and negative the imaginary part the better suited to rotate the flux linkage space phasor backwards.

Let us consider the inverter switching state (11110) during a time interval at which the first harmonic flux linkage space phasor lies, e.g., within sector 14 while, at this same time, the third harmonic flux linkage space phasor lies in sector 11. Figure 3 shows for the mentioned switching state index, *sw* = (11110), the corresponding real and imaginary parts of the fundamental voltage space phasor (calculated in a reference frame aligned with the fundamental flux linkage space phasor). Analogous information provides Figure 4 related to the third harmonic voltage space phasor.

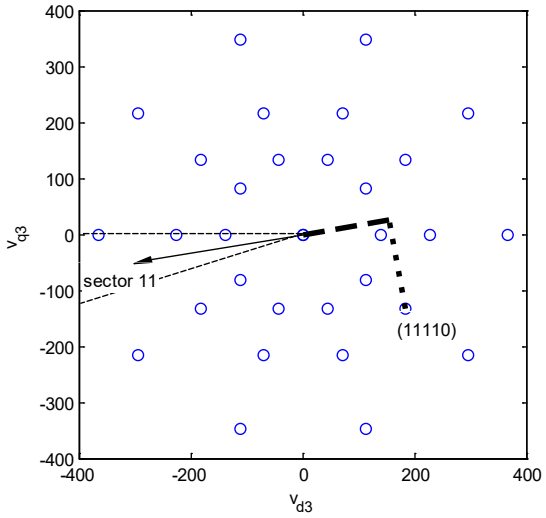

Figure 4. Similar to Fig. 3, but for the third harmonic space wave and when Ψ_3 lies in sector 11

The result of these operations performed for all sectors and all switching states are four 32x20 matrices (matrices M_{T1} M_{T3} $M_{\Psi 1}$ and $M_{\Psi 3}$ in Figure 6). These matrices, (13), are the imaginary or real parts of the matrices obtained as the complex product of the voltage space phasors column vectors times $(\mathbf{u}_{\gamma/2})^*$:

$$\begin{aligned}
[M_{T1}] &= \mathrm{Im}\left(\vec{u}_1 \times \left(\vec{u}_{\gamma/2}\right)^*\right) \\
[M_{\Psi 1}] &= \mathrm{Re}\left(\vec{u}_1 \times \left(\vec{u}_{\gamma/2}\right)^*\right) \\
[M_{T3}] &= \mathrm{Im}\left(\vec{u}_3 \times \left(\vec{u}_{\gamma/2}\right)^*\right) \\
[M_{\Psi 3}] &= \mathrm{Re}\left(\vec{u}_3 \times \left(\vec{u}_{\gamma/2}\right)^*\right)
\end{aligned} \tag{13}$$

where $(\mathbf{u}_{\gamma/2})^*$ is the row vector formed by the complex conjugates of the 20 sector central unitary vectors, according to the following equation:

$$\vec{u}_{\gamma/2} = \left[e^{+j\frac{2\pi}{40}} \quad e^{+j3\frac{2\pi}{40}} \quad e^{+j5\frac{2\pi}{40}} \quad \ldots \quad e^{+j39\frac{2\pi}{40}} \right] \tag{14}$$

In these matrices, each row is associated with one of the 32 available switching states in the 5-phase converter, while each one of the 20 columns is associated with one of the 20 sectors in which the phasorial domain for the fundamental and 3rd harmonic has been split into.

Notice that, once selected, e.g., sector 11, Figure 4 shows how the imaginary and real parts of the third harmonic voltage space phasor for one specific switching state can be obtained. Yet, this operation has to be performed, in this sector, for the 32 possible inverter switching states. The 32 x 2 values obtained this way are just the 32 values in column 11 of matrices M_{T3} and $M_{\Psi 3}$. Thus, matrices M_{T1} M_{T3} $M_{\Psi 1}$ *and* $M_{\Psi 3}$ express the ability of the 32 inverter switching state combinations to modify angle (torque) or magnitude (flux) of the fundamental or of the third harmonic flux linkage space phasors when these phasors lie in each one of the 20 sectors. From each one of these four matrices, and by means of the actual **Ψ** sector calculators, the system extracts the appropriate column, Figure 6, that is, the column corresponding to the sector in which the actual fundamental (or third harmonic) flux linkage space phasor lies (the actual sector is simply and directly determined from the **Ψ** phasor angle). Each one of these four columns is then weighted; or, more precisely, it is multiplied by the normalized desired trend (obtained from the *torque and flux linkage comparators*) in magnitude and angle of both flux linkage space phasors.

These weights for the stator and rotor fundamental and third harmonic torque and flux control are those shown in Figure 6 as *dt1, dp1, dt3, dp3*. They are equal to the actual torque or flux error (ΔT, $\Delta \Psi$) in per unit of the corresponding rated value multiplied by a suitable weighing factor, *k*, that is:

$$\begin{aligned}
dt1 &= \frac{\Delta T_1}{T_{1,rated}} k_{T1}; \quad dp1 = \frac{\Delta \Psi_1}{\Psi_{1,rated}} k_{p1} \\
dt3 &= \frac{\Delta T_3}{T_{3,rated}} k_{T3}; \quad dp3 = \frac{\Delta \Psi_3}{\Psi_{3,rated}} k_{p3}
\end{aligned} \tag{15}$$

where the k-values in (15) have been chosen in this paper equal to:

$$\begin{aligned}
k_{T1} &= \frac{T_{1,rated}}{T_{rated}}; \; k_{T3} = \frac{T_{3,rated}}{T_{rated}} \\
k_{p1} &= \frac{\Psi_{1,rated}}{\Psi_{rated}}; \; k_{p3} = \frac{\Psi_{3,rated}}{\Psi_{rated}}
\end{aligned} \tag{16}$$

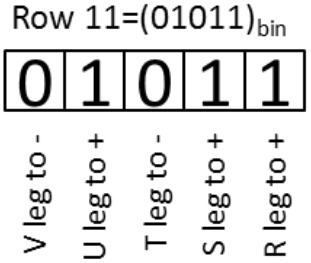

Figure 5. Five-phase Inverter switching legs status as determined by individual bits of row number conversion to binary: example for row number = 11. Inverter output phases are designed in this figure as *V, U, T, S* and *R*

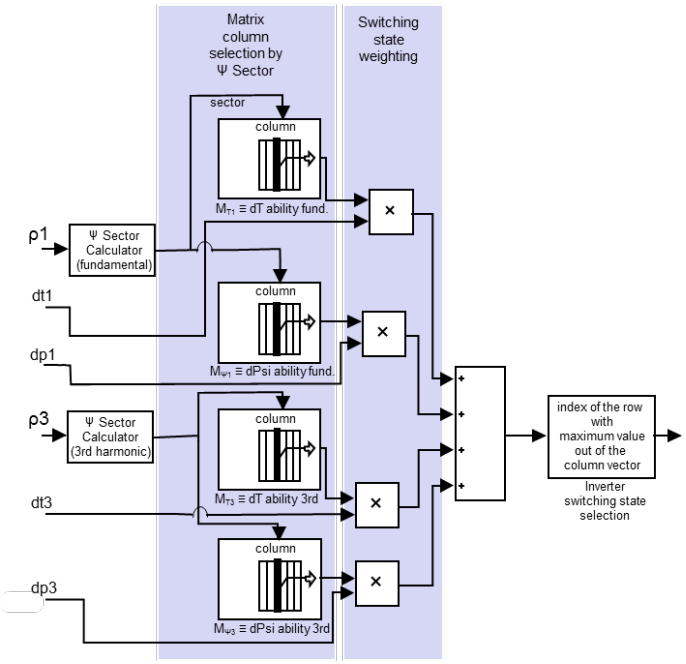

Figure 6. Operations flow for the 5-phase DTC: sector calculators, columns selection, weighing (products), combined switching state ability to modify magnitude/angle of the flux linkage space phasors (addition), best inverter switching state selection and, finally, binary conversion to get the inverter legs switching states. ρ_x: flux linkage space phasor angle (1: fundamental; 3: 3rd harmonic); dt_x and dp_x: normalized desired trend in magnitude and angle of the flux linkage space phasors.

The four column vectors mentioned above are added up to form a single column vector, and then its row with the highest value is selected. From this selected row the inverter switching state is obtained immediately: indeed, in accordance with the comments just after eq. (12), the row number conversion to binary directly yields the required switching state for all five inverter legs, Figure 5. This procedure overcomes the unsolved problem found in switching-table based operation strategy of multiphase VSIs in order to select the inverter switching state which is best suited to *simultaneously modify* magnitude and angle of the fundamental and also of the higher harmonic flux linkages space phasors in the way prescribed by the external control loops. (Remember that the space phasors **Ψ** play the central role in the GAFTOC strategy).

In summary, the switching state selection process is divided into two main steps. First, each switching state ability to force changes in the magnitude and angle of the flux linkages space phasors of fundamental and third harmonic is calculated (this step is carried out off-line and stored as an array in the controller memory). Second, depending on the magnitude and torque/angle errors for the flux linkage space phasors, the best suited out of the 32 available switching states is selected (this step needs only real products to be performed and is carried out on-line).

The whole process is then very light in terms of computational requirements as only basic operations and in small number are required. It needs to be carried out just once in every modulation period. The most computationally heavy operations for the matrices calculation are carried out off-line and only the resulting arrays are stored in the control system memory. It is important to notice too that this strategy can directly be extended to inverters with more than 5 phases and/or to multilevel inverters.

4. Independent and Very Fast Control of the Fundamental and Harmonics Torques of Multiphase Doubly Converter-Fed Asynchronous Machines

The Direct Torque and Stator and Rotor Flux Control (DTSRFC) of the three phase DCFAM in [4] actually set the basis for the very fast control of the fundamental and harmonics torques of the multiphase DCFAM.

The fundamental idea behind a very fast torque control strategy was already applied to develop the DTSRFC: In steady state of polyphase machines only rotational emfs appear in all of their windings and, therefore, these are just the emfs (that is, the ones related to the electromechanical energy conversion process) that have to be enhanced. The pulsational emfs (that is, the ones associated to amplitude variations of the flux linkage space phasors) should be kept null. This essential idea (pulsational emfs are a waste of resources and time as to the torque production) should be extended to transient states too if a torque control with very fast dynamic response and an efficient utilization of the machine (and of the power conditioning unit) is desired. This is the GAFTOC principle [6].

The three phase doubly converter-fed asynchronous machine is especially well suited to put into practice such control strategy. Indeed, to keep the pulsational emfs null in all of its windings, it suffices to operate the stator and rotor converters so as to maintain $\mathbf{\Psi_{str}}$ and $\mathbf{\Psi_{rot}}$ magnitudes constant. Should there still be any degree of freedom in the operation of the converters, it must be used so as to force the biggest possible rotational emfs (speed of the flux linkages space phasors).

In a three phase machine, the following equations hold [3,4]:

$$T = -\frac{m}{2} p \frac{L_\mu}{\left(L_{str} L_{rot} - L_\mu^2\right)} \left(\vec{\Psi}_{str} \times \vec{\Psi}_{rot}\right)$$

$$T = \frac{m}{2} p \frac{L_\mu}{\left(L_{str} L_{rot} - L_\mu^2\right)} \Psi_{str} \cdot \Psi_{rot} \cdot \sin\delta \tag{17}$$

It should be noticed [5] that space phasors are not physical vectors but (mathematically seen) complex time-varying quantities. Thus, the vectorial product in (17) should be interpreted as a formal operation.

Therefore, in the three phase machine the control is performed, [4], by keeping the $\mathbf{\Psi_{str}}$ and $\mathbf{\Psi_{rot}}$ modules constant and adjusting the torque through the angle, δ, between both phasors, Figure 7, according to (17). This same procedure must simply be extended to all of the fictitious independent machines of the multiphase machine.

A multiphase inverter enables, for each one of these fictitious machines, two degrees of freedom, that is, to freely adjust magnitude and angle of the corresponding flux linkage space phasors, **Ψ** [5]. Therefore, in a multiphase DCFAM (two inverters) this control strategy still leaves one degree of freedom to completely define the $\mathbf{\Psi_{str}}$ and $\mathbf{\Psi_{rot}}$ references in each fictitious machine. In the particular case of three phase machine this remaining degree of freedom is used to force a balanced share of electric power between both inverters. For more details, see [4].

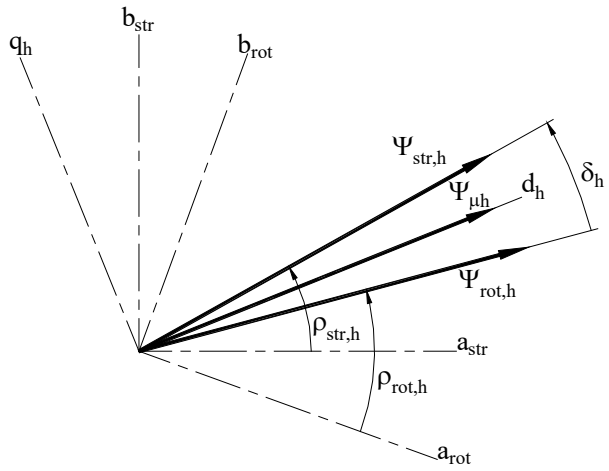

Figure 7. Stator, rotor and magnetizing flux linkage space phasors and flux load angle δ for the space harmonic of relative order h. Systems (a_{rot},b_{rot}), (a_{str}, b_{str}), (d_h, q_h): rotor, stator and magnetizing phasorial reference frames for the harmonic h.

In multiphase machines a new additional and important control task arises, namely how to adjust the suitable value and orientation of the harmonic magnetizing flux linkage space waves with regard to the fundamental one. In this sense, in a machine with the classical sinusoidal air-gap induction distribution only in the narrow region where the induction is maximum becomes the iron saturated to the desired value at any one instant. Yet, it seems clear that the magnetic circuit would be better utilized if the air-gap induction wave approximates a nearly rectangular one. Notice, nevertheless, that the control scheme in Figure 8 below enables to easily obtain any desired induction waveform. To this end, it suffices to choose the suitable amplitudes of the different harmonic flux linkage space waves (block flux linkage reference distribution in Figure 8) and their orientations with respect to the fundamental magnetizing flux linkage wave (18). These values are chosen to obtain (in machines with a high number of phases) an air gap induction wave of quasi-rectangular shape.

Notice too, from another perspective, that the possibility of obtaining almost any desirable air gap induction waveform in machines with a high number of phases relies on the fact that, with increasing phase number, the converters can inject additional current DmPhSs of different sequences, g, with the appropriate $\varepsilon(t)$ values in (1), which is valid for steady and transient states.

In this regard, it should be remembered from section 2 that the only condition to have different waves groups is to inject (through the suitable currents) dynamic time current phasors of different (and not complementary) sequences. For instance, in the particular case of steady state of a five phase machine, in order to get the two wave groups of $h = 5q \pm 1$ and h = $5q \pm 2$, it is only required to feed the winding, simultaneously, with two suitable sinusoidal polyphase current systems, A and B. In system A the phase angle between the currents of two consecutive winding phases should be γ or 4γ (that is, g_A = 1 or 4), with γ=2π/5. In system B it should be 2γ or 3γ (g_B = 2 or 3). Obviously, the functions $\varepsilon(t)$ are in this case of sinusoidal currents: $\varepsilon_A(t) = \omega_A t$ and $\varepsilon_B(t) = \omega_B t$, where ω_A and ω_B are two arbitrary constant values. If *in addition* it is desired that the head members of both wave groups turn in the same direction and at the same speed, then one must choose g_A =1, g_B =3 (or g_A =4, g_B =2) and ω_B=$3\omega_A$. In other words, and contrary to some statements in the literature, the frequency $\omega_B = 3\omega_A$ does not imply the existence of a third harmonic wave (which is tied to the sequence g of the current DmPhS) but only determines its speed [5].

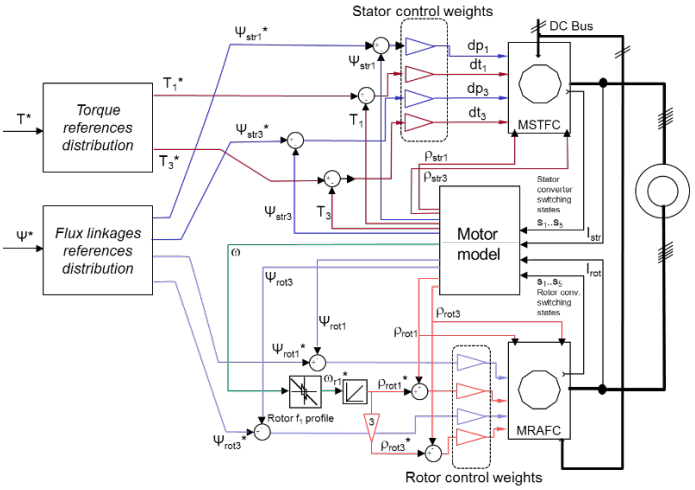

Figure 8. DTC diagram of a five phase doubly converter-fed asynchronous machine incorporating the harmonic torques. Symbol * stands for reference values. For a detailed explanation, see text.

The fact that, as above indicated, the air gap induction wave approximates a quasi-rectangular shape leads to a resultant magnetizing flux linkage wave that approximates a symmetrical triangular distribution so that one peak of all the magnetizing flux linkage space waves for the space harmonics of relative order 1, 3, … must occur at the same air gap angular position. In other words, the magnetizing flux linkage space phasors must be oriented in such a way that their angles (measured in their respective phasorial domains) meet the following equation:

$$\rho_{\mu 1} = \frac{1}{3}\rho_{\mu 3} = \frac{1}{5}\rho_{\mu 5} = \ldots \tag{18}$$

The diagram in Figure 8 shows the global control structure. It starts with the machine total torque and flux linkages references: the machine torque reference is the output of the speed controller (not shown in the figure) while the flux linkages reference can be either kept constant or suitably adjusted in the case of field weakening operation. The torque references distribution block provides the torque share for the fundamental and the third harmonic. An analogous statement hold for the flux linkages references distribution block. Then, the stator flux linkage and torques references are compared with the actual machine values and the errors are divided by the corresponding rated values and multiplied by the suitable weighing factors. The results of these operations, (15), are the inputs *dt1, dp1, dt3, dp3* to the stator Multiphase Stator Torque and Flux Controller (MSTFC) block, which has the structure of Figure 6. As for the rotor, the flux linkages comparators are similar to those of the stator. However, the role of the stator torque comparators is played here by the flux linkage space phasor angle comparators: the machine speed sets (by means of the rotor frequency profile, Figure 9) the rotor fundamental frequency. This rotor frequency is integrated to provide, first, the rotor fundamental flux linkage space phasor angle and thereafter, making use of (19), Figure 8 bottom, the angle of the rotor third harmonic space phasor. Then, the references for amplitude and

angle of the first and third harmonic rotor flux linkage phasors are compared with the actual values in the machine, and the errors are multiplied by the corresponding rotor control weights. Finally, the results of these operations are the inputs *dt1, dp1, dt3, dp3* to the rotor Multiphase Rotor Angle and Flux Controller (MRAFC) block, which also has the structure of Figure 6.

To synthetize and highlight the hard core of the diagram in Figure 8 let us consider as a first step only the fundamental waves. The input data required to operate the rotor converter are, in summary, the magnitude and angle errors of the rotor flux linkage space phasor. In turn, the input data required to operate the stator converter are the magnitude and angle errors of the stator flux linkage space phasor (this last one, that is, the error of the stator flux linkage space phasor orientation with respect to the rotor flux linkage phasor is indirectly given by the required fundamental torque, according to (17)). This way, both fundamental flux linkage space phasors can be forced upon the stator and the rotor by the corresponding converter. This scheme is repeated for all of the harmonic waves in a decoupled way (for the harmonics, the rotor phasor angle is given by specifying the position of the harmonic magnetizing space wave with respect to the fundamental one). And since, moreover, the modules of all of the harmonic flux linkage phasors are always kept constant, there are no pulsational emfs induced in the machine (GAFTOC principle) and, therefore, the torque contribution of the fundamental and the harmonics can be adjusted independently and very quickly.

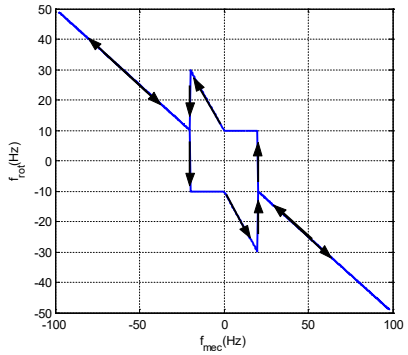

Figure 9. Rotor frequency profile

Let us introduce a final and brief comment on the rotor frequency vs. speed profile chosen, Figure 8 and Figure 9. This profile, as explained in [4], assures a balanced power share between the stator and the rotor converters and, at the same time, avoids operation at voltages close to converter ceiling voltage (higher frequencies) but maintaining a similar minimum converter frequency both in stator and rotor all over the speed range. A minimum frequency is important to allow accurate estimation of stator and rotor total flux linkage space phasors with simplified machine models.

5. Simulation Results and Discussion

There are several proposals to distribute the torque and flux linkages between the fundamental and the higher harmonic waves in asynchronous multiphase machines [28,29]. All of them have in common that the increase in machine torque is achieved through an increase of the fundamental air gap induction, Figure 10. This way, the machine pole flux is increased too. However, as the maximum value of the air gap magnetic induction is kept equal to that of sinusoidal operation, iron losses are accepted in the mentioned proposals to be scarcely affected. In accordance with these ideas, in this paper the third harmonic induction amplitude has been set to 0.18 of the fundamental wave. This results in a third harmonic torque contribution equal to 3.6% that of the fundamental for a total rms current equal to the one for sinusoidal operation.

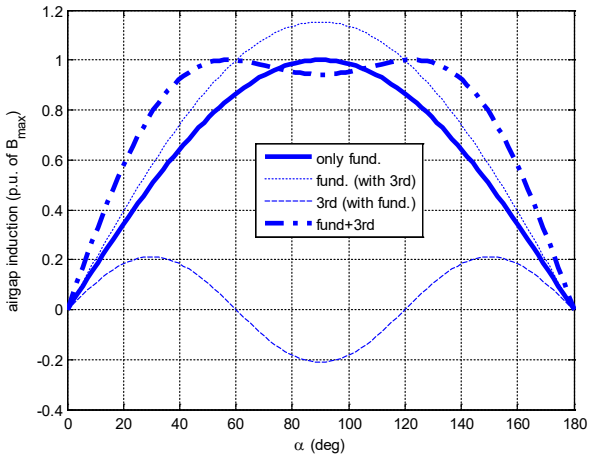

Figure 10. Air gap induction wave in a 5-phase machine for sinusoidal (solid line) and quasi-square wave operation (dash-dor line). The maximum value of the air gap induction is equal in both cases.

An extensive set of simulations, the results of some of which are displayed below, have been carried out on a five phase machine using Matlab-Simulink. The main machine parameters are listed in table 1.

Table 1 5.5 kW Drive Main Parameters

General	P=5,5kW, n=1438 rpm, η=0.863, cos φ=0.83 J=0.05 kg·m^2, stator and rotor phases: 5 Converter maximum frequency 8 kHz
Stator	U=138 V, I=10.9 A, f=50 Hz R=0.75Ω, L_σ=4.3mH (leakage,), $L_{\mu,1}$=80.4mH (main ind.) ; concentrated winding (one full pitch coil per pole pair).
Rotor	U=138 V, I=9.4 A, f=50 Hz R=0.54Ω, L_σ=3.1mH (leakage) $L_{\mu,1}$=80.4mH (main ind.); concentrated winding (one full pitch coil per pole pair).

The first point to note, Figure 11, is the ability of the control system to comply with one of its main objectives: the fast and decoupled control of the torques produced by the harmonics 1 and 3, while keeping constant the stator and rotor flux linkages space phasors magnitudes of both fundamental and third harmonic, as required by the GAFTOC. In the first row of graphs the step torque changes attest the very high dynamic response to torque reference changes while in the second and third row the excellent decoupling between torque and flux linkage, both for stator and rotor and for the fundamental and third harmonic, is clearly apparent. The last row of graphs shows on the one hand (by comparison with the first row) the direct relationship between torque and q-axis current and, on the other hand, the approximate sharing of the magnetizing current between stator and rotor. (Although only the stator d-axis current is plotted, it can be seen how it is approximately kept to

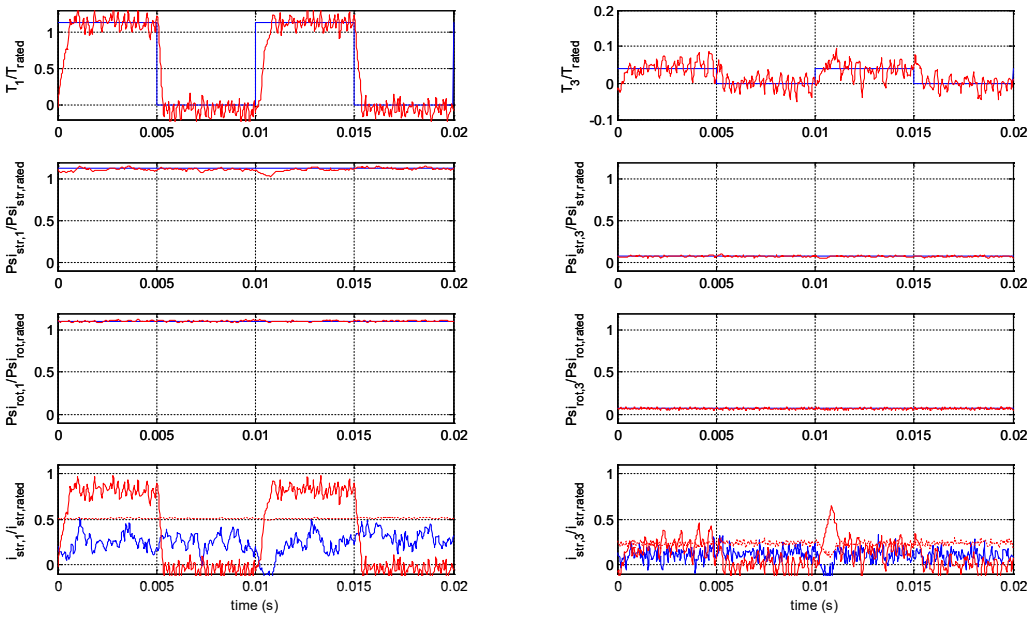

Figure 11. Rated torque step response at rated speed: left fundamental, right third harmonic. Up: Torque reference and actual value. Center: stator (above) and rotor (below) total flux linkage magnitude. Bottom: stator d, q currents and machine magnetizing current (dotted).

one half of the machine magnetizing current, meaning that the rotor provides the remaining half).

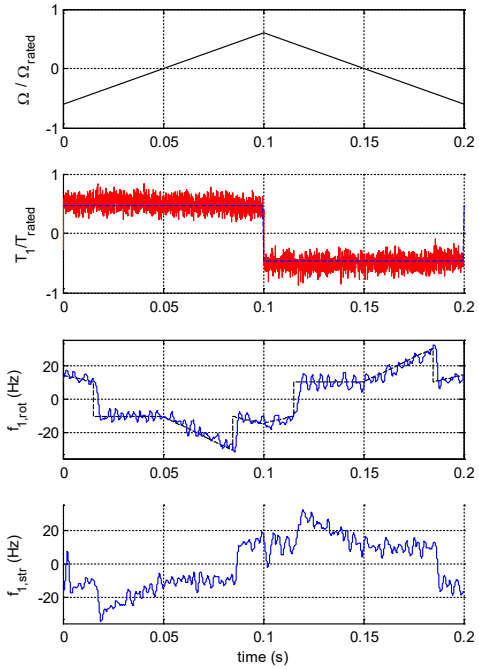

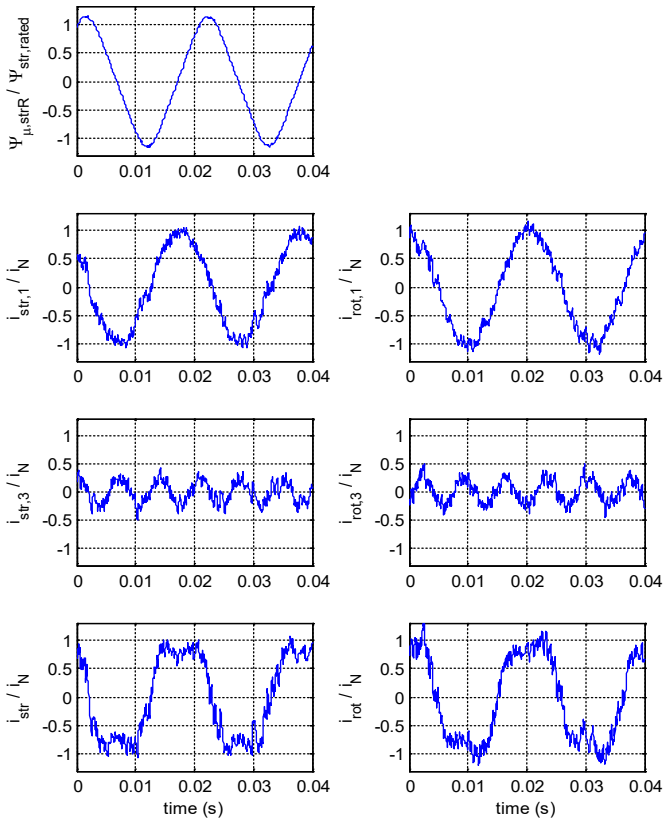

Figure 13. Machine operation at full load and twice rated speed. Left: Normalized magnetizing flux linkage of stator phase R (top), stator phase currents for sequence 1 (above) and 3 (center) and total phase current (below). Right: rotor phase currents for sequence 1 (above) and 3 (center) and total phase current (below).

Figure 13 shows the stator and rotor phase currents at full load (rated stator rms current) and twice rated speed operation and the quasi-triangular magnetizing flux linkage of phase R. This figure shows, for stator and rotor, the current share between the

fundamental and the third harmonic to provide the total required machine torque. The quasi-square waveform of the total phase current (as opposed to the sinusoidal current waveforms only possible up to now with previous multiphase DTC) clearly shows the third harmonic contribution to the torque enhancement achieved not exceeding the rms current rated value. It is worth noticing how a total torque of 116% of rated torque requires a relatively modest third harmonic torque of about 4% of rated torque to be added to the 112% of rated torque provided by the fundamental space waves.

The torque increase because of the third harmonic contribution appears also clearly when the 5-phase drive is compared with an equivalent three-phase drive with the same rated power and phase current as in Fig. 14 and Fig. 15. The right side in both figures shows the performance of the conventional 3-phase DCFAM under DTSRFC (as introduced in [4] and also explained in [6]) with the expected sinusoidal phase flux linkage and phase currents both in stator and in rotor. On the contrary, the left side in Fig. 15 clearly shows the quasi-triangular phase flux linkage and the associated quasi square-wave stator and rotor phase currents as in Figure 13. The reduced maximum current for the 5-phase drive (due to the harmonic content with equal rated rms total current) can be clearly appreciated also in comparison with the sinusoidal phase current in the 3-phase drive.

One can easily check that the results on the right side of Fig. 14 and Fig. 15 are a particular case of the results on the left side. Mathematically: reducing the degrees of freedom in the DTC of the multiphase DCFAM while keeping the GAFTOC strategy results in the DTC scheme of the three-phase machine (no contribution of the harmonic torques, associated to the fictitious harmonic machines). Three-phase DCFAM have already been dealt with in the literature, since they show the great advantage over three-phase IM and PMSM of having an extended operating range of up to twice the rated speed while keeping the ability to provide full rated torque and a balanced power share between the stator and rotor inverters. Yet, multiphase DCFAM have not been dealt with so far, not even in the simpler case of only fundamental wave operation. This problem has been addressed in this paper in the general case (arbitrary odd number of phases and contribution of harmonic torques). And, as shown by the figures and discussion in this section, the system presented keeps the main advantages of both the three-phase DCFAM (doubling the power) and of the multiphase configuration (greater fault tolerance, reduced ratings of the electronic converters components and torque enhancement through harmonics contribution).

6. Conclusions

Constant air gap multiphase PMSM, IM and DCFAM can be decomposed into an equivalent set of three-phase machines mechanically coupled but electrically independent. Thus, their torques can be controlled independently. On the other hand, each multiphase inverter enables for each one of these fictitious machines two degrees of freedom, so that magnitude and angle of either $\boldsymbol{\Psi}_{str}$ or $\boldsymbol{\Psi}_{rot}$ can be adjusted in each machine trough the inverter.

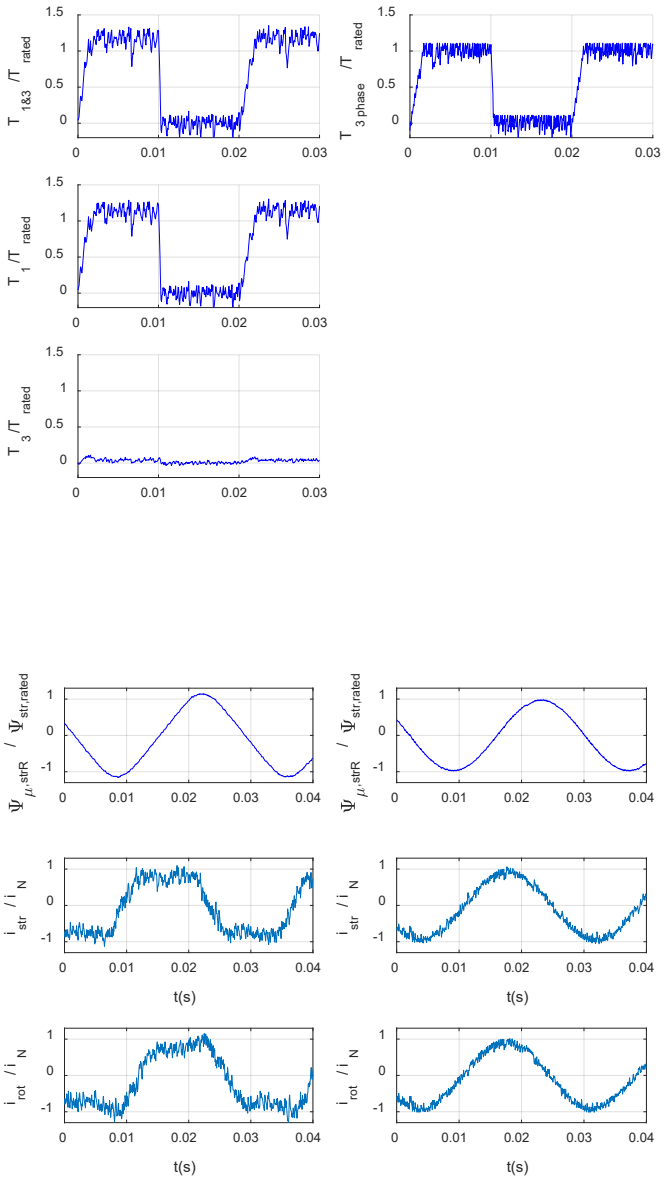

Figure 15. Direct torque and stator and rotor flux control of a DCFAM steady state operation at rated phase current: comparison for 5-phase (left) and 3-phase (right) drives. Top: stator phase flux linkage in p.u. of rated phase flux linkage. Middle and bottom: stator and rotor phase current, respectively, in p.u. of rated phase maximum current.

fictitious machines. GAFTOC states that the magnitudes of both $\boldsymbol{\Psi}_{str}$ and $\boldsymbol{\Psi}_{rot}$ of each machine must remain constant and that its torque must be adjusted by means of the angle between $\boldsymbol{\Psi}_{str}$ and $\boldsymbol{\Psi}_{rot}$, This strategy, with two inverters available, still leaves one degree of freedom to completely define the $\boldsymbol{\Psi}_{str}$ and $\boldsymbol{\Psi}_{rot}$ references. This degree of freedom has been used, in the main machine (which provides most of the power) to force a balanced power share between both inverters, and, in the remaining machines, to suitably align their magnetizing flux linkage space waves to the fundamental one.

In addition, in order to be able to apply the mentioned DTC to a DCFAM with an arbitrary odd number of phases, this paper also presents a new and very general switching-table based mode of operation for multiphase VSIs that, moreover, is computationally very light and can be easily extended to multilevel inverters.

Previous switching-table based mode of operation for multiphase VSIs enabled to take profit only of the machine fundamental wave (harmonic suppression schemes).

The whole system has been tested through an extensive set of simulations in a five phase DCFAM. They show that, as predicted by the theory, a very fast torque control of the DCFAM is possible: a) throughout the whole operational speed range b) keeping an excellent decoupling between torque and flux linkage, and c) independently for the fundamental and the harmonic torques. As to this point it should be underlined that the control of multiphase DCFAM is far more complete and versatile than that of multiphase IM and PMSM, simply because the degrees of freedom to design the control system are now double than before (two inverters instead of one). Reducing in different ways the degrees of freedom in the DTC of the DCFAM while keeping the GAFTOC strategy leads to the different DTC structures presented in the literature for the classic three-phase machines.

The main disadvantage of the DCFAM versus the alternative with IM or PMSM is the need for a slip rings rotor. However, even if the drive design around an IM or a PMSM were always the best option (which is dubious for high power applications), the multiphase machine decoupling and the fast and independent harmonic torque control proposed in this paper can still be applied to the DTC of multiphase IM and PMSM to great advantage.

This research did not receive any specific grant from funding agencies in the public, commercial, or not-for-profit sectors.

Conflict of Interest

The authors declare no conflict of interest.

References

[1] E. Levi, R. Bojoi, F. Profumo, H. Toliyat, S. Williamson, "Multiphase induction motor drives - a technology status review," Electric Power Applications, IET, vol. 1, no. 4, pp. 489–516, July 2007.

[2] Y. Kawabata, E. Ejiogu, T. Kawabata, "Vector-controlled double-inverter-fed wound-rotor induction motor suitable for high-power drives," Industry Applications, IEEE Transactions on, vol. 35, no. 5, pp. 1058–1066, 1999.

[3] G. Poddar V. T. Ranganathan, "Direct torque and frequency control of double-inverter-fed slip-ring induction motor drive," Industrial Electronics, IEEE Transactions on, vol. 51, no. 6, pp. 1329–1337, Dec 2004.

[4] J. Martinez-Roman L. Serrano-Iribarnegaray, "Direct torque and stator and rotor flux control doubly converter fed induction machines," in IEEE Mediterranean Electrotechnical Conference, 2006. MELECON 2006. IEEE, 2006, pp. 1158–1161.

[5] L. Serrano-Iribarnegaray, "Space phasor theory and control of multiphase machines through their decoupling into equivalent three-phase machines," Electrical Engineering, vol. 96, no. 1, pp. 79–94, 2014.

[6] L. Serrano-Iribarnegaray J. Martinez-Roman, "A unified approach to the very fast torque control methods for dc and ac machines," Industrial Electronics, IEEE Transactions on, vol. 54, no. 4, pp. 2047–2056, Aug 2007.

[7] H. Xu, H. Toliyat, L. Petersen, "Five-phase induction motor drives with dsp-based control system," Power Electronics, IEEE Transactions on, vol. 17, no. 4, pp. 524–533, Jul 2002.

[8] L. Zheng, J. E. Fletcher, B. W. Williams, X. He, "A novel direct torque control scheme for a sensorless five-phase induction motor drive," IEEE Transactions on Industrial Electronics, vol. 58, no. 2, pp. 503–513, Feb 2011.

[9] D. Casadei, G. Serra, A. Tani, L. Zarri, "Direct torque control for induction machines: A technology status review," in Electrical Machines Design Control and Diagnosis (WEMDCD), 2013 IEEE Workshop on, March 2013, pp. 117–129.

[10] M. Bermúdez, H. Guzmán, I. González-Prieto, F. Barrero, M. J. Durán, X. Kestelyn, "Comparative study of dtc and rfoc methods for the open-phase fault operation of a 5-phase induction motor drive," in IECON 2015 - 41st Annual Conference of the IEEE Industrial Electronics Society, Nov 2015, pp. 002702–002707.

[11] X. Kestelyn, E. Semail, D. Loroil, "Direct torque control of multi-phase permanent magnet synchronous motor drive: application to a five-phase," in IEEE International Conference on Electric Machines and Drives, 2005., May 2005, pp. 137–143.

[12] Y. Gao L. Parsa, "Modified direct torque control of five-phase permanent magnet synchronous motor drives," in APEC 07 - Twenty-Second Annual IEEE Applied Power Electronics Conference and Exposition, Feb 2007, pp. 1428–1433.

[13] A. Yousefi-Talouki, S. A. Gholamian, M. Yousefi-Talouki, R. Ilka, A. Radan, "Harmonic elimination in switching table-based direct torque control of five-phase pmsm using matrix converter," in 2012 IEEE Symposium on Humanities, Science and Engineering Research, June 2012, pp. 777–782.

[14] K. D. Hoang, Z. Q. Zhu, M. Foster, "Optimum look-up table for reduction of current harmonics in direct torque controlled dual three-phase permanent magnet brushless ac machine drives," in 6th IET International Conference on Power Electronics, Machines and Drives (PEMD 2012), March 2012, pp. 1–6.

[15] X. Ma, Y. Yu, H. Zhang, W. Wang, L. Liu, "Study on direct torque control of dual y shift 30 degree six-phase pmsm," in 2015 IEEE 10th Conference on Industrial Electronics and Applications (ICIEA), June 2015, pp. 1964–1968.

[16] K. D. Hoang, Y. Ren, Z. Q. Zhu, M. Foster, "Modified switching-table strategy for reduction of current harmonics in direct torque controlled dual-three-phase permanent magnet synchronous machine drives," IET Electric Power Applications, vol. 9, no. 1, pp. 10–19, 2015.

[17] Y. Zhao T. Lipo, "Space vector pwm control of dual three-phase induction machine using vector space decomposition," Industry Applications, IEEE Transactions on, vol. 31, no. 5, pp. 1100–1109, Sep 1995.

[18] H.-M. Ryu, J.-H. Kim, S.-K. Sul, "Analysis of multiphase space vector pulse-width modulation based on multiple d-q spaces concept," Power Electronics, IEEE Transactions on, vol. 20, no. 6, pp. 1364–1371, Nov 2005.

[19] D. Casadei, D. Dujic, E. Levi, G. Serra, A. Tani, L. Zarri, "General modulation strategy for seven-phase inverters with independent control of multiple voltage space vectors," Industrial Electronics, IEEE Transactions on, vol. 55, no. 5, pp. 1921–1932, May 2008.

[20] O. Lopez, D. Dujic, M. Jones, F. Freijedo, J. Doval-Gandoy, E. Levi, "Multidimensional two-level multiphase space vector pwm algorithm and its comparison with multifrequency space vector pwm method," Industrial Electronics, IEEE Transactions on, vol. 58, no. 2, pp. 465–475, Feb 2011.

[21] G. Carrasco C. Silva, "Space vector pwm method for five-phase two-level vsi with minimum harmonic injection in the overmodulation region," Industrial Electronics, IEEE Transactions on, vol. 60, no. 5, pp. 2042–2053, May 2013.

[22] O. Lopez, J. Alvarez, J. Doval-Gandoy, F. Freijedo, "Multilevel multiphase space vector pwm algorithm," Industrial Electronics, IEEE Transactions on, vol. 55, no. 5, pp. 1933–1942, May 2008.

[23] J. Alvarez, O. Lopez, F. Freijedo, J. Doval-Gandoy, "Digital parameterizable vhdl module for multilevel multiphase space vector pwm," Industrial Electronics, IEEE Transactions on, vol. 58, no. 9, pp. 3946–3957, Sept 2011.

[24] I. Takahashi T. Noguchi, "A new quick-response and high-efficiency control strategy of an induction motor," Industry Applications, IEEE Transactions on, vol. IA-22, no. 5, pp. 820–827, Sept 1986.

[25] L. Gao, J. E. Fletcher, L. Zheng, "Low-speed control improvements for a two-level five-phase inverter-fed induction machine using classic direct torque control," IEEE Transactions on Industrial Electronics, vol. 58, no. 7, pp. 2744–2754, July 2011.

[26] R. Karampuri, J. Prieto, F. Barrero, S. Jain, "Extension of the dtc technique to multiphase induction motor drives using any odd number of phases," in 2014 IEEE Vehicle Power and Propulsion Conference (VPPC), Oct 2014, pp. 1–6.

[27] E. Semail, A. Bouscayrol, J.-P. Hautier, "Vectorial formalism for analysis and design of polyphase synchronous machines," The European Physical Journal Applied Physics, vol. 22, no. 3, pp. 207–220, 2003.

[28] D. Casadei, M. Mengoni, A. Tani, G. Serra, L. Zarri, "Torque maximization in high-torque density multiphase drives based on induction motors," in Energy Conversion Congress and Exposition (ECCE), 2010 IEEE, Sept 2010, pp. 3896–3902.

[29] L. A. Pereira, S. Haffner, L. F. Pereira, R. S. da Rosa, "Torque capability of high phase induction machines with sinusoidal and trapezoidal airgap field under steady state," in Industrial Electronics Society, IECON 2013-39th Annual Conference of the IEEE. IEEE, 2013, pp. 3183–3188.

[30] J.-A. Echeverria-Villar, J. Martinez-Roman, L. Serrano-Iribarnegaray, "Transient harmonic torques in induction machines: measurement and impact on motor performance," Electrical Engineering, vol. 94, no. 2, pp. 67–80, 2012.

ASTES

Advances in Science, Technology and Engineering Systems Journal Vol. 3, No. 4, 45-52 (2018)

www.astesj.com

Special Issue on Multidisciplinary Sciences and Engineering

ASTESJ

ISSN: 2415-6698

A detailed step-by-step electrical parameters identification method for photovoltaic generators using a combination of two approaches

Selma Tchoketch Kebir*, Mohamed Salah Ait Cheikh, Mourad Haddadi

Laboratoire des Dispositifs de Communication et de Conversion Photovoltaïque, Département d'Électronique, École Nationale Polytechnique, 10 Avenue Hassen Badi El Harrach, Algiers, Algeria

ARTICLE INFO

Article history:
Received: 19 May, 2018
Accepted: 02 July, 2018
Online: 11 July, 2018

Keywords :
Photovoltaic Generators
Data acquisition
Identification
Least Squares
Levenberg-Marquardt
PSO algorithm

ABSTRACT

The object of this paper is to identify the unknown electrical parameters of solar photovoltaic generators in real time, through the application of a novel suggested hybrid method. The identification process is discussed with details, about the four steps of identification. In this issue, the first step describes the experimental data acquisition work done to obtain data from a real photovoltaic system. For the second step, a model of a cell's corresponding electrical circuit is selected. In the third step, the estimation of the parameters 'values is done using two combined optimization approaches, such as Levenberg-Marquardt combined with Particle Swarm Optimization. The fourth step describes the validation of the selected model. The benefit of this work compared to those before, is in the use of real data, in the use of smart optimization technics and the hybridization between two methods, which provides best results.

1. Introduction

This paper is an extension of work originally presented in 2017 at the 5th International Conference on Electrical Engineering-Boumerdes (ICEE-B) [1]. In the order to well detail, explain and develop the previous work presented in this latter conference. In nature, many processes can be modelled by a system of mathematical expressions [2]. Models usually contain some unknown parameters. In the object to find the values of these unknown parameters, some real measurements from the system are required, to be compared with the output of the models proposed through minimizing of some errors [3]. This problem is known as the parameters' identification problem. In these systems, there is the process of modeling and after that, there is an identification process of the unknown parameters for the selected model [4]. In this order, we have used this discipline in a solar photovoltaic (PV) system, in order to identify the electrical parameters of the PV generators. These parameters are very necessary for simulating solar PV production's behavior and therefore control it. As the high non-linearity found in PV cell's models, we present in this work, the combination of two optimization algorithms for identifying the electrical PV generator's unknown parameters from real experimental data. The PV parameters identification process for PV generators is shown in the Figure 1 below.

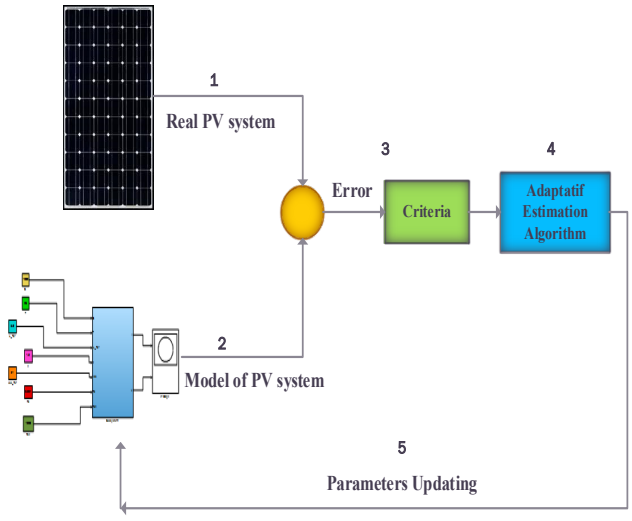

Figure 1. Parameters Identification for PV generators.

The process of PV parameters identification is based on a prediction of the error between the real system and the theoretical model. This error is used with an appropriate algorithm that has to

*Selma TCHOKETCH KEBIR, Ecole Nationale Polytechnique Algiers, Algeria, Email : selma.tchoketch_kebir@g.enp.edu.dz

be modified at each iteration. In this order, the PV parameters are found through the main steps cited below, as illustrated in the above Figure 1:

1- Obtain experimental data from a real PV installed system.

2- Obtain data from a selected model representing a PV system.

3- Minimize the error between the real data and the data of the selected model, using some criteria.

4- Application of an appropriate identification adaptation algorithm.

5- Update the PV parameters values that validate the final selected model representing the real system.

The organization of this paper is as follows: after having introduced the subject in this first section. The second section, gives a state of the art about the PV parameters identification existed methods. Then, the third section focuses on the major steps of PV parameters identification, with more details about each step. Herein, the use of the suggested combined optimization approaches. In the fourth section, a discussion is given concerning the obtained results, before some conclusions in the fifth section.

2. State of the art

In literature, many different methods exist to allow determining the electrical parameters values for the PV generators [5], [6]. Primary, scientific researchers have focuses on the parasitic resistances (series and shunt) determination [7], [8] by the cause of their major influences on the PV performances. Then, it was also observed some influences of all PV electrical parameters on the performances [9], which leads for doing a large number of studies for obtaining their accurate values. The elaborated studies are classified into several categories [5]. Certain methods are classified as theoretical methods such as analytic [10], numeric [11], [12]. Certain other methods are based on an experimental process and are known as identification methods [13], [14], [15]. All methods have their own advantage and inconvenient, to be chosen for using in such application, based on some criteria (complexity, convergence speed, precision …). In this work, we are going to well develop our identification approach.

3. Steps of Photovoltaic Parameters Identification

Parameters identification is an automatic technic, which consists to get a mathematical model, for certain system using some experimental measures. Therefore, the identification process is based on the development of a mathematical representation for a physical system by the use of experimental data [16] [17], through details explained in the main steps cited in the points below of Figure 2.

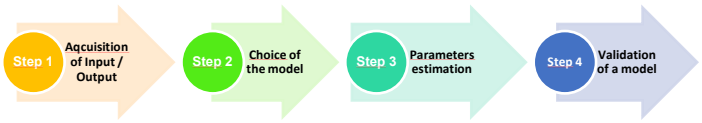

Figure 2. Major steps of parameters identification in systems.

The above major steps of the identification process for PV generators, are well developed in the following points.

2.1. First Step- "Acquiring of Real Data"

A description of our experimental work is giving in this subsection, for obtaining the real PV measured data information [18]. The data acquired issued from a PV system located at our laboratory, (*Laboratoire de Dispositifs de Communication et de Conversion Photovoltaique, LDCCP*). This acquisition work is schematized in Figure 3. The PV system contains a photovoltaic generator, which is composed of four PV panels associated in series, where each panel generate about 55 Watts of power. The measured parameters are the temperature, the solar irradiation, as well as the voltages and currents. In order to collect data, the different components of the proposed PV measurement system are:

- A sensor of temperature 'T', the LM35.
- A sensor of solar irradiation 'G', the pyranometer.
- PV generator associated with the electronic load.

In order to draw the real current-voltage (I-V) curve of PV generators under real conditions, these generators are associated with an electronic load. The process of information reception is made using a computer, which consists of the unit of treatment and control. In this context, we set up an experimental manipulation based on an Arduino-Uno card [19] that allows us the acquisition of data issued from a PV system installed in our laboratory. The transmission of these acquired data to a personal computer is ensured by a USB connection port (serial communication).

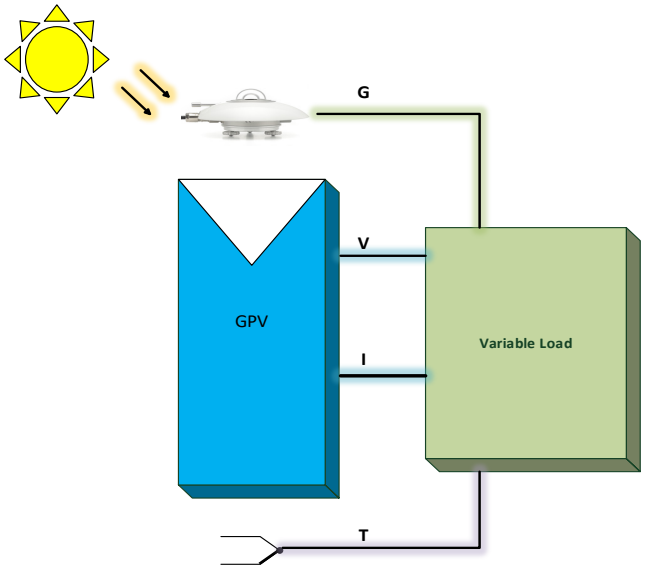

Figure 3. Sensors and PV generator related to a variable load.

The proposed system consists of a set of sensors for measuring both meteorological (e.g. temperature, irradiation) and electrical parameters (photovoltaics voltage and current). The collected data are first conditioned using precision electronic circuits and then interfaced to a PC using a data-acquisition card (Arduino-Uno) [16]. The LABVIEW program is used to further process, display and store the collected data in the PC disk. We have conceived an electronic load based on a MOSFET transistor of power [20]. The variable load allows the measures of a couple of the current-voltage (I–V) along the curve. The obtained current–voltage characteristic (I–V) curve of our photovoltaic generator is

illustrated in Figure 4, which was operated under the real environmental conditions (794.46W/m2, 30.85°C).

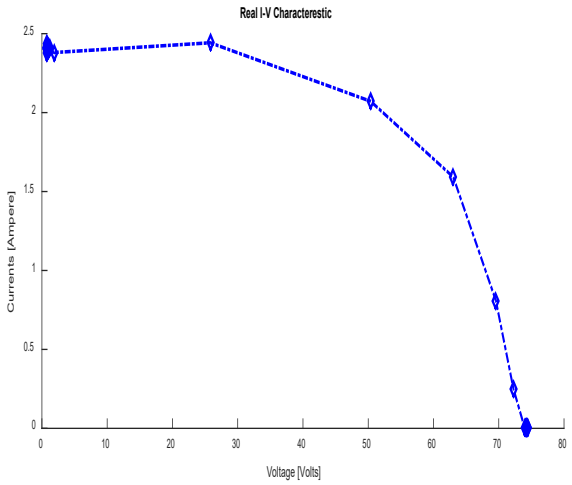

Figure 4. The obtained Current–Voltage experimental curve at (794.46W/m2, 30.85°C) for the four series PV panels of type SM55.

The following *Table I* shows the PV manufacturer's datasheet information of the SM55 PV panel used in this work [21].

Table 1. Specification of Siemens SM55 solar PV panel used, from datasheets under Standard-Test-Conditions : STC (T = 25 °C & G= 1 000 W/m^2).

Parameters		**Mono Crystalline Silicon**
		Panel
Open Circuit Voltage (Volts)	***Voc***	21.7
Short Circuit Current (Ampere)	***Isc***	3.45
Maximum Power Voltage (Volts)	***Vmpp***	17.4
Maximum Power Current (Ampere)	***Impp***	3.15
Maximum Power Point (Watts)	***Pmpp***	55
Number of cells in series	**Ns**	36

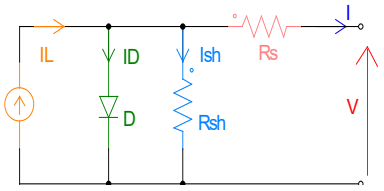

Figure 5. Solar photovoltaic cell's electrical equivalent circuit (The one diode model).

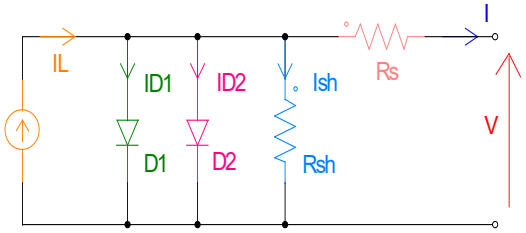

Figure 6. Solar photovoltaic cell's electrical equivalent circuit (The double diode model).

2.2. Second Step- "Selection of the appropriate model"

An accurate mathematical model is an important tool for researchers. The one and double diode PV models, with 5 and 7 unknown parameters respectively, are represented as follow in Figure 5 and Figure 6 [22], [23], [24].

The mathematical equations related the Current-Voltage, (I-V) relationship of the electrical models are given below.

(a) The one diode model

$$I = I_L - I_D - I_{sh} \quad (1)$$

$$I = I_L - I_{ds}.\left(exp\left(\frac{V+R_S.I}{n.V_t}\right) - 1\right) - \frac{V+R_S.I}{R_{sh}} \quad (2)$$

(b) The double diode model

$$I = I_L - I_{D1} - I_{D2} - I_{sh} \quad (3)$$

$$I = I_L - I_{ds1}.\left(exp\left(\frac{V+R_S.I}{n_1.V_t}\right) - 1\right) - I_{ds2}.\left(exp\left(\frac{V+R_S.I}{n_2.V_t}\right) - 1\right) - \frac{V+R_S.I}{R_{sh}} \quad (4)$$

The PV panel contains cells associated in series manners through the mathematical expression below.

$$I = I_L - I_{ds}.\left(exp\left(\frac{V+R_S.I.N_S}{n.V_t.N_S}\right) - 1\right) - \frac{V+R_S.I.N_S}{R_{sh}.N_S} \quad (5)$$

Where:

(a)The one diode model

- I_L: Light current.
- I_{ds}: Diode saturation current.
- n: Diode ideality factor.
- R_s: Series resistance.
- R_{sh}: Shunt resistance.

(b) The double diode model

- I_L: Light current.
- I_{ds1}: Diode saturation current.
- I_{ds2}: Reverse diode saturation current.
- n_1: Diode ideality factor.
- n_2: Second diode ideality factor.
- R_s: Series resistance.
- R_{sh}: Shunt resistance.

The PV Generator contains N_{ms} series branches and N_{mp} parallel branches.

$$I = I_L N_{mp} - I_{ds}.N_{mp}\left(exp\left(\frac{V.N_{mp}+R_S.I.N_S.N_{ms}}{n.V_t.N_S.N_{ms}}\right) - 1\right) - \frac{V.N_{mp}+R_S.I.N_S.N_{ms}}{R_{sh}.N_S.N_{ms}} \quad (6)$$

N_s**:** Number of series cells. N_{ms}: Number of modules in series branches. N_{mp}: Number of modules in parallel branches.

The next Figure 7 shows the PV generator located at our laboratory.

Figure 7. Photovoltaic system mounted at our laboratory.

In our work (Figure 8), the PV generator has N_s of about ***36***, N_{ms} of about ***4*** and N_{mp} is ***1***.

2.3. Third Step- "Parameters estimation"

In this step, the application of the chosen optimization algorithm to identify and obtain the optimal values of PV parameters. The idea is based on a prediction error between the output of the real PV process and the output predicted by the PV model [3], as explained before. This prediction error is used by a Parametric Adaptation Algorithm (A.A.P), which at each iteration will modify the parameters of the model in order to minimize the error, which will be detailed through the next subsections, as schematized in Figure 8.

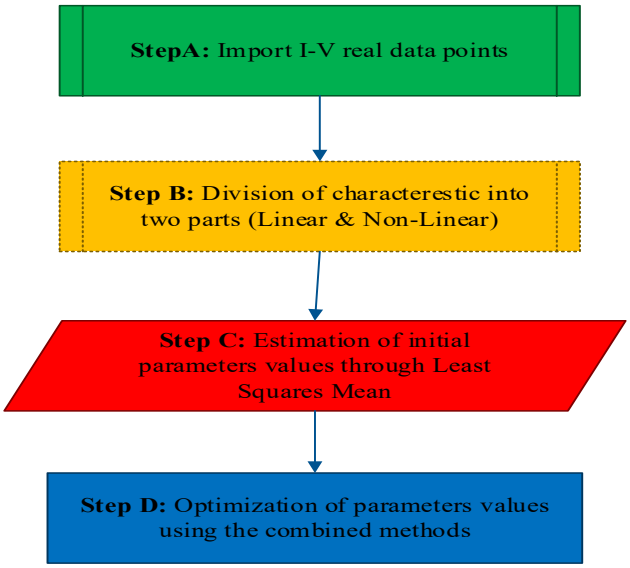

Figure 8. Major steps to estimate, determine and optimize the PV parameters values.

These points will be well explained in the next subsections.

2.3.1. The Least Squares Mean (LSM)

Different approaches allow the **initial estimate** of parameters values such as Least Squares (LS), Least Squares Mean (LSM), Recursive Least Squares (RLS), Recursive Extended Least Squares (RELS) and Newton stochastic (NS) [25]. In an optimization algorithm, the step of initialization of the unknown PV parameters is very necessary for converging to solution. In this regard, we have chosen for obtaining the initial values of our PV parameters the Least Squares Mean (LSM). The benefit of this developed LSM approach is in her non-iterative process. Then, the obtained initial values will be optimized through our developed hybrid approach (Levenberg-Marquardt with PSO). The curve characteristic of the PV generator has two distinct regions as shown in Figure 9, Linear and Non-linear parts. For the linear part, the LSM method is applied merely, while in the non-linear part, it is done through a suitable approximation by a linearization in a logarithmic way [26].

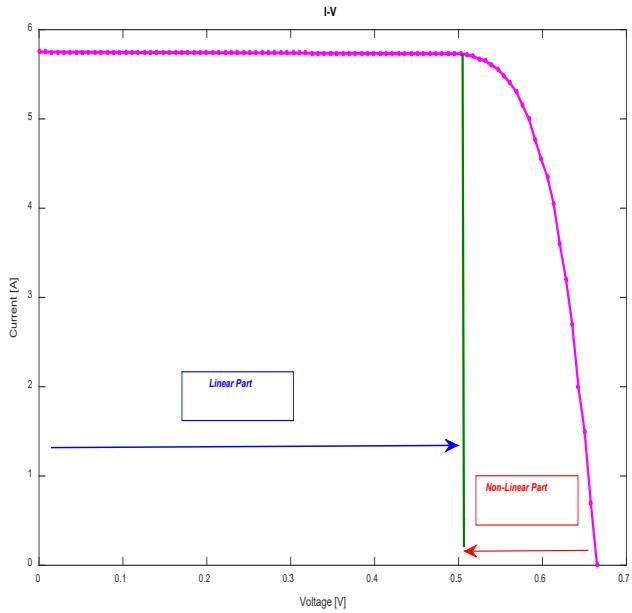

Figure 9. Linear and Non-Linear parts of the I-V characteristic.

The Least Squares Mean approach is based on the minimization of a quadratic function defined as below [14].

$$G = \sum_{i=1}^{n} \varepsilon(i)^2 \quad (7)$$

Where ε is defined as the prediction error between the PV model and the real PV system [14].

$$G = \sum_{i=1}^{n} [I_{Real}(i) - I_{Model}(i)]^2 \quad (8)$$

In order to identify the PV parameters from the real I-V characteristics, we fitted to the best the model to the real (I-V) data, through the minimization of squared errors between the theoretical and experimental curves [27]. In this regard, the cost function used in the optimization process is the Sum of Squared Error (SSE) [28]. Where I_{Model} is the output vector of the PV model, I_{Real} is the PV measured process output and N is the total number of the measured points.

$$G(I,V,X) = \sum_{i=1}^{n} [I_{Real}(i) - f(I,V,X)_i]^2 \quad (9)$$

Where: X is a vector that contains the PV parameters, for example, $\{I_L, I_{ds1}, I_{ds2}, n_1, n_2, R_s, R_{sh}\}$, in the two-diode model. The minimum of Sum Squared Errors "SSE" leads to optimal values of the PV parameters [28]. The minimization of the objective function cannot be done in analytically way due to the strong nonlinearity of the I-V curve characteristics. Therefore, the numerical methods for the nonlinear regression based on the least squares principle are more appropriate to minimize such function.

2.3.2. The Levenberg-Marquardt (LM)

The traditional technic of Levenberg-Marquardt contains inside its process two technics declined from Gradient orders such as the steepest descent and the Gauss-Newton with their complementary features [29]. Generally, the LM approach starts through the steepest descent technic because of her low sensitivity for initial parameters values. Then, after calculating the parameters values and near approaching to the final solution, the Gauss-Newton technic take over and lead to end of the LM process, with a fast convergence. The control parameter δ called damping factor is the responsible parameter in the LM approach that allows switching from steepest descent to Gauss-Newton. The PV parameters to be determined as in [30], are updated at each iteration using the following expression [29].

$$X_{k-1} = X_k - \left[\frac{J'\varepsilon}{J'J+\delta J}\right]_{X=X_k} \quad (10)$$

Where

- J : Jacobian matrix $\left[\frac{\partial f(x)}{\partial x}\right]_{X=X_k}$ which contains a derivative for the function $f(I,V,X)$ regarding each parameter.
- I: Identity matrix.

The damping factor, which his value must be found at each iteration of Levenberg-Marquardt approach, is considered as a crucial factor in the convergence process of the algorithm, for this reason we optimize their value by using PSO approach.

2.3.3. The Particle Swarm Optimization approach (PSO)

This subsection focuses on the evolution study of the function $G(I,\ V,\ X,\ \delta)$, indicated by $G(\delta)$ for X fixed at X_k, regarding many diverse values of the damping factor, at each iteration of the Levenberg-Marquardt algorithm. Herein, it is observed that at each iteration, a presence of various local minimums of $G(\delta)$. For this reason, and in order to achieve the global minimum of $G(\delta)$ corresponding to the best minimizing of the objective function $G(I,\ V,\ X)$, we suggest using the PSO approach. The basic idea of this latter approach was inspired from social behaviour of certain animals such as birds, fishes, and ants and so on. The PSO process is like the natural process existing in groups when they are communicating together, such as a group of birds when they search for migration way or such as ants when they search for food. Herein, it is observed that those animals or insects do not know their best position. Consequently, if a certain member can find the best way to go and achieve the objective, the rest of members, will follow [31]. For mathematical modelling of PSO approach, the population is called a swarm, the individuals are termed as particles and the objective function to be optimized is called fitness. Each particle possesses:

- Its own position

$$P(i+1) = P(i) + V(i+1) \quad (11)$$

- Its own velocity

$$V(i+1) = w * V(i) + c_1 * \left(PL_{best} - P(i)\right) + c_2 * \left(PG_{best} - P(i)\right) \quad (12)$$

- Its neighbourhood (Local and Global)

The local best position is calculated as:

$$PL_{best}(i) = \begin{cases} PL_{best}(i-1) & if\ F(P(i)) \geq F(PL_{best}(i-1)) \\ P(i) & if\ F(P(i)) < F(PL_{best}(i-1)) \end{cases} \quad (13)$$

The global best position is calculated as:

$$PG_{best} = min\left\{F(PG_{best}1), F(PG_{best}2), \ldots, F(PG_{best}N)\right\} \quad (14)$$

The following Flowchart, Figure 10, shows the major steps of the PSO's algorithm.

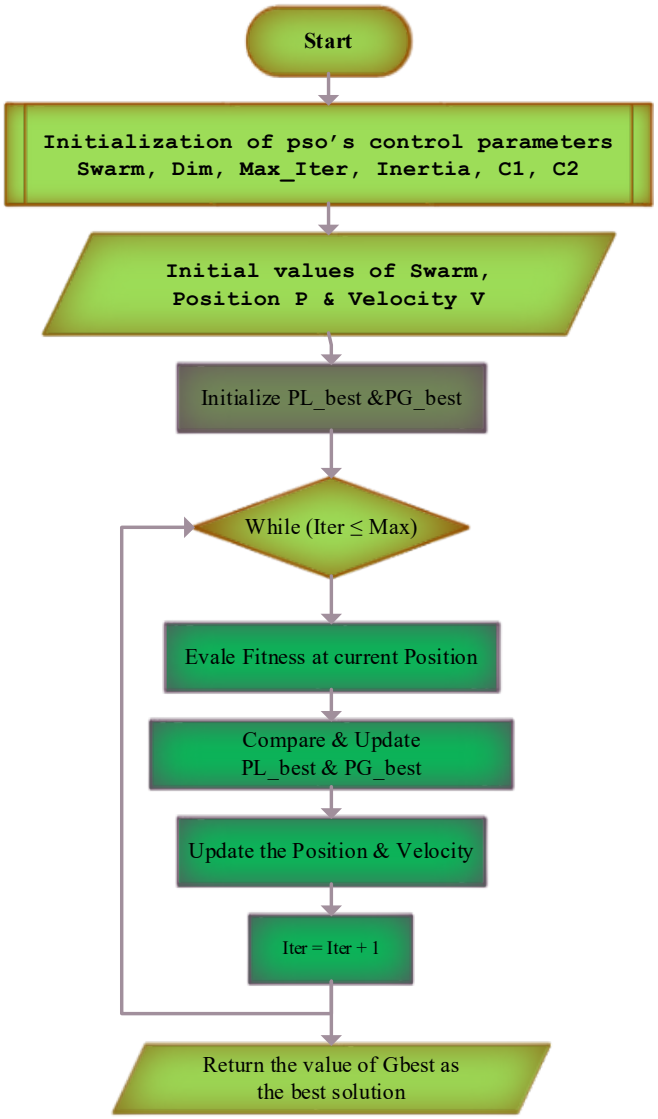

Figure 10. Flowchart of the general steps of PSO algorithm.

This algorithm requires a number of parameters to be set, namely, Inertia W, velocity V, position P, local and global components C_1 & C_2, Number of search agents (the swarm of N visited sites), Maximum number of iteration and the stopping criterion.

2.3.4. *The hybridization of LM with PSO*

The PV identification process, including initialization of PV parameters values through LSM and then optimize their values through the combined Levenberg-Marquardt with Particle-Swarm-Optimization (LM-PSO) developed approach is presented step by step, in what follows Figure 11.

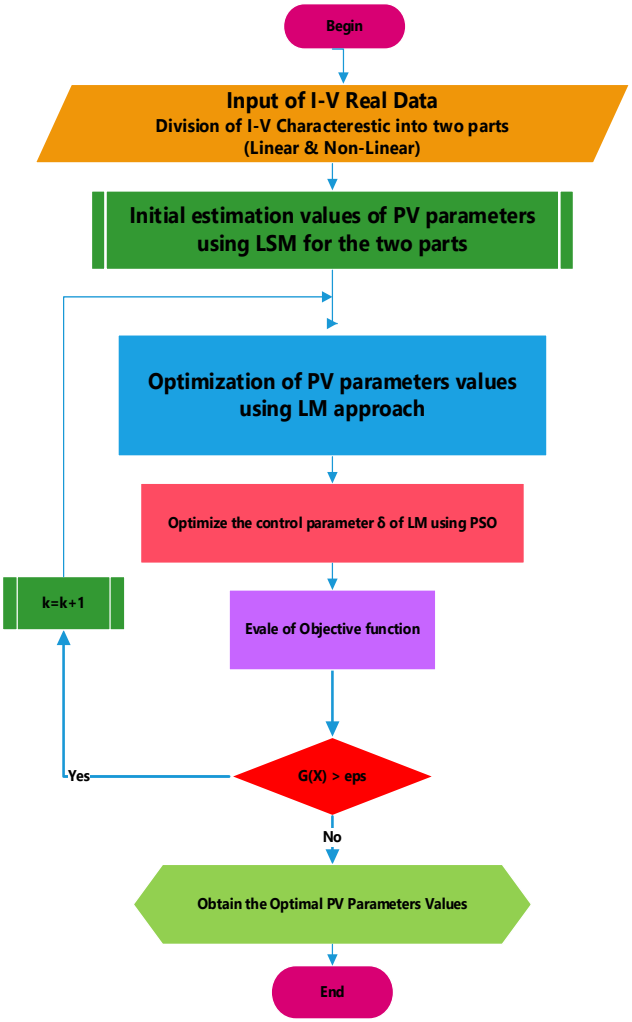

Figure 11. PV parameters identification steps using the hybrid LM approach with PSO approach.

The organigramme of Figure 11 resume the PV parameters identification steps done in this work. After obtaining real data through the acquisition work we used them in a process of algorithms, such as the LSM and the hybrid optimization approach. The advantage of hybridization of two optimization technics is observed in the optimization process of the damping factor of the LM technic, at each iteration, using the PSO technic.

2.4. *Fourth Step "Validation of the model"*

After the estimation process, the obvious query is whether the derived model is adequate for its intended use or not. This is the subjective and overall hard problem of model validation [32]. The sound way to attack the matter is to confront the model with all available type of information, including a priori knowledge, experimental data, and experience of the used model. The selected PV model from the steps before will be validated in this final identification step, after attaining the final obtained results and once fitting all of the entire curve characteristics. The developed approach was tested for other real data of PV cells such as (A-300 of SunPower) as shown in the Figure 12 below, for the one diode model, at STC: Standard-Test-Conditions (T=25°c & G=1000W/m^2).

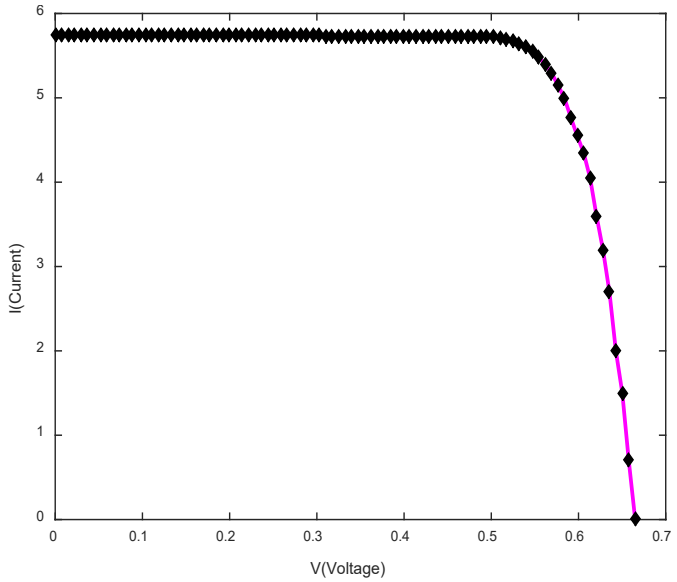

Figure 12. The fitted I-V curve characteristic for the (A-300 SunPower) solar PV cell at STC.

From the above Figure 12, it is clear that once obtaining a good confrontation between the two curves, the model is well chosen to represent the real system.

4. Results & Discussions

This section presents the results obtained for identifying PV parameters values, using the developed combined approach. The following Table II illustrates the results obtained for the electrical PV parameters values of the generator installed in our Laboratory (LDCCP).

Table 2. The obtained parameters values from our developed approach for PV generator.

(a) The one diode model

Parameters	*Obtained values*
I_L	2.45
I_{ds}	3.166611e-07
n	1.279182
R_s	0.036461
R_{sh}	53.271523

(b) The double diode model

Parameters	*Obtained values*
I_L	2.45
I_{ds1}	3.166611e-07
I_{ds2}	3.266611e-07
n1	1.279182
n2	1.379182
R_s	0.036461
R_{sh}	53.271523

The two above tables show that the obtained values for PV parameters models have good values as compared to the values mentioned in literature [33]. The final curves results that validate the model selected for representing our PV generator's behavior, are shown in the fitting I-V curves below, Figure 13.

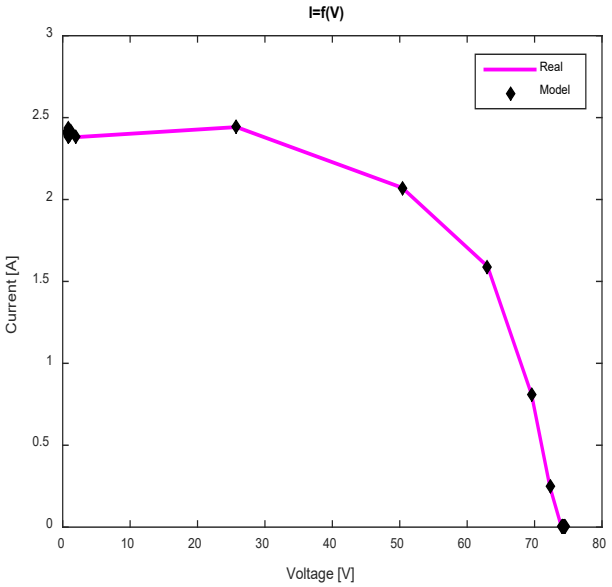

Figure 13. The fitted final I-V curve characteristic for our PV generator (4 associated modules in series of SM55).

It is clear from Figure 13 that the two curves (from the model and the real systems) are well fitted and adjusted. Therefore, the selected model is approximately near of the real behavior of PV generator.

5. Conclusion

In this paper, a detailed study is provided for determining, estimating, identifying and obtaining of the electrical PV parameters values in real time, through combining two algorithms (Levenberg-Marquardt with Particle-Swarm-Optimization). The novelty of this method is that it uses least-squares regressions to initialize the PV parameters values before optimizing their values. The process of identification was elaborated with details, containing all of the four basic steps of identification, as data acquisition, selection of model, PV parameters estimation values and model validation. The obtained results show that the developed approach has the capability to achieve higher PV parameters values with a best precision. The effectiveness is proved by the best approximation obtained between the real data and the data predicted from the curve fitted. This work allows as studying the PV generator's behavior under real conditions, through the detailed steps of the identification process.

Conflict of Interest

The authors declare no conflict of interest.

Acknowledgment

The experimental part presented by this paper was done at the LDCCP Laboratory of the Electronic Departement at Ecole Nationale Polytechnique, Algiers, Algeria.

References

[1] S. Tchoketch Kebir, M. S. AIT CHEIKH, M. Haddadi, B. Boumaaraf, "Step by step Parameters Identification for Photovoltaic Generator" in the 5th International Conference on Electrical Engineering – Boumerdes (ICEE-B), Boumerdes, Algeria, 2017.

[2] Karel J. Keesman, System Identification: an introduction, Springer-Verlag London, 2011.

[3] I.D. Landau. System identification in closed loop. Marie Curie Action TOK 3092, 2004.

[4] Gonzalo Cabodevila, Identification des systèmes, École Nationale Supérieure de Mécanique et des Microtechniques, France, 2010.

[5] Ali M. Humada, Mojgan Hojabri, Saad Mekhilef, Hussein M. Hamada, "Solar cell parameters extraction based on single and double-diode models: A review". Renewable and Sustainable Energy Reviews, Volume 56, April 2016, Pages 494-509.

[6] M.A. Hasan S.K. Parida, "An overview of solar photovoltaic panel modeling based on analytical and experimental viewpoint". Renewable and Sustainable Energy Reviews Volume 60, July 2016, Pages 75-83.

[7] J. Thongpron, K. Kirtikara, C. Jivacate. "A method for the determination of dynamic resistance of photovoltaic modules under illumination". Solar Energy Materials & Solar Cells 90 (2006).

[8] Vincenzo d'Alessandro, Pierluigi Guerriero, Santolo Daliento, Matteo Gargiulo. "A straightforward method to extract the shunt resistance of photovoltaic cells from current–voltage characteristics of mounted arrays". Solid-State Electronics 63 (2011) 130–136.

[9] Kenneth, L. Kennerud. "Analysis of Performance Degradation in CdS Solar Cells". IEEE Transactions on aerospace and electronic systems. NOVEMBER 1969.

[10] Valerio Lo Brano, Giuseppina Ciulla, "An efficient analytical approach for obtaining a five parameters model of photovoltaic modules using only reference data". Applied Energy Volume 111, November 2013, Pages 894-903

[11] T.R. Ayodele, A.S.O. Ogunjuyigbe, E.E. Ekoh, "Evaluation of numerical algorithms used in extracting the parameters of a single-diode photovoltaic model". Sustainable Energy Technologies and Assessments Volume 13, February 2016, Pages 51-59.

[12] F.Ghani G.Rosengarten M.Duke J.K.Carson, "The numerical calculation of single-diode solar-cell modelling parameters". Renewable Energy Volume 72, December 2014, Pages 105-112.

[13] Alireza Askarzadeh, Alireza Rezazadeh, "Parameter identification for solar cell models using harmony search-based algorithms". Solar Energy Volume 86, Issue 11, November 2012, Pages 3241-3249.

[14] M.F. AlHajri, K.M. El-Naggar, M.R. AlRashidi, A.K. Al-Othman, "Optimal extraction of solar cell parameters using pattern search". Renewable Energy Volume 44, August 2012, Pages 238-245.

[15] M.Zagrouba, A.Sellami, M.Bouaïcha, M.Ksouri, "Identification of PV solar cells and modules parameters using the genetic algorithms: Application to maximum power extraction". Solar Energy, Volume 84, Issue 5, May 2010, Pages 860-866.

[16] D. Ucinski, Optimal Measurement Methods for Distributed Parameter System Identification: CRC Press; 1 edition (August 27, 2004), 2004.

[17] O. Nelles, Nonlinear System Identification: from classical approaches to neural networks and fuzzy models, 1 ed.: Springer-Verlag Berlin Heidelberg, 2001.

[18] M. Benghanem, "Low cost management for photovoltaic systems in isolated site with new IV characterization model proposed," Energy Conversion and Management, vol. 50, pp. 748-755, 2009.

[19] https://store.arduino.cc/arduino-uno-rev3

[20] H. Belmili, M. S. Ait Cheikh, M. Haddadi, and C. Larbes, "Design and development of a data acquisition system for photovoltaic modules characterization," Renewable Energy, vol. 35, pp. 1484-1492, 2010.

[21] http://www.siemen.co.uk/sm55_sm50.html

[22] Hongmei Tian, Fernando Mancilla-David, Kevin Ellis, Eduard Muljadi, Peter Jenkins, "A cell-to-module-to-array detailed model for photovoltaic panels". Solar Energy, Volume 86, Issue 9, September 2012, Pages 2695-2706.

[23] K. Ishaque, Z. Salam, and H. Taheri, "Simple, fast and accurate two-diode model for photovoltaic modules," Solar Energy Materials and Solar Cells, vol. 95, pp. 586-594, 2011.

[24] Mohsen Taherbaneh ,A. H. Rezaie,H. Ghafoorifard,K. Rahimi Iranian, Iran,M. B. Menhaj &J. M. Milimonfared, "Evaluation of two-diode-model of a solar panel in a wide range of environmental conditions". International Journal of Electronics, Volume 98, Issue 3, 2011.

[25] K. Madsen, H.B. Nielsen, O. Tingleff, Methods for Non-Linear Least Squares Problems, 2nd Edition, April 2004.

[26] K. Bouzidi, M. Chegaar, A. Bouhemadou. "Solar cells parameters evaluation considering the series and shunt resistance". Solar Energy Materials & Solar Cells 91 (2007) 1647–1651.

[27] K.F. Alvina, A.N. Robertson, G.W. Reichc, K.C. Parkd, "Structural system identification: from reality to models". Computers & Structures Volume 81, Issue 12, May 2003, Pages 1149-1176.
[28] Valerio Lo Brano, Giuseppina Ciulla, and Mariavittoria Di Falco. "Artificial Neural Networks to Predict the Power Output of a PV Panel". Volume 2014.
[29] Henri P. Gavin. "The Levenberg-Marquardt method for nonlinear least squares curve-fitting problems". Department of Civil and Environmental Engineering. May 4, 2016.
[30] A. Malaoui, A. Elmansouri, "Deux nouvelles methodes complementaire pour l'extraction optimale des parametres electriques des jonctions". Revue des Energies Renouvelables Vol. 13 N°2 (2010) 199-212.
[31] Satyobroto Talukder. "Mathematical Modelling and Application of Particle Swarm Optimization". Blekinge Institute of Technology, Master of Science, February 2011.
[32] Peter Lindskog. "Algorithms and Tools for System Identification Using Prior Knowledge". Linköping University, September 1994.
[33] Kashif Ishaque, Zainal Salam, Hamed Taheri, Amir Shamsudin. "A critical evaluation of EA computational methods for Photovoltaic cell parameter extraction based on two diode model". Solar Energy 85(9):1768-1779 · April 2011.

ASTES

Advances in Science, Technology and Engineering Systems Journal
Vol. 3, No. 4, 53-58 (2018)
www.astesj.com
Special Issue on Multidisciplinary Sciences and Engineering

ASTES Journal
ISSN: 2415-6698

Dc-link voltage drift compensation in a four level Double-Star Converter using redundant states via phase-shifted PWM strategy

Carlos A. Reusser*

Universidad Tecnica Federico Santa Maria, Department of Electronics, 2390123, Valparaiso, Chile

ARTICLEINFO

Article history:
Received: 07 May, 2018
Accepted: 30 June, 2018
Online: 14 July, 2018

Keywords:
Double-Star Converter
Redundant Switching States
DC-Voltage Drift

ABSTRACT

The following work introduces the use of the available Redundant switching states introduced by the double star four level converter topology, for its application in a medium voltage variable speed drive under a wide range of operation loads. Redundant switching states are obtained using multi-carrier phase-shifted pulse width modulation (PWM) strategy. The converter performance is evaluated in terms of the dc-voltage drift and the torque ripple on the load side, when compared with a classical level-shifted PWM modulation.

1 Introduction

Modern industrial high demanding processes are commonly based on medium voltage induction machines (MV-IM) AC-drives with Field Oriented Control (FOC) scheme [1]. In this field of applications, voltage source multi-level converters are the dominant topologies used in industry, rather than two-level voltage source converters (2L-VSC), in order to reduce the blocking voltage rating of power switches (semi-conductors) as well as conduction losses; harmonic distortion is also minimized ensuring a low rate of torque ripple [2].

Commonly adopted converter topologies for industrial applications are based on cascade H-Bridge (CHB), neutral point clamped (NPC) and flying capacitor (FC) converters [3, 4, 5, 6]. This configurations can be considered as the today's industry standard, because they have reached heir technological maturity proven during the past couple of decades in high demanding industrial processes. However, due the fact that variable speed drives operate within a wide range load profile, most of the time at a fraction of their nominal load, multi-level converters have to deal with this fact, operating in their low modulation index region.

Nowadays, level-shifted PWM (LS-PWM) strategy has become a standard as modulation strategy for multi-level converters. However this modulation technique has a poor performance at low modulation indexes, resulting in dc-link voltage unbalance and the consequent torque ripple in the mechanical drive [7].

The recent diversification of the power electronics market, has open a new scenario for medium voltage converter topologies that can compete with today's industrial standards, improving the disadvantages of classical converter topologies and keeping their advantages (medium voltage capability, low Total Harmonic Distortion (THD) and low semi-conductor stress) [8].

Following this motivation, in this work a double star four level medium voltage converter topology [9] is introduced for its application in medium-voltage AC-drives. However the topology offers many advantages over commonly used industrial standards, it shows the same problem introduced by level-shifted PWM at low modulation index, as reported in [9].

The main contribution of the of the present work, is referred to the use of the redundant switching states available in the double star topology, to deal with the dc-link voltage unbalance, in low modulation index operation. Redundant switching states are synthesized using a phase-shifted PWM (PS-PWM) scheme. The performance of the proposed solution, is analysed via simulation results using an induction machine Filed Oriented Control drive as industrial load.

2 Double Star Multi-level Converter Topology

The double-star converter (DSC) topology is based on a three-level NPC (3L-NPC) configuration, but with the absence of clamping diodes or switches (as in the case of the ANPC) [9]. The converter front-end is arranged

*Corresponding Author: Carlos A. Reusser; Av. Espana 1680, Valparaiso, Chile; carlos.reusser@usm.cl

https://dx.doi.org/10.25046/aj030407

with an 18-pulse diode rectifier, fed from the main grid via a multi-winding zig-zag phase-shifting transformer so that a shifting in -20, 0 and 20 degrees, is achieved. Each diode rectifier is connected to a dc-link capacitor (each level) and are also interconnected in series to each other as presented in Fig. 1.

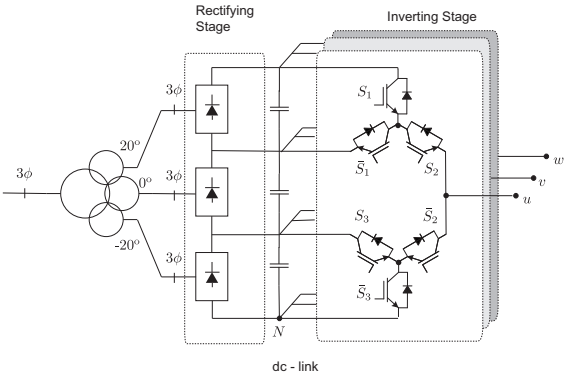

Figure 1: Double Star converter topology

The most remarkable features of this topology are:

1. 6 active switches per phase like the three-level Active Neutral Point Clamped converter (3L-ANPC).

2. 4 voltage levels; one more than the 3L-ANPC and using less number of active switches.

3. no need of clamping diodes or switches (ANPC and NPC topologies), isolated DC-sources (Cascaded H-bridge CHB) or flying capacitors.

The absence of clamping devices makes that each capacitor is in a floating condition, respect to ground, such as in a three level Flying Capacitor converter (3L-FC). The converter fundamental cell (per leg) is presented in Fig. 2 and its corresponding allowed switching states are listed in Table 1

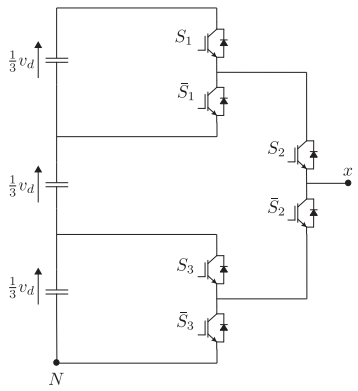

Figure 2: Fundamental converter cell

Table 1: Switch stages per leg (fundamental cell)

#	S_1	S_2	S_3	v_{xN}
1	0	0	0	0
2	0	0	1	$\frac{1}{3}v_d$
3	0	1	0	$\frac{2}{3}v_d$
4	0	1	1	$\frac{2}{3}v_d$
5	1	0	0	0
6	1	0	1	$\frac{1}{3}v_d$
7	1	1	0	v_d
8	1	1	1	v_d

Pulse width modulation techniques for multi-level converters, such as level-shifted PWM (LS-PWM) and phase-shifted PWM (PS-PWM), are based on the use of multiple carriers, as an extension of two-level PWM methods. Level-shifted PWM (LS-PWM) strategy has become a very popular multi-level modulation technique, because it is suitable for any multi-level converter topology and presents low harmonic distortion [10, 11]. The corresponding output voltage is synthesized as given in eqs. (1) - (5)

$$v_{xn} = \frac{1}{3} v_d \left(S_1 + S_2 + S_3 \right) \quad \forall x \in [a, b, c] \tag{1}$$

$$S_1 = \begin{cases} 1 & |u^*_{xn}| \geq |u_{c1}| \\ 0 & |u^*_{xn}| < |u_{c1}| \end{cases} \tag{2}$$

$$S_2 = \begin{cases} 1 & |u^*_{xn}| \geq |u_{c2}| \\ 0 & |u^*_{xn}| < |u_{c2}| \end{cases} \tag{3}$$

$$S_3 = \begin{cases} 1 & |u^*_{xn}| \geq |u_{c3}| \\ 0 & |u^*_{xn}| < |u_{c3}| \end{cases} \tag{4}$$

where u^*_{xn} stands for the voltage reference corresponding to the x phase, and u_{c1}, u_{c2}, u_{c3} for the corresponding level-shifted carriers. Each PWM voltage reference corresponds to a min-max optimization strategy, which ensures improvement of the corresponding duty cycles, thus reaching the maximum possible modulation index by including the effect of common mode voltage, as presented in eq. (5)

$$u^*_{xn} = v^*_{xn} - \frac{1}{2}\left\{ min(v^*_{an}, v^*_{bn}, v^*_{cn}) + max(v^*_{an}, v^*_{bn}, v^*_{cn}) \right\} \tag{5}$$

As presented in eqs. (1) - (4) using the LS-PWM scheme only switching states 1, 2, 4, 8 are synthesized, neglecting the extra degrees of freedom that offers the converter topology with the redundant switching states, presented in Table 1. When low modulation index operation is required (for the proposed topology $m \leq 0.33$), because only the lowest voltage levels are being synthesized, a voltage unbalance in the dc-link starts to build-up, thus requiring the implementation of an additional dc-link voltage balance strategy, as reported in [9, 12, 13].

To deal with the previous described problem, the double star converter extra degrees of freedom can be exploited by implementing a PS-PWM modulation scheme, thus introducing a phase-shifting for the k^{th} carrier denoted by θ_k and given in eq. (6)

$$\theta_k = (k-1)\frac{2\pi}{\ell-1} \quad k \in [1 \dots \ell-1] \tag{6}$$

where ℓ represents the number of voltage levels of the converter. All available switching states shown in Table 1 are then used. Redundant switching states are synthesized, according to eq. (5), (7) - (9), introducing redundant switching states to those allowed in the LS-PWM scheme.

$$S_1 = \begin{cases} 1 & |u^*_{xn}| \geq |u_{c1}(\theta_1)| \\ 0 & |u^*_{xn}| < |u_{c1}(\theta_1)| \end{cases} \tag{7}$$

$$S_2 = \begin{cases} 1 & |u^*_{xn}| \geq |u_{c2}(\theta_2)| \\ 0 & |u^*_{xn}| < |u_{c2}(\theta_2)| \end{cases} \tag{8}$$

$$S_3 = \begin{cases} 1 & |u^*_{xn}| \geq |u_{c3}(\theta_3)| \\ 0 & |u^*_{xn}| < |u_{c3}(\theta_3)| \end{cases} \tag{9}$$

PS-PWM scheme ensures that each capacitor will be delivering energy at its corresponding duty cycle, independently of the modulation index, thus reducing the natural voltage unbalance, without the need of an external voltage drift control scheme.

It also has to be noted, that for this particular application in a medium voltage AC-drive, using field oriented control scheme, the modulation strategy has to deal with the dc-link voltage unbalance, without the use of a voltage-drift control, thus the converter voltage references are set by the FOC control scheme, as a function of speed (within a certain load) and flux.

3 Induction machine Field Oriented Control drive

Squirrel cage induction machines (SCIM) are widely used in heavy industrial environments and applications. The three-phase SCIM mathematical model in the natural stator reference frame $\alpha\,\beta$ in state variables $\boldsymbol{i_s^{(\alpha\beta)}}$, $\boldsymbol{\psi_r^{(\alpha\beta)}}$, ω_r in the state space form (10)

$$\begin{aligned} \frac{d}{dt}\boldsymbol{x}(t) &= f_c\left(\boldsymbol{x(t)}, \boldsymbol{u(t)}\right) \\ \boldsymbol{y(t)} &= g_c\left(\boldsymbol{x(t)}, \boldsymbol{u(t)}\right) \end{aligned} \tag{10}$$

$$\boldsymbol{x(t)} = \begin{bmatrix} i_s^\alpha & i_s^\beta & \omega_r \end{bmatrix}^T \quad \boldsymbol{u(t)} = \begin{bmatrix} v_s^\alpha & v_s^\beta \end{bmatrix}^T$$

$$f_c = \begin{bmatrix} -\frac{1}{\tau_\sigma'} i_s^\alpha + \frac{L_m}{L_r r_\sigma \tau_\sigma' \tau_r} \psi_r^\alpha + \frac{L_m}{L_r r_\sigma \tau_\sigma' \tau_r} \omega_r \psi_r^\beta + \frac{1}{r_\sigma \tau_\sigma'} v_s^\alpha \\ -\frac{1}{\tau_\sigma'} i_s^\beta + \frac{L_m}{L_r r_\sigma \tau_\sigma' \tau_r} \psi_r^\beta - \frac{L_m}{L_r r_\sigma \tau_\sigma' \tau_r} \omega_r \psi_r^\alpha + \frac{1}{r_\sigma \tau_\sigma'} v_s^\beta \\ \frac{L_m}{\tau_r} i_s^\alpha - \frac{1}{\tau_r} \psi_r^\alpha + \omega_r \psi_r^\beta \\ \frac{L_m}{\tau_r} i_s^\beta - \frac{1}{\tau_r} \psi_r^\beta - \omega_r \psi_r^\alpha \\ \frac{3}{2}\frac{p}{J}\frac{L_m}{L_r} \psi_r^\alpha i_s^\beta - \frac{3}{2}\frac{p}{J}\frac{L_m}{L_r} \psi_r^\beta i_s^\alpha \end{bmatrix}$$

$$g_c = \begin{bmatrix} i_s^\alpha & i_s^\beta \end{bmatrix}^T$$

Control goals for the induction motor drive can be summarize as the following:

1. Maximum torque per Ampere operation.
2. Control of nominal flux.
3. Control of rotor speed.

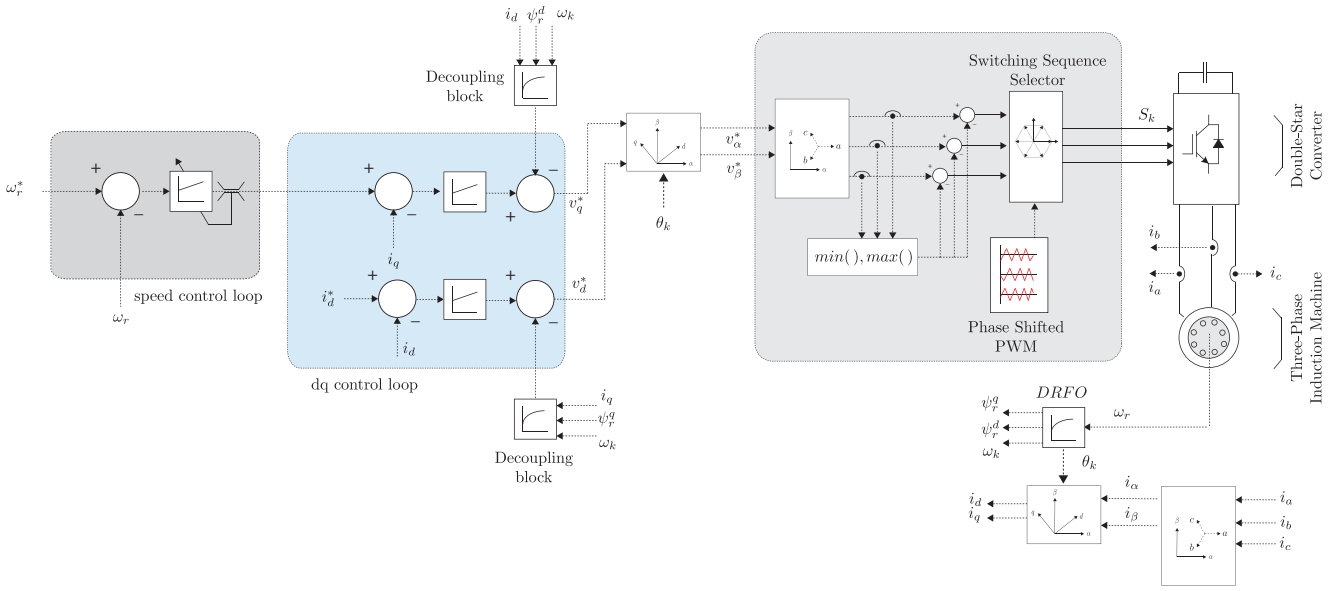

Figure 3: Field Oriented Control scheme with non-linearities compensation

The characteristics of FOC, have made this control strategy the most widely used for high demanding industrial applications [11]. Field Oriented Control (FOC) is based in the decoupling of the current space vector into a flux producing current and a torque producing current [14]. This is achieved by rotating the current space vector $i_s^{\alpha\beta}$ into a synchronous rotating reference frame dq, which is oriented by the rotor flux linkage space vector. Rotation of the state variables is achieved by means of the rotation matrix U given in eq. (11)

$$U = \begin{bmatrix} \cos\theta_k & \sin\theta_k \\ -\sin\theta_k & \cos\theta_k \end{bmatrix} \tag{11}$$

The dynamics in the dq synchronous reference frame are obtained by applying eq. (11) to eq. (10) . State variables $\boldsymbol{\psi}_r^{(dq)}$ $\boldsymbol{i}_s^{(dq)}$ can then be obtained as in (12), (13).

$$\boldsymbol{\psi}_r^{(dq)} = U \cdot \boldsymbol{\psi}_r^{(\alpha\beta)} \tag{12}$$

$$\boldsymbol{i}_s^{(dq)} = U \cdot \boldsymbol{i}_s^{(\alpha\beta)} \tag{13}$$

The implementation of the IM FOC control scheme is shown in Fig. 3. Compensation of non-linearities was achieved by including feed-forward compensation for the dq control loop PI controllers.

4 Simulation Results

Dc-link voltage stability performance simulation results, for the double-star converter, are presented for an industrial application consisting in a field oriented controlled induction machine industrial drive, under variable load and speed conditions.

Constant load and variable speed operation results are presented in Fig. 4. Simulations include the initial system speed start-up from 0 to 0.5 $[pu]$ of rated speed in ① and a speed step-up from 0.5 to 1.0 $[pu]$ of rated speed in ② under a linear torque characteristic such as $T_L = k\,\omega_r$

As shown in Fig. 4, during the speed start-up at ① using LS-PWM strategy the Upper and Middle capacitor voltages raise, because of the floating condition of ground, meanwhile the Lower capacitor voltage drops due the fact that only the lowest voltage level is being used and all energy is drawn only from this capacitor. On the other hand, when implementing PS-PWM scheme, there is no voltage drift. During the speed step-up at ② implementing LS-PWM the initial observed voltage drift increases, symmetrical from each other. With PS-PWM there is a natural voltage drop in all levels with a small voltage drift but only in the Lower capacitor.

Results for variable load and constant speed operation are shown in Fig. 5. They include the performance

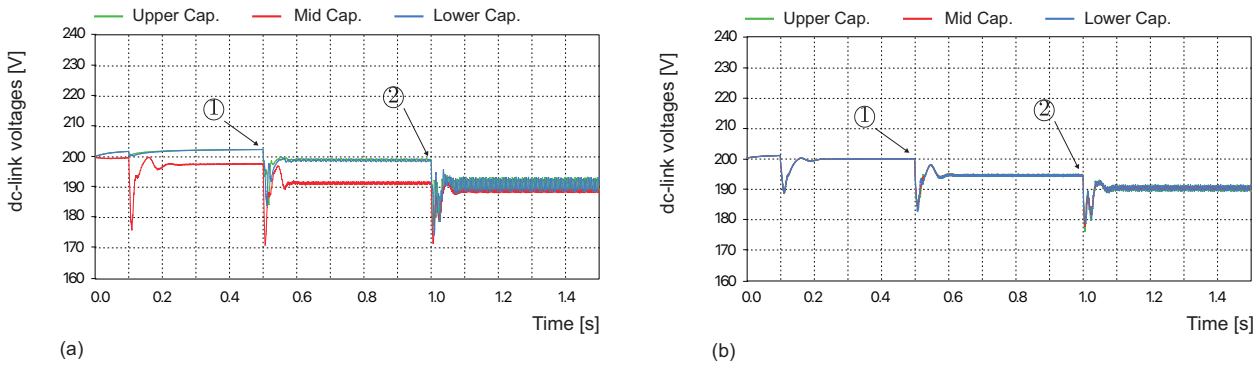

Figure 4: Simulation results for constant load-variable speed operation: (a) dc-link voltages using LS-PWM modulation (b) dc-link voltages using PS-PWM modulation

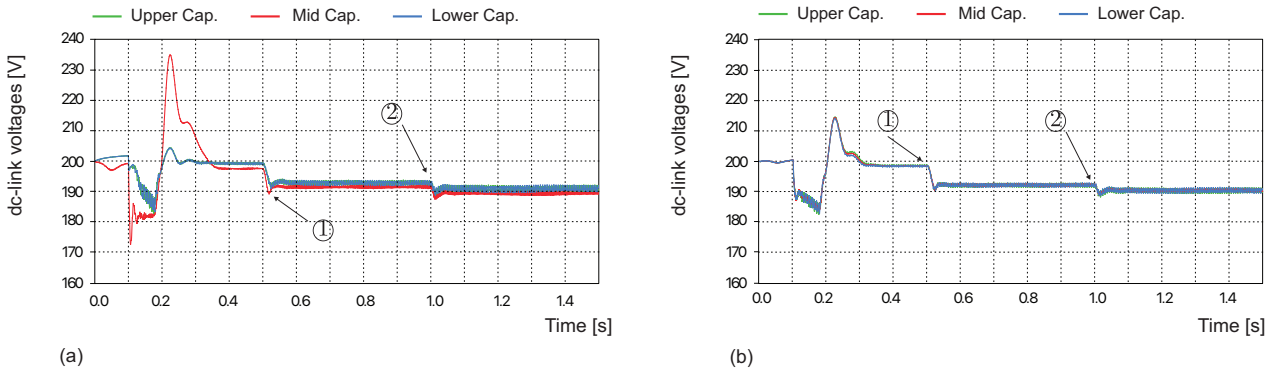

Figure 5: Simulation results for load impact under constant speed operation: (a) dc-link voltages using LS-PWM modulation (b) dc-link voltages using PS-PWM modulation

of dc-link capacitors voltages and the line - line output voltage, for the following operational conditions: initial speed-up transient under no-load condition, a first load impact of 0.6 [pu] at ① and a second load impact of 1.0 [pu] of rated load at instant ②

An evaluation of the actual benefits of PS-PWM strategy for this particular application in the DSC, can be made by comparing the capacitors dc-voltage drift and the output current THD, for both LS-PWM and PS-PWM strategies. These results are shown in Fig. 6 and in Fig. 7 respectively.

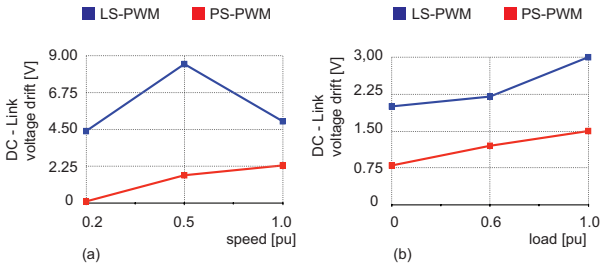

Figure 6: Total dc voltage drift: (a) constant load - variable speed (b) constant speed - variable load

The dc-link voltage drift is shown, for variable speed, constant load operation shown in Fig. 6 (a) and in constant speed, variable load operation as presented in Fig. 6 (b); in both cases, PS-PWM generates a lower voltage drift as with LS-PWM (it has to be noted that no voltage-drift control is implemented).

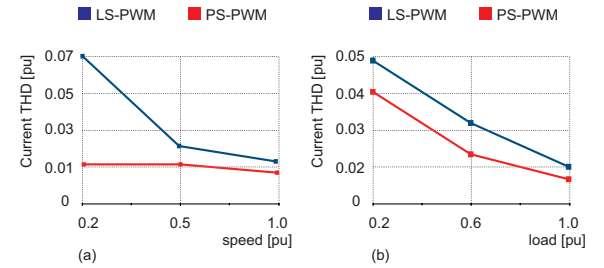

Figure 7: Line current Total Harmonic Distortion (THD), in per unit [pu] (a) constant load - variable speed (b) lconstant speed - variable load

In Figs.7 (a) and (b) the output currents THD performance is shown, for constant speed and constant load operation conditions, using both, LS-PWM and PS-PWM strategies. On each case the PS-PWM strategy presents a lower THD index.

The harmonic content of the output currents, has a directly impact on the electrical torque developed by the induction machine, due the fact that the electromechanical torque is a function of the stator currents and the rotor flux linkage space vectors.

In Fig. 8 the results for the i_d i_q current control loop, and the developed torque performance are presented. As shown in Fig. 8 (a) and (d) the i_d i_q current control loop (inner control loop) exhibits a good performance either using level shifted or phase shifted PWM. However, results for the electromechanical torque developed by the induction machine, when using LS-PWM strategy, shown in Fig. 8 (b) and (c), exhibit a more scattered harmonic pattern, with higher order frequency components, compared to the results obtained with the PS-PWM strategy, discussed previously.

As shown in Fig. 4 and Fig. 5 PS-PWM modulation strategy offers a better performance during the initial speed-up transition (low modulation index operation region), in terms of dc-link undershoot and voltage unbalance, when compared with LS-PWM modulation. Moreover, DC-link voltages show less voltage unbalance between each capacitor, resulting in lower THD for the output currents, as presented in Fig. 7.

Output currents with lower harmonic distortion, ensures low electrical torque ripple, as shown in Fig. 8 (c), so the torque harmonics are concentrated in the low frequency range, as presented in Fig. 8 (f), while, on the other hand, LS-PWM shows a very distributed torque harmonic profile, with high order frequencies, which can be a source of mechanical stresses.

5 Conclusions

In the present work a double-star converter application for a medium voltage induction motor drive under variable speed and load operation has been presented. The particular characteristics of the double-star topology, enables this multi-level voltage source converter to use the extra degrees of freedom, by synthesizing the redundant switching states via the phase-shifting PWM strategy.

The use of redundant switching states also improves the natural voltage-drift between the dc-link capacitors, due to its floating condition, resulting output currents with low harmonic content. Moreover, the developed torque shows a more symmetrical harmonic distribution, concentrated in the low frequency range, compensating the torque ripple, and thus preventing mechanical stresses on the output shaft. These characteristics make the double-star converter topology using PS-PWM modulation strategy, suitable for medium voltage drive applications.

The converter advantages for its application in medium voltage AC-drives, over classical medium-voltage voltage-source converters topologies, are based in the simplicity of its topology (no flying capacitors and clamping devices are required) and to fact that redundant switching states are available via conventional pulse-width modulation methods, reducing harmful high order torque harmonics.

Conflict of Interest The authors declare no conflict of interest.

Acknowledgment The author also wish to thank the financial support from the Chilean Found for Human Resource Development (CONYCIT) through its Ph.D. scholarships (CONICYT/21130448).

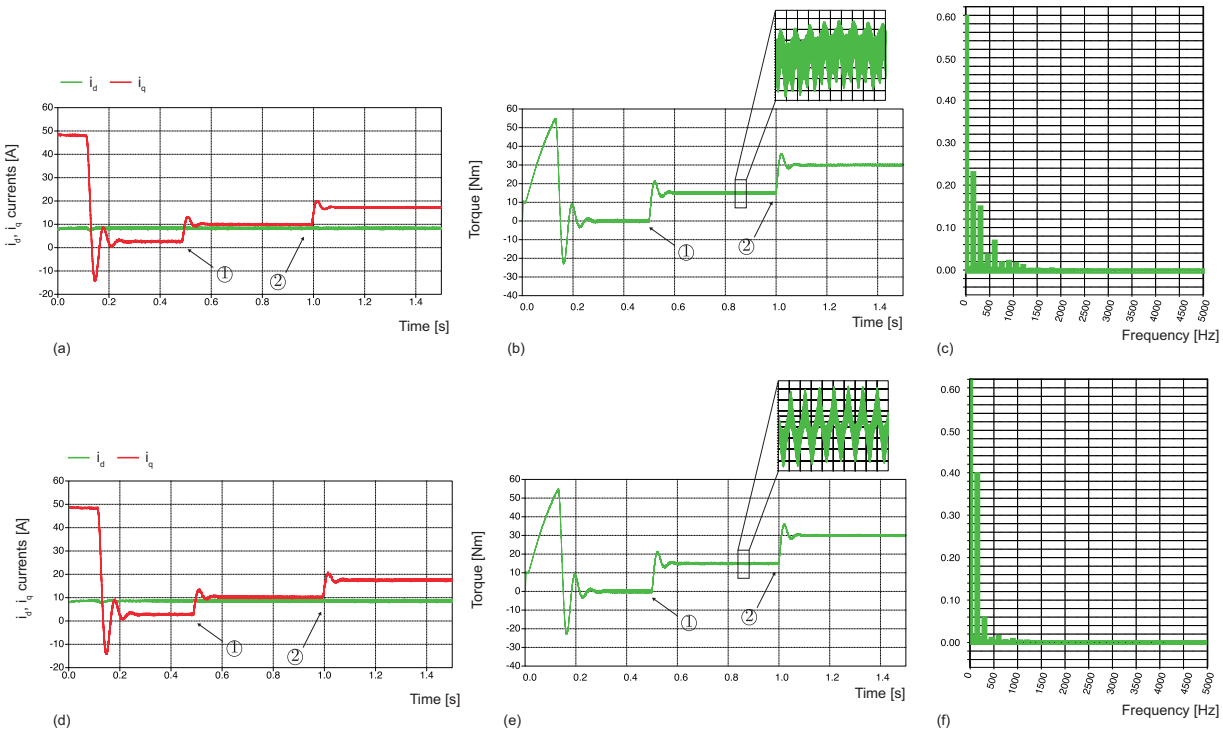

Figure 8: Simulation results under constant speed - variable load: (a) $i_d\, i_q$ currents using LS-PWM modulation (b) electric torque using LS-PWM modulation (c) torque harmonic profile using LS-PWM modulation (d) $i_d\, i_q$ currents using PS-PWM modulation (e) electric torque using PS-PWM modulation (f) torque harmonic profile using PS-PWM modulation

References

[1] I. Boldea and S. A. Nasar, "Electric drives," *CRC Press*, vol. 24, June 30 2016.

[2] J. I. Leon, S. Vazquez, and L. G. Franquelo, "Multilevel converters: Control and modulation techniques for their operation and industrial applications," *Proceedings of the IEEE*, vol. 105, no. 11, pp. 2066–2081, Nov 2017.

[3] S. Kouro, M. Malinowski, K. Gopakumar, J. Pou, L. G. Franquelo, B. Wu, J. Rodriguez, M. A. Perez, and J. I. Leon, "Recent advances and industrial applications of multilevel converters," *IEEE Transactions on Industrial Electronics*, vol. 57, no. 8, pp. 2553–2580, Aug 2010.

[4] L. G. Franquelo, J. I. Leon, and E. Dominguez, "New trends and topologies for high power industrial applications: The multilevel converters solution," in *2009 International Conference on Power Engineering, Energy and Electrical Drives*, March 2009, pp. 1–6.

[5] X. Yuan, "Derivation of voltage source multilevel converter topologies," *IEEE Transactions on Industrial Electronics*, vol. 64, no. 2, pp. 966–976, Feb 2017.

[6] J. Rodriguez, S. Bernet, B. Wu, J. O. Pontt, and S. Kouro, "Multilevel voltage-source-converter topologies for industrial medium-voltage drives," *IEEE Transactions on Industrial Electronics*, vol. 54, no. 6, pp. 2930–2945, Dec 2007.

[7] D. G. Holmes and T. A. Lipo, "Pulse width modulation for power converters: Principles and practice," *Wiley-IEEE Press*, vol. 24, October 3 2003.

[8] S. alberto Gonzalez, S. andres Verne, and M. I. Valla, "Multilevel converters for industrial applications," *CRC Press*, vol. 8, July 22 2013.

[9] S. Kouro, M. Perez, J. Rodriguez, and B. Wu, "Four-level medium voltage multilevel converter for high power applications," in *ECCE Asia Downunder (ECCE Asia), 2013 IEEE*, June 2013, pp. 1028–1033.

[10] L. M. Tolbert, F. Z. Peng, and T. G. Habetler, "Multilevel pwm methods at low modulation indices," *IEEE Transactions on Power Electronics*, vol. 15, no. 4, pp. 719–725, Jul 2000.

[11] W. Bin, "High-power converters and ac drives," *Wiley-IEEE Press; 1 edition*, pp. 1–468, 2006.

[12] C. A. Reusser, S. Kouro, A. Llor, R. Cardenas, and V. Yaramasu, "Permanent magnet synchronous generator wecs based on a four-level double star converter," in *2017 IEEE 8th International Symposium on Power Electronics for Distributed Generation Systems (PEDG)*, April 2017, pp. 1–6.

[13] A. M. Llor, S. Kouro, C. Reusser, V. Yaramasu, and B. Wu, "Medium voltage 4-level double-star multilevel converter using model predictive control," in *2017 IEEE International Conference on Industrial Technology (ICIT)*, March 2017, pp. 136–140.

[14] J. Holtz, "The representation of ac machine dynamics by complex signal flow graphs," *IEEE Transactions on Industrial Electronics*, vol. 42, no. 3, pp. 263–271, Jun 1995.

ASTES

Advances in Science, Technology and Engineering Systems Journal
Vol. 3, No. 4, 59-71 (2018)
www.astesj.com
Special Issue on Multidisciplinary Sciences and Engineering

ASTES Journal
ISSN: 2415-6698

An FPGA Implementation of Resource-Optimized Dynamic Digital Beamformer for a Portable Ultrasound Imaging System

Jingwei Xu[*,1], Yi Zheng[2], Mohan Chirala[3], Mohamed Almekkawy[2]

[1]*Department of Electrical and Computer Engineering, Texas A&M University, College Station, Texas, USA*

[2]*Department of Computer Science and Engineering, Penn State University, University Park, Pennsylvania, USA*

[3]*Samsung Research America, Dallas, Texas, USA*

ARTICLEINFO

Article history:
Received: 01 June, 2018
Accepted: 01 July, 2018
Online: 14 July, 2018

Keywords:
Medical Ultrasound
Digital Beamforming
Linear array
FIR Polyphase Filter
FPGA

ABSTRACT

This paper presents a resource-friendly dynamic digital beamformer for a portable ultrasound imaging system based on a single field-programmable gate array (FPGA). The core of the ultrasound imaging system is a 128-channel receive beamformer with fully dynamic focusing embedded in a single FPGA chip, which operates at a frequency of 40 MHz. The Rx beamformer is composed of a midend processing module, a backend processing module, and a control block. The midend processing module is established using the implementation of the delay summation through coarse delays and fine delays, with which delays could vary continuously to support dynamic beamforming. In order to enhance spatial and contrast resolution, the Rx beamformer is further accommodated by employing a polyphase filter, which improves the effective beamforming frequency to 240 MHz. The control block generates control signals based on a memory management block, which doubles the data transfer rate. The processed data is wirelessly sent to a commercial Android device. The low cost ultrasound imaging system supports real-time images with a frame rate of 40 fps, due to the limitation imposed by the wireless backhaul process. To reduce power consumption, a dynamic power management technique is used, with which the power consumption is reduced by 25%. This paper demonstrates the feasibility of the implementation of a high performance power-efficient dynamic beamformer in a single FPGA-based portable ultrasound system.

1 Introduction

Ultrasound imaging is the most commonly-used noninvasive real-time diagnostic tool in clinical applications because of its free of radiation and ease of use [1]. However, traditional ultrasound devices are bulky because of the large amount of digital data that needs to be simultaneously processed. For greater operational convenience, low power hand-held devices have come into prominence [2–4]. To minimize the size of ultrasound imaging systems, research laboratories continue to propose approaches based on modern signal and image processing methods. Their intent is to improve the image quality and diagnostic accuracy, without compromising imaging performance [5]. Medical ultrasound imaging has been used for imaging organs in human body and measuring the blood flow in vessels through Doppler shift [6].

A number of approaches have been reported for ultrasound imaging using both linear array and phased array [7–11]. One-dimensional ultrasound transducer arrays are used to get 2D images, and two-dimensional transducer arrays have been applied to produce 3D ultrasound images [12–14]. The ultrasound produces images through the backscattering of the mechanical energy from boundaries through tissues. Because of this property, a 1D image could be produced by 1 transducer element exciting ultrasound waves along a

[*]Corresponding Author: Jingwei Xu, Department of Electrical and Computer Engineering, Texas A&M University, College Station, Texas USA, Email: xujw07@tamu.edu

https://dx.doi.org/10.25046/aj030408

straight line, called scanline (SL), and a 2D image could be generated by repeating the same step for all transducer elements. With a frame rate of approximately 30 fps, ultrasound imaging is considered to be a real-time imaging technique. However, the relatively poor soft tissue contrast limits the performance of ultrasound imaging technique. In addition, the increase in integration density tends to increase the power consumption, which is a major constraint in the implementation of digital signal processing (DSP) architectures especially for hand-held ultrasound imaging system. Although some ultrasound devices are implemented based on application-specific integrated circuits (ASICs) to reduce cost and power consumption [15], the ASIC-based design is not preferred by researchers due to its inflexibility for advanced applications. On the contrary, FPGA, because of its reconfigurability, has become an ideal alternative to ASIC. There are some existing FPGA based designs on ultrasound, but these designs are limited by several criteria discussed below.

First, it is hard to implement the DSP portion of the system with a low hardware complexity, while not impacting the spatial and temporal resolutions of the system. In fact, portable ultrasound imaging systems are limited by the low resolution and high power consumption. Increased number of transducer elements, though providing higher resolution, making the entire data rate at ADC interface reach a forbidding level that challenges not only the power consumption but also the data transmission ability. In addition, such large transducer array requires hugh analog-front-end (AFE) and digital circuitry operates in parallel, such as low-noise-amplifier (LNA), time-gain controller (TGC), and analog-to-digital converter (ADC). However, the large number of hardware duplication may cause a lot of implementation issues when integrated into portable form factors, including heat dissipation, crosstalk interface, I/O packaging. Several prior methods have been developed to reduce hardware complexity. A 64 channel power-efficient architectures version without the real time controller (RTC) has been shown by [16]. Other schemes described the DSP algorithms used in digital beamforming [17–19]. In addition, an ASIC-based programmable ultrasound image processor is shown by [20]. A 16-channel FPGA-based real-time high frequency digital ultrasound beamformer is discussed by [21], but it could only support 30 fps frame rate, which constrains the image quality.

Seconds, the temporal resolution is bounded by the bandwidth of the ultrasound imaging system, which is limited by the ADC implementation [22, 23]. The temporal resolution in digital beamforming systems can typically be improved in two ways: either using phase rotation, also known as direct sampled in-phase/quadrature (DSIQ) beamforming, or through interpolation-based filtering. However, phase rotation degrades image quality as it assumes the ultrasound signal to be a narrow band [4, 24], and interpolation-based filtering requires up-sampling before low-pass filtering, which requires the operation of the DSP portion on high frequencies, and therefore raises the energy cost. Therefore, we need to improve the methods above to reduce power consumption.

Third, applying exact delays on corresponding signals is a challenge, because the amount of delay between two subsequent sampled signals may vary based on the nature of dynamic beamforming. An iterative algorithm for calculating delay information in real-time has been implemented by [25]. However, the delay resolution in that system is bounded by the frequency of the delay calculation module. Therefore, a higher operating frequency is necessary to acquire more accurate delay information. Another widely used method is precomputing the delays. However, to overcome the impending memory limitation of FPGAs, only a pseudo-dynamic focusing technique is utilized where delay information is only updated for a pre-determined depth rather than for a pre-determined delay resolution [26]. Different articles introduced the digital beamformer design using a 5 MHz center frequency beamformer linear array implemented on FPGA as discussed by [27] and with a 50 MHz center frequency annular array by [28,29]. A research-aimed FPGA-based digital transmit beamformer system for generating simultaneous arbitrary waveforms has been developed by [30]. Others have applied over sampling techniques and single transmit focusing as other methodologies for digital beamforming [31].

Therefore, there is a need to develop resource-friendly, power-efficient, and space-efficient architectures and methods for both properly delaying sampled signals and correctly acquiring delay information for a portable ultrasound device, where innovative designs of AFE and mixed-signal interface are keys to the next generation portable ultrasound devices. State-of-the-art portable ultrasound typically operates at 2 to 4 MHz with less than 64 active transducer elements.

In this paper, we present our 128-channel portable ultrasound imaging system embedded in an Arria V FPGA (Altera Inc., San Jose, CA, USA), where several methods are introduced, such as polyphase filter, memory management block, and active aperture, with which we resolve the issues discussed above so as to deliver a resource friendly ultrasound imaging system. Our ultrasound imaging system, compared to prevailing 32-channel [26] and 64-channel ultrasound imaging system [32], outputs higher resolution images with the better use of FPGA area. An overview architecture block diagram of the developed N-channel power-efficient and space-efficient ultrasound imaging system is shown in Figure 1. For the AFE part, a serial low voltage differential signaling (LVDS) interface protocol is used to get a fast analog acquisition, which serves as a serial way to recover parallel data. In addition, the echo-backed signal on each channel is amplified by a TGC amplifier to compensate for signal attenuation through propagation in the medium. The TGC amplifier is implemented on the AFE part as shown in Figure 2. The AFE implementation is out of the scope of this paper and will not be discussed in detail. The delay-and-sum (DAS) module in the midend processing module receives the compressed

timing information and outputs beamformed signal without decompression.

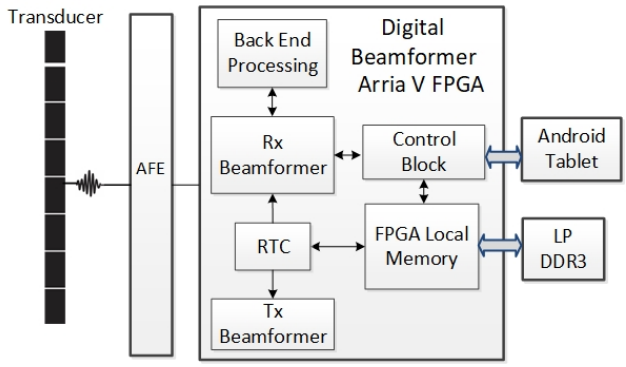

Figure 1: Architecture block diagram of the ultrasound digital beamformer based on a single FPGA.

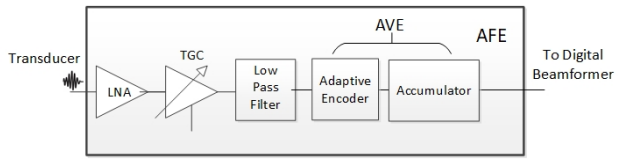

Figure 2: AFE architecture block diagram in the ultrasound digital beamforming system.

2 System Architecture

Figure 3 shows the detail of the beamforming architecture of the N-channel FPGA-based ultrasound imaging system. The midend beamformer will first pass the signal to S2P module to parallel the signal, since the AFE will serialize 2 signals from neighboring channels. Then, each signal will be passed into a coarse delay module, which delays the signal from the corresponding channel by integer numbers of the sampling period, T_s. The signal is then passed into a fine delay module, which delays the signal from coarse delay module by a fraction of T_s, and an apodization weight module, which multiplies the signal by a weight window function. The coarse delay block is achieved through controlling the writing process to the first-in-first-out (FIFO) memory to get valid data. The fine delay block is employed to replace the traditional way of optimizing the resource and is accomplished by a polyphase FIR filter. Finally, the processed signals from the N channels will be summed and sent to the backend processing module. The back end processing module processes acquired data based on an user-defined imaging mode, which can be selected via the Android tablet. The FPGA local memory is connected with an external memory, LP DDR3 to store the large amount of pre-computed delay information. The architecture of the ultrasound imaging system supports apodization and dynamic focusing, and is able to achieve a high-performance imaging system. In the following subsections, we will present the architecture of the Tx and Rx beamformer, the implementation of the midend processing module, the backend processing module, the control signal generation, and the calculation of the propagation delay.

2.1 AFE Architecture

AFE contains an LNA, an LVDS interface protocol, a TGC amplifier, and a low-pass filter, as shown in Figure 2. The LNA is used for amplifying small echoed back signals; LVDS interface protocol is used for getting a fast analog acquisition; the low-pass filter is used for cutting off the high-frequency noises. Inside the AVE, an adaptive encoder and an accumulator is employed. The accumulator detects transition edge of each piecewise-constant section and calculate the length. The adaptive encoder module performs adaptive thresholding and converts the amplitude variation into ternary timing information. The adaptive encoder consists of a comparator and a threshold generator. Two 1-bit ADCs are with in the comparator, and each receives input of the input signal and a low-threshold or a high-threshold signal, generated by the threshold generator. The comparator will outputs +1 or -1 if the input signal is greater than the high threshold or low than the low-threshold, respectively, and then requires the threshold generator to update the comparison parameter for the next comparison based on the input variation; otherwise, the comparator simply outputs 0. In this way, unit amplitude +1 or -1 could be assigned without loss of generality.

Some modulation methods, including the time encoding machine (TEM) [33], delta modulation [34], and integrate-and-fire scheme [35], converts amplitude information into timing information, and both TEM and delta modulation include a negative feedback loop to lock the input signal. In addition, these techniques will force the entire circuit keeps on flip-flopping, similar to a sigma-delta modulator output with constant input, and firing all the time even when there is no input signal. Also, typical integrate-and-fire scheme calculates the running average and also fires even when no variation occurs, resulting in unnecessary power overhead. Whereas in our adaptive encoder, the circuits fire only when significant variation occurs. As a result, the proposed adaptive encoder modulates the amplitude variations into delay information more efficiently.

2.2 Tx and Rx Architecture

The Tx beamformer supports 128 channel ultrasound beamforming signals, formed by two essential parameters: pulse-shape, assumed to be the same for all channels, and channel-delay, the value of which may vary among channels, and some channels could even be disabled. The two parameters are inputs to SPI ports, governed by the SPI clock. The SPI clock may run at different frequency compared to Tx clock which provides the Tx delay granularity.

Figure 4 shows the architecture of Rx beamformer, which receives control signals from both RTC and local memory management block, which will be discussed in

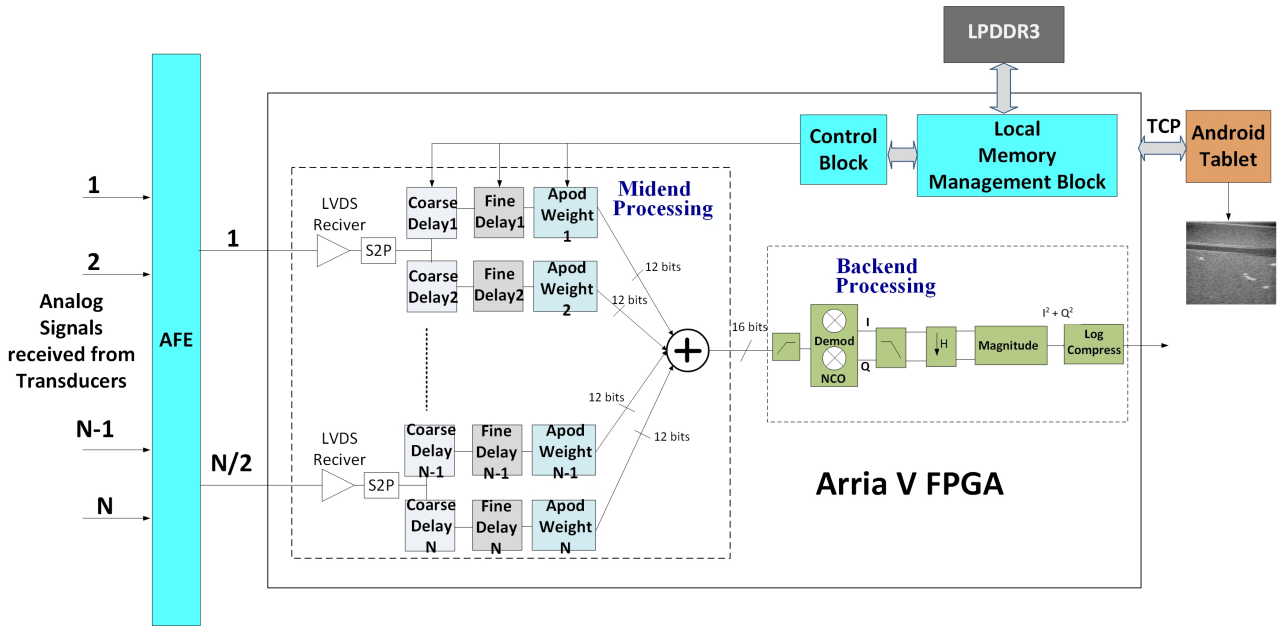

Figure 3: Architecture of ultrasound receiver of the single FPGA-based the ultrasound digital beamformer, showing the midend processing and the backend processing module with the control block and the local memory management block.

section 2.5, and outputs control signals to AFE. Eight sub-blocks made up the frame of the Rx block, and each comprises an LVDS receiver, a Frame Align module, a data management block, and a FIFO memory block. The Rx AFE SPI module outputs control signals serially.

2.3 Midend Processing Architecture

The core of midend processing module is coarse delay filters and find delay filters. The coarse delay filter delays the signals by the integer number multiplication of the sampling period, T_s. This block is implemented as a FIFO buffer. The coarse delay outputs a buffered signal when the desired control delay equals to the number of signals stored in the FIFO buffer. In the dynamic beamforming, some signals are used twice for the alignment. It is satisfied by this mechanism. As a result, if the control signal is greater or equal to the number of signal in the FIFO buffer, it is possible that when the control signal increment by 1, the coarse delay output remains the same. Hence, to get the same sampled signal, the coarse delay should be incremented by one as well, which prevents updating output signals. Therefore, by focusing the points from the nearest to the farthest along a scanline, the desired delays for all channels increase simultaneously.

Fine delay filter delays signals by a fraction of the sampling period, T_s. Figure 5 shows the architecture of the fine delay filter. As shown in Figure 5, the fine delay filter uses 48 FIR low-pass filters, from C0 to C47. Their parameters are calculated based on the baseband width and the carrier frequency. The 48 filters are grouped into 8 taps, with 6 phase coefficients per tap. Each set serves to multiply the input signals, or buffered signals, by the corresponding coefficients. Then, the multiplied signals are summed up to produce the interpolation signals.

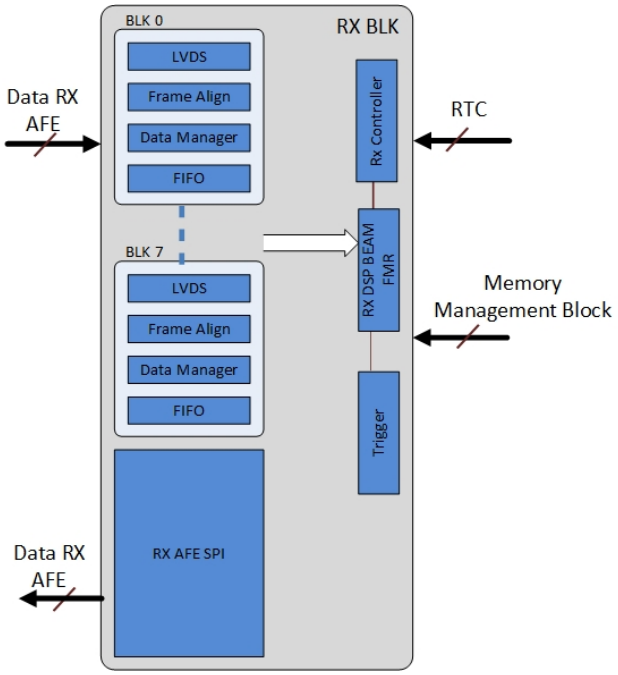

Figure 4: The Rx block diagram, showing Rx block is controlled by the control signal and RTC, and contains several subblocks 8 LVDS blocks, 8 frame align blocks, 8 data management blocks, and 8 FIFO memory blocks.

Based on the desired phase shift, the control signals generated by the control block select which set of coefficients will be used to multiply the input signals. The purpose of using register buffer is to reject the last repeated signals, because it is possible that when the coarse delay increases by 1 the output of coarse delay

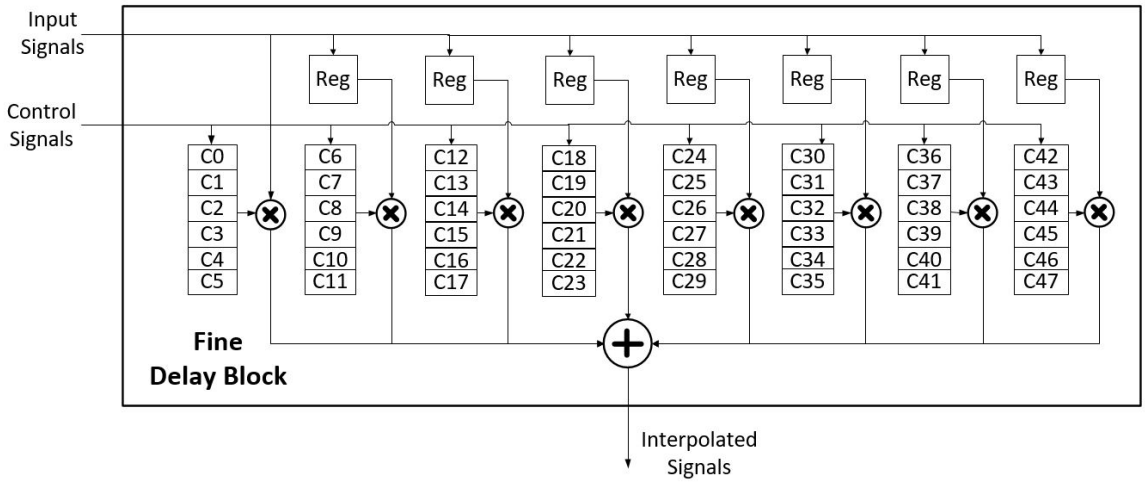

Figure 5: Block diagram of poly-phase fine delay filter with 7 registers for rejecting the last repeat signals and 8 × 6 low-pass filters for interpolation.

blocks are not updated. Therefore, the clock-gating scheme is introduced to prevent such hazard. Once the coarse delay is increased by 1, the pipeline enable signal will be pulled down to gate the clock. Therefore, the pipeline in the fine delay block will be stalled in one cycle to reject data input.

2.4 Backend Processing Architecture

Figure 3 also shows the architecture of the backend processing module. The backend processing module includesa high-pass filter, a demodulator, a numerically controlled oscillator (NCO), and a low-pass filter. The parameters of demodulation block are determined using Matlab (TheMathwork's Inc., Natwick, MA, USA). The data in this block is beamformed in 2 steps: before quadrature demodulation and after quadrature demodulation. The first step is the high pass filtering followed by the low pass filtering. This allows users to define filter option through the Android GUI. The second step architecture contains a down-sampling block, a magnitude I/Q demodulation block, and a log compression block. The I/Q demodulation block is used to extract the amplitude from the compressed data and outputs the interpolated data, where I and Q are 12 bits signed signal. The magnitude calculator outputs $I^2 + Q^2$, a 23-bit value. The log compression block is used to compress the data by taking its natural log value, which reduces the dynamic range, and outputs a 8-bit value.

2.5 Control Signals Generation

Control signals are generated by 2 blocks: RTC and the control block. Figure 6 is an overview of RTC. RTC contains 2 major blocks: the memory and RTC finite state machine (FSM). RTC FSM generate control signals based on data loaded from memory and controls Tx and Rx block along with memory.

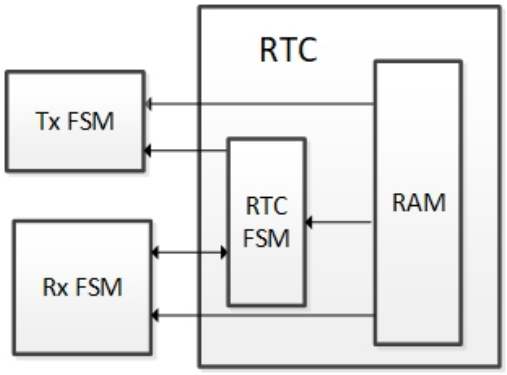

Figure 6: RTC block diagram showing the how RTC communicates with Tx and Rx block.

All N datapathes in Figure 3 are controlled by the control block. The control block generates control signals based on information passed from the local memory management block, where the FPGA local memory locates. An external memory is used to accommodate the FPGA local memory to store the large amount of pre-computed delay information. The corresponding delay information will be loaded into FPGA local memory based on the imaging mode that is selected on the user side, and the command will be sent wirelessly to the control block. The control block controls all delay filters by loading pre-computed data stored in the FPGA local memory. The FPGA local memory updates itself by reading data from an external memory. However, since it takes much more time to retrieve data from the external memory than from the local memory, it is necessary to adjust the data load process, necessitating the memory management block. Figure 7 shows the architecture of the memory management block. The FPGA local memory receives data from the external memory. The input data is passed into a demux, which is controlled by the number of scan-lines processed. Each demux output is connected to half of the FPGA local memory, the output of which is connected to a mux, which is controlled by the num-

ber of scanlines processed. The output of the mux is the output of this block. Local memory A and B are used as buffers, where A is used to buffer the current scanline and B is used to buffer the next scanline. The demux will pass input data to local memory A if the number of scanline processed is an odd number, and to B otherwise, represented by $2k+1$ and $2k$, respectively, where k is a non-negative integer. The mux will output data from local memory A if the number of scanline processed is an even number, and from local memory B otherwise. With this technique, the FPGA local memory is always passing the current scanline data and next scanline data, reducing the time spent on transferring data from the external memory to the control block.

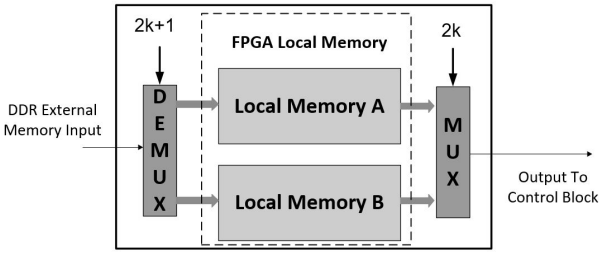

Figure 7: Block diagram of local memory management system for control signal generation process.

3 Propagation Delay Calculation

Beamforming is a algorithm which takes inputs from the transducer elements and outputs the summed signals. The implementation of beamforming algorithms is one of the deterministic factors in the ultrasound imaging quality [36]. In this paper, a delay-and-sum beamformer is used, because of its high accuracy on close-range beamforming, which is a dominant in medical ultrasound systems. Several focusing techniques have been developed for delay-and-sum beamforming, including the fixed focusing, dynamic focusing, and composite focusing techniques. The composite focusing technique is simply a special case of dynamic focusing [37] and will not be discussed in this paper.

Figure 8 shows how the signals alignment system (SAS) works. As Figure 8 presents, the signals echoed back from the focal point reach different channels at different time, which causes delay. The SAS module is used to align the signals and then pass them into the summer, which outputs the summed signal.

The difference between dynamic focusing and fixed focusing is that dynamic focusing requires the focal point to be continuously changed. Dynamic focusing could extend the field depth without satisfying the frame rate [38]. Therefore, the dynamic focusing technique is used when the SAS operates in the receive phase, and the delays of all channels are adjusted, because of the requirement of dynamic focusing. Figure 9 demonstrates the changes in the signals' flight paths during the receive phase. In Figure 9, multiple channels are used to receive ultrasound signals. Focal points on the same scanline are under detection. By assuming the scanline begins from the position of channel A, we can determine the focal points of the signals sampled by channel A. There exists a depth in the physical positions between every two sampled data points which is clearly evident in Figure 9. The distance, d, between two focal points, P_1 and P_2, satisfies that $d \approx (c \times T_s)/2$, given that d is small enough. Here, c is the average ultrasound speed in human body.

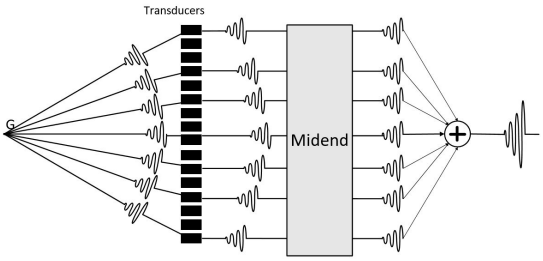

Figure 8: Signals alignment in ultrasound digital beamforming system.

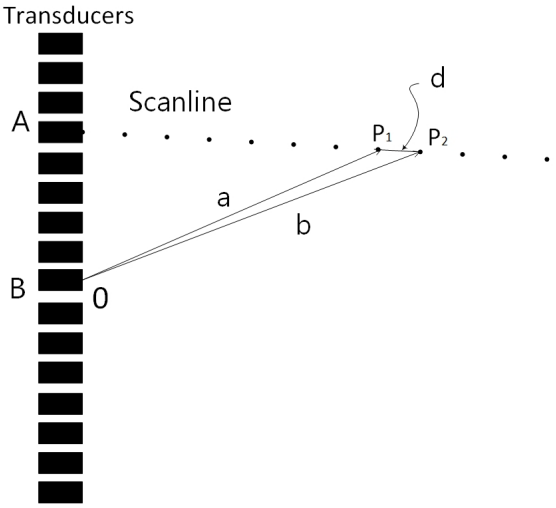

Figure 9: Variations of echo paths in receiving signals used in dynamic focusing technique.

Now, the signals that are variably received by the transducer elements should be delayed using dynamic beamforming. For the focal point P_1 in Figure 9, it is assumed that the time interval between transmission and reception by channel A is T_1. The time interval for channel B to receive it is T_2, where $T_2 > T_1$. Consequently, a delay of $(T_2 - T_1)$ in the signal echoed back from P_1 is observed to be aligned with the signal in channel B. For the subsequent focal point P_2, the time that corresponding signals are received by Channel A and Channel B, $\hat{T_1}, \hat{T_2}$ respectively, are:

$$\begin{aligned} \hat{T_1} &= \Delta T_1 + T_1 \\ \hat{T_2} &= \Delta T_2 + T_2 \end{aligned} \tag{1}$$

According to the property of the triangle, we have

$b - a < d$, where a is the distance between P_1 and channel B, and b is the distance between P_2 and channel B. Thus it is derived that:

$$\begin{aligned} \Delta T_2 &= \frac{d+b-a}{c} < \frac{2d}{c} \\ \Delta T_1 &= \frac{2d}{c} \end{aligned} \tag{2}$$

It implies that the corresponding signal of P_2 has arrived at channel B before its next sampling. We can retrieve the fraction delay between two samples after sampling the next signals in channel B provided that $\Delta T_1 - \Delta T_2$ is relatively short. But if we get a large enough $\Delta T_1 - \Delta T_2$, the corresponding signal has to be accessed without sampling the next signal. Here, we use the previous sampled signal from channel B twice and align with both signals received from the channel for P_1 and P_2. The resolution our system can support is $\lambda/16$. There are techniques that use a 100 MHz sampling rate with digital interpolation filters [21], which allow the signals to be sampled at a lower frequency and concurrently get more precise delays [39, 40].

The delay values are pre-computed and pre-loaded to the external memory, as mentioned in the previous section.

4 System Specifications

The T_x firing frequency, also called pulse repetition interval (PRI), is constrained by several theoretical limitations: the round trip delay (RTD), the wireless backhaul limitation (WBL), and the DDR to FPGA interface limitation.

First, PRI is given by:

$$PRI = \frac{1}{N_s \times FR} \tag{3}$$

where N_s refers to the number of samples per scanline, and FR is the frame rate of the system.

N_s could be calculated by:

$$N_s = f_s \times RTD \tag{4}$$

where f_s indicates the ADC sampling rate, as defined previously, and RTD is calculated by 5,

$$RTD = \frac{2l}{c} \tag{5}$$

where l is the penetration depth. The penetration depth varies among different mediums. Theoretical time for penetration depth is shown in Table 1:

WBL is given by

$$WBL = \frac{N_s N_b}{W_b} \tag{6}$$

where N_b is the number of bits per sample; and W_b, the wireless bachhaul speed, is determined by the device employed. The WBL indicates the lower bound for PRI.

Table 1: Theoretical RTD for Different Penetration Depth.

Depth of Penetration (cm)	RTD (μs)
9	116.88
7	90.10
5	64.94
3	38.96

5 Dynamic Power Management

To reduce power consumption, we modified the traditional B-mode imaging to perform the following scans: for each focal point on a specific scanline, excite a pulse from the transducer corresponding to that scanline, and receive signals with all transducers within active aperture. Repeat this procedure for all scanlines. The reason this method is able to reduce power consumption and conserves the image quality is because of 7:

$$F_n = \frac{f}{D} \tag{7}$$

where F_n is the f-number, a fixed number for one transducer, f is the focal depth and D is the diameter of the hypothesis aperture. According to 7, the maximum hypothesis aperture size is proportional to the depth of the furthest focal point, which indicates that channels outside the hypothesis aperture does not help the preservation of image quality. Figure 10 shows how this equation helps reduce the power consumption. As shown in Figure 10, for focal point B, the hypothesis aperture is the black region in the center. When focal point B is processed, all transducers outside the hypothesis aperture could be turned off. When the focal point is changed from B to A, the size of the hypothesis aperture increases, so more channels could be turned on to receive signals. The transducers in the white region are still off, because they are outside the hypothesis aperture for focal point A.

To further reduce power consumption, we consider turning off additional transducer elements with negligible image quality degradation. The idea is to choose a range of transducer elements, the range of which is called limited aperture, shown in Figure 11, and listen from the transducer elements within the limited aperture. However, there are cases where the transducers are not enough to cover the whole limited aperture, as illustrated in Figure 12. In this case, the aperture covering both transducers and limited aperture is called active aperture, and only the channels within the active aperture are turned on.

To get better image quality, the received signal for a focal point is the sum of all signals received by different active transducer elements. This can be achieved by a simple transducer elements shift operation shown in Figure 13. When processing SL_1, the transducer elements within the active aperture only are turned; for SL_2, the limited aperture is shifted down by 1 transducer element, so that one more transducer element

is turned on to receive signals; and when SL_n is processed, all transducer elements within the limited aperture are turned on. This shift operation will last until all scanlines are processed.

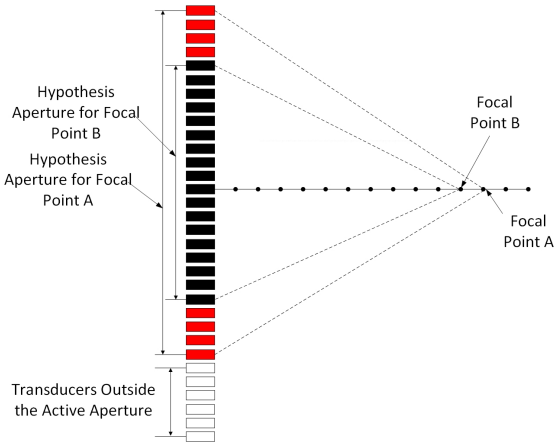

Figure 10: Hypothesis aperture for different focal points on one scanline, showing the variation of hypothesis aperture with the change of focal depth.

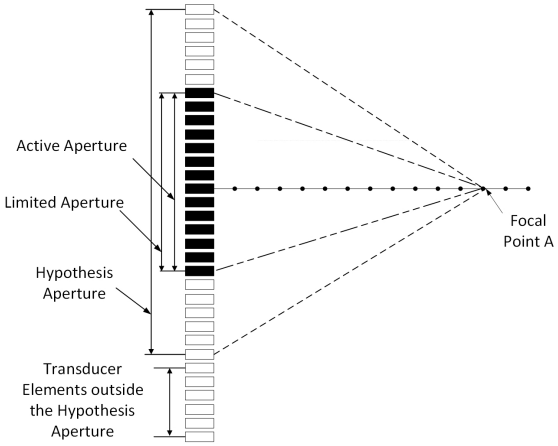

Figure 11: Limited aperture size for further focal points showing the relationship between active aperture, limited aperture, and hypothesis aperture in the normal case.

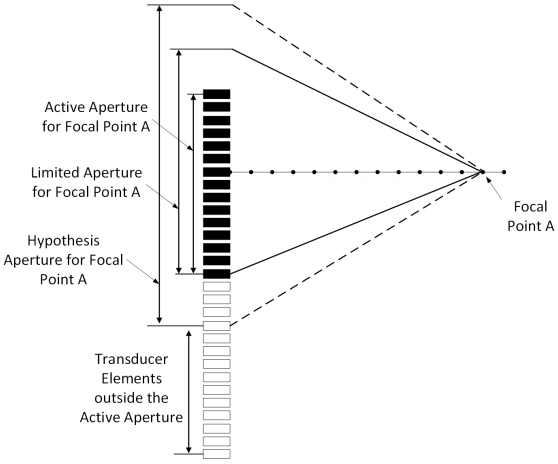

Figure 12: Limited aperture size for further focal points showing the relationship between active aperture, limited aperture, and hypothesis aperture when the transducer elements cannot cover the whole limited aperture.

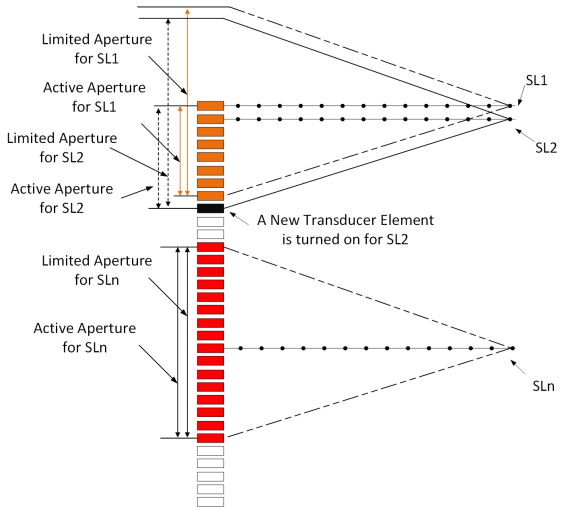

Figure 13: Transducer elements shift operation illustration. The limited aperture will be shifted based on the location of scanlines.

For a 128-channel ultrasound system, the maximum hypothesis aperture size could reach up to 256, including a virtual array consisting of 128 elements (the intersection between hypothesis aperture and aperture out of limited aperture) and physical aperture consisting of 128 elements. To observe the degradation on performance, different sizes of the limited aperture are used to receive echoed back signals. The corresponding images are shown in Figure 14. These images show that with the receive aperture increasing, a higher imaging contrast resolution could be achieved. When the limited aperture is larger than half of the effective aperture (the whole transducer array), the degradation is conceptually negligible. With the aperture size less than half of the effective aperture, most parts of the image such as blood vessels could still be clearly imaged. However, the bright spots are spread around. Hence, when the aperture size increases, a better signal-to-noise ratio (SNR) is achieved. To acquire a good measurement of the degradation, the formula below is applied to quantitatively check the difference among those images.

$$CR = 10log_{10}[\frac{\bar{I}_2}{\bar{I}_1}] \tag{8}$$

where CR is the contrast ratio, and $\bar{I}_1, \bar{I}_2$ are the average intensities in the region of interest and the region of reference, respectively. This provides a quantitative assessment of the performance of contrast restoration, the result of which is shown in Table 2.

As we discussed above, we know that the image quality will vary depending on the active aperture size. Thus, for the case we illustrated, we could merely keep the 128-channel aperture instead of the 256-channel aperture. Therefore, based on the analysis above, we could turn off all transducers outside the active aperture to reduce power consumption, while still conserving the image quality.

To estimate the power consumption, we assume that each transducer element could be independently

Table 2: Contrast Ratio of the Images with Different Limited Aperture Values.

Aperture	128	96	64	32	16	8
CR	16.3842	16.0634	15.4241	14.7033	14.637	14.637

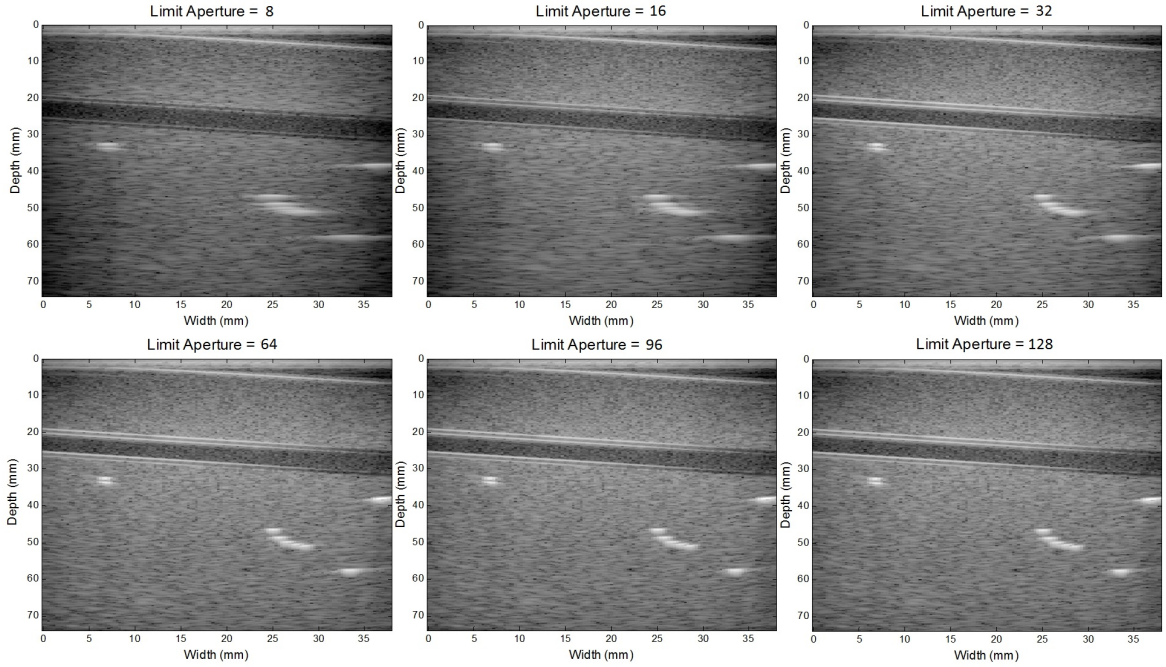

Figure 14: Ultrasound images generated with different limited aperture size chosen, showing that the image quality reserves when the limited aperture size is greater than or equal to half of the effective aperture.

switched "on" and "off" by using power-gating technology. For a linear array, the power consumption is approximately proportional to the total number of active elements used during scanning one frame:

$$Power \propto \sum_{i=1}^{128} N_i \tag{9}$$

where N_i is the number of data channels used for the i^{th} scanline. N_i could be represented by

$$N_i = Ch_{right} - Ch_{left} + 1 \tag{10}$$

where Ch_{right} and Ch_{left} are the indexes of right most and left most active transducer element, respectively. They can be represented as in 11 and 12.

$$Ch_{right} = \begin{cases} i + LA & \text{if } i + LA < 128 \\ 128 & \text{if } i + LA \geq 128 \end{cases} \tag{11}$$

$$Ch_{left} = \begin{cases} i - LA & \text{if } i - LA \geq 1 \\ 1 & \text{if } i + LA < 1 \end{cases} \tag{12}$$

where LA is the size of limited aperture. The index of the very right channel is on the right of the channel which is in the position of the current scanline. The limitation of aperture allows the channels whose index is larger than $i + LA/2$ to be turned off. If the very right channel outside the zone of the transducer, i.e. whose index is larger than 128. The 128^{th} channel will be the right bound.

According to 9, the normalized power consumption for different aperture limitations are calculated and plotted in Figure 15. With negligible degradation, the 128-channel ultrasound device will consume 75% of the power that the all-channel effort devices consume.

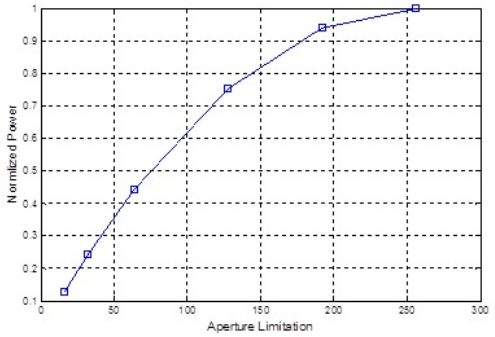

Figure 15: Normalized power consumption for different limitations of aperture.

6 Results and Discussion

The timing of the beamforming architecture is shown in Figure 16. Initially, the system is powered up, allowing switching mode power supplies (SMPSs), AFE ICs, FPGA, and wireless to be on. When the user selects the smart probe function via tablet GUI, a data packet containing initial system configuration is sent to the RTC wirelessly. The RTC will extract the imaging mode, application, array type, FR, Ns, and number of scanlines (NSL) from this packet. Then the RTC will continue to

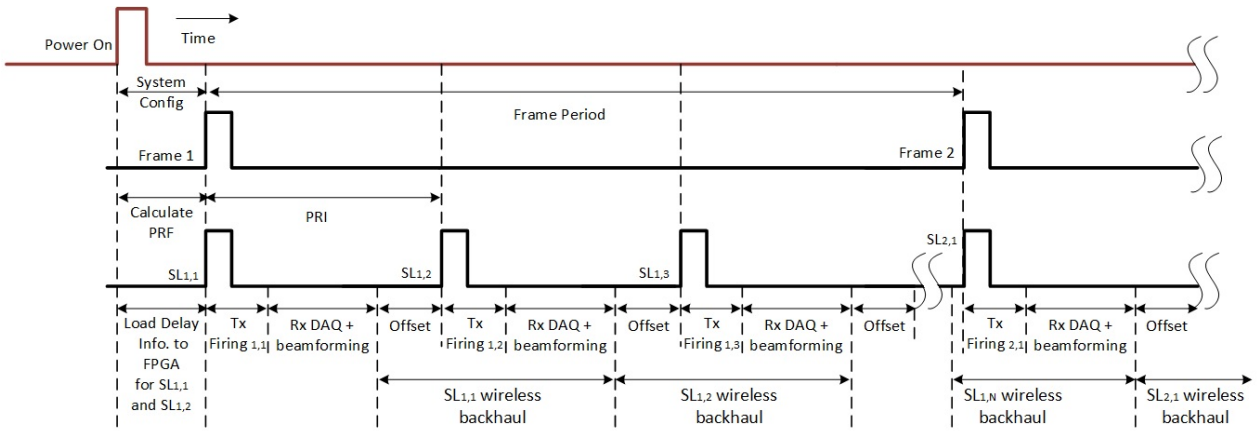

Figure 16: PRI adjustability based on system requirements, showing the conceptual timing of the single-FPGA-based ultrasound imaging system.

load and send delay information for SL_1 and SL_2 into Rx beamformer using the mechanism described in section 2.5. The delay information for SL_1 in frame 1 will also be loaded into the T_x beamformer inside the 128-channel Tx AFE (in Figure 16, $SL_{a,b}$ indicates the b^{th} scanline in the a^{th} frame). This configuration time is pre-determined, and this allows the Tx beamformer to send a "Ready" signal to the RTC. Upon receiving the signal, the RTC initiates the Tx pulse firing by sending pulse-in, pulse-enable, and scan-enable signals. After Tx firing, the Rx beamformer begins to listen and beamform received signals. The data is sampled based on the ADC sample rate. DDR3 control data has already been preloaded into FPGA local memory for SL_1, so this is applied to the coarse delay for beamforming. The I/Q data is then backhauled throught the PCIe solution based wireless module. Notice there is a gap named "Offset" in Figure 16. This offset time is used when the R_x beamformer sends beamformed data to the display device and the T_x beamformer receives the 3 signals (pulse-in, pulse-enable, and scan-enable) from the RTC. This offset time is the reason why the WBL is the lower bound for PRI, as mentioned in section 4.

The program on Android device, once the system starting up, will wirelessly send the pre-calculated delay information to the probe, which will send the Android device the digitized data pack during the wireless backhaul after applying the information and beamforming. Upon receiving the package, the program will create an image and apply a filter on it. The filtered image will finally be displayed.

The dynamic power management approach allows power reduction on a high end system with higher channel count and operating at higher supply voltages. The approach allows dynamic control of the AFE operational state based on the ultrasonic pulse repetition frequency (PRF). The PRF of an ultrasonic smart probe is dictated primarily by the speed of its wireless backhaul. Regardless of the depth of penetration, there is going to be a sizable offset after the successful reception of the furthest received signal, and the beginning of the next transmit firing. This offset region, as has been discussed above, is where the receiver is sitting in an idle state and burning DC power. Hence, we would prefer to turn off the most power inefficient regions of the receiver.

Our ultrasound imaging system supports 40 MHz ADC sample rate (25 ns temporal resolution) with 12 MHz max fundamental frequency and 80% bandwidth. Also, a max pass band of 16.8 MHz is available with 20 dB rejection. For the fine delay filter, each filter is implemented based on 48 FIR filter, which has 0.2 dB ripple and 20 dB rejection. The PRI we used is 200 μs with FR of 39 fps for 128-channels, limited by RTD of 65 μs at penetration depth of 5 cm, and a WBL of 180 μs (N_b = 12 bits/sample, W_b = 140 MHz). The TDL of 51.2 μs, constrained by the bus speed of 40 MHz. The digital beamformer is implemented with register-transfer level (RTL) in Verilog and synthesized by Quartus II (Altera Inc., San Jose, CA, USA) for Altera Arria V. The flow chart of the RTC is shown in Figure 17. The Android GUI program has been developed with C++ to control the system. All the control signals were generated in the tablet and are transferred wirelessly to the prototype board after the user configures the required input data via the tablet.

To improve the utilization of memory, a delta-coding scheme is used. From the previous mechanism, we know that the coarse delay for each channel monotonously increases and the maximum difference of coarse delay signals between two focal points for each channel is one. One bit is enough to be used as the delta between two coarse control signals. The absolute values of coarse delays for the first focal point are given at the beginning of scanning a line. The delays change according to the delta value. The fine delay has 3 bits, which are updated every sample. Therefore, there are 4 bits to be stored for each sample and each channel. Figure 18 shows the data organization in local memory. The memory is updated every scanline. The beginning 9 bits are used for initial absolute coarse delay. Subsequent 3 bits are used to indicate the fractional delay for the first focal point. Following 4-bit words are used to update delay information, whose first bit is the increment of coarse delay and other 3

bits are the fractional delay.

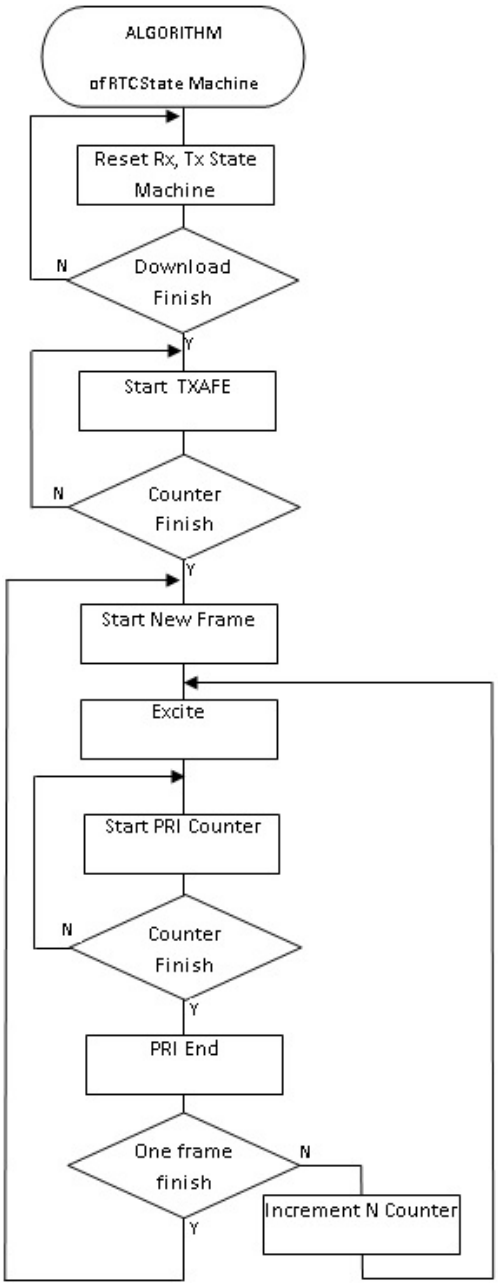

Figure 17: Flow chart of the real time controller for the ultrasound digital beamformer.

The system provides 128-channels of transmitter channels with a maximum of 32 excited pulses while simultaneously receiving signals at a 40 MHz sampling rate and converting them to a 12-bit binary number. The digitized data from all channels are first fed through the processor in the FPGA, and then stored in LPDDR3 memories by using direct memory access. These raw data are accessed by the beamforming processor to build the image that will be sent to the Android device wirelessly for further processing.

Figure 19 shows the finite state machine (FSM) used to coordinate the data flow of the local memory to dynamically generate the control signals (Coarse Delays and Fine Delays). Since there is limited bandwidth between the receiver and the memory, we introduced the scheme to dynamically change delays to accommodate the dynamic beamforming. To do that, last-level local memory is used on the receiver, which is 16×4×9 large for 16 channels. The memory is organized so that each channel has 4 × 9 bits in the local memory. Initially, those memories are filled by 4 × 9 bits of data, so that the initial fine delays and fraction delays are known (This is done in the first 4 status S0, S1, S4, S5). Once those 4 statuses are set, the delays can be initialized. Then the delays are held until the receiver starts working (state S2). As the receiver starts receiving data, the delays change. The new delay information (4 bits, 1 for coarse delay change, 3 for new fine delay) is sent into the control blocks in each cycle. In this phase, the local memory needs to keep updating data (S3 does this). When the counter hits the length of the scanline depth, one scanline is done. It then reverts to the initial state.

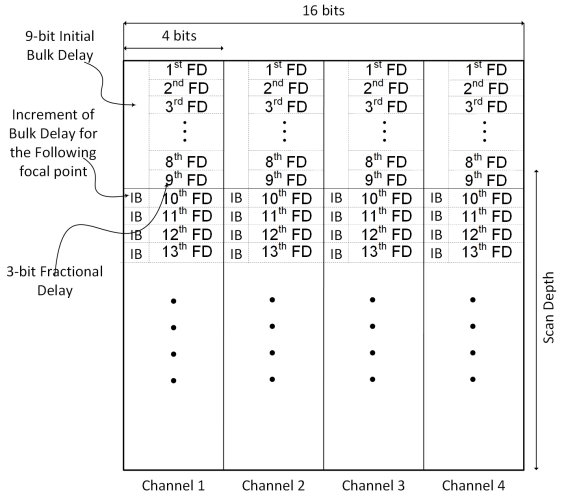

Figure 18: Flow chart of the real time controller for the ultrasound digital beamformer.

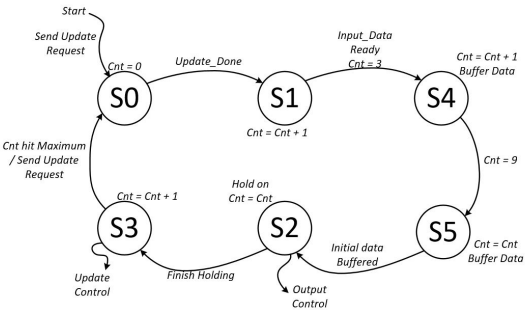

Figure 19: Finite state machine for generating the control signal for the ultrasound digital beamformer based on a single FPGA.

The beamformer that applies delays to the echoes of each channel is implemented by the strategy that combines coarse and fine delays (4 ns). This system is capable of achieving a maximum frame rate of 50 fps; this is mainly limited by the maximum speed we can achieve while wirelessly backhauling the data to the Android device. Table 3 shows the device utilization for the

whole architecture, mid-end and the control block. The 128-channel model consumes 130,547 adaptive logic modules (ALMs), the beamforming block consumes 128,044 ALMs, and the control section consumes 2,147 ALMs. The designed board contains the architecture in FPGA and DDR3, which is the external memory to store all delay information. We use the FPGA Mezzanine Card (FMC) connector to feed testing data into FPGA from stimulus boards. The board wirelessly backhauls the ultrasound image for display on a tablet or smart phone as shown in Figure 20(a).

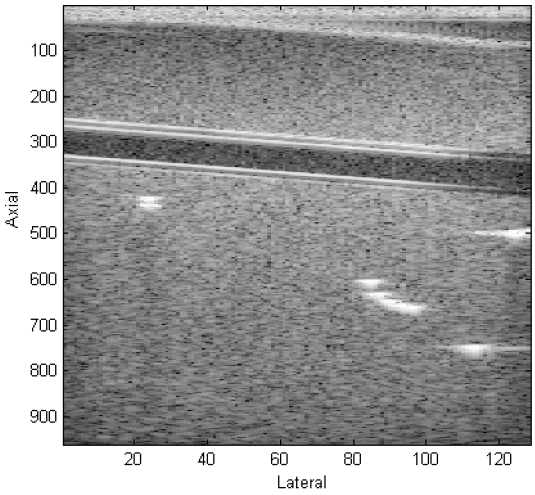

(a)

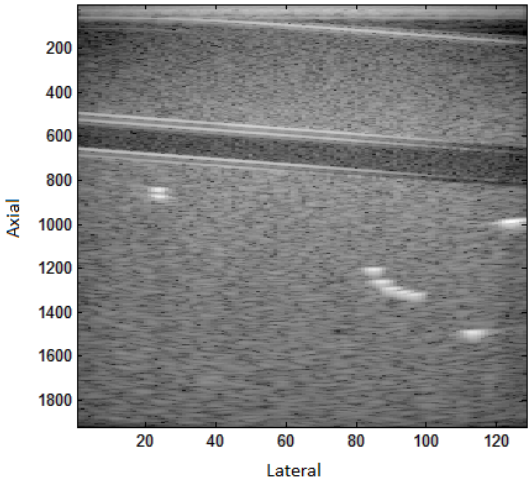

(b)

Figure 20: Ultrasound images displayed on tablet processed by (a) single Altera Arria V FPGA based ultrasound digital imaging system and (b) Simulink.

To validate our design, another FPGA is added for testing purposes: the beamformed data is stored temporarily in the added FPGA and will be sent to the Android device after testing. A software-based beamformer is simulated by Matlab and Simulink. Data generated by a quantized Matlab module is used to verify the output of the board, as shown in Figure 20(b). The sum operation across all channels is pipelined to incorporate numerous inputs and process them at a high clock frequency. The first stage in the pipeline contains 64-inputs, each producing the sum of the incoming 12-bits from 2 channels. The resulting 32 outputs are summed in pairs in the second pipeline stage. The last summation stage is truncated to a 12-bit number and fed into the high pass filter. The image is generated from a Verasonics machine (Vantage 128, Verasonics Inc., Kirkland, WA, USA).

Table 3: Implementation Parameters

Parameter	Value	Percentage
ALMs	130,547	96
Registers	41,450	-
Pins	263	40
Block memory bits	2,754,067	18
PLLs	3	8
DLLs	1	25

7 Conclusion

In this paper, we present a series of techniques: interpolation filter, limited aperture size and dynamic power management to improve the efficiency of a fully dynamic ultrasound beamformer for a handhold real-time 128-channel ultrasound system, providing higher image resolution compared to the 32-channel [26] and 64-channel beamformer [32]. The proposed architecture is programmed and synthesized in a single Arria V FPGA using Verilog, allowing fully dynamic beamforming in a low-cost single FPGA implementation. This proposed digital beamformer can be used in generic ultrasound imaging systems, personal portable ultrasound health care, as well as the cart ultrasound machine. It is useful for portable low-power ultrasound and high performance ultrasound imaging with the genuine support of dynamic beamforming, while most current ultrasound devices employ pseudo dynamic beamforming. In addition, the power consumption and hardware utilization was reduced by a huge amount.

References

[1] J. A. Jensen, "Medical ultrasound imaging," *Progress in Biophysics and Molecular Biology*, vol. 93, pp. 153-165, no.1, 2007.

[2] J. J. Hwang, J. Quistgaard, J. Souquet, and L. A. Crum, "Portable ultrasound device for battle field trauma," in *Proc. IEEE Ultrason. Symp.*, vol. 2, pp. 1663-1667, 1998.

[3] M. Karaman, P. c. li, and M. odonnell, "Synthetic aperture imaging for small scale systems," *IEEE Trans. Ultrason. Ferroelectr. Freq. Control*, vol. 42, no. 3, pp. 429-442, 1995.

[4] C. Yoon, J. Lee, Y.M. Yoo, T.-K. Song, "Display pixel based focusing using multi-order sampling for medical ultrasound imaging,", 3rd ed. *Electronics Letters*, vol. 45, no.25, pp. 1292-1294, Dec. 3, 2009.

[5] A. Assef, J. Maia, E. Costa "A flexible multichannel FPGA and PC-based ultrasound system for medical imaging research: initial phantom experiments," *Research on Biomedical Engineering*, vol. 31, pp. 277-281, Sept. 2015.

[6] A. Murtaza, D. Magee, and U. Dasgupta. "Signal processing overview of ultrasound systems for medical imaging," *SPRAB12, Texas Instruments*, Nov. 2008.

[7] J. A. Jensen, O. Holm, L. J. Jensen, H. Bendsen, H. M. Pedersen, K. Salomonsen, J. Hansen, and S. Nikolov, "Experimental ultrasound system for real time synthetic imaging," *IEEE Ultrasonics Symp*, pp. 1595-1599, 1999.

[8] M. O'Donnell, M. J. Eberle, D. N. Stephens, J. L. Litzza, B. M. Shapo, J. R. Crowe, C. D. Choi, J. J. Chen, D. W. M. Muller, J. A. Kovach, R. J. Lederman, R. C. Ziegenbein, K. San Vicente, and D. Bleam, "Catheter arrays: can intravascular ultrasound make a difference in managing coronary artery disease," *IEEE Ultrasonics Symp*, pp. 1251-1254, 1997.

[9] J. Schulze-Clewing, M. J. Eberle and D. N. Stephens, "Miniaturized circular array," *IEEE Ultrasonics Symp*, pp. 1253-1254, 2000.

[10] J. P. Stitt, R. L. Tutwiler and K. K. Shung, "An improved focal zone high-frequency ultrasound analog beamformer," *IEEE Ultrasonics Symp*, pp. 617-620, 2002.

[11] C. Dusa, P. Rajalakshmi, S. Puli, U. B. Desai and S. N. Merchant, "Low complex, programmable FPGA based 8-channel ultrasound transmitter for medical imaging researches," in *2014 IEEE 16th International Conference on e-Health Networking, Applications and Services (Healthcom)*, Natal, 2014, pp. 252-256.

[12] A. Bhuyan *etal*., "Integrated circuits for volumetrix ultrasound imaging with 2-D CMUT arrays," *IEEE Trans. Biomed. Circuits Syst.*, vol. 7, pp. 796-804, Dec. 2013.

[13] J. W. Choe, O. Oralkan, and P. T. Khuri-yakub, "Design optimization for a 2-D sparse transducer array for 3-D ultrasound imaging," *Proc. IEEE Ultrason*. Sysmp., 2010, pp. 1928-1931.

[14] J. Song *etal*., "Reconfigurable 2D cMUT-ASIC arrays for 3D ultrasound image," *Proc. SPIE Meidcal Imaging*, vol. 8320, p. 83201A, Feb. 2012.

[15] V. S. Gierenz, R. Schwann,T .G. Noll, "A low power digital beamformer for handheld ultrasound systems," in *Solid-State Circuits Conference, Proceedings of the 27th European*, pp. 261-264, 18-20 Sept, 2001.

[16] M. Almekkawy , J. Xu and M. Chirala, "An optimized ultrasound digital beamformer with dynamic focusing implemented on FPGA," in *36th Annual International Conference of the IEEE Engineering in Medicine and Biology Society*, Aug 26, pp. 3296-3299, 2014.

[17] C. Fritsch, M. Parrilla, T. Sanchez, O. Martinez, "Beamforming with a reduced sampling rate," *IEEE Ultrasonics*, vol. 40, pp. 599-604, 2002.

[18] S. R. Freeman, M. K. Quick, M. A. Morin, R. C. Anderson, C. S. Desilets, T. E. Linnenbrink, and M. ODonnell, "Delta sigma oversampled ultrasound beamformer with dynamic delays," *IEEE Trans. Ultrason.*, Ferroelect., Freq. Contr., vol. 46, pp. 320-332, 1999.

[19] M. Kozak and M. Karaman, "Digital phased array beamforming using single-bit delta-sigma conversion with non-uniform oversampling," *IEEE Trans. Ultrason.*, Ferroelect., Freq. Contr., vol. 48, pp. 922-931, 2001.

[20] C. Basoglu, R. Managuli, G. York, and Y. Kim, "Computing requirements of modern medical diagnostic ultrasound machines," *Parallel Computing*, vol. 24, pp. 1407-1431, 1998.

[21] C. H. Hu, X. C. Xu, J. M. Cannata, J. T. Yen and K. K. Shung, "Development of a real time high frequency ultrasound digital beamformer for high frequency linear array transducers," *IEEE Trans. Ultrason.*, Ferroelect., Freq. Contr., vol. 53, no. 2, pp. 317-323, 2006.

[22] D. K. Peterson and G. S. Kino, "Real-time digital image reconstruction: A description of imaging hardware and an analysis of quantaization errors," *IEEE Trans. Sonics Ultrason*, vol. SU-31, pp. 337-351, 1984.

[23] B. D. Steinberg, "Digital Beamforming in ultrasound," *IEEE Trans. Ultrason.*, Ferroelect., Freq. Contr., vol. 39, no. 2, pp. 716-721, 1992.

[24] H. Sohn, S. Seo, J. Kim and T. Song, "Software implementation of ultrasound beamforming using ADSP-TS201 DSPs," *Proceedings of SPIE*, vol. 6920, pp. 69200Z-69200Z-11, 2008.

[25] H. T. Feldkamper, R. Schwann, V. Gierenz, T.G. Noll, "Low power delay calculation for digital beamforming in handheld ultrasound systems," *IEEE Ultrasonics Symposium*, vol. 2, no., pp. 1763-1766, Oct 2000.

[26] Gi-duck Kim, Changhan Yoon, Sang-Bum Kye, Youngbae Lee, Jeeun Kang, Yangmo Yoo, Tai-Kyong Song, "A single FPGA-based portable ultrasound imaging system for point-of-care applications," *IEEE Trans. Ultrason.*, Ferroelect., Freq. Contr., vol. 59, no. 7, pp. 1386-1394, July 2012.

[27] B. Tomov and J. A. Jensen, "A new architecture for a single chip multi-channel beamformer based on a standard FPGA," *IEEE Ultrasonic Symp.*, pp. 1529-1533, 2001.

[28] P. J. Cao and K. K. Shung, "Design of a real time digital beamformer for a 50 MHz annular array transducer," *IEEE Ultrasonic Symp.*, pp. 1619-1622, 2002.

[29] P. J. Cao,C. H. Hu and K. K. Shung, "Devolepment of a real time digital high frequency annular array ultrasound imaging system," *IEEE Ultrasonics Symp*, pp. 1867-1870, 2003.

[30] A. A. Assef, J.M. Maia, F.K. Scheneider, E.T. Costa, V.L. Button, "A programmable FPGA-based 8-channel arbitrary waveform generator for medical ultrasound research activities," in *Engineering in Medicine and Biology Society (EMBC), 2012 Annual International Conference of the IEEE*, vol., no., pp. 515-518, Aug. 28 2012-Sept. 1, 2012.

[31] M. A. Hassan, and Y. M. Kadah, "Digital signal processing methodologies for conventional digital medical ultrasound imaging system," *American Journal of Biomedical Engineering*, vol. 3,no. 1, pp. 14-30, 2013.

[32] C. Hu, L. Zhang, J. M. Cannata, J. Yen, K. K. Shung, "Development of a 64 channel ultrasonic high frequency linear array imaging system," *Ultrasonics*, vol. 51, no. 8, pp. 953-959, 2013.

[33] A. A. Lazar and L. T. Toth, "Perfect recovery and sensitivity analysis of time encoded bandlimited signals," *IEEE Trans. Circuits Systems 1*, vol. 51, no. 10, pp. 2060-2073, Oct. 2004.

[34] N. S. Jayant and A. E. Rosenberg "The preference of slope overload to granularity in the delta modulation of speech," *Bell System Technical Journal*, vol. 50, no. 10, Dec. 1971.

[35] A. S. Alvarado and J. C. Principle, "From compressive to adaptive sampling of neural and ECG recordings," in *Proc. of IEEE Int. Conf. on Acoustics, Speech, and Signal Processing (ICASSP)*, pp. 633-636, Apr. 2011.

[36] J. Lu, H. Zou, and J. F. Greenleaf, "Biomedical ultrasound beam forming," *Ultrasound in Med. and Biol.*, vol. 20, pp. 403-428, 1994.

[37] H. Yao, "Synthetic aperture methods for medical ultrasonic imaging,", Ph.D. thesis, Univ. of Oslo, Norwa, 1997.

[38] I. LIE, M. E. TANASE, D. LASCU, and M. LASCU, "Ultrasonic beamforming with delta-sigma modulators," in *Proc. of the 10th WSEAS International Conference on CIRCUITS*, 2006, pp. 344-349.

[39] R. A. Mucci, "A comparison of efficient beamforming algorithms," *IEEE Trans. Acoust. Speach Signal Processing*, vol. ASSP-32, no. 3, pp. 548-558, 1984.

[40] T. I. Laasko, V. Valimaki, M. Karjalainen, and U .K. Laine "Splitting the unit delay," *IEEE Signal Processing Mag.*, vol. 13, pp. 30-60, 1996.

ASTES

Advances in Science, Technology and Engineering Systems Journal Vol. 3, No. 4, 72-82 (2018)

www.astesj.com

Special Issue on Multidisciplinary Sciences and Engineering

ASTESJ

ISSN: 2415-6698

Interactive Virtual Reality Educational Application

Shouq. Al Awadhi, Noor. Al Habib, Dalal Al-Murad, Fajer Al deei, Mariam Al Houti, Taha Beyrouthy, Samer Al-Kork*

American University of Middle East, Egaila, Kuwait

ARTICLE INFO

Article history:
Received: 19 May, 2018
Accepted: 09 July, 2018
Online: 11 July, 2018

Keywords:
Computer software and applications
Engineering
Information Technology

ABSTRACT

Virtual Reality (VR) technology has become one of the most advanced techniques that is used currently in many fields. The role of education is extremely important in every society; therefore, it should always be updated to be in line with new technologies and lifestyles. Applying technology in education enhances the way of teaching and learning. This paper clarifies a virtual reality application for educational resolutions. The application demonstrates a virtual educational environment that is seen through a Virtual Reality headset, and it is controlled by a motion controller. It allows the user to perform scientific experiments, attend online live 360° lectures, watch pre-recorded lectures, have a campus tour, and visit informative labs virtually. The application helps to overcome many educational issues including hazardous experiments, lack of equipment, and limited mobility of students with special needs.

1. Introduction

"This paper is an extension of work originally presented in BioSMART, the 2nd International Conference on Bio-engineering for Smart Technologies" titled 'Virtual Reality Application for Interactive and Informative Learning' [1]. Significantly, education has been improving throughout the past years by involving technology in this field. In addition, teaching and learning methods are being enhanced by using software and high-tech devices which are making education more effective. Assuming that, every new technology gets linked to education can solve at least one of the problems that face the field especially the students and the teachers. However, a lot of problems are still hindering students and teachers in schools and universities. Distractions and loss of attention during the lecture due to many factors are some of the problems that face the students, and that may lower their educational skills and scores. Furthermore, students are taking the lessons with lack of interest and excitement in the classroom. It is also difficult to visualize the explication of the lessons for some students [2]. Nevertheless, hazardous mistakes, which require practical implementation, are done in labs. For example, some chemical interactions and electrical experiments mistakes lead to considerable serious injuries.

Another problem is, some schools and universities cannot afford some expensive experimental materials. Also, it is hard to provide some biological organs all the time in schools. Finally, the lack of resources plays a huge role in decreasing the educational level of students with disabilities because some of them find it difficult to interact and perform experiments easily due to their special needs and the movements struggles that they face. Therefore, with the purpose of eliminating all these educational matters, technology must be involved with education essentially to build a better sophisticated and educative society.

2. Objectives

Virtual Reality (VR) is defined as "a computer with software that can generate realistic images and sounds in a real environment and enable the user to interact with this environment" [3]. Developing Virtual Reality applications is benefiting education in many aspects. Creating a virtual educational environment can help with solving a lot of educational problems. To be able to have this virtual educational environment different devices have to be connected together. Those devices are Virtual Reality headset, gesture controller or motion sensor, and 360° camera. For the VR headset, it will allow the user to be a part of the virtual world and see the virtual environment. The gesture controller will help him to interact inside this virtual environment. However, the 360° camera will take a realistic 360° images and videos, which will be

*Samer Al Kork, American University of the Middle East, +965 2225 1400 Ext. 1732, samer.alkork@aum.edu.kw

displayed inside the VR environment. In the other hand, many objectives are obtained by developing an educational virtual reality application. Assisting students in comprehending lectures easily and attracting students' attentions by using virtual visualized clarifications of the lecture are some of those objectives. Moreover, the application gives instructors a huge benefit in delivering information easily to the students by supporting their ideas with virtual visualizations. It helps also in performing hazardous experiments without being in danger since the experiments are going to be performed virtually, or student can practice those experiment virtually to be more cautious when they perform it in real-life. In addition, it can solve lack of equipment in labs and affording luxurious equipment problems because the equipment can be provided virtually. Finally, integrating the VR headset with the motion controller will give students with special needs the chance to perform experiments with less movements struggles.

3. Background and Literature Review

Since 1950s, virtual reality was on the boundary of technology but with lack of achievements [4]. However, there was a huge improvement in the virtual reality field in 2012 [5]. The VR headsets are considered as the main tool that enters the user to the virtual world. They are designed to able the user to see the virtual world through special lenses. Also, having a three-dimensional environment is required to be displayed on those VR headset. There are some useful software which help with creating those virtual three-dimensional environments. Those environments can be used as applications that allow the users to learn, watch videos and pictures, and play games.

The literature review discusses the required hardware and software to create a virtual environment and interact with it. First, the hardware part is divided into gesture sensors, VR headsets, and 360º cameras. Second, the software part compares some common software that are used in creating virtual environments and building three-dimensional (3D) applications. Lastly, some existing VR application were mentioned with their purposes.

3.1. Hardware

3.1.1. Gesture Sensors

Gesture controlling technology is a way that is used to detect body motion and gesture. This technology will enable users to interact with some objects and devices without physically touching them [6]. There are many kinds of gesture controllers that can work with the VR technology.

Myo armband is a gesture controller that controls arms' motion [7]. Moreover, Microsoft has produced a sensor controller called Kinect. The motion controller Kinect can be fixed separately on any object like a desk for example, and it is used mostly for gaming [8]. On the other hand, Oculus VR, which is an American technology company, produces touch controllers that are named Oculus touch that are consisting of two controllers that have buttons to control motion by thumbs [9].

Another controller is Leap Motion which is a small device that helps the user to interact with the objects using their free hands. This controller tracks fingers and hands by using three sensors. It can be connected to the PC through a USB port. In addition, it has its own Software Development Kits (SDKs) that helps in programming [10].

3.1.2. Headsets

VR headsets allow the users to enter through a Three-dimensional sphere, so they can look at, move around, and interact with the 3D virtual environments as if they are real environments.

As an example of the VR headsets, HTC Vive headset is considered as a complete set that contains a headset, two motion controllers, and two base stations for defining a whole-room area. HTC Vive has a unique tracking system that tracks the users' movements in 10-foot cube from his position. Also, it provides SDKs for the VR devices in order to simplify the programming process for developers. In addition, it has 32 sensors for 360º motion tracking and a front facing camera which helps in making the virtual world more realistic. The motion tracking system of HTC Vive has two controllers which come with two wireless Lighthouses cameras that senses the signals coming from the headset and the controller's sensors. Then, it programs these signals to make the users moves and interacts virtually in the virtual environment [11].

On the other hand, Samsung Gear VR is considered as one of the most affordable VR headsets. However, it needs specific Samsung Galaxy smartphones to work with. This need constricts the users of Samsung Gear VR headsets because they have to use one of those specific Samsung phones which are Galaxy note 7, S7, S7 Edge, Note 5, S6, S6 edge, and S6 Edge Plus [12].

Oculus Rift headset is another example of the existing VR headsets. This headset can make the user totally immersed inside the virtual environment. In addition, it provides the user with precise picturing scenes and enjoyable interactive experience. It works with 2160 x 1200 resolution, and it is considered to be lighter than its first competitor HTC Vive, which is mentioned previously, since it only weights 470 grams. Oculus offers a package consisting of a single VR headset along with touch controllers for 798$ [13].

However, Oculus Rift DK2 is the oldest version of Oculus Rift. It is a VR headset that provides a stereoscopic 3D view which maintains excellent depth and scale. Oculus Rift DK2 has a 360º head tracking technology and an external camera for enhancing the Rift's positional tracking ability. In addition, its motherboard contains an ARM Cortex-M3 microcontroller that is used to utilize the ARM Thumb-2 Instruction Set Architecture, so the device provides full programmability and enables high performance [14].

Lastly, Google Cardboard is a VR headset that was released in 2014. It considered as one of the lightest VR headsets due to the light materials which are used to build it with. Those materials are cartoon, woven nylon, and rubber as the outer headset, and it

comes with two lenses. Also, it has some specifications that able the users to enter the virtual world [15].

3.1.3. 360º Cameras

360º cameras are common nowadays. They are provided with one or more lenses to take a certain degree photos and videos. There are many available types in the market.

As an example of the 360º cameras, the Bubl 360º camera utilize four lenses to capture the images, and it can capture 14 mega pixel spherical images and videos. It uses Wi-Fi to able the users to share the recorded videos and photos through social network. It also allows live-streaming directly to the user's PC or mobile. Bubl 360º camera also have the MicroSD card which save all the contents [16].

The 360fly 4K camera is also one of the common 360º cameras, and it has the ability to capture 16 mega pixel photos and videos. It has a water resistant up to 1 ATM, so it can capture photos and videos under the water. Furthermore, it allows user to live-steam directly, and it has a high resolution [17].

However, the Gear 360º camera records and capture videos and photos with 15 mega pixels. It has two lenses that are horizontal and vertical. Each lens captures 180º of the view, so the view in total will be 360º. It also has water resistant. The Gear 360º camera was invented for the Samsung VR headset and Samsung smartphone [18].

In addition, the LG 360º camera can capture both 360º and 180º images and videos. Also, it allows the users to capture those images with 13 mega pixels. Android 5.0 or later updates and IOS8 or later updates devices holders can use this camera. It is friendly to use with YouTube and Google Street view applications which allow the users to explore some of the 360º videos and photos and share them as well [19].

Finally, Ricoh Theta S camera is a small 360º camera that has two lenses each with 180º field of view. It can take 360º images and video, and it also support the live-streaming mode. It can be connected to the PC through a USB port or a Wi-Fi connection [20].

3.1.4. Software

There are many existing software that provide creating virtual environments like Unity3D, Open Wonderland, and Unreal.

First, Open Wonderland is considered as a 3D toolkit which can build virtual reality environments. It is a Java based application that has many services. Also, it supports many platforms such as IOS, Android, Mac, and Windows [21].

Second, Unreal is a software that support C# and Blueprints programming languages. Blueprints Visual Scripting System helps those users who are unused to deal with programming languages to create their virtual environments easily in this software. Moreover, it has many services including multiplayer capability, more detailed graphics, and flexible plugin architecture [22].

Lastly, Unity 3D software is a software that helps the developer to create the virtual scenes. It supports three programming languages which are Boo, C#, and JavaScript. It also has existed tutorials and online chat, where all of the users can communicate and help each other, on their official website. Furthermore, it has a free version which helps with lowering the cost of building a virtual application [23].

3.1.5. Existing Application

Virtual Reality is used in different fields, so many VR application were created in order to so some tasks in each of those fields.

One of these VR applications is the "Interactive Pedestrian Environment Simulator". This Simulator is used for cognitive monitoring and evaluation. It demonstrates a virtual traffic environment that helps in ensuring the safety of pedestrian and elderly people at the road. The application was built by using Unity3D software [24] and was demonstrated using Oculus Rift DK2 connected to Leap Motion and Myo by Thalmic Labs [25].

Moreover, Titan of Spare application, which is considered to be as an educational simulator, which allows students to orbit the solar system and discover the planets virtually. It provides the chance for them to learn and discuss about the space in an exciting and motivating technique. Students are allowed to perform several errands including zooming in and out the system, discovering the planets in the solar system, and gaining information about each planet. The application was developed for Google cardboard, Oculus Rift, HTC Vive, and Samsung Gear platforms [26].

Another simulator is Virtual Electrical Manual 'VEMA' which is a virtual electronics lab that facilitate the way of learning and understanding the electrical circuits. It allows the students performing circuits virtually to prevent dangerous incidents with electricity. It contains different menus such as equipment menu, capacitor menu, construction of Direct Current (DC) circuits menu, Alternating Current (AC) menu, and resonance menu. Several information is demonstrated in each menu to unsure the students' understanding. The developers of this application used Wirefusion software to build up the 3D objects in the virtual lab, and they used JavaScript as a programming language in order to interact with the 3D objects [27].

Additionally, the Chemistry Lab Application was developed as an educational animated application to provide the chance for students to perform chemical experiments virtually. It reduces the chances of having real-life injuries and causing serious damages due to the chemicals use. Developers used Autodesk Maya software for creating the 3D objects in this virtual lab. HTC Vive headset and its controllers were used to enter user to the virtual world of this application and to interact with the 3D objects inside the labs there. Unity3D software was used to build this application [28].

4. Methods

The proposed system of the application consists of both hardware and software modules. After comparing the common existing devices together and doing some calculations to see which fits our needs, the hardware module was designed. First, the common VR headsets were compared deepening on the frequency, price, angle of view, weight, resolution, connection, SDKs, platforms, and integration. Meanwhile, the common 360º cameras were compared depending on price, SDKs, number of lenses, connection, resolution, RAM, Angle, battery life, frequency, and integration. For the gesture controllers, there were few controllers on the market, so it was easy to take a decision. The most important criteria that was taken into consideration while choosing the motion controller was the accuracy because it will affect the whole project. Without an accurate controller, the application will not work in an effective way. Moreover, the tracking area of the motion sensor should be wide as much as possible to make sure that the motions will be within the range. In addition, the controller must be easy to use, so the user feels comfortable while moving. Since there is a limited budget, so the price of the motion sensor must be affordable. As a result, for the hardware implementation, Oculus Rift as VR headset, Leap Motion as gesture motion controller sensor, and Ricoh Theta S as 360º camera were chosen to be integrated together with a VR ready PC. Figure 1 shows the connections between all the devices that are used in this project. As shown in Figure 1, Oculus Rift should be connected to the PC using USB and HDMI ports. Moreover, Leap Motion controller should be connected to the PC using USB port, and Ricoh Theta S 360º camera can be connected to the PC using USB port or Theta's Wi-Fi connection that it provides. All the devices should be initialized on the PC at the beginning. The software and the needed SDKs of each device should be installed on the PC.

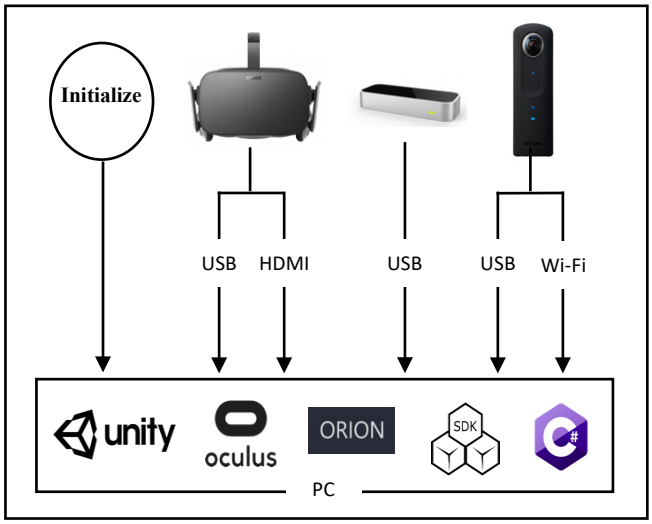

Figure 1: High Level Design Flowchart

Before choosing a software to build the application with, the specifications of the most common software that provide building a virtual environment were compared together in order to get the final decision. Those common software are Unity3D, Open Wonderland, and Unreal. Some of the main criteria of choosing the software were, the software should be easy to be dealt with and there should be existing tutorials to help with learning how to use it well. In addition, the programming languages, graphics capability, and the services that each software provides were taken into consideration. As a result, Unity3D game engine was chosen because it satisfies all the needs of this project.

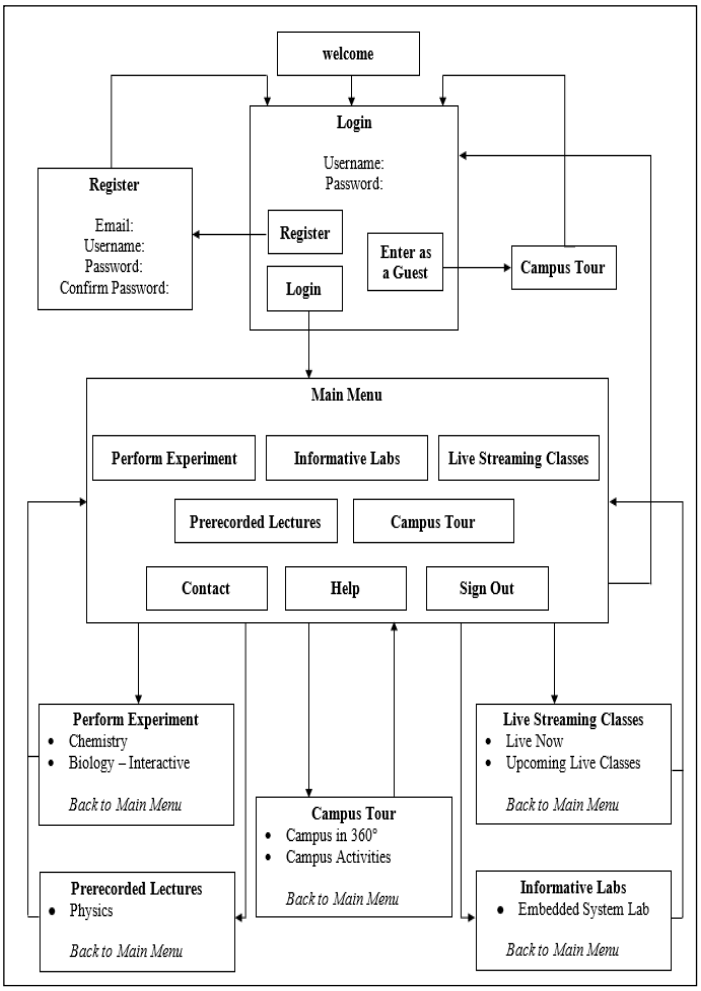

Figure 2: User Interface Hierarchy Flowchart

For the software implementation, Figure 2 shows the user interface hierarchy, and it describes the flow of the application in general. Each box in the flowchart shown in Figure 2 represents a main scene. Meanwhile, each main scene has some sub-scenes that execute a specific task such as performing experiments, watching pre-recorded lectures, having a campus tour, attending online live-streaming classes, and identifying elements and components in the informative labs. To perform those tasks, many taught courses such as Biology, Chemistry, and Physics were referred to in those scenes.

As a start, a welcome scene will be showed to the user once he plays the application. Then, he will be directed to the "Main Menu" where three main buttons which are "Enter as a Guest", "Register", and "Login" can be found. The "Enter as a Guest" button will give the user an access to have a tour around the campus only, so the user will have to register in order to get a full

access to the application. However, the application needed to be secured since it is used for an educational purpose, so a registration and a login feature were added. The user is required to fill in the needed information which are the "Username", "Email", "Password", and "Confirm Password" in the registration scene. Once the user is done with filling the information there, the system will check if the "Username" is valid or not and if the "Password" and "Confirm Password" fields are identical or not. If there is any error, the system will show a message regarding the error. Otherwise, the system will complete the registration process and add the user to the database. After that, the user will be able to login, and once he enters his username and password, the system will check the database if this user has an authorization or not. If the username is not found or the password is not correct, the system will show a message about this error. If the login is successful, the user will be directed to the "Main Menu" where he can choose to enter to one of the provided sub-scenes. If the user chose "Perform experiment" scene, he will be directed to that scene where he can choose between entering the Biology or the Chemistry labs to either interact with the objects or perform experiments virtually ending up with small quizzes to test his understanding. On the other hand, if the user chose to enter the "Informative labs" scene, he will be directed to a scene where he can visit an embedded system lab virtually to notify and learn about each equipment and their location inside the lab. For the live-streaming sub-scene, the user can enter "Upcoming Live Classes" scene to check the time schedule of the upcoming live classes. Then, if there is an available live class at any time, the user can enter "LIVE NOW" scene to attend the given lecture virtually. Moreover, by entering the "Prerecorded Lecture" scene, the user will be able to choose the "Physics Lecture" scene where a physical experiment was recorded to be displayed to the user, so he can refer to it whenever needed. In the "Campus Tour" scene, the users can choose to attend a scene where they can watch 360^0 pictures and videos of the campus facilities or visit a scene where they can display photos and videos of the campus activities taken with Ricoh Theta S 360^0 camera. Each sub-scene has a "Back to Main Menu" button, so the user can easily shift between scenes. Finally, the users can find the contact information of the university, manage the settings, get some help, and sign out from their accounts by clicking on the required button showed on the "Main Menu". Some Assets, codes, equations, object, and animations were used to implement the application.

4.1. Assets and codes

To be able to build the application using Unity3D game engine many assets and codes, which were written with different programming languages, were used. To show the hands, interact with the objects, and trigger the items inside the scenes Leap Motion assets [29] were used. In addition, Curved Keyboard [30] asset was used to show the keyboard that helps the users with entering characters in the "Login" and "Register" scenes. Furthermore, Curved UI assets [31] were downloaded into unity3D software to provide a curved interface that has 180^o of view, so the interface will be flexible and easy to use. It is also a scalable interface, and it can support different VR Headsets including Oculus Rift, Gear VR, HTC Vive, and Google Cardboard. In addition, it supports many controllers other than the Leap Motion, which is the used gesture controller sensor for this project, such as the mouse, Vive controller and Oculus Touch. Lastly, Theta Wi-Fi Streaming asset [32] were downloaded to be able to have online live-streaming classes.

For codes and programing, Unity3D software support C# and JavaScript as programming languages. Both of these languages were used to write some codes in order to perform some actions inside the application. In this application, many functions were programmed to transfer the user from scene to scene, show and hide User Interface (UI) elements, display two-dimensional (2D) and 360^o videos, generate animations by using Unity3D particle systems, login, register, and calculate the grades of the Biology and Chemistry experiments based on the user performance. In addition, a virtual tutor was programmed to give the user immediate instructions and feedbacks depend on his actions, so the user will be helped to move easily through the application in general.

4.2. Equations

Since there are quizzes and graded experiments in the application, few equations were used to calculate the score of the students' performance. First, the Chemistry lab has two multi-leveled experiments and a quiz. The total score of the Chemistry lab is divided to cover all those multi-leveled experiments and the final grade of the quiz. In total of a 100 scores, the first multi-leveled experiment worth 25%, the second multi-leveled experiment worth also 25%, and the quiz worth 50%. Equation 1 is used to calculate the grade of each level of the experiments. The symbol *TIME* represents the time consumption of each student to finish each experiment. Depending on the code, if the time consumption of the user is 60 seconds or below, *TIME* will get the value 60. In addition, the symbol *TRIALS* represents the number of trials the student use to complete the experiment. However, both of *TIME* and *TRIALS* mentioned in "(1)" have 50% of each level's grade which is already worth 25% of the total score as previously mentioned.

$$Score = ((50/TRIALS) + ((50*60) /TIME))/2 \qquad (1)$$

The quiz of the Chemistry lab is divided into five questions, so each one worth 10 scores out of 50% of the total score. Equation 2 is used to calculate the quiz grades. The symbol x represents the answer of each question, so if the right answer is chosen the value of x will be 1. Otherwise, the value of x will be 0. The symbol *TIME* in "(2)" represents the time consumption of the user to solve each question in the quiz. Depending on the code, if the time consumption of the user is 15 seconds or less, *TIME* will be valued as 15.

$$Score = (((15 * x) /TIME) * 10) \qquad (2)$$

For the Biology lab, it was built to be more interactive than being experimental, so the student will be only evaluated depending on the quiz grades. Equation 2, which is used to

calculate the Chemistry lab quiz, is also used to calculate the grade of the Biology lab quiz too. As the Chemistry lab, the Biology lab is divided into five questions, and each of them worth 10 scores out of 50. Since there is no experimental part on the Biology lab, the total score of it is 50.

4.3. Three-Dimensional (3D) Objects and Animations

Inside the virtual environment of this application some animations and three-dimensional objects were used. For example, Chemistry and Biology labs are animated labs which are based on animations, 3D objects, and 3D characters. In addition, the pre-recorded class in this application was built to have a combination between those 3D objects and a 2D video. Furthermore, the virtual tutor was created using 3D objects and characters. Some of those three-dimensional objects were built using tools from Unity3D game engine, and some of them were predefined from the software itself. The location, position, size, and color of those objects and animations were modified and customized to fit the project's needs. Some of these objects are interactive, so the user can hold, release, and move them inside the scenes. Those objects were created and designed in a way that appears close to the real-life objects. Hence, the objects which some of them are the labs equipment will be recognizable and observable to the user while doing the experiments or moving through the application. Moreover, fire, bubbles, and liquid drops are examples of the animations that are used in the Chemistry lab scene. Those specific animations were created using particle systems offered by Unity3D software.

5. Final Results and Achievements

As a result, Oculus Rift as a virtual reality headset, Leap Motion as a motion sensor and gesture controller, and Ricoh Theta S 360º camera were integrated together with a PC that has Unity3D game engine to build a fully interactive educational VR application. Users can interact with the application using their free hands as shown in Figure 3. The interaction between the hands and the application was done due to the detection of the users' gestures using Leap Motion controller.

Figure 3: Hardware Integration

5.1. User Interface

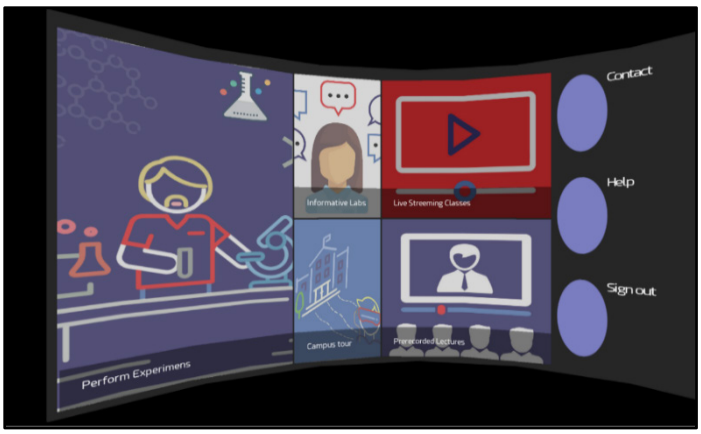

Figure 4: Main Menu User Interface

The user interface was constructed to be curved using the CurvedUI asset [31], and it was customized to fit the application's needs. Having a curved user interface can give the user 180º cylindrical view, which will make the menu fully interactive from any angle. Figure 4 shows the use of the CurvedUI asset on the "Main Menu" inside the application.

5.2. Chemistry Lab Scene

The Chemistry lab scene is divided into five levels scenes other than the main scene where the student will be able to identify the equipment that will be used during the coming levels virtually. This feature will help in solving the problem of lack of equipment and the problem of affording expensive ones in real life. In level 1 and 2, experiment 1 will be demonstrated. However, in level 3 and 4, experiment 2 will be demonstrated. Students will not be able to choose the number of the level, so he will start by level 1, pass through the next levels ascendingly, and end up with the quiz.

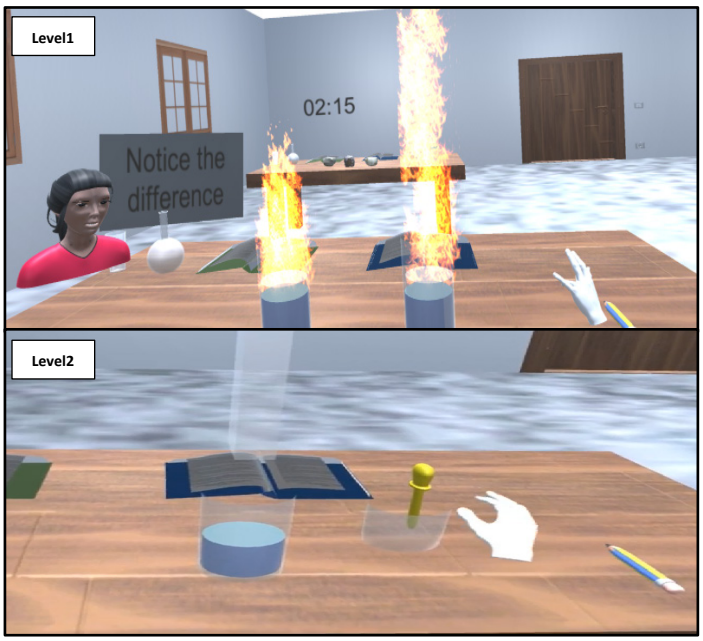

Figure 5: Chemistry Lab Scene Level 1 and Level 2

In the first level, the students will be allowed to perform a dangerous real-life experiment which is "The Reaction of Sodium with Water" that produces fire [33], so the user will try to place two virtual different sized pieces of Sodium into water and notice the difference between the reactions them. In fact, the larger the amount of Sodium the more fire will be produced as shown in Figure 5. Then, the students will check the acidity of the product in level 2 by dropping Phenolphthalein virtually on it. After dropping Phenolphthalein, if the product color turned to pink color, the product will be considered as a base.

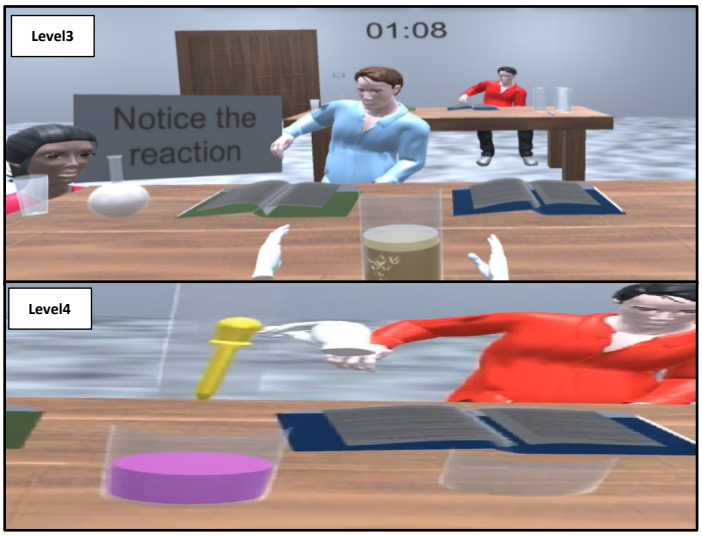

Figure 6: Chemistry Lab Scene Level 3 and Level 4

In level 3, the students will be able to recognize the reaction between Sodium and Alcohol. As level 1, the student will try to place two different sizes of Sodium inside the Alcohol. Then, they will try to notice the reaction. Unlike the reaction of Sodium with water, the reaction between Sodium with Alcohol will produce bubbles in real-life [34]. The more the amount of Sodium is used, the more bubbles will be produced. As level 2, the student will check the acidity of the product by dropping Phenolphthalein into it, and if the color of the product is changed into pink as shown in Figure 6, it will be considered as a base [35].

After the experimental part, a quiz will be provided in level 5 including five questions to test students' understanding as shown in Figure 7.

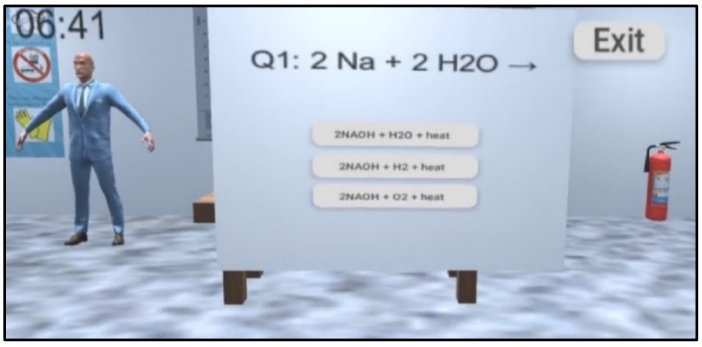

Figure 7: Chemistry Lab Quiz

Finally, the scores of experiment 1, experiment 2, and the quiz will be displayed on the score scene as shown in Figure 8.

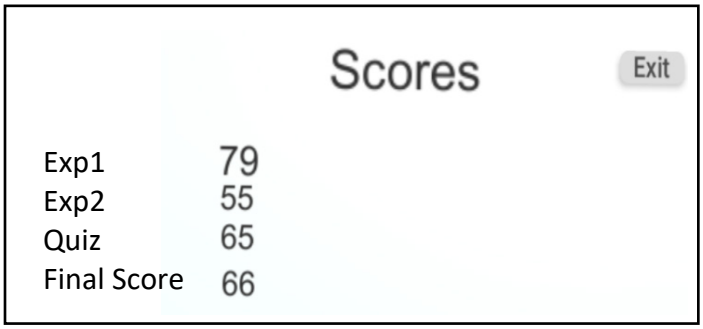

Figure 8: Chemistry Lab Scores

Regarding the applicability of VR teaching within the Chemistry lab scene, some situations are programmed to be aligned with the real-life incidents. For example, if the sodium was dropped by mistake on the ground in this application, the student can sit and pick it up as if it is real. This will give the students the chance to try and learn about how to do it in reality. Also, as mentioned previously, the different amounts of produced fire and bubbles due to the size of Sodium are examples of the applicability of VR teaching because this virtual experimental practice will lead the student to get main idea. However, some other incidents are not programmed yet. In brief, applying this experiment virtually will give the students the chance to practice the experiment and see its reaction, so if this experiment is performed in real-life the students will be more cautious. As a result of using this education supplementary virtual reality application, serious injuries will be prevented or reduced.

5.3. Biology Lab Scene

The Biology lab was built in order to help the students with learning and interacting with the biological organs virtually because it is hard to deal with them in real-life. Also, it is difficult to afford real biological organs, so this lab helps solving this problem. In the Biology interactive and informative lab scene, the user can interact with the different virtual biological objects such as human muscle, human heart, human skeleton, and a plant cell. A box of information about each object will appear to the user by triggering the objects.

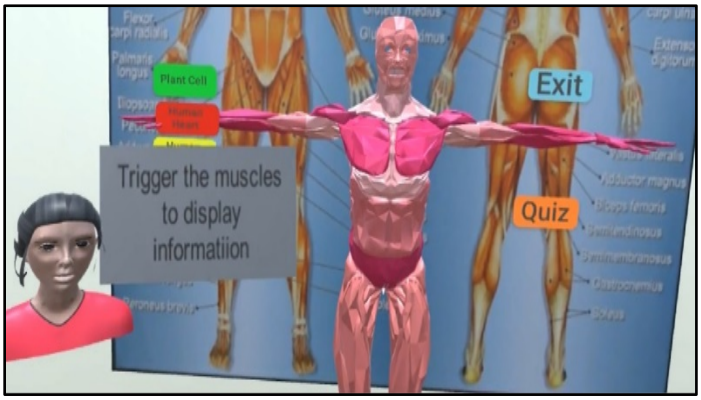

Figure 9: Human Muscles Scene

Figure 9 represents the human muscles scene, where students can see a 3D virtual human muscle module. By following the virtual tutor guidance, the student will be asked to trigger the human muscle module so that a list of information about the human muscles will be displayed in the information box.

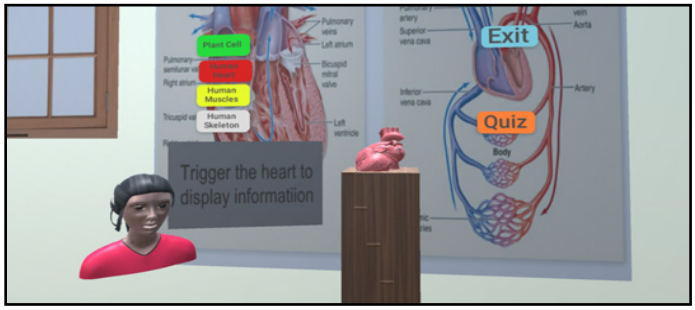

Figure 10: Human Heart Scene

The human heart scene shown in Figure 10 includes a 3D human heart module. By triggering this heart module, a list of general information about the human heart will be appeared to the student. Students will be asked in the quiz later questions which are related to the information.

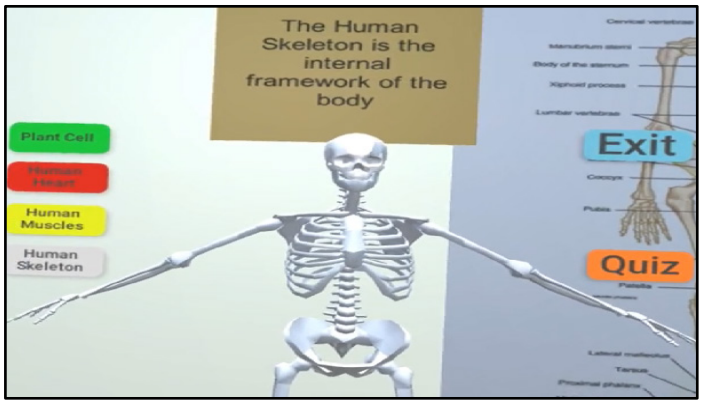

:Figure 11 Human Skeleton Scene

The human skeleton shown in Figure 11 will be displayed in the human skeleton scene in the Biology lab. In this scene, students will be asked to trigger the skeleton itself, so a box of information about this body part will be shown to them.

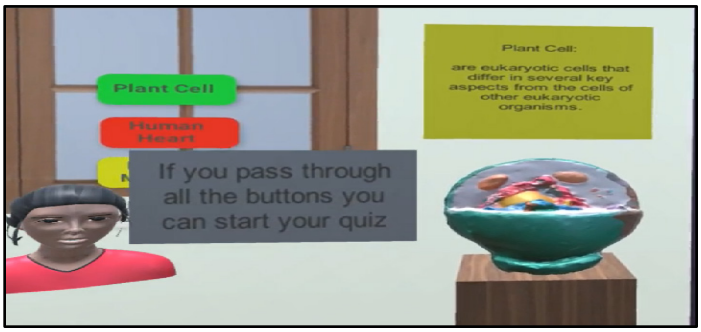

Figure 12: Plant Cell Scene

Moreover, the plant cell scene shown in Figure 12 includes a 3D plant cell module. Students can see the small components of the cell in a clear and interesting way that will help them to understand easily. Also, they can gain some information about the plant cell after looking at the information box that will be displayed when the plant cell is triggered.

After recognizing all the elements in the Biology lab, students can take a provided quiz that consist of five questions to test their understating. Then, the scores scene, where only the quiz grades will be appeared since there is no experimental part in the Biology virtual lab, will be displayed.

5.4. Pre-recorded Physics Lecture Scene

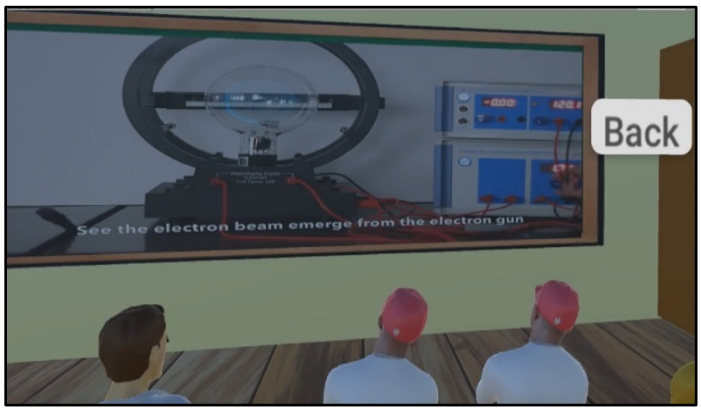

Figure 13: Prerecorded Physics Lecture Scene

A pre-recorded Physics lecture scene was created in this application to include one of the Physics experiments that need expensive equipment. Some educational societies cannot afford the equipment, so this feature provides a way to visualize what are being taught in the class with a lower cost. The recorded experiment in this scene is known as “Charge to Mass Ratio experiment” [36]. As shown in Figure 13, this scene is a combination between animated 3D characters and a 2D video.

5.5. Informative Lab Scene

Figure 14: Informative Embedded System Lab Scene

In the informative lab scene as shown in Figure 14, the user can attend a real-pictured 360º embedded system lab. This picture was taken using Ricoh Theta S 360º camera. Some floating buttons were added to the scene, so when the user press those buttons, a clear image of different equipment that are used inside the lab with its description will be shown. This lab will help students to gain more information about the use of those equipment in real-life.

5.6. Live-streaming Scene

Figure 15: Live-streaming Scene

In the live-streaming scene shown in Figure 15, the live-streaming feature was developed to provide the chance to attend virtually 360º online live classes after checking the lectures' timing on the provided schedule. To be able to have the live-streaming feature, the PC should be connected with Ricoh Theta S 360º camera's wi-fi that it provides. Having this attribute will help in increasing the number of the available seats in some particular classes that are full seated in real-life.

5.7. Campus Tour Scenes

Campus Tour considered as multiple scenes where the user can have a virtual tour inside the campus. He can see a gallery where 360º images and videos of the campus facilities are provided including the activities that have been done in the campus. All of the 360º photos and videos were taken using Ricoh Theta S 360º camera to make the user's tour be close to the reality. One of the advantages of this tour is having a virtual orientation around the campus, which will help in recognizing the campus before applying to this university or this school for example. Another advantage is, the virtual campus tour will help new students in recognizing the campus's facilities. In addition, it will allow the students, who missed the activities, to attend them virtually as if they were there.

5.8. Virtual Tutor

Figure 16: Virtual Tutor

A virtual tutor, which is shown in Figure 16, was created to guide the user inside the application. It was programmed to give immediate instructions and feedbacks depending on the user's actions. For example, it gives the user the instruction on doing the experiment inside the Chemistry lab, and it tells him well done if he passed the experiment. Also, it is used to tell the user which button to click or what movement should he do in order to perform the tasks.

5.9. Testing and Evaluation

In order to evaluate the performance of the application and to achieve the design specifications, different methods were applied to the hardware and software. First method, we moved through the application step by step and checked whether all the scenes are operating correctly or not. At the same time, the functionality of the hardware parts such as sensors were checked to make sure they are working and tracking well. In addition, all the bugs and errors that were found have been fixed.

Another followed method was, evaluating the application by multiple users and to get their feedbacks regarding their experience and the issues they faced. This includes their technical experience about the functionality of the buttons, effects, clicks, animations, and the response time of the actions. The application was tested with an approximate total of more than 50 students and 20 instructors from our university which is the American University of the Middle East, 16 instructors and 12 students from the BioSMART conference which is the Second International Conference on Bio-engineering for Smart Technologies held in Paris, and over 200 people with different positions in Knowledge Summit held in Dubai. Most of the feedbacks supported the idea of having a fully interactive educational application for practical and informative learning. On the other hand, some of them concerned about the difficulty of dealing with the virtual environment using Leap Motion gesture controller. In fact, this concern is normal because the Leap Motion controller needs some practice in order to get used to it. Some people refused the idea of replacing real teaching process with VR teaching. However, this application is an education supplementary application that will help in reducing some educational issues, so it will support the real teaching processes. At last, it was important to take these feedbacks into consideration to give the user a better experience and to improve the quality and the performance of the application. As a future plan, when there is an availability the application will be tested on people with disabilities to check their performance and to see their acceptance to the idea of this application.

5.10. New-Work

Additional to what was presented on BioSMART conference, some upgrades to the application were added. A Database using C# was created to collect data and results in one place, so it can be easily accessed and tracked. This Database keeps profile of each user whether instructor or student. Having the Database in the application will help the user to know how well he is doing, and it will help instructors in evaluating the students based on their reports easily. As shown in Figure 17 below, each user's folder contains three file which are the user's information file, the Chemistry lab scene scores file, and the Biology lab scene scores file. For the user's information file, it contains the username, email,

and password of the user as shown in Figure 17. On the other hand, the scores scenes will contain only numbers that represents the scores of each experiment and quiz in those scenes. On the other hand, the database can be used also to report the user's activity and attendance of live streaming classes and prerecorded lectures for example. However, it is a basic database, so some other upgrades will be provided to add some more professional features like those.

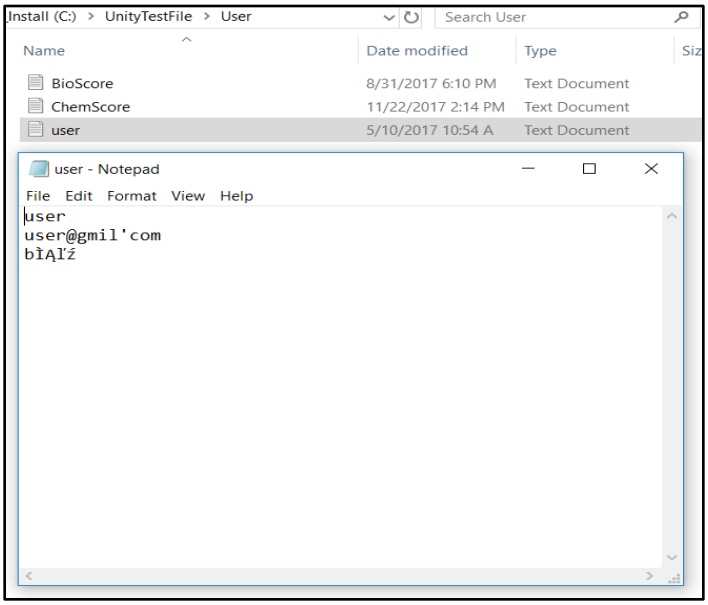

Figure 17: User's File

6. Conclusion

In conclusion, the evolution of technology succeeded in spreading the use virtual reality nowadays in several fields including education. Since that, a virtual reality application for educational purpose such as practical learning was built to solve some of the educational issues. This provided solution will facilitate the way of learning and teaching. Student's understanding and attention will be increased, and teachers will have an easier way to deliver the information to them using this application. In addition, dangerous mistakes in labs will be prevented or reduced due to the practical virtual implementation, so students will be able to practice dangerous experiments safely. Also, the number of lack of equipment problems will be decreased since those equipment will be provided simply inside the virtual environment. Nevertheless, students with disability will be involved in performing experiments with less movements struggles. Furthermore, this application is supporting gaining information in an interesting way because of the use of virtual reality technology. As an outcome, Oculus Rift as a virtual reality headset, Leap Motion as a motion sensor and gesture controller, and Ricoh Theta S as a 360° camera were integrated together with Unity3D game engine to produce this educational tool that can help in developing the educational field.

Conflict of Interest

The authors declare no conflict of interest.

Acknowledgment

This project was supported and Funded by the American University of the Middle East (AUM) where we spent time doing the project at the Research and Innovation Center with endless support from the professors, instructors, and engineers. We would like to show our gratitude to them for assisting, helping, and shearing their pearl of wisdom with us to complete this project.

References

[1] S. AlAwadhi N. AlHabib, D. Murad, F. AlDeei, M. AlHouti, T.Beyrouthy, S. AlKork., "Virtual reality application for interactive and informative learning," 2017 2nd International Conference on Bio-engineering for Smart Technologies (BioSMART), Paris, 2017, pp. 1-4. doi: 10.1109/BIOSMART.2017.8095336
[2] G. Leman and W. Tony, "Virtual worlds as a constructivist learning platform: evaluations of 3D virtual worlds on design teaching and learning," Journal of Information Technology in Construction (ITcon), pp. 578-593, 2008.
[3] P. Brey, "Virtual Reality and Computer Simulation," The handbook of information and computer ethics, pp. 361-363, 2008.
[4] G. Burdea and P. Coiffet, Virtual Reality Technology, Canada: John Wiley & Sons, 2003.
[5] G. V. B. Yuri Antonio, "Overview of Virtual Reality Technologies," Southampton, United Kingdom, 2013.
[6] G. Daniel, "Will gesture recognition technology point the way?," vol. 37, no. 10, pp. 20 - 23 , 2004.
[7] N. Rachel, "Armband adds a twitch to gesture control," *New Scientist,* vol. 217, no. 2906, p. 21, 2013.
[8] X. Zhang, Z. Ye and L. Jin, "A New Writing Experience: Finger Writing in the Air Using a Kinect Sensor," vol. 20, no. 4, pp. 85 - 93, 2013.
[9] Higgins, Jason Andrew, Benjamin E. Tunberg Rogoza, and Sharvil Shailesh Talati. "Hand-Held Controllers with Capacitive Touch Sensors for Virtual-Reality Systems." U.S. Patent Application 14/737,162, 2016.
[10] "Leap Motion Unity Overview," Leap motion, 2016. [Online]. Available: https://leapmotion.com.
[11] L. Prasuethsut, "Why HTC Vive won our first VR Headset of the Year award," WAREABLE, 2 November 2016. [Online]. Available: https://www.warea [2]ble.com.
[12] G. Carey, "Spec Showdown: Oculus Rift vs. Samsung Gear VR," 6 January 2016. [Online]. Available: http://www.digitaltrends.com.
[13] "intoducing Oculus Ready PCs," 2016. [Online]. Available: https://www.oculus.com.
[14] B. Lang, "Oculus Rift DK2 Pre-order, Release Date, Specs, and Features," Road to VR, 5 October 2016. [Online]. Available: http://www.roadtovr.com.
[15] "Cardboard," google, 2016. [Online]. Available: https://vr.google.com.
[16] "Be a part of 360 Spherical Movement," Bublcam, 2015. [Online]. Available: https://www.bublcam.com.
[17] "360fly 4K Specifications," 360fly, 2016. [Online]. Available: https://360fly.com.
[18] "GEAR 360," samsung, 2016. [Online]. Available: http://www.samsung.com.
[19] "LG 360 CAM," LG, 2016. [Online]. Available: http://www.lg.com.
[20] "High-spec model that captures all of the surprises and beauty from 360°," THETA, 2016. [Online]. Available: https://theta360.com.
[21] J. Kaplan and Y. Nicole, "Open Wonderland: An Extensible Virtual World Architecture," vol. 15, no. 5, pp. 38 - 45, 2011.
[22] G. A. Kaminka, M. M. Veloso, S. Schaffer, C. Sollitto, R. Adobbati, R. Adobbati, A. Scholer and S. Tejada, "GameBots: a flexible test bed for multiagent team research," *Communications of the ACM - Internet abuse in the workplace and Game engines in scientific research,* vol. 45, no. 1, pp. 43-45, 2002.
[23] "Unity 3D," Unity 3D, 2016. [Online]. Available: https://unity3d.com.
[24] J. Orlosky and M. Weber, "An Interactive Pedestrian Environment Simulator for Cognitive Monitoring and Evaluation," pp. 57-60 , 2015.
[25] N. Owano, "Thalmic Labs' Alpha users explore Myo with Oculus," 2014.
[26] "Titans of space," 2016. [Online]. Available: http://www.titansofspacevr.com.
[27] V. M. Travassos and M. C. Ferreira, "Virtual labs in electrical engineering education - The VEMA environment," Information Technology Based Higher Education and Training, 2014.

[28] C. Smith, "Chemistry Lab VR," 2016. [Online]. Available: https://devpost.com.
[29] "Leap Motion Unity Overview," Leap motion, 2016. [Online]. Available: https://leapmotion.com.
[30] "Unity 3D," Unity 3D, 2016. [Online]. Available: https://unity3d.com.
[31] "Curved UI - VR Ready Solution To Bend / Warp Your Canvas!," Unity 3D, 2016. [Online]. Available: https://www.unity3d.com
[32] High-spec model that captures all of the surprises and beauty from360°," THETA, 2016. [Online]. Available: https://theta360.com
[33] C. Bobbert, "Solvation and chemical reaction of sodium in water clusters," The European Physical Journal D - Atomic, Molecular, Optical and Plasma Physics, vol. 16, no. 1, p. 95–97, 2001.
[34] J. Clark, "REACTING ALCOHOLS WITH SODIUM," 2009. [Online]. Available: http://www.chemguide.co.uk/.
[35] Repp, Julia, Christine Böhm, JR Crespo López-Urrutia, Andreas Dörr, Sergey Eliseev, Sebastian George, Mikhail Goncharov, "PENTATRAP: a novel cryogenic multi-Penning-trap experiment for high-precision mass measurements on highly charged ions." Applied Physics B 107, no. 4 (2012): 983-996.
[36] Al Kork SK, Denby B, Roussel P, Chawah P, Buchman L, Adda-Decker M, Xu K, Tsalakanidou F, Kitsikidis A, Dagnino FM, Ott M, Pozzi F, Stone M, Yilmaz E, Uğurca D, Şahin C "A novel human interaction game-like application to learn, perform and evaluate modern contemporary singing: "human beat box"". In: Proceedings of the 10th international conference on computer vision theory and applications (VISAPP2015), 2015
[37] Ulmer, S., C. Smorra, A. Mooser, Kurt Franke, H. Nagahama, G. Schneider, T. Higuchi et al. "High-precision comparison of the antiproton-to-proton charge-to-mass ratio." Nature 524, no. 7564 (2015): 196, 2015.
[38] Al Kork S, Amirouche F, Abraham E, Gonzalez M. "Development of 3D Finite Element Model of Human Elbow to Study Elbow Dislocation and Instability". ASME. Summer Bioengineering Conference, ASME Summer Bioengineering Conference, Parts A and B ():625-626, 2009
[39] E. Saar, "Touching reality: Exploring how to immerse the user in a virtual reality using a touch device," p. 43, 2014.
[40] D. D. Carlos, Corneal Ablation and Contact Lens Fitting: Physical, Optical and Visual Implicatios., Spain: Universidad de Valladolid, 2009.
[41] Patrick CHAWAH et al., "An educational platform to capture, visualize and analyze rare singing", Interspeech 2014 conference, Singapore, September 2014

ASTES

Advances in Science, Technology and Engineering Systems Journal Vol. 3, No. 4, 83-98 (2018)

www.astesj.com

Special Issue on Multidisciplinary Sciences and Engineering

ASTESJ

ISSN: 2415-6698

Theory Building of Quattro Bottom Line Approach for Sustainable Reverse Logistics from Government Perspective: the Indonesia Evidence

Hesti Maheswari*, Gatot Yudoko, Akbar Adhiutama

School of Business and Management. Institut Teknologi Bandung, Bandung 40132, Indonesia

ARTICLE INFO

Article history:
Received: 11 June, 2018
Accepted: 7 July, 2018
Online: 23 July, 2018

Keywords:
Sustainable reverse logistic
Quattro bottom line
Government perspectives

ABSTRACT

Reverse logistics activities are widely used application to preserve the environment in many developed countries from e-waste problem. Due to lack of public awareness in many emerging countries, implementation of reverse logistics program must be initiated by government. Besides that, reverse logistics practices often fail to balance among profit target achievement, the environmental conservation, and social harmony. Moreover, in the recent years, triple bottom line is not enough since many parties are only focused on their reputation due to they are afraid to be blame as the source of problems. Therefore, this research aims to build sustainable reverse logistics theory for emerging countries through quattro bottom line approach from government perspectives. Theory building process consists of systematic literature review, triangulation of data collection, major part of theory description, conceptualization and operationalization of theory. The result indicates a number of obligation that must be regulated by government for all parties that was divided into four categories, i.e. infrastructures and facilities provision, human resource commitment, regulation establishment, and managerial orientation. This theory can be adopted to measure performance of SRL Implementation.

1. Introduction

This paper is an extension of work originally presented in Industrial Engineering and Engineering Management Conference, IEEM 2017 [1] that wants to prove the need for government role in building sustainable reverse logistics (SRL) theory by using quattro bottom line approach. This study departs from the researcher's belief that the success of handling e-waste depends on an active role of government. At least there are three roles of government in supporting reverse logistics (RL) implementation. First, as a policy maker, government makes regulations and policies in preserving the environment [2], second, as a regulator, government arranges RL implementation, and third, as a facilitator, government provide facilities to conduct RL activities. Actually, electronic and electrical products are considered as luxurious and unaffordable things for middle-lower income country. However, due to the increasing of the Indonesian income per capita that almost reached 4 million per month, communities consumptive behavior, and the growth of industrial capability reflected in gross domestic products (GDP) of Indonesia more than 5%, the third highest in the Group of Twenty (G20) after China and India [3], lead the community to replace electronic products faster than it should be. Generally, the Indonesian people persist on using their mobile phone (MP) are not more than three years [4], which causes these products contribute the largest amount of e-waste compared with other electronic devices [5].

Along with the highest rate of electronic products replacement, increase also the amount of e-waste, while, only a few of them are recycled. Nokia mobile phone survey noted that only 9% of e-waste mobile phones are recycled in India and China, and only 1% in Nigeria and Indonesia [6]. The biggest role in recycling activities comes from informal businesses [7] that pay more attention only to target profit achievement and do not care with the environment. This is the reason for the great role of government to control recycling programs. Through government policies and regulation, not only balancing profit and reputation achievement, but also protecting the environment and social harmony. The rules and regulations should be designed properly to arrange how to take benefit from recycling process without disturbing other interest.

As mentioned before, the success of a a country in conducting recycling program depends on the role of government to encourage

*Hesti Maheswari, Jl. Rudal Raya No. 3A Joglo West Jakarta 11640 - Indonesia, +62 82123596058 email: hesti.maheswari@sbm-itb.ac.id

and regulate it [2]. Providing a high technology recycling needs enormous budget allocation. In developed countries, the amount of e-waste is regarded as a resource for other business. They convert e-waste into energy or other valuable products. Furthermore, the government early anticipate the number of product produced in forward chain. They think early to create a handling mechanism by making RL activity as an obligation for everyone, either businesses or societies. Unlike in developed countries, regulations in emerging countries are always left behind. The rules or acts will be created after government feels there is a crucial problem. Even though RL activity is conducted, they are often ignoring the environmental friendly way. The main characteristics of emerging countries RL model as compared to international models [7] is depicted in Table 1.

Table 1: Comparison of RL models in developed and emerging countries

	Developed Countries		Emerging Countries		
	Switzerland	Sweden	China	India	Brazil
Government	Active	Participative	Inactive	Inactive	Active
Industry	Total Mgt.	Transportation	Ships WEEE		Total Mgt.
Consumer	Pays ARF returns	Return			Pays embedded fee and returns
Informal S			Excluded	Pre-processing	No training

There is no opportunity for informal sector in developed countries to get profit through RL activities. The government strictly prohibits informal sector to recycle used electronic products because they are often ignoring the environmental sustainability. While, in many emerging countries, the informal sector plays a major role in recycling e-waste activities, even becoming home industry but illegal.

According to my preliminary research, in fact, there are many Indonesian people want to participate in recycling MP program by sending it to collecting point [4]. Unfortunately, most of them said that they do not know where to bring it for recycling since they are hard to find the drop box facility [4]. Some of them are reluctant to send their used MP, and prefer to keep it at home due to unreasonable of reimbursement. They are also hard to find someone else who really want to use it. Others explained that it is very difficult to sell the obsolesce or out of date electronic product to secondary market [4]. These phenomena show that recycling mechanism in many emerging countries that actually can be used for handling e-waste problem, are not built yet.

From literature reviews, we found that since 1990s until now, people all over the world have felt the need for RL, although their aims are not purely to protect the environment. They are focus on profit or embarrassment if their activities are littering surrounding [8, 9]. Therefore, in that era, many researchers studied about how to improve firms' performance in reverse chain. Evolution of RL theories refer to original constructs built by some previous studies such as reverse logistics network that explored the types of RL activities [10] and motivation [11], organizational commitment [11-14], and RL performance [15]. The author is hard to find a research that explores the role of government in encouraging communities to participate actively in RL program, how the government regulates RL mechanism, how the government assigns businesses to conduct RL activities, and how the government oblige societies to participate. Therefore, today it is relevant to sift the research idea to focus on government role in preserving the environment through RL program that consider not only profit, planet, and people elements, but also consider reputation factor. Due to low of public awareness in emerging countries even they pollute the environment although they conduct RL activities, therefore, the researcher believes that RL concept is not enough and this study proposes to use sustainable reverse logistics (SRL) terminology. Moreover, the researcher believes that SRL concept must be explored and created from government policies, regulations, perspectives and expectations. So, by investigating the linkage and the gaps among theories, finding the governments expectation by interviewing them, and generating a suitable pattern of the program, this study wants to build a SRL theory based on quattro bottom line (QBL) approach, include reputation terminology as a new idea and very relevant with current situations but has not emerged in the research publication.

The rest of this paper is organized as follows. The second section explores literatures related to sustainable reverse logistics, government rules, policies, and performance. The third section discusses the research method, data collection process and highlight the variables for building a theory. The fourth section explains the main finding. Finally, the fifth section summarizes the research and suggests further research.

2. Literature Review on Sustainable Reverse logistics

Exploration of sustainable reverse logistics concepts are directed to prove that the main purpose of conducting SRL programs are protecting the environment. Furthermore, the success of this program particularly in emerging countries, depends on the role of government to encourage other stakeholders. Therefore, the actions that support RL implementation, governments' performance, and sustainability concept will be the main themes in this paper. Related to sustainability concepts, this paper uses quattro bottom line approach because the researcher believes that it is not enough without spelling out reputation concepts for research in the context of emerging countries.

2.1. Sustainable Reverse Logistics Actions

Reverse logistics is the process of planning, implementing, and controlling the efficient, cost effective flow of used electronic products from the point of consumption to the point of origin for the purpose of recapturing or creating value to prevent environmental pollution [11]. From this definition, it is illustrated that RL activities should be able to protect the environment and one of the ways is adding span of life electronic products especially for MP that has the shortest product life cycle.

There are 8 types of reverse logistics activities [16], namely remanufactured, reconditioned, refurbished, re-process, repair, recycle, reuse, and disassembly. However, only 5 types are commonly done in emerging countries, i.e.: refurbished, repair, recycle, reuse, and disassembly [17] and usually many informal businesses are doing these activities. On the contrary, only a few manufacturers take a part in RL program and only a little role of government in regulating mechanism of RL implementation. Therefore, this research seeks to find actions that support SRL theory building, either from literatures or practices.

This research divides type of reverse logistics actions based on who is recommended by government to perform the activity, whether businesses (manufacturer or intermediary business), consumers, or governments itself. Knowledge, willingness, and awareness of all stakeholders to the environmental sustainability are believed to be a strong foundation to commit in supporting SRL program.

2.2. Sustainability

In manufacturing industries, after the achievement of quality, differentiation, and cost leadership as the leverage of their competitive advantage, management has to concern about strategic issue such as the environment. The most integrated performance of supply chain either in forward or reverse network is the business development in line with sustainability. Sustainability is a set of skill and concepts that allow all parties to obtain competitive returns without sacrificing people and environment interest [8]. Aptly joining the definition of reverse logistics and sustainability brings about sustainable reverse logistics (SRL). The industry must control not only financial achievement, but also consider its impact on economic as a whole, environmental protection, and social responsibility which conform to the triple bottom line (3BL): economic value, environmental and social responsibility (Figure 1) [18]. Others stated that the most important reasons in implementing RL activities are economic (decreasing the use of raw materials, reduction of disposal cost, creation of added value for and-of-use products, and demonstrating of environmentally responsible behavior), legal (implementing extended producer responsibility as follow the government rule), and social (preventing environmental pollution from carbon emission and e-waste generation) [19, 20]. The worries on corporate image, government responsibility, and communities' awareness are sometimes become the reason of all stakeholders to conduct RL programs.

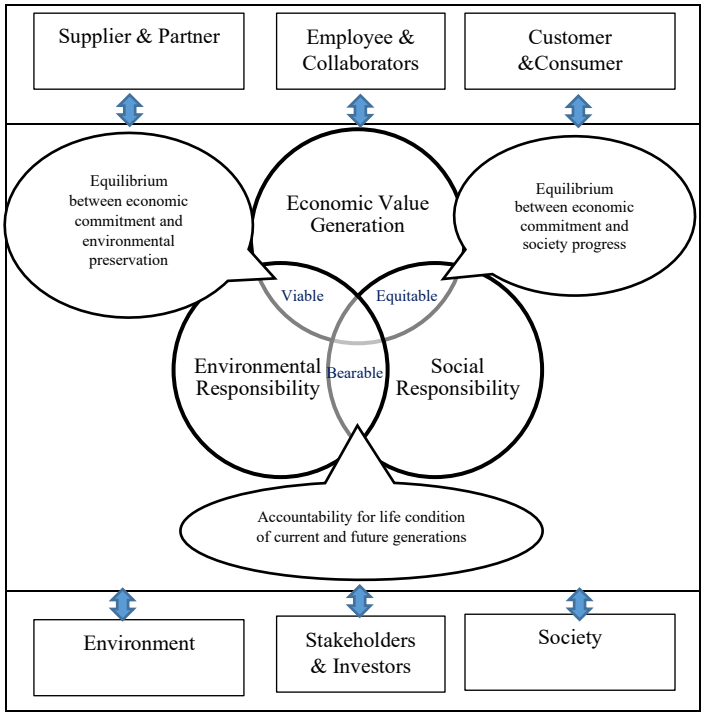

Figure 1: The triple bottom line [Pedroso in [16]

Figure 1 explains about interactions among social, environmental and economic spheres result in deeper and more complete aspects of sustainability. The relation between economic and social prioritizes job creation and income to improve living standards, economic welfare and growth that favor social aspects, besides increase level of education and professional development. Intersection between the economic and environmental spheres stresses to create benefit from various activities but still pay attention to environmental sustainability such as designing eco-friendly products and developing methods for electronic product volume reduction [21]. Further, interaction between social and environmental spheres indicates that communities have to use electronic products properly reflected in accountability for life condition of current and future generations. Finally, intersection of the three spheres represents sustainability in a broader sense. These issues will be the central topic in this study because most parties are often fail to maintain the balance among the profit target achievement, planet conservation, and social harmony.

2.3. Reputation

Reputation in an organizational context, is generally related to two dimensions, first, how stakeholders perceive the quality of specific attributes, and second, the degree to which an organization or company is recognized collectively [22]. From a business perspective, reputation has been defined as the combination of a company's public prominence, its public esteem, and the qualities or attributes associated [22, 23]. In other word, a company or organization is recognized on a large-scale and salient in the minds of stakeholders. From government perspective, reputation concepts are defined as responsibility of a country from various problems especially that giving negative impacts and disturbing to other countries. While, for the communities, reputation is related to their willingness to actively involved in preserving the environment.

There are six dimensions of reputation [24], namely:

- Emotional appeal (likeability, respectfulness, and trustworthiness);
- Physical appeal (attractiveness of an infrastructure);
- Financial appeal (favorable environment for stakeholders);
- Leadership appeal (charismatic leadership and a clear vision);
- Cultural appeal (socio-cultural diversity, history, entertainment);
- Social appeal (the perceived responsibility as a member of the global community and the manifest support for good causes)

2.4. Government Policy, Regulations, and Performance

Government has a range of policy instruments that can be divided into six broad categories to reduce the environmental impact of freight logistics [25], namely: taxation; financial incentives; tariff regulation; liberalization and privatization of freight markets; infrastructure and land using planning; as well as advice and exhortation. Government as a regulator can run e-waste management system through realizing extended producer responsibility (EPR) implementation; corporate social responsibility (CSR) mechanism, energy and row material control, take back program application, environmental-friendly product utilization, e-waste budget allocation, deposit fund requirement, international end-of-life standard, 4Rs program application [21]

and skill accreditation [26, 27]. Government as a facilitator should provide drop box that easy to find by communities, storage point, and landfill areas. Indonesia Waste Forum (IWF) requires five aspects which must be considered to solve waste problem in emerging countries they are law and national policy, national institution for integrated implementation, financial investment, community involvement, and technology creation [28].

3. Research Method

3.1. Method

The perfect research design is built to ensure all research questions will be answered [29]. This research uses quantitative and qualitative approaches and the design is divided into five steps that depicted in Figure 2.

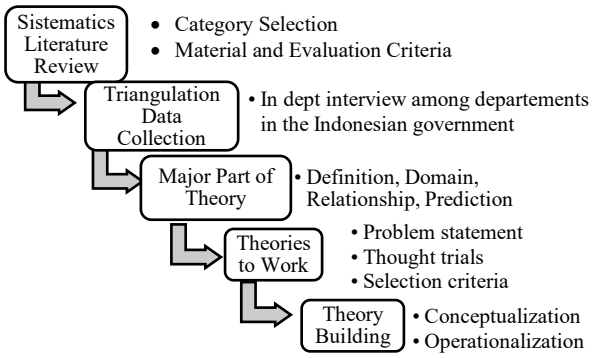

Figure 2: The research flow

First, in quantitative approach, this research chooses systematic literature review [30], that comprised of two steps i.e.: category selection and material evaluation. In the category selection step, firstly this study defines and refines a topic, then designs a search and locate research report. This study uses two main topics namely: reverse logistics and sustainability. This study explored many researches without limiting the year of their publication. After that, they are reviewed and classified by differing their characteristics and distinguished and then recorded in a prepared spreadsheet to be analyzed holistically. The different characteristics in reverse logistic concept are its activities and network while the sustainability concept refer to the fulfillment of Quattro bottom line approach. Secondly this study determines how to evaluate the material by using validity test, crosschecked for ensuring the enrichment of study such as Scopus indexed, journal accredited, and the research quality that answering its research question.

Because this research wants to build SRL theory from government perspective and expectation, therefore in the end of this section will be served the measurement of government performance that conduct RL activities. For evaluating performance of government, this research chooses three types of evaluations [31], namely: criterion-focused evaluation (by what criteria shall the SRL program be evaluated?), impact focus (what are the direct and indirect SRL program impacts, not only on participants, but also on larger systems and the community), and implementation focus (to what extent was the program implemented as designed? What issue surfaced during implementation that need attention in the future?)

Second, to complete the constructs, this research applies a qualitative method by using triangulation data collection (i.e. in-depth interview between departments in the Indonesian government) for six months from January 2017 to April 2018. *Third*, this research adopts that theory comprises of four major parts, i.e.: definitions, domain, relationships, and predictions [32]. Definitions translate the concepts, constructs, or variables used in the theory by using "what?" and "who?" questions. Domains refers to where the theory applies with answer the questions of "where?" and "when?". Relationships shows the nature of causality among those concepts, constructs, or variables selected by answering "why?" and "how?" questions. Predictions reflects whether the theory will give impact in the field by applying the questions of "could, should, and would?" *Fourth*, Weick's theorizing as disciplined imagination provide three tools for theorist to work with in crafting theories, i.e.: problem statement, thought trials, and selection criteria [29]. and *Fifth,* the general method of theory building in applied discipline comprises of five nonlinear phases: conceptualization, operationalization, confirmation, application and refinement [29]. This research is only use the first two phases, i.e.: conceptualize and operationalize. The purpose of conceptualization phase is to develop a sound conceptual framework that provides an initial understanding and explanation of the nature of problem and phenomena. While, the purpose of operationalization phase is to bridge the concept and practice. Although, the operationalization of a theory needs to be tested or confirmed, in this paper, the confirmation phase is not conducted because of the interview results refer to government policies and regulations. In turn, the theory is likely to result in better outcomes and appropriate to be implemented.

3.2. Samples

Since lack of community awareness in emerging countries to reduce e-waste and preserve the environment, so the theory formation must be generated from government perspectives.

Table 2: Government and selected respondents

National Agencies	Selected Respondents
• Ministry of Environment and Forestry (MEF)	• The head of sub directorate of e-waste and recycle • Directorate General of Waste, E-Waste, Hazardous and Toxic Material
• Ministry of Industry (MI)	• Directorate Industry of Electronic and Telematic • Directorate Small Medium Industry of Metal, Machine, Electronic and Conveyance
• Ministry of Trade (MT)	• The Head Agency of Assessment and Development of Trade Policies
• Ministry of National Development Planning (MNDP)	• Directorate of Environment
• Ministry of Cooperation, Micro and Small Medium Enterprise (MCSMEs)	• Secretary for Deputy Minister of Business Restructuring
• Environment and Hygiene Office (EHO)	• The Head of Environment and Hygiene Office • The Head of Hygiene Management • The Head Control of Environmental Impact
• Cooperation, Small Medium Enterprise, and Commerce Office (CSMEs C)	• The Head of Cooperation, Small Medium Enterprise, and Commerce Office

By interviewing the government officials, this research wants to catch the various constructs considered for implementing SRL activities. This research chooses five ministries and two government agencies that are predicted influencing the successful of SRL implementation. Not all of divisions in those ministries made as respondent. Table 2 is detailing who the respondents are.

4. Result and Discussion

This section consists of five parts following the research flows. The first part is exploring the existing theory include the evolution of RL and further about SRL theory. The second part is recording the government policies and regulation plus roles and responsibilities from in dept interview. Then, the third part is elaborating the definition, domain, relationships, and prediction of SRL theory, the fourth part is selecting the SRL criteria through problem statement and thought trials, and the last part is pattern matching of the concept with the practices to create the sound of sustainable reverse logistics theory.

4.1. Evolution of Reverse Logistics and Sustainable Reverse Logistics Theory

Firstly, some businesses conducted reverse logistics activities for getting profit from used electronic product [4, 11, 12, 15, 18, 33-35]. Actually, the idea of returning electronic product emerged around 1940s to 1970s. They did not recycle or conduct other form of RL activities. Usually they resell used electronic products to other. If those products cannot be sold, they kept it at home, sometimes become a children's toy, or throw them in the bin mixed with household waste. However, in the recent years, they began aware with environmental condition which resulted by more and more used electronic product that make the narrowness of dumping grounds. Actually, RL activities are closely related to sustainability concepts with the three perspectives (triple bottom line, 3BL), namely: profit, planet, and people [8]; economic value, environmental and social responsibility based on Pedroso and Swicker [18]. Types of reverse logistics activities such as remanufactured, reconditioned, refurbished, re-process, repair, recycle, reuse, disposal, and disassembly [10, 15, 18] are manifestation of sustainability movement. However, for many emerging countries, the use of 3BL concept is not enough. RL managed efficiently and effectively has the potential to gain economic value and enhance the positive image of the firm in the consumers' perception and the distribution chain [33]. RL managed effectively help to improve after-sales service as fast to respond to complaints and solve problems which is able to provide certainty that the returns enhance the positive image of firms [20]. The firms deliberately doing RL activity to get attention from societies because mitigating environmental, health, and safety impacts can enhance a firm' reputation [8]. For the government, they worry if their e-waste pollutes neighboring countries and they get negative image from them. Today, societies also worry about getting social sanction, if their behavior is not responsible or lack awareness to the environment. Social perspective to assess reverse logistics performance is also considered as part of reputation concept with some indicators such as market reputation of the enterprise if they produce unqualified product and do not have a technology for handling their own e-waste [15]. This matter makes the researcher believe that not only businesses but also government and communities expecting a good reputation in realizing it [4].

Discussion of sustainability are driven by the basic concept that reverse logistics' performance should be measured not only by profits and reputation, but also by the impact of activities on environmental and social systems. Therefore, there is a tight correlation between reverse logistics and sustainability. Unfortunately, in many emerging countries, in fact, RL activities are often not managed and controlled properly by government. They are still concern to produce a new qualified electronic product in forward chain, provide technology to develop features, promote, and sale it in the market as much as possible. They forget to early anticipate e-waste problem. Meanwhile, the informal sector from community more quickly respond by looking at it as a business opportunity. After that, a new problem emerges in almost all emerging countries as they move without government permission and ignore health and safety work. They only think about how to fulfil their needs or how to earn a lot of money. These phenomena make the author convince to use sustainable reverse logistics terminology if we want to study about all activity in reverse chain.

4.2. Government Policies and Regulations plus Roles and Responsibilities

Many emerging countries have no rules, act, or legislation completely related to SRL implementation. Some rules bellow will be used as a foundation of building SRL theory. For example, Indonesia just made a rule about the obligation of businesses to manage their used product, if it is hard to decompose by natural process in Act No. 18 of 2008, article 15.

The last government regulation related to face e waste problem is No 101 of 2014, article 1, verse 11 – 31 that concern with managing e-waste. Indonesian government also prohibit businesses to import used electronic product, e-waste, hazardous, and toxic material as shown on Decision of The Ministry of Trade No. 229/MPP/Kep/7/97 and Basel Convention of 1989. Polluter pay principle is also set in Act No. 32 of 2009 article 2 verse (i) and Government Regulation No.18 of 1999 article 9 verse (1, 4, 5). For reducing e-waste, government assesses and control the quality of product through national standard of Indonesia (SNI) that enforced mandatory for electronic product in regulation of The Ministry of Industry No. 36/M-IND/PER/9/2017. Indonesian government form adjusted assessment institution in order to SNI enforcement.

Ministry of Industry has machines restructuration and/or other equipment program for small and medium industries in rule of Ministry of Industry No. 20/M-IND/PER/3/3/2016to help them improve the quality of products. So, the procurement of machine should not be a problem anymore for converting e-waste to other valuable product. Government also encourage all businesses to reach green industry certification as arranged in rule of The Ministry of Industry No. 18/M-IND/PER/3/2016. For increasing the number new of entrepreneurs, Indonesian government makes new business invention program and train them until it becomes an established business as shown on Act no 20 of 2008. Government make serious effort to link and match small and medium enterprises with the big industry to learn the technology and improve their skill that arranged in PP No. 17 of 2013. There is no rule, act, and other form of regulation that organize how to conduct SRL activities, who should be responsible, what the role

of each actor is, and what kind of punishment if they are breaking the rule. As explained in previous section, because of community lack awareness the concepts of SRL must derive from government initiative. Therefore, this author formulates the theory of SRL from the government perspective.

This research explores the roles and responsibilities of national agencies related to SRL implementation by interviewing them. These roles and responsibilities will be a fundamental construct in building SRL theory (Table 3)

Table 3: Government roles and responsibilities

National Agencies	Roles and Responsibilities
• Ministry of Environment and Forestry (MEF)	• Define responsibilities for stakeholder • Define SRL categories for business • Establish and manage e-waste collection channel and systems • Establish e-waste treatment standard • Manage licensing system for business • Monitor and evaluate business' environmental performance
• Ministry of Industry (MI)	• Encourage eco-design product • Finding RL technology • Create technology e-waste conversion
• Ministry of Trade (MT)	• Prohibit import of used electronic product. • Define product quality
• Ministry of National Development Planning (MNDP)	• Develop financing scheme SRL • Define and manage subsidies
• Ministry of Coop. Micro and SME (MCSMEs)	• Training the business • Create link and match with big industry

4.3. The Major Part of Sustainable Reverse Logistics Theory for Emerging Countries

The SRL theory especially for mobile phone industry has not been extensively studied and conceptual models explaining the possible recovery network have not been abundantly created [8]. So, the implementation of RL activities in almost all emerging countries is more damaging the environment because it still does not consider sustainability concepts since there is no theory that fortifies these activities. For gaining the sound theory, four major parts of theory (definition, domain, relationship, and prediction) [32] will be described in table 4-7. This research explains what SRL is, who should play a role, when and where it must be implemented, why it is important, how it is applied, whether it can be implemented, how it should be implemented, and will all parties participate.

Table 4: Definition component

Questions	Description
What?	Sustainable reverse logistics is designed as an attempt to guarantee activities in reverse chain in line with the primary goals such as profit, social harmony, and environmental preservation. This theory is really needed especially in emerging countries to fortify community activity in utilizing used electronic products to get profit.
Who?	Governments are the backbone in enforcing sustainable reverse logistics implementation who formulate the mechanism includes educating and socializing to community and also organizing it. Due to implementation of sustainable reverse logistics theory requires collaboration of all parties, therefore not only government, but also manufacturer or producer, intermediary business, and society should be involved

Table 5: Domain component

Questions	Description
When?	Sustainable reverse logistics should be done when production of electronic products in forward chain takes place and followed by consumptive behavior, to anticipate e-waste generation
Where?	Sustainable reverse logistics is designed for community in emerging countries especially in a country where the population has low of the environmental preservation awareness

Table 6: Relationships component

Questions	Description
Why?	The Indonesian government, through Ministry of Environment and Forestry, Ministry of Industry, Ministry of Trade, Ministry of National Development Planning, and Ministry of Cooperation, Small Medium Enterprise should concern with the environmental quality degradation due to a lot of e-waste. Because of lack community awareness, the sustainable reverse logistics theory must be developed from government side. Government policy and intervention will be the right breakthrough for encouraging all parties aware with environmental sustainability. Finally, this theory is expected become a guidance for all parties who are looking for profit on reverse chain.
How?	The Indonesian government can apply sustainable reverse logistics theory by arranging its mechanism, making the rules and regulations, determining the role of each stakeholder, developing infrastructures or facilities, preparing the community knowledge, and controlling the implementation continuously. The expected outputs from this theory building refer to sustainability achievement through quattro bottom line approach, encompass business profit either for producers or intermediary businesses, local and national economic growth, social welfare, and environmental preservation as well as all parties' reputation since their effort and participation.

Table 7: Prediction component

Questions	Description
Could?	The Indonesian Government believes and expects that sustainable reverse logistics theory could be implemented in emerging countries for handling e-waste problems.
Should?	To implement sustainable reverse logistics theory, the activities should refer to quattro bottom line fulfilment. The balancing among profit target achievement, social value creation, environmental preservation, and reputation acquisition should become a fundamental orientation.
Would?	All parties would adhere to government regulation since they receive equal treatment between the fulfilment of rights and the implementation of obligation

4.4. The Categories Selected for Sustainable Reverse Logistics Theory for Emerging Countries

The SRL categories combining literatures, field practices, and also government roles, responsibilities, regulation and expectation are summarized in table 8. This research found 53 categories which will be used as the constructs for SRL theory, while the definitions of each categories are provided in the appendix. There are 17 constructs are not found in literature, but regarded very important in building SRL theory for emerging countries. They are standard equipment utilization; training for SMEs in reverse logistics activities; inclusion of product content and duration; fairness in using electronic product; illegal import restriction, Electronic product national standard arrangement; vocational education for human resource preparation; business localization; tax arrangement; restructuration machine program; budget provision; rules alignment; social punishment; control

mechanism of RL implementation; SMEs-industry link and match; Modernization of SMEs; and social and public facility utilization. We give star mark for the seventeenth constructs to differentiate the both constructs source clearly.

Government recommends 18 actions of SRL for businesses. Three of them are found from interview result, namely encouraging utilization of standard equipment to avoid hazardous and toxic materials from e-waste; giving training to small medium enterprise in e-waste processing and use of e-waste conversion technology, and writing down the product life and product content on the packaging. Although other 15 action are found from literature, however only 2 actions have been conducted in Indonesia, i.e. giving after sales service and providing drop box facilities but with limited number.

Table 8: Sustainable reverse logistics concepts for emerging countries: summary of in depth interview results and literature review

Sustainable Reverse Logistics Categories	Actions Recommended by Governments							Literatures
	MEF	MI	MT	MNDP	MCSMEs	EHO	CSMEC	
Businesses:								
Eco-friendly product design	√	√	-	-	-	-	-	[20]
After sales service	√	√	√	-	-	-	-	[38]
Packaging reduction	√	-	-	-	-	-	-	[39]
Deposit fund	√	-	-	-	-	-	-	[26]
Take back obligation	√	-	-	-	-	√	√	[9]
Drop box facility	√	-	-	√	-	√	√	[5]
Recycling technology creation	√	√	√	√	-	√	√	[16, 26, 38]
Standard equipment utilization*	√	√	-	-	√	√	√	-
Skill accreditation (employee competency)	√	√	-	√	√	√	√	[14]
Quality of product (longevity of extension)	√	√	√	-	√	√	-	[26]
Organizational commitment	√	√	-	-	-	√	-	[11, 35]
Budget allocation	√	√	-	√	√	√	√	[13]
Inclusion of post-use product handling	√	-	√	-	-	-	-	[34]
Technology conversion	√	√	-	√	√	√	√	[14, 26]
SMEs coaching*	-	√	√	√	√	-	√	-
Enterprise alliances	-	√	-	-	√	-	-	[14, 36, 38]
Inclusion of product content and duration*	√	-	-	√	-	-	-	-
Corporate citizenship	-	-	-	-	-	-	-	[41]
Public:								
Public participation awareness	√	-	-	√	√	√	√	[14, 9]
Eco shopping decision	√	-	-	-	-	√	-	[20]
Reduce replacement frequency	√	-	-	√	-	√	-	[16, 26]
Separate own e-waste	√	-	-	√	-	√	-	[40]
Reasonable reimbursement (incentives)	√	-	-	-	-	√	-	[8, 40]
Willingness to pay recycling cost		-	-	√	-	-	-	[40]
Fairness in using electronic product*	√	-	-	-	-	√	-	-
Government:								
Illegal import restriction*	√	-	√	-	-	-	-	-
Electronic product national standard arrangement*	-	√	√	-	√	-	-	-
Collecting point extension	√	-	-	√	-	√	√	[26]
Invention of handling mechanism	√	-	√	√	√	√	√	[37]
Health and social awareness instillation	√	-	-	√	√	√	√	[6, 14]
Vocational education for human resource preparation*	-	-	-	√	-	-	-	-
Storage point	√	-	-	√	-	√	-	[10, 37]
Professional management of secondary market	-	-	√	-	-	-	√	[26]
Business localization*	-	-	-	-	-	√	-	-
Tax arrangement (additional or reduction) *	√	-	-	-	-	-	-	-
Jobs creation	√	-	-	-	√	-	√	[37]
Knowledge building and deployment	√	-	√	√	√	√	-	[20]
Program of restructuration machine*	-	√	-	-	-	-	-	-
Budget provision from APBN*	√	√	-	√	-	√	√	-
Regulation alignment between departments*	√	-	√	√	√	√	-	-
New entrepreneur invention program	-	√	-	-	√	-	√	[14, 36, 38]
Third party provision	√	√	-	-	-	√	-	[8, 20, 9, 37, 44]
Social Punishment*	√	-	-	-	-	√	-	-
Synergy of key actors	√	√	√	√	√	√	√	[34, 37]
Integrated implementation	√	√	-	√	√	√	√	[34, 36]
Control mechanism of RL implementation*	√	-	-	-	-	-	-	-
Green industrial development	-	√	-	√	-	√	-	[36]
SMEs-Industry link and match*	-	√	-	-	√	-	√	-
Process modernization of SMEs*	-	-	-	-	√	-	√	-
Tariff adjustment	-	-	-	-	-	-	-	[8, 10]
Waste to energy program	√	√	-	-	-	√	-	[8, 10]
Social and public facility utilization*	-	-	-	-	-	-	√	-
Monopolistic collective systems	-	-	-	-	-	√	-	[42]
All Stakeholders:								
Environmental preservation	√	√	√	√	√	√	√	[3, 6, 8, 10, 26, 34]
Prestige consideration (image, reputation)	√	√	-	√	-	√	√	[6, 14, 36, 41]

After sales service is needed to extend the life of electronic products. Usually, damaged electronic products are repaired for reuse. If those products cannot be used anymore, the owner will trade in with the new one in a secondary market. Unfortunately, usually retailers are only willing to buy these products at the lowest price, so that, the owners often cancel to sell it and prefer to keep it at home.

There are 7 actions recommended by government for community and only one action was not found in literature, i.e. fairness in using electronic product. Finally, this research found 28 actions that must be done by government itself. These phenomena give an impression that governments in many emerging countries have not paid great attention to SRL implementation, so they get the most responsibility than others.

Table 9: Linkage of reverse logistics and sustainability concept

Sustainable Reverse Logistics Categories	The Reasons to Conduct SRL			
	Profit	People	Planet	Reputation
Businesses:				
Eco-friendly product design		√	√	√
After sales service		√		√
Packaging reduction	√		√	√
Deposit fund	√			
Take back obligation			√	√
Drop box facility		√	√	
Recycling technology creation			√	√
Standard equipment utilization		√	√	
Skill accreditation (employee competency)		√		
Quality of product (extension of longevity)	√			√
Organizational commitment				√
Budget allocation	√			
Inclusion of post-use product handling		√	√	
Technology conversion			√	√
SMEs coaching		√		
Enterprise alliances	√		√	
Inclusion of product content and duration		√		
Corporate citizenship		√	√	√
Public:				
Public participation awareness			√	√
Eco shopping decision	√		√	√
Reduce replacement frequency			√	√
Separate own e-waste		√	√	√
Reasonable reimbursement (incentives)	√			
Willingness to pay recycling cost			√	√
Fairness in using electronic product			√	√
Government:				
Illegal import restriction			√	
Elect. prod. national stand. arrangement		√	√	√
Collecting point extension			√	
Invention of handling mechanism			√	
Health and social awareness instillation		√		
Vocational education for HR preparation		√	√	
Storage point			√	
Professional mgt. of secondary market	√	√		
Business localization		√	√	
Tax arrangement	√			
Jobs creation		√		
Knowledge building and deployment		√		
Program of restructuration machine		√		
Budget provision from APBN	√			
Regulation alignment between departments			√	
New entrepreneur invention program		√		√
Third party provision			√	
Social Punishment		√		
Synergy of key actors		√	√	
Integrated implementation			√	√
Control RL implementation			√	
Green industrial development			√	√
SMEs-Industry link and match		√	√	
Process modernization of SMEs		√	√	
Tariff adjustment	√			
Waste to energy program	√	√	√	√
Social and public facility utilization		√		
Monopolistic collective systems		√	√	√

To ensure that RL activities are very closely with sustainability concepts, each construct is grouped into four elements of sustainability depicted in Table 9. Interaction between RL categories and each element in sustainability concepts reflects the reasons why the stakeholders conduct SRL activities. However, government has never taken profit for government itself. The benefits gained from SRL activities are used for community welfare in form of circular economy.

Based on literature review and interview results, the duties of businesses suggested by government encompass creating eco-friendly electronic product design for easy features upgrading, providing after sales service to avoid quick replacement, reducing product package to save resources, initiating deposit fund to pay the environmental recovery, obligating take back program to provide collecting facilities, building drop box to facilitate community disposing used electronic product, finding recycling and e-waste conversion technology, utilizing standard equipment for maintaining society health, improving employee competency in e-waste processing. The business should strive to create an extension longevity of product, increase the organization commitment to implement RL especially in budget allocation, train the SMEs to process e-waste, publish how to handle product after using and product content, and overall, grow corporate citizenship. Government expects society to aware and participate in recycling program, by separating their own e-waste, eco-shopping, and reducing electronic product replacement. Government also hopes the public willing to pay cost of environmental recovery. Using electronic product fairly is an assertion that cannot be avoided. Although communities have also an obligation to protect the environment, they still expect to receive the reasonable reimbursement of their used electronic product unless they are reluctant to give their product.

The first government action to ensure SRL program will be implemented properly is restriction of illegal import used electronic products, since those products and their parts often cannot be utilized and only littering the environment. Moreover, informal businesses that seeks to profit from those products often ignoring safety and health process in reverse chain. Therefore, government should immediately make a regulation and national standard of import electronic product that will be sold in Indonesia and how to treat them, so they are not quickly pollute the environment.

This research finds some communities' expectations from a preliminary research, for example, collecting point facility to get a lot of amount of e-waste should be provided by government, because e-waste is a resource for SRL activities [4]. They should also easy to find a drop box by providing it close to the community. While based on businesses perspectives, government should motivate communities to give their used electronic product by giving a magnitude incentive. Regarding incentive for communities, the researcher suggests to government to make an incentive mechanism or regulation The Environment and Hygiene Office has a pick-up program for used electronic products, however, they do not give incentive to owners so they are often unmotivated to hand over those products for recycling. So that, instillation of health and social awareness in conducting SRL activities are also a big homework for government in emerging countries.

4.5. The Sound of Sustainable Reverse Logistics Theory building for Emerging Countries

Building SRL theory particularly for emerging countries is not an easy problem. Government should start from providing a good infrastructure including technology, setting up human resource capacity including their awareness and knowledge maturity, formulating the regulation and policies, arranging the mechanism, and designing monopolistic collective system. If the process mechanism in reverse chain has been running, the next step is providing professional management of secondary market. According to the head of sub directorate of e-waste and recycle, for implementing SRL program, Indonesian Government must depart from making a policy. After that the policy should be socialized so community wants to participate. While communicating the program, government must immediately build the infrastructure, and the last step is program enforcement at all level of society, if needed, mechanism enforcing of punishment should be prepared. Integrated implementation and all stakeholder involvement are also needed to ensure that all RL activities are in line with quattro bottom line concept.

This research is categorizing the stakeholder into two groups, i.e. internal and external stakeholder. Internal stakeholder consists of consumer, manufacturer, and intermediary business. While, external stakeholder comprises of environment, society, and government itself. Government intervenes other stakeholders to support and conduct SRL program with regard to the principle of sustainability in order not to harm other interests (Figure 3).

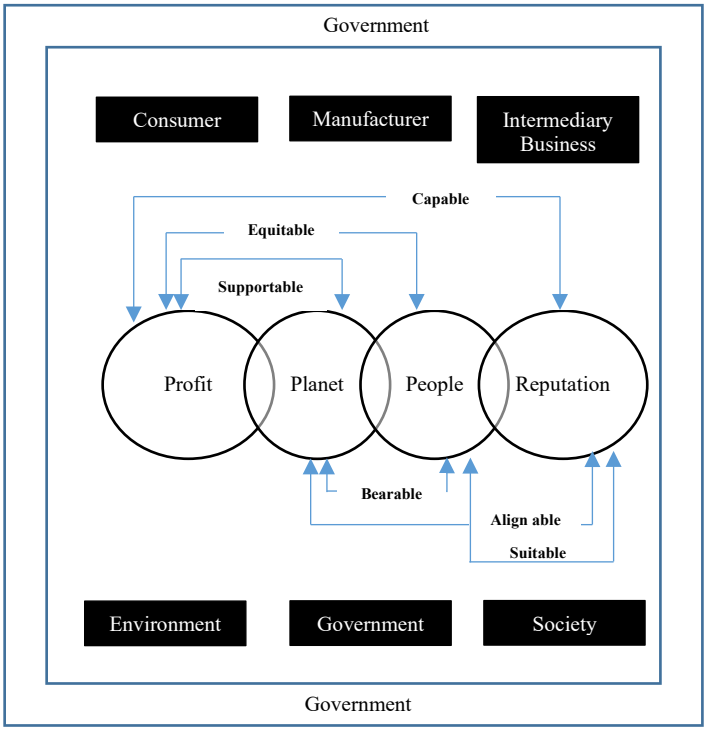

Figure 3: Quattro Bottom Line Approach for Sustainable Reverse Logistics Theory

The next step in building SRL theory is rearranging individual practices and literatures into "meta" constructs. In general literature review that had low levels of adoption, limited applicability and/or which did not relate to other practices were dropped so for further analysis we only use 51 constructs. The SRL theory to be built refers to two themes, namely activities related to RL implementation that must be conducted by all stakeholders based on government perspective and sustainability concepts with its four elements, i.e. profit, planet, people, and reputation (Figure 3). In building the SRL theory, the researcher seeks to balance between two interests. Therefore, this research formulates the sixth balancing constructs, namely: supportable, equitable, capable, bearable, align able, and suitable that will be described below,

- Supportable, re-design the way our economy works and re-build a restorative economy through creativity and also innovation, generate business and economic opportunity (Profit) and provide environmental benefits through renewable and reusable resources as materials in an efficient way (Planet).
- Equitable, conformity between opportunities to create greater value and align incentives (Profit) and societal benefits through invention of job creation and additional income in reverse chain (People)
- Capable, ability to maximize resources in-use, maintain, repair, and upgrade the lifetime of electronic products will bring benefit (Profit) and demonstrate positive image (Reputation).
- Bearable, alignment of responsibility to maintain the environmental preservation (Planet) and global healthcare activity in reverse chain (People)
- Align able, fair phone design in using materials, good working conditions to enable the reuse and recycling of parts (Planet) will anchor deep niche position in the market (Reputation)
- Suitable, worthy activities in supporting the program to reach social welfare (People) and to be responsible in using electronic product and/or handling their own e-waste (Reputation).

Ideally a theory is built by adjusting why the theory is needed, where that theory will be applied, who the actor is, and what the outcome and expectation are. As explained in previous section, the SRL theory is needed for handling e-waste problem due to low of public awareness in using electronic product especially MP and almost of them do not know how to treat the used MP that is no longer used. Therefore, the SRL theory that will be applied in emerging countries, has to be made and initiated by government. The theory is designed to encourage other stakeholders conduct RL practices accordance with expected output and outcomes. After describing the constructs, either from literature or individual practice (Table 8 and 9) and exploring the possible interaction between sustainable constructs (Figure 3), this research categorizes these constructs to adopt parsimony and complete requirement in theory building. As explained in this research method section, this research uses three types of evaluations, namely criterion-focused evaluation, impact focus, and implementation focus. Table 10 is the end result of this analysis. Due to this theory building is built from government perspective, this research has to consider the overall vision, mission, function, and primary task of government. This research summarized those considerations into four categories, namely infrastructure and facilities provision, human resource commitment, regulation, and managerial orientation.

Table 10: Rearranging literatures review and individual practices into meta constructs

Meta Constructs	Literatures Review and Individual Practices	Number of Government Recommendation
Infrastructures and Facilities	1. Converting technology creation	6
	2. Government budget provision	5
	3. Drop box facilities	4
	4. Collecting point extension	4
	5. Additional storage point	3
	6. Job creation	3
	7. Social and public facility utilization	1
Human Resource Commitments (behavior and attitude)	1. Standard equipment utilization	5
	2. Health and social awareness instillation	5
	3. Public participation awareness	5
	4. Reduce replacement frequency of electronic product	3
	5. Individual commitment	3
	6. Eco-shopping decision	2
	7. Willingness to pay recycling cost	2
	8. Fairness in using electronic products	2
	9. Corporate citizenship	-
Regulations	1. Synergy of key actors	7
	2. E-waste handling mechanism	6
	3. Integrated implementation	6
	4. Skill accreditation	6
	5. Regulation alignment between departments	5
	6. Building knowledge and deployment	5
	7. Coaching for SMEs	5
	8. Separate own e-waste	3
	9. Take back obligation	3
	10. Waste to energy program	3
	11. SMEs-Industry link and match	3
	12. Third party recycling business provision	3
	13. New entrepreneur invention program	3
	14. Enterprise alliance	2
	15. Inclusion of product content	2
	16. Inclusion of post-use product handling	2
	17. Reasonable reimbursement	2
	18. Illegal import restriction	2
	19. Social punishment	2
	20. Professional management of secondary market	2
	21. Preparation vocational education to increase individual capability	1
	22. Localization of reverse logistics business	1
	23. Tax arrangement both additional for new product or reduction for second hand product	1
	24. Program of restructuration machine	1
	25. Control mechanism of RL implementation	1
	26. Process of SMEs modernization	1
	27.Monopolistic collective system	1
	28. Deposit fund	1
Managerial Orientation, Vision and Mission	1. Budget allocation	6
	2. Product quality	5
	3. National standard arrangement particularly for electronic product	3
	4. Green industrial orientation	3
	5. After sales service	3
	6. Eco-friendly product design	2
	7. Packaging reduction	1

Category 1 – Infrastructure and Facilities. There are 7 selected constructs in this category. Converting technology creation is the most recommendation from government. It was recommended by 6 national agencies. if an emerging country has this technology, a lot of e-waste will not be a problem instead a resource. For providing it, government should prepare a large budget. Moreover, the budget is not only for technology procurement, but also to add drop box facilities, and extend the collecting and storage point.

Although Ministry of Environment and Forestry has the largest responsibility, however, RL cannot be implemented without supporting from all parties include from other departments. Two of departments did not have good alignment between the element of sustainability, especially between profit and other elements. Some efforts to reduce plastics usage will never work due to other departments (Ministry of Industry and Ministry of trade) encourage precisely to produce it for the reason gaining economics and industrial growth.

Actually, Indonesia has a regulation to ban importing waste and used electronic product from other countries, however, we often still found those products in many places such as Wakatobi, Batam, Surabaya, Pare-Pare, and even in the capital city of Indonesia, Jakarta. There is no control mechanism to prevent importing e-waste, integrated RL implementation for handling e-waste problems, and significant investment for building a big industry in reverse chain.

Category 2 – Human Resource Commitment. This research finds 9 constructs in category of human resource commitment. This category describes communities' (people) attitude toward SRL program. Public awareness is the central issue in this category for conducting SRL program. We divided public awareness into three dimensions, namely 1) awareness to use basic standard equipment such as rubber gloves, masker, and so on include taking care of community health; 2) awareness to actively participate in recycling program such as separating their own e-waste and willing to pay the recycling cost; and 3) awareness to prevent the increasing amount of e-waste by reducing replacement frequency, eco-shopping, and fairness in using electronic products. That e-waste problem is a small matter that does not need to get priority attention, e-waste is invaluable product and not as energy resources, e-waste problem is not my backyard and other negative syndrome have to be eliminated from societies' mind. Not only societies that should be aware, but also businesses and government itself must be conscious and should be the first guard of environment protecting initiative. Environment and Hygiene Office Jakarta Province failed to put the drop box facilities in each Transjakarta bus stop until now for a reason they do not know. Commitment to successfully implementing activities in reverse chain were evidenced in seventh ways [28], i.e.: 1) credibility of decision maker, in this case is government; 2) implementation mechanism include incentive to market; 3) significant attention of secondary market; 4) societies involvement; 5) sustainable commitment to high quality of operation facilities for managing e-waste; 6) Effectiveness evaluation to the strategy chosen; and 7) the clear legal protection for handling e-waste by government.

Category 3 – Regulation. This research found a lot of government responsibilities to regulate SRL program. The researcher believes these regulations (categories) will be the measurement of government performance in SRL implementation.

In the first type evaluation, this research found five evaluation criteria of SRL implementation. The evaluation criteria are classified into five dimensions, namely integrated enforcement of SRL program by all parties even among government agencies, obligation compliance to support SRL implementation, competency improvement to prevent SRL activities polluting the environment, creative ideas development to create income in reverse chain, and professional management to arrange SRL implementation properly.

This research establishes synergy of key actors such as government, businesses, and community; integrated SRL implementation; regulation alignment between department; and enterprise alliances as government responsibilities in integration enforcement of SRL program. While, obligation compliance dimension has seven indicators, namely willingness to separate e-waste by sorting the valuable material, conduct take back scheme, publish product content and post-use product handling in packaging, arrange reasonable reimbursement system, prevent illegal import of used electronic products, and socialize restructuration machine program to everyone that needs recycling machine but does not have enough money to buy it. Improvement of human resource competency is very important for implementing SRL, because to process used electronic product required a specific skill. Therefore, government responsible to increase return handling capability by giving a training and an accreditation certificate for individual or firm that really has recycling ability. Big companies are usually obliged to train small medium enterprises to transfer their skill in recycling process. Many developed countries such as Sweden and Japan provide vocational education specifically for increasing the skill in reverse chain, so they can operate the RL activities without damaging the environment and community interests.

The government responsibilities in creative idea development criteria comprise five indicators, namely building waste to energy (WTE) program, providing third party recycling business, inventing new entrepreneur in reverse chain field, organizing monopolistic collective system, and constructing deposit fund scheme. Many emerging countries have not been able to take benefit from e-waste, whereas developed countries import a lot of e-waste from their neighboring countries to be converted into energy. WTE needs a lot of resources, so the government in developed countries organizes monopolistic collective system to avoid informal group intervention. Nevertheless, Indonesian government is always trying to find new entrepreneurs in reverse chain field, due to many people in emerging countries make this activity as their primary livelihood. For businesses that have not been able to recycle their used product or to neutralize their hazardous products, government should provide third party recycling business. Since converting used electronic product into energy or other valuable products needs a lot of funds, constructing deposit fund scheme is urgent to do immediately.

The last regulation for SRL implementation is professional management that has the most number of indicators, i.e. professional in e-waste handling mechanism to avoid too large intervention of informal group, SMEs-industry link and match to improve employees' skill, social punishment application for tight SRL implementation in avoiding environmental pollution, secondary market management to develop business in reverse chain, business localization in reverse chain for easy controlling the SRL activities, SMEs modernization, and tax arrangement to grow the business spirit.

Category 4 – Managerial Orientation. In the forth category, this research found seven dimensions. The first government duty is providing budget for the expensive technology, facilities, and infrastructures and guarantee the quality of import electronic products that will be sold in Indonesia to prevent those products littering the environment quickly. Today, Indonesian government does not have a national standard for electronic products, so there are many unqualified products sold in Indonesian market. Besides easily damaged, these products are harmful to human body since they contain toxic and hazardous materials.

In managerial orientation, vision, and mission, government also should think about how to manage SRL activities from collecting process until selling the products to secondary market by using environmental friendly ways through reducing the use of packaging and trying to create eco-friendly products. Besides that, after sales service believed can reduce e-waste generation since this action adds life span of the products. Actually, all government agencies (respondents) recognize that environmental preservation is their responsibility. They are conscious that to protect the environment they should cooperate with others [2].

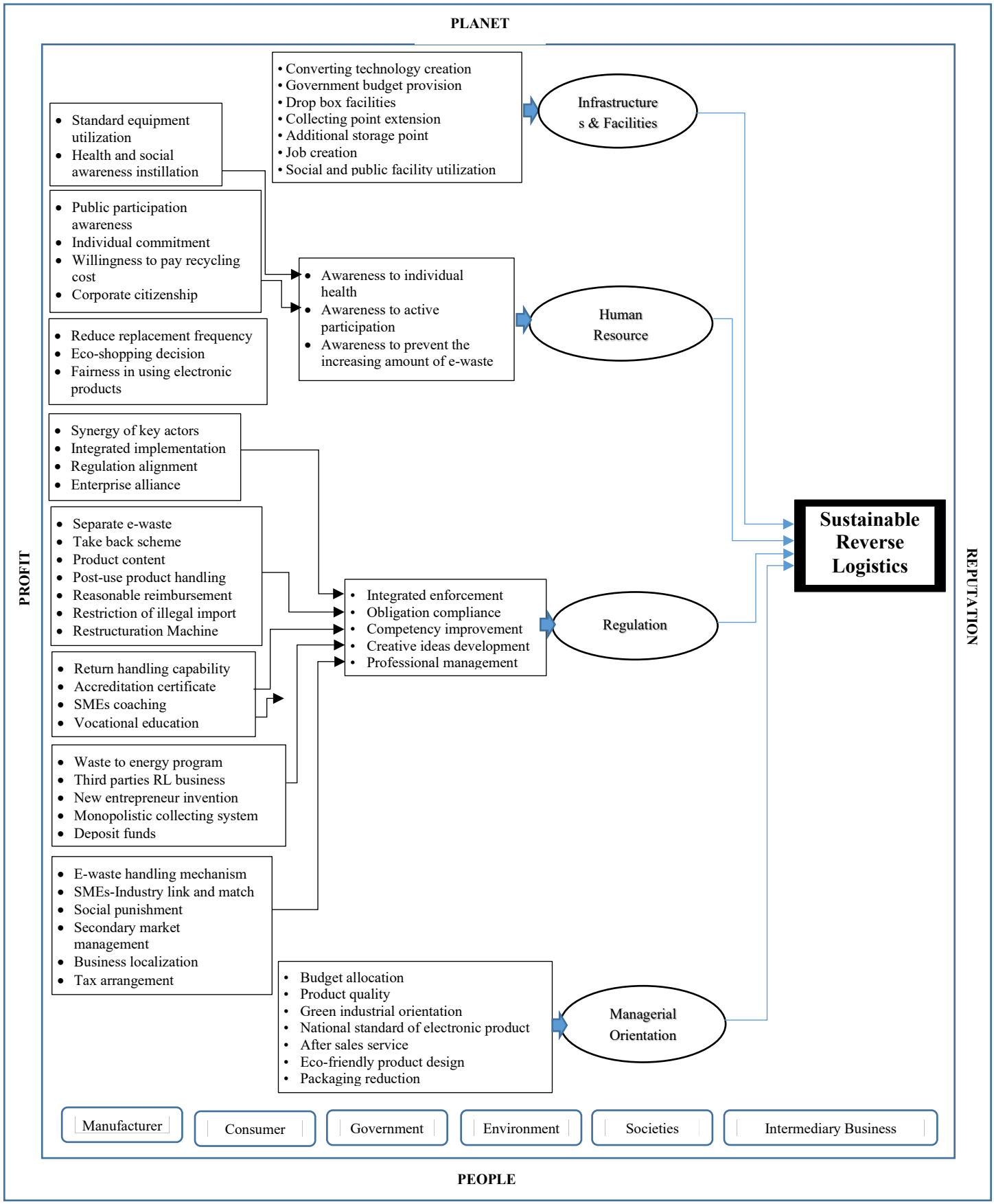

Figure 4: A model of sustainable reverse logistics for emerging countries from government perspectives

They know also that community in emerging countries usually have low awareness to protect the environment, therefore, the initiative must come from the government. Unfortunately, in many emerging countries, the government itself has often not felt that activity in reverse chain currently is very important due to the abundant of production in forward chain. Some respondents, especially Ministry of Environment and Forestry and Environment and Hygiene Office plans to apply punishment to arouse community awareness. They believe that must use the hard way. Besides that, they have to think how to implement and control that regulation.

After finding the evaluation criteria, this research uses impact evaluation for describing the direct and indirect impact of the use of indicators, dimensions, and variables formatted to measure the successful of SRL theory implementation, that is a reverse logistics theory that constantly in line with four elements in sustainability concepts, i.e. profit, planet, people, and reputation. SRL theory is recommended if activities in reverse chain will be applied in emerging countries. Using reverse logistics terminology is perceived to be no longer appropriate since many people ignore environmental friendly way. Therefore, sustainable reverse logistics concept is a theory which should be standardized for emerging countries.

Figure 4 is the last figure and the end of finding in this research that summarize all constructs for building SRL theory from government perspectives. Quattro bottom line as an approach that can preserve RL activities will not interfere other interests and the sixth ability to keep the balancing among interests and stakeholders will consider to be used in this research.

This research uses implementing-focused evaluation in the last step to test the theory building. For this type of evaluation, this research has two main propositions and eighteen proponent propositions to build a whole theory of sustainability reverse logistics and explain each interaction between two spheres, i.e.: capable, equitable, align able, supportable, suitable and bearable. However, this research does not examine the theory, but only formulate the propositions.

Proposition 1: The infrastructures and facilities provision, human resource commitment, regulation establishment, and managerial orientation are required to build a sustainable reverse logistics.

Proposition 1a: Converting technology creation, budget provision by government, providing drop box facilities, collecting point extension, additional storage point, job creation, and social and public facility utilization are needed for infrastructures and facilities provision.

Proposition 1b: Awareness to individual health, active participation, and prevent the increasing amount of e-waste are needed to build human resource commitment.

Proposition 1b1: Utilization of standard equipment and instillation of health and social awareness are needed to build individual health awareness

Proposition 1b2: Public participation, individual commitment, willingness to pay recycling cost, and corporate citizenship are believed can build awareness to active participation.

Proposition 1b3: Reduce replacement frequency, eco-shopping decision, and fairness in using electronic product are needed to prevent the increasing amount of e-waste.

Proposition 1c: Integrated enforcement, obligation compliance, competency improvement, creative idea development, and professional management should be regulated immediately.

Proposition 1c1: Synergy of key actors, integrated implementation, alignment of regulation, and enterprise alliance are needed to integrate the implementation.

Proposition 1c2: Separating own e-waste, taking back scheme, inclusion of product content and post-use product handling, reasonable reimbursement, restriction of illegal import, and restructuration machine are the form of obligation compliance.

Proposition 1c3: Return handling capability, accreditation certificate, SMEs coaching, and vocational education are needed to improve the competency.

Preposition 1c4: Waste to energy program, third parties recycling business, new entrepreneur invention, monopolistic collecting system, and deposit funs are the creative ideas that should be regulated immediately.

Preposition 1c5: E-waste handling mechanism, link and match between industry and SME's, social punishment, management of secondary market, business localization, tax arrangement, and modernization of SMEs need professional management.

Preposition 1d: Budget allocation, product quality, green industry, national standard for electronic products, after sales service, eco-friendly product design, reduce packaging are the types of managerial orientation.

Preposition 2: Sustainable reverse logistics could be realized by referring quattro bottom line conceptual framework.

Proposition 2a (capable): Stakeholders capability to balance target profit achievement and reputation recognition is required to create sustainable reverse logistics.

Proposition 2b (equitable): Stakeholders fairness between obtaining profit and preserving social harmony is required to realize sustainable reverse logistics.

Proposition 2c (align able): Align able of Stakeholders interest between to reach reputation recognition and environmental conservation is required to establish sustainable reverse logistics.

Proposition 2d (bearable): Stakeholders responsibility to preserve social harmony and environmental conservation is required to create sustainable reverse logistics.

Preposition 2e (suitable): worthy activities in supporting the program to reach social welfare and to be responsible in using and producing electronic product and/or handling their own e-waste are the suitable components to format sustainable reverse logistics

Preposition 2f (supportable): re-design the way our economy works and re-build a restorative economy through creativity and also innovation, generate business and economic opportunity and provide environmental benefits through renewable and reusable resources as materials in an efficient way.

5. Conclusion and Further Research

This research uses criteria of good theory [29, 32] to break down few conclusions. First, this research highlights 51 selected constructs for building sustainable reverse logistics theory that categorized into 4 dimensions to fulfil parsimony requirement and evaluation criteria in building a theory. They are infrastructures and facilities provision, human resource commitment, regulation, and managerial orientation. Second, the causality relationship of major constructs both direct and indirect impact of SRL implementation, is used to explain the internal consistency and impact criteria. Third, the implementation criteria are met by finding the stakeholders obligations to realize SRL program. There is a small chance for community or businesses in emerging countries to initiate conduct SRL activities, therefore these constructs are the obligations for them. In the case of Malaysia, manufacturers are not proactive in taking advantage of product take back since they regard it as service cost [36, 46]. While in Thailand, they still face many problems in conducting RL such as return policy, procedure management, transportation and communication [6]. The author believes that many poor and emerging countries still grapple with the same problem. Fourth, in term of fulfilling generalization criterion, it is better to test in some emerging countries with the same phenomena before using this theory. For further research, it is needed to explore the new constructs based on businesses and communities' inspirations. Furthermore, for managerial implication, government will adopt those constructs to measure SRL performance.

Conflict of Interest

The authors declare no conflict of interest.

Acknowledgment

This study would not have been possible without support material and non-material from LPDP scholarship from The Ministry of Finance and The Ministry of Research Technology and Higher Education. The author would like to thank and appreciate the invaluable constructive views and comments by reviewers.

References

[1] H. Maheswari, G. Yudoko, A. Adhiutama, "Towards sustainable reverse logistics: A conceptual framework of quattro bottom line approach" in Indstr. Eng. and Eng. Mgt Confr. 2017, 1377-1381,

[2] G. Yudoko, "Integrated municipal solid waste planning and management (IMSWPM) in developing countries: A conceptual framework", J. Mgt. Tech., 2007

[3] Organization for Economic Cooperation and Development (OECD), "OECD economic survey: Indonesia", OECD Publishing, 2010

[4] H. Maheswari, G. Yudoko, A. Adhiutama, "Stakeholder engagement model in quattro helix model for mobile phone reverse logistics in Indonesia: A conceptual framework" in IOP Conf. Series: Mat. Sci. and Eng., 2017. https://doi:10.1088/1757-899X/277/1/012062

[5] P. Andarani, N. Goto, "Potential e-waste generated from households in Indonesia using material flow analysis" J Mater Cyc. Waste Mgt., **16**, 306-320, 2014. http://doi.org/10/1007/s10163-013-0191-0

[6] P. Tanskanen, Electronics waste: recycling of mobile phones, INTECH Open Access Publisher, 2012

[7] J.D. Demajorovic, E.E.F. Augusto, M.T.S. De Souza, "Reverse logistics of e-waste in developing countries: challenges and prospects for the Brazilian model", Ambt. And Soc, **19** (2), 117-136, 2016

[8] P.R. Kleindofer, K. Singhal, L.N.V Wassenhove, "Sustainable operations management" Prod. and Oprt. Mgt., **14** (4), 482-492, 2005. ABI/INFORM Global

[9] P.J. Daugherty, A.E. Ellinger, "Reverse Logistics: The relationship between resorce commitment and program performance", J. of Busn. Logst., **22** (1), 107-123, 2001

[10] L. Paquette, "Reverse logistics and the creations of reverse flows for the mobile phone industry" Thesis, Aarush University, 2009

[11] D.S. Rogers, P. Tibben-Lembke, "Going Backwards: Reverse Logistics Trends and Practices", Reverse Logistics Executive Council, University of Nevada, Reno Center for Logistics Management, 1998

[12] H.C. Pfohl, A. Bode, H.T.V. Nguyen, "Adaptability to reverse logistics – An empirical study in European electronics industry", Journal of Glob. Strat. Mgt., **6** (1), 89-102, 2012. http://doi.org/10.20460/JGSM.2012615789.

[13] I. El-Nakib, "Reverse logistics: A comparison of electronic waste recycling between Switzerland and Egypt" in Global Conference on Operations and Supply Chain Management, 2012, ISBN No. 978-967-5705-06-9

[14] M.D. Abdulrahman, N. Subramanian, "Barriers in implementing reverse logistics in Chines Manufacturing Sectors: An Empirical Analysis" in the 23rd Annual POMS Conference, 2012

[15] A. Agrawal, "Reverse logistics: Performance measure and their effect in product lifecycle" in Inter. Jour. of Core Eng. and Mgt, **1** (2) 14-23, 2014, ISSN: 2348 9510

[16] S. Emmet, V. Sood, Green Supply Chain, A John Wiley and Sons, Ltd. Publication, United Kingdom, 2010

[17] E. Damanhudi, "The role of informal collector of recyclable waste and used goods in Indonesia", Post-Cons. Waste Rec. and Opt. Prod., Intechopen.com, 2012, Croatia

[18] R.F. dos Santos, F.A.S. Marins, "Integrated model for reverse logistics management of electronic products and components" Procedia Computer Science, **55**, 575-585, 2015

[19] M. Thierry, M.J.V.N. Salomon, J.V. Nunen, L.V. Wassenhove, "Strategic issue in product recovery management", California Mgt. Rev., **37** (2), 114-135, 1995, http://doi.org/10.2307/41165792

[20] M.P. De Brito, R. Dekker, "A framework for reverse logistics", ERIM Rep. Series, 1-23, 2003, http://doi.org/10.1007/978-3-540-24803-3_1

[21] S.S. Khan, S.A. Lodhi, F. Akhtar, "Sustainable WEEE management solution for developing countries applying human activity system modeling", Mgt. of Envr. Qual., **26** (1), 84-101, 2014, http://doi.org/10.1108/MEQ-05-2014-0072

[22] V.P. Rindova, I.O. Williamson, A.P. Petkova, J.M. Sever, "Being good or being known: An empirical examination of the dimensions, antecedents, and consequences of organization reputation", The Acadm. Of Mgt Journ, **48** (6), 1033-1049

[23] C.E. Carroll, "Corporate Reputation and the News Media in the United States" New York, NY: Routledge, 2011

[24] T. Passow, R. Fehlmann, H. Grahlow, "Country reputation – from measurement to management: The case of Liechtenstein, Corport. Rept. Rev, **7** (4), 309-326, 2005, http://doi.org/10.1057/palgrave.crr.1540229

[25] A. McKinnon, The role of government in promoting green logistics", The Chart. Inst. of Log. and Transp., 342-360, ISBN 97807494567888, 2010, United State.

[26] J. Aitken, A. Harrison, "Supply governance structures for reverse logistics systems", Intr. J of prt. and Prod. Mgt., **33** (6), 745-764, 2012, DOI: 10.1108/IJOPM-10-2011-0362

[27] W. Wilhelm, A. Yankov, P. Magee, "Mobile phone consumption behavior and the need for sustainability innovation", J. of Strt. Innvt. and Sust., **7** [2] 20-38, 2011

[28] M.A.P. Sari and Rustan, Implementation of good governance in waste management", PKP2A III LAN Samarinda (2013)

[29] R. Swanson, T.J. Chermack, Theory Building in Applied Disciplines", Berrett-Koehler Publ., 2013, San Fransisco

[30] D.K. Beckley, W.B. Logan, "The Retail Sales Person at Work", Gregg Publs., New York, NY, 1948

[31] M.Q. Patton, "Utilization-Focused Evaluation: The New Century Text", Sage Publicatio, UK, 1997

[32] J.G. Wacker, "A definition of theory: Research guidelines for different theory building research method in operation management", J. Opr. Mgt., **16,** 361-385, 1998

[33] M. Bernon, J. Cullen, "An integrated approach to managing reverse logistics", Intrn. J. of Log. Resrc. and Applc., **10**, 41-56, 2007

[34] C.H. Chiou, "Dynamic capabilities, collaborative network and business model: An empirical analysis of Taiwan HTC corporation", Affrican J. of Busn. Mgt. **5** (2), 299-305, 2011

[35] H.L Correa, L.H. Xavier, "Concepts, design, and implementation of reverse logistics systems for sustainability supply chain in Brazil", J. of Oprt. And Supp. Cha. Mgt., **6** (1), 1-25, 2013

[36] S.M. Budijati, Model of Reverse Logistics Management: Close Loop and Opened Loop as well as Consumer Behavior Accommodation, Dissertation, UGM, 2016

[37] J-B. Sheu, "Green supply chain collaboration for fashionable consumer electronics products under third-party power intervention-a resources dependence perspective" Sustainability, **6**, 2832-2875, 2014. http://doi.org/10.3390/su6052832

[38] R.G. de Sauza, J.C.N. Climaco, A.P. Sant'Anna, T.B. Rocha, R.A.B. Valle, O.L.G. Quelhas, "Sustainability assessment and prioritization of e-waste management", Wst. Mgt., **57**, 46-56, 2016, http://dx.doi.org/10.1016/j.wasman.2016.01.034

[39] I. Vlachos, "A conceptual framework of reverse logistics impact on firm performance", Brit. Acdm. of Mgt (BAM) Confr., 2014

[40] P. Rajagopal, V.P.K. Sundram, B.M. Naidu, "Future direction of reverse logistics in gaining competitive advantage: A review literature", Int. J Sup. Chain. Mgt, **4** (1), 39-48, 2015

[41] J. Yin, Y. Gao, H. Xu, "Survey and analysis of consumers' behavior of waste mobile phone recycling in China", J of Clean. Prod., 1-9, 2013, http://dx.doi.org/10.1016/j.jclepro.2013.10.006

[42] R. Pinna, P.P. Carrus, "Reverse logistics and the role of fourth party logistics provider", Pathw. to Sup. Ch. Exc., www.intechopen.com

[43] A. Atasu, L.V.N. Wassenhove, "An operation perspective on product take-back legislation for e-waste: Theory, practice, and research need", Prod and Opr. Mgt., **21**, (3), 407-422, 2012, ABI/INFORM Research

[44] H. Maheswari, "Supply Chain Management", Cent. Of Teach. Mat. Dev., Economic Faculty, Mercu Buana University, 2008.

[45] K.S. Khor, Z.M. Udin, "Impact of reverse logistics product disposition towards business performance in Malaysian E&E companies", J. of Sup. Ch. And Cust. Rel. Mgt., 19 pg., 2012, DOI: 10.5171/2012.69946

Appendix

Constructs	Definition
Eco-friendly product design	Designing an electronic product that using eco-friendly resources and easy to upgrade the feature
After sales service	Giving service after selling electronic product
Packaging reduction	Reducing the use of packaging by alternating usage
Deposit fund	Providing budget by collecting from community for normalizing environmental condition
Take back obligation	Designing return electronic product mechanism from point of consumption (consumer) to point of origin (producer)
Drop box facility	Providing drop box to facilitate community bring and collect used electronic product
Recycling technology creation	Creating a technology to recycle used electronic product
Standard equipment utilization	Enforcing employee to use standard equipment when conducting RL activities
Skill accreditation (employee competency)	Accrediting the employee to standardize competency of employee
Quality of product (longevity of extension)	Establishing the quality of product by adding longevity of extension
Organizational commitment	Preparing commitment of organization to conduct RL activities
Budget allocation	Allocating budget to convert e-waste to be a valuable product
Inclusion of post-use product handling	Publishing how to handle after using electronic product
Technology conversion	Inventing a technology to convert e-waste to energy
SMEs coaching	Coaching small medium enterprise to recycle safely used electronic product
Enterprise alliances	Alliancing enterprises for easy sharing the knowledge and facility
Inclusion of product content and duration	Writing electronic product content and duration in guidance book for informing the when they allow to replace it
Corporate citizenship	A set of values or principles that drive an organization to become responsible engaged with particular RL activities [36]
Public participation awareness	
Eco shopping decision	Warning community to be aware to participate in RL program
Reduce replacement frequency	Buying electronic product when it is needed
Separate own e-waste	Reducing the frequency of electronic product replacement
Reasonable reimbursement (incentives)	Separating communities' own e-waste from household waste so that easy to recycle
Willingness to pay	Giving reasonable incentive to motivate owner of used electronic product to bring it for recycling
Fairness in using electronic product	Influencing community want to pay e-waste converting cost
	Using electronic product with reasonable way
Illegal import restriction	
Electronic product national standard arrangement	Preventing import of electronic product illegally
Collecting point extension	Making national standard for electronic product
Invention of handling mechanism	Adding collecting point for electronic products in many place
Health and social awareness instillation	Inventing mechanism of e-waste handling for each stakeholder
Vocational education for HR preparation	Bringing strong understanding of health and social awareness
Storage point	Developing vocational education to teach safety recycling technology
Professional mgt. of secondary market	Building storage point to relocate used electronic products from drop box
Business localization	Managing secondary market professionally to facilitate circulation of used electronic product
Tax arrangement	Placing businesses in reverse chain on particular area
Jobs creation	Arranging tax reduction for reselling used electronic products
Knowledge building and deployment	Creating a new job in reverse chain to help uneducated people as part of recycling program e.g. as scavenger.
Program of restructuration machine	Building knowledge to community about waste, hazardous and toxic materials
Budget provision from APBN	Subsidizing businesses by giving a new machine that is needed for converting e-waste to energy
Rules alignment	Providing budget to run RL program
New entrepreneur invention program	Aligning rules and regulation in each department for integrating RL program
Third party provision	Inventing new entrepreneurs that do business in recycling used electronic product
Social Punishment	Providing a company that certified by government to conduct RL activity for firms that do not have recycling technology
	Giving punishment to communities that avoid to separate their own e-waste from other kinds of waste, wasteful in using electronic product
Synergy of key actors	Integrating key actors to implement RL activities together
Integrated implementation	Integrating RL activities to reduce e-waste faster
Control RL implementation	Controlling implementation of RL program to ensure not damaging the environment
Green industrial development	Developing green industrial by making a competition
SMEs-Industry link and match	Creating link and match between SMEs and industry
Process modernization of SMEs	Improving process modernization of SMEs in managing business in reverse chain
Tariff adjustment	Adjusting tariff for electronic products that have longer life time
Waste to energy program	Implementing waste to energy program
Social and public facility utilization	Using social and public facility to facilitate business in reverse chain
Monopolistic collective systems	Dominating collective system of used electronic product to avoid uncertain timing and quantity of returns

ASTES

Advances in Science, Technology and Engineering Systems Journal Vol. 3, No. 4, 99-111 (2018)

www.astesj.com

Special Issue on Multidisciplinary Sciences and Engineering

ASTESJ

ISSN: 2415-6698

Extendable Board Game to Facilitate Learning in Supply Chain Management

Linda William*[1], Za'Aba Bin Abdul Rahim[1], Robert de Souza[1], Eko Nugroho[2,3,4], Rio Fredericco[2]

[1] *The Logistics Institute Asia Pacific, National University of Singapore, 21 Heng Mui Keng Terrace #04-01, Singapore 119613*

[2] *Kummara Studio, Jl. Sidomukti no. T1, Bandung 40123 Indonesia*

[3] *Center for Research on Information & Communication Technology, Institute Technology Bandung, Jl. Ganesha No.10, Lb. Siliwangi, Coblong, Kota Bandung, Jawa Barat 40132, Indonesia*

[4] *GameLab, Computer Science Program, Bina Nusantara University, Joseph Wibowo Center Campus, Jl. Hang Lekir I No. 6 Senayan, Jakarta 10270, Indonesia*

ARTICLE INFO

Article history:
Received: 14 June, 2018
Accepted: 08 July, 2018
Online: 23 July, 2018

Keywords:
Game-based learning
Facilitate learning
Supply chain management
Board game
Expandable framework

ABSTRACT

Game-based learning has been introduced as an interactive tool to facilitate learning and training processes in various fields, including supply chain management (SCM). Most of these games are specifically designed to focus on certain scenarios and concepts. For example, the original beer distribution game focuses on a single product supply chain without considering capacity and process reliability into account. This creates challenges for extending the games to cover other concepts in SCM. To tackle this problem, we propose a board game, titled ThinkLog, as a face-to-face extendable framework to facilitate learning in SCM. It can be extended to generate different scenarios for various concepts in SCM without changing the basic game structure. Using this principle, we have extended the basic version of ThinkLog to two other scenarios, namely: humanitarian logistics and urban logistics, by simply modifying the rule of the game. Each scenario would have different learning objectives embedded in the gameplay. The game is also complemented with a computer-based application (digital application) to enhance the overall learning experience and collect relevant data (data gathering) during a game session. These three scenarios have been evaluated on four-interactive sessions with government officials and policy- makers in Indonesia. Each session has been consistent in its acceptance of the game as a tool to facilitate learning in SCM, regardless of the scenarios that we played. Our learning objective evaluation also shows that the game is effective in deepening the players' understanding of SCM concepts.

1. Introduction

This paper is an extension of work originally presented in 2017 IEEE 6th International Conference on Teaching, Assessment, and Learning for Engineering (TALE) [1]. It focuses on developing and evaluating an extendable board game as a game-based learning framework to facilitate teaching and learning in Supply Chain Management (SCM).

Game-based learning has been introduced to improve training activities and initiatives by stimulating learning engagement and motivation through role playing and repeatability for the players to learn new skills and concept voluntarily [2, 3, 4, 5, 6]. It is a subset of serious games which includes the use of any medium of games (e.g. board games, card games, sports or digital games) for learning purposes [7]. It has been implemented in various fields, such as healthcare [8, 9, 10], military applications [11], city planning [12] and supply chain management [13, 14, 15, 16, 17].

Previous studies have identified the benefits of these type of games in a variety of critical-contexts [3]. It includes enhancing engagement and motivation, improving self-monitoring, recognizing and solving problems, improving decision making, and developing social skills for collaboration and negotiation [3,

*Corresponding Author: Linda William, The Logistics Institute Asia Pacific, National University of Singapore, 21 Heng Mui Keng Terrace #04-01, Singapore 119613, Telp: +65-6516 4281, Email: Lindawati.tliap@nus.edus.ag

18, 19]. It would advance the players' understanding and learning in a scientific knowledge [20]. By using games, players become more involved in solving multiple tasks or challenges. Games provide a hand-on experience where the players need to plan appropriate strategies based on their knowledge and skills, implement these strategies in the experimented environment and respond to the consequences of their strategies. It would promote players' motivation and knowledge transfers in a subsequent realistic context [20, 21].

However, most of the game-based learning in SCM focus on one or a limited number of scenarios. For example, the original beer distribution game is designed for a pure retail distribution game without taking product conversion, capacity and process reliability into account [22] or the blood supply chain only focuses on perishable goods [23]. It cannot be extended (or difficult to be extended) to cover different SCM concepts without changing the game structure or game components. Hence, it is limiting the implementation of the games.

Recognizing this problem, we propose a board game, titled ThinkLog, as an extendable face-to-face learning framework for SCM concept. It uses role-playing and simulation to stimulate discussion and interaction between the players. It creates a safe environment for the players to share their thoughts and practice their new skills without the threat of real-world consequences. ThinkLog can be extended to generate different scenarios for various concepts in SCM without changing the basic game structure. To demonstrate its capability, we have extended the basic scenario of ThinkLog [1] to cover two more complex SCM concepts, namely: humanitarian logistics and urban logistics. These new concepts can be embedded in the game by modifying the rules of the game.

We also develop a digital companion application to complement our board game. Companion apps have been used in several games, such as Dungeon Master's Assistance for Dungeons and Dragon game [24] and smart play system for Yes or Know board game [25], to guide the players during the game and provides a simple calculation for fastening the game processes. Our companion app aims to enhance the overall learning experience and collects the relevant data (data gathering) during a game session. The data collected can be analyzed further to understand the players' behavior and game experience. Using this insight, we would be able to adjust and customize the game to fit with individual learning behavior.

To evaluate the effectiveness of ThinkLog, we conducted four interactive sessions with government officials and policy makers in Indonesia using different scenarios. From those sessions, we learnt that the game (with or without the companion app) is highly accepted by the players. The players were also able to grasp the learning objectives of the game easily. Other than these four sessions, we also conducted a game session with master students in the National University of Singapore, as part of their SCM course, to evaluate the game in a larger group setting. The game acceptance and learning objective evaluation of the players resonates throughout the game session.

The remaining of the paper will be organized as follows: Section 2 presents the literature review and section 3 presents the proposed board game. Section 3 includes the game design, components, scenarios and its companion app. Section 4 discusses the evaluation method to measure the effectiveness of ThinkLog in facilitating learning in SCM. Section 5 reviews ThinkLog adjustment for adoption in classroom with large group setting and Section 6 presents the conclusions and future research direction.

2. Literature Review

In this section, relevant literature in the areas of board games and games for SCM are reviewed.

2.1. Board Games

Board games have been used as entertainment for centuries, starting from the ancient games such as *Go* and *Backgammon* that are still used today [26]. Generally, board games are played using an artwork [27] which incdice the main board, balls, dices, and cards. It has a set of rules that need to be obeyed by all the players. Points or rewards are given according to the rules. The players have a flexibility to change the rules based on the consensus from all the players [25]. They would take turns to play and receive feedbacks immediately. The actions and feedbacks are all apparent to all the players. The players would also be able to discuss with each other openly.

Although it has not been explored extensively as digital games, board games show promising opportunities to facilitate learning and training [28, 29, 30]. It has been proven to be as effective as digital games to facilitate learning [31]. As part of game-based learning, board games are able to enhance the players' engagement and motivate them to learn new skills, including social skills, to get potential rewards from the game through interaction and discussion with other players. It can stimulate the players' ability to think and solve problems and challenges. The nature of board games also implies transparencies and interactions as the core mechanism of the game. Hence, these board games are suitable for collaborative games where all players need to work together as a team to win the game [29] or other similar contexts which highly depend on real human interaction [28].

Board games have been successfully implemented to support learning and training in healthcare [32]. It shows a significant increment of knowledge on nutrition labeling [31], dengue hemorrhagic fever [32], healthy eating [33], chronic disease and risk factors [34], tooth morphology [35], pediatric [36], and cancer treatment [37]. Other than healthcare, board games have also been implemented in urban planning [38], agriculture [39], and software design [40]. The Beer Distribution Game, a well-known game in SCM, is also available on board game version [13, 41].

2.2. Games for SCM

A number of games have been introduced to facilitate learning of Supply Chain Management (SCM) concepts [6], among which are the famous Beer Distribution Game [13, 42, 43], Blood Supply Chain Game [23, 44], Mortgage Service Game [15] and Distributor Game [16, 17].

The beer distribution game is the most well-known game in SCM and part of many SCM curriculum since it was being developed by MIT in the 1960s [43]. There are several variants of the beer distribution game in the literature, these includes the stationary beer game [14], computer simulated beer game (e.g. [45, 46]) and online beer game [42]. This game aims to introduce the

basic concepts of the bullwhip effect and the benefits of information sharing and lead-time reduction. It simulates a supply chain for a single product involving a four-level supply chain composed of a retailer, a wholesaler, a distributor and a manufacturer. Each player takes one role and for each turn, he/she follows the same set of activities, that is to fulfil customer demand, order from supplier, and manage inventories. The goals of this game are to minimize the total holding and backorder costs incurred in the entire supply chain.

Blood Supply Chain Game demonstrates supply and demand balance in healthcare perishable products with limited shelf life and production. It simulates the simplified supply chain of blood units from donors to patients based on a real case study modelling the UK blood supply chain [23]. This game is played from the perspective of the distributor which is the middle-player in the blood supply chain network. It has different game options and parameters to determine the probability of blood supply and demand and fulfillment policy. Each player aims to maximize the number of order fulfillment to the hospitals by considering the limited stock.

Different from beer distribution game and blood supply chain game that focus on a supply chain with finished goods inventory, Mortgage Service Game is intended to teach service-oriented SCM concepts [15] that typically do not hold any inventory and can only manage backlogs through capacity adjustment (such as number of employee's adjustment). It aims to introduce the bullwhip effect resulting from information and capacity adjustment lags and impact of end-user demand information in the service industry. This game represents a simplified mortgage approval process that has four stages, namely: initial processing, credit checking, surveying and title checking. Each player or team of players controls a particular stage and able to adjust its capacity by hiring or firing employees to check all mortgage applications in its backlog for each turn. Depending on the setup, the other stages may be managed by artificial agents or real players. The game also introduces lags on the capacity adjustment processes. The goal of this game is to minimize the total cost for the entire supply chain, resulting from employee salaries and service delays (certain fine or backlog fee would be added to the total cost).

Lastly, distributor game, is operating at a continuous clock with ongoing events and responses to individual decision to mimic the real-time global supply chain [17]. It is different from the other three games where the players need to wait for their turns to make their actions. Distributor game is a specific instance of Global Supply Chain Game (GSCG). It aims to educate the players on critical leadership skills for global supply chain in real time. These skills include strategic leadership, operations management, financial management and information technology.

Table 1. SCM Game Comparison

Category	Beer Distribution Game	Blood Supply Chain Game	Mortgage Service Game	Distributor Game	ThinkLog
Game world					
Type	Role-playing simulation	Role-playing simulation	Role-playing simulation	Role-playing simulation	Role-playing simulation
Platform	Board, Digital, Online	Board, Digital (Excel-based)	Digital	Online	Board
Technical Features	Multi players with four roles; Players wait for their turn to make their actions	Single player from the perspective of distributor	Single player/multi players; Players wait for their turn to make their actions	Single player; Players do not need to wait for their turn to make their actions	Multi players; Players wait for their turn to make their actions
Game Event					
Subject or content areas	Industrial production and distribution system	Supply and demand balance for perishable goods	Service-oriented SCM	Global supply chain	Supply Chain Management
Scenario	One scenario; Single product in a four level supply chain	One scenario; Blood supply chain	One scenario; Mortgage approval process that has four stages	One scenario; A four-level global supply chain	Expendable to different scenarios with different gameplay
Learning objective	Introduce the basic concepts of the bullwhip effect and the benefits of information sharing and lead-time reduction	To improve understanding of complex principles of supply chain for perishable goods	Introduce bullwhip effect resulting from information and capacity adjustment lags and impact of end-user demand information in the service industry	To learn leadership skills that are critical to manage real-time global supply chain.	Different scenarios would have different learning objectives

All players take a role as a distributor in a distribution center in a four level supply chain. Other levels, including competing distributors are played by artificial agents to create a complex and dynamic global environment.

The summary and comparison of these four games and our proposed board game are presented in Table 1. The comparison is based on game categories adapted from [47]. Other than these four games, there are other games designed to illustrate different SCM concepts (see, for example, Lean Leap Logistics Game [48] and The Chain Game [49]).

3. ThinkLog: An Expandable Learning Framework

This section would describe ThinkLog as a special board game designed to enable the extension in the scenarios without changing the basic game structure. The game design, components, scenarios and companion app are reviewed.

3.1. Game Design

As an interactive board game for game-based learning, ThinkLog is carefully designed to balance the entertainment components and the pedagogy (i.e. learning objectives and outcomes). The game needs to have a clear objective, derived from specific SCM concepts, research outcomes and case studies. It also needs to have a clear pedagogy to influence learning and motivate the players to gain specific knowledge and skills related to the learning objectives. However, the game would also need to maintain the enjoyment and fun components, such as fantasy [50, 51], challenge [52, 53], choice [54], mechanism and playability [55]. It enables the players to engage and immerse into the game which would eventually motives the players to achieve new skills and understands new concepts voluntarily in a greater speed.

To balance these factors, ThinkLog is developed by following the game base learning framework [56], as illustrated in Figure 1. The framework has been adapted to include board game elements, such as interaction between the players. For each scenario, specific concepts are translated to the learning objectives and then converted into the specific scenario with clear goals for the players.

The entertainment components are captured by the game characteristics that allow players to be involved and engaged in the game. The characteristics can be categorized into 6 criteria, namely: challenge [52, 53], choice [54], competition, fantasy [50, 51], goal, and rule [57]. The summary of these characteristics is shown in Table 2.

3.2. Game Components

There are four main components of ThinkLog, namely: main board, demand cards, gameplay/rules and game master. These are essential components to play ThinkLog regardless of the scenarios played.

3.2.1. Main board

ThinkLog's main board is a symmetrical map to visualize actions and responses during the game. It is a center of the whole activities in the game. It is also the base for all the engagements and twists during the game. By design, the board serves as a platform that gives players a (pseudo) control of the entire game environment. This sense of control is important to keep the player focus and bring more excitement to the game. The board also shows the player' actions and (action) feedbacks.

To represent the supply chain network and logistics activities, several nodes for the players' logistics facilities or other logistics assets are included. Depending on the game scenarios, the players may be able to determine their facility locations. Logistics activities will occur on the map between these facilities. Common disruptions such as traffic congestions, flooding and facilities' breakdown can be shown in the main board to introduce risk and uncertainty aspects of the supply chain.

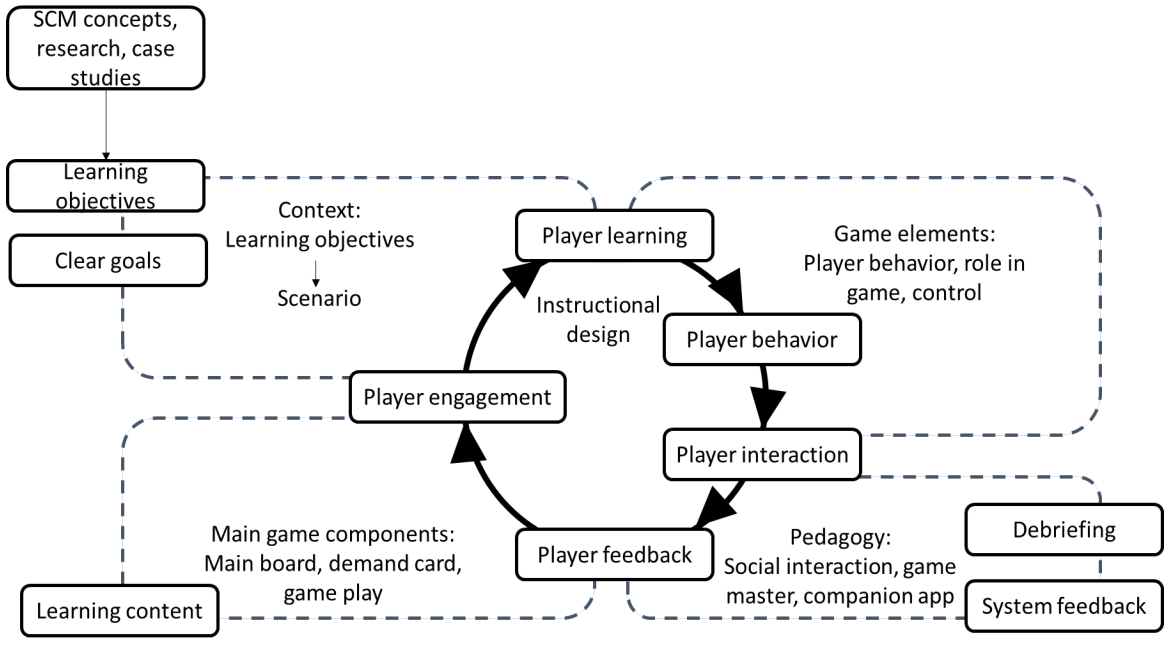

Figure 1. ThinkLog Game Design

Table 2. ThinkLog Characteristics

Challenge	• The difficulty level is determined by the lead time and demand level. • Various disruptions (such as traffic congestions, flooding and facilities' breakdown) would be added.
Choice	• Depending on the scenarios, the players may need to decide the locations of their facilities and consolidate their orders. • Players need to select their vehicle's delivery route. • Players need to decide the number of goods to ship to the next level node in the supply chain and the number of goods to order from the previous level node in the supply chain
Competition	• Depending on the scenarios, the players may compete with the other players to win the game. • The players may compete to get the highest performance (in term of money or other points)
Fantasy	The game uses the main board and other components (i.e. vehicles) to help the players imagine the logistics environment.
Goal (Game Objective)	The general goal is to create an efficient supply chain network.
Rule	• Each player needs to wait for his/her turns to take actions. • Interaction between players and game master are encouraged.

There are two variations of the main board depending on the point or node locations as shown in Figure 2. The first variation, named basic main board, has eight facility locations, while the second variation, named flexible main board, has several alternative locations where the players can choose to locate their facilities or assets.

3.2.2. Demand cards

During the game, players will be introduced to "Demand Cards", as shown in Figure 3. It represents the market demands that need to be fulfilled during the game and players can either work together or individually to do so. The demand values are dependent on the scenarios; it can be randomly generated or based on a certain distribution to mimic real demands for a particular good in the particular scenario.

3.2.3. Gameplay

The gameplay core mechanic in ThinkLog is point to point delivery where the players need to deliver a certain amounts of goods to a certain point. Players main objective is to develop a strategy for efficient and effective deliveries which include managing their delivery timing, amounts, and resupplying their stocks. It will determine the result of the game and players' performance in the game.

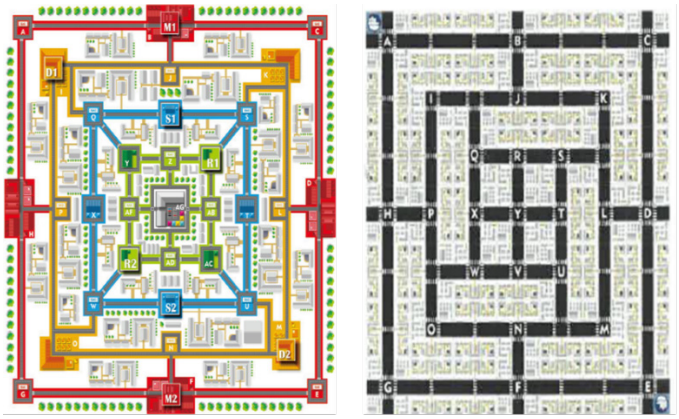

(a) Basic Main Board with fixed warehouse locations

(b) Flexible Main Board with alternative warehouse's locations

Figure 2. ThinkLog Main Board

Figure 3. ThinkLog Demand Cards

To develop their delivery strategies, the players must consider the following criteria: locations, management cost, facilities and vehicle constraints, and supply availability. Tweaking these criteria would create different situations in the game and eventually resulting in different scenarios. There are 3 main activities for the players within a round of the game as follows.

1. **Ship**. The players send the exact amount of goods ordered by the next level node in the supply chain (i.e. the player's customer). If the players do not have enough goods and cannot fulfil all the order, they will get a backlog token.
2. **Pay.** The players pay inventory cost and backlog cost (if any).
3. **Order**. The players give order to the previous level in the supply chain (i.e. the player's supplier) and pay the price.

The 3 main activities can be re-arranged and adjusted if needed in specific scenarios.

3.2.4. Game Master

A game master guides the overall gameplay of the game session and ensures players understand and follow the rules accordingly. Depending on the number of players and the game master's availability, the game session may be led by one main game master and several supporting/group game masters. For each game session, the game master would need to do the following:

1. **Briefing**. The game master initiates a discussion highlighting on: 1) the concept of the game and its relations with the logistics/supply chain topic; and 2) the overview of the game rules and objectives to guide the players on how to play the game.

2. **Playing**. The game master would be involved in the game, by:

    - Observing the group dynamics.
    - Providing some additional information/motivation to make sure all participants actively involved in the session.
    - Intervening the game in case there are some (unwanted) conflicts. The game master may take necessary action to minimize any possible risk of distraction.

3. **Debriefing**. The game master conducts a discussion after the game session. The game master would motivate the players to share their experience and highlighting some learning points that they found during the playing phase. Later the game master summarizes those findings by emphasizing on main learning points of the game.

Other than these four main components, there are other components for ThinkLog game. It includes player board, truck token, facility token, good token, congestion token, paper money and order form. Some scenarios may need additional components. The use of these components is also depending on the scenarios played. Several components can be replaced by a feature in the companion app. For example, paper money can be replaced by virtual money in the companion app.

3.3. ThinkLog Scenarios

There are 3 scenarios of ThinkLog that have been developed, namely: basic, humanitarian logistics and urban logistics. The two later scenarios are the extensions of the basic scenario. Each scenario is designed to accommodate a certain theme and focuses on different learning objectives. The basic scenario focuses on information flow and coordination challenge in supply-chain and logistics sector. At the same time, it provides an overview of risk management in supply chain and the bullwhip effect. The second scenario focuses on introducing the Multi Criteria Decision Making (MCDM) procedure [58, 59] and its implementation in a simplified humanitarian logistics setting. And the third scenario focuses on important aspects of facility management in the context of last mile delivery. A summary of these scenarios is presented in Table 3.

3.3.1. Basic Scenario

Similar to the Beer Distribution Game [13, 42, 43], each player would choose one out of four available roles, namely: manufacturer, distributor, wholesaler, or retailer. Each role represents one level in the overall supply chain network. Each player or a team of players (2-3 players per team) will take the role of a supply chain coordinator and is responsible in managing their goods, supplies and facilities to fulfil the demand from their customers (or the next level in the supply chain). The learning points for the basic scenario are bullwhip effect, lead time, and stock management. The game can be played by 4 to 10 players for approximately 90-120 minutes.

3.3.2. Humanitarian Logistics Scenario

The humanitarian logistics scenario adapts Multi Criteria Decision Making (MCDM) concept to determine the locations of the warehouses/distribution centers for relief supply stocks in humanitarian setting [60]. MCDM is a structured framework to analyze decision problems that involve complex multiple objectives [58, 59]. It can be used to accommodate complex decision processes involving various criteria and various decision makers with different viewpoints.

For this scenario, players are divided into different teams. Each team represents an expert team of regulators in humanitarian disaster relief. Their aim is to provide a continuous delivery of relief goods to the disaster area. To do so, each team first need to determine the optimal location for their warehouse and later to optimize their operation (delivery). Failure to deliver the required relief goods at the right time would be penalized with a failure token for the team. The team with the least failure token at the end of the game is the winner. The game can be played by 6-10 players with 60-90 min duration of play.

The game is divided into two stages, namely: preparation and respond stage. In the preparation stage, the players need to decide the optimal warehouse location(s) by MCDM methodology by considering a list of decision criteria, described in [60]. While in the respond stage, the players need to deliver the goods to the main disaster area. The game play at this stage is similar to the basic scenario.

3.3.3. Urban Logistics Scenario

Urban logistics scenario focuses on last mile deliveries in urban areas. It has four different roles, namely: port, distributor, wholesaler and retailer. Ideally, the game should be played by 8 players where 1 player as the port, 2 players as distributors, 2 players as wholesalers and 3 players as retailers. Each player is competing with each other to optimize their logistics activities.

This scenario has two stages, namely: preparation and respond stage. Similar to humanitarian logistics scenario, in the preparation stage, the players (except for the port) need to decide the optimal warehouse location(s) using MCDM methodology. But, the criteria used are different from the humanitarian logistics scenario. On the respond stage, the players need to deliver the goods to their customers. It is similar to the basic scenario, with the following differences: 1) the demand locations are random for each round and scattered all over the map; 2) each

Table 3. ThinkLog Scenarios

	ThinkLog		
	Basic scenario	Humanitarian logistics scenario	Urban logistics scenario
Learning objective	• To provide an overview of information flow and coordination challenges in supply chain and logistics • To introduce the bullwhip effect	• To introduce the concept of Multi Criteria Decision Making (MCDM) for selecting warehouse location for relief supply stocks in humanitarian logistics	• To introduce MCDM for selecting warehouses/collection and delivery points (CDP) and last-mile challenges in urban distribution
Game components			
Main board	Basic main board	Basic main board	Flexible main board
Demand card	Demand card shows the demand value	Demand card shows demand value	Demand card shows demand value and demand location. Note: demand locations are scattered and dispersed all over the map.
Gameplay	1 stage	2 stages, namely: • preparation stage (to determine the warehouse location) • respond stage (to deliver certain amount of relief goods to the main disaster area)	2 stages, namely: • preparation stage (to determine the warehouse location) • respond stage (to deliver certain amount of goods to the urban area)
Roles	4 roles, namely: manufacturer, distributor, wholesaler, and retailer	1 roles: regulator in humanitarian disaster relief	4 roles, namely: port, distributor, wholesaler, and retailer
Relation between roles	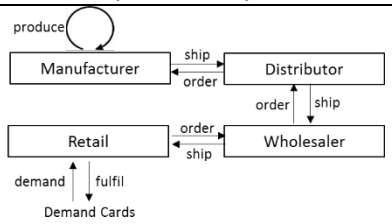	-	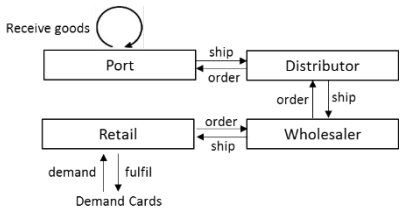
Game setup			
Number of players	4-10 players	6-10 players	4-8 players
Game duration	90-120 minutes/session	60-90 minutes	60-90 minutes
Performance measurement	Remaining money and backlogs	Remaining money and saved lives (represented by failure token)	Remaining money and backlogs
Twists	Common disruptions such as traffic congestions and flooding may be introduced on certain part of the game		

retailer would receive the same demand value and location; 3) retailers would be able to order goods from any wholesaler; 4) wholesalers would be able to order goods from any distributor; 5) port has two dedicated warehouse locations and the delivery will start from these two locations; and 6) the players are able to consolidate the shipments from two or more orders.

3.4. Companion Digital Application

From our first interactive session, we noted some improvements were needed to maximize the players' experience, such as in auto-tracking and graphical presentation of players' actions. These improvements may help to disseminate certain concepts better. For example, by producing a graph at the end of the game session, it may help to explain the bullwhip effect more effectively and help the players to review their decisions throughout the game and how it had affected the whole supply chain performance. In addition to that, several scenarios, such as humanitarian and urban logistics scenarios, may require some complex steps and calculations to determine the best location for the warehouse. It can be very time-consuming and prone to human error if it is to be done manually.

Based on the above improvement needs, we develop a digital companion application. It is designed not only to assist in complex calculation and display information, but also to guide the players during the game, support the game master (especially the non-experience game master) and record the player's actions and decisions during the game. We believe that with the companion app, the gameplay can be more interactive and lively,

not only between players but also between the game and the players.

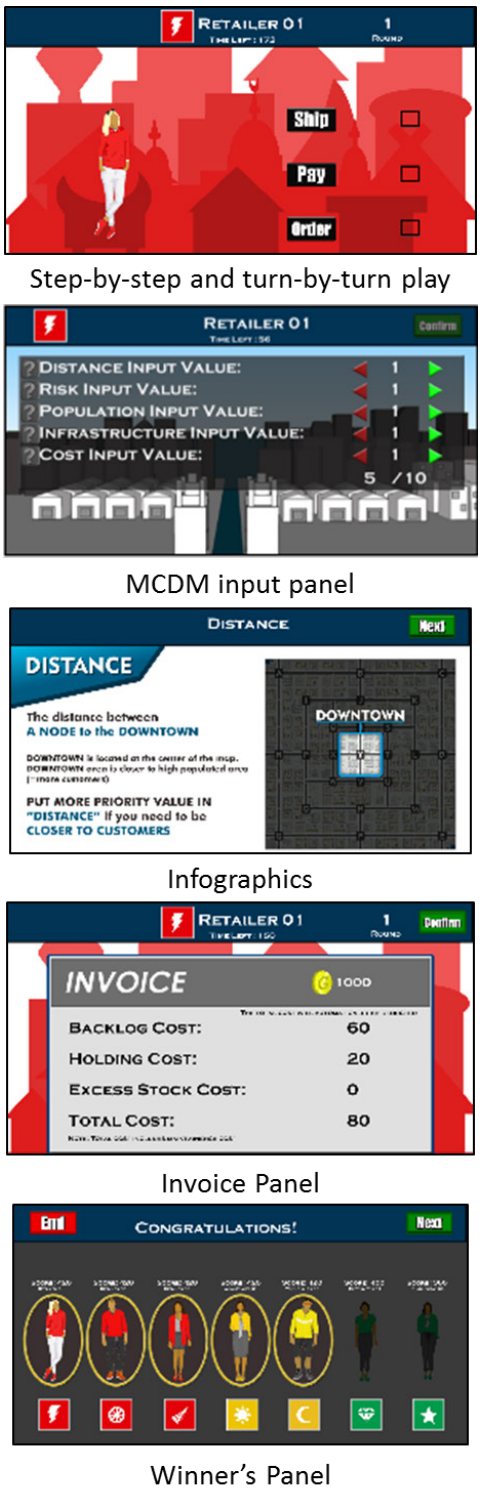

Figure 4. Examples of the Companion App Interfaces

The companion app is developed as desktop and mobile application. Several interfaces of the companion app are shown in Figure 4. Ideally, the companion app should be provided to all the players, downloadable for their digital devices. The features of the companion app include:

- Provides step-by-step, turn-by-turn play instructions to the players
- Serves as timekeeper for each player. Failing to keep to the time, the app will assume that no action is required from the player and ends the player's turn
- Captures the transaction inputs from the players and displays them as graphs at the end of the game
- Auto-generates a list of the most suitable locations for the player to choose based on the players' input for the MCDM (for scenarios that use MCDM)
- Provides a function to randomize the congestion locations for each round
- Provides infographics on the different criteria available for the MCDM
- Auto-deducts the cost incurred by each player and presenting its breakdown cost at each turn
- Auto-generates the winner(s) at the end of the game

4. Evaluation Method

To evaluate the effectiveness of ThinkLog, we conducted four interactive sessions with senior government officials and supply chain specialists as part of a three-day workshop in SCM. The sessions were held in different cities in Indonesia from August 2016 to April 2018 with different players for each session. Different sessions were played in different ThinkLog scenarios with or without the companion app. Summary of the sessions played is presented in Table 4.

In each session, we divided the players into small groups of eight to ten players where each group would have a mixed composition of players with different background. During the game session, the players were able to interact and discuss with the game masters and other players. Examples of that interaction without and with companion app are shown in Figure 5 and Figure 6 respectively.

We consider Session 1 as a trial session to measure the players' acceptance. For this session, we focused on observing the players' interaction and collecting their sentiments toward the game. In the subsequent sessions, we gathered more feedbacks from the players as well as from the game masters. These include players' sentiment, game experience, learning objective and feedback for companion app. Since the interactive sessions were run under different experimental conditions (i.e. using different scenario, different location and different game masters), we decided to treat the feedback from each session separately.

4.1. Sentiment Analysis

To gather the players' sentiments toward the game, we asked the players to provide their comments in an open-ended question. We then applied sentiment analysis method in R to evaluate these comments. Sentiment analysis has been widely used to study opinions, sentiments and emotions expressed in texts to identify positive or negative opinions based on a set of positive and negative lexicon [61].

Table 4. Summary of the Interactive Sessions

Interactive Session	Period	Location	Number of players	Using companion app	The scenario played	Feedback gathered	
						Players [feedback(#valid responses)]	Game Masters
1	August 2016	Jakarta	45	No	Basic	• Players' sentiment (13)	-
2	May 2017	Bandung	63	No	Humanitarian	• Players' sentiment (15) • Game experience (34) • Learning objective evaluation (34)	-
3	November 2017	Makassar	54	Yes	E-Commerce	• Players' sentiment (13) • Game experience (28) • Learning objective evaluation (28) • Companion app (28)	companion app
4	May 2018	Yogyakarta	44	Yes	E-Commerce	• Players' sentiment (20) • Game experience (25) • Learning objective evaluation (33) • Companion app (33)	companion app

Figure 5. Interactions between the players without companion app

Due to limited positive and negative lexicon database in Bahasa Indonesia, for this study, we used English positive and negative lexicon database [62, 63]. Before applying the sentiment analysis method, we translated the comments/feedback in English. The survey responses and sentiment analysis score are shown in Figure 7. The result shows that the average sentiment score is above 0. This indicates positive sentiments toward the game.

4.2. Game Experience

We further evaluated the players' game experience in session 2 to 4. We developed a questionnaire comprising 9 questions focuses on four experience categories, namely: positive, negative, flow, and learning experience. Flow experience is defined as a total engagement in the game that motives the players to win the game by achieving new skills and understanding new concepts voluntarily [64], while learning experience is defined as an ability of the game to transfer its learning objectives to the players [65]. The questionnaire used the 4-point Likert scale (4=strongly agrees, 1=strongly disagrees). Summary of the responses is shown in Figure 8.

Figure 6. Interactions between the players with companion app

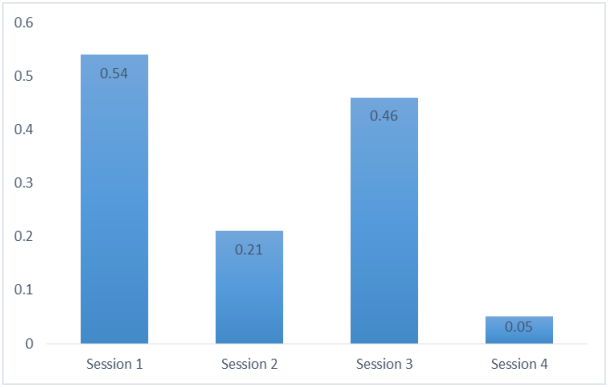

* = score <0 represents negative opinion, score =0 represents neutral opinion and score >0 represents positive opinion

Figure 7. The Players' Sentiment Analysis Score

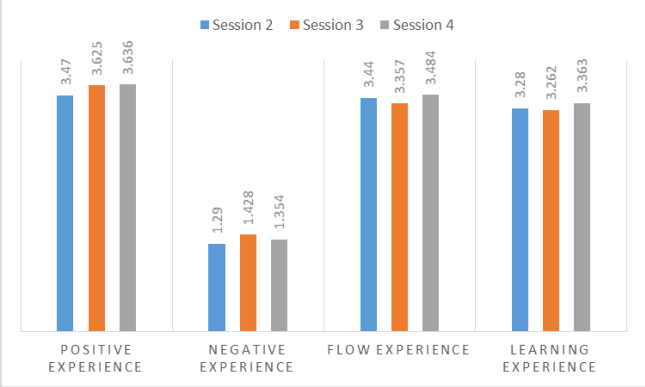

Figure 8. The Players' Overall Game Experience

Figure 8 shows that the average score for two experience categories (positive experience and flow experience) is above 3.3 and the average score for negative experience is below 1.5 for all the game sessions. It indicates that the players have a good experience with the game. For the learning experience, the result shows that the average score is above 3.2 which suggests that the players are able to understand the learning objectives.

4.3. Learning Objective

The learning objective is evaluated in the sessions 2 to 4. Session 2 used the humanitarian logistics scenario, while session 3 and 4 used the urban logistics scenario. The intended learning objectives for these two scenarios are described in Table 3. These intended learning objectives are to be evaluated against the learning points from the players' perspective.

In session 2, we collected the players' feedback by asking each group of players to list down learning points from the game after they have completed the game. A sample of those lists is shown in Figure 9. In this figure, the players mentioned that their learning points from the game were understanding criteria for determining the location of warehouse/distribution center for relief supply stocks in humanitarian logistics. Those criteria are distance, disaster location, congestions, infrastructure and maintenance cost.

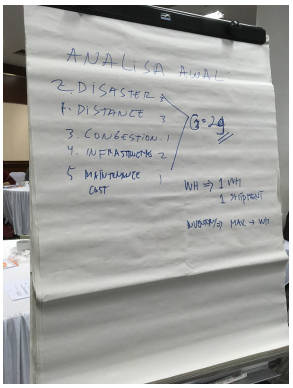

Figure 9. Sample of poster for the players' learning points

The summary of the learning points from the players' perspective in session 2 is as follows:

1. There are a lot of criteria to consider when determining the location of warehouse/distribution center, such as distance to the demand area, congestion, access to infrastructure and cost.
2. The decision makers need to consider some trade-off between those criteria.
3. Communication and coordination are essential to fulfil the demand effectively and efficiently.

These learning points are aligned with the intended learning objectives for humanitarian scenario. In session 3 and 4, we gathered the players' learning points individually. Each player was able to list down one or more learning points. Since we were playing the same scenario in these two sessions, we combined the players' learning points and summarized it in Table 5. From the result, we learnt that the players' learning points are aligned with the intended learning objectives for urban logistics.

4.4. Feedback on Companion App

The companion app was first introduced at interactive session 3 and 4. We gathered feedbacks on the companion app from the players and game masters. For the players, we asked them to evaluate the companion app usefulness in two criteria, namely: helping the players to understand the rule of the game and helping the players to learn about SCM concepts and used a 4-point Likert scale (4=strongly agrees, 1=strongly disagrees) to evaluate the criteria. We received 61 valid responses from interactive session 3 and 4. The average score for both criteria is above 3 (3.1 for helping the players to understand the rule and 3.2 for helping the players to learn). It indicates the companion app was well received by the players and it helps with the understanding and learning of the supply chain concepts embedded in the game.

Table 5. Learning Points absorb by the Players in the Third and Fourth Sessions

Learning Points	Number of Players
Importance of warehouse location	24
Warehouse selection criteria	11
Order planning and fulfillment	10
Stakeholders' coordination	8
Inventory management	6
Supply chain strategy and management	6
Warehouse and route optimization	5
Cost management	5
Demand forecasting	3
Communication	3
Simulation	1
Supply chain risk	1

To gather feedbacks from the game masters, we conducted group discussions after the game sessions were completed. From the discussions, we learnt that the companion app is able to speed up and smoothen the game process, but the interface may need to be improved especially for small screen devices. The information shown in the companion app may also need to be filtered or re-arranged to avoid information overload that would confuse the players.

5. Incorporating ThinkLog into Supply Chain Courses

With its expandable capability, ThinkLog has great potential to be incorporated into supply chain courses with large number of students. ThinkLog scenario can be adjusted to fit in different

courses. For example, the basic scenario is suitable to provide an introduction of SCM, while the humanitarian logistics scenario is suitable for more advance courses or special topics in SCM.

However, there are several challenges to incorporate ThinkLog in courses, especially for classes with a large number of students. Firstly, board game is usually played in small groups to encourage interaction within the group itself [66]. With limited number of game resources (i.e. boards and game masters), it may be impossible to divide large number of students into smaller groups. Secondly, it would be difficult to maintain the level of experience from all the students because the lecturer may not be able to engage with all of the students. Hence, it would be difficult for the students to relate their game experience with the course material.

To mitigate these challenges, we adjust the setup and components of ThinkLog as follows.

1. **Group formation**. The students are divided in two competing groups. Each group would have its own board. Within each group, students are equally divided to take a particular role (i.e. manufacturer, distributor, wholesaler, and retailer) in the game.
2. **Main board.** Instead of using real board game, a digital board, projected on the big screen is used to improve visibility for all the students.
3. **Demand card.** Demand card will be randomly generated using the companion app and shown on the big screen.
4. **Game Master**. The course lecturer would replace the role of the game master.
5. **Companion app**. The app would help to keep track of the goods' movement and show it on the digital screen. Virtual money is also used to replace the "game" money.

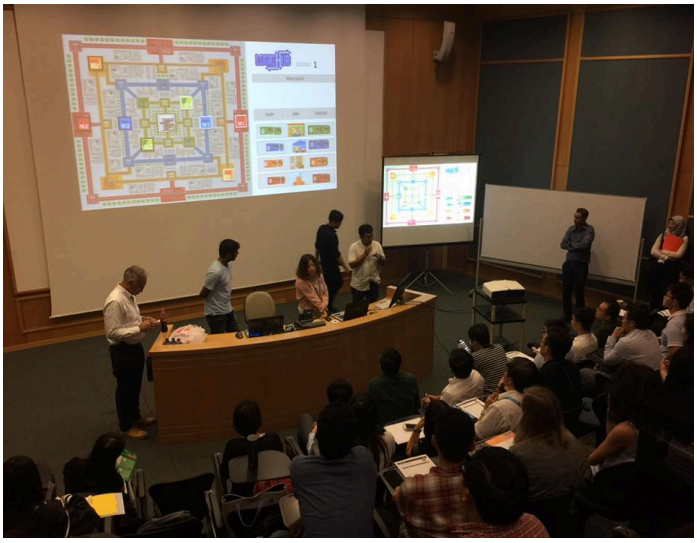

Figure 10. ThinkLog session in a supply chain course in National University of Singapore

We applied these adjustments (with the exception of the Companion app) and tested it on one supply chain course for master students in the National University of Singapore. The class was conducted on August 2017 and attended by 90 students from various backgrounds. Most of the students had background knowledge about SCM. During the game session, we observed that the students were able to discuss within their group and able to raise questions to the lecturer. An example of that interaction is shown in Figure 10.

Based on our observation and discussion with some of the students after the game session, we conclude that the students enjoy the game and highly accept it as part of their course. It's also apparent that the game helps them to understand about the course content better by applying it in the simulated environment within the game.

6. Summary and Future Work

In this paper, we focus our study on developing and evaluating an expandable board game, named ThinkLog, as an interactive tool to facilitate learning in Supply Chain Management (SCM). There are four main components in ThinkLog, namely: main board, demand card, gameplay and game master. One unique feature in ThinkLog is that this game can be extended to generate different scenarios for various concepts in SCM without changing the basic game structure. The gameplay can be adjusted to include various scenarios for different learning objectives. To date, we have extended the ThinkLog basic scenario to include two other SCM concepts, namely: humanitarian and urban logistics.

Four interactive sessions as part of three-day SCM workshops were conducted to evaluate ThinkLog. We use different scenarios for each session. Based on our observation, survey and sentiment analysis of the interactive sessions, we learnt that ThinkLog is highly accepted by the players to deepen their understanding of SCM concepts. The result of the learning objective evaluation in sessions 2, 3 and 4 also confirms that the players were able to absorb the learning objectives of the game regardless of the scenario played in the sessions. We also tested our proposed game in a big class environment as part of a supply chain course at the National University of Singapore. The acceptance and learning objective evaluation of the players resonates throughout the game session.

Nonetheless, we see four possible extensions that we would like to study in the near future. First, we would like to test our game in wider audiences and incorporate the game in different supply chain management courses. Further adjustment to the game setup may be needed to cater for different class environment. Second, we would like to embed more scenarios into the game such as healthcare logistics. We may also want to introduce supply chain credibility concept where each role or player would have its own rating or random rating to describe actual distribution processes. It would enrich the game as a platform for learning SCM concepts. Third, we would like to develop a more comprehensive evaluation method to measure the learning outcome of the game. It may include having a third party team to objectively evaluate the players' learning points and compare it with the intended learning objectives of the game. Last but not least, we would like to conduct comprehensive data analysis for each game session to further understand the players' behavior and their actions. For example, the data captured from companion app would help to indicate whether the time allocated for the game session is sufficient or if there is a correlation between the players' background knowledge and the decisions made.

Conflict of Interest

The authors declare no conflict of interest related to this paper.

Acknowledgment

The work is part of solutions/case studies developed as part of "Temasek Foundation International – National University of Singapore Urban Transportation Management Programme in Indonesia" programme. It is supported by Temasek Foundation International and Coordinating Ministry for Economic Affairs of Indonesia.

References

[1] Lindawati, E. Nugroho, R. Fredericco, Z. Abdul Rahim and R. de Souza, "ThinkLog: Interactive Learning for Supply Chain Management," in *IEEE 6th International Conference on Teaching, Assessment, and Learning for Engineering (TALE)*, Hong Kong, 2017.

[2] S. Tobias, J. Fletcher and A. Wind, "Game-based learning," in *Handbook of research on educational communications and technology*, New York, Springer, 2014, pp. 485-503.

[3] M. Ma, A. Oikonomou and L. Jain, "Innovations in Serious Games for Future Learning," in *Serious Games and Edutainment Applications*, London, Springer, 2011, pp. 3-7.

[4] T. Susi, M. Johannesson and P. Backlund, "Serious games: An overview," Technical Report, School of Humanities and Informatics, University of Skövde, Skövde, Sweden, 2007.

[5] S. de Freitas and F. Liarokapis, "Serious Games: A New Paradigm for Education?," in *Serious Games and Edutainment Applications*, London, Springer, 2011, pp. 9-21.

[6] J. Riedel and J. Hauge, "State of the art of serious games for business and industry," in *Concurrent Enterprising (ICE), 2011 17th International Conference* , 2011.

[7] J. Breuer and G. Bente, "Why so serious? On the Relation of Serious Games and Learning," *Journal for Computer Game Culture,* vol. 4, no. 1, pp. 7-24, 2010.

[8] M. Garcia-Ruiz, J. Tashiro, B. Kapralos and M. Martin, "Crouching Tangents, Hidden Danger: Assessing Development of Dangerous Misconceptions within Serious Games for Healthcare Education," in *Gaming and Simulations: Concepts, Methodologies, Tools and Applications*, Hershey, PA, Information Resources Management Association, 2011, pp. 1712-1749.

[9] S. de Freitas and S. Jarvis, "Towards a development approach for serious games," in *Games-based learning advancements for multi-sensory human-computer interfaces: Techniques and effective practices*, T. Connolly, M. Stansfield and E. Boyle, Eds., Hershey, PA, IGI Global, 2008, pp. 215-231.

[10] M. Graafland, J. Schraagen and M. Schijven, "Systematic review of serious games for medical education and surgical skills training," *British Journal of Surgery,* vol. 99, no. 10, pp. 1322-1330, 2012.

[11] C. Lim and H. Jung, "A study on the military Serious Game," *Advanced Science and Technology Letters,* vol. 39, pp. 73-77, 2013.

[12] A. Gómez-Rodríguez, J. González-Moreno, D. Ramos-Valcárcel and L. Vázquez-López, "Modeling serious games using AOSE methodologies," in *11th International Conference on Intelligent Systems Design and Applications (ISDA), IEEE*, 53-58, 2011.

[13] J. Sterman, "Modeling Managerial Behaviour: Misperceptions of Feedback in a Dynamic Decesion Making Experiment," *Management Science,* vol. 35, no. 3, pp. 321-339, 1989.

[14] F. a. S. R. Chen, "The stationary beer game," *Production and Operations Management,* vol. 9, no. 1, pp. 19-30, 2000.

[15] E. Anderson and D. Morrice, "A Simulation Game for Teaching Service-Oriented Supply Chain Management: Does Information Sharing Help Managers with Service Capacity Decision?," *Production and Operations Management,* vol. 9, no. 1, pp. 40-55, 2000.

[16] S. van Houten, A. Verbraeck, S. Boyson and T. Corsi, "Training for today's supply chains: an introduction to the distributor game," in *The 37th Winter Simulation Conference*, 2005.

[17] T. Corsi, S. Boyson, A. Verbraeck, S. Van Houten, C. Han and J. Macdonald, "The real-time global supply chain game: New educational tool for developing supply chain management professionals," *Transportation Journal,* vol. 45, no. 3, pp. 61-73, 2006.

[18] L. Rieber, "Seriously considering play: Designing interactive learning environments based on the blending of microworlds, simulations, and games," *Educational Technology Research and Development,* vol. 44, no. 2, pp. 43-58, 1996.

[19] J. Knight, S. Carly, B. Tregunna, S. Jarvis, R. Smithies, S. de Freitas, K. Mackway-Jones and I. Dunwell, "Serious gaming technology in major incident triage training: A pragmatic controlled trial," *Resuscitation Journal,* vol. 81, no. 9, pp. 1174-1179, 2010.

[20] H. Hou, "Integrating cluster and sequential analysis to explore learners' flow and behavioral patterns in a simulation game with situated-learning context for science courses: A video-based process exploration," *Computers in human behavior,* vol. 48, pp. 424-435, 2015.

[21] J. Hamari, D. Shernoff, E. Rowe, B. Coller, J. Asbell-Clarke and T. Edwards, "Challenging games help students learn: An empirical study on engagement, flow and immersion in game-based learning," *Computers in Human Behavior,* vol. 54, pp. 170-179, 2016.

[22] L. Zhou, Y. Xie, N. Wild and C. Hunt, "Learning and practising supply chain management strategies from a business simulation game: a comprehensive supply chain simulation," in *Simulation Conference, 2008*, 2008.

[23] K. Katsaliaki, N. Mustafee and S. Kumar, "A game-based approach towards facilitating decision making for perishable products: An example of blood supply chain," *Expert Systems with Applications,* vol. 41, no. 9, pp. 4043-4059, 2014.

[24] T. Nilsen, S. Linton and J. Looser, "Motivations for augmented reality gaming," in *Game Developers Conference, FUSE 4*, New Zealand, 2004.

[25] S. Gobel, "Serious Game Application Examples," in *Serious Game: Foundations, Concepts, and Practice*, R. Dörner, S. Göbel, W. Effelsberg and J. Wiemeyer, Eds., Darmstadt, Wiesbaden, Springer, 2016, pp. 319-405.

[26] R. Dörner, S. Göbel, W. Effelsberg and J. Wiemeyer, Serious games: foundations, concepts and practice, Darmstadt, Wiesbaden: Springer, 2016.

[27] E. Nugroho and A. Hariyadi, "Creative Learning and Research Through Modern Board Game," in *Triple Helix 10 th International Conference*, Bandung, 2012.

[28] B. Lamey and C. Bristow, "The Game as a Talking Tool: Using a Board Game for Creative Consultation, Engagement and Inclusion," in *Creative Education, Teaching and Learning: Creativity, Engagement and the Student Experience*, G. Brewer and R. Hogarth, Eds., London, UK, Palgrave Macmillan, 2015, pp. 243-.

[29] J. Zagal, J. Rick and I. Hsi, "Collaborative games: Lessons learned from board games," *Simulation & Gaming,* vol. 37, no. 1, pp. 24-40, 2006.

[30] A. d'Astous and K. Gagnon, "An inquiry into the factors that impact on consumer appreciation of a board game.," *Journal of Consumer Marketing,* vol. 24, no. 2, pp. 80-89, 2007.

[31] M. Grechus and J. Brown, "Comparison of individualized computer game reinforcement versus peer-interactive board game reinforcement on retention of nutrition label knowledge.," *Journal of Health Education,* vol. 31, no. 3, pp. 138-142, 2000.

[32] J. Lennon and D. Coombs, "The utility of a board game for dengue haemorrhagic fever health education," *Health Education,* vol. 107, no. 3, pp. 290-306, 2007.

[33] S. Amaro, A. Viggiano, A. Di Costanzo, I. Madeo, A. Viggiano, M. Baccari, E. Marchitelli, M. Raia, E. Viggiano, S. Deepak and M. Monda, "Kaledo, a new educational board-game, gives nutritional rudiments and encourages healthy eating in children: a pilot cluster randomized trial," *European journal of pediatrics,* vol. 165, no. 9, pp. 630-635, 2006.

[34] W. Bartfay and E. Bartfay, "Promoting health in schools through a board game," *Western Journal of Nursing Research,* vol. 16, no. 4, pp. 438-446, 1994.

[35] A. Vahed, "The tooth morphology board game: an innovative strategy in tutoring dental technology learners in combating rote learning," in *2nd European Conference on Games Based Learning*, 2008.

[36] P. Ogershok and S. Cottrell, "The pediatric board game," *Medical Teacher,* vol. 26, no. 6, pp. 514-517, 2004.

[37] S. Fukuchi, L. Offutt, J. Sacks and B. Mann, "Teaching a multidisciplinary approach to cancer treatment during surgical clerkship via an interactive board game," *The American journal of surgery,* vol. 179, no. 4, pp. 337-340, 2000.

[38] I. Mayer, L. Carton, M. de Jong, M. Leijten and E. Dammers, "Gaming the future of an urban network," *Futures,* vol. 36, no. 3, pp. 311-333, 2004.

[39] E. Speelman, L. García-Barrios, J. Groot and P. Tittonell, "Gaming for smallholder participation in the design of more sustainable agricultural landscapes," *Agricultural Systems,* vol. 126, pp. 62-75, 2014.

[40] K. Slegers, S. Ruelens, J. Vissers and P. Duysburgh, "Using game principles in ux research: A board game for eliciting future user needs," in *33rd Annual ACM Conference on Human Factors in Computing Systems*, 2015.

[41] A. Van Ackere, E. Larsen and J. Morecroft, "Systems thinking and business process redesign: an application to the beer game," *European Management Journal,* vol. 11, no. 4, pp. 412-423, 1993.

[42] F. Jacobs, "Playing the beer distribution game over the internet," *Production and Operations Management,* vol. 9, no. 1, pp. 31-39, 2000.

[43] J. Wisner, K. Tan and G. Leong, Principles of supply chain management: A balanced approach, Cengage Learning, 2014.

[44] N. Mustafee and K. Katsaliaki, "The blood supply game," in *Winter Simulation Conference 2010*, 2010.

[45] D. Simchi-Levi, E. Simchi-Levi and P. Kaminsky, Designing and managing the supply chain: Concepts, strategies, and cases, New York: McGraw-Hill, 1999.

[46] P. Kaminsky and D. Simchi-Levi, "A new computerized beer game: A tool for teaching the value of integrated supply chain management," *Global supply chain and technology management,* vol. 1, no. 1, pp. 216-225, 1998.

[47] A. Abdul Jabbar and P. Felicia, "Gameplay engagement and learning in game-based learning: A systematic review," *Review of Educational Research,* vol. 85, no. 4, pp. 740-779, 2015.

[48] M. Holweg and J. Bicheno, "Supply chain simulation - a tool for education, enhancement and endeavour," *International Journal of Production Economics,* vol. 78, no. 2, pp. 163-175, 2002.

[49] T. Muller, R. Müller, K. Zedel, G. Zomer and M. Engler, "Enhancing awareness on the benefits of supply chain visibility through serious gaming," in *Conference on e-Business, e-Services and e-Society*, 2015.

[50] D. R. Cruickshank and R. Telfer, "Classroom games and simulations," *Theory Into Practice,* vol. 19, pp. 75-80, 1980.

[51] M. R. Lepper and D. L. Cordova, "A desire to be taught: Instructional consequences of intrinsic motivation," *Motivation and Emotion,* vol. 16, pp. 187-208 , 1992.

[52] T. W. Malone and M. R. Lepper, "Making learning fun: A taxonomy of intrinsic motivations for learning," in *Aptitude, learning and instruction*, vol. 3, R. Snow and M. Farr, Eds., Hillsdale, NJ, Erlbaum, 1987, pp. 223-253.

[53] R. Rouse, Game design: theory & practice, Plano, TX: Wordware Publishing, Inc , 2005.

[54] M. J. Hannafin and K. Peck, The design, development and evaluation of instructional software, New York: MacMillan Publishing Company, 1988.

[55] A. Wilson, C. Broadbent, B. McGrath and J. Prescott, "Factors Associated with Player Satisfaction and Educational Value of Serious Games," in *Serious Games and Edutainment Applications*, Springer, 2017, pp. 513-535.

[56] J. Van Staalduinen and S. de Freitas, "A game-based learning framework: Linking game design and learning," in *Learning to play: exploring the future of education with video games*, M. Khine, Ed., New York, Peter Lang, 2011, pp. 29-54.

[57] S. M. Alessi and S. R. Trollip, Multimedia for learning: Methods and development, Boston: Allyn and Bacon, 2001.

[58] P. Vincke, "MCDM: Past decade and future trends—A source book of multiple criteria decision making," *European Journal of Operational Research,* vol. 26, no. 1, pp. 179-780, 1986.

[59] M. Köksalan, J. Wallenius and S. Zionts, "An Early History of Multiple Criteria Decision Making," *Journal of Multi-Criteria Decision Analysis,* vol. 20, no. 1-2, pp. 87-94, 2013.

[60] G. Timperio, G. Panchal, R. De Souza, M. Goh and A. Samvedi, "Decision making framework for emergency response preparedness: A supply chain resilience approach," in *IEEE International Conference on Management of Innovation and Technology (ICMIT)*, 2016.

[61] G. Miner, J. Elder IV and T. Hill, Practical text mining and statistical analysis for non-structured text data applications, Academic Press, 2012.

[62] M. Hu and B. Liu, "Mining and Summarizing Customer Reviews,," in *ACM SIGKDD International Conference on Knowledge Discovery and Data Mining (KDD-2004)*, Seattle, Washington, USA, 2004.

[63] B. Liu, M. Hu and J. Cheng, "Opinion Observer: Analyzing and Comparing Opinions on the Web," in *the 14th International World Wide Web conference (WWW-2005)*, Chiba, Japan, 2005.

[64] K. Kiili, "Evaluations of an Experiential Gaming Model," *An Interdisciplinary Journal on Humans in ICT Enviroments,* vol. 2, no. 2, pp. 187-201, 2006.

[65] H. Kelly, "How Games and Simulations Can Help Meet America's Challenges in Science Mathematics and Technology Education," in *Serious Game Design and Development: Technologies for Training and Learning*, IGI Global, 2010, pp. 117-133.

[66] S. Fukuchi, L. Offutt, J. Sacks and B. Mann, "Teaching a multidisciplinary approach to cancer treatment during surgical clerkship via an interactive board game," *The American journal of surgery,* vol. 179, no. 4, pp. 337-340, 2000.

ASTES

Advances in Science, Technology and Engineering Systems Journal Vol. 3, No. 4, 112-121 (2018)

www.astesj.com

ASTESJ

ISSN: 2415-6698

Effectiveness of Routing Protocols for Different Networking Scenarios

Akbor Aziz Susom*

Institute of Information and Communication Technology, Bangladesh University of Engineering and Technology,1205, Bangladesh.

ARTICLE INFO

Article history:
Received: 01 June, 2018
Accepted: 26 June, 2018
Online: 23 July, 2018

Keywords:
Routing Protocols
Hybrid Networks
Throughput
Jitter
Packet Length
Packet Loss

ABSTRACT

Selection of a routing protocol is vital for modern arena of Internet communication as network traffic and network complexities are rapidly increasing. This paper evaluates the effectiveness of three routing protocols namely routing information protocol version 2 (RIPv2), open shortest path first (OSPF), enhanced interior gateway routing protocol (EIGRP), and hybrid protocols based on these three. These stand-alone and hybrid protocols are compared in terms of four metrics: throughput, jitter, packet length and packet loss. Different kinds of networks are developed using Graphical Network Simulator-3 (GNS3) network software emulator. The network performance measurement of those four metrics is done with the help of Wireshark and Iperf tools. Besides, three network topologies termed as 'experimented', 'retracted' and 'extended' networks are created using 7, 3, and 9 routers. Simulation results indicate that EIGRP protocol performs the best showing the highest average throughput (28 packet/sec), while RIP-OSPF hybrid protocol has the lowest average throughput (16 packet/sec). Moreover, EIGRP has the lowest value of packet loss of 2.66. The lowest jitter value is obtained for hybrid RIP-OSPF-EIGRP protocols. However, EIGRP has a moderately high jitter value. Furthermore, EIGRP has standard size of packet length. Hence, EIGRP can be a good selection as a routing protocol for different sized networks.

1. Introduction

Connection of group of routers that are used to build different networking systems based on the requirements and affordability mainly follow two functions – select a path through networks and then transmit information packet across that fixed path to reach the determined destination. In doing so, [1] routing protocols and algorithms play most significant role to plot the routes through networks so that packet can transmit to the most efficient possible paths. First routing protocol shares information among immediate neighbors, and then throughout the network [2]. This way, routers gain information of the topology of the network. Throughout this process, routing protocols follow some criteria based on throughput, delay, efficiency, simplicity, low overhead, reliability/stability, and flexibility [3]. Therefore, performance and efficiency of a networking system is dependent on the routing protocols. As it varies protocol to protocol as well as performance changes in different networking systems. In this experiment, the purpose is to find throughput, jitter, Packet length and packet loss in three different networks with seven different combinations of protocols. Then to compare those results with each other from protocols to protocols, and system to system.

As with most complex technologies and requirements for diversity, there's no one-size-fits-all solution when it comes to develop networking systems [5]. The necessity and resources of each unique sector will correlate to a different set of networking systems and solutions. [6] Therefore, development and changes in the development of the networking systems has been a vital need for fulfilling different demands and requirements. It is needed to carefully consider the situation and determine to change the network design for their situation to create an optimized networking solution for that situation [7]. For that reason, in this research paper we have analyzed with three different networks on the basis of experimented networks that uses 7 routers then we extended and retracted the system by corresponding 9 and 3 routers respectively to diversify the networking systems.

A network that has been well designed is characterized by consistency and performance of some parameters and protocols used in the networks. A consistently high level of performance is

*Akbor Aziz Susom, Bangladesh University of Engineering and Technology
Email: akb.susom@gmail.com

observed with the good combination of different networking protocols [8]. As Routing protocols has significant influence on networking system also each routing protocols have both positive sides and negatives sides on different networking systems.

So, we have selected three routing protocols-RIP, OSPF, EIGRP and the hybrid protocols consisting of these three individual ones. [9] An important point to note that all through this study, RIPv2 is considered as RIP. The hybrid protocols considered are RIP-OSPF, RIP-EIGRP, OSPF-EIGRP and RIP-OSPF-EIGRP. It can be noted that the three individual protocols: RIP (version 2), OSPF and EIGRP are supported by VLSM, and these have built in algorithms of Bellman-Ford, Dijkstra and Dual, respectively [10].

These protocols are used for evaluating not any single networking system rather focusing on different networking systems to find the effective and efficient match of routing protocols and algorithms for that specific system [11] and also to suggest whether it satisfies the need of design or redesign of different networking infrastructure based on some parameters like throughput, Jitter, Packet Length and Packet Loss.

This research is determined to do a comparative analysis of routing protocols alone and combined routing protocols performance in different networks [12]. Finally, to suggest the best combination of routing protocols that will meet the requirements of the networking system as well as to show the best performance for the particular computer networks.

The rest of the paper is organized as follows. Section 2 presents the methodology of the study, Section 3 describes the related work, and Section 4 presents the performance results obtained from computer simulations. Finally, Section 5 provides the concluding remarks and future research directions.

2. Methodology

2.1. Procedures

With seven combination of routing protocols in three different networks, first to establish twenty-one different networks with specific router configuration that are all configured with real time topology. This research then executed to create traffic with transmission of information packet over a fixed time period to observe the real time figure and values of different performance measuring parameters of the networks and analyzing the captured traffic based on these parameters. This paper first measured each protocols throughput and jitter value both in software and manually with raw data for every networks using the same resources and conditions. Showing each protocols graph for both throughput and jitter value is demonstrated in section 4 (simulation results portion of the paper). Similarly packet length value and packet loss percentage are measured with the same conditions of the networks. Finally, to demonstrate the comparison graph for each routing protocols in three different networks provide the significant ideas of the protocols performance and efficiency. Depending on the comparison graph, decision has been made in the conclusion section to determine the best combination of routing protocols that can be implemented in a particular networking system.

2.2. Software and Simulation Tools

The Network has been established in Graphical Network Simulator 3 (GNS3) version 2.1.5 using VirtualBox version 5.2.12 that runs on the Windows 10 operating system. The Router 3725 Series with Cisco IOS operating system enabled that runs in GNS3, and Windows 10 operating system is running in VirtualBox as a PC. For simulation purpose, Wireshark software version 2.5.1 is used and version 3.1.3 Iperf applications running on the PC.

2.3. Prototype Modeling

Simulation will be performed in three different networks named as Experimented, Extended and Retracted Networks with a combination of routing protocols in seven different scenarios following as RIP, OSPF, EIGRP, RIP-OSPF, RIP-EIGRP, OSPF-EIGRP, RIP-OSPF-EIGRP.

2.4. System Design

We consider three different networking models – retracted network, experimented network and extended network, for this experiment. The models have been developed on the basis of real time topology with combination of 3, 7 and 9 routers respectively. Two computers are also connected with the networks for the transmission of the packet to create traffic that is used for simulation purpose of the network [13]. GNS3 software has been used to design the network that is as followed:

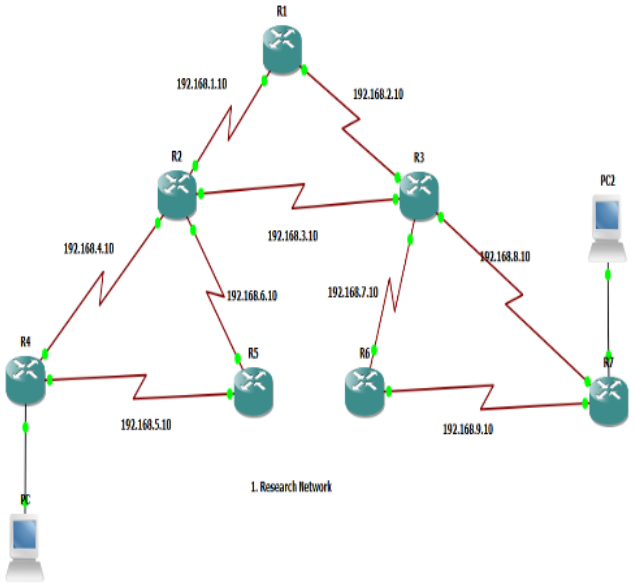

Figure 1: Experimented Network

2.5. Parameters to evaluate the protocols

A. Throughput:

Network throughput refers to the average data rate of successful communication of a network or message delivery over a specific networking link**. [**11**]** It measures a comparable effectiveness and efficiency of an operation or a system. It defines how strong and consistent the connection is maintained during the session. It is calculated by a theory as:

Throughput for each connection(i)

$$= \sum \frac{(\text{Throughput (i)})}{\sum_{J-1}^{N} \text{Throughput (j)}}$$

In our experiment, we have measured throughput value for each system to find the throughput for that specific protocol or combined protocols to see the transmission of packet over that fixed period in a network.

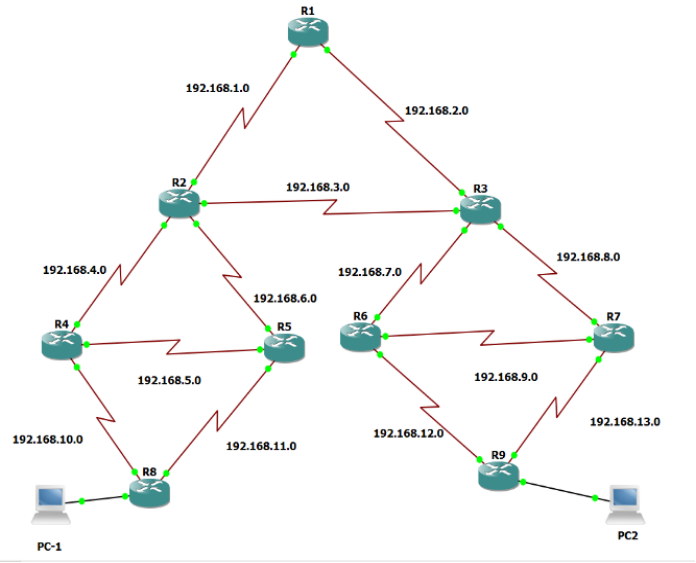

Figure 2: Extended Network

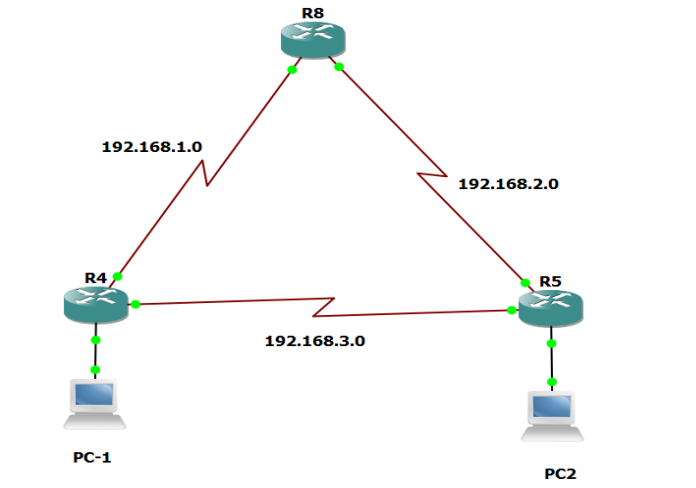

Figure 3: Retracted Network

B. Jitter

Jitter refers to statistical variation of Packet Delay and it is cited in IETF RFC 3393 and 5481.It is calculated to find the delay for all the packets from a source to a destination. Here, we have both calculated the jitter value in iperf software and taking the raw data from Wireshark that is calculated as follows:

Jitter rate $= \text{Total Variant Delay} / \text{No. of packet sent} - 1$

Measuring the total delay,

Total Variant Delay = (Ri -Si) (R i+1 -Sj+1)

Here, Ri = Received Time
Si = Sent Start time

C. Packet Length

Packet size is a considerable issue for energy constrained and performance evaluation of a network. Because of larger size of packets, data bit corruption creating higher frequency of re-transmission may be caused. And bigger packet might have problem if it is above the size of MTU (Maximum Transmission Unit). Moreover, NIC (Network Interface Controller) and OS has memory size restriction [14]. On the other hand, small size packets are more efficient but creating too short packet size might cause faults, like higher overhead and startup energy consumption for each packet can degrade the network performance. Besides, small size packets have issues with fragmentation and security problem. For this reason, Packet length for protocols and combination of the protocols in three different networks is measured to evaluate the particular networking system.

D. Packet Loss

Packet loss refers to small bits of lost data over a transmission period to or from one networking equipment to another equipment. Some amount of packet loss, generally just a small percentage can be available in a connection of a network. However, Packet loss is closely associated with quality of service considerations as network performance is impacted by packet loss and retransmission. Because of saturation, bandwidth outage, misconfiguration, network may be defected to lose acknowledge when retransmission is needed although the packet was transmitted. Moreover, TCP congestion window size is affected for packet loss when it will not accept optimal throughput value for the network.

3. Related works

There are several papers related to evaluation of networking protocols performance like dynamic routing protocols- RIP, OSPF and EIGRP and using these protocols to conduct the other scientific research. In paper [2] author describes the routing protocols using same Opnet software while they considered point to point throughput, querying delay and convergence time to compare the protocols. They both suggested EIGRP protocols for best choice In paper [4] they analysis performance of Virtual private Lan service network using Kerberos-enabled protocols (alternative authentication protocols) to measure the throughput value with respect to Normal VPLS network using Wireshark software IO graph. However, some other parameters like Delay, time factor, transmission efficiency is also important to precisely measure the performance of an authentication protocols in VPLS network. Paper [5] evaluated the routing protocols while they also considered combined routing protocols performance in Ipv6 network using iperf software which measured the throughput, jitter and packet loss value in a same networks platform. After all this result may change with the demand or design of different other computer networks. In the paper [6], author examined the performance of Ipv4 and Ipv6 when routing protocols have been utilized in both Ipv4 and Ipv6 virtual networks using GNS3

simulator software. They compared end to end delay and latency result for Ipv4 and Ipv6 and commented Ipv6 is the better choice for these two parameters. In paper [10] author analysis of RIP, OSPF and EIGRP protocols performance using Opnet software where they considered network convergence, Average Delay, Average email uploads response time, protocols traffic etc. to compare the performance.

But they have performed all these simulation experiment in fixed network structure that results from each simulation might not be the same when network design changes. Besides, Paper [11] compared the routing protocols performance in Big data application using Riverbed Modeller Simulator while they made comparison based on convergence duration, video conferencing packet end-to-end delay, jitter of voice and voice packet end-to-end delay.

4. Simulation Results:

4.1. Throughput

This experiment has been done to measure the throughput value in terms of different protocols and hybrid protocols for three types of networks. Here, x and y axis are considered as time and average packet sent over that time period. The average throughput value is calculated as packet per second. For the simulation purpose, SMA period is set as 10 interval SMA and corresponding value for y axis is considered as 1000 interval SMA. Specific protocol is selected every time to find the throughput value for the graph.

For Experimented Network:

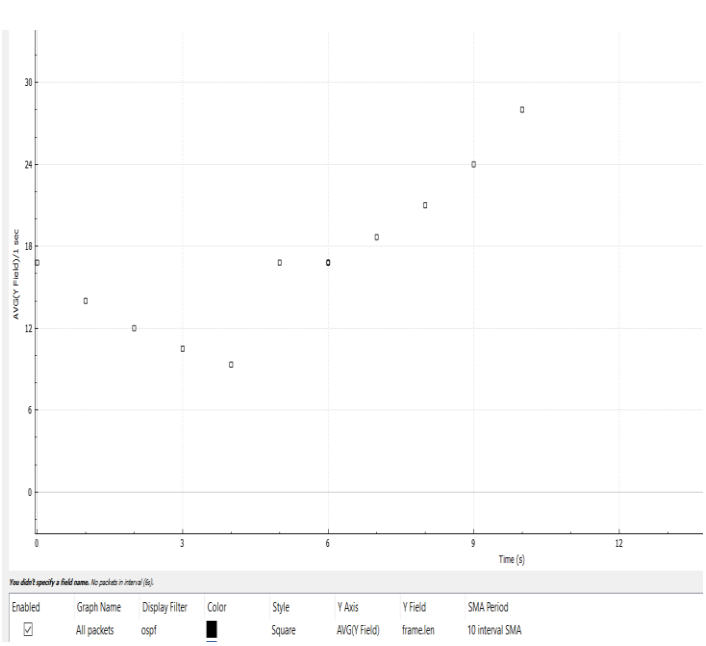

Figure 4: Average Packet / sec as throughput vs time for OSPF

In this figure, we have found that the average throughput value for this network using ospf protocol is 18 packet / sec which show maximum throughput is 28. The value of throughput initially got down up to 5 secs then went upward.

For extended Network:

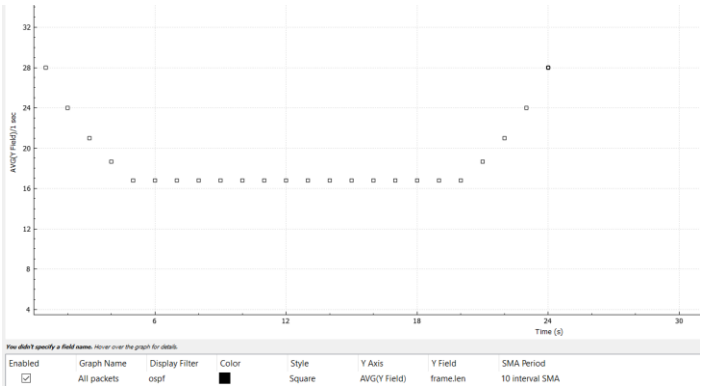

Figure 5: Average Packet / sec as throughput vs time for OSPF

In this figure, the average throughput value for this network using ospf protocol is 17 packet / sec which show maximum throughput is 26.

For Retracted Network:

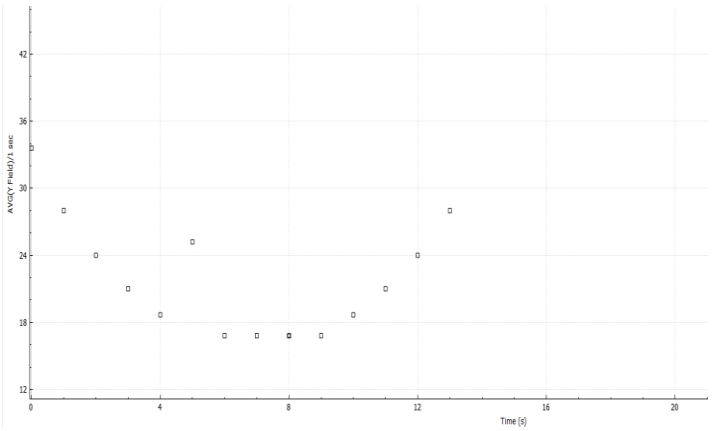

Figure 6: Average Packet / sec as throughput vs time for OSPF

In this figure, the average throughput value for this network using ospf protocol is 20 packet / sec which show maximum throughput is 34. Above the simulation figure has been shown for OSPF protocols in three different networks. The similar way is followed for valuation of other protocols to finally demonstrate the comparison graph for standalone and hybrid protocols.

Valuation:

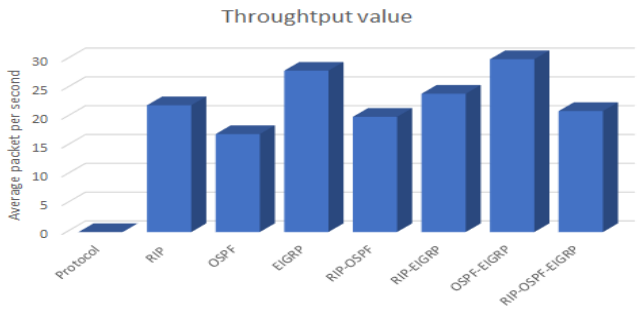

Figure 7: Comparison graph of Protocols vs average packet per second as Throughput for Extended Network.

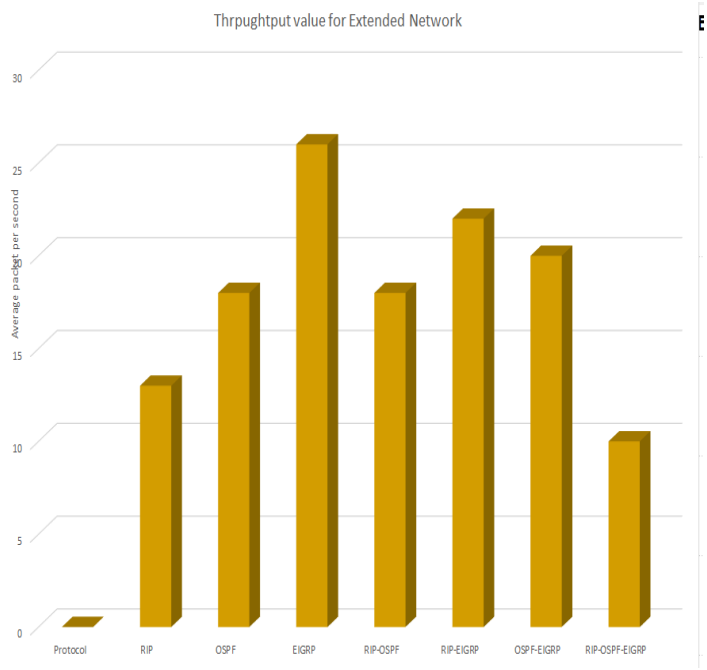

Figure 8 Comparison graph of Protocols vs average packet per second as Throughput for Extended Network.

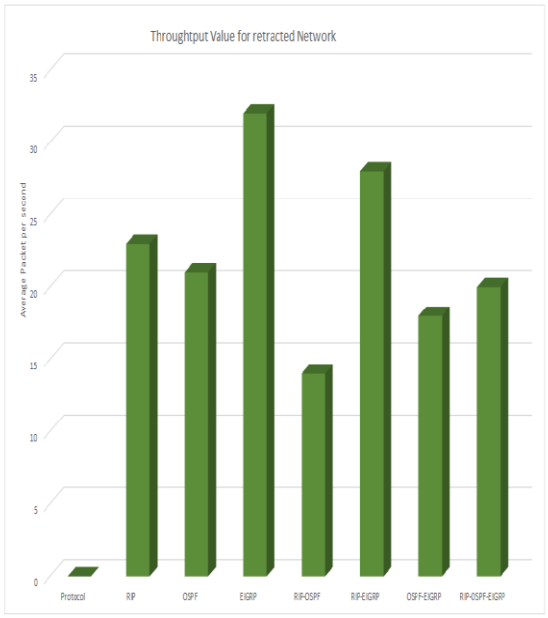

Figure 9: Comparison graph of Protocols vs average packet per second as Throughput for Retracted Network.

Results Analysis and decision:

Analyzing the above figures, combined OSPF-EIGRP protocol performs better for experimented network with maintaining average throughput almost 30 packets per sec. Here alone EIGRP and combined RIP-EIGRP maintains average throughput 28 and 23 respectively. Poor performance is observed for OSPF and RIP-OSPF protocols that are below throughput value of 20.

Extending the network, best performance is obtained for alone EIGRP (above 25 packets per second) which was actually proposed by researchers for big networking system. Lower performance is shown for combination of three protocols and RIP protocols that is below 13 packets per second. Similarly, EIGRP protocol achievement for retracted network is also the highest number of throughput value that is 32 packets per second while RIP-EIGRP and alone RIP protocols have shown considerable performance for this networking system. However, least throughput is attained for combined RIP-OSPF protocols.

Performance gain is obtained for RIP and EIGRP protocols for Retraced Network compared to Experimented network that are 9.52% and 23.07% while performance penalty is observed for combined RIP-OSPF protocols (46.15%).

Compared to extended network with experimented network, Performance penalty is obtained for combined OSPF -EIGRP (27.27%) which was the suggested for experimented network.

4.2. Jitter

In this simulation process, jitter value is calculated maintaining seven different scenarios in three different networks. It shows the deviation during the transmission of the packets as shown in x axis with respect to time in y axis for every particular networking system.

Jitter value is calculated in both ways by iperf application and manually to take the raw data from capture data in each networking module for specific protocols to find the actual figure and then to compare those to select the best one.

Below the simulation figure for jitter has been shown for OSPF protocols in three different networks. The similar way is followed for valuation of other protocols to finally demonstrate the comparison graph for standalone and hybrid protocols.

For Experimented Network:

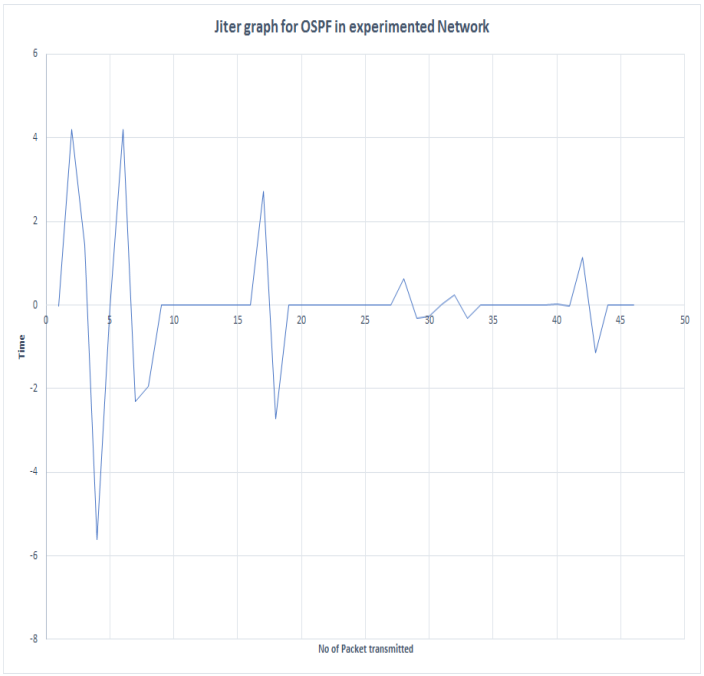

Figure 10: Variation of time as Jitter graph for OSPF

For Extended Network:

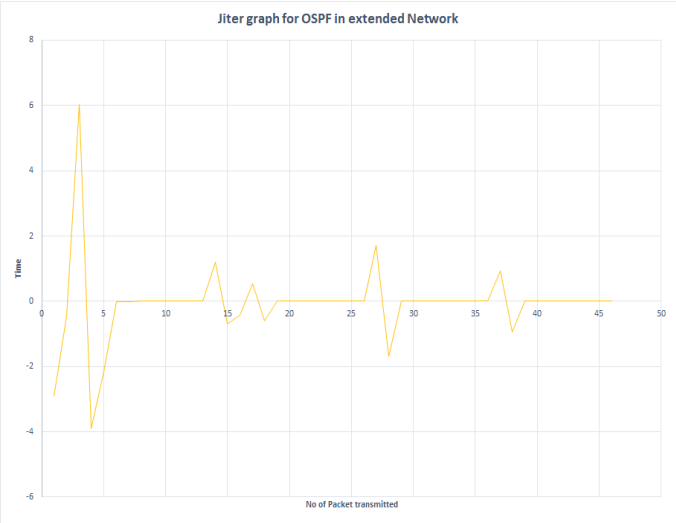

Figure 11: Variation of time as Jitter graph for OSPF

For Retracted Network:

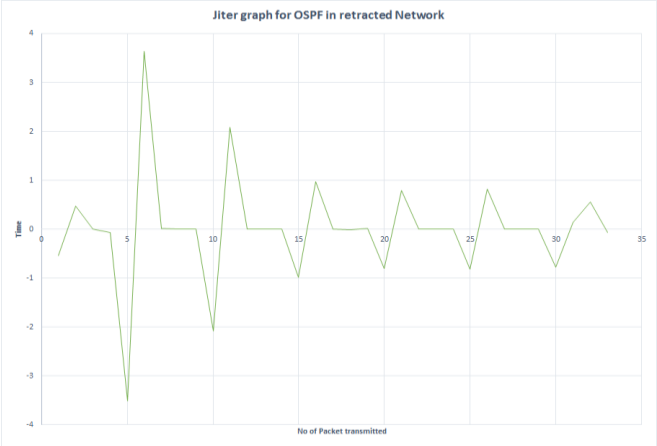

Figure 12: Variation of time as Jitter graph for OSPF

Valuation:

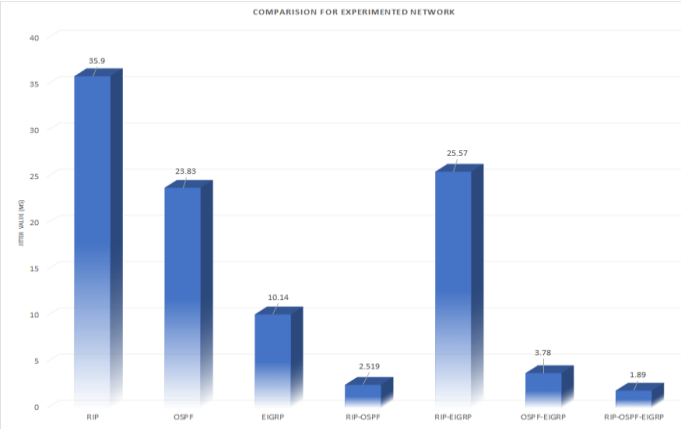

Figure 13: Comparison of Jitter Value in ms through y axis for Experimented Network

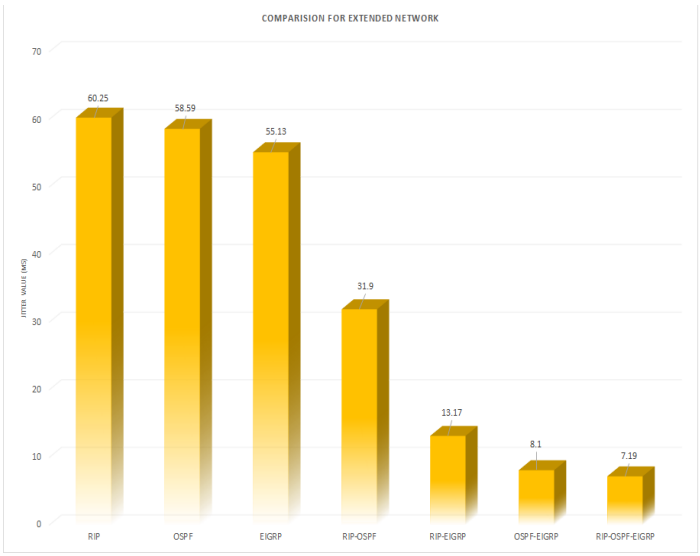

Figure 14: Comparison of Jitter Value in ms through y axis for Extended Network

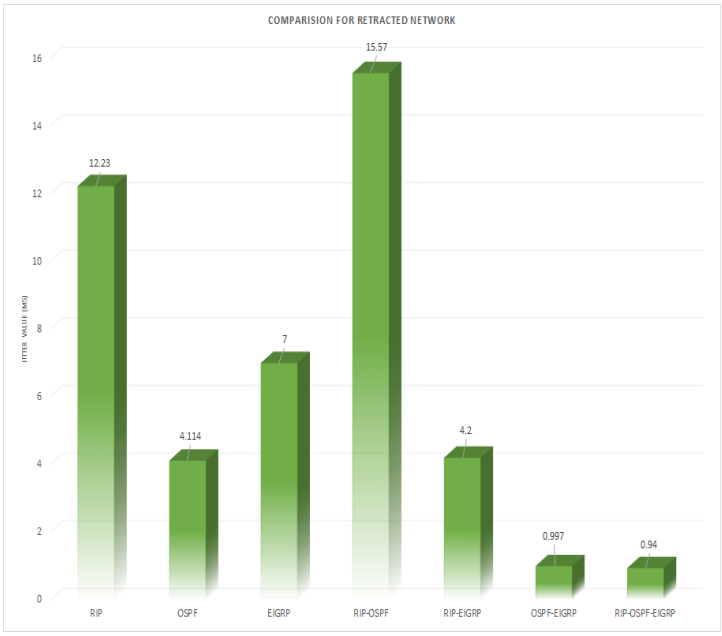

Figure 15: Comparison of Jitter Value in ms through y axis for Retracted Network

Result analysis and decision:

Minimum jitter value captured for the protocols is considered the best one for that particular networking system. Following the experimented network, the lowest jitter value is got for combination of three protocols in a network “RIP-OSPF-EIGRP” that is 1.89ms. RIP-OSPF and OSPF-EIGRP also show the good result for jitter are 2.5 and 3.78 respectively. The very poor result observed for the protocol of RIP (35.9ms). Similar result is also obtained for retracted and extended network considering the flow graph performance of the protocols that RIP-OSPF -EIGRP combined networking protocols show the best performance for every networking design. However, for retracted network, performance increased for every combination and alone protocols comparing the jitter value. Considerable performance shown for

RIP, OSPF, RIP-EIGRP that are gained by 65.93%, 81% and 83.57% respectively for retracted network. Only combine RIP-OSPF performance got down as jitter value increased from 2.51 to 15.57 in Retracted network.

4.3. Packet Length

Packet Length is measured considering ten different range of the size of the packet that is described through x axis and y – axis is cited as the number of packet in a particular range in percentage. The result is obtained first for each protocol and combined protocols then showing the comparison graph on the basis of the simulation results. Below the table for packet length has been shown for OSPF protocols for three different networks. The similar way is followed for valuation of other protocols to finally demonstrate the comparison graph for standalone and hybrid protocols.

Scenario 1.

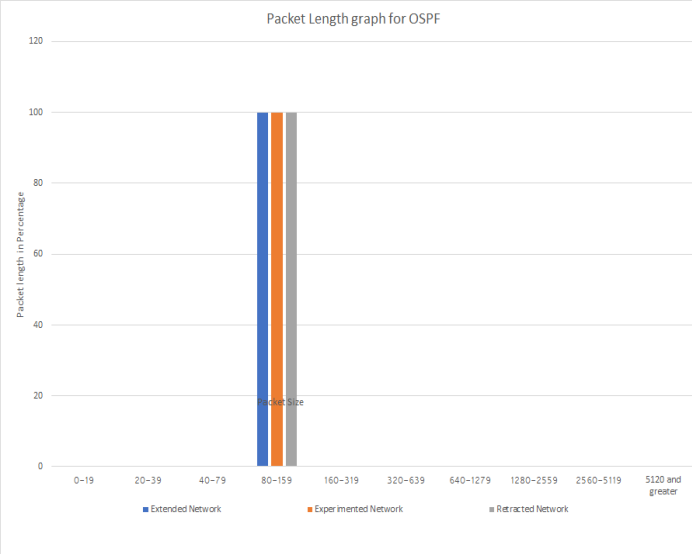

Figure 16: Packet Size for OSPF.

Valuation:

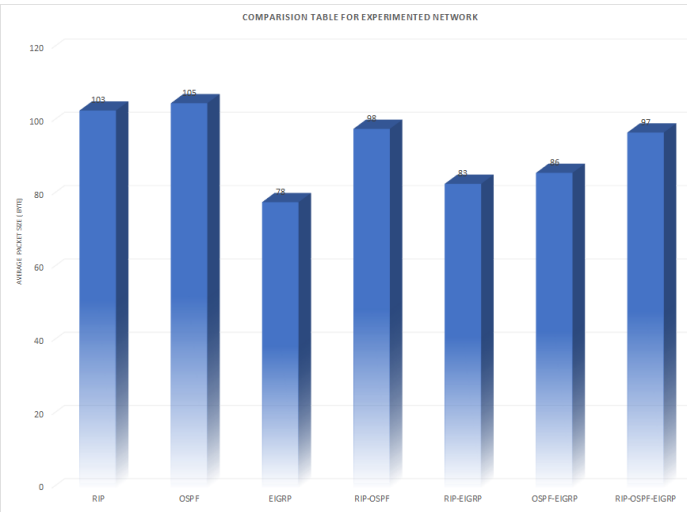

Figure 17: Comparison for protocols vs average packet size in byte for Experimented Network.

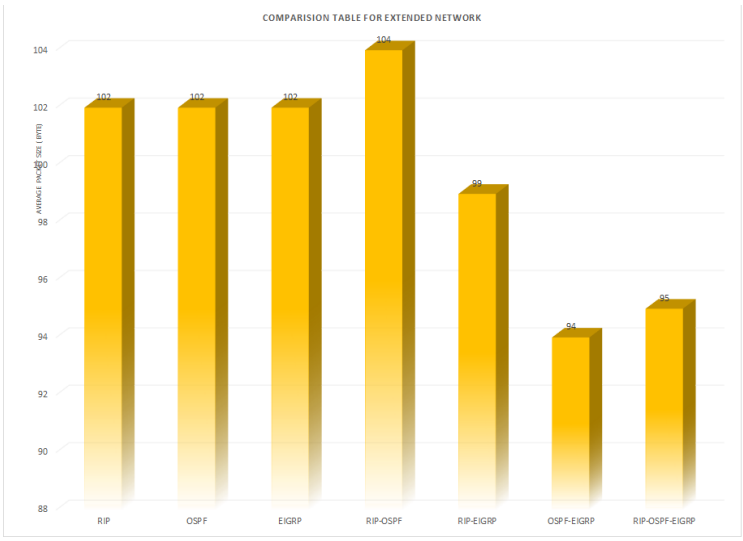

Figure 18: Comparison for protocols vs average packet size in byte for Extended Network.

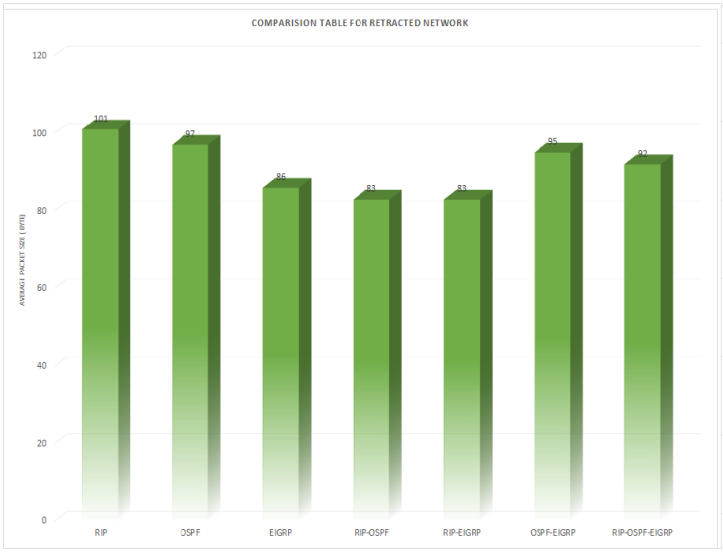

Figure 19: Comparison for protocols vs average packet size in byte for Retracted Network.

Result Analysis and Decision:

There is no big difference found in packet size during the transmission of the packet in all there networking system. For experimented network, packet size ranges from 78 to 106 for protocols while highest average packet size got for OSPF is 106 and lowest size for EIGRP is 78. In the case of extended network, it ranges from 94 to 104 while considerable expansion of average packet size captured for RIP-OSPF is 104 that was 83 for experimented network. No similar size packet is seen for extended network compared to retracted network.

On the contrary, average packet size for retracted network ranges from 83 to 101 which shows minor difference in packet length for all protocols. Here, same average packet size is obtained for RIP-OSPF and RIP-EIGRP, is 83. The maximum packet size is seen for RIP is 101 that is somewhat similar to all other networking systems. Overall, RIP and OSPF protocols show bit higher packet size for the network.

4.4. Packet Loss Comparison Graph

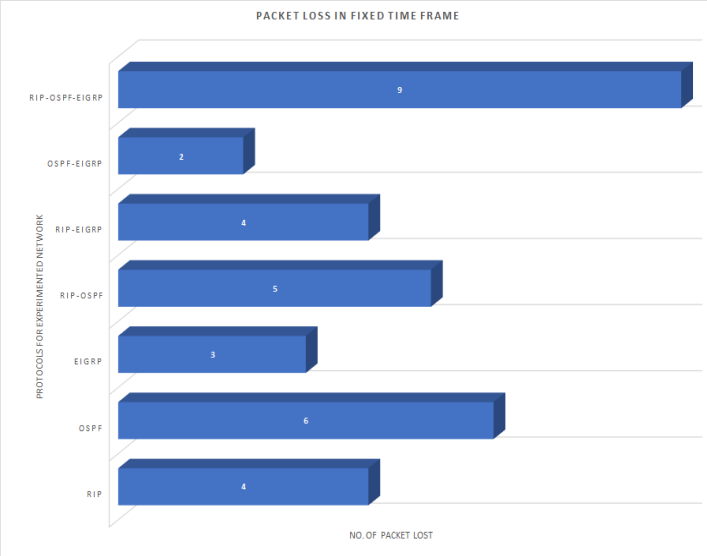

Figure 20: Protocols vs No of Packet loss in Experimented Network.

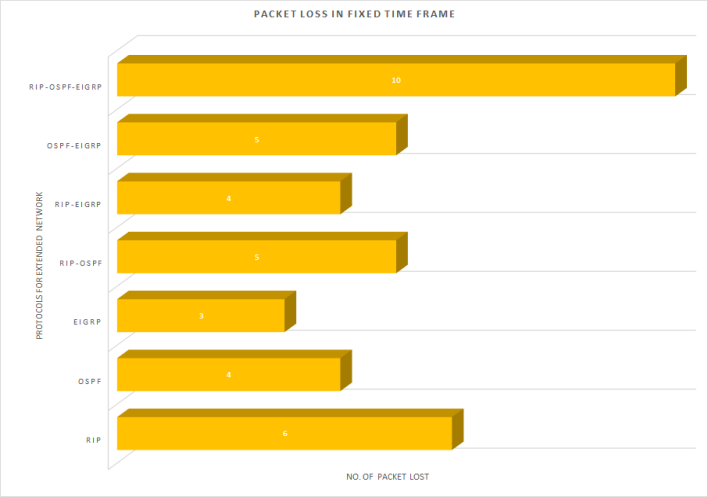

Figure 21 Protocols vs No of Packet loss in Extended Network.

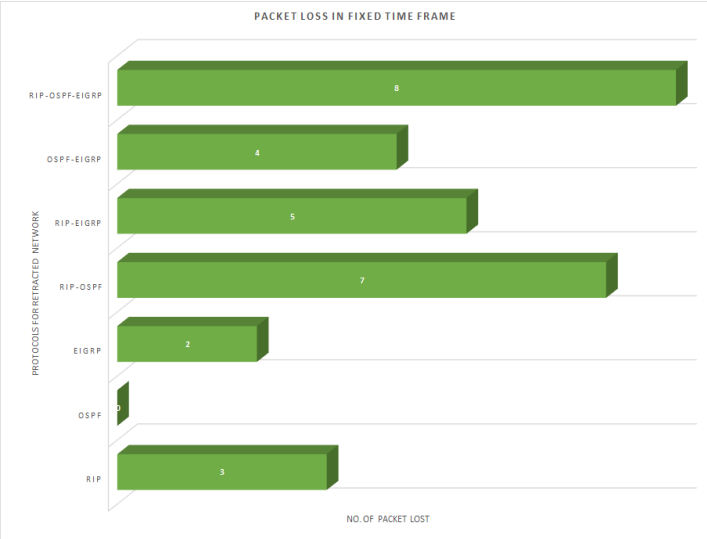

Figure 22: Protocols vs No of Packet loss in Retracted Network.

Result Analysis and Decision:

Comparison graph for experimented network indicated that the average percentage of the packet loss is lowest for OSPF-EIGRP as it shows packet loss value is 2 during the transmission steam of the packet. The second-best performance shown for this network is EIGRP having packet loss value 3. However, poor performance is shown for RIP-OSPF-EIGRP and OSPF for this network that shows 6 and 9 packet loss value during the transmission of the packet.

The performance is still satisfactory for EIGRP in extended network while OSPF and RIP-EIGRP show the same value of packet loss in this network. Combination of three protocols show the maximum packet loss value in extended network is 10 while it was 9 for experimented network. In the case of retracted network, excellent result shown by OSPF having zero packet loss while RIP-OSPF and RIP-OSPF-EIGRP depicts poor performance as usual in packet loss for all networking systems. Finding the reason for this result for these two protocols, raw data shows many number of retransmission request and drop packet that causes higher packet loss percentage for RIP-OSPF and RIP-OSPF-EIGRP.

5. Conclusion and Future works:

In this paper, we designed and evaluated Routing protocols namely RIP, OSPF, EIGRP along with its all possible combinations for three different networks and applied it to measure throughput, jitter, packet length and packet loss to demonstrate its performance and utility. We demonstrated how the results obtained in one network design can change for the configuration of the same protocol in response to dynamically changing conditions of another network. On comparing the results of the simulation of different protocols and combined protocols, the overall best performance is shown for throughput value by EIGRP protocols while only for experimented network, OSPF-EIGRP combined protocol is suggested to implement that give the highest throughput. In fact, RIP-EIGRP and OSPF-EIGRP can be chosen as the second-best selection for the networks. The average throughput considering all networks for EIGRP is 28.00 packet/sec while the lowest obtained by combined RIP-OSPF-EIGRP average 14.00 packet/sec respectively. After that, the suggestion goes to combined protocols of either RIP-OSPF-EIGRP or OSPF-EIGRP in term of jitter value, that shows minimum packet delay in all networks conditions. The average minimum jitter value for RIP-OSPF-EIGRP and OSPF-EIGRP are 3.34ms and 4.29ms respectively while the poor performance having maximum jitter is examined for RIP is average 36.12ms meaning all three networks. Moreover, mixed results are captured for packet length in different networks. In general, RIP, OSPF and RIP-OSPF shows the standard and largest packet size during the networks communication. Finally, for the best possible value for packet loss is obtained by EIGRP which average packet loss value is 2.66 in overall all three networks whereas RIP-OSPF has overall 5.66 packet loss. The results backed by simulation evaluation and validation demonstrate that EIGRP and combined OSPF-EIGRP are best solution to choose routing protocols for enhancing networking performance especially for extended (large-scale) networks while RIP or OSPF can have moderate performance for retracted (small-scale) network.

Table 1: Comparison Table for routing protocols in terms of performance justification of four different parameters

Protocols	Experimented Network				Extended Network				Retracted Network				Average			
	Throughput	Jitter	Packet Length	Packet Loss	Throughput	Jitter	Packet Length	Packet Loss	Throughput	Jitter	Packet Length	Packet Loss	Throughput	Jitter	Packet Length	Packet Loss
RIP	21	35.9	103	4	12	60.25	101	6	22	12.23	102	3	18.33	36.12	102.00	4.33
OSPF	16	23.83	105	6	17	58.59	97	4	20	4.114	102	0	17.67	28.84	101.33	3.33
EIGRP	26	10.14	78	3	26	55.13	86	3	32	7.0	102	2	28.00	24.09	88.66	2.66
RIP-OSPF	19	2.519	98	5	17	31.9	83	5	12	15.57	104	7	16.00	16.66	95.00	5.66
RIP-EIGRP	22	25.57	83	4	22	13.17	83	4	27	4.2	99	5	23.67	14.31	88.33	4.33
OSPF-EIGRP	30	3.78	86	2	19	8.1	95	5	17	0.997	94	4	22.00	4.29	91.66	3.66
RIP-OSPF-EIGRP	15	1.89	97	9	8	7.19	92	10	19	0.940	95	8	14.00	3.34	94.66	9.0

There are several future research areas including (I) exploring other routing protocols and its combination with which we could further demonstrate the performance and utility of the network; (II) designing and implementing modern communication secured networks is inevitable for more scientific research in future to combat cybercrimes and network vulnerabilities where different types of cryptographic algorithms like encryption protocols, authentication and hashing protocols are utilized. Therefore, further research will be conducted also to evaluate the particular routing protocols performance in case of using different security protocols in the networks; (III) Our proposed protocols from this research paper will be further examined and validated for different other security- enabled networking environments.

Conflict of Interest

There is no conflict of interest for this research work.

Acknowledgment

This research work has been done in Advanced Networking Lab in Institute of Information and Communication Technology with the equipment supported by Bangladesh University of Engineering and Technology.

References

[1] K. Akunuri, R. Arora, and I. G. Guardiola, “A study of speed aware routing for mobile ad hoc networks” in International Journal of Interdisciplinary Telecommunications and Networking, Vol 3, pp. 40-61, 2011. https://dl.acm.org/citation.cfm?id=2440280

[2] S. Y. Jalali, S. Wani, M. Derwesh, “Qualitative Analysis and Performance Evaluation of RIP, IGRP, OSPF and EGRP Using OPNET” Research India Publications., Vol. 4, pp. 389-396, 2014. https://pdfs.semanticscholar.org/b616/f7b1a8e13f18b71998c557dc6f18d1fcba33.pdf

[3] M. Abdulkadhim, “Routing Protocols Convergence Activity and Protocols Related Traffic Simulation with Its Impact on the Network" in international Journal of Computer Science Engineering and Technology (IJCSET), vol. 5, no. 3, pp. 40-43 (2015).http://ijcset.net/docs/Volumes/volume5issue3/ijcset2015050302.pdf

[4] C. Fancy, L. M. M. Thanveer,“An evaluation of alternative protocols-based Virtual Private LAN Service (VPLS)” in IoT and Application (ICIOT), International Conference, Nagapattinam, India, May. 2017, pp. 1-6 (2017) https://ieeexplore.ieee.org/document/8073621/

[5] S.U. Masruroh, F. Robby, and N. Hakiem, “Performance Evaluation of Routing Protocols RIPng, OSPFv3, and EIGRP in an IPv6 Network” in International Conference on Informatics and Computing (ICIC), Mataram, Indonesia Oct. 2016, pp. 111-116 (2016). https://ieeexplore.ieee.org/document/7905699/

[6] D. R. Al-Ani, A. R. Al-Ani, “The performance of IPv4 and IPv6 in terms of Routing Protocols using GNS 3 Simulator” in 9th International Conference on Ambient Systems, Networks and Technologies, ANT-2018 and the 8th International Conference on Sustainable Energy Information Technology, SEIT 2018, May. 2018, pp. 1-6 (2018). https://dl.acm.org/citation.cfm?id=3223610

[7] B. Swami,, and R. Singh,, "Performance analysis of DFS based ordered walk learning routing protocol in MANET" in Green Computing and Internet of Things (ICGCIoT), 2015 International Conference, Noida, India, Oct. 2015. https://ieeexplore.ieee.org/document/7380456/

[8] S. G. Thornier, "Dynamic routing protocol implementation decision between EIGRP, OSPF, and RIP based on technical background using OPNET Modeler" in Proc. Second International Conference on Computer and Network Technology (ICCNT), Bangkok, Thailand, Apr. 2010, pp. 191–195. https://ieeexplore.ieee.org/document/5474509/

[9] X. Du, M. Guizani, Y. Xiao, H. H. Chen, "A Routing-Driven Elliptic Curve Cryptography based Key Management Scheme for Heterogeneous Sensor Networks" *IEEE Transactions on Wireless Communications*, vol. 8, no. 3, pp. 1223-1229, March 2009. https://ieeexplore.ieee.org/document/4801475/

[10] D. Xu, and L. Trajkovic, "Performance Analysis of RIP, EIGRP, and OSPF using OPNET" Simon Fraser University., British Columbia, Canada,2012. https://www.researchgate.net/publication/267385378_Performance_Analysis_of_RIP_EIGRP_and_OSPF_using_OPNET

[11] E. Balasas, M. Roumeliotis, K.E. Psannis, "Performance Evaluation of Routing Protocols for BIG Data application," in University of Macedonia.,Thessaloniki, Greece, May,2018. https://www.researchgate.net/publication/322291489_Performance_Evaluation_of_Routing_Protocols_for_BIG_Data_application

[12] S. Corson and J. Macker. "Mobile Ad Hoc Networking (MANET): Routing Protocol Performance Issues and Evaluation Consideration" available at http://www.ietf.org/rfc/rfc2501.txt

[13] K. A. Zahoor, "A Novel Patient Monitoring Framework and Routing Protocols for Energy & Qos Aware Communication in Body Area Network," PhD thesis, Dalhousie University, June 2013

[14] T. S. Andrew, W. J. David, Computer Networks, Prentice Hall, 2010.

[15] L. Chappell, Wireshark Network Analysis. Protocol Analysis Institute, San Jose, CA 95129 USA, 2012.

ASTES

Advances in Science, Technology and Engineering Systems Journal Vol. 3, No. 4, 122-129 (2018)

www.astesj.com

ASTESJ

ISSN: 2415-6698

Complete Modeling of the Hydrogen Stored in a Spherical Cavity

Kamel. Idris-Bey[*,1], Sofoklis S. Makridis[2]

[1]*Matter Science Department, Faculty of Sciences, Laboratory of Physics Experimental Techniques and Applications University Yahia Fares- Medea, 26000, Algeria*

[2]*Department of Environmental and Natural Resources Management, University of Patras, GR30100 Agrinio, Greece*

ARTICLE INFO

Article history:
Received: 17 April, 2018
Accepted: 18 July, 2018
Online: 29 July, 2018

Keywords:
Hydrogen energy storage
Modeling
Thermodynamic functions

ABSTRACT

Hydrogen is the lightest of gases and possesses the lowest density. However at ambient temperature and pressure it occupies a large volume. This necessitates compressing it at high pressures up to 800 Bars to minimize the volume. The immense interest generated by hydrogen comes from the fact that it has the best energy per weight ratio of all fuels and the ecological nature of the combustion product. From the pedagogical point of view, it is also the most taught and involved in research, in particular in quantum mechanics. This aspect is treated in this article in order to solve the problem of storage of the hydrogen by minimizing losses. The solutions envisaged are, first, the improvement of the theory to understand the physical phenomena that occur in the physical system, especially the resolution of the transcendental equation, and then the means of perfecting the materials constituting the cavity.

Quantum scale investigations began with solving the Schrodinger equation at three-dimensional spherical symmetry, taking into account the boundary conditions of Victor Gustave Robin on the inner walls of the envelope. The clean energies that are stored in a spherical-shaped cavity have been modeled theoretically by solving the transcendental equation. The last part of the article is devoted to the thermodynamic properties of the hydrogen gas, particularly the dependence of the energy with the pressure and the temperature.

1. Introduction

At all times, energy has been indispensable for maintaining the life of living beings on our planet earth. It first appeared as fossil energy in the form of coal, which originated from the rapid burial of trees and plant debris within some sedimentary basins. This fossil energy remained for a long time in the primitive state until the 19th century era of running in search of black gold. Fossil fuels then include coal, oil and gas and are essential for transport, power generation, heating, plant operation and others.

Through many scientific meetings on renewable energies, the discusses in current research focuses on hydrogen as an energy carrier. This implies that, in order to control this renewable energy, four levels of interventions have to be considered simultaneously, along a complete path leading to its proper use and management.

- The production or source of energy.
- The transportation.
- The storage.
- The distribution.

The origin of the vector being the source of artificial production since hydrogen does not exist in the natural state and must be extracted by reforming from hydrocarbons or by hydrolysis from water, and the arrival tip is the distribution to the consumers.

This article is devoted to the storage of hydrogen, with two major difficulties to be answered: the safety and the miniaturization of the storage tanks because hydrogen is an explosive product and little dense which implies that it occupies a large volume even in small quantity. The density of hydrogen at the temperature T = 273 K and the pressure P = 1 atm is d = 0.0899 g/L equivalent to $8.99.10^{-5}$ g/cm3 [1]. Numerous storage means have been envisaged for hydrogen and are currently competing: gas storage under pressure, cryogenic storage in liquid form, solid storage in hydrides and adsorbent materials [2].

[*] Kamel. Idris-Bey, University of Medea, Faculty of Sciences
Email: idrisbeykamel@gmail.com

2. The gas storage

The innovative solution for pressure storage today comes from wound fiber and resin structures that provide much higher storage pressures while reducing envelope mass. At present, operating pressures of 350 bars are commonly proposed and the research is directed towards even greater pressures in the order of 700 to 800 bars [3]. The structure of a composite fiber and resin tank is more complex than that of a steel tank. At least three envelopes are used which each fulfill a different function.

The internal envelope, made of aluminum, does not contribute to the mechanical strength of the tank but must; however, withstand the high stresses induced by the load variations during the filling and use cycles. To replace aluminum, some research is directed towards polymeric materials such as high density polyethylene. These materials are even lighter than metal, stress resistant, easy to work with and inexpensive but they still suffer from the fact that they are significantly more permeable to hydrogen than aluminum.

The middle envelope ensures the mechanical strength of the tank it is the working structure. It is obtained by winding a continuous network of carbon or glass fibers coated with a thermosetting or thermoplastic resin directly on the internal envelope. This winding is affected by rotating the inner envelope and by scanning the fibers in and out at a given angle up to the total overlap. It is thus possible to produce a composite structure of several covering layers with different angles. A firing phase then allows the polymerization of the resin and finishes the production phase.

The outer casing acts as a protector against external aggressions such as moisture, shocks or friction, which can cause the carbon or glass fiber to become brittle and the tank to become brittle locally. This envelope is most often made of cheap fiberglass and can be completed with a foam thickness.

Finally, pressure storage must be evaluated according to the risks of use, particularly in the case of on-board tanks. This involves a series of homologation tests involving the validation of the storage system for various accidental scenarios such as gas leakage, crash, fire, impact, as well as corrosion resistance and behavior in cycling and fatigue.

3. Mathematical theory

To solve theoretically, hydrogen gas transmission phenomenon that is enclosed in a spherical cavity under high pressure, two equations are necessary: the Schrödinger equation (1), which is well known with the Hamiltonian H and the energy E, and the Victor Gustave Robin boundary condition (2),

$$H.\psi(\vec{x}) = \mathrm{E}(\vec{\mathrm{k}}).\psi(\vec{x}) \quad (1)$$

$$\gamma(\vec{x})\psi(\vec{x}) + \vec{n}(\vec{x}).\vec{\nabla}\psi(\vec{x}) = 0, \quad \vec{x} \in \partial\Omega \quad (2)$$

The self-adjoint extension parameter $\gamma(\vec{x})$ takes into account the constituent material of the cavity, $\psi(\vec{x})$ is the wave function, $\partial\Omega$ is the limit of a spatial region Ω and $\vec{n}(\vec{x})$ is the unit vector perpendicular to the surface. As usual, the wave function can be factored as the product of a radial function $\psi_{\nu\ell}(r)$ with a spherical harmonic function $Y_{lm}(\theta,\varphi)$ according to the following expression

$$\psi(\vec{x}) = \psi_{\nu\ell}(r).Y_{\ell m}(\theta,\varphi) \quad (3)$$

3.1. The transcendental equation of the energy spectrum

When replacing (3) in (2) and for a spherical cavity, the most general perfectly reflecting boundary condition of (2) takes the form

$$\gamma\psi_{k\ell}(R) + \partial_{\mathrm{r}}\psi_{k\ell}(R) = 0 \quad (4)$$

The Hamiltonian radial equation of the hydrogen atom, in spherical coordinates, takes the expression:

$$-\frac{1}{2\mathrm{M}}\left(\partial_{\mathrm{r}}^2 + \frac{2}{\mathrm{r}}\partial_{\mathrm{r}} - \frac{\ell(\ell+1)}{\mathrm{r}^2} - \frac{\mathrm{e}^2}{\mathrm{r}}\right)\psi_{\nu\ell}(r) = E\psi_{\nu\ell}(r) \quad (5)$$

In this case, the parameterized energy is as [4]

$$E = -\frac{Me^4}{2\nu^2} \quad (6)$$

While in the infinite volume the quantum number ν takes integer values for the bound state spectrum, in the cavity ν is in general real-valued. Introducing the Bohr radius

$$a = \frac{1}{Me^2} \quad (7)$$

The energy with function of the Bohr radius is

$$E = \frac{e^2}{32\,a} \quad (8)$$

and the normalizable wave function is given by

$$\psi_{\nu\ell}(r) = A\left(\frac{2r}{\nu a}\right)^{\ell} L_{\nu-\ell-1}^{2\ell+1}\left(\frac{2r}{\nu a}\right) exp\left(\frac{-r}{\nu a}\right) \quad (9)$$

where $L_{\nu-\ell-1}^{2\ell+1}\left(\frac{2r}{\nu a}\right)$ is an associated Laguerre function, a is the Bohr radius and A is a constant.

When resolving (4), the energy spectrum is then determined by the transcendental equation [4]

$$\left(\frac{\gamma\nu a}{2} - \frac{1}{2} + \frac{\ell\nu a}{2R}\right) L_{\nu-\ell-1}^{2\ell+1}\left(\frac{2R}{\nu a}\right) - L_{\nu-\ell-2}^{2\ell+2}\left(\frac{2R}{\nu a}\right) = 0 \quad (10)$$

3.2. Resolution of the transcendental equation

Hydrogen energies are quantified by the two parameters ν and ℓ, these energies depends on the self-adjoint extension parameter (as possible) which identify the materiel properties of the inner cavity wall, many scientists consider the cavity envelopes made with nanotechnology, fibers and polymers, [5-13]. The energies of the hydrogen are also a function of the radius R of the spherical cavity. Consider the case $\nu = 4$, (10) takes the form

$$\left(2\gamma a - \frac{1}{2} + \frac{2\ell a}{R}\right) L_{3-\ell}^{2\ell+1}\left(\frac{R}{2a}\right) - L_{2-\ell}^{2\ell+2}\left(\frac{R}{2a}\right) = 0 \quad (11)$$

For $\ell = 0$, (11) becomes

$$\left(2\gamma a - \frac{1}{2}\right) L_3^1\left(\frac{R}{2a}\right) - L_2^2\left(\frac{R}{2a}\right) = 0 \quad (12)$$

replacing the expressions of the generalized Laguerre polynomials $L_3^1\left(\frac{R}{2a}\right)$ and $L_2^2\left(\frac{R}{2a}\right)$

$$L_3^1\left(\frac{R}{2a}\right) = -\frac{1}{6}\left(\frac{R}{2a}\right)^3 + 2\left(\frac{R}{2a}\right)^2 - 6\left(\frac{R}{2a}\right) + 4 \quad (13)$$

$$L_2^2\left(\frac{R}{2a}\right) = 2 \quad (14)$$

Doing calculations, one can arrive to (15)

$$X^3 - 12\,X^2 + 36\,X - 24 = 0 \qquad (15)$$

where $$X = \left(\frac{R}{2a}\right) \qquad (16)$$

Equation (15) is a polynomial equation of degree three, with using the informatics processing, the solutions are found using the roots Matlab procedure, there is three distinct values for X, then from (16), three values for the cavity radius are deduced. The solutions are reported in the Table 1

Table 1: values of X, and corresponding values for the radius R *calculated.*

X=R/2a	R(x10^{-10} meter)
7.7588	8.2116
3.3054	3.4983
0.9358	9.9041

For $\ell = 1$:

In this case, the quantify parameter of the energies is always equal to four ($\nu = 4$), and the azimuthally parameter is changed equal to one ($\ell = 1$), (11) becomes

$$\left(2\gamma a - \frac{1}{2} + \frac{2a}{R}\right) L_2^3\left(\frac{R}{2a}\right) - L_1^4\left(\frac{R}{2a}\right) = 0 \qquad (17)$$

replacing the expressions of the generalized Laguerre polynomials $L_2^3\left(\frac{R}{2a}\right)$ and $L_1^4\left(\frac{R}{2a}\right)$

$$L_2^3\left(\frac{R}{2a}\right) = \frac{1}{2}\left(\frac{R}{2a}\right)^2 - 5\left(\frac{R}{2a}\right) + 10 \qquad (18)$$

$$L_1^4\left(\frac{R}{2a}\right) = -\left(\frac{R}{2a}\right) + 5 \qquad (19)$$

Then, taking into account (18) and (19), (17) becomes

$$\left(2\gamma a - \frac{1}{2} + \frac{2a}{R}\right)\left(\frac{1}{2}\left(\frac{R}{2a}\right)^2 - 5\left(\frac{R}{2a}\right) + 10\right) - \left(-\left(\frac{R}{2a}\right) + 5\right) = 0 \qquad (20)$$

After calculations (20) takes the form

$$m\,X^3 - 2(5m-3)X^2 + 20(m-2)X + 40 = 0 \qquad (21)$$

Where X is the new variable, which is defined by the (16), and m is real number parameter defined as

$$m = 4\gamma a - 1 \implies \gamma a = \frac{m+1}{4} \qquad (22)$$

This is a third order equation. To find the solutions use the graphic informatics processing, with resolving the system

$$\begin{cases} G(X) = 0 \\ where \\ G(X) = m\,X^3 - 2(5m-3)X^2 + 20(m-2)X + 40 \end{cases} \qquad (23)$$

The calculations were done with five different values of the parameter m. For each curve it exist two positive solutions, the results are written in the Table 2

In this case, the energy E_{41} corresponding to $E_{\nu\ell}$ when $\nu = 4$ and $\ell = 1$, is stationary and stay constant along all the abscises axes.

For $\ell = 2$:

As well as the section before, the quantify parameter of the energies is always equal to four ($\nu = 4$), and the azimuthally parameter is change equal to two ($\ell = 2$), (11) becomes

$$\left(2\gamma a - \frac{1}{2} + \frac{4a}{R}\right) L_1^5\left(\frac{R}{2a}\right) - L_0^4\left(\frac{R}{2a}\right) = 0 \qquad (24)$$

Table 2: The solution points of (21)

m	X= R/2a	R=2aX (x10^{-10} meter)	E=e^{2}X/(16R) (x10^{-30}Joule)
First points			
11	2.5876	2.7386	15.118
19	2.6604	2.8157	15.118
27	2.6907	2.8477	15.118
35	2.7073	2.8653	15.118
43	2.7177	2.8763	15.118
Second points			
11	7.0658	7.4782	15.118
19	7.1347	7.5511	15.118
27	7.1639	7.5820	15.118
35	7.1801	7.5991	15.118
43	7.1903	7.6099	15.118

The graphic resolution is reported in the Figure 1

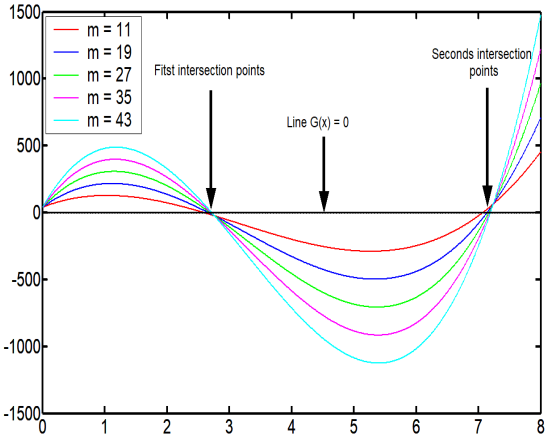

Figure 1: Graphic resolution of (23), showing the curves G(X) and the two solution points.

replacing the expressions of the generalized Laguerre polynomials $L_1^5\left(\frac{R}{2a}\right)$ and $L_0^4\left(\frac{R}{2a}\right)$

$$L_1^5\left(\frac{R}{2a}\right) = -\left(\frac{R}{2a}\right) + 6 \qquad (25)$$

$$L_0^4\left(\frac{R}{2a}\right) = 1 \qquad (26)$$

Doing calculations, one can arrive to the equation below

$$X^2 - 6(m-1)X - 24 = 0 \qquad (27)$$

the variable X and the parameter m are defined by respectively (16) and (22). Solutions can be found graphically from the curve with resolving the equality

$$\begin{cases} mH(X) = 0 \\ where \\ H(X) = mX^2 - 6(m-1)X - 24 \end{cases} \qquad (28)$$

It exists only one positive solution, the unique value for X and the radius R are obtained when the parameter m is fixed equal to $2{,}1167.10^{30}$, with one great value of the self-adjoint extension parameter γ ($\gamma = 1.10^{40}$), this maximizes the hydrogen energy storage. The result is reported in Table 3

Table 3: value of the radius R.

m (x10^{30})	X= R/2a	R(x10^{-10} meter)
2.1167	6.0000	6.3502

The graphic resolution is reported in the Figure 2

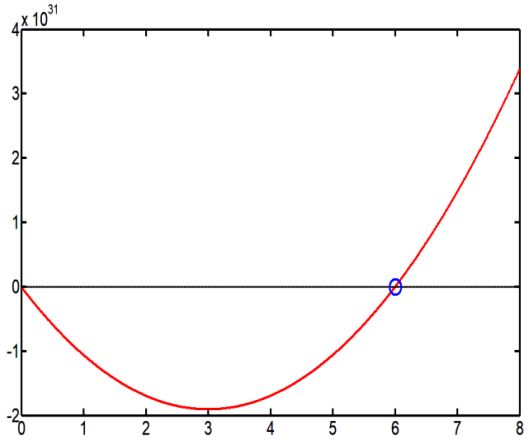

Figure 2: Graphic resolution of (28), showing the red curve H(X) for $m = 2{,}1167.10^{30}$ and the unique solution (blue point).

For $\ell = 3$:

Consider here the quantify parameter of the energies equal to four ($\nu = 4$), and the azimuthally parameter is change equal to three ($\ell = 3$), (11) becomes

$$\left(2\gamma a - \frac{1}{2} + \frac{6a}{R}\right) L_0^7\left(\frac{R}{2a}\right) - L_{-1}^8\left(\frac{R}{2a}\right) = 0 \qquad (29)$$

With: $$L_0^7\left(\frac{R}{2a}\right) = 1 \quad and \quad L_{-1}^8\left(\frac{R}{2a}\right) = 0 \qquad (30)$$

Then: $$2\gamma a - \frac{1}{2} + \frac{6a}{R} = 0 \qquad (31)$$

Resolving (31), the Bohr radius, a, depend on the cavity radius R according to the form

$$a = \frac{R}{4(\gamma R + 3)} \qquad (32)$$

And, by (8) and (32), the energy is

$$E_{43} = \frac{e^2}{32\,a} = \frac{(\gamma R + 3)e^2}{8R} \qquad (33)$$

4. Graphics processing of the energies

The informatics processing of the hydrogen energies is made in the Matlab R2009a environment. All the expressions of the energies decrease with the cavity radius R in the function form

$$E = \frac{C}{R},\ C\ is\ a\ constant \qquad (34)$$

except the last energy E_{43}.

4.1. Hydrogen energies E_{40} graphics

It exists three possible energies corresponding, respectively to three different radius of the spherical tank storing the hydrogen. These values are reported in the Table 4.

Table 4: values of the cavity radius and their corresponding energies E_{40}

R (x10^{-10} meter)	E_{40}=e^2X/(16R) (x10^{-30} Joule)
0.9904	125.30
3.4982	035.50
8.2114	015.10

The Figure 3 shows the behavior of the energy E_{40} with function of the radius R, it decreases like the function $\frac{1}{R}$. The three solution points of the radius are fixed in the curve. One can remark that the radius axes coordinates are very small, atomic scale, because there is no correlation between the energy E_{40} and the self-adjoint extension parameter.

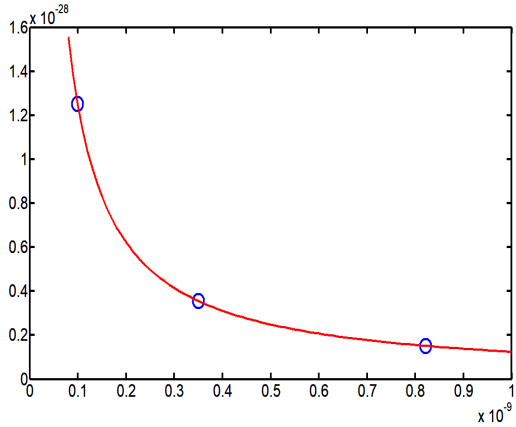

Figure 3: Curve of the energy $E_{40}(R)$ with the three solutions (blue points).

4.2. Hydrogen energy E_{41} graphics

From the Table 2, there are two different points which are the solution of (21). Because the values are nearer in each point, it is necessary to make the average of the values. The two points radius average, with different positions, have the same energy, they are reported in the Table 5

Table 5: energyE_{41} corresponding to the two radius position average

R (x10^{-10}meter)	E_{41}=e^2X/(16R) (x10^{-30} Joule)
2.8287	15.118
7.5639	15.118

In the Figure 4, the two average points occupy two different positions, supported by two different energy curves in 1/R, but possess the same energy $E_{41} = 15{,}118.10^{-30}$ Joule. Also the radius axes coordinates are very small, atomic scale, because there is no correlation between the energy E_{41} and the self-adjoint extension parameter.

4.3. Hydrogen energy E_{42} graphics

The energy E_{42} possess one solution value, because (27) has only one approximate best solution which is $X = 6$. The corresponding values of the cavity radius R and the energy E_{42} are reported on the Table 6

Table 6: values of the cavity radius R and the energy E_{42}

R (x10^{-10}meter)	E_{42}=e^2X/(16R) (x10^{-30} Joule)
6.3500	15.118

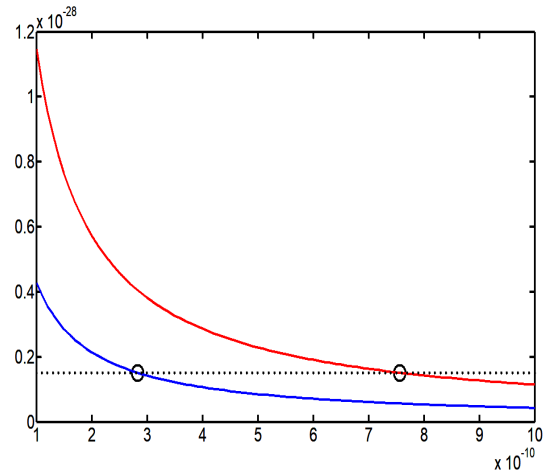

Figure 4: Curve of the energy E_{41}(R) with the two solutions points, different positions and same energy.

The Figure 5 shows the behavior of the energy with function of the cavity radius, but the energy E_{42} possesses only one value, equal to 15.118x10^{-30} Joule, which is very small.

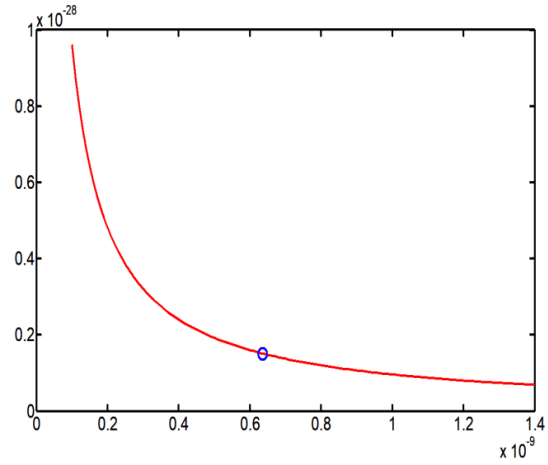

Figure 5: Energy E_{42} (R) behavior with function on the cavity radius R, and the point solution is fixed on the curve.

4.4. Hydrogen energies E_{43} graphics

Expression (33) gives the relation between the energy E_{43} with the self-adjoint extension parameter γ, and as well as it is known, γ greater make favorable the hydrogen storage. The calculations were made with three different values of this extension parameter. To be realist, the cavity radius dimension is set to be between 0 to 0.4 meter and the best dimension of one hydrogen tank is when its radius is equal to 0.2 meter. Also to have a great energy, extension parameter γ is take with great values about 1.10^{40}. The results values are report in the Table 7

Table 7: three values of the extension parameter generate three different values of the energy E_{43}, when the cavity radius is equal to 0.2 meter

R (meter)	E_{43}= (γR+3)e^2/(8R) (Joule)	γ (x10^{40})
0.2	160	5
0.2	800	25
0.2	1600	50

Informatics processing of (33) and the graphic study of the function $E_{43} = f(R, \gamma)$ gives the Figure 6

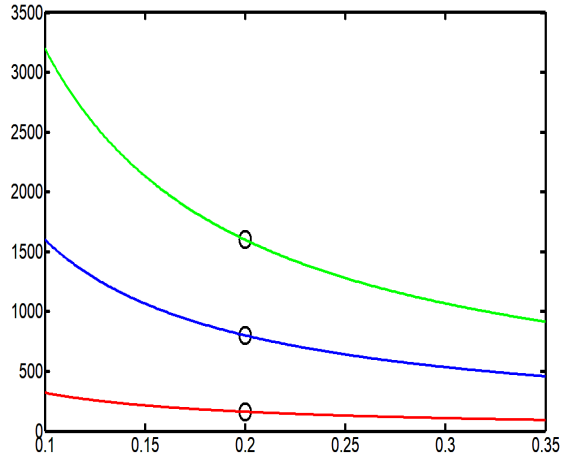

Figure 6: Three point values of the energy E_{43} (R) are marked on three different curves of energy (in 1/R) with three different values of the extension parameter γ.

5. Thermodynamic model

Thermodynamic properties of hydrogen storage systems, such as temperature and pressure, are required in order to evaluate and optimize their performance. The thermodynamic models of hydrogen storage systems are based on the mass and energy balance equations [14].

To simply model the hydrogen stored in a spherical cavity of radius r, with taking into account the thermodynamic phenomena, the knowledge of the thermodynamic state functions and there states variables becomes necessary. It exists the intensive state variables as the temperature T, the pressure P, the density d and the extensive state variables as the volume V, the masse m, the mole number Nor the mole number per unit volume

$$n = \frac{N}{V_0} \tag{35}$$

where V_0 is the final volume of the tank ($V_0 = constant$).

5.1. Hypothesis

The volume V of the spherical cavity of radius r is define by the geometrical relation

$$V = \frac{4}{3}\pi\, r^3 \tag{36}$$

The clean or internal energy E decrease with the radius r according to the relation

$$E = \frac{A}{r} \quad with \;\; A = \frac{e^2 X}{16} = \frac{e^2 R}{32\, a} = constant \tag{37}$$

Where X is the solution of the polynomial equation obtained from the transcendental equation, it is define by (16).

Hydrogen in state gas can appear as perfect gas or real gas, in practice the real gas is always used. The density of hydrogen at elevated pressure can be estimated using the principles of thermodynamics. While the behavior of most gases can be

approximated with a high accuracy by the simple equation of state of an ideal gas with the constant R_{IG}

$$P\,V = n\,R_{IG}T \tag{38}$$

that relates the pressure, the volume and the temperature of a given substance, the behavior of hydrogen deviates significantly from the predictions of the ideal gas model. The resulting deviation from the ideal gas law is always in the form of expansion – the gas occupies more space than the ideal gas law predicts. One of the simplest ways of correcting for this additional compression is through the addition of a compressibility factor, designated by the symbol$Z$. Compressibility factors are derived from data obtained through experimentation and depend on temperature, pressure and the nature of the gas. The Z factor is then used as a multiplier to adjust the ideal gas law to fit actual gas behavior as follows [15]

$$P\,V = n\,ZR_{IG}T \tag{39}$$

5.2. Thermodynamic functions

Replacing the volume expression, (36), in (39), the cavity radius is expressed with function on the pressure and the temperature

$$r(P,T,Z,n) = \left(\frac{3n\,Z\,R_{IG}}{4\pi}\right)^{\frac{1}{3}}\left(\frac{T}{P}\right)^{\frac{1}{3}} \tag{40}$$

The internal energy form is obtained by replacing the cavity radius (40) in (37).

$$E(P,T,Z,n) = A\left(\frac{4\pi}{3nZR_{IG}}\right)^{\frac{1}{3}}\left(\frac{P}{T}\right)^{\frac{1}{3}} = A\left(\frac{4\pi}{3}\right)^{\frac{1}{3}}\left(\frac{P}{nZR_{IG}T}\right)^{\frac{1}{3}} \tag{41}$$

The internal energy is function of the pressure, the temperature, the compressibility factor and the mole number per unit volume. It increase with the pressure rising and it decrease when the temperature raise. Also, the inner energy is quantified by two parameters ν *and* ℓ, the total energy in the tank storing hydrogen is the addition of all the individual energies corresponding to different states of the energy parameterized by the constant A_i

$$A_i = \frac{e^2X_i}{16} = \frac{e^2}{32\,a}R_i \tag{42}$$

The final cavity radius takes one realistic value manufacturing the tank

$$R_i = R_1, R_2, R_3, \dots\dots\dots R_c \quad c\ integer > 0 \tag{43}$$

Then

$$E_i(P,T,Z,n) = A_i\left(\frac{4\pi}{3nZR_{IG}}\right)^{\frac{1}{3}}\left(\frac{P}{T}\right)^{\frac{1}{3}} \tag{44}$$

The partition function z is then defined by the relation

$$\mathrm{z}(P,T,Z,n) = \sum_i exp\left(-\beta E_i(P,T,Z,n)\right)$$

$$= \sum_i exp\left(-\beta A_i\left(\frac{4\pi}{3nZR_{IG}}\right)^{\frac{1}{3}}\left(\frac{P}{T}\right)^{\frac{1}{3}}\right) \tag{45}$$

with $\beta = \frac{1}{K_BT}$ K_B *is the Boltzmann constant* (46)

For the construct tank of hydrogen the radius is equal to R_c then the true partition function z take the form

$$z(P,T,Z,n) = exp\left(-\frac{\beta e^2R_C}{32\,a}\left(\frac{4\pi}{3nZR_{IG}}\right)^{\frac{1}{3}}\left(\frac{P}{T}\right)^{\frac{1}{3}}\right) \tag{47}$$

The free energy F is then deduce from (46) by the relation

$$F(P,T,Z,n) = -K_BTLnz = \frac{e^2R_C}{32\,a}\left(\frac{4\pi}{3nZR_{IG}}\right)^{\frac{1}{3}}\left(\frac{P}{T}\right)^{\frac{1}{3}}$$

$$= \frac{e^2}{32\,a}\left(\frac{4\pi}{3}\right)^{\frac{1}{3}}R_C\left(\frac{P}{nZR_{IG}T}\right)^{\frac{1}{3}} \tag{48}$$

The free energy is also function of the internal energy E, the entropy S and the temperature T, with the following relation

$$F(E,S,T) = E - TS \tag{49}$$

Then

$$S = \frac{E-F}{T} \tag{50}$$

By substituting the E and F expression, respectively (41) and (48), in (50), the entropy S takes the form

$$S(P,T,Z,n) = (R - R_C)\left(\frac{e^2}{32\,a}\right)\left(\frac{4\pi}{3}\right)^{\frac{1}{3}}\left(\frac{P}{nZR_{IG}T^4}\right)^{\frac{1}{3}},\ R > R_C \tag{51}$$

The Gibbs G energy is function of the free energy F the pressure P and the volume V, like

$$G = F + PV \tag{52}$$

By replacing V and F with their expressions, (36) and (48), in (51)

$$G(P,T,Z,n) = \frac{e^2}{32\,a}\left(\frac{4\pi}{3}\right)^{\frac{1}{3}}R_C\left(\frac{P}{nZR_{IG}T}\right)^{\frac{1}{3}} + \frac{4}{3}\pi\,r^3P \tag{53}$$

Then taking into account of the radius r (40),

$$G(P,T,Z,n) = \frac{e^2}{32\,a}\left(\frac{4\pi}{3}\right)^{\frac{1}{3}}R_C\left(\frac{P}{nZR_{IG}T}\right)^{\frac{1}{3}} + \left(n\,Z\,R_{IG}T\right) \tag{54}$$

The chemical potential μ is define like

$$\mu = \left(\frac{\partial G}{\partial N}\right)_{P,T} = \left(\frac{\partial G}{\partial n}\right)_{P,T}\left(\frac{\partial n}{\partial N}\right) \tag{55}$$

Knowing (35)

$$\mu = \left(\frac{\partial G}{\partial N}\right)_{P,T} = \frac{1}{V_0}\left(\frac{\partial G}{\partial n}\right)_{P,T} \tag{56}$$

The calculation arrive to the final expression

$$\mu = -\frac{e^2R_C}{96\,a\,V_0}\left(\frac{4\pi}{3}\right)^{\frac{1}{3}}\left(\frac{P}{n^4ZR_{IG}T}\right)^{\frac{1}{3}} + \frac{ZR_{IG}T}{V_0} \tag{57}$$

With

$$V_0 = \frac{4\pi}{3}{R_C}^3 \tag{58}$$

6. Graphic processing

The data are set with the following values in the international unit system (IS):

the Bohr radius is $a = 0{,}52918x10^{-10}\,meter$, the constant of real gas is $R_{IG} = 8{,}3143\,J.K^{-1}.mol^{-1}$, the mole number per unit volume is equal to the Avogadro number $n = 6{,}0225.10^{23}\,particles\ per\ mole$, the cavity radius $R = 0.2\,m$ and from (37) the constant $A = 3{,}0312.10^{-30}\,J.m.$

The values of the compressibility factor were taken from the experimental curve of the compressibility factor as a function of the pressure at different temperatures [15]. The experimental data are shown in Table 8

Table 8: dataset for calculations

P (Bar)	0	50	100	200	300	400	500	600
T1=100 (K)								
Z1	1	0.98	1.06	1.22	1.44	1.66	1.88	2.05
T2=150 (K)								
Z2	1	0.98	1.08	1.18	1.32	1.46	1.59	1.72
T3=200 (K)								
Z3	1	0.98	1.08	1.16	1.26	1.36	1.46	1.56
T4=300 (K)								
Z4	1	0.99	0.98	1.07	1.12	1.18	1.25	1.39

6.1. Energy with function on the pressure and the temperature

Knowing the energy relation as function of the pressure and the temperature (59)

$$E(P,T,Z,n) = A\left(\frac{4\pi}{3nZR_{IG}}\right)^{\frac{1}{3}}\left(\frac{P}{T}\right)^{\frac{1}{3}} \qquad (59)$$

The curves of the energies are shown in the Figure 7

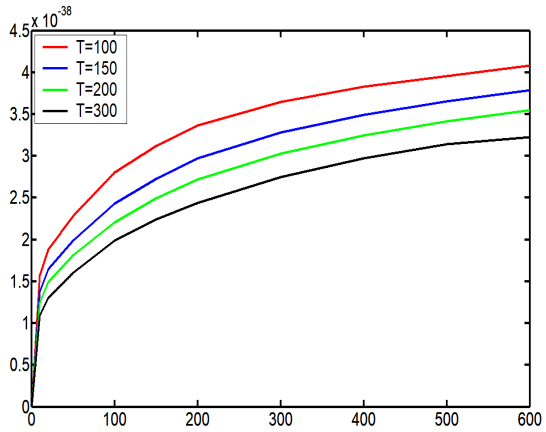

Figure 7: Energy, (59), as function of the pressure and the temperature.

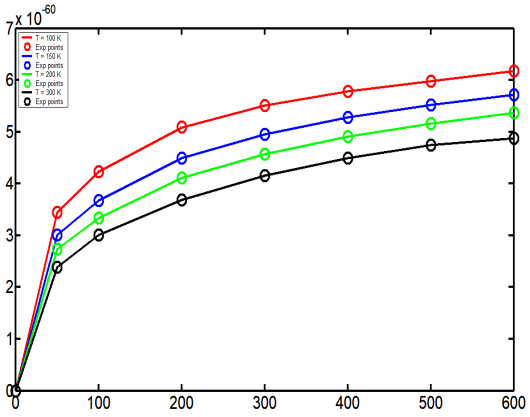

Figure 8: Energy with function of the pressure and the temperature including the experimental points.

Considering the experimental values of the compressibility factors, and with one scale factor equal to $sf = 1{,}511.10^{-22}$, the curves were adjusted using the function of the energy (59). The Figure 8 shows the behavior of the energies with the experimental values of the compressibility factor.

7. Conclusion

This article has examined the hydrogen storage phenomenon in a spherical cavity. Especially the hydrogen gas subjected to high pressures, leading to significant loss of mass of hydrogen, and requiring materials that can withstand these high pressures and minimize losses. For all these reasons, the problem is considered at the quantum scale. So the first part of the article is dedicated to the quantum mechanics, it studies the theory of the radial functions corresponding to the hydrogen by resolving the Schrödinger equation with adding the boundary condition of Robin. The second part was devoted to solving the transcendental equation that is the result of the first part and has resulted in the relations of the energies. The mathematical studying of the transcendental equation has given three polynomial equations which are independent on the self-adjoint extension parameter. The energies in this case are very small, E_{40} # E_{41} # E_{42} # 1.10^{-28} Joule. Only the case where the energy E_{43} is function of the self-adjoint extension parameter is acceptable and important. This energy is estimated between 160 J and 1600 J, because of the high value of the self-adjoint extension parameter about 1.10^{40}. The conclusion from this part is that all the energies depend on the radius R of the cavity according to the form (Constant/R). The third part studies the thermodynamic modeling, which made it possible to express all the thermodynamic functions with function of the pressure and the temperature. With considering the experimental curve of the compressibility factor as a function of the pressure at different temperatures, the expression of the energy was adjusted very well with the model of the theoretical energy. The energy increase with the pressure P rising and decrease with the increasing of the temperature T. This made it possible to validate the model, since there is a perfect agreement between the experimental values of energy and the theoretical model.

References

[1] Sofoklis S. Makridis, Hydrogen storage and compression, Methane and hydrogen for energy storage, Chapter 1 p 4, CH001, eprint arXiv: 1702.06015, 02/2017.

[2] Durbin DJ, Malardier-Jugroot C, Review of hydrogen storage techniques for on board vehicle applications. International Journal of Hydrogen Energy 2013; 38:15595–14617.

[3] U. Bossel, Renewable Energy World, March-April (2004) 155-159.

[4] M.H.Al-Hashimi, U.-J. Wiese, Self-adjoint extensions for confined electrons: From a particle in a spherical cavity to the hydrogen atom in a sphere and on a cone, Annals of Physics 327, 2012, 2742-2759.

[5] Ravindra Shinde and Meenakshi Tayade, Remarkable Hydrogen Storage on Beryllium Oxide Clusters:First Principles Calculations, Maharashtra 400076, INDIA., and Mumbai, Maharashtra 400019, INDIA, 25 Jul 2016.

[6] D. Harrison, E. Welchman and T. Thonhauser, H4-Alkanes: A new class of hydrogen storage material? Department of Physics, Wake Forest University, Winston-Salem, NC 27109, USA. 22 May 2017.

[7] Vito Dario, Camiola Riccardo Farchioni,Tommaso Cavallucci, Antonio Rossi, Vittorio Pellegrini, ValentinaTozzini, Hydrogen storage in rippled graphene: Perspectives from multi-scale simulations, Pisa Italy, 2013.

[8] Sarah Goler, Camilla Coletti, Valentina Tozzini, Vincenzo Piazza, Torge Mashoff, Fabio Beltram, Vittorio Pellegrini, and Stefan Heun, The Influence

of Graphene Curvature on Hydrogen Adsorption: Towards Hydrogen Storage Devices, Piazza San Silvestro 12, 56127, Pisa Italy, 2010.

[9] Kelly NA,Gibson TL, Cai M, Spearot JA, Ouwerkerk DB, Development of a renewable hydrogen economy: optimization of existing technologies. International Journal of Hydrogen Energy 2010; 35:892–899.

[10] Jain IP, Hydrogen, the fuel for the 21st century. International Journal of Hydrogen Energy 2009; 34:7368–7378.

[11] Wang X, Chen R, Zhang Y, Chen C, Wang Q, Hydrogen storage alloys for high-pressure supra-pure hydrogen compressor. Journal of Alloys and Compounds 2006; 420:322–325.

[12] Hui L, Xinhua W, Zhaohui D, Lou X, Changpin C, A study on 70MPa metal hydride hydrogen compressor. Journal of Alloys and Compounds 2010; 502:503–507.

[13] S.S. Makridis, E. Gkanas, G. Panagakos, E.S. Kikkinides, A.K. Stubos, P. Wagener and S. Barcikowski, Polymer-Stable Magnesium Nanocomposites Prepared By Laser Ablation For Efficient Hydrogen Storage. International Journal of Hydrogen Energy 30 August 2013; Volume 38, Issue 26, Pages 11530-11535.

[14] Xiao J, Bénard P, Chahine R, Charge-discharge cycle thermodynamics for compression hydrogen storage system. International Journal of Hydrogen Energy 41 (2016), pp. 5531-5539.

[15] Hirscher M (ed.). Handbook of hydrogen storage: new materials for future energy storage. Weinheim: Wiley-VCH Verlag GmbH & Co. KgaA; 2010.

ASTES

Advances in Science, Technology and Engineering Systems Journal Vol. 3, No. 4, 130-172 (2018)

www.astesj.com

Special Issue on Multidisciplinary Sciences and Engineering

ASTESJ

ISSN: 2415-6698

Acoustic Signal Processing and Noise Characterization Theory via Energy Conversion in a PV Solar Wall Device with Ventilation through a Room

Himanshu Dehra*

Egis India Consulting Engineers Pvt. Ltd., Egis Tower, Plot # 66, Sector 32, Gurugram (Haryana), 122001, India

ARTICLEINFO

Article history:
Received: 04 June, 2018
Accepted: 24 July, 2018
Online: 29 July, 2018

Keywords:
Acoustics
Signal Processing
Noise Characterization
Energy Conversion
Ventilation
Loudspeaker
PV Solar Wall Device

ABSTRACT

Noise defined as 'a sensation of unwanted intensity of a wave', is perception of a pollutant and a type of environmental stressor. The unwanted intensity of a wave is a propagation of noise due to transmission of waves (viz. physical agents) such as light, sound, heat, electricity, fluid and fire. The characterization of noise interference, due to power difference of two intensities in a wave is presented. Noise interference characterization in a wave is obtained depending on type of wave. Standard definitions of noise sources, their measurement equations, their units and their origins under limiting reference conditions are derived. All types of wave form one positive power cycle and one negative power cycle. The positive and negative noise scales and their units are devised depending on speed of noise interference in a wave. A numerical and experimental study was conducted for supporting the noise characterization theory via ascertainment of energy conversion characteristics of a pair of photovoltaic (PV) modules integrated with solar wall of an outdoor test-room. A pre-fabricated outdoor room was setup for conducting outdoor experiments on a PV solar wall with ventilation through the outdoor room. Acoustic signal processing is supported with some experimental and numerical results of a parallel plate PV solar wall device installed in an outdoor test-room to authenticate the noise interference equations. Detailed discussions on noise characterization theory along with some examples of noise filter systems as per noise sources are also presented. The noise characterization theory is also exemplified with some noise unit calculations using presented noise measurement equations.

1. Introduction

The aim of this paper is to present acoustic signal processing and noise characterization theory with support of energy conversion models and experiments on a photovoltaic (PV) solar wall with ventilation through a room. This paper is an extension of work originally presented in conference [1, 2].

Noise, defined as 'a sensation of unwanted intensity of a wave', is perception of a pollutant and a type of environmental stressor. An environmental stressor such as noise may have detrimental effects on various aspects of health. The unwanted intensity of a wave is a propagation of noise due to transmission of waves (viz. physical agents) such as light, sound, heat, electricity, fluid and fire [1]. A unified theory for stresses and oscillations is applicable so as to take into effect of all the physical agents as an environmental stressor on a human body [3]. As per the theory, the stresses acted on a particle due to interaction of many forces are distinguished as fundamental, internal and external stresses. The existence of fundamental stresses is due to presence of electromagnetic and gravitational forces. The internal stresses are acted under the influence of fundamental stresses and are constituted by composition and properties of a particle. The external stresses are acted under the existence of an external source of energy.

Solar energy conversion occurs at solar cells and solar intensity of incident solar energy is converted into electric power and waste heat. The photovoltaic devices with ventilation provide means for converting waste heat lost to surrounding environment into useful thermal power [2-7]. The composite waves are transmitted in photovoltaic (PV) devices due to stresses and oscillations of incident solar and ventilation energy. In this way solar power intensity is converted into heat, fluid, electricity, light, sound and fire depending on intensities

* Corresponding author: Himanshu Dehra, Email: anshu_dehra@hotmail.com

of its transmitted composite waves in a PV solar wall device.

1.1. Methodology

This paper has summarized the concept of acoustic signal processing and noise characterization theory with aid of energy conversion in a PV solar wall device. Basic definitions on noise characterization are presented in Appendix. Sources of noise are characterized as per physiological responses from human senses. Definitions of various types of noise as per type and speed of wave are presented. Noise measurement equations are deduced from the wave theory. Acoustic or noise filters as per source of various power systems are defined and illustrated with examples. Experimental results on energy conversion are presented on a PV solar wall device. Sensible heat storage capacity and thermal storage capacities are explained for their energy conversion phenomenon.

Some numerical results are also presented to support the noise characterization. In order to further authenticate the noise wave characterization, signal processing is achieved from a PV device composed of RC analogue signal. Acoustic signal processing is supported with some experimental and numerical results of a parallel plate PV solar wall device installed in an outdoor test-room for verification of the noise interference equations. Some noise unit calculations deduced from the numerical model based on newly devised noise measurement equations are also presented in tables. Detailed discussions are also presented on significance of noise characterization theory for: i) cities; ii) acoustics; iii) electrical engineering, instrumentation & control; iv) energy conversion in engines; v) noise pollution and control; vi) fire alarm systems; vii) operation of power systems; viii) friction & oscillations; ix) noise instrumentation; x) automatic control & management in noise systems; xi) potential research themes and graduate teaching subjects.

The following sections define and describe 'noise', its sources, its measurement equations with support of experimental and numerical results of a PV solar wall device with ventilation through a room. Discussions of noise characterization theory on solar energy acoustics, energy conversion model and experiments, acoustic signal processing, noise filters & their examples with description of sensors & transducers for a human brain along with human comfort & health are presented in later sections.

2. Noise Characterization

2.1. Source & Sink of Noise

The strength of a source is defined as total energy flow per unit time and unit length of line. A line which is drawn hypothetically perpendicular to the plane, from which energy is assumed to flow uniformly in all directions at normal angles to it, is defined as a source. It acts as a point in the usual two-dimensional energy flow diagram. The flow is in imaginary radial lines from the source, the current of energy flow is at a distance r from the source. The current is determined by the strength divided by the energy flow area [8-10].

2.2. Psychoacoustics in New Dimensions

The standard sources of noise along with their definitions, their measurement equations and measurement units are presented. A contemporary theory of psychoacoustics was presented for characterization of interference of noise waves due to difference of power of two intensities [11]. The difference of two intensities of power is due to transmission of heat, fluid, light, electricity, fire and sound into a particle body. The sources of noise are classified according to the type of wave of interference. The various types of noise are defined with factors of speed of wave, areas of energy stored in a wave, due to interference and difference of power between two intensities of wave. Noise filters as per source of noise signals from noise power systems are differentiated for filtering unwanted frequencies from solar power, electric power, light power, sound power, heat power, fluid power and fire power.

The interference of noise arises due to difference of power of two intensities [1-13]. The intensity of power for any particle body is a function of development of various stresses. The phenomenon of acoustic resonance arises due to matching of critical stress level with the natural stress level necessary for oscillation of a particle body. The criteria for generation of acoustic resonance include waves propagated with transmission of light, sound, noise, heat, electricity, fluid and fire from a particle body. The psychological feeling of sensation and perception of noise from light, sound, heat, electricity, fluid and fire is a physiological response from the sensory organs of a standard (average) human body.

3. Sources of Noise

The sources of noise are classified according to the type of wave of interference:

Light: In the electromagnetic radiation wavelength band from approximately between 380-765 nm, the visual sensation of light is tested by the eye of an observer with seeing of a radiant energy. The physiological response from an average eye defines units of light. The sensitivity of human eye is not same in all wavelengths or colors. The contribution of adding daylight is visual sensation in the visible region of the solar energy spectrum.

Sound: In the range of frequencies between 20 Hz and 20,000 Hz, the sound is evaluated due to presence of fluid pressure energy as a hearing sensation by the ear. The sound units are based on the functional feedback of an average ear. The sensitivity of sound to the whole frequency band is not same for human ear.

Heat: In the electromagnetic radiation between 0.1 μm to 100 μm, the heat as a temperature sensation is examined by the human body. The sensation function of temperature defines units of heat. The temperature sensation function is a measure of coldness and hotness. The comfort zone of temperature is evaluated from functional feedback of a human body which also defines thermal comfort. The contribution to discomfort of human body is in the ultra violet region of solar energy spectrum.

Electricity: With passing of direct current or an alternating

current, the electricity as a shock sensation is evaluated by skin of an observer due to electromagnetic energy stored in a conductor which is short-circuited by a human body.

Fluid: The fluid as combined ventilation and breathing sensation is evaluated by amount of fluid passed either externally or internally through a standard (average) human body.

Fire: The exposure of radiant energy and fluid acting on skin surface of an average human body, defines the fire as a sensation of burning.

4. Noise Measurement Equations

The following standard measurement equations are derived and adopted from the standard definitions for sources of noise interference as mentioned in Appendix.

Noise of Sol: For a pack of solar energy wave, the multiplication of solar power storage and the velocity of light gives solar power intensity I. On taking logarithm of two intensities of solar power, I_1 and I_2, provides intensity difference. It is mathematically expressed as:

$$Sol = \log(I_1)(I_2)^{-1} \quad (1)$$

Whereas logarithmic unit ratio for noise of sol is expressed as *Sol*. The oncisol (oS) is more convenient for solar power systems. The mathematical expression by the following equality gives an oncisol (oS), which is $1/11^{th}$ unit of a *Sol*:

$$oS = \pm 11\log(I_1)(I_2)^{-1} \quad (2)$$

Noise of Therm: For a pack of heat energy wave, the multiplication of total power storage and the velocity of light gives heat power intensity I. The pack of solar energy wave and heat energy wave (for same intensity I), have same energy areas, therefore their units of noise are same as *Sol*.

Noise of Photons: For a pack of light energy beam, the multiplication of total power storage and the velocity of light gives light power intensity I. The pack of solar energy wave and light energy beam (for same intensity I), have same energy areas, therefore their units of noise are same as *Sol*.

Noise of Electrons: For a pack of electricity wave, the multiplication of total electrical storage and the velocity of light gives electrical power intensity I. The pack of solar energy wave and electricity wave (for same intensity I), have same energy areas, therefore their units of noise are same as *Sol*.

Noise of Scattering: For a pack of fluid energy wave, the multiplication of total power storage and the velocity of fluid gives fluid power intensity I. On taking logarithm of two intensities of fluid power, I_1 and I_2, provides intensity difference. It is mathematically expressed as:

$$Sip = \log(I_1)(I_2)^{-1} \quad (3)$$

Whereas, logarithmic unit ratio for noise of scattering is *Sip*. The oncisip (oS) is more convenient for fluid power systems.

The mathematical expression by the following equality gives an oncisip (oS), which is $1/11^{th}$ unit of a *Sip*:

$$oS = \pm 11\log(I_1)(I_2)^{-1} \quad (4)$$

For energy area determination of a fluid wave, the water with a specific gravity of 1.0 is the standard fluid considered with power of ±1 Wm^{-2} for reference intensity I_2.

Noise of Scattering and Lightning: For a pack of fire wave, the intensity I, of fire flash with power of light, is the multiplication of total power storage and the velocity of light. Whereas for a pack of fire wave, the intensity, I, of fire flash with power of fluid, is the multiplication of total power storage capacity and velocity of fluid.

- For a noise due to fire flash, the collective effect of scattering and lightning is to be obtained by superimposition principle.
- For same intensity I, the pack of solar energy wave and a fire flash with light power have same energy areas, therefore their units of noise are same as *Sol*. The therm power may also be included in fire flash with power of light.
- For same intensity I, the pack of fluid energy wave and a fire flash with fluid power have same energy areas, therefore their units of noise are same as *Sip*. In determining the areas of energy for the case of fluids other than water, a multiplication factor in specific gravity of fluid is to be considered.

Noise of Elasticity: For a pack of sound energy wave, the product of total power storage and the velocity of sound gives sound power intensity I. On taking logarithm of two intensities of sound power, I_1 and I_2, provides intensity difference. It is mathematically expressed as:

$$Bel = \log(I_1)(I_2)^{-1} \quad (5)$$

Whereas, logarithmic unit ratio for noise of elasticity is *Bel*. The oncibel (oB) is more convenient for sound power systems. The mathematical expression by the following equality gives an oncibel (oB), which is $1/11^{th}$ unit of a *Bel*:

$$oB = \pm 11\log(I_1)(I_2)^{-1} \quad (6)$$

4.1. Limiting Conditions

The Table 1 summarises units of noise and their limiting conditions.

Table 1: Noise under Limiting Conditions

Reference[a] (I_2 = ±1 Wm^{-2})	Noise Scales and limiting Conditions		
	Noise of Sol	**Noise of Scattering**	**Noise of Elasticity**
Units	**Sol**	**Sip**	**Bel**
I_1 = 1 Wm^{-2}	No Positive Solar Energy	No Positive Fluid Energy	No Positive Sound Energy
I_1 = 1+→0 Wm^{-2}	Decreasing Solar Energy	Decreasing Fluid Energy	Decreasing Sound Energy
I_1= + ve	Increasing Solar Energy	Increasing Fluid Energy	Increasing Sound Energy
I_1 = -1 Wm^{-2}	Negative Solar Energy	Negative Fluid Energy	Negative Sound Energy
	Darkness	Low Pressure	Inaudible range
I_1 = -ve	Darkness increasing, distance from point source of light increasing	Low pressure increasing, vacuum approaching	Inaudible range increasing, vacuum approaching
I_1 = -1+→0 Wm^{-2}	Negative Solar Energy	Negative Fluid Energy	Negative Sound Energy
	Decreasing Darkness	Decreasing Low Pressure	Decreasing inaudible range
* Reference value of I_2 = ±1 Wm^{-2} signifies the limiting condition with areas of noise interference approaching to zero.			

There are following elaborative points on choosing an *onci* as $1/11^{th}$ unit of noise [1]:

i) Reference value used for I_2 is -1 W m^{-2} on positive scale of

noise and 1 W m^{-2} on negative scale of noise. In a power cycle, all types of wave form one positive power cycle and one negative power cycle (see Figure 10). Positive scale of noise has 10 positive units and one negative unit. Whereas, negative scale of noise has 1 positive unit and 10 negative units;

ii) Each unit of sol, sip and bel is divided into 11 parts, 1 part is $1/11^{th}$ unit of noise;

iii) The base of logarithm used in noise measurement equations is 11;

iv) Reference value of I_2 is -1 W m^{-2} with I_1 on positive scale of noise, should be taken with negative noise measurement expression (see Eqs 2, 4 and 6), therefore it gives positive values of noise;

v) Reference value of I_2 is 1 W m^{-2} with I_1 on negative scale of noise, should be taken with positive noise measurement expression (see Eqs 2, 4 and 6), therefore it gives negative values of noise.

5. Noise Filters

The noise filters are classified as per source signal of unwanted frequencies from solar power, electric power, light power, sound power, heat power, fluid power and fire power. An acoustic filter is an electrical analog circuit of various combinations of RC feedback circuit with an operational amplifier and is used to filter unwanted frequencies of oscillations from a power system [14]. It is a network with selective transmission for currents from a power system of varying frequency. The unwanted frequencies generated from a power system are removed by using an operational amplifier with different combination of filter arrangements. An operational amplifier is an integrated circuit that consists of several bipolar transistors, resistors, diodes, and capacitors, interconnected so that amplification can be achieved over a wide range of frequencies [15].

The action of filtering the frequency from a power system is based on the variation in the reactance of an inductance or a capacitance with change in frequency. The band of frequencies that can be removed from a power system can be at the low frequency end of frequency spectrum, at the high frequency end, at both ends, or in the middle of the spectrum. The filters to perform each of these operations are known respectively as low-pass filters, high-pass filters, band-pass filters and band-stop filters. There are many configurations of design of filters. The filters are divided into passive and active configurations. The passive filters are less effective simple circuits constructed with resistors, capacitors, and inductors. The active filters are useful in providing an effective filtering action than passive filters. The active filters require a source of operating power.

5.1. Noise Filter Systems

The criteria for definitions of filters for noise filtering is based on areas of energy stored in a wave due to noise interference, speed of wave and difference of power between two intensities of wave. The filtered noise signals are considered from systems of solar power, electric power, light power, sound power, heat power, fluid power and fire power. The noise filters as per sources of noise are defined as follows:

Filter for noise of sol: This filter is used to filter noise due to difference of power intensities between two solar power systems. Example: window curtain, window blind, wall and glass.

Filter for noise of therm: This filter is used to filter noise due to difference of power intensities between two heat power systems. Example: house, insulation, clothing and furnace.

Filter for noise of photons: This filter is used to filter noise due to difference of power intensities between two light power systems. Example: 3-D vision of any object, electric bulb, television, computer and LCD screen laptop.

Filter for noise of electrons: This filter is used to filter noise due to difference of power intensities between two electrical power systems. Example: AM/FM radio clock with ear phones, telephone instrument with ear phones and CD audio player with ear phones.

Filter for noise of scattering: This filter is used to filter noise due to difference of power intensities between two fluid power systems. Example: electric fan, pump, motor vehicle, river stream and tap water.

Filter for noise of scattering and lightning: This filter is used to filter noise due to difference of power intensities between two fire power systems. Example: lighter, matchstick, gas stove, locomotive engine and thunder-bolt.

Filter for noise of elasticity: This filter is used to filter noise due to difference of power intensities between two sound power systems. Example: your vocal apparatus, organ pipe, thunder-bolt and drum beats.

6. Some Examples of Noise Filters

Some examples of noise filters are enumerated as under.

6.1. Human Voice Production

The example of phonetics of filtering sound of a human speech is illustrated. The human speech is synthesized due to development of stresses at vocal folds [16-17]. The smoothening of the sound is function of its amplitude and its shape of oscillations at vocal tract of a human being. The vocal tract is a resonant cavity wall with sound energy stored in oscillations of its vocal folds. The vocal chords showing mechanism of synthesis of human speech is illustrated in Figure 1.

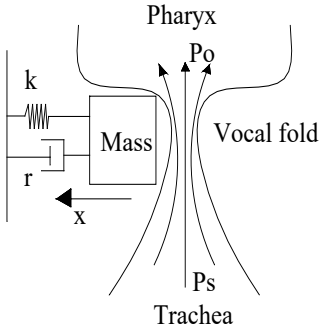

Figure 1: A human vocal mechanism

6.2. An Airflow Window with a Photovoltaic Solar Wall

The filtering of solar energy is illustrated through an example of an airflow window attached with a shading device. An airflow window is fixed with a movable roller blind to control the transmission of daylight as well as amount of solar heat. The bottom portion of photovoltaic solar wall is used for controlling the amount of air ventilation along with generation of solar electric power. The example is illustrated in Figure 2.

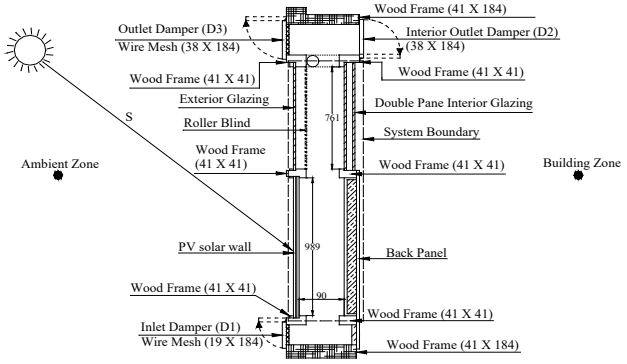

Figure 2: An Airflow window with a Photovoltaic Solar Wall (Dimensions shown are in mm).

6.3. Psychrometric Air Conditioner

An elementary air conditioner for summer comfort conditioning consists of a cooling coil, a cooling fluid with a filter [18]. The schematic of operation of a psychrometric air conditioner is illustrated in Figure 3.

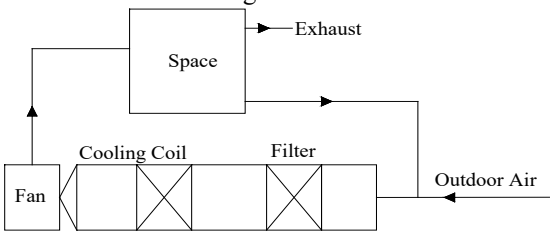

Figure 3. A psychrometric air conditioner

6.4. Telephone Line

The impedance of a telephone line is composed of distributed resistance, capacitance, and inductance [19]. The impedance of telephone line is proportional to the insulation, loop length and whether the wire is buried, aerial or bare parallel wires strung on telephone pole. A telephone line is usually supplied with a 48 VDC from the telephone exchange. The schematic of operation of a telephone line with telephone instrument is illustrated in Figure 4.

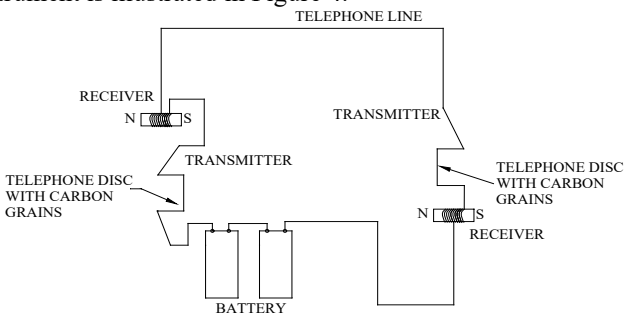

Figure 4: Operation of a Telephone Line.

6.5. Fire and Smoke Detection System

A fire detection system consists of a control system with interconnected alarms, smoke and heat detectors. A fire detector is a device which is used for presetting an alarm at a particular temperature. A smoke detector is a device which is used for presetting an alarm when a certain percentage of smoke accumulates. The photovoltaic cell activates the smoke alarm only if it senses requisite obscuration of light over a unit area with control from BMS [20]. The schematic of various components for fire detection system is illustrated in Figure 5. The detail description of a fire alarm systems is provided later in discussions.

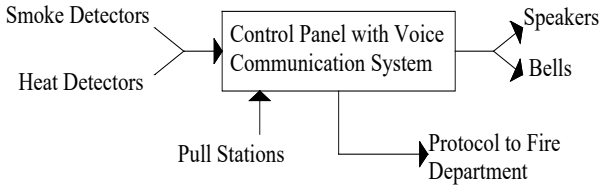

Figure 5: A fire detection system

7. Experiments

Many studies on facade integrated PV system are focused on the model simulation of radiation and convection [21-36]. Kim and Kim [28] compared three different types of integrated PV-thermal system configurations. The study analyzed the system performance as well as the building performance. Various researchers [29-30] have also conducted research on the energy performance and efficiency of actively air cooled PV modules integrated into facades.

In the present study, the salient feature of a pair of PV modules used in solar wall was the glass coating surrounding the semiconductor material of solar cells [24-25]. The manufacturing of glass coated PV modules was based on multi-crystalline solar cell technology. The operating conditions were selected for conducting various experiments on a PV solar wall. The indoor solar simulator tests were conducted for PV modules under standard operating conditions. The outdoor tests were conducted under available climatic conditions for obtaining temperatures, air velocities, thermal time constants, heat capacity, and thermal storage capacity of a PV solar wall. The PV modules used for experiments were having a glass coating of 3 mm attached on its exterior and interior sides. The glass coating was attached to exterior and interior sides of PV modules in the form of glass sheets by a double-glass (PWX) manufacturing technology. Each PV module was having 36 multi-crystalline solar cell units, with thin transparent gaps in between them. The glass coating on PV modules has improved the overall performance of PV modules in many ways; it has: i) protected semi-conductor material from weather deterioration; ii) absorbed ultra violet rays of solar energy and trap solar heat in glass coating, thus increasing the temperature of the surrounding environment; iii) reduced the reflection losses of sunlight rays reflected from PV module; iv) improved the aesthetic appearance of PV module; v) increased the thermal

mass of PV module; and vi) enhanced the structural strength of PV module. The pictorial view of glass coated PV module used in experiments is illustrated in Figure 6. The typical characteristics of glass coated PV module without frame were: dimensions of 993 mm by 453 mm and a thickness of 6.2 mm with glass coating, typical current of 2.8 A, typical voltage of 17 V, temperature coefficients of current and voltage were + 0.034 %/°C and -2.17 mV/°C/solar cell at standard test conditions [2, 24].

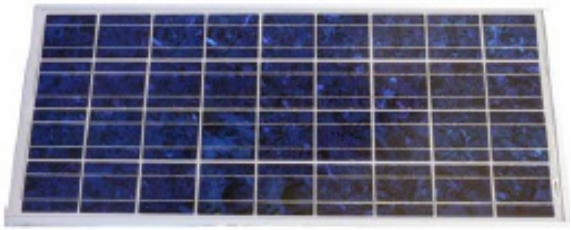

Figure 6: Glass coated PV module used in experiments

The indoor measurement tests were carried out in an indoor simulation test facility of CANMET Energy Technology Centre of Natural Resources, Varennes, Québec, Canada [2]. The schematic of indoor solar simulator used for establishing characteristics of glass coated PV modules is illustrated in Figure 7.

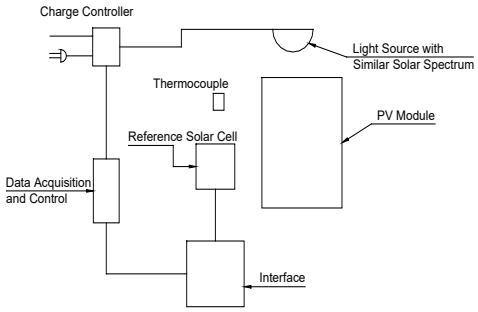

Figure 7 Block diagram of an indoor solar simulator

The current-voltage and power-voltage characteristics of one of the PV modules are shown in Figs. 8 and 9 [2]. Table 2 has presented characteristics of a pair of PV modules established with an indoor solar simulator [2]. As presented in Table 2, electrical conversion efficiency to the order of 8.9% was reported from indoor simulator tests. The current-voltage and power-voltage characteristics of tested PV module are illustrated in Figs. 8 and 9.

Table 2: Characteristics of glass coated pv modules established with an indoor solar simulator

PV Module	Solar Intensity (Wm^{-2})	Spectrum	Isc (A)	Voc (V)
PW30	1009.11	1.5 A.M. Class B	2.833	21.296
PW31	1007.58	1.5 A.M. Class B	2.829	21.352
PV Module	Vmax (V)	Pmax (Watts)	Fill Factor	Efficiency (%)
PW30	16.198	42.157	0.6985	8.703
PW31	16.503	43.435	0.7188	8.981

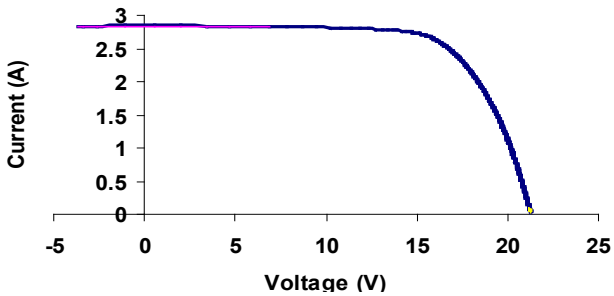

Figure 8: Current-voltage characteristics of PW30

After determining current-voltage and power-voltage characteristics from an indoor solar simulator, the pair of glass coated PV modules was installed in the test section of an outdoor test-room. The outdoor experiments were conducted on PV modules in order to determine energy conversion characteristics and further improving the overall performance of PV modules by using thermal mass of an outdoor room.

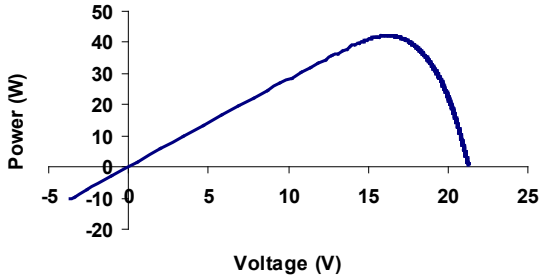

Figure 9: Power-voltage characteristics of PW30

The outdoor room was a pre-fabricated structure that was delivered into the premises of Concordia University in Montréal, Québec, Canada for conducting experiments on glass coated PV modules [2]. The test section with vertical PV modules, was aligned 10° East of South for receiving maximum solar radiation between 8.00 and 14.00 hrs solar time and also avoiding shading from adjacent buildings. The schematic of an outdoor room used for conducting outdoor experiments is illustrated in Figure 10. The outdoor experiments were conducted on a solar wall section built with two commercially available glass coated PV modules, an air passage with gap width of 90 mm, an insulating panel, side walls made up of Plexiglas and connected wooden frames. The insulation panel was assembled with 7 mm thick plywood board enclosure filled with 26 mm polystyrene. The steady state average resistance of the composite plywood board-polystyrene section of insulation panel obtained from the heat flow meter test was 1.0 m^2 °C W^{-1} [2]. The side wall of wooden frame was fixed with Plexiglas of thickness 12 mm (k = 0.1316 W m^{-1} K^{-1}) placed perpendicularly facing air-gap for view of the air passage from inside the test room.

A series electrical circuit connection was established for a pair of vertical PV modules installed on a solar wall for determining the current-voltage measurements and electric power output. The electrical circuit for two PV modules connected in series for generation of electric power with a

rheostat of maximum varying resistance up to 50 Ω is illustrated in Figure 11. A circular variable resistor of 50 Ω was a wire-wound coil with a sliding contact that was used to vary electrical resistance without interrupting the current. The Joule heating at a rate of 73 cal/s (305 W) was predictable at a typical current rating of 2.8 A for a PV module. The null resistance of rheostat was calculated to be 39 Ω at a current of 2.8 A, which was not having any potential difference across it. In Figure 6, the sliding contact of rheostat has a resistance of R_s, with a current ($i= V_r/R_s$) flowing across the circuit; V_r is potential difference across the resistance, R_s.

The passive air ventilation was created in the PV module test section by natural wind or through buoyancy effect in the absence of wind. The active fan pressure was used to achieve higher air velocities by operation of the exhaust fan fixed on opposite façade with respect to the PV test section. The slight negative pressure was induced for drawing low air velocities in absence of wind-induced pressure from the inlet damper into the PV test section through the outdoor room. The exhaust ventilation fan was rated at 270 CFM (ft3/min) (0.127 m3 s-1) at standard atmospheric pressure so as to create between 10-25 Pa of negative pressure depending on the air leakage from the outdoor room.

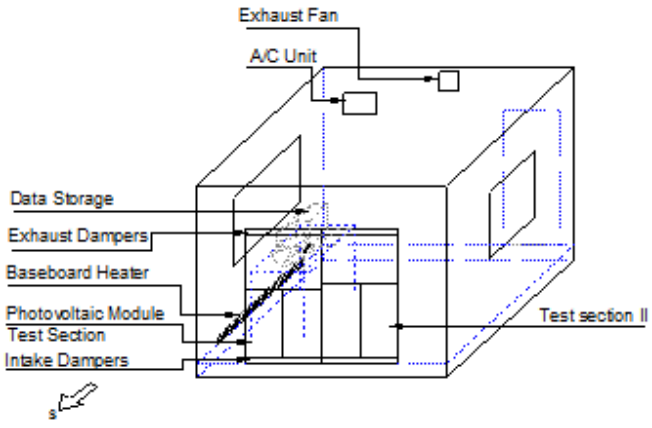

Figure 10: Schematic of a pre-fabricated outdoor room with PV solar wall test section

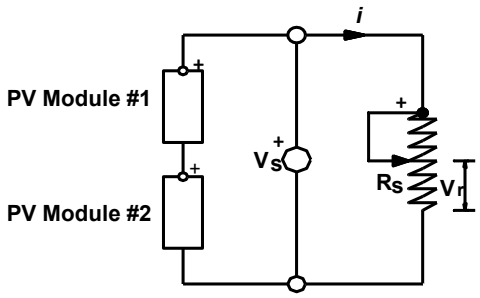

Figure 11: Electric circuit for PV modules

The air velocities near the exit of PV modules were obtained both as a measure of buoyancy and fan induced hybrid ventilation. The fan pressure was created with an exhaust fan fixed on wall of an outdoor room opposite to wall with a wooden frame installed with glass coated PV modules. The air velocity sensor was placed perpendicular to the walls of the PV solar wall section for measuring axial air velocities near its outlet.

In order to minimize boundary layer effect in air velocity measurement, air velocity sensor was placed at middle air-gap width at a distance of 45 mm from either of the walls of the PV solar wall. To minimize turbulence effects in air velocity measurement, air velocity sensor was placed near the outlet (at 1100 mm from the bottom) of the PV test section with total air passage length of 2100 mm in the test section. To minimize three-dimensional effect in air velocities, fan-induced active ventilation was achieved by developing air velocities by the induced draft fan fixed on the opposite wall so that it was placed at a distance from the walls of PV module test section. It was validated by one of the experiments that measured surface temperatures of the two adjacent glass coated PV modules were within ±0.5 °C under similar operating conditions.

7.1. Outdoor Measurements

Three thermocouple sensors were placed at the top, middle, and bottom locations in the PV module, air-passage, and insulating panel. They were used to measure their local temperatures at their defined fixed positions. Two thermocouples were used to measure the inside test room air temperature and ambient air temperature. One differential thermocouple was used to check the air temperature difference between top and bottom sections of the PV module test section. The thermocouple outputs, current, voltage, solar irradiation, and air velocity signals were connected to a data logger and a computer for data storage. The copper-constantan junction (T-type) thermocouples were used for measurements for generating voltage signals to the data logger. As mentioned earlier, the air velocity sensor (make-Dwyer instruments, model no. 640-0) was used to collect air velocity measurements. The solar intensity measurements were collected with a photometer sensor fixed on the south wall of an outdoor room. The schematic of outdoor experimental apparatus for a PV solar wall device is illustrated in Figure 12.

7.2. Temperature Plots

The measurements collected from the sensors were recorded in a data logger as a function of air velocities through a PV solar wall for the cases of passive ventilation and active ventilation with use of fan pressure. Similarly, temperature measurements were obtained from the PV solar wall section as a function of air velocities. The temperatures for PV module, air passage, and insulating panel in the PV solar wall were obtained. The sample measurements obtained from outdoor experimental setup are presented in Table 3.

The temperature plots for PV module, insulating panel, and air for different conditions of ventilation are illustrated in Figs. 13 and 14. The temperature plots with respect to height of a PV solar wall for the data provided in Tables 3 to 5 are obtained. The variation of mean temperatures of PV module, insulating panel, and air in a PV solar wall with approximately steady solar noon irradiation with varying air velocities for the case of active ventilation and passive ventilation are illustrated in Figs. 15 to

16. Temperature differences for various cases of ventilation are provided in Figure 17(a) and 17 (b).

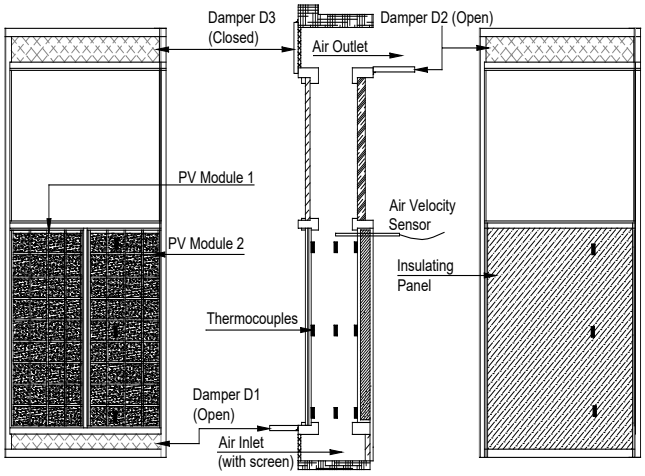

Figure 12: Schematic of outdoor experimental apparatus for a PV solar wall installed on a wooden frame

7.3. Sensible Heat Storage Capacity

The PV solar wall test section with wooden frame was composed of non-homogeneous materials having different densities, specific heats, and thicknesses. The pair of PV modules was fixed with three layers of material, viz. a flat sheet of solar cells, glass sheets on its exterior and interior sides. It was assumed that surface temperature of PV module was uniformly distributed in the three layers. It was also assumed that the heat capacity of the wooden frame and sealing material was having little effect on the temperature of PV module, air or insulation panel. This was because of the fact that wood was used as a construction material, and moreover, the magnitude of the heat capacity of wood framing material was not proportional to the face area of glass coated PV modules. The sensible heat capacities of glass faces, solar cells, air and polystyrene filled plywood board are presented in Table 4. It was observed that the difference of temperatures recorded by the top and bottom sensors for PV module, air and insulating panel were 6.9 °C, 8.1 °C, and 9.9 °C, respectively, for the critical case of passive ventilation of Run no. 4 in Table 3. Furthermore, the temperature differences were used for obtaining sensible heat storage capacities of various components in y-ordinate. The heat storage capacities obtained were 59.6 kJ, 0.755 kJ, and 510.7 kJ for PV module, air and insulation panel respectively. The heat capacities obtained were negligible in comparison with the total daily solar irradiation on PV modules on the day of conducting the outdoor experiments. It was also assumed that there were constant surface properties and ideal still air at the instance of collection of the measurements. Heat storage capacity in x-ordinate was also obtained from the similar procedure by assuming same proportionate temperature difference along thicknesses in x-ordinate. It was found that heat capacity in x-ordinate was nil in comparison with the value of heat capacity obtained for y-ordinate.

Table 3: Outdoor Measurement

Run No.	S ($W\ m^{-2}$)	E_p (W)	T_o (°C)	T_s (°C)	V ($m\ s^{-1}$)
		Active ventilation (Fan-assisted)			
1	716.1	30.7	15.2	22.4	0.68
2	716.1	30.7	13.4	22.4	0.53
		Passive ventilation (Buoyancy-induced)			
3	697.5	28.9	13.2	25.1	0.13
4	697.5	28.8	13.3	24.9	0.17

Run No.	T_p(b) (°C)	T_p(m) (°C)	T_p(t) (°C)	T_b(b) (° C)	T_b(m) (°C)	T_b(t) (°C)	T_a(b) (°C)	T_a(m) (°C)	T_a(t) (°C)
				Active ventilation (Fan-assisted)					
1	35.4	33.8	36.8	20.6	24.7	29.1	18.8	21.7	19.4
2	35.9	34.6	37.9	20.9	25.0	29.5	19.3	22.5	19.9
				Passive ventilation (Buoyancy-induced)					
3	40.8	44.9	46.8	27.9	34.8	38.0	21.3	29.5	29.8
4	39.9	45.0	46.8	28.4	35.0	38.3	21.7	28.3	29.8

Distance as per locations shown in Figure 7	T_p(b) (°C)	T_p(m) (°C)	T_p(t) (°C)	T_b(b) (°C)	T_b(m) (°C)
y (cm)	15	55	94	15	55
z (cm)	60	60	60	60	60
x (mm)	6.2	6.2	6.2	96.2	96.2

Distance as per locations shown in Figure 7	T_b(t) (°C)	T_a(b) (°C)	T_a(m) (°C)	T_a(t) (°C)	Air velocity sensor
y (cm)	94	15	55	94	99
z (cm)	60	60	60	60	60
x (mm)	96.2	51.2	51.2	51.2	51.2

Note: x is horizontal; y is vertical; z is adjacent 3rd axis of x-y plane

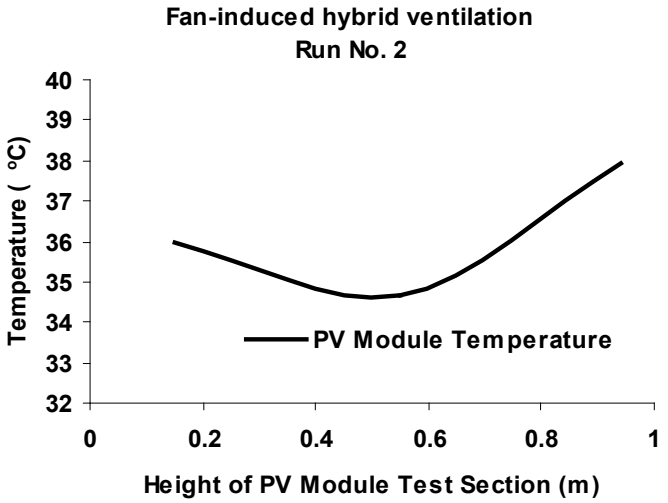

Figure 13: (a) Temperature plot of PV module for fan-assisted ventilation with height of PV solar wall section

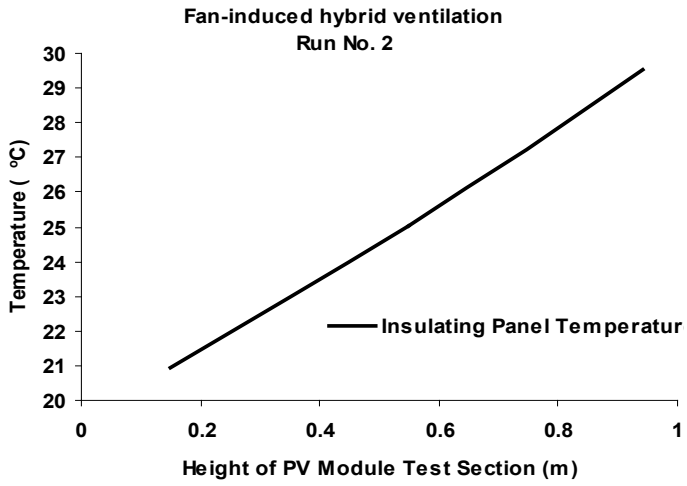

Figure 13: (b) Temperature plot of insulating panel for fan-assisted ventilation with height of PV solar wall section

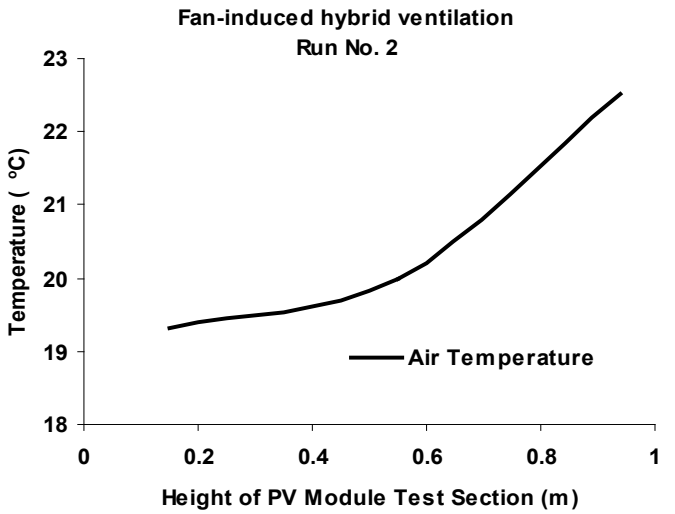

Figure 13: (c) Temperature plot of air for fan-induced hybrid ventilation with height of PV solar wall section

Table 4: Sensible heat storage capacities

Component	ρ_n (kg m^{-3})	C_n (J kg^{-1} K^{-1})	d_n (m) X 10^{-3}	$d_n\rho_nC_n$ (J m^{-2}K^{-1})	H_{pv-T} (J K^{-1})
Glass coating	3000	500	3	4500	4171.5
PV module	2330	677	0.2	315.48	292.45
Glass coating	3000	500	3	4500	4171.5
Sub-total	-	-	-	-	8635.5
Air	1.1174	1000	90	100.56	93.22
Plywood	550	1750	7	6737.5	6245.66
Polystyrene	1050	1200	26	32760	30368.5
Plywood	550	1750	7	6737.5	6245.66
Sub-total	-	-	-	-	42953.0
Total	-	-	-	-	51588.5

Note: Heat capacities were calculated for face area of PV module test section of 0.927 m^2.

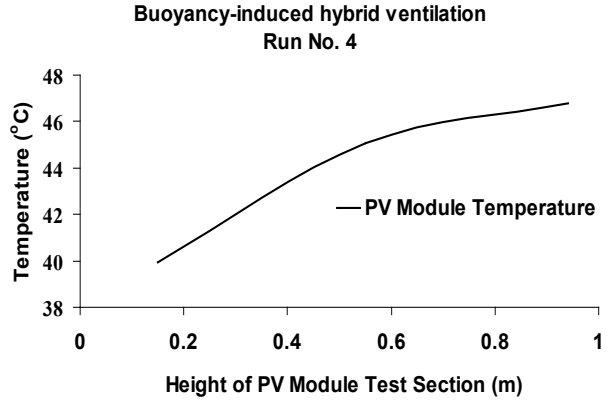

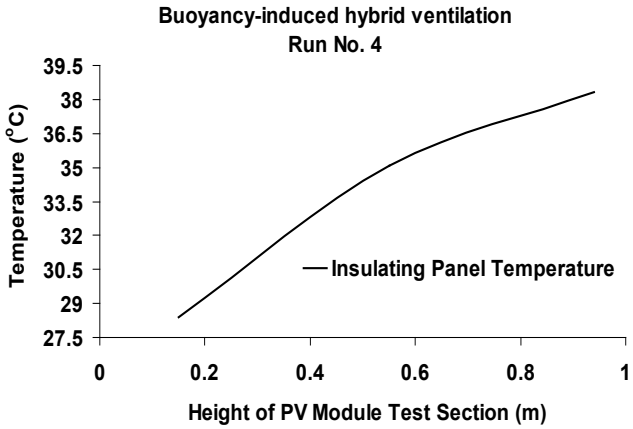

Figure 14: (b) Temperature plot of insulating panel for buoyancy-induced hybrid ventilation with height of PV solar wall section

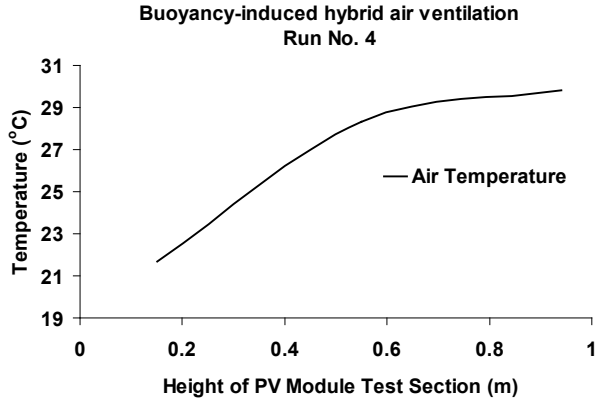

Figure 14: (c) Temperature plot of air for buoyancy-induced hybrid ventilation with height of PV solar wall section

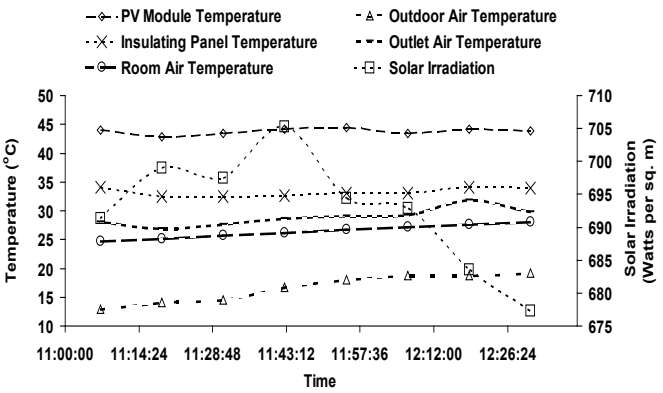

Figure 16: Variation of mean temperatures of PV module, air and insulating panel with solar irradiation under buoyancy-induced hybrid ventilation

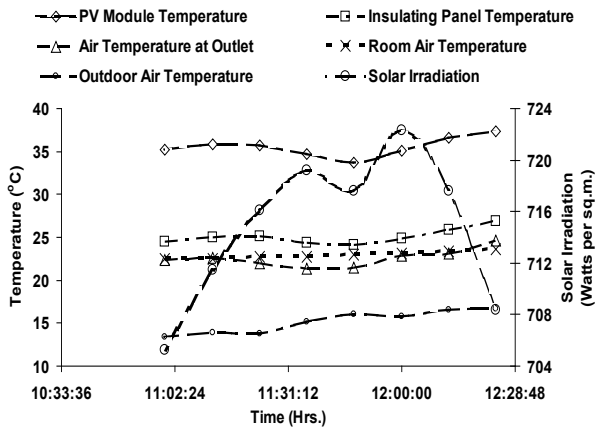

Figure 15: Variation of mean temperatures of PV module, air and insulating panel with solar irradiation under fan-induced hybrid ventilation

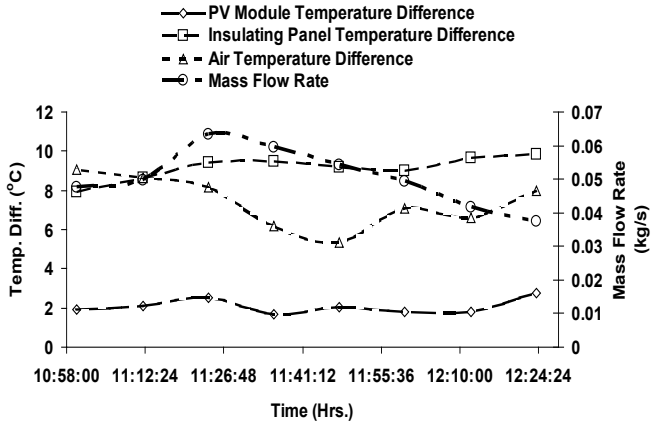

Figure 17(a): Temperature difference for PV module, insulating panel and air with height of PV solar wall under fan-induced hybrid ventilation

Table 5: Thermal storage capacities

Component	k_d (W m^{-1} K^{-1})	$d_n\rho_nC_n$ (J $m^{-2}K^{-1}$)	H_d ($Wm^{-2}K^{-1}$)	T (sec)	ΔT_V (K)	ΔT_H (K)	Q_V (kJ)	Q_H (J)
PV module	0.91	9315.48	10	932	6.9	0.04	5.8	0.2
Air	0.02624	100.56	10.0	10	8.1	0.75	0.0	0.0
Plywood	0.0835	6737.5	10.0	674	9.9	0.40	0.55	0.16
Polystyrene	0.02821	32760	1.0	32760	9.9	0.40	9.0	9.6
Plywood	0.0835	6737.5	10.0	674	9.9	0.40	0.55	0.16
Total	-	-	-	-	-	-	15.9	10.12

Notes:

1. Equivalent thermal conductivity of glass coated PV module was calculated to be 0.91 W m^{-1} K^{-1}
2. Temperature differences along y-direction i.e. along height of PV module test section (0.993 m) were obtained from Table III for Run No. 4 in the case of buoyancy-induced hybrid ventilation.
3. Temperature differences along x-direction i.e. along thicknesses of each component of PV module test section were obtained proportionate to temperature differences along y-direction.

Table 6: Temperature difference and noise of sol with solar irradiation (air velocity: 0.75 $m \cdot s^{-1}$)

Solar irradiation ($W \cdot m^{-2}$)	Air Temperature Difference (ΔT) °C	Noise of Sol oS (oncisol)
450	15.50	28
550	18.90	28.93
650	22.40	29.7
750	25.90	30.36
850	29.40	30.91

Table 7: Temperature difference and noise of scattering with air velocity (S = 650 W·m^{-2})

Air velocity (m·s^{-1})	Fluid Power (W·m^{-2})	Air Temperature Difference (ΔT) °C	Noise of Scattering oS (oncisip)
1.35	47.62	15.28	17.72
1.05	37.0	18.22	16.50
0.75	26.45	22.40	15.02
0.45	15.87	28.15	12.65
0.15	05.29	29.80	07.64

Table 8: Mass flow rate and noise of therm with (ΔT) °C

(ΔT) °C	Mass flow rate (Kg·s^{-1})	Thermal Power (W·m^{-2})	Noise of Therm oS (oncisol)	(ΔT) °C	Mass flow rate (Kg·s^{-1})	Thermal Power (W·m^{-2})	Noise of therm oS (oncisol)
15.50	0.01376	71.09	19.5602	15.28	0.0231	117.65	21.868
18.90	0.01275	80.325	20.119	18.22	0.0171	103.85	21.296
22.40	0.0120	89.6	20.614	22.40	0.0120	89.6	20.614
25.90	0.0115	99.2833	21.043	28.15	8.1 X 10^{-3}	76.0	19.866
29.40	0.0111	108.78	21.505	29.80	6.2 X 10^{-3}	61.59	18.898

Table 9: Noise of elasticity with air particle velocity (Impedance Z_0 = 413 N·s·m^{-3} at 20°C)

Air velocity (m·s^{-1})	Fluid Power (W·m^{-2})	Noise of Scattering oS (oncisip)	Sound Pressure (N·m^{-2})	Sound Power Intensity (W·m^{-2})	Noise of Elasticity oB (oncibel)
1.35	47.62	17.72	557.5	752.7	30.36
1.05	37.0	16.50	433.65	455.33	28.05
0.75	26.45	15.02	309.75	232.31	24.97
0.45	15.87	12.65	185.85	83.63	20.24
0.15	05.29	07.64	61.94	09.29	10.12

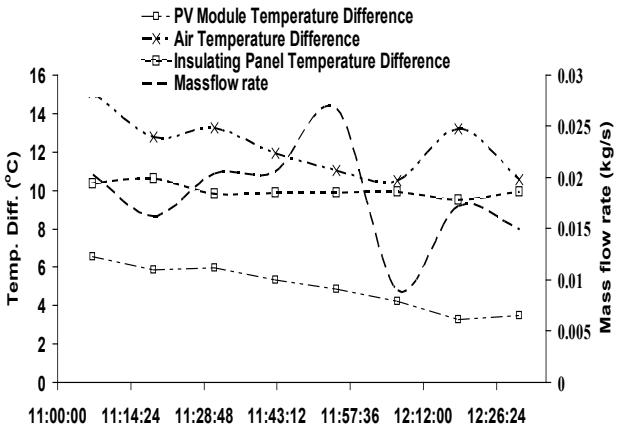

Figure 17(b): Temperature difference for PV module, insulating panel and air with height of PV solar wall under buoyancy-induced hybrid ventilation

8. Numerical Model

The initial boundary values in the model are based on the measured values of quasi steady-state solar irradiation, ambient air temperature, and room air temperature and air velocities. The measured boundary values were then used to obtain solutions for heat equations of the photovoltaic solar wall section. The actual observed temperatures from the experimental apparatus were then compared with the simulated temperatures obtained from the model.

The results of noise unit calculations using Equations 2, 4 and 6 for an outdoor duct exposed to solar radiation are tabulated in Tables 6 to 9. The results of the 2-D numerical model are presented in Table 10 and are obtained by assuming constant fluid and surface properties.

The variation of temperature of air with height of the photovoltaic solar wall test section is illustrated in Figure 18. Figure 18 also illustrates the deviation caused in the proposed model solution in comparison with the ideal exponential or logarithmic temperature variation.

The profiles of surface temperatures of PV module and back panel along the height of the solar wall section are illustrated in Fig, 19. The deviation from the ideal exponential and logarithmic temperature profiles of PV module and back panel is also presented in Figure 19. It was observed that significant cooling of surface of PV module was achieved by radiation heat exchange with the back panel. The surface temperatures of PV module and back panel for four different runs representing variation in solar intensities are presented in Table 10.

8.1. Thermal Time Constant

The thermal time constant is defined as the time required for the outlet air temperature to attain 63.2% of the total difference in value attained in air temperature following a step change in temperature of outdoor air crossing the inlet opening of the PV solar wall. Data for a step change were selected for observing the ambient air temperature. The data selected were in a steady state before and after the time-interval during the unsteady state response of the outlet air temperature with the step change in ambient air temperature. From the graphs, it was observed that thermal time constant under passive air ventilation was between 8-10 minutes in comparison to 2 minutes under active air ventilation. Therefore, it was decided that duration of time

Table 10: Results obtained from 2-d numerical model

Input values	Run no. 1			Run no. 3			Run no. 5			Run no. 7		
S (W m^{-2})	65.1			362.7			520.8			725.4		
E_p (W)	1.2			29.5			31.3			31.1		
T_o (° C)	10.6			11.1			10.8			14.5		
T_s (° C)	15.8			17.9			18.8			22.6		
v (m s^{-1})	0.794			0.597			0.642			0.425		
y (m)	T_a (°C)	T_p (°C)	T_b (°C)	T_a (°C)	T_p (°C)	T_b (°C)	T_a (°C)	T_p (°C)	T_b (°C)	T_a (°C)	T_p (°C)	T_b (°C)
0.0495	10.63	12.97	11.27	11.28	23.66	16.13	11.03	25.67	15.02	15.25	33.87	19.91
0.1485	10.66	12.95	11.57	11.47	23.53	17.19	11.36	25.56	16.14	16.01	33.90	21.57
0.2475	10.69	12.95	11.64	11.66	23.53	17.52	11.69	25.61	16.62	16.76	34.14	22.49
0.3465	10.72	12.96	11.68	11.84	23.57	17.74	12.02	25.72	16.98	17.49	34.45	23.17
0.4455	10.75	12.96	11.70	12.02	23.62	17.89	12.35	25.86	17.28	18.21	34.80	23.80
0.5445	10.79	12.98	11.73	12.21	23.69	18.01	12.67	26.01	17.53	18.91	35.16	24.37
0.6435	10.82	12.99	11.75	12.39	23.76	18.09	12.98	26.18	17.74	19.60	35.53	24.89
0.7425	10.85	13.01	11.75	12.56	23.85	18.12	13.29	26.36	17.89	20.27	35.87	25.32
0.8415	10.88	13.04	11.74	12.74	23.99	18.04	13.60	26.62	17.93	20.92	36.39	25.62
0.9405	10.90	13.09	11.67	12.91	24.25	17.65	13.89	27.02	17.66	21.55	37.01	25.56

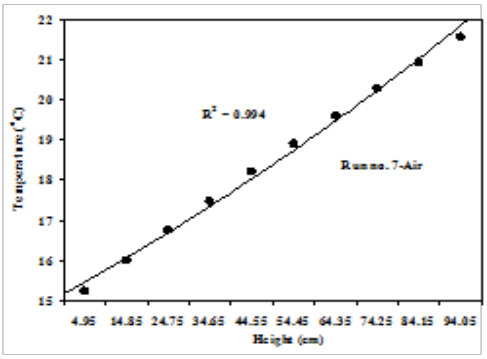

Figure 18: Temperature profile for Air for S=725.4 W m^{-2} (Run no. 7)

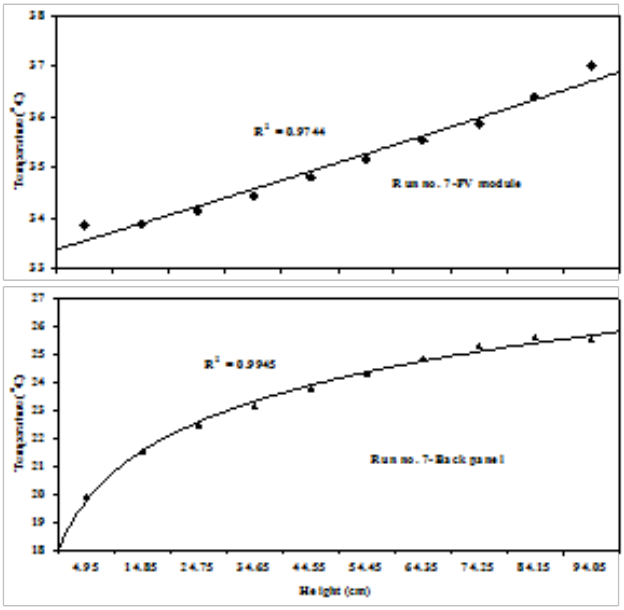

Figure 19: Temperature profile for PV module and Back Panel for S=725.4 Wm^{-2} (Run no. 7)

interval was selected for a minimum of two minutes to record any subtle temperature changes for obtaining measurements from the data logger [34]. The graphs of ambient and outlet air temperatures were plotted against the time-interval of measured data for the two cases of passive and active ventilation are presented in Figure 20(a) and 20 (b). Thermal time constants of the PV solar wall section were function of ambient air temperatures and air velocities and were therefore approximately calculated under conditions of passive and active air ventilation.

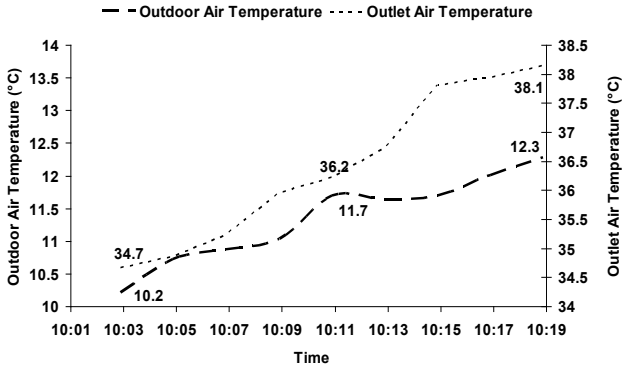

Figure 20 (a): Changes in outlet air temperature from a PV solar wall with a step change in outdoor air temperature under passive (buoyancy-induced) ventilation

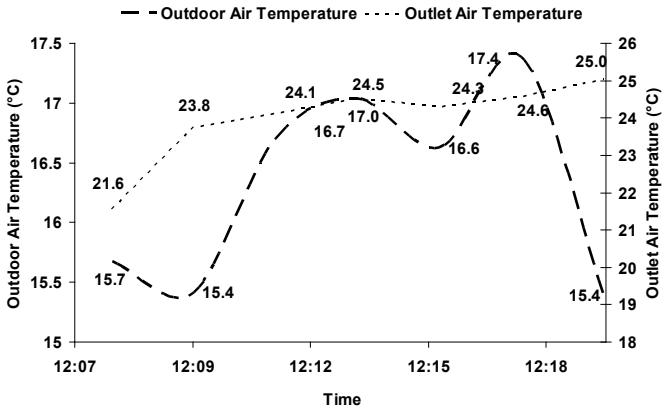

Figure 20 (b): Changes in outlet air temperature from a PV solar wall with a step change in outdoor air temperature under active (fan-induced) ventilation

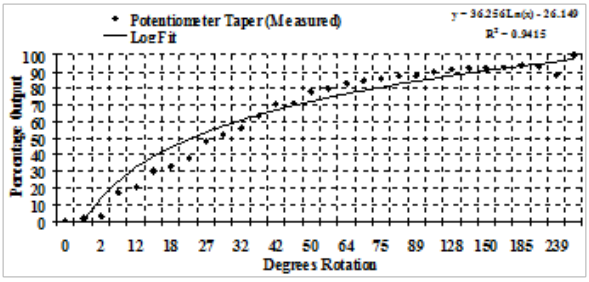

Figure 21: Potentiometer Taper (Measured) with percentage voltage output

8.2. *Photovoltaic Amplification*

In a parallel plate PV device, the temperatures were measured as a function of its volume. The measurements of temperatures for PV modules, insulating panel and ventilated air column in the wooden frame were non-linear. In the ventilated PV solar wall device for transportation of heat, the air velocities were developed both as a measure of buoyancy-induced and fan-assisted ventilation. The measurements of PV solar wall device, ambient air and room air temperatures, air velocities and solar intensities are presented in Table 10. The location and nomenclature of sensors is presented in Table 3. The power output results from a potentiometer with rotation of its circular knob are illustrated in Figure 21. From the graphs of Figs. 13, 14, 18, 19 and 20, phenomenon of photovoltaic amplification is observed. For a PV solar wall device, the gain is a function of its resistance or volume of steady state thermal and electrical functions. A loudspeaker has similar operational characteristics.

9. Signal Processing Parameters for a PV Device

The sinusoidal steady-state response was applied in performing the analysis of the parallel plate PV device circuit, because of the advantage of representing a periodic function in terms of a sinusoidal exponential function. Electrical analog RC circuit parameters of a parallel plate PV device are enumerated as under [4, 22]:

Capacitance: The capacitance of a parallel plate PV device with air as a dielectric medium was calculated to be 91.2 picofarads.

Resistance: The electrical resistances of various components were calculated as: glass coated PV modules were approximated as 5.3 kΩ, air was approximated as 1200 MΩ, and plywood board was approximated as 26.5 Tera Ω. The total equivalent electrical resistance of a parallel plate PV solar wall device was approximated as: 5.3 kΩ.

Time Constant: The time constant, which is product of resistance and capacitance, was calculated to be: 0.5 microseconds. The frequency with this time constant was calculated to be 2 MHz.

Capacitive Reactance: The capacitive reactance was calculated to be: 872.5 Ω.

Impedance: The impedance of the circuit was calculated to be: 5.4 kΩ.

The Phase angle θ: The phase angle between capacitance and reactance was calculated to be 9°.

The Phasor representation:

$Z = 5.300 - j\,0.8725 = 5.4\ \text{k}\Omega \angle -9°$.

Capacitive Heating: The joule law gives instantaneous power absorbed by the capacitive impedance which is converted to heat. The heat capacities under critical operation of buoyancy-induced ventilation were calculated to be 59.6 kJ, 0.755 kJ and 510.7 kJ for PV module, air and plywood board respectively. The total average value of joule heating for the parallel plate PV device was calculated to be 571 kJ.

Induction Losses: The induction losses due to thermal storage effect in the parallel plate PV device were calculated to be 15.9 KJ.

Power Factor: The power factor was calculated to be cos θ = 0.911 lag.

Current function ($i^2(t)$): Using the current function, $i^2(t) = I_m^2 \sin^2(\omega t + \theta)$, the effective (root mean square) value of current was calculated to be 10.4 amps and maximum value of current was calculated to be 14.71 amps.

Voltage function: The voltage function is defined as per the sine wave: $v = V_m \sin(\omega t)$. The effective value of the voltage was calculated to be 60.4 volts and maximum value of the voltage was calculated to be 85.42 volts.

Power function: The instantaneous power is given by the expression:

$$p(t) = \frac{V_m . I_m}{2} . \cos(\theta) - \frac{V_m . I_m}{2} . \cos(2\omega - \theta) \qquad (7)$$

The Plots: The time diagram for current, voltage is plotted in Figure 22 (a). The time diagram for power is plotted in Figure 22 (b).

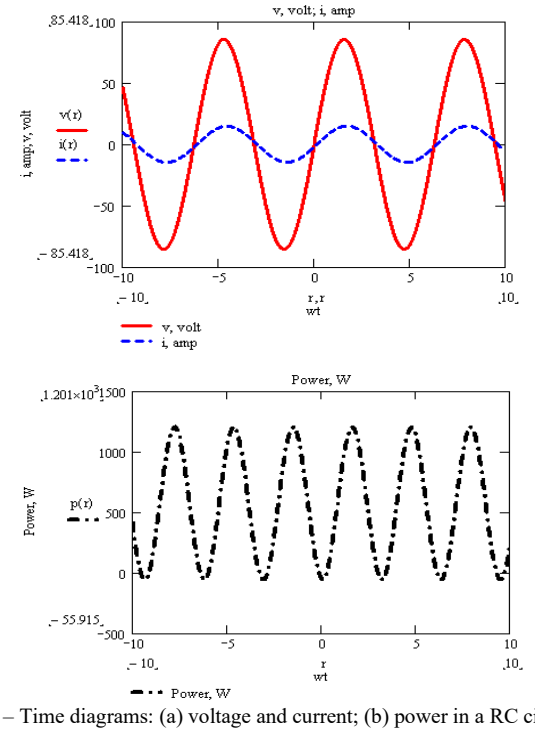

Figure 22 – Time diagrams: (a) voltage and current; (b) power in a RC circuit amplifier

Power Transfer: To describe the resonance phenomenon for

equivalent mechanical, hydraulic and thermal systems of PV solar wall device, an electrical analog was used.

The Figure 22 shows that the instantaneous power is negative whenever the voltage and current are of opposite sign. However, as is illustrated in the Figure 22 that positive area of p(t) energy exceeds the negative area. Therefore, the average power is finite. Since the angle, θ, is small between current and voltage, the negative area of energy become very small. The induction losses due to thermal storage amount to 1.5% in comparison to the capacitive heating. Thus induction losses cannot be avoided in any electrical circuit, but can be minimized.

10. Solar Energy Acoustics

10.1. Theory

A theory of acoustics in solar energy was proposed by the author [10], which can be arrived and deduced from definitions of Noise of Sol and Equations (1) and (2).

A brief on the theory of a solar energy absorber is presented here in this paper. On the transparent surface of a solar energy absorber, direct rays from the sun are incident. The diffuse rays from the sky, clouds, and surrounding objects are also incident, which is also partly reflected and partly transmitted from a solar energy absorber. In addition to this, the selective coating on the surface of a solar energy absorber absorbs some part of the radiation. The reflected part of the incident flux is called the reflectance p, the absorbed part of radiation is called the absorptance α, and the transmitted part of radiation is called the transmittance τ. The sum of absorptance, transmittance and reflectance is unity, or

$$\alpha + \tau + p = 1 \quad (8)$$

There are non-constant distributions of radiations over the directions of incidence and over the wavelength (or frequency) scale on a solar energy absorber. A sample of selective material of a solar energy absorber has radiation properties of transmittance, reflectance and absorptance, which are function of a specific thickness. For a solar energy absorber, the emittance ε is defined as the division of the thermal radiant flux emission from a surface to the black body radiant flux emitted at the same temperature.

The evaluation of radiation properties from angular dependence point of view is explained through geometry theory of a solid angle formed by all rays joining a point to a closed curve. The solid angle is defined as the ratio of the projected area A on the sphere to the square of length R and radius R. A sphere is considered to be having a solid angle of 4π steradians. For a solar energy absorber, the solar radiation incident on a point at a surface is presumed to be coming from many directions in a conical solid angle. For a cone of half angle θ, the solid angle defined by the circular top of the cone and point bottom of that cone is given by expression as:

$$\Omega = 2\,\pi\,(1-\cos\theta) \quad (9)$$

In measuring the transmittance or reflectance, a sample is illuminated over a specified solid angle. The flux is then collected for a given solid angle for measurement of reflectance or transmittance. A conical solid angle is bound through a right circular cone. The source of solar radiation is sunlight.

The radiation properties of sunlight essential for performance analysis of daylighting and lighting are defined as follows:

The luminous flux is directed outward from a source, it ultimately strikes on many surfaces, where it is reflected, transmitted and absorbed. The illuminance is the density of the luminous flux incident on that surface.

The luminance is defined as the intensity of the source or the sink in the direction of an observer divided by the area projected on the source or sink as viewed by an observer.

Luminous intensity is defined as the power due to generation of the luminous flux. A source of sunlight is depicted to be having a luminous intensity in a particular direction. The inverse square law demonstrate that the illuminance incident perpendicular to the line from the point source of sunlight to the surface is directly proportional to the intensity of the source and inversely proportional to the square of the distance from the source of sunlight to the incident surface.

The luminous flux is defined as the rate of flow of light. A receiver surface receives watts of sunlight and it emits luminous flux. The measure of the success rate in converting watts of sunlight to lumens is called efficacy.

Quantity of sources is defined as luminous energy and is related to luminous flux, which is luminous power per unit time.

The luminance exitance is defined as the density of luminous flux leaving a surface of a solar energy absorber. The reflectance is defined as the ratio of the luminous flux reflected from a surface to the luminous flux incident on that surface. The transmittance is defined as the ratio of the luminous flux transmitted through a surface to that incident on the same surface.

10.2. Source and Sink of Solar Energy

The planet earth and its surrounding environment is absorber of solar energy. Examples of solar energy absorbers are civil structures such as green houses, buildings, panels, collectors, thermal power plants, roads, ports, bridges and canals. The earth-atmosphere system is an absorber for a portion of the incident solar energy radiated from the sun. The surface of the earth is also heated by a flux from its interior region from the decay of radioactive isotopes of the earth. The tides on earth occur due to the earth-moon system, result in viscous friction, energy input that affects the surface energy balance of the earth. To the extent that the earth is at a steady state and is not changing, the heat radiated by the surface of the earth is equal to the sum of the heat inputs. The solar radiation sources consist of many waves of interference in its radiation spectrum. The absorbed sources of waves of interference of light, sound, heat, electricity, fluid, fire are function of absorptivity for a solar intensity. The sink of solar energy is the earth and its earth-moon system. The temperature of the earth is raised by absorbed solar radiation as incident solar energy is the dominant energy input. The radiation absorbed by the earth is proportional to the earth's cross-sectional area perpendicular to the sun's flux. The earth is acting as a black body radiator with actual power radiated by the earth is determined

from the radiative temperature of the earth-atmosphere system.

10.3. Radiation Sources and Life on Earth

Life on the earth is completely dependent upon the energy radiated by the sun. By photosynthesis green plants convert solar energy into chemical energy. All biological processes are either directly or indirectly reliant upon photosynthesis. In addition to the primary role of light in a living economy, a constant environment of radiations from various sources produces other effects, reactions and adaptations. These radiations have receptiveness to influence the life activities. The solar radiation, while passing through the atmosphere is reflected, scattered, and absorbed by gas molecules, ozone, water vapour, clouds and dust. The atmospheric length path traveled by sun rays is obtained by the air mass *m*, which is the ratio of the mass of atmosphere to the mass which would exist if the sun was directly overhead at sea level. In this case of overhead earth-sun path, *m* is equal to 1.0.

The sunlight on the earth is the major source of radiations. The spectrum of sunlight constitutes ultraviolet radiation, visible light, infrared rays and radio waves. The x-rays are originated by solar flares and their ionization due to absorption happens high in the earth's atmosphere. From various celestial sources, x-rays also reach the earth's atmosphere. About 60 per cent of the sunlight energy is in the invisible infrared region's indefinite limit in radiation spectrum. Before radiations of shorter wavelengths reach the surface of earth, they are absorbed in the earth's atmosphere. The artificial radioactive elements are produced by bombardment through high energy particles, examples include helium nuclei. The radioactive emanations consist of three components: i) alpha particles, which are positively charged helium nuclei; ii) gamma rays, which are penetrating radiations of very short wavelength but otherwise like x-rays; and iii) beta particles, which are rapidly moving electrons.

10.4. Greenhouse Gases

The most of ultraviolet solar radiation is absorbed by the ozone in the upper atmosphere. The part of the solar radiation in the shortwave region is scattered by the air molecules. The ozone layer is formed high above the atmosphere through absorption of ultraviolet radiation by oxygen. The reversible reaction again turns the ozone into oxygen through absorption of longer ultraviolet rays. The strength of the absorption of solar energy is proportional to the wavelength and absorption bands that are formed at regions of strong absorption. The examples of important atmospheric gases forming part of absorption bands are oxygen (O_2), ozone (O_3), carbon dioxide (CO_2), methane (CH_4), water vapour (H_2O), nitrogen dioxide (NO_2) and chlorofluorocarbons (CFC).

11. Sensors and Transducers for a Human Brain

Your body has feedback systems that regulate the internal environment of your body. The feedback systems make use of storage depots and numerous feedback loops. The monitoring of plasma calcium is a good example of negative feedback. The bones constitute large storage depots for calcium, for the plasma to withdraw these storage supplies in times of need. Our body's homeostatic regulatory systems are represented by feedback loops. The feedback is considered negative, when it is compensating or negates any change. The negative feedback is essential to stabilize a system.

The gastrointestinal tract, the lungs, the kidneys, and skin of your body make exchange of materials and energy between the internal and the external environments. A steady state is achieved by regulatory mechanisms involving the balance between the inflow and outflow of the internal environment that stabilizes the composition of the internal environment. The tendency to regulate the internal environment so that it is maintained in a steady state is called homeostasis [1, 7].

11.1. Heat Stress

When vulnerable to solar radiation, your body acts as a solar energy absorber. This enables your senses for interpretation of our surrounding environment. The amount of heat you lose is dependent on the difference in temperature between the environment and the surface of your body. The heat loss from your body is directly proportional to this difference in temperature. The heat would be released from your body, if the surface temperature of your body is at a higher level than that of the environment. If due to excessive solar radiation, the environmental temperature rises above your body temperature, you will gain heat from the environment.

11.2. Effects of Intense Heat in a Room

Your presence in a room with solar radiation, high room air temperature and conduction do not count in your favour for loss of body heat. In this situation, your body gain heat from the surrounding environment. You have the chance to survive, but only through mechanism of sweating for losing heat. The normal response of your body is resulting in intense heat strains through the body's circulatory system. This happens because the hypothalamus reacts to the heat through expansion of the blood vessels in your skin. As a consequence, it results in decreased resistance to blood flow and your blood pressure falls. The reflexes happen, which prevent large changes in blood pressure, ultimately begin to operate and the decreased resistance to blood flow is compensated through the heart working much harder. The expanded blood vessels create it potential for large amounts of blood to pool in the vessels of your skin at the price of other organs. You will faint as a result of sufficiently low blood supply to your brain.

11.3. Sweating

Through sweating, a circulatory problem occurs, because of the salt and water loss. A decreased plasma volume occurs because of excessive fluid loss. As a result, the output of blood from the heart is slowed down, which could lead to decreased blood flow to the skin, which ultimately could reduce sweating. If this occurred, your main avenue for heat loss would be shut down. In this case, heat production would continue and your body temperature would rise until your whole body system is collapsed. The body's ability to control heat loss is very limited. A vicious circle may occur as

a result of heat not losing rapidly enough to prevent a rise in body temperature. When heat regulation fails, the positive feedback loop occurs into operation in your body (Heat production – metabolism – temperature control); if unchecked it results in heat stroke and death.

11.4. Evaporation

Sweating is an evident method to lose heat by evaporation. Water continuously evaporates from your skin during the process of sweating. When you breathe, there is also a small loss of water from the surface of the lungs. When you breathe or sweat, the amount of water that evaporates is proportional to the humidity of the air. At high humidity of the surrounding air, water evaporates much slowly and therefore contributes less to the cooling process. One of the important methods of losing heat from the surface of your body is through evaporation. There is evaporation of water from your skin after swimming and you feel cool. There should have minimum amount of energy of the water molecules on your body's surface for evaporation to happen. The speeding water molecules on the surface of skin beat the forces holding them in the liquid state. This finally results in evaporation into the air as water vapour molecules. The cooler molecules are left behind in the whole process. As a result, heat pours from the warmer surface of your skin to the cooler water molecules. This heat flow transfers energy to the water, increasing the number of evaporating water molecules. Furthermore, the cooling of your skin also cools any underneath blood which tends to flow through that part of your body.

11.5. Protection through Noise Filters

The keeping of face beard (facial hair) and wearing of a knitted head cloth (*patka*) and a turban (*pag*) on your body has a logical and a scientific significance. The daily self-making folds of hair knots and making round folds of turban over the head of your body with colourful cotton cloths has following historical, medical benefits: i) it indicate, protects and concentrate the disciplinary physical and mental strength of a person; ii) it gives hair tonic to the growth of hairs on your body due to solar energy; iii) the whole system acts as noise filter and provides immunity to your body; and iv) the folded *Patka* with style, folded design of hair knots on top of your head is your identity in time domain, the face beard on your body is a measuring ration and a sign of man, the turban with style, colour, design is your identity in space domain.

12. Comfort and Health

The ASHRAE handbook of fundamentals has provided a detailed discussion of the physiological principles of human thermal comfort [37]. The amount of heat generated and dissipated by your body varies considerably with activity and age as well as with size and gender. The complex regulatory system of your body act to maintain the temperature of your body to about 36.9 °C regardless of the environmental conditions.

The environmental factors that affect thermal balance of your body for influencing thermal comfort are [38]: i) the dry bulb temperature of the surrounding air; ii) the humidity of the surrounding air; iii) the relative velocity of the surrounding air; iv) the temperature of any surfaces that are in direct view to any part of your body and thus exchange radiation. In addition the personal variables that affect the thermal comfort of your body are activity and clothing. The physiological mechanisms that your body uses to control your body temperatures are metabolism, blood circulation, near the surface of the skin termed as cutaneous blood circulation, respiration and sweating. The metabolism rate determines the rate at which energy is converted from chemical to thermal form within your body and blood circulation controls the rate at which the thermal energy is carried forward to the surface of your skin. In respiration, air is taken in at ambient conditions but leaves saturated with moisture and very near the temperature of your body. The sweating has a significant effect on the rate at which energy is carried away from the skin of your body by heat and mass transfer.

The energy generated by metabolism rate of your body varies considerably with the activity of your body. A unit to express the metabolic rate per unit of area of your body is termed as met (1 met = 58.2 W m^{-2}), defined as the metabolic rate for your body while seated quite (called sedentary). The variable which affects the comfort of your body is the type and amount of clothing that you are wearing. The insulation of clothing is defined as a single equivalent uniform layer over your whole body. The insulation value for clothing of your body is expressed in terms of clo units (1 clo=0.155 m^2CW^{-1}). A heavy business suit with accessories has insulation value of 1 clo, whereas a pair of shorts has 0.05 clo. ASHRAE Standard 55 provides comfort conditions for an acceptable thermal environment [38]. The most comfort studies involve use of the ASHRAE thermal sensation scale. The scale relates words describing thermal sensations to a corresponding number. These are enumerated below:

+3	hot
+2	warm
+1	slightly warm
0	neutral
-1	slightly cool
-2	cool
-3	cold

The operative temperature is the average of the mean radiant and ambient air temperatures, weighted by their respective heat transfer coefficients. Energy balance equations are developed that use a predicted mean vote (PMV) index. The PMV index predicts the mean response of a large group of persons. The coordinates of the comfort zones are:

Winter: Operative temperature of 20 to 23.5 °C at 18 °C wet bulb temperature; operative temperature of 20.5 to 24.5 °C at 2 °C dew point.

Summer: Operative temperature of 22.5 to 26 °C at 20 °C wet-bulb temperature; operative temperature of 23.5 to 27 °C at 2 °C dew point.

The loss of hearing is a serious occupational hazard. Factory workers, truck drivers and other workers are exposed to noise levels that are harmful. The continuous exposure to harmful noise

level results in hearing impairment of your ear. The federal Occupational Safety and Health Administration (OSHA) in the Department of Labour has maintained noise exposure limits. The noise exposure is expressed in daily noise for an 8-hour shift.

13. Discussions

13.1. Experiments

The electrical characteristics that were obtained for a pair of glass coated PV modules with indoor experiments under standard operating conditions were performed under ideal conditions. The ideal test conditions gave inconclusive characteristics which certainly are not suitable for consideration during design of PV module system connected to buildings. Additional information under available operating conditions was essential for system design of the PV module system. The results of outdoor experiments revealed that thermal characteristics of PV modules were improved with a glass coating. There was considerable loss in generation of electrical power from a pair of glass coated PV module in comparison to typical rated electrical power for a PV module. The glass coating was responsible for increasing thermal storage along the major dimensions of the PV module system. The conduction heat flow along the height of the glass coated PV module resulted in rise of temperature along its height. This resulted in formation of thermal gradients along the volume of PV module system. The original metallic frame of the glass coated PV module was replaced with a wooden frame to minimize the effect of thermal gradients. The insulating panel in the wooden frame was a plywood board filled with polystyrene which is used in a modern building for insulation. A comparison of experimental results of passive and active ventilation envisaged that active ventilation was necessary to reduce high temperatures of PV modules. The heat storage capacities and thermal storage capacities of various components of PV module system were calculated. The major heat storage in the PV module system was due to heat capacities of the insulating panel. The result was loss of heat along the height of the PV module system. The packed polystyrene with loose fills in the plywood board was responsible for increasing thermal storage capacity of insulating panel. The rise in temperature along the thickness was calculated proportionally from the observed temperature rise along the height of the PV module system. Hence, the temperature measurements were also obtained along the volume, viz. height of a PV solar wall system.

13.2. Numerical Model

The temperature plots of Figure 18 and Figure 19 show that there was steep rise in temperature of insulating panel in comparison to glass coated PV module. The air temperature of air passage in the PV module test section was increased considerably due to increase in thermal mass of the PV module system connected to a building.

A periodic solar heat flux was subjected to heat exchange with ambient and heated air in the PV solar wall. With the assumption of lumped parameter applicability in x-direction imposed a very small percentage of error in the solution of the model. More elaborate solution techniques for heat exchange analysis though improve the accuracy of solution method but certainly were not realistic in environmental conditions involving large deviation due to variation in convection heat exchange coefficients but no deviation with simulated periodic variation of solar intensity.

13.3. Composite Waves due to Stresses and Oscillations

The following composite waves are generated due to development of stresses and oscillations on a PV solar wall device with incident short wavelength electro-magnetic waves: (i) due to connected external electrical load, transmission of electrical energy wave; (ii) due to exchange of viscous dissipation with air, the propagation of heat waves at longer wavelength; (iii) due to thermal stress generation with propagation of heat waves, elastic waves are transmitted in a PV solar wall device; (iv) due to combination of stress development with heat waves, elastic waves and applied external source of energy, the fluid surface waves are propagated; (v) due to climate-particle oscillations of wind and fan induced pressure, applied external waves are propagated; In absence of wind and fan pressure, thermosyphon based oscillations are propagated due to thermal buoyancy.

Such as in an organ pipe, the sound waves can transmit with combination of applied external source of energy and fluid surface waves. From the surrounding environment due to air-borne sound transmission, the sound waves are propagated. Due to various stresses and oscillations acting on a static particle body, the transmission of composite waves is generated. With action of composite forces acting on a PV solar wall device, the developed stresses are classified as: (i) fundamental; (ii) internal; and (iii) external. Due to presence of electromagnetic and gravitational forces of a solar system, the fundamental stresses are generated. Under the influence of fundamental stresses, internal stresses are generated with characterization of composition properties at chemical, atomic and molecular level. With application of external source of energy such as fan based force used for active air ventilation in PV solar wall device, the external stresses are generated. With stress development due to periodic force of expansion/compression, cooling/heating and night/day, the oscillations are assumed to be generated on PV solar wall device. On a PV solar wall device, climate-particle oscillations due to wind force are also transmitted. Due to superposition of composite waves, the fluctuating forces are generated.

13.4. Resonance

The parallel and series cases of LCR circuit resonance are briefed here. With the aid of presented modelling and experimental data, the cases of resonance are visualized. For elastic waves transmission, the inductance force exists due to mass of the mechanical system. The capacitance force exists due to heat storage capacities of PV solar wall device (PV modules, air and polystyrene filled plywood board). The polystyrene filled plywood board is vulnerable to heat stress of fire as soon as heat waves propagated with frequency matching with its latent heat of vaporization is achieved. Due to thermal and fluid resistance in energy storage elements of PV solar wall device, equivalent

electrical analog resistance is developed. The parallel case of LCR resonance happens with fluid surface waves (RC) and heat waves (RC) in conjunction with inductance (L) due to mass of PV solar wall device and resistance (R) due to temperatures of ambient air and ground surface. The series case of LCR resonance occurs with propagation of elastic waves of a PV solar wall device.

13.5. Human Regulatory Feedback Mechanism

Our body has feedback systems that regulate the internal environment of our body. The feedback systems make use of storage depots and numerous feedback loops. The monitoring of plasma calcium is a good example of negative feedback. The bones constitute large storage depots for calcium, for the plasma to withdraw these storage supplies in times of need. Our body's homeostatic regulatory systems are represented by feedback loops. The feedback is considered negative, when it is compensating or negates any change. The negative feedback is essential to stabilize a system. The gastrointestinal tract, the lungs, the kidneys, and skin of your body make exchange of materials and energy between the internal and the external environments.

A steady state is achieved by regulatory mechanisms involving the balance between the inflow and outflow of the internal environment that stabilizes the composition of the internal environment. The tendency to regulate the internal environment so that it is maintained in a steady state is called homeostasis. The coordination of the activities of the various sensory organs within your body is controlled by the secretion of hormones and by transmission of nerve impulses. The nerve impulses travel along axons.

The sensory nerve axons carry impulses from different parts of your body to the central nervous system (brain and spinal cord). Although parts of your brain involved in various physiological functions have been located, research attempts to localize complex behavior patterns in sensory areas of your brain have failed. The sensory areas are located for the impulses on the cortex. The motor areas are also located where "command" impulses leave the cortex. The cerebellum receives impulses from sensory receptors and interacts with motor cortex, insuring smooth muscular movements. The reticular formation receives sensory impulses from the environment and sends impulses to the cortex.

13.6. Noise Filters and Kinetic Theory of Gases

The behavior of gases over wide range of temperatures is predicted through kinetic theory model by average kinetic energy of translation. The noise filters are defined based on the model of kinetic theory of gases for filtering unwanted frequencies of oscillations from a power system. It is a network with selective transmission for currents from a power system of varying frequency. The noise filter is used to filter unwanted frequencies of oscillations from a power system. The noise protection and security is a crucial operation for obtaining a desired output from a power system.

13.7. Significance of Noise Characterization Theory in Cities

Energy & Entropy: Developed cities are highly reliant on continuous inputs of energy to provide goods, services and environment associated with a high standard of well-being. Energy is typically thought of in purely sensible terms of heat and work consumption of a city, but the process development itself may be shown to be theoretically dependent upon inputs of energy in a city. Primarily, energy is required to achieve an increase in order and knowledge (since thought process of an individual requires a metabolic input). The theoretical basis for this concept of increase in order and knowledge is based on principle of kinetic theory of gases. The laws of mechanics are insufficient to predict the behavior of a gas, since they provide no preferred direction for time. With some limitations, the concept of increasing entropy, however, provides a direction for time. Since the entropy of a system is associated with its lack of order, the concept of entropy also applies to non-thermodynamic systems [39].

Biological System and Entropy: Biological system represents an increase in order for the evolved material (i.e. a decrease in entropy) and is termed as 'complexification' by the biologists. Cultural evolvement and industrialization also signify movement by a developing city from less order to greater order. Additionally, life also requires continuous input of low entropy energy to recompense for the ultimate entropy increase experienced by all living material, i.e. death.

Photosynthesis is directly reliant upon energetic photons of shorter wavelength visible light. By means of photon-activated chemical reactions, plants are able to produce organic material from carbon dioxide and water. Since the energy potential of the organic material is greater than that of constituents, an entropy decrease is achieved. The organic material has higher order degree than the carbon dioxide and water from which it was produced. The process of respiration both by the plants and living organisms which depend either directly or indirectly through plants, achieves in low-temperature waste heat. It is this biological heat engine upon which life on earth is almost entirely dependent.

Knowledge, Order and Well-Being: Knowledge is gained mostly through social-economic process, which requires inputs of low entropy reserves. Well-being of a city also increases through knowledge even though history has been marked with short-term reversals such as in the event of a war. Smart improvements in a city represent an increase in order i.e. a decrease in entropy. Improvement in well-being of a city is often the result of endeavours that have very subtle effects such as an insight of a new scientific theory, which represents a more ordered image of the world. In addition to increases in order, human created systems frequently produce undesired forms of disorder, i.e. environmental pollution. For example, emissions (indoor and outdoor) represent a 'scattering' to the winds of pollutants, an increase in disorder.

Solar Energy and Waste Recycling: Recycling of wastes is equivalent to interconnecting the material inputs and outputs. Energy though conserved cannot be completely recycled, due to inevitable increase of entropy. A shift from the present dependence upon conventional energy resources to either a direct

or indirect usage of solar energy is already happening. A complete recycling of materials and a total reliance upon solar energy would lead to sustainable and smart economy. Energy derived from the sun is obtained without entropy increase. There is generation of waste heat irrespective of energy source. However, a solar energy system results in no greater increase of entropy in comparison which occurs without the system. Entropy is an indicator of non-utilization. The increase in entropy specifies a decrease in low entropy sources of energy with high utilization, which occurs irrespective of energy conservation in a system.

Noise and Noise Behaviour: It is recognized that many proposed methods of energy conservation also results in reduction of energy cost. For example, an improved transportation system would not only result in energy conservation, economical affordability but also generates less Noise. As is the case of increased energy consumption, increased quantities of goods and services result in generation of more noise behaviour in a city. As stated previously, 'Noise' is defined as a sensation of unwanted intensity of a wave. It is perception of a pollutant and a type of environmental stressor. An environmental stressor such as noise may have detrimental effects on various aspects of health. The unwanted intensity of a wave is a propagation of noise due to transmission of waves (viz. physical agents) such as sun, light, sound, heat, electricity, fluid and fire. Noise Behaviour is checked by identifying a source and a sink of noise i.e. a person making noise in the environment and a person affected by such noise in the environment.

The omnipresent characteristic of the urban environment is its exposure to environmental noise. The excessive noise is accepted by the public health doctors and professionals as an undesirable feature of the urban environment. Noise is indisputably perceived to be an irritant, interfering into personal privacy, and causing displeasure and diminishing the worth of a person and his health. As health is largely defined to include quality of life and displeasure, therefore noise undoubtedly affects health.

The effects of stress due to noise of physical agents are consideration to contribute to a range of disorders as wide as impairment of hearing, cancer, heart disease, musculoskeletal conditions, skin disease, gastrointestinal and other disorders. The evidence is strongest for links between certain types of prolonged stress and heart disease, hypertension, and mental illness. Most of the evidence for such links is epidemiological. It is possible that what is bad for the individual employee is also bad for the organisation. Organisational worries connected with work related stress include high absenteeism, increased staff turnover, low job satisfaction, low morale, poor organisational commitment, poor performance and productivity, possible increased accident and near miss rates, and, in some cases, an increase in employee and client complaints and litigation.

All such unwanted disturbances of noise caused by a person or deviation from a normal behaviour so as to distract attention of a normal person are termed as 'Noise behaviour'. There is always a source of noise and a sink of noise i.e. a person making the noise in the environment and a person affected by such noise in the environment. A person making the noise in the environment is also affected. The occurrences of noise related stress alters the way people think, feel, and behave. Many of the changes that occur are diffident and potentially reversible, although harmful to the person's value of life at the time. Other changes may be more enduring, and have substantial consequences for health. Behavioral changes include increases in health risk behavior, such as smoking and drinking, and decreases in health positive behavior, such as exercise and relaxation. Many behavioral changes represent attempts to cope with the emotional experience of stress due to noise—for example, by making noise due to presence of physical agents in the environment or because of other person's noise behavior in the form of polluting the environment. The noise in the environment is associated with poor decision making, impaired concentration, reduced attention span, impaired memory, and confusion. People who report under stress due to noise also admit that not being able to think straight forward. Social behavior and interpersonal relations of the person affected by noise may also be demolished, possibly reflecting these and other psychological changes such as tiredness and increased irritability.

Biomedical Instrumentation for a Noise System: Biomedical instrumentation for measurement and monitoring of noise from human systems in a city require real time informatics capabilities. Sensing and actuating capabilities as well as measurement systems for noise can be 'in vivo' and 'in vitro'. The signals can be classified as bio-electric, bio-sound sample, bio-mechanical, bio-chemical, bio-magnetic, bio-optic and bio-impedance depending upon origin of 'stresses and oscillations' in a noise system.

Energy Conversion, Energy Processes and Noise: Energy conversion materials and devices convert one form of energy into another form. The energy conversion efficiency of a device is an expression of energy balance between energy input and energy output. Materials play important role in conversion efficiency due to involvement at molecular and atomic level. Energy conversion is deeply associated with energy processes of heat, fluid, electricity and HVAC devices.

Combustion is primary form of energy conversion of low grade fuels such as biomass and municipal solid waste. Energy conversion of low grade fuels from solid to a liquid or gaseous state is through various techniques for enhancement of calorific value of fuel. Inefficient fuel combustion is wasteful as well as generates higher level pollutants. The pollutants and solid wastes generated during energy conversion must be controlled to protect public health and well-being of the affected environment in an ecosystem.

Energy conversion efficiency can be increased through cogeneration. A cogeneration plant consists of energy equipment to produce both electric energy and useful forms of thermal energy such as heat or steam for commercial, industrial, heating, or cooling purposes. Cogeneration plant is designed as either topping-cycle or bottoming-cycle process. Either of these cycles can utilize thermal energy to meet process heating, ventilating, and air-conditioning (HVAC) or built environment comfort requirements for steam or for hot/cold water.

There is generation of waste heat, entropy and noise in all energy conversion devices and systems, which can be minimized by selective materials, optimized design configurations and performing high-resolution modelling and simulations.

13.8. Significance of Noise Characterization Theory in Acoustics

Traditionally acoustics is associated with sound. Nearly all life activities result in generation of sound. However, in traditional acoustics only vibrations by way of pressure difference is associated with sound. In noise characterization theory, apart from sound, acoustics is associated with composite wave elements of light, heat, fluid, electricity, fire and sun. Since all life activities are associated with these composite waves, therefore contemporary acoustics should also involve these wave elements. In this way, knowledge of wave theory principles enables the requirements for the control of noise due to these composite wave elements.

A clear differentiation must be made between the objective specification and measurement of noise field due to these composite wave elements and its subjective appraisal or the sensation it produces on people exposed to it. Many kinds of subjective judgment are possible, according to the particular circumstances, but no objective measurement can determine subjective response directly. Although much of the discussion of noise can be in objective terms and be concerned with quantities which can be evaluated and measured, it is essential to introduce the subjective aspect since noise is associated with people and their routine lives.

Investigation of the noise quantities due to composite wave elements vary with frequency. Frequency is normally plotted on a logarithmic scale because the pitch, which is a subjective assessment of frequency of composite waves (viz., physical agents) perceived by human senses, varies approximately in this way. Usually, measurements are normally made in ranges of frequency bands, or at frequency intervals which are equal steps on a logarithmic scale. Octave steps may be suitable in many cases of composite wave elements, but narrower bands may be more appropriate where applicable. For comparison purposes, certain standard frequencies and frequency bands may need to be developed for these composite wave elements.

For some cases, such as expressing the reduction or insulation provided by a particular building wall, the relative values in *oncibel* and *oncisol* are sufficient. A wall with reduction in sound power intensity and thermal power intensity is given by a certain ratio. Sound pressure measurements are normally made in terms of Root Mean Square (r.m.s) value of the alternating pressure of the sound wave. Similar r.m.s values can be obtained for light, heat, fluid, electricity, fire and sun. Objective measurements and specification of intensity level is to be made on a hexagonal noise scale with seven edges. Figure 23 has presented a double-sided hexagonal slide rule with seven edges for noise measurement representing seven sources of noise [6]. In subjective assessment, however, we are concerned with the way people perceive and respond to various physical agents, and the response of human senses play important role. Contours of equal loudness (pressure level) can also be determined for a number of similar conditions using bands of noise and perceiving conditions of physical agents more closely resembling under practical conditions. A number of other criterion curves, similar in form to the equal contours, are in use for assessment of subjective attributes of noise, such as noisiness, disturbance etc. A simple subjective assessment is presented in Table 11, in which grades and flag colors of noise are notated under limiting conditions [6].

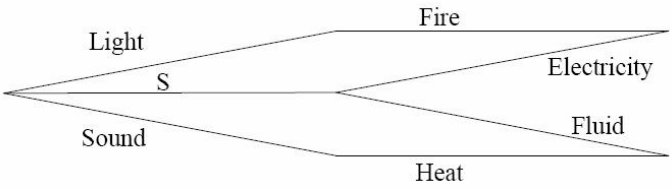

Figure 23: A Double-Sided Hexagonal Scales of Noise with Seven Edges (S denotes Sun)

13.9. Significance of Noise Characterization Theory in Electrical, Instrumentation and Control

Electrical noise is defined as unwanted signals that interfere with the wanted signal output. In electrical engineering, noise is associated with circuits, devices, power systems, electronics, instrumentation and control.

There are many sources of measurement noise. It is mainly caused by the sensor physical mechanism. In general, for sensors and transducers, there are many sources of noise that lead to: i) Johnson's noise; ii) radiation noise; iii) shot noise due to recombination; iv) flicker or contact noise; and v) interference noise.

A control system is gained in measurement noise by way of amplification and it is fed into the whole system. This results in substantial variations in the signal for control of process variable. In this way measurement noise, disturbs the information about the process variable which is delivered by the sensor. Measurement noise has high frequencies in most cases. It is essential that the fluctuations in the control signal are maintained to minimum and not so large to cause the actuator to steep. Measurement noise and its actuator steep leads to inevitable gain of high frequency in the controller and therefore results in its rapid response speed.

In computer controlled systems it is also caused by the resolution of the analog to digital converter. The signal to noise ratio (SNR) is plotted for example with a Bit Error Rate (BER) in a digital communication system. The units expressed in various types of electrical noise should be in *oncisol* which can be plotted on a log scale against frequency or any other parameter. Similarly noise due to an actuator for example a stepper motor, can be expressed in terms of electrical noise (*oncisol*) and its motion noise (*oncisip*).

13.10. Noise Fields

In a free space, noise travels away from a point source, and is small compared with the wavelength. In this case, there is spherical radiation and the intensity at a remote point varies inversely as the distance from the source. There is another case

when noise source is large or extended and the distance is not large compared with the noise source size, in this case the inverse square relation does not hold. Noise fields are complex pattern. Wave theory is necessary to estimate the complete behaviour of noise and even in simple cases, analysis is complex. In actual field practice, only geometrical and statistical methods are used.

Table 11: Noise Grades and Flag Colors under Limiting Conditions

Grades	Noise Grades and Flag Colors under Limiting Conditions		
	Noise of Sol	*Noise of Scattering*	*Noise of Elasticity*
$G_2^a = \pm U$	Sol	Sip	Bel
$G_1 = G_2 = U$	No Positive Solar Energy	No Positive Fluid Energy	No Positive Sound Energy
Base Color for $G_1 = G_2$			
$G_1 = U+\rightarrow 0\ Wm^{-2}$	Decreasing Solar Energy	Decreasing Fluid Energy	Decreasing Sound Energy
Base Color for G_2			
G_1= + ve	Increasing Solar Energy	Increasing Fluid Energy	Increasing Sound Energy
Base Color for G_2			
$G_1 = -U\ Wm^{-2}$	Negative Solar Energy	Negative Fluid Energy	Negative Sound Energy
	Darkness	Low Pressure	Inaudible range
Base Color for G_2			
G_1 = -ve	Darkness increasing, distance from point source of light increasing	Low pressure increasing, vacuum approaching	Inaudible range increasing, vacuum approaching
Base Color for G_2			
$G_1 = -U+\rightarrow 0\ Wm^{-2}$	Negative Solar Energy	Negative Fluid Energy	Negative Sound Energy
	Decreasing Darkness	Decreasing Low Pressure	Decreasing inaudible range
Base Color for G_2			

a. Reference value of $G_2 = \pm U$ signifies the limiting condition with areas of noise interference approaching to zero.

We need to define the system boundary in a noise system. Noise is radiated initially from a source, but due to finite dimensions of the system and as per wave theory some portion of the noise is reflected, whenever it strikes a bounding surface. The resulting noise field at any other point is made up partially of noise radiated directly and partially of the reflections from the system boundaries. When the system surfaces are made as reflecting as possible and the system boundary is irregular with reflections occurring in all directions, the noise field is effectively diffuse. There is no preferred direction in which the noise is travelling at any point and the noise pressure level is assumed to be uniform throughout the volume of the system. There is exception when the noise pressure is not uniform, when the point investigated is close to the noise point source.

Materials play important role in noise absorption. Most of the materials available are not complete reflectors. In many cases, noise is partially reflected, partially absorbed and partially transmitted through the system surfaces forming the system boundaries. The magnitude and direction of noise field depends on the material and surface characteristics of the system boundary. Therefore, the noise fields occurring in practice are rarely completely diffuse. In most of the cases, in the system boundary, there are surface irregularities which are sufficient to provide diffusion at the higher frequencies, where wavelength is short. In the cases, where the noise source wavelength is comparable with the dimensions of the investigated system (such as a cubical or rectangular), complete diffusion may occur at lower end of the frequency range. For many practical cases, it is assumed that the noise fields in the system are diffuse, with support of the measurements made at a number of different positions throughout the investigated system under steady state conditions, which do not show much variation, hence the average of a suitable number is normally taken.

Insulation and Absorption: Physical agents which are propagated into the system fall into two classes, wanted and unwanted. The wanted physical agents are the new field of acoustics. The unwanted physical agents, noise, are controlled in a system in two ways, by insulation and by absorption. Energy is removed from the system containing the sources of physical agents by the absorption at the bounding surfaces. The steady state level to which the physical agent builds up with a given source is determined by the volume and total absorption of the system. Small proportions of the non-reflected composite wave elements of physical agents, which are incident upon a system surfaces, are transmitted through the structure of the material and may be radiated from the other side of the system. In this case the surface acts as an insulating barrier between the source of physical agent and the remote position. Materials which are good absorbers of physical agents are rarely effective insulators if used in the form of barriers in a system. However, the principal requirements for each function are completely different. Thus it is important to distinguish between the two mechanisms by which intensities of composite waves are reduced. The reduction of noise field and kinds of materials suitable for insulation and absorption can also be investigated.

When an insulation panel acts as a barrier to a noise field the practical insulation or reduction to intensities of composite wave elements is given by the amount by which the noise pressure level due to a source is reduced by the barrier. The surface densities, thermal, optical and elastic properties, of the insulation panel are direct factor influencing insulation. It cannot be expected that this simple statement will take into account all the factors which are likely to affect the insulation of a panel in practice. However, it gives an extremely good indication of the values likely to be expected. The noise insulation expression is required, which gives a good indication of the insulation to be expected from an insulation panel at sufficiently low and sufficiently high frequencies depending on the particular physical characteristics of the panel. Between these frequencies there is a band where the material stiffness and the corresponding bending wave pattern in the panel influences its noise insulation behaviour. The panel is

forced by the noise field into bending waves of this wavelength and at the same frequency as is present in the incident composite wave. If the physical constants of the panel-stiffness, density, thickness, optical and thermal characteristics, for example – are such that a free bending wave of this wavelength coincides with this frequency, there is theoretically the possibility of total transmission, with the panel, being freely excited and radiation from the other side occurring. At a particular frequency the bending wavelength imposed on the panel is smallest for noise fields near grazing incidence and largest towards normal incidence. At normal incidence the imposed bending wavelength is infinite and true bending waves cannot be excited. In this case the panel can be forced into uniform oscillations of physical agents. This effect is only possible above the critical frequency for which the bending wavelength in the wall is equal to the wavelength in contact medium since only then is the bending wavelength larger than the wavelength of contact medium. It is simply experienced in practice that this effect has some influence on the insulation values of panel when the appropriate conditions are satisfied. Although noise fields in a closed system (such as rooms) are reverberant and partitions are not normally exposed to plane composite waves, at particular angles of incidence. Although the transmission is never total nor the insulation reduced to zero (because of finite dimensions, the damping in the material and at the edges, and the random noise fields which exist in practice). The depression or dip in composite wave which is obtained can have a significant subjective effect. One way of increasing the critical frequency to above the practical range and hence increasing the insulation is to reduce the stiffness of a panel.

Radiation from Panel: The power of panel radiating noise field is also closely connected with the critical frequency. The depression or dip in the behaviour of insulation occurs because noise is freely radiated when the wavelength in the material is greater than the corresponding wavelength in contact medium. At frequencies for which wavelength in contact medium is greater than wavelength of the material, the value of incidence angle is imaginary and radiation no longer occurs, the oscillations of composite waves in the panel occurs without much stress or pressure field. On the basis of this radiation theory it is expected that thicker panels for which wavelength in material is larger would radiate better than thin ones, and this is so when the amplitudes of oscillations are the same. For the same amount of energy used to excite a panel, however, the thick panel has a lower amplitude of oscillation but better radiating power and thin panel the higher amplitude and the lower radiating power; the net effect of a given excitation, is to have the same order of noise.

Factors affecting Insulation: There are a number of interacting factors which affect the insulation. Mass is normally of greatest importance and determines the insulation at low frequencies. At the lowest frequencies it is possible that the normal resonances or modes of oscillation of panel of typical size may affect the insulation but the practical difficulties of determining the insulation at low frequencies are such that the measurements are not as reliable or reproducible as measurements at higher frequencies. Therefore, any effect caused due to low frequency resonance is difficult to detect.

Heat transmission also plays important role in thermal insulation [40]. The three types of heat transfer affecting the comfort level is radiation, conduction and convection. The integrated thermal and sound insulation is to be determined by various factors such as climate, heat transfer rate, solar energy intensity, elastic, thermal and optical transmission properties. Water vapour barrier and insulation play important role in comfort and wellness of the occupants. In warmer climates, water vapour barriers on exterior side of panel or wall are normally not provided because: i) the temperature drop across the insulation is usually less, and because of this vapour migration would be slower; ii) there are less chances of condensation due to less temperature difference; iii) the built environment is subjected to significant amount of cooling in summer, the vapour barrier would be on the wrong side of the panel much of the yearly time. This is because when the vapour barrier is on the cold side of the insulation, the barrier traps moisture inside the wall. A good integrated insulation will act as noise filter to prevent unwanted oscillations of composite wave elements. Other factors affecting insulation of a system are infiltration. Air and moisture leak into the closed system (or building) through cracks around openings such as windows and doors. This leakage is caused by a combination of the wind pressure on the system and the difference in temperature between the inside and the outside. Sound insulation will depend on the materials and methods used in a system. As mentioned before sound transmission through a panel depends on mass of the panel and on its inelasticity. Massive, thick walls provide excellent sound barriers, but there is a diminishing point when mass alone is not an economical solution.

Integrated noise insulation ratings depend on materials and assemblies of materials. Integrated Noise Transmission Class (INTC) can be used to represent the transmission loss performance of the panel construction over a broad range of frequencies. The results can be plotted, and a standard curve based on human senses response at the various measuring frequencies can be used to determine the rating. The higher the rating, the better will be the construction of a panel in terms of reducing composite wave elements. Average Integrated Transmission Loss (AITL) can be used to check performance of the panel over a range of different frequencies. The results of these performance tests, at each frequency, should be averaged together for integrated transmission loss rating. In these performance tests, the effect of various people sensitivities to various types of noise over various frequency ranges is not taken into consideration. Integrated Noise Reduction Coefficient (INRC) rating could be used to measure the ability of a material to absorb various physical agents rather than reflecting them.

Double or Cavity Walls: When a single panel or wall does not provide sufficient insulation and it is impracticable either to increase the weight or to gain adequate advantage from single wall or panel, a system of double wall construction could be used. The double wall insulation obviously depends on the overall behaviour of each panel, on their relative spacing along with their structural joints for support and interconnection. In the case of

double wall, the air cavity acts as a coupling. If the air in the cavity between the two panels of a double wall is prevented from moving laterally, i.e. along the width and height, rather than across the cavity, the lower frequency resonances due to noise field at oblique incidence and the resulting effect on the insulation are less noticeable. Such a lateral restriction occurs whenever a suitable absorbing material is put into the airspace. The effect of such materials is most noticed at the lower and upper ends of the frequency range and their influences least at mid-frequencies. The best type of material should have a reasonably high resistance, good damping, and stiffness adequately high but not higher than the air. Complete isolation of the two panels of a cavity wall is normally impracticable. Even when the two adjoining panels are capable of standing independently it is normal practice to link them together for structural stability. The way in which these links provide integrated thermal and sound bridges between the panels is likely to have a marked effect on the resultant integrated insulation. Sufficiently light or resilient bridges on the one hand or sufficiently heavy or rigid bridges on the other are likely to have least influence on the insulation, since in either case the impedance of the bridging element, i.e. resistance to being driven into oscillations due to composite wave elements, is different from that of the two panels. It is difficult however, to ensure that a bridge used in practical situation, falls into either of these two categories, hence the use of bridges in cavity wall structures is likely to result in lower values of integrated airborne sound and thermal insulation than expected, and should be avoided if at all possible in practical situations.

Building Structures: In addition to being excited by various airborne physical agents, building structures can also be directly excited by direct impact forces, oscillating bodies such as machine vibrations and footsteps. These forces can also be natural such as wind, thunderstorm, earthquake, lightning etc. One difference between these two methods of excitation is the effective area of the structure which is excited. With airborne physical agents, it is normally the whole area of wall or surface exposed to the noise field, unless the source is particularly directional and these are marked differences in level between the direct and reverberant noise field exciting the structure. With direct impact forces, the area directly excited is more limited, although the structure-borne waves produced may travel through the structure and be radiated from larger areas remote from the noise source. The degree of excitation close to the source may, however, be much greater than with airborne physical agents at the levels normally experienced.

Direct structural excitation may frequently be considered to act at a point and the amplitude of oscillation in the immediate area may well be large although when the energy is spread to other parts of the structure. The resultant amplitude of oscillations is of the same order of magnitude as with airborne composite wave elements. The obvious solution for most impact force transmission problems lies in preventing the impact stresses or pressures, which give rise to oscillations in the main body of the structure, either by providing surfaces which act as cushion absorbers, or by having a discontinuous structure preventing the oscillations implanted on the noise source side from being transmitted to and radiated from surfaces beyond.

With thicker constructions the local elasticity at the point of impact of physical agent may be such that the simple expression for the velocity cannot be used since the noise fields from all types of physical agents not on their velocities but on the resultant velocity subsequently produced in adjacent regions, and on the local resilience at the point of impact. The radiating power of the surface excited also has an effect and this in turn depends on the ratio of the frequency to the critical frequency of the panel. Further, the level of radiated noise field, which can be obtained from the resultant velocity, assumes a constant bandwidth with respect to frequency whereas practical spectra are normally obtained in terms of constant percentage bandwidth.

Design and Insulation: Ventilation systems such as an airflow triple glazed window with an automated roller blind and photovoltaic solar wall which include adequate noise attenuation can be provided in new building construction. At present they are expensive, and the problem of adapting existing buildings for such type of acoustic filter is difficult though not impossible. In particular situations where noise due to physical agents is intermittent, automation of the integrated noise and ventilation system could be performed. The provision of adequate noise insulation in a new building is always possible providing the standards which have to be achieved are known and the appropriate decisions are made at the planning and design stage. In many cases the appropriate standards can be met without extra expense at planning and design stage but it is extremely difficult to make any appreciable changes when the building is already in existence, particularly when high values of insulation are required. At the higher level of insulation, however, the effect of flanking transmission via the supporting structure is most marked and slight changes in structure may give significantly different results. It is at these higher levels of insulation that the results of field and laboratory measurements of noise insulation show the greatest difference. If a completely new form of construction is planned for which no corresponding field results are available, a laboratory measurement will indicate the potential insulation which the construction could give.

Maximum intruding noise levels: In every case, before the acoustic design is considered, the problem of eliminating external noise has to be solved, removing the unwanted physical agents, so that wanted composite wave elements can be perceived to the best advantage. The principles of noise insulation has been described, but in practice an appreciable proportion of the overall design is concerned with ensuring that these principles are adequately applied in practice to eliminate all the possible weak links in the external structure, and to ensure that no noise comes from plant or equipment which would produce any undesirable physical changes in the system.

The particular integrated insulation required will obviously depend on the level of external noise and the degree of disturbance to be eliminated. Various criteria can be put forward for the maximum levels of intruding noise permissible in acoustic design of systems. If the intruding noise is intermittent rather than continuous some account will normally have to be taken in

practice of the proportion of time for which these criteria levels may be exceeded. It is impossible to lay down hard and fast rules but the best attempt must be made within the bounds of practicability to reduce the intruding noise levels.

Absorption: All kinds of materials absorb a certain amount of composite wave elements (viz., physical agents). In noise control problems, it is necessary to predict as accurately as possible the amount by which surfaces, furnishings or materials affect noise fields by absorption. The absorption provided by many materials can be measured and tremendous practical data is available for comparison analysis. In noise control such data is essential to enable the best ways to be used to reduce the integrated noise.

The energy absorbed from noise of composite wave elements incident on a surface is most frequently converted into heat in the material, the remaining energy, transmitted or reflected, appearing as diffuse physical agents. The amount of energy absorbed obviously depends on the kind of material, but it also depends on other factors such as shape, angle of incidence and frequency of the incident noise field due to composite wave elements. The absorption coefficient, defined as the ratio of non-reflected to incident energy, can have values between 0 and 1. Absorbers can be used in situations in which noise fields are reverberant and composite wave elements are incident on the surface at all angles. For some materials the absorption does not vary appreciably with angle of incidence and data obtained with one kind of noise field may be more or less appropriate for other noise fields. For many kinds of materials and situations, however, there are differences and it cannot always be assumed that absorption charts obtained in one way can be used comprehensively.

Absorption mechanism play important role in classifying various types of absorbers.

Porous Absorbers: There are many materials commercially available for noise control fall come into porous absorbers. These are usually most suitable for general purpose treatment in noise reduction. The pores of such materials have to be interconnected so that fluid can flow right into the material and they absorb principally because of the viscosity of fluid. The noise waves cause motion of fluid relative to the adjacent material generating heat by friction and the constant compression and expansion of fluid in the pores with the resultant heating and cooling also contributes to the energy losses.

The factors which are responsible for absorption characteristics of such materials are the thickness, frequency, stiffness, porosity and structure factor. Some materials are essentially rigid and the absorption increases with frequency and thickness. The absolute values depend largely on the structure of the material. The principal disadvantage of such materials is the durability and appearance of the surface when used as a finishing material in wall. For example, rock wool and glass wool blankets are excellent absorbers but normally are unacceptable as a surface finish.

Panel Absorbers: Composite wave elements form noise field and which is acting over a thin impervious panel. Oscillations are set due to energy dissipated in the material and at the edges. The mass and stiffness of the panel on its supports and stiffness of the space behind govern a resonant frequency at which the absorption is at a maximum. Thin roofing sheets can be used over deep spaces to provide very low frequency absorption, and stiffer panels have their resonant frequency towards the low end of the spectrum. It is only at the low frequencies that this mechanism is effective since panels designed to resonate at high frequencies only provide absorption over a very narrow band of frequencies.

Resonant Absorbers: Any enclosed volume of fluid can act as a resonator. Such resonators are thought to have been used for noise control purposes since ancient times. Resonators tuned to a single frequency are rarely used in practice.

13.11. Energy Conversion in Engines and their Noise Fields

Energy balance of an engine: Energy or heat balance in an engine is an experimentally determined distribution of heat, which is added to the engine together with the fuel [41]. The energy balance is composed of input heat added to the engine together with the fuel in a definite time interval. The input heat is converted into: i) definite amount of useful work; ii) the amount of heat given to cooling fluid; iii) the amount of heat given to the lubricating oil; iv) the heat carried away from the engine by exhaust gases; v) the amount of heat that does not come out because of incomplete combustion; and vi) the remainder heat, which theoretically cannot be converted into useful work.

Thermal loads and thermal stress level: Thermal load is defined as the value of specific heat flux transferred from the working medium to the surface of a part. Transfer of heat from the working medium to the surface is affected in two ways: i) by radiation; and ii) convection. In engines, radiation is of particular importance, because mainly diffusion combustion occurs in them, which is accompanied by formation of soot which burns out subsequently. The soot content in the flame is the cause of its high degree of blackness and, therefore, of high emissive power of the flame. In practice, diesel flame temperature is much higher than the volume averaged thermodynamic temperature. High flame temperatures and degrees of blackness of flame are the cause of a high fraction of heat transferred by radiation. In practice, it is estimated that up to 45% or more heat is transferred by radiation. Radiation of tri-atomic gases also plays partial role in radiation transfer. The thermal stress level of separate parts of engine depends mainly on the disposition of the portion relative to the flame and is therefore not the same. In some engines, zones of the parts like the cylinder liner, cylinder head and piston are shielded by the piston body from the flame during intense radiation.

Heat transfer includes the convective heat exchange in the bulk of the charge and transfer of heat by conduction via the boundary layer of the charge. The heat transfer intensity is determined to a great extent by local conditions of mixture formation and heat liberation. Many case studies have revealed that the intensity and nature of motion of the charge in the cylinder and combustion chamber, formed during the intake, have not much effect on thermal loads in engine parts with variation of the motion of the charge initiated during combustion and the distribution of fuel over the combustion chamber volume. The fuel distribution

depends on the number and location of the fuel sprays and the dimensions and configuration of combustion chamber. These factors determine the local temperature of the charge. In summary, it has been revealed that the heat exchange in piston type engines is markedly nonstationary and the distribution of thermal loads in its parts is rather non-uniform. The nonstationary nature of the heat exchange depends on all the time-variable factors such as state variables of the charge, charge velocity, flame structure etc., which affect radiation and heat transfer. In such a heat exchange, the maximum specific heat flux may be several factors higher than time-averaged value. The greatest part of heat is transferred in the period of intense burning.

The type and dimensions of a combustion chamber have a significant effect on the non-uniformity of distribution of the thermal loads. Thus, in the piston type engines, the non-uniformity of thermal loads increases with a decrease of the relative diameter of the combustion chamber. In divided chamber engines, the non-uniformity of distribution of specific flux over the piston and cylinder head surface is, as a rule, more than in the open chamber engines. The level of thermal loads is to a great extent determined by the engine rating (brake power per litre). It is, as a rule, higher in two-stroke engines. Thermal loads appreciably increase with an increase in external loads (decrease in excess-air coefficient), speed, pressure and temperature of air at the engine intake. Also the injection (ignition) advance angle has a definite effect on the thermal loads. With an increase in this angle, the thermal loads grow owning to the increase in maximum pressure and temperature of the cycle. As time elapses, after a new or overhauled engine is put into service, the thermal fluxes transferred from the working medium to the parts decrease due to the accumulation of partial oxidation, cracking and polymerization products of lube-oil and fuel on the parts. Further, the transferred fluxes tend to stabilize. When the engine operates at variable conditions, the heat fluxes transferred from the working medium to the parts vary not only throughout every cycle but also from cycle to cycle. Abrupt variation of the time-averaged thermal loads in one cycle due to racing, loading, unloading, and stopping of engine is known as the heat shock. The nature and frequency of heat shocks affect the reliability of engine operation.

The term thermal stress level is used to express a set of phenomena related to the thermal state of engine parts. The thermal state of the parts has an effect on the strength characteristics of the material of which the parts are made, on the rate at which deposits appear on the parts, on the lubrication conditions of the parts, on friction, wear and stresses in the parts. Temperature stresses appear because of uneven distribution of temperature in the parts and also because the majority of parts do not enable the most heated portions to expand freely. Therefore, the thermal stress level depends on the distribution of temperature in the parts. Thermal stress is a function of the heat load, part design and its cooling conditions. The distribution of local thermal resistances depends on the design of parts. The cylinder head and piston are the most thermally stressed parts. The thermal state of the cylinder liner is also of importance, because it has an appreciable effect on the thermal state of the piston.

The methods of controlling the thermal stress level are, of course, dependent on the factors which determine the thermal stress. A definite permissible level of thermal loads corresponds to specific designs of parts, to the materials used and cooling conditions. Thermal loads can be reduced by the use of cooled constructions, which makes it possible to appreciably lower the temperature of piston. Heat insulating coatings aid in reducing the temperatures and temperature gradients of the parts. An appreciable reduction in the thermal stress level can be achieved through the use of rational design of the cooling system. Fluid cooling systems are, as a rule, more effective than air cooling systems.

Internal losses in engines: By internal losses is meant all kinds of friction losses, gas-exchange losses, auxiliary mechanisms (water, oil and fuel pumps, fan, generator, etc.) drive losses, ventilation losses due to the movement of engine parts in air-oil emulsion and atmosphere, the engine being running at high speeds, and also the compressor drive (two- and four-stroke engines supercharged by a drive supercharger) losses. In the divided-chamber engines, the hydro-dynamic losses due to the flow of the charge between the cavities of the combustion chamber are also classified as internal losses. The greater part (up to 80%) of the internal losses is frictional losses. Much of the friction losses are accounted for by the piston liner and piston rings-liner pairs. The bearing friction losses amount to 20% of the total internal losses. The following forces load the rubbing pairs: the forces of inertia, the forces exerted by gases and the elastic forces (of rings, springs). The estimation of time-averaged values of the forces acting on the parts is of significant importance for frictional losses. The time-averaged forces of inertia in absolute value are much higher than the time-averaged forces exerted by gases. Of the elastic forces, the elastic forces of the piston rings which are independent of the engine speed have the maximum effect on the frictional losses.

The following factors have a significant effect on frictional losses: i) thermal conditions of the engine affect the oil viscosity which essentially determines the forces of friction of complete fluid lubrication. When the engine runs at sub-zero temperatures the frictional losses increase and the effective characteristics of the engine deteriorate. The most appreciable decrease in the viscosity of motor oils occurs when the oil temperature mounts up to 60 °C; ii) Speed. Increasing the speed causes the forces of inertia and the relative rate of travel of parts to grow. At the same time the temperature slightly rises and the viscosity of the lubricating oil decreases. The friction forces of the complete fluid lubrication increase mostly due to the growth in the relative rate of travel of parts. The friction forces of the boundary lubrication grow due to the increase in the loads acting on the rubbing pairs. On the whole, the frictional losses appreciably increase with growing speed. Increasing the load leads to growing the gas forces, rising the temperature of parts and decreasing the viscosity of oil. Note that the speed, load, supercharging pressure, and compression ratio, on the one hand, and the design, dimensions of rubbing parts, quality and thermal conditions of lubrication, on

the other hand, should be correlated with the aim of ensuring reliable friction of the complete fluid lubrication. If these conditions and the engine operating rules are observed, then the frictional losses first decrease due to the running-in of parts and then stabilize.

Acoustic parameters of engines: The concentrations of a large number of mechanisms and machines equipped with engines are the cause of increased noise due to various physical agents at construction sites. These noise levels interfere in doing work and disturb the people in taking rest. Noise has an adverse effect first of all on the sensing organs of operators of machines equipped with engines, annoys people by getting on to the nerves, reduces the output and hinders in picking up of warning noise signals and human physiological responses. The standards as well as a correct estimation of the noise level at a work place serve as bases for the organization who handle the in-service engines. Generally the external and internal engines are normalized. There is definite tendency to lower the admissible values of the engine noise, which demands the development of new and innovative designs. The total noise level may serve as an integral characteristic of the quality of engine and of the culture of production and production processes. These separate characteristics of the engine noise are used as diagnostic parameters.

By engine noise is meant the acoustic radiation emitted by the engine when in operation. The engine noise is measured by the noise level and the noise spectrum. These are the engine noise characteristics at a point in the space. As a source of acoustic radiation, an engine is characterized by the emitted acoustic power, its spectrum and the directional diagram. Integrated noise spectrum is a very important characteristic of physical agents. The reaction of human sensing organs to physical agents of one kind of amplitude but of different frequencies is not the same. The integrated engine noise spectrum should show the distribution of the emission energy over the frequency range. Discrete components which are multiples of speed and number of cylinders can be plotted with a continuous region in integrated noise spectra. The integrated octave band spectra of all the powers of physical agents may serve as one principal characteristic of the machine noise.

Energy balance of acoustic parameters in an engine: Physical agents are known to appear due to-i) the interaction of vibrating body with the medium; ii) upon rapid liberation of heat in a finite volume of the medium; iii) during addition and outflow of a finite amount of substance to a definite finite region of the medium; iv) upon interaction of the flow of substance with a solid body. These physical processes occur precisely in time domain during accomplishment of the working cycle. Here, in all the cases of various physical agents, the acoustic emission will account all the oscillations and propagation of oscillations in this system and subsequent energy emission process in the surroundings. The combustion chamber walls deform during compression, combustion and expansion, which causes the outer walls of the engine to oscillate. The energy of wall oscillations in the form of dissipated energy is emitted to surroundings. During combustion, the heat added to working medium in the cylinder gives rise to the acoustic emission. The tilting moment will set the suspension-mounted engine into oscillations whose energy in the form of noise will partly dissipate to the surroundings. When in operation, shocks of contact parts may appear in the mechanisms and this produces additional noise. The work of units (fan, fuel feed pump, etc.) disposed on the engine also gives rise to one more noise term. During the exhaust, the substance inflows into the region adjacent to the exhaust manifold, which is liberated with a certain amount of energy. This gives rise to exhaust noise. Comparing the energy balance of acoustic parameters in an engine makes it possible to determine the most significant components of the engine noise, to indicate the causes of noise, to study the noise-formation process, and to find the most rational ways of reducing the engine noise.

Noise reduction in engines: The oscillating systems with distributed parameters of elasticity, inertia, and energy distribution are known to have an infinitely large series of frequencies of free oscillations. In reducing the engine noise, focus is to study the number of low-frequency free oscillations of parts, which fall in the range of the action of the force and its spectra. These set of low frequencies in combinations with the construction properties to absorb oscillations is called the amplitude-frequency characteristics of an engine part. The ability of the force to set up oscillations of the part on which it acts is determined first by the amplitude of the component force estimated by the coordinate of the spectrum. The larger the ordinate of spectrum, the greater is action of its force at a given frequency. Another important characteristic of the spectrum is its width. The wider the force spectrum, the greater will be its given force over a wider range of frequencies. This force can set up oscillations in the construction. Coincidence of frequencies of the amplitude-frequency characteristic of a part and the force spectrum is indicative of the development of oscillations of the part at the given frequency and thus, of the generation of noise. The release of energy of engine outer wall oscillations to the surroundings depends on the radiation resistance. In the general case, this results in active and reactive components of the radiation resistance. The active component reveals what part of the energy of oscillations is radiated as noise to the surroundings, and the reactive component gives the fraction of energy which the medium and oscillating body exchange during the period of oscillations.

The intake and exhaust noise are traditionally reduced by installing silencers. The intake silencer is usually designed integral with the air cleaner. Note that the air cleaner lowers the intake noise to a definite extent. However, modern engines are often equipped with additional mufflers at the intake. These are, as a rule, resonance chambers. The ability of a resonance chamber to muffle noise depends on its volume, the length and the area of the section of the connecting neck. Theoretically, the muffling would be the maximum only at a one resonance frequency which depends on the combination of these parameters. If an integrated noise absorbing material is disposed in this resonance chamber, then the muffling at the resonance frequency will slightly decrease but the frequency range of muffling will widen. For a better muffling, an exhaust system consisting of an exhaust silencer can

be designed. As a rule, the exhaust system designed for an engine to be used in an automobile or a tractor cannot be utilized in road building machines due to design complexities.

Noise can be reduced by applying the methods that involve vibro and noise proofing, vibro and noise absorption muffling. Vibro-absorption methods are widely used in the motor engine industry. The vibro-absorption effect resides in making use of internal friction of structural materials to absorb the vibration energy. As a result, the vibration energy converted into heat energy. This property of the construction can be enhanced, i.e. special devices –vibration energy absorbers – can be created and the engine is equipped with them. It is good experience to choose structural materials for engine parts with due regard for the internal friction. The characteristic of dissipative properties of a material, the coefficient of losses or any other characteristic should be taken into consideration along with the strength and wear-resistance characteristics. Use is also made of the oscillation or sound isolation properties which hinder the vibration energy propagation over the construction or in the engines.

Internal combustion engines may be equipped with special noise proof devices-capsules. The capsule does not contact the engine surface. Here, the engine supports are made in such a way that they exhibit high vibration oscillation properties. In designing other devices such as noise control units, similar requirements are complied with to prevent vibrations from appearing at the outer surface of the capsule, otherwise the useful effect will be lost. The noise proof devices are shields which partly block the way for a flux of a physical agent. Here it is possible to act on one or several components of energy balance of acoustic parameters on the surface. On the whole, it should be said that the maximum noise reduction can be obtained if vibro and noise proofing devices are used in combination with the vibro and noise absorbing constructions.

13.12. Noise Pollution & its Control

Our earth environment is composed of air, water and land and these are known as atmosphere, hydrosphere and lithosphere respectively. All these spheres make the biosphere. In the biosphere, apart from human beings, plants, animals, birds, fishes, insects and microorganisms also exist. The atmosphere provides oxygen, while the hydrosphere and lithosphere are responsible for water, food and space. Whenever a change, physical or chemical, occurs in the biosphere, all living beings get affected. This change is termed as pollution and the agents that institute these changes are called pollutants. Noise pollution is caused by unwanted intensity of these agents; it may be due to pollutants of air, water, light, sound, heat, radiation, fire and electromagnetic waves. The major sources of noise pollution are: i) industry and machinery; ii) transportation (surface, air and sea); iii) community activities (construction works, events, entertainment, etc.).

The main menace of noise is the transport systems. Noise from road transport, particularly heavy diesel vehicles and motor bicycles, can be a nuisance. The use of larger and faster jet aircraft is a menace if the airfield happens to be in one's neighbourhood. It causes significant damage to property besides giving freight to humans and animals. It can cause mental anguish too.

Noise pollution control is achieved by: i) reduction of noise at the source. For example, noise from a fan can be reduced by increasing the number of blades or by decreasing the rotational speed without reduction of airflow; ii) noisy machinery or equipment may be covered with insulating material; iii) protection devices like breathing masks, scarfs, mufflers, earmuffs may be used to prevent body from heat, air pollutants and excessive sound; iv) Acoustic zones should be created to prevent propagation of noise; v) trees can be planted in and around the noise sources to attenuate noise.

Noise pollution control by road transport can be reduced by using transport services like metro, bus, electric or CNG vehicles and by preventing honking of horns. The sides of the roads or highways could be lined with trees, which act as a buffer and reduce the noise pollution. New traffic regulations enforcing lower speed limits can prove beneficial. Old vehicles which produce lot of noise pollution should be taken off the road. Noise pollution at community level can be curbed by imposing a ban on: i) disposal of solid & kitchen wastes; ii) a ban on blaring loudspeakers and by reducing their pitch; iii) ban of sale and use of crackers during festivals, and processions.

Of all the measures of noise control the elimination of noise at the source, i.e. directly in the apparatus or industrial process mechanism is most effective. Some of the measures for the suppression of noise at the source are: i) substitution of non-percussion processes and tools for percussive ones, e.g., use of hydraulic drives instead of cam or eccentric mechanisms, welding instead of impact riveting and straightening instead of forge-rolling, etc.; ii) use of rotational, preferably uniform, motion instead of reciprocating motion; iv) replacement of spur and chain gearing with Y-belt and simple gear-belt transmissions; and v) replacement of spur chain pinions with helical and shevron gears.

Integrated noise proofing includes construction of barrier structures, such as walls or partitions, to safeguard the workers from external noise. Integrated noise proofing utilizes principle of reflection of composite wave elements, i.e., the greater part of the energy incident on a surface is reflected and only its smallest part penetrates through it. Ideally a noise proof structure should not let noise into an enclosure it safeguards. For the case of sound energy, it penetrates through obstacles using their own vibrations. In other words, the obstacle itself becomes the source of noise and radiates sound energy into the room, it is supposed to protect. Therefore, the more heavy (massive) the barrier structure, the more sound-proofing is achieved. As the acoustic resistance of the surface is determined by its acoustic inertance it is more sound proof to high frequency waves than to waves of low frequency.

Noise absorption is the process by which energy of composite wave elements is diminished in passing through a medium or striking a surface. Another benefit from noise absorption is the possibility of easy checking of human senses, due to operation of industrial processes, where direct composite wave elements succeed noise from every apparatus. Ceilings and the upper portions of walls above the floor level should be lagged with noise-absorbing material.

Aerodynamic noises are sharp pulses of velocity and pressure of air or gas flowing in conduits, occurring during the operation of pneumatic machines, engines, compressors, turbo-blowers, fans, ejectors, etc. To abate such noises at the source is practically impossible so they have to be suppressed or silenced. This aim is achieved by using various types of silencers and exhaust mufflers which deaden the noise by weakening the pulsations of pressure in a flow of air without causing resistance to the flow at the outlet.

13.13. Fire Alarm Systems

The objective of fire alarm signalling system is to detect and warn people in due time and inform the public fire station about the place of fire. In a building, an alarm system should be available to warn everybody in case of fire. If the alarm is not given automatically this can be done by installing alarm bells, whistles, or sirens in different parts of the building, and push-button or handles in all workrooms to operate the alarm, if necessary. The automatic fire alarm system comprises of fire-detectors (transducers), a power source, and a fire alarm station connected electrically. Electric fire-signalling system can be of two types: the radial line and the closed loop system. In a radial type fire alarm system each transducer is connected to the receiving station by a separate two wire (out and in going) line. The receiving station is designed similarly to a telephone switching center to receive all the signals from fire detectors. The system has proved reliable and effective as it provides simultaneous reception of signals from all lines.

Fire alarm warning devices, called fire-detectors, are in fact transducers that convert the physical quantities characterizing fire into electric quantities, i.e., signals which are collected at the receiving station. The signal can be initiated manually (push-button) or automatically as soon as the parameters of the environment change due to fire (temperature, flame, smoke). Fire alarms can be heat, smoke and light detectors, or detectors that use more than one parameter, such as heat-smoke sensitive detectors.

According to the principle, the fire-detectors are designed to operate on alarm and a distinction is made between the maximal, differential and maximal-differential types of detectors. The maximal-type fire detectors are designed to operate as the temperature in the room reaches the pre-set value (+60 or + 80 °C, regardless of the rate at which the temperature rises). The differential type detectors operate as the rate of temperature rise reaches a pre-set value. There are however quick-response heat detectors that ensure as instantaneous warning at the very onset of fire or even when the environmental changes preceding fire such as flashes, flames, sparks or smoke are low-key. This is ensured by using photo-cells, ionizing chambers, semiconductors, thermocouples, etc.

Some heat detectors are thermocouple devices, the operation of which depends on the difference in temperature between the junctions of two dissimilar metal conductors. In a closed circuit, this temperature difference generates an emf, thermos-electromotive force, which provides a thermoelectric current. The magnitude of the thermos-emf depends on the nature of metals and difference in temperature. A combination of two dissimilar metals having a junction which can be maintained at the temperature which it is desired to measure in terms of the thermoelectric current produced is known as a thermocouple. An individual thermocouple produces a small thermos-emf of several millivolts. To increase the thermos-emf a number of thermocouples are connected in series or in parallel or both to form a thermopile.

Some heat fire detectors use a temperature-sensitive resistor with a negative temperature coefficient. Heating increases its resistance due to increased number of free charge carriers. Resistors are normally fabricated from oxides, sulfides, and metal carbides (iron, nickel, manganese, titanium). Smoke detectors employ photo-cells or ionizing chambers or differential photo-relays. Ionizing chambers using alpha rays proved most popular. The ionizing power of alpha particles is higher than of beta or gamma rays and less harmful to the human body. Light detectors are designed to respond to different regions of the open flame light spectrum. Most popular are light detectors which respond to the ultra-violet region of the optical spectre and which may include thermos-resistors, photo-cells, photo-resistors or photo-counters, etc.

Fire alarm receiving stations or centres are designed to monitor and detect faults in the circuits, receive alarm signals, and to actuate automatic fire-fighting devices and installations. Radial type optical fire alarm station is designed for use in industry. It consists of a receiving unit with a power source and 10 radial terminals connected to it electrically. The number of fire detectors on each terminal is not limited. The centre receives alarm signals, checks the circuits for faults, warns the fire-brigade and operates automatic fire-fighting.

Radioisotope (fire-guard) stations employ smoke detectors, light and audible fire alarm indicators and are intended for use in industry. One such station is capable of initiating a fire alarm, controlling automatic fire-fighting and guarding premises against trespassing by controlling the integrity of the interlocking loops and giving audible and light signals as soon as the contacts of the lops are closed. Automatic fire alarm-guarding stations are designed to detect smoke, heat and open flames, indicate places of fire and warn the fire-brigade by light and audible signals. Such stations can also operate automatic fire-fighting and safeguard the premises.

Photoelectric fire alarm-guarding systems intended to receive and register fire-alarm signals coming from smoke detectors. It operates automatic fire-fighting and an audible alarm. The system ensures that a warning ‘Attention’ is given after one fire-detector operates, then it starts an ‘Alarm’ and automatic fire-fighting after two or more fire-detectors have operated. The system monitors and checks all the circuits and detectors, received the signals and transmits the information to the fire station. Concentrators of the fire-guard signalling system safeguard the building premises against trespassing and fire. Using one receiving station, the system serves the dual purpose of giving fire-alarm warning and safeguard signalling.

13.14. Noise Instrumentation

In order to measure intensities of physical agents, various types of sensors, transducers and meters are required. The sensing and transducing capability depends on the signal strength and its conversion into electrical signal for further processing, conditioning and data storage. Frequency analysis of the signal is required for its noise characterization. Much discussion on instruments for noise measurement is given in Purkis [42, 43].

Microphones: The prime necessity in any instrument for measurement is a microphone capable of reproducing as closely as possible in electrical terms the characteristics of the sound wave to which it is exposed. Although in some cases only relative measurement is required, such as when measuring the reduction afforded by a particular construction or device, in most cases an absolute measurement of pressure is required, i.e. the sensitivity or electrical output for a given sound field should be known, and the way in which the sensitivity varies with frequency and with angle for fields in which the sound is coming from a particular direction. Non-linear distortion will occur at sufficiently high sound pressure. The characteristics of microphones can be best categorized into electrical and sound. For electrical parameters, unit of *oncisol* should be used, whereas for their sound related parameters *oncibel* should be used. For louder noises, specially designed insensitive microphones may be required, since normal microphones may suffer actual physical damage.

Noise level indicators: The most common form in which intensity of a physical agent can be measured can be noise level meter, which can be built into the measuring amplifier. Indication of the r.m.s. value of the voltage or pressure is most often required. Thermocouples can be used to give direct reading but their use in practice is limited by their slow response and inability to withstand overloading without damage.

The noise measurements can be stored in a noise data recorder with computer storage. All the indicating devices give relative readings and for absoluter readings (of flux, pressure, intensity of a physical agent for example), a calibration signal, either of known level or electrical in relation to the sensitivity of the sensor used, is necessary.

Frequency analysis: In noise control, a single reading corresponding to the overall pressure, flux, intensity of a noise source, at a particular instant of time, is of limited use. Many practical measures for the control of noise by insulation or absorption are frequency dependent, i.e., have more or less effects for some frequencies in comparison with other frequencies. In subjective assessment, the spectral constant is used. Thus a frequency analysis of many noises is essential. The degree of analysis required varies with the kind of spectrum likely to be obtained and the purpose for which it is required. Although when presented with a completely unknown noise, it is only possible to find out whether the spectrum is highly irregular and has discrete components by a narrow band analysis. However, it is only experienced by practice that when a broad band and when a narrow band analysis is desirable.

Most of the filters used for broadband analysis are passive, i.e. consist only of arrangements of inductances, capacitances or resistances with no additional amplification and their specification in terms of the centre frequencies and response outside the pass band are a standard practice internationally.

Vibration measurement: Vibration is measured by instruments based on the mechanical and electric methods of measurement. Mechanical measuring devices, due to gaps and lag of the indicating and recording mechanism, give rather accurate readings only at relatively large amplitudes (more than 0.05 mm) and at low frequencies (up to 30 Hz). Electrical instruments are superior to and more precise than the mechanical devices. They permit measurement over a wide range of frequencies for vibrations of a large and low intensity; vibrograms are obtainable at a considerable distance from the vibration body, which is both safe and convenient. Vibration meters are used to measure vibration of surfaces. They are connected through transition adapters to the vibration transducers with the output characteristics corresponding to those of the sound level meter to indicate levels of the oscillatory velocity, instead of sound levels of pressure.

Integrated noise measuring instruments: Various instruments are used to measure noise levels among which noise meter is the commonest. This can be any form of meter which allows the operator to measure either objectively or subjectively. The measurement of loudness can be measured objectively. The principle of instrumentation is conversion of sound energy into electric energy and consists of non-directional piezo-electric microphone, an amplifier, connective filters, a detector, and an indicator. The overall circuit design is such that the meter's characteristics should approximate the response of human senses. Vibration noise meter (vibrometer) is an apparatus for the measurement in the octave band frequency or generally of the root mean square pressure levels of noise.

The levels of ultrasonic radiation can be measured by ultrasonic detectors and devices for the measurement and detection of ultrasonic waves. Such devices can be mechanical, electrical, thermal, or optical in nature [44].

To estimate electromagnetic radiation intensity in close vicinity of HF sources, measurements of electric and magnetic field strength are made separately. It is necessary because an electromagnetic field in the induction zone is a totality of independent electric and magnetic fields. The electric or magnetic field strength at a given location results from the passage of radio waves. In the case of a sinusoidal wave, the root-mean-square (RMS) value is commonly used. Unless otherwise stated, it is taken in the direction of maximum.

The principal instrument for measuring the intensity of electromagnetic fields is the radio –field strength meter, a devise consisting of an amplifier, dipole and frame antennas, and a voltage divider. The devise is calibrated using the range of the working frequencies to give readings of the effective field intensities from 5 to 1000 V/m for the electric field component, and from 0.5 to 300 A/m for the magnetic field component. The error of measurement does not exceed 20%. The antenna is placed in the magnetic field to be measured, and its position is varied until the scale gives a maximum reading.

Measuring noises from physical agents require sensing and transduction of certain parameters. Light meters can be used to measure illumination levels. Infrared thermometers can be used to measure thermographic imaging with temperature measurements. Solar intensity measurements can be made from a pyranometer. There are many heat flux sensors available to measure intensity of a heat source. A simple voltmeter can be used for measuring operating voltages of electrical equipment. Other electrical instruments are wattmeter and power factor meter for measuring power consumption and power factor. Combustion analyzer is used to measure combustion efficiency of furnaces, boilers in order to estimate energy losses and draw Sankey diagrams for exergy analysis. Ultrasonic leak detector is used for compressed air leak detection. These are electronic ultrasonic receivers that are tuned very precisely to the frequency of the hissing sound of an air leak. Airflow can be measured by a velometer, an anemometer, or an airflow hood.

Variation with time: Many of the noises requiring measurement are non-steady, and although it is possible, perhaps with the aid of measurements, to make an analysis of such noises and to obtain a response of noise level variation with respect to time, either for the full frequency range or in particular bands. Counters can be used to measure the noise band intervals. For example noise level ranges of 66 *oncibel* (oB), with a counter each placed at 6 oB range would require 11 counters to cover the entire 66 oB range. A fast counting rate, such as 11 per second, will be satisfactory for most kinds of noise where the intensity level is not varying too quickly with time, or alternatively a slower rate with some means of adding a number of very short intervals can also be used in the analysis.

13.15. Operation of Power Systems

Operating conditions and characteristics: The principal operating objective for any plant equipment and devices is to satisfy the output demand according to the load curve and ensure the highest service life and highest efficiencies with minimum noise generation in the plant. The load curve of plants is mostly non-uniform which is determined by variations of services and goods as received by the consumers. There are daily, weekly and seasonal load curves. Any plant equipment may operate in the base, semi-peak or peak modes. In a base regime, the load is essentially constant, though certain variations are allowed in this regime and even shut-down to reserve on non-working days. In semi-peak regime, the equipment is shut down to reserve in the off peak and weekends. In peak regime, the equipment is in operation only during peaks of the load.

The following principal characteristics are adopted to describe the operating conditions of any equipment: i) the net efficiency of the equipment at rated load and the average efficiency for a particular operating period; ii) the operation factor which is essentially the ratio of the actual operating time of the equipment to the calendar time of the period considered; iii) the availability factor, i.e., the ratio of the total time during which the equipment was in operation and reserve to the calendar time; iv) the capacity factor which is the ratio of the generated product to the probable product generation during the calendar time if the equipment operated at the rated product generating capacity; and v) the average and maximum time of a campaign or, using terminology from the reliability theory, the operating time to failure (a failure is understood as an event such as noise generation that reduces the output as well as disturbs the operating ability of any equipment).

Equipment operating in the base regimes should have the highest values of the indicated characteristics. It should be clear that such high indices cannot be attained by the equipment operating in semi-peak and peak regimes.

Since monobloc units gradually replace older equipment, some of them, including those are employed increasingly for supplying the variable portion of the load curve. In that respect, the manoeuverability of equipment is a characteristic that grows in importance. The concept of manoeuverability of monobloc units includes: the characteristics which determine the range of operating loads of a unit; the startup-shutdown characteristics; the dynamic properties; the characteristics at sudden sheddings and surges of the load. The conditions of operation of equipment at various loads are characterized by the load control range and the range of allowable loads. In the load control range, the automatic control system of equipment should quickly respond to load variations without interference of the operating personnel. In this range, it is not allowed to change the composition of the auxiliary equipment and the adjustment of automatic regulators. The concept of the allowable load range includes, in addition the region of loads from the lower limit of the control range to the lowest capacity at which the equipment can operate steadily. In this range, the load varies relatively slowly according to the load-dispatching curve and it allowed varying the adjustment of the auxiliary equipment to stabilize the process load.

Regimes of operation at any load with insignificant variations of output parameters are called steady. In contrast, regimes characterized by load variations and deviations of output parameters due to internal and external disturbances are called unsteady. Internal disturbances of an operating regime are caused by variations of one or more equipment inlet parameters. External disturbances are caused by variations in the external conditions. An important characteristic of equipment is its ability to change the load quickly, which is called the acceleration characteristic. It is determined mainly by the dynamic properties of equipment, i.e. by its response to regime disturbances.

The characteristic of manoeuverability of the equipment are determined largely by startup-shutdown regimes. The principal types of equipment shutdown are as follows: i) shutdown to reserve or for some types of repair work; ii) shutdown for repairs of whole plant; and iii) emergency shutdown; it is carried out by the prescribed procedure which is determined by the cause of shutdown and the possibility of restarting.

To illustrate the process of operation of power systems, the case of boiler combustion of thermal power plant is mentioned herewith [45].

Power systems operation under steady conditions: In general, equipment operation is carried out according to a regime chart which gives the principal characteristics of the regime

obtained by the equipment tests. Modern monobloc units are equipped with computer panels which make it possible to determine the current or average efficiency characteristics and the process stream characteristics. This information is used for the optimization of equipment operation. In addition, a number of automatic regulators maintain the process parameters at optimal values. For these devices the regime chart gives the extreme variations of the variables, above which the personnel should correct the operation of the controllers or change to manual operation. Steady regimes of the equipment operation may be different depending on the load. Variations of a particular process parameter or regime characteristics as a function of load are described by what is called the static characteristics.

For the case of thermal power plant, controlling the efficiency of combustion process consists in maintaining the optimal excess air ratio in the furnace and in distributing the airflow between the burners in accordance with fuel distribution. Uniform distribution of fuel and air between the boiler burners is favourable for decreasing the maximum temperatures of water-wall tubes, decreasing temperature stratification of flue gases at the furnace outlet, and preventing slagging of the heating surfaces. The temperatures conditions of the heating surfaces are also impaired if some tubes have leaks or bursts. Tube-burst indicators of the acoustic type based on sound sensing are finding increasing use for detecting bursts and leaks in boiler tubes. If the temperature behind particular heating surfaces has increased above the allowable level or if a tube burst has been detected, the boiler is shut down.

With an increase of load, the temperature of flue gases at the furnace outlet increases, resulting in a greater volume of combustion products and higher temperature gradients in the convecting heating surfaces whose heat absorption thus increases with this result. As has been established by boiler tests and by experience of boiler operation, the lower limit of the load control range is: i) 40-50% of the rated load in the combustion of fuel oils, gas and high-volatile coals; ii) 50-60% for lean solid fuels; and iii) 60-75% for slagging-bottom boilers. The lowest load for stable operation of a boiler is usually 30-40% of the rated load.

Power systems operation under unsteady conditions: Specific processes occurring in drum-type and once through boilers are determined by the differences between these boiler types: the position of the boundaries of the steam-generating portion, its filling mass and capacity of heat accumulation. For a drum-type boiler, a change in load is done by changing simultaneously the fuel consumption and the capacity of blowers, with subsequent variation of feed water flow rate which is controlled by the water level in the drum, with leading pulses from variations of the steam and feed water flow rates. The load of a once-through boiler can be varied by similar procedures, with the sole difference being that feed water flow rate is controlled by the fluid temperature in an intermediate portion of the path. A different control procedure is often employed in the automatic control systems of once-through boilers: first the feed water flow rate is varied according to the load and the flow rates of fuel and air are controlled in proportion to it and corrected by the fluid temperature in the intermediate portion of the path. In monobloc units, two versions of load variations are employed. For planned load variations, the load of the turbine is changed by varying the steam-generating capacity of the boiler so as to maintain a constant pressure of live steam. When the unit operates in a regime controlled by the power controller of the turbine, the load of the turbo-generator is changed first and the boiler load is then corrected.

Starting-up circuits: The starting-up circuit includes special starting devices, which are used only at start-up, shut-down and during load shedding of the equipment. Taking example of a boiler unit in thermal power plant, these starting-up circuits include devices for discharging the steam from the boiler into the atmosphere before the boiler is connected to the steam main header. In Monobloc units, the start-up and shut-down regimes of the boiler and turbine are interrelated more closely and are much more complicated. In this connection, starting-up circuits, operating instructions and automatic control systems for monobloc units have been symbolized. They are based on a standard procedure of starting up a unit by ‘sliding’ regime, i.e. by gradually increasing the flow rates, pressures and temperatures of live and reheated steam. This procedure creates the most favourable conditions for starting the turbine and decreases starting-up losses. The procedure requires no special devices for its realization in monobloc units with drum type boilers. For the quick starting-up of a boiler, the starting circuit has a pipeline for steam discharge from the drum into the atmosphere, which is in use during the period when pressure rises roughly to 0.6 MPa. The sliding regime of starting-up of a once-through boiler cannot be performed without special devices, since from the requirements of reliable temperature conditions and hydrodynamics of steam generating water walls, the starting-up flow rate of feed water must be less than a specified value and the fluid pressure in the water walls must be maintained at a level close to the nominal pressure. For a sliding starting-up regime, a once-through boiler is provided with an internal starting-up unit which comprises an internal gate valve, an internal separator, and pipelines with throttle valves for the supply of working fluid to the internal separator, drainage of moisture, and steam removal from the internal separator. The starting-up circuit for any type of boiler has a bypass line around the turbine which connects the steam main directly with the condenser. A startup-shutdown device in this line comprises a closing throttle valve, a noise absorber for sound waves, and a spray-type steam attemperator. Live steam is discharged through the turbine bypass line in the following cases: i) at starting-up of the unit, for a period when steam temperature is raised to the level determined by the thermal conditions at the turbine inlet; ii) at shut-down, for the period during which steam is discharged from the boiler and the latter is cooled; and iii) at load shedding, for the period when the turbine is idle-running or supplies only the auxiliary load of the unit. Starting-up circuits have special devices to maintain the temperature of live and reheated steam. A characteristic feature of drum-type boilers is that their steam-generating capacity during start-up lags substantially behind the increasing fuel consumption, so that the

temperature of tubes of super-heater rises substantially and may exceed the allowable limit. Besides, it is essential to maintain the specific schedule of live steam temperature variation before the turbine. On the other hand, the condensate-spraying system of the main circuit can operate only at boiler loads not less than 30% of the rated value. For this reason, there is provision of a starting-up spray system with atomizing nozzles arranged in the condensate-spray diffusers.

In most cases, the starting regime of a monobloc unit should ensure a reduced reheated steam temperature level and further control of this temperature according to the specified schedule. In view of the dynamic properties of the re-heater and some other factors, the main means of control can be used only beginning from loads 25-30% of the rated value. A method for starting control that is widely used in all types of monobloc units is steam bypassing in the reheating system. Part of the steam is passed from the cold reheat line into the hot reheat line thus lowering the temperature gradient, and therefore, the heat absorption in the re-heater. As steam from the cold reheat line is mixed with that in the hot reheat line, the temperature of the reheated steam can be controlled at the lower level. In once-through boiler units, a starting spray is additionally provided in the steam main, which is used to control the temperature of reheated steam upon closing the steam bypass. Feed water to the starting spray is supplied at a pressure of more than 7 MPa from the intermediate stage of the feed pump, so that there is no need to control the water pressure in the spray line. In some cases, only one means of reheated steam temperature control is employed. It is possible to employ steam bypassing only, if it has been established by boiler tests that the re-heater has reliable temperature conditions at the maximum load at which the steam bypass will be used. The allowable conditions for starting spray are determined by the minimal flow rate and pressure of steam at which moisture will be evaporated completely in the steam flow and will not precipitate on the internal surface of the steam main header, especially in the nearest bend after the spray.

Power system shut-down and load shedding: Before normal shutdown, the boiler of a monobloc unit should be unloaded, i.e. its load should be shedded. When shutting down for short time (for instance, overnight), the hot state of the plant is usually retained wherever possible, so that load shedding is limited (for the most part not less than 50% of the rated load). When shutting down for a longer time, it is advisable to utilize the accumulating capacity of the boiler as much as possible. This is favoured by the deep unloading of the unit with sliding (variable) pressure of live steam. In addition to this, upon flame extinction in the boiler furnace, the turbo-generator is left for a certain time connected to the system so as to work off the accumulated steam in the boiler. The load shedding conditions in a drum type boiler are determined by the rate at which the saturation temperature in the drum decreases; this should not exceed 1.5-2 °C/min. The rate at which load shedding is occurred in the once through boiler by the action of its automatic control system can be determined by the dynamic properties of the boiler.

A boiler is shut down by interrupting the fuel supply to the burners and the supply of feed water. In drum-type boilers, the drum is first filled with water to the upper working level. Upon flame extinction in the furnace, the draft fans remain in operation for 10-15 minutes to prevent the accumulation of an explosive mixture in the gas-air path, which is thus ventilated. During the standstill, measures are taken to prevent the condensation of steam in super-heater tubes, since this might involve complications in subsequent firing of the boiler and decrease the boiler reliability. In view of this, as a once-through boiler is shut down to reserve and the feed water supply to it is discontinued, the water path up to the internal gate valve is closed (by closing the feed water valve, and the fittings of the internal separator) and steam is discharged from the super-heater (via the start-up and shut down device) and re-heater (via the discharge line from the steam mains) into the condenser. When shutting down a drum type boiler, the pressure in it is reduced gradually (by steam discharging through the start-up shut down device of the de-super heater), so as to maintain the saturation temperature below the temperature of flue gases in the super heater, i.e. by forming conditions preventing the condensation of live steam in the super heater. The drum is periodically fed with water. The re-heater is freed from steam in the same way as in a once-through boiler.

When the cold shut-down of a monobloc unit must be performed, requiring that all boiler equipment be cooled, load shedding is carried with the gradual reduction of the pressure of live steam. In a once-through boiler, the internal gate valve is closed at a load roughly 60% of the rated value and the pressure in the path up to this valve is then maintained constant. In both types of boilers, the temperature of live steam is lowered together with its pressure at a rate allowed by thermal stresses in metallic elements of the boiler, pipelines and turbine. At the same time, the temperature of reheated steam is lowered. The super heater and re-heater can thus be cooled roughly to 300 °C.

In emergency situations, a boiler is shut down with ‘pressure retention’. As the furnace is extinguished, the feed water control valve and the team outlet valve are closed, the turbo-generator is switched off, and the start-up shutdown device is kept closed if the pressure of the live steam is below the actuating pressure of the boiler safety valves. In this method, the pressure and temperature of fluid along the boiler path are first held at the same values as in normal operation. After that they diminish slowly owing to heat transfer to the surroundings and loose fittings of the water steam path. If the trouble is eliminated quickly, this method of shutting down makes it possible to start the boiler from the state of hot reserve. Otherwise, shutting down is continued and steam from the super-heater is discharged.

Emergency shut-down of a boiler must be carried out immediately in the following situations: i) when the water level in the drum passes beyond the safety marks or the supply of feed water to one of the flows in a once-through boiler is interrupted for more than 30 secs; ii) on failure of the water level gauges in a drum type boiler or of the feed water flow meters in a once-through boiler; iii) when there is no flow of steam through the re-heater; iv) when the pressure has risen intolerably (in once-through boilers, a pressure drop is also dangerous); v) on rupture

of tubes in the water steam path; vi) on flame extinction in the furnace, explosions in the furnace or gas ducts, or inflammation of combustible deposits in convective heating surfaces; vii) on an intolerable reduction of the pressure of gas or fuel oil the control valve; viii) when there is no voltage at remote-control devices and measuring and control instrumentation; and ix) on switching off of the turbine (in monobloc units) or of some of the auxiliary equipment (draft fans, blowers, etc.). In all such cases, a delayed shut-down can aggravate the situation and cause serious damage, so that the boiler operator is instructed to stop the boiler without waiting for permission from the management. An emergency shut down of a boiler is affected by the protection system on receiving the signal as per appearance of some or other emergency situation.

Firing system for thermal power generation: Firing system operation consists of preparatory procedures, firing, and raising the load to its specified rated capacity. The first preparatory stage includes assembling the water-steam, fuel, and gas-air paths, preparing all mechanisms and systems, creating vacuum in the turbine condenser, pre-starting de-aeration of feed water, etc. A drum type boiler is filled with water as required. The water level in the drum should be somewhat below the normal mark so as to allow swelling. A once-through boiler is to be filled with water in all firing regimes, except for firing from the state of hot reserve. As water is fed into the boiler, it displaces air from the system (provided that the air pressure is not excessive). In a once-through boiler, the feed water flow rate is adjusted at the starting-up level and the water pressure is raised to the working value by closing the throttle valve, In boiler firing from the hot state, first a reduced flow rate of water is established (10-15% of the nominal value), which makes it possible to slowly cool the boiler path up to the internal gate valve and internal separator. The starting-up flow rate of water is set in upon raising the water pressure before the internal gate valve. Water from the internal separator is discharged into the start-up expander and further into the circulation conduit. The start-up and shutdown device is opened to create vacuum in the super heater. This procedure is also carried out in a drum type boiler if there is no excessive pressure in it; this ensures a slower rise in the saturation temperature of the drum during firing. In cases when the start-up and shutdown device is initially closed, its opening is performed only upon firing the furnace, so as to maintain a constant pressure of live steam that has been generated to that moment.

During boiler standstills, moisture may accumulate in some stages of the super heater, which can be prevented through certain measures. Besides, un-tightness of the internal gate valve and throttle valve in a once-through boiler may lead to moisture accumulation in the pipeline and the first heating surface behind the internal gate valve. This moisture can be pushed out into the hot headers of the boiler during firing and cause their cracking. In a drum-type boiler, this may result in a quicker pressure rise in the drum at the initial stage of firing, which in turn diminishes the allowable heating intensity in the furnace. By opening the start-up shutdown device, the super heater is connected with the condenser which promotes the evaporation of moisture from the super heater tubes during boiler firing.

After switching on the draft fans, ventilating the gas air path, and preparing fuel supply mechanisms, the regime of burner firing is carried out. It is advisable to carry out the boiler firing by igniting as many burners as possible with the least fuel flow rate through each of them; this is essential for the uniform heating of the water walls around the furnace periphery and for minimizing local thermal stresses; in drum type boilers, this measure is additionally essential for the development of circulation in all water walls. In boiler starting from a cold or warm state, the initial flow rate of the fuel is controlled at a level of 12-15% of the nominal value. In a drum type boiler, this ensures the quick development of circulation in water walls and, on the other hand, the rate of pressure rise in the drum is within tolerable limits. In starting from the hot state, the fuel flow rate in the initial period is established at 20% of the nominal value or, if there is steam flow through the super heater, is increased additionally so as to attain the required temperature of live and reheated steam.

As the initial flow rate of fuel has been established in a once-through boiler, the flow rate of the feed water and the pressure of fluid before the internal gate valve are maintained constant. As the pressure of fluid in the start-up expander has risen up to 0.4-0.5 MPa, steam from the expander is removed to the deaerator and, when a sufficient quantity of drain water has been accumulated, the cycle is closed. In boilers with boiling-type economizers, the regime with periodic water feeding and a low constant flow rate of water can in some cases lead to a substantial maldistribution of heat along with hydraulic maldistribution. Some water-distributing tubes may supply the fluid of a higher enthalpy (up to super-heated steam) to the drum. This is prevented by maintaining the specified temperature of fluid in an intermediate section and at the economizer outlet by properly controlling the flow rate of water and by increasing the rate of blowdown on an increase in the water level in the drum. As the initial flow rate of fuel has been established, it is possible to raise the flow rate and parameters of live steam in a drum type boiler or the temperature of fluid before the internal gate valve, in a once-through boiler. The temperature of fluid determines its moisture content on entry to the internal separator.

As the super-heater is connected to circuit, as a result the temperature of tube metal in the heating zone decreases. At the same time, the temperature of steam at the boiler outlet gradually increases, since the heat transfer coefficient increases with the flow rate of steam. As the steam flow rate through the super heater increases, the steam mains are gradually heated. Steam is discharged from them through the start-up shutdown device and the drainage of the dead-end sections. Heating is usually carried out until the temperature of steam before the high pressure cylinder of the turbine is roughly 100 °C higher than the temperature at the steam inlet. In units provided with a pressure reducing de-super-heater, the re-heater system is heated by supplying live steam to the cold reheat pipeline and discharging it from the hot reheat pipeline into the condenser. This heating is only started when the temperature of steam before the de-super-heater exceeds the temperature at the discharge end of the high-pressure cylinder of the turbine, so as to avoid cooling of that

section. The end of heating of the hot reheat pipeline is determined by the temperature of steam before the intermediate-pressure cylinder of the turbine which exceeds the temperature at the steam inlet by 50-80 °C.

In some regimes, a monobloc unit can be started without preheating the steam pipelines, in particular, the regime of starting from the hot state. Moreover, when the thermal insulation is in proper condition, a unit can be started without preheating the re-heater system after a standstill for 1-2 days. A criterion of such regimes is a decrease in the steam temperature by not more than 20-30 °C compared with the temperature at the steam inlet to the turbine. As pre-heating is completed, the flow rate of fuel is corrected so as to ensure the steam-generating capacity of the boiler at which the initial load of the turbo-generator will be around 5% of the rated value. In starting up from a cold or a warm state, the flow rate of the fuel is usually established at the minimal level so as to obtain more easily the required low temperature of live and reheated steam. In starting up from hot state, however, the flow rate of fuel is increased to the upper limit (30% of the nominal value in the circuits with single bypass) to obtain a steam temperature close to the nominal value. Before pushing the turbine rotor, the starting sprays are switched on and the temperature of live steam is established at a desired level. In a once-through boiler, the throttle valve in the line of water recirculation to the deaerator is set so as to obtain a steam pressure before the starting spray nozzles that is 1.5-2.0 MPa higher than the pressure of live steam. In a drum-type boiler, the desired steam temperatures behind the stages of the super-heater are additionally pre-set. In units of higher capacities there is no steam bypass and only the starting sprays to the steam main, which are put in operation before connecting the turbo-generator to the electric network, are used. Before connecting the turbo-generator to the network, when its rotor is accelerated and synchronized, the steam-generator capacity of the boiler and the temperature of live steam are maintained constant. During this period, the temperature of the re-heated steam gradually increases for the same reasons as on connection of the super-heater.

The temperature of the re-heated steam rises especially sharply on connection of the turbo-generator, i.e. when the steam flow rate through the re-heater system is almost doubled. For this reason, it is important to switch on in due time the devices which control the temperature of re-heat. In units with once-through boilers, the start-up and shutdown device is not closed during the period of turbo-generator synchronization, so that all the control valves of the turbine are opened (and heated) due to a drop of pressure in the live steam. In units with drum type boilers, the start-up and shutdown device is partially closed to maintain a constant pressure of live steam, which improves the operating conditions of the boiler drum and control over the steam temperature. As the turbo-generator is connected to the network, the start-up and shutdown device is closed and the unit begins to supply the initial load.

At the third stage of starting (loading) a monobloc unit, its elements are heated from the initial temperature to the final temperature corresponding to its operation under the rated conditions. An attempt to shorten the time of loading may result in the quick heating of the boiler elements and the appearance of high temperature gradients. The highest temperature gradients and highest temperature stresses can appear in massive thick-walled elements, such as the housing and rotor of a turbine, the drum and headers of a boiler, and fittings of the steam mains. In such cases, compressive stresses appear in the heated surface of an element and tensile stresses in its unheated surface. Upon heating an element, temperature stresses diminish to zero and often even change sign. Stresses of an inverse sign can form in elements on the reduction of the steam temperature or shutdown of the unit. With frequently repeated start-up and shutdown regimes, thermal stresses vary cyclically and can cause fatigue cracking of the metal. These stresses determine the allowable heating rates of these elements.

Solid fuel-fired boilers are transferred from starting fuel (gas or fuel oil) to solid fuel, if the load is 15-30% of the nominal value, and the consumption of the firing fuel is gradually reduced. As the boiler begins to supply the specified load, the elements of the starting circuit which are used only at start-up and shutdown are switched off and the voltage supply to the corresponding drive means is discontinued. Some monobloc units, which supply a variable portion of the load curve, are started by an automatic process control system. Such systems can perform automatic control of a given process and carry out discrete operations by means of logic control units. These units an switch on and off the mechanisms of auxiliary system of a boiler, change the position (open or close) of closing valves, switch on and off automatic controller, switch over the controllers from some actuators to others, alter the structural schemes of the controllers, etc. Before performing a particular operation, a logic control unit checks that the operation is allowed. In monobloc units provided with an automatic control system of this type, the boiler operator has following additional functionalities: i) to perform preparatory operations for starting the unit and select the reserve mechanisms which will be switched on automatically; ii) to supervise the functioning of the equipment and perform manual control should a failure occur in the operation of a particular automatic controller; iii) to correct the operating conditions (when needed) by adjusting the set-point devices of automatic controllers; and iv) to check the state of the equipment upon completion of a particular stage of the starting regime and issue commands for a next stage. Thus the automatic control system of a monobloc unit is complex of the technical means of control and the operating personnel which co-operates with these means.

13.16. Friction and Oscillations

Friction and oscillations are closely interrelated, friction is capable of generating oscillations, and oscillations have influence on friction [46]. The discussions are presented here on the concept that the friction force is mainly formed by a load normal to the rubbing surface and by the corresponding normal contact deformation. Important is also the concept that the oscillations in complex elastic systems are interdependent. This means, that the normal and tangential oscillations of a slider cannot arise

irrespective of one another. When one kind of oscillation occurs, the others usually take place too. This interdependence is determined by how close the natural frequencies of the respective oscillations are and by the character of their relation.

Normally directed oscillations generated by friction: If a sliding body or slider has a height that is not much greater than its transverse dimensions, i.e. this slider is other than a rod sliding on its end face, the elastic compliance of the slider in the normal direction is dozen of times lower than the compliance of the contact layer, the latter being a layer formed by the peaks and valleys of micro irregularities of the rubbing surfaces. In this case, the slider is roughly similar to an absolutely rigid body that rests on a number of minute springs which simulate the peaks of surface irregularities. Some of these are in contact and carry the normal load, while others, the smaller ones, are out of contact. Any casual normally directed pulse acting on the slider will cause its free oscillations in the normal direction. These oscillations are non-linear and asymmetrical, because more and more new smaller peaks come into contact as the slider moves downwards, and because the contact rigidity is variable: it rises when the slider moves down and drops when the slider moves up. An increase in the amplitude of these oscillations causes the mean level of the slider over the counter face to rise and thereby the total real contact area to decrease.

As the slider moves along the counter-face, its surface asperities receive micro-pulses from the asperities of the counter-face. The normal components of these micro-pulses continuously generate the oscillations of the slider as a whole in the normal direction. These micro-pulses, chaotic as they are, maintain permanent quasiperiodic sustained oscillations of the slider in the normal direction. These asymmetrical oscillations lift the slider and reduce the friction force. The higher the speed of sliding, the more intensive are the normal components of micro-pulses between the surface asperities, and hence the greater is the amplitude of the oscillations, the higher is the mean level of the slider movement, the smaller is the real contact area, and the weaker is the friction force. That may explain the drooping of the friction force-speed characteristic, i.e. reduction in the friction force with increase in the speed of sliding in the absence of lubrication. Oscillograms of oscillations, which are contact oscillations, show that their amplitude grows linearly with the sliding speed.

Effect of forced oscillations on friction force: To reduce friction, use is made of normally-directed forced oscillations whose frequencies are usually very different from the contact resonant frequency. For this reason a tangible reduction of friction force requires the application of powerful vibrators. The selection of a vibrator is determined by the construction of the tribological joint and by the mass of the vibrating element. Piezo-electric vibrators are convenient to use for small masses, whereas electrodynamic vibrators are used for large masses. The quantitative problem of power rating of the vibrator depending on the slider mass and the rubbing surface properties can also be solved. The power of the vibrator must increase with an increase in its mass. Piezoelectric vibrators are attached symmetrically to the top surface of the slider so that they extend radially from the surface far enough to provide the coincidence of their natural bending oscillation frequencies with the resonance frequency of the contact oscillations and, at the same time, with that of the vibrator. That increases the magnitude of the friction force resonance minimum without changing the frequency. For gradual control, the forced oscillation frequencies should be farther from the resonant frequency.

Normal micro-pulses are proportional to the speed of sliding. With tangential oscillations at work, the normal micro-pulses reach its maximum twice for one period of the tangential oscillations. As there is the natural frequency of the normal oscillations, the frequency of the forced tangential oscillations (which is half that of the normal oscillations), must act as a resonance frequency for inducing the maximum amplitude normal oscillations.

Frictional self-excited oscillations: A non-uniform sliding of solids rubbing against each other under a constant reactive force may involve more or less periodic halts; this uniformity is called frictional self-excited oscillations. A possible explanation for non-uniform sliding is a drooping sliding speed-friction force characteristic. In this case a casual acceleration of sliding reduces the friction force and leads to a further acceleration until the slider has slipped into the position where its external elastic constraints develop a reactive force which causes the slider to slow down. The slow-down increases the friction force and therefore leads to a further slow-down. In some cases the slider slows down to a stop, and then the pull of the elastic drive rises until it dislodges the slider by causing it to skip once again. The non-uniformity occurs when the gradient of the drooping characteristic, i.e. a negative derivative of the friction force with respect of the sliding speed, becomes greater than te coefficient of damping of the drive's oscillating system. The greater this gradient, the more intensive oscillations take place and the higher is the speed below which the slider oscillations are attended with halts. The main practical recommendation for eliminating the non-uniformity of sliding is to increase the damping capability of the slider drive and to lower the gradient of the friction force-sliding speed characteristic or to remove completely the factors which give rise to a drooping characteristic.

13.17. Automatic Control and Management of Noise Systems

Definition of noise systems: The physical structure of a noise system is extremely diverse and complicated. A noise system consists of noise fields of composite wave elements due to physical agents. Noise systems therefore are hard to formalize and deny a uniformly valid straightforward methodology which could be helpful in their analysis and handling. The choice of noise system parameters involves such methods based on experience of handling a noise system by way of system control theory. However, experience obtained in handling one noise system cannot be used in assessing the behaviour of another system, so each noise system has to be described by a separate model. The model evaluator, therefore, has to adopt a multimethod, multidisciplinary approach which naturally, prevents tracing even

general equivalence relations between various noise systems. The introduction of computers brought about a variety of simulation techniques based on the generation of random variables and functions. However, applied to noise system problems, these programs are cumbersome, computer time intensive, and may even fail to warrant optimal solutions. The existent techniques of system control theory – the vector matric approach in the state space and frequency domain techniques – and software package based computational procedures are of limited value for noise system modeling and design [47].

Noise systems operating in the presence of uncertainty or in conflict situations may be handled to advantage by the methods of game theory. These methods are efficient in solving the synthesis problems in noise systems and searching for their optimal system arrangements. Some of the above-mentioned directions pertaining to noise characterization theory for noise system studies have not yet received a due development to become suitable for practical problem solving, mainly owning to the complexity of the respective computational procedures and the need for powerful software packages. Most of these shortcomings can, in all probability, be overcome by establishing super-high efficiency computer aided noise system networks with elements of artificial intelligence. This however, may require a few years of research of many institutions in electronics, instrumentation, computing and information science. The development of appropriate versatile software to support complex design of a noise system may take even longer time. Therefore power design procedures for a noise system capable of optimizing the system arrangements and parameters of noise systems will evolve unless both measurement hardware and simulation and computing software are available.

Wide scale introduction of industrialization, fast transportation systems and modern engineering systems in daily lives of people have led to the development of complex noise systems. Over and above, these noise systems came into existence when they received powerful computers for their control. As a result, a new class of noise systems engineering has appeared in which operating instructions, realized as computer routines, monitor and control continuous subsystems for their automation. Such noise systems are referred to discrete-continuous systems and their design faces certain problems due to the intrinsic complexity and lack of well-established mathematical methods of analysis and synthesis. On the advantage side, computer simulation can be employed even in the absence of analytical methods for noise system design and it is simple for monitoring the time evolution of the noise process concerned. Among the disadvantages, simulation is hard in deriving a model adequate to the actual noise system. Moreover, it cannot generate its own decisions (which can be made with analytical design techniques), and the last but not least, the procedure of noise characterization simulation is rather long as it has to evaluate the effects of a large number of variables, controls, and disturbances. The pursuit for elimination of these shortcomings has led to the development of analytical techniques, facilitated by the recent advancements in computer hardware and software along with internet of things (IoT).

The flexible automated lines, for example in industry and transportation systems are a very broad class of noise systems. They offer improved output at minimum costs due to an organizational approach, which is directed towards mechanized systems, which lack in optimization and control of noise from these systems. This approach takes account of all the ingredients of production cycle including raw material supply, manufacturing, and transportation of finished items for further processing and assembly, or toward warehouses. This implies that these automated lines are multistep noise systems with a given subsystem arrangements. The intrinsic constraints for such noise systems due to composite wave elements (viz., noise fields) are energy and materials balances in the form of inventories in stock, production resources and storage capacity for raw materials and display capacity for ready products.

The mathematical models for this type of noise systems take the form of multivariate algebraic equations and inequalities. Optimal parameter search under large number of noise system constraints is achieved by high capability software programs with linear and non-linear variables. To simplify computational procedures, both the direct and decomposition techniques assume that the matrix of constraints is rather sparse, i.e., contains many zeros and linear terms. In the direct methods based on linear programming and the simplex method, the main computational procedure is the manipulation of the inverse of the base case. To compute the inverse matrix it is decomposed into a product of elementary matrices each containing maximum possible number of zeros. The inverse matrix can also be represented as a product of two triangular matrices, which significantly reduces the amount of computations. If the algorithms of storing the matrix are such that the columns are stored with the use of special markers introduced into the code, then what is stored is a reduced-size matrix of elements alien to the initial matrix.

Decomposition methods represent a large system as a number of individual subsystems. Decomposition can exploit the techniques for linear and nonlinear compensation of interconnections, and the sequential elimination of low-impact controls and disturbances. These methods are normally realized in the form of structural transformations. The computational procedure of large problem decomposition is built around column generation. Columns are generated where necessary, but none of them is stored so that the main storage requirements are considerably reduced. The decomposition method is an iterative procedure comprising a sequential solution of the noise systems problem and its subsystems involved. Once the initial feasible basis of the noise system problem is generated, one can derive the dual variables to determine the objective function of its subsystems. Solving the subsystems in turn generates new columns for the noise system, which give rise to a new basis and dual variables and the computational procedure is done with recycled iteration.

The above mentioned process is a simplex algorithm which converges to an optimal solution in a finite number of iterations. For cycling of iteration, additional manipulations are necessary to ensure convergence of the iterative process. With an appropriate

modification of the problem formulation, the decomposition principle can be used to solve problems of large and complex noise systems. New control languages and data processing codes introduced for solving large scale linear programming and mixed integer programming problems are well adapted for computer aided modeling and control of noise systems. Synthesis of flexible automated noise flow fields and noise control systems should allow for time dependent functions governed by the probabilistic behaviour of input constraints and their associated service times. These noise systems are multilevel arrangements with an arbitrary structure, and their modeling may be achieved with advantage on the lines of queueing theory. Because of the complicated structure of the processes in noise systems the modeller has to allow for a multitude of various factors, the complete list of which is not always attainable. A much higher efficiency than in deriving analytical dependences can be achieved with asymptotic techniques. These exploit the fact that physical parameters of the system can be treated as small variables. In the context of modeling a noise system, asymptotic techniques perform in much the same manner as exact methods: both yield dependencies which form a base for exhaustive search algorithms of the parameters essential for the system development.

Noise management systems would require the need for introducing priority servicing strategies. As a rule, priority is assigned on the basis of service time. Another approach is to assign priority in accordance with the value of the service-time to waiting-cost ratio, so that the highest priority is assigned to the arrival of service with the smallest ratio. Numerous other methods may be invoked for priority assignment. However, in noise systems, a priority strategy does not always result in analytical relationships for modeling, forcing the choice of parameters to be performed by complex methods of mathematical modeling.

Modeling studies in queueing theory have received wide application areas in noise systems comprising of communications, computer networks, transportation systems, equipment maintenance scheduling, resource management etc. It should be noted that many areas of the current research in queueing theory resulted because of the advancements of computer information systems. This expanded the range of solvable problems, and gave rise to new methods of decision making helpful in deriving arrangements of noise systems for their modeling, simulation and control.

There exist a class of noise systems operating under uncertainty and conflict conditions. Each conflict situation taken from the practical experience is normally extremely complicated and its analysis is hampered by a multitude of secondary factors. Modellers would require analyzing such noise systems with simplified game models. The salient feature of these models is that none of the players is informed in advance on the decision made by the others, i.e., the player has to choose his strategy under uncertainty. At times the uncertainty of the outcome may be due to a priori unknown external disturbances. The game theory models involved in the solution of noise system synthesis include finite and infinite zero-sum games, cooperative games and differential games. Finite non-cooperative games are used to study discrete noise systems, or continuous noise systems which can be reduced to the discrete counterparts. In synthesis problems, utility functions are formulated in terms of payoff matrices. In n-person games, each player has its own utility function.

In infinite zero-sum games, players tend to reach antagonistic objectives and the set of feasible solutions is infinite. This feature of the games makes them a suitable tool for the synthesis of continuous noise systems. Cooperative games are involved when the noise system problem allows pre-play coalitions concerning players' strategies to be set up, and the payoff to be distributed among the players on a pre-arranged basis. Differential games are, essentially, multistage games with continuous time. The transition from state to state is then described by a set of differential equations. The usual assumption is that two players together control the motion of a particle in n-dimensional space, and controls for this motion are chosen by means of a vector or scalar performance criterion. Game theory models are fairly unwieldy and have come into use for system synthesis after information and computing system science became available. For most practical problems the analyst has to invoke heuristic approaches and interactive optimization systems.

Computer simulation: In complicated noise systems, dynamic automatic control can be described by high-order differential or difference equations. In order to arrive at the precision and quality of the performance specification for a noise system modeled, the modeller has to adjust parameters many times so the procedure may run into long simulation times. The modules of a computer simulation program in the noise characterization field can be compiled by means of a vector matrix description of dynamics in state space. Matrix representation in frequency domain can be very useful for algorithms computing transfer functions, frequency characteristics, transient processes, and studying the dynamic accuracy of continuous and discrete automated noise control systems. This approach to analysis and synthesis of complicated automatic noise control systems may relieve the modeller from routine operations. The engineer or modeller engaged in computer simulation normally has to analyze many sets of different alternatives for the noise system to choose one which most fully meets the performance specifications. At the final stage of analyses, procedures of search theory and decision making theory may be invoked. The chosen alternative is decided by two factors: i) by the probabilities of the outcomes that would take place; and ii) by the priorities used in comparison of alternative outcomes. Most widely used techniques rely on decision making with priority subject to a given objective function. These techniques are supported by the respective algorithms of quasi-optimal or optimal decisions. The complexity of automatic noise control systems decreases the modeller's capability of treating all the information concerning priority in a non-formal manner. Therefore, new decision making techniques are developed which are based on judgmental assessments. These assessments are generated as the modeller subjects various system alternatives to his judgement with account of numerous relevant factors such as precision, quality, cost, reliability, weight and size, and most importantly noise pollution control factors and the

information on the interconnection of these factors. In addition, the technique takes into account the judgemental assessments of experts in the noise characterization and control field. Since these assessments are performed by several experts, the designer ranks them and evaluates correlated judgements, and the level of significance for the performed expertize. If the deviation of the judgemental assessments is insignificant, then the correct decision may be evaluated with a very high significance coefficient. On the other hand, deviation of judgements may be used to advantage in a collective assessment. Collective brainstorming sessions may bring about interesting results, without a total comparison with the individual priorities derived. In all the situations considered, decision analysis offers advantages over analytical techniques because it allows formalized account of numerous subjective factors essential for the problem on hand. Some decision making techniques rely on multi-critical methods of optimal control. In some situations, the multi-criteria problem of optimal control reduces to one with a scalar criterion. The further development of decision making is seen on the way of implementing the methods of finite games using vector criteria.

To date decision making has reached a status when it can handle complicated problems of noise system design. However to ensure correct decisions to be made more versatile methodological procedures are needed, that are built around multifactor priorities and collective actions of experts, as well as the related computer simulation software. The above mentioned methods of noise system analysis enable the modeller not only to obtain optimal arrangements, but also to determine their numerous characteristics of a noise system. Solution to the noise system problem encounters considerable difficulties because of inadequate information on the capabilities of the existent noise systems either because of a small size of the respective system's family or because of total lack of the respective analogs. Practical prognosis includes several methods such as the analogs technique, trend extrapolation, the development model, construction trees of objectives, and statistical estimation. As a rule these methods are backed up by individual or collective expert assessments. Certain disadvantages have been noted for these methods. More specifically: The analogs technique is difficult to derive identical characteristics. The trend extrapolation cannot ensure a correct choice of the characteristics being forecast not to say about a large amount of statistical data required for its realization.

The best forecasting technique is the statistical method because it ensures a high reliability of prognoses at a rather scarce initial data input. However its use incorporates a reduction in the space of characteristics. The significance of a particular characteristic for the noise system's potential evaluation depends on its contribution to the accuracy of the noise system's class identification. Normally this contribution is measured in terms of losses, specified by a loss matrix. The statistical approach also requires a model which separates all evaluated noise systems into feasible and infeasible categories. Then the potential of the noise system may be assessed from the probability of the parameter vector in each of the classes concerned. However, often the scarcity of initial data prevents this operation from being implemented. Therefore, the characteristics are combined in groups. The number of combinations is to be determined from modeling. These combinations are used to estimate the accuracy of the classification and the loss matrix is set-up. If the expected losses computed with such matrices are minimal, then the system may be classed as feasible one. After this, it is assumed again that each combination is a signature and they are classified. The process continues until the accuracy of classification ceases to alter.

For automatic noise control systems, consideration should be given to the non-linearity involved and the random nature of the signals. The behaviour of such noise systems is described by stochastic differential equations. When these equations run into high dimensionality their solution encounters significant difficulties. The analyst has to invoke various linearization techniques for nonlinear functions, including statistical techniques. It should not be overlooked, however, that these models are valid so long as the assumptions fundamental to the statistical linearization principle hold true. This limitation can be removed by invoking the path integral technique which expands the range of nonlinear problems handled. Basically the path integral technique consists in representing the solution of nonlinear stochastic equation as a sum over all feasible paths of the dynamic noise system. The set of these paths can be finite or enumerable for discrete systems, and have the power of continuum for continuous noise systems.

The state of art in noise system theory is such that the necessary prerequisites are existent for solving problems of the noise management of multilevel economic systems. These problems include integration of noise generation activities, scheduling, transportation planning, optimal facilities location and layout and project management. For their solution, one may exploit systems analysis and certain methods and their state of art algorithms. Most of these are heuristic techniques which yield only approximate solutions. The quality of solutions improves when the problems are solved systematically in an iterative manner so that final decision is made by the modeller. Further development of noise system theory can be motivated by the cumulative number of problems which can give rise to a variety of research efforts tailored to suit numerous applications.

Automatic control in noise systems: The main direction of current technological development would be to control the process variables in the noise system and arranged the system as per desired objectives. The field is however materially penalized by lack of research in the development of rigorous mathematical methods which would allow the modeller to select the most efficient arrangement and parameters for constitutive modules of the noise system. In noise systems, which are made for automatic controlling of either complicated or simple objects, the streams of data and controls may be of essentially diverse physical nature, which significantly hampers the formulation of mathematical models and consequently the development of its design and modeling methodology. The most complicated group of noise systems are those involving as one of the control links a human operator or a group of people coordinating, matching, or

predicting control actions.

Actual noise systems consist of a wealth of individual interdependent subsystems of various levels, of hierarchy. The behaviour of these subsystems varies under the impact of the environment and control instructions issued for the system to accomplish its objectives. A multilevel arrangement of the noise system leads to the need for a sequential stage-by-stage coordination of activities within the noise system. The efficiency of such coordination depends on the choice of local controls at each stage such that it ensures an optimal performance of the noise system. The process of sequential coordination with iterative procedure can be used for improving the global performance of a noise system.

The number of levels used in devising the hierarchy of a noise system is conditioned by the adopted mathematical model. In an elementary description the arrangement may be treated as consisting of a number of interrelated subsystems of the noise system. The hierarchical arrangements can pave the way for a general approach to their buildup. All the arrangements have a vertical system with the control actions formed at the upper level flowing downwards. Three basic types of multilevel noise systems, most frequently occurring in practical situations are as follows: i) with vertical flow of control actions; ii) with controls applied via feedforward and feedback loops; and iii) with the use of matched control actions in feedback loops. The modellers need to breakdown such noise systems into simpler components with the use of decomposition techniques. The decomposition is known to boil down to the synthesis of a noise coordination system modification device. Accordingly, the condition central to a decomposition is that the noise system is coordinated. Once the noise system is decomposed into separate subsystems, the synthesis problem is solved for each of them and the optimal arrangement and parameters derived that satisfy certain deterministic local criteria. This is done in such a way that the recombination of so derived subsystems into a single noise system may ensure extremity of the global deterministic performance measure formed from the adopted local criteria by some elementary operations. Then the parameters of subsystems are varied to arrive at the given stochastic performance specification. It should be recognized that this approach is valid only for noise systems described by differential and difference equations reducible to linear equations. Its applicability to nonlinear noise systems requires additional validation based on the methods of operations research. Two step optimization – first with the deterministic and then with the stochastic performance measures – considerably simplifies the estimation of effectiveness and modeling of noise systems.

In the absence of random external disturbances and equipment failures, all multilevel noise systems can be synthesized with a deterministic performance criterion allowing only two outcomes (if the noise system accomplished the objective or not) and subject to a number of constraints imposed on the time of accomplishing all the stages of the operation. However, actual noise systems operate in random environments, under the conditions of randomly varying parameters. For recurrent operating cycle the effectiveness of design alternatives can be assessed using stochastic performance measures.

Noise control system and its characterization: The increasing complexity of noise control systems has led to the call for their refinement of the formal models used in their design. Such a model describes in a formal manner how the process being controlled interacts with the environment. In the classical context of automatic control, including a controlled process, a decision making block, and feedforward and feedback loops, a control action is generated from information on the controlled process and its state, the data on the state arriving through the feedback loop. If the controlled process is a continuous noise system, it is described by laws specifying its functions as a rule in the form of integro-differential equations in which the state of the controlled process is a continuous function of time. From the practical viewpoint, however, controlled processes in the form of discrete systems are characterized by: i) a finite set of events that transfer the noise system from one state into another (including the transitions that occur as a result of control actions); ii) a finite set of conditions defining noise system's states; and iii) a finite set of controls. Such a noise system normally denies a description by equations including time functions. A decision on a control is made upon assessing the current state of the object. Such an estimate is a function of the parameters defining the arrangement properties of the noise system rather than its numerical characteristics, as is the case with continuous noise systems. The noise system may contain resources that cannot be shared – a typical situation in practice – then a request for this resource may not be honored immediately and the process will have to wait for this resource a certain time. The management of a system thus reduces to allowing certain processes to hold resources and taking a resource away from a process, so that the process is blocked. The quality of management is then decided by the number of processes in the wait condition and the number of resources being held by blocked processes, i.e., waiting processes and resources held by them are undesirable.

Noise management systems: A variety of methods may be involved in building a model for a multilevel noise system with hierarchical control, called a noise management system. These are simulation techniques, queueing theory, various optimization techniques, game theory etc. The methods are combined in order to achieve more or less comprehensive models. Such multifaceted approach hampers establishing the interconnection between subsystem descriptions and, when in an industrial context, the erection of a model for enterprise noise management. These problems owe their existence in the large part to the absence of a clear cut global comprehension of the system being controlled, specifically of the noise system structure. Noise management system modeling presents the analyst with particular problems.

Assume that the noise system to be modeled is a transportation network. What should be meant by the element in such a noise system? Since the task of transportation is to provide the shipment of goods, it would be logical to assume that this element is a complex of three types of facilities, namely, loading means, carrier vehicles, and unloading means. Such a complex

aggregated for a shipment disintegrates when the process of shipment is over and its components are available for the formation of new complexes which in turn disintegrate. Thus the mentioned noise system will be conceived as a multitude of elements being integrated and disintegrated in a random fashion. Consequently, it is difficult to reveal regularity and to define the noise system structure. However, for the noise system to perform its main function, consistent with the objective for which it has been devised, it is immaterial what the specific complexes will be, i.e., which facilities will be integrated in them. This implies that there must be a noise system structure that is sufficiently stable and adequately defines noise system components.

Every noise system can be described either in the lines of transforming the input excitations into the output quantities, or by way of a process aimed at achieving a certain objective or performing a certain function. The first approach is referred to as the cause-effect process. Essentially, it decomposes the noise system on hand into simple elements interconnected by cause-effect ties according to the input-output principle. Each element is to perform a certain, logically completed, specific function, the union of which, upon interconnecting the elements under the set principle, is to achieve the global function of the noise system. Exciting the input of such an element by a standard waveform, one may evaluate how the element functions by recording its output and describe this function by a model. All these activities identify the physical element having input and output ports with the function it performs. By identifying an element or module with the function it performs, elements are represented by different structures – physical and functional. This identification is valid until cause-effect, or input-output, connections can be traced out in the noise system and this is decomposable into elements in accordance with this principle. Unlike engineering, physical and other types of system, noise management systems are never closed, therefore their evolution or purposeful development is an integral factor of their existence. Owing to this fact, the control of the development of such noise systems is the most important type of control as it defines not only the improvement of the management system but also the quality of its performance and its very existence.

13.18. Research Areas in Noise Characterization Theory

Human noise behaviour: a) Developing a slide rule for noise measurement; b) Acoustic/Noise Filters, built environment analysis, human comfort & health through selective acoustic/noise filter configurations; c) Physiology and epidemiology of human noise behaviour.

Integrated control of built environment parameters for comfort and wellness: Providing acceptable Indoor Environmental Quality is a critical function of built environment system through characterization and measurement (odors, dust, pollen, light, humidity, heat, sound, electricity, airflow, air temperature, fire etc.). With integrated environmental control, these environmental parameters are to be characterized and checked through sensation and perception of occupants for comfort and wellness and controlled through various environmental monitoring sensors. The effect of these human behavioural parameters is to be characterized and measured on a logarithmic noise scale.

Distributed/Noise generation characterization & modelling; health effects (+/-); comfort/discomfort indices: a) Aero-acoustics/wind-induced natural ventilation; b) Pedestrian comfort/discomfort/noise indices with wind-induced corner peak pressure on tall buildings; c) Solar & wind energy conversion acoustics on PV/T collectors; d) Hybrid wind and solar PV systems (off Grid) for serving remote city areas; e) Wind energy conversion acoustics/electromagnetic interference due to wind mills; f) Heat transfer, thermal compression oscillations, thermo-acoustics.

Energy conversion materials characterization and noise insulation: a) Novel solar energy conversion materials, their properties & characterization for selective configurations of solar photovoltaic, thermoelectric and solar thermal collectors; b) Integrated insulation materials properties; c) Heat transfer, energy, entropy & noise generation modelling.

Energy conversion materials and noise generation modeling: a) Solar energy conversion by biological & photosynthetic materials; b) Hydrogen production through solar energy conversion; c) Biomass/Waste-to-Energy Conversion; d) Energy, exergy, thermodynamic, entropy & noise generation modelling.

Energy conversion (materials, devices) and noise: a) Investigating solar energy acoustics by using/devising geothermal energy to supply power of a mega power size plasma torch for plasma gasification of waste; b) Investigation on their control system using wireless power transfer; c) Energy, combustion, exergy, thermodynamic, entropy & noise generation modelling.

Industrial energy conversion (materials, devices) and noise management: a) Industrial energy conversion, waste/biomass combustion/incineration and cogeneration for electric power and HVAC comfort requirements; b) Energy conversion in engines and noise reduction; c) Noise reduction in transportation systems; d) Noise systems modeling and control.

Instrumentation: a) Sensors & transducers for measurement, monitoring and control of noises (light, sound, heat, fluid, electricity, fire and the sun); b) Electromagnetic, thermoelectric and piezoelectric transducers for noise measurement.

Graduate teaching courses: a) Building Insulation; b) Sustainable Eco-Cities; c) Human Environmental Health; d) Noise Systems Engineering; e) Occupational Cellular Physiology; f) Solar Energy Acoustics; g) Measurement Systems and Units.

14. Conclusions

A study on acoustic signal processing and noise characterization theory via energy conversion in a PV solar wall device with ventilation through a room is performed. The noise interference and characterization as per speed of a composite wave is presented. The sources of noise waves (sun, light, sound, heat, electricity, fluid and fire) are described depending on their speed of noise interference. Noise measurement equations and their units are coined. The power systems are classified as per

source signals of solar power, electric power, light power, sound power, heat power, fluid power and fire power. The noise filters for filtering noise from power systems are defined with examples.

Energy conversion is investigated in a PV solar wall by means of experiments and numerical model. The outdoor experiments were conducted on a PV solar wall installed on a wooden frame connected to a room with passive and active ventilation. Further, outdoor experiments were established under available operating conditions. The experiments conducted on a PV solar wall have taken into consideration the effect of heat capacity, thermal time constant, and thermal storage losses. The experimental results along with results of simulation model for noise filtering for a PV device are presented.

The electrical and thermal characteristics were established for a PV solar wall. The sensible heat storage capacities of a PV solar wall installed on a wooden frame were higher in comparison to a window glass or a stand-alone PV module. The electrical and thermal characteristics were function of both outdoor air temperature and thermal storage losses. Finally, production of heat and electricity was a nonlinear function of volume of electrical and thermal resistances developed across a PV solar wall similar to a loudspeaker. The active ventilation was deemed to be essential in order to avoid over-heating of a PV solar wall and to maintain adequate outdoor ventilation in a room under mild climate conditions.

Some noise unit examples for an air duct exposed to solar radiation are tabulated. A phenomenon of photovoltaic amplification for a pair of photovoltaic modules connected to a potentiometer is enlightened. The time plots of power function were used to support and devise noise measurement expressions and noise characterization in a power system as per speed of a wave.

A simple theory is outlined in this paper which gives an indication of the way in which noise due to physical agents are attenuated by a complex system or building elements. In practice due to complex elements, the noise transmission due to composite waves comes both via the common partition panel and the balance from the supporting structure. Theory and measurement applicable to panels can be extended to complex building systems, since it is the objective to devise the lightest and simplest panels with the highest values of insulation. It is the net effect of the panel partition with its associated structure which decides the insulation obtained in practice and which is difficult to predict.

Detailed discussions of noise characterization theory in various disciplines are presented through energy conversion model and experiments with emphasis on cities, acoustics, electrical, control, noise fields, energy conversion in engines, noise pollution & control, fire alarm systems, noise instrumentation, operation of power systems, friction & oscillations along with some discussions on automatic control & management of noise systems. The paper has also introduced theory and concept of solar energy acoustics. Description of sensors & transducers for a human brain with example of human comfort & health are also presented. Research areas in noise characterization theory along with its graduate teaching subjects are briefly outlined.

Appendix has presented some basic definitions to understand the noise characterization theory.

Acknowledgment

Part of the work was conducted by the author at Department of Building, Civil and Environmental Engineering, Concordia University, Montréal, Québec, Canada.

References

[1] H. Dehra, **"**A Paradigm for Characterization and Checking of a Human Noise Behavior", WASET Proceedings of 19th International Conference on Psychological and Brain Sciences, pp. 658-666, May 11-12, 2017, Montréal, Canada.

[2] H. Dehra, **"**Electrical and Thermal Characteristics of a Photovoltaic Solar Wall with Passive and Active Ventilation through a Room", WASET Proceedings of 19th International Conference on Sustainable and Renewable Energy Engineering, pp. 584-592, May 11-12, 2017, Montréal, Canada.

[3] H. Dehra, "A unified theory for stresses and oscillations", *Proc. Canadian Acoustical Association (CAA) Montréal 2007 Conf*, Concordia University, Montréal, Québec, Canada , pp. 132-133, 2007.

[4] H. Dehra, "Power transfer and inductance in a star connected 3-phase RC circuit amplifier", *Proc. AIChE 2008 Spring Meeting,* New Orleans, LA, USA, session 96a, 2008.

[5] H. Dehra, "The noise scales and their units", *Proc. Canadian Acoustical Association (CAA) Vancouver 2008 Conf*, Vancouver, B.C., Canada, pp. 78-79, 2008.

[6] H. Dehra, "A benchmark solution for interference of noise waves", *Proc. AIChE 2009 Spring Meeting*, Tampa, FL, USA, session 67c, 2009.

[7] H. Dehra, "A guide for signal processing of sensors and transducers", *Proc. AIChE 2009 Spring Meeting*, Tampa, FL, USA, session 6b, 2009.

[8] H. Dehra, "Solar energy absorbers", chapter 6 in *Solar Collectors and Panels, Theory and Applications*, edited by Reccab Manyala, InTech Publication, pp. 111-134, 2010.

[9] H. Dehra, "Acoustic filters", chapter 5 in *Ventilation: Types, Standards and Problems* edited by Vincent A. Romano and Allison S. Duval, Nova Publishers, pp. 135-154, 2012.

[10] H. Dehra, "A theory of acoustics in solar energy", *Natural Resources*, pp. 116-120, 4 (1A)**,** 2013.

[11] H. Dehra, "A novel theory of psychoacoustics on noise sources, noise measurements and noise filters"*, Proc. NoiseCon16*, Providence, Rhode Island, pp. 933-942, 13-15 June, 2016, Publisher: Institute of Noise Control Engineering, USA, 2016.

[12] H. Dehra, "On Sources and Measurement Units of Noise", Proc. International Conference on Innovation, Management and Industrial Engineering (IMIE 2016), Kurume, Fukuoka, Japan, 05-07 August 2016, 219-227, ISSN: 2412-0170, 2016.

[13] H. Dehra, "A Slide Rule for Noise Measurement", 10th International Conference on Sustainable Energy Technologies (SET 2011), Istanbul, Turkey, September 4-7, 2011, 5 p.

[14] V. Del Toro, *Electrical Engineering Fundamentals*, 2nd ed., Prentice-Hall of India, New Delhi, India, 1986.

[15] Robert H. Randall, *An Introduction to Acoustics*, Dover Publications, USA, 1951.

[16] Ingo R. Titze, *Principles of Voice Production*, Prentice Hall, Englewood Cliffs, NJ, USA, 1994.

[17] J. C. Lucero, "Dynamics of the vocal fold oscillation", *TEMA Tend. Mat. Apl. Comput.*, 6, No. 1, pp. 11-20, 2005.

[18] J.L Threlkeld, *Thermal Environmental Engineering*, Englewood Cliffs, NJ, USA, 1962.

[19] H. Dehra, "*A heat transmission model for a telephone line",* Proc. of 21st CANCAM, Department of Mechanical and Industrial Engineering, Ryerson University, Toronto, Ontario, Canada, June 3-7, 2007, pp. 356-357, 2007.

[20] H. Michael Newman. *Direct Digital Control of Building Systems,* John Wiley and Sons, New York, USA, 1994.

[21] H. Dehra, **"**Photovoltaic Solar Wall: 2-D Numerical Modeling and Experimental Testing under Fan induced Hybrid Ventilation", proceedings of the IEEE International Conference on Energy Efficient Technologies for Sustainability, April 7-8, 2016, St. Xavier's Catholic College of

Engineering, Nagercoil, Kanyakumari District, Tamilnadu, India, IEEE Xplore, ISBN: 978-1-4673-9925-8, Page(s): 668-676.
[22] H. Dehra, "A Multi-Parametric PV Solar Wall Device", in proceedings of IEEE International Conference on Power, Control, Signals and Instrumentation Engineering (ICPCSI-2017), 978-1-5386-0814-2/17/$31.00 ©2017 IEEE, Chennai, India on Sep 21-22, 2017, pp. 392-401.
[23] H. Dehra, "Characterization of Noise in Power Systems", proceedings of IEEE International Conference on Power Energy, Environment & Intelligent Control (PEEIC2018), 978-1-5386-2341-1/18/$31.00 ©2018 IEEE, Greater Noida, India on April 13-14, 2018, pp. 321-330.
[24] H. Dehra, "A numerical and experimental study for generation of electric and thermal power with photovoltaic modules embedded in building façade," submitted/un-published Ph.D. dissertation, Dept. Building, Civil and Environmental Engineering, Concordia University, Montréal, Québec, Canada. August 2004.
[25] H. Dehra, "Experiments on photovoltaic modules embedded in building façade," AIChE Spring 2010, San Antonio, TX, USA, March 21-25, 2010.
[26] H. Dehra, "The effect of heat and thermal storage capacities of photovoltaic duct wall on co-generation of electric and thermal Power," AIChE 2007 Spring Meeting, Houston, Texas, USA, April 22-26, 2007, session 36a.
[27] C. Muresan, C. Ménézo, R. Bennacer, R. Vaillon, "Numerical simulation of a vertical solar collector integrated in a building frame: radiation and turbulent natural convection coupling," Heat Transf Eng, pp. 29-42, 27, 2006.
[28] J. H. Kim, J. T. Kim, "A simulation study of air-type building-integrated photovoltaic-thermal system," Energy Procedia, pp. 1016-1024, 30, 2012.
[29] Y. Lin, C. Chiang, C. Lai, "Energy efficiency and ventilation performance of ventilated BIPV walls," Eng Appl Comput Fluid Mech, pp. 479-486, 5, 2011.
[30] C. J. Ho, A. O. Tanuwijava, C. Lai, "Thermal and electrical performance of a BIPV integrated with a micro encapsulated phase change material layer," Energy Build, pp. 331-338, 50, 2012.
[31] H. Dehra, "The effect of heat and thermal storage capacities of photovoltaic duct wall on co-generation of electric and thermal Power," AIChE 2007 Spring Meeting, Houston, Texas, USA, April 22-26, 2007, session 36a, 9 pages.
[32] H. Dehra, "The Entropy Matrix Generated Exergy Model for a Photovoltaic Heat Exchanger under Critical Operating Conditions", International Journal of Exergy, Vol. 5, Issue 2, pp. 132-149 (2008).
[33] H. Dehra, "A Two Dimensional Thermal Network Model for a Photovoltaic Solar Wall", *Solar Energy*, 83 (11) 1933-1942 (2009).
[34] H. Dehra, "An investigation on energy performance assessment of a photovoltaic solar wall under buoyancy-induced and fan-assisted ventilation system", Applied Energy, pp. 55-74, 191, 1 April 2017.
[35] H. Dehra, "A Combined Solar Photovoltaic Distributed Energy Source Appliance", Natural Resources, June 2011, Issue 2, pp. 75-86.
[36] H. Dehra, "A Mathematical Model of a Solar Air Thermosyphon integrated with Building Envelope", International Journal of Thermal Sciences, Vol. 102, April 2016, pp. 210-227.
[37] ASHRAE Handbook, *Fundamentals Volume* (1997), American Society for Heating, Refrigerating and Air-Conditioning Engineers, Inc., Atlanta, GA, USA, 1997.
[38] ANSI/ASHRAE Standard 55-2004. *Thermal environmental conditions for human occupancy*, American Society of Heating, Refrigerating and Air-Conditioning Engineers, Inc., Atlanta, GA, USA, 2004.
[39] Jerrold H. Krenz, *Energy Conversion and Utilization, 2nd Edition,* Allyn and Bacon, Inc,, Boston, USA, 1984.
[40] Larry Gay, *The Complete Book of Insulating,* The Stephen Greene Press, Vermont, USA, 1980.
[41] V. Lukanin, *Internal Combustion Engines,* Mir Publishers, Moscow, 1990.
[42] H.J. Purkis, *Building physics: Acoustics*, Oxford, New York: Pergamon, 1966.
[43] H J Purkis, "Instruments for noise measurement", Journal of Scientific Instruments, Volume 41, Number 5, pp.284-289, 1964.
[44] M.K. Poltev, *Occupational Health and Safety in Manufacturing Industries*, Mir Publishers, Moscow, 1985.
[45] M. I. Reznikov and Yu. M. Lipov, *Steam Boilers of Thermal Power Stations*, Mir Publishers, Moscow, 1989.
[46] I.V. Kragelsky, *Friction, Wear, Lubrication – Tribology Handbook*, Vol. 2, Mir Publishers, Moscw, 1986.
[47] A. A. Voronov, *Management and Control in Large Systems*, Mir Publishers, Moscow, 1986.

Appendix

Definitions

Energy Area: The definitions of noise sources are characterized by energy area stored in a wave with its speed and difference due to power intensities of two waves due to interference.

Noise of Sol: The difference of power intensities between two solar power systems causes noise of sol (S). The power storage on a unit area per unit time defines amplitude of a solar energy wave. The storage of solar power is defined by a solar energy wave pack of unit cross sectional area and of length s, the velocity of light.

Noise of Therm: The difference of power intensities between two heat power systems causes noise of therm. The power storage on a unit area per unit time defines amplitude of a heat wave.

The storage of heat power is defined by heat energy wave pack of unit cross sectional area and of length s, the velocity of light.

Noise of Photons: The difference of power intensities between two lighting power systems causes noise of photons. The power storage on a unit area per unit time defines amplitude of a light beam.

The storage of light beam is defined by light beam packet of unit cross sectional area and of length s, the velocity of light.

Noise of Electrons: The difference of power intensities between two electrical power systems causes noise of electrons. The power storage on a unit area per unit time defines amplitude of an electricity wave.

The storage of electrical power is defined by an electricity wave pack of unit cross sectional area and of length s, the velocity of light.

Noise of Scattering: The difference of power intensities between two fluid power systems causes noise of scattering. The power storage on a unit area per unit time defines amplitude of a fluid wave.

The storage of fluid power is defined by fluid energy wave pack of unit cross sectional area and of length s, the velocity of fluid.

Noise of Scattering and Lightning: The difference of power intensities between two fire power systems causes noise of scattering and lightning. The power storage on a unit area per unit time defines amplitude of a fire flash.

The storage of fire power of light is defined by fire pack of unit cross sectional area and of length s, the velocity of light. The storage of fire power of fluid is defined by fire pack of unit cross sectional area and of length s, the velocity of fluid.

Noise of Elasticity: The difference of power intensities between two sound power systems causes noise of elasticity. The power storage on a unit area per unit time defines amplitude of a sound wave. The storage of sound power is defined by sound energy wave pack of unit cross sectional area and of length s, the velocity of sound.

Nomenclature

T_p	Temperature of PV module
T_b	Temperature of insulating panel
T_a	Temperature of air
S	Solar Intensity
E_p	Electric power
V	Air velocity
T_o	Ambient air temperature

T_s	Room air temperature
$H_{pv\text{-}T}$	Heat capacity
ΔT_v	Temperature difference (y-ordinate)
ΔT_H	Temperature difference (x-ordinate)
ρ_n	Density
K_d	Thermal conductivity
H_d	Film coefficients
T	Thermal time constant
Q_v	Thermal storage capacity (y-ordinate)
Q_H	Thermal storage capacity (x-ordinate)
C_n	Specific heat
d_n	Thickness
$d_n\rho_nC_n$	Energy stored/m^2/K
I_{sc}	Short circuit current
V_{oc}	Open circuit voltage

ASTES

Advances in Science, Technology and Engineering Systems Journal Vol. 3, No. 4, 173-186 (2018)

www.astesj.com

Special Issue on Multidisciplinary Sciences and Engineering

ASTESJ

ISSN: 2415-6698

Supporting Active Aging Through A Home Automation Infrastructure for Social Internet of Things

Vittorio Miori*, Dario Russo, Luca Ferrucci

Institute of Information Science and Technologies (ISTI), CNR-National Research Council of Italy, Via Moruzzi 1, Pisa 56124, Italy

ARTICLE INFO

Article history:
Received: 30 May, 2018
Accepted: 05 July, 2018
Online: 29 July, 2018

Keywords:
SIoT
IoT
Interoperability
SOA
SOCIALIZE
AAL
Smart Home
Active Ageing

ABSTRACT

The number of smart devices inside the living environments grows more and more every day, and with it the need to interface them in order to share data and activate functions. Each day, new scenarios and new applications emerge to make our lives easier in many different contexts. The AAL SOCIALIZE project aims to create a new reference platform for active ageing by applying technological solutions to care for the health of the elderly, facilitate their daily activities, simplify their access to dedicated services.
The work presented herein describes the "Elderly Monitoring service" – an IoT module of the SOCIALIZE platform, whose aim is to monitor elderly people's activities and physiological parameters and to combine smart device functions. This modeling process can actively contribute to anticipating, and thereby preventing, emergency situations, increasing elderly autonomy and making them feel "protected" and "safe".
In this regard, the system implements a practicable, scalable solution that allows heterogeneous devices belonging to different domotic systems using diverse protocols to interact with each other, share data and services and bind together through 'friendship', thereby creating an infrastructure suitable for the creation of a true Social IoT (SIoT).

1. Introduction

This paper is an extension of the work originally presented in *2017 Global Internet of Things Summit* (*GIoTS*) [1].

The issues involved in welfare and health costs sustainability are currently the focus of widespread discussion in many nations of the world. Of such issues, one of the most frequently addressed is population ageing. The ageing population will soon become one of the most demanding Big Societal Challenges that the world will face [2]. Over the last 150 years, life expectancy has risen by 50 years, and over the last half century alone it has increased by three years every decade.

Hand in hand with ageing, it is highly likely that the elderly will experience an increase in disability and dependence, along with a greater incidence of age-related illnesses and the need for medication [3]. The majority of the ageing population experiences progressive deterioration of their health from 50 to 80 years of age. As a result, there is an interval of 30 years during which subjects age with deteriorating health – a critical aspect to take into consideration when seeking to preserve good quality of life for the elderly. Over recent years the elderly population has been growing. This is mainly due to the progressive increase in life expectancy and the low fertility rates affecting an ever greater proportion of the overall population [4]. This progressive increase in the elderly population has led to a new phenomenon: so-called active ageing. According to the definition of the *World Health Organization* [5], active aging is "a process of optimization of opportunities for health, participation and safety in order to improve the quality of life of older people". Active aging is epitomized by elderly people who, rather than spend their entire day sitting at home, bored, in an armchair, voluntarily stay in the workforce for as long as they can, they exercise, they train, they take care of their children and grandchildren. They are over 65-70 years of age, they are healthy, they are satisfied and they often have acquired skills, including on the technological and logical levels. In the near future, the upcoming candidates to join the ranks of the active aging are currently in the age range of 50-60 years. The European Community is actively involved in caring for the active ageing, and to such end has launched the programme "Ageing well in the information society". Moreover, the European Commission declared 2012" The Year of Active Ageing and Solidarity between Generations". One result of the measures adopted in 2012 is the formulation of the active ageing index, which measures the ability of older people to achieve their full potential in terms of

* Corresponding author: Vittorio Miori, Email: vittorio.miori@isti.cnr.it

employment, social and cultural participation and maintaining autonomy.

In an information society, *Information and Communication Technology* (*ICT*) plays an important role for the active elderly. Utilizing the *WWW*, for example, they can get information, have social interactions, participate in social and political life, enjoy simplified access to administrative and commercial transactions, find online entertainment and leisure activities, and so on [6]. Moreover, *ICT* offers a great opportunity for older people living home alone. According to the *Internet of Things* (*IoT*) paradigm, objects are rendered 'intelligent'– they can be discovered, localized, and acquire, process and exchange data. Smart Home & Building applications are particularly important in the *IoT* scenario, as they are the link between the individual (citizen, consumer) and the overlying layers implementing the *IoT* paradigm (Smart City, Smart Grid) [7].

The *IoT* is however not merely a distant vision of the future – it is already here and is having an impact on more than just technological developments. It permits sophisticated devices to share information directly with each other and the cloud, making it possible to collect, record and analyze new data streams faster and more accurately. So, it is now possible to exploit a broad set of services able to improve the autonomy of the elderly [8] and constantly monitor their health status and identify any potentially hazardous conditions [9]. Connected 'smart objects' can be used to collect data on the health status of home residents, particularly those at risk. The *IoT* will thus make possible to create environments equipped with such intelligent devices in which an older person's state of health is constantly monitored, allowing for more effective management of his or her long-term well-being. The advent of the *IoT* and its new technological capabilities offers many advantages over traditional health monitoring. In particular, conventional monitoring systems are not predictive, that is, they cannot offer the same accuracy as modern biometric detection systems, which are capable of recognizing emergencies before they occur, and they do not have the ability to "automatically" launch a warning to formal and/or informal caregivers without direct action by the elderly person.

Instead, by combining wearable devices with *IoT* these limitations can be overcome. Commercial products offering similar such features already exist: intelligent watches whose functions range from detecting movements indicating a possible fall and contacting the authorities or relatives, to the ability to "learn" a person's normal activities and send an alert by text message, email, or other app if a significant change occurs (e.g. a user lies in bed for an entire weekend).

The last frontier of the *Internet of Things* is the evolution of objects that are 'merely' smart to objects that can be social. This paradigm is called *Social Internet of Things* (*SIoT*) [10,11]. The *SIoT* is defined as an *IoT* in which objects are capable of establishing social relationships with other objects, independently of human intervention, thereby creating a social network of objects.

The key principle guiding the *SOCIALIZE* project [12] is to create a complete technological solution which effectively fulfills the general objectives of the third call of the *EU – AAL* (Ambient Assisted Living) programme. The *SOCIALIZE* project is creating a new, specialized platform expressly dedicated to today and tomorrow's active ageing people in order to facilitate their participation in social life.

The authors' main contribution to the project presented in this work is the study and development of a *SIoT* ready service, called the *Elderly Monitor*, which is fully integrated into the *SOCIALIZE* platform. The function of the service is to monitor the activities of home occupants, collect and analyze personal and environmental parameters from various, technologically heterogeneous devices and enable them to cooperate and share data. The results of the monitoring can be accessed by doctors, relatives and/or caregivers as deemed appropriate with regard, for example, to the cognitive, health status and wishes of the person in question.

The paper is organized as follows: in *The Social IoT (SIoT)* section is introduced the feature and advantages of the *SIoT* apprach, in the *Related work* section are shown the most significant solutions for the monitoring and analysis of the user's health parameters, the main applications of the *IoT* in the health field and the most widely used *SIoT* approaches. In the section *Socialize Project* is presented the *SOCIALIZE* project with its main features and objectives. This section allows to illustrate the context in which the application presented in this work was studied and developed. In the section *SmartSMILE framework* is described in detail the ideas of the proposed solution. In the *Implementation* section are described how some domotic technologies have been integrated in the framework. In the *Field trials* section are shown the deployment and the experiments carried out to verify the correct functioning of the system. Finally, we have the *Conclusions* section that summarizes and concludes the work.

2. The Social IoT (SIoT)

Adoption of the *SIoT* paradigm presents several further advantages: (*i*) the resulting structure of such object networks can be shaped as required to guarantee network navigability and effectively perform the discovery of objects and services, thereby guaranteeing scalability, just as in human social networks; (*ii*) a level of trustworthiness can be established to leverage the degree of interaction among things that are 'friends'; (*iii*) models designed to study social networks can be reused to address *IoT* related issues (intrinsically related to extensive networks of interconnected objects). Thanks to the implementation of this paradigm, devices become part of a social network of objects. As in human social networks, the concept of "friend" plays a key role in *SIoT*. By exploiting device friendship, things can be made to interoperate autonomously by implementing intelligent behaviors [13]. This scenario has opened up the possibility for new object intelligence: the ability to discover new services, activate new contacts with other objects, share information with them, and use the capabilities of other objects towards the attainment of a common goal.

In order for *SIoT* principles to be effectively applied, the communication and integration infrastructure of *IoT* devices must be built in such a way as to address specific challenges. If we consider the domestic environment, most of them concern the lack of interoperability between the diverse installed home automation systems, but not only. The *SIoT* must be based on an infrastructure able to support the following services:

- *Discovery*: the ability for devices to detect the functions of other devices. This service is useful to automatically identify device functions that could be combined together to create new, more advanced ones. This implies that each service of each device must be identified, addressed and described using an ontology, taxonomy or free-text description that follows predefined rules in order to be computed.

- *Composition*: the ability to combine the functions of different devices to create new system capabilities. To do this, the constituent devices of a system have to "speak" the same language. This can only be obtained either by using devices that adopt the same communication technology or by implementing interoperability between natively incompatible devices to share states, values and function calls. Interoperability is the ability of two or more incompatible systems to communicate in a way to create a functional dependence between them, allowing them to act like a single system that behaves as a single entity [14].
- *Trustworthiness management*: the ability to understand how to use the information provided by other devices. To implement this service, it is useful to apply the concepts of centrality, prestige and reliability. Centrality measures the number of contacts any given device has within the network; prestige measures how many other devices seek that device. Centrality and prestige are summarized in a value called reliability. These measures are particularly interesting in big *IoT* scenarios, in which the network is made up of numerous devices and a mechanism is needed to determine which are most dependable for reaching a particular goal.

On the contrary, the vast majority of existing *IoT* interoperability platforms are not designed to offer all these features in an integrated way. Devices and applications do not communicate directly between each other, but use cloud connectivity, computing and storage features as intermediaries.

In fact, in January 2016, with the *Horizon 2020 research programme*, the European Commission funded seven projects to address the interoperability of the *Internet of Things*: *Inter-IoT* [15], *BIG IoT* [16], *AGILE* [17], *symbIoTe* [18], *VICINITY* [19], *bIoTope* [20]. In general, the most widely followed technical approach to address these issues is the implementation of a hierarchical *IoT* stack connecting smart objects and *IoT* gateways with the cloud. In these projects, interoperability is implemented by collecting device data in the cloud (typically in a database) where they can be queried in order to process information.

3. Related work

The current scientific literature addresses the issue of elderly health monitoring with solutions that are able to collect and then display data, typically through a web interface, to formal and / or informal caregivers who can check them to oversee an elderly person's health status. In addition to allowing viewing of the collected data, most of the proposed solutions include a preliminary automatic analysis of the occupant's health. Such analyses take different approaches. Some check whether a prefixed threshold for some specific health parameter (e.g. heart rate) has been exceeded and then send a notification to designated recipients. Others use more advanced intelligent systems that are able to understand trends in a set of specific user parameters and thereby make decisions and automatically launch alarms and warnings when vital sign values are considered suspicious. Some examples of this kind of systems are those that analyze data in real time. In [21], the author proposes a pervasive patient health monitoring (*PPHM*) system based on wireless wearable devices integrated through a cloud computing infrastructure. The work presents also a solution based on *ECG* to monitor patient suffering of congestive heart failure; in [22], the author proposes a system to monitor cardiac activities using wireless wearable sensors and an *Android* device, taking into consideration cost and ease of use; *GiraffPlus* [23] project belongs to the Programme for Research and Technological Development in the Seventh Framework (2007-2013), which proposes a monitoring system solution based on environmental wireless sensors and a robot recognising user's activities and physiological parameters; in [24], the author proposes a work to monitor in mobility patients using *6LoWPAN* (*IPv6 over Low-Power Wireless Personal Area Networks*) devices in a hospital; in [25], the author presents an *NFC* and *RFID* based telemonitoring mobile solution to monitor blood pressure and heart rate; in [26], the author shows a mobility medication control system exploiting *RFID* technology.

With the growth of information coming from numerous sensors, the management of health data is crucial. Literature presents two interesting and innovative approaches to health data management: in [27], the author offers an engine for querying data from heterogeneous sources; in [28], the author presents a cloud computing system based on data mining procedures to correlate health and lifestyle.

All the presented works are examples of *IoT* technology applied to the health field. Unfortunately, virtually all have been designed for, and are strictly tied to, specific proprietary hardware or devices and technological communication standards, creating quite strong constraints on the choice of devices to be used for monitoring. To overcome such limitation and enable devices to be chosen based on their functionalities, cost and performance, regardless of purely technical and compatibility aspects, a system is needed that allows different devices using different communication standards to work together at the same time.

Current literature studies apply the social concept to *IoT* in two different ways: devices interacting directly with humans, following the example of Social Networks (*SIoT* between devices and humans) [29] and devices that interact amongst themselves in a *Social IoT* way (*SIoT* between devices). This twofold interpretation of *SIoT* has been described in [30], which also provides some examples of interactions between devices. In [31], the author extends and formalizes the differences between these two scenarios by defining the integration of devices within Social Networks as the *Web of Things* (*WOT*) and direct interactions between devices as the *SIoT* proper. They also detail the state of the art of the underlying technologies and apply these concepts to Wireless Sensor Networks. In [32], the author presents a solution and a prototype able to establish communications between two or more heterogeneous devices by exploiting their proximity (the communication takes place only when devices are near each other). Once again, most of the *SIoT* approaches proposed in the literature are designed for specific proprietary hardware or devices.

With regard to the current state of the art, herein we present a new home automation interoperability architecture based on the "friend" concept applied to services and devices. The greatest advantage offered by the system is that it is designed to integrate new devices, home automation systems or sensor networks, even if they communicate through different, incompatible native protocols. Exploiting the *SIoT* paradigm, devices and services communicate and share values and states with each other directly, without the need for intermediary components such as a database.

One direct consequence of Social paradigm approach is the advantage of being able, as needed or convenient, to freely replace any device or appliance of a specific brand with another brand's device without interfering with the functioning of the entire system. It moreover allows for the possibility of supporting the

network application layers implementing the *SIoT* functions for different purposes, as well.

4. Socialize Project

The *SOCIALIZE* (Service Oriented Assisted Living Infrastructure) project aims to meet the needs of today's (and future) active ageing. The projects aims to create a complete technological Web solution which integrates into a single platform a multiplicity of services designed specifically for the senior population and their caregivers (secondary end users). These services aim to strengthen social relations among the elderly, and with their relatives, who often live far away, and to create a sense of security and autonomy at home. The distance separating relatives from and older person living alone at home represents a potential health and security risk. In fact, the elderly are more subject to chronic diseases and unexpected critical health events. For these reasons, it is crucial to be able to monitor their health status and activities in order to identify any possible worsening of their conditions and avoid dangerous situations.

Although the *SOCIALIZE* Project is currently aimed at active ageing people with a certain degree of knowledge about the use of technological equipment, the ultimate goal is to make the platform accessible to all elderly people, including and especially, the large proportion of the older population that nowadays has great difficulty accessing and using *ICT*. For this reason, the user interfaces have been given rather simplified designs to make them easy to use, thereby permitting the inclusion of the largest number of elderly as possible.

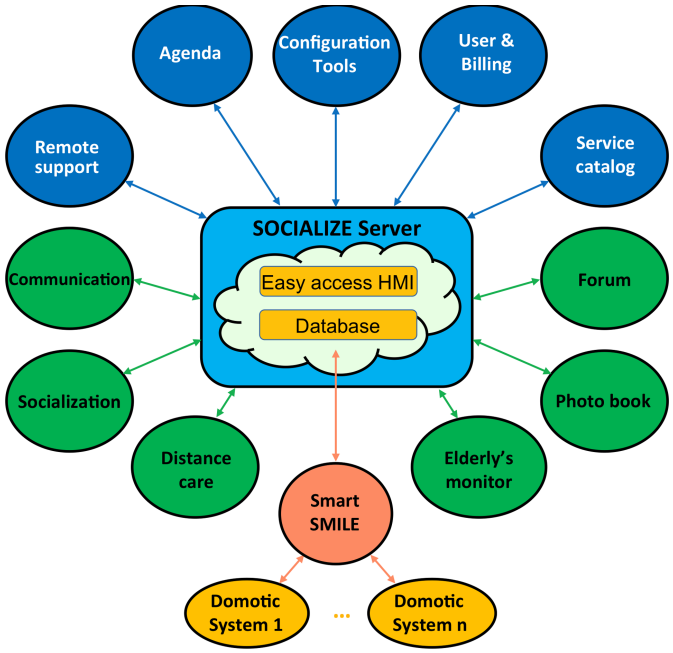

Figure 1: SOCIALIZE services

The services supplied by the project (Figure 1) can be divided in three categories:

- *Socialization* services: which aim to improve older people's social interactions. These include: (a) *communications*: enables exchanging messages and making audio / video call between the members of the *SOCIALIZE* community; (b) *socialization*: a dedicated social network between *SOCIALIZE* members; (c) *forum*: an advanced application for discussion of topics of general and personal interest; it can also highlight the most interesting discussions; (e) *photo book*: for storing and organizing photos and videos; (f) distance care: can follow the member's movements and monitor daily activities, and even warn of any threats; (g) *monitor*: analyzes user activities, as well as personal and environmental parameters; the results of this monitoring can be supervised by doctors, relatives and / or caregivers as is deemed appropriate with regard, for example, to the cognitive, health status and wishes of the elderly;
- *Cross services*: vertical applications common to all socialization services. The cross services currently implemented are: (a) *configuration tool*: provides for configuration of the system and services; (b) *user & billing*: manages *SOCIALIZE* platform users and their access credentials; (c) *remote support*: which provides help on using the *SOCIALIZE* platform or, more generally, computers or the device used; (d) *agenda*: collects all the events and date/time-related activities for a given user; (e) *service catalogue*: manages the available services, enabling them to communicate through the use of an enterprise bus system;
- *Cloud services*: it allows to the different services provided by the platform to communicate by sharing data and functionalities and it hosts the database containing data coming from the different Socialize service components. It consists of: (a) *easy access Human Machine Interface (HMI),* a web application with public and private content that acts as the entry point to the *Socialize* platform; (b) *database*, containing all the information related to users and services.

5. SmartSMILE framework

5.1. Concepts and use cases

The elderly monitor service is part of the *SOCIALIZE* platform. Its aim is, on one hand, to monitor elderly people's activities and physiological parameters to display processed data to caregivers, doctors, and relatives, to notify them of suspicious values, and on the other, to combine device functions to improve the individuals' life at home, increasing their autonomy and making them feel "protected" and "safe". To these ends, the *SmartSMILE* (Socialize MIddLeware Elderly) framework was created. *SmartSMILE* is a monitoring and interoperability *SIoT* ready software infrastructure for the socialization between devices. It is based on *SOA Web Services* and *XML* technologies to create intelligent domestic environments whose components collaborate to provide for the integration and interoperability of devices and household utilities belonging to different, incompatible native technologies. In fact, *SmartSMILE* creates an abstraction layer that overcomes the limitations of device compatibility, thereby enabling both the monitoring and composition services to work irrespective of the technologies of individual devices.

Figure 2 shows a monitoring use case. When a device changes its state, the new value is collected in a repository. When needed, all stored values are retrieved to be displayed to caregivers, doctors and family members. A device state change can in general occur for three main reasons:

- Direct interaction: the user physically acts on the device to change its status (e.g. pressing a button);

- Indirect interaction: the user acts on the device without touching it (e.g. through a smartphone);
- Involuntary interaction: the user does not interact with the device, but its state changes as the result of some event (e.g. a PIR sensor detects a presence in the environment).

Figure 3 shows a use case related to activation of the interoperability function. When a device changes its state, *SmartSMILE* verifies the condition to activate interoperability between devices. To do this, *SmartSMILE* (Figure 3) activates a *friendship manager* that searches for a friend relation that involves the device. If one is found, the other device is identified and the corresponding function is automatically activated. A device function is a command that any given smart device can execute. For example, the functions for a lamp can be *switch on*, *switch off* and *getStatus*. The *friendship manager* is a special component of *SmartSMILE* that defines which devices can interact with each other, and how, to create a composition of functions. As friends, two or more devices are trusted and are thus enabled to access each other's private data and functions, thereby providing interoperability.

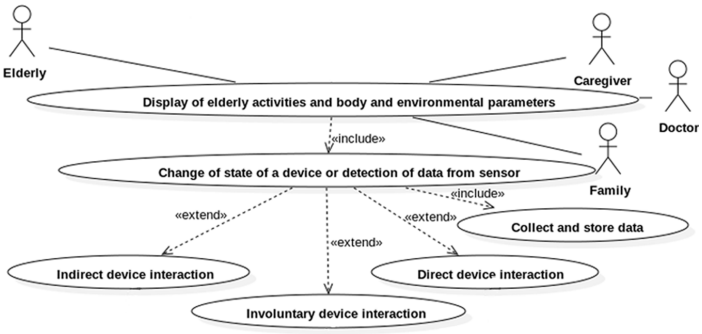

Figure 2: Monitoring use case

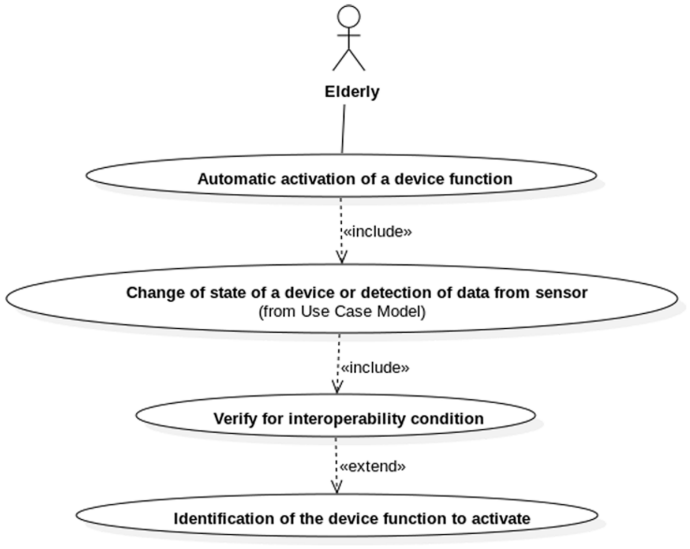

Figure 3: Interoperability use case

5.2. Architectural description

The *SmartSMILE* architecture (Figure 4) is made up of a set of sub-modules, called gateways. Each gateway interfaces with specific domotic systems expressly installed inside the home. The gateway serves the function of managing its own set of devices, integrating and interfacing them with the platform. To uniformize devices belonging to different gateways, *SmartSMILE* uses a high-level ad hoc language, called *SmartSmileML*, to describe devices in a technology-independent fashion. Such description includes their main characteristics, and the functions that they can execute, along with their input and output parameters and defined data types. Moreover *SmartSmileML* describes the possible events (e.g. device state change) specific to the supported domotic technologies for processing. To describe devices, functions and events, *SmartSmileML* uses an XML based language. Its functioning does not require prior definition of taxonomies or classifications for devices and events. By avoiding the use of pre-defined devices, the system is able to manage any kind of device, exploiting all the available functions that are automatically identified during its creation.

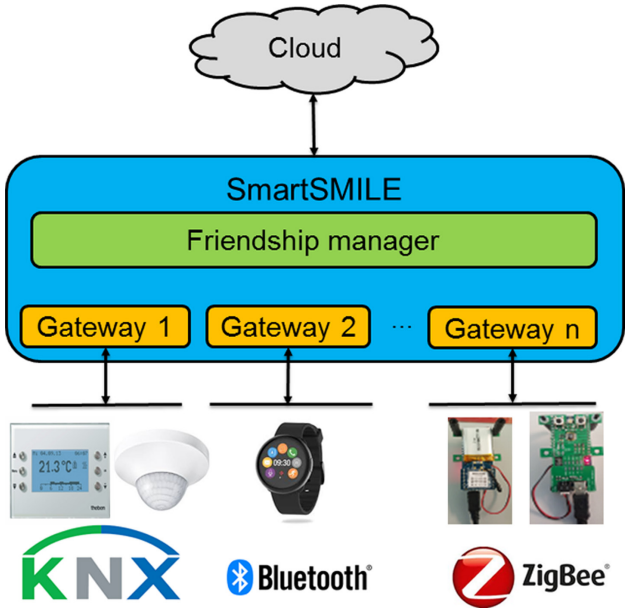

Figure 4: SmartSMILE architecture

In order for the system to work, each gateway has to implement some basic features; these are:

- Creation of the high-level description of devices belonging to its network: This operation enables having a unique view of, and access to all the devices belonging to *SmartSMILE*. In this way, *SmartSMILE* can use a unified way to interact with them. For this to work, the gateway must be able to map the device descriptions with the corresponding real devices.
- Capture of events that occur in the automated home network and translation into the *SmartSmileML* language. This allows for monitoring events in the domotic bus and enables *SmartSMILE* to react accordingly. The obtained information are translated into the *SmartSmileML* and are sent to the cloud server for collection and querying as needed.
- Translation of a *SmartSmileML* function description into the corresponding domotic command. This enables *SmartSMILE* to invoke commands in devices. To do this the system must know the corresponding gateway managing each device.

5.3. SmartSmileML language

SmartSmileML consists of two main formalisms: *SmartSMILE Device* and *SmartSMILE Message.*

SmartSMILE Device

SmartSMILE Device: defines devices and their functions. In particular, it describes the characteristics of each device and the processes by which it interacts with other *SmartSMILE Devices*. The XML description includes the following tags:

- *device*: the *root* element that is the *parent* of all other elements. The main attributes contained in this tag are: (a) *description*: a free text field; (b) *id*: the identifier of the device within the *SmartSMILE* framework; such identifier must be clearly unique; (c) *serialNumber*: a device identifier in the domotic technology; (d) *tech:* the domotic technology employed by the device; this allows for immediate assignment of the device to the proper gateway; (e) *type*: the kind of device; this can be a free text field or contain pre-defined values;
- *service*: *child* of the *device* tag. There is a *service* tag for each device function,. The main attributes are: (a) *name*: the name used in the relevant domotic technology to call that function; (b) *output*: the *SmartSMILE* data type; this attribute is defined, only if the function returns a value;
- *input*: *child* of the *service* tag. There is an *input* tag for each input parameter that the function requires,. The main attributes are: (a) *name*: a label for the input; (b) *type*: the *SmartSMILE* data type;
- *allowed*: *child* of the *input* tag. There is a tag for each possible value that that input value can take. If no allowed tags are defined, it means that any value is allowed for the declared *SmartSMILE* data type (e.g. if the type is *int,* and no *allowed* tags are defined, the input can be any integer value. The main attribute is *value*: the allowed value;
- *linkedService*: *child* of *service* tag. If defined, it describes friendship relations with other devices. The main attributes are: (a) *id:* the id used in *SmartSMILE* to identify the friend device; (b) *service*: the name of the function of the friend device to invoke to create compositions;
- *linkedInput*: *child* of *linkedService*. There is a *linkedInput* tag for each input of the friendly device function to invoke,. The main attributes are: (a) *from*: the name of the input to the described function whose value is needed in order to be shared with the friend device function named in the *linkedService* tag; (b) *to*: the name of the input of the friendly device function whose value has to be assigned using the shared one; (c) *value*: if *from* attribute is not defined, this defines a fixed value for the *to* input name.

SmartSMILE Message

SmartSMILE Message formally describes events, commands and responses. The XML description establishes the following tags:

- *message*: the *parent* tag. The main attributes contained in this tag are: (a) *message*: the name of the function involved in the message; (b) *messageType*: defines the scope of the message: the possible options are: *COMMAND*, when the message is addressed to a gateway for translation into a domotic message and written to the domotic bus for execution. In this case, the *message* attribute is related to the function to activate; UPDATE, when an event related to a device change of state is captured on the domotic bus, it is transmitted to the *Friendship manager* to check whether the conditions for interoperability are satisfied. In this case, the *message* attribute regards the device function that can be correlated to the change of state; (c) *senderId*: if the message is of type *UPDATE*, the id of the *SmartSMILE* device involved in the message; (d) *receiverId*: if the message is of type *COMMAND,* the id of the *SmartSMILE* device involved in the message;
- *input*: *child* of the *message* tag. This describes the values that are involved in the message. The main attributes are: (a) *name:* the name of the value; (b) *type*: the *SmartSMILE* data type; (c) *value*: the new value.

5.4. SmartSMILE SIoT features

Using *SmartSmileML*, it is possible to achieve interoperability among services and devices by taking advantage of a single means of communication and data sharing. Thus, it is possible to achieve a social network of intelligent objects, whereby devices are tied to each other by social relationships in order to collaborate and provide a common *SIoT* application. When a message passes through a domotic bus, it is captured by its gateway. The gateway identifies the correspondence between the device that sent the message and the associated description in *SmartSMILE Device*. Using the information in the device description, the captured event is translated into the *SmartSmileML* language, inserted into *SmartSMILE Message* and forwarded to the *Friendship manager* to check for the existence of relations, and finds the device and its function that can achieve the necessary interoperability. To verify and activate the friendship, the *Friendship manager* checks the *linkedService* and *linkedInput* tags to verify the relation between the involved devices, and if it exists, it shares input and output values between them.

By way of example, let us assume we have two devices belonging to different domotic systems whose functions have to be combined as shown in Figure 5. The first device is a "wall switch" employing the *KNX* [33] technology. It has a function named SET_STATUS (the content of the tag *service name*), whose input name *status* is an *OnOff* data type. The values of *OnOff* can be *on* or *off*. The second device is a "lamp", which instead uses *UPnP* [34] technology. It has two functions: *getState* and *setPower*. Both use a value of type *OnOff* as output and input respectively. The *device description* of the function *SET_STATUS* of the wall switch has a special tag, named *linkedService*. This tag permits the *Friendship manager* to establish a friend relation between the two devices and to create a composition of functions. When the *Friendship manager* receives the event that the wall switch is set to *on* (Figure 6), it 'knows' that it has to invoke the function *setPower* of the device with *id = 3* (the lamp). The content of the *linkedInput* tag specifies that the wall switch shares the *status* value with the lamp. In the end the *Friendship Manager* invokes the lamp's *setPower* function, which will have the value *on* within the input named *power* (Figure 7).

The device descriptions are for the most part created automatically by the gateway. The complexity involved in this depends on the standard to be managed. For example, in *UPnP* the creation is completely automated because the devices present and

describe themselves each time they enter the network. For *KNX*, the descriptions are made by parsing a configuration file created by the configuration software named *ETS* [35]. In some cases, automating the process is not possible and it is necessary to write them manually.

```
<device description="wall switch" id="1"
  serialNumber="123" tech="KNX" type="switch">
  <service name="SET_STATUS">
    <input name="status" type="OnOff">
      <allowed value="on" />
      <allowed value="off" />
    </input>
    <linkedService id="3" service="setPower">
      <linkedInput from="status" to="power" />
    </linkedService>
  </service>
</device>

<device description="energetic saving lamp" id="3"
  serialNumber="456" tech="UPNP" type="lamp">
  <service output="OnOff" name="getState"  />
  <service name="setPower">
    <input name="power" type="OnOff">
      <allowed value="on" />
      <allowed value="off" />
    </input>
  </service>
</device>
```

Figure 5: Two device descriptions in smartSMILE Device

```
<message message=" SET_STATUS " messageType="UPDATE"
senderId="1">
  <input name="status" type="OnOff" value="on" />
</message>
```

Figure 6: The description of an event in SmartSMILE Message

```
<message message="setPower" messageType="COMMAND"
 receiverId="3">
  <input name="power" type="OnOff" value="on"/>
</message>
```

Figure 7: Command representation in SmartSMILE Message

6. Implementation

SmartSMILE exploits W3C-recommended standard Web technologies. It exposes services using *Web Services*, *SOA* and *XML* technologies. The advantage of using *W3C* standard solutions is that they ensure that the developed applications are fully compatible with other standards-based software and are not tied to any particular software system, programming language or computer architecture.

illustrates the deployment of the *SmartSMILE* component used in the *SOCIALIZE* Project. *SmartSMILE* is connected on one side to the Cloud server, where the values coming from devices are stored and recovered for any further analysis, and on the other side, to the wired or wireless domotic buses. Through the intervention of *SmartSmileML*, communications between the Cloud server and *SmartSMILE* are performed using high-level messages as shown in Figure 6. In this way, the cloud does not need to 'know' how the different domotic technologies work in order to understand messages – it just needs to be able to "speak" *SmartSmileML*. In addition to collecting values, the *Cloud* provides a web server environment and a web application to show each user's data to the caregivers. To match the received values from *SmartSMILE* with the respective user, the *Cloud* is previously configured associating devices to consumers.

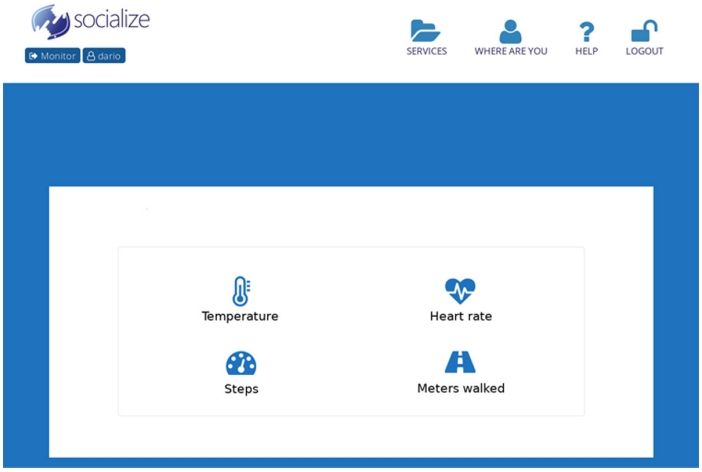

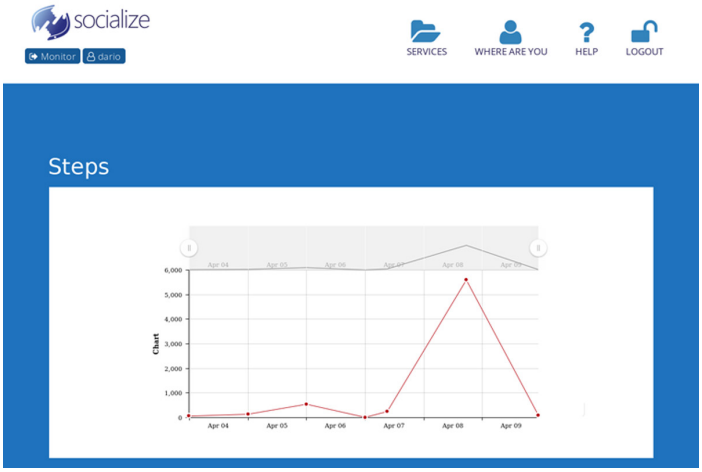

Figure 9: Example of "Steps" page of the web application

The different domotic technologies used in the project were: KNX, UPnP, MyHome [36], ZigBee and Bluetooth [37] KNX gateway. Table 1 shows the implemented classes for each developed *SmartSMILE* gateway. A brief description of each class is provided in the following subsections.

6.1. KNX gateway

To integrate *KNX* into *SmartSMILE*, the gateway exploits the API provided by the *Calimero 2* [38] libraries to connect to, capture and write KNX messages to and from the domotic bus. At startup time the gateway connects to the bus and initializes the required structures for translation of the data types and values used in *SmartSmileML* to KNX *Datapoint* identifiers and vice-versa. Then, the gateway loads the *ETS* (KNX Engineering Tool

Software) configuration file that contains information about different *KNX* devices connected to the KNX bus, such as their description, their application programs, and their functionalities. It then implements a listener on the KNX bus to manage events. Captured message are translated into *SmartSMILE Message* and can be of two types: a reply to a read request for a device state, or detection of an event that implies a device change of state that can trigger a composition of functions. To invoke functions, *SmartSMILE Message* are translated into KNX packages and written to the bus.

Table 1:Used Java Classes to implement gateways

Gateway	*Java Classes*
KNX	*KNX* *KNXListener* *KNXServiceMapping* *SSServiceData* *KNXServiceData* *SSParamterMapping* *KNXDriverException* *SSTypeValueXlator* *SSTypeValue*
UPnP	*UPnPManager* *UPnPManagerPoint* *UPnP2SmartSmile*
MyHome	*BTicino* *BTicinoDeviceData* *BTicinoDeviceManager* *BTicinoMsgsVerifier* *BticinoServiceData* *BticinoServiceManager* *BTicinoDeviceManager* *BTicinoDimensionValuesMapper* *SSServiceData*
SmartSmileML	*SmartSmileMLGateway*

To implement the gateway, 9 Java classes have been developed (Figure 10):

- *KNX*: this is the main class that acts as a communications bridge between *KNX* and *SmartSMILE*. It checks all the parameters of configuration files and establishes connections with the *KNX* bus via the *KNX/IP* gateway device. This makes it possible to read and write to the *KNX* bus. Moreover, it creates abstract instances of the *KNX* devices in *SmartSMILE* and maps them to the actual ones, so they can be used by the platform. The class also implements the reading and writing operations on the bus, and their conversion from *KNX* to *SmartSmileML* format and vice versa, including the values of the different data types.
- *KNXListener*: this class implements the functions and interactions with the *KNX* bus. It creates and manages the data flow to and from the *KNX* bus by providing: (a) synchronous reading of data (when the value of a datapoint is explicitly requested through a group address); (b) asynchronous reading (the system furnishes the value of a datapoint through the group address without any explicit request, such as a thermostat that periodically reports the temperature, or notification of a user activating a device); (c) writing for activation of functions. Using the configuration data of *KNX* devices in *SmartSMILE*, it is possible to associate the correct coding/decoding type of data (*DTP*) to each *group address*.
- *KNXServiceMapping*: defines the mapping between the *KNX group address* and the associated *KNX* data type.
- *SSServiceData*: once both the *individual address* of the device and the corresponding *KNX group address* are known, this Java Class obtains the appropriate *SmartSMILE* function.
- *KNXServiceData*: takes as input the *SmartSMILE* function and finds both the *individual address* and the *KNX group address.*
- *SSParamterMapping*: represents the data structure that allows mapping a *SmartSMILE Message* to the available input and output parameters.
- *KNXDriverException*: defines the exceptions generated during interactions with *KNX*.
- *SSTypeValueXlator*: implements the functionalities to convert a *KNX* value into a *SmartSMILE* value and vice versa, according to the respective data types. By way of example: a) the *KNX* value "on" can be converted to a *SmartSMILE* "true" Boolean value; b) the *SmartSMILE* percentage scale has a range of 0 to 100, while in *KNX* it ranges from 0 to 255; it is thus necessary to convert the values between the two scales.

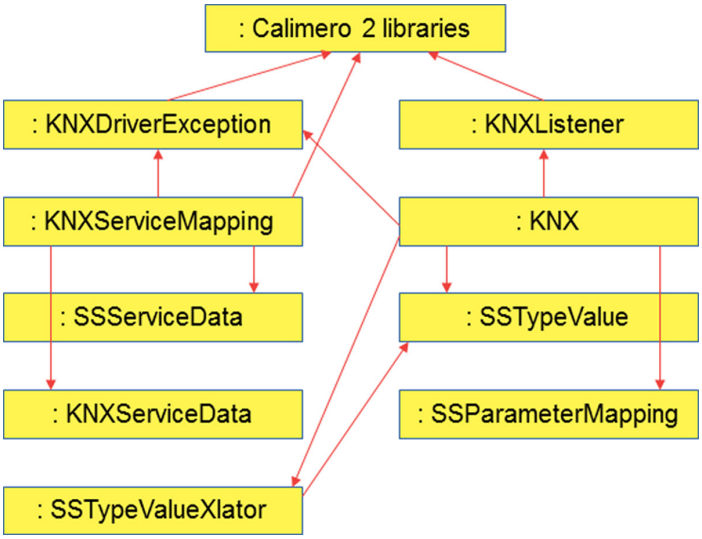

Figure 10: Developed classes for KNX gateway

When a function is invoked using the *SmartSMILE Message* formalism, the *KNX* class searches for the corresponding *KNX* service retrieved via the *KNXServiceMapping* class (using the *getKNXService* method). The value initially expressed in *SmartSMILE* format, is taken from the *KNXServiceData* class using the *GetValue* method. It is converted to the *KNX* value using the *SSTypeValueXlator* class with the get *getKNXParameterValue*

method. The data are then written to the *KNX* bus using the *KNXListener* class. In the end, a reply indicating the execution of the command is sent back, once again using the *KNXServiceMapping* class (method *getSSService*) in order to generate confirmation of execution. (Figure 11).

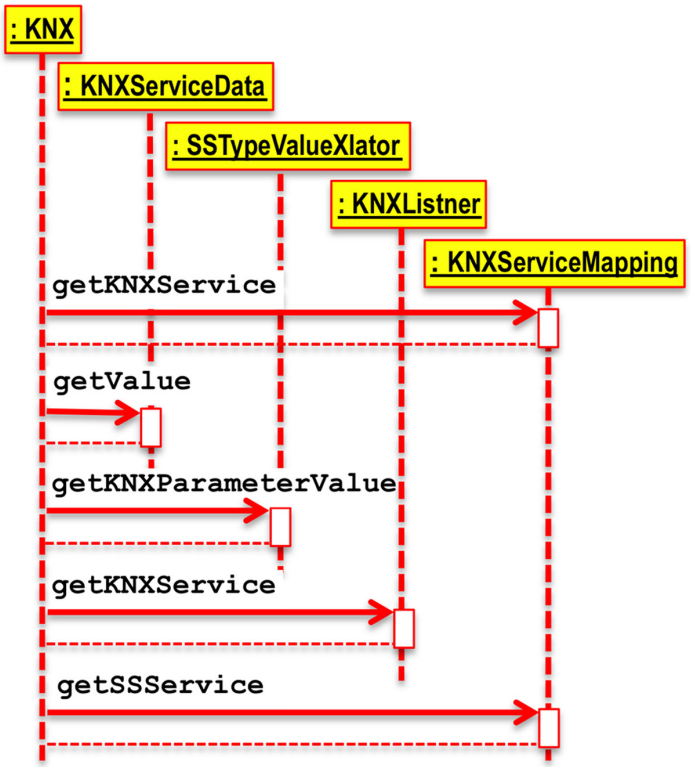

Figure 11: Write operation on KNX gateway

These operating principles of the *KNX Gateway* have also applied to the other gateways implemented in the project. In particular, regarding the development of the *UPnP* and *MyHome* Gateways.

6.2. UPnP gateway

nP technology, the gateway exploits the API provided by the *Cyberlink* and *Cidero* libraries [39]. At startup time, the gateway initializes the *ManagerPoint*, which is a *UPnP listener* that enables adding, removing and executing functions on devices. The gateway initializes the data structures for the translation from *SmartSmileML* to the corresponding *UPnP* values and types, and vice-versa. When a new device enters the *UPnP* network, it announces itself and provides a description of itself together with a list of functions that it can offer. This information is represented using *XML* structures that the *ManagerPoint* parses to create the *SmartSMILE Devices*.

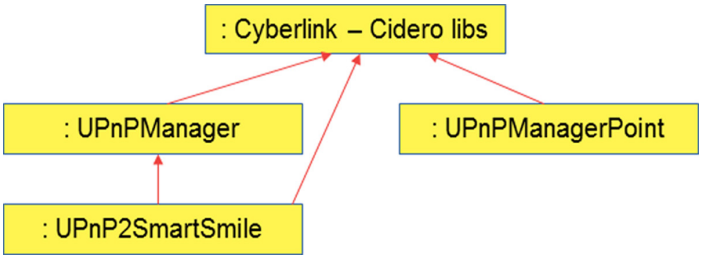

Figure 12: Developed classes for UPnP gateway

Three Java classes have been developed to implement the gateway (Figure 12):

- *UPnPManager*: this is the main class that acts as a communication bridge between *UPnP* and *SmartSMILE*. It checks all the parameters of configuration files and establishes interactive connections with *UPnP*. Moreover, it creates abstract instances of the *UPnP* devices in *SmartSMILE* and maps them to the actual ones. The class also implements the reading and writing operations on the *UpnP* bus and their conversion from *UPnP* to *SmartSmileML* format and vice versa, including the values of the different data types.
- *UPnPManagerPoint*: this class implements the functions of and interactions with *UPnP*. It creates and manages the data flow to and from the *UpnP* system by providing the synchronous and asynchronous functions for reading and writing to the bus.
- *UPnP2SmartSmile*: implements all the data structures and methods to convert descriptions, commands and values of *UPnP* into *SmartSmileML,* and vice-versa.

6.3. MyHome gateway

library was used, though modified to add the authentication functionalities offered by the *AndroidBetaOwnAuthentication* library. This library makes it possible to manage communications through an *OpenWebNet* (*OWN*) server by formatting messages according to the *OWN* syntax. It moreover serves to open sessions, creating special threads, and send and receive reply messages as well as syntactic and communication errors. At startup, the gateway opens communications with the *OpenWebNet* server that interfaces with the *MyHome* technology. The server works using two sessions: monitor and command. During the monitoring session the gateway starts a thread that remains in execution to asynchronously intercept the events that it reads from the bus. Messages are parsed by an *LL(1)* [41] grammar. During the command session, instead, the gateway establishes a connection with the server when it has to invoke a function. Unfortunately, auto discovery and auto configuration of *SmartSMILE Devices* is not available because the technology does not offer any device discover process. Hence, it is necessary to create the *SmartSMILE Devices* manually.

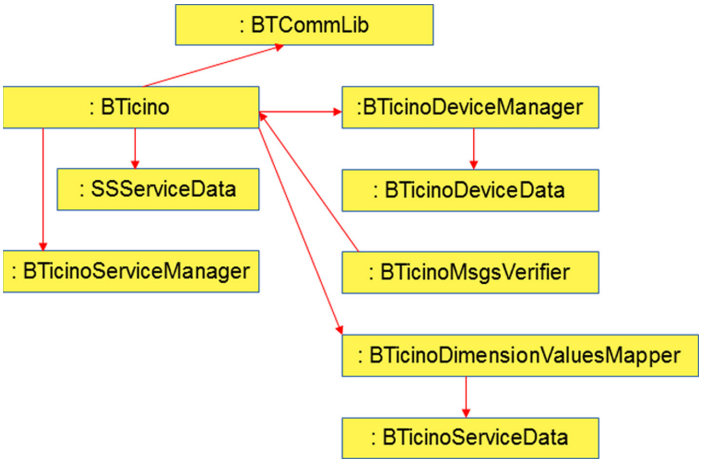

Figure 13: Deployed classes for MyHome gateway

To implement the gateway, 8 Java classes were developed (Figure 13):

- *BTicino*: this is the main class that manages devices and creates all the structures needed to interact with *MyHome* systems. It creates the two threads needed to interface with the monitoring and command sessions.
- *BTicinoDeviceData*: contains data and information related to a *BTicino* device for interactions.
- *BTicinoDeviceManager*: manages *BTicinoDeviceData*, organizing them in a Hash table.
- *BTicinoMsgsVerifier*: checks messages from the monitoring session.
- *BTicinoServiceData*: contains data and information related to *BTicino* messages.
- *BticinoServiceManager*: organizes BTicinoServiceData in a Hash table.
- *BTicinoDimensionValuesMapper*: translates quantities from *SmartSmileML* to *OWN* and vice-versa.
- *SSServiceData*: contains data and information useful for executing a *SmartSmile Message*.

6.4. *SmartSmileML* gateway

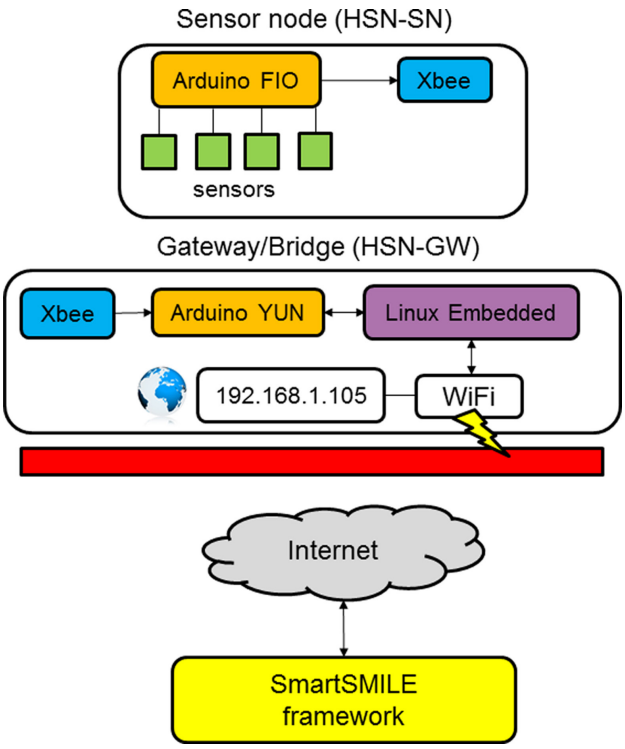

Figure 14: ZigBee architecture

The *ZigBee* architecture (Figure 14) used in the project is fully IEEE 802.15.4 and ZigBee 2007/PRO compliant. The transmitting protocol is ZigBee HA profile. It is composed by two main elements:

- *Smart node* (HSN-SN): this is a device made up of a sensor, an *XBee S2* radio module configured as a *ZigBee* router and a node. The core of the node is an *Arduino FIO* board with one or more sensors connected to its I/O ports (input/output lines, either digital or analog). Each sensor node receives broadcast messages from the *coordinator* (bridge) and sends events only to the *coordinator* in a so-called *star* network topology. Events generated from sensor nodes are changes in the state of a sensor, power up or reset, low battery and heartbeat (a timed event indicating the node is alive).

A simple character-oriented communications protocol has been implemented on the smart node for bi-directional communication, network management and control of the input/output lines between smart nodes and the gateway/bridge. Events notification messages are forwarded directly, while the incoming commands require some tweaks on the server side. Although the communication protocol is able to manage bidirectional messages (from sensor node to gateway and vice versa), only one way is used (Figure 15).

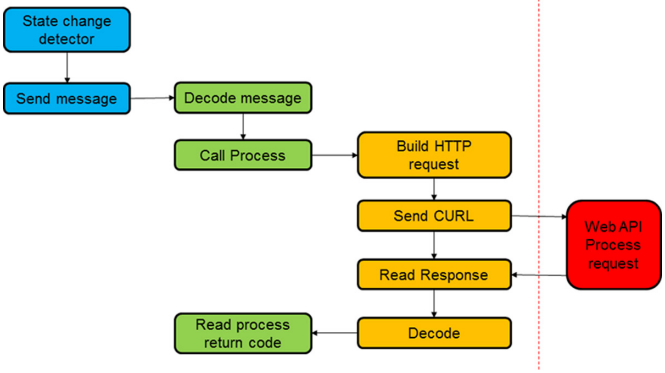

Bluetooth devices in the project are interfaced using an *Android Smartphone* app (Figure 16).

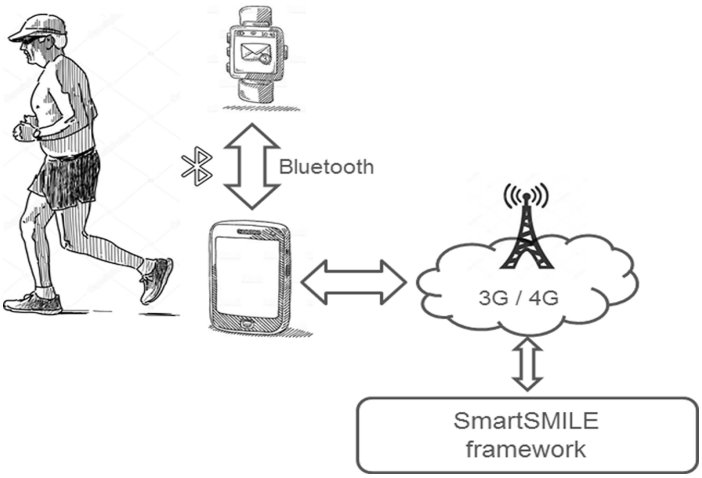

Figure 16: Bluetooth device connected to a Smartphone

Both the *ZigBee* Gateway and the *Android* app for *Bluetooth* are specifically designed to communicate through the *SmartSmileML* language. This provides *SmartSMILE* with a native *SmartSmileML* gateway, which has the task of setting up a connection as a *TCP* or *UDP* socket or a *REST* service to which devices can send messages. Incoming messages are directly forwarded to the *SmartSMILE* core for analysis by the *Friendship manager* and then forwarded on to the cloud server. Since this gateway does not require any special implementations to convert data, values and functions, it was sufficient to include all the features described in a single class called *SmartSmileMLGateway*.

In order to make devices able to 'speak' *SmartSMILEML*, device developers can refer to a document describing how *SmartSmileML* works and how to use it.

When a device becomes active, it sends a message in which it describes itself using a *SmartSMILE Device* description, as shown in Figure 5. In this case, the attribute *tech* is *SmartSMILE*. The *id* has been left blank because *SmartSMILE* will automatically fill it in. The assigned *id* will be used by the device for its communications. When the device is deactivated, it sends a special *SmartSMILE Message* of the type *REMOVE* containing its *id* (Figure 17).

```
<message id="90A2DAF501A4.ROOM105.NODE101"
messageType="REMOVE" />
```

Figure 17: SmartSMILE Message of type REMOVE

Leveraging the *IoT* capabilities of *SmartSMILE*, we ran a pre-test of the proposed system using remote devices during the development stage. A *SmartSMILE* server was deployed in ... with various devices employing *KNX*, *UPnP* and *MyHome* technologies, including a thermostat, motion detectors, gas and smoke detectors, electrical load control of instantaneous consumption, power actuators, a cooking gas electromagnetic valve and smart TV. All the appliances and devices are part of a demonstration installation that simulates an actual home. *ZigBee* environmental sensors, including temperature and humidity, were fitted at the *SUPSI University* in *Switzerland* in *Manno*. A *Bluetooth* Smartwatch able to capture users' heart rates, number of steps and sleep duration was set up at *Spring Techno* in *Bremen Germany* (Figure 18).

Figure 18: Smartwatch and ZigBee sensors

7. Field trials

The test and validation processes of the *SOCIALIZE* platform were performed by the end-user partners in the project.

In Switzerland it has been tested in a retirement home, while the Italian test involved two regions (Tuscany and Sicily), making sure in each case to involve different types of target users in the test:

- Care-dependent elderly people in residential facilities;
- Partially autonomous elderly people assisted at their own residence/homes;
- Autonomous elders who are not beneficiaries of social care or healthcare assistance and participate in associational activities.

Regarding the elderly monitoring service, the test was conducted inside a residential facility in Tuscany. The aim was to collect data from sensors and ensure that they were understandable, and that they were able to constantly follow and track the evolution of those parameters deemed significant for the health and safety of the older persons involved.

A technologically enriched environment was recreated in this residence by assembling and recreating within the pilot site the same*IoT* device configuration already used in the earlier design stage.

The testing period was two weeks. *SmartSMILE* was installed on a computer located inside the residence and connected to the Internet through an *ADSL* connection.

The devices installed were (Table 2): a wireless ambient temperature and humidity sensor in the cafeteria (*ZigBee* technology), a temperature and humidity sensor as well as a SmartTV and Media Server (*UPnP* technology) in the dining room, two PIR wired presence sensors, one in a bedroom and one in the kitchen, which was also equipped with gas electrovalve actuator, push button, gas, water, smoke sensors (*KNX* technology) and electrical load control (*MyHome* tecnology), and finally two SmartWatches worn respectively by two guests (*Bluetooth* technology). Almost all *IoT* devices used are powered by a mains power source, only the *ZigBee* temperature and humidity monitoring devices could have a battery life problem.

Table 2: Devices in field tials

Device	Technology	Location
Ambient temperature and humidity sensor	ZigBee: wireless bus with plug and play feature. Battery power supply	Cafeteria Dining room
Smart TV and Media Server	UPnP: wireless WiFi bus. Mains electricity supply	Dining room
PIR presence sensor	KNX: wired bus. Mains electricity supply	Bedroom Kitchen
Gas, water and smoke sensors Gas electrovalve and push button Power actuator	KNX: wired bus. Mains electricity supply	Kitchen
Electrical load control	BTicino: Wired bus. Mains electicity supply	Kitchen
Smartwatches	Bluetooth: wireless bus. Rechargeable battery power supply	Wearable device

They have 2 AA (LR-03) batteries and their measured energy consumption is 35mA in transmission and 2.1uA in sleep mode. The run time is 1 year based on sending data per 20 min. Both *SmartSMILE* framework and the corresponding gateways to manage the domotic technologies run on a *Raspberry Pi 3 Model B+* [42].

The data collected by these heterogeneous home automation devices was converted, standardized and normalized by *SmartSMILE*. The data were then sent to a database managed in Cloud Computing mode residing at the Digimat company, in Matera, Italy.

The results of the experimentation made it possible to verify the correct functioning of the entire system. In particular, through the use of dedicated Web interfaces it was verified that data were stored correctly. These interfaces have enabled simple, intuitive aggregation of the data over fixed periods of time and their display in clear, easily understandable graphics.

In fact, the information is displayed as simply as possible, with icons corresponding to the requested service (for example Physical Activity or Heart Rate monitoring). The end user needs only click the corresponding icon to show a graphical representation of the acquired data with the possibility to adjust the timeframe.

The proper functioning of the collaboration and interoperability between the devices has also been verified, as these features are necessary for the implementation of a *SIoT* based on the *SmartSMILE* infrastructure.

The tested monitoring activities included:

- Temperature control inside the home environment. This has led to the discovery that people who tend to keep the room temperature either too hot or too cold are subject to falling ill more frequently;
- Supervision of elderly people who do not get enough physical activity with respect to doctors' recommendations;
- The feeling of safety older people experiences with regard to the hazards of fire, flooding and gas leaks that may occur within the environment.

The strength of the *SIoT*-ready infrastructure is highlighted by the following composite functions:

- Following the voluntary provocation of conditions of flooding, gas leaks and smoke in the kitchen using dedicated *KNX* devices (Figure 19), when a hazardous event was recognized, the corresponding alarm signals from the *UPnP* media server were promptly displayed on the television, together with the simultaneous activation of an acoustic alarm.
- When one or more appliances requiring high power consumption were turned on at the same time (specifically the microwave oven, the traditional oven, the boiler and the washing machine), the electrical load monitoring system of detected an overload. Power actuators were deactivated according to a preset priority until the situation returned to normal. When the load reduced because one of the still functioning household appliances finished, the load control detected this change and reactivated the appliances that were previously stopped. The functionalities were implemented using *MyHome* electrical load control of instantaneous

);

Figure 20: Electrical load control and power actuator

witching on the cooking gas requires pressing a button. After a pre-set period of time, an acoustic and luminous alert was activated, and an appropriate message displayed on the TV to remind the user that to continue cooking the button had to be pressed again. This prevented the user forgetting food on the cooker. The combined timer and smart TV functionalities were composed using the *KNX* electromagnetic cooking gas valve (Figure 21).

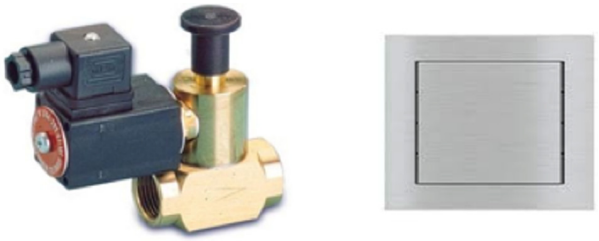

Figure 21: Gas electrovalve and push button

The most significant anomalies identified were long periods of no information coming from both SmartWatches. For the first incident, the reason was that the person took off the watch for 5 nights consecutively, while the second was due to the fact that twice (3 hours and 5.5 hours, respectively) the other person did not notice that the device was no longer working because the battery needed recharging.

8. Conclusions

The paper presented *SmartSmile*, a framework that solves the main issues so that *SIoT* paradigms can find actual application. This software infrastructure was developed as an activity of the *Socialize* project, to address the problem of monitoring older

people within the living environment.

Thanks to the potential of *SmartSmileML language*, the framework implements an abstraction layer that hides the underlying, often proprietary technologies, of the integrated devices, leveling them out. In addition, *SmartSmileML* defines a strategy to define the "friendship" relation between devices permitting the sharing of information amongst them even if they are not natively interoperable. On the one hand, *SmartSmile* permits to users to choose the most suitable sensors/actuators for the specific case without concern for their compatibility with the devices or systems already installed and, on the other hand, it provides developers with a unique representation of the acquired data without the need to know the technical details of each single technology.

Summarizing, the most significant features that have allowed the creation of a *SIoT* environment supporting the services of device discovery, combination of device functions and reliability, are:

- Interoperability: the ability of the devices to interoperate with each other even if they belong to natively incompatible home automation systems, thereby permitting full interconnection and interaction amongst them.
- Service-to-service communications: the service provided via a device can share its input and output with the services of other “friends” to achieve a common objective.
- Scalability: in order to attain a certain goal, devices can collaborate with each other; moreover, when changes occur (new devices become available or some are missing), tasks can be re-distributed.

As a future work, *SmartSMILE* will allow to expose its own devices externally. Exploiting the results of the work described in [43], every device within the system will be reachable using an *IPv6* address, and socialization will be achieved between devices belonging to different *SmartSMILE* instances. In addition, the stored data could be made available to special machine learning algorithms that could launch alarms automatically, learning the user's habits.

SmartSMILE is released under the *GPL licence* [44]. Its code is shared on GitHub [45].

Conflict of Interest

The authors declare no conflict of interest.

Acknowledgment

The *SOCIALIZE* project has been financed by the *European Commission* through the *Ambient Assisted Living Joint Programme* (AAL JP).

References

[1] V. Miori, D. Russo, "Improving life quality for the elderly through the Social Internet of Things (SIoT)" in IEEE Global Internet of Things Summit (GIoTS), 1-6, 2017. https://doi.org/10.1109/GIOTS.2017.8016215

[2] A. Börsch-Supan, M. Brandt, C. Hunkler, T. Kneip, "Data resource profile: the Survey of Health, Ageing and Retirement in Europe (SHARE)" International Journal of Epidemiology, 2013, https://doi.org/10.1093/ije/dyt088

[3] A. Hofman, D. E. Grobbee, P. De Jong, F. A. Van den Ouweland, "Determinants of disease and disability in the elderly: the Rotterdam Elderly Study" European journal of epidemiology 7.4, 1991. 403-422. https://doi.org/10.1007/BF00145007

[4] Kaare Christensen, Gabriele Doblhammer, Roland Rau, James W Vaupel, "Ageing populations: the challenges ahead", The Lancet, 374(9696), 2009. https://doi.org/10.1016/S0140-6736(09)61460-4.

[5] World Health Organization, World report on ageing and health, ISBN: 978 92 4 156504 2, 2015.

[6] M. Sánchez-Valle, M. Vinarás Abad, C. Llorente-Barroso, "Empowering the Elderly and Promoting Active Ageing Through the Internet: The Benefit of e-inclusion Programmes" Safe at Home with Assistive Technology, Springer, Cham, 95-108, 2017. https://doi.org/10.1007/978-3-319-42890-1_7

[7] J. Gubbi, R .Buyya, S. Marusic, M. Palaniswami, "Internet of Things (IoT): A vision, architectural elements, and future directions" Future Generation Computer Systems, Volume 29, Issue 7, 1645-1660, 2013. http://dx.doi.org/10.1016/j.future.2013.01.010.

[8] C. Christophorou, S. Kleanthous, D. Georgiadis, D. M. Cereghetti, P. Andreou, C. Wings, E. Christodoulou, G. Samaras, "ICT services for active ageing and independent living: identification and assessment" Healthcare technology letters, 3.3: 159, 2016. https://doi.org/10.1049/htl.2016.0031

[9] V. Miori, D. Russo, "Preventing Health Emergencies in An Unobtrusive Way", Internet of Things. User-Centric IoT. Springer, Cham, 242-247, 2015. https://doi.org/10.1007/978-3-319-19656-5_35

[10] L. Atzori, A. Iera, G. Morabito, M. Nitti, "The social internet of things (siot)-when social networks meet the internet of things: Concept, architecture and network characterization" Computer Networks 56(16), 3594-3608, 2012. https://doi.org/10.1016/j.comnet.2012.07.010

[11] L. Atzori, A. Iera, G. Morabito, "From "smart objects" to "social objects": The next evolutionary step of the internet of things" Communications Magazine, IEEE 52.1, 97-105, 2014. https://doi.org/10.1109/MCOM.2014.6710070

[12] http://www.socialize-project.eu/

[13] V. Miori, D. Russo, "Domotic Evolution towards the IoT" in 28th International Conference on Advanced Information Networking and Applications Workshops (WAINA 2014), Victoria, Canada, 809-814, 2014. https://doi.org/10.1109/WAINA.2014.128

[14] British Standards Institute. Industrial Automation Systems – Concepts and Rules for Enterprise Models, BS ISO 14258, London: British Standards Institute, 1998

[15] M. Ganzha, M. Paprzycki, W. Pawlowski, P. Szmeja, K. Wasielewska, "Semantic Technologies for the IoT - An Inter-IoT Perspective" in IEEE First International Conference on Internet-of-Things Design and Implementation (IoTDI), Berlin Germany, 271-276, 2016. https://doi.org/10.1109/IoTDI.2015.22

[16] A. Broering, S. Schmid, C. K. Schindhelm, A. Khelil, S. Kaebisch, D. Kramer, D. Le Phouc, J. Mitic, D. Anicic, E. Teniente, "Enabling IoT Ecosystems through Platform Interoperability" IEEE Software, vol. 34, no. 1, 54-61, 2017. https://doi.org/10.1109/MS.2017.2

[17] S. Kubler, J. Robert, A. Hefnawy, K. Främling, C. Cherifi, A. Bouras, "Open IoT Ecosystem for Sporting Event Management," IEEE Access, vol. 5, 7064-7079, 2017. https://doi.org/10.1109/ACCESS.2017.2692247

[18] S. Soursos, I. Podnar Zarko "symbIoTe: Symbiosis of Smart Objects Across IoT Environments, in Digitising the Industry" Internet of Things Connecting the Physical, Digital and Virtual Worlds, IERC Cluster Book, 303-307, 2016. https://doi.org/10.1109/EuCNC.2016.7561070

[19] Y. Guan, J. C. Vasquez, J. M. Guerrero, "An open virtual neighbourhood network to connect IoT infrastructures and smart objects — Vicinity: IoT enables interoperability as a service" in Global Internet of Things Summit (GIoTS), Geneva Switzerland, 1-6, 2017. https://doi.org/10.1109/GIOTS.2017.8016233

[20] S. Kubler, J. Robert, A. Hefnawy, C. Cherifi, A. Bouras, K. Främling, "IoT-based Smart Parking System for Sporting Event Management" in 13th International Conference on Mobile and Ubiquitous Systems: Computing, Networking and Services (MOBIQUITOUS 2016), ACM, New York USA, 104-114, 2016. https://doi.org/10.1145/2994374.2994390

[21] J. H. Abawajy, M. M. Hassan, "Federated internet of things and cloud computing pervasive patient health monitoring system" IEEE Communications Magazine, 55(1), 48-53, 2017. https://doi.org/10.1109/MCOM.2017.1600374CM

[22] P. Kakria, N. K.Tripathi, P. Kitipawang, "A real-time health monitoring system for remote cardiac patients using smartphone and wearable sensors" International journal of telemedicine and applications, 8-19, 2015. https://doi.org/10.1155/2015/373474

[23] S. Coradeschi, A. Cesta, G. Cortellessa, L. Coraci, C. Galindo, J. Gonzalez, L. KarlssonA. Forsberg, S. Frennert, F. Furfari, et al., "GiraffPlus: a system for monitoring activities and physiological parameters and promoting social

interaction for elderly" Human-Computer Systems Interaction: Backgrounds and Applications 3, Springer, Cham, 261-271, 2014. https://doi.org/10.1007/978-3-319-08491-6_22
[24] M. S. Shahamabadi, B. B. M. Ali, P. Varahram, and A. J. Jara, "A Network Mobility Solution Based on 6LoWPAN Hospital Wireless Sensor Network (NEMO-HWSN)" in Seventh International Conference on Innovative Mobile and Internet Services in Ubiquitous Computing, Taichung Taiwan, 433-438, 2013. https://doi.org/10.1109/IMIS.2013.157A
[25] A. Dohr, R. Modre-Opsrian, M. Drobics, D. Hayn, G. Schreier, "The Internet of Things for ambient assisted living" in 7th International Conference on Information Technology: New Generations (ITNG 2010), Las Vegas USA, 804–809, 2010. https://doi.org/10.1109/ITNG.2010.104
[26] F. Goncalves, J. Macedo, M. J. Nicolau, A. Santos, "Security architecture for mobile e-health applications in medication control" in 21th International Conference on Software, Telecommunications and Computer Networks (SoftCOM 2013), Split - Primosten Croatia, 1–8, 2013, https://doi.org/10.1109/SoftCOM.2013.6671901
[27] L. Nie, T. Li, M. Akbari, J. Shen, T. Chua, "Wenzher: Comprehensive vertical search for healthcare domain" in ACM SIGIR Conf. Res. Develop. Inf. Retrieval, Gold Coast Australia, 1245–1246, 2014. https://doi.org/10.1145/2600428.2611176
[28] H. Takeuchi, N. Kodama, "Validity of association rules extracted by healthcare-data-mining" in IEEE 36th Annu. Int. Conf. EMBC, Chicago USA, 4960–4963, 2014. https://doi.org/10.1109/EMBC.2014.6944737
[29] A. M. Ortiz, D. Hussein, S. Park, "The cluster between internet of things and social networks: Review and research challenges" IEEE Internet of Things Journal, 1.3, 206-215, 2014. https://doi.org/10.1109/JIOT.2014.2318835
[30] T. Y. Chung, I. Mashal, O. Alsaryrah, V. Huy, W. H. Kuo, D. P. Agrawal, "Social Web of Things: A Survey" in International Conference on Parallel and Distributed Systems (ICPADS), Seoul South Korea, 570-575, 2013. https://doi.org/10.1109/ICPADS.2013.102.
[31] H. Lee, J. Kwon, "Survey and Analysis of Information Sharing in Social IoT" in 8th International Conference on Disaster Recovery and Business Continuity (DRBC), Jeju South Korea, 15-18, 2015. https://doi.org/ 10.1109/DRBC.2015.13
[32] L. E. Holmquist, F. Mattern, B. Schiele, P. Alahutha, M. Beigl, H. Gallersen, "Smart-its friends: a technique for users to easily establish connections between smart artefacts" in ACM UbiComp'01, Atlanta USA, 2001. https://doi.org/10.1007/3-540-45427-6_10
[33] S. D. Bruyne, "Finding your way around the KNX Specifications" in KNX Technology Tutorial Workshop, Deggendorf Germany, 2004.
[34] B. A. Miller, T. Nixon, C. Tai, M. D Wood, "Home networking with Universal Plug and Play" IEEE Communications Magazine, vol. 39, no. 12, 104-109, 2001. https://doi.org/10.1109/35.968819
[35] https://www.knx.org/knx-en/software/ets/about/index.php
[36] http://www.bticino.com/solutions/home-automation/
[37] J. S. Lee, Y. W. Su, C. C. Shen, "A Comparative Study of Wireless Protocols: Bluetooth, UWB, ZigBee, and Wi-Fi" in IECON 2007 - 33rd Annual Conference of the IEEE Industrial Electronics Society, Taipei Taiwan, 46-51, 2007. https://doi.org/10.1109/IECON.2007.4460126
[38] B. Malinowsky, G. Neugschwandtner, and W. Kastner, "Calimero: Next Generation", in Konnex Scientific Conference, 2007.
[39] A. Bobek, H. Bohn, F. Golatowski, G. Kachel, A. Spreen, "Enabling workflow in UPnP networks" in INDIN'05 3rd IEEE International Conference Industrial Informatics, 166-171, 2005. https://doi.org/10.1109/INDIN.2005.1560370
[40] https://www.myopen-legrandgroup.com
[41] A. V. Aho, M. S. Lam, R. Sethi, J. D. Ullman, Compilers: Principles, Techniques, and Tools (2nd Edition), Addison-Wesley Longman Publishing Co. Inc., 2006.
[42] https://www.raspberrypi.org/products/raspberry-pi-3-model-b-plus/
[43] V. Miori, D. Russo "Home automation devices belong to the IoT world" ERCIM News, 101, Special theme: The Internet of Things and the Web of Things, ERCIM, 22 - 23, 2015.
[44] A. G. González, GNU General Public License v3: A Legal Analysis SCRIPT-ed, 155-163, 2006
[45] https://github.com/darioxrusso/smartSMILE

ASTES

Advances in Science, Technology and Engineering Systems Journal Vol. 3, No. 4, 187-192 (2018)

www.astesj.com

ASTESJ

ISSN: 2415-6698

Vertical Accuracy Assessment of DSM from TerraSAR-X and DTM from Aerial Photogrammetry on Paddy Fields – Karawang, Indonesia

Bambang Riadi[1], Yustisi A. Lumban-Gaol[*,1], Bimo Wicaksono[2] and Sekar Pranadita[2]

[1]*Geospatial Information Agency, Jalan Raya Jakarta-Bogor Km.46, Cibinong 16911, Indonesia*

[2]*University of Indonesia, Kampus Universitas Indonesia Depok, Depok 16424, Indonesia*

ARTICLE INFO

Article history:
Received: 17 April, 2018
Accepted: 25 July 2018
Online: 29 July 2018

Keywords:
Accuracy
DSM
DTM
Check points
Stereo-plotting

ABSTRACT

A Digital Terrain Model (DTM) is a digital model representing the earth 's surface topography in three dimensions (3D) while a Digital Surface Model (DSM) represents the whole terrain including the objects on it such as trees and buildings. DTMs can be created through stereo-plotting. The advantage of this method is that the 3D data can be obtained with a high level of accuracy, but the data is limited in cloudy areas. This problem can be solved by using DSM, which can be created using TerraSAR-X and TanDEM-X Satellites with Synthetic Aperture Radar (SAR) system. This research aims to analyze the accuracy of DSMs from TerraSAR-X alongside DTMs extracted from aerial photogrammetry. The accuracy assessment of vertical height was completed by choosing 121 check points spread systematically on a paddy field in Karawang Regency, West Java. As paddy field was chosen to minimize errors between the DSM and DTM. The average, minimum, and maximum value of height differences between the DSM and DTM was calculated to obtain the standard deviation. The result showed that the average height difference between the DSM and DTM was 3.4 m with a minimum and maximum difference as 0.2 m and 10.808 m respectively. The standard deviation obtained was 4.9 m.

1. Introduction

Spatial data acquisition technology from above the earth's surface to obtain three-dimensional (3D) data can be completed using aerial photogrammetry and radar. The representation of topography on a specific reference system is generally related to Digital Terrain Models (DTMs). DTMs can be created with a terrestrial survey or remote sensing in areas where remote sensing is faster than a survey. Remote sensing technologies that can be used to produce data and information about the objects on the surface are aerial photogrammetry and radar. The height data model from those technologies will represent the DTM and the Digital Surface Model (DSM). DSMs represent the height of objects such as trees, buildings, ground level, and so on. This data is formed after orthorectification, a geometric correction process using satellite imagery to fix geometric errors related to topography, sensor geometry, and other factors. The height information is obtained for any point on the earth's surface by calculating the phase difference received by the two antennas on the mission's two satellites with X-band radar signals, such as TerraSAR-X or TanDEM-X [1]. DSM as one of height data model with grid spacing between 5-10 m is a digital earth surface model represented the earth surface height. The elevation model is based on a pair of stereo TerraSAR-X StripMaps with 3 m resolution. Then, the StripMaps are processed using the radargrametric technique by matching a homolog point from two images in the same area with different geometry [2]. The vertical accuracy value of an object showed the uncertainty of geometry of the height value on an object in the image towards an object which is considered correct in the actual position. The vertical accuracy of an object is the LE90 value, and it is based on a comparison between the height data values of a point that has been examined and is considered correct. Height value accuracy of any examined point should not fall below 90% [3].

The rapid development of technology for photogrammetry data processing, especially aerial photos, can fulfill several needs and purposes. DTMs provide information on the height of the earth's surface in digital format (raster or vector) that shows the earth's

*Yustisi A. Lumban-Gaol, Email: yustisi.ardhitasari@big.go.id

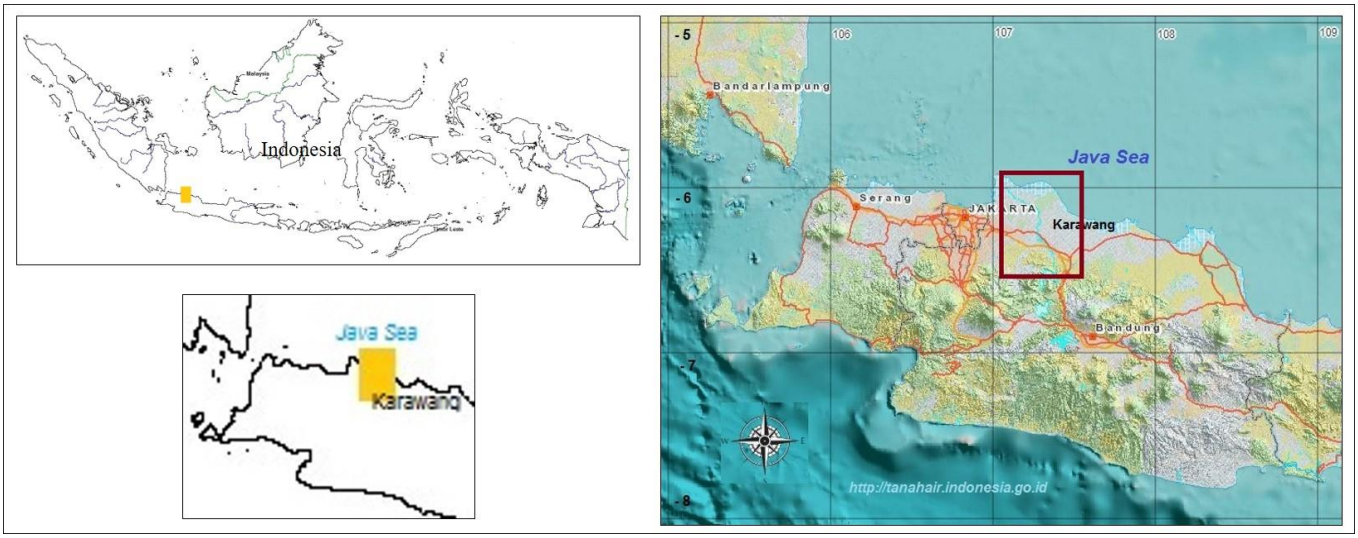

Figure 1. The location of Karawang Regency, West Java.

surface topography. Digital aerial photogrammetry is an advance tool used to build models of the earth's surface that can produce high resolution DTMs by image matching automatically. Currently, acquisition technology uses digital cameras that provide direct, high-resolution images. The dimension of internal DTMs are measured in pixels and are related to the camera metrics quality, photo scale, flight height, Ground Sample Distance (GSD), surface morphology, vegetation, shadows, and atmospheric conditions. Digital photogrammetry can produce a 3D height point with high spatial resolution, and the image correlation method is applied to DTM extraction automatically. Standard procedure for producing DTM is based on basic steps consisting of internal orientation, external orientation, and point extraction.

Internal orientation aims to assign the position of the frame inside the camera to fix the distortion and set the known coordinate values on certain points. External orientation consists of two steps: relative orientation, and absolute orientation. Relative orientation is done to build a stereoscopic model. Automatic procedure for image processing and DTM extracting generates a high precision model in a very short time, which reduce manual editing. DTM accuracy is related to image quality and terrain features.

The accuracy level of TerraSAR-X along with spatial resolution is very high, and a DTM generated from TerraSAR-X is 90% accurate within a range of 9.75 m [4]. The same research was completed by Seferick et al. (2012) [5] and their results showed that the accuracy of DEM TerraSAR-X was between 8 to 10 m depending on a slope with an RMSEz value of approximately 2.5 m. The purpose of this research was to analyze the vertical accuracy of DTMs by comparing the vertical value of DSMs from TerraSAR-X with DTMs from aerial photos.

2. Materials and Method

2.1. Study area

This research was completed from July 2017 through November 2017 at Indonesia Geospatial Information Agency (BIG). This study is located in the Karawang Regency in the north part of the West Java Province. Geographically, it is located between Longitude 107º15'33" - 107º21'31" East and Latitude 6º13'32" - 6º21'36" South as is shown in Figure 1.

2.2. Materials and data used

The primary data used in this study consists of DTMs from aerial photos and DSMs from TerraSAR-X. The aerial data acquisition process including Ground Control Point (GCP) survey was not discussed in this article. Details of the materials used are provided in Table 1.

2.3. DTM Photogrammetry Process

Digital aerial photos from acquisition contain information about the camera, images, and external orientation (EO). Beforehand, premark was installed as a GCP so the control point could be captured in the images, which is very important in aerial triangulation. Global Positioning System (GPS) survey was done on each premark to obtain an accurate geo-reference point for image processing so that each image had a reference system in line with the needs of mapping the results. GCP was used to process data for geometric correction on mosaic orthophoto to produce a highly accurate map.

Table 1. DSM and aerial photogrammetry specification.

Materials	Specifications
DSM TerraSAR-X in 2011, orthorectification	Resolution: 9 m
Aerial photogrammetry in November 2016	Leica RDC30 60MP 6 micron Ground sample distance 10 cm Flight height 1000-1300 m Photo scale 14000-16000 Overlap 65% Sidelap 30%

Scale uniformity on each photo required several control points. Photogrammetric work covers a wide area which produces a lot of images, so the control points were with aerial triangulation. Aerial triangulation is a coordinate transformation from image to ground using GCP. Aerial triangulation was used to establish a direct relationship between the photo and ground coordinate systems without a relative and absolute orientation process [6].

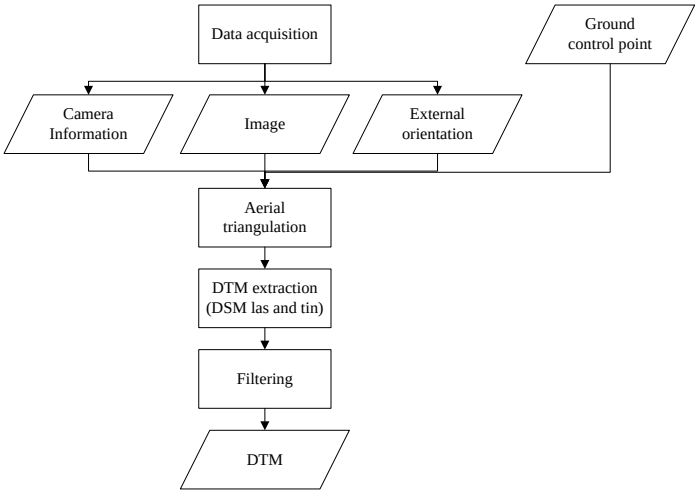

Figure 2. DTM photogrammetry flowchart.

The DTM photogrammetry was extracted from aerial photos after the aerial triangulation process using Inpho 5.4 to produce a DSM. After that, the DSM was filtered using software Terrasolid to obtain a DTM (Figure 2).

DTMs are used to describe terrain or relief models in 3D. DTMs depict actual shapes in the real world and is visualized using graphic computers and virtual reality technology [7]. The utilization of aerial photo techniques to produce 3D data has been heavily studied and is discussed in several publications. A discussion on the utilization of medium format cameras for producing 3D images was written by Warner et al. and used medium format Rollei 6006 cameras that could obtain a horizontal accuracy of 0.5 m and vertical accuracy of 1 m (1996) [8]. Currently, data acquisition and aerial photo processing uses the full digital system [9]. The provider and developer of photogrammetry software integrated data processing using AutoCAD and ArcGIS for vector data [6].

2.4. The determination of check points

Hereafter, the DTM from aerial photogrammetry was compared to the DSM from TerraSAR-X to find out the accuracy of the DSM. From the research location, an area was chosen to be an examination sample area. The sample area was a paddy field, based on the assumption that a paddy field is relatively flat. A DSM was examined directly without smoothing to eliminate spikes. The comparison between both elevation models was performed using the Combine/Compare Terrain Layers menu on Global Mapper with sample spacing matching the higher resolution, 0.5 m x 0.5 m.

The retrieval of sample points for examination (Figure 3) began by looking at the visual area of the paddy field, and a maximum limit of the coordinates was determined. From that boundary, the sample points were taken systematically with a range of 500 m between each point in either a north-south or east-west direction. This range was decided by assuming that each point represented the paddy field and was accurate enough to represent the elevation difference between DTM and DSM [10]. The selected points still had spikes or extreme values due to normal error. To reduce the effect of such error, any points with an elevation difference of more than 5.2 m were eliminated [3].

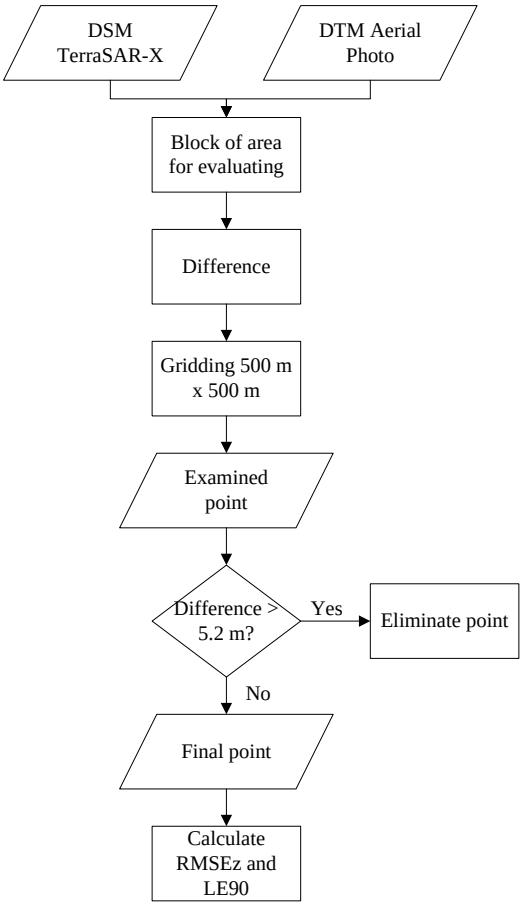

Figure 3. Statistic examined process for DSM and DTM.

The vertical accuracy of points was calculated using the RMSE (Root Mean Square Error) method from the difference between vertical values of a DSM TerraSAR-X and a DTM Aerial Photo on 90% confidence level. A total of 121 points were examined. RMSE and LE90 values were obtained from the equation below [11]:

$$RMSEz = \sqrt{\Sigma}(zDSM - zDTM) \quad (1)$$

$$LE90 = 1.6499 \times RMSEz \quad (2)$$

where

zDSM : vertical value on the DSM
zDTM : vertical value on the DTM
RMSEz : RMSE on z (vertical)
LE90 : confidence level 90%

3. Results and Discussion

The accuracy information of orthorectification of the DSM TerraSAR-X from BIG was presented in Table 2. The difference between the DSM and the DTM of the sample area can be seen in Figure 6. and Table 3. A negative value indicates that the DSM TerraSAR-X elevation was lower than in the DTM aerial photo, while a positive value means the opposite. Then, the examined point was taken systematically on paddy field. The total number of examine point was 121 with range 500 m both directions, north to south and west to east (Figure 5). Based on statistical results from the examined points, the difference in maximum value was 10.8 m, minimum value was 0.2 m, and average value was 3.4 m. The RMSEz and LE90 values were 4.2 m and 6.9 m respectively.

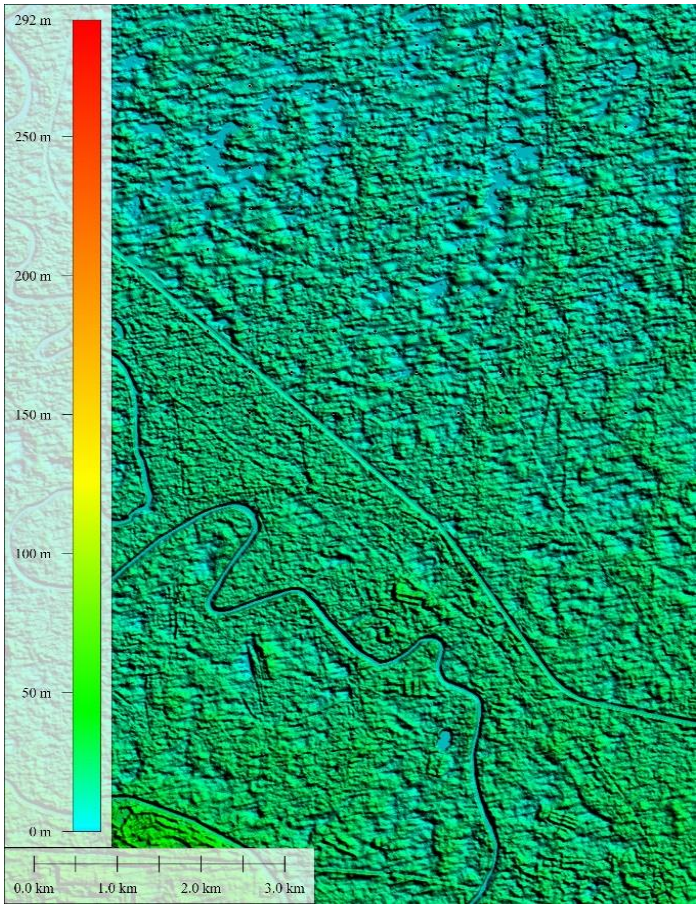

Figure 4. DSM TerraSAR-X elevation range.

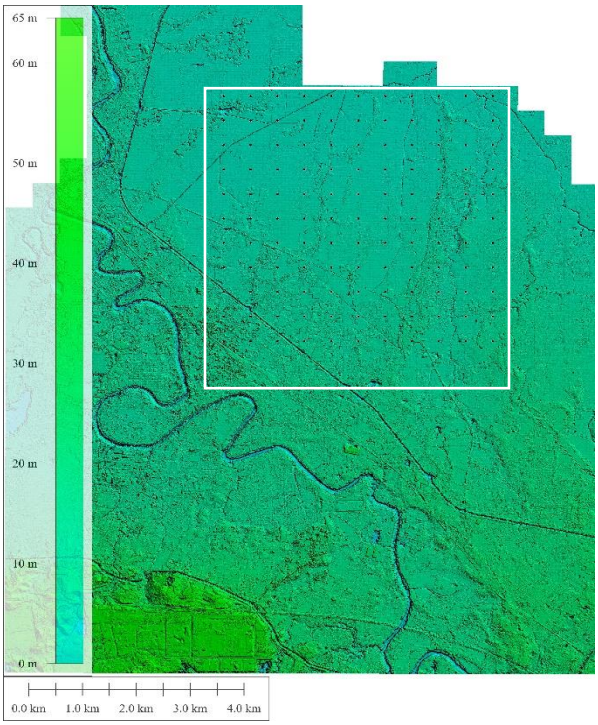

Figure 5. DTM aerial photogrammetry elevation range, white box was the examined area.

Table 2. DSM TerraSAR-X resolution.

Image statistics		ICESat statistics	
Min (m)	0	Nu. of points	135
Max (m)	292	RMSE (m)	2.4
Mean (m)	41.6	LE90 (m)	5.4
STD (m)	35.9		

From 121 examined points, there were 23 points with a difference greater than 5.2 m. After those points were eliminated, the RMSEz value become 2.9 m with LE90 4.9 m, which means the vertical accuracy value at a 90% confidence level was 4.9 m. This result fulfills the specification for a base map on a 1:25.000 scale class 1 in line with [1] BIG Regulation Nu. 15 Year 2014.

To see the form of a cross-section from the DTM and the DSM, a cross-section graphic analysis was done. The sample cross-section of a DEM can be seen in Figure 6.

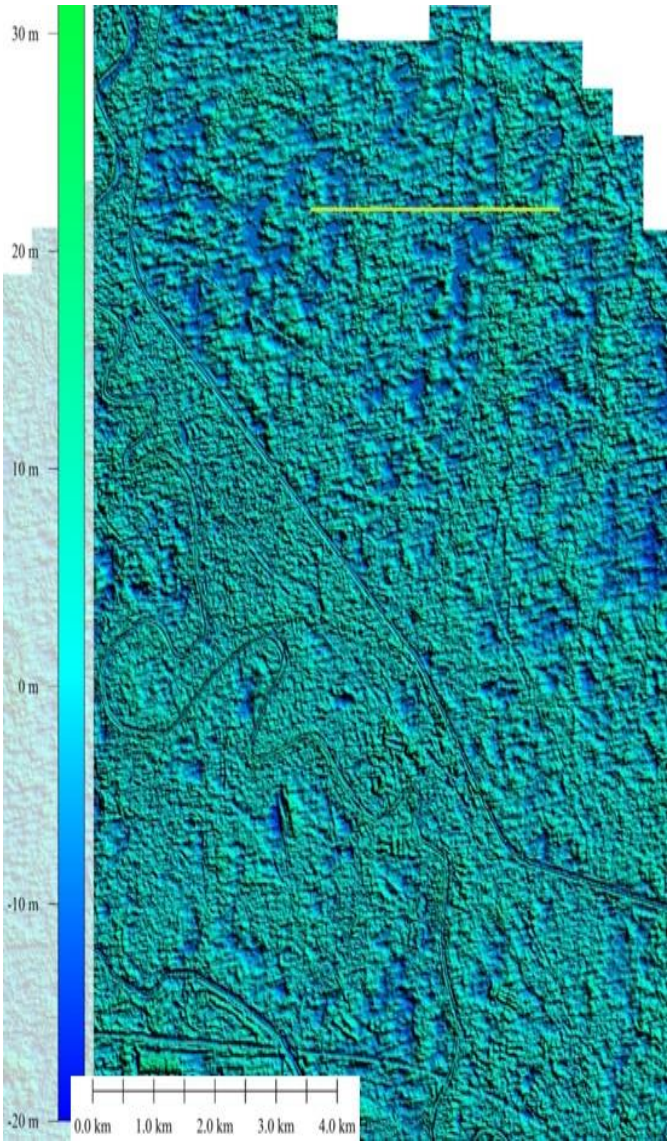

Figure 6. The elevation difference between DTM and DSM, yellow line was the sample for cross-section.

Table 3. The difference between DSM TerraSAR-X and DTM aerial photogrammetry.

No	X	Y	Z	No	X	Y	Z	No	X	Y	Z
1	754000	9308000	-3.972	41	755500	9304500	3.894	81	757500	9306500	-3.942
2	754000	9307500	0.376	42	755500	9304000	-1.51	82	757500	9306000	-8.44
3	754000	9307000	4.577	43	755500	9303500	-0.161	83	757500	9305500	-9.351
4	754000	9306500	-3.641	44	755500	9303000	3.192	84	757500	9305000	-10.808
5	754000	9306000	-5.727	45	756000	9308000	-4.453	85	757500	9304500	-1.558
6	754000	9305500	-8.806	46	756000	9307500	4.249	86	757500	9304000	0.576
7	754000	9305000	2.005	47	756000	9307000	3.477	87	757500	9303500	-6.552
8	754000	9304500	7.152	48	756000	9306500	7.737	88	757500	9303000	-0.257
9	754000	9304000	4.728	49	756000	9306000	4.026	89	758000	9308000	3.985
10	754000	9303500	1.038	50	756000	9305500	5.134	90	758000	9307500	-6.659
11	754000	9303000	-4.375	51	756000	9305000	2.249	91	758000	9307000	-1.072
12	754500	9308000	0.472	52	756000	9304500	-7.246	92	758000	9306500	-1.328
13	754500	9307500	-2.82	53	756000	9304000	-3.047	93	758000	9306000	3.581
14	754500	9307000	0.155	54	756000	9303500	-1.152	94	758000	9305500	-1.052
15	754500	9306500	4.278	55	756000	9303000	-7.689	95	758000	9305000	4.863
16	754500	9306000	-9.396	56	756500	9308000	-6.606	96	758000	9304500	-0.42
17	754500	9305500	-3.316	57	756500	9307500	-6.262	97	758000	9304000	6.261
18	754500	9305000	-6.891	58	756500	9307000	4.802	98	758000	9303500	4.378
19	754500	9304500	0.745	59	756500	9306500	-0.775	99	758000	9303000	-5.167
20	754500	9304000	0.248	60	756500	9306000	0.798	100	758500	9308000	-2.864
21	754500	9303500	-4.528	61	756500	9305500	-4.061	101	758500	9307500	5.298
22	754500	9303000	0.661	62	756500	9305000	-0.314	102	758500	9307000	3.358
23	755000	9308000	-1.839	63	756500	9304500	-3.851	103	758500	9306500	1.638
24	755000	9307500	4.869	64	756500	9304000	1.045	104	758500	9306000	4.5
25	755000	9307000	0.957	65	756500	9303500	4.311	105	758500	9305500	8.423
26	755000	9306500	3.702	66	756500	9303000	-3.555	106	758500	9305000	0.763
27	755000	9306000	2.996	67	757000	9308000	-2.406	107	758500	9304500	1.855
28	755000	9305500	-1.624	68	757000	9307500	0.925	108	758500	9304000	4.613
29	755000	9305000	2.933	69	757000	9307000	3.056	109	758500	9303500	3.655
30	755000	9304500	1.499	70	757000	9306500	3.89	110	758500	9303000	3.465
31	755000	9304000	3.986	71	757000	9306000	-7.521	111	759000	9308000	3.18
32	755000	9303500	3.635	72	757000	9305500	-9.084	112	759000	9307500	0.357
33	755000	9303000	3.241	73	757000	9305000	-2.893	113	759000	9307000	0.466
34	755500	9308000	-4.334	74	757000	9304500	-1.636	114	759000	9306500	-3.496
35	755500	9307500	0.523	75	757000	9304000	4.002	115	759000	9306000	-0.502
36	755500	9307000	0.482	76	757000	9303500	-4.239	116	759000	9305500	3.17
37	755500	9306500	-0.927	77	757000	9303000	-2.274	117	759000	9305000	-1.703
38	755500	9306000	1.573	78	757500	9308000	6.151	118	759000	9304500	-7.686
39	755500	9305500	-0.345	79	757500	9307500	5.917	119	759000	9304000	-2.701
40	755500	9305000	-1.809	80	757500	9307000	-0.722	120	759000	9303500	0.876
								121	759000	9303000	-0.658

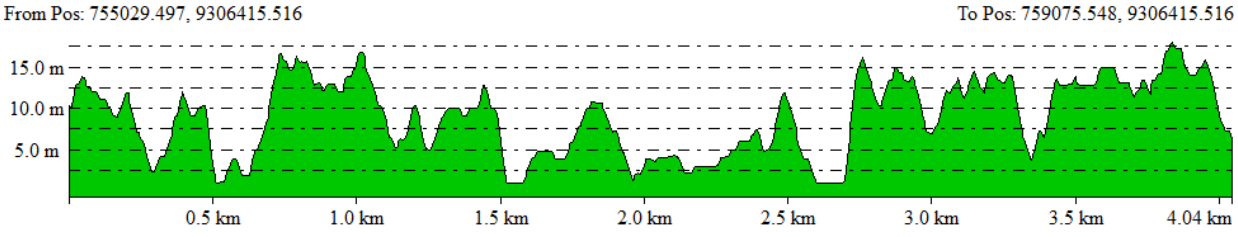

(a)

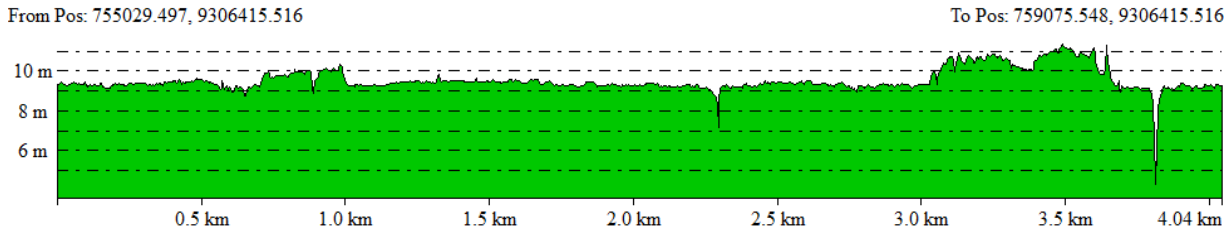

(b)

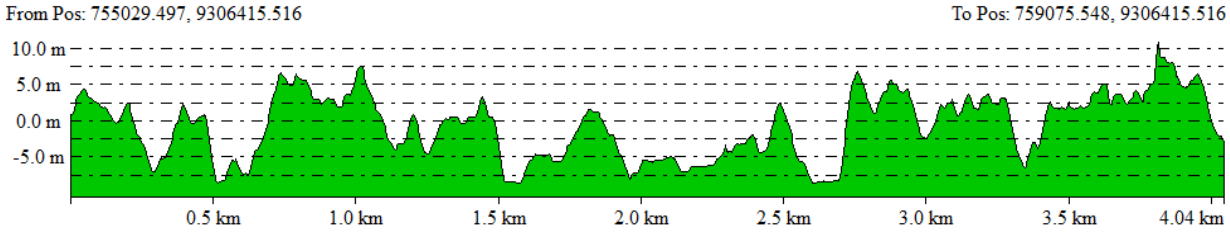

(c)

Figure 7. Cross-section of (a) DSM TerraSAR-X; (b) DTM aerial photogrammetry; (c) The elevation differences between DSM and DTM.

Figure 7b above shows that the surface from a DTM aerial photo was relatively flat while on the DSM spikes were still occur (Figure 7a). Additionally, the DSM from TerraSAR-X was rougher than the DTM aerial photo because DSM has a lower spatial resolution. Smoothing the DMS using validated points can be done to eliminate spikes, but this step was not completed in this research. The elevation differences between DSM and DTM was seen in Figure 7c where the metrics value had already discussed before.

4. Conclusion

Until now, a DTM from aerial photography was the most ideal for finding basic data for topographic mapping. From this study, the vertical accuracy of a DSM TerraSAR-X was 4.9 m with an average value of 3.4 m and standard deviation of 2.9 m. This result leads to the conclusion that on a paddy or flat area, a DSM TerraSAR-X can also be used for situations that need high vertical accuracy.

Conflict of Interest

The authors declare no conflict of interest.

Acknowledgment

Thanks to the Geospatial Information Agency for data and equipment support for data processing of DSM TerraSAR-X and DTM photogrammetry, so this article can be resolved.

References

[1] Collins J., Riegler G., Schrader H., Tinz M., 2015. Applying Terrain and Hydrological Editing to TanDEM-X Data to Create a Consumer-ready WolrdDEM Product. 36th International Symposium on Remote Sensing of Environment, Berlin, Germany.

[2] Infoterra. 2010. TerraSAR-X Elevation DSM. Regional Digital Surface Models worldwide. E.info@infoterra-global.com.

[3] Prihanggo M, Geofana A, Mulyana AK. 2015. Uji Akurasi Ketelitian Vertikal DSM TerraSAR-X (studi kasus : Kota Banjarmasin dan Kota Palangkaraya). Prosiding Forum Ilmiah Tahunan Ikatan Surveyor Indonesia 2015.

[4] Susetyo, D.B., Syafiudin, M. F., Prasetyo, Y. 2017. DTM Generation from TerraSAR-X Using TIN Algorithm in Papua Island, Indonesia. ISPRS Hannover Workshop, Germany.

[5] Seferick, U. G., Schunert, A., Soergel, U., Watanabe, K. 2012. Validation of DEMs Derived from High Resolution SAR Data: A Case Study on Barcelona. XXII ISPRS Congress, Melbourne, Australia.

[6] Pranadita S and Harintaka. 2013. Digital Elevation Model Development from Interactive Stereo-plotting of Medium Format Aerial Photo Using DiiCam Camera. *Jurnal Ilmiah Geomatika* Vol. 19 No.2, Desember 2013.

[7] Fabris, M and Pesci, A. 2005. Automated DEM extraction in digital aerial photogrammetry: precisions and validation or mass movement monitoring. *Annals of Geophysics*, Vol. 48, N. 6, December 2005.

[8] Warner WS, Graham RW, Read RE. 1996. *Small Format Aerial Photography*. ISBN 1-870325-5-7, Whittles Publishing. Scotland, UK.

[9] Höhle, J. 2011. DEM Generation by Means of New Digital Aerial Cameras. *International Archives of Photogrammetry, Remote Sensing and Spatial Information Sciences* 38 (3/W22).

[10] Karabork, H., Yildiz, F., Coskun, E., a, Yilmaz, H.M., Yakar, M. 2007. Investigation of Accuracy for Digital Elevation Models Generated With Different Methods In Photogrammetry. Engineering Faculty, 42031 Kampus-Konya, Turkey.

[11] Badan Informasi Geospasial. 2014. Peraturan Kepala Badan Informasi Geospasial tentang Pedoman Teknis Ketelitian Peta Dasar. Nomor 15 Tahun 2014.

ASTES

Advances in Science, Technology and Engineering Systems Journal Vol. 3, No. 4, 193-200 (2018)

www.astesj.com

Special Issue on Multidisciplinary Sciences and Engineering

ASTESJ

ISSN: 2415-6698

Design of smart chess board that can predict the next position based on FPGA

Alaa Hamza Omran*,1, Yaser Muhammad Abid[2]

[1]*Department of Information System Management, University of Information Technology and Communication, Baghdad, 00964, Iraq*

[2]*Department of Business Information Technology, University of Information Technology and Communication, Baghdad, 00964, Iraq*

ARTICLE INFO

Article history:
Received: 29 June, 2018
Accepted: 26 July, 2018
Online: 29 July, 2018

Keywords:
Artificial Neural Network
Smart Chessboard
Back propagation algorithms
Chess game, intelligent chessboard
Intelligent controller and Supervised feed forward algorithm

ABSTRACT

The abilities of human brain to discover solutions for many problems is a great gift that motivate the scientists to develop the revolution of the artificial intelligence and using it in many areas. This paper proposed an intelligent chessboard which works in a way that similar to the human brain that predicts the next positions for any piece of the chess. MATLAB is used in the training of the artificial neural networks of the chessboard and implemented on FPGA as a hardware part; the proposed system has many advantages such as the low cost of production with a high efficiency in the prediction of the position of any piece on the chessboard and the similarities to the human brain.

1. Introduction

This paper is an extension of work originally presented in 4th IEEE International Conference on Engineering Technologies and Applied Sciences (ICETAS) [1].

In the early centuries, wars among major countries were in the zenith of prosperity, and the countries that have consultants who develop strategic plans for the Wars were prevail these wars; therefore, a game known as "kings game" was appeared. This game helps in developing the strategic plans without any human losses; it was spread rapidly in most countries and enticing many people because of its ability to motivate the human mind to think in a smart way. Furthermore, many schools in the world start to teach this game and considering it as the one of the games that test the intelligence [2]. Currently, and due to the tremendous evolution of the modern technology, many researches tries to make this game plays on the computers [3] [4]. They start to develop many programs that simulate chess game, however, playing this game can take many hours as known and sitting on computers for many hours can leads to serious problem such as headache, blurred vision and back pain etc. a large number of papers proved that the neural networks and intelligent systems have great dependency in many areas [5] [6] [7]. Many attempts in papers to build intelligent chess games have been done with disadvantages of very high costs used for designing the systems and complex electrical circuit.

However, there are a great number of researches in this area; [8] presents chess game in real time by using MATLAB environment without using for any chess engine, the system designed to detecting the chess movements depending on RGB webcam, and that means the complexity in the system designed may obtain incorrect positions during the game, the system have high cost with low accuracy. [9] presents chess board that can play against human depending on robotic arm which is five degree of freedom, the control system designed to control the speed and the position of the robotic arm, the designed system depend on the use of computer and that too expensive with very complex in the design that take long period of time to control the speed and the position. [10] Presents an attempt to design chess play against human and calculate its moves, the system implemented on microcontroller and the computer used to control chess movement, the system gave not perfect results and the use of computer also

* Corresponding author: Alaa Hamza Omran, Email: engineeralaa90@gmail.com

have disadvantages as mentioned. [11] Presents a robotic system play chines chess with human that can recognize pieces on the designed chessboard, the system designed to move the pieces of chess with the help of mechanical arm of robot, the system designed with expensive components. [12] Presents the chess game designed using MATLAB and electronics circuit for educational reasons, the system implemented on Arduino and the detection process for any piece to his place and type done by using Infrared light-emitting diode and photodiode, extra multiplexers, encoders and shift registers to increase the no. of I/P or O/P pins, this system have complex designed electronics circuit and high cost. [13] [14] present the FPGA in different systems and producing great efficiency in different area of researches and high speed in response. This paper merges two methods; the first one, is the ordinary method which used in the playing of the chess game. And the second method is the newest that used the technology methods to facilitate the playing of the game without using any computer device to decrease the damage that can be caused from playing the game as much as possible. The main contribution of this paper is to design an intelligent chessboard that can present the next positions for each piece and the avoidance of using computer due to different disadvantages that can occurred as a results of using it such as headache and blurred vision etc. The chessboard is designed by using a simple and low cost of electronics components that can compensate the using of computers which are used in many other chess game application.

2. Proposed System

Intelligent chessboard that can predict the next positions for all pieces of chess game is designed in this paper. Figure (1) shows the block diagram of the proposed system.

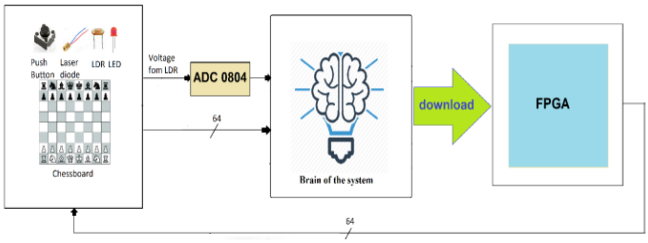

Figure 1: Block diagram of intelligent chessboard system

It consists of 64 push buttons which are equally distributed, one button for each square on the chessboard; a simple press on any push button of the intelligent chessboard would send a notification to the proposed system with the exact position and the needing to predict the next positions. There are also 64 LASER diodes which are equally distributed as the push buttons, one LED for each square of the chessboard. In the chess game, there are 32 pieces which are divided equally into 16 pieces, (king, queen, rooks, Bishop, knights and pawns), for each player. Therefore, 32 LDR sensors were used and equally distributed as one sensor for each piece. Furthermore, the pressing of any piece would make the LEDs of chessboard glowed in order to notify the user with the next positions were the pressed piece can move on. The LDR sensors were used to distinct among the 32 pieces; they are connected serially with a constant resistance for each piece as that shown in Figure (2)

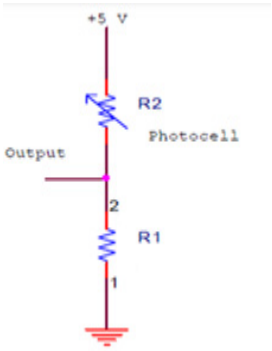

Figure 2: Constant resistance connected with LDR sensor

The light falling on the LDR sensor will produces a fixed range of voltage for each piece; because for each piece there is a different constant resistance; table (1) shows chess's piece types with corresponding voltages in the proposed system.

Table 1: Chess's piece types with corresponding voltages

Piece type	Range of voltage
Rook pieces	(from 0 to 0.5) volt
Knight pieces	(From 0.6 to 1)volt
Bishop pieces	(From 1.1 to 1.5) volt
King pieces	(From 1.6 to 2) volt
Queen pieces	(from 2.1to 2.5) volt
White pawn pieces	From (2.6 to 3) volt
black pawn pieces	(from 3.1to 3.5) volt

In the chess game, there are 8 pawns for each player which can move in different paths and opposite direction; therefore, the range of voltages differ and divided into two team white pawns and black pawns as shown in table (1).

3. Simulation Results of Training

The human brain handles the processes in an amazing and smart way that distinct it from any other machines. Therefore, the neural networks of the proposed system trained in such a way that is similar to the human brain in order to notify the players with the next positions of the movement for every piece in a smart way. Super vised Feed forward neural networks were used to train all the pieces of chess game depending on back propagation algorithm [15]; and each piece types in chess was trained individually. The determination of the No. of neurons in the input layers, No .of neurons in the hidden layers, the No. of layers and also the activation functions in each network all done using Try and error method.

3.1. Rook

Finally, the rook piece in the chess game moves in different paths as compared with the other pieces, it has specific paths of movements on chessboard which can moves horizontally or vertically. Four no. of rook pieces in chess game which are divided equally into two teams, all rooks piece have the same paths of movements on the chessboard; therefore, the training of the rook

was done individually for the first piece and repeated to the other pieces. In order to train the neural networks with the path of movements of the rook piece to act such as human brain, every square of the chessboard has sequential number begins with 1 and ends with 64. Any square which carry the rook piece will predict a different probability of the movements for the next positions of rook. Therefore, the networks of the chessboard trained with all possibility of movements for the rook piece on the chessboard. They are trained with six neurons in the hidden layer and fifteen neurons in the output layer as shown in Figure (3)

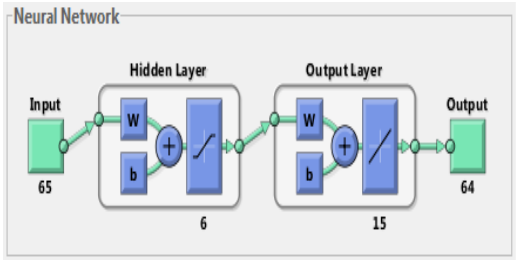

Figure 3: Final neural network used for rook pieces

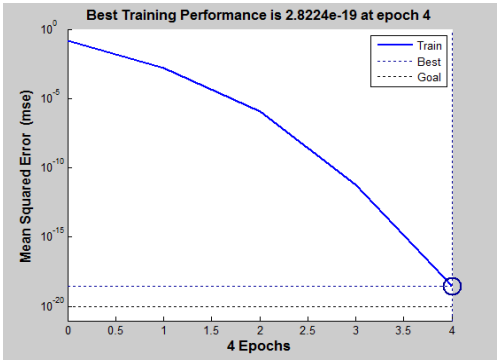

Figure 4: The simulation results of training the rook pieces

Figure (4) shows the simulation results of training the rook pieces; if the square with the number one carry the rook piece, all the several paths for the next position of the rook piece are shown in figure (5).

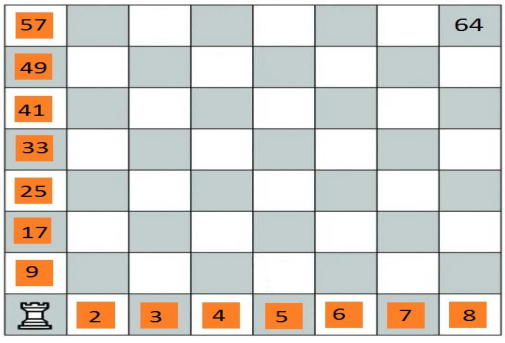

Figure 5: The way of movements of rook piece on the chessboard.

In the proposed chessboard a simple press over the rook piece, will lead to press the push button at the square with number one at the chessboard which will activate the laser diode to fall its light on the LDR sensor and depending on the voltage which produced from the LDR sensor and according to the range of voltage specified previously in table (1), the rook piece will be recognized. In more details, the reorganization process will lead to change the state of the LEDs to ON state over the designed chessboard and the exact squares (2, 3, 4, 5, 6, 7, 8, 9, 17, 25, 33, 41, 49, and 57) will be glowed to notify the player with the next available positions that the rook can move on.

The trained networks of rook piece converted into Simulink in order to test it and connect it with other networks in the next steps. The simulation results of rook piece movement for next positions shown in figure (6)

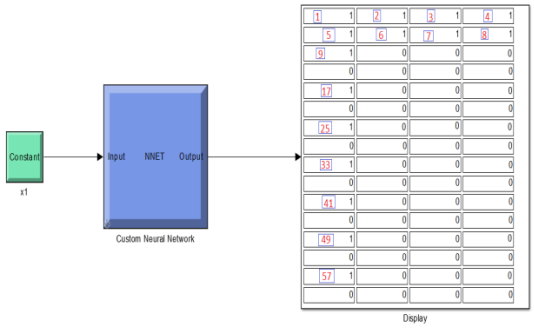

Figure 6: Simulation results of rook pieces for next positions movements

The trained networks of the rook pieces converted into VHDL code by using MATLAB that have HDL coder in order to implement it on FPGA, figure (7) shows the RTL of rook pieces used in proposed system and figure (8) shows the simulation results of intelligent networks of rook by using Xilinx ISE Design Suite 13.3.

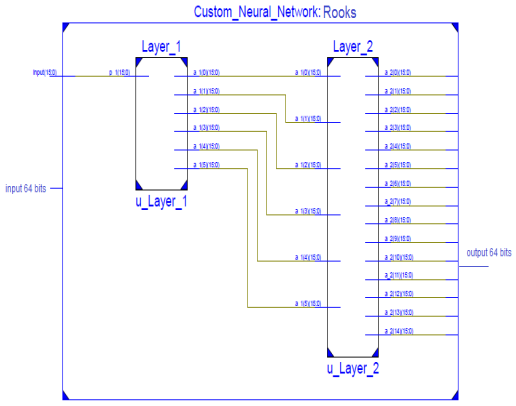

Figure 7: The RTL of rook pieces used in proposed system

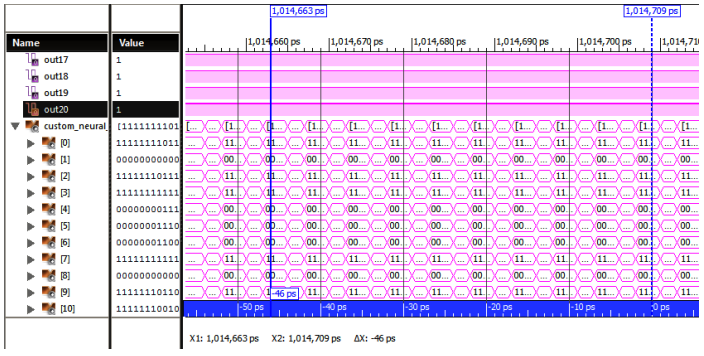

Figure 8: The simulation results of intelligent networks of rook

3.2. Bishop

The Bishop piece in the chess game moves in different paths as compared with the other pieces, it has specific paths of

movements on chessboard which can moves diagonally. The chess game has four pieces of bishop which are divided equally into two teams, all bishops piece have the same paths of movements on the chessboard; therefore, the training of the bishop was done individually for the first piece and repeated to the other pieces. In order to train the neural networks with the path of movements of the bishop piece to act such as human brain, every square of the chessboard has sequential number begins with 1 and ends with 64. Any square which carry the bishop piece will predict a different probability of the movements for the next positions of bishop. Therefore, the networks of the chessboard trained with the all possible movements of the bishop piece on the chessboard. They are trained with eight neurons in the hidden layer and twenty neurons in the output layer as shown in Figure (9).

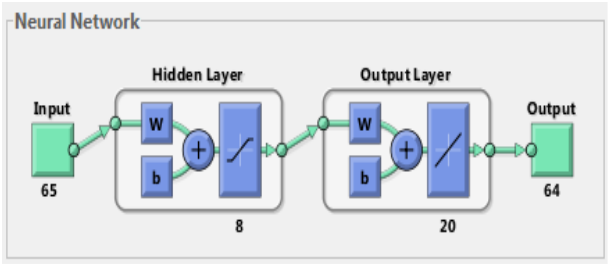

Figure 9: Final neural network used for bishop pieces

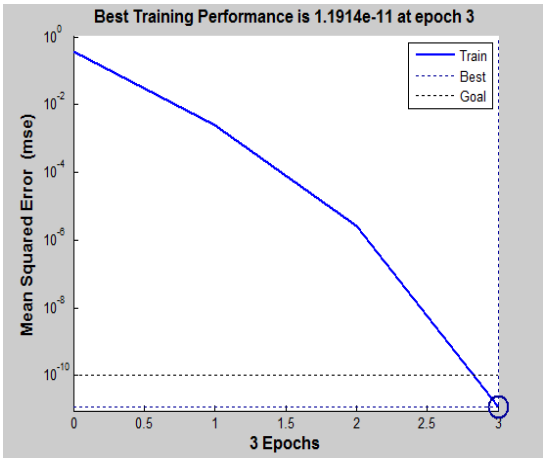

Figure 10: The simulation results of training bishop pieces

Figure (10) shows the simulation results of training bishops; if the square with the number twenty two carry the bishop piece, all the several paths for the next position of the bishop piece are shown in figure (11).

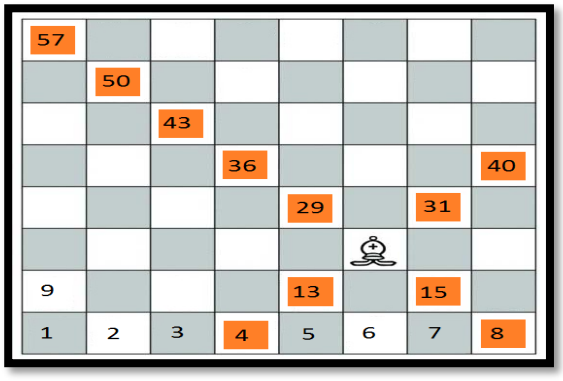

Figure 11: The way of movements of bishop pieces on the chessboard.

In the proposed chessboard a simple press over the bishop piece at square twenty two, will lead the same processes mentioned in the rook piece and the bishop piece will be recognized. In more details, the reorganization process will lead to change the state of the LEDs to ON state over the designed chessboard and the exact squares (4, 8, 13, 15, 22, 29, 31, 36, 40, 43, 50, and 57) will be glowed to notify the player with the next available positions that the bishop can move on.

The trained networks of bishop piece converted into Simulink in order to test it and connect it with other networks in the next steps. Figure (12) show the simulation results of bishop piece movement for next positions.

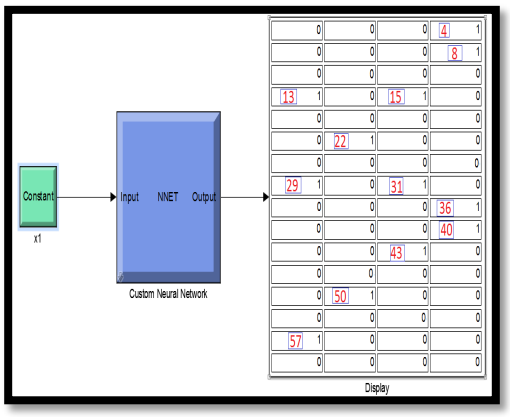

Figure 12: Simulation results of bishop pieces for next positions movements

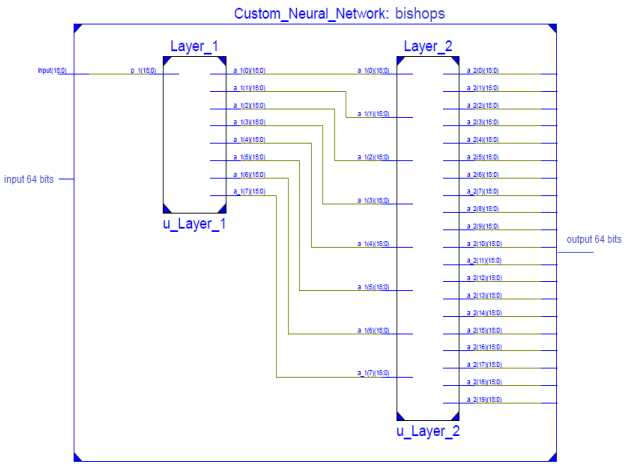

Figure 13: The RTL of bishop pieces used in proposed system

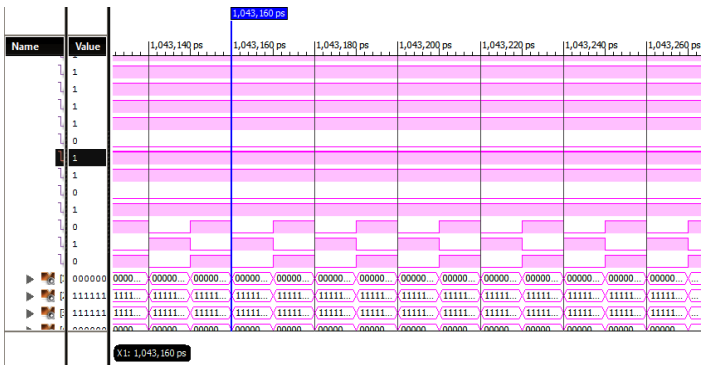

Figure 14: The simulation results of intelligent networks of bishop

The trained networks of the bishop pieces converted into VHDL code by using MATLAB that have HDL coder in order to implement it on FPGA, figure (13) shows the RTL of bishop pieces used in proposed system and figure (14) shows the simulation results of intelligent networks of bishop by using Xilinx ISE Design Suite 13.3.

3.3. Knights

The knight piece in the chess game moves in different paths as compared with the other pieces, it has specific paths of movements on chessboard which can moves in the shape of **L** for two square and can jumps on other pieces on the chessboard. The chess game has four pieces of knights which are divided equally into two teams, all knights piece have the same paths of movements on the chessboard; therefore, the training of the knight was done individually for the first piece and repeated to the other pieces. In order to train the neural networks with the path of movements of the knight piece to act such as human brain, every square of the chessboard has sequential number begins with 1 and ends with 64. Any square which carry the knight piece will predict a different probability of the movements for the next positions of knight. Therefore, the networks of the chessboard trained with the all possible movements of the knight piece on the chessboard. They are trained with twelve neurons in the hidden layer and eleven neurons in the output layer as shown in Fig (15).

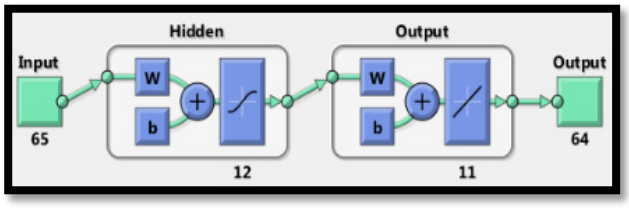

Figure 15: Final neural network used for knight pieces

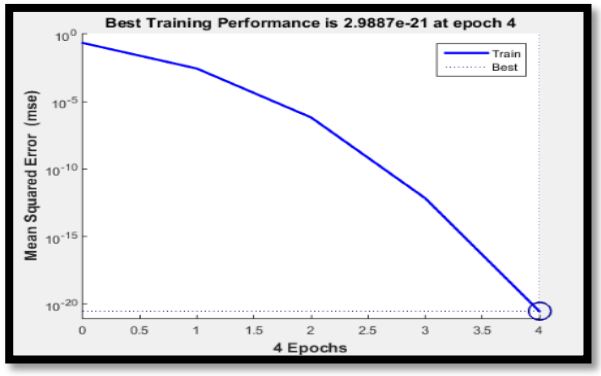

Figure 16: The simulation results of training the knight pieces

Figure (16) shows the simulation results of the knight movements; if the square with the number thirty seven carry the knight piece, all the several paths for the next position of the knight piece are shown in figure (17).

In the proposed chessboard a simple press over the knight piece at square thirty seven, will lead the same processes mentioned in the rook piece and the knight piece will be recognized. In more details, the reorganization process will lead to change the state of the LEDs to ON state over the designed chessboard and the exact squares (20, 22, 27, 31, 37, 43, 47, 52, and 54) will be glowed to notify the player with the next available positions that the knight can move on.

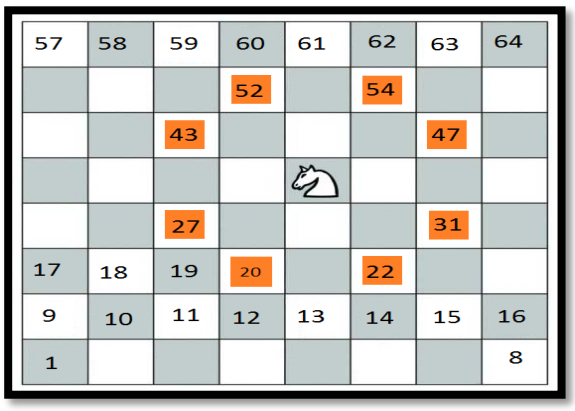

Figure 17: The way of movements knight pieces on the chessboard.

The trained networks of knight piece converted into Simulink in order to test it and connect it with other networks in the next steps. The simulation results of knight piece movement for next positions shown in figure (18)

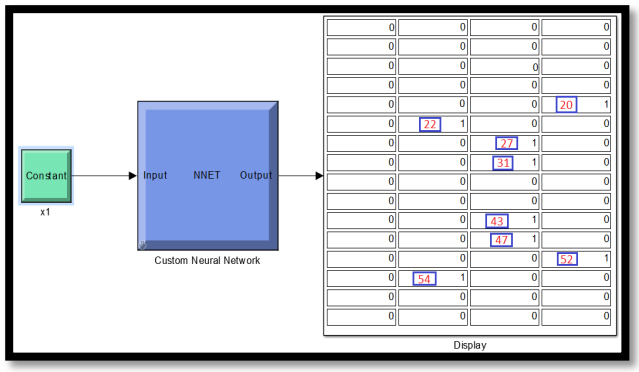

Figure 18: Simulation results of knight pieces for next positions movements

The trained networks of the knight pieces converted into VHDL code by using MATLAB that have HDL coder in order to implement it on FPGA, figure (19) shows the RTL of knight pieces used in proposed system and figure (20) shows the simulation results of intelligent networks of knight by using Xilinx ISE Design Suite 13.3.

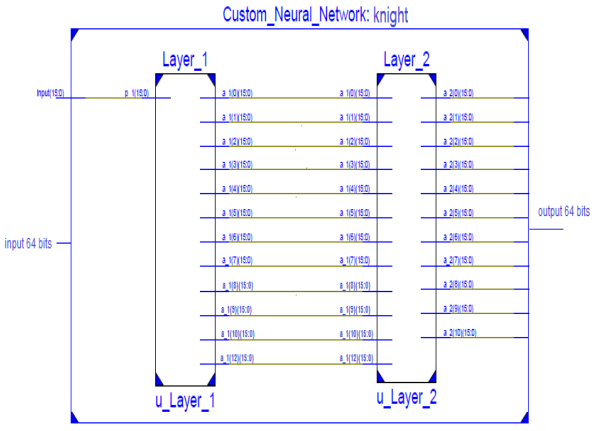

Figure 19: The RTL of knight pieces used in proposed system

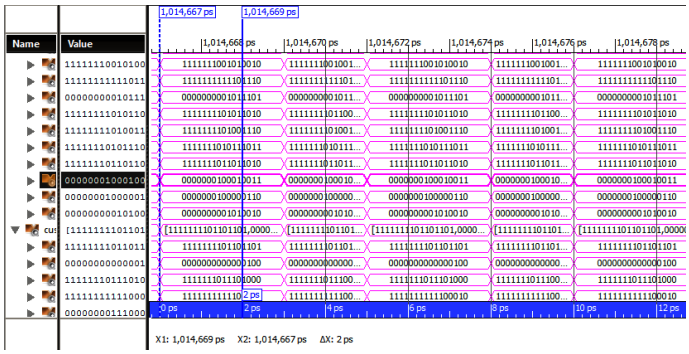

Figure 20: The simulation results of intelligent networks of knight

3.4. Queens

The queen piece in the chess game moves in different paths as compared with the other pieces, it is the strongest piece and has specific paths of movements on the chessboard, it can moves at paths that collect the both paths of the rook and bishop pieces at the chessboard. The chess game has two pieces of queen which are divided equally into two teams, all queen pieces have the same paths of movements on the chessboard; therefore, the training of the queen was done individually for the first piece and repeated to the other piece. In order to train the neural networks with the path of movements of the queen piece to act such as human brain, every square of the chessboard has sequential number begins with 1 and ends with 64. Any square which carry the queen piece will predict a different probability of the movements for the next positions of queen. Therefore, the networks of the chessboard trained with the all possible movements of the queen piece on the chessboard. They are trained with four neurons in the hidden layer and twenty neurons in the output layer as shown in Figure (21).

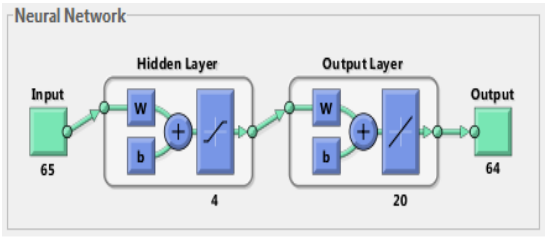

Figure 21: Final neural network used for queen pieces

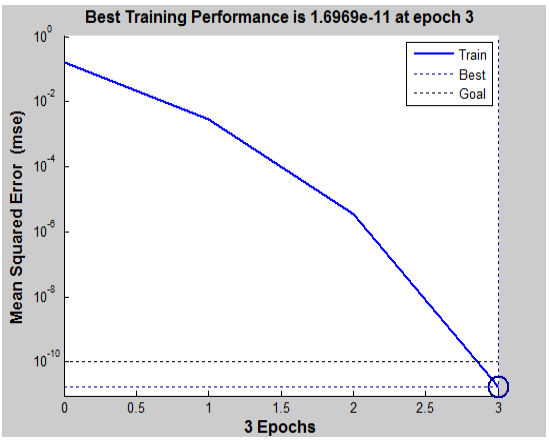

Figure 22: The simulation results of training queen pieces

Figure (22) shows the simulation results of training the queen pieces; if the square with the number thirty three carry the queen piece, all the several paths for the next position of the queen piece are shown in figure (23).

Figure 23: The way of movements queen pieces on the chessboard.

In the proposed chessboard a simple press over the queen piece at square thirty one, will lead the same processes mentioned in the rook piece and the queen piece will be recognized. In more details, the reorganization process will lead to change the state of the LEDs to ON state over the designed chessboard and the exact squares (4, 7, 13, 15, 22, 23, 24, 25, 26, 27, 28, 29, 30, 31, 32, 38, 39, 40, 45, 47, 52, 55, 59, 63) will be glowed to notify the player with the next available positions that the queen can move on.

The trained networks of knight piece converted into Simulink in order to test it and connect it with other networks in the next steps. The simulation results of queen piece movement for next positions shown in figure (24)

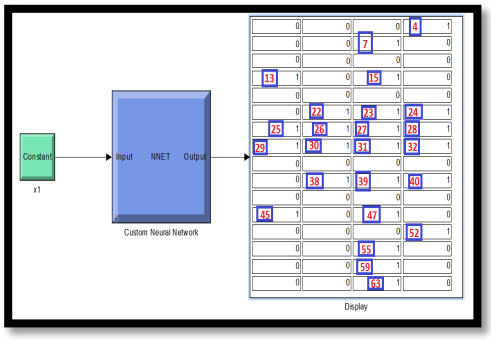

Figure 24: Simulation results of queen pieces for next positions movements

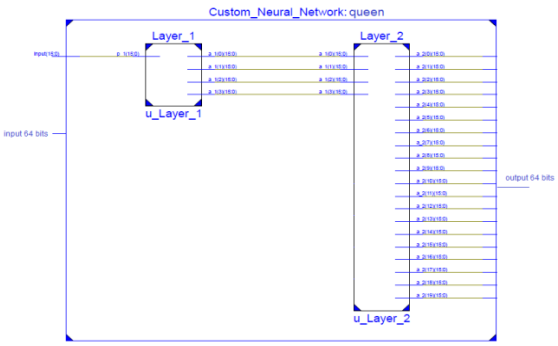

Figure 25: The RTL of queen pieces used in proposed system

The trained networks of the queen pieces converted into VHDL code by using MATLAB that have HDL coder in order to implement it on FPGA, figure (25) shows the RTL of queen pieces used in proposed system and figure (26) shows the simulation results of intelligent networks of queen by using Xilinx ISE Design Suite 13.3.

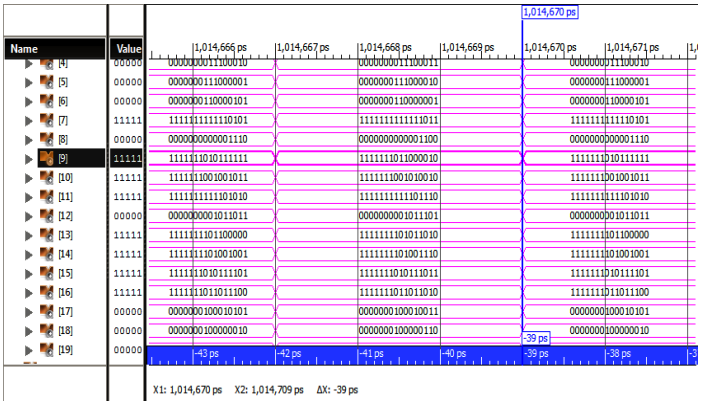

Figure 26: The simulation results of intelligent networks of queen

3.5. Kings

The king piece in the chess game moves in different paths as compared with the other pieces, it has specific paths of movements on the chessboard, it moves such as the queen piece with only one square. The chess game has two pieces of king which are divided equally into two teams, all king pieces have the same paths of movements on the chessboard; therefore, the training of the king was done individually for the first piece and repeated to the other piece.

In order to train the neural networks with the path of movements of the king piece to act such as human brain, every square of the chessboard has sequential number begins with 1 and ends with 64. Any square which carry the king piece will predict a different probability of the movements for the next positions of king. Therefore, the networks of the chessboard trained with the all possible movements of the king piece on the chessboard. They are trained with nine neurons in the hidden layer and twenty neurons in the output layer as shown in Figure (27).

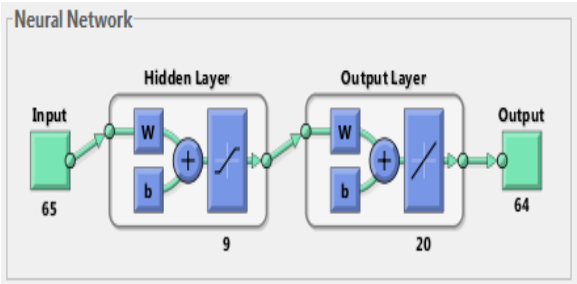

Figure 27: Final neural network used for king pieces

Figure (28) shows the simulation results of training the king pieces; if the square with the number forty-three carry the king piece, all the several paths for the next position of the king piece are shown in figure (29).

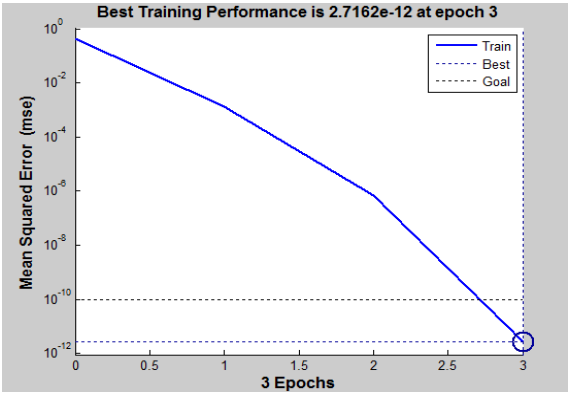

Figure 28: The simulation results of training the king pieces

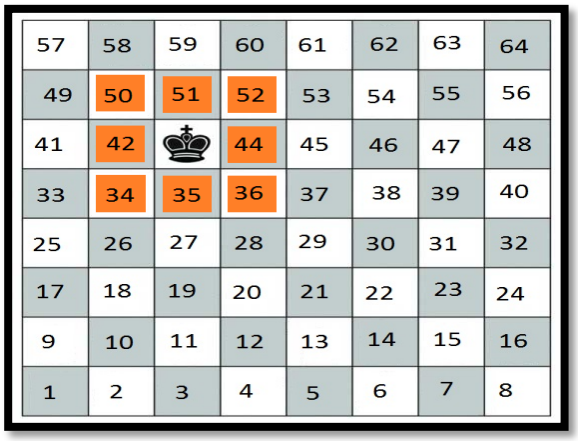

Figure 29: The way of movements of the king pieces on the chessboard.

In the proposed chessboard a simple press over the king piece at square forty three, will lead the same processes mentioned in the rook piece and the king piece will be recognized. In more details, the reorganization process will lead to change the state of the LEDs to ON state over the designed chessboard and the exact squares (34, 35, 36, 42, 43, 44, 50, 51 and 52) will be glowed to notify the player with the next available positions that the king can move on.

The trained networks of king piece converted into Simulink in order to test it and connect it with other networks in the next steps. The simulation results of king piece movement for next positions shown in figure (30)

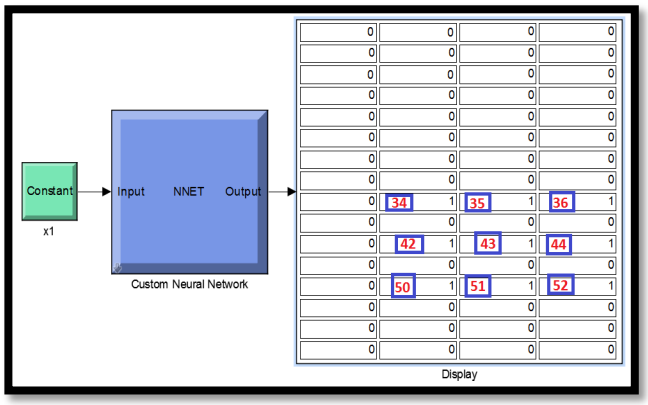

Figure 30: Simulation results of king pieces for next positions movements

The trained networks of the king pieces converted into VHDL code by using MATLAB that have HDL coder in order to implement it on FPGA, figure (31) show the RTL of king pieces used in proposed system and figure (32) shows the simulation results of intelligent networks of king by using Xilinx ISE Design Suite 13.3.

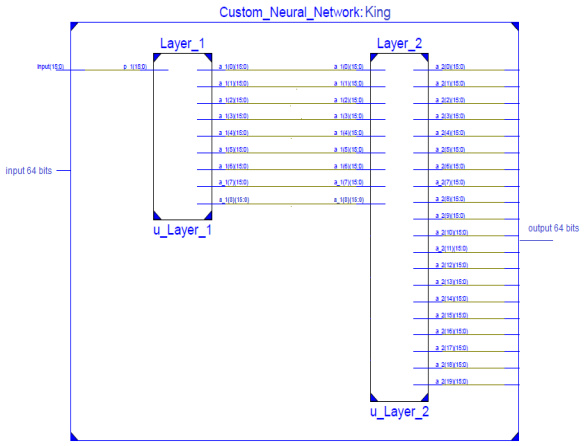

Figure 31: The RTL of king pieces used in proposed system

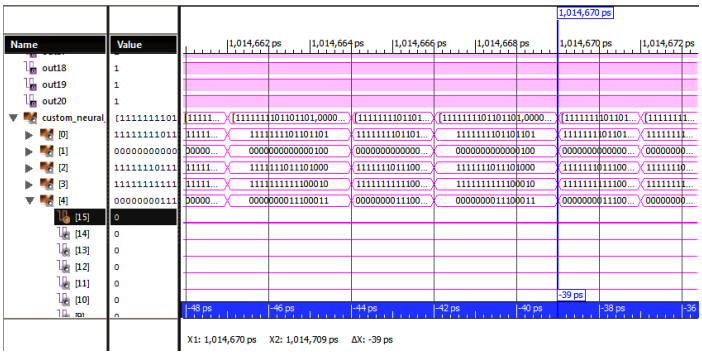

Figure 32: The simulation results of intelligent networks of king

3.6. Pawns

The movement of pawn piece was the simplest and the easiest to know as compared with the other pieces as well as to reduce the cost of the internal design, whereas knowing the movement of the pawn piece was just single step either to the straight ahead or diagonally one step in the case of attack. Therefore, it was not mentioned with the other scenarios.

4. Conclusion

In this paper an intelligent chessboard designed to handle the processes such as human brain through predict the next positions of any piece at the chessboard. Different algorithms used in the training of the chessboard and the best one were used in the proposed system. Each piece of chess game trained individually by using MATLAB and the results tested with different states, all networks of pieces trained was combined together in one system that produce the intelligent chessboard. It converted into VHDL code by using HDL coder in MATLAB, the VHDL code of the proposed system tested with different states by using ISE Design Suite 13.3.

References

[1] Alaa Hamza Omran, Yaser M. Abid, Dr. Huda Kadhim, “Design of Artificial Neural Networks System for Intelligent Chessboard”, 4th IEEE international conference on engineering technology and applied scince (ICETAS), Manama, Bahrain, NOV. 2017

[2] Manish A. Chhangani, “ Arduino based Wireless Powered Chess “, International Journal of Innovative Research in Computer and Communication Engineering,, Vol. 3, Issue 4, April 2015.

[3] Wang LinLin, Wu YuNu, Wang YaJie, Cao Guoqiang, “Research on the Surakarta chess game program based on Unity 3D”, IEEE, 2017.

[4] NasrulHumaimi Mahmood1, Che Ku MohdSalahuddinChe Ku Long, IsmawatiAbdGhani, RubitaSudirman, “Low Cost Electronic Chess Set for Chess Tournament”, IEEE 7th International Colloquium on Signal Processing and its Applications, 2011.

[5] Diwas Sharma, Udit Kr. Chakraborty, “An Improved Chess Machine based on Artificial Neural Networks”, International Journal of Computer Applications® (IJCA) (0975 – 8887) National Conference cum Workshop on Bioinformatics and Computational Biology, NCWBCB- 2014.

[6] Panos J. Antsaklis, “Neural Networks in Control Systems”, IEEE Control Systems M agazine , Vol.10, No.3, pp.3-5, April 1990; Special Issue on 'Neural Networks in Control Systems' of the I EEE Control Systems Magazine , Vol.10, No.3, pp.3-87, April 1990.

[7] Kuo-Lan Su, Bo-Yi Li, Jr-Hung Guo, Kuo-Hsien Hsia, “Implememtation of The Chess Game Artificial Intelligent Using Mobile Robots”,SCIS&ISIS 2014, Kitakyushu, Japan, December 3-6, 2014.

[8] Can Koray , Emre Sumer, “A Computer Vision System for Chess Game Tracking”, 21st Computer Vision Winter Workshop Luka Cehovin, RokMandeljc, Vitomir ˇ Struc (eds.) ˇ RimskeToplice, Slovenia, February 3–5, 2016

[9] Firas Abdullah Thweny Al-Saedi , Ali H. Mohammed, “Design and Implementation of Chess-Playing Robotic System”, IJCSET(www.ijcset.net) | May 2015 | Vol 5, Issue 5,90-98.

[10] Gurjit Kaur, Anil K. Yadav, VarunAnand, “Design and Implementation of Artificially Intelligent Microcontroller based Chess Opponent”, Proceedings of the World Congress on Engineering 2010 Vol I WCE 2010, June 30 - July 2, 2010, London, U.K.

[11] Guofeng Tong, Ying Qu, Tong Cheng, “Human-computer interactive gaming system - a Chinese chess robot” Intelligent Robots and Systems, 2009, IEEE/RSJ International Conference.

[12] SitiZarinaMohdMuji, MohdHelmy Abdul Wahab, RadziAmbar, “Design and Implementation of Electronic Chess Set”, International Conference on Advances in Electrical, Electronic and System Engineering, 14-16 Nov 2016, Putrajaya, Malaysia, 2016.

[13] Zhang Baofeng, Wang Ya, Zhu Junchao “Design of High Speed Data Acquisition System Based on FPGA and DSP” IEEE 2010.

[14] Jing pang “intelligent traffic light controller design using PFGA digest of technical papers”, international Conference on consumer electronics (ICCE), IEEE, 2016.

[15] J. Zurada, “Introduction to Artificial Neural Network System”, West Publishing Company, ISBN: ISBN 0-3 14-93391 -3, 1992.

ASTES

Advances in Science, Technology and Engineering Systems Journal Vol. 3, No. 4, 201-210 (2018)

www.astesj.com

Special Issue on Recent Advances in Engineering Systems

ASTESJ

ISSN: 2415-6698

Experimental Investigation of Human Gait Recognition Database using Wearable Sensors

Sherif Said[*,1], Samer Al-Kork[1], Vishnu Nair[1], Itta Gowthami[3], Taha Beyrouthy[1], Xavier Savatier[3], M Fayek Abdrabbo[2]

[1]*American University of Middle East, Egaila, Kuwait*

[2]*Shoubra Faculty of Engineering, Benha University Shoubra, Cairo, Egypt*

[3]*IRSEEM, ESIGELEC Saint-Etienne du Rouvray, France*

ARTICLE INFO

Article history:
Received: 01 July, 2018
Accepted: 26 July, 2018
Online: 30 July, 2018

Keywords:
Gait Recognition
Biometrics
Wearable sensors
Accelerometer
Shimmer

ABSTRACT

In this research human gait database is collected using different possible methods such as Wearable sensors, Smartphone and Cameras. For a gait recognition accelerometer data from wearable shimmer modules and smartphone are used. Data from different sensors location is compared to know which sensor location have better recognition rate. Different walking scenarios like slow, normal and fast walk were investigated. Wearable sensors and smartphone data are compared to know whether mobile phones can be used for gait recognition or not. Also effects of age, height, weight on gait recognition are also studied. The obtained results of gait biometric matrices like Genuine Recognition Rate (GRR), Total Recognition Rate (TRR) and Equal Error Rate (EER) showed better results. EER in different walking scenarios ranged from 0.17% to 2.27% for the five wearable sensors at different locations, whereas EER results of smartphone data ranged from 1.23% to 4.07%. For sensors located at leg, pocket and hand the average GRR value falls with increase in age group, while for sensors located at upper pocket and bag, the GRR value doesn't follow any trend. Moreover GRR results on all sensors show no significance regarding height or weight variations.

1. Introduction

This paper is an extension of work originally presented in BioSMART, the 2nd International Conference on Bio-engineering for Smart Technologies" titled 'Biometric Database for Human Gait Recognition using Wearable Sensors and a Smartphone' [1]. Biometrics identifiers are typical, quantifiable characters that can be used to identify and label individuals. The identifiers can be either physiological or behavioural. Physiological characteristics include, but are not limited to fingerprint, iris recognition, face recognition, retina, and palm print etc., everything related to shape of the body. Behavioural characteristics include, but are not limited to gait, voice, typing rhythm etc. They are related to pattern of behaviour of a person. Biometric identifiers are unique for each person and they can be used as a reliable means to verify identity or as a means of authentication. But collection of biometric identifiers might raise concerns about privacy and questions about how secure the collected data is. Extensive use of biometric systems has been done in different fields such as forensics for criminal identification, electronic gadgets access, human activity recognition, health status [2]. Although extensive research has been going on in the field of biometric identification and authentication for the last decade, all this has been limited to the topics of face recognition, iris recognition, voice recognition, fingerprint recognition etc. Identification of individual using their gait is an idea which is least explored and not put into practise extensively [3]. Gait recognition is defined as "automatic identification of an individual based on the style of walking" [3]. Gait is the manner in which a person walks and it is more distinctive than we realise and so a person can be identified using his walking pattern from a distance [4]. Lot of research and thought has been put into human gait recognition using floor sensors (FS), machine vision (MV) and wearable sensors (WS) [5]. Most of previous works in gait recognition were based on machine vision techniques, i.e. analysing video or a sequence of images to collect patterns. Both MV and FS based techniques have their disadvantages. MV based techniques have many interfering variables [6] and FS based technique have costly floor sensors. Recently WS using accelerometers were used for gait recognition

[*]Sherif Said, American University of the Middle East, +965 2225 1400 Ext. 2168, sherif.said@aum.edu.kw

and nowadays every smartphone has an accelerometer giving a new direction to the gait recognition researches. Our model incorporates different widely used emerging technologies in human gait recognition. Wearable sensors, and Smartphone accelerometer two such technologies. In our experiment thought has been given to various walking scenarios and other variables such as age, weight, and height. The data acquired from the various sensors are then compared with testing data set. Different comparison methods give the matching percentage and best suited gait data. Figure 1 shows the outline of the data process that takes place in our work.

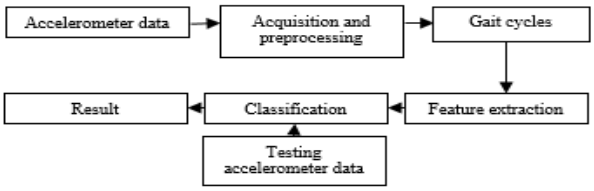

Figure 1. Overall process of gait cycle signal processing

2. Methodology

2.1. Database Collection

In a hall of 10x25 meters (indoor experiment), human gait database was collected using five wearable shimmer [7] sensor modules (integrated 3 axis MEMS accelerometer and gyroscope), and one smartphone Samsung Galaxy Note (with inbuilt NT70000 K3DH acceleration and K3G gyroscope sensors) [8], [9]. Data collected from these three techniques are saved with details like participant name, participant ID and type of walk in .dat, .csv, and .jpg formats respectively for further processing. None of the subjects has any known gait abnormalities. Figure 2 shows the overall setup for gait data collection. In this section we will talk in details about our experimental setup and collected methodologies.

Figure 2. Experimental lab used in our study

2.2. Wearable Accelerometer and Gyroscope Sensors

From a group of 50 people comprising of 37 males and 13 females of varying age range from 14 to 52 years' accelerometer and gyroscope data regarding gait is collected. The average age, height and weight of subjects is 26.6 years, 173.8cm and 71.2 Kg respectively. The general information regarding each subject like name, age, height, weight, and footwear are collected and kept securely for further data analysis. A walking protocol was developed and each subject were follow that protocols, which includes walking with different speeds like slow, normal and fast walk throughout the experiment. i.e. subjects should wait for 3 seconds before they start walking, then walk for a distance of four meters, then wait another 3 seconds and then walk the same distance to and fro for a duration of 45 seconds. The above same procedure was repeated for all other three types of walk.

Five wireless sensors modules (Shimmer 2r) are attached to different locations on human body like on L/R hand, L/R leg, L/R pant pocket, L/R shirt pocket and hand bag (Figure 3). The sensor locations for this study are chosen based on where a normal person carries his phone (like in pant pocket, hand, bag, upper pocket).

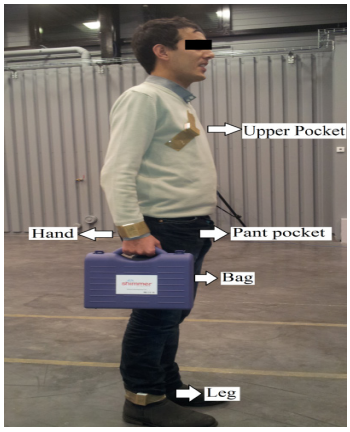

Figure 3. Shimmer sensor locations

Shimmer sensor module is a small wireless sensor platform that can record and transmit physiological and kinematic data in real-time (Figure 4). Each shimmer wireless sensor has on-board microcontroller (MSP430), wireless communication via Bluetooth or 802.15.4 low power radio and local storage to micro SD card [10], [11]. The unit also has integrated 3 axis MEMS accelerometer (Free scale MMA7361) and gyroscope for motion sensing, activity monitoring and inertia measurement application. All five Shimmer sensor modules are calibrated using 'Shimmer 9DOF Calibration application'.

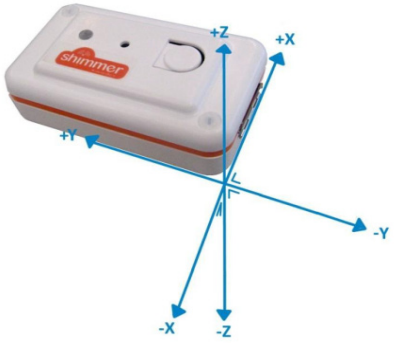

Figure 4. Shimmer 2R wearable sensor

Data acquisition software named 'Multi-Shimmer Sync' developed by shimmer research group was used to synchronize all five shimmer modules and to transmit streamed data to PC through Bluetooth. Multi-Shimmer Sync is an application which allows for the configuration and synchronized data capture from multiple Shimmers (Figure 5) [12], [13]. All five shimmer sensor modules are configured with ±1.5g acceleration range, this range is chosen because most of the smartphone's inbuilt accelerometers have same range. Sampling rate is set to 51.2 Hz

to avoid any data transmission loss. Total data collection time for each subject is approximately 4.5 minutes. Collected data are finally stored in PC in .dat format for further processing in MATLAB.

2.3. Smartphone accelerometer and Gyroscope

From a group of 23 subjects comprising of 16 males and 7 females of a varying age group from 21 to 39 years. The average age, height and weight of collected subjects is 27 years, 172.2cm and 72.08 Kg respectively. Smartphone Samsung galaxy note, with inbuilt NT70000 K3DH acceleration [14] and K3G gyroscope sensors are used to capture data [15]. Android application named 'Sensor pro list' is used to capture sensor data. Captured sensor data is then transferred to PC through Bluetooth. [16], [17]. Each subject is asked to hold the phone in hand like how they normally carry it [18]. Each subject is also asked to select the log on and log off (i.e. to start and stop) of mobile android application and walk in similar walk protocol as explained earlier [19], [20]. Table 1 shows the comparison study of database collected using two techniques.

3. Processing of Accelerometer Data

Raw data from all shimmer sensors modules is saved in DAT file format. Each subject file contains information of the five sensors. Each sensor data consists of time stamp, accelerometer

(in x, y, and z axis) and gyroscope (in x, y, and z axis). similarly, smartphone data is a saved in CSV file format. Each subject smartphone sensor data also consists of time stamp, accelerometer (in x, y, and z axis) and gyroscope (in x, y and z axis).

3.1. Data Preprocessing

3.1.1 Data reading

The data reading procedure is divided into three steps. In first step, each participant data such as name, ID, height, weight, gender, age, sensor location is read one by one which are stored in excel file. In second step, sensor data files of each participant are read from assigned folders and subfolders for creation of gait data base features. Finally, all data files are exported to MatLab and headers of each file are read to identify each subject recorded

Figure 5. Sample gait data collection with Multi shimmer sync software

Table 1. Comparison of the two techniques

	Wearable Shimmer sensor	*Smartphone*
Sensor specification	Five Shimmer 2r's with inbuilt 3-axis MEMS Freescale MMA 7361 accelerometer	One Samsung Galaxy Note (inbuilt K3DH acceleration & K3G gyroscope sensors)
Computer interface	Bluetooth	Bluetooth
Software used	Multi Shimmer Sync	Sensor Pro list
Range of sensor	+/-1.5 g	+/-1.5 g
Sensor sampling frequency	51.5 Hz	
Location of sensor	Leg, Hand wrist, pant pocket, Shirt pocket and bag (left and right side)	Hand
Number of participants	50(37 male, 13 female)	23 (16 male, 7 female)
Range of age	14 to 52 years	21 to 39 years
Mean of age	26.6 years	27
Range of height	150-193 cm	154-189 cm
Mean height	173.8 cm	172.2 cm
Range of weight	50 to 107 kg	50 to 105 kg
Mean weight	71.2 kg	72.08 kg

sensor data belong to which sensor location (like leg data\hand data\pocket data etc.) and to which data such as accelerometer, gyroscope and time stamp values. Since each sensor at different body location has different processing techniques such as data recorded from leg is entirely different from data recorded from pocket; therefore, data each particular sensor is identified and processed with techniques explained below. Processing methods also depends on the sensors used for data collection, like sampling frequency of sensor, location of sensor. Effective preprocessing techniques improve recognition rate. Figure 6 shows a flow chart of data processing of testing and training data.

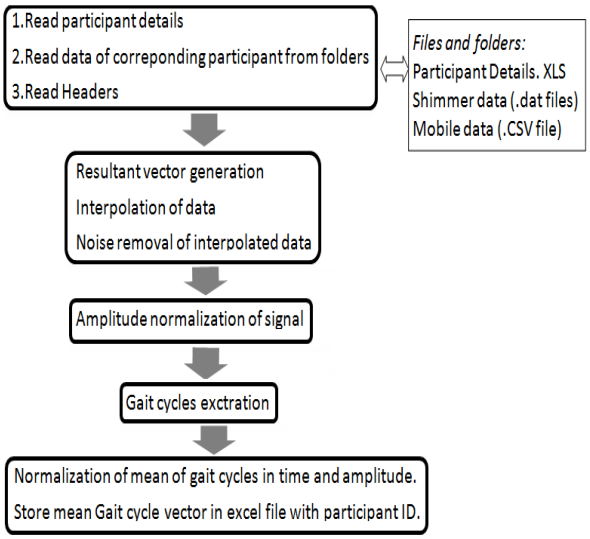

Figure 6. Flow chart of data processing of testing and training data

3.1.2 *Data processing*

Resultant vector: The output from various accelerometers data will vary depending on how the shimmer sensor modules are oriented and also all three different axes have varying moments. To overcome this problem, the resultant vector (xyz) of the accelerometer in X, Y, and Z axis output is calculated using Euclidean norm as given in (1). The first three plots of Figure 7 shows X, Y, Z plots. The last plot in Figure 7 shows the resultant vector of all axes.

$$xyz = \sqrt{x^2 + y^2 + z^2} \quad (1)$$

Interpolation: Raw accelerometer data has irregular periodic intervals therefore interpolation is needed to have data samples at regular intervals. Interpolation [21] is a method of constructing new data points within the range of a discrete set of known data points. Many interpolation methods like linear, polynomial, spline interpolation methods can be used. In our work, spline interpolation of period 10 m sec is used. Spline interpolation [22] uses low-degree polynomials in each of the intervals, and chooses the polynomial pieces such that they fit smoothly together [23].

Noise removal: Weighted moving average (WMA) method is applied to our interpolated data to remove unwanted noise from the signal. This method is fast and easy to implement. In WMA method, the nearest neighbors are more important than those more away, while in other methods all the neighbors have equal weight. The formula for WMA with a sliding window of size 5 is given in (2).

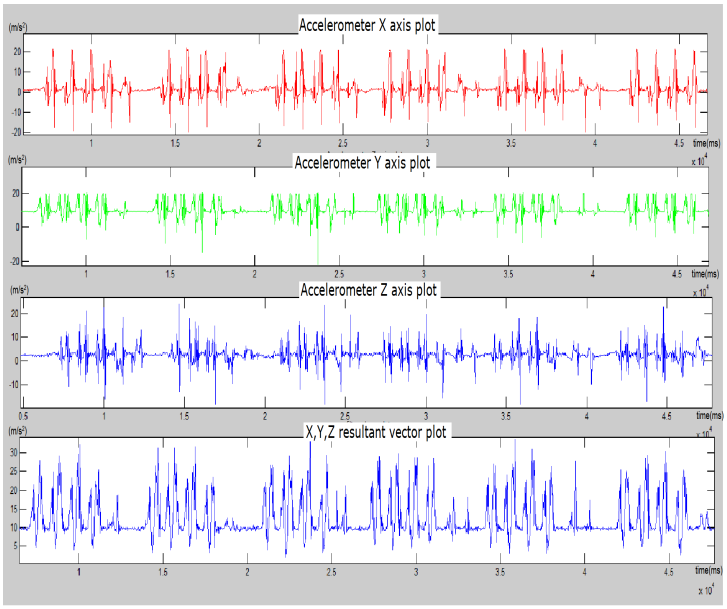

Figure 7. Unprocessed raw gait signals

$$wma = \frac{(x_{t-2}*1)+(x_{t-1}*2)+(x_t*3)+(x_{t+1}*2)+(x_{t+2}*1)}{5} \quad (2)$$

where: x_t is the acceleration value at position t

Amplitude Normalization: For easy computations, raw accelerometer data is normalized from 0 to 1 as shown in Figure 8 by applying (3)

$$\text{newsi} = \frac{\text{xyzif}-\text{mi}}{\text{ma}-\text{mi}} \quad (3)$$

Where: newsi - amplitude normalized signal

xyzif - interpolated and filtered signal of accelerometer resultant vector signal

mi - minimum range of sensor

ma - maximum range of sensor

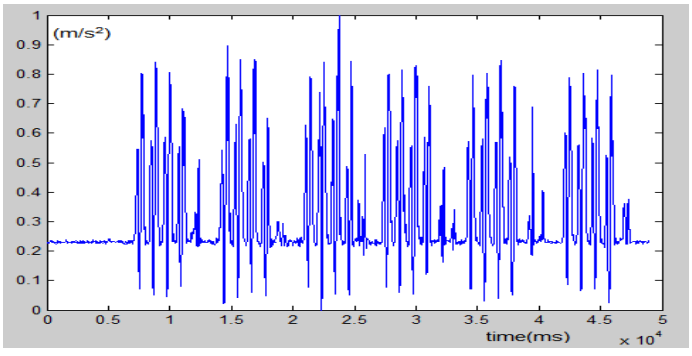

Figure 8. Amplitude normalization of whole gait signal

3.1.3 Gait cycles extraction and Time Normalization

Cycle Detection: A gait cycle will comprise of two footsteps and it is detected by finding the minimum points in a given cycle.

The end of the preceding one will mark the start of each cycle up to final cycle of the gait signal. Fake minimum points are eliminated by calculating mean cycle time and standard deviation. If a gait cycle has a cycle length which falls outside of the mean time ± standard deviation is considered to be as fake cycles and will be eliminated. Since all sensors collect gait data whose minimum points should mark the start of another gait cycle, the gait detection algorithm will work for all the sensors used. In Figure 9, the first plot shows extracted gait cycles from an amplitude normalized signal. Cycle length as well as mean length of all gait cycles are estimated and saved as feature vectors. There are chances that the length of each gait cycle might vary from cycle to cycle; therefore, normalization of signal in time is needed. Gait cycles are normalized to 1 second duration. Here 1 second is chosen as a random standard value. Figure 9 shows difference between normalized and un-normalized gait cycles.

In some cases, after time normalization also fake cycles are observed, so again these fake cycles are eliminated by calculating trimmed mean cycle (TM cycle). TM cycle is calculated by calculating mean and standard deviation (SD) of all gait cycles and if point lies beyond ±SD of mean cycle then that particular cycles eliminated. Figure 10 shows a normalized trimmed gait cycle.

3.1.4 *Normalization of Mean gait*

After elimination of fake cycles, Mean cycle, Median cycle and Trimmed mean cycle are calculated to represent a gait cycle feature vectors. Mean cycle refers to the time domain waveform at which each time sample represents the mean cycle value over a fixed time window of the gait cycle length. Median cycle refers to the time domain waveform at which each time sample represents the median cycle value over a fixed time window of the gait cycle length. Mean, Median and TM gait cycle which is normalized in time (for 100 samples) and in amplitude (0 to 1 range) is then stored in an array of 100 values are stored in Microsoft excel.

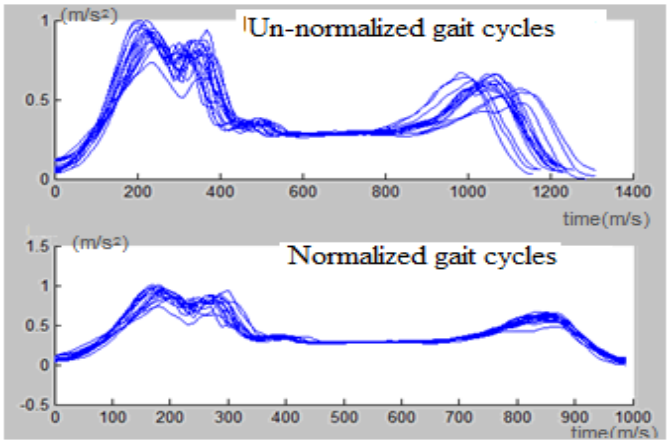

Figure 9. Un-Normalized and Normalized gait cycles

Since each sensor at different body location has different processing techniques such as data recorded from leg is entirely different from data recorded from pocket; therefore, each sensor is identified and processed with techniques explained below. Processing of different sensors varies in cutoff and in elimination of fake cycles techniques.

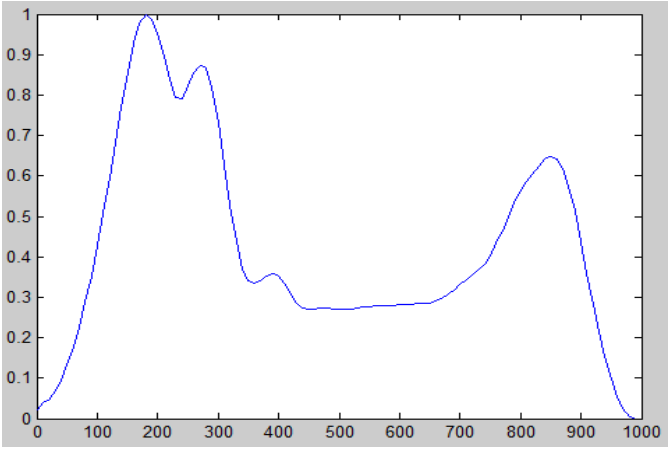

Figure 10. Normalized Trimmed Mean Gait Cycle

3.2. *Elimination of fake cycles*

Before calculating average gait cycle fake cycles can be eliminated by using following techniques:

1. By calculating mean cycle length(MCL) and standard deviation (SD) of all identified cycles. Cycle length falling beyond MCL ± SD are eliminated.
2. By calculating trimmed mean(TM) cycle of all cycles. TM cycle is obtained by calculating mean of cycle points which lie in between Mean cycle point ± SD of cycle point and cycle points which lie beyond range are eliminated.
3. By matching maximum point of all gait cycles i.e. by calculating mean gait cycle and searching maximum point of each cycle around SD of mean gait cycle maximum point.

3.3. *Data analysis for obtaining results*

This section explains how data has been analysed for obtaining results.

3.3.1 *Analyzing methods*

This sub section explains the calculation of gait biometric system performance metrics like FAR,FRR,EER,TRR and FRR [24]. The performance metrics are calculated by creating Distance score tables and explained below.

Distance score table calculation: Obtained average gait cycles for all subjects for different walks(SW, NW, FW) at different sensor location for both smartphone data and wearable data are compared against each other. Distance metrics like Manhatten and Euclidean methods are used and explained below:

Manhatten distance: This is also known as absolute distance and the formula is shown in (4). Manhattan distance between two points is the sum of the absolute difference in their Cartesian coordinates. In addition, this distance metric is the computationally least expensive one.

$$dm = \sum |(x1 - x2)| \tag{4}$$

Hamming distance: Hamming distance is utilized to detect and correct errors in digital communication. Hamming distance between two data are said to be the least number of changes that could make both the data same. For example, the hamming

distance between 'name" and 'meme" is 2 and between 337895 and 235817 is 4.

Euclidean distance: This is a slight modification of the Manhattan distance, see (5). Instead of taking the sum of the absolute differences we now take the square root of the sum of all differences squared.

$$dh = \sqrt{\sum(x1 - x2)^2} \quad (5)$$

From distance metric methods a score tables are generated. Valid subject has a less distance score as compared to not valid subjects. Distance score table is classified into accepted and rejected matches based on classifier cutoff. Classifier cutoff is choosen from percentage of maximum score value from score table. Accepted matches again have two cases like Genuine Accepted Match (GAM) and Fraud Accepted Match (FAM). GAM is accepted match of correct subject i.e. accepted match is of correct subject and is recognized by classifier. FAM is counted when a false match is accepted and recognized as correct match. Similarly rejected matches have two cases like Genuine Rejected Match (GRM) and Fraud Rejected Match (FRM). GRM is genuine match is supposed to be accepted but is not recognized. FRM is counted when false match is accepted and recognized as an incorrect match. FRM is fraudulent match is supposed to be accepted but is recognized as incorrect.

Biometric matrices like False acceptance rate (FAR), false reject rate (FRR), Total recognition rate (TRR), Genuine recognition rate (GRR) and Equal error rate (ERR) are calculated from generated score table and are explained as below.

False acceptance rate (FAR) is a measure of how precisely biometric data can be compared and recognized (6). It represents the chance that the comparison will accept a wrong input as an affirmative match. The input is not supposed to match with the template data but invariably the system considers this match to be correct. FAR is calculated by testing known biometric templates against a huge collection of data.

$$FAR(\%) = \frac{number\ of\ fraud\ accepted\ samples(FAM)}{total\ number\ of\ samples} * 100 \quad (6)$$

False rejection rate (FRR) is a measure of the chance that the system will wrongly reject a genuine input as a match that doesn't fit (7).

$$FRR(\%) = \frac{number\ of\ genuine\ rejected\ samples(GRM)}{total\ number\ of\ samples} * 100 \quad (7)$$

EER is the value at which FRR and FAR are equal and is obtained by plotting graph between FAR and FRR. TRR and GRR are calculated using (8) and (9). In TRR number of recognized samples is sum of genuine accepted and fraud rejected samples but GRR is calculated only for genuine accepted samples.

$$TRR(\%) = \frac{number\ of\ recognised\ samples(GAM+FRM)}{total\ number\ of\ samples(N)} * 100 \quad (8)$$

Where N is the total number of comparison samples.

$$GRR(\%) = \frac{number\ of\ genuine\ recognised\ samples(GAM)}{total\ number\ of\ samples} * 100 \quad (9)$$

For data collected from wearable sensor for 50 subjects, two files for each of three different walking scenarios (SW, NW and FW) we have total 300 (50*3*2) gait features for one sensor location. So total of 100 gait features of each scenario (e.g. for normal walk sensor at leg have 100 templates) are compared against each other and with other scenario i.e. comparison with walks like slow-slow(S-S), normal-normal (N-N), fast-fast (F-F), slow-normal(S-N), slow –fast(S-F), normal-fast (N-F). In comparison of same sensor location and same walk there are five cases, there are case 0: don't count (DC), case 1: GAM, case 2: GRM, case 3: FAM, case 4: FRM. DC case is when comparing two similar files because each subject has two files when we compare first file of a subject to the first file of subject it is obvious match. So this case is not counted for metric calculation. Also if there is match between first file of subject to second file this is counted in GAM. So cases 0, 2, 3 are not valid (error matches), FAR and FRR are calculated using FAM and GRM respectively. In comparison with other different walks like), slow-normal(S-N), slow –fast(S-F), normal-fast (N-F) case 0 (DC) will not be there.

Table 2 shows the FAR, FRR, TRR and GRR values with different classifier cutoffs. Consider FW-FW comparison with cutoff 40%, it has FAR of 2.92% which says that 2.92 subjects out of 100 subjects are falsely accepted, FRR of 0.07% means 0.07 subjects which are genuine are rejected, TRR of 97.01% says how efficiently a classifier can classify matches correctly whether it is genuine accepted match or fraud rejected match and GRR of 93% represent the ability of classifier to identify genuine accepted matches. From Table 2, as cutoff percentage increases GRR increases at the cost of increase in sum of errors (FAR+FRR). So classifier cutoff is chosen such a way by having tradeoff between GRR and errors.

Table 2. Pocket hamming method results

100 samples	Classifier Cut-off=10%				Classifier Cut-off=20%				Classifier Cut-off=30%				Classifier Cut-off=40%				Classifier Cut-off=50%			
Pocket	FAR	FRR	TRR%	GRR	FAR	FRR	TRR%	GRR	FAR	FRR	TRR%	GRR	FAR	FRR	TRR%	GRR	FAR	FRR	TRR%	GRR
S-S	0	0.67	99.3300	33.00	0.72	0.3900	98.8900	61.00	3.0800	0.2200	96.7000	78.00	6.2900	0.1200	93.5900	88.00	8.4500	0.0300	91.5200	97.00
s-n	2.3300	1.55	96.1200	22.50	7.30	1.0800	91.6200	46.00	12.9800	0.8500	86.1700	57.50	17.9900	0.6500	81.3600	67.50	20.4500	0.5300	79.0200	73.50
s-f	1.9700	1.77	96.2600	11.50	10.88	1.3200	87.80	34.00	23.6700	0.9100	75.4200	54.50	31.4400	0.6900	67.8700	65.50	34.3100	0.6000	65.0900	70.00
n-n	0.1800	0.22	99.6000	78.00	0.93	0.0800	98.99	92.00	1.8800	0.0500	98.0700	95.00	2.4800	0.0200	97.5000	98.00	3.0600	0.0200	96.9200	98.0000
n-f	5.5000	1.03	93.4700	48.50	12.77	0.6500	86.58	67.50	15.1800	0.5800	84.2400	71.00	17.9300	0.5100	81.5600	74.50	19.1300	0.4700	80.4000	76.50
f-f	0.0500	0.50	99.4500	50.00	0.63	0.1500	99.22	85.00	1.8800	0.0900	98.0300	91.00	2.9200	0.0700	97.0100	93.00	3.9100	0.0400	96.0500	96.00

4. Results

Figures 11 and 12 shows the recognition rate of all wearable sensors using Hamming method of classification. Figures 13 and 14 shows the recognition rate of all wearable sensors using Manhattan method of classification Same sensor to sensor walk (like S-S, N-N, F-F) comparison have highest recognition rate value than comparison with other walks (S-N, S-F, N-F). In Figures 11,12,13 and 14 shows that Manhattan classifier has better classification results than Hamming method. Sensor located at Pocket and Leg has highest recognition rate than other sensor location. Results in table shows the EER value of different sensors. The EER values ranges from 0.21 to 2.258. Same sensor to sensor walk EER values (for S-S, N-N, F-F) comparison have less error values than comparison with other walks (S-N, S-F, N-F). EER rate of F-F comparison is more than S-S and N-N because when a subject is asked to walk fast, walk becomes unstable. Also among all six scenarios S-F comparison has highest EER as there is template mismatching and comparison between stable (SW) and unstable walk (FW) gives higher EER.

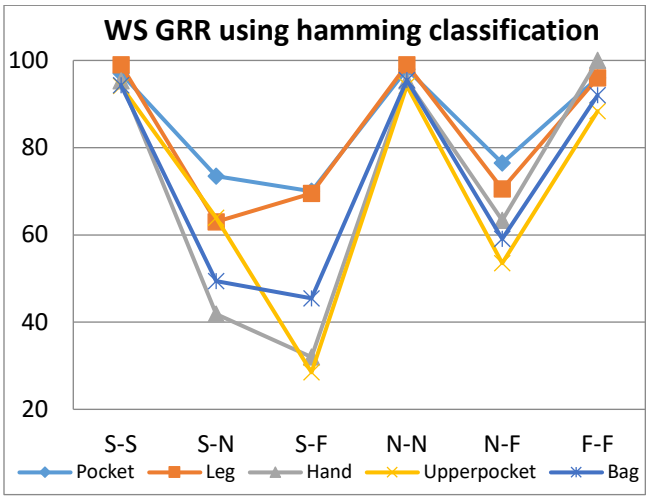

Figure 11. Wearable sensors GRR values using hamming method

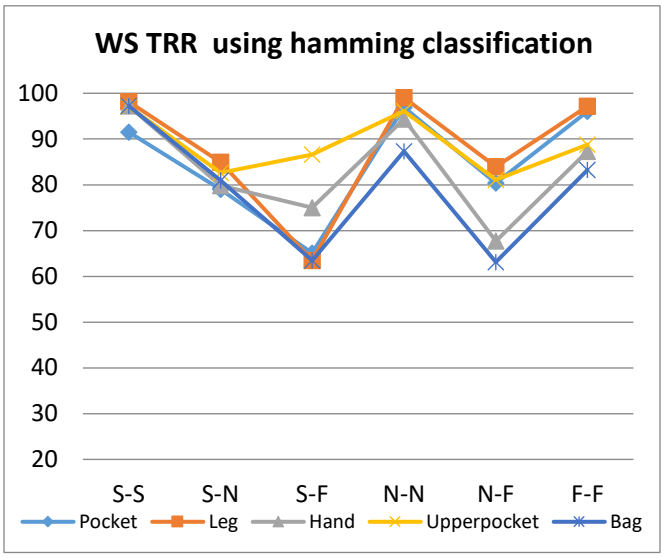

Figure 12. Wearable sensors TRR values using hamming method

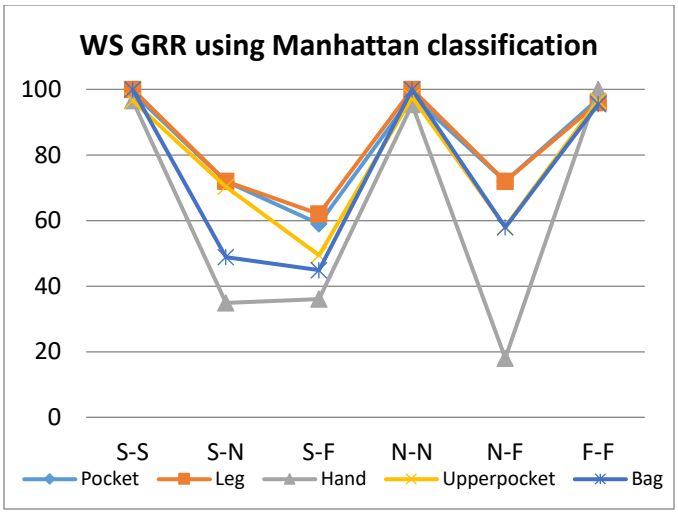

Figure 13. Wearable sensors GRR values using Manhattan method.

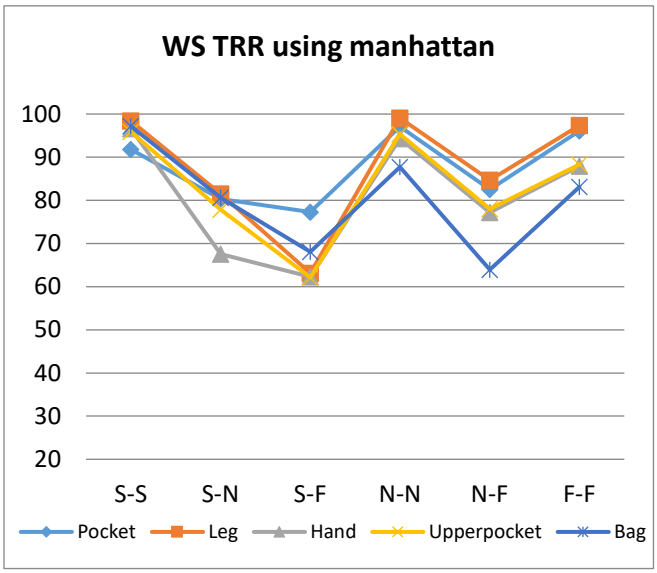

Figure 14. Wearable sensors TRR values using Manhattan method

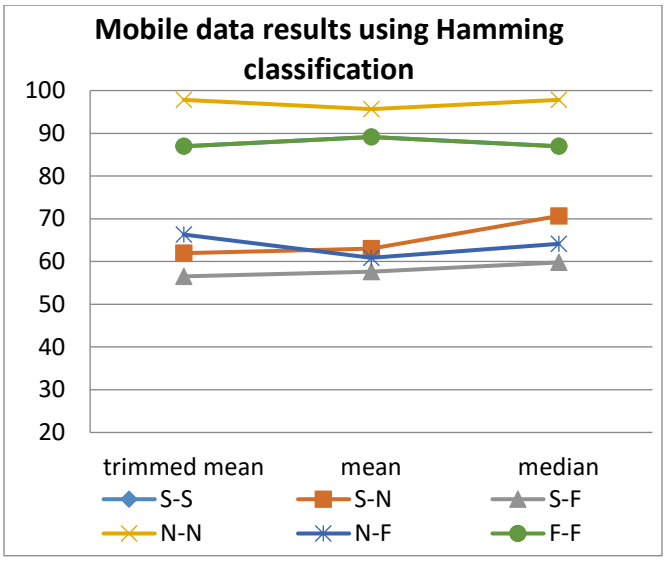

Figure 15. Mobile data results of Hamming method

Table 3. EER table of Hamming and Manhattan tables

	Hamming					Manhattan				
	Pocket	Leg	Hand	Upper Pocket	Bag	Pocket	Leg	Hand	Upper Pocket	Bag
S-S	0.44	0.2700	0.3245	0.3786	0.3874	0.4400	0.2700	0.3245	0.3786	0.3616
s-n	1.6200	1.6000	1.9605	1.3521	1.7691	1.6100	1.6100	2.2445	1.3386	1.7562
s-f	1.7900	1.9200	2.2039	2.0146	2.1436	1.7800	1.8900	2.2580	2.0687	2.1823
nn	0.2100	0.1700	0.4867	0.4056	0.8781	0.1900	0.1700	0.4867	0.4056	0.8781
n-f	1.3600	1.5000	2.0822	2.0416	2.0919	1.4600	1.5000	2.2715	2.0416	2.0919
f-f	0.2400	0.2600	0.5949	0.6760	0.8910	0.2300	0.2600	0.6084	0.6760	0.8910

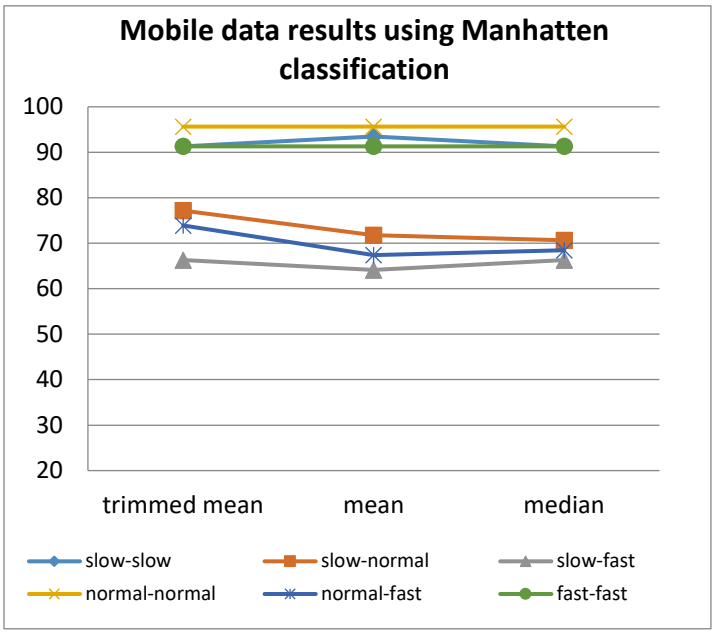

Figure 16. Mobile data results of Manhattan method

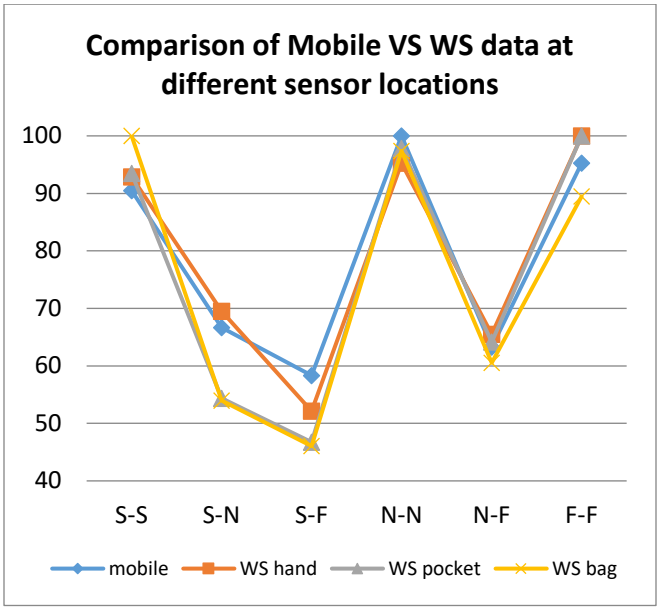

Figure 17. Comparison of mobile data results with wearable sensors location like hand, pocket and bag data

Figures 15,16 shows the results of Manhattan and Hamming methods for six different walk scenarios for which comparisons are done TM, mean and median cycles respectively. Table 3 shows the EER values, whose range is from 1.2287 to 4.0643. EER values of mobile data are more than wearable sensors data.

In real life people hold\place their phones in different location on body such as (pocket, hand, suit case etc...). Figure 17 shows the comparison results of GRR for 23 participants' data of mobile, wearable sensors at hand, pocket and bag. Even though mobile data have more or same wearable sensors recognition rates, mobile data has more EER values. Smartphone's have accelerometers that are good enough to detect human gait with slight modification on their frequency range and sensitivity of sensor. Although investigations are going on extensively in this field of research, an attempt to include comparison of different techniques and that to taking into account different walking scenarios was never seen before. This paper will give insight into how different walking posters will affect the gait recognition of different sensors.

Table 4. Mobile data EER rate

	Hamming			Manhattan		
	Trimmed mean	Mean	Median	Trimmed mean	Mean	Median
S-S	1.6068	1.7013	1.6068	1.6068	1.6068	1.6068
s-n	3.5917	3.6389	3.5444	3.5917	3.6389	3.5444
s-f	4.0643	4.0643	4.0170	4.0643	4.0643	4.0170
n-n	1.7486	1.7958	1.7958	1.6541	1.7486	1.7013
n-f	3.5917	3.6389	3.3554	3.5917	3.6389	3.3081
f-f	1.3233	1.2287	1.3233	1.2287	1.2287	1.2760

Human gait is affected by many factors, and changes in the normal gait pattern can be transient or permanent. The factors can be of various types:

- Extrinsic: Several extrinsic factors such as terrain, footwear, clothing, cargo(luggage).
- Intrinsic: Intrinsic factors are sex (male and female), weight, height, age, etc.
- Physical: Physical factors such is the weight, height, physique

- Psychological: Psychological factors are the type of personality, emotions
- Physiological: When talking about is physiological anthropometric characteristics
- Pathologic, pathological factors can be for example trauma, neurological diseases, musculoskeletal, psychiatric disorders
- Intrinsic factors such as age, height and weight are also analyzed in our work.

The entire sample was divided into three equal groups as shown in Figure 18 for comparing wearable sensors for different weight range. And it was found that the average TRR for range of 50 to 58 Kg is more than other two ranges.

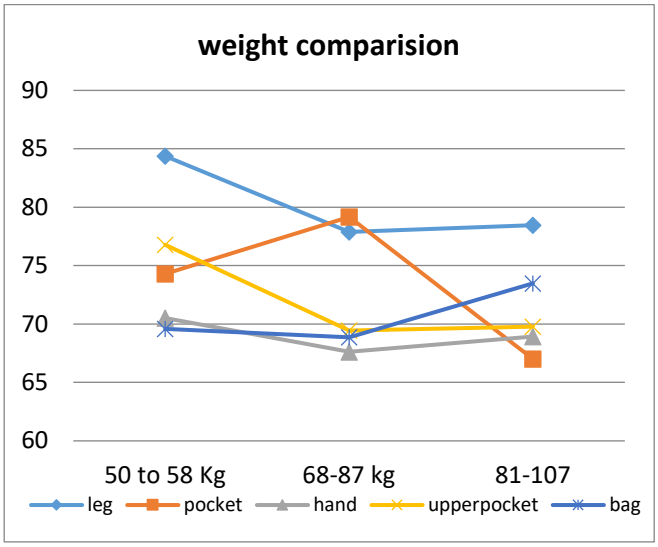

Figure 18. Average GRR (of six scenarios) value of wearable sensor data comparison for different weights range

For sensors located at leg, pocket and hand the average GRR value falls with increase in age group, while for sensors located at upper pocket and bag, the GRR value doesn't follow any trend. In general, average recognition rate decreases as age increases, which has been explained by Richard W. Bohannon [25] in his work. Many other physiological factors like brain stability, thoughts etc. changes as age increases (Figure 20). Weight and height factors are studied as shown in Figure 18 and Figure 19 respectively. Different walks had different energy of signal which can be used for activity recognition. Even though three walks have different energies, they have more or less same gait features in common.

5. Conclusion

Our future work needs to give emphasis to increasing the number of participants in the experiment to about 120-150 because the number of participants affect the calculated recognition rate by a great deal and helps in making the calculations accurate. Time elapsed and activity recognition are some other factors that will have to be pondered over. This research will provide us with an idea of how changes in subject's daily routine affect the rate of recognition. How a person walks can vary depending on different parameters such as footwear, type of clothing, with or without luggage, walking surface and terrain, human factors; thus the above mentioned issues needs to be looked into further. Our research needs to be further extended to include other types walking patterns including running, climbing stairs up/down, jumping and sitting. The smartphone data used in the study was exclusive to one smartphone and one data processing software. More work is to be done on this part. Data from different smartphones having a variety of built in accelerometers and using some other data processing software. Effect of Gait difference of same height subjects with different weight and effect of load are also to be studied further. Insight was also provided on how other co parameters affect the gait recognition of the sensors.

Figure 19. Average GRR (of six scenarios) value of wearable sensor data comparison for different heights range

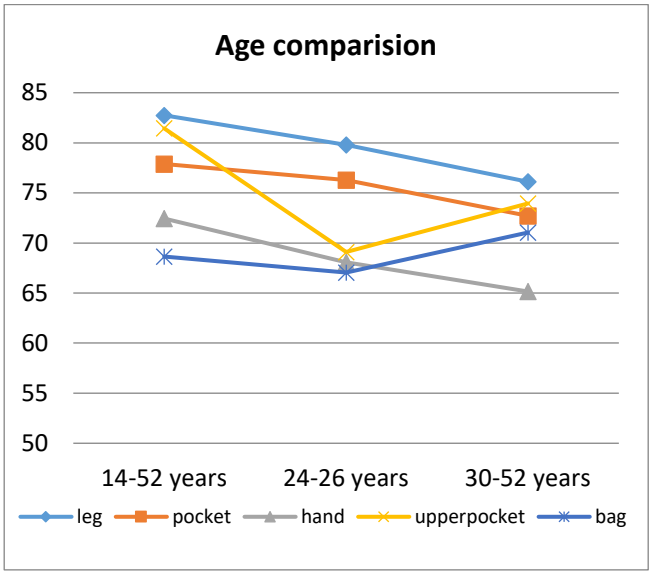

Figure 20. Average GRR (of six scenarios) value of wearable sensor data comparison for different weights range

Conflict of Interest

The authors declare no conflict of interest.

Acknowledgment

This work was supported by Haute-Normandie Region as part of The Nomad Biometric Authentication (NOBA) project.

References

[1] S. K. A. Kork, I. Gowthami, X. Savatier, T. Beyrouthy, J. A. Korbane and S. Roshdi, "Biometric database for human gait recognition using wearable sensors and a smartphone," 2017 2nd International Conference on Bio-engineering for Smart Technologies (BioSMART), Paris, 2017, pp. 1-4

[2] Qian Cheng, Yanen Li_, Joshua Juen, "Classifier of Gait Pattern for Detecting Abnormal Health Status", SenSys'12Toronto, ACM 978-1-4503-1169-4, Canada 2012.

[3] D. Hodgins, "The Importance of Measuring Human Gait," European Medical Device Technology, 2008.. F Sayegh, F Fadhli, F Karam, M BoAbbas, F Mahmeed, JA Korbane, S AlKork, T Beyrouthy "A wearable rehabilitation device for paralysis," 2017 2nd International Conference on Bio-engineering for Smart Technologies (BioSMART), Paris, 2017, pp.1-4.

[4] Mark Ruane Dawson, "Gait Recognition",(technical report) Department of Computing Imperial College of Science, Technology & Medicine London 2002.

[5] Q. Meng b, B. Li a, H. Holstein, "Recognition of human periodic movements from unstructured information using a motion-based frequency domain approach," Volume 24, Issue 8, Pages 795–809, Department of Computer Science, University of Wales, August 2006.

[6] T. Massart, C. Meuter and V. B. Laurent, "On the complexity of partial order trace model checking, Inform. Process," 2008.

[7] M. Davis and H. Putnam, "A computing procedure for quantification theory.," in Journal of ACM, 1960

[8] E. Abraham, S. Alkork, F. Amirouche, E. Hande, S. P. Rai and S. Biafora, "Experimental Investigation of Posterior Elbow Dislocation in a Primate Model," 2007 29th Annual International Conference of the IEEE Engineering in Medicine and Biology Society, Lyon, 2007, pp. 5099-5102

[9] Al Kork S, Amirouche F, Abraham E, Gonzalez M. Development of 3D Finite Element Model of Human Elbow to Study Elbow Dislocation and Instability. ASME. Summer Bioengineering Conference, ASME 2009 Summer Bioengineering Conference, Parts A and B ():625-626

[10] S. Said, S. AlKork, T. Beyrouthy and M. F. Abdrabbo, "Wearable bio-sensors bracelet for driver as health emergency detection," 2017 2nd International Conference on Bio-engineering for Smart Technologies (BioSmart), Paris, 2017, pp. 1-4.

[11] F Sayegh, F Fadhli, F Karam, M BoAbbas, F Mahmeed, JA Korbane, S AlKork, T Beyrouthy "A wearable rehabilitation device for paralysis," 2017 2nd International Conference on Bio-engineering for Smart Technologies (BioSMART), Paris, 2017, pp.1-4.

[12] Ho, N. S. K., Tong, K. Y., Hu, X. L., Fung, K. L., Wei, X. J., Rong, W., & Susanto, E. A. (2011, June). An EMG-driven exoskeleton hand robotic training device on chronic stroke subjects: task training system for stroke rehabilitation. In 2011 IEEE

[13] Taha Beyrouthy, Samer Al. Kork, J. Korbane, M. Abouelela, "EEG Mind Controlled Smart Prosthetic Arm – A Comprehensive Study", Advances in Science, Technology and Engineering Systems Journal, vol. 2, no. 3, pp. 891-899 (2017).

[14] "http://www.shimmer-research.com.," [Online].

[15] Sung-Jung Cho, Eunseok Choi, Won-Chul Bang, Jing Yang, "Two-stage Recognition of Raw Acceleration Signals for 3-D Gesture-Understanding Cell Phones," Tenth International Workshop on Frontiers in Handwriting Recognition 2006.

[16] M. O. Derawi, "Accelerometer-Based Gait Analysis A survey," in NISK conference., 2010.

[17] Mohammad Omar Derawi, "Accelerometer-Based Gait Analysis A survey," pp 33-44, NISK-2010 conference.

[18] Tobias Stockinger, " Implicit Authentication on Mobile Devices," Ubiquitous Computing, Media Informatics Advanced Seminar LMU, Summer Term 2011(Tech Report), University of Munich, Germany 2011.

[19] Jani Mäntyjärvi, Mikko Lindholm, "Identifying Users of Portable Devices from Gait Pattern with Accelerometers," pp. ii/973 - ii/976 Vol. 2, IEEE 2005.

[20] Yuzuru Itoh, Manabu Miyamoto, "Convenient use of Accelerometer for Gait Analysis," pp 21-31, Bulletin of the Osaka Medical College, 2008

[21] M. Lindholm and J. Mäntyjärvi, "Identifying Users of Portable Devices from Gait Pattern with Accelerometers," IEEE, vol. Vol 2, pp. 973-976, 2005.

[22] S.-J. Cho, E. Choi, W.-C. Bang and J. Yang, "Two-stage Recognition of Raw Acceleration Signals for 3-D Gesture-Understanding Cell Phones," in Tenth International Workshop on Frontiers in Handwriting Recognition, 2006.

[23] Jordan Frank, Shie Mannor, "Activity and Gait Recognition with Time-Delay Embeddings," Twenty-Fourth AAAI Conference on Artificial Intelligence 2010.

[24] Martin Hynes, Han Wang, "Off-the-Shelf Mobile Handset Environments for Deploying Accelerometer based Gait and Activity Analysis Algorithms," Engineering in Medicine and Biology Society, pp. 5187 – 5190, IEEE 2009.

[25] R. W. Bohannon, "Comfortable and maximum walking speed of adults aged 20—79 years: reference values and determinants," 1997.

Advances in Science, Technology and Engineering Systems Journal Vol. 3, No. 4, 211-217 (2018)

www.astesj.com

Special Issue on Multidisciplinary Sciences and Engineering

ASTESJ

ISSN: 2415-6698

Psychoacoustical Approach in Soundscape Characterization

Mia Suhanek*, Ivan Djurek, Sanja Grubeša, Antonio Petošić

University of Zagreb, Faculty of EE and Computing, Department of Electroacoustics, Unska 3, HR-10000 Zagreb, Croatia

ARTICLE INFO

Article history:
Received: 21 June, 2018
Accepted: 28 July, 2018
Online: 31 July, 2018

Keywords:
sound environment
soundscape
loudness
noise

ABSTRACT

Four different soundscapes with different loudness and spectral distributions were recorded in Zagreb (capital of Croatia) and reproduced to two groups of listeners while they were performing a concentration demanding task – a simplified variation of the memory game. These two groups of test subjects listened to the same soundscapes but with different loudness distribution. The game results versus time were recorded, analyzed and compared to questionnaire answers, along with loudness and property changes of each soundscape. The goal was to determine which of the sound events causes the largest distraction and to establish a connection between these results and the annoyance level of each soundscape. As expected, the loudest soundscape resulted in the lowest score and caused the largest annoyance. However, other factors proved to cause listeners' distraction, mainly unexpected sounds that differ from the main sound print. In that sense, this paper also deals with a concept of creating enjoyable sound environment in urban places.

1. Introduction

The initial concept of soundscape was proposed as an attempt to create an analytical perspective that would explain the total acoustic environment over time and across cultures [1]. Schafer wrote in 1977: "Ecology is the study of the relationship between living organisms and their environment. Acoustic ecology is the study of sounds in relationship to life and society." He also suggested three different types of noise: 1) unwanted sound, 2) unmusical sound (defined as non-periodic vibration and 3) any loud sound and disturbance in signaling systems. In his book he deals with the idea that every city has a unique urban soundscape and furthermore, every part of the city has a unique soundscape. An example for that is a siren in a noisy environment can be barely noticeable, while the same siren in a different but calmer neighborhood can result in a temporal or chronic hearing loss if the attack is sudden [2],[3]. The soundscape studies are multidisciplinary and include: acoustics, psychoacoustics, otology (study and treatment of the ear) and noise reduction. Most soundscape studies concern the qualitative analysis of soundscapes; however, the methods for evaluating a soundscape vary depending on the purposes of the studies and the researchers conducting them [4],[5]. So far soundscape research has been oriented mainly on evaluating a soundscape in a qualitative way, e.g. assessing the soundscape pleasantness or rather its unpleasantness [6]-[9]. In order to describe a certain soundscape in greater detail and provide a more comprehensive approach to soundscape research, it is necessary to use other methods which could also define soundscape characteristics quantitatively. The basis for acoustical characterization can be achieved by using a set of subjective descriptors, for example bipolar adjectives, that describe specific soundscape characteristics such as loudness or a level of distraction or annoyance by a certain sound and are then assigned a numerical score which enables and facilitates the statistical analysis of specific sound properties [2],[10]-[12].

From a quantitative point of view, statistical relevance is of utmost importance in efforts to describe or quantify a listener's perception and evaluation of a soundscape. Taking into account several variables such as loudness, pitch strength and fluctuation of pitch strength among others, it is possible to calculate the annoyance level of a certain sound or a soundscape [13]-[16]. Another part of soundscape and sound analysis deals with their distraction properties and the way in which characteristic sounds influence people performing logical, mathematical and other concentration demanding tasks [10],[11].

People are exposed to different sound environments on a daily basis. Long exposure to a specific sound environment results in eventual adaptation to that environment, and small and expected loudness changes in soundscape do not significantly influence one's perception of that soundscape [2]. Frequent exposure to even a slight change in our everyday sound environment would also result in adaptation; furthermore, providing the loudness levels were not significantly higher, these changes would not be perceived as annoying [3].

*Mia Suhanek, University of Zagreb, Croatia, 00385 1 6129840,
Email: mia.suhanek@fer.hr

In this paper, we aimed at analyzing and comparing in what way certain soundscapes with different loudness distributions distract listeners performing a rather simple but concentration-demanding task, like a simplified variation of the memory game. Since the test subjects received no training prior to undergoing the testing and were only given technical information pertaining to the testing environment, this game was chosen due to the familiarity of the test subjects with its format. Furthermore, the level of concentration required for this simplified variation of the game corresponds to day-to-day situations where people perform basic tasks while being exposed to different sounds which do not require their focus, but only cause distraction. We wanted to monitor listeners' reactions to different sounds in the background of the main theme of a soundscape and to determine whether these sound events cause the distraction on the same level as louder, familiar and expected sounds of a certain soundscape.

In general, we intentionally opted for different spectral content, loudness distribution, duration and rate of change of individual louder events in the recorded soundscapes. The underlying idea was that the listeners perform a certain task for the duration of all soundscapes. We wanted for the listeners to perceive the soundscapes subconsciously, rather than actually listen to the recordings. The task involved playing a game, thus requiring a higher level of concentration. The results of the game for all listeners were compared to questionnaire responses which lead us to conclude that, when analyzing soundscape in general, listeners base the level of their annoyance mainly on loudness. On the other hand, distraction can also be attributed to unexpected sounds that are somewhat different from the main sound print.

Furthermore, a soundscape by definition includes a certain environment and therefore a large number of sound sources that affect human activity, concentration and mood which is why soundscape research investigates the conditions and reasons of its origin as well as the level of human soundscape perception and evaluation[1].

Tim Beatley also explains in his paper "Celebrating the Natural Soundscapes of Cities" (2013) the importance of soundscape of the city in a way that the city should be enriched with natural sounds. There are also other studies that have shown that people especially enjoy the sound of water[6]. In that sense, we can conclude that the real challenge is how to create an enjoyable soundscape in nowadays overpopulated cities.

Unfortunately, the main concern of the society in general, is still only noise management and legislative. We can conclude that nowadays, urban planners have a big challenge before them. While fitting visual aesthetics with solutions for transport, waste and energy, they need to bear in mind the natural soundscape preservation perspectives.

2. Urban Soundscapes in Zagreb

The first recorded soundscape was a children's park situated in the western suburb of Zagreb and surrounded by large housing blocks. Figure 1 shows a spectrogram of the recorded children's park environment excerpt. The spectrogram is relatively wide stretching above 10 kHz, with very short leaps in loudness change which are up to 20 dB higher when compared to the steady part of the recording.

The second recorded soundscape was the expressway stretching from the east to the western exit of the city. Traffic in this avenue is almost always heavy and dense so the soundscape included sounds coming from cars, buses and trucks passing by and an audible traffic signal for the visually impaired (see Figure 2). The frequency spectrum is narrower compared to the children's park environment and is mainly concentrated at frequencies below 1 kHz. Sudden and large changes in loudness were not as unexpected for the expressway environment as they were in the case of the children's park.

The third soundscape was a stream on the outskirts of western part of Zagreb, in a small forest surrounded with local roads. The recording included sounds coming from the stream, nearby traffic, children playing and a small dog barking. Figure 3 shows the frequency spectrum of this recording excerpt. It is narrow and concentrated in the low frequencies making the sudden loudness changes (dog barking, children screaming etc.) very discernible.

The fourth soundscape was an industrial hall which produces rail vehicles situated in the eastern part of Zagreb. Figure 4 is a spectrogram of this soundscape which included the sounds of power tools such as grinders and drills, the sound of a hammer hitting metal and music coming from the radio. These specific sounds are very loud, as shown on the spectrogram (see Figure 4). The frequency spectrum is up to 10 kHz wide, with short loudness changes rising to 30 dB above the average level.

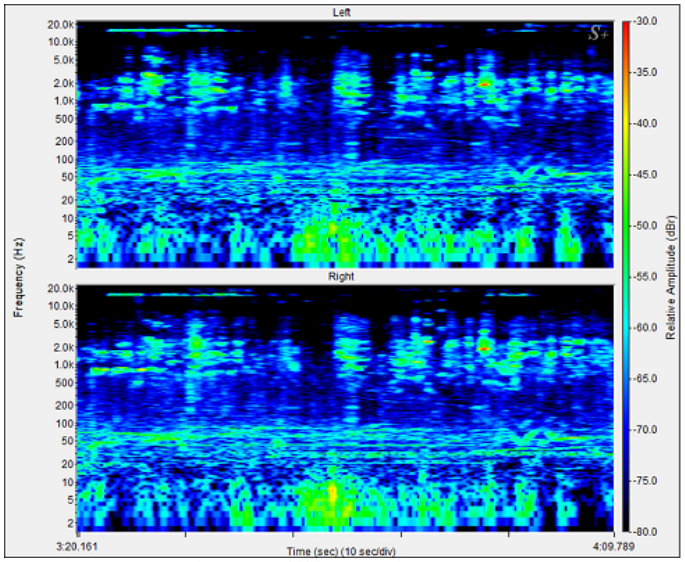

Figure 1. Children's park spectrogram

These four soundscapes were chosen due to their relatively different sound characteristics. An average person living in an urban environment is familiar with three of them: the children's park, the expressway and the stream soundscape. However, the industrial hall soundscape is less common, to say the least. For the research, comparing familiar with unfamiliar soundscapes enabled us to analyze whether the former was perceived less distracting than the latter. The research participants were divided into two groups: the control (marked *CG*) and experimental group (marked *EG*). The experimental group listened to the soundscapes with frequent sudden and short loudness changes, and the control group listened to the same soundscape but with lower loudness changes. Loudness versus time diagram were also created for a specific soundscape and listening group (see Figures 5a, 5b, 5c and 5d)

based on Figures 1 to 4. In Figures 5a, 5b, 5c and 5d the soundscape recording for the experimental group is marked with a solid line while the recording for the control group is marked with a dotted line.

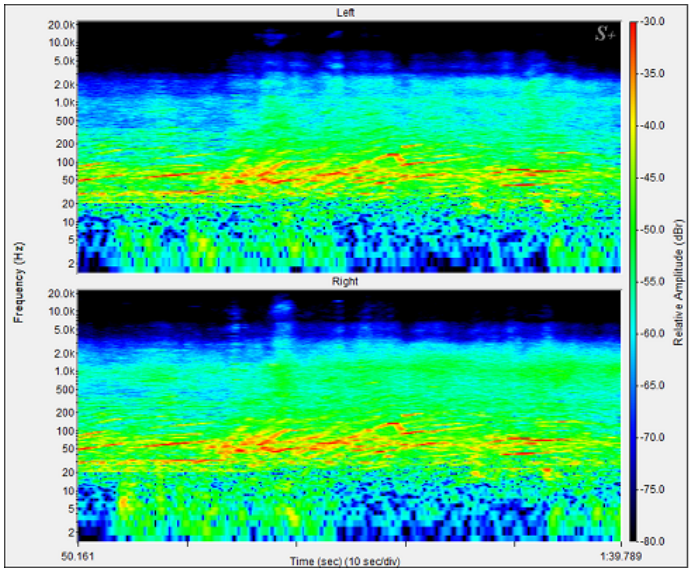

Figure 2. Expressway spectrogram

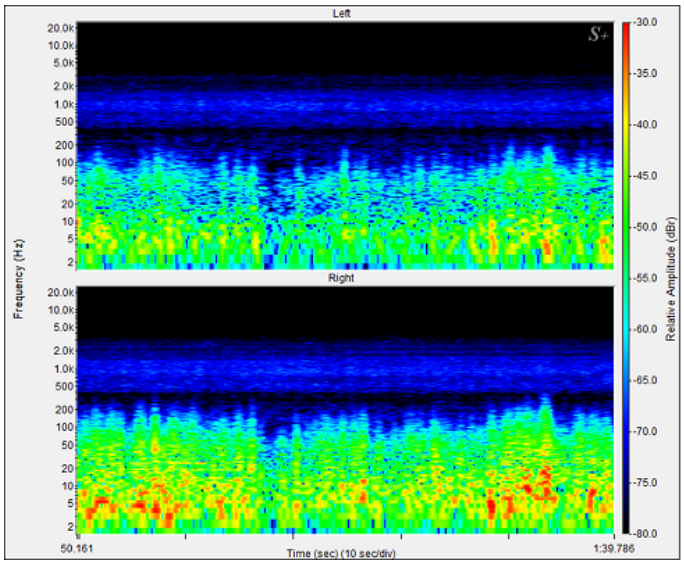

Figure 3. Forest stream spectrogram

3. Listening Tests

Four characteristic urban soundscapes were recorded using the *soundwalk* method [5,17]. The soundscape samples were recorded using the M-AUDIO recorder [18] and a pair of binaural microphones, with a 48 kHz sampling rate and a 16 bit quantization standard. The *soundwalks* were performed at different times of the day, different days of the week, always in nice, dry and sunny weather in March 2018. These recordings were performed at the *soundwalker's* height so that the patterns obtained would be as similar to the natural binaural listening of people residing in these soundscapes. The recordings were then reproduced to two groups of listeners: the control group (CG) and the experimental group (EG). The experimental group listened to the soundscapes with frequent sudden and short loudness changes, and the control group listened to the same soundscape but with lower loudness changes.

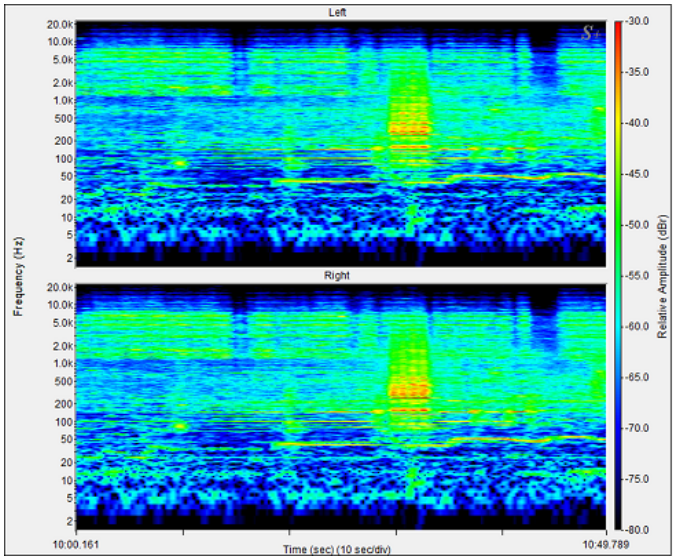

Figure 4. Industrial hall spectrogram

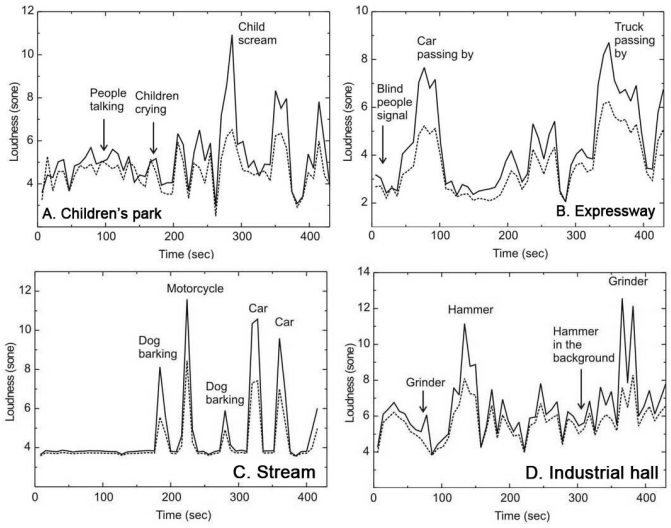

Figure 5. Average loudness versus time diagram for (the control group is presented with a dotted line and experimental group with a solid line): a) children's park, b) expressway, c) stream and d) industrial hall

The recordings were reproduced using AKG K55 closed electrodynamic headphones with an average sound pressure level of 50 dB(A) in the steady part of the recorded soundscape. Loudness was calculated using the established Zwicker method [13],[14]. Free field equalization was used. It is important to emphasize that average sound pressure level of 50 dBA refers to the recordings listened by the experimental group while the recordings for the control group are corrected by a compressor with a limit value of 60 dBA and a compression ratio of 3:1. The listeners' groups had equal female-to-male ratio, with median age of 24. Each of the listeners listened to all four recordings with a time gap of at least one week in order to facilitate recovery time and eliminate any potential influence of one recording on another. The listeners were not informed as to the content of the recording. The order of the listening of the soundscapes was fixed for all listeners which is in line with the established psychological and statistical research methodology and praxis [19],[20], and is as

follows: the children's park soundscape, the expressway soundscape, the industrial hall soundscape and the stream soundscape. The results wouldn't have been different if we chose a different order of the soundscape listening. However, once you have chosen the order of the listening it has to remain the same for all participants of the study. For example: if a participant is placed in a control group (he or she is not of course aware of it) then he or she has to stay in the control group till the end of the study. Furthermore, if one participant listened the soundscapes in a certain order then the rest of the participants must have the same order due to psychological methodology and its requirement that all participants have to have the same testing conditions. Thus, this way of research enables the researcher to have a better control over the study.

Table 1 Most annoying sounds for the experimental and control groups (EG- experimental group, CG- control group)

Children's park	**EG**	**CG**
children screaming	44,8%	34,7%
sound of the swing	27,6%	20,4%
children crying	10,4%	8,2%
kindergarten teacher	13,8%	16,3%
all of the above	1,7%	8,2%
nothing bothered me	1,7%	12,2%

Expressway	**EG**	**CG**
vehicle horn	13,3%	2,4%
audible traffic signal for the visually impaired	11,1%	17,1%
sound of cars	21,1%	43,9%
all of the above	0,0%	7,3%
nothing bothered me	24,5%	29,3%

Industrial hall	**EG**	**CG**
sound of power grinders	18,2%	41,9%
sound of hammers	70,4%	38,7%
music from the radio	0,0%	1,6%
all of the above	2,3%	1,6%
nothing bothered me	9,1%	16,2%

Stream	**EG**	**CG**
small dog barking	27,6%	5,2%
children screaming	20,7%	10,7%
bus passing by	37,9%	7,3%
stream bubbling	0,0%	10,5%
all of the above	13,8%	0,0%
nothing bothered me	0,0%	66,3%

Additionally, a questionnaire was composed in order to get a more detailed description of which particular sounds in a given soundscape were the most annoying and why. The listeners had to provide an answer to a direct question: Which of the given sounds in the soundscape bothered you the most? This form of research enabled us to establish a connection between annoying sounds and the results of the game (e.g. listeners' distraction). For every soundscape we have supplied a list of potentially most annoying sounds. However, the list was far from selective as it contained all the characteristic sound events appearing in a certain soundscape. Our intention was to provide a reminder for the listeners considering the long duration of the soundscape samples, rather than to influence their answers. These results are laid out in Table 1. In addition to the list of the characteristic sound events, the questionnaire provided the "all or nothing of the above" answer options for each soundscape.

4. The Game

During the first listening of each soundscape, the listeners had to solve an interactive game, similar to the traditional children's memory game, programmed in MATLAB (see Figure 6).

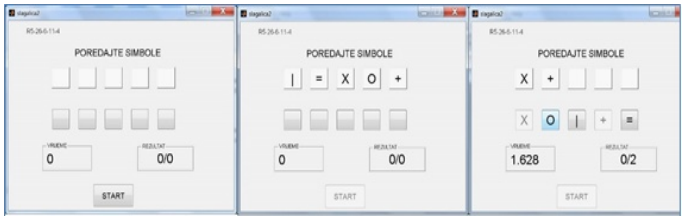

Figure 6. The game interface in MATLAB

The listeners played the game on the computer, while at the same time listening to a certain soundscape. The game uses five cards with simple mathematical symbols (X, O, I, +, =). The symbols on the cards are revealed to the listener in a random order for four seconds. The goal is for the listener to line up the symbols on the cards according to the order in which they appeared. Time allotted for this task is seven seconds, with a two second pause before the next layout of the cards. If the listener makes a mistake while arranging the symbols on cards, a new hand of cards is drawn automatically. The game is not intended to be difficult or complicated, but rather to serve as means of assessing listener's concentration or the absence thereof during specific sound events in each soundscape, i.e., sudden loudness changes. For the duration of each soundscape, the program generates orders of symbols and records the listener's score. In this way we could establish and analyze the potential correlation between the results of the game and time, as well as identify certain parts of a soundscape that could have caused the distraction occurring at a specific point in time. The results of the game, representing the success ratio of each move, are generated numerically. For instance, if a listener successfully arranged all the cards in the given time frame, their result for this move equaled 1. If a listener successfully arranged only 3 out of 5 cards, the result was 3/5 = 0.6. We then calculated and compared the average scores for each soundscape overall.

Finally, for each listener, we created an average score versus time diagram for a specific soundscape and listening group. All of these were then used in calculating the overall average score

versus time diagram. Figure 7a, 7b, 7c to 7d show these diagrams for all four soundscapes.

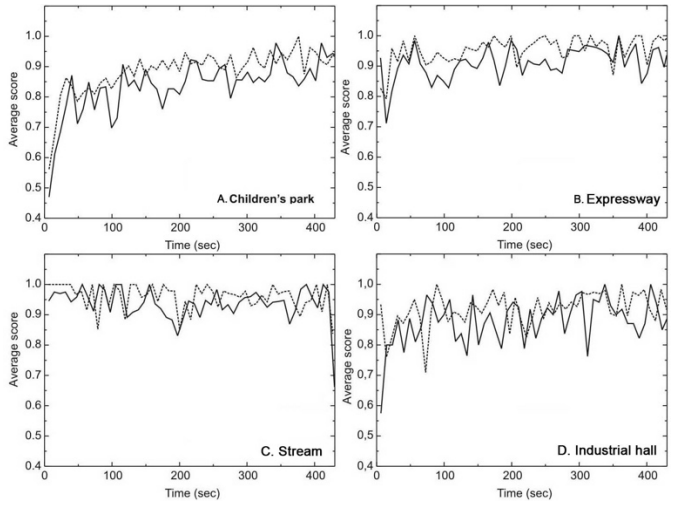

Figure 7. Average score versus time diagram for (the control group is presented with a dotted line and experimental group with a solid line): a) children's park, b) expressway, c) stream and d) industrial hall

5. Research Results

The questionnaire responses describing the listeners' assessment of the soundscapes showed that, in the majority of cases, annoyance can be assigned to loud sounds - mainly those louder than the main theme of the soundscape. Furthermore, a comparison between the experimental and control group soundscapes shows that, in general, loudness has the strongest influence on the annoyance factor. On the other hand, a more detailed analysis shows that significant loudness changes are not the only factor contributing to listeners' distraction.

It is interesting to notice that when comparing two relatively loud soundscapes - the children's park and industrial hall soundscapes, the percentage of listeners not bothered with any of the characteristic sound events was higher in the case of the loudest soundscape with artificial sounds – the industrial hall. Based on the content, the comparison of these two soundscapes shows that the louder sounds are much more varied in the former soundscape. Even though the industrial hall soundscape features a greater number of louder sounds, they are quite similar and consist mainly of the sound of power tools. In the case of the children's park soundscape, individual sound events are much more varied in terms of frequency content, loudness distribution and rate of change.

In the case of the expressway soundscape, a larger percentage of listeners stated that nothing bothered them. This soundscape is in general quieter, but also consist mainly of the same sounds, with very narrow loudness distributions. In addition, fewer loud sounds differ from the main soundscape print in a way to annoy and distract the listeners.

The specific nature of the stream soundscape reflects in the longest period of the steadiness of the main theme. However, all the listeners in the experimental group reported some type of annoyance. Even though this soundscape features less sudden loudness changes than the previous three, these transitions are considerable in comparison with the steady part of the recording. Also, a large number of listeners in the control group stated that nothing bothered them which is in compliance with various studies in this field in terms of conclusion that people prefer the sound of water.

Upon careful examination of the game results, all the diagrams show a similar pattern (Figure7a, 7b, 7c and 7d). The average move score tends to slightly increase toward the end of the soundscapes. This effect is most evident in the children's park soundscape. Moreover, the first moves for all listeners are most inaccurate, while the average scores tend to increase toward the end of the soundscape. The reasons for this are twofold: adaptation to the game environment and adaptation to the soundscape. Despite the fact that all the listeners played some type of a memory game prior to this testing and were therefore familiar with the pattern of the game, their initial moves were considerably less accurate than those made later in the game. The recorded average move time stabilized after the first few moves, and this can be attributed both to the adaptation to the game environment and adaptation to the soundscape factors. This effect is less obvious for soundscapes with smaller loudness change and for the control group soundscapes where loudness changes were intentionally lower, which is indicative of the importance of the occurrence of sudden and unexpected sounds.

Comparing the average score for all four soundscapes (see Table 2), the children's park soundscape has the lowest average score, immediately followed by the industrial hall soundscape, expressway and stream soundscapes. There is an obvious difference for the experimental and control group soundscapes. As mentioned, soundscapes with lower loudness changes have lower distraction properties than those with higher loudness changes. This corresponds to the questionnaire results, where larger percentage of listeners of the control group soundscapes stated that nothing bothered them.

If we compare the average score with loudness diagrams for a specific soundscape, in some cases the lower score did not correspond to higher loudness change, as would be expected. Several other factors that affected a lower game score must be taken into consideration. For example, the time segment around the 100th second in the children's park soundscape for the experimental group shows a lower average score even though there are no considerable loudness changes in this part of the soundscape. However, this interval features a short conversation which immediately distracted the majority of listeners. The same distraction pattern occurred whenever an indistinct conversation could be overheard in this soundscape. It seems that larger loudness changes in the form of children screaming did not distract the listeners playing the game as would be expected.

A similar example can be found in the industrial hall soundscape for the experimental group. Around the 300th second, a sound of a hammer could be heard in addition to that of power grinders. This sound stimulus proved to be unexpected and very distracting despite the fact that the main theme of the soundscape was louder (see Table 1). The sound of hammers was a high pitched sound of metal hitting metal, while the sound of power grinders was a constant noise. In the questionnaire, many of the listeners stated that the sound of hammers was the most annoying and disturbing in a generally loud soundscape.

As far as the expressway soundscape is concerned, the lower score can be attributed to the sounds of fast-passing cars which stood out from a generally noisy environment. In this case, there were no sudden and large loudness changes that would distract the listeners, thus the scores were relatively high.

Similarly, when it comes to the stream soundscape, lower results occurred at the moment of the dog's first bark since this sound event was unexpected after a longer period of no loudness changes. After that, the listeners expected similar distracting sounds and, consequently, the scores were higher.

Table 2. The game results for the experimental and control groups

	Children's park		Expressway		Industrial hall		Stream	
Group	EG	CG	EG	CG	EG	CG	EG	CG
Average score	0.86	0.92	0.93	0.96	0.88	0.92	0.94	0.96
Stand. deviation	0.091	0.071	0.058	0.041	0.074	0.056	0.055	0.043
The lowest score	0.47	0.56	0.67	0.79	0.58	0.71	0.83	0.84
N_5 (sone) (7 min)	8.1	6.1	8	6.5	10.5	8.1	9.5	6

6. Future Work

Taking into account the questionnaire and the game results, we can conclude that higher loudness in a certain soundscape is the most annoying factor. It determines general annoyance perception and influences the distraction features of a soundscape considerably. On the other hand, loudness is not the only distraction feature and other sound characteristics must be considered. After being exposed to sudden loudness changes, the listeners adapted, and the only remaining factors of distraction were the sounds perceived as different, unexpected or not corresponding to general soundscape characteristics.

Finally, we can conclude that the results of the testing showed that there is a sophisticated distinction between annoyance and distraction, and that these two terms should be distinguished from each other in the future. Further research on this topic should focus on determining in what way particular sounds differ from their background, as well as identifying the factors that influence human perception which defines these sounds as unexpected for a given soundscape.

One more way that we could proceed is preserving and/or creating ”silent places” within a certain urban soundscape. This research also showed that people prefer the sound of water. This can be a valuable information in soundscape studies in terms of masking the annoying soundscape with the soundscape that consist of water and natural sounds. We could also work on developing innovative design and materials: green spaces, green walls, water walls and other unrecognized ecosystem services.

7. Conclusion

In spite of adapting to a certain sound environment, providing it is not too loud, people still get distracted by unexpected sounds not ”belonging” to the main soundscape print. A soundscape may be loud but, at the same time, not perceived as such; whereas a somewhat different sound in that soundscape, no matter how short, could be the source of annoyance and the reason for distraction.

Finally, we can conclude that urban planning should include zoning requirements for new buildings and constructions, which would offer us the possibility for designing soundscapes.

Acoustic ecology is not just an interesting new aspect of urban studies. In our opinion soundscape designing will be one of the most important part for future city planning in a way to create sustainable and pleasant cities. Natural and water sounds in soundscape can be used as a tool when masking the undesirable sounds and soundscapes.

Conflict of Interest

The authors declare no conflict of interest.

Acknowledgment

This work has been supported by the European Union from European regional development fund (ERDF) under the project number KK.01.2.1.01.0103 Acoustical Camera (in Croatian: Akustička kamera).

References

[1] R. M. Schafer, Our Sonic Environment and the Soundscape: The Tuning of the World, Destiny Books, 1994.

[2] H. Fastl, S. Kerber, N. Guzsvány, ”Aspects of startling noises” in Proceedings of Euronoise 2009, Edinburgh, 2009. ISBN: 978-1-61567-680-4

[3] J. Vos, ”The Loudness of Impulse and Road-Traffic Sounds in the Presence of Masking Background Noise”, Acustica – Acta Acustica, **84**(6), 1119-1130, 1998. ISSN 1610-1928

[4] B. Schulte-Fortkamp, A. Fiebig, ”Soundscape Analysis in a Residential Area: An Evaluation of Noise and People’s Mind”, Acta Acustica united with Acustica, **92**(6), 875-880, 2006. ISSN 1610-1928

[5] B. Berglund and M. E. Nilsson, ”On a tool for measuring soundscape quality in urban residential areas”, Acta Acustica united with Acustica, **92**(6), 938-944, 2006. ISSN 1610-1928

[6] J. Y. Jeon. P. J. Lee, J. You, J. Kang, ”Perceptual assessment of quality of urban soundscapes with combined noise sources and water sounds”, Journal of the Acoustical Society of America, **127**, 1357-1366, 2010. https://doi.org/10.1121/1.3298437

[7] A. Torija, D. Ruiz, A. F. Ramos-Ridao, ”Application of a Methodology for Categorizing and Differentiating Urban Soundscapes Using Acoustical Descriptors and Semantic-Differential Attributes”, Journal of the Acoustical Society of America, **134**, 791-802, 2012. https://doi.org/10.1121/1.4807804

[8] A. Ozcevik, Z. Yuksel Can, ”A Laboratory study on Evaluation of Soundscape”, in Proceedings of the Acoustics 2012, Nantes, France, 2012. https://hal.archives-ouvertes.fr/hal-00810900

[9] M. Suhanek, I. Djurek, ”Perception and Evaluation of Sudden Loudness Changes in Urban Soundscapes”, in Proceedings of the 5th Congress of the Alps Adria Acoustics Association 2012, Petrčane (Zadar), Croatia, 1-7, 2012. ISBN 978-953-95097-1-0

[10] E. E. Ryherd, L. M. Wang, ”The Effects of Noise from Building Mechanical Systems with Tonal Components on Human Performance and Perception”, ASHRAE Transactions, AB-10-018 (RP-1322), 2010. http://digitalcommons.unl.edu/archengfacpub/6

[11] L. M. Wang, ”Effects of Building Mechanical System Noise on Worker Performance and Perception”, in Proceedings of NOISE-CON 2010, 2010. http://digitalcommons.unl.edu/archengfacpub/6/

[12] M. Suhanek, I. Đurek, ”Implementation of Bipolar Adjectives pairs in Analysis of Urban Acoustic Environments”, Promet - Traffic & Transportation. **28** (5), 461-470, 2016. https://doi.org/10.7307/ptt.v28i5.2089

[13] E. Zwicker, ”Procedure for calculating loudness of temporally variable sounds”, Journal of the Acoustical Society of America, **62**, 675-682, 1977. https://doi.org/10.1121/1.381580

[14] E. Zwicker, H. Fastl, Psychoacoustics: Facts and models, 2nd ed. Springer-Verlag, Berlin, Heidelberg, New York, p. 220, 1999.
[15] U. Widmann, "A psychoacoustics annoyance concept for application in sound quality", The Journal of the Acoustical Society of America **101**, 3078 (1997); https://doi.org/10.1121/1.418779
[16] S. Viollon and C. Lavandier, "Multidimensional Assessment of the Acoustic Quality of Urban Environments", in Proceedings of Internoise, Nice, France, 2000. ISBN 2951561962, 9782951561960
[17] C. Semidor, "Listening to a City With the Soundwalk Method", Acta Acustica united with Acustica, **92**(6), 959-964, 2006. ISSn 1610-1928
[18] http://www.m-audio.com/, 20.09.2013.
[19] G. Milas, Istraživačke metode u psihologiji i drugim društvenim znanostima (Research Methods in Psychology and other Social Sciences), Naklada Slap, p. 91-118, 153-216, 2009. ISBN 978-953-191-283-9
[20] M. Mejovšek, Metode znanstvenog istraživanja u društvenim i humanističkim znanostima (Methods of Scientific Research in Social Sciences and Humanities), Naklada Slap, p. 71-158, 2007. ISBN 953-191-342-3

ASTES

Advances in Science, Technology and Engineering Systems Journal Vol. 3, No. 4, 218-223 (2018)

www.astesj.com

ASTESJ

ISSN: 2415-6698

Textural Analysis of Pap Smears Images for k-NN and SVM Based Cervical Cancer Classification System

Abraham Amole[*,1], Bamidele Sanya Osalusi[2]

[1]*Department of Electrical, Electronic and Computer Engineering, Bells University of Technology, Ota, P.M.B. 1015, Nigeria.*

[2]*Neurology Unit, Department of Medicine, Olabisi Onabanjo University Teaching Hospital, Sagamu, Ogun State, Nigeria*

ARTICLE INFO

Article history:
Received: 15 February, 2018
Accepted: 17 July, 2018
Online: 05 August, 2018

Keywords:
Cervical Cancer
Morphological
Wavelet
GLCM
k-NN
SVM

ABSTRACT

Early detection and treatment of cervical cancer is crucial to patients' recovery with a reported success rate of nearly 100%. Presently, Pap smear test which is a visual inspection of cells collected from the ectocervix is the screening tool mainly used in cancer prevention programs. The Pap smear is relatively easy to handle however, it is time-consuming and requires wet fixation of the cytological material. Thus, there is great demand for an automated-screening system that exhibits high sensitivity, high specificity and high-throughput. Hence, a textural based cervical cancer classification system has been developed in this research work. The wavelet transform was used to denoise 120 Pap smear images to enhance its visual quality while the images were segmented using the morphological operations. Eight textural features of GLCM that serve as inputs into the k-NN and SVM classifiers were extracted from each of the images and the performance was evaluated using accuracy, sensitivity and specificity. The result of the developed system shows that clustering shade SVM classifier out-performs entropy k-NN classifier in terms of classification accuracy of 90.0% and 88.3% respectively and vice visa in terms of sensitivity and specificity.

1. Introduction

Cancer is characterized by uncontrolled growth and spread of abnormal cells and is one of the currently most ravaging diseases and if its spread is uncontrolled, can result in death [1, 2]. Cancer is a complex genetic disease that is potentially fatal and caused mainly by environmental factors that mutate genes encoding critical cell-regulatory proteins [3]. Also, it has been reported by [2] that cancer may be caused by external factors like tobacco, infectious organisms, unhealthy diet and internal factors, such as inherited genetic mutations, hormones and immune conditions. Currently, cancer constitutes public health problem for men and women, it has been reported as the leading cause of death for human being in worldwide, because the cause of the disease is unknown and the early detection of cancer is also tedious [4]. Cancer has variants like breast cancer, prostrate cancer, skin cancer and cervical cancer depending on the organ of the body affected. Cervical cancer is caused by human papillomavirus (HPV) which is a common virus that is passed from one person to another during sex. At least half of sexually active people will have HPV at some point in their lives, but few women will get cervical cancer [5].

Cervical cancer was reported the third most common cause of death among the female [6, 7]. It is a less aggressive cancer that tends to grow slowly with a development rate of several years and in the pre-cancerous stages it may be completely asymptomatic with preinvasive cervix lesions that can only be detected by screening methods [8]. Cervical cancer mostly occurs in women of over age 30 and it remains a challenge for the health care sector because of the numbers of invasive cancer that are involved and the high cost of maintaining quality screening programs. In fact, WHO maintained that cervical cancer constitutes approximately 12% of all cancers in women worldwide and that is a leading cause of mortality and morbidity. For instance, according to [5] approximately 12,000 women in the United States get cervical cancer each year. Cervical cancer can be prevented with regular screening tests and follow-up when found and treated early [2].

Early detection and treatment of cervical cancer is crucial to patients' recovery with a reported success rate of nearly 100% [8]. Treatments of cervical cancer may include but not limited surgery,

[*]Amole Abraham, ECE Dept., Bellstech, P.M.B. 1015, Ota, Ogun State, Nigeria 2348067612133, latidassah@gmail.com

radiation, chemotherapy, hormone therapy, immune therapy and targeted therapy. There are a number of different methods like Automated cervical screening techniques, Neuromedical systems, HPV testing, Polar probe [9], flow cytometry [10], colscopy [8] and Pap smear [11] that have been proposed and tested for early detection and diagnosis of cervical cancer. Presently, Pap smear test which is a visual inspection of cells collected from the ectocervix is the screening tool mainly used in cancer prevention programs. The Pap smear looks for precancers and cell changes on the cervix for treatment thus preventing cervical cancer. The use of Pap smear test has led to a considerable reduction in the cases of cervical cancer though it is not a diagnostic but a screening tool [12, 13]. The Pap smear is important in diagnostic cytology because it uniquely stains pattern with differentially smeared cytoplasm. The Pap smear is relatively easy to handle however, it is time-consuming and requires wet fixation of the cytological material. Thus, there is great demand for an automated-screening system hat exhibits high sensitivity, high specificity and high accuracy.

2. Related Works

Several studies, majority of which aimed at early detection and classification of cervical cancer have been developed and reported in literatures. In [5], intelligent classification of cervical pre-cancerous cells based on the FTIR spectra in which peak-corrected area-based features' extraction (PCABFE) was used and the Hybrid Multilayered Perceptron (HMLP) network was employed for classification with a reported performance of 97.4%. Likewise, [14] worked on identification of abnormal cervical regions from colposcopy image sequences using an algorithm that automates identification of abnormal cervical regions based on a set of low-level feature vectors as input to the support vector machine (SVM) classifier. The highest classification rate obtainable was 94.6% with linear kernel thus made the algorithm accurate and effective. The work of [15] was based on color histogram features used as an input to k-NN, NaiveBayes, and SVM classifiers to detect the Aceto White Region (AWR) with accuracy of over 85% and average sensitivity of over 74%. A comparative study between multi-sparse representation classification with accuracy of 93.3% and classical classifiers like ANN and NaiveBaiyes on cervical cancer cell images trained on genetic algorithm was done in [16]. In [17], a pap smear images classification for early detection of cervical cancer was performed using SVM classifier that gave promising results with average accuracy of 92.961%, sensitivity 90.833% and specificity 80.39%. Also, [11] presented a computer assisted pap smear analyser for cervical cancer screening system that produces higher sensitivity of 93% and 95% in HSIL and SCC grades respectively and was found to reduce the workload of cytologist to almost 60%. In [18] classification of MR Images of cervical cancer using SVM and ANN with classification accuracy found to be 92% and 84% respectively. Finally, [19] worked on improvement of features extraction process and classification of cervical cancer for the Neuralpap System based on Hybrid RBF (HRBF) networks with increase in the accuracy of the classification of cervical cancer to 76.35%, compared with 73.40% which is obtained from the previous NeuralPap system.

3. Materials and Methods

This section presents the stepwise approach towards the development of the developed k-NN and SVM based cervical cancer classification system.

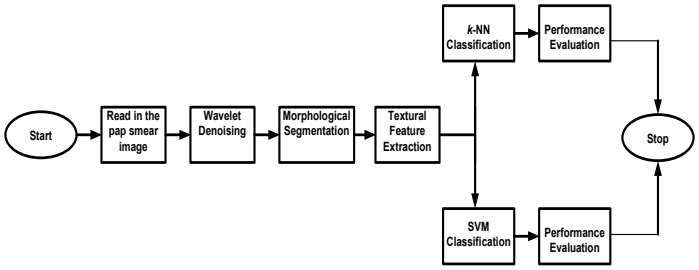

Figure 1: Block Diagram of the Developed System

3.1. Image Data Preparation

The images used in this work was collected online from the smear2005 database of the Herlev University Hospital and sample of the Pap Smear images used in this work were presented in Figures 3 and 2. These smear images were taken at a resolution of 0.201µm/pixel by skilled cyto-technicians with a microscope connected to a frame grabber. Light dysplasia in Figure 3 is one of the three variants of the dysplasia which is characterized by enlarged and light nucleus hence; it has similar features to the carcinoma-in-situ. Figure 2 presented images of cervical carcinoma-in-situ and is also characterized by very large nucleus. One hundred and twenty of these images were selected for use in this work out which sixty were used for training and the remaining sixty were used for testing.

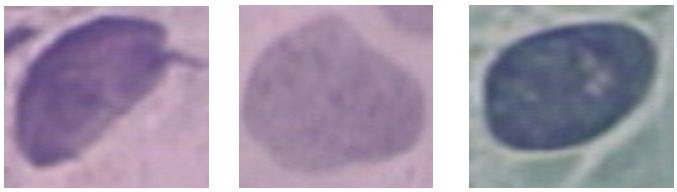

Figure 2: Images of Carcinoma-in-situ before Segmentation

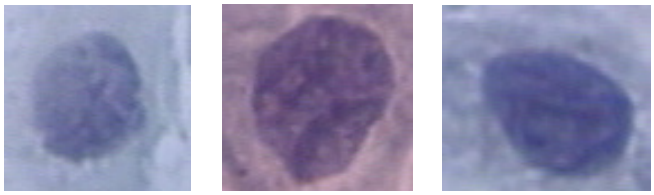

Figure 3: Images of Light Dysplasia before Segmentation

3.2. Wavelet based Denoising

The wavelet system builds a set of blocks to represents a signal or function by giving a time frequency localization of the signal [20, 21]. Wavelet systems are generated from single scaling function by scaling and translation. Hence, wavelet transform has become an important tool for denoising corrupted images by

reconstructing the signal on the basis of the observations of a useful signal corrupted by noise [22, 23, 24]. The pap smear images were denoised based on the wavelet system using symlet 4 as the wavelet family.

3.3. Image Segmentation

Image segmentation is the process of partitioning a digital image into multiple segments with the goal of easing the representation of an image into a more meaningful and easy to analyze version. Image segmentation is basic to most medical image classification system hence; several approaches like Fuzzy clustering [25] have been used in the literatures. The morphological operation which applies a structuring element to an input image, creating an output image of the same size based on erosion and dilation was used in this work. Dilation adds pixels to the boundaries of objects in an image, while erosion removes pixels on object boundaries.

3.4. Feature Extraction

Feature extraction is an important step in any detection and classification system, and it has been reported that the key to successful classification is the ability of representing images based on visual characteristics such as texture, color and shape [26]. Texture is the basic and most widely used techniques for analyzing medical images [27, 28] through the gray level co-occurrence matrix (GLCM) which is a second-order statistical measure of image intensity variation. GLCM considers both the intensities distribution and the position of pixels. It has capability of revealing certain properties about the spatial distribution of the gray levels in the texture. It provides the basis for a number of texture features hence; we built GLCM of the smear images region of interest (ROI) defined as 50 pixel by 50 pixel from which 8 texture features were computed as follows [29, 30]:

1. Contrast measures the intensity contrast between a pixel and its neighbour over the whole image. For a "constant" image (no variation) contrast is zero.

$$contrast = \sum_i \sum_j |i-j|^2 \, p(i,j) \tag{1}$$

2. Local homogeneity measures the closeness of the distribution of elements in the GLCM to the GLCM diagonal. For a diagonal GLCM, homogeneity is 1.

$$Homogeneity = \sum_i \sum_j \frac{1}{1+|i-j|^2} p(i,j) \tag{2}$$

3. Correlation is a measure of how correlated a pixel is to its neighbour over the whole image. It is 1 or -1 for a perfectly positively or negatively correlated image and infinity for a constant image.

$$Correlation = \sum_i \sum_j \frac{1(i-\mu_i)(j-\mu_j)p(i,j)}{\sigma_i - \sigma_j} \tag{3}$$

where; μ_i and μ_j are the GLCM mean of the first and second components

σ_i and σ_j are the GLCM variances of the first and second components

4. Cluster shade and cluster prominence characterises the tendency of clustering of the pixels in the region of interest.

$$Cluster\ shade = \sum_i \sum_j \left(i + j - \mu_i - \mu_j\right)^3 p(i,j) \tag{4}$$

$$Cluster\ prominence = \sum_i \sum_j \left(i + j - \mu_i - \mu_j\right)^4 p(i,j) \tag{5}$$

5. Entropy is a measure of randomness that can be used to characterise the texture of an image

$$Entropy = \sum_i \sum_j p(i,j) log p(i,j) \tag{6}$$

6. Maximum probability describes the maximum likelihood of producing the pixels of interest.

$$Maximum\ probability = \max\ p(i,j) \quad for\ all\ i,j \tag{7}$$

7. Energy returns the sum of squared elements in the GLCM, it has values between 0 and 1, it is 1 for a constant image.

$$Energy = \sum_{i,j} P(i,j)^2 \tag{8}$$

These texture features formed feature vectors which were used as input into two the classifiers whose performance were evaluated using accuracy, sensitivity and specificity.

3.5. Classification

Subsequent to feature extraction is the classification stage where the images were classified using the support vector machine (SVM) and the k-Nearest Neighbors classifiers.

k-NN Classifier is based on the idea that a sample is classified by a majority vote of its neighbors, with the sample being assigned to the class most common amongst its k nearest neighbors. Let the training samples be described by *n* attributes thus each sample represents a point in *n* - dimensional space. Therefore, all the training samples form an *n* - dimensional pattern space. At the instance of an unknown sample, the *k*-nearest neighbor (k-NN) classifier searches the pattern space for the k training samples which are closest to the unknown sample where the k training samples are the k-nearest neighbors of the unknown sample [31, 32]. Assuming the number of voting neigbours are $k = k_1 + k_2 \ldots k_N$, where k_i is the number of samples from *i* in the k sample neighborhood of the test samples. The test sample is assigned to class *e* if

$$K_2 = max(k_i; i = 1,2,3 \ldots \ldots \ldots . N) \tag{9}$$

For this work, 7 nearest neighbours were used throughout the experimental set up.

SVM is one of the most widely used classifiers in medical image analysis [33, 34]. SVMs are primarily two-class classifiers that have been shown to be an attractive and more systematic approach to learn linear or non-linear decision boundaries [35, 36]. It performs classification by constructing a hyperplane in a high-dimensional feature space for linearly separable classes as follows [37];

$$g(x) = w_x^T + w_0 = 0 \quad (10)$$

This can be can be further written as

$$w_x^T + w_0 = \pm 1 \quad (11)$$

This implies that the support vectors lie on either of the two hyperplanes and they form the critical elements of the training set. Also;

$$w = \sum_{i=1}^{N_s} \lambda_i y_i x_i \quad (12)$$

Where w = parameter or support vector, λ_i = Langrange multiplier, *Ns* = feature vector.

SVM can be used for classification purpose under different types of kernel function. Gamma kernel function with $\gamma = 6$ was used in this work. The choice of SVM lies in its flexibility due to parameters that can be adjusted to achieve better classification rate. The dimensionality of the feature space is determined by the number of support vectors extracted from the training data [38]. It performs structural risk minimization to achieve good generalization [35, 36].

3.6. Performance Evaluation

The performance of the developed cervical cancer classification system was evaluated based on sensitivity, specificity and accuracy defined as follows;

1. Sensitivity is the ability of a system to identify the presence of disease and it has no dependence on the disease prevalence

$$TP/(TP+FN) \quad (13)$$

2. Specificity Ability to identify the absence of disease and has no dependence on the disease prevalence

$$TN/(TN+FP) \quad (14)$$

3. Accuracy represents the global reliability of the classification system but depends on the disease prevalence

$$(TP+TN)/(TP+TN+FP+FN) \quad (15)$$

The performance of the developed system was evaluated using confusion matrix that shows the percentages of correct and incorrect classifications from which accuracy, sensitivity and specificity were computed. These indices indicate an increasingly high diagnostic performance of the examination under investigation the closer they are to unity [39, 40]. The overall process was implemented using MATLAB 8.5.

4. Results Discussion

This section presents the results of the developed texture based pap smear classification system for cervical cancer. Figure 4 presents some of the morphological operations and wavelet segmented images of carcinoma-in-situ. By visual inspection and comparison of Figure 2 and 4, it can be inferred that the wavelet is effective in remove artifacts from the pap smear images and that the morphological operations effectively segment the nucleus area of the image. Also, Figure 5 presents some of the morphological operations and wavelet segmented images images of light dysplasia. Figure 3 and 5 also gave a comparable result to that of Figure 2 and 4.

Figure 6 present confusion matrix classification results of clustering shade SVM and entropy k-NN with 90.0% and 88.3% respectively. According to Figure 6a, 55 of the images are not cancer whereas 5 are cancer, the SVM algorithm with clustering shade feature predicted 49 as not cancer and 11 as cancer; this translates to 90.0% accuracy. Similarly, in Figure 6b, 1 of the images are not cancer whereas 59 are cancer, the k-NN algorithm with entropy feature predicted 8 as not cancer and 52 as cancer; this translates to 88.3% accuracy. In Table 1, the summary of classification accuracy, sensitivity and specificity for SVM and k-NN classifiers with all texture features were presented. From the table, a general inference that can be drawn is that the SVM classifier with clustering shade out-performs the k-NN classifier with entropy in terms of classification accuracy of 90.0% and 88.3% respectively. On other hand, k-NN classifier with entropy out-performs the SVM classifier with clustering shade in terms of sensitivity and specificity with a value of 1.00 and 0.82 respectively for k-NN classifier and a value of 1.00 and 0.45 respectively for SVM classifier. This result is comparable to the work of [17] in terms of accuracy and sensitivity for SVM classifier.

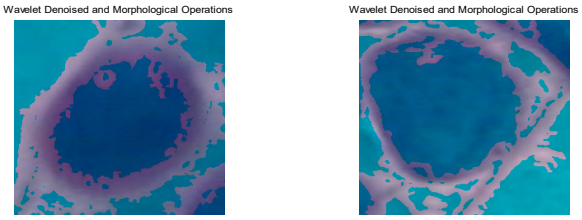

Figure 4: Denoised images of carcinoma-in-situ wavelet and morphological operations.

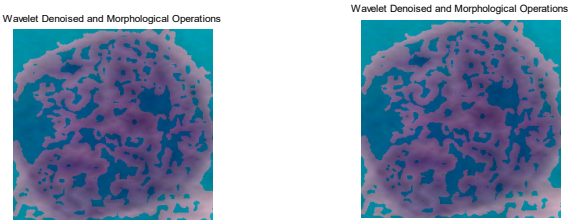

Figure 5: Denoised images of light dysplasia using wavelet and morphological operations.

Table 1: Summary of performance evaluation for SVM and k-NN classifiers

Textural Features	SVM Classifier			k-NN Classifier		
	Acc. (%)	Sen.	Spec.	Acc. (%)	Sen.	Spec.
CP	65.0	0.51	0.36	86.7	0.90	0.00
CS	90.0	1.00	0.45	86.7	1.00	0.00
Energy	65.0	0.80	0.00	86.7	1.00	0.82
Entropy	61.7	0.84	0.00	88.3	0.80	1.00
Cor	63.3	0.00	1.00	86.7	0.80	0.27
Con	81.7	0.73	0.36	86.7	1.00	0.00
Hom	66.7	0.78	0.18	86.7	1.00	0.00
MP	63.3	0.73	0.18	81.7	0.94	0.00

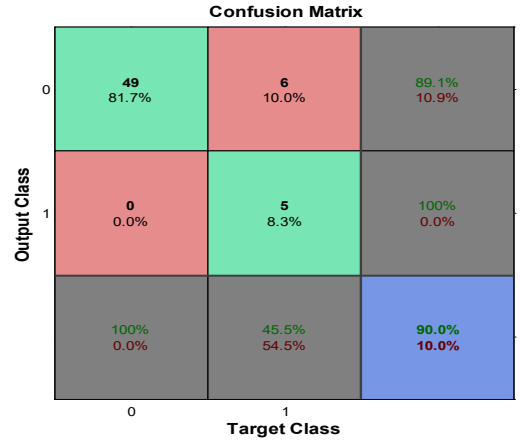

(a) Clustering Shade SVM

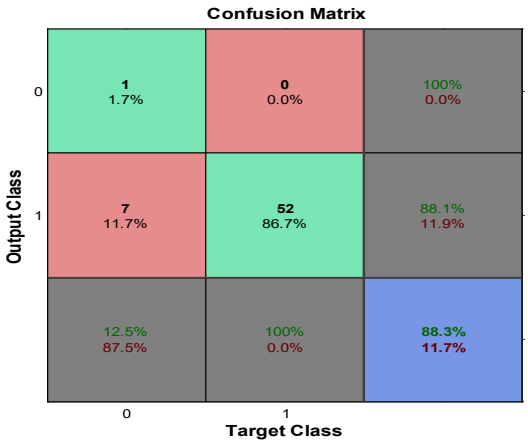

(b) Entropy k-NN

Figure 6: SVM and k-NN confusion matrix classification results with clustering shade and entropy.

5. Conclusion

With this paper our contribution is that we have shown the potential of textural features derived from GLCM in classifying cervical cancer Pap smears images. Generally, the result of the developed system shows that clustering shade SVM classifier out-performs entropy k-NN classifier in terms of classification accuracy of 90.0% and 88.3% respectively and vice visa in terms of sensitivity and specificity.

Acknowledgements

The authors wish thank the Herlev University Hospital for making available smear2005 database from which the test Pap smear image was obtained and Prof. Tope Bello at LAUTECH Teaching Hospital, Osogbo for his assistance and constructive criticism towards the success of this work.

References

[1] U.S. Department of Health and Human Services (2016, May 2). Centers for Disease Control and Prevention [Online]. Available: http://www.cdc.gov/cancer.

[2] American Cancer Society. *Cancer Facts & Figures 2015*. Atlanta: American Cancer Society; 2015.

[3] R. A. Malcolm, *Cancer, Encyclopedia of Life Sciences.* Nature Publishing Group, 2001.

[4] R.R. Jemila and S. Allwin, "Computerized Cancer Detection and Classification Using Ultrasound Images: A Survey" *International Journal of Engineering Research and Development*, Vol. 5, Issue 7, PP. 36-47, 2013

[5] J. Yessi, C. N. Siew and A. A. O. Noor, "Intelligent screening systems for cervical cancer" *the Scientific World Journal*, Vol. 2014, Article ID 810368, pp: 1-15, 2014.

[6] S. Rubina, A. Maheswari, K. K. Deodhar, B. Rekhi and K. C. Murali, "Raman spectroscopic study on classification of cervical cell specimens", *Vibrational Spectroscopy,* vol. 68, pp: 115– 121, 2013.

[7] P. Sukumar and R. K. Gnanamurthy, "Computer aided detection of cervical cancer using pap smear images based on hybrid classifier", *International Journal of Applied Engineering Research,* Vol. 10, no. 8, pp. 21021-21032, 2015.

[8] D. G. Juan, K. Jan and L. Wenjing, "Automatic colposcopy video tissue classification using higher order entropy-based image registration", *Computers in Biology and Medicine* 41, pp: 960–970, 2011.

[9] K. Duraisamy, K.S. Jaganathan and J. C. Bose, "Methods of detecting cervical cancer " *Advances in Biological Research*, vol. 5, no. 4, pp: 226-232, 2011.

[10] H. Xiaotian, P. Bo, M. Masakatsu, E. Ryuichiro, I. Junya, T. Yosuke, C. Ying, W. Xiaochun, Y. Wentao, C. Bin and W. Xiaohua, "A novel highly sensitive and specific flow cytometry system for cervical cancer screening", *Gynecologic Oncology,* 139 pp: 52–58, 2015.

[11] R.U. Deepak, R. R. Kumar, N. B Byju, P. N. Sharathkumar, C. C. Pournami, S. Sibi, E. Bengtsson and K. Sujathan, "Computer Assisted Pap Smear Analyser for Cervical Cancer Screening using Quantitative Microscopy", *Journal of Cytology & Histology,* pp: 1-6, 2015.

[12] J. Coste , B. Cochand-Priollet, P. deCremoux, C. Le Gales, I. Cartier, V. Molinie, S. Labbe, M. Vacher-Lavenu and P. Vielh, "Cross sectional study of conventional cervical smear, mono layer cytology, and human papilloma virus DNA testing for cervical cancers creening", *BMJ*, vol. 326, pp: 733, 2003.

[13] C. Mathers, G. Stevens and M. Mascarenhas (2009), "Global Health Risks: Mortality and Burden of Disease Attributable to Selected Major Risks", in *World Health Organization*, Geneva, Switzerland, 2009.

[14] L. Mingpei, Z. Gaopin, H. Xinyu, M. Gaolin and T. Alade, "Identification of abnormal cervical regions from colposcopy image sequences", in *Proceeding of 21st International Conference on Computer Graphics, Visualization and Computer Vision* Plzen, Czech Republic, 2013.

[15] P.S.P. Rama and H. Ranganathan (2013), "Comparing different classifiers for automatic lesion detection in cervix based on colour histogram", *Journal of Computer Applications (JCA)*, vol. 6, issue 1, pp: 15-18, 2013

[16] S. S. Simi, V. M. Anit and S. Subha, "Comparative study between sparse representation classification and classical classifiers on cervical cancer cell images" *International Journal of Advanced Research in Computer and Communication Engineering*, Vol. 3, Issue 8, 2014.

[17] H. M. Ayubu and Z. Pei, "Pap smear images classification for early detection of cervical cancer", *International Journal of Computer Applications*, vol. 118, No. 7, 2015.

[18] S. P. Aabha and B. B. Ashwini, "Classification of MR Images of Cervical Cancer Using SVM and ANN", *IJSR - International Journal of Scientific Research*, vol. 4, Issue 5, pp: 3-6, 2015.

[19] S. N. Sulaimana, N. A. Mat-Isab, N. H. Othmanc and F. Ahmada, "Improvement of features extraction process and classification of cervical cancer for the neuralpap system", in *Proceeding 19th International Conference on Knowledge Based and Intelligent Information and Engineering Systems*, Procedia Computer Science 60, pp: 750 – 759, 2015.

[20] P. Rathore and P. Dutta, "Implementation of noise removal methods of images using discrete wavelet transform and filters", International *Research Journal of Engineering and Technology*, vol. 03 issue. 02, pp: 870-877, 2016.

[21] A. K. Sevcan, "Diagnosis of cervical cancer cell taken from scanning electron and atomic force microscope images of the same patients using discrete wavelet entropy energy and Jensen Shannon, Hellinger, Triangle Measure classifier", *Spectrochimica Acta Part A: Molecular and Biomolecular Spectroscopy* vol. 160, pp: 39–49, 2016.

[22] M. Misiti, Y. Misiti, G. Oppenheim and J. M. Poggi, "Wavelets and their applications", UK, ISTE, 2007.

[23] M. Sonka,V. Hlavac and R. Boyle, "*Image processing, analysis, and machine vision*", Pp10-210 & 646-670
[24] M. Raghuveer, A.S. Rao and Bopardikar, "*Wavelet Transforms: Introduction to Theory and Application*", Addison-Wesley, 2001.
[25] J. Talukdar, C. K. Nath and P.H.Talukdar (2013), "Fuzzy Clustering Based Image Segmentation of Pap smear Images of Cervical Cancer Cell Using FCM Algorithm, *International Journal of Engineering and Innovative Technology (IJEIT)*, vol. 3, Issue 1, pp: 460-462, 2013.
[26] L. Alessandra, N. Loris and B. Shery, "Multilayer descriptors for medical image classification", *Computers in Biology and Medicine* 72, pp. 239–247, 2016.
[27] R. M. Rangayyan, Biomedical Image Analysis, Boca Raton FL: CRC Press, 2005.
[28] F. Lucas, M.R. Rangaraj, A. M. Guilherme, M. A. Paulo and H. N. Marcello, "Shape, texture and statistical features for classification of benign and malignant vertebral compression fractures in magnetic resonance images", *Computers in Biology and Medicine,* 73, Pp: 147–156, 2016.
[29] D. O. Aborisade, J. A. Ojo, A. O. Amole and A. O. Durodola A.O (2014), "Comparative analysis of textural features derived from glcm for ultrasound liver image classification", *International Journal of Computer Trends and Technology (IJCTT)* – vol. 11 no. 6, pp: 239-244, 2014.
[30] R.M. Haralick R.M., Shanmugam K. and I. Dinstein, "Textural features for image classification", *IEEETrans. Syst.ManCybern*, vol. 3, no. 6, pp. 610–621, 1973.
[31] R. E. Maleki, A. Rezaei and B. M. Bidgoli, "Comparison of Classification Methods Based on the Type of Attributes and Sample Size" Department of Computer Engineering, Iran University of Science & Technology (IUST), Tehran, Iran.
[32] J. Han and M. Kamber, *Data Mining: Concepts and Techniques,* Elsevier, Second Edition, 2006.
[33] E. Kim, and X. Huang, "A data driven approach to cervigram image analysis and classification", In: *Color Medical Image analysis, Lecture Notes in Computational Vision and Biomechanics*, Vol. 6, 113, 2012. N No 2277 - 9
[34] J. Zhang and Y. Liu, "Cervical cancer detection using SVM based feature screening", In: *MICCAI*, Vol. 3217, pp: 873-880, 2004.
[35] V. Vapnik, *The Nature of Statistical Learning Theory*, Berlin, Springer, 1995.
[36] C. Burges, "Tutorial on support vector machines for pattern recognition", *Data Mining Knowledge Discovery,* vol. 2, no. 2, pp; 955-974*,* 1998.
[37] K. Fukunaga, *Introduction to Statistical Pattern Recognition*. Academic Press. USA, 1990.
[38] J.A.K. Suykens, T.V. Gestel, J.D. Brabanter and J.V.B.De Moor, *Least Squares Support Vector Machines.* Singapore, World Scientific Pub. Co., 2002.
[39] S. Francesco and D.L. Giovanni, *Biostatistics for Radiologists*, Italia, Springer-Verlag, 2008.
[40] J. Yessi, A. M. Nor, A. Rohana and H. O. Nor, "Intelligent classification of cervical pre-cancerous cells based on the FTIR spectra, *Ain Shams Engineering Journal* 3, Pp: 61–70, 2012.

ASTES

Advances in Science, Technology and Engineering Systems Journal Vol. 3, No. 4, 224-229 (2018)

www.astesj.com

Special Issue on Multidisciplinary Sciences and Engineering

ASTESJ

ISSN: 2415-6698

A Dual-Band 90-Degree SiGe HBT Active Phase Shifter Based on Band-Pass and Band-Stop Designs Using Dual-Band Resonators

Yasushi Itoh*

Shonan Institute of Technology, Electrical and Information Engineering, 251-8511, Japan

ARTICLE INFO

Article history:
Received: 22 June, 2018
Accepted: 14 July, 2018
Online: 05 August, 2018

Keywords:
Microwaves
Phase Shifter
Differential Amplifier
Dual-Band

ABSTRACT

A dual-band 90-degree SiGe HBT active phase shifter based on band-pass and band-stop designs using dual-band resonators is presented in this paper. The active phase shifter employs differential configuration and has band-pass and band-stop filters in the load circuit. By switching two output ports of the differential amplifier, 90-degree phase shifting has been realized at dual bands. The implemented dual-band active phase shifter using 0.35 micron SiGe HBT has achieved a gain of 9.3 dB and a phase shift of 95 degrees at 0.74 GHz as well as a gain of 8.9 dB and a phase shift of 98 degrees at 0.88 GHz. This is the first paper to present a dual-band active phase shifter based on band-pass and band-stop designs using dual-band resonators.

1. Introduction

This paper is an extension of the work originally presented in the 47th European Microwave Conference, 2017 [1]. Recently, multi-band phase shifters are being developed for the next generation multi-band and multi-mode wireless communication systems using active phased array modules and/or beam-forming networks [2]-[3]. Various types of multi-band phase shifters have been reported, including reflection-type [4]-[5], loaded-line type [6]-[7], vector-sum type [8] and wideband distributed amplifiers with varactor-tuned LC networks [9]-[10]. However, there was no report on the low-pass high-pass phase shifters for the multi-band or multi-mode applications. In order to address this issue, a novel dual-band active phase shifter using band-pass and band-stop designs has been presented in [1]. The active phase shifter is based on a differential amplifier and employs two types of different loads, that is, band-pass or band-stop filters. With the use of abrupt phase shifting characteristics at around cutoff frequencies of the filters [11]-[12], variable phase shifting can be easily achieved at multiple bands by switching band-pass and band-stop filters. Although the conventional low-pass high-pass phase shifters [13]-[14] are limited to single-band operation, band-pass and band-stop designs can make multi-band operation available. In [1], 90-degree phase shifting has been successfully achieved at dual-band by switching two output ports of the differential amplifier. From the viewpoint of multi-band phase shifting as well as high gain, the active phase shifter is considered to be one candidate for achieving various phase shifting at multiple bands, which would be used in the next generation multi-band or multi-mode wireless communication systems with active phased array antenna and beam forming networks. To extend the work [1], the dual-band passive phase shifter based on band-pass and band-stop designs is newly described, showing that the dual-band 90-degree phase shifting is unavailable because of a low Q-factor of the circuit elements. Then how to address this design issue is presented by utilizing 180-degree out of phase performance of the differential amplifier. It is also added in description that an impedance matching has to be taken into account since the band-pass and band-stop filters using dual-band resonators are actually employed in the output matching circuit of the differential amplifier. The outstanding features of the multi-band active phase shifter based on band-pass and band-stop designs over the previously published multi-band phase shifters are high gain and digital control. Thus the measured input and output return losses are newly added for multi-bit applications.

In Chapter 2, the design, simulation, fabrication and performance of the dual-band band-pass/band-stop switching passive phase shifter are presented, showing that the dual-band 90-degree phase shifting becomes unavailable because of a low Q-factor of the circuit elements. In Chapter 3, the design, simulation, fabrication and performance of the dual-band band-pass/band-stop switching active phase shifter are presented, showing that the dual-band 90-degree phase shifting becomes available by utilizing 180-degree out of phase performance of the differential amplifier. Moreover, it is clearly shown as a comparative analysis that the dual-band active phase shifter based on band-pass and band-stop

*Corresponding Author: Yasushi Itoh, 1-1-25 Tsujido-Nishikaigan, Fujisawa, Kanagawa, 251-8511 Japan, +81-466-30-0185 | Email: itoh@elec.shonan-it.ac.jp

designs has an advanced feature in performance and controllability over the previously published multi-band phase shifters.

2. Dual-Band Band-Pass/Band-Stop Switching Passive Phase Shifter

2.1. Circuit Design

A schematic diagram of the dual-band band-pass/band-stop switching passive phase shifter is shown in Figure 1. It employs band-pass/band-stop filters comprised of dual-band resonators and SPDT switches. A 90-degree phase shifting can be accomplished by switching band-pass and band-stop filters.

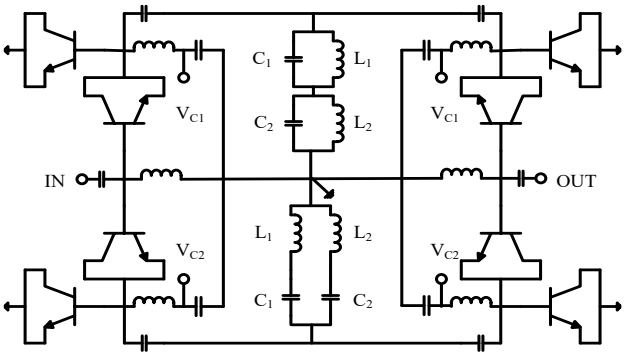

Figure 1: Schematic diagram of the dual-band band-pass/band-stop switching passive phase shifter

A dual-band phase shifting technique by switching band-pass and band-stop filters is illustrated in Figure 2. Figures 2(a) and 2(b) present band-stop and band-pass filters, respectively. The magnitude and phase shift of the band-stop and band-pass filters are illustrated in Figure 2(c) and Figure 2(d), respectively. The band-stop filter is comprised of two parallel LC circuits in a stacked form. It has a single band-stop frequency of f_{3a} and dual band-pass frequencies of f_1 and f_2, which are given as the following equations [11]-[12]:

$$f_1 = \frac{1}{2\pi\sqrt{L_1 C_1}} \tag{1}$$

$$f_2 = \frac{1}{2\pi\sqrt{L_2 C_2}} \tag{2}$$

$$f_{3a} = \frac{1}{2\pi}\sqrt{\frac{1/L_1 + 1/L_2}{C_1 + C_2}} \tag{3}$$

On the other hand, the band-pass filter is constructed from two series LC circuits. It has a single band-pass frequency of f_{3b} and dual band-stop frequencies of f_1 and f_2. f_{3b} is given as the following equation [11]-[12]:

$$f_{3b} = \frac{1}{2\pi}\sqrt{\frac{1/C_1 + 1/C_2}{L_1 + L_2}} \tag{4}$$

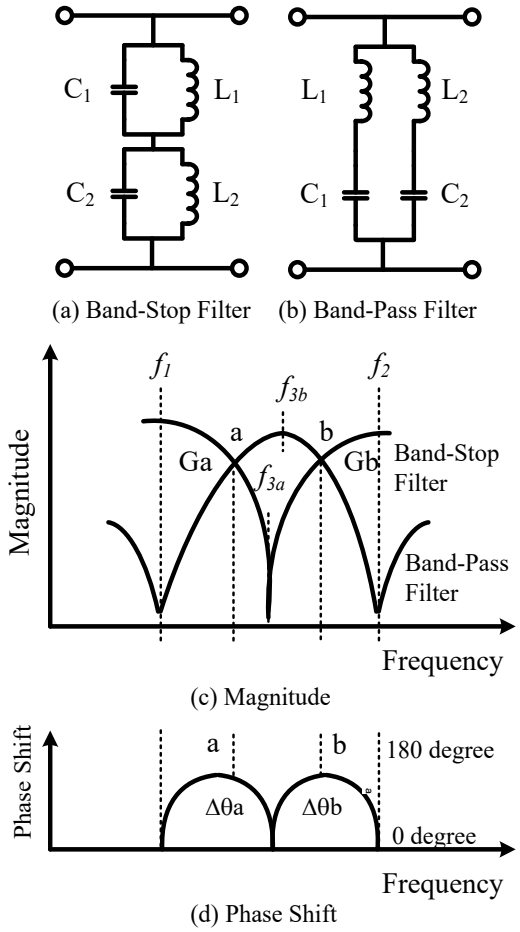

Figure 2: Dual-band phase shifting technique by switching band-pass and band-stop filters

At around transition frequencies in Figure 2(c), the impedance drastically changes from open to short, or short to open. Moreover, a low-pass filter shows a negative phase shift and a high-pass filter provides a positive phase shift. Due to the actual low Q factor, however, the phase shift obtained by switching band-pass/band-stop filters has a limit shown in Figure 2 (d). Now it is assumed that the gain is expressed as G_a, G_b and the phase shift is $\Delta\Phi_a$, $\Delta\Phi_b$ at the frequency points a or b, respectively. The circuit design has to focus mainly on how to determine L_1, C_1, L_2 and C_2 to meet with $G_a = G_b$ and/or $\Delta\Phi_a = \Delta\Phi_b$ at dual-band of the frequency points a and b.

2.2. Circuit Simulation

A circuit simulation is performed by using ADS2016 for the schematic diagram shown in Figure 1. 1005-type chip elements are used as R, L or C as well as 0.35 μm SiGe HBT with an f_t of around 25GHz is used as a switching element by taking into account the operating frequency around L-Band as well as better performance of SiGe HBTs over CMOS devices. The circuit element values are listed in Table 1. The simulated S_{21} and a phase shift ΔΦ is shown in Figure 3. At the frequency points a and *b*, ΔΦ becomes around 80 and 50 degrees, respectively

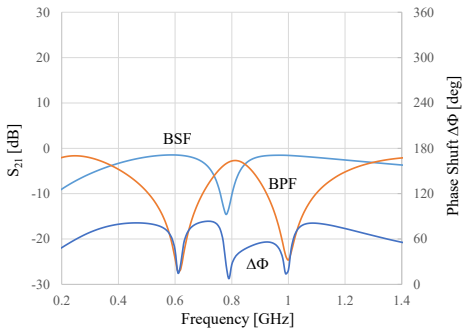

Figure 3: Simulated S_{21} and a phase shift ΔΦ

Table 1: Circuit element values

Element	Value
L_1 [nH]	8
L_2 [nH]	6.2
C_1 [pF]	8
C_2 [pF]	3

2.3. Circuit Fabrication and Performance

A photograph of the dual-band band-pass/band-stop switching passive phase shifter is shown in Figure 4. The phase shifter was fabricated on the FR-4 substrate with a dielectric constant of 4.4 @ 1 GHz and a tanδ of 0.016 @ 1 GHz. 1005-type chip resistors, capacitors, and inductors are mounted on the substrate by soldering. A surface mount type of the 0.35 µm SiGe HBT with an f_t of around 25 GHz (Toshiba MT4S102T) is used as a switching device. The circuit size is 16 x 16 x 1.2 mm^3.

The measured S_{21} and phase shift of the dual-band band-pass/band-stop passive phase shifter are demonstrated in Figure 5. The measured results are basically in good agreement with the simulated results of Figure 3. A slight discrepancy appears for the phase shifting value at G_a and G_b. This is most likely due to the error in the modeling of Q-factor. Bias conditions are V_{C1}=-1V and V_{C2}=+1V for BPF as well as V_{C1}=+1V and V_{C2}=-1V for BSF.

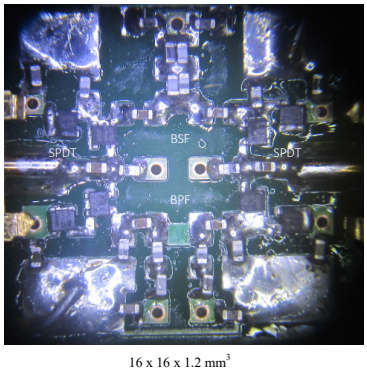

Figure 4: Photograph of the dual-band band-pass/band-stop switching passive phase shifter

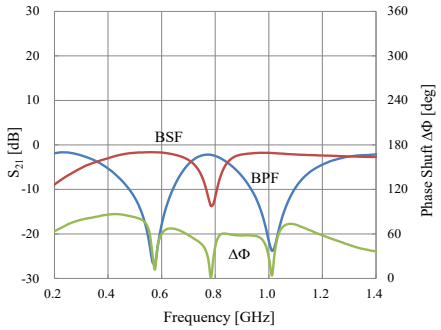

Figure 5: Measured S_{21} and phase shift of the dual-band band-pass/band-stop switching passive phase shifter

3. Dual-band Active Phase Shifter Based on Band-Pass and Band-Stop Designs Using Dual-Band Resonators

3.1. Circuit Design

A schematic diagram of the dual-band active phase shifter based on band-pass and band-stop designs is shown in Figure 6. It is comprised of a differential amplifier and a SPDT switch. The differential amplifier employs two different loads of Z_{L1} and Z_{L2}. Z_{L1} corresponds to the band-stop filter in Figure 2(a) and Z_{L2} in Figure 2(b). To supply a voltage to differential transistor pairs, a large inductance of L_3 (100nH) is connected in parallel with C_1 and C_2. Z_S is a series feedback circuit comprised of two resistors R_S. R_E is a current source. Differential outputs of OUT+ and OUT- are connected to a SPDT switch.

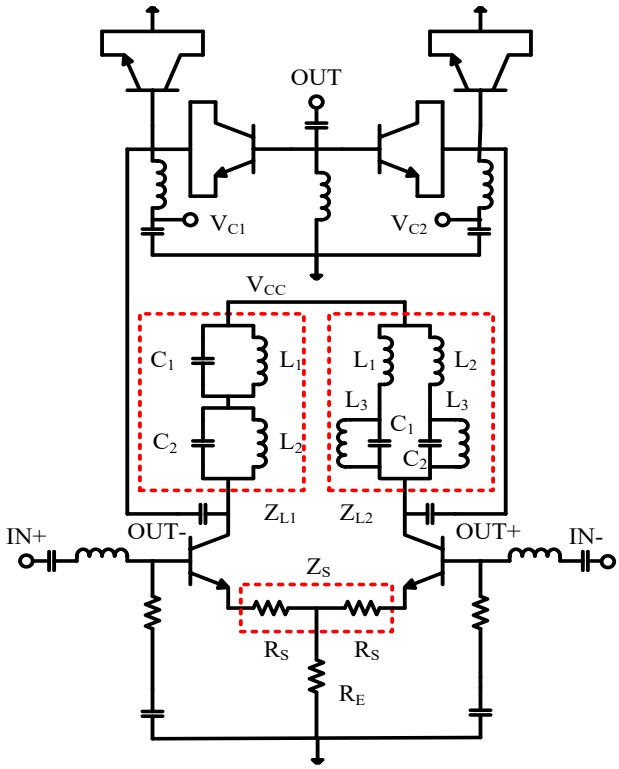

Figure 6: Schematic diagram of the differential amplifier and dual-resonant RLC circuit

The SPDT switch employs a series-shunt configuration for a high isolation. Since the collector and emitter are short-circuited, the transistor acts as a switching diode. V_{C1} and V_{C2} are a control voltage. Input matching circuits employ a lossy match configuration to improve an input matching as well as stabilize the circuit. The base bias resistors for a differential transistor pair are not shown in Figure 6 because of a circuit simplicity. V_{CC} is a supply voltage.

The phase shifting performances are compared for the passive phase shifter of Figure 1 and the active phase shifter of Figure 6, which is shown in Figure 7. Since the output signal from the differential amplifier is already 180 degrees out of phase, the phase shifting performance of the active phase shifter is a complementary value of the passive phase shifter.

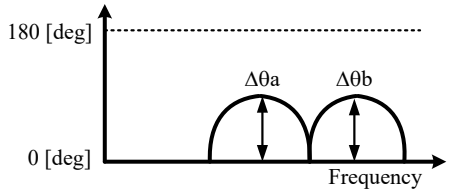

(1) Phase Shift (BPF/BSF Switching)

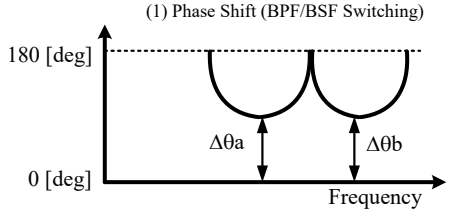

(2) Phase Shift (Differential)

Figure 7 Phase shifting performances of the passive phase shifter (Figure 1 and the active phase shifter (Figure 6)

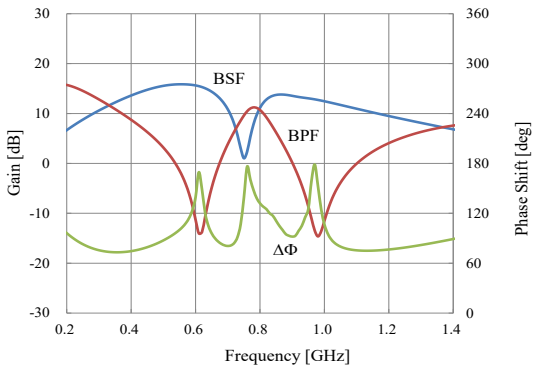

Figure 8: Simulated gain and phase shift of the dual-band active phase shifter using band-pass and band-stop designs

3.2. Circuit Simulation

The circuit simulation has been done by using ADS2016 for the schematic diagram in Figure 6 with the circuit element value of Table 1. V_{CC} is 6 V. V_{C1} and V_{C2} are +1 V or -1 V. Simulated gain and phase shift of the dual-band active phase shifter using band-pass and band-stop designs are shown in Figure 8. First, it is clearly shown that 180-degree phase shifting has been obtained at f_1, f_2, f_{3a} or f_{3a}. Moreover, a phase shift of 80 to 180 degrees can be realized between f_1 and f_{3a} or f_{3b} as well as between f_2 and f_{3a} or f_{3b}. It must be noted that the phase shifting value is greatly dependent on the frequency separation of f_1 and f_2 in addition to Q-factors of the band-pass and band-stop filters.

3.3. Circuit Fabrication and Performance

A photograph of the dual-band active phase shifter using band-pass and band-stop designs is shown in Figure 9. In a similar way as Figure 4, the active phase shifter was fabricated on the FR-4 substrate with a dielectric constant of 4.4 @ 1 GHz and a tanδ of 0.016 @ 1 GHz. 1005-type chip resistors, capacitors, and inductors are mounted on the substrate by soldering. A surface mount type of the 0.35 μm SiGe HBT with an f_t of around 25 GHz (Toshiba MT4S102T) is used as an amplifier device as well as a switching device. The circuit size is 16 x 16 x 1.2 mm^3. The circuit has two SMA connectors on the bottom side for differential inputs and a single SMA connector on the upper side for the output of the SPDT switch.

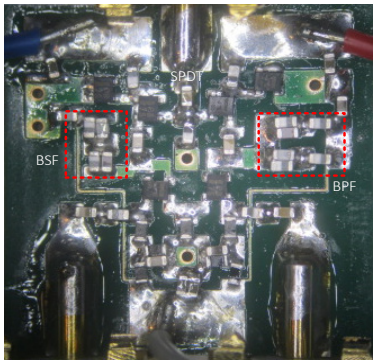

16 x 16 x 1.2 mm^3

Figure 9: Photograph of the dual-band active phase shifter using band-pass and band-stop designs

The measured gain and phase shift of the dual-band active phase shifter using band-pass and band-stop designs using dual-band resonators are demonstrated in Figure 10. The measured results are basically in good agreement with the simulated results of Figure 8. The active phase shifter has achieved a gain of 9.3 dB and a phase shift of 95 degrees at 0.74 GHz as well as a gain of 8.9 dB and a phase shift of 98 degrees at 0.88 GHz. Small gain ripples appear in Figure 10. This is most likely due to the stability problem. Although the stability problem can be improved with the use of the load resisters, the phase shifting amount becomes smaller due to a low Q-factor, which provides a design tradeoff. Bias conditions are V_{CC}=6 V and V_{C1}, V_{C2}=+1V or -1V, respectively.

The measured input and output return losses of the dual-band active phase shifter using band-pass and band-stop designs are demonstrated in Figures 11 and 12, respectively. The input return loss was 11.8 dB at 0.74 GHz and 16.3 dB at 0.88 GHz. The output return loss was better than 8 dB at both 0.74 GHz at 0.88 GHz. As mentioned above, the load resistor also improves the output return loss but the Q-factor becomes worse.

Table 2: Comparative analysis

References	Year	Application	Phase Shifter Type	Dual-Band Method	Active/Passive	Controllability	Frequency	Phase Shifting	Insertion Gain	Return Loss
[4]	2006	WLAN	Reflection	Switching Varactor Diodes	Passive	Analog	2.4/5.2 GHz	120°/180°	-3.0/-5.0 dB	-15/-10 dB
[6]	2011	Doherty PA	Loaded-Line	Switching Capacitive Loads	Passive	Analog	2.1/2.2 GHz	90°	not shown	not shown
[8]	2004	WLAN	Vector-Sum	Switching Phase Shifters	Active	Analog	2.4/5.2 GHz	360°	+4.0/+3.5 dB	not shown
This Work	2018	under R&D	BPF/BSF	Switching BPF/BSF	Active	Digital	0.74/0.88 GHz	90°	+9.3/+8.8 dB	-8 dB

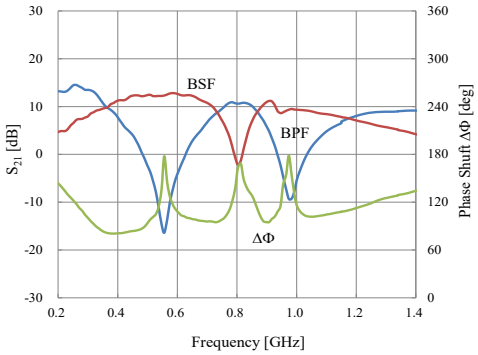

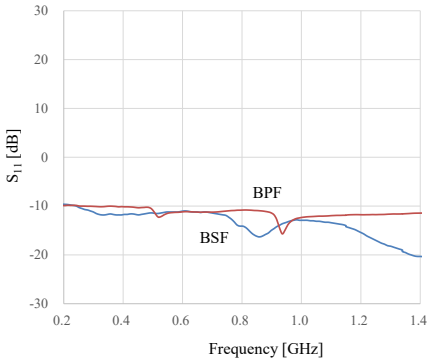

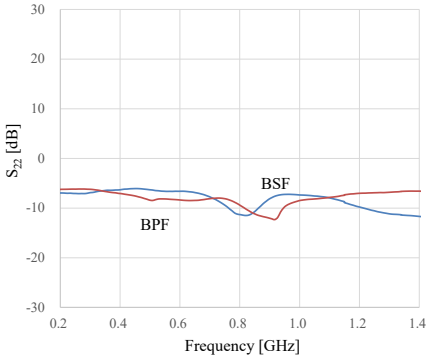

3.4. Comparative Analysis

A comparative analysis is summarized in Table 2. Since this paper is the first report on the dual-band phase shifter using BPF/BSF or LPF/HPF switching, the results obtained from this work are compared with the other multi-band phase shifting methods. All of the multi-band phase shifters in Table 2 have achieved a multi-band phase shifting by switching devices or circuits. The reflection type [4] and the loaded-line type [6] are based on passive phase shifter designs and thus the insertion loss is large. On the other hand, the vector-sum type [8] and our work [1] are an active phase shifter and thus have an insertion gain. Moreover, the phase shifters in [4], [6] and [8] are analogously controlled and thus the complex control is needed. It can be concluded from these viewpoints that the dual-band phase shifter using band-pass and band-stop designs of our work can provide several advantages especially in performances and controllability over the previous ones.

4. Conclusions

Design, fabrication and performance of the dual-band active phase shifter based on band-pass and band-stop designs using dual-band resonators have been presented. It can be clearly shown that the dual-band 90-degree phase shifting is unavailable for the passive phase shifter merely using band-pass and bandstop switching but becomes available for the active phase shifter using a differential amplification. The implemented dual-band active phase shifter using 0.35 μm SiGe HBT has achieved a gain of 9.3 dB and a phase shift of 95 degrees at 0.74 GHz as well as a gain of 8.9 dB and a phase shift of 98 degrees at 0.88 GHz. 180-degree phase shift can be easily obtained with the use of the differential amplifier, In addition, a lower bit of 45-, 22.5- and 11.25-degrees can be achieved by using the same band-pass and band-stop designs. With the use of these techniques, digitally-controlled 5-bit multi-band active phase shifters having a high gain can be realized for use in the next generation, multi-band and multi-mode wireless communication systems.

References

[1] Y. Itoh, H. Takagi, “A Dual-Band 90-Degree SiGe HBT Active Phase Shifter Using Band-Pass and Band-Stop Designs”, in 47th European Microwave Conference, pp. 232-235, October 2017.

[2] T. Nakagawa, M. Kawashima, H. Hayashi, K. Araki, “A 0.9-2.5 GHz Wideband Direct Conversion Receiver", in IEEE GaAs IC Digest, pp. 37-40, 2001.

[3] H. Kamizuma, T. Yamawaki, Y. Akamine, K. Maeda, S. Tanaka, “A Quad Band WCDMA Transceiver with Fractional local divider", in Symposium on VLSI Circuits Digest, pp. 96-99, 2008.

[4] Ocera, E. Sbarra, R. Vincenti Gatti, R. Sorrentino, “An Innovative Reconfigurable Reflection-Type Phase Shifter for Dual Band WLAN Applications", in European Microwave Association, pp. 64-67, 2006.

[5] Y. Shoji, K. Sakamoto, Y. Itoh, “A Dual-Band Reflection Type Phase Shifter Using Active Loads”, in Contemporary Engineering Sciences, Vol. 7, No. 20, pp. 957-964, 2014.

[6] N. Park, J. Gwan, Y. Kim, C. Lee, "Dual-band Switching Doherty Power Amplifier using Phase Shifter Composed of PIN Diode", in 6th European Microwave Integrated Conference, pp. 300-3003, 2011.
[7] M. Maassel, B. D. Braaten, D. A. Rogers, "A Metamaterial-Based Multiband Phase Shifter", in IEEE International Conference on Electro/Information Technology, pp. 533-535, 2014.
[8] D. R. Banbury1, N. Fayyaz2, S. Safavi-Naeini1, S. Nikneshan, "A CMOS 5.5/2.4 GHz Dual-band Smart-antenna Transceiver with a Novel RF Dual-band Phase Shifter for WLAN 802.11a/b/g", in IEEE RFIC Symposium Digest, pp. 157-160, 2004.
[9] Lu, A. Pham, D. Livezey, "On the Linearity of CMOS Multi-band Phase Shifters", in Topical Meeting on Silicon Monolithic Integrated Circuits in RF Systems, Page 4, pp., DOI: 10.1109 /SMIC.2005.1587973, 2006.
[10] Z. El-Khatib, L. MacEachern, S. A. Mahmoud, "Fully-Integrated Multi-band Tunable Linearized CMOS Active Analog Phase Shifter with Active Loss Compensation for Multiple Antenna Wireless Transceiver Applications", in International Symposium on Circuits and Systems, pp. 2966-2969, 2009.
[11] G. L. Matthaei, L. Young, E.M.T. Jones, Microwave Filters, Impedance-Matching Networks, and Coupling Structures, Artech House, ISBN: 978-0-89006-099-5, 1965.
[12] M. Poger, "Microwave engineering education: From field theory to circuit theory", in IEEE/MTT-S International Microwave Symposium Digest, 2012.
[13] Y. Ayasli, S. W. Miller, R. Mozzi, L. K. Hanes, "Wide-Band Monolithic Phase Shifter", in IEEE Trans. ED-31, No. 12, pp. 1943-1947, 1984.
[14] J. P. Comeau, M. A. Morton, J. D. Cressler, J. Papapolymerou, M. Mitchell, "A High-Linearity 5-bit, X-band SiGe HBT Phase Shifter", in IEEE MTT-S Digest, pp. 1668-1671, 2006.

Advances in Science, Technology and Engineering Systems Journal Vol. 3, No. 4, 230-235 (2018)

www.astesj.com

ASTESJ

ISSN: 2415-6698

A Modular Design Process for Developing Humanoid Mobile Robot Viebot

Hung Chan Nguyen[1], Ha Xuan Nguyen[2], Ngoc-Anh Mai[*,3], Lam Bao Dang[2], and Hai Minh Pham[2]

[1]*CMC Institute of Science and Technology, Duy Tan str. 11, Hanoi, Vietnam*

[2]*Hanoi University of Science and Technology, Dai Co Viet str. 1, Hanoi, Vietnam*

[3]*Le Quy Don Technical University, Hoang Quoc Viet str. 236, Hanoi, Vietnam*

ARTICLE INFO

Article history:
Received: 14 June, 2018
Accepted: 30 July, 2018
Online: 05 August, 2018

Keywords:
Modular design process
Humanoid mobile robot
VieBot

ABSTRACT

This paper introduces a design process for developing a humanoid mobile robot, namely VieBot. Stemming from the design process, it is easy to adjust the design and extent robot behaviors to meet customer needs. Our key solution is to split the design into three modules related to robot behavior, kinematic computation and motion control. Base on the results from testbed module under comprehensive testing, the design is gradually improved to satisfy sophisticated requirement of assisting disabled people.

1. Introduction

This paper is an extension of work originally presented in the 2017 IEEE International Conference on Robotics and Biomimetics (ROBIO 2107) [1], which introduced the performance evaluation of a humanoid mobile robot, namely VieBot, using MS Kinect. This paper focuses on a modular design process for developing VieBot.

VieBot is a humanoid mobile robot shaped like a woman (see Figure 1) with some basic components including a head, neck, torso and two arms. It has a vision ability to observe the working environment and to avoid collision via sensor devices working as human senses such as listening, seeing and touching. Its vision ability is based on a Kinect.

Kinect camera is a sensor device using depth and RGB camera images to support robots an outstanding capability to identify human gestures and motions. According to [2], the second generation of the Microsoft Kinect for Windows V2 is based on the Time-of-Flight (ToF) principle and offers a higher resolution and a wider field of view. Based on the properties of high-definition, low-cost image reproduction, this device is often chosen for observing and imitating human behavior and gestures. This device supports many robots in imitating human behaviors in real time or in the recorded data.

Figure :. VieBot's appearance

The kinect images are processed to regenerate the human skeletal structure. Stemming from the regenerated skeletal structure, the robot control system calculates the poses of robot's joints and links by means of inverse kinematic expressions and then controls motions of robot's arm and hand. Based on these flexible motions, VieBot is able to carry out many sophisticated tasks by mimicing complex human behaviors such as greeting,

*Corresponding Author: Ngoc-Anh Mai, Le Quy Don Technical University
Email: maingocanh.atc@mta.edu.vn

guiding, talking, etc. For this reason, VieBot has been applied for several supportive activities similar to other robots in the world such as guiding visual impaired men [3], assistance robots in hospitals [4], or advertising for clients [5].

According to [6], *modular design* is aim to select the best assembly of modules for a given task in a design space. The approach of modular design allows a sufficient, cost-effective and rapid design for different specific tasks. For more details, the modular design process is proposed by a hierarchical approach with three levels of filters, simulations, and tests. In our research, a modular design process is modified from [6] by using parallel sub-modules instead of hierarchical sub-modules. The parallel sub-modules concern the designs of robot's behaviors, kinematic computation for controlling arms and hands, and motion control for travelling.

As stated in [7], behavior-based robot control provides good capabilities to design complex behaviors for robots. The key idea of behavior-based control is a divergence design of a complex behavior by multiple easier designs. This key idea is adopted for building a design module of VieBot's behavior definition.

To control VieBot's arms and hands, a design module is created for computing direct and inverse kinematics. The more flexible the arm and hand are, the more complicated the inverse kinematic problem becomes. The most popular solutions for dealing with the inverse kinematic problems concerning three following methods: interactive method [8, 9], geometric method [10, 11, 12] and inverse-transformation method [13, 14]. In this research, the mechanical structure and joint variable constraints of VieBot are applied for controlling the arms and hands based on the method of inverse kinematic computation presented in [14] with a modification of the extensional constraints on joint variables corresponding to the specific mechanical design of VieBot. The movements of VieBot's arms and hands are controlled based on the result of processing images taken from the MS Kinect V2. The data of Kinect image processing is also used for choosing a suitable solution among multiple ones. The more details of the modification are analyzed in [1].

To travel around surrounding environment, a design module is necessary for motion control. VieBot moves as a mobile robot on a chassis with three wheels. According to [15], static stability requires a minimum of three wheels, with the additional condition that the center of gravity must be contained within the triangle formed by the ground contact points of the wheels. Besides the localization, the path planning is also important to guide the robot moving to a desired target. According to [16], the path planning problem is divided hierarchically into two problems: global path planning and local path planning. In our research, VieBot deals with the second problem based on a Kinect camera and some sonar sensors to easily move to a human target and quickly change direction to avoid obstacles.

In the next section, the modular design process of VieBot is presented with the modules concerning behavior definition, kinematic computation, and motion control. After that, the experiments in a lab environment and in a meeting hall are implemented with regarding specific design modules and evaluating the whole system operation. Finally, the conclusion and future orientation is given.

2. Modular Design Process

The design process for developing VieBot is depicted in Figure 2. It is organized with six modules including CN, BD, KC, MC, DA, and TE.

Module CN contains customer needs such as functionalities, technical requirements, term of service, workplace features. Some other customer needs will be not mentioned such as, time, price, hair color, type of dress.

Module BD defines the basic behaviors based on the existing behaviors designed for VietBot. After defining, these behaviors are sent to the next module for computing kinematics. In case a basic behavior has not defined before, a new definition will be carried out in a sub-module and added to module BD. In fact, the behaviors may be sorted in order of priority. This modular organization allows easy creating of new behaviors.

Module KC provides general direct and inverse kinematic equations for the arms and hands. These equations are supported with technical requirements to form activities matching the identified behaviors. In case there are many solutions due to inverse kinematics, the system must select the best one. The method to select the best solution was described in our other publication [1].

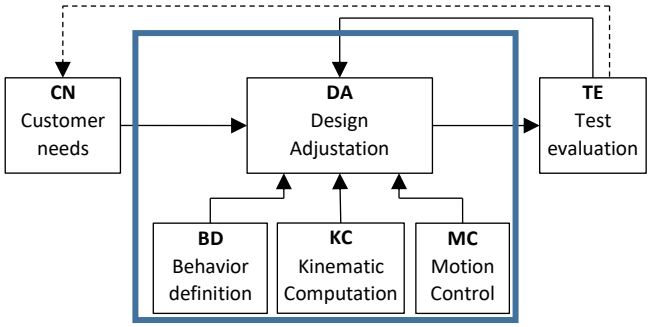

Figure 2: Modular design process for developing VieBot

Module MC provides functions of motion control such as obstacle avoidance and approaching human target. The motion control is computed based on the sensor data and it is constrained by given workplace properties.

Module DA carries out a mechanical design adjustation concerning behavior definition, kinematic computation and motion control for VieBot concerning prioritized behaviors to meet well the customer need. This module provides a concept-to-launch process including modification and refinement.

Module TE performs tests for evaluating the whole design adjustations. Some errors will be detected in this module. Then it feeds back the test results to module DA to ensure the final design meets customer functional or non-functional requirements, and detailed specifications.

It should be noticed that customer needs directly affect module DA in design. The design is refined by cross-checking between the module TE output and the customer needs. If any changes are required, the adjustments are performed again in module DA. This iterative procedure of improvement between TE and DA is performed until satisfying the customer needs.

3. Behavior definition

In this design module, robot behavior definition is a mapping of gestures of human arms and hands to positions and angles of robot's arms and hands as shown in Figure 3.

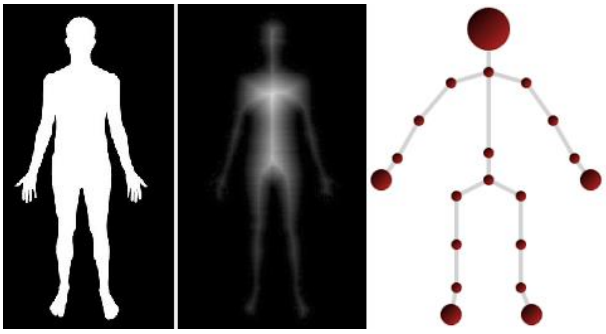

Figure 3: Definition of behavior

Based on customer needs and the behavioral design, the mechanical design inside DA is accomplished to help align the joints and links of the skeleton. For example, a greeting behavior is defined by imitating a human gesture for welcoming by raising hand and waving hand as shown Figure 4. This behavior is designed in module BD with the length of links and joint angles between shoulders, upper arms, elbows, forearms, and wrists. After that, the data of the behavior definition are provided for module DA to design feasible mechanical parts of the arms and their constraints in joint and operational spaces.

Figure 4: Definition of greeting behavior (Left: human, right: Robot mimicking human)

By the similar way, different behaviors are defined to meet the customer needs. Actually, some behavior definition contains a multi-solution, e.g. left hand or right hand, upper elbow or below elbow, palm of hand or back of hand. In these cases, an additional condition must be included to limit number of solutions.

More details of modular system diagram of behavior-based control can be seen in [16].

4. Kinematic Computation

The design of kinematic computation is carried out in module KC. The kinematic structure of VieBot concerning the arms and hands are shown in Figure 5. The arm has six degree of freedom (DoF) corresponding to the six joints involving the shoulder, elbow, upper arm, forearm and wrist. Furthermore, VieBot has one DoF for controlling the five-finger hand to open and close.

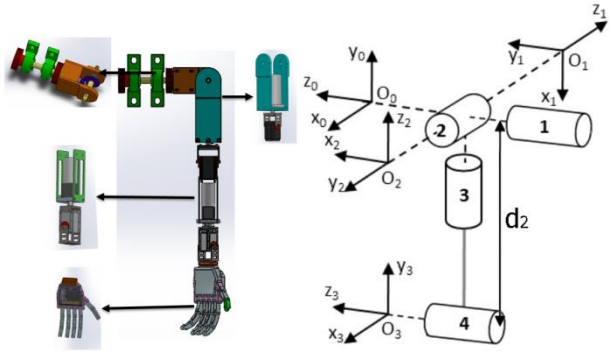

Figure 5: Kinematic structure of VieBot's arm and hand

Joint	θ_i	α_i	a_i	d_i
1	q_1-90°	90°	0	0
2	q_2+90°	-90°	0	0
3	q_3+90°	90°	0	$-d_2$
4	q_4	90°	0	0
5	q_5	90°	0	d_3
6	q_6+90°	90°	a_6	0

Figure 6: Table of Denavit-Hartenberg parameters of VieBot's arm

The kinematic parameters of VieBot's arm is expressed by Denavit – Hartenberg table shown in Figure 6. The kinematic parameters are symbolized as follows:

- θ_i : angle between axes $x_{(i-1)}$ and x_i about axis $z_{(i-1)}$.
- α_i : angle between axes $z_{(i-1)}$ and z_i about axis x_i.
- a_i : length between $O_{(i-1)}$ and O_i along x_i.
- d_i : length between $O_{(i-1)}$ and O_i along $z_{(i-1)}$.
- q_1, q_2, q_3, q_4, q_5, q_6 are angular rotation of respective joints in VieBot's hand.

The kinematic relationship between the shoulder and the hand (considered as the end-effector) is represented by the following equations:

$$\mathbf{T}_6^0 = \mathbf{T}_1^0 \mathbf{T}_2^1 \mathbf{T}_3^2 \mathbf{T}_4^3 \mathbf{T}_5^4 \mathbf{T}_6^5 = \begin{bmatrix} \mathbf{R}_6^0 & \mathbf{p}_6^0 \\ \mathbf{0}^T & 1 \end{bmatrix} \quad (1)$$

$$\mathbf{R}_6^0 = \begin{bmatrix} n_x & s_x & a_x \\ n_y & s_y & a_y \\ n_z & s_z & a_z \end{bmatrix} \quad (2)$$

$$\mathbf{p}_6^0 = \begin{bmatrix} p_x \\ p_y \\ p_z \end{bmatrix} \quad (3)$$

where $\mathbf{T}_6^0, \mathbf{R}_6^0, \mathbf{p}_6^0$ are transformation matrix, orientation matrix, and position matrix of the hand in comparison with the shoulder; Symbols n_x, n_y, n_z, s_x, s_y, s_z, a_x, a_y, a_z stand for rotation vectors of a frame attached to the hand; Symbols p_x, p_y, p_z express position vectors of the hand.

Due to the real mechanical structure of the arm and anthropomorphic motion, the joint variables are constrained to

$$\begin{aligned} 0^0 \le q_1 \le 180^0 \quad & 0^0 \le q_4 \le 120^0 \\ 0^0 \le q_2 \le 180^0 \quad & -90^0 \le q_5 \le 90^0 \\ -90^0 \le q_3 \le 90^0 \quad & -90^0 \le q_6 \le 90^0 \end{aligned} \tag{4}$$

The inverse kinematic equation has the following form:

$$\mathbf{T}_0^6 = \left(\mathbf{T}_6^0\right)^{-1} = \begin{bmatrix} \left(\mathbf{R}_6^0\right)^T & \left(-\mathbf{R}_6^0\right)^T \mathbf{p}_6^0 \\ \mathbf{0}^T & 1 \end{bmatrix} \tag{5}$$

The details of the kinematic computation are written in [1].

This module supports the kinematic computations which are used with the behavior definitions and technical requirements.

5. Motion Control

The design of motion control is performed in module MC concerning avoiding obstacle and planning path. The principle diagram of VieBot's motion control is shown in Figure 7. This diagram is built based on the generic system architecture for robot control in [7] with four functional modules: Sensor-based Localization - SL, Obstacle Avoidance - OA, Target Approaching - TA and Motion Fusion - MF.

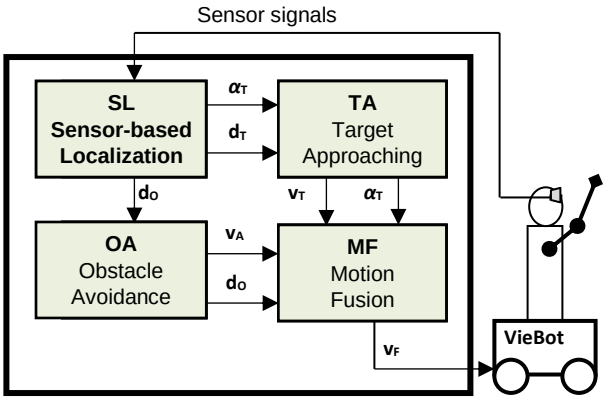

Figure 7: Generic diagram of motion control

Module SL carries out sensor-based signal processing to determine the position and direction of VieBot, human objects and obstacles from the sensors such as Kinect camera and sonar sensors. The outputs of module SL are distance $\mathbf{d}_O$ of obstacle, distance $\mathbf{d}_T$ and angle a_T of a human target closest to VieBot.

Module TA processes information concerning target distance $\mathbf{d}_T$, and target angle a_T to reckon behaviors for approaching the human target. Module TA provides a velocity command $\mathbf{v}_T$ to control the robot approach the human target. It provides a target angle a_T for collaborating motion later.

Module OA calculates behaviors for avoiding obstacles on the way to the target. Module OA give out a velocity command $\mathbf{v}_A$ for driving the robot safely and the obstacle distance $\mathbf{d}_O$ for collaborating motion later.

Module MF performs a coordination between the behaviors of approaching target $\mathbf{v}_T$ and avoiding obstacle $\mathbf{v}_A$ to compute a final velocity command $\mathbf{v}_F$ to control VieBot to the target without any collision.

The motion coordination has the following form:

$$\mathbf{v}_F = k_T \mathbf{v}_T + k_A \mathbf{v}_A \tag{6}$$

where k_T and k_A are functional factors changed after the target angle a_T from module TA and the obstacle distance $\mathbf{d}_O$ from module OA.

6. Experiments and results

VieBot looks similar to a woman with a height of 1.6 meters and a weight of 55kg. Its computer-based brain is built on an Intel Core i7 Mini-PC with 16GB RAM running MS Windows 10. VieBot's data base of robot is connected with MS Azure cloud through 4G LTE mobile network to use advanced Microsoft Azure cloud services including Face API, Computer Vision and Machine learning that support VIEBOT to recognize human face, gender, age and surrounding objects.

6.1. The experiment objective

The experiments are designed to evaluate VieBot's modular designs related to defining robot behaviors based on imitating human behaviors, computing kinematics for arms and hands, controlling its motion for travelling around and approaching a human, performing sophisticated tasks involving making conversation and helping an visual impaired man.

Figure 8: Experiment setup

VieBot communicates with people in the experimental area as illustrated in Figure 8. While Viebot mimicking human gesture, a second Kinect Camera is used to analyze Viebot gestures. Then, two data streams from Viebot Kinect and the second Kinect is compared and processed to calculate errors using MS Excel and some statistical tools.

6.2. Experiment implementation

We did the following three groups of experiments :

GR1: Test the design of human-mimiced behaviors and kinematic computation.

GR2: Test the design of motion control for avoiding obstacle and approaching a human target.

GR3: Performance of sophisticated tasks for helping visual impaired people travel around.

In experiments GR1, VieBot has to mimic some human gestures such as raising and stretching the arm and hand. Its joint parameters are measured and collected to evaluate the accuracy of the design concerning kinematic computation.

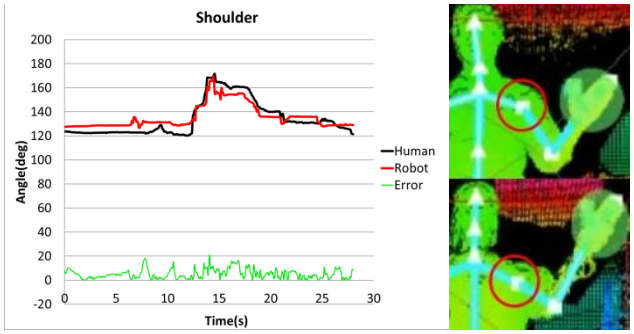

Figure 9: Deviation of VieBot's shoulder joint compared to the human one

The measured differences of the human and robot raising hand behaviors are shown in Figure 9 for the shoulder joint, in Figure 10 for the elbow joint and in Figure 11 for the wrist joint. The black line demonstrates the human movement, the red one illustrates the robot movement, and the green one is the error between the black and red lines.

Base on the analysis, the mean errors of the joint angles concerning shoulder, elbow, and wrist are computed at 4.32%, 5.73% and 3.12%, respectively. These data demonstrate the effectiveness of design taken on the perceived angles of 51 data points.

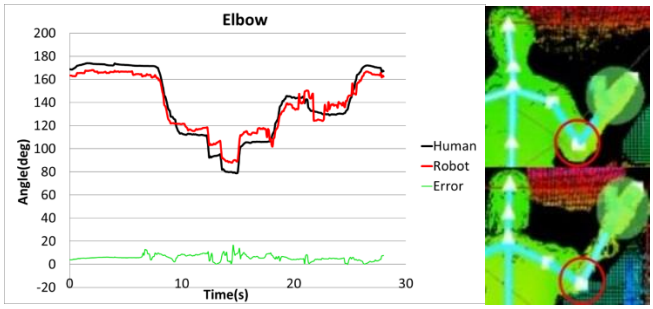

Figure 10: Deviation of VieBot's elbow joint compared to the human one

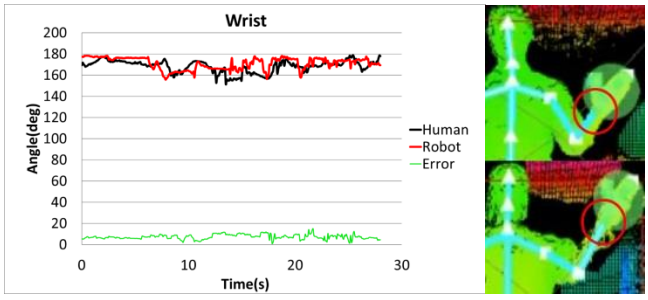

Figure 11: Deviation of VieBot's wrist joint compared to the human one

Figure 12 demonstrates the dependency of the deviations on the magnitude of joint angles. The results show three error trends of the shoulder (blue), elbow (red) and wrist (green). It is noticeable that the trends depend on the joints differently. In other words, the wrist joint errors depend on the input angles much stronger than the others; the shoulder joint errors weakly depend on the input angles; the wrist joint errors strongly depend on the input angles in the range from 150 to 180 degree. These errors are necessary for the design modification in module DA. Bases on them, the design in DA module can be improved by either way: 1) improve the design of mechanical parts or 2) add automatic offset mechanism into the design of kinematic computation inside sub-module KC to be aware of input angle ranges or 3) refine the behavior design inside sub-module BD.

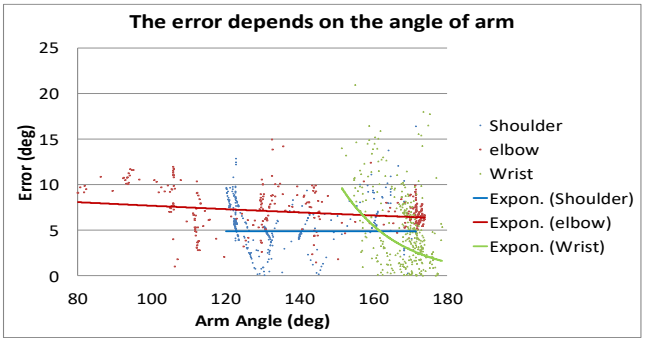

Figure 12: Dependency of deviations on the magnitude of the joint angles

Figure 13: Approaching a human target and avoiding obstacles

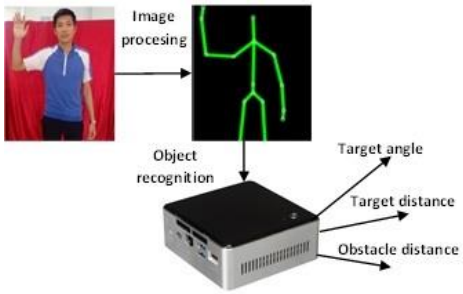

Figure 14: Principle from human recognition to motion control

In experiments GR2, the design of motion control is evaluated by testing the motion of approaching a human target and avoiding some obstacles randomly arranged along the corridor shown in Figure 13. The corridor width is less than 2m and the distance between the obstacles is less than 1.8m. The robot avoids the obstacles with the closest distance of over 15cm and approaches the human target with a distance of about 60cm.

The data of human and obstacle recognition used for motion control is illustrated in Figure 14. The images and depth streams taken from the MS Kinect v2 are processed in a computer Intel NUC. The image processing concerns image enhancement, color processing, segmentation, representation, and object recognition. Stemming from object recognition, the computer extracts object information concerning target angle a_T, target distance $\mathbf{d}_T$, and obstacle distance $\mathbf{d}_O$. These parameters are used for motion control mentioned above in Figure 7.

The experiment results prove that VieBot's mechanical design under the motion control design can help the robot approach a human target safely without collision with obstacle and maintain a safe distance to the human. If any additional behavior is required, it can be added and adjusted inside sub-module BD to satisfy safety requirements.

In experiments GR3, VieBot carried out some sophisticated tasks concerning helping a visual impaired man reach a given position as shown in Figure 15. Firstly, VieBot approached a visual impaired man in a safe distance approximately 60cm, raised its hand toward the man and asked him to give his hand forward and take its hand. Then, VieBot observed the furniture obstacles on the way to plan a path for safely moving and led him to the given position.

Figure 15: VieBot is guiding a visual impaired man to his desired position.

While guiding the visual impaired man, since the furniture in the room is considered as obstacles, the behavior of avoiding obstacles is always activated beside the leading behavior. The test results demonstrate the ability to coordinate the design for complex missions.

7. Conclusion

This paper presents the modular design process of VieBot, a humanoid mobile robot developed in Vietnam. The novel design approach facilitates easy extension of new behaviors as well as improve robot performance and precision both robot arm and movement control.

Three groups of experiment in real-world conditions show the advantage of this modular design approach in quickly satisfying user requirements and improving robot performance in sophisticated activities such as assisting visual impaired people.

In further research, more collaborative scenarios will be studied such as access elevator, assisting disabled people in the variety of environments both indoor and outdoor.

Conflict of Interest

The authors declare no conflict of interest.

Acknowledgment

The authors express their high appreciation for the World Bank project FIRST (Fostering Innovation through Research, Science and Technology) for the financial supports.

References

[1] H. X. Nguyen, H. C. Hung, N. A. Mai, H. T. Nguyen, D. X. Tran, L. D. Dang, H. M. Pham and L. N. Dinh, "Performance evaluation of an inverse kinematic based control system of a humanoid robot arm using MS Kinect", in IEEE ternational conference on Robotics and Biomimetics (ROBIO), 2017, pp. 469-474.

[2] P. Fankhauser, M. Bloesch, D. Rodriguez, R. Kaestner, M. Hutter, and R. Siegwart, "Kinect v2 for mobile robot navigation: evaluatiion and modeling", in International Conference on Advanced Robotics (ICAR), 2015, DOI: 10.1109/ICAR.2015.7251485.

[3] T. C. Pham, "Robotic research trends in the world and robotic research and development in Vietnam", in Journal of Computer Science and Cybernetics, Vol. 26, No. 3, 2010, pp. 197-212.

[4] T. S. Dahl and M. N. K. Boulos, "Robots in Health and Social Care: A complementary Technology to home care and telehealthcare?", in Journal of Robotics, Vol. 3, 2013, ISSN 2218-6581, pp. 1 – 21.

[5] P. Kucsera, "Autonomous advertising mobile robot for exhibitions, developed at BMF, Towards Intelligent Engineering and Information Tech. SCI 1243, 2009, pp. 295 -303.

[6] S. Farritor and S. Dubowsky, "On modular design of field robotic systems", Autonomous Robots 10, 2001, pp. 57-65

[7] N. A. Mai and K. Janschek, "Generic system architecture for behavior-based mobile robot control using fuzzy logic", in International Conference on Control, Automation and Information Sciences (ICCAIS), 2012, pp. 253-258.

[8] Riadh Zaier, "The Future of Humanoid Robots - Research and Applications", Text book, ISBN 978-953-307-951-6, 310 pages, Publisher: InTech, 2012. (Edited Volume)

[9] R. Arnay, H. A. Javier, G. Evelio, and L. Acosta, "Teaching kinematics with interactive schematics and 3D models", in Computer Applications in Engineering Education, vol. 25, Iss. 3, 2017, pp. 420-429.

[10] K. Tokarz and S. Kieltyka "Geometric approach to inverse kinematics for arm manipulator", in Journal of latest trends on systems, vol. II, ISSN 1792-4235, ISBN 978-960-474-214-1, pp. 682 - 687

[11] G. Tevatia and S. Schaal, "Inverse kinematics for humanoid robots," in Proc. IEEE International Conference on Robotics and Automation (ICRA), vol. 1, 2000, pp. 294–299.

[12] J. Wang and Y. Li, "Inverse kinematics analysis for the arm of a mobile humanoid robot based on the closed-loop algorithm," in Proc. of the IEEE Information and Automation (ICIA), 2009, pp. 516–521.

[13] T. Asfour and R. Dillmann, "Human-like motion of a humanoid robot arm based on a closed-form solution of the inverse kinematics problem", in Proceeding of the IEEE/RSJ International Conference on Intelligent Robots and Systems (IROS 2003), 2003.

[14] J. I. Zannatha and R. C. Limon, "Forward and inverse kinematics for a small-sized humanoid robot," in Proc. of the IEEE Intl. Conf. on Electrical, Communications, and Computers, 2009, pp. 111–118.

[15] K. Goris, "Autonomous Mobile Robot Mechanical Design", Report, Vrije Universiteit Brussel, 2005, p. 19.

[16] N. A. Mai, Optical flow-based perception, behavior-based control, and topological path planning for mobile robot using fuzzy logic concepts, TUDpress, 2012.

ASTES

Advances in Science, Technology and Engineering Systems Journal Vol. 3, No. 4, 236-240 (2018)

www.astesj.com

Special Issue on Multidisciplinary Sciences and Engineering

ASTESJ

ISSN: 2415-6698

A novel mixed-mode universal biquad employing plus current output DVCCs

Takao Tsukutani*,[1], Yasutomo Kinugasa[2], Noboru Yabuki[3]

[1] *Professor Emeritus, National Institute of Technology, Matsue College, 690-8518, Japan*

[2] *National Institute of Technology, Matsue College, Department of Electrical and Computer Science, 690-8518, Japan*

[3] *National Institute of Technology, Tsuyama College, Department of Integrated Science and Technology, 708-8509, Japan*

ARTICLE INFO

Article history:
Received: 02 June, 2018
Accepted: 28 July, 2018
Online: 05 August, 2018

Keywords:
Analog signal processing
Mixed-mode biquad circuit
Plus current output DVCCs

ABSTRACT

This paper refers to a novel mixed-mode universal biquad employing plus current output differential voltage current conveyors with grounded passive components. The circuit performs mixed-mode operation with the selection of the input and output terminals, and it enables low-pass, band-pass, high-pass, band-stop and all-pass responses choosing suitable input signals. The circuit needs no component matching constraints for obtaining five basic circuit responses above, and can adjust orthogonally the characteristic parameters by the circuit component. Additionally, the circuit has extremely low sensitivities with respect to the circuit components. A circuit design is performed with PSPICE simulation in order to verify the workability of the circuit.

1. Introduction

Active circuit with high performances (i.e. high frequency operation, low power dissipation, wide dynamic range, etc.) is receiving significant attention. Numerous circuit designs using some active devices such as operational trans-conductance amplifiers (OTAs), second generation current conveyors (CCIIs) and differential voltage current conveyors (DVCCs), etc. have been reported in the literature earlier [1-12].

A DVCC is a very useful active device, and DVCC-based circuit is adaptable to wideband operation. A plus current output DVCC (PO-DVCC) is composed of simpler circuit configuration than a minus current output one. Hence it has low power performance compared to the minus current output DVCC. Several voltage-mode (VM) and current-mode (CM) circuits have been synthesized by employing the DVCCs previously [8-11].

A biquad circuit is a typical second-order building block, and it is used for configuring various types of high-order circuits. It is required for circuit designers that the circuit enables some kinds of circuit responses without any component matching constraints, and that it has orthogonal or independent adjusting for characteristic parameters. Additionally, the circuit configuration employed grounded passive components is much recommended for CMOS implementation.

In actuality, active circuit may be claimed to operate in the mixed-modes (i.e. the VM, CM, trans-admittance-mode (TAM) and trans-impedance-mode (TIM)) from a broad viewpoint. So far, there are some research reports concerning OTA-based mixed-mode biquads [1-3]. But the OTA-based biquads above are not applicable to wideband behavior compared with the DVCC-based ones. If the mixed-mode biquad utilizing the PO-DVCCs is devised, the circuit has some excellent performances (i.e. wideband operation, low power dissipation, etc.) in comparison with conventional ones. However, such PO-DVCC-based biquad has not been well researched as yet.

This article focuses on a novel mixed-mode universal biquad using only the PO-DVCCs with grounded passive components as mentioned above. The biquad circuit configuration is consisted of an integrator loop structure with loss-less integrators [4]. The circuit performs the VM, CM, TAM and TIM operations with the selection of the input and output terminals, and it enables the low-pass (LP), band-pass (BP), high-pass (HP), band-stop (BS) and all-pass (AP) characteristics by suitably choosing the input signals with no component matching constraints. The characteristic parameters ω_0 and Q are set orthogonally by the circuit components. Additionally, the sensitivity analysis leads that the

*Dr. Takao Tsukutani, 2682-1 Watari, Sakaiminato, Tottori, 684-0072 Japan, Contact No 18M-06-086 & Email: t.tsukutani@sea.chukai.ne.jp

biquad has extremely low sensitivities with respect to circuit components.

A versatile mixed-mode biquad employing current controlled DVCCs (DVCCCs) is inducted. A DVCCC is an active device utilized effectively the parasitic resistance at the x-terminal of the DVCC. The circuit is composed of plus current output DVCCCs (PO-DVCCCs) and grounded capacitors. And the circuit performance can be controlled electronically with the bias currents of the PO-DVCCCs.

A biquad circuit design is carried out with PSPICE simulation, and the simulation responses are favorable sufficient over a wideband of frequencies. The biquad has several excellent performances in terms of the wideband operation, low power dissipation, orthogonal adjusting for the characteristic parameters, etc., and it suits well for CMOS implementation.

2. Plus current output DVCC

The symbol of the PO-DVCC is given in Figure 1, and hereinto it shows dual plus current output DVCC.

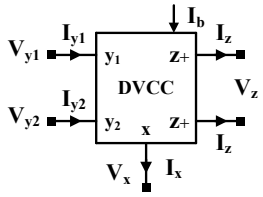

Figure 1: Symbolic representation of PO-DVCC

The PO-DVCC is characterized by the terminal equations [8] below:

$$V_x = V_{y1} - V_{y2}, \quad I_z = I_x \tag{1}$$

The MOS PO-DVCC configuration [11] is shown in Figure 2. It is an active device modified differential difference current conveyor (DDCC) [12], namely one y-terminal with plus polarity is grounded in the DDCC.

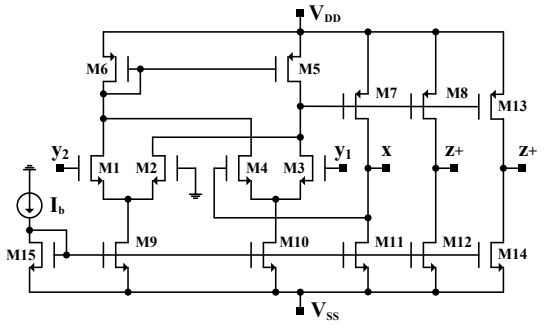

Figure 2: Plus current output DVCC configuration with MOS transistors

3. DVCC-based biquad and its performances

The mixed-mode universal biquad circuit configuration is shown in Figure 3. The circuit is consisted of four single PO-DVCCs, one dual PO-DVCC with grounded resistors and capacitors. This circuit is configured utilizing a second-order loss-less integrator loop structure [4].

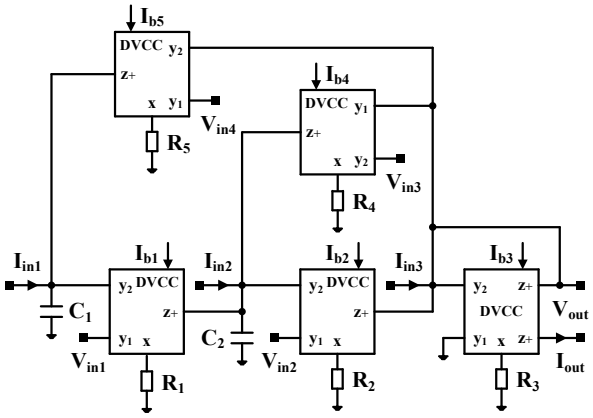

Figure 3: DVCC-based biquad circuit configuration

The voltage and current outputs $V_{out}(s)$, $I_{out}(s)$ are given as:

$$V_{out}(s) = \frac{N_v(s)}{D(s)} \tag{2} \qquad I_{out}(s) = \frac{N_i(s)}{D(s)} \tag{3}$$

where

$$N_v(s) = R_3[\{I_{in3}(s) + \frac{V_{in2}(s)}{R_2}\}s^2 - \frac{1}{C_2R_2}\{I_{in2}(s) + \frac{V_{in1}(s)}{R_1} - \frac{V_{in3}(s)}{R_4}\}s + \frac{1}{C_1C_2R_1R_2}\{I_{in1}(s) + \frac{V_{in4}(s)}{R_5}\}] \tag{4}$$

$$N_i(s) = -\frac{1}{R_3}N_v(s) \tag{5}$$

$$D(s) = s^2 + \frac{R_3}{C_2R_2R_4}s + \frac{R_3}{C_1C_2R_1R_2R_5} \tag{6}$$

It is obvious from the equations above that the circuit performs the mixed-mode behavior with the selection of the input and output terminals, and it enables the various kinds of the circuit responses choosing the input signals suitably.

In the CM operation (i.e. $V_{in1}(s)=V_{in2}(s)=V_{in3}(s)=V_{in4}(s)=0$), the circuit transfer functions are realized as below:

LP: $I_{in1}(s)=I_{in}(s)$, $I_{in2}(s)=I_{in3}(s)=0$

$$T_{LP}(s) = \frac{I_{out}(s)}{I_{in}(s)} = -\frac{1/C_1C_2R_1R_2}{D(s)} \tag{7}$$

BP: $I_{in2}(s)=I_{in}(s)$, $I_{in1}(s)=I_{in3}(s)=0$

$$T_{BP}(s) = \frac{I_{out}(s)}{I_{in}(s)} = \frac{(1/C_2R_2)s}{D(s)} \tag{8}$$

HP: $I_{in3}(s)=I_{in}(s)$, $I_{in1}(s)=I_{in2}(s)=0$

$$T_{HP}(s) = \frac{I_{out}(s)}{I_{in}(s)} = -\frac{s^2}{D(s)} \tag{9}$$

BS: $I_{in1}(s)=I_{in3}(s)=I_{in}(s)$, $I_{in2}(s)=0$

$$T_{BS}(s)=\frac{I_{out}(s)}{I_{in}(s)}=-\frac{s^2+1/C_1C_2R_1R_2}{D(s)} \tag{10}$$

AP: $I_{in1}(s)=I_{in2}(s)=I_{in3}(s)=I_{in}(s)$

$$T_{AP}(s)=\frac{I_{out}(s)}{I_{in}(s)}=-\frac{s^2-(1/C_2R_2)s+1/C_1C_2R_1R_2}{D(s)} \tag{11}$$

The characteristic parameters ω_0 and Q are represented as:

$$\omega_0=\sqrt{\frac{R_3}{C_1C_2R_1R_2R_5}},\quad Q=R_4\sqrt{\frac{C_2R_2}{C_1R_1R_3R_5}} \tag{12}$$

Thus the circuit enables five basic circuit responses with no component matching constraints, and the characteristic parameters ω_0 and Q are set orthogonally by the passive components.

Especially the deviation of the circuit components affects the circuit performance. Hence we examine the effects with sensitivity analysis. The component sensitivities concerning ω_0 and Q are shown in Table 1. These values clarify that the circuit has low sensitive performance. It is an additional note that the sensitivities are not dependent on the component values.

Table 1: Component sensitivities

x	ω_0 sensitivity	Q sensitivity
R_1	-0.5	-0.5
R_2	-0.5	0.5
R_3	0.5	-0.5
R_4	0.0	1.0
R_5	-0.5	-0.5
C_1	-0.5	-0.5
C_2	-0.5	0.5

Successively we examine the performance of the VM circuit. The circuit responses in the VM operation (i.e. $I_{in1}(s)=I_{in2}(s)=I_{in3}(s)=0$) are found with the choice of the input voltages as below:

LP: $V_{in4}(s)=V_{in}(s)$, $V_{in1}(s)=V_{in2}(s)=V_{in3}(s)=0$

$$T_{LP}(s)=\frac{V_{out}(s)}{V_{in}(s)}=\frac{R_3/C_1C_2R_1R_2R_5}{D(s)} \tag{13}$$

BP: $V_{in1}(s)=V_{in}(s)$, $V_{in2}(s)=V_{in3}(s)=V_{in4}(s)=0$

$$T_{BP}(s)=\frac{V_{out}(s)}{V_{in}(s)}=-\frac{(R_3/C_2R_1R_2)s}{D(s)} \tag{14}$$

HP: $V_{in2}(s)=V_{in}(s)$, $V_{in1}(s)=V_{in3}(s)=V_{in4}(s)=0$

$$T_{HP}(s)=\frac{V_{out}(s)}{V_{in}(s)}=\frac{R_3}{R_2}\frac{s^2}{D(s)} \tag{15}$$

BS: $V_{in2}(s)=V_{in4}(s)=V_{in}(s)$, $V_{in1}(s)=V_{in3}(s)=0$

$$T_{BS}(s)=\frac{V_{out}(s)}{V_{in}(s)}=\frac{R_3}{R_2}\frac{s^2+1/C_1C_2R_1R_5}{D(s)} \tag{16}$$

AP: $V_{in1}(s)=V_{in2}(s)=V_{in4}(s)=V_{in}(s)$, $V_{in3}(s)=0$

$$T_{AP}(s)=\frac{V_{out}(s)}{V_{in}(s)}=\frac{R_3}{R_2}\frac{s^2-(1/C_2R_1)s+1/C_1C_2R_1R_5}{D(s)} \tag{17}$$

The VM circuit can also realize the LP, BP, HP, BS and AP transfer functions like as the CM one. The characteristic parameters ω_0, Q and component sensitivities are same as the current-mode ones.

In addition, the TAM and TIM operations are performed selecting the input terminal $I_{in}(s)/V_{in}(s)$ and output terminal $V_{out}(s)/I_{out}(s)$, respectively. Also, the circuit responses are derived with the above-mentioned ways in these operational modes.

4. Current controlled DVCC and biquad circuit configuration

In reality, the DVCC has parasitic resistance existing at the x-terminal, and the resistance varies with the bias current. The parasitic resistance R_x is given as:

$$R_x=K\left(\mu C_{ox}\frac{W}{L}I_b\right)^{-\frac{1}{2}} \tag{18}$$

where μ, C_{ox}, W/L, I_b and K denote the electron mobility, gate oxide capacitance per unit area, MOS transistor aspect ratio, bias current and constant parameter, respectively. Equation (18) shows that the parasitic resistance R_x is electronically adjusted with the bias current I_b. An active device made good use of the parasitic resistance is named DVCCC.

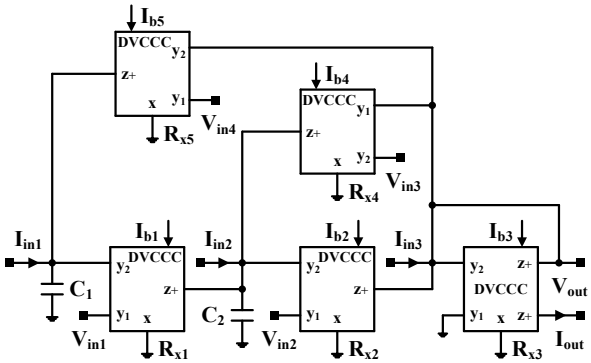

Figure 4: DVCCC-based biquad circuit configuration

Figure 4 illustrates the biquad circuit configuration employing the PO-DVCCCs. The circuit is composed of the PO-DVCCCs and grounded capacitors. The voltage and current outputs $V_{out}(s)$, $I_{out}(s)$ are given replacing the external resistance R_i to the parasitic resistance R_{xi} from (4) to (17). The characteristic parameters ω_0 and Q are also obtained with the same replacement.

The PO-DVCCC-based biquad has electronic tunability for the characteristic parameters with the bias currents. In addition, it can

be expected that the circuit has a high potential for low power performance, because the circuit configuration is without external resistors.

5. A circuit design and simulation responses

In order to confirm our proposal, we tried to realize a CM circuit using PSPICE simulation. As a circuit design, we deal a specification with the cut-off frequency f_0=1MHz, quality factor Q=1.0 and gain constant H=1.0. A macro model of the PO-DVCC in Figure 2 was used in this simulation.

To achieve the specification above, we set that the circuit components were R_i (i=1, 2, 3, 4, 5)=12kΩ and C_1=C_2=12pF, and that the bias currents (i=1, 2, 3, 4, 5)=10μA, DC supply voltages V_{DD}=-V_{SS}=0.8V and input current I_{in}=10μA, respectively.

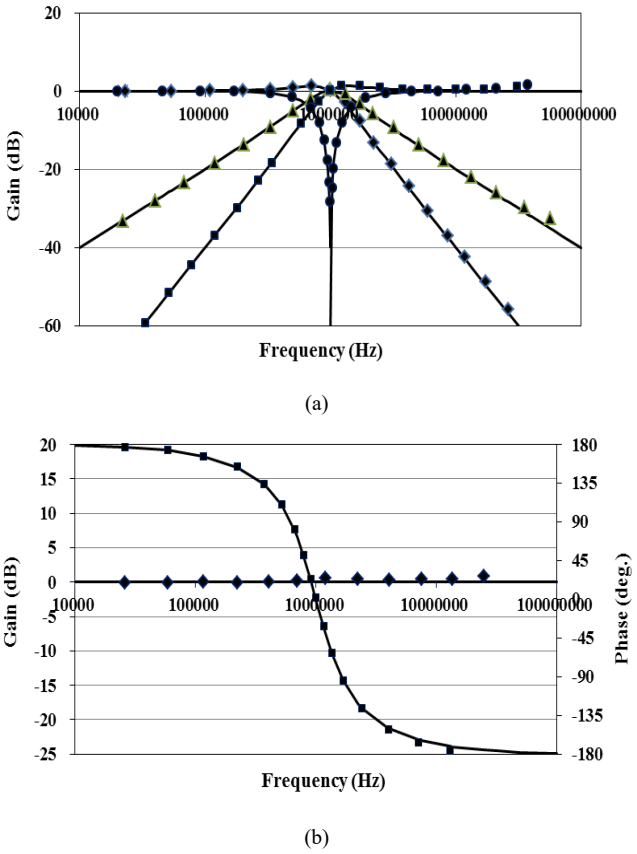

Figure 5: Simulated circuit responses

The simulation responses are given in Figure 5. Figure 5 (a) presents the LP, BP, HP and BS responses, and meanwhile the AP response is indicated in Figure 5 (b). In the figures, the marks signify the simulated responses, and the continuous lines show the theoretical responses. The simulated responses agree very well with the ideal values over a wide range of frequencies. The consumed power dissipation was 0.439mW. It's rather small.

The MOS transistor aspect ratios [10] are given in Table 2. Additionally, we utilized device parameters of MOSIS 0.5μm for other parameters.

Table 2: MOS transistor aspect ratios.

MOS transistors	W / L
M1-M4	20μm / 0.5μm
M5-M8, M13-M15	30μm / 2μm
M9-M12, M16-M19	10μm / 2μm

6. Conclusions

In this paper, we have proposed a novel mixed-mode universal biquad employing plus current output DVCCs with grounded passive components. Additionally, we demonstrated that the circuit accomplishes the mixed-mode behavior, and it enables five kinds of basic circuit responses without any component matching constraints. The circuit is capable of orthogonally adjusting the characteristic parameters by the circuit components. It has also been revealed that the component sensitivities were extremely low in the circuit.

The versatile plus current output DVCCC-based biquad has been inducted. The circuit can adjust electronically the circuit performances with the bias currents.

A circuit design was performed with SPICE simulation, and the simulated responses were sufficient good over a wideband of frequencies.

Our proposed biquad possesses several advantages concerning the wideband operation, low power dissipation, orthogonal adjusting for the characteristic parameters, etc., and it is easily capable of integrating in CMOS technology.

In reality, the DVCC has non-ideal elements (i.e. voltage and current tracking errors, etc.), and especially they affect the circuit performances. An appropriate solution on this must be found out in the future.

Acknowledgment

The authors would like to thank to Mr. David Martin for his helpful suggestions. Especially we are grateful to him for editing our manuscript properly.

References

[1] M.T. Abuelma'atti, et al, "A novel mixed-mode OTA-C universal filter" Int. J. Electron., 92(7), 375-383, 2005. https://doi.org/10.1080/08827510412331295009

[2] C.N. Lee, "Multiple-mode OTA-C universal biquad filters" Cir. Syst. Sig. Proc., 29, 263-274, 2010. DOI 10.1007/s00034-009-9145-0

[3] T. Tsukutani, et al, "A mixed-mode biquad employing OTAs and grounded capacitors" J. Elec. Eng., 6(3), 151-155, 2018. DOI: 10.17265/2328-2223/2018.03.003

[4] E. Sanchez-Sinencio, et al, "Generation of continuous-time two integrator loop OTA filter structures" IEEE Trans. Cir. Syst., 35(8), 936-946, 1988. DOI: 10.1109/31.1840

[5] Y. Tao, J.K. Fidler, "Electronically tunable dual-OTA second-order sinusoidal oscillators/filters with non-interacting controls: a systematic synthesis approach" ibid., 47(2), 117-129, 2000. DOI: 10.1109/81.828566

[6] S.H. Tu, et al, "Novel versatile insensitive universal current-mode biquad employing two second-generation current-conveyors" Int. J. Electron., 89(12), 897-903, 2002. https://doi.org/10.1080/0020721031000121262

[7] J.W. Horng, "High input impedance voltage-mode universal biquadratic filters with three in-puts using plus-type CCIIs" ibid., 91(8), 465-475, 2004. https://doi.org/10.1080/00207210412331294612

[8] H.O. Elwan, A.M. Soliman, "Novel CMOS differential voltage current conveyor and its applications" IEE Proc. Cir. Dev. Syst., 144(3), 195-200, 1997. DOI: 10.1049/ip-cds:19971081

[9] M.A. Ibrahim, et al, "A 22.5MHz current-mode KHN-biquad using differential voltage current conveyor and grounded passive elements" Int. J. Electron. Com., 59, 311-318, 2005. https://doi.org/10.1016/j.aeue.2004.11.027

[10] S. Minaei, M.A. Ibrahim, "General configuration for realizing current-mode first-order all-pass filter using DVCC" Int. J. Electron., 92(6), 347-356, 2005. https://doi.org/10.1080/00207210412331334798

[11] T. Tsukutani, et al, "Novel current-mode bi-quadratic circuit using only plus type DO-DVCCs and grounded passive components" ibid., 94(12), 1137-1146, 2007. DOI: 10.1080/00207210701791085

[12] W. Chiu, et al, "CMOS differential difference current conveyors and their applications" IEE Proc. Cir. Dev. Syst., 143(2), 91-96, 1996. DOI: 10.1049/ip-cds:19960223

ASTES

Advances in Science, Technology and Engineering Systems Journal Vol. 3, No. 4, 241-253 (2018)

www.astesj.com

Special Issue on Multidisciplinary Sciences and Engineering

ASTESJ

ISSN: 2415-6698

Pole-Changing Windings for Close Ratio and 1:N Ratio Using the 3//Y / 3//Y Method

Gabor Kovacs*

Ganz Electric Works, 1095 Budapest, Soroksari ut. 30-34. Hungary

ARTICLE INFO

Article history:
Received: 02 June, 2018
Accepted: 28 July, 2018
Online: 05 August, 2018

Keywords:
Induction motor
Pole changing 3Y / 3Y method
Pole changing 1:N

ABSTRACT

Requirement for pole-changing motors emerged at the very early times of asynchronous motor design. Different solutions have been elaborated and some of them are generally used. One of these solutions in use is the so called pole phase modulation method. The so called 3 Y / 3 Y pole-changing winding being subject of this paper belongs to this group. This paper presents a new approach to this method. A new, complete and comprehensive study is introduced, including features and, moreover, detailed design guidelines. The method is applicable for any pole combination for the so called close ratio without any further particular consideration. As the target of the paper is to provide solution for high power application, it does not deal with balancing methods, but as a novelty, calculates the effect of those disadvantageous phenomena (asymmetries, even harmonics) in order to enable the designer for evaluation and decision. The study also reveals as a novelty that the same method is suitable for wide ratio as well, moreover, a new solution for theoretically infinite ratio expressed in 1:N, with supply voltage system of N phase is proposed. Using this motor, a new and complete drive system has been proposed with subject pole changing motor as core element as the most appropriate arrangement of high power main marine propulsion drive.

1. Introduction

This paper is an extension of work originally presented at the International Conference on Electrical Machines 2018. organized by the World Academy of Science, Engineering and Technology [1].

The original work is extended in terms of

- much wider references are presented and deeply analyzed
- in case of close ratio,
    - the effect of the unavoidable even harmonics are not only generally analyzed but calculation methods are given as well; the limits for omitting balancing measures are clearly given and are supported by calculations
    - calculation methods are given to support the work of a designer of such motor (such as: winding pitch, maximum fundamental torques, air gap induction, harmonic torques, current imbalance).
- in case of wide ratio,
    - the necessity of NxN-times phase supply on the lower pole number is clearly explained by voltage vector diagram; winding pattern also for 1:5 is given demonstrating how to create the winding of any ratio for 1:N by applying N-phase supply system and N//Y / N//Y connection
    - supply strategies are given supported by calculation.

2. Pole changing motors

The objective of motor designers for industrial use was, from the beginning, to provide two speeds in a single motor instead of one speed only.

There are two main methods for pole changing of motors which are most generally used. The first method creates two independent windings in the stator, which is basically two motors in one: both windings can be ideally designed for their respective speeds in the meaning that the number of turns per slot may be chosen freely corresponding to the number of the pole. Due to the fact, however, that only one of the windings works at a time, the size of such motors is much bigger than the size of a corresponding single speed

*Gabor Kovacs, Ganz Electric Works, Email gabor.kovacs.ganz@gmail.com

motor. The method is generally used for close ratio, practically any pole combination can be implemented [2].

The second method is based on changing the connection of parts of a winding called pole amplitude modulation (PAM motor): a part of the winding is connected in a to-and-back direction in order to achieve the basic and then the modulated pole number. Although the entire winding is working on both speeds at any given moment, two inherent disadvantages cannot be avoided: a number of additional terminals are required, therefore the drive must be fitted with a specially designed switching apparatus, and the magnetic field/wave in the airgap is always considerably distorted on the modulated speed. With this method, the possible pole combinations are limited. The method is used both for close ratio as well as for wide ratio.

Another group of methods is the one so called pole phase modulation. With this method, subdivided parts of the winding belong to one phase for one pole number while some of them will be moved to another phase for forming the other pole number. Intensive research has been performed on this field so far. Although the method is suitable for both close and wide ratio, the research is more focusing on the wide ratio nowadays.

Serious proposals for wide ratio might have started with the pioneer works of [3] and [4] both research groups working parallel to each other, reaching almost the same result, proposing 1:3 ratio pole changing winding with ideal (inherently balanced) characteristics. They admit, however, "it is not suggested that this phenomenon is likely to have any application but is of interest as an instructional demonstration". [5] gives design criteria for pole changing motors as a summarizing work of the results till that time. 3 parallel connection was proposed at an early time by that milestone work of [6], with advantageous 6 terminals only. Its strategy is, however, completely different from that given in present paper. Yet, it was expressly stated by them that the method is suitable for close ratio only. Further, each pole combination required special considerations to implement, sometimes with coil omission; and for low power only. Current imbalance between parallel branches was just mentioned, but not discussed, not explained, even not calculated. [7] states to have developed a computer program for any pole combination of close as well as wide ratio prevailing on the previous results of the technique. 1:4, even 1:7 ratio machines were tested but at laboratory size only. [8] gives again a special solution for 1:4 ratio, again for low power. In [9], a 1:3 pole ratio motor was developed for a 9-phase supply on the lower pole number. Moreover, they studied and solved the smooth transition from one pole to the other by the control of the inverter supply, marking out a direction for future research for others. [10] and [11] were dealing with the same motor. The connection for a pole number to the other and for a phase number to the other are not made within the motor but by the control of the 9-phase supply. Therefore, the solution is rather a pole changing system than a pole changing winding. [12] is again a paper with summarizing value by giving general winding design rule for the pole phase modulation. Control algorithms were also developed. [13] and others not listed here are strongly working on eliminating imbalance of the winding for close ratio, proposing successful balancing methods.

These methods, however, although being suitable for low power but cannot be applied for high power motors (e.g. different turn numbers per slot). [14] is one example for the seemingly recent direction of research where as many as 5 different pole numbers are integrated in one motor. The solution is again such that the connection (and the pole changing at all) is not made within the motor but by the control of the supply (each slot being controlled by its own inverter).

Generally, it can be stated that the works are related to low power, laboratory size and they propose particular solution only. Some solutions are proposed for close ratio only while the rest only for wide ratio, respectively. Also the help of the supply is required in many cases for implementing the pole changing effect.

Approach of each paper (and of those not listed here) is different from that presented in this paper; work presented in [15] and [16] was not taken by anybody into consideration.

3. 3//Y / 3//Y Method

Belonging to the family pole-phase-modulation, another alternative is the so-called 3//Y/3//Y method. It is a real pole changing winding. Advantages of this solution are that the entire winding is working at any given moment and only 6 terminals are needed. At the same time, however, certain characteristics may be unfavorable. There may be certain asymmetries and additional even harmonics values. Therefore, calculation methods shall be given for those undesirable phenomena, in order to evaluate their importance.

As the 3// connection is inherently suitable for high power and balancing measures proposed by others are hardly feasible on that field, this paper will not deal with them. Instead, calculation methods will be introduced in order to enable the designer to evaluate those unfavorable phenomena.

It will be shown that both close ratio as well as wide ratio pole changing winding can be implemented by this single method.

4. Basic Idea behind the 3//Y/3//Y Method

Figure 1 (see [15] and [16]) shows a pole-changing connection for 4/6 pole. Instead of the usual 60° phase belt, such connections are prepared with a 120° phase belt and two-layer winding. Figure 1 (a) and (b) shows the upper layer for 4-pole and 6-pole connections, respectively. Figure 1 (c) shows the necessary subdivision into parts being smaller than q slot (slot number per phase per pole) on 4 pole.

The figure indicates the relationship between those subdivided parts of the winding and phases, indicating a 4-pole connection in one case (d) and a 6-pole connection in the other (e). It is clear that certain winding parts belong to a certain phase for 4-pole and to another phase for 6-pole.

In subject case, winding group 1, 4, 7 remains in the same phase; however, all the rest is moved to another phase. Because the groups are connected into series, 15 terminals and an appropriate switch are required.

It is clear that the elements of groups 2, 5, 8 as well as 3, 6, 9 shall be identical among each other; otherwise they could not be interchanged with each other.

Considering those three groups as a whole, it becomes clear that group 1, 4, 7, group 2, 5, 8 and group 3, 6, 9 are also identical with each other allowing them to be connected in parallel.

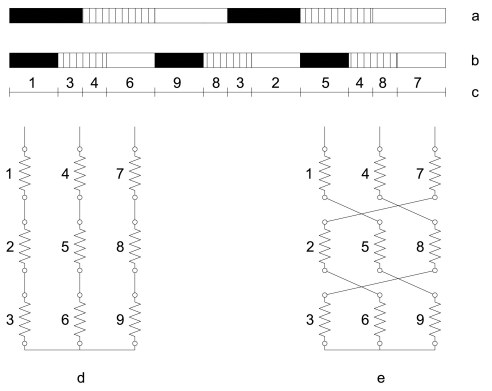

Figure 1. Classical pole changing winding according to [15] and [16]
(a) upper layer for 4-pole connection
(b) upper layer for 6-pole connection
(c) subdivision of the winding
(d) connection of winding for 4-pole
(e) connection of winding for 6-pole

This consideration opens a new way for a much simpler solution.

See connection pattern on Figure 2.

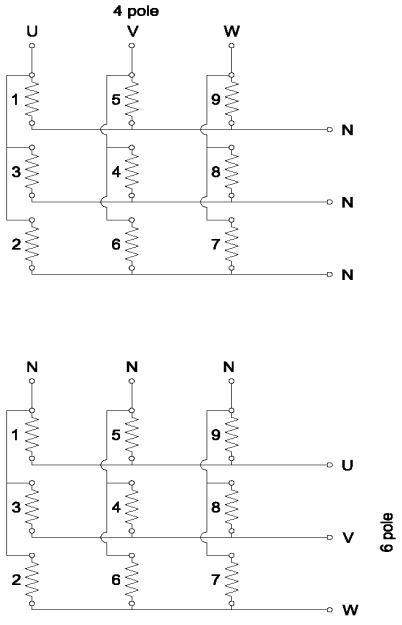

Figure 2. Pole changing winding by 3//Y / 3//Y method

5. Application of the method for close ratio

5.1. Phase Imbalance between Groups to be connected in Parallel

Such question does not arise for the original series connection, as just because of the series connection, the system is inherently balanced. The same is not evident, however, for the parallel connection. Therefore, Figure 1. and Figure 2. shall be considered again showing the origin and the derivation of the method.

The method of derivation for the 6-pole connection will be analyzed first. It is clear that always full poles are connected into the final scheme (no further subdivision for these) and these full poles are obviously always in the right phase angles. Therefore the 6-pole connection is always and inherently balanced.

In another case when 6 pole is the lower pole number, its full poles are, however, necessarily subdivided. Yet these subdivided parts (taken from different poles) are in the end always connected into series in a way as to always create full poles again see and consider Figure 5a. Generally, it stands that if the pole number is an integer multiplier of 6, it is always balanced, regardless of whether it is the higher or the lower pole number.

Returning to the derived 4-pole connection and in order to make the explanation more transparent, some of the already subdivided parts "are further cut" in order to better illustrate the phase angle of the voltage induced in them see Figure 3a. Then, in Figure 3b. the resulting induced voltage pattern are provided for each 3-phase group to be connected into parallel.

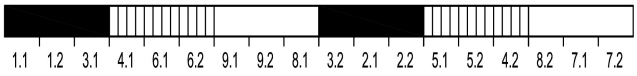

Figure 3a. Sketch for 4-pole connection serving as reference for Figure 1a.

The voltage values of the 3 groups to be connected in parallel are not balanced. It is clear that the vector difference between the supply and the induced voltage of each group (being always 20°) will drive equalizing currents in each group. In order to extend the picture the same pattern is provided for 8 pole as well. Figure 4. indicates the final result only.

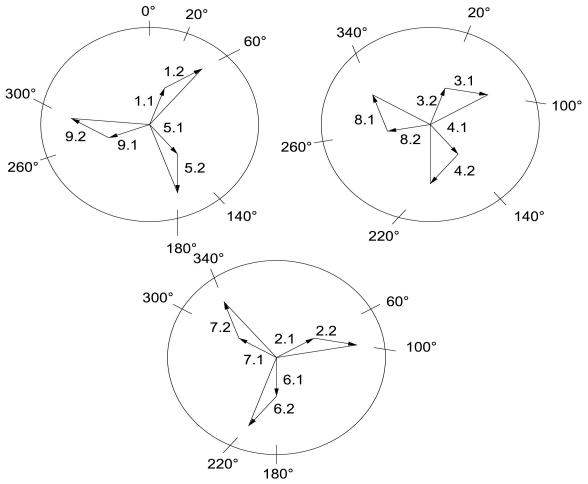

Figure 3b. Voltage vector pattern for 4-pole connection

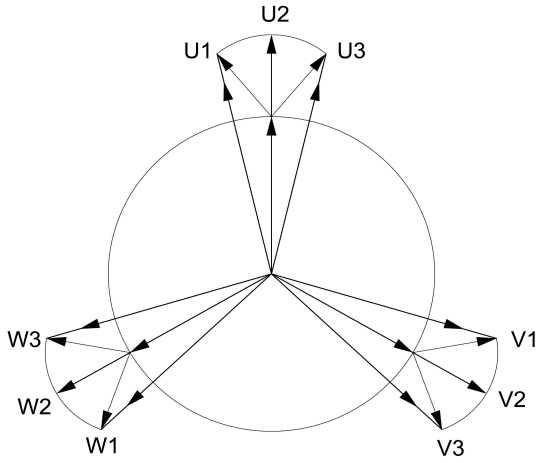

Figure 4. Voltage vector pattern for 8 pole connection acc. to Winding Scheme on Figure 5b.

As seen the imbalance is less. The reason for this is that, in case of 4 poles, all poles are subdivided into 3 parts that results necessarily in no right phase angle. At 8 poles, however, regardless of whether it is the higher or the lower pole number, the "first 6 poles" are always being put together creating full poles (and symbolized by those 3 vectors in the circle being 120° from each other), and only the "last 2 poles" are subdivided in an undesirable way (symbolized by those 3 vectors starting from those previous ones, always 40° from each other). Therefore, the 8 pole connection contains definitely fewer imbalances. The same consideration applies for higher pole numbers. Both Figure 3b and Figure 4 show the vectors in a true scale.

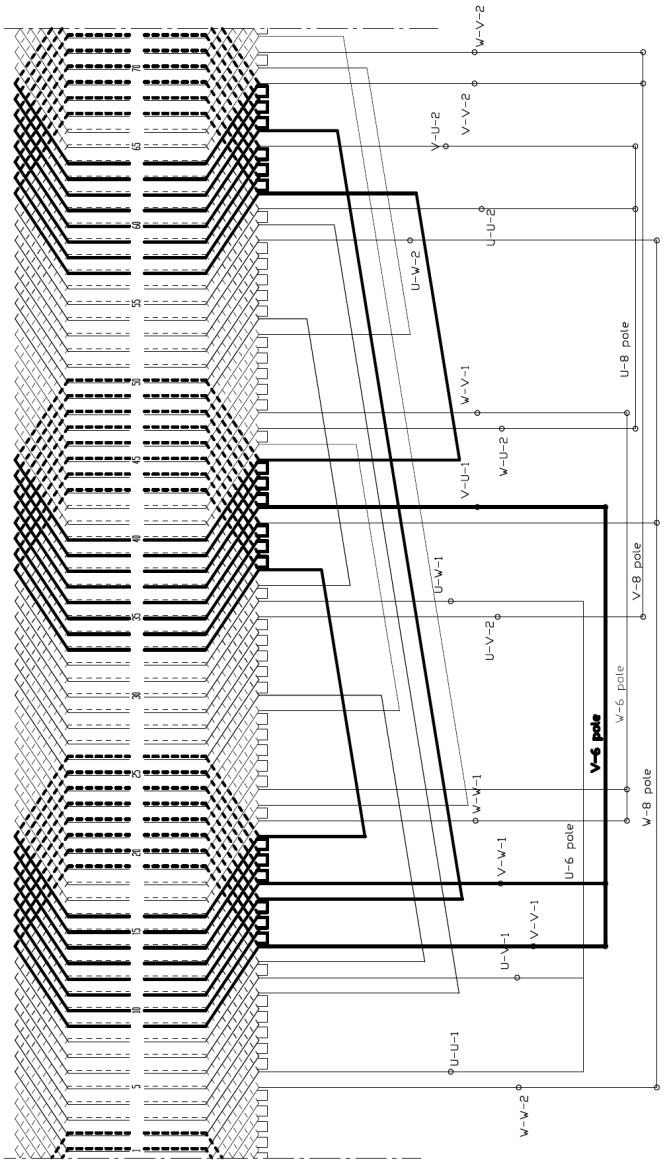

Figure 5a. Winding Scheme when supplied on the terminals marked by 6 pole

The induced voltages as well as (obviously) the supply voltage of each group constitute a symmetrical 3-phase system. It is the vector difference between them which drives the equalizing currents. Therefore no negative sequence currents will arise. The equalizing current will be appr. perpendicular to the magnetizing current in group 1 and group 3, while it will be parallel and in the sense against the magnetizing current in group 2. Then, the superposition method shall be used for the resulting current (and resulting air-gap induction) in each group. Local irregularities (copper losses, air gap & iron core induction) arise in this way. A short approximate calculation method will be given for the equalizing currents in the Appendix.

5.2. Actual implementation

An actual implementation by showing both layers of the winding is presented on Figure 5. as an example and demonstration. It shows how the winding of a real motor looks like in the high power industry, not in a laboratory. From now on a 6/8-pole winding will be taken as an example for further considerations.

Figure 5a shows the result supplied at the terminals marked for 6-pole, while Figure 5b shows the result supplied at the terminals marked for 8-pole.

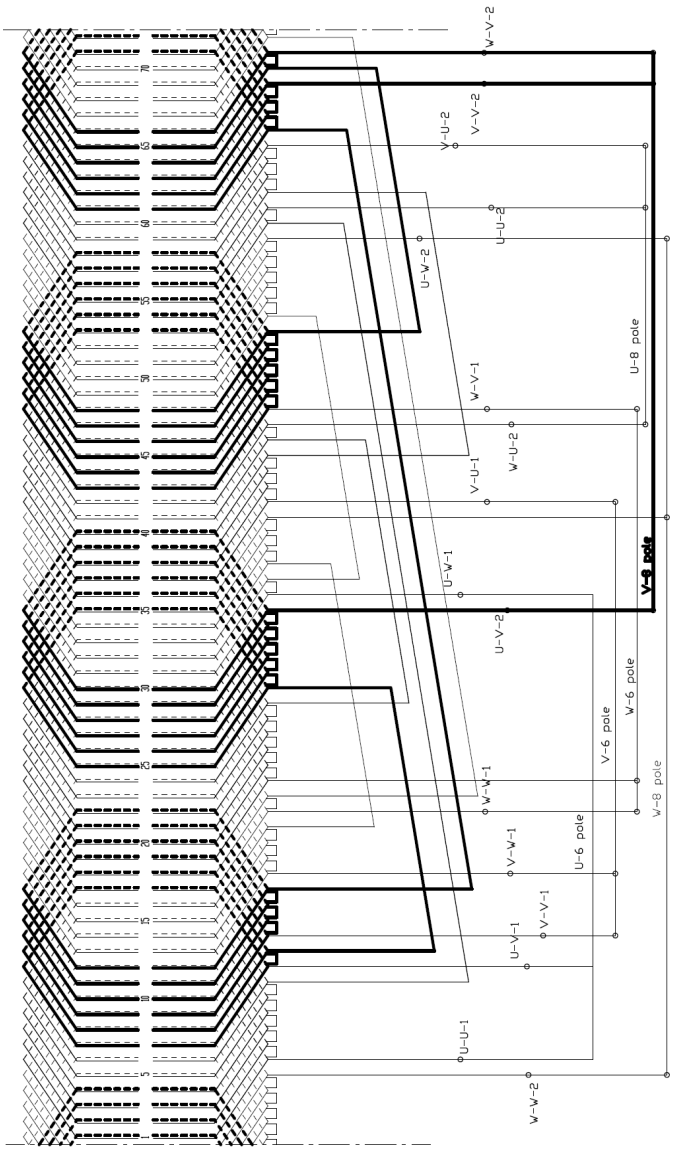

Figure 5b. Winding Scheme when supplied on the terminals marked by 8 pole

There are three terminals for both pole numbers: one group is used for power supply for 6-pole, whereas the other three terminals are used as the star points, therefore these latter remain idle. The opposite is true for 8-pole: the other group of three terminals, used

earlier as star points, is used now for power supply, whereas the former group remains idle as star points. Those terminals, serving actually for star-points, do not need to be short-circuited.

The basic connection scheme in [15] and [16] see Figure 1. implies the concept of subdivision of the winding (=of the poles) and then the re-grouping as well. It is presented there as a particular solution, only for 4/6 poles. By understanding the concept, however, a winding for any pole combination can be created with no limitation. Endwinding connections are "longer" than those of usual single speed motors but note that each of them shall be dimensioned on the 1/3 of rated current only.

5.3. Design Aspects

5.3.1. Stator slot number

The possible stator slot numbers are considered for this method now. Because the slots are subdivided into nine groups, the slot numbers must be integer multiple of 9, no matter which are the pole combinations.

The best is to apply the rule for slot numbers in case of two independent windings [2]. Three-phase motor slot numbers are always integer multiple of 3. Slot numbers possible generally for pole changing motors with two independent windings are integer multiple of a further coefficient of 3 if any of the pole numbers is integer multiple of 6, so the slot numbers suitable for pole changing winding will be inherently integer multiple of 9 in such cases. For the rest of combinations like 8 – 10, 10 – 14, 14 – 16, etc., that above resulting slot number must be multiplied by 3.

5.3.2. Rotor slot number

The subject method does not imply any new requirement regarding rotor slot number, therefore traditional considerations may be applied. Yet, because of the even harmonics, in order to reduce the magnitude of their counteraction with other fields, rotor slot numbers higher than that of the stator may be recommended.

5.3.3. Winding pitch

The main (or perhaps the only) tool for the designer having in hand: the winding pitch. This fact has gained little consideration so far, it is for this 120° phase belt, however, of basic importance. Again, see Figure 5a for the lower pole number and then Figure 5b for the higher pole number.

In case if the pitch would be 1 – 13, this would mean full pitch for 6 pole, the arrangement is symmetrical, that is no even harmonic, the consecutive poles (N – S ...) are equal. It is clear at the first glimpse that the picture for the higher pole number cannot be symmetrical at the same time. In this case, pitch is 240° for the 8-pole, therefore (considerable) even harmonics will evolve.

If the slot pitch is, however, not 1 – 13 but 1 – 10, the situation is just the opposite: the winding of 8 pole is symmetrical (= no even harmonic) and 6-pole is (extremely) not symmetrical. If the pitch is in between, like 1 – 11 as on Figure 5. indeed, both are non-symmetrical but just on a moderate extent.

It is not usual to choose a pitch over 180° for the usual 60° phase belt winding; but this value is exceeded at such pole-changing winding for the higher pole number. The right choice of pitch is the key in designing such pole-changing motor where the actual drive and operation must always be taken into consideration. For example, if the higher pole number, that is lower rated speed, is applied only for starting and the standard operation always occurs on the lower pole number, then selecting a pitch which is symmetrical on the lower pole number (= higher operating speed) is recommended.

The following considerations will help in the decision:

- Max. 2nd harmonic will evolve: pitch degree 270°
- Disappearing 2nd harmonic: pitch degree 180°
- Max. 4th harmonic evolves: pitch degree 135° or 225°
- Disappearing 4th harmonic: pitch degree 180° or 270°

Based on this, the target is to choose a pitch that gives a degree between 135° and 225° on both pole numbers. This is possible for pole numbers being "close" to each other, e.g. 6 – 8, 8 – 10, 10 – 12, etc.. On those pole numbers which are "far" from each other as 4 – 6, 6 – 10, etc., only those pitches are possible where the pitch degree for the lower pole number is between 135° and 225° and the pitch degree for the higher pole number is over 225°. Vicinity of 225°, however, must be avoided in any case.

In order to give proposals in this respect the designer shall make some calculations first; it can be analyzed only after whether the right or even ideal pitch might be determined if such exists at all.

5.3.4. Harmonic Phenomena

In this chapter the winding factors will be determined first and then conclusions will be drawn regarding harmonic leakage, attenuation and harmonic torques. For reasons of generalization, an infinite number of slots will be applied. Then, as soon as the actual slot number is known, the known formulas may be used.

5.3.4.1. Distribution factor

ν =	Distribution factor
1	$\sqrt{3}\cdot 3/2\pi$
2	$-\sqrt{3}\cdot 3/4\pi$
3	
4	$\sqrt{3}\cdot 3/8\pi$
5	$-\sqrt{3}\cdot 3/10\pi$
6	
7	$-\sqrt{3}\cdot 3/14\pi$
	…….

(1)

5.3.4.2. Chording factor:

$$\sin(\nu\cdot\pi/2\cdot y/\tau) \quad \text{where } \tau \text{ is full pitch} \tag{2}$$

Based on the above the differential leakage and the attenuation factor can be calculated acc. to the theory but with even harmonics also involved.

5.3.4.3. Differential Leakage Coefficient:

$$\sigma_1 = \sum_{\nu}\left(\frac{\xi_\nu}{\nu\cdot\xi_1}\right)^2 \tag{3}$$

For $\nu = 2, 4, 5, 7, 8, 10, 11, 13 \ldots$

5.3.4.4. Attenuation Factor:

$$\Delta = 1 - \frac{\sum_{\nu} \eta_\nu^2 \cdot \left(\frac{\xi_\nu}{\nu \cdot \xi_1} \right)^2}{\sum_{\nu} \left(\frac{\xi_\nu}{\nu \cdot \xi_1} \right)^2} \tag{4}$$

where

$$\eta_\nu = \frac{\sin\left(\nu \frac{p \cdot \pi}{N_2} \right)}{\frac{p \cdot \pi}{N_2}}$$

with the N_2 rotor slot number that cannot be infinite here.

5.3.5. Harmonic Torque:

It is not within the scope of this paper to take a position between the different approaches on how to calculate harmonic torques. For the sake of good transparency, the method given in [17] p. 112. (240a) will be followed here:

$$M_\nu = \frac{3}{2} \frac{U}{I_{m0}} \frac{\nu}{\omega} \frac{I_k^2}{1 + \tau_d} \frac{\xi_\nu^2}{\nu^2 \cdot \xi_1^2} \tag{5}$$

Where

U – phase supply voltage
I_{m0} - magnetizing current (fundamental)
I_k - short circuit current (fundamental)
τ_d - differential leakage coefficient

For obtaining a more simple formula that gives quick values for comparison, some further formulas will be introduced and certain approximation will be made as follows:

$\tau_d \to 0$

$M_{\max} = \frac{3}{2} \frac{U^2}{X_s} \frac{1}{\omega}$ fundamental

$I_k = U / X_s$ - with X_s stray reactance

$I_{m0} = U / X_m$ - with X_m magnetizing reactance

By inserting the above three approximate relations into (5) and by rewriting the following formula will be obtained:

$$M_\nu = M_{\max} \frac{X_m}{X_s} \frac{\xi_\nu^2}{\nu \cdot \xi_1^2} \tag{6}$$

If both X_m and X_s will be put in p.u. a quick estimation will be obtained for the maximum torque of the ν^{th} harmonic in relation to the maximum torque of the fundamental wave.

This formula must be applied for $2p_1$ and $2p_2$ pole number separately because also p.u. values of X_m and X_s are different on each pole number.

From parasitic torque point of view the 4th harmonic is the critical one, because its rotation is in the motor range, in other words the sense of rotation is the same as that of the fundamental field. The 2nd harmonic is rotating opposite sense therefore it has no influence on the motor range unless its break-down torque is extremely high and its effect (although acting in brake-range) "reaches" the motor range. Anyway, harmonics' torque may be reduced linearly by reducing magnetizing reactance (= increasing no-load current) see [17] p. 112, equ (240a): which may be a reasonable compromise. 4th harmonic torque has less effect at a drive with parabolic counter-torque like pump, fan etc. Corresponding effect on motor derating k3 is discussed under item *5.3.9.* Derating. of this chapter.

From differential leakage point of view, however, the 2nd harmonic is the critical one, because its influence on the differential leakage may be dramatic, although having highest attenuation. Therefore, for example, pitch degree of 270° is not recommended, although 4th harmonic would disappear but 2nd harmonic is just on maximum.

In case of critical situation regarding too high 4th harmonic, the following method can be applied: the "last" slot or slots in each phase belt will be left without winding. By doing so the phase belt will be less than 120°, or with other words, it gets one-step closer to phase belt 90°. If 90° phase belt were reached, there would be no 4th harmonic – as known from the theory.

Obviously, each "empty" slot requires further derating of the motor, therefore just a moderate use of this method is recommended, also because further harmonics may be generated at the other pole number; see k4 under item *5.3.9.* Derating. of this chapter. Calculations show that practically no change of differential leakage is expected by doing so.

5.3.6. Maximum Fundamental Torque on p_1 and p_2 Pole Numbers, Air-gap Induction

The fundamental air gap flux will be determined first and then the maximum torque will be estimated on both pole numbers. The expression of voltage and flux will be written as known:

$$U = \sqrt{2} \cdot \pi \cdot f \cdot N \cdot \xi_1 \cdot \Phi \tag{7}$$

with f – supply frequency
Φ – flux per pole
N – number of turns per phase.

As the N number of turns per phase is definitely identical on both pole numbers, it follows that $\xi_1 * \Phi$ is necessarily identical also. Because the maximum torque is proportional to

$$M_{\max} \approx p * \xi_1^2 * \Phi^2 \tag{8}$$

the following will be obtained:

$$M_{\max p2} \approx p_2/p_1 \cdot M_{\max p1} \tag{9}$$

This means the absolute value of maximum torque on the higher pole number is definitely higher than that on the lower pole number. The motor operation may be called as "constant power operation".

Furthermore, with

$$\Phi = D \cdot \pi/2p \cdot L \cdot B$$

with D – air gap diameter
L – equivalent length of iron core
B – air gap induction mean value

Inserting it into (7) the following formula is obtained:

$$B_{p2} = (p_2/p_1) \cdot (\xi_{1p1}/\xi_{1p2}) \cdot B_{p1} \tag{10}$$

As important information for the designer, it is established that the air-gap induction on the higher pole number is (much) higher than that on the lower pole number.

5.3.7. Ideal pitch

Because the pitch is practically the only tool in the hand of the designer the question arises whether the optimum or "ideal" pitch may be found or not. Figure 6. will help in the consideration.

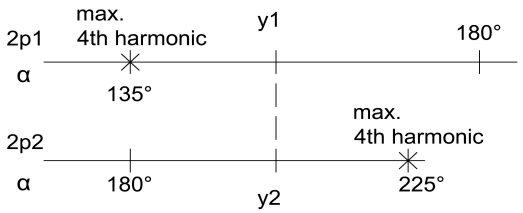

Figure 6. Sketch for explaining "ideal" pitch

The sketch indicates the electrical angles of both pole numbers, around 180° as "full pitch", as well as those dangerous pitches which should be avoided. The coincidence of y_1 and y_2 demonstrates that the mechanical pitch is necessarily identical. Therefore

$$y_2 = p_2/p_1 \cdot y_1$$

While moving y_1 towards 180°, the harmonic content (incl. 4th harmonic) on the lower pole number will always be more and more advantageous, but, at the same time it will always be more and more disadvantageous on the higher pole number until it reaches unacceptable extent, and vice-versa see also in *5.3.3.* above.

The right pitch shall be somewhere in between. A possibility to choose y_1 and y_2 in a way that

$$180^0 - y_1 = y_2 - 180^0$$

At such choice the winding factors of all harmonics as well as the fundamental will be identical on both pole numbers.

The resulting pitches are

$$y_1 = \frac{p_1}{p_1 + p_2} \cdot 360^0 \quad y_2 = \frac{p_2}{p_1 + p_2} \cdot 360^0 \tag{11}$$

Harmonic torques p.u. value as given in (6), however, will still not be identical because they are further dependent on the ratio of X_m and X_s, and those are different for each pole number. Further consideration is necessary in this respect.

Passing over detailed deduction it is obtained that

X_m is proportional to $(1/p)^2 \cdot \xi_1^2$

while X_s however, remains approximately constant (more precisely it reduces slightly).

It is obtained at the end that the ratio X_m / X_s valid for the lower pole number will change when connected to the higher pole number according to the following way:

$$(X_m/X_s)\big|_{p2} \approx \left(\frac{p_1}{p_2}\right)^2 \cdot \frac{\xi_{1p2}^2}{\xi_{1p1}^2} \cdot (X_m/X_s)\big|_{p1} \tag{12}$$

This expression shall be inserted into (6) for direct calculation of harmonic torques on the higher pole number. It is underlined that the formulas give the harmonic torque referred always to its own maximum fundamental torque (in p.u.).

Targeting equal 4th harmonic torque (p.u.) on both pole numbers as a good compromise, the above formula tells that y_1 and y_2 according to (11) will not provide the expected results as the harmonic torques will be much less for the higher pole number. Therefore, y_1 may be moved a bit towards 180° by reducing chording on the lower pole number. Because of the non-linearity (sin() in both winding factors, ξ^2 in the torque expression) this "ideal" pitch cannot be given in a definite formula.

y_2 – obviously - must not be moved too close to 225°.

For a full picture, the calculations by the formulas in *5.3.4.3* and *5.3.4.4* give that

- this "targeted" pitch (although for infinite slot numbers) will result in such "high" magnitude of differential leakage coefficients as given in the literature for q = 3 or so. This is due to the presence of (low-order) even harmonics.
- at the same time it results in lower attenuation factors than given in the literature due to the strong attenuation effect of the rotor just on the low-order even harmonics.

Expected approximate harmonic torques for 6/8 pole at that chording for best compromise:

6 pole		8 pole	
M_4 / M_{max}	0.16	M_4 / M_{max}	0.16
M_7 / M_{max}	0.007	M_7 / M_{max}	0.006
M_{10} / M_{max}	0.023	M_{10} / M_{max}	0.001

This example represents the limit of application in respect of pole ratio (min. 0.75) without balancing measures.

5.3.8. Parallel Connection of the Winding

For high power motors, further parallel connection of the winding may become necessary. It is, unfortunately, not possible for the smallest pole numbers, e.g. for 6-8 pole or such. It is possible, however, for higher pole numbers: for 12-16 pole further 2// connections, for 18-24 pole further 3// connections become possible, for example.

5.3.9. Necessary Derating of the Basic One-Speed Motor

Based on the above considerations, the necessary derating of such double-speed motor can be defined compared to the basic single-speed motor. To put it differently: considering a certain size of a single-speed motor with P [MW] power and $2p_1$ pole number, what can be the power P1 of such double-speed motor with the same lower pole number $2p_1$. P2 belonging to $2p_2$ (the higher one) is not important, because the load at the higher pole number is always considerably lower.

There are 4 factors for necessary derating:

$$P1 = k1 * k2 * k3 * k4 * P \tag{13}$$

Each coefficient is < 1, according to the followings:

k1 derating due to the ratio of the winding factor for 60° and 120° belt and for the pitch. The belt factor ratio is always the same: 0.827 / 0.955 = 0.866 which is the value of inherent derating necessity derived directly from the theory of this method. Then, this should be multiplied by the ratio of the actual (lower pole number) pitch shortening factor compared to the usual 5/6 shortening factor. This later ratio is usually again less than 1.

k2 derating due to excess loss caused by the balancing currents due to imbalance of stator phase angles. This only applies in case the lower pole number is not integer multiple of 6, otherwise k2 = 1

k3 derating necessity due to eventual excess loss caused by eventual necessity of increasing no-load current, which causes the rated current to increase because of the decreased cos φ. For further details see Harmonic Torque *5.3.5.*

k4 derating necessity in case where phase belt should be less than 120°, again see Harmonic Torque *5.3.5.*

Overall derating necessity is expected to be 75 – 80% (example: a 6 MW single speed motor size may be loaded by 4.5 – 4.8 MW if wound for 3// Y / 3 //Y for any pole number).

5.4. Conclusion, proposal for application

Any pole number combination can be implemented by the prescribed method.

Based on the voltage imbalance and the calculation of the harmonic torques it can be established, however, that the method may be applied

- for 6 poles and above and
- for pole ratios of 0.75 and higher (very close ratios)

without any balancing measures in the winding.

The method is recommended especially for driving such machines as pumps, fans etc.

It is underlined that such pole combinations like 4-6, 6-10 etc. can be implemented also. The high unfavorable effects of the even harmonics and phase imbalance appearing here may be eliminated by balancing measures.

6. Application of the method for wide ratio

6.1. General Considerations

Now it will be investigated as a new field of research whether the method can or cannot be applied for pole numbers being very far from each other, generally called wide ratio. The easiest investigation involves a 1 : N ratio where N is integer.

If N is even, such as 2, 4, 8, etc. and symmetrical pitch (=full pitch) is chosen on the lower pole number, as logical first approach for avoiding even harmonics, there will be no excitation on the higher pole number (it is easy to understand that U and –U are in the same slot and therefore magnetomotive force of each slot is zero). As a consequence, such motor simply does not work. If, however, y_1 will be moved to either direction, but preferably towards lengthening, the machine will work on both pole numbers, but even harmonics appear also on both pole numbers; the calculation method can be obtained again from the previous chapter.

If N cannot be divided by 3 such as 4, 5, 7, 8 etc. the 3// connection cannot be implemented at all, because the 3 groups cannot be identical, as one phase is always and considerably different from both the other phases.

If N = 3 (3, 9 etc.), however, like a 6 – 18 pole changing winding, the result is absolute ideal, no even harmonic will appear on either pole number, therefore the motor's behavior on both pole numbers is identical to the corresponding single-speed motor.

This statement may be supported very easily.

If "full pitch" will be chosen on the lower pole number, as the logical first approach for avoiding even harmonics as before then the same mechanical pitch will result in

$$y_2 = p_2 / p_1 \cdot y_1 = \ldots = N \cdot 180^0$$

electrical pitch for the higher pole number.

If N is even the electric angle for the higher pole number is always

$$y_2 = N \cdot 180^0 = \ldots = 360^0$$

It means that there will be no fundamental wave on $2p_2$ at all.

If N is odd, however, the electric angle for the higher pole number is always

$$y_2 = N \cdot 180^0 = \ldots = 180^0 \text{, full pitch}$$

This is the reason why the machine will work as a standard one on both pole numbers, but always with full pitch. No further

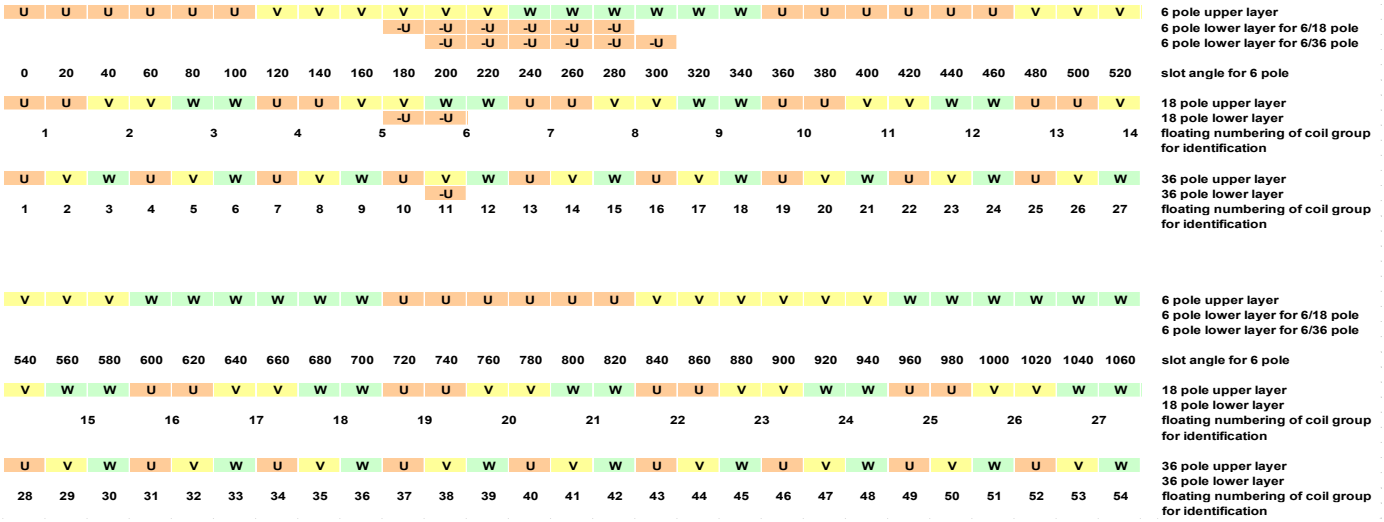

Figure 7. Slot distribution pattern for 1:3 as well as for 1:6 pole ratio

scientific considerations are required and the designer may apply basically his standard software (but for 120° phase belt).

However, further investigation shows that in such cases (N=3, N=6 etc.), phase asymmetry will always appear again, on the lower pole number only, the nature of which is the same as in *5.1*, but the magnitude is much higher. It is even so high that a solution must be found to eliminate it.

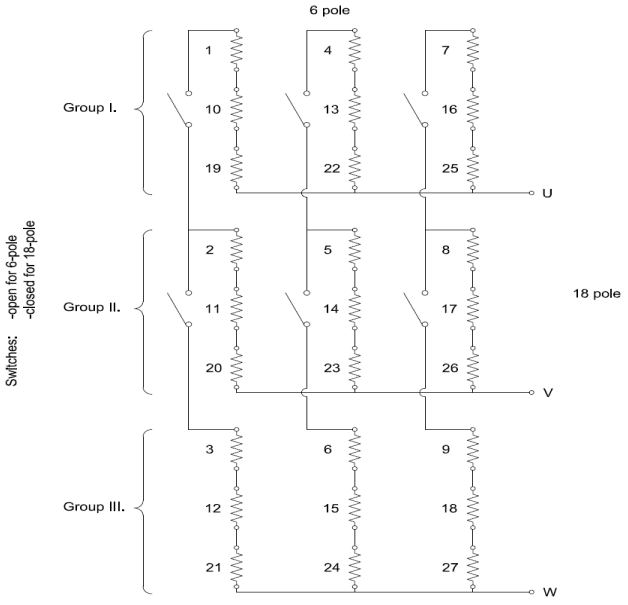

Figure 8. Pole changing connection pattern for 1:3 pole ratio

6.2. Specific Considerations for the Lower Pole Number

The lower pole number on Figure 7. will be discussed again. Comparing it with Figure 8.. it comes clear that Group I. contains always the "beginning part" of the pole, Group II. the "middle part", Group III. the "last part".

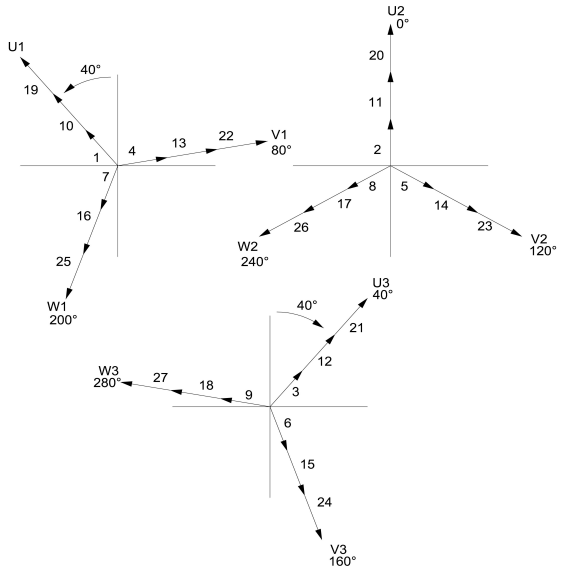

Figure 9. Voltage vector pattern for 1:3 pole ratio

Supplying the – parallel connected – Group I, Group II and Group III. with the same 3-phase system, then considerable balancing currents will be generated by that always 40° phase imbalance. Although there is wide ratio here, the approach of calculation method given in Appendix may be applied. Nevertheless, no need for any further calculation (neither that of extreme difference in the currents nor additional torque ripples in the motor caused by local air gap induction variation) to see that it exceeds any tolerance range.

Instead of looking for solutions in the machine (losing its simplicity) a solution in the supply is more recommended this time.

Group I. shall be supplied
by a 3-phase system -40° – 80° – 200°
Group II. shall be supplied
by a 3-phase system 0° – 120° – 240°
Group III. shall be supplied
by a 3-phase system 40° – 160° – 280°

Just a clear 9-phase supply system has been reached in this way.

Consequently, the only possibility for avoiding balancing currents in pole numbers 2p – 3x2p or 2p – 6x2p, etc. is to have nine terminals for the lower pole number.

Such solution was already proposed by [9], but through a completely different way of consideration and actual connection arrangement, and then continued in [10] and [11] but as a result of a particular consideration, only for 1:3 ratio.

For creating 9-phase system, frequency converters may be used. The converter is connected into 3-parallel (not unusual for high power) and the regulation of each parallel branch is shifted by 40° from each other, see Figure 10.

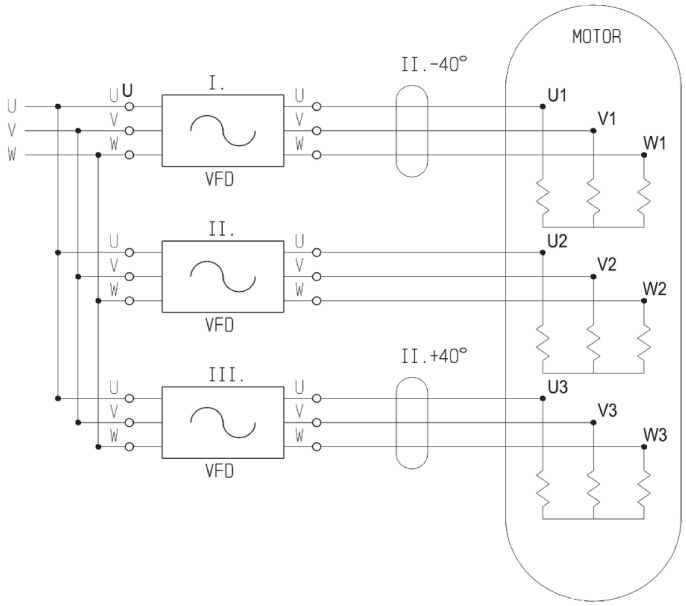

Figure 10. Proposal for supply of the stator winding on the lower pole number

As a consequence, no further derating other than the inherently k1 = 0.866 is necessary to apply in case of 1:3 (1:9 etc.) pole combination.

Such shifting of 40° is not necessary for the higher pole number, which may thus preserve its 3-phase winding – 3-phase supply – 3-terminal. When changing the supply to the higher pole number, the nine terminals of the lower pole number (always 3-3-3 of the same phase) must be short circuited by a separate switch.

The same energy supply concept shall be applied for the lower pole number in case of 6-36 pole, 6-54 pole etc. that means for 1:6, 1:9, etc. pole ratio as well.

Mechanical pitch corresponds always to that of the lower pole number. This mechanical pitch (endwinding construction) is very far from the usual ones at standard high pole motors. That is the only fact to be taken into consideration when electromagnetic calculation is being performed by standard calculation software.

6.3. Further extension of the approach: 1:4, 1:5, 1:7… pole ratio

A motor winding supplied by the usual 3-phase network has been investigated so far. Therefore, some limitations have appeared, such as 1:4, 1:5, 1:7 etc ratios have not been possible. If, however, this approach is exceeded, and the number of the phases is extended, as a very new approach, those missing pole ratios became possible immediately and very easily. 1:4 pole ratio is possible to achieve by 4-phase supply and 4//Y / 4//Y connection, 1:5 pole ratio by 5-phase supply system and 5//Y / 5//Y connection, 1:7 pole ratio by 7-phase supply system and 7//Y / 7//Y connection and so on.

As an example, the slot distribution pattern as well as connection pattern for 5 phase 5//Y / 5//Y connection is given on Figure 11. and Figure 12., resp. just for demonstration (for which the slot distribution pattern is only its beginning part, for the sake of good visibility and readability only). It is to be continued for N phase N//Y / N//Y connection in the same way.

Some conclusions found before still valid. Supply concept on the lower pole number must be applied similarly to Figure 10. in order to avoid those extreme balancing currents.

As a consequence, the number of the terminals will increase according to the number of the phases, also because NxN phase supply is necessary for the lower pole number.

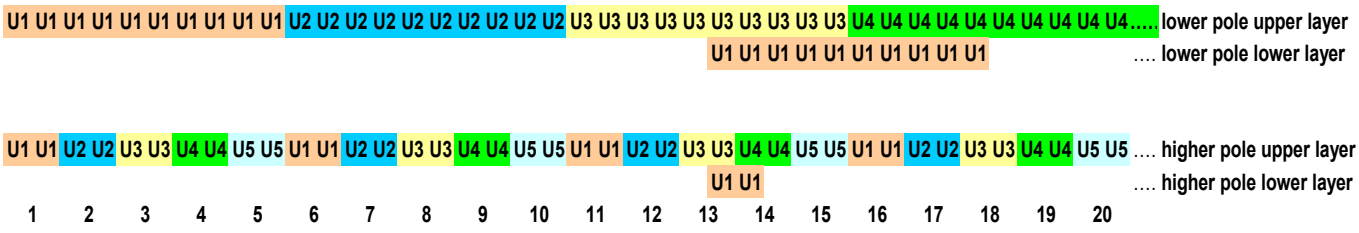

Figure 11. Slot distribution pattern for 1:5 pole ratio

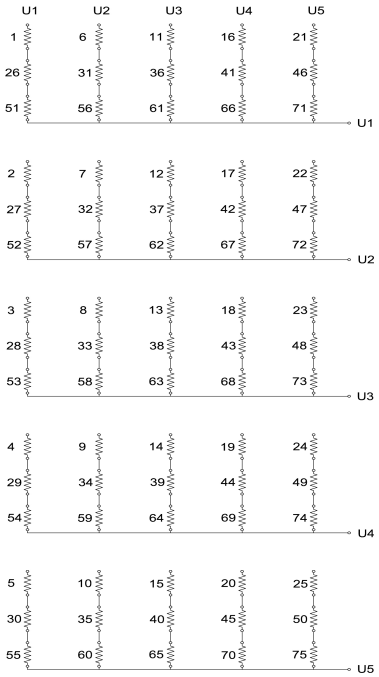

Figure 12. Connection pattern for 1:5 pole ratio (5 phase supply)

Further, what found before for the case if N is even or odd, is still valid. If N is even, like 1:4, even harmonics will appear. If N is odd like 1:5, 1:7 etc. the result again is absolute ideal, no even harmonic will appear on either pole number, therefore the motor's behavior on both pole numbers is identical to the corresponding single-speed motor. Derating factor of k1=0.866 is still valid.

Due to the high number of parallel connection – high number of phases is also a certain kind of parallel connection – the method is inherently suitable for high power.

6.4. Rotor slot numbers

The literature gives little support for how to choose the rotor slot numbers.

- q number of slots per pole per phase must not be an integer (for avoiding synchronous harmonic torque at zero speed)
- number of rotor slot number per 2p must be an integer (for avoiding imbalanced magnetic pull).

Considering these for both the higher as well as the lower pole number a clear picture can be obtained, preferable on a usual spreadsheet.

The result is the following:

- there is no common slot number on the sheets because
- each slot number proposed acc. to 2nd requirement for higher pole number are forbidden slot numbers acc. to 1st requirement for the lower pole number. The reason is that each gives an integer q for the latter.
- no any on the (long) list of proposed slot numbers of the lower pole number can be found on the (shorter) list of the higher pole number.

It is clear in this way that it is impossible to find a rotor slot number which would fulfill even those minimum requirements above at the same time.

What in this situation can be preferred is the lower pole number – because of the higher speed – unless the generally higher air gap induction on the higher pole number seems to make more problems.

6.5. Supply voltage strategy

It was obvious in the chapter *5*. for close ratio that the supply voltage for both pole numbers is the same. It is not necessarily the case, however, here. Therefore, it may be discussed shortly what supply strategy may be possible when switching from the lower pole number to the higher pole number and what the consequences are.

The formulas already found in chapter *5.3.6.* will be applied. The case for N = odd will be discussed only just for more compact formulas because here the pitch is identical (full) pitch on both pole numbers therefore: $\xi_{1p1} = \xi_{1p2}$ and the consideration can focus on the important phenomena.

The logical target – when determining the power - will always be to obtain identical maximum torque expressed in p.u. on both pole numbers (M_{max} /M_{rated} remains). Therefore, the ratio of the maximum torque absolute values will be expressed as being proportional with the square of the voltage.

6.5.1. Same voltage

$$U_{p2} = U_{p1}$$

$$M_{\max p2} = \left(U_{p1}/U_{p2}\right)^2 * p_2/p_1 * M_{\max p1} = ... = N * M_{\max p1} \tag{14}$$

$$P_{p2} = M_{ratedp2} * \omega_{p2} = N * M_{ratedp1} * \omega_{p1}/N = P_{p1}$$

$$I_{p2} = P_{p2}/U_{p2} = ... = I_{p1}$$

$$B_{p2} = N * B_{p1} \quad (!)$$

The operation corresponds to "constant power".

The result is obviously identical to that obtained in *5.3.6* for close ratio.

6.5.2. Voltage reduced by $\sqrt{N}$

$$U_{p2} = U_{p1}/\sqrt{N}$$

$$M_{\max p2} = ... = M_{\max p1}/N * N = M_{\max p1} \tag{15}$$

$$P_{p2} = M_{ratedp2} * \omega_{p2} = M_{ratedp1} * \omega_{p1}/N = P_{p1}/N$$

$$I_{p2} = P/U = P_{p1}/N/U_{p1}/\sqrt{N} = I_{p1}/\sqrt{N}$$

$$B_{p2} = N/\sqrt{N} * B_{p1} = \sqrt{N} B_{p1}$$

The operation corresponds to “constant torque”.

6.5.3. Voltage reduced by N

$$U_{p2} = U_{p1}/N$$

$$M_{\max p2} = \ldots = M_{\max p1}/N \qquad (16)$$

$$P_{p2} = M * \omega = M_{ratedp1}/N * \omega_{p1} \quad /N = P_{p1}/N^2$$

$$I_{p2} = \ldots = 1/N^2 * 1/N * I_{p1} = I_{p1}/N$$

$$B_{p2} = B_{p1}$$

The operation could be named as “constant stress of motor”.

It shall be remarked that all the above formulas regarding the current are valid only if the (eventual) change of η and cos φ is out of consideration.

It shall be remarked also that - when connected to p2 - the induction in the iron core will be changed in an unusual way:

B_{tooth} changes proportional to B_{airgap} ;

B_{yoke} changes proportional to B_{airgap} / N .

The right strategy may be chosen acc. to the torque requirements of the drive.

7. Conclusion

In this paper, a complete analysis of 3//Y / 3//Y pole changing method has been provided through a unique approach, including application, characteristics and design aspects in a comprehensive way, especially for high power motors.

The main finding of the analysis is that the method is suitable for any pole combination, with no limitation for both close ratio as well as for wide ratio pole changing windings.

It has been proven for close ratio that the method is well applicable without balancing measures for practically the whole range required by the industry. The limits are given and are supported by calculations.

Moreover, as a fundamental novelty, a solution for a theoretically infinite range of 1:N pole change ratio winding connection has been given (N phase N//Y / N//Y connection), with no need for further scientific considerations, that means it is suitable for a direct industrial use. The designer may use his standard calculation software.

A new, complete drive system for main marine propulsion has been proposed, with the pole changing motor with 1:N ratio as the core element.

8. Appendix

8.1. Approximate calculation of balancing currents discussed in connection of Figure 4.

The phenomenon was simple mentioned already in [6] but with little explanation, no calculation.

Because the phenomenon arises in no-load as well, even, the phenomenon is in connection with the main flux and the induced voltage by the main flux, the simplified equivalent circuit known from the theory may be applied.

This simplified equivalent circuit shall be applied for each parallel branch see Figure 13.. The voltage of the branches is the same: U, the supply voltage. The currents, however, are obviously different: they will be expressed by the sum of the common, resulting (magnetizing) current and the equalizing current I + ΔI. Regarding reactance and the induced voltage, not only the value but its direction must be taken into consideration in the meaning that the phase of the induced voltage will be different in different winding parts acc. to their position: that is why the reactance representing those “last 2 poles” are multiplied by $e^{j\alpha}$, *1*, $e^{-j\alpha}$ resp.

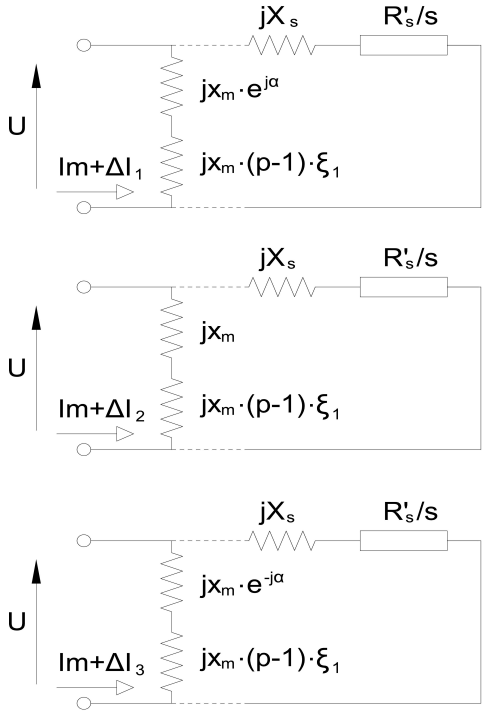

Figure 13. Simplified equivalent circuit

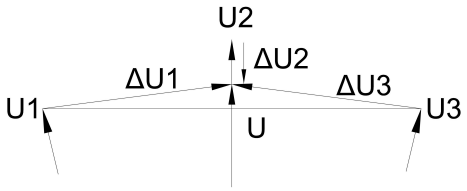

Figure 14a. Voltage vector diagram

Vector diagrams of the voltages and of the currents for no-load and load – based on Figure 4. - are shown on Figure 14a. and Figure 14b. The latter one is not in true scale.

The equations for the 3 parallel branches will be:

$$(I_m + \Delta I_1) * jX_m((p-1) * \xi_1 + e^{j\alpha}) = U$$

$$(I_m + \Delta I_2) * jX_m((p-1) * \xi_1 + 1) = U \qquad (17)$$

$$(I_m + \Delta I_3) * jX_m\left((p-1) * \xi_1 + e^{j-\alpha}\right) = U$$

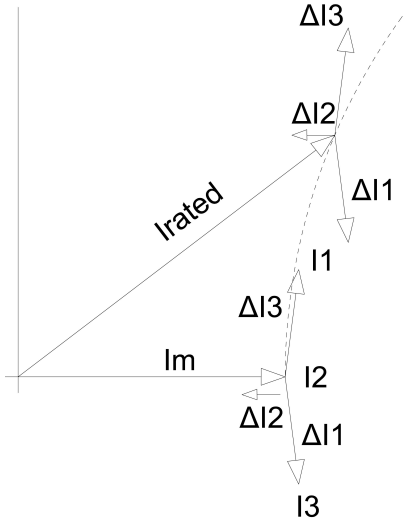

Figure 14b. Resulting equalizing currents

where

I_m - resulting, equivalent magnetizing current of one parallel branch

X_m - magnetizing reactance per pole per branch

$p-1$ - takes into account that the "first 6 poles" are full poles $e^{j\alpha}; 1; e^{-\alpha}$

U - supply voltage.

Because the sum of the equalizing currents is per definition zero, if all three equations are added, it yields

$$I_m = \frac{U}{jX_m} \frac{1}{\left((p-1)\xi_1 + (2\cos\alpha + 1)/3\right)} \qquad (18)$$

Actually, although I_m is given in this way, the main target is to know ΔI_n compared to I_m as the imbalance in p.u.:

$$\Delta I_1 = I_m \frac{(2\cos\alpha + 1)/3 - e^{j\alpha}}{(p-1)\xi_1 + e^{j\alpha}}$$

$$\Delta I_2 = I_m \frac{(2\cos\alpha + 1)/3 - 1}{(p-1)\xi_1 + 1} \qquad (19)$$

$$\Delta I_3 = I_m \frac{(2\cos\alpha + 1)/3 - e^{-j\alpha}}{(p-1)\xi_1 + e^{-j\alpha}}$$

Magnitudes of the equalizing currents are (for 8 poles) approximately:

$\Delta I_1 \approx \Delta I_3 \approx 0.19 I_m$

$\Delta I_2 \approx 0.05 I_m$

The phase angle is also interesting in case of further considerations because e.g. ΔI_2 results in local decrease while ΔI_1 and . ΔI_3 do so in local (half so much) increase of airgap induction which causes torque ripples and local radial force fluctuation.

Above equations are valid for 8, 14, 20 etc. poles. In case of 10, 16, 22 etc. poles

$(p-1)$ shall be substituted by $(p-2)$ and

$e^{j\alpha}, 1, e^{-j\alpha}$ shall be substituted by $2e^{j\alpha}, 2, 2e^{-j\alpha}$ resp.

Conflict of Interest

The author declares no conflict of interest.

References

[1] G. Kovács, "A 3Y / 3Y Winding for high Power Asynchronous Motors", World Academy of Science, Engineering and Technology International Journal of Electrical and Computer Engineering Vol:12, No:1, 2018. p. 1367-1374

[2] Lengyel Zoltán, "Korszerű kéttekercselésű motorok", in Hungarian. Ganz Közlemények, Proceedings of Ganz Electric Works 1964. p. 31 – 36.

[3] G. H. Rawcliff, B. V. Jayawant, "The development of a new 3: 1 pole-changing motor". Proceedings of the IEE – Part A Power Engineering 1956. p. 306 – 316.

[4] T. H. Barton, O.I. Butler, H. Sterling, "The theory and Characteristics of the new 3:1 pole changing induction motor", Proceedings of the IEE – Part A: Power Engineering 1956 p.285 – 294.

[5] K.C. Rajaraman, "Design criteria for pole-changing windings", Proceedings of the Institution of Electrical Engineers (Volume: 124, Issue: 9, September 1977) 775 – 783, https://doi/org/10.1049/piee.1977.0171

[6] A.R.W. Broadway ; K.S. Ismail , "Phase modulated 3-phase pole changing windings", IEE Proceedings B - Electric Power Applications 1986 p. https://doi.org/10.1049/ip-b.1986.0011

[7] P. Chidambaram ; M. Subbiah ; M.R. Krishnamurthy, "Developments in Pole Changing Windings using Star/Star-Delta Switching", IEEE Transactions on Energy Conversion (Volume: EC-1, Issue: 4, Dec. 1986) p. 135 – 141 https://doi/org/10.1109/TEC.1986.4765787

[8] K.C. Rajaraman, W. Ranjith Perera, G. Subramaniam, "New wide-ratio pole-changing motors", IEE Proceedings B - Electric Power Applications (Volume: 134, Issue: 4, July 1987) p. 211 - 214 https://doi.org/ 10.1049/ip-b.1987.0036

[9] J.W. Kelly ; E.G. Strangas ; J.M. Miller, "Control of a continuously operated pole-changing induction machine", IEEE International Conference on Electric Machines and Drives. 2003 IEMDC'03. https://doi.org/10.1109/IEMDC.2003.1211265

[10] Gautam, J. Ojo, " Variable speed multiphase induction machine using pole phase modulation principle", IECON 2012 – 38th Annual Conference on IEEE Industrial Electronics Society 2012. https://doi/org/10.1109/IECON.2012.6389310

[11] Umesh B S, Kiran Kumar N, Sivakumar K, "Performance improvement of a nine phase pole phase modulated induction motor drive". IEEE International Conference on Industrial Technology, 2015 p.812-817. https://10.1109/ICIT.2015.7125198

[12] Baoming Ge ; Dongsen Sun ; Weiliang Wu ; Fang Zheng Peng , "Winding Design, Modeling, and Control for Pole-Phase Modulation Induction Motors" IEEE Transactions on Magnetics (Volume: 49, Issue: 2, Feb. 2013) p. 898 - 911 https://doi/org/10.1109/TMAG.2012.2208652

[13] Dawei Meng, Qian Wang, Research on Balanced Winding Used in 3Y/3Y pole changing Motor, - International Journal of Automation and Power Engineering (IJAPE) Volume 2 Issue 4, May 2013

[14] H. Liu, J. Wang, Z. Zhang, Performance analysis of variable speed multiphase induction motor with pole phase modulation, Archives of Electrical Engineering, Vol. 65(3) 2016. p. 425-436

[15] W. Nürnberg, "Die Asynchronmaschine", in German, Springer Verlag 1952. p.299.

[16] Liska József, "Villamos gépek, IV. Aszinkron gépek", In Hungarian, Tankönyvkiadó Budapest 1960. p. 126.

[17] Bedrich Heller, Václáv Hamata, "Harmonic Field Effects in Induction Machines", ELSEVIER Scientific Publishing Company Amsterdam, Oxford, New York 1977

ASTES

Advances in Science, Technology and Engineering Systems Journal Vol. 3, No. 4, 254-259 (2018)

www.astesj.com

Special Issue on Multidisciplinary Sciences and Engineering

ASTESJ

ISSN: 2415-6698

Wireless Channel Measurement and Modeling in Industrial Environments

Kun Zhang[1], Liu Liu[*,1,2], Cheng Tao[1], Ke Zhang[1], Ze Yuan[1], Jianhua Zhang[3]

[1]*School of Electronic and Information Engineering, Beijing Jiaotong University, 100044, P.R.China*

[2]*National Mobile Communications Research Laboratory, Southeast University, Nanjing 210096, P.R.China*

[3]*Beijing University of Posts and Telecommunications, 100876, P.R.China*

ARTICLE INFO

Article history:
Received: 08 June, 2018
Accepted: 03 August, 2018
Online: 05 August, 2018

Keywords:
IIoT
Wireless channel
K factor
Time delay
Path loss

ABSTRACT

The Industrial Internet of Things (IIoT), a typical use case of the Internet of Things, has been a great prospect for development in the near future. In the developing fifth generation mobile communications, the IIoT is an extremely important application case. In this paper, the channel propagation properties are researched and modeled based on the measurement data in an automobile welding factory. The results of the path loss exponent values are around 2.5 and 3.3 in line of sight propagation (LOS) and obstructed line of sight (OLOS) propagation scenarios, respectively. In LOS and OLOS propagation scenarios, K factor values are around 5 dB and 4 dB, respectively. Meanwhile, in these two-propagation environment, the amount of multipath components (MPCs) and the root mean squared (RMS) delay are extracted and compared. Particularly, a special case is considered that the sensor/actuator is placed inside the metallic body of a machine, which affects the path loss exponent values and K factor values. These measurement results are of great significance to the development of IIoT.

1. Introduction

In recent years, the Internet of things has become a hot research topic in industry and academia. In the developing fifth generation wireless mobile communications, the IIoT is an extremely important application case. The IIoT is particularly important in the application of the fifth generation of wireless communications. In the IIoT wireless communications, there are two different types of radio signals: narrow band (NB) and wide band (WB). In the industrial environment, there are a great quantity of mobile equipments work at WB to transmit surveillance video. Basically, there are an enormous amount of sensors work at NB to obtain all kinds of temperature, humidity or pressure information These signals also have different central frequencies. This paper mainly investigates the wireless channel of industrial environment and it is an extension of work originally presented in 2018 20th International Conference on Advanced Communication Technology [1].

The IIoT generally includes three different layers: application layer, perception layer and network layer. The first layer is to be used intelligent sensing technology, such as various sensors, to collect industrial data anytime and anywhere; the second layer is to be used communication technology, such as the Zig-bee, the Narrow Band Internet of Things (NB-IoT), and so on, to build a communication network. The third layers is to be used data processing and analysis technology, such as cloud computing, and so on, to make deep mining and utilization of these data, and then to realize the management and optimization of the industrial process [2]. At the IIoT network layer, huge amounts of sensors connect to the access point by wireless communication technologies. Wireless communication links will be obstructed and shadowed by industrial equipment or metallic materials in the industrial propagation environments. The propagation of electro-magnetic waves will generate strong reflection due to the role of these obstructions. However, in the industrial propagation case, wireless communication technology has not been completely researched. There are many differences between IIoT and cell communication systems. It is important to get a thorough knowledge of the IIoT wireless channel characteristics.

At present, researches on the influence of modern industrial environment on electromagnetic wave propagation are relatively

[*]Liu Liu, Beijing Jiaotong University No.3 Shangyuancun Haidian District Beijing China, Email: liuliu@bjtu.edu.cn

limited. Reference [3] extracted wireless channel parameters of path loss and time delay power based on the measured data of five factories. Reference [4] studied the characteristics of the typical industrial environment by channel measurement based on manufacturing plant. The related parameters obtained from the average time delay and RMS delay obtained from the 2.4GHz center frequency were found to be dependent on the LOS condition and related to the distribution of metal hindrance. Reference [5] measured four typical factory environments (corridors, offices, laboratories and large industrial manufacturing halls) at 1.9GHz center frequency, and analyzed shadow fading, K factor and delay spread which according with log-normal distribution. Reference [6] considered the large-scale characteristics based on measurement data in several factory buildings. Reference [7] researched NB propagation at 900 MHz, 2400 MHz and 5200 MHz. Reference [8] studied the effects of two important industrial environments on electromagnetic wave propagation, including channel path loss and multipath component (MPCs). One is high absorption environment, the other is high reflection environment. In the same year, reference [9] proposed a broad-band channel model for industrial wireless networks. This model takes into account the influence of noise in the harsh factory environment and uses the first order two state Markov process to describe the characteristics of the typical burst pulse noise in the industrial environment. Authors in reference [10] modelled the industrial wireless channels using Saleh-Valenzuela models. In 2017, reference [11] conducted seven scene measurements at three locations, studied the LOS and OLOS scenarios with a frequency of 5.8GHz, and analyzed the wireless channels.

The main contribution of this paper is to employ a vector signal generator and spectrum analyzer as a channel sounding system to probe realistic automobile factory environments. Three frequency bands, 1.1GHz, 2.55GHz, and 5.8GHz are considered in this paper. The frequency bands of 1.1GHz and 2.55GHz are corresponding to narrow band (NB) (0.8MHz) and 5.8GHz is corresponding to wide band (WB) (8MHz). In the NB case, we consider a special condition that the sensor/actuator (receiver antenna of the channel sounder in our channel measurements) is placed inside the metallic body of a machine, an industrial computer box with the thickness of 2 mm in the measurement. The channel parameters of time dispersion including RMS delay spread, number of MPCs, power difference and the K factor in different scenarios are extracted from the measurement data.

The paper is organized as follows. In Section 2, the system model and measurement system are described. Then raw data are analyzed to show the results of measurement and give the reasonable explanation in Section 3 . In Section 4 the conclusion is given.

2. System model and measurements description

As shown in Figure 1, a vector signal generator (Rhodes &Schwartz SMBV100A) and a spectrum analyzer (Agilent N9010B) are employed as a channel sounder. Two local rubidium clocks are employed to ensure efficiency and accuracy synchro-nization between the Tx and Rx. In Table 1 channel measurement parameters are listed.

As shown in Figure 3, two different propagation types of LOS (100 measurement spots) and OLOS (100 measurement spots) are considered in this measurement. In OLOS propagation case, the wireless links are semi-blocked (shadowed) by metal machines and buildings. And as mentioned in the previous part, a special case is considered that the sensor/actuator (receiver antenna of the channel sounder in our channel measurements) is placed inside the metallic body of a machine, as shown in Figure 2. The dimension of the measurement factory is 120 m×59 m×8 m, the Tx antenna height is 5 m and the Rx antenna height is 1.4m.

Table 1: Measurement Parameters.

Bandwidth Type	Frequency	Bandwidth	Power	Antenna Gain
NB	1.1GHz	0.8 MHz	33dBm	0dBi
NB	2.55GHz	0.8MHz	33dBm	0dBi
WB	5.8 GHz	8MHz	33dBm	16dBi

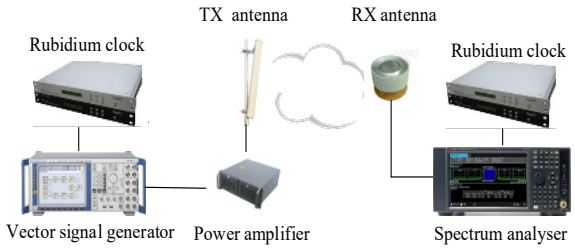

Figure 1: Channel sounding system

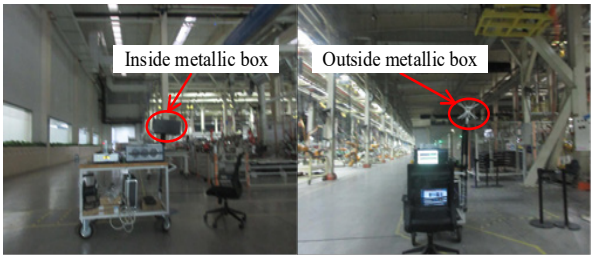

(a) Receiver inside (b) Receiver outside

Figure 2: Measurement setup

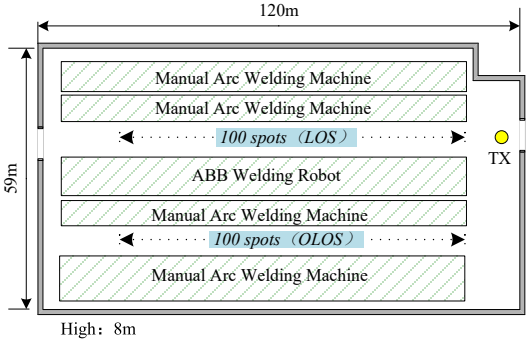

Figure 3: Environment map of the automobile factory

In the measurement, in order to extract the channel impulse response (CIRs), the frequency-domain method (OFDM signal) is

used. There are N subcarriers in one OFDM symbol with transmitted. $X[m]$ denotes the excitation signal on the m-th subcarrier. The discrete time excitation signal $x(n)$ can be given after N-point IFFT

$$x(n)=\frac{1}{N}\sum_{m=0}^{N-1}X[m]\exp\left(j2\pi\frac{mn}{N}\right) \tag{1}$$

The convolved output between the excitation signal and the time-variant CIRs denoted as a function of the discrete time variable (n) and the time delay (τ) can be expressed as

$$\begin{aligned} y(n)&=h(n,\tau)*x(n)+w(n)\\ &=\sum_{\tau=0}^{L-1}h(n,\tau)x(n-\tau)+w(n)\end{aligned} \tag{2}$$

where $w(n)$ is the additive white Gaussian noise (AWGN), L denotes the amount of MPCs. In the duration of one OFDM signal, the channel is assumed as constant, i.e., $h(n,\tau)=h(\tau)$. The received signals can be obtained as follows after removing the CP and FFT operation:

$$\begin{aligned} Y[m]&=\left(\sum_{\tau=0}^{L-1}h(\tau)e^{-j2\pi\tau k/N}\right)X[m]+W[m]\\ &=H[m]X[m]+W[m]\end{aligned} \tag{3}$$

Then the frequency domain correlation processing is performed as

$$\tilde{H}[m]=\frac{Y[m]X^{*}[m]}{|X[m]|^{2}}=H[m]+W'[m] \tag{4}$$

Finally, the extracted CIR can be obtained from (4) via the Fourier series as

$$\tilde{h}(\tau)=\sum_{n=0}^{N-1}\tilde{H}[m]e^{j2\pi\tau m/N} \tag{5}$$

Finally, the real MPCs from $\tilde{h}(\tau)$ can be extracted. And then the method in reference [12] is used to the noise threshold determination and path searching.

3. Results and Analysis of Measurement Data

3.1. Path Loss Characteristics

Path loss is an important parameter, which reflects the energy loss of electromagnetic wave in the environment. Usually, previous researchs and results show that the path loss power is mainly related to the distance between the receiver and the transmitter. And when acquiring the propagation loss power and the distance between the receiver and the transmitter, path loss prediction can be described with the empirical path loss model which can be written as

$$PL(d)=A+10\cdot n\cdot\log10(d)+X_{\sigma} \tag{6}$$

where n represents the path loss coefficient, d denotes the distance in meters between the receiver and the transmitter, X_{σ} is the shadowing term, and A represents the intercept. The least square (LS) method is adopted to the linear fitting and estimate n in the measurement data processing. In TABLE 2, the results are listed.

Table 2: Path Loss Parameters

Frequency	LOS		OLOS	
	n^{Ous}	n^{Ins}	n^{Ous}	n^{Ins}
1.1GHz	2.5	2.6	3.1	3.4
2.55GHz	2.4	2.5	3.4	3.7
5.8 GHz	2.6	-	3.2	-

The superscript *Ous* and *Ins* represent cases that the receiver antenna of the channel sounder is outside and inside of the metallic box respectively.

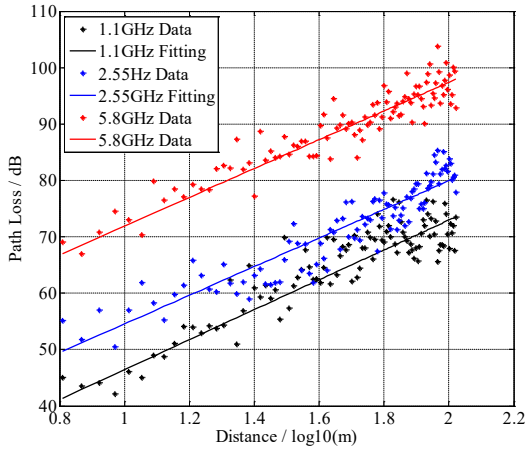

(a) Path Loss in LOS Scenario

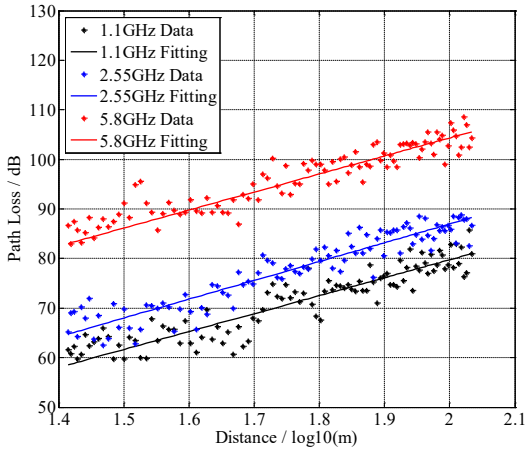

(b) Path Loss in OLOS Scenario

Figure 4: Path Loss Exponent Extraction

Different frequency bands are measured in the same route (LOS and OLOS). The LS method is used to fit the path loss model, as shown in Figure 4, which is the situation of LOS and OLOS outside of metallic body respectively. The estimated path loss coefficient is around 2.6 in LOS, and the value in OLOS is relatively larger, around 3.2 as showed in Table 2. This is due to

the fact the propagation link is semi-blocked by the metal machines and other objects. Path loss coefficient in the industrial scenarios exhibits a higher value compared to the path loss coefficient (n=2.0) in the free space model. In contrast, path loss exponent value inside metallic box is a little bit larger than the value extracted outside. This is mainly because of the energy loss of electromagnetic waves penetrating metal boxes. Moreover, it can be found that there is no clear relationship between frequency band and path loss coefficient. In reference [13] there is also similar conclusion that path loss coefficient is independent of the frequency band. Furthermore, the results in Table 2 change significantly with the path loss coefficient acquired from different industrial wireless channel measurements summarized in [14] (Table I). It can be assumed that the path loss coefficient varies with the environment (the position, the size, the height, and density of Metallic materials or machines in the industrial factory), links configuration and frequency. In a consequence, when planning wireless communication systems in the industrial factories, it is suggested that a larger path loss coefficient should be used.

And what's more, according to the characteristics of the workshop in the industrial environment, under the same propagation conditions, if the receiver exists inside the large machine or inside the metallic body, a greater path loss coefficient should be selected compared to the external. Therefore, receiver location and environmental conditions in the workshop should be investigated before selecting the appropriate path loss coefficient.

3.2. K Factor

Two different types propagation LOS and OLOS scenarios are considered in the industrial environment. The envelope of the received signal is according with Rician distribution which varies with the probability density function written as

$$P(r) = \frac{r}{\sigma^2} \cdot \exp\left(-\frac{r^2 + s^2}{2\sigma^2}\right) \cdot I_0\left(-\frac{rs}{\sigma^2}\right) \tag{7}$$

where σ^2 represents the variance of the diffuse components, $I_0(\cdot)$ is the nth-order modified Bessel function of the first kind, and s^2 represents the power of the LOS path. A moment-based K-factor estimator is used to extract the K-factor [14]

$$\hat{K}_{2,4} = \frac{-2\hat{\mu}_2^2 + \hat{\mu}_4 - \hat{\mu}_2\sqrt{\hat{\mu}_2^2 - \hat{\mu}_4}}{\hat{\mu}_2^2 - \hat{\mu}_4} \tag{8}$$

where the closed forms of the even moment are $\hat{\mu}_2 = E\left[r^2\right]$ and $\hat{\mu}_4 = E\left[r^4\right]$, respectively.

In Table 3, K factor values of LOS and OLOS scenarios are shown. In LOS scenario, K factor values are about 5 dB, and due to metallic materials or equipments, the values in OLOS are little smaller than that in LOS scenario. Moreover, it is expected that when the center frequency increasing, the wavelength decreasing and more objects playing a role as reflectors, the K factor value decrease. Besides, K factor inside metallic body is smaller than outside. That is due to the metallic body generates additional penetration loss, so the dominant signal is attenuated. Meanwhile, the reflection scattering in the metallic body may be enhanced. This give rise to the occurrence of deep fades and yield small Rician factors.

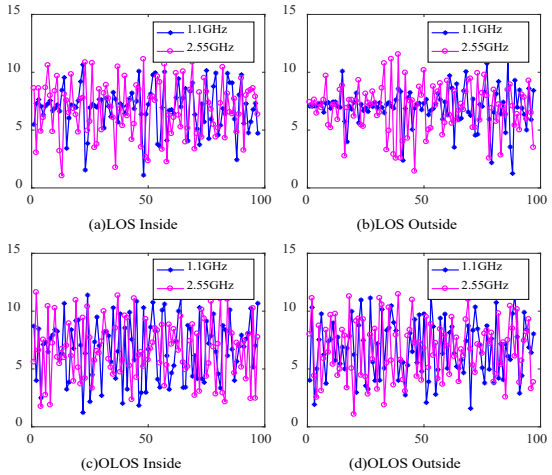

Figure 5: The change of channel envelope values

Table 3: K-Factor

Frequency	LOS (dB)		OLOS(dB)	
	K^{Ous}	K^{Ins}	K^{Ous}	K^{Ins}
1.1GHz	4.8	4.2	3.8	3.2
2.55GHz	5.2	4.5	4.6	2.8
5.8 GHz	7.3	-	4.3	-

The superscript *Ous* and *Ins* represent cases that the receiver antenna of the channel sounder is outside and inside of the metallic box respectively.

Figure 5 shows the channel envelope which represents the fluctuation degree of the receiving signals at different propagation scenarios (Figure 5 a, b, c, d) and the variances σ^2 of channel envelope in all scenarios are extracted in Table 4, which are 5.5, 3.7, 6.5, 5.6. It can be seen that when the Rx antenna is in the same environment, for example, inside of the metallic body under LOS propagation case of Figure 5(a), the envelope fluctuation of the received signals of different frequencies is basically the same. And in the same scenarios (LOS or OLOS), σ^2 inside metallic body is larger than outside. That means the fluctuation of signals envelope is more serious. This is because reflected and scattered waves in the metallic body are much more those outside of the metallic body. More MPCs give rise to significant fluctuation of the channel envelope and cause larger variance σ^2. Furthermore, it also can be found that variance σ^2 in OLOS scenarios is larger than that in LOS environments. This is due to the rich MPCs. These MPCs give rise to the severe fluctuation of the channel envelope.

Table 4: Variances σ^2 of Channel Envelope

LOS		OLOS	
Ins	Ous	Ins	Ous
5.5	3.7	6.5	5.6

3.3. Time Delay Characteristics

The time delay spread is important to digital communication system. It reflects the delay time of a multipath channel and can

represent the time dispersion characteristic parameters of the channel. The statistical results are mainly the multipaths delay spread to estimate the small-scale fading of wireless channel. The RMS delay is used to quantify the parameters of the multipath channel, the following definition of RMS delay parameters is given by

$$\sigma_\tau = \sqrt{\frac{\int_0^\infty (\tau-\bar{\tau})^2 p(\tau)d\tau}{\int_0^\infty p(\tau)d\tau}} = \sqrt{\int_0^\infty (\tau-\bar{\tau})^2 p(\tau)d\tau} \quad (9)$$

where τ is time delay, $p(\tau)$ is power delay profile (PDP), $\bar{\tau}$ is average time delay which can be expressed as

$$\bar{\tau} = \frac{\int_0^\infty \tau p(\tau)d\tau}{\int_0^\infty p(\tau)d\tau} = \int_0^\infty \tau p(\tau)d\tau \quad (10)$$

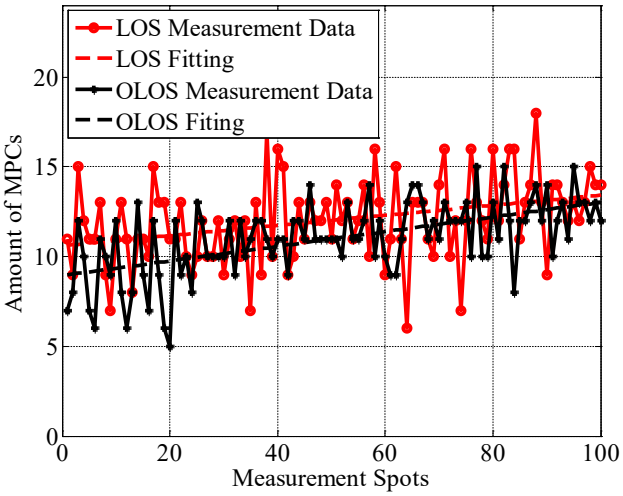

Figure 6: The amount of MPCs of 5.8GHz in LOS and OLOS

In this section, the RMS delay spread values and the number of MPCs of LOS and OLOS scenarios are researched with 8 MHz bandwidth, whether it is LOS or OLOS scenario, Out or Ins condition, there is only one main path can be obtained when the excitation signal bandwidth is 0.8 MHz (corresponding to 1.1 GHz and 2.55 GHz). And more echo waves can be obtained when the excitation signal bandwidth is 8 MHz. The main reason is that when the bandwidth is 0.8 MHz, the resolvable distance of the excitation signal is 375 m, whereas, when the bandwidth is 8 MHz, the resolvable distance is 37.5 m. So, it's much easier to make detecting MPCs when the bandwidth wider. For this reason, time delay parameters are extracted with the bandwidth in 8MHz, however, the channel envelope (not resolvable MPCs and the time delay spread) is the primary parameter extracted when the bandwidth is 0.8MHz.

Figure 6 shows the amount of MPCs of 5.8GHz in LOS and OLOS propagation conditions. It can be seen that the number of MPCs in the OLOS propagation condition is obviously more than that under the LOS propagation condition, which is mainly due to the scattered around the OLOS propagation is more abundant, and the electromagnetic waves mainly arrive at the receiving antenna by the way of reflection and diffraction. In addition, it can be seen that the number of MPCs increases slightly with the increase of distance in both LOS and OLOS propagation conditions, which is mainly due to the greater density of metal or equipment in the actual factory environment, far from the receiving end of the transmitting antenna. Meanwhile, when the bandwidth of the excitation signal is 8 MHz, the RMS results are shown in Table 5. RMS in OLOS propagation condition is larger than that in LOS, which also shows that the phenomenon of multipaths is more serious in OLOS propagation condition.

Table 5: RMS Delay Spread

Frequency	LOS	OLOS
5.8 GHz	9.37 us	15.3 us

4. Conclusions

Measurement results and analysis of the propagation fading behaviour in industrial factory environments has been presented in this paper. And two propagation types LOS and OLOS cases are considered. Particularly, special industrial propagation cases, sensors/actuators are equipped in metallic machine bodies. The results of the path loss exponent values have been reported. The estimated values are around 2.5 and 3.3 in LOS and OLOS propagation scenarios, relatively, which are larger than that of the free space model. In the research, K factor is used to described the power ratio between the direct ray and the sum of the powers of other rays. As the results shown, in LOS and OLOS scenarios, the K factor values are around 5 dB and 4 dB, respectively. And when the receiver antenna is equipped in metallic machine bodies, the path loss exponent is larger and K factor values are smaller. These are due to the metallic body generates additional penetration loss, so the dominant signal is attenuated. Further-more, channel envelope fluctuation in OLOS is more serious than LOS, and the channel envelope fluctuation inside the metallic body is more serious than outside. These are mainly because of MPCs in LOS and inside of metallic body are more abundant. What's more, in this paper time delay parameter and the number of MPCs are researched. The RMS delay spread are 9.37us and 15.3us in LOS and OLOS scenarios. The research results are important to the design of the IIoT for industrial scenarios.

Conflict of Interest

The authors declare no conflict of interest.

Acknowledgment

The research was supported in part by the Key Laboratory of Universal Wireless Communications (BUPT, KFKT-2018 105), Ministry of Education, P.R.China, Beijing Natural Science Foundation(NO. L172030), the Beijing Municipal Natural Science Foundation under Grant 4174102, and the Open Research Fund through the National Mobile Communications Research Laboratory, Southeast University, under Grant 2017D01 and 2018D11.

References

[1] L. Liu, K. Zhang, C. Tao, K. Zhang, J. Zhang. "Channel measurements and characterizations for automobile factory environments." International

Conference on Advanced Communication Technology 2018:234-238. https://doi.org/10.23919/ICACT.2018.8323708

[2] S. Mumtaz, A. Alsohaily, Z. Pang, A. Rayes, K. F. Tsang, J. Rodriguez, "Massive Internet of Things for Industrial Applications: Addressing Wireless IIoT Connectivity Challenges and Ecosystem Fragmentation." IEEE Industrial Electronics Magazine 11.1(2017):28-33. https://doi.org/10.1109/MIE.2016.2618724

[3] T. S. Rappaport, C. D. Mcgillem. "UHF fading in factories." IEEE Journal on Selected Areas in Communications 7.1(2015):40-48..https://doi.org/10.1109/49.16842

[4] A. Miaoudakis, A. Lekkas, G. Kalivas, S. Koubias, "Radio channel characterization in industrial environments and spread spectrum modem performance." Emerging Technologies and Factory Automation, 2005. Etfa 2005. IEEE Conference on IEEE, 2006:7 pp.-93. https://doi.org/10.1109/ETFA.2005.1612506

[5] C. Oestges, D. Vanhoenacker-Janvier, B. Clerckx. "Channel Characterization of Indoor Wireless Personal Area Networks." IEEE Transactions on Antennas & Propagation 54.11(2006):3143-3150. https://doi.org/10.1109/TAP.2006.883962

[6] E. Tanghe, W. Joseph, L. Martens, H. Capoen, K. Van Herwegen, W. Vantomme. "Large-scale fading in industrial environments at wireless communication frequencies." Antennas and Propagation Society International Symposium, Conference IEEE, 2007. https://doi.org/10.1109/APS.2007.4396167

[7] M. Cheffena."Propagation Channel Characteristics of Industrial Wireless Sensor Networks." IEEE Antennas & Propagation Magazine 58.1(2016): 66-73.https://doi.org/10.1109/MAP.2015.2501227

[8] B. Holfeld, D. Wieruch, L. Raschkowski, T. Wirth, C. Pallasch, W. Herfs, C. Brecher. "Radio channel characterization at 5.85 GHz for wireless M2M communication of industrial robots." Wireless Communications and NETWORKING Conference IEEE, 2016. https://doi.org/10.1109/WCNC.2016.7564890

[9] J. Ferrer-Coll, P. ÄNgskog, J. Chilo, P. Stenumgaard. "Characterisation of highly absorbent and highly reflective radio wave propagation environments in industrial applications." Communications Iet 6.15(2013): 2404-2412.https://doi.org/10.1049/iet-com.2012.0028

[10] J. Karedal, S. Wyne, P. Almers, F. Tufvesson. "Statistical analysis of the UWB channel in an industrial environment." Vehicular Technology Conference, 2004. https://doi.org/10.1109/VETECF.2004.1399930

[11] Şeyma Tütüncü, A. Kara. "UHF propagation measurements in heavy industry." Signal Processing and Communication Application Conference IEEE, 2016.https://doi.org/10.1109/SIU.2016.7495797

[12] L. Liu, C. Tao, R. Sun, H. Chen, Z. Lin. "Non-stationary channel characterization for high-speed railway under viaduct scenarios." Science Bulletin 59.35 (2014):4988-4998.https://doi.org/10.1007/s11434-0140606 -x

[13] Cheffena M. "Propagation Channel Characteristics of Industrial Wireless" IEEE Antennas & Propagation Magazine 58.1(2016): 66-73. https://doi.org/10.1109/MAP.2015.2501227

[14] Nikolic, B. Zorica "Principles of Mobile Communication: Gordon L. Stuber; Second Edition; Kluwer Academic Publishers, Boston, 2001, 752 pages, ISBN 0-7923-7998-5." Microelectronics Journal 32.12(2001):10 50-1051.https://doi.org/10.1016/S0026-2692(01)00119-7

ASTES

Advances in Science, Technology and Engineering Systems Journal
Vol. 3, No. 4, 260-269 (2018)
www.astesj.com
Special Issue on Multidisciplinary Sciences and Engineering

ASTES Journal
ISSN: 2415-6698

Topology, Discontinuities and Dimension Effects on CMOS Rotary Traveling Wave Oscillators

Rogelio Manuel Higuera Gonzalez [*,1], Mónico Linares Aranda[2], Luis Hernández Martínez[2], Carlos Sanabria Díaz[2]

[1]*Electronics Department, Tecnológico de Estudios Superiores de Ixtapaluca (TESI), 56580 México*

[2]*Electronics Department, Institute of Astrophysics, Optics and Electronics (INAOE), 72840 México*

ARTICLEINFO

Article history:
Received: 30 June, 2018
Accepted: 31 July, 2018
Online: 12 August, 2018

Keywords:
RTWO
Oscillator
Transmission lines

ABSTRACT

In this article, a new method to extract the RLC parameters from the structure of a Rotating Traveling Wave Oscillator (RTWO) is described. The use of a 3D simulator (EMPRO) allow us to develop a precise analysis of the impact of the topology, the geometrical discontinuities, and the dimensions of the transmission lines, on the performance parameters of the RTWO, i.e. frequency of oscillation and power consumption. The results show that a right angle discontinuity compensation can reduce the power consumption up to 3.34% and, for RTWOs with a frequency range between 11.4 GHz and 11.5 GHZ, narrow transmission lines (as the technology is able) can reduce the power consumption up to 98%. Additionally, it was observed that the topology used affects the performance parameters, as there are more folds and overlaps between metal levels in the RTWO structure, and the frequency increases by 2.9% while the power consumption increases by 10.52%.

1 Introduction

Nowadays, the high and very high-frequency ranges (millimeter range: 10-66Hz, and THz range: 0.1THz-10THz) are an object of study due to their promising applications in the military, commercial, communications and medical fields; which include spectroscopy, remote environmental sensing, high-resolution biological imaging, mobile telecommunications, and broadband satellite communications, among others [1, 2, 3]. On the other hand, in the past, only critical circuits, essentially high-precision clock systems, operated at high frequency.

However, this is no longer true at the present high-speed digital design. Many of the signal processors and their interconnections operate and transmit signals at frequencies in the MHz range and even in the GHz range. This is the case of high-performance information systems, which after the current demand of developing faster and faster electronic devices able to perform a wide number of functions (computers, telephones, tablets, and so on), generate the need to increase the operating frequency of the microprocessors to the GHz range with a minimum power consumption. Consequently, the conventional systems of clock generation and/or distribution, commonly used in the current ICs (H-tree, X-tree, mesh, etc.), become obsolete.

The common element used in the previously mentioned applications is the oscillator: a periodic signal generator circuit that operates at the highest frequency in any synchronous system. In communications systems, the clock element is the Voltage Controlled Oscillator (VCO), usually included in the Phase Tie Loop (PTL) and in microprocessor systems. Currently, there is a new resonant oscillator type based on transmission lines. To synchronize signals on CMOS chips, different high-speed resonant oscillator structures have been created: distributed differential oscillators [4], fixed wave oscillators [5], and Rotary Traveling Wave Oscillators (RTWO) [6], among others. From these technologies, the RTWO stands out for its multiple advantages such as high oscillation frequencies, low power consumption, multiphase signals, low jitter, low skew and simple design [7].

The RTWO is an innovative approach which takes

[*]Rogelio Manuel Higuera Gonzalez, Carretera Coatepec s/n Km. 7, San Juan, 56580 Ixtapaluca, México, (+32) 555-477-3941 & m.sc.hgrm@ieee.org

https://dx.doi.org/10.25046/aj030426

advantage of the distributed Inductive and Capacitive (LC) nature of the interconnection lines, present at the CMOS processes used for the manufacture of integrated electronic systems. RTWOs are used for the generation of multi-GHz signals in communication systems, and the generation/distribution of clock signals in high-performance microprocessors [6].

The RTWO generates the oscillations through the LC elements associated with the transmission lines which form the resonant structure. Hence, the operation and performance of an RTWO depend on the physical properties of the materials used, the dimensions of the transmission lines (width W, length l, and thickness T), the discontinuities of the line (curves, crossings, vias, joints, etc.), and the topological structure used (circular, square, hexagonal, etc.).

Several works have been published concerning the design of the RTWOs. In [11], a rectangular topology was implemented and analytical approaches were used to obtain the RLC parameters. [19, 20] implemented different RTWOs in a 180 nm technology with a frequency range from 2GHz to 12GHz, using a rectangular topology and a 2D electromagnetic simulator to extract the RLC parameters. In [17], RTWOs were designed in a 65nm technology achieving a frequency range from 110 GHz to 152GHz. That work implemented an octagonal topology while the extraction of the RLC parameters was done by means of a 2D electromagnetic simulator. [23] used a 180nm technology with a frequency range from 3GHz to 11GHz, and although the extraction of the RLC parameters was done by a 3D electromagnetic simulator, they segmented the ring to perform the simulation, so they did not take into account many of the effects obtained when the complete ring is simulated.

Most of the mentioned previous works used analytical approximations or 2D simulators for the extraction of the RLC parameters. Since the analytical approximations are not exact and the 2D simulators do not take into account some electromagnetic effects on the ground plane, such as skin effect and proximity effect, the designed RTWO could not oscillate at the desired frequency or, in the worst case, could not oscillate.

In this work, a new design method was developed. A 3D electromagnetic simulator was used to extract the RLC parameters of the RTWO structure, which allows us to perform an accurate analysis of how the frequency of oscillation and power consumption are affected by the dimensions of the RTWO (length, width and gap between the transmission lines), right-angle discontinuities, and the different topologies used in RTWO design. In this way, it is possible to simultaneously analyze the effect of the geometric discontinuities and the topology on the operating parameters of the RTWOs.

2 The RTWO

The Rotatory Traveling Wave Oscillator (RTWO) is a closed loop implemented with a differential transmission line (displaying LC characteristics) with a connected crossing from the inner conductor to the outer

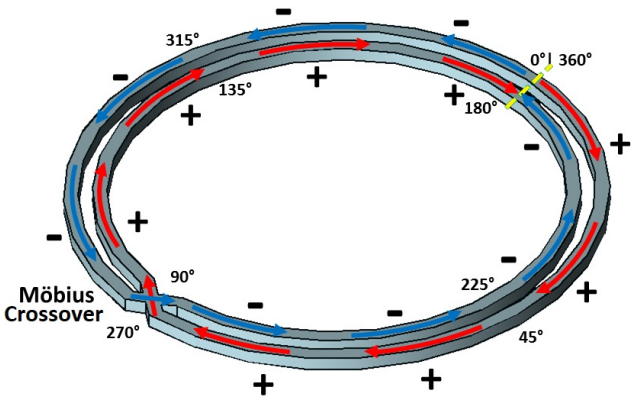

Figure 1: Typical circuit topology of a RTWO.

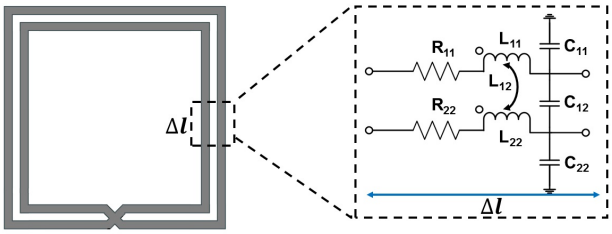

Figure 2: Equivalent electrical circuit of an infinitesimal section of an RTWO.

conductor (Möbius crossing), which causes a reversal in the signal (Figure 1). Oscillation begins with any noise event. If there were no losses, a wave would travel in the ring indefinitely, providing a complete clock cycle every two rotations to the ring (Möbius effect).

To model the electrical behavior of the RTWO resonant circuit, an equivalent electrical circuit of distributed elements (RLC) is used. The effects of the transmission line are modeled by resistance (R_{11} and R_{22}), self-capacitance (C_{11} and C_{22}) and self-inductance (L_{11} and L_{22}), while the magnetic and electrical coupling are modeled by mutual inductance (L_{12}), and mutual capacitance (C_{12}), respectively. The equivalent electrical circuit is shown in Figure 2.

Since there are losses in the conductor due to discontinuities or the dielectric, the signal will be attenuated while it travels through the resonant circuit. Therefore, an amplification stage is required to compensate the losses of the resonant circuit. For the amplification stage, a topology consisting of two inversers antiparallely connected (CCIP) were used. Additionally, the CCIPs block the phase, which causes the odd propagation mode, i.e. a signal in one line will be offset by 180° from the signal in the other line. The compensation stage configuration is shown in Figure 3. The CCIP stages will generate negative resistance

(transconductance), which compensates the resistive losses of the resonant circuit. These compensation stages are evenly redistributed throughout the ring.

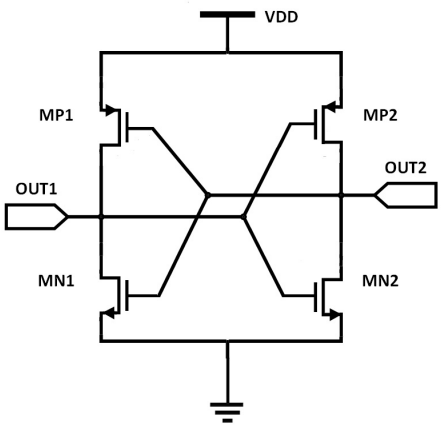

Figure 3: RTWO compensation stage.

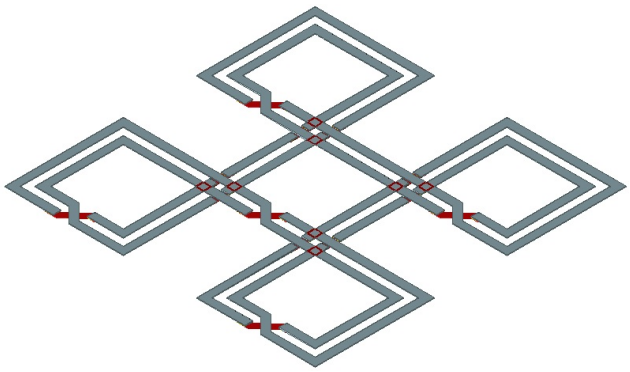

Figure 4: Rotary Oscillator Array (ROA).

2.1 Rotary Oscillator Array (ROA)

Multiple RTWOs can be connected together to form an array of rotating oscillators that distribute a signal to the entire chip. Figure 4 shows a basic structure of a ROA constituted by five RTWO rings connected in a checkerboard topology.

The inner rings and outer rings of the adjacent RTWOs are physically connected for synchronization purposes [14]. The advantage of implementing a ROA instead of a single RTWO is that a ROA provides more interconnection points, which eliminates the need of using too long interconnections between the synchronous element and the oscillator. The decrease in interconnection length provides the reduction in signal delay caused by the effects of high-frequency interconnections.

2.2 RTWO design parameters

Two of the main design parameters of a RTWO are power consumption and frequency of oscillation, which will be described in the following sections.

2.2.1 Power consumption

The power consumption of the RTWO is the sum of the contribution of the resonant circuit and the compensation stages, where the power dissipated by the resonant circuit P_{lt} can be calculated by Equation 1:

$$P_{lt} = \frac{{V_{DD}}^2}{{Z_c}^2} \tag{1}$$

The power consumption of the compensation stage P_{CCIP} is divided into three components: the static power consumption, which is negligible; the dynamic power, which is recirculated and converted into energy for the resonant circuit; and the short circuit power, which cannot be ignored and is consumed when both NMOS and PMOS transistors are switched on [15]. P_{CCIP} is expressed by Equation 2 as:

$$P_{CCIP} = \frac{I_s V_{DD}(t_r + t_f)}{T} \tag{2}$$

Where I_s is the saturation current, t_r is the signal rise time, t_f is the signal fall time and T is the signal period.

2.2.2 Frequency of oscillation

The frequency of oscillation f_{osc} is a factor of the total capacitance C_t and the total inductance L_t, as is expressed in Equation 3.

$$f_{osc} = \frac{1}{2\sqrt{L_t C_t}} \tag{3}$$

L_t is just related with the differential transmission line, while C_t depends on Equation 4. C_{lt} is the capacitance of the differential transmission line, C_{comp} is the capacitance of the compensation stage and C_{load} is the load capacitance.

$$C_t = C_{lt} + C_{comp} + C_{load} \tag{4}$$

As is seen from Equations 3 and 4, f_{osc} will strongly depend on the geometry of the RTWO and the compensation stage.

2.3 RTWO structure and manufacture

The RTWO of the present work was built using a 180 nm mixed-mode UMC manufacturing technology, which uses a single level of polysilicon and 6 levels of metal (1P6M), P-type substrate, and RFCMOS. The structure was made of aluminum at level 6, with the Möbius crossing at level 5. Figure 5 shows a schematic of the technology used. The main physical and electrical parameters of the RTWO are shown in Table 1.

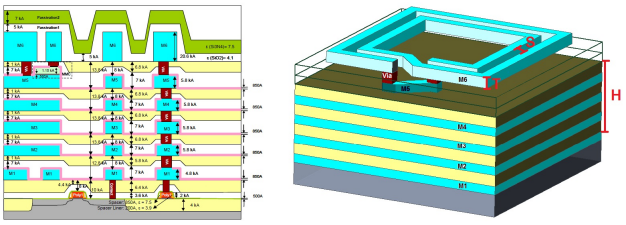

Figure 5: (a) Cross-section view of the UMC 180 nm RFCMOS manufacturing technology, (b) 3D structure of the RTWO.

Table 1: UMC 180 nm CMOS manufacturing process parameters, and RTWO geometrical features.

Parameter	Symbol	Value
Conductivity (S/m)	σ	37×10^6
Material permitivity	ε_r	3.8
Vacuum permitivity (F/m)	ε_0	8.854×10^{12}
Vacuum permeability (H/m)	μ_0	$4\pi \times 10^{-7}$
Line thickness (μm)	T	2.06
Oxide thickness (μm)	H	6.52
Line length (μm)	l	1000

2.4 Geometrical discontinuities

The abrupt changes in the conductor geometry of the transmission line cause geometrical discontinuities. Consequently, the electric and magnetic field distributions are modified near the discontinuity when high-frequency signals are transmitted through them.

In RTWOs design, right-angled corners origin a build-up of load particularly on the outside of the corner, which causes capacitance overload. Similarly, the interruption of the current flow produces inductance overload [8, 9]. Since the excess of capacitance and inductance change the frequency of oscillation and the power consumption of the RTWO, it is necessary to use a compensation technique for this type of geometrical discontinuity.

There are different useful techniques to compensate the excess of capacitance and inductance caused by 90° corners. These techniques remove some of the metal from the corners. Figure 6 shows the full-wave results from a geometrical discontinuity simulation. The current density is best redistributed by a 45° chamfer, 1 side [16]. Therefore, the less load build-up at the corners decreases the capacitance, compared to a right angle corner.

2.5 Topologies

In RTWO design, several topologies of different shapes are known, such as circular, hexagonal, octagonal, and square with different number of crossings. These topologies have been applied in [10, 17, 18, 21]. However, there is no analysis joining the effect of the diffrent discontinuities on the answer of an RTWO. In RTWO design, the dimensions of the oscillator, the design of the compensation stage, the geometric discontinuities, and the topology used for the oscillator, have a high impact on the inductance and capacitance of the differential transmission lines from which the oscillator is built. As consequence, they affect the oscillation frequency and the power consumption of the RTWO.

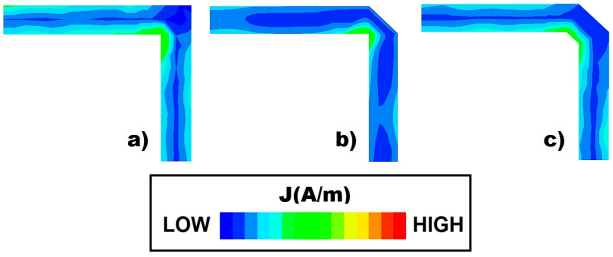

Figure 6: Current distribution on transmission line using mitered techniques: (a) Right angle bend (no mitered), (b) 45° chamfer - 1 side, (c) 45° bend - 2 sides.

3 Methodology

In order to include the effects of the geometrical discontinuities, in [19] and [23] the transmission lines of the rotating ring were divided into uniform segments. However, the union of the different segments presents differences in contrast with the superposition of the effects by segments. Both technique differ from the simulation of a complete ring [22]. Thus, to minimize the discrepancies and to consider the greatest number of electromagnetic effects in the structure of a RTWO, the methodology used in this work includes the simulation of the full ring.

Different software tools were used to simulate the RTWO due to the fact that the 3D electromagnetic simulator used (EMPRO) only extracts the S-parameters from the full-wave simulation. Then, it requires the use of an additional software to calculate the parameters of the RTWO through the S-parameters (MATLAB in this work), and another one to simulate the electrical circuit of the RTWO (HSPICE). Therefore, in this work the first step was to use EMPRO to develop the 3D geometrical structure of the RTWO. Then, a full-wave simulation was performed by means of the Finite Element Method (FEM). The resulting S-parameters from the simulation were exported to MATLAB. With MATLAB, the RLC parameters, the transistor size of the compensation stage, the power consumption and the oscillation frequency by analytical approaches were calculated. Finally, HSPICE was used to implement the RTWO considering the RLC parameters of the resonant circuit and the compensation stage, simulating the circuit of the distributed elements of the resonant circuit and the compensation stages of the RTWO.

At first, a working frequency range from 11 to 12 GHz was defined. In the simulations of [22], it was determined that with a length of 1000μm, the frequency

of oscillation range required was obtained. Therefore, different simulations of the RTWO were carried out varying the width W, the separation between the transmission lines S, and the topology of the RTWO, to observe the impact of these factors over the oscillation frequency and the power consumption. In the simulations developed with HSPICE, eight uniformly distributed amplification stages were used.

4 Effect of W and S on f_{osc} and P_t

All the electrical properties of the interconnections are due to the arrangement of the conductors and dielectrics and the way they interact with the electrical and magnetic fields of the signals. The total resistance of the interconnections depends on the signal strip and the return plane; both resistors depend on the geometry of the conductors and the current distribution in them. The inductance is also composed of two terms, the first related to the inductance inside the conductors and the second term, called external inductance, produced in the proximities of the conductors. Both inductances, as well as the resistance, depend on the current distribution in the conductors. On the other hand, the value of the capacitance depends on the distribution of the charge on the surface of the conductors.

As it was seen, inductance, resistance and capacitance in the interconnections, depend strongly on their geometry. Since the resonator circuit of the RTWO is built by the interconnections of the integrated circuits, and the frequency of oscillation depends on the capacitive and inductive effects of the interconnections, the impact of the width of the interconnections on the frequency of oscillation and the power consumption of the RTWO must be analyzed. Therefore in this work, several simulations were performed considering W in the range of 5 μm to 25 μm. Moreover, the value of S was set at the minimum value of W, in this case, 5 μm.

Figure 7 shows the variation of the total inductance L_t and the total capacitance C_t for the different values of W. As W increases, the cross-sectional area over which the current is distributed increases, so the total number of magnetic field line loops decreases and, therefore, L_t decreases. When increasing the size by W, the transconductance g_m required to compensate the losses must increase, so larger transistors are required and, as consecuence, C_{comp} increases. In the same way, considering the analogy of a parallel plate capacitor, when increasing the width of the line, the capacitance C_{lt} increases. The increment of both capacitances (C_{comp} and C_{lt}) produce the increment of the total capacitance.

Figure 8 shows the variation of the characteristic impedance Z_c and the resistance R when varying W. In this case, it can be seen that both parameters decrease with the increase of W because there is a larger cross-section where the current flows through the transmission line. Figure 9 shows how the frequency of oscillation and power consumption varies by increasing W. The low dependency of f_{osc} to W is due to the fact that the increase of C_t is compensated by the decrease of L_t (Figure 7).

Setting the values of l=1000 μm and W=5 μm, another parameter that can be varied is the separation between the transmission lines S. In this case, values from 5 μm to 15 μm were taken for S. Figure 10 shows the variation of L_t and C_t depending on the different values of S.

Due to the separation of the transmission lines, a smaller number of magnetic field lines are annulled, which causes the increase of the mutual inductance and therefore the increase of L_t. On the other hand, as the transmission lines are separated, fewer losses are required to be compensated for, so the size of the transistors decreases and C_t decreases. Figure 11 shows the variation of R and Z_c depending on the different values of S. It can be seen from the graph that both R and Z_c have little dependence on the separation of the transmission lines.

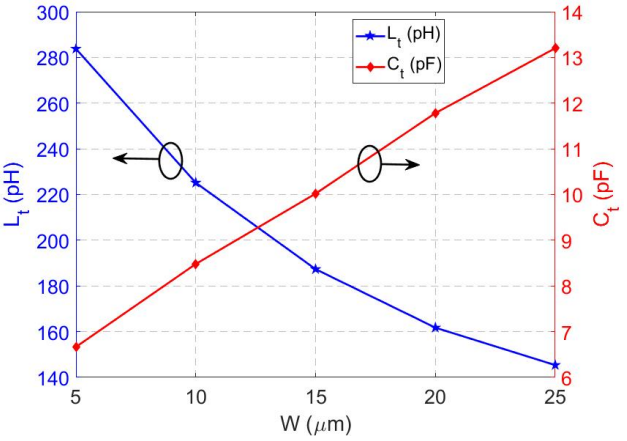

Figure 7: Variation of L_t and C_t when increasing W.

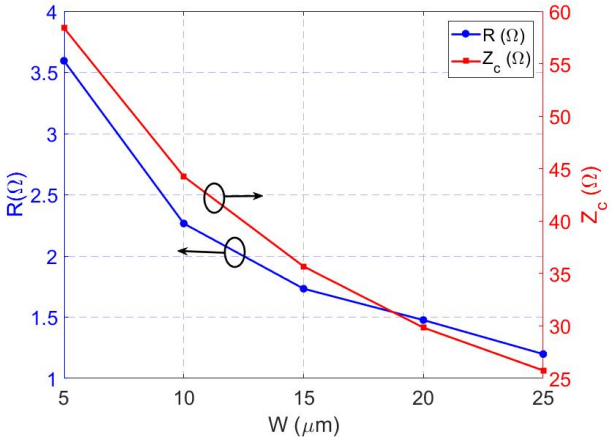

Figure 8: Variation of R and Z_c when increasing W.

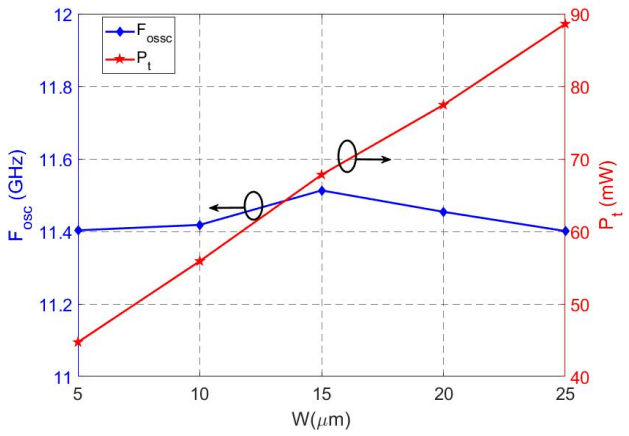

Figure 9: Variation of f_{osc} and P_t when increasing W.

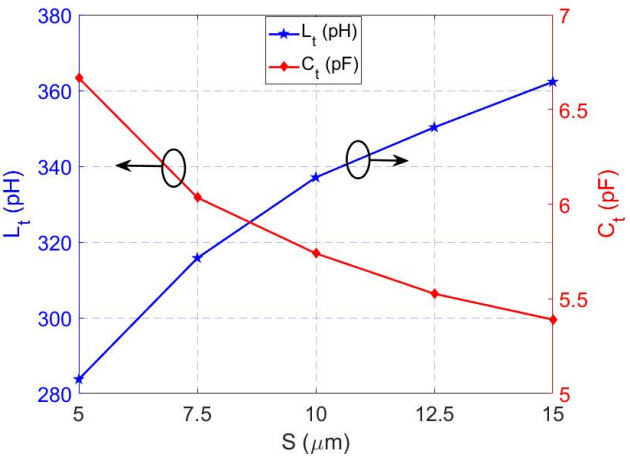

Figure 10: Variation of L_t and C_t when increasing S.

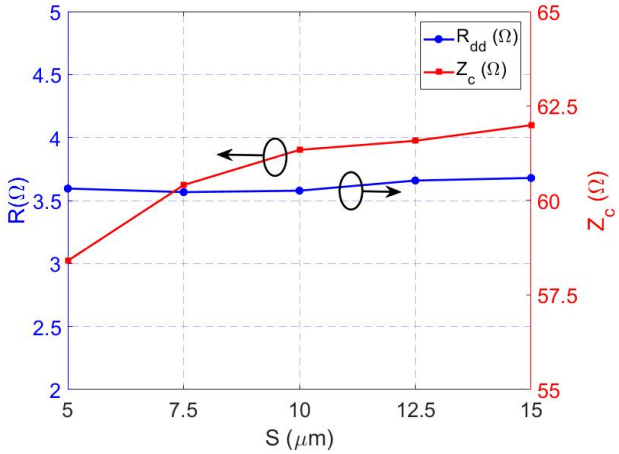

Figure 11: Variation of R and Z_c when increasing S.

Finally, Figure 12 shows that f_{osc} remains approximately constant. On the other hand, the power consumption P_t decreases when separating the transmission lines, due to the decrease of the power consumption of the compensation stage.

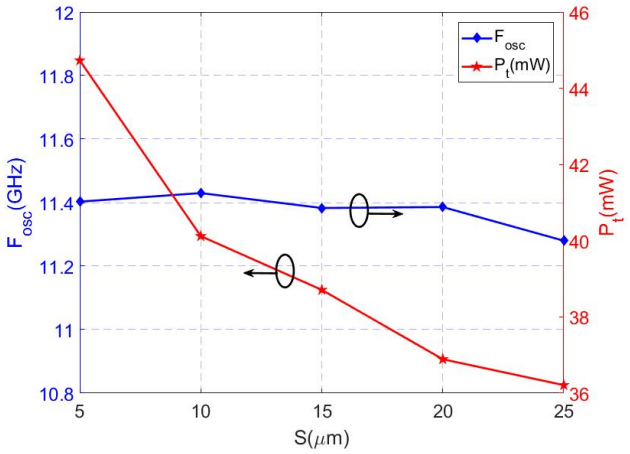

Figure 12: Variation of f_{osc} and P_t when increasing S.

5 Discontinuities compensation effect in squared topology

Prior to the simulation of the different RTWO topologies, the squared RTWO design was optimized by applying two mitered techniques: 45° miter - 1 side, and 45° miter - 2 sides (Figure 6). Three layouts were developed using the squared topology with a Möbius crossing, by means of the Mentor Graphics Design Editor (Figure 6a). In Layout 1 no mitered was implemented, but in Layout 2 the 45° mitered corner - 1 side was implemented, and in Layout 3 the 45° mitered corner - 2 sides. For the hexagonal and octagonal layouts, any mitered technique was applied. The performance parameters of the oscillators applying the different mitered techniques are shown in Table 2. It is worth to mention that Layout 4 corresponds to the squared topology of the RTWO built directly with the EMPro electromagnetic simulator, and not with Mentor Graphics, but for ease, it is also included.

Table 2: RTWO performance parameters using different mitered techniques.

Layout	F_{osc}**(GHz)**	P_t **(mW)**
1	11.66	41.18
2	11.82	39.28
3	12.07	37.74
4	11.43	40.12

From Table 2 is inferred that the 45° mitered on both sides of the line (Layout 3), is the most effective mitered technique because it allows to the RTWO having the highest oscillation frequency, in agreement with [16], due to its less capacitance and total inductance variation. In the same way, when comparing values of extracted capacitance, there is a variation of 5% in the total capacitance where EMPro is used directly (Layout 4) and when the RTWO layout is done in Mentor Graphics (Layout 3). This variation is due to the fact that in the layout from Mentor Graphics several vias (small contacts between the different metals of the technology) were used to connect the 5th and

6th levels of metal, while in Layout 4 only one single contact is used, which is unsuitable for real integrated circuits.

6 Topology effect

Figure 13 shows the total variation of the resistance, inductance, and capacitance for the different topologies of the RTWO analyzed. As is shown, the total capacitance increases since there are more crossings in the metal 5 (see topologies in Figures 14d to 14f). This effect is due to the increase in capacitance coming from the crossing. Figure 14(b) shows how the crossing in metal 5 (topologies 4, 5 and 6) increase resistance due to the smaller thickness of the metal 5 in contrast with metal 6. Therefore, the cross-section through which the current flows is lower causes an increase in the resistance.

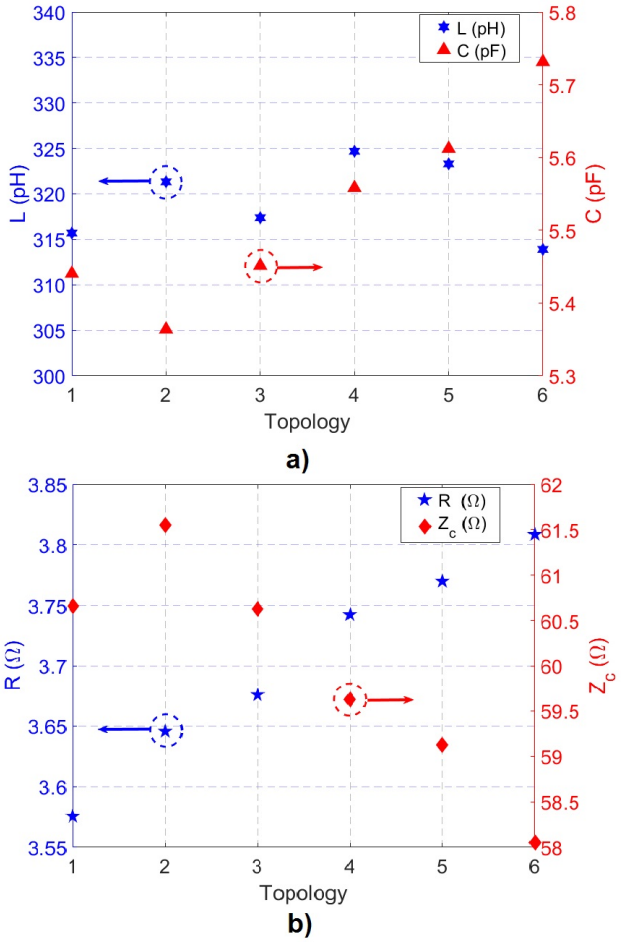

Figure 13: Electrical parameters of the different topologies: Resistance (R), Inductance (L), Impedance (Zc) and Capacitance (C).

Table 3 shows the performance parameters of the RTWO using different topologies. In this table, two crossing types are identified: one where metal levels 5 and 6 intersect diagonally (Möbius crossing), and the other one where metal levels 5 and 6 intersect orthogonally (simple crossing). It is observed that the oscillation frequency between oscillators having only one metal crossing (topologies 1, 2 and 3) is approximately the same; whereas if the number of crossings in metal 5 increases, the oscillation frequency decreases due to the increase of the inductance and the capacitance in the crossings. On the other hand, the power consumption increases as the number of metal 5 crossings increase (topologies 4, 5, and 6), due to the increase of the resistance and the reduction of the characteristic impedance.

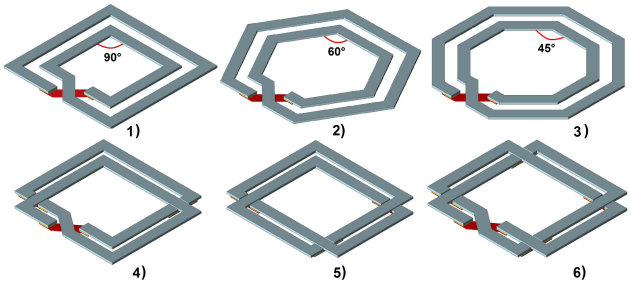

Figure 14: RTWO topologies analyzed: 1) Square with 1 Möbius crossing, 2) Hexagonal with 1 Möbius crossing, 3) Octagonal with 1 Möbius crossing, 4) Square with 2 crossings and 1 Möbius crossing, 5) Square with 3 crossings, 6) Square with 4 crossings and 1 Möbius crossing.

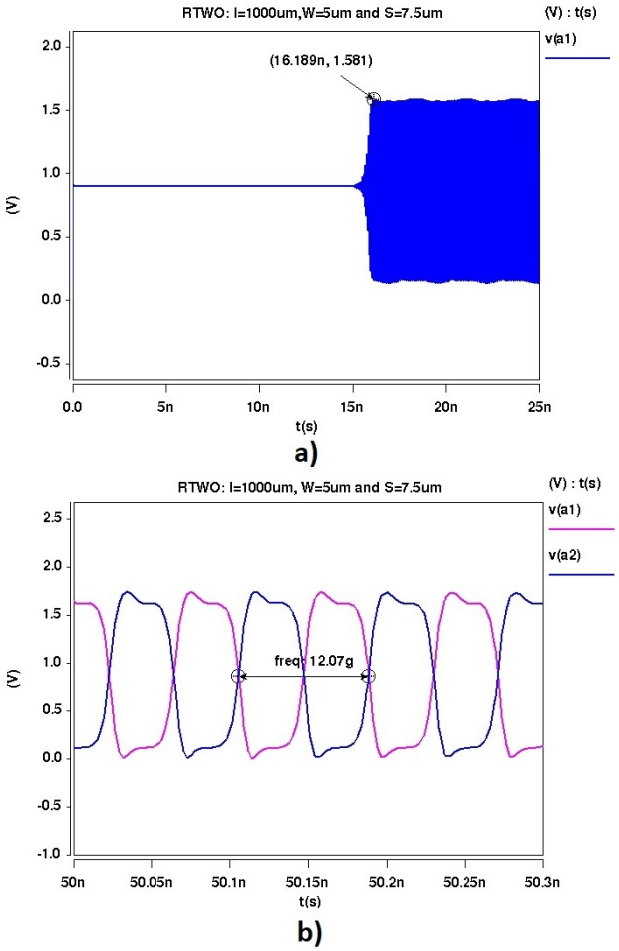

Figure 15: Waveforms of the RTWO oscillator: a) Beginning of the oscillation, b) oscillation of stable complementary nodes.

Table 3: RTWO performance parameters using diferent topologies.

Topology	F_{osc}(GHz)	P_t (mW)
1 (Squared-1 Möbius)	12.051	37.44
2 (Hexagonal-1 Möbius)	11.972	39.00
3 (Octagonal-1 Möbius)	11.937	39.67
4 (Squared-2 crossings-1 Möbius)	11.706	40.40
5 (Squared-3 crossings)	11.741	39.85
6 (Squared-4 crossings-1 Möbius)	11.701	42.18

Figure 15 shows the waveforms of the RTWO. In Figure 15a, is observed that, after 16.189 ns, the RTWO starts to oscillate in a stable form to a frequency of 12.07 GHz with an amplitude of 1.581 V. Figure 15b shows how the waveform of a node is offset by 180° from its complementary node. To observe the band nature of RTWO, the spectrum was observed over a span of 100GHz. Figure 16 shows the results of this simulation.

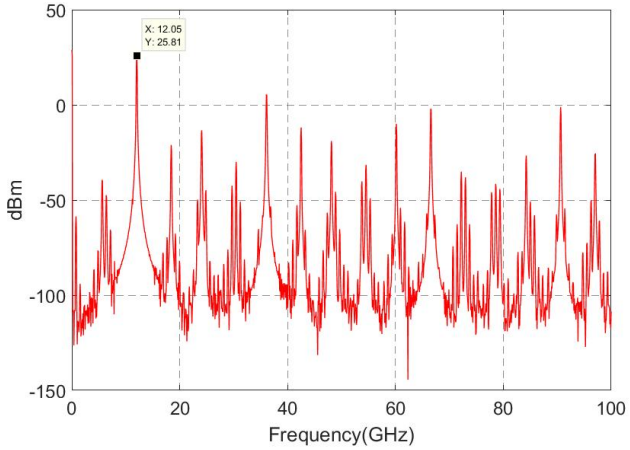

Figure 16: Typical power spectrum-wide band.

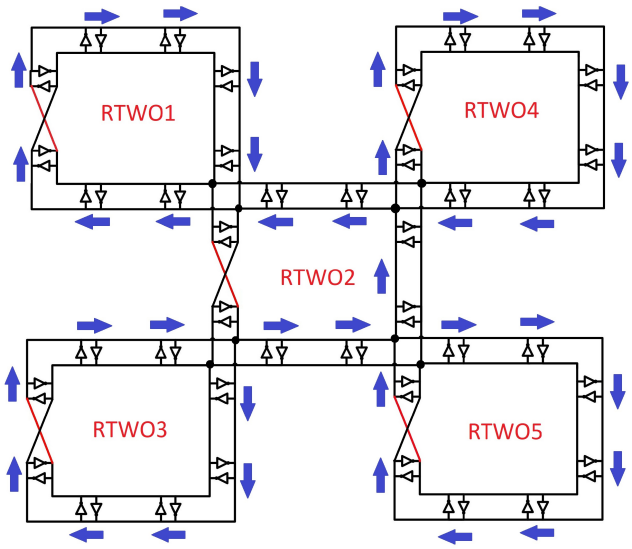

Figure 17: Diagram of the simulated ROA.

7 Design of an ROA

After designing a RTWO, an array of RTWO oscillators was made. In this case, a checkerboard configuration was used in which five RTWOs were connected (Figure 17). Each of the RTWOs is in phase with the others at the connection node. The advantage of a ROA is that multiphase signals can be obtained anywhere in the integrated circuit by reducing the skew and jitter of the signal.

The signal of each of the RTWOs of the ROA is shown in the Figure 18. In this case, only the signal of the external nodes of every RTWO is shown. It can be seen that the signals travel in clockwise direction, while in the middle RTWO (RTWO2) they travel in the opposite direction. Similarly, as the signal passes from one compensation stage to another, the signal is offset. For this case, the offset is given by Equation 5:

$$\Delta\Theta = \frac{180°}{\#stages} = 22.5° \tag{5}$$

Nevertheless, if small oscillation frequencies are desired, they must be made with maneuverable lengths so that L_t and C_{lt} increase their value and therefore the oscillation frequency decreases. This is a disadvantage in the design of RTWOs and ROAs because they will consume a larger area on the chip. Another way to decrease the frequency of oscillation is to be able to increase C_{comp}, which can be achieved by making larger transistors for the compensation stage. The disadvantage is that having very large transistors increases the power consumption, therefore there is a strong compromise between the area of the chip and the power consumption in low frequency RTWOs.

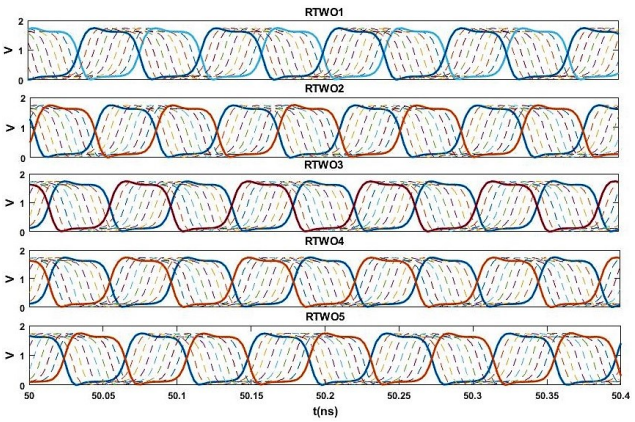

Figure 18: Simulated output waveforms.

8 RTWO performance comparison against existing works

In order to show the efficiency of the designed method applied at the present work, a comparison was made with two published methodologies: the methods of Chen et al. [11] and Aidoo et al. [15]. Chen et al. used analytical approximations in the determination

of the electrical parameters R, L and C of the RTWO, including different RTWOs at different frequencies simulated in HSPICE with parameter values of a technology 0.18μm SMIC and a 1.8 V power supply. In contrast, Aidoo et al. divided the RTWO structure into segments with equal dimensions while the parasite parameters were extracted from every segment using a 2D simulator. By this method of bonding segments, Aidoo et al. designed and manufactured different RTWOs using an IBM 0.18μm CMOS technology.

Using as reference the RTWO manufactured by Aidoo et al. at the present work (which oscillates up to 12.2 GHz), two RTWOs were designed with the same ring dimensions as well as of its compensators, but using 8 compensation stages for the design 1, and 28 for the design 2. Later, both the method used by Chen et al. and the one proposed in this work, were applied to extract the parasite parameters from the RTWO. The specifications of the different designs are shown in Table 4.

Since the comparison made in Table 4 considers RTWOs designed by parameters of different technological processes, this might not be a good comparison. In order to improve the comparison, two RTWOs were designed using the same technology (UMC 180 nm RFCMOS): one of them applying the method of Aiddo et al. and another one applying the method proposed in this work. Table 5 shows a comparison of the parasite parameters variations (R, L and C), the size of the transistors, the oscillation frequency and the amplitude of both designs. K_m represents the magnetic coupling coefficient of the ring differential line used to develop the electrical simulation in HSPICE. W_p and W_n are the dimensions of the transistors of the compensating circuit.

Table 4: RTWOs specifications using different manufacturing technologies (l= 880 μm, W =10 μm , S = 20 μm).

Parameter	Aidoo [15]	Chen [11]	Design 1	Design 2
$W_n(\mu m)$	48	52.1	52.1	15.3
$W_p(\mu m)$	115	140.6	140.6	41.4
Compensation stages number	8	8	8	28
f_{osc} simulated (GHz)	11.9	12.83	12.205	12.19
f_{osc} experimental (GHz)	12.2	—-	—-	—-
$f_{osc-sim}$- $f_{osc-exp}$ (%)	-2.45	5.16	0.04	-0.08

In Table 5, it is possible to observe that the oscillation frequency increases by 0.53% with respect to the one obtained by the method of Aidoo et al. This increase in the oscillation frequency agrees with the behavior between the simulated and the experimentally measured values of Aidoo et al. Moreover, the value of the resistance obtained from the simulation when applying the method of Aidoo et al. is lower than the extracted through the method developed at the present work. This is because the method of Aidoo et al. does not contemplate the proximity effect nor the skin effect on the return plane, and this variation in resistance directly affects the amplitude value. Therefore, the greatest number of electromagnetic effects must be considered to obtain more accurate results.

Table 5: Comparison between designed methods using the same technology.

Parameter	Aidoo [15]	This work	Variation (%)
$\Delta R(\Omega)$	0.231	0.286	23.78
$\Delta C(fF)$	15.753	14.720	-6.55
$\Delta L(pH)$	33.364	32.581	-2.34
$\Delta C_m(fF)$	1.548	2.252	45.45
K_m	0.072	0.052	-27.77
W_n (μm)	52.060	52.060	—-
W_p (μm)	140.580	140.580	—-
F_{osc} (GHz)	12.140	12.205	0.53
V_{out} (V)	1.770	1.685	-4.80

9 Conclusions

In this paper the impact of topology, dimensions and geometric discontinuities on power consumption and frequency of oscillation in an RTWO were investigated. To obtain RLC values with greater accuracy than other previous works [11, 19, 20, 17, 23] , the use of a 3D electromagnetic simulator was implemented. From the results presented, it is shown that the correct dimensioning of the resonator is vital in this type of oscillator. It was observed that at a frequency range of 11.4GHZ-11.5GHz it is possible to save up to 98% of the power consumption by making the transmission line with a W=5um. It is recommended to choose a W as small as possible where the resistive losses in the conductor allows the RTWO oscillate as it was designed.

Additionally, it is recommended to compensate the discontinuities using some mitered technique. According to the results obtained, it is possible to improve (increase) the frequency of oscillation up to 3.34% when changing the corners from 90° to corners at 45°. The simulations results show that the RTWO topology has a strong influence on the oscillation frequency and the power consumption, i.e. when the number of crossings in a lower metal increases, the oscillation frequency decreases and the power consumption of the resonator increases. Consequently, we conclude that it is better to elaborate the structure of the RTWO with only one crossing in a lower metal level.

References

[1] Samar Hussein, and Ahmed Eladawy, Design of a 85 GHz Rotary Traveling Wave Oscillator for Imaging Applications, International Journal on Recent and Innovation Trends in Computing and Communication,. vol. 4, no. 6, pp. 321 324, 2016.

[2] Paolo Maffezzoni, Bichoy Bahr, Zheng Zhang, and Luca Daniel, Oscillator Array Models for Associative Memory and Pattern Recognition, IEEE transactions on circuits and systemsregular papers, vol. 62, no. 6, pp. 1591-1598, June 2015.

[3] Omeed Momeni, and Ehsan Afshari, High Power Terahertz and Millimeter-Wave Oscillator Design: A Systematic Approach, IEEE Journal of solid-state circuits, vol. 46, no. 3, pp. 583- 597, March 2011

[4] A. J. Drake, K. J. Nowka, T. Y. Nguyen, J. L. Burns, and R. B. Brown, Resonant clocking using distributed parasitic capacitance, IEEE Journal of Solid-State Circuits, vol. 39, no. 9, pp. 1520 1528, Sept. 2004.

[5] J. Wood, T. Edwards, and S. Lipa, Rotary traveling-wave oscillator arrays: A new clock technology, IEEE J. Solid-State Circuits, vol. 36, no. 11, pp. 16541665, Nov. 2001.

[6] OMahony, F. ; Yue, C.P. ; Horowitz, M.A. ; Wong, S.S. A 10-GHz global clock distribution using coupled standing-wave oscillators, IEEE Journal of Solid-State Circuits, vol. 38, no. 11, pp. 1813- 1820, 2003.

[7] Zhengtao Yu, Xun Liu, Low-Power Rotary Clock Array Design, IEEE Transactions on Very Large Scale Integration (VLSI) Systems, pp. 5 12, 2007.

[8] A. K. Rastogi, Munira Bano, Manisha Nigam, Microstrip Line Discontinuities Simulation at Microwave Frequencies, Advances in Physics Theories and Applications, vol.19, pp. 38-48, 2013.

[9] Sara Hosseini, Majid Shakeri, Sara Ebrahimian, Fatemeh Arastoonejad, A New Survey on Comparative Analysis of Discontinuities at Microstrip Lines Using Quasi-Static TLM SCN,. Journal of Basic and Applied Scientific Research, vol 3, no. 2, pp. 126-134, 2013.

[10] Koji Takinami, Rich Walsworth, Saleh Osman, and Steve Beccue , Phase-Noise Analysis in Rotary Traveling-Wave Oscillators Using Simple Physical Model, IEEE Transactions on microwave theory and techniques, vol. 58, no. 6, pp. 1465-1474, June 2010.

[11] L. Chen, H. Zhang, J. Zhou, and K. Chen, Efficient design of rotary traveling wave oscillator array via geometric programming, Journal of Zhejiang University-SCIENCE A, vol. 10, no. 12, pp. 18151823, 2009.

[12] C. Zhuo, H. Zhang, R. Samanta, J. Hu, and K. Chen, Modeling, optimization and control of rotary traveling-wave oscillator, in Proceedings of the 2007 IEEE/ACM international conference on Computer-aided design, pp. 476480, IEEE Press, 2007.

[13] Gonzalez, R. M. H., Aranda, M. L., Martínez, L. H., & Díaz, C. A. S. (2017, October), "Topology and discontinuities effect on CMOS rotary traveling wave oscillators". In Electrical Engineering, Computing Science and Automatic Control (CCE), 2017 14th International Conference on (pp. 1-5). IEEE.

[14] Y. Teng, J. Lu, and B. Taskin, Roa-brick topology for rotary resonant clocks, in Computer Design (ICCD), 2011 IEEE 29th International Conference on, pp. 273 278, IEEE, 2011.

[15] M. Aidoo, N. S. Dogan, Z. Xie, H. Savci, and P. Roblin, A power-aware rotary traveling wave oscillator (rtwo) design in 0.18 um cmos, in 2014 IEEE MTT-S International Microwave Symposium (IMS2014), pp. 14, IEEE, 2014.

[16] Chang, Richard Weng-Yew and See, Kye-Yak and Tan, Yang-Long, Impacts of bends and ground return vias on interconnects for high speed GHz designs, in Electromagnetic Compatibility and 19th International Zurich Symposium on Electromagnetic Compatibility, (APEMC2008), pp. 502-505, IEEE, 2008.

[17] L. Wu, R. Sebsebie, M. Kirkman-Bey, M. Aidoo, Z. Xie, and N. S. Dogan, Design of 110152 ghz rotary traveling wave oscillators in 65 nm cmos technology, in IEEE SOUTHEASTCON 2014, pp. 14, IEEE, 2014.

[18] Ma. Wei Fei, Hao Yu, and Junyan Ren, A 75.7 GHz to 102 GHz Rotary-traveling-wave VCO by tunable composite Right/left Hand Tline, IEEE Custom Integrated Circuits Conference, pp. , 2013.

[19] Armenta Márquez, Linares Aranda, and Hernández Martínez, Influence of discontinuities in Resonant Oscillators based on Transmission lines, 12th International Conference on Electrical Engineering, Computing Science and Automatic Control, pp. 593-598, 2015.

[20] M. Aidoo, CMOS Rotary TravelingWave Oscillators (RTWOs). PhD thesis, North Carolina AT State University, 2014.

[21] Raleigh Smith, Tuning of the Relative Phases of a Rotary Travelling Wave Oscillator, M. Sc. Thesis, 2014.

[22] Higuera Gonzalez, Caraterización de osciladores resonantes RTWO en tecnología CMOS, M. Sc. Thesis, 2017.

[23] Armenta Márquez, Oscilador Resonante de onda Rotatoria en Tecnologa CMOS, M. Sc. Thesis, 2015.

ASTES

Advances in Science, Technology and Engineering Systems Journal Vol. 3, No. 4, 270-275 (2018)

www.astesj.com

Special Issue on Multidisciplinary Sciences and Engineering

ASTESJ

ISSN: 2415-6698

Sequential Card Activities of Recollect Experience for Elderly with Dementia

Fang Lin Chao*, Boxiu Fanjiang

Department of Industrial Design Chaoyang University of Technology, 436, Taiwan R.O.C

ARTICLE INFO

Article history:
Received: 11 May, 2018
Accepted: 28 July, 2018
Online: 10 August, 2018

Keywords:
Sequential card
Dementia
QR code
App.

ABSTRACT

In this study, the authors propose a modified design of sequential card activities to recollect experience for the elderly with Dementia. The cards and App were designed to complement each other for Nostalgia-based support. Image and text are utilized to trigger memories that bring out shared experience from the patient. By using suitable trigger elements, group sharing, and physical objects, one can enhance the memory recall. The procedure of rice dumpling preparation and making were listed in a sequential step and printed on cards. Cards are shuffled, and the elderly are asked to sort these cards to right sequence with the help of QR scanner. In multiple theme scenarios, different groups of object making steps were mixed, and the player needs to select cards that related to a specific group. Using actual items and activities, the triggered of elder's experience was confirmed. The qualitative testing results showed that the elderly enjoyed the activities. Those events verified the effectiveness of the proposed method.

1. Introduction

There had been an increasing trend for the number of patients with dementia in recent years, as well as a trend in which the average age for patients with dementia is becoming younger. This situation has been a challenge in the country where the amount of caregivers is low compared to the elderly population. The medical community has not found a cure for dementia; however, the condition often follows some pattern. Characteristically, foreign workers hired as caregivers do not make use of community-based services as they care for the elderly. Many efforts had been developed to support the elderly with dementia. For instance, training program, caring direction and technologies have been utilized to investigate and improve patient well-being [1-3]. The designer should realize that an integrated approach is necessary to address the cognitive, emotional and motivational aspects.

Although low-tech external memory aids have limitations, these limitations may be addressed by smart assistive technologies. Mihailidis and Fernie had concluded in a study that people with dementia assisted by context-aware computing [4]. "The research illustrates developmental training needs for dementia nursing to improve the efficacy of assessments and therefore interventions" was proposed by Carradice et al. [5]. Banerjee discuss the quality of care in dementia, co-resident spouse care with Alzheimer's dementia. Training benefits on cognitive, behavioral, and global functioning in patients with Alzheimer's disease were reported [6]. If possible, technologies should be designed to be friendly and noninvasive.

We had observed that some patients fail to remember recent events quickly, but can recall events from the distant past. To address this, designers need to include an individual's environmental context and social relationship during their design process. Group-based nostalgia induced recollect experience may take different forms in the lives of each elderly. "During bus trip in a distant city, nostalgia was identified as a key element of the experience for socializing" [7]. In elder care center in Taiwan, some may reminisce through sing old traditional songs together, while others may look at old photos of buildings or sceneries, or read letters from the past from acquaintances. Recollect experience can be an image, text or sound track that can trigger the memory. In the instance where the caregiver and the elder have no close relationship, the activity seldom triggers any feedback. This problem indicates that the event is not sufficient, and the reaction was rendered as non-existent. As shown in Figure 1, it's difficult to communicate since they may not know much about the elder's background, so professional activities are needed.

2. Objectives and Methods

The goals and approaching of this study are:

1. Design sequential card activities of recollect experience that are suitable for patients with memory loss; trigger feedbacks from them using the appropriate images and text.

*Corresponding Author: Fang Lin CHAO, email: flin@cyut.edu.tw

Figure 1. Relationships between person help recollect experience: A foreign helper has less in common with the elder, which causes less memory recollect .

2. To propose a group activity, through the mutual agitation among members; the seniors with dementia can discover the differences between others and arouse interest. Based on personal characteristics, actual items were utilized to trigger past experience.

An improved design was used so that participants can use it actively without technology barrier. In the nostalgia-based supporting, different presentation of information and background memory elements can enrich interaction. During this study, the designer and the elderly play with the sequential card game together. The designer can test the system, collect feedback, and implement improvements in the newer version. Sections III, IV and VI describe our evolutional development cycles from the initial concept.

3. Arrange Sequential Card Activities

There are memories or facts in memory backtracking. Consciousness not only contains symbols, words, or phenomena but a combination of life experiences. The feature of cards game is that each card has its facts and events. When any card wakes up the user's memory, he can continue to explore the relationship between the cards. At the time of exploration, the life experience began to be excavated. The card game proposed in the previous reference applied to the wake of the experience of the elderly [8]. This article will further elaborate on the relevant content and details.

3.1. Design approach

Information technology used in many ways. For example, we can implement card games within touchscreens with software; because the one operating the app needs to be familiar with the use of mobile phones, the elderly may not suitable. Although the design has the greatest flexibility, we still adopt "supportive" proposals. The APP is only a supporting character. If there is any doubt, one can use a scanner to get help. It is as though we are asking others a question. Because the sequential card games are with a physical object that can be touched, it is suitable to link with the life experience of the elderly and reduces the fear.

3.2. Concept realization

Software is used as a means to reduce the stress in taking care of elderly with dementia; since they often repetitively ask the same questions, the average caretaker may be irritated from answering the same questions over and over again. Thus, the app is advantageous in that it can make a reply anytime, and answer related questions immediately, and won't be irritated from repeating the same answers.

Table 1. The concept shifts concerning the user confidence, where fluency means "the possibility of without obstacles during the game."

	standalone within screen	supportive explanation
flexible	+++	- -
fluency	+	++
affordance	- - -	+++

Based on Table 1, we utilize app as a supporter or explainer. Sequential card was designed (Figure 2) with the theme of wrapping rice dumplings (zongzi). For each step card, a proper image and description text should be matched. The cards are shuffled in random order before the game, and the elderly are asked to sort these cards into the correct sequence.

As technology is added in design, we have to consider whether the senior will reject or not feel accommodated to using these tools. Thus, in the card design, pictures or text is still shown on the front side, while the tag placed on the back side. The user won't often be distracted by tag. When the user wishes to seek help, they can get pertinent information by moving the card to a fixed position. QR code was placed on the back of each card. While the elderly see the image, the scanner read the QR code and activate necessary audio explanation with adjustable volume and speed (Figure 3, 4). During the process, if the elderly ever want to express anything about personal experience, question or feedback, the elder's voice response would be collected.

Remaking the step cards would be inconvenient when there are plenty of triggering elements. A reconfigurable card holder can be used to different sequential cards. Considering game's flexibility, while selecting the proper subject, the card's corresponding QR code [8] will not require re-setting.

Figure 2. Continuous applicable card holder. A reconfigurable slot is placed on the side wall for inserting a card. A user can change the theme more efficiently with this design.

Figure 3. Scanning will take some time for elderly.

Figure 4. QR code placed at the back of the sequential card. With an unstable hand, the user need moves the card to the designated position stably to scan the code.

During the trial, we noticed a few unstable hands during code scanning. In the modified design, QR code is placed at the back of the card to make it more convenient for the elderly. When the user can't hold the phone steadily with their hands, scanning will take some time. We can make the response time from scanning faster by placing the phone in a fixed position (Figure 5). If the user can hold the phone steadily and successfully operate the app, then a fixture for scanning won't be necessary.

Figure 5. When the user can't hold the phone steadily with their hands, the supporting fixture make the response time from scanning faster

4. Mobile App Design

The app was made using MIT App Inventor 2 which use module block in programming. App design arranged procedure screens as Figure 6. App Inventor programs blocks (Figure 7) represent sensing the measured value through the QR connection.

Figure 6. When the user clicks on an image, a scanner pops up. As the user scans the corresponding image on the card, texts detailing each step of the food preparation process pops up.

Students in the industrial design department seldom use programs, so they often forget the syntax and structure of the program. The module block can connected to another neighborhood block. It will be pushed apart automatically if it is not appropriate. Therefore, the designers pay attention to the main logical relationship between the program block and the selection of the module. The connection between Bluetooth blocks, we need to setup the paired connection and send the appropriate data to the other party. As shown in Figure 7, the program block and the link of the modules is quite simple; although the blocks are simple, they still achieve powerful functions.

An event is an action that takes place. App Inventor II uses event handler blocks to specify how the program responds to individual circumstances. There is a user-initiated and automatic event. Every time the interval is up, a timer event triggered. Build-in sensors also initiated events when the user made a specific movement or orientation.

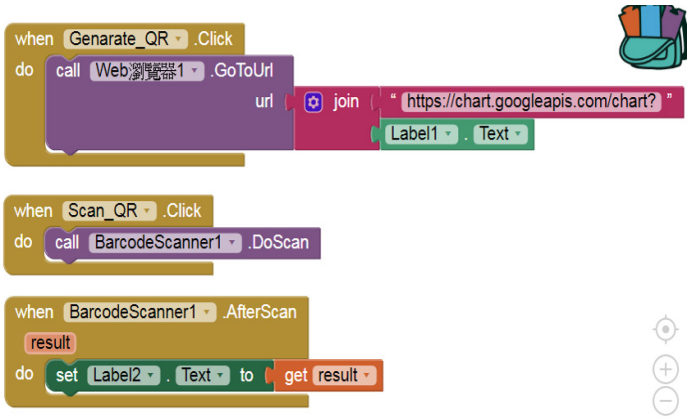

Figure 7. QR scan programming with modulated App Inventor blocks.

5. Multiple theme Scenarios

The more advanced games are organized for higher-skilled people; three recollect experience activities are available with different series of cards. Six step card blocks are cut to be in a 45-degree plane. By touching the magnets on each side, we can assemble six side blocks into a cube (Figure 8).

In multiple theme scenarios, different object making process are mixed, the player needs to select cards that related to specific objectives. After grouping those cards, one need to arrange those cards in proper sequence. When the blocks are organized into a cube, there is more variation for the player. The player cannot see all figures at once. The elderly need rotate the cube, and think about the category relationship between the images, and try to exercise their memorization ability more.

Assuming three recollect experience activities are available (making of rice dumpling, red turtle cake, and rice noodle soup), and each of these three groups has 6 step cards to be reordered. Put together cards of the same order, and make six cubes, and give those to the user. The researcher provides a questionnaire to the player. For example, if a user chose a turtle cake theme, the user has to make the related sides of each cube face upwards and rearrange these cubes.

(a)

(b)

Figure 8. Three-dimensional sequential card game, (a) magnets on the edge of a card allows each card to be attached to the cube, (b) the combined cube. In multiple theme scenarios, each card belongs to a different theme.

The flow chart for the sequential card game indicated in Figure 9. The explanations of each card are stored at separate lists. Player need recall experience about the steps of trigger elements and the timing relationship between cards. The cards help people focus and trigger the memory of a player.

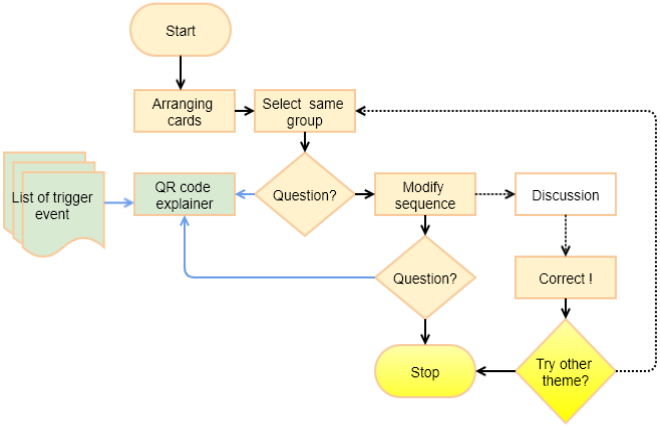

Figure 9. Sequential card and app flow chart indicates recollect experience with the support of QR code explainer. Question and discussion may be triggered while modifying sequence. After finish the sequential placement, users can try another theme.

6. User Testing

6.1. Elderly center interview

During the evaluation process, the participants actively talked to us about their experiences in making rice dumplings. For example, one mentioned a tip on how to make tastier dumplings, and one made a suggestion based on how her mother made it. The two testers shared the experiences with each other, which enhanced the recollect experience treatment's effect. The lady (in Figure 10) talked about when she was little, her family made red turtle cake during Christmas time, because her family treats Christmas like Lunar New Year, and this was their way of celebration. Tester C came from mainland China. She is a retired teacher. She is quiet and not very talkative to others. She likes to cook at home; she usually eats noodles and knows how to wrap rice dumplings herself. She prefers plain or slightly sweet rice dumplings with red bean paste or red dates added. Tester D is also a quiet lady with dementia. She often repeats the same thing over and over. She has more of a monotonous lifestyle and regularly watches TV. She likes to cook at home; usually, eat rice and prefer meat dumplings.

During the evaluation process, participants had made feedback about the using the sequential card. The shared message was recorded by a researcher. A five points Likert scale survey about playing the game were collected, the averaged of the score are shown in Table 2. The single theme achieved better manipulation experience, less skill and explanations were requested. When four people play a single theme sequential card game together, the games are fluent and emotional engagement (talkative to others) are high (score above the average value). This activities indicated positive feedback. They are grateful to share individual experiences. The communication links those elderlies together, and make nostalgia-based treatment more effective.

The multiple theme achieved less manipulation experience, more skill and memory function are request for proceed the game. More explanations were requested. Arranging magnets placed at sides and organized into a cube is a challenge for elderly with less detail manipulation skill. We suggested multiple theme is suitable only for advanced users.

Figure 10. User observation of multiple theme, to provide proper image with good resolution and teach user to get explanations through the support of QR code.

6.2. Follow-up personal activity

Through group activities, the mutual interaction among members, old people with dementia discovered the differences of others. Then, a follow-up private action based on actual items and

activities was conducted to confirm when measurable memory is triggered.

Table 2. averaged feedback about using the product (5 points Likert scale)

	single theme	multiple themes
manipulation skill	4.25	3.25
request explanation	3.00	4.50
fluent of game	4.25	3.00
emotional engage	4.25	3.25
talkative to others	3.75	3.00

Our participant is a 90-year-old woman with dementia; she often repeats the same thing and does not notice it. She has a monotonous lifestyle, and usually watches TV, and sleeps for longer durations. Based on past life experience, the selected personal activity is rice dumpling making. We prepared objects such as bamboo leaves, strings, and red dates (Figure 11).

Figure 11. The prepared objects and items during personal practice and interview.

Through the initial guidance, the participant gradually recall her past experiences with rice dumpling making. We then made recordings of her descriptions with different aspect of experiences (Figure 12).

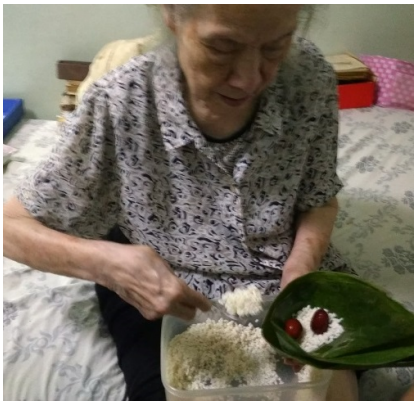

Figure 12. Personal practice and interview

Second, we will analyze the sentences (underline) in her descriptions, and categorize them into facts, estimations based on events, phenomena that may result from situations, and personal emotions. The subject's narrative was classified, and her depth of participation is presented in Table 3. During 3 hours of communication, we collect 24 minutes of voice records which are summarized below. Some paragraph was repeated to show her traits.

1. *How many kilograms of rice do you have to buy?* Now you can only get one serving. You have to buy a kilo of rice and soak the rice in water. Bamboo leaves must be soaked before they become soft.
2. *Do you know how to wrap a rice dumpling?* I thought these [strings] were worms! We put red beans with sugar, like cooking porridge. Rice must wash first. A cup of rice is fine. The rice must wash for preparing quickly.
3. Bamboo leaves must first be soaked water to be softened, which is not easy to be torn. Just put a few red dates on it. Wash them first and soak them in water, and throw a few into the rice dumplings. It will swell as soon as it cooked, and it will be delicious.
4. *What is the use of dates?* Red dates are used for eating ah! The boiled berry swell while cooking. There are hard shells inside the red dates, and your teeth may hurt if you accidentally bite on them. The price of bamboo leaves is high. Someone in the market sells USD, and another sells only $2. Larger leaves are more expensive because fewer people are selling them.
5. *When there is no bamboo leaf, how should you pack the rice dumplings?* Smaller leaves can be used, a few pieces together. If you don't break it, you can dry it and re-use it. Bamboo leaves have a scent! Maybe someone thinks it's smelly odor.
6. *How do you buy the leaf?* I guess. Do you mean to purchase bamboo leaves? Would you put pork or salted eggs in dumplings? We usually eat sweet rice dumplings. Let's start wrapping! I dumped the water and, here is the material for you, bamboo leaves and rice, and strings.
7. *Why is water dripping out from the rice dumplings?* There is water flowing out, and a hole on the side of the rice dumplings and rice inside may come out. Why do you use two leaves to wrap it? Because a piece of a leaf will quickly be torn with force and with two pieces, it will be firm.
8. *How do you tie the rope while bundling?* Hold it with one hand and use the other to help. This one was too flat and not wrapped well. Someone will use teeth to help bite the string and tie it so that it's tighter.

Owing to the capacity disorder of poor hearing, the participant would often say "what you are saying I can't hear". Sometimes she asks, "Where do you come from," "Where do you go to work?" and similar typical questions. This is the typical response of dementia patients.

The details response of those activities contains logical relations and inferential information, which are different from her usual behavior. In addition to the characteristics of the sentence analysis of her recorded response, there is also the presentation of actions. For instance, each of the steps of wrapping a rice dumpling is hidden as procedural memory in the cerebellum. When the hand touches these objects, such as materials for wrapping a rice dumpling, those memories are evoked; and the previous situations can emerge.

Table 3. The summary of voice recording and categorizing into facts, estimations, inductions and emotions.

facts	estimation	induction	emotion
hard shells inside fewer people are selling soak the rice red dates with sugar, wash first usually eat sweet water flowing out	hard shells inside only get one serving. buy a kilo of rice a cup of rice rice inside may run out will be firm two leaves to wrap	become soft will swell will be delicious cooked quickly Small pieces dry it and re-use it use teeth to help have a scent	I thought these were worms! Red dates are used for eating ah! I guess. Do you mean to buy bamboo leaves someone thinks it's smelly odor

The academic reference [9] indicates “Imagery and motion were found to share common cerebellar circuitry;” “which reflect a higher demand for the cerebellum as compared to a motion." The activation pattern observed during the execution of the finger-to-thumb movement (motor preparation and timing) is in agreement with theories [9]. “Specific localizations of right superior cerebellar activation, the reaction times were significantly increased for the verbal working memory and motor control tasks” were reported [10]. From the academic reference and user observation, the presentation of actions is another crucial trigger element. It may conduct in the future design of sequential card game.

7. Conclusion

The main contributions in the paper are an implementation of the sequential card activities with different themes to recollect experience. The steps for rice dumpling preparation and making were printed on cards. The elderly are asked to sort these cards to right sequence with the help of a QR scanner. The qualitative testing results showed that the elderly enjoyed the activities. Through the game and trigger elements, non-family members or caregivers have more social interaction and involvement in personal experiences. The communication appeared among members during the group activity. The old people with dementia discovered their differences and enabled passing experiences between each other.

Based on individual characteristics, we also conducted actual items and physical activities; the participant is triggered to find out his experience that has been identified. Concerning unique features of dementia, understanding of the activation made by the elderly was confirmed. In future, the app will extend with remote communication ability to share with the friends. The presentation of motion actions is another crucial trigger element. It will conduct in future card game design.

References

[1] M.S. Bourgeois, C. Camp, M. Rose, B. White, M. Malone, J. Carr, and M. Rovine, “A comparison of training strategies to enhance use of external aids by persons with dementia,” J. Commun. Disorders, **36**, 361-378, 2003. https://doi.org/10.1016/S0021-9924(03)00051-0

[2] L. Clare, B.A. Wilson, G. Carter, and J.R. Hodges, "Cognitive rehabilitation as a component of early intervention in Alzheimer's disease: A single case study," Aging Mental Health, **7**, 15–21, 2003. https://doi.org/10.1080/1360786021000045854

[3] S. Josefsson, L. Backman, L. Borrel, B. Bernspang, L. Nygard, and L. Ronnberg, "Supporting everyday activities in dementia: an intervention study,” Int. J. Geriatric Psychiatry, **8**, 395–400, 1993. https://doi.org/10.1002/gps.930080505

[4] A. Mihaildis and G. Fernie, “Context-aware assistive devices for older adults with dementia,” Gerontechnology, **2**, 173–189, 2002. https://doi=10.1.1.588.447&rep=rep1&type=pdf

[5] Carradice, Angela, Marie Claire Shankland, and Nigel Beail. "A qualitative study of the theoretical models used by UK mental health nurses to guide their assessments with family caregivers of people with dementia." International Journal of Nursing Studies 39.1 (2002): 17-26. https://doi.org/10.1016/S0020-7489(01)00008-6

[6] Banerjee, Sube, et al. "Improving the quality of care for mild to moderate dementia: an evaluation of the Croydon Memory Service Model." International Journal of Geriatric Psychiatry: A journal of the psychiatry of late life and allied sciences 22.8 (2007): 782-788.

[7] S. Fairley “In search of relived social experience: group-based nostalgia sport tourism,” Journal of Sport Management, **17**(3), 284-304, 2003. https://doi.org/10.1123/jsm.17.3.284

[8] Chao, Fang-Lin, et al. "Design Jigsaw puzzle and app for Recollect experience support on elderly with Dementia." Awareness Science and Technology (iCAST), 2017 IEEE 8th International Conference on. IEEE, 2017. DOI: 10.1109/ICAwST.2017.8256464

[9] Luft, A.R., Skalej, M., Stefanou, A., Klose, U. and Voigt, K., 1998. Comparing motion‐related and imagery‐related activation in the human cerebellum: A functional MRI study. Human brain mapping, 6(2), pp.105-113. https://doi.org/10.1002/(SICI)1097-0193(1998)6:2<105::AID-HBM3>3.0.CO;2-7.

[10] Desmond, John E., SH Annabel Chen, and Perry B. Shieh. "Cerebellar transcranial magnetic stimulation impairs verbal working memory." Annals of Neurology: Official Journal of the American Neurological Association and the Child Neurology Society 58, no. 4 (2005): 553-560. https://doi.org/10.1002/ana.20604

ASTES

Advances in Science, Technology and Engineering Systems Journal Vol. 3, No. 4, 276-283 (2018)

www.astesj.com

Special Issue on Multidisciplinary Sciences and Engineering

ASTESJ

ISSN: 2415-6698

The Impacts of Distribution Generators' Size and Location on Power Efficiency and Voltage Profile in Radial LV Networks

Maher M.A Al-Maghalseh*,1,2

[1]*Electrical Engineering Department, Palestine Polytechnic University, Palestine*

[2] *Renewable Energy and Enviermental Research Unit (REERU), Palestine Polytechnic University, Palestine*

ARTICLE INFO

Article history:
Received: 20 June, 2018
Accepted: 31 July, 2018
Online: 10 August, 2018

Keywords:
Distribution generations (Distribution generators)
Off Grid systems
Grid connected systems
Voltage profile
Power losses

ABSTRACT

This paper presents analytical methods for optimum allocation of distribution generators in a radial distribution network. The aim is to increase power efficiency and reduce loss of power. The ideal size of each distribution generator unit at the identified locations has been carefully selected by making adjustments to loss saving equations and the voltage on a radial feeder. The experimental system is located in the governorate of Bethlehem specifically within the district served by the Jerusalem Distribution Electricity Company (JDECO). The NEPLAN simulator has been utilized in the verification process of the aforementioned experimental system. It entails of several nodes and 400 V-buses that feed up to five household loads. The size and location of each has been carefully chosen. Consequently, significant loss saving, and voltage profile improvement have been reported. Hence, the use of Renewable Distribution Generators (DGs) systems is highly desirable for various reasons including increased system reliability, decreased loss of power, and enhanced voltage profile. Notably, cutting back on the use of conventional fuel will in turn reduce the negative environmental impacts.

1. Introduction

Electric supply companies incur losses of supply on its way to final consumers mainly manifested in the quantities of power infused into distribution grids and the transmission which users are not charged for. Mainly there are two main types of losses: technical and non-technical. This paper will address the technical losses which are losses that occur naturally mainly due to electricity dissipation in power system machineries such as transmissions and distribution channels, transformers, and measurement systems. The losses in electricity are quite higher at the distribution lines compared to that at the transmission systems. This is usually due to the R/X ratio which is higher at the distribution lines. Consequently, reducing the technical losses will increase technical and cost efficiency while relieving the community from the economic and environmental costs of power generation.

Several methods have been implemented in order to save power at distribution systems. Some of which were network reconfiguration and capacitor placement. Notably, the staggering growth of distribution generation may contribute to both the increase in power losses as well as the reduction in power quality at the distribution system. On the other hand, distribution generators, if managed efficiently, can enhance the system's performance.[1]. This paper is an extension of work previously presented in 2017 [2]. This paper presents a thorough technical and economic analysis of standalone and grid connected photovoltaic (PV) systems. A considerable amount of literature has already been published [3] on studies that showcased the latest technologies in distribution reconfiguration. Optimization of technical losses in electricity has sure been deemed an engineering issue that includes designing the system in addition to planning and modeling.

Among several techniques implemented were selecting the distribution generators' optimum locations and size. To that end, Adefarati and Bansal have proposed the Markove model to evaluate the reliability of the distribution system with a wind turbine generator (WTG), an electric storage system (ESS), and a photovoltaic (PV) [4]. Several case studies have been conducted to

*Corresponding Author: Maher M.A Al-Maghalseh, maher4xp@yahoo.com

assess reliability,it was found that using distribution generators does in fact improve the reliability of the distribution system.

Moreover, researchers have found that embedded generation on distribution systems can increase the fault level in the system. Hence, Orozco-Henao et al. [5] have presented a fault location (FL) analytical methodology for active distribution networks. The suggested technique has been used to assess the ideal fault level and location. The ATP/EMTP software has been utilized in modeling the test feeder. The results have emphasized the accuracy of this methodology and its potential for success in real-life applications. Additionally, Kaveh et al. [6] have performed a new analytical method to assess the influence of distribution generators.. It was found that the proposed method can be used to specify the ideal location to set the distribution generator to thus reduce phase imbalance, increase power efficiency, and enhance the voltage profile. Another study by Soroudi et al. [7] has presented analytical methods to assess the effects of wind power on the distribution networks. The proposed methods were applied on a distribution network, namely a 69 bus. Interestingly, the numerical method can be used to specify the optimum location, the capacity of renewable energy sources, and to minimize the power losses.

Pukhrem et al. [8] have studied the effects of Rooftop Solar PV Installation in a low-voltage distribution network. To that end, reactive power control and active power curtailment control methods have been applied to reduce voltage fluctuation into the distribution system. The result of merging both approaches has indicated a positive impact on managing and regulating the voltage profile of the system. A numerical study developed by Matlab Simulink [9] to study the influence of the distribution network on the annual energy yield of residential PV systems with variables of increased PV penetration. The study has been conducted upon actual residential PV systems within the UK distribution network. The results have revealed that the level of PV generation would reduce should network voltage rise beyond grid limits. Additionally, the percentage of the annual energy yield, and the economic performance of the systems have been analyzed.

In [10], the author presented the Monte Carlo-based method to analyse the effects of Rooftop photovoltaic (PV) on voltage quality. While in [11] conducted a numerical study of hybrid photovoltaic (PV) and wind turbine (WT) rooftop generation systems (hybrid systems).it has been found that enhanced penetration level of the hybrid system in turn results in maintaining the voltage within range. In [12], the researcher presented an economic analysis of the installation of PV generation on-site (self-consumption) compared to generating solar energy and exporting it to the grid. The study has been conducted on 302 households which have taken part in a UK smart grid project. It was found that 45% of self-consumption can be supplied by the PV generation. This has resulted in decreasing the average annual electricity demand which amounts to 24 percent reduction. In [13], the author provided a review of high penetration of photovoltaic micro-generation on a low voltage distribution network. The study proposed an analytical method to study the effects of high penetration of PV on the radial distribution network. It has been indicated that 'self-consumption with storage' is the most efficient method; to reduce overvoltage, to prevent reverse power flow, and in turn reduce power losses.

A noteworthy analysis and discussion on the subject has been presented by Al-Maghalseh [14-16] on several real-life case studies of embedded distribution generations. Interestingly, the effects of different types of renewable energy distribution generation have been clearly evaluated. Horowitz et al. [17] provided an extensive review on the cost of integrating PV systems into distribution networks. Omar and Mahmoud [18] explored grid connected PV home systems in Palestine. A significant amount of published literature has discussed the effects of high PV penetration on low voltage distribution networks [19]. Furthermore, a detailed review of PV in the distribution systems has been carried out in [20-22].

This paper exhibits an ideal blueprint of standalone and grid connected photovoltaic systems which cover the networks' demand. The blueprint specifies the ideal size and location of the distribution generator at which it will incur slightest technical losses while enhancing the voltage profile.

2. Proposed Methodology

Recently, many studies have been used to optimize the allocation and size of distribution generators. Different analytical approaches have been applied by [1, 23, 24]. Mixed integer non-linear programming method has been used by [25-28]. Atwa and Saadany have used the evolutionary algorithms (EA) technique [28]. Recently, an alternate method has been adopted for the optimization process [19]. This approach has utilized the equivalent current injection technique and neglected the Jacobian matrices. Furthermore, this approach is in line with the analytical method presented in [1]. hence, it is essential to examine the effects of the reactive loss and the real power loss in the system.

In this paper, a simplified analytical method is applied to examine the distribution generation active and reactive branch currents and the related loss savings of a distribution generation located in the radial distribution system. Figure 1 exhibits the N-bus radial distribution system.

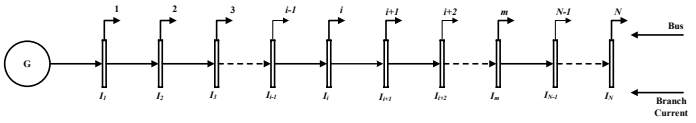

Figure 1. An N-bus radial distribution network.

The total power loss, P_L, of N-bus radial DS having n number of branches, (Figure 1) can be presented as:

$$P_L = \sum_{i=1}^{N-1} I_i^2 . R_i = \sum_{i=1}^{N-1} \left(I_{ai}^2 + I_{ri}^2 \right) . R_i \quad (1)$$

whereas I_i is the complex current, I_{ai} and I_{ri} are the real and imaginary parts of $I_i=(I_{ai} + jI_{ri})$ respectively, while R_i is the resistance of the i_{th} branch. The value of I_i can be obtained from the load flow solution of the given DG.

Figure 2 exhibits the N-bus radial distribution system with a DG. Upon DG placement in the system, the current (I_i^{new}) for the branch i, at m_{th} bus can be presented by the following illustration:

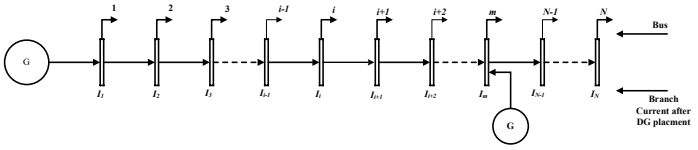

Figure 2. N-bus radial distribution network after distribution generation locating.

$$I_i^{new} = I_i - D_i.I_d g^m = (I_a i - D_i.I_d ga^m) + j(I_r i - D_i.I_d gr^m) \quad (2)$$

whereas,

$$I_i = I_{ai} + jI_{ri} \quad (3)$$

$$I_{dg}^m = I_{dga}^m + jI_{dgr}^m \quad (4)$$

Infusing a current I_{dg}^m influences the currents along the network branches in the area between the substation and the m_{th} bus, while the currents within the rest of the branches remain unaffected. However, I_{dga}^m and I_{dgr}^m are the real and imaginary components of I_{dg}^m and D_i can be illustrated as follows:

$$D_i = \begin{cases} 1; \text{ if branch } i \text{ is between bus 1 and } m \\ 0; \text{ otherwise} \end{cases} \quad (5)$$

To that end, the formula for the total compensated losses P_L^{new} after DG placement may be conveyed as:

$$P_L^{new} = \sum_{i=1}^{N-1} \left(I_i^{new}\right)^2 .R_i = \sum_{i=1}^{N-1} \left[\left(I_{ai} - D_i.I_{dga}^m\right)^2 + \left(I_{ri} - D_i.I_{dgr}^m\right)^2 \right].R_i \quad (6)$$

The related power losses saving, S_L, can be exhibited using (1-6) as:

$$S_L = P_L - P_L^{new} = \sum_{i=1}^{N-1} [\left(I_{ai}^2 + I_{ri}^2\right) - \{\left(I_{ai} - D_i.I_{dga}^m\right)^2 + \left(I_{ri} - D_i.I_{dgr}^m\right)^2 \}].R_i \quad (7)$$

By simplifying the above equation, we arrive at:

$$S_L = 2\sum_{i=1}^{N-1} \left[I_{ai}.I_{dga}^m - I_{ri}.I_{dgr}^m\right].D_i. - \sum_{i=1}^{N-1} \left[\left(I_{dga}^m\right)^2 + \left(I_{dgr}^m\right)^2\right].D_i^2.R_i \quad (8)$$

The highest loss saving is due to the DG currents I_{dga}^m and I_{dgr}^m and can be arrived at using (8) given that the following prerequisites are fulfilled:

$$\frac{\partial S_L}{\partial I_{dgn}^m} = 0 \quad (9)$$

As such, based on equation (9) we can derive :

$$\frac{\partial S_L}{\partial I_{dga}^m} = 2.\sum_{i=1}^{N-1} I_{ri}.D_i.R_i - 2\sum_{i=1}^{N-1} I_{dga}^m.D_i^2.R_i = 0 \quad (10)$$

$$\frac{\partial S_L}{\partial I_{dgr}^m} = 2.\sum_{i=1}^{N-1} I_{ri}.D_i.R_i - 2\sum_{i=1}^{N-1} I_{dgr}^m.D_i^2.R_i = 0 \quad (11)$$

Upon simplifying equations (10) and (11), the active distribution generation current I_{dga}^m and reactive current I_{dgr}^m representing the highest loss saving formula can be respectively depicted as follows:

$$I_{dga}^m = \frac{\sum_{i=1}^{N-1} D_i.I_{ai}.R_i}{\sum_{i=1}^{N-1} D_i^2.R_i} \quad (12)$$

$$I_{dgr}^m = \frac{\sum_{i=1}^{N-1} D_i.I_{ri}.R_i}{\sum_{i=1}^{N-1} D_i^2.R_i} \quad (13)$$

The subsequent DG size is arrived at from equations (11-13):

$$S_{dg}^m = V_m.\left(I_{dg}^m\right)^* = V_m.\left(I_{dgn}^m - I_{dgr}^m\right) \quad (14)$$

where, S_{dg}^m is the capacity of m_{th} DG in complex form, and V_m is the phasor voltage at the bus.

3. The Test System

Using NEPLAN software the presented analytical methods have been utilized on a real-life test radial distribution system, for the purpose of optimal DG allocation and sizing. The selected sample involves a system utilized by the Jerusalem District Electricity Co. (JDECO) in the vicinity of the city of Bethlehem. A balanced constant load radial distribution system particularly of a single source (see Figure3). Voltage limitation has been set to a range between -5% and +5%. The DG has been placed south facing the PV systems at a tilted angle of 15° degrees. The type of systems utilized include standalone and grid connected without the effect of shading. Various setups for positioning the DGs have been taken into account. To decrease loss, several possible solutions have been carefully analyzed. Furthermore, a detailed analysis along with a simulation have been conducted for the radial configuration while changing the variables as deemed necessary. The blueprint of the electric network for the aforementioned site is illustrated in Figure3.

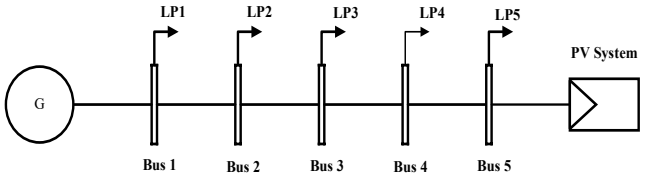

Figure 3. A schematic diagram for the test radial distribution network.

Figure 4. below depicts consumers power consumption in kWh/day. Furthermore, the yearly sun light hours for each month are shown in Figure5.

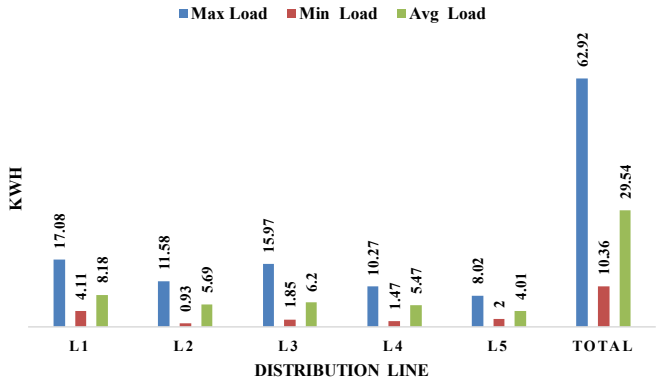

Figure 4. The loads at the distribution line.

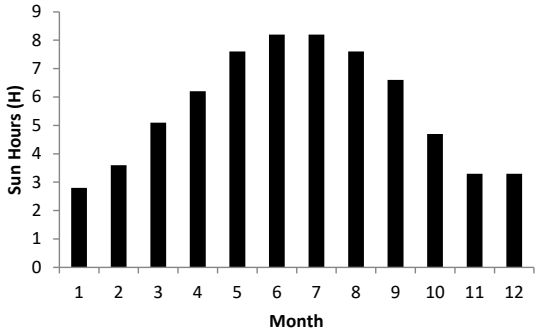

Figure 5. Yearly Sun light hours.

3.1. Photovoltaic system design

The methodology of this study has included researching inputs and the required calculations to determine the potential for either types of solar photovoltaic generation according to the amount of solar radiation.

Grid connected system design:

The electrical characteristics for the panels and the inverter used in the grid connected system are exhibited below in Table 1 and Table 2, respectively.

Table.1. Electrical characteristics for the PV panels under Standard Test Conditions (STC).

Nominal Maximum Power (Pm) in Watts	315
Power tolerance	0 / + 5 W
Open Circuit Voltage (Voc) in Volts	45.25
Short Circuit Current (Isc) in Amps	9.29
Voltage at Maximum Power (Vmp) in Volts	36.75
Current at Maximum Power (Imp) in Amps	8.58
Maximum System Voltage in Volts	1000
Module Efficiency (%)	16.25

Table.2. Technical characteristics of 10 kW inverter

Inverter Type	AS-IC01-xxx-2 (2 MPPT)
Recommended Max. DC voltage (V)	1000
Maximum efficiency	98.30%
MPPT range (V)	200-800
Max. DC power (W)	10000
Max. input current (A)	12.5 x 2
Rated output power (W)	9800
Max. AC output current (A)	14

The system has been designed based on actual figures collected from average power consumption per day. Accordingly, recorded inputs were as follows the consumed energy at an average of 29.54 kWh per day, while sun peak hour approximately 5.58H, whereas the system losses reached approximately 30%, and the future expansion estimated at 20%. Hence, the solar module capacity can be calculated using the equation below as follows:

$$\begin{aligned} Energy\ per\ year &= 29.54\ \text{k}WH * 365\ day \\ &= 10,783.65\ \text{kWH / year} \end{aligned} \tag{15}$$

$$Solar\ module\ capacity = \frac{Energy\ per\ year}{365 * \text{SPH} * \left(1 - SYS_{Loss}\right)} \tag{16}$$

$$= \frac{10,783.65}{365 * 5.58 * 0.7} = 7.75\ \text{k}W$$

where, SPH stands for sun peak hours

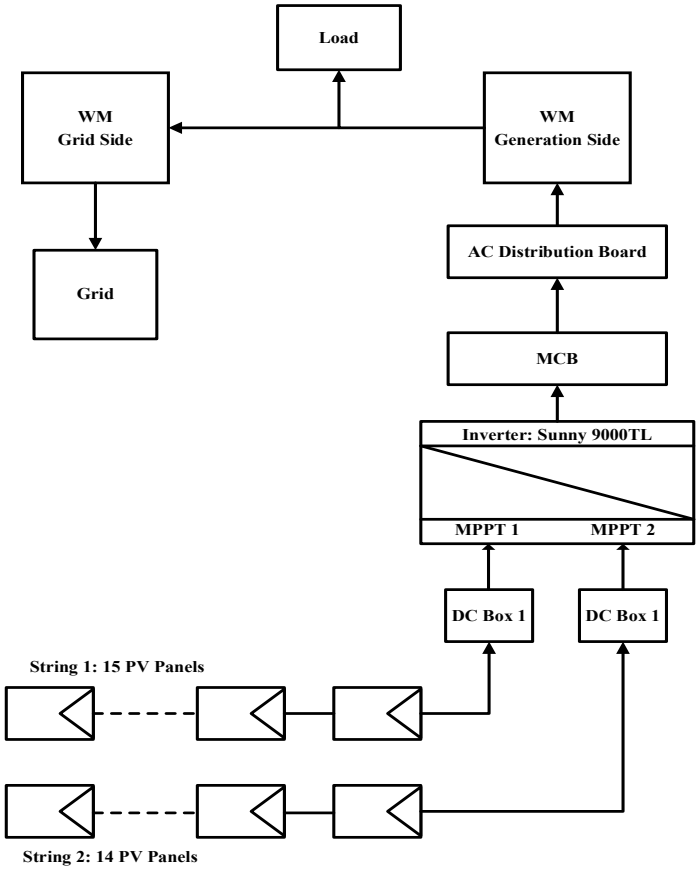

Figure 6. A schematic diagram for the grid connected system.

Adding +20% for future and load growth, the number of modules and energy per year can be calculated using the equation below as follows:

$$\text{Required Capacity} = 7.75 * 1.2 = 9.08\ \text{k}W \tag{17}$$

$$\text{Number of module} = \frac{9.08}{315} = 28.57 = 29\ Panels \tag{18}$$

$$\text{Actual system capacity} = 29 * 315 = 9135\,W \tag{19}$$

$$\text{Energy/year} = = \frac{\textit{Actual system capacity} * 365 * \text{SPH}}{\left(1 - SYS_{Loss}\right) * 1000} = \frac{9135 * 365 * 5.58}{0.7 * 1000} = 13,016.93 \text{ kWh} \quad (20)$$

The schematic diagram for the grid connected system design is shown in Figure 6. It exhibits 15 panels connected at input A of the inverter, and 14 panels connected at input B.

Standalone System Design:

The design has been based on the average consumption per day. The energy was recorded at 29.54 kWh per day, the sun peak hour at approximately 2.79H, system losses have reached about 30%, whereas the battery bank can provide up to two autonomy days upon having three sunny days. Panels and an inverter similar to those applied in the grid connected system have been used for the standalone system. Using equation 14, the value of solar module capacity has been approximately 15.11 kW, while accounting for autonomy days.

$$\textit{autonomy factor} = x + \frac{2}{3}x = \frac{5}{3}x = 1.667\,x \quad (21)$$

Consequently, the capacity of the solar system is calculated using equations (15-18) which has been estimated at 25.08 kW. Since the required capacity is approximately 25.08 kW, the estimated number of PV modules needed is 80 Panels. Noting that the system capacity mounted to approximately 25.2 kW, while the general energy generated per year estimated at 17,986 kWh. Hence, to calculate the inverter inputs, we have assumed that: input A= 3 x 16 string panels, and input B = 2 x 16 string panels. In addition, two island inverters have been used. An island inverter to incorporate the storage systems into the standalone systems. Hence, DC voltage for the batteries has been estimated at 48 V. The storage energy for up to two days is calculated using the following formula:

$$Es = \frac{\textit{Generated energy per year}}{365} \times 2 = \frac{17,986.13}{365} x2 = 98.55 \text{ kWH} \quad (22)$$

To assess the needed number of DC batteries, we have assumed using 24V/ 100A batteries. For energy safety:

$$E_{safe} = \frac{E_{rough}}{MDOD} = \frac{98}{0.75} = 130.67\,KWH \quad (23)$$

To estimate the capacity of the battery bank needed the following formula has been used:

$$C = \frac{E_{safe}}{V_b} = \frac{130.67}{24} = 2722\ Amps.h \quad (24)$$

The total number of batteries has been thus obtained using the following formula:

$$N_{batteries} = \frac{C}{C_b} = \frac{2722}{100} = 28\ Batteries \quad (25)$$

The number of batteries in each series has been determined by the following formula:

$$N_s = \frac{48}{24} = 2 \quad (26)$$

Finally, the number of parallel paths N_p has been obtained by the following formula:

$$N_p = \frac{N_{batteries}}{N_s} = \frac{28}{2} = 14 \quad (27)$$

The number of batteries required is 28 batteries (14 parallel branches and 2 series of batteries). In Taking into account the estimated sun peak hours of 2.79, the energy required for 2 days can be verified as follows:

$$H = \frac{\text{energy required for 2 days}}{\textit{No. of inverters} * \textit{inverter capacity} * \textit{No. of off days}} = \frac{98.55}{2 * 6 * 3} = 2.74 < 2.79 \quad (28)$$

The system has indeed been able to charge batteries to feed the loads for 2 days. Figure7 exhibits the schematic diagram for the standalone system design.

4. Simulation results

In order to select the ideal location to place the DG, the NEPLAN simulator was utilized in testing four case scenarios. Moreover, DG buses have been designed as PQ bus with a power factor of less than one. Listed below are the abovementioned tested case scenarios respectively;

1. The impact of highest load with lowest generation
2. The impact of highest load with maximum generation
3. The impact of lowest load with lowest generation
4. The impact of lowest load with highest generation.

Figure 8 below exhibits a schematic of the designated locations of the DG systems in cases 2 and 4.

Figure9 below exhibits the voltage profiles for cases 1 to 4. According to the voltage profile results, it is evident that mounting the PV system at buses 7 and 5 enhances the voltage levels at all buses thus maintaining a range of ±5%. The voltage profiles for cases 3 and 4.

According to the figure, it is evident that the buses increase in voltage levels is recorded at 1.01 Pu and 1.02 Pu. it is highly unlikely for this case to occur, and even if it were to occur during daylight hours, the voltage range will fall within normal rates. Mounting the DG nearby the loads has resulted in quite enhanced voltage profile This indicates that mounting the DG close to the loads enhances the overall voltage profile curve. To conclude, mounting the DG at bus 4 ensures the lowest energy losses and improves the voltage profile thus keeping it within a normal span.

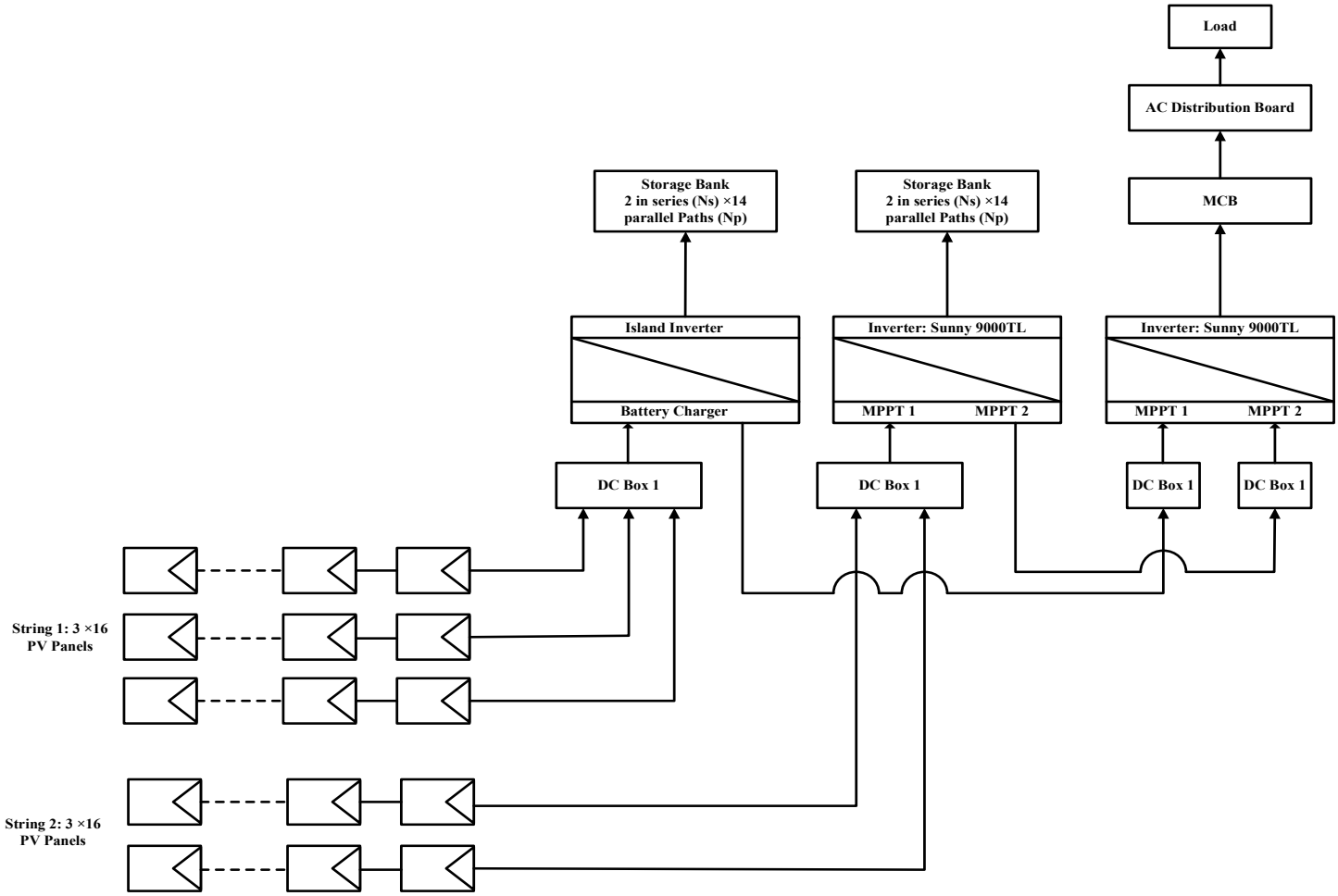

Figure 7. A schematic diagram for grid connected system.

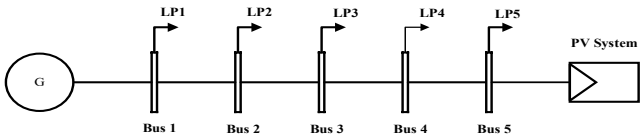

Figure 8. designated locations for the DGs.

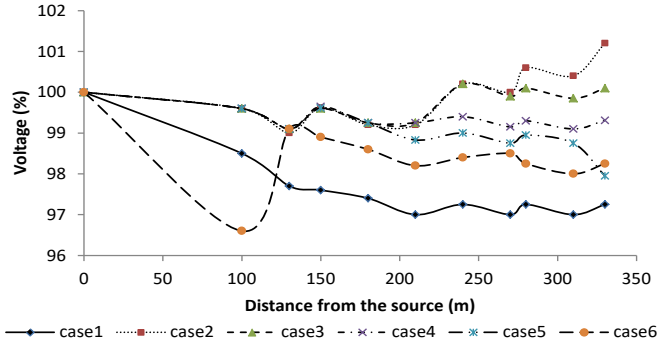

Figure 9. Voltage profiles of the system

In this section, an economic analysis for both standalone and grid connected systems will be featured along with a feasibility evaluation for each option. The evaluation methodology has been based on some financial principles such as: payback period, internal rate of return (IRR), the levelized cost of electricity (LCOE), and the net present value (NPV).

Payback is among widely used methods to estimate the value of a project. Its value is determined by comparing the cumulative cash investments against the cumulative benefits. The payback period formula is calculated by dividing the initial investment over the cash inflow per period:

$$Payback\ Period = \frac{Initial\ Investment}{Cash\ inflow\ per\ period} \tag{29}$$

The following formula to calculate the net present value NPV gathers the total net benefits of a project upon deducting the costs, thus turning the final value into dollar terms as presented below;

$$NPV = \sum_{t=1}^{T} \frac{C_t}{(1+r)^t} - C_o \tag{30}$$

where; Ct = net cash inflow during the period t, Co= total initial investment costs, r = discount rate, and t = number of time periods

The internal rate of return (IRR) is favorably used for comparing projects. It is simply defined as the interest rate which

the project is able to produce for the investors, and is calculated as the discount value that when applied in the NPV formula drives the NPV formula to zero. The formula for IRR is:

$$0 = P0 + \frac{P_1}{(1+IRR)} + \frac{P_2}{(1+IRR)^2} + \frac{P_3}{(1+IRR)^3} \\ ..... + \frac{P_n}{(1+IRR)^n} \quad (31)$$

where, P_0, P_1, . . . P_n equals the cash flows in periods *1, 2, . . .n*, respectively.

The levelized cost of electricity (LCOE) in electrical energy production is considered an essential tool to decide whether to move forward with a said project as it allows us to compare varied technologies of unequal life spans, project size, different capital cost, risk, return, and capacities. It is also described as the current value of the cost of the electrical energy generated over an assumed lifetime in cents/kW.hr. In other words, it is the cost of electricity needed when revenues equal costs. Thus, obtaining a RoC invested equivalent to rebate rate. The following formula exemplifies (LCOE) [29]:

$$LCOE = \frac{\sum_{t=0}^{t=n} \frac{I_t + O\&M_t - PTC_t - D_t + T_t + R_t}{(1+i)^t}}{C\sum_{t=0}^{t=n-1} \frac{P_t}{(1+i)^t}} \quad (32)$$

where *LCOE* is Generation Cost (cents/kWh), I_t is Investment made per year ($), $O\&M_t$ is Operating and maintenance per year ($), PCT_t is Production Tax Credit ($), D_t is Depreciation credit ($) , T_t is Tax levy ($), R_t is Land rent ($), P_t is Electrical generation capacity (Kwh) and *i* is the Discount rate fraction.

Table 3: Constant cost analysis, operation costs, and LEOC for both systems.

Item	Off- Grid	On-Grid
System Size (kW-DC)	$25.20	$9.13
1st-Year Production (kWh)	$17,986.36	$13,017.00
Annual Degradation	0.50%	0.50%
Cost ($/W)	$1.47	$1.57
Initial Rebate/Incentive	$2,343.05	$2,343.05
Total Investment cost	$36,930.00	$9,137.00
O&M Cost ($/kW)	$10.00	$15.00
O&M Escalator (%)	3.00%	3.00%
PPA Rate ($/kWh)	$0.13	$0.13
PPA Escalator	3.00%	3.00%
PPA/20 years	$0.1738	$0.1738
PPA/20 years	$0.1881	$0.1881
LCOE Outputs/20 years	$0.1205	$0.0631
LCOE Outputs/25 years	$0.1033	$0.0554
Discount rate	0.06	0.06
NPV	15097.56	17737.57
IRR	10.66%	25.36%

Table 3 exhibits the analysis for constant cost analysis, operation and maintenance costs, payback period, NPV, IRR, and LEOC for each item. Figure 10 below illustrates the cumulative cash flow for both systems. In general, the feasibility of installing a grid connected system is higher than standalone. Grid connected systems are usually cheaper with better efficiency rates considering the costs associated with the batteries and other standalone equipment which add to cost as well as maintenance. However, standalone systems provide a good alternative to supply remote areas or remote loads in which the investment in installing new electric network is quite higher compared to installing a standalone system. Choosing between a grid-connected and a standalone system is subject to case specifications, and is therefore deemed for the discretion of decision makers.

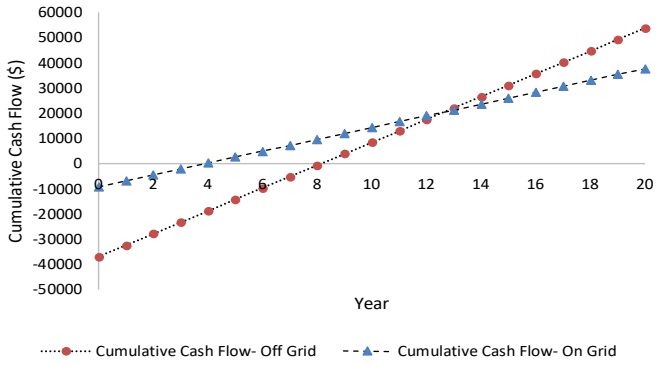

Figure 10. The cumulative cash flow for standalone and grid connected systems.

6. Conclusion

DG's flexibility, small size, minimum investment expenditure, and ecofriendly interests have the potential to improve distribution system performance. Moreover, DG also supplies increased load over time which in turn has a significant impact decreasing the needed investment. DGs have an advantage over central power plants since they can be mounted at or close to the load. The impact of distributed generation has multi-faceted effects on the system and its machinery including stability, reliability, steady-state procedure, power quality, dynamic procedure, and safety for consumers and power suppliers. Effects could be classified as either positive or negative, contingent upon several factors including the distribution system, distributed generators locations and sizing, and the load characteristics. Positive effects are usually referred to as "system support benefits," and entail: decrease in loss, enhanced reliability of the utility system, voltage support and enhanced power quality, transmission and distribution capacity release, deferrals of new or upgraded transmission and distribution infrastructure, quick and convenient installation on account of mass-produced components, reducing expenses by evading long distance high voltage transmission, and nature friendly where renewable sources are used.

Optimal allocation of distributed resources will in turn lead to realizing the potential positive impacts of distributed generation. Particularly, because it utilizes the actual function, limits and utilizes a suitable optimization algorithm. To that end, financial performance indicators (internal rate of return (IRR), net present value (NPV) and payback periods) have been assessed for both systems. To conclude, grid connected systems have the upper hand in terms of technical feasibility and economic viability compared to standalone system.

References

[1] R. Viral and D. K. Khatod, "An analytical approach for sizing and siting of DGs in balanced radial distribution networks for loss minimization,"

International Journal of Electrical Power & Energy Systems, vol. 67, pp. 191-201, 2015/05/01/ 2015.

[2] M. Al-Maghalseh, S. Odeh, and A. Saleh, "Optimal sizing and allocation of DGs for real power loss reduction and voltage profile improvement in radial LV networks," in *Smart Cities: Improving Quality of Life Using ICT & IoT (HONET-ICT), 2017 14th International Conference on*, 2017, pp. 21-25: IEEE.

[3] O. Badran, S. Mekhilef, H. Mokhlis, and W. Dahalan, "Optimal reconfiguration of distribution system connected with distributed generations: A review of different methodologies," *Renewable and Sustainable Energy Reviews,* vol. 73, pp. 854-867, 2017/06/01/ 2017.

[4] T. Adefarati and R. C. Bansal, "Reliability assessment of distribution system with the integration of renewable distributed generation," *Applied Energy,* vol. 185, pp. 158-171, 2017/01/01/ 2017.

[5] C. Orozco-Henao, A. S. Bretas, R. Chouhy-Leborgne, A. R. Herrera-Orozco, and J. Marín-Quintero, "Active distribution network fault location methodology: A minimum fault reactance and Fibonacci search approach," *International Journal of Electrical Power & Energy Systems,* vol. 84, pp. 232-241, 2017/01/01/ 2017.

[6] M. R. Kaveh, R.-A. Hooshmand, and S. M. Madani, "Simultaneous optimization of re-phasing, reconfiguration and DG placement in distribution networks using BF-SD algorithm," *Applied Soft Computing,* vol. 62, pp. 1044-1055, 2018/01/01/ 2018.

[7] A. Soroudi, A. Rabiee, and A. Keane, "Distribution networks' energy losses versus hosting capacity of wind power in the presence of demand flexibility," *Renewable Energy,* vol. 102, pp. 316-325, 2017/03/01/ 2017.

[8] S. Pukhrem, M. Basu, M. F. Conlon, and K. Sunderland, "Enhanced Network Voltage Management Techniques Under the Proliferation of Rooftop Solar PV Installation in Low-Voltage Distribution Network," *IEEE Journal of Emerging and Selected Topics in Power Electronics,* vol. 5, no. 2, pp. 681-694, 2017.

[9] G. Pillai, G. Putrus, N. Pearsall, and T. Georgitsioti, "The effect of distribution network on the annual energy yield and economic performance of residential PV systems under high penetration," *Renewable Energy,* vol. 108, pp. 144-155, 2017/08/01/ 2017.

[10] R. Torquato, D. Salles, C. O. Pereira, P. C. M. Meira, and W. Freitas, "A Comprehensive Assessment of PV Hosting Capacity on Low-Voltage Distribution Systems," *IEEE Transactions on Power Delivery,* vol. 33, no. 2, pp. 1002-1012, 2018.

[11] V. Behravesh, R. Keypour, and A. A. Foroud, "Stochastic analysis of solar and wind hybrid rooftop generation systems and their impact on voltage behavior in low voltage distribution systems," *Solar Energy,* vol. 166, pp. 317-333, 2018/05/15/ 2018.

[12] E. McKenna, J. Pless, and S. J. Darby, "Solar photovoltaic self-consumption in the UK residential sector: New estimates from a smart grid demonstration project," *Energy Policy,* vol. 118, pp. 482-491, 2018/07/01/ 2018.

[13] F. M. Camilo, R. Castro, M. E. Almeida, and V. F. Pires, "Assessment of overvoltage mitigation techniques in low-voltage distribution networks with high penetration of photovoltaic microgeneration," *IET Renewable Power Generation*, vol. 12, no. 6, pp. 649-656Available: http://digital-library.theiet.org/content/journals/10.1049/iet-rpg.2017.0482

[14] M. Al-Maghalseh and W. Saleh, "Design and cost analysis of biogas based power plant: Jenin perspective," in *Smart Cities: Improving Quality of Life Using ICT & IoT (HONET-ICT), 2017 14th International Conference on*, 2017, pp. 31-35: IEEE.

[15] M. M. Al-Maghalseh, A. K. Abutemeha, and M. Iyadiyyeh, "Modeling a hybrid system for electrical generation and wastewater treatment using photovoltaic and fuel cells," (in English), *Desalination and Water Treatment,* vol. 100, pp. 250-257, 2017.

[16] M. M. A. Al-Maghalseh, "Evaluating the Reliability worth Indices of Electrical Medium Voltage Network: Case Study," *Procedia Computer Science,* vol. 130, pp. 744-752, 2018/01/01/ 2018.

[17] K. A. W. Horowitz, B. Palmintier, B. Mather, and P. Denholm, "Distribution system costs associated with the deployment of photovoltaic systems," *Renewable and Sustainable Energy Reviews,* vol. 90, pp. 420-433, 2018/07/01/ 2018.

[18] M. A. Omar and M. M. Mahmoud, "Grid connected PV- home systems in Palestine: A review on technical performance, effects and economic feasibility," *Renewable and Sustainable Energy Reviews,* vol. 82, pp. 2490-2497, 2018/02/01/ 2018.

[19] P. Chaudhary and M. Rizwan, "Voltage regulation mitigation techniques in distribution system with high PV penetration: A review," *Renewable and Sustainable Energy Reviews,* vol. 82, pp. 3279-3287, 2018/02/01/ 2018.

[20] D. S. Pillai and N. Rajasekar, "A comprehensive review on protection challenges and fault diagnosis in PV systems," *Renewable and Sustainable Energy Reviews,* vol. 91, pp. 18-40, 2018/08/01/ 2018.

[21] I. Ali, G. M. Shafiullah, and T. Urmee, "A preliminary feasibility of roof-mounted solar PV systems in the Maldives," *Renewable and Sustainable Energy Reviews,* vol. 83, pp. 18-32, 2018/03/01/ 2018.

[22] A. Zurita *et al.*, "State of the art and future prospects for solar PV development in Chile," *Renewable and Sustainable Energy Reviews,* vol. 92, pp. 701-727, 2018/09/01/ 2018.

[23] D. K. Khatod, V. Pant, and J. Sharma, "Evolutionary programming based optimal placement of renewable distributed generators," *IEEE Transactions on Power Systems,* vol. 28, no. 2, pp. 683-695, 2013.

[24] D. Q. Hung and N. Mithulananthan, "Multiple Distributed Generator Placement in Primary Distribution Networks for Loss Reduction," *IEEE TRANSACTIONS ON INDUSTRIAL ELECTRONICS,* vol. 60, no. 4, 2013.

[25] D. Q. Hung, N. Mithulananthan, and R. C. Bansal, "Analytical strategies for renewable distributed generation integration considering energy loss minimization," *Applied Energy,* vol. 105, pp. 75-85, 2013/05/01/ 2013.

[26] R. S. A. Abri, E. F. El-Saadany, and Y. M. Atwa, "Optimal Placement and Sizing Method to Improve the Voltage Stability Margin in a Distribution System Using Distributed Generation," *IEEE Transactions on Power Systems,* vol. 28, no. 1, pp. 326-334, 2013.

[27] Y. M. Atwa, E. F. El-Saadany, M. M. A. Salama, and R. Seethapathy, "Optimal Renewable Resources Mix for Distribution System Energy Loss Minimization," *IEEE Transactions on Power Systems,* vol. 25, no. 1, pp. 360-370, 2010.

[28] Y. M. Atwa and E. F. El-Saadany, "Probabilistic approach for optimal allocation of wind-based distributed generation in distribution systems," *IET Renewable Power Generation,* vol. 5, no. 1, pp. 79-88, 2011.

[29] M. M. Al-Maghalseh and E. M. Maharmeh, "Economic and Technical Analysis of Distributed Generation Connection: A Wind Farm Case Study," *Procedia Computer Science,* vol. 83, pp. 790-798, 2016.

Advances in Science, Technology and Engineering Systems Journal Vol. 3, No. 4, 284-294 (2018)

www.astesj.com

Special Issue on Multidisciplinary Sciences and Engineering

ASTESJ

ISSN: 2415-6698

The experience of implementation with Agile Business Process Management

Denis Rodríguez*, Enrique Silva Molina

Electrical-Electronic-Computer Faculty, National Engineer University, Nicaragua

ARTICLE INFO

Article history:
Received: 29 June, 2018
Accepted: 02 August, 2018
Online: 12 August, 2018

Keywords:
Agile Business Process Management
Business Process Management
Wiki

ABSTRACT

This paper is an extension of work originally presented at the Convention of Central America and Panama XXX VII- The Institute of Electrical and Electronic Engineers -2017. We have extended our previous work by presenting the initial results of how social technologies in particular wikis has the potential for Information Technology support of a cooperative community knowledge generation.
This paper outlines an experience in the implementation of a multidisciplinary research project – AGILe busIness PrOcess (AGILIPO), applied to an important organization in Nicaragua. In addition, it focused on improving key process by describing through collaborative tools which foster end user collaboration and organization knowledge.
We gathered evidence that blogs and podcasts couldn't afford to allow users on collaborative tasks of AGILIPO. The principal contributions of this work are the lessons learned from the experience of applying AGILIPO to an organization in Nicaragua, the key elements in achieving success in the application, the conditions that were brought together in order to use AGILIPO, the drawbacks during the experience and the relevant limitations of AGILIPO and how we can improve process by agile Business Process Management.

1. Introduction

Business Process Management (BPM) is a discipline which has been around since the early 90s, launched by the article by Hammer (1990) and reinforced by the book by Hammer and Champy (1993) on Business Process Reengineering (BPR). Hammer (1990) stressed that Information Technology (IT) made it possible for companies to undertake major revisions in the way they did work [1].

One of the methodologies of BPM agile found in the bibliographic searches carried out in this work was AGILIPO. In this literature review they were not experiences prior documented of the implementation of the AGILIPO methodology in an organization. Thus, what is innovative of this work is to implement AGILIPO in an organization in Nicaragua [2].

Agile BPM represents the next generation of business process management designed to flexibly address all types of processes to support all forms of work. It combines traditional Business Process IT-Management (BPM) style predefined processes, along with Adaptive Case Management (ACM) style dynamic work support. Agile BPM is designed to flexibly address all types of processes used to conduct business: structured, unstructured, and hybrid process types to support all forms of work [3].

The methodology used in researching this paper has a qualitative approach with a practical action-oriented research design, which the investigator carried out a literature review of the area of the knowledge of BPM and Agile BPM. It deepened through an analysis of the background of BPM and Agile BPM. The result of this analysis was the selection of a multidisciplinary research project AGILe busIness PrOcess (AGILIPO). Next, the investigator developed the experience to apply AGILIPO to an organization in Nicaragua. Based on this experience of applying AGILIPO, we learned a group of lessons [4].

This research project shows the lessons learned from the experience of applying AGILIPO to an organization in Nicaragua, the key elements to achieve success in the application, the conditions that we should have in order to use AGILIPO, the drawbacks during the experience and the relevant limitations of AGILIPO [4].

The principal contributions of this work are the lessons learned from the experience of applying AGILIPO to an organization in

*Corresponding Author: Denis Rodríguez, FEC-UNI, Managua, Nicaragua, +1202-974-3009, rodrigde@paho.org

Nicaragua. On the basis of this experience some limitations of AGILIPO were found [2].

From the experience of applying AGILIPO evidence it was learned that this increases the participation of the users in the phase of modeling and implementation of key processes. On the other hand, the search in the databases for research during this work showed the lack of research on the methodology agile BPM.

2. Analysis of BPM background

2.1. Definitions

What is a process?

A process corresponds to the representation of a set of actions (activities) that are done (carried out), under certain conditions (rules) and that can trigger or cause events [5].

What is a business process?

A business process is a set of activities, which promoted by events and carried out in a certain sequence create value for a client (internal or external) [5].

What is a key process?

A business process which, from management's point of view, is critical to customer service and satisfaction, has a competitive advantage, or has the success of the firm's strategy [2].

What is Business Process Management (BPM)?

Business Process Management (BPM) is a management discipline that integrates the strategy and goals of an organization with the expectation and needs of customer by focusing on end-to-end process. BPM comprises strategies, goals, culture, organizational structures, roles, policies, methodologies, and IT tools to (a) analyze, design, implement, control, and continuously improve end-to-end processes, and (b) to establish process governance [6].

After WWII, applying science to process became front and center as W. Edwards Deming and Joseph Juran taught the Japanese about the power of quality management. Their work and the work of others triggered a wave of Total Quality Management (TQM), spurred on by the publications of Deming and Juran in 1982 as shown below. The emphasis was not so much on the design of new processes, but on statistical measurements as a means of improving existing work practices and quality [7].

Then a decade later, the 1992 blockbuster books, Process Innovation and Reengineering the Corporation, hit corporate board rooms, and reengineering work through information technology took off. In this second wave of business process management, processes were manually reengineered, and through a one-time, big-bang activity, cast in concrete in the bowels of today's automated Enterprise Resource Planning (ERP) and other packaged systems. Although "downsizing" is the moniker most remembered from Business Process Reengineering (BPR), it was technological enablement—including office automation—that allowed companies to tear down internal silos and reengineer end-to-end business processes that spanned individual functional departments (silos) [7].

In the third wave of process management, the business process was freed from its concrete castings and made the central focus and basic building block of automation and business systems. Processes became first-class citizens in the world of automation. Change was the primary design goal because in the world of business process management: the ability to change is far more prized than the ability to create in the first place. It is through agile business process management that end-to-end processes can be monitored, continuously improved and optimized. Feedback of results, agility and adaptability are the bywords of the third wave [7].

Industry 4.0 denotes the Fourth Industrial Revolution, a term introduced in 2011 at the Hannover Messe, one of the world's largest trade shows, and since then widely used by German industry and government [8-5].

BPM as Support for Industry 4.0 and E-Commerce

The new industrial revolution will have a strong impact on the relation of BPM and e-Commerce because it moves manufacturing and production from a centralized to a decentralized paradigm. This will require a widespread adoption of smart interconnection of machinery and systems, not only at the same production site but also across the entire organizational ecosystem. An enormous potential opens up for innovation in business processes and in the way society interacts at a global level [9].

Agile BPM

One of the reasons why BPM is losing momentum is the lack of strategic alignment of its programs. On the one hand, organizations involved in BPM initiatives still mainly focus their efforts on the early stages of the BPM lifecycle, i.e. on process identification and discovery [10].

For many years, we have been arguing that traditional models of management, sponsorship, and project management have not coped with the increasing rate of change. In two separate Harvard Business Review articles, Donald Sull argues for a values-based agile model of business and Gary Hamel presents 25 grand challenges designed to redesign all aspects of management theory and practice to address the fact that "modern models of management" have reached their limits [11].

Business process management (BPM) encompasses the discovery, modelling, monitoring, analysis, and improvement of business processes. Traditional BPM limitations in addressing changes in business requirements have resulted in a number of agile BPM approaches that seek to accelerate the redesign of business process models [12].

Another alternative to highly engineered processes might he called "agile" methods. They are less focused on the specific steps to be followed in a process, and more oriented to the managerial and cultural context surrounding the process. Instead of detailed process flows, for example: agile methods might emphasize the size and composition of process teams, a highly iterative workflow, and a culture of urgency. This is the case, for example, in the agile method known as "extreme programming." [13].

Next-generation Agile BPM is designed to address all of the requirements of managing work in today's enterprise: from streamlining routine, repeated business processes to managing

dynamically evolving business cases involving teamwork, collaboration, and judgment across and among diverse sets of process participants [3].

Achieving successful BPM solutions starts with an agile approach. An agile approach supporting stronger business and IT collaboration on BPM and minimizes the challenges of ineffective requirement definition. By engaging business in the actual development process, design problems can be surfaced more quickly and this helps to reduce the typically long development cycles often seen in BPM. Finally, and perhaps most importantly, an agile BPM approach can institutionalize a partnership between business and IT by providing a foundation for shared commitment, role management and process ownership [14].

AGILe busIness PrOcess (AGILIPO)

AGILIPO - AGILe busIness PrOcess - is a multidisciplinary research project that has been put forward within the scope of a wide-raging research programme aimed at integrating the development of computer-based artifacts for organizations with the accumulated knowledge on organizational design [15].

AGILIPO approach is based on the following steps:

1. Defining the process according to its goals.
2. Defining the process according to its agency and context, using a classificatory framework based on organizational routines.
3. Describing the process using a wiki-like approach, where collaboration, user empowerment and tacit knowledge usage are key principles.
4. Fine-tuning the description through an ontological approach known as folksonomy.
5. Validation of the process.

AGILIPO approach steps are shown in Figure 1.

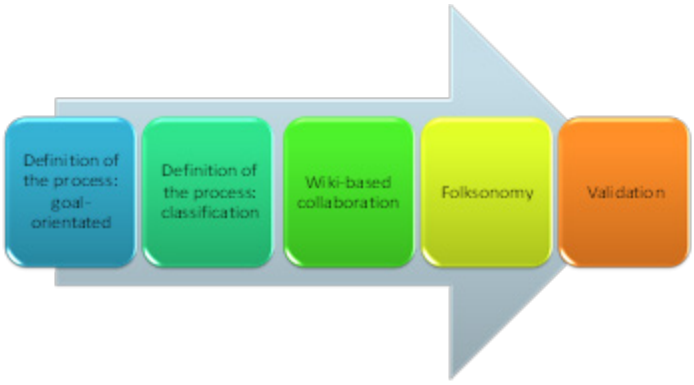

Figure 1: Proposal AGILIPO approach

Definition of the process: goal-oriented

Goal-orientation mirrors the approach we take to goals in our own lives and lends itself to business user involvement in the creation and management of processes. This also extends to routine tracking of plan execution to detect problems as they occur, or even better before they do, in order to take timely and appropriate actions [15].

Definition of the process: classification

On the topic of standardization (and eventual reuse) if we know the process type(s) and the process instance(s) that we are dealing with, this will save much time and effort at the outset. Classification of processes is a method which has been talked about in the literature. There have been many initiatives aimed at cataloguing generic business processes, each proposing classifications of their own, including the MIT process handbook (Malone, 1999) or the Process Classification Framework by the American Productivity and Quality Center's International Benchmarking Clearinghouse (APQC, 2006) [15].

Wiki-based collaboration

In the context of an agile BPM methodology, we proposed that a wiki-type tool can be created for the collective description of business processes. In this context, three aspects may be considered when evaluating wiki-type scenarios [15]:

1. The degree of organization of the BPM team.
2. The degree of specificity of wiki objects (goals, sub-goals, activities, roles, etc.).
3. The degree of desired process completeness.

Wikis, blogs/photoblogs and podcasts (and its video incarnation, the vodcast) carry the potential of complementing, improving and adding new collaborative dimensions to the many Web-based medical/health education, Continuing Professional Development (CPD), and research services currently in existence. They offer many unique and powerful information sharing and collaboration features. They also afford users the added advantage of reducing the technical skill required to use these features, by allowing users to focus on the information and collaborative tasks themselves with few delivery obstacles [16].

Folksonomy

Folksonomies are an emergent phenomenon of the social Web. They arise from data about how people associate terms with content that they generate, share, or consume (Gruber, 2006). It is claimed that Folksonomies have many advantages over controlled vocabularies or formal taxonomies. Tagging has dramatically lower costs because there are no complicated, hierarchically organized nomenclatures to learn. Users simply create and apply tags on the fly. Folksonomies are inherently open-ended and therefore respond quickly to changes and innovations in the way users categorize content (Wu et al., 2006) [15].

Validation

The modeling of business processes is never finished because the process itself is never complete. In order to overcome such a realization, a validation step must be adopted (Kuhne, 2008). Validation should give immediate and continuous feedback to business process designers about weaknesses and inconsistencies in possibly incomplete models. The established modeling process with sequential modeling, validation and evolution stages should be replaced by a modeling process with integrated validation support [15].

This research is not an attempt to generalize probabilistically the results to broader populations, nor necessarily obtain representative samples. This approach used interpretive practices that make the organization visible where research was developed and proposals made to transform the way in which people interact with the key processes. This became a representation in the form

of observations for the AGILIPO proposed methodology, academic articles, and diagrams of modeled key processes [2].

3. The experience of implementing AGILIPO in an organization in Nicaragua

Current approaches to BPM still work on the AS-IS/TO-BE paradigm, inherited from the Business Process Reengineering (BPR) era from the nineties. BPR is a top-down, holistic, and cross- cutting approach that takes months of analysis and impact assessment to achieve. [17-18]. The problems with the AS- IS/TO-BE approaches are related to the temporal gap between the modeling and implementation phases as well as the lack of involvement of the users [15]. These problems have been little addressed by BPM and agile BPM. That is why they are important at present.

After searching the databases of Scopues–Elsevier, ScienceDirect, Google Scholar and IEEE, articles on neither the implementation of AGILIPO nor experiences of AGILIPO in Nicaragua were found. Thus, what is innovative in this work is to implement AGILIPO in an organization in Nicaragua with live business processes.

Although Business Process Management implementation is usually associated with large scale business, implementing it on small medium enterprise may also be a good consideration for Small Medium Enterprises (SMEs) owners. SMEs are non-subsidiary, independent firms which employ fewer than a given number of employees [19]. Upon regarding this organization in Nicaragua as a SMEs, the implementation of AGILIPO should be taken into account.

The experience was carried out in the natural and daily environment of the PAHO/WHO Representative Office in Nicaragua in 2015 and included the key processes for the biennium 2014-2015 [2].

The key processes were:

1. Local and international purchases (procurements of goods).
2. Service contracts (contracts of providers).
3. Temporary advisor contracts (contract of temporary people).

Furthermore, this experience responds to the AGILIPO team requirement to improve even more the key processes of PAHO/WHO Nicaragua of the biennium 2016-2017. Besides, it tries to respond what types of other social network tools as blog and podcast could be feasible for AGILIPO.

The experience was divided into three stages:

The first one included semi-structured interview of project's managers and administrative-technical committee (operational structure linked with the review of processes in the Representative Office) [2].

The second stage included development of the experience using the proposal methodology AGILIPO with the key processes. For this activity there was created the AGILIPO team, which was integrated by a representative of each level of the organization chart of the Representative Office and the investigators [2].

The third one included an evaluation of the use of other social network tools (blogs and podcasts) for step 3 to 5 of AGILIPO and improves the key process of PAHO/WHO Nicaragua of the biennium 2016-2017 by using the best practices of modeling with Bizagi.

3.1. Results obtained in the first stage of the experience

The purpose of the first interview of the four project managers was to compile information on the knowledge of the interviewees of the methodology of process management that the organization has used in the last 6 years. In the interview all the interviewees agreed that the organization had tried to be efficient and that the companies should be flexible and adapt to change [2].

The preliminary results of the first interview warn the AGILIPO team that the project managers had little knowledge about BPM and agile BPM. Thus the investigators trained the interviewees on the basic concepts of BPM and agile BPM. In the opinion of the investigators a condition for using AGILIPO should be training of the interviewees and the AGILIPO team on the basic concepts of BPM and agile BPM to improve the knowledge of the interviewees about BPM and agile BPM.

The second interview of the project managers and the administrative technical committee, through questionnaire No. 2, had the purpose of compiling information on the knowledge of the interviewees on the possibility of the use of methodology agile BPM for management of the processes of the Representative Office. 89% of the participants thought that the agile BPM could be used in the operational processes. 100% believed that increasing the participation of the users could help to improve the management. 89% believed that it was feasible to use collaborative tools that exist in the organization [2].

The AGILIPO team agreed with the interviewees who were open to changes and improvements in the processes of the organization and in strengthening the use of tools already existing in the organization. The opinion of the interviewees were taken into account to help improving the process and to empower the users to share their ideas and proposals to work on the issues.

3.2. Results obtained in the second stage of the experience

In the second stage of the experience had participated five peoples of the administrative technical committee (75% of the committee) through a Wiki site [2].

The first round of the experience was carried out with the three operational processes of the general services unit. The definition of the process aimed at step 1 was complicated since the participants could not link the modeled processes with the goals of the Representative Office. The definition of the processes according to this agency (organization) and context was complicated because the participants did not understand the classification approach defined by AGILIPO and they did not reach a consensus. That issue did not allow participants to describe the process with the Wiki in conjunction of the folksonomy approach [2].

Based on the results of the first round; the Representative took a decision on how to model the key process of the WHO/PAHO Nicaragua. Below are the results of the execution of the key

processes of procurements of goods shown using the five steps of AGILIPO [2].

Step 1: Definition of the process: goal-oriented

In this step 75% of the interviewees did not link the process of procurement of goods to any product of its corresponding project in the Plan of the bi-annual Budget 2014-2015. Furthermore 100% of the interviewees did not define the objectives of the process. 75% of the interviewees did not reach a consensus on who should do the tasks (human or technological actors).

The definition of the process was guided by AGILIPO approach; it helped to detect the inconsistency that existed in the products of the projects of the biennium 2014-2015, which were not linked clearly to the key processes of the organization [2].

Step 2: Definition of the process: classification

Defining the process according to its agency and context, using a classificatory framework based on organizational routines [15].

Due to the difficulties that the members of the technical committee–administrator had in using the classification of step 2 of AGILIPO, the investigators decided to obtain evidence of this difficulty applying the third interview through questionnaire No. 3. The purpose of this questionnaire was to compile information on how they used the classification based on Howard-Grenville (2006) [4].

The questions of the questionnaire No. 3 were coded in the Figure 2 with this syntax: Questionnaire number X and Question number Y. Example: Q3Q1.

The questions of the questionnaire No. 3 for the process of procurements of goods are listed below:

1. Do you believe that the process of procurements is necessary? [Q3Q1]
2. Do you believe that the process of procurements has a clear definition? [Q3Q2]
3. You believe that the process of procurements has a clear definition of who should do it? [Q3Q3]
4. Do you believe that the process of procurements has a weak embeddedness ? [Q3Q4]
5. Do you believe that the process of procurements is flexible? [Q3Q5]
6. Do you believe that the process of procurements has some change probabilities? [Q3Q6]

Regarding the classification based on Howard-Grenville (2006), all the participants agreed on what had to be made. Although 75% believed that the process was not flexible, and they did not reach a consensus on who should make this process. Using this classification was complicated for the interviewees, due to a lack of understanding that the columns were related. For example, the embeddedness of the process, with the actors primary orientation, the performances of the flexible process, the changes in process over time, process labels and characteristics over time[2]. The overall of the answers of the questionnaire No.3 is shown in Figure 2.

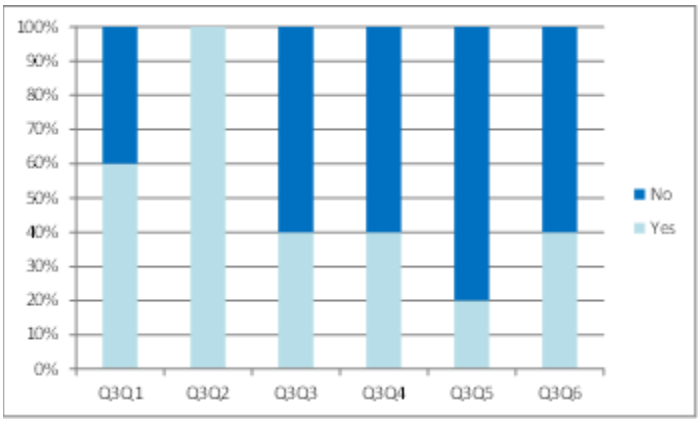

Figure 2: Abstract of responses to the questions of the questionnaire No.3

The classification of processes constituted a limitation of AGILIPO. Since all the participants did not understand how to use it. The author suggests changing to the MIT process classification or the framework of classification of processes of APQC [2].

Step 3: Wiki-based collaboration

Social technologies provide a range of collaboration and communication tools such as blogs, wikis, forums, chat platforms, etc. that support user interaction through social computing features. These features enable users to easily capture and share the knowledge and expertise that is needed to do their work. This sharing of information encourages collaboration, improves innovation, and targets relevant content to the people who have to see it [20].

Traditional process elicitation methods are expensive and time consuming. Recently, a trend toward collaborative, user-centric, on-line business process modeling can be observed [21].

Enterprise social networks are gaining momentum as a platform for collaboration between members of an enterprise, leading to the notion of Enterprise 2.0 [22].

Upon considering the issues suggested by the authors for the use of the Wiki:

- The level of organization of the team AGILIPO, in this case is made up of the investigator and the members of the technical committee–administrator. The mapping and description of the process, including the number of participants of different organizational units, were based on the rules established by the Representative Office in order to guarantee their consistency. The Wiki have a mechanics of horizontal work that provided the proposals of the participants in the description of the process.
- The degree of specificity of the objects of the Wiki (goals, activities, roles). The structure of the data, related to the definition of the process was based on the knowledge of the participants in the experience maintaining the greatest possible simplicity.
- From the standpoint of social intelligence, we can observe that the more collective intelligence is needed for a given task, a lesser degree of organization is required. . In other words to greater participation in the development of an artifact, the greater the probability of its completion is increased. During

the execution of the experience, a description by consensus was obtained for the most part.

Wiki was used to model the key processes, through the cooperative knowledge of the AGILIPO team. With the Wiki an active participation of the AGILIPO team in the modeling of the key process was seen. This participation made it possible to carry out contributions to the modeled key process [2].

Step 4: Folksonomy

The folksonomy was the most interesting step in the experience. Since the participants were accustomed to working with methodologies of structured management as the logical Framework and the Results-based Management. These methodologies are from the top down. In the opinion of the participants, this made it difficult for them to be able to prepare the labels without a hierarchy resulting in the participants having equal decision-making power [2].

The transcription of the Wiki in the creation of labels of the process of procurement of goods, through the folksonomy, was developed in four interactions. The last round is shown below [2]:

- Create request of purchase
- Confirm if it is planned
- Authorize request
- Notify It staff member the change
- Generate offers
- Approve offer
- Notify there is not offer
- Review budget
- Notify change in budget
- Create purchase order
- Authorize purchase order
- Cancel purchase order
- Send purchase order to supplier
- Receive products
- Review products
- Notify claim of goods
- Pay invoice to supplier
- Close purchase order

The labels created by the members of the AGILIPO team are tabulated in Table 1. These labels described the process of procurement of goods (Process 1). These labels were grouped by synonyms synthesizing them in verbs or actions that describe the analyzed process. Finally, the labels are ordered by coincidences in order which they were written by the members of the AGILIPO team and the results of the tasks of the process analyzed [2].

Table 1: Review of labels of the folksonomy – Process 1

Labels	Person 1	Person 2	Person 3	Person 4	Person 5
Create	1				
Request		1	1		
Request purchase				1	
Authorize request		1			1
Quotations		1			1
Authorize quotation	1				
Create purchase			1		1
Notify vendor		1		1	
Reject request			1	1	
Receive goods	1				1
Check goods			1	1	
Goods claim		1		1	
Business rules ok	1				
Pay to vendor				1	1
No money	1			1	1

Finally, the labels are ordered by coincidences and in order in which they were written by the members of the AGILIPO team and the results of the tasks of the process analyzed [2].

- Register
- Request
- Request purchase
- Authorize request
- Offers
- Approve offer
- Create purchase
- Notify supplier
- Reject request
- Receive goods
- Review goods
- Demand of purchase
- Business rules OK
- Pay supplier
- Defund

The folksonomy used jointly with the Wiki was the reason the participants described the key processes and created the labels that helped to improve the key processes [2].

Step 5: Validation

Taking into consideration that PAHO/WHO Nicaragua cannot implement changes in their key processes as part of this work. The

investigators took a decision of carry out a simulation in order to validate the modeled processes [2].

The procurement units had six kinds of purchases services. As part of the validation, the investigators reviewed those six cross functional flowchart and create one. Based on that cross functional flowchart, the investigators create the old BPM diagram of procurements process. The old BPM diagram of procurements is shown in Figure 3.

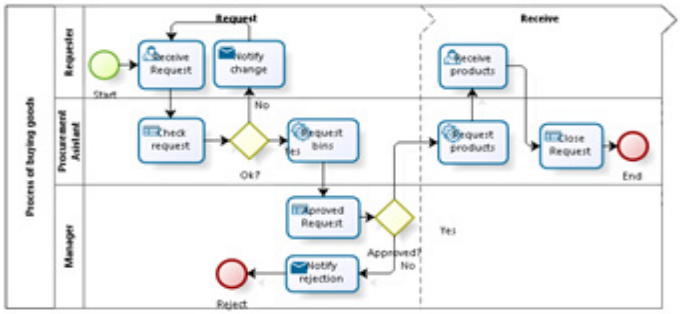

Figure 3: Old BPM diagram of procurements process

The procurement units had two kinds of services contracts. As part of the validation, the investigators reviewed those tow cross functional flowchart and create one. Based on that cross functional flowchart, the investigators create the old BPM diagram of services contracts. The old BPM diagram of services contracts is shown in Figure 4.

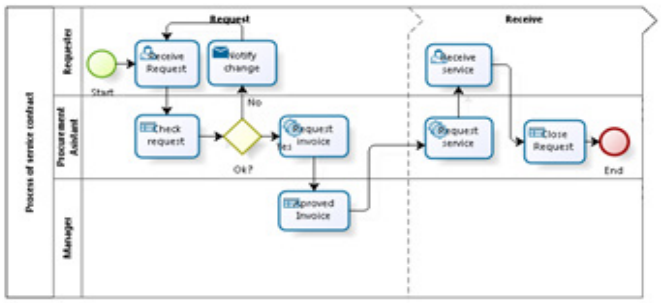

Figure 4: Old BPM diagram of services process

The Human Resources (HR) units had three kinds of services contracts. As part of the validation, the investigators reviewed those three cross functional flowchart and create one. Based on that cross functional flowchart, the investigators create the old BPM diagram of recruitment temporary staff. The old BPM diagram of temporary staff is shown in Figure 5.

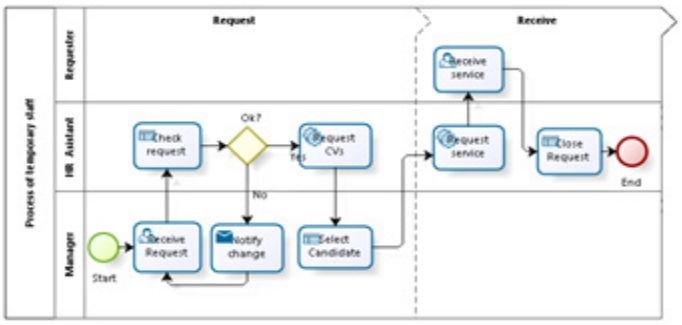

Figure 5: Old BPM diagram of temporary staff

Based on the log of the Wiki in conjunction with the labels produce through the folksonomy process we create a new BPM diagram of the process of procurement of goods, services contracts, and recruitment of temporary staff.

The resulting new BPM diagram of procurements process based on the best practices in modeling of Bizagi is shown in Figure 6. The improvements of the old BPM diagram were the following:

- Use the standard BPMN (Do not use unit names).
- Simplification of the diagrams (Combine two roles which bellow to the same organizational unit).
- Maintain the logical sequence and cleaning (Eliminate duplicated end events).

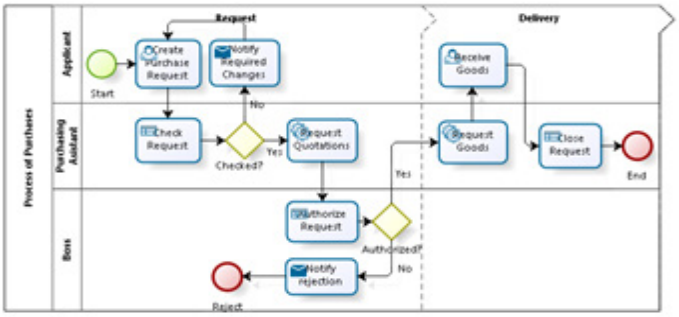

Figure 6: New BPM diagram of procurements process

The resulting new BPM diagram of service contracts process based on the best practices in modeling of Bizagi is shown in Figure 7. The improvements of the old BPM diagram were the following:

- Use the standard BPMN (Use standard job title).
- Maintain the logical sequence and cleaning (Add rejection task after authorize tasks).

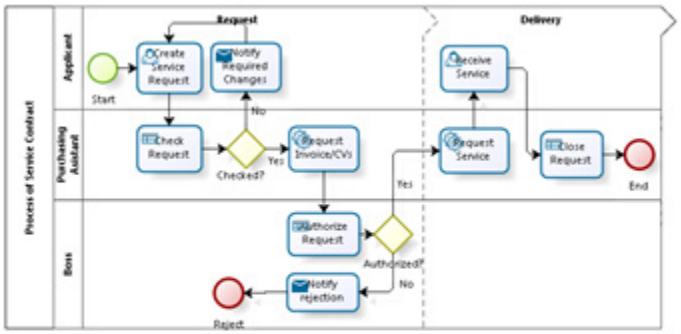

Figure 7: New BPM diagram of service contracts process

The resulting new BPM diagram of recruitment temporary staff process based on the best practices in modeling of Bizagi is shown in Figure 8. The improvements of the old BPM diagram were the following:

- Simplification of the diagrams (Combine two roles which bellow to the same organizational unit).
- Maintain the logical sequence and cleaning (Transfer two tasks from the boss to the applicant, Add a rejection task after a decision task).

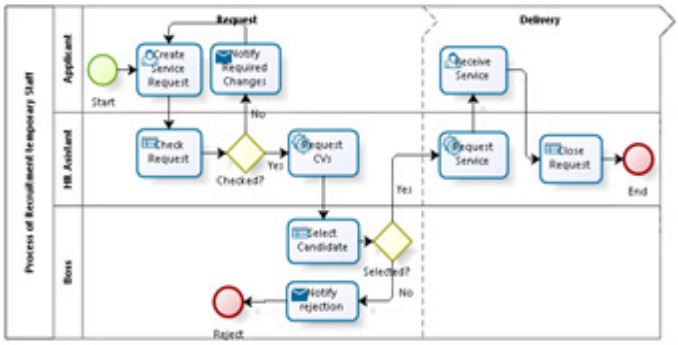

Figure 8: New BPM diagram of recruitment temporary staff process

Considering the limitations of time on the work of the thesis and the regulations of PAHO/WHO to authorize changes in their processes, a validation was carried out through a simulation on the basis of a scenario: 30 calendar days of execution, along with the personnel that worked in the Representative Office during the development of this research [2].

Bizagi Simulation comprises of four levels. Each subsequent level incorporates additional information exhibiting more complexity than the preceding one, thereby providing a detailed analysis of your processes [23].

1. Process Validation
2. Time Analysis
3. Resource Analysis
4. Calendar Analysis

To illustrate each of the simulation levels let us consider the level 1 for the Procurement Process.

Level 1: Process Validation

This level of the simulation validates gateways, messages, decisions and routing and all the sequence flow are fine. The results of the Bizagi simulation level one for Procurement Process are tabulated in Table 2.

Table 2.Results of process validation of Procurement Process

Name	Type	Tokens completed
Process of Purchases	Process	1000
Start	Start event	1000
Checked?	Gateway	2022
Authorized?	Gateway	1000
Reject	End event	504
End	End event	496
Create Purchase Request	Task	2022
Check Request	Task	2022
Request Quotations	Task	1000
Notify Required Changes	Task	1022
Authorize Request	Task	1000
Notify rejection	Task	504
Request Goods	Task	496
Receive Goods	Task	496
Close Request	Task	496
Process of Purchases	Process	1000

3.3. Results obtained in the third stage of the experience

In the third stage of the experience participated five peoples of the administrative technical committee (75% of the committee) through a Google's blogger, WordPress site with podcast, a SharePoint blogs site with podcasts, and a SharePoint blogs site.

The AGILIPO team tested the Google's blogger site. Only 20% of the AGILIPO team created his/her account. Besides, the team tested Apple's Podcasts. The team was unable to subscribe to a podcast channel on iTunes. The team agreed that they preferred a technology available in his working environment. Microsoft SharePoint is a technology that includes blogs and RSS feeder and is available on PAHO/WHO.

As part of evaluate the use of podcast and blog for step 3 to 5 of AGILIPO. The AGILIPO team used the outcome of the step 1 and 2 in stage two of this experience.

Step 3: Podcast-based collaboration

The investigators created a SharePoint blogs site with RSS feeds and configure the Outlook RSS reader watching the SharePoint site. After that, they made a quick guide to help AGILIPO team to create a short podcast and upload the audio files on the SharePoint site. Only 20% of the team could create three small audio files of one or two minutes. To deal with this issue the investigators trained to AGILIPO team how to create an audio file. After that, only 40% of the team could create three additional small audio files of two minutes. All the AGILIPO team agreed that describing the process using podcast approach was not easy to follow the discussion and describe the process. They spent much time listening all audio files.

Step 4: Folksonomy through Podcast

The AGILIPO team used the SharePoint blogs site to tune the description through folksonomy. Only 40 % of the AGILIPO team could create eight audio files for same number of labels. The AGILIPO team agreed that tune the description by folksonomy through Podcast was very confused. They said that was so complicated listened audio files and understand the labels.

Step 3: Blogs-based collaboration

The investigators created a SharePoint blogs and a quick reference guide to help AGILIPO team to post information on the SharePoint site. The investigators started the blogs and all AGILIPO team members posted information to describing the key process of PAHO/WHO Nicaragua. All AGILIPO team agreed that they felt a little concern about who posted which information, rejected or support some information. They preferred the Wiki approach, because they do not see audit tracks and felt more comfortable given feedbacks.

Step 4: Folksonomy through Blogs

In the case of fine-tuning the description of the process through folksonomy the AGILIPO team agreed that was more complicated to follow the comments, feed backs and get a consensus. They spend more time reading the blogs to label the key process of PAHO/WHO Nicaragua. The AGILIPO team agreed that the Wiki approach was easier to describing the process and tune the description through folksonomy.

The transcription of the SharePoint blogs in the creation of labels of the process of service contracts through the folksonomy, was developed in four interactions. The last round is shown below

- Create request of contract
- Authorize request
- Notify changes
- Review budget
- Notify change in budget
- Authorize contract of service
- Cancel contract of service
- Send to review in department of legal advisory services
- Sign contract
- Request payment
- Pay invoice to provider
- Provider offers services
- Request report of services
- Pay the bill
- Close contract of service

The labels created by the members of the AGILIPO team are tabulated in Table 2. These labels described the process of services (Process 2). This process combines the process of services and recruitment of temporary staff and this is an improvement of both services. These labels were grouped by synonyms synthesizing them in verbs or actions that describe the analyzed process. Finally, the labels are ordered by coincidences in order which they were written by the members of the AGILIPO team and the results of the tasks of the process analyzed.

Table 3: Review of labels of the folksonomy – Service 2

Labels	Person 1	Person 2	Person 3	Person 4	Person 5
Create	1			1	1
Check		1	1		
Request invoice		1		1	
Authorize request	1				
Request service				1	1
Authorize Invoice	1	1			
Notify vendor					1
Notify changes		1		1	1
Receive services	1			1	
Pay the bill	1				
Close request		1	1	1	
Service claim				1	
No money			1		

Finally, the labels are ordered by coincidences and in order in which they were written by the members of the AGILIPO team and the results of the tasks for the improve process of services are:

- Create
- Check
- Request invoice
- Request service
- Authorize invoice
- Notify changes
- Receive services
- Close request

Improve the key process of PAHO/WHO Nicaragua 2016-2017

After analyzing the description of the improved process of service contracts using blogs approach and applying the best practices of Bizagi, the investigators create a new BPM diagram of the improved process of service contract. The AGILIPO team agreed that some steps of both process could be combined and improve the logic sequence of the process. The result diagram was easy to understand for the team.

The resulting new BPM diagram of procurements process based on the best practices in modeling of Bizagi is shown in Figure 9. The improvements of the old BPM diagram were the following:

- Simplification of the diagrams (Combine two roles which bellow to the same organizational unit).
- Maintain the logical sequence and cleaning (Eliminate duplicated tasks).

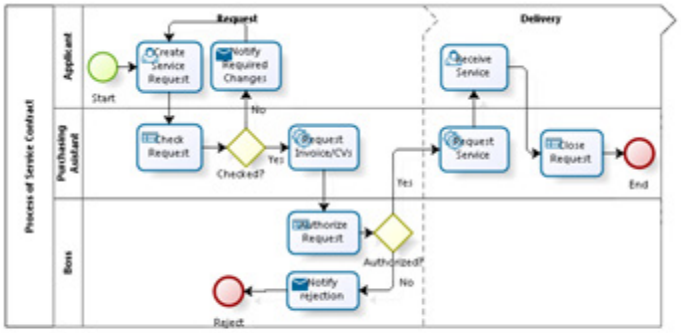

Figure 9: New BPM diagram of the improved process of service

4. Learning Lessons of the experience

The principal contribution of this research project carried out and synthesized in this article is described as a group of lessons learned about the basis of the experience to apply AGILIPO to an organization in Nicaragua. The lessons learned are detailed below [2]:

- Based on the experience of applying AGILIPO, we learned that a key element to achieve success is to write questions in order to determine the key processes.

- It was learned that a condition to use AGILIPO should be the training about BPM concepts for the members of the AGILIPO team..
- It was found that another condition to use AGILIPO should be the definition of the level of training, roles, and level of the organization chart of the participants who will be part of the AGILIPO team.
- It was noticed that the AGILIPO team had several drawbacks in classifying the processes; it was very difficult for the participants to use of AGILIPO classification.

In the second stage of the experience we modeled no key process and the AGILIPO team realized that the outcomes of this approach did not have sense. After that, the manager of this organization recommended model key process. The AGILIPO methodology does not provide any information about it and based on this experience, we learned that we should model key process with this methodology.

The experience in applying AGILIPO provided evidence of the conditions necessary to use AGILIPO. One is the training of the basic concepts of BPM and BPM of the AGILIPO team [2]. During the first stage of the experience the investigators interviewed project managers and realized that they had few knowledge about BPM and agile BPM. The investigators suggest to the AGILIPO team to have a training session for all interviewers and the AGILIPO team.

The experience to apply AGILIPO gave evidence on the conditions in order to use AGILIPO. One is to define the roles and the levels of the organization chart that they should be represented in the equipment AGILIPO [2]. Based on experience the investigators suggested including all levels of the organization chart and key persons with a deep knowledge of the unit and organization.

In addition, the experience in applying AGILIPO, there is evidence of some limitations in the application of AGILIPO, which are the classification of the processes. Thus, the investigators suggest change to the classification of processes of the Massachusetts Institute of Technology (MIT) or the framework of classification of the processes of the American Productivity and Quality Center. (APQC) [2].

The experience to apply AGILIPO gave evidence on the issues of working with podcasts to implement AGILIPO. The AGILIPO team agreed that was hard to follow a description of a process listening podcasts. Besides, tune the description by folksonomy. In the case of using blogs to describe and fine-tuning the description of the process through folksonomy the AGILIPO team agreed that was more complicated to follow the comments, feed backs and get a consensus. They spend more time reading the blogs to label the key process of PAHO/WHO Nicaragua.

The experience in applying AGILIPO, there is evidence of some limitations of podcasts and blog and the Wiki is feasible for AGILIPO.

In this paper it was verified that the use of social network tools is useful in the management of business processes. Since these can facilitate the interaction within the organization [24].

In addition, the experience in applying AGILIPO and responding a request of the AGLIPO team for improve the process obtained in the second stage of the experience. The improved process of services contracts combined effectively the process of recruitment temporary staff and services contracts. The result diagram was very easy to understand and few tasks.

After analyzing the description of the improved process of service contracts using blogs approach and applying the best practices of Bizagi, the investigators create a new BPM diagram of the improved process of service contract. The AGILIPO team agreed that some steps of both process could be combined and improve the logic sequence of the process. The result diagram was easy to understand for the team. In 2016 PAHO/WHO started the second phase of the implementation of the new Enterprise Resources Planning (ERP) and that ERP reduced most of the process.

The authors hope that other research of the proposal of the AGILIPO methodology is developed in other organizations using the Wiki.

Conflict of Interest

The authors declare no conflict of interest.

Acknowledgment

The authors thank Dr. Socorro Gross, Representative of PAHO/WHO Nicaragua to permit use information on the Representative Office to conduct this research.

References

[1] M. Hammer, Reengineering Work: Don't automate, obliterate, Harvard Business Review, vol. 68, 1990.
[2] D. Rodríguez, "Gestión por Procesos de Negocio (BPM) – Una experiencia de aplicación de AGILIPO en una organización en Nicaragua", 2017.
[3] T. Koulopoulos, "Taming the Unpredictable". Future Strategies Inc. 1st Edition.
[4] D. Rodriguez, E. Silva, The experience of implementation with Agile Business Process, Management, CONCAPAN XXX –VII-IEEE, 2017.
[5] B. Hitpass, "BPM: Business Process Management - Fundamentos y Conceptos de Implementación". BHH Ltda. Cuarta edición. 2017.
[6] T. Benedict, N. Bilodeau, P. Vitkus, E. Powell, D. Morris, M. Scarsig, D. Lee, G. Field, T. Lohr, R. Saxena et al., "BPM CBOK Version 3.0: Guide to the Business Process Management Common Body Of Knowledge version 3.0", 3nd Edition, CreateSpace Independent Publishing Platform,2013.
[7] J. Sinur, J. Odell, P. Fingar. Business Process Management: The Next Wave, 2013.
[8] Germany Trade and Invest (GTAI), Promoted by Federal Ministry for Economic Affairs and Energy in Accordance with a German Parlament Resolution. Berlin, 2016.
[9] B. Hitpass, H. Astudilo, Industry 4.0 Challenges for Business Process Management and Electronic-Commerce, Journal of Theoretical and Applied Electronic Commerce Research, Universidad de Talca, Chile, 2019.
[10] M. La Rosa, "Strategic Business Process Management", Queensland University of Technology, 2016.
[11] R. Thomsett, "Agile Business: The Final Frontier", www.cutter.com. 2010.
[12] M. Zacarias, P. Ventura, "Agile Business Process and Practice Alignment Methodology: A Case-Study-Based Analysis".IGI Global, 2018..
[13] P. Bernus, J. Blazewiez, G. Schmidt, M. Shaw, "International Handbooks on Information Systems", 2010.
[14] S. Simmons, Steele, M., "BPM Voices: Synchronicity: An agile approach to business process management". 2012.
[15] R. Meziani, R. Magalhaes, "Proposal for an Agile Business Process Management Methodology". First International Workshop on Organizational Design and Engineering. 2009.
[16] M. Kamel, I. Maramba, S. Wheeler, "Wikis, blogs, and podcasts: a new generation of Web-based tools virtual collaborative clinical practice and education", BMC Medical Education, 2006.

[17] T. Morgan, Business Rules and Information Systems: Aligning IT with Business Goals, Addison Wesley, 2002.
[18] M. Cumberlidge, "Business Process Management with JBoss, jBPM", Packt Publishing –Birmingham, 2012.
[19] S. Allibang, "BPM: Business Process Management (BPM) of Small and Medium Enterprises", DBest Reads, 2016.
[20] A. Kumar, Business Process Management, Taylor and Francis, 2018.
[21] F. Dengler, D. Vrandecic, "Wiki-Based Maturing Of Process Descriptions". International Conference on Business Process Management. 2011.
[22] O. Hatzi, G. Meletakis, M. Nikolaidou, D. Anagnostopoulos, "Collaborative management of applications in enterprise social networks". International Research Challenges in Information Science, 2014.
[23] Bizagi Process Modeler User Guide, 2016.
[24] M. Rosing, A. Scheer, H. Scheel, "The Complete Business Process Handbook: Body of Knowledge from Process Modeling to BPM", Volume I, Morgan Kaufmann Publisher, 2015.
[25] M. Zacarias, P. Ventura, "Agile Business Process and Practice Alignment Methodology: A Case-Study-Based Analysis".IGI Global, 2018.

ASTES

Advances in Science, Technology and Engineering Systems Journal Vol. 3, No. 4, 295-307 (2018)

www.astesj.com

ASTESJ

ISSN: 2415-6698

Defined Limited Fractional Channel Scheme for Call Admission Control by Two-Dimensional Markov Process based Statistical Modeling

Md. Asadur Rahman[*,1], Md. Shajedul Islam Sohag[2], Rasel Ahmmed[3], Md. Mahmudul Haque[1], and Anika Anjum[1]

[1] *Department of Biomedical Engineering, Khulna University of Engineering & Technology (KUET), Khulna, Bangladesh*

[2] *Dhaka Power Distribution Co. Ltd., Dhaka, Bangladesh*

[3]*Department of Electronics and Communication Engineering, East West University, Dhaka, Bangladesh*

A R T I C L E I N F O

Article history:
Received: 07 July, 2018
Accepted: 31 July, 2018
Online: 12 August, 2018

Keywords:
Call admission control (CAC),
Handover call dropping probability (HCDP)
New call blocking probability (NCBP)
Quality of services (QoS)
Thinning schemes
Acceptance factor
Defined limited fractional channel (DLFC)
Channel utilization

A B S T R A C T

The increasing demand for advanced services in wireless networks raises the problem for quality of service (QoS) provisioning with proper resource management. In this research work, such a provisioning technique for wireless networks is performed by Call Admission Control (CAC). A new approach in CAC named by Defined Limited Fractional Channel (DLFC) is proposed in this work for the wireless networks in order to provide proper priority between the new calls and handover calls. This DLFC scheme is basically a new style of handover priority scheme. Handover priority is provided by two stages in this scheme which helps the network to utilize more resources. The first priority stage is a fractional priority and the second stage is an integral priority. Fractional priority is provided by the uniform fractional acceptance factor that accepts new calls with the predefined acceptance ratio throughout the fractional priority stage. The two significant parameters of QoS: new call blocking probability and handover call dropping probability of single service wireless network have been analyzed under this DLFC scheme. Besides, the results of the proposed scheme have been compared with the conventional new thinning scheme and cut-off priority scheme and we found that our proposed scheme outperforms than the conventional schemes. Integral priority is given to the handover calls by reserving some channels only for handover calls. In this work, it is shown that DLFC scheme proves itself as optimal call admission controlling technique which is concerned about not only the QoS but also the proper channel utilization with respect to conventional thinning scheme and fractional channel schemes. The handover call rate estimation and its impact on QoS provisioning is discussed widely to attain the optimum QoS in the proposed handover priority scheme. We hope this proposed DLFC scheme will contribute to design high performance CAC in the wireless cellular network.

1. Introduction

With the blessing of the communication system, the modern civilization has achieved an unbelievable pace. Because of the revolution of communication system, the whole world is becoming closer day by day. In this modern era, there is a lot of communicating ways like telephone, fax, television, radio, email, mobile phone, video conferencing, etc. those can be broadly classified into two categories - Wired and Wireless. Nowadays, the cellular communication technique becomes the most preferred compared to the other communicating ways of the wireless communication systems because of its vigorous number of facilities like mobility, intelligent network system, and various services in single network, convergent capability of different network system etc. That is why the demand of cellular network is increasing tremendously which leads to notable curiosity and improvement in the arena of wireless infrastructures [1].

The area covered by the cellular network is allocated into different precise sections which are termed as cells. When a mobile user exceeds the boundary of the cell or the wireless link quality

[*]Md. Asadur Rahman, Dept. of BME, KUET, bmeasadur@gmail.com

becomes unacceptable, usually, the procedures of the handover call are originated [2]. Therefore, there are two categories of calls those can be commenced in a cell. One is a new call and another is a handover call which comes from the neighboring cell. Recently, a significant propensity in scheming the wireless cellular network is reducing the area of cell size and increasing the mobility of the users. This designing proposition results in frequent call handovers in wireless communication systems [3]. The probability of blocking a new call request by the network due to the lack of resources is called new call blocking probability (NCBP). On the other hand, an accepted enduring call is being terminated due to the lack of recourses is often termed as a handover call dropping probability (HCDP). In addition to that, NCBP and HCDP are two important qualities of service (QoS) parameters in single service cellular networks. According to the survey [4], the HCDP of a cellular network must be less than 2%. That's why for giving the priority to the handover call, an intelligent network should be designed. A call admission control (CAC) is such an intelligent call management scheme that purposes to uphold the delivered QoS to the different calls of the network at the target level by off-putting the number of continuing calls in the system [5-6].

A number of CAC schemes have been proposed by considering different aspects. Among them, providing the priority to the handover calls several CAC schemes have been suggested in [1], [7]-[20]. Most of these propositions [1], [7-13] considered identical channel holding time regarding both the new and handover calls those specify one-dimensional Markov queue process. On the other hand, the research works proposed in [14-20] have been claimed that this one-dimensional queue method is not accurate and therefore they proposed different channel holding time approaches which are more suitable to evaluate the QoS of a CAC scheme. It is obligatory to reserve a few channels devoted for the exceptional type of calls like handover call for providing the priority. Since the bandwidth of the cellular network is inadequate, the proper utilization of the channels (or bandwidth) become challenging due to the channel reservation. On the other hand, the non-priority scheme offers maximum utilization of the radio resources but this scheme is completely unable to guarantee the gratified level of QoS. Therefore, there is always a tradeoff relationship between QoS and channel reservation.

Based on several original CAC schemes, some researchers suggested QoS optimization methods in several approaches as thinning scheme I [13], thinning schemes II and new call bounding (NCB) schemes [21], new thinning scheme [21], [22], cutoff priority scheme [20], [23], etc. The NCB and thinning II schemes use the method of restriction over the acceptance of the new calls. The thinning scheme I is designed based on the defined the edge value of occupied channels as well as thinning scheme II works based on the probability of the new call acceptance at different numbers of new calls existed in the cell of the network. The new thinning scheme is another CAC policy that offers to fractionise the acceptance of the new call on only one channel which is basically designed considering the idea of limited fractional channel scheme (LFC) [13] in two dimensional Markov environments. The authors of the LFC scheme claimed that this CAC scheme is optimum with respect to thinning scheme I. On this contrary, the new thinning scheme is optimum with respect to NCB and thinning scheme II. The authors of the research works proposed in [13], [21-22] did not explicate the effects of fractionizing more than one channel. Although for the first time the concerning effect is interpreted in the method named uniform fractional band (UFB) scheme [24], the performance measurement is performed by considering one dimensional Markov process. It is already clarified that among the aforementioned CAC schemes, the LFC and new thinning schemes are optimum CAC schemes in one dimensional and two dimensional Markov process, respectively. Nevertheless, both research works also did not state the effect on QoS parameters in case of fractionizing more than one channel. Therefore, the consequential demand is to determine the effects of fractionizing more than one channel under two dimensional Markov process. Elsewhere, the mathematical model of fractionizing more than one channel under two dimensional Markov process is quite complex because of its *curse of dimensionality* [25].

Considering the previous scopes, this research work proposes a new CAC policy considering two dimensional Markov process based statistical model entitled by defined limited fractional channel (DLFC) scheme. It is also mentionable that this DLFC scheme was primarily proposed by our conference paper in [26] but the detail performance and mathematical details have been presented in this work.

This paper contributes in some specific points those can be mentioned as: (*i*) In UFB scheme NCBP was reduced where HCDP remained constant. But in DLFC scheme the HCDP has been reduced where NCBP is often constant. In this case, it is analyzed that the QoS in the DLFC scheme is better than that of the UFB scheme. (*ii*) For the different number of fractional channel, both the HCDP and NCBP have been analyzed and graphical and tabular presentations have been presented in the DLFC scheme which wasn't analyzed in the UFB scheme. (*iii*) HCDP and NCBP have been examined and presentations regarding graphical and tabular have been presented in DLFC scheme for different values of acceptance factor. (*iv*) HCDP and NCBP have been also studied for LFC and new thinning schemes and compared with the DLFC scheme. From the analysis, it is shown that the QoS of the proposed DLFC scheme is better than the conventional schemes.

2. Parameters Portrayal

2.1. Call Admission Control

Call admission control or CAC is basically an algorithm that regulates the traffic volume in cellular networks. CAC can also be used to maintain QoS by providing priority to a specific class of traffic. Generally, there are two kinds of CAC schemes, in broader senses and those are static CAC and dynamic CAC [7]. In this paper, we are concerned about the Static CAC scheme for the augmentation of the QoS. Static CAC schemes use the avowed traffic profile with no effort to estimate the authentic traffic. A proper CAC scheme depends on some parameters. Most significant parameters are: call holding time, cell dwell time, average call holding time, call arrival rate, call termination rate, and handover probability

- **Call Holding Time**: The call holding time means the call length in second from the initiation to termination of the call. The call may either stays in the cell or be handed over to another cell during this time. Generally, the parameter $1/\mu$ is used to define the call holding time, T_n in units of seconds to

designate the average call length of time. Here, μ denotes the average channel departure rate. It is often assumed that the average call length time is a random quantity with exponential distribution.

- **Cell Dwell Time**: In a modern high-speed communication system, it is always considered that the mobile users randomly move from one cell to another. Therefore, call handover is a very common case in the mobile cellular network. The time T_h what actually spent in a specific cell only before handed over the call is known as the cell dwell time. It means the average duration the calls dwell in the cell. The average dwell time is presented as $1/\eta$, where η denotes the call termination rate in that cell only.
- **Average Call Holding Time**: The average holding time is the average time occupied for an operating network to response a call or the time a mobile user waits in the queue for the response. If the average dwell time is $1/\eta$ and the average call length is $1/\mu$, then the average call holding time, $1/\mu_c$ is found as,

$$\frac{1}{\mu_c} = \frac{1}{\mu + \eta} \tag{1}$$

- **Call Arrival Rate**: At which rate, the new calls and the handed over calls from the neighbor cell arrive in a cell are called the call arrival rate and often denoted by the symbol λ . In a mobile cellular network, two kinds of calls are generated- new calls and handover calls. The new call arrival rate is denoted by λ_n and handover call arrival rate is denoted by λ_h .
- **Call Termination Rate:** The amount of terminating calls in a cell in unit time is called the call termination rate, μ . The new call termination rate is denoted by μ_n and for the handover call, it is denoted by μ_h . In practice, these parameters are not equal. If these parameters are considered as equal the system can be modeled by one dimensional Markov process. Whereas, on the consideration of $\mu_n \neq \mu_h$ requires two dimensional Markov process.
- **Handover Probability:** The call handover probability, P_h is the probability of a call being handed over from one cell to another. Generally, in the case of a handover call, the call holding time T_n is greater than the call dwell time, T_h. Since both $T_n(1/\mu)$ and $T_h(1/\eta)$ are considered as exponentially distributed according to the call arrival characteristics. The handover probability, P_h of a call in a particular time can be calculated as,

$$P_h = \frac{\eta}{\mu + \eta} \tag{2}$$

2.2. The significance of CAC and Resource Reservation

CAC and resource reservation (RR) for mobile communication are of the most important issues that guarantee system efficiency and QoS required for different services in a very scarce resource as the radio spectrum. As forced call termination due to the handover call dropping are generally less desirable than blocking a new one, handover calls should have a higher priority than new calls [26].

2.3. Mathematical Modeling of CAC schemes

Mathematical model subjected to a CAC scheme can help to indicate the performance of the network. This modeling is based on some probability theory due to its random nature. Therefore, a basic discussion over CAC scheme modeling with possible terminology have been explored and explained, gradually.

- **Queuing Theory**: The queuing theory is a mathematical approach of waiting in lines or queues. In queuing theory a model is constructed so that queue lengths and waiting time can be predicted. Networks of queues are systems in which a number of queues are connected by customer routing. When a customer is serviced at one node it can join another node and queue for service, or leave the network. For a network of m, the state of the system can be described by an m–dimensional vector $(x_1, x_2, x_3, ..., x_m)$ where x_i represents the number of customers at each node. Queuing theory maintains the birth and death process.
- **Markov Process**: Markov process is a statistical method which is used to predict the forthcoming behavior of a variable or system whose existing behavior does not depend on its behavior at any time in the past. In other words, this procedure works with random variables. Basically, a Markov process works with a sequence of random variables suppose $x_1, x_2, x_3, ...$ with the Markov property, such as the current, future, and past states are independent. Formally,

$$P_r(X_{\{n+1\}} = xX_1 = x_1, X_2 = x_2, ..., X_n = x_n) \tag{3}$$

If these two conditional probabilities are properly defined, i.e. if,

$$P_r\left(X_1 = x_1, \ldots\ldots, X_n = x_n\right) > 0 \tag{4}$$

The probable values of X_i construct a countable set, S which is known as the state space of the chain. This Markov chain may be either single dimensional or multidimensional.

- **Multidimensional Markov Model:** Suppose that, we have s categorical sequences and each sequence has m possible states in M. In addition, let $x_n^{(k)}$ be the state probability distribution vector of the j^{th} sequence at time n. Therefore, if the probability of founding the j^{th} sequence in state j is one at time n, the following relation can be considered.

$$x_n^{(k)} = e_j = \left(0,0,...,0, \underbrace{1}_{j^{th}\text{ state}}, ... ,0,.....\right)^T \tag{5}$$

Furthermore, it can also be assumed that the following relationship exists among the sequences.

$$x_{n+1}^{(j)} = \lambda_{jj} P(jj) x_n^{(j)} + \sum_{k=1, k\neq j}^{s} \lambda_{jk} x_n^{(k)}, \quad for \ \ j = 1, 2, ..., s \tag{6}$$

$$where, \lambda_{jj} \geq 0, \ 1 \leq j, \ k \leq s \ \text{ and } \sum_{k=1}^{s} \lambda_{jk} = 1, \quad for \ j = 1, 2, ..., s$$

This mathematical relationship basically represents that the

state probability distribution of the j^{th} chain at the time $(n+1)$ and it totally depends on the weighted average of $P(jj)x_n^{(j)}$ and the probability distribution of the state at the other chains at time n. Here $P(jj)$ denotes the one-step transition probability matrix of the j^{th} Sequence. We can write the system in matrix form as,

$$x_{n+1} \equiv \begin{bmatrix} x_{n+1}^{(1)} \\ x_{n+1}^{(2)} \\ \vdots \\ x_{n+1}^{(s)} \end{bmatrix} = \begin{bmatrix} \lambda_{11}P^{(11)} & \lambda_{12}I & \dots & \lambda_{1S}I \\ \lambda_{21}I & \lambda_{22}P^{(22)} & \dots & \lambda_{2S}I \\ \vdots & \vdots & \vdots & \vdots \\ \lambda_{S1}I & \lambda_{S2}I & \dots & \lambda_{SS}P^{(SS)} \end{bmatrix} \begin{bmatrix} x_n^{(1)} \\ x_n^{(2)} \\ \vdots \\ x_n^{(s)} \end{bmatrix} \equiv Qx_n \quad (7)$$

For the relation (7), the following proposition can be considered as a generalized version of the *Perron Frobenius* theorem [27].

From the above theoretical view of multidimensional Markov chain model, we get the concept of using two dimensional Markov chain model for the purpose of call admission control in a wireless network. It provides desired QoS for handover calls and guarantees that the QoS of new calls still meets the requirements. When congestion occurs, we may lose both of these purposes. The average service rate of the new call and handover call μ_n and μ_h are not the same. Different CAC schemes are designed under 2D Markov process. Among them cut off priority and limited fractional channel CAC schemes are most common those have been discussed here. These methods have also been widely examined to compare with our proposed scheme.

- **Cut off Priority CAC Scheme:** The transition rate diagram of two dimensional Markov chain model for the cutoff priority CAC scheme [20], [23] is given in Figure 1. In this figure, n_1 denotes the number of new calls, n_2 denotes the number of handover calls and M is the defined threshold for new call acceptance. New traffic load and handover traffic load are defined as $\rho_n = \frac{\lambda_n}{\mu_n}$ and $\rho_n = \frac{\lambda_h}{\mu_h}$ where λ_n and λ_h are the new call and handover call arrival rate respectively and μ_n μ_h are the average termination rate for new and handover calls, respectively. If $P(n_1, n_2)$ denotes the steady state probability, then from the balance equation we have [21],

$$\begin{aligned} P(n_1, n_2) &= P(n_1, 0) \times P(0, n_2) \\ &= \frac{\rho_n^{n_1}}{n_1!} \times \frac{\rho_h^{n_2}}{n_2!} \times P(0,0) \end{aligned} \quad (8)$$

$$\text{where,} \quad P(0,0) = \left[\sum_{n_1=0}^{M} \frac{\rho_n^{n_1}}{n_1!} \sum_{n_2=0}^{C-n_1} \frac{\rho_h^{n_2}}{n_2!} \right]^{-1} \quad (9)$$

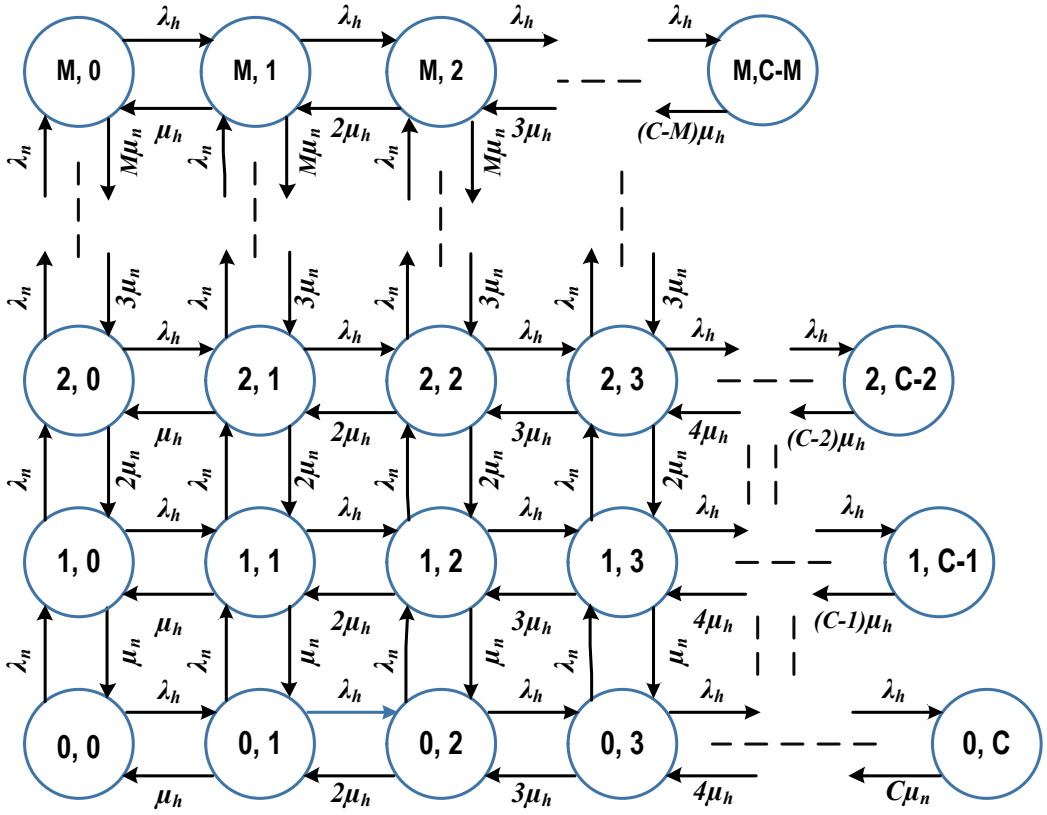

Figure 1: Transition rate diagram based on two-dimensional Markov model obeying the Cut off Priority scheme of CAC

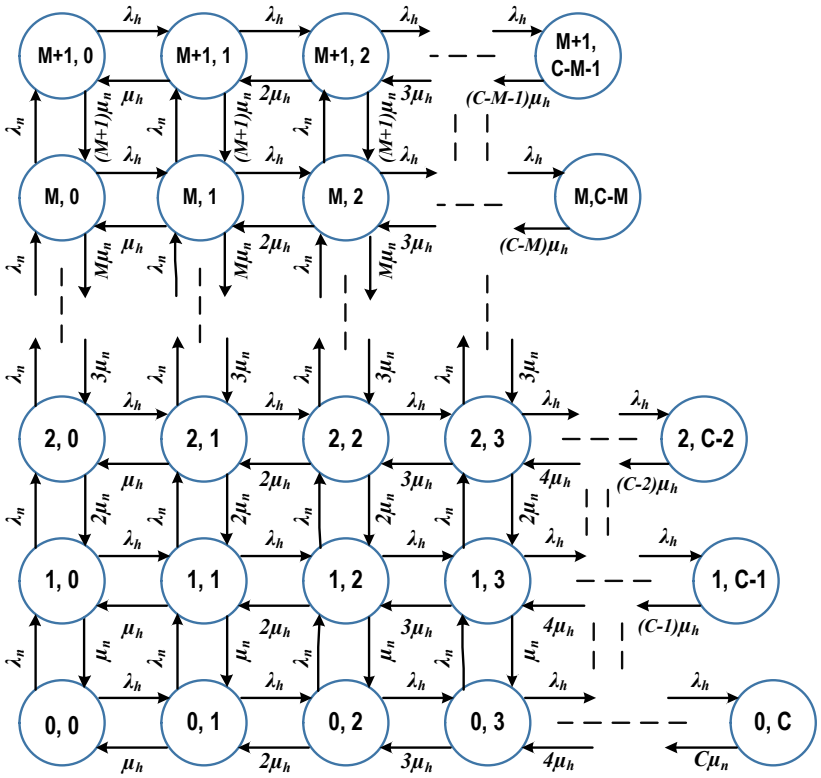

Figure 2: Transition rate diagram of LFC scheme under two dimensional Markov chain model

The new NCBP, P_B and HCDP, P_D can be derived from the above equation as the relation given below:

$$P_B = \frac{\sum_{n_2=0}^{C-M}\left[\frac{\rho_n^M}{M!}\times\frac{\rho_h^{n_2}}{n_2!}\right]+\sum_{n_1}^{M-1}\left[\frac{\rho_n^{n_1}}{n_1!}\times\frac{\rho_h^{C-n_1}}{(C-n_1)!}\right]}{\sum_{n_1=0}^{M}\frac{\rho_n^{n_1}}{n_1!}\sum_{n_2=0}^{C-n_1}\frac{\rho_h^{n_2}}{n_2!}} \tag{10}$$

$$P_D = \frac{\sum_{n_1}^{M}\left[\frac{\rho_n^{n_1}}{n_1!}\times\frac{\rho_h^{C-n_1}}{(C-n_1)!}\right]}{\sum_{n_1=0}^{M}\frac{\rho_n^{n_1}}{n_1!}\sum_{n_2=0}^{C-n_1}\frac{\rho_h^{n_2}}{n_2!}} \tag{11}$$

- **Limited Fractional Channel (LFC) Scheme:** This scheme was first introduced by R. Ramjee in [13] as optimal CAC. But he assumed μ_n and μ_h equal as it was designed under the one-dimensional Markov process. In practical case $\mu_n \neq \mu_h$ [26-28]. Then LFC scheme has been discussed under two dimensional Markov process in [22] which was named as new thinning scheme. In this paper, one channel was fractionally used for accepting new calls with an acceptance factor, α. But the authors did not discuss the situation while more than one fractional channel are considered. The transition diagram of the LFC scheme under two dimensional Markov process has been given in Figure 2.

From the Figure 2, the mathematical expressions can be derived. If $P(n_1,n_2)$ denotes the steady state probability when there are n_1 new calls and n_2 handover calls in the cell, then from balance equation we have,

$$P(n_1,n_2) = \begin{cases} \frac{\rho_n^{n_1}}{n_1!}\times\frac{\rho_h^{n_2}}{n_2!}\times P(0,0), & 0 \le n_1 \le M \\ \frac{(\alpha\rho)^1\rho_n^M}{(M+1)!}\times\frac{\rho_h^{n_2}}{n_2!}\times P(0,0), & n_1 = M+1 \end{cases} \tag{12}$$

$$\text{where, } P(0,0) = \left[\sum_{n_1=0}^{M}\frac{\rho_n^{n_1}}{n_1!}\times\sum_{n_2=0}^{C-n_1}\frac{\rho_h^{n_2}}{n_2!}+\frac{\alpha\rho_n^{M+1}}{(M+1)!}\times\sum_{n_2=0}^{C-M-1}\frac{\rho_h^{n_2}}{n_2!}\right]^{-1} \tag{13}$$

The NCBP and HCDP of the new thinning scheme are estimated by the mathematical relation given by (14) and (15), respectively.

$$P_B = \sum_{n_1=0}^{M}\left[\frac{\rho_n^{n_1}}{n_1!}\times\frac{\rho_h^{C-n_1}}{(C-n_1)!}\right]P(0,0)+\sum_{n_2=0}^{C-M-1}\left[\frac{\alpha\rho_n^{M+1}}{(M+1)!}\times\frac{\rho_h^{n_2}}{n_2!}\right]P(0,0)+(1-\alpha)\sum_{n_2=0}^{C-M-1}\left[\frac{\alpha\rho_n^{M+1}}{(M+1)!}\times\frac{\rho_h^{n_2}}{n_2!}\right]P(0,0) \tag{14}$$

$$P_D = \sum_{n_1=0}^{M}\frac{\rho_n^{n_1}}{n_1!}\times\frac{\rho_h^{(C-n_1)}}{(C-n_1)!}P(0,0)+\frac{\alpha\rho_n^{M+1}}{(M+1)!}\times\frac{\rho_h^{(C-M-1)}}{(C-M-1)!}P(0,0) \tag{15}$$

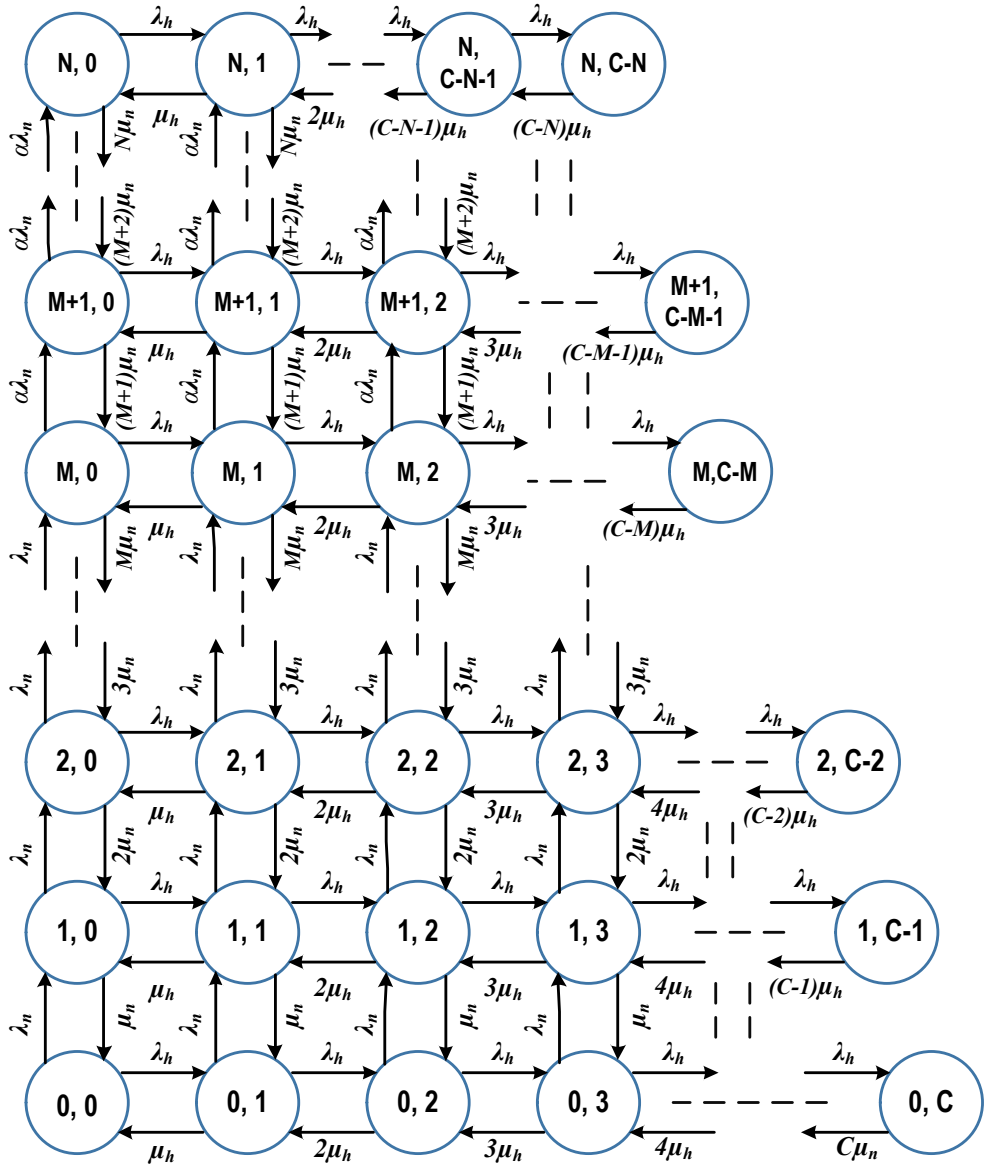

Figure 3: Transition rate diagram of proposed DLFC scheme of CAC under two dimensional Markov chain model

3. Proposed DLFC

3.1. Mathematical Modeling of the Proposed DLFC Method

This CAC scheme is proposed under two-dimensional Markov process where, $\mu_n \neq \mu_h$. For increasing channel utilization fractional channel scheme is used and the number of fractional channels is considered more than one. That's why this scheme is named Defined Limited Fractional Channel scheme (DLFC). After occupying the M channels, the additional new calls will be admitted with a certain probability "α". Therefore, the new calls will be opposed with probability 1-α in those states. Finally, only handover calls will be acceptable from M+N to C. If all channels are busy, handover calls will be dropped. The proposed scheme with its transition properties is illustrated in Figure 3. In this scheme, we have assumed a different channel holding time for each type of calls. Thus, the different channel holding time ($\mu_n \neq \mu_h$) offers the state transition rate diagram to be two dimensional. In Figure 3, n_1 and n_2 denotes states new calls and handover calls, respectively. The ρ_n and ρ_h indicates the new call traffic load and handover call traffic load, respectively. For call admission controlling of DLFC scheme, a flowchart is given below in Figure 4. From this figure, it can be explained that at first, the system will analyze the call type either handover or a new call. If the call is a handover call then the availability of the channel less than C will be checked. If yes then the call will be accepted if not then it will be blocked. If the call is a new call then the availability of channel less than M will be checked. If yes then the call will be accepted and if not then the availability of channel M to N-1 will be checked for their availability. For being available the call will be accepted with predefined acceptance factor α. If not then it will be blocked.

From the Figures 3 and 4, mathematical terminologies of the DLFC scheme have been derived. If $P(n_1, n_2)$ denotes the steady state probability considering that there present n_1 new calls and n_2 handover calls in the cell. From the balance equation we have,

$$P(n_1,n_2)=\begin{cases}\dfrac{\rho_n^{n_1}}{n_1!}\times\dfrac{\rho_h^{n_2}}{n_2!}\times P(0,0), & 0\le n_1\le M\\ \dfrac{(\alpha\rho)^{n_1-M}\rho_n^{M}}{n_1!}\times\dfrac{\rho_h^{n_2}}{n_2!}\times P(0,0), & M<n_1\le N\end{cases} \tag{16}$$

From normalization we get,

$$P(0,0)=\left[\sum_{n_1=0}^{M}\frac{\rho_n^{n_1}}{n_1!}\times\sum_{n_2=0}^{C-n_1}\frac{\rho_h^{n_2}}{n_2!}+\sum_{n_1=M+1}^{N}\frac{(\alpha\rho_n)^{n_1-M}\rho_n^{M}}{n_1!}\times\sum_{n_2=0}^{C-n_1}\frac{\rho_h^{n_2}}{n_2!}\right]^{-1} \tag{17}$$

where, M and N denote the threshold channel and priority to the channel, respectively.

The NCBP and HCDP of the DLFC scheme can be found as (18) and (19), respectively.

$$P_B=\sum_{n_1=0}^{M}\left[\frac{\rho_n^{n_1}}{n_1!}\times\frac{\rho_h^{C-n_1}}{(C-n_1)!}\right]P(0,0)+\sum_{n_2=0}^{C-N}\left[\frac{(\alpha\rho_n)^{N-M}\rho_n^{M}}{N!}\times\frac{\rho_h^{n_2}}{n_2!}\right]P(0,0)+(1-\alpha)\sum_{n_1=M+1}^{N-1}\sum_{n_2=0}^{C-n_1}\left[\frac{(\alpha\rho_n)^{n_1-M}\rho_n^{n_1}}{n_1!}\times\frac{\rho_h^{n_2}}{n_2!}\right]P(0,0) \tag{18}$$

$$P_D=\sum_{n_1=0}^{M}\frac{\rho_n^{n_1}}{n_1!}\times\frac{\rho_h^{(C-n_1)}}{(C-n_1)!}P(0,0)+\sum_{i=1}^{N-M}\frac{(\alpha\rho_n)^{i}\rho_n^{M}}{(M+i)!}\times\frac{\rho_h^{(C-M-i)}}{(C-M-i)!}P(0,0) \tag{19}$$

when $N-M=0 \rightarrow$ (Simple guard channel (GC))

$N-M=1 \rightarrow$ (LFC) [13], [21]

$N-M>1 \rightarrow$ (Defined limited fractional channel) again $\alpha=0\rightarrow$ GC;

$\alpha=1\rightarrow N-M$; These channels show the non-priority characteristics.

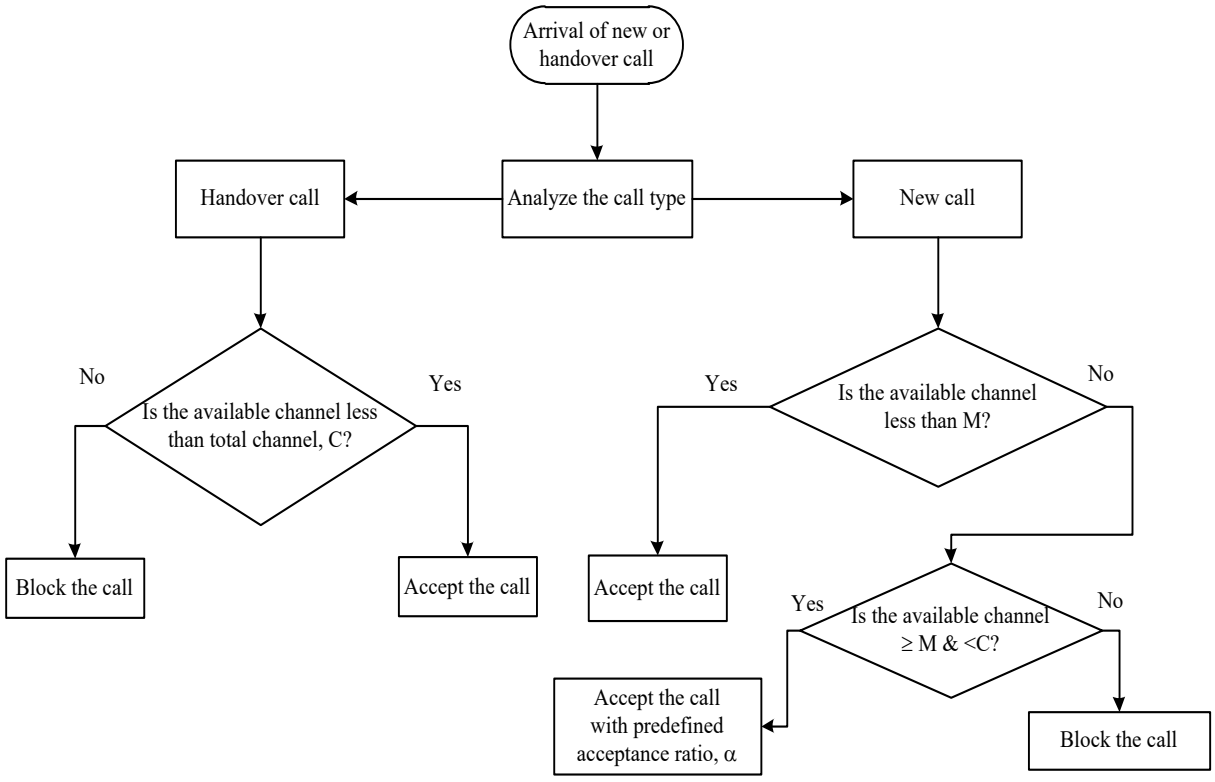

Figure 4: The conditional steps of call admission according to the DLFC scheme

3.2. Numerical Evidence of Optimality for DLFC scheme

For designing a CAC scheme it is important to ensure QoS. In [13] it is stated that cut off priority scheme is the optimal CAC scheme. But DLFC is more optimal than cut off priority scheme because the HCDP is less than cut off priority scheme in DLFC where NCBP is almost constant. As λ_n and λ_h are not linearly related [1] it is too complicated to prove the optimality for DLFC. Here, numerically we have proven the optimality of the NCBP and HCDP based estimation by the proposed DLFC scheme individually.

Numerical Evidence of Optimality for NCBP (P_B): Let us consider, total channel=C and guard channel= M, for Fixed Guard Band (FGB) or cut off priority scheme. From the relation (9) we get,

$$P_{FGB}(0,0)=\left[\sum_{n_1=0}^{M}\frac{\rho_n^{n_1}}{n_1!}\times\sum_{n_2=0}^{C-n_1}\frac{\rho_h^{n_2}}{n_2!}\right]^{-1}$$

$$=\left[\sum_{n_1=0}^{M-i}\frac{\rho_n^{n_1}}{n_1!}\times\sum_{n_2=0}^{C-n_1}\frac{\rho_h^{n_2}}{n_2!}+\sum_{n_1=M-i+1}^{M}\frac{\rho_n^{n_1}}{n_1!}\times\sum_{n_2=0}^{C-n_1}\frac{\rho_h^{n_2}}{n_2!}\right]^{-1}$$

$$=[x_1]^{-1}\quad \text{where, } x_1=\sum_{n_1=0}^{M-i}\frac{\rho_n^{n_1}}{n_1!}\times\sum_{n_2=0}^{C-n_1}\frac{\rho_h^{n_2}}{n_2!}+\sum_{n_1=M-i+1}^{M}\frac{\rho_n^{n_2}}{n_1!}\times\sum_{n_2=0}^{C-n_1}\frac{\rho_h^{n_2}}{n_2!} \tag{20}$$

Again acceptance factor, $0<\alpha<1$; Fractional priority to $N=M$ and number of fractional channel = N-M= i; for proposed DLFC scheme. From the relation (17) we get,

$$P_{DLFC}(0,0)=\left[\sum_{n_1=0}^{N-i}\frac{\rho_n^{n_1}}{n_1!}\times\sum_{n_2=0}^{C-n_1}\frac{\rho_h^{n_2}}{n_2!}+\sum_{n_1=N-i+1}^{N}\frac{(\alpha\rho_n)^{n_1-N+i}\rho_n^{N-i}}{N!}\times\sum_{n_2=0}^{C-n_1}\frac{\rho_h^{n_2}}{n_2!}\right]^{-1}$$

$$=\left[\sum_{n_1=0}^{M-i}\frac{\rho_n^{n_1}}{n_1!}\times\sum_{n_2=0}^{C-n_1}\frac{\rho_h^{n_2}}{n_2!}+\sum_{n_1=M-i+1}^{M}\frac{\alpha^{n_1-M+i}\rho_n^{n_1}}{n_1!}\times\sum_{n_2=0}^{C-n_1}\frac{\rho_h^{n_2}}{n_2!}\right]^{-1}$$

$$=[x_2]^{-1}\ \text{ where, }\ x_2=\sum_{n_1=0}^{M-i}\frac{\rho_n^{n_1}}{n_1!}\times\sum_{n_2=0}^{C-n_1}\frac{\rho_h^{n_2}}{n_2!}+\sum_{n_1=M-i+1}^{M}\frac{\alpha^{n_1-M+i}\rho_n^{n1}}{n_1!}\times\sum_{n_2=0}^{C-n_1}\frac{\rho_h^{n_2}}{n_2!} \tag{21}$$

Since $0<\alpha<1, x_1>x_2$ and $\frac{P_{FGB}(0,0)}{P_{DLFC}(0,0)}=\frac{x_2}{x_1}=x'\le 1\begin{bmatrix}x'\approx 1 \text{ when offered load is low}\\ x'<1 \text{ when offered load is high}\end{bmatrix}$, $P_{FGB}(0,0)\le P_{DLFC}(0,0)$

Now for blocking probabilities from equations (10) and (20), we can estimate NCBP for FGB scheme as,

$$P_B^{\ FGB}=\left[\sum_{n_2=0}^{C-M}\left[\frac{\rho_n^{M}}{M!}\times\frac{\rho_h^{n_2}}{n_2!}\right]+\sum_{n_1=0}^{M-1}\left[\frac{\rho_n^{n_1}}{n_1!}\times\frac{\rho_h^{C-n_1}}{(C-n_1)!}\right]\right]P_{FGB}(0,0) \tag{22}$$

Handover dropping probability for DLFC scheme,

$$P_B^{\ DLFC}=\left\{\sum_{n_1=0}^{M}\left[\frac{\rho_n^{n_1}}{n_1!}\times\frac{\rho_h^{C-n_1}}{(C-n_1)!}\right]+\sum_{n_2=0}^{C-N}\left[\frac{(\alpha\rho_n)^{N-M}\rho_n^{M}}{N!}\times\frac{\rho_h^{n_2}}{n_2!}\right]+(1-\alpha)\sum_{n_1=M+1}^{N-1}\sum_{n_2=0}^{C-n_1}\left[\frac{(\alpha\rho_n)^{n_1-M}\rho_n^{n_1}}{n_1!}\times\frac{\rho_h^{n_2}}{n_2!}\right]\right\}P_{DLFC}(0,0)$$

$$\therefore\frac{P_B^{\ FGB}}{P_B^{\ DLFC}}=\frac{P_{FGB}(0,0)}{P_{DLFC}(0,0)}\left\{\frac{\sum_{n_2=0}^{C-M}\left[\frac{\rho_n^{M}}{M!}\times\frac{\rho_h^{n_2}}{n_2!}\right]+\sum_{n_1=0}^{M-1}\left[\frac{\rho_n^{n_1}}{n_1!}\times\frac{\rho_h^{C-n_1}}{(C-n_1)!}\right]}{\sum_{n_1=0}^{M}\left[\frac{\rho_n^{n_1}}{n_1!}\times\frac{\rho_h^{C-n_1}}{(C-n_1)!}\right]+\sum_{n_2=0}^{C-N}\left[\frac{(\alpha\rho_n)^{N-M}\rho_n^{M}}{N!}\times\frac{\rho_h^{n_2}}{n_2!}\right]+(1-\alpha)\sum_{n_1=M+1}^{N-1}\sum_{n_2=0}^{C-n_1}\left[\frac{(\alpha\rho_n)^{n_1-M}\rho_n^{n_1}}{n_1!}\times\frac{\rho_h^{n_2}}{n_2!}\right]}\right\}$$

$$= x'.x'' \quad \text{where, } x'' = \frac{\sum_{n_2=0}^{C-M}\left[\frac{\rho_n^M}{M!}\times\frac{\rho_h^{n_2}}{n_2!}\right]+\sum_{n_1=0}^{M-1}\left[\frac{\rho_n^M}{n_1!}\times\frac{\rho_h^{C-n_1}}{(C-n_1)!}\right]}{\sum_{n_1=0}^{M}\left[\frac{\rho_n^{n_1}}{n_1!}\times\frac{\rho_h^{C-n_1}}{(C-n_1)!}\right]+\sum_{n_2=0}^{C-M}\left[\frac{(\alpha\rho_n)^{N-M}}{N!}\times\frac{\rho_h^{n_2}}{n_2!}\right]+(1-\alpha)\sum_{n_1=M+1}^{N-1}\sum_{n_2=0}^{C-n_1}\left[\frac{(\alpha\rho_n)^{n_1-M}}{n_1!}\times\frac{\rho_h^{n_2}}{n_2!}\right]} > 1$$

because, $0 \le \alpha \le 1$ and $\frac{P_B^{FGB}}{P_B^{DLFC}} = X \approx 1$, therefore it can be said that $P_B^{FGB} \approx P_B^{DLFC}$. From this relation, it is proved that NCBP is almost same in FGB and DLFC. A truth table for this evidence is given in Table 1 where M=80; C=100; i=1 and α=0.5.

Table 1: Truth table of optimality test for DLFC regarding NCBP

Serial No	Erlang	x′	x″	X=x′*x″	P_B^{DLFC}-P_B^{FGB}
1	72	0.95396	1.125123788	1.07	0.002533046
2	108	0.814726	1.242736145	1.01	0.003510861
3	144	0.739994	1.358456043	1.01	0.002376509
4	180	0.693542	1.446178112	1.00	0.00167154
5	216	0.662022	1.51347319	1.00	0.001234904
6	252	0.639281	1.566425511	1.00	0.000948721
7	288	0.622116	1.609086009	1.00	0.000751506
8	324	0.608707	1.644154299	1.00	0.00060996
9	360	0.597946	1.673476122	1.00	0.000504963

Numerical Evidence of Optimality for DLFC by HCDP (P_D): Similarly for HCDP of FGB scheme from equation (11) we get,

$$P_D^{FGB} = \sum_{n_1=0}^{M}\left[\frac{\rho_n^{n_1}}{n_1!}\times\frac{\rho_h^{C-n_1}}{(C-n_1)!}\right]P_{FGB}(0,0)$$

HCDP of DLFC from equation (19) we get,

$$P_D^{DLFC} = \left\{\sum_{n_1=0}^{N-i}\left[\frac{\rho_n^{n_1}}{n_1!}\times\frac{\rho_h^{C-n_1}}{(C-n_1)!}\right]+\sum_{n_1=N-i+1}^{N}\frac{\alpha^{n_1-N+i}\rho_n^{n_1}}{n_1!}\times\frac{\rho_h^{n_2}}{(C-n_1)!}\right\}P_{DLFC}(0,0)$$

$$\therefore \frac{P_D^{FGB}}{P_D^{DLFC}} = \frac{P_{FGB}(0,0)}{P_{DLFC}(0,0)}\left\{\frac{\sum_{n_1=0}^{M-i}\left[\frac{\rho_n^{n_1}}{n_1!}\times\frac{\rho_h^{C-n_1}}{(C-n_1)!}\right]+\sum_{n_1=M-i+1}^{M}\frac{\rho_n^{n_1}}{n_1!}\times\frac{\rho_h^{C-n_1}}{(C-n_1)!}}{\left\{\sum_{n_1=0}^{N-i}\left[\frac{\rho_n^{n_1}}{n_1!}\times\frac{\rho_h^{C-n_1}}{(C-n_1)!}\right]+\sum_{n_1=N-i+1}^{N}\frac{\alpha^{n_1-N+i}\rho_n^{n_1}}{n_1!}\times\frac{\rho_h^{C-n_1}}{(C-n_1)!}\right\}}\right\}$$

$$= x'.x''' \quad \text{where, } x''' = \frac{\sum_{n_1=0}^{M-1}\left[\frac{\rho_n^{n_1}}{n_1!}\times\frac{\rho_h^{C-n_1}}{(C-n_1)!}\right]+\sum_{n_1=M-i+1}^{M}\left[\frac{\rho_n^{M}}{n_1!}\times\frac{\rho_h^{C-n_1}}{(C-n_1)!}\right]}{\sum_{n_1=0}^{N-i}\left[\frac{\rho_n^{n_1}}{n_1!}\times\frac{\rho_h^{C-n_1}}{(C-n_1)!}\right]+\sum_{n_2=N-i+1}^{N}\frac{\alpha^{n_1-N+i}\rho_n^{n_1}}{n_1!}\times\frac{\rho_h^{C-n_1}}{(C-n_1)!}} > 1 \text{ hence, } 0 < \alpha < 1$$

$$= X > 1 \text{ and } P_D^{FGB} > P_D^{DLFC} \tag{23}$$

Finally, it is also proved that HCDP of DLFC scheme is less than that of FGB. A truth table for this evidence is given in Table 2 where M=80; C=100; i=1 and α=0.5. From the table, it is found that the previously claimed condition has been successfully achieved. The value of X corresponding to every value of the Erlang* is greater than 1. This condition is hypothesized by the proved relation given in (23).

[*An Erlang is a unit to measure the traffic load or total traffic volume of one hour in telecommunication systems. Therefore, Erlang = number of calls × duration]

Table 2: Truth table of optimality for DLFC by HCDP

Serial No	Erlang	x′	x‴	X
1	36	1	1.256047896	1.26
2	72	0.95396	1.343211738	1.28
3	108	0.814726	1.524809854	1.24
4	144	0.739994	1.614197079	1.19
5	180	0.693542	1.675859871	1.16
6	216	0.662022	1.720978322	1.14
7	252	0.639281	1.755288598	1.12
8	288	0.622116	1.782196438	1.11
9	324	0.608707	1.803834919	1.10
10	360	0.597946	1.821599044	1.09

4. Results and Discussions

In this section, the simulation results have been presented for the assessment of the proposed DLFC scheme with the other conventional schemes under 2D Markov process based on statistical modeling. These results show how much deviation may take place for applying the proposed scheme with respect to the other traditional CAC schemes. On the other hand, the various features of the proposed scheme have been also described gradually. First of all, investigations of all the CAC schemes were carried out considering some basic assumptions. For simulating the proposed methodology regarding CAC scheme designing in 2D Markov process, we assumed some parameters as the numerical values represented in Table 3. These parameters were always considered in a similar manner for all the performance analysis of the conventional schemes as well as the proposed DLFC scheme.

Table 3: Basic assumptions of some parameters

Parameters	Nomenclature	Values
Total Channel	C	100
Guard Channel	M	80
Fractional Guard Channel	M	75~79
Fractional Priority Channel	N	80
Traffic Load (New Call)	ρ_n	0~360
New Call Termination Rate	μ_n	1/120
Handover Call Termination Rate	μ_h	1/60
Acceptance Factor	α	0~1

In numerical results, the new NCBP's and handover HCDP's of the DLFC cut off a priority, and LFC schemes were examined in two dimensional Markov process. The performances of all the schemes were analyzed with different conditions like fractional channel numbers and different values of acceptance factor. According to the basic assumption of the system parameters, all the mathematical calculation has been performed in MATLAB 2012b. The two dimensional Markov model was prepared by MATLAB code and based on this model all the traffic load was analyzed to estimate the performances of the different schemes.

The HCDP of the wireless network under the conditions of given parameters of Table 3 regarding different traffic load were analyzed and compared the performances. Figure 5 presents such a comparison among the various popular CAC schemes as well as the proposed scheme regarding their HCDP performances. This figure shows that the proposed scheme confirms the lowest HCDP than the others and the highest HCDP occurs in case of the cut off priority scheme. DLFC scheme has a lower HCDP than LFC and cut off priority schemes.

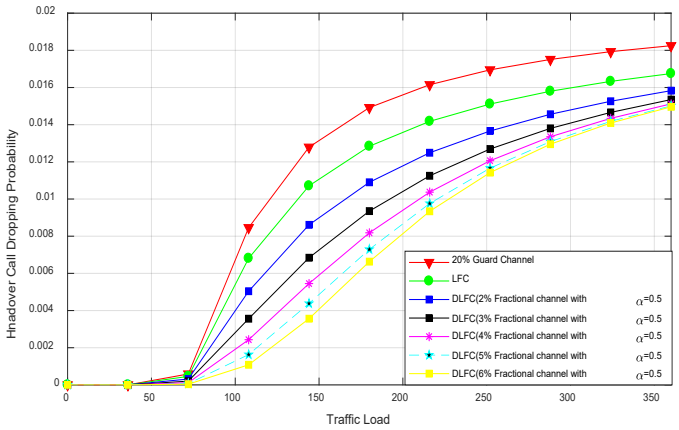

Figure 5: Handover call dropping probabilities for the different number of fractional channel for DLFC with Cut off Priority and LFC scheme

It is also observed that by increasing the number of the fractional channels the HCDP can be reduced. But there is a limit to increasing the number of fractional channels. After increasing the value to the limit the HCDP remain almost the same. In Figure 5, it was found that the values of HCDP for 5% and 6% fractional channels of the assumption are almost the same for the high traffic load.

The NCBP of the cutoff priority scheme, LFC, and proposed DLFC schemes have been calculated and presented to show the comparison among their performances and presented in Figure 6. Here it is observed that the NCBP are almost same for cut off priority, LFC, and proposed DLFC scheme at higher traffic load which is our real concern. DLFC scheme has a marginally higher NCBP than LFC and cut off priority schemes at the lower new call arrival rate but same performance in the higher new call arrival rate. In this analysis, the basic assumptions were the same as in Figure 5.

We assumed that all the parameters became same except acceptance factor and for different acceptance factors the HCDP have been calculated. The results concerning this consideration have been presented in Figure 7. The value of α must be $0 \le \alpha \le 1$. In this analysis acceptance factor is assumed as α=0.2, 0.3, 0.5, 0.75 & 0.9. It is observed that with the increment of acceptance factor the HCDP increased. The less the acceptance factor is presented in the system, we found the less HCDP. Figure 7 presents the HCDP's of DLFC scheme for the different values of α. Here, one thing can be approached that if we choose the acceptance factor to be 0.5 the dropping probability remains at a satisfactory level. For the value of acceptance factor 0.75 and 0.9, the HCDP increases drastically, which is a threat for the QoS.

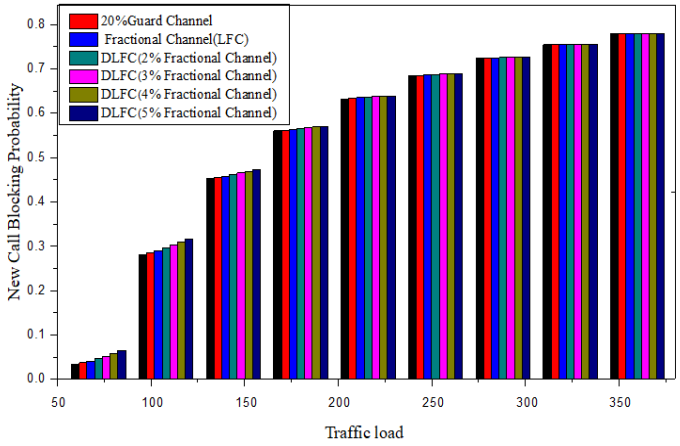

Figure 6: New Call Blocking Probabilities for different no of the fractional channel for DLFC with cut off priority and LFC scheme

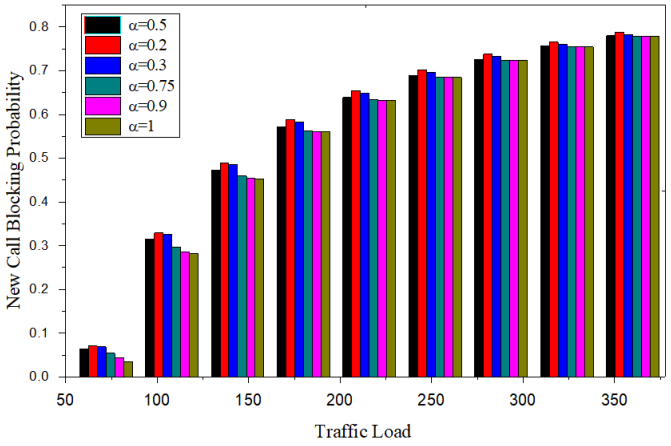

Figure 8: New Call Blocking Probabilities for different values of acceptance factor for DLFC

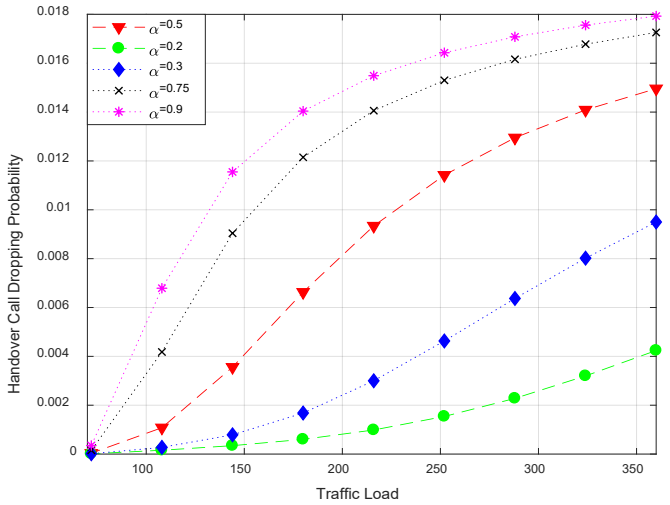

Figure 7: Handover Call Dropping Probabilities for different values of acceptance factor for DLFC

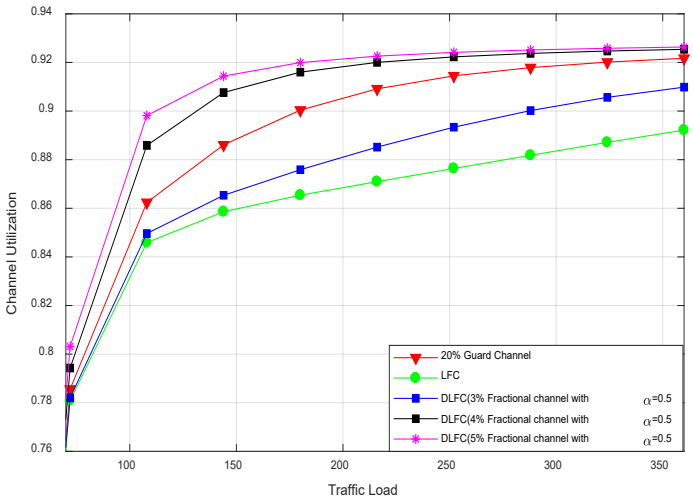

Figure 9: The performance of channel utilization by the DLFC, cut off priority, and LFC scheme regarding different traffic load

In addition to that, with the similar conditioning, the performances regarding NCBP of the proposed DLFC scheme have been also assessed. The results we found have been presented in Figure 8. From this figure, we can perceive that there are some effects of the acceptance factor at the lower traffic load. On the other hand, at the higher traffic load, this effect does not carry any significance which is very concerning the issue of the proposed scheme.

This scheme offers a system where the HCDP will be decreased without affecting the NCPB which has been achieved by the results given in Figure 8. Therefore, the proposed scheme improves the QoS of the wireless network where we are concerned about the HCDP at the very high traffic load. So, the results clarify that the DLFC scheme reduces HCDP without hampering the performance of the system's NCPB. The additional benefit of the proposed scheme is the regulating properties of the acceptance factor. To achieve a certain level of QoS, we can select our acceptance factor to maintain the HCDP and NCBP at our satisfactory level with respect to the load. In addition, it can be chosen according to traffic load arrived in the cellular network.

Extra concerning issue for the QoS associated with the CAC policy is channel utilization. In Figure 9, the channel utilization performance of the proposed DLFC scheme has been presented comparing with the conventional cut off priority scheme and LFC scheme. Channel utilization of all the schemes discussed here remains the same for almost all the cases. Although the cut-off priority scheme shows the highest performance of channel utilization, the proposed DLFC scheme has also almost similar channel utilization performance by tuning the acceptance factor.

In Figure 10, channel utilization of DLFC scheme has been shown under various values of acceptance factor α. This acceptance factor has a nice tuning effect on the performance of the channel utilization. Therefore, it is easier to attain the required system's channel utilization performance by the proper selection of the call acceptance factor. It should be mentioned here that, with the help of reducing the NCBP we can increase the channel utilization but in this case, it will be difficult to maintain the QoS. To maintain the importance of handover call we should take into account not only the blocking probability but also the channel utilization as well. To optimize the system performance, we can regulate the acceptance factor through the DLFC scheme.

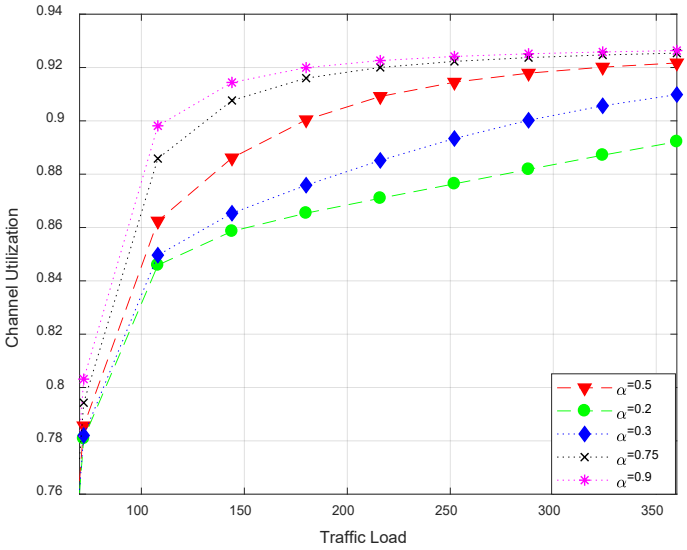

Figure 10: The performance of channel utilization by the DLFC, cut off priority, and LFC schemes regarding different acceptance factors

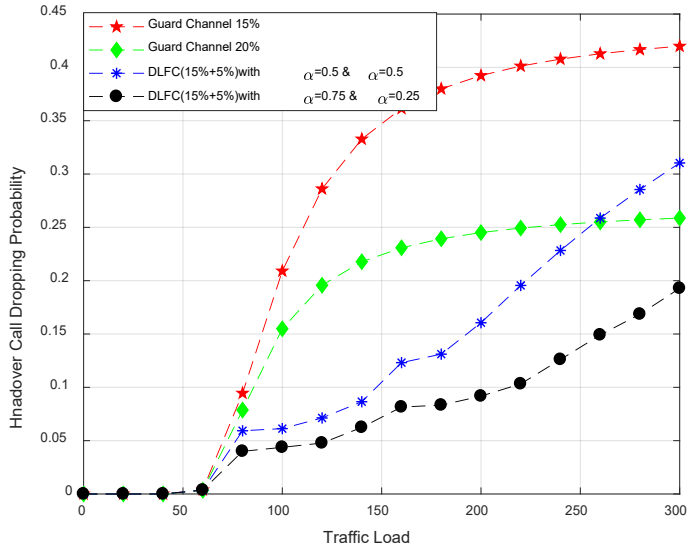

Figure 11: The performance of the DLFC scheme while it is used as a hybrid approach with compared to the guard channel scheme.

This DLFC scheme has another beautiful feature which is its utility of hybrid approach of call acceptance rate. If we consider 15% guard channel and 20% guard channel in cutoff priority scheme, there we find a major difference in handover call dropping probability. On the other hand, we can solve this problem with the proposed DLFC scheme. We can reduce the handover call dropping probability to a satisfactory level by using the utility of the regulation of the acceptance factor. Such a result has been given in Figure 11. Here, we can observe that if we divide the 20% guard channel as 15%+5% and choose different acceptance factors for two different divided channel groups, the HCDP reduces significantly. Here, acceptance factor 0.75 has been chosen for the 1st 15% guard channel and for the rest 5%, the acceptance factor has been chosen 0.25. For both (15% and 5%) guard channel the acceptance factor 0.5 has been used in Figure 11 to show the reference performance of the proposed DLCF scheme.

5. Conclusions

The radio resource is limited to a system. For this reason, providing a priority to one class in its call admission is a cause to increase the call blocking probabilities of other classes. Since handover call dropping is practically much more annoying than the new call blocking, in this research paper, a new call admission control scheme has been proposed which is termed as a defined limited fractional channel or DLFC scheme. The NCBP and HCDP of the proposed scheme have been estimated from the model designed MATLAB 2012b and also compared to the existing methods under two dimensional Markov process based statistical modeling. In this case, it has been observed that the HCDP is decreased where NCBP is almost the same with respect to the cut off priority scheme and LFC schemes. It has been perceived from the simulation results that the performance of the DLFC depends upon the number of fractional channels and the values of the acceptance factor. So, it becomes a major concern to choose the number of fractional channels and the value of the acceptance factor.

This DLFC scheme has been investigated in a two-dimensional Markov process. There is scope to analyze this idea under multidimensional Markov process for multi-service wireless network and to find out the effect on performances of this scheme and its curse of dimensionality.

Conflict of Interest

The authors of this paper declare that there is no conflict of interest and commercial engagement with other parties regarding this research work.

Acknowledgment

All authors of this paper would like to thank Prof. Dr. Mostafa Zaman Chowdhury, Dept. of EEE, Khulna University of Engineering & Technology (KUET), for his valuable guidance from the beginning of this research work.

References

[1] M. A. Rahman, M. A. Hossain, S. Ahmed, and M. Z. Chowdhury, "A New guard-band call admission control policy based on acceptance factor for wireless cellular networks," International Conference on Informatics, Electronics & Vision (ICIEV), pp. 1-5, May 2014. DOI: 10.1109/ICIEV.2014.6850803.

[2] A. Sgora, Vergados, and D. Dimitrios, "Handover prioritization and decision schemes in wireless cellular networks: A survey," IEEE Communications Surveys and Tutorials, vol. 11, no. 4, pp. 57-77, December 2009. DOI: 10.1109/SURV.2009.090405.

[3] M. Z. Chowdhury, Y. Min Jang, and Z. J. Haas, "Call admission control based on adaptive bandwidth allocation for wireless networks," Journal of Communications and Networks, vol. 15, no. 1, pp. 15-24, February 2013. DOI: 10.1109/JCN.2013.000005.

[4] Y. Fang, "Modelling and performance analysis for wireless mobile networks: A new analytical approach," IEEE/ACM Transaction on Networking, vol. 13, no. 5, pp. 989-1002, October 2005. DOI: 10.1109/TNET.2005.857119.

[5] M. Z. Chowdhury, M. S. Uddin, and Y. M. Jang, "Dynamic channel allocation for class-based QoS provisioning and call admission in visible light communication," Arabian Journal for Science and Engineering, vol. 39, no. 2, pp. 1007-1016, February 2014. DOI: 10.1007/s13369-013-0680-4.

[6] M. Mamman, Z. M. Hanapi, A. Abdullah and A. Muhammed, "An adaptive call admission control with bandwidth reservation for downlink LTE networks," IEEE Access, vol. 5, pp. 10986-10994, 2017. DOI: 10.1109/ACCESS.2017.2713451

[7] M. Schneps-Schneppe and V. B. Iversen, "Call Admission Control in Cellular Networks," Mobile Networks, Chap. 6, pp. 111-136, InTech Publisher, 2012. DOI: 10.5772/35866.

[8] M. Ghaderi and R. Boutaba, "Call admission control in mobile cellular networks: A comprehensive survey," Wireless Communication and Mobile Computing, vol. 6, no.1, pp. 69-93, February 2006. DOI: 10.1002/wcm.246

[9] K. Bhoite and S. Gengaje, "Handoff Prioritize Call Admission Control Policy for Integrated Macrocell-Femtocell Network," International Journal of Computer Applications, vol. 164, no. 2, pp. 21-26, April 2017. DOI: 10.5120/ijca2017913593.

[10] M. Jain and R. Mittal, "Adaptive call admission control and resource allocation in multiserver wireless/cellular network," Journal of Industrial Engineering International, vol. 12, no. 80, pp. 71-80, November 2015. DOI: 10.1007/s40092-015-0129-3.

[11] H. Beigy and M.R. Meybody, "A new fractional channel policy," Journal on High-Speed Networks, vol. 13, no. 1, pp. 22-36, 2004.

[12] J. L. V. Avila, A. Flipe, C. Perez, and L.O. Guerrero, "Performance analysis of fractional guard channel policies in mobile cellular networks," IEEE Transactions on Wireless Communications, vol. 5, no. 2, pp. 301-305, February 2006. DOI: 10.1109/TWC.2006.1611053.

[13] R. Ramajee, R. Nagarajan, and D. Towsley, "On optimal call admission control in cellular networks," Wireless Networks, vol. 3, pp. 29-41, 1997. DOI: 10.1109/INFCOM.1996.497876.

[14] M. B. A. Sadi and A. Nadia, "Call admission scheme for multidimensional traffic assuming finite handoff user," Journal of Computer Networks and Communications, vol. 2017, Article ID 6101568, 5 pages, 2017. DOI:10.1155/2017/6101568.

[15] J. Hou and Y. Fang, "Mobility-based call admission control schemes for wireless mobile networks," Wireless Communication and Mobile Computing, vol. 1, pp. 269-282, 2002. DOI: 10.1002/wcm.18.

[16] Y. Fang, "Thinning scheme for call admission control in wireless networks," IEEE Transactions on Computers, vol. 52, no. 5, pp. 685-687, May 2003. DOI: 10.1109/TC.2003.1197135.

[17] J. L. V. Avila, A. Flipe, C. Perez, and L.O. Guerrero, "Performance analysis of fractional guard channel policies in mobile cellular networks," IEEE Transactions on Wireless Communications, vol. 5, no. 2, pp. 301-305, February 2006. DOI: 10.1109/TWC.2006.1611053.

[18] X. Wang, P. Fan, and Y. Pan, "A more realistic thinning scheme for call admission control in multimedia wireless networks," IEEE Transactions on Computers, vol. 57, no. 8, pp. 1143-1148, 2008. DOI: 10.1109/TC.2008.29.

[19] Y. Zhang and D. Liu, "An adaptive algorithm for call admission control in wireless networks," IEEE Telecommunications Conference, vol. 10, no. 4, pp. 3628-3632, 2001. DOI: 10.1109/GLOCOM.2001.966358.

[20] Y. Fang and Y. Zhang, "Call admission control schemes and performance analysis in wireless mobile networks," IEEE Transactions on Vehicular Technology, vol. 51, pp. 371-382, 2002. DOI: 10.1109/25.994812.

[21] Z. Firouzi and H. Beigy, "A new call admission control scheme based on new call bounding and thinning II schemes in cellular mobile networks," IEEE Conference on Electro/Information Technology, vol. 09, pp. 40-45, June 2009. DOI: 10.1109/EIT.2009.5189581.

[22] Z. Firouzi and L. M. Far, "Defining interval for threshold in new thinning scheme," Computer Science and Information Technology (ICCSIT), 2010 3rd IEEE International Conference, vol. 09, pp. 108 – 112, July 2010. DOI:

[23] D. Hong and S. S. Rappaport, "Traffic model and performance analysis for cellular mobile radio telephone systems with prioritized and no prioritized handover procedures," IEEE Transaction on Vehicular Technology, vol. 35, no. 3, pp. 77-92, 1986. DOI: 10.1109/T-VT.1986.24076.

[24] M. A. Rahman, "QoS Provisioning Using Optimal Call Admission Control for Wireless Cellular Network," M. Sc. Thesis Paper, KUET, 18 December 2014.

[25] E. Keogh and A. Mueen, "Encyclopedia of Machine Learning," pp. 257-258, Springer 2010.

[26] M. A. Rahman, M. S. I. Sohag, and M. Z. Chowdhury, "A new fractional channel call admission control for handover priority," International Conference on Informatics, Electronics and Vision (ICIEV), June 2016. DOI: 10.1109/ICIEV.2016.7759997.

[27] M. A. Rahman, A. S. M. Z. Shifat, and M. S. I. Sohag, "The effect of average channel holding time to estimate the QoS parameters of cellular network through guard channel scheme," International Conference on Electrical Engineering and Information Communication Technology, May 2015. DOI: 10.1109/ICEEICT.2015.7307484.

[28] Y. Fang and I. Chlamtac, "Teletraffic analysis and mobility modeling for PCS networks," IEEE Transaction on Communication, vol. 47, pp. 1062–1072, July 1999. DOI: 10.1109/26.774856.

ASTES

Advances in Science, Technology and Engineering Systems Journal Vol. 3, No. 4, 308-317 (2018)

www.astesj.com

Special Issue on Multidisciplinary Sciences and Engineering

ASTESJ

ISSN: 2415-6698

Synthesis of QDI Combinational Circuits using Null Convention Logic Based on Basic Gates

Duarte Lopes de Oliveira[*,1], Orlando Verducci[1], Vitor Leandro Vieira Torres[1], Robson Moreno[2], Lester de Abreu Faria[1]

[1]*Electronics Engineering Division, Technological Institute of Aeronautics, 12227-000, São José dos Campos - SP, Brazil*

[2]*IESTI, Federal University of Itajubá, 35903-087, Itajubá – MG, Brazil*

ARTICLE INFO

Article history:
Received: 01 July, 2018
Accepted: 04 August, 2018
Online: 12 August, 2018

Keywords:
Asynchronous logic
QDI circuits
Dual-rail code
FPGA
NCL gates

ABSTRACT

Currently, synchronous digital circuits (SDC) may require certain design conditions, such as power consumption, robustness, performance, etc. These design conditions are more difficult to satisfy when SDC are implemented in VLSI (Very Large Scale Integration) technology and in the deep-sub-micron MOS (DSM-MOS) technology. The asynchronous design style has properties that serve as an alternative to design DSM-MOS technology circuits and it can satisfy these design conditions. Quasi Delay-Insensitive (QDI) circuits is a class of asynchronous circuits, they have properties where the DSM-MOS technology design is applied, because they are robust to noise, temperature and voltage variations, as well as low electromagnetic emissions, and they are tolerant to certain faults. An interesting style of QDI combinational circuits are NCL (NULL Convention Logic) circuits, because they accept conventional Boolean functions and it can achieve a better optimization. This paper presents an approach and an architecture based in basic gates for the synthesis of NCL gates, therefore its implementation uses only standard libraries and Field Programmable Gate Array (FPGA). The proposed QDI combinational circuits are implemented in the approach that uses only NCL gates.

1. Introduction

This paper is an extension of work originally presented in *2017 IEEE XXIV International Conference on Electronics, Electrical Engineering and Computing* (INTERCON) [1].

Synchronous digital circuits are quite popular and conventionally use a global clock to synchronize their operations. The reason for this popularity is the simplicity of the design. There is also an abundant offer of commercial EDA (Electronic Design Automation) tools for their automatic synthesis. Synchronous circuits have been implemented in deep-sub-micron MOS (DSM-MOS) technology, but global clock signal leads to different problems of synchronous design, such as: a) less tolerance to noise and electromagnetic interaction which increase due to high clock frequency; b) distributing of clock signal is increasingly difficult; c) rise in the delay time variation (Tp-MAX, Tp-MIN) in a gate or wire results in loss of performance, because clock must be adjusted to the maximum delay; d) intensification of drivers amount in the clock signal, consuming a significant part of total energy; e) aggravation of the clock skew; and f) significant delay in wires causes an increase in time analysis complexity [2].

The asynchronous paradigm is a promising alternative to digital design because it eliminates problems related to clock signal and also it increases the robustness of circuits. These circuits operate by events, so there is no overall signal to synchronize operations. Synchronization in asynchronous circuits is performed by protocols of type handshake. In the asynchronous paradigm, there are different classes of asynchronous circuits [3]. The class is defined by its delay model in which the circuit operates correctly and by its operation mode in which it describes how communication works with the environment [4]. The delay models can be classified, such as: a) Bounded Gate and Wire Delay which is similar to the synchronous paradigm [2]; and b) Unbounded Gate and Wire Delay (UGWD). In the UGWD model, the delays of gates and wires can be undefined (any delay value), but finite. In this class, we have the delay-insensitive (DI) circuits that are free of timing analysis. Martin [5,6] shows that DI circuits are very restricted. They can only be synthesized using C elements and inverting gates. Two less restricted variants of the UGWD model

* Duarte Lopes de Oliveira, Email: duarte@ita.br

are: b1) speed-independent (SI) circuits that obey the model in which it has as restriction the delay in wires equal to zero, i.e., the unbounded gate delay and zero wire delay model [3]; and b2) quasi delay-insensitive (QDI) circuits, they have as a constraint the delays in wires when they form a fork, i.e., wires with fan-out > 1 must have approximately equal delays [4,6], so QDI circuits obey the UGWD model and isochronic fork constraint. The interaction of these circuits, for example, DI, SI, QDI with the environment is performed in the I/O_M mode [3, 4, 6]. In I/O_M mode, any change in the output signal can immediately activate a change in the input signal.

For DSM-MOS technology, the asynchronous circuits that best meet the requirements of digital design are the QDI circuits [7]. The QDI circuits have important properties, such as: a) potential to have better latency time, because it works with real delays and not with maximum delays; b) greater robustness to PVT (variations of Process, supply Voltage and Temperature); c) greater robustness to interaction with environment and Stuck-at faults (class of faults tested easily); d) it allows high reuse, because they are highly modular, so they can be used as intellectual property - IP [8]; e) better performance in design of security systems (e.g., encryption) [9]; and f) highly simplified timing analysis.

In QDI combinational circuits (QDI_CC), the data are represented by DI codes of type m-of-n and the most usual processing is the "4-phase" protocol. Several styles were proposed for the synthesis of QDI_CC [10-31]. Firstly, we quote the Minterm Insensitive Delay Synthesis (DIMS) [12] which is quite popular because of its simplicity, but it has a large overhead in area. In DIMS functions, products are implemented with C-elements. Figure 1a shows the operations table of C-element, Figure 1b and 1c show implementations as semi-static CMOS and basic gates, respectively. Another style is the NULL Convention Logic (NCL) proposed by Kant et al. [13]. The NCL style is based on a set of 27 complex gates implemented at the CMOS transistor level [14, 15]. The method for designing QDI_CC based on NCL gates departs from conventional minimized Boolean functions that are transformed into dual-rail Boolean functions and then, the technological mapping is performed using an NCL gates library [16]. The QDI_CC style based on NCL gates has the difficulty of implementing NCL gates in programmable devices, such as Field Programmable Gate Array (FPGAs) [21, 22], while for Very Large Scale Integration (VLSI) it is used standards libraries.

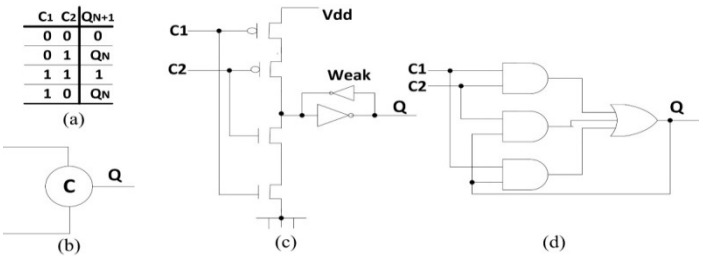

Figure 1. C-element: a) table of operation; b) symbol; c) semi-static version; d) version based on basic gates.

The operating table of NCL gates, not considering the weights, is shown in Figure 2a. The symbol for an THmn NCL gate is shown in Figure 2b, where *n* is the input number and *m* represents the minimum number of inputs that are activated with value one, so that the output is activated with value one. For output to be enabled at zero, all *n* inputs must be enabled at zero. For illustration, the TH23 NCL gate shown in Figure 3 has been implemented in static CMOS technology. In [17-20] three basic gates architectures that implement NCL threshold gates have been proposed for applications that involve standard-cell VLSI or FPGA platforms. In order to operate correctly, these architectures must obey the fundamental mode (FM), therefore they are not QDI.

The interaction with the environment proposes that in the FM mode, "for a new activation of some input signal, the circuit must be stabilized in a stable state, therefore without any electrical activity" [1]. The C-element implemented with basic gates, as shown in Figure 1c, is not QDI because when Q goes from 0 to 1, the circuit must satisfy the fundamental mode to change the inputs again. The QDI_CC design styles of [11, 26-31] are based on basic gates, but they use additional circuits to detect the indicatability which is the requirement to be free of timing analysis.

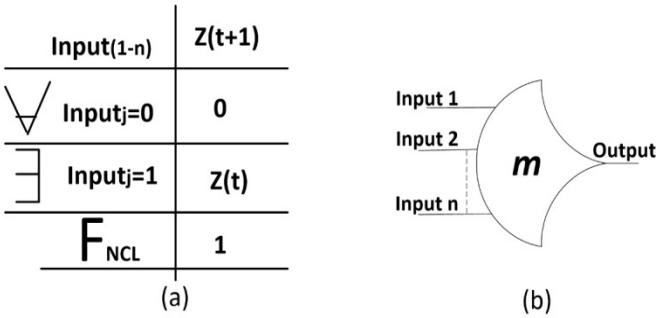

Figure 2. THmn NCL gates: a) table of operations; b) symbol.

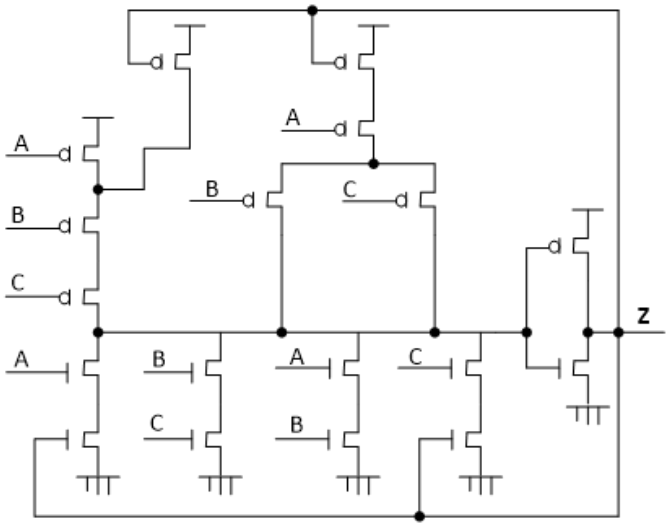

Figure 3. TH23 NCL gate of [16].

To implement THmn NCL gates, this paper proposes a new architecture based on basic gates (see Figure 4). The resulting NCL gates operate in I/O_M mode, therefore they are QDI. Because the NCL gates library is synthesized with only basic gates, then these NCL gates can be easily mapped to platforms of type FPGA or type standard-cell VLSI. This paper also proposes an approach that synthesizes Boolean QDI functions with strong indication using only proposed NCL gates.

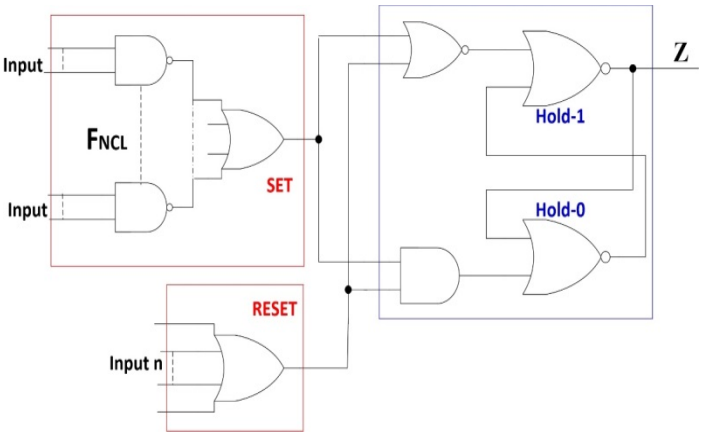

Figure 4. Proposed architecture for THmn NCL gates.

2. Synthesis of NCL Gates: Overview

In order to implement NCL gates, different architectures were proposed at the transistor level [14, 15]. We can also cite architectures that use basic gates, such as proposals [1, 17]. The architecture of [17] is based on Huffman's machine, and the architecture of [1] uses RS latches, which is a semi-static CMOS version of [15].

2.1. Synthesizing Huffman machines as NCL gates

The implemented THmn NCL gates in the Huffman machine architecture [17-20] (see Figure 5) can be synthesized by the Huffman method [3]. We chose the NCL TH23 gate to illustrate method and architecture. The first step of design procedure started with the generation of operations table from the Z function of TH23 NCL gate, as shown in Figure 6a, its function being Z = AB + AC + BC. In the second step, the operations table is represented in the Karnaugh map. In final step, it is realized conventional logic minimization, extracting next-state equations Z(t+1), shown in Figure 6b. The final Z(t+1) equation was extracted by an algebraic manipulation. The logic circuit of TH23 gate is shown in Figure7.

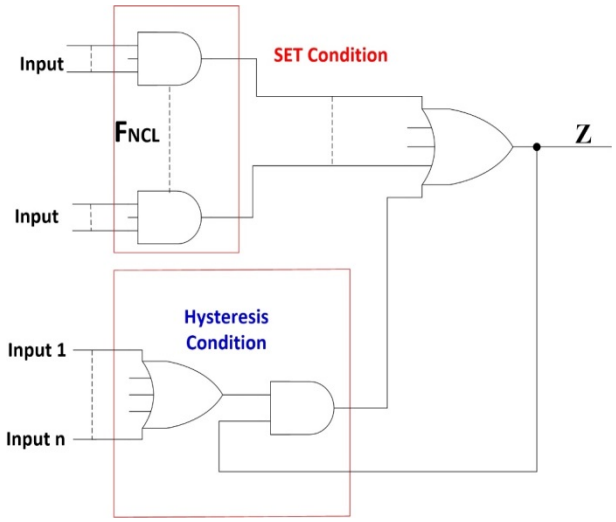

Figure 5. Architecture in the FM for NCL gates of [17-20].

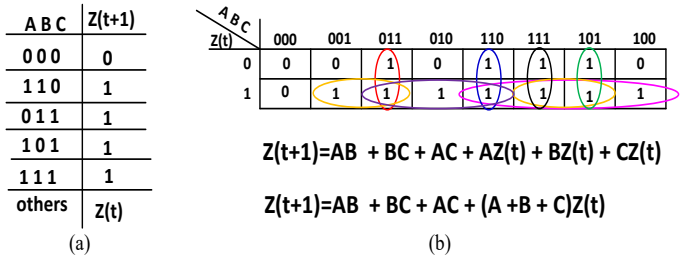

Figure 6. Synthesis of TH23 gate in architecture of [17-20]: a) Operations table; b) Next-state equation.

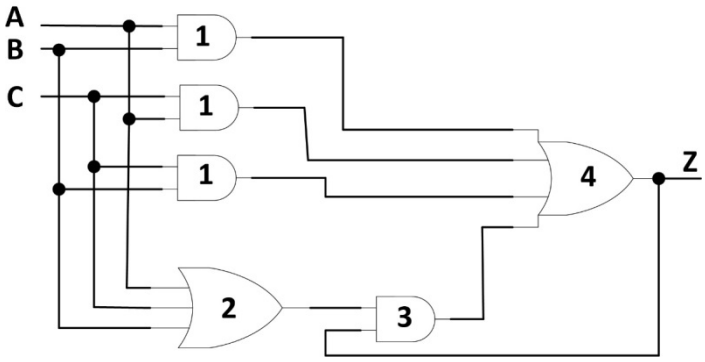

Figure 7. FM architecture of [17-20]: netlist of TH23 gate.

2.2. Synthesizing standard RS as NCL gate

The synthesis of NCL THmn gates in standard RS architecture based on [15] (see Figure 8) extracts the F_{SET} and F_{RESET} functions as shown in [3]. For NCL gate THmn the F_{SET} function is the Z function itself, but using its complemented products. The F_{RESET} function can be described by an OR gate of fan-in=n, which detects when the n input signals are set to zero. The TH23 gate will be used to illustrate method and architecture. Since the Z function of TH23 gate is AB + AC + BC, then the F_{SET} function is {(AB)', (BC)', (BC)'}. Figure 9b shows the F_{SET} function extraction, starting from the operations table and Myers' [3] method, as well as the extraction of F_{RESET} function. The logic circuit of TH23 gate is shown in Figure 10.

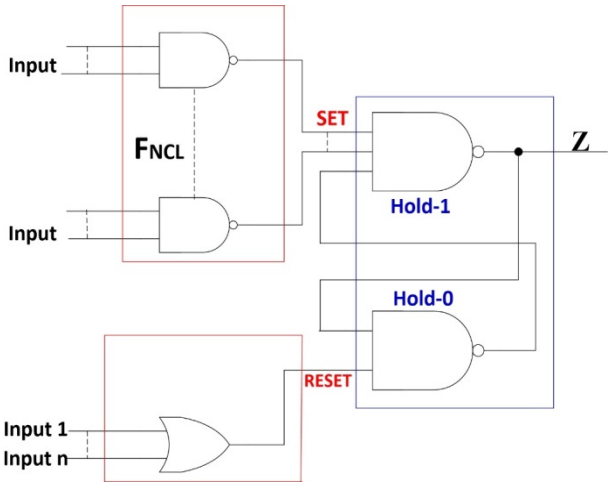

Figure 8. Standard RS architecture in the FM for NCL gates.

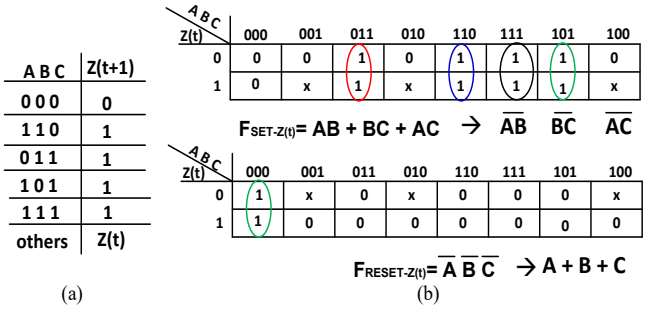

Figure 9. Synthesis of TH23 gate in the standard RS architecture: a) Operations table; b) Fset and Freset equations.

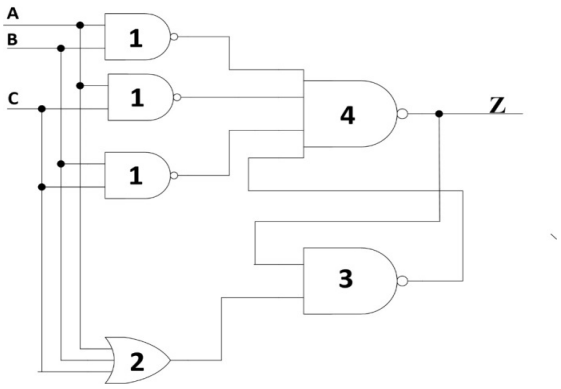

Figure 10. Standard RS architecture: netlist of TH23.

2.3. Synthesizing modified RS as NCL gates

The implementation of THmn NCL gates in modified RS architecture was proposed in [1] (see Figure 11). It follows conventional extraction of the F_{SET} and F_{RESET} functions as shown in section 2.2, but products of F_{SET} are not complemented. To illustrate the method and architecture, it is used the same TH23 gate. Equation 1 describes the architecture of [1] that is composed by the $F_{NCL\text{-}SET}$ and $F_{NCL\text{-}RESET}$ equations. Equations 2 and 3 are extracted using the same procedure described in Figure 9, where $F_{NCL\text{-}RESET}$ is complemented. Finally, equation 4 is obtained from equations 2 and 3, which is the next-state equation of the TH23 gate. Figure 12 shows the logic circuit of TH23 gate in this architecture.

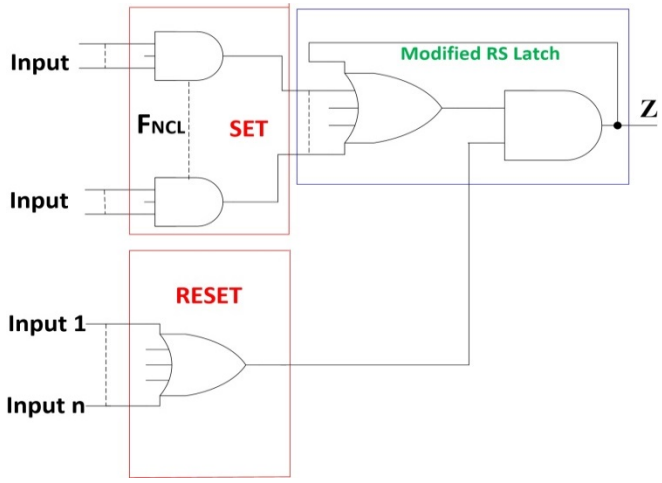

Figure 11. Modified RS architecture in the FM for NCL gates of [1].

$$Z(t+1)=(F_{NCL\text{-}SET}+Z(t)).F_{NCL\text{-}RESET} \quad (1)$$

Where,

$$F_{NCL\text{-}SET}=AB+BC+AC \quad \text{and} \quad (2)$$

$$F_{NCL\text{-}RESET}=\overline{\overline{A}\ \overline{B}\ \overline{C}}=A+B+C \quad (3)$$

$$Z(t+1)=(AB+BC+AC+Z(t)).(A+B+C) \quad (4)$$

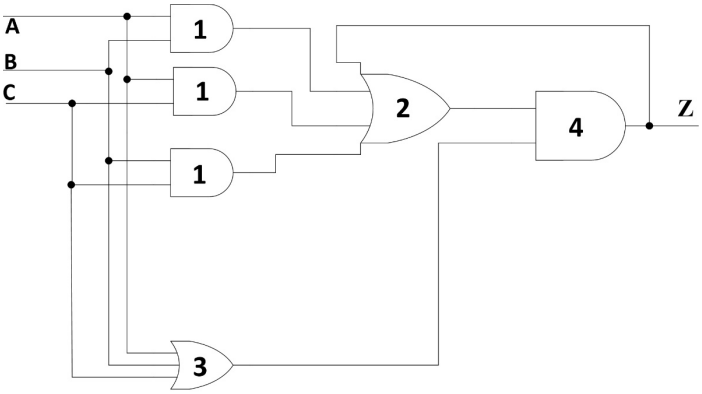

3. QDI Boolean Function: Concepts

Boolean functions for QDI are called function blocks (QDI_FB) and they are synthesized in DI codes. There are different DI codes and in this paper, we adopted the dual-rail coding [32]. The QDI_FB circuits that will be synthesized operate behaving according to the 4-phases handshake protocol [4]. In the dual-rail code, each variable is encoded with two bits. For the variable A, we have A1A0=00 (null - space), A1A0=01 (data 0), A1A0=10 (data 1) and A1A0=11 (never occurs). The DI codes generate the operation completion signal without need of a delay element and with a relatively simple circuit.

3.1. Boolean function: QDI condition

The delay-insensitive (DI) combinational circuits are subject to hazard. Hazardous circuit means that there is a potential for glitches to occur, so it may lead to malfunctioning. The hazard manifests in DI circuits through gate orphan and wire orphan, i.e., a circuit is DI if it is free of gate orphan and wire orphan.

Definition 1 - Gate orphan: Being a function block called FB; it has a gate orphan if a sequence of signal transitions across a path of one or more gates is not recognized by a transition signal on any primary output.

Definition 2 - Wire orphan: Being a function block called FB; it has a wire orphan if the signal transition on a line is not recognized by a transition signal on any primary output.

Since QDI combinatorial circuits satisfy the isochronic fork assumption then these are free of wire orphan, so the combinatorial circuit is QDI if it is free of gate orphan. Figure 13a shows a circuit where input signal transition acts on gates 1 and 2, but it is not recognized by the output signal related to gate 2, so we have a wire orphan. Figure 13b shows the transition of two input signals that activate the OR gate, but it is not recognized by the output signal

related to gate 3, so there is a gate orphan, which means that the circuit is not QDI.

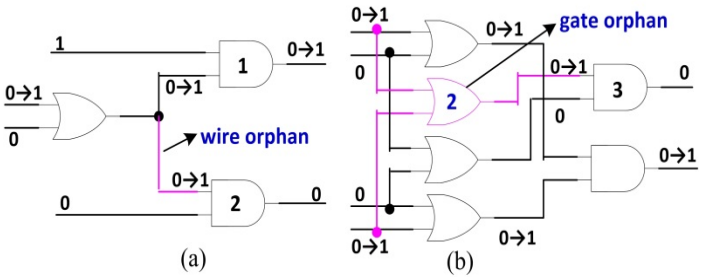

Figure 13. Hazard delay-insensitive of [14]: a) wire orphan; b) gate orphan.

3.2. QDI Boolean function: interaction with environment

A function block for a QDI circuit is required to indicate when its cycles of operations NULL and Valid Data are completed. Hence, by observing the function block outputs, the environment must be able to determine when all input and internal signals have settled. This behavior is shown by a property called indicatability [30, 31]: the signal transition *a* is indicated by *b* since the occurrence of *b* indicates that *a* has already occurred. We say that *a* circuit is indicating if it possesses the indicatability property [30, 31]. The indicatability property ensures that no circuitry outruns a signal which changes slowly. Furthermore, the presence of hazards in an indicating circuit is excluded [30, 31].

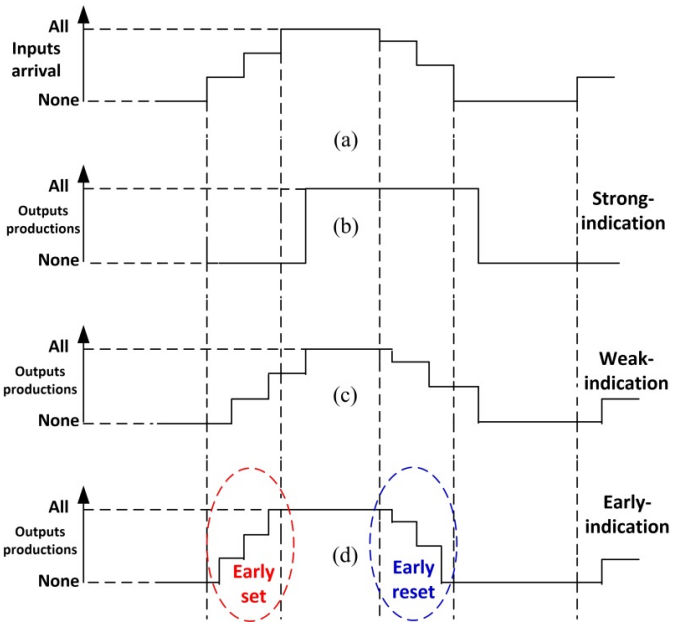

Figure 14. Input-output timing behavior of QDI circuits: a) input arrival; b) strong-indication; c) weak-indication; d) early-indication.

The indicatability property tells you how robust the circuit is in aspect of timing analysis and freedom of orphan. Figure 14 shows the three types of interaction where strong indication is the most robust and, early indication (output) is the least robust. Strong indication means that the output signal transitions will only occur when all input signals are NULL (space processing) or all input signals are valid (data processing). Weak indication means that some transition of the output signal may occur without all input signals being NULL or valid, but for the last transition of the output signal, all input signals are NULL or valid. Early indication means that for all transition of output signals be NULL or valid, the input signals are not necessarily NULL or valid.

If the function block does not indicate inputs on the outputs, it is necessary to add circuitry to ensure correct QDI operation. The inputs are indicated through circuitry with a single Boolean output, whose only purpose is to indicate transitions on the input variables. This circuit is called a status detector. The output from status detector together to the output from function block is used by the environment to ensure correct QDI operation [30, 31].

3.3. Timing analysis

The basic assumption behind QDI circuits is that gates and wires have unbounded unknown delays; the only timing assumption permitted is the isochronic fork – whenever a wire forks to two destinations or more, delays on the forks are approximately equal [3, 4]. In contrast, our approach assumes that the delay of gates and wires are bounded by given time intervals:

($Tp_{MIN\text{-}G}$, $Tp_{MAX\text{-}G}$) for a gate and ($Tp_{MIN\text{-}W}$, $Tp_{MAX\text{-}W}$) for a wire, these intervals represent the lower- and upper-bound delays for propagating an input change to the output in a gate. These delays can either be obtained from standard-cell library characterizations or they can represent the theoretical limits of parametric variation. For simplicity, we despised the delays in wires and we will analyze the three architectures presented in Figures. 5, 8 and 11.

I. NCL gates as Huffman machine

By making a timing analysis of the circuit of Figure 7, we have the inequality 5 that reports QDI constraint of the circuit. Analyzing (5), Tp is the propagation time of a gate, and it can be anywhere in range {minimum, maximum}. If the inequality is not satisfied, we will have glitches in output which occur in reason of the fundamental mode violation. As an example, assuming that A and B go from 0→1 and C=0, Z goes from 0→1 and immediately, A goes from 1→0. So Z can vary 1→0→1→0 if (5) is not satisfied. This case shows clearly that to the TH23 gate to operate correctly it must obey to the fundamental mode, so it is not QDI.

$$2xTp_{MIN\text{-}AND1} + Tp_{MIN\text{-}OR4} > Tp_{MAX\text{-}OR2} + Tp_{MAX\text{-}AND3} \quad (5)$$

II. NCL gates as standard RS

The inequality 6 shows QDI constraint of Figure 10 circuit. By analyzing (6), we can have glitches if the inequality is not satisfied. As shown in the architecture of Figure 5, glitch in the output occurs because of fundamental mode violation, so the TH23 gate is not QDI.

$$2xTp_{MIN\text{-}NAND1}+Tp_{MIN\text{-}NAND4} > Tp_{MAX\text{-}OR2} + Tp_{MAX\text{-}NAND3} \quad (6)$$

III. NCL gates as modified RS

The inequality 7 shows QDI constraint of Figure 12 circuit. By analyzing (7), we can have glitches if the inequality is not satisfied, for the processing of valid data → null data → valid data. As shown in the architecture of Figure 8, the glitch in the output

occurs because of fundamental mode violation, so the TH23 gate is not QDI.

$$2xTp_{MIN\text{-}OR3} + Tp_{MIN\text{-}AND4} > Tp_{MAX\text{-}AND1} + Tp_{MAX\text{-}OR2} \quad (7)$$

4. Synthesis of QDI NCL Gates: Proposed

The design of NCL THmn gates, in case TH23, THand0, TH24comp and TH34w3, will illustrate the approach in the proposed architecture of Figure 4. For THand0 gate, the function is Z = AB + BC + AD while for TH24comp gate, the function is Z = AC + AD + BC + BD. For TH34w3 gate, the function is Z = A + BCD.

4.1. Synthesis of NCL gates

The implementation of proposed THmn NCL gates follows the conventional extraction of F_{SET} and F_{RESET} functions, as shown in section B. F_{SET} function is the NCL gate function itself. F_{RESET} function is the detection of *n* signals going to zero, therefore being an OR gate with fan-in equaling to *n*. Figure 15 shows the logic circuit of NCL TH23 gate where FS_{ET} = AB + AC + BC and F_{RESET} = A+B+C. Figures 16, 17 and 18 show the THand0, TH24comp and TH34w3 gates in the proposed architecture, respectively.

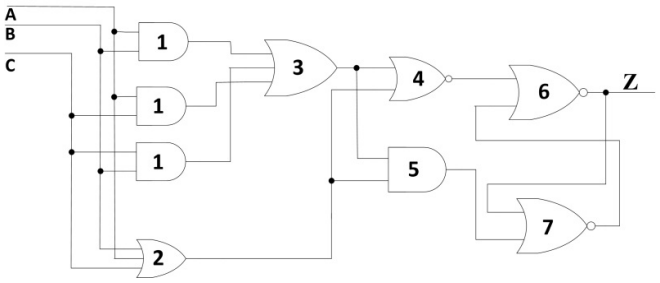

Figure 15. Proposed architecture: netlist of TH23 gate.

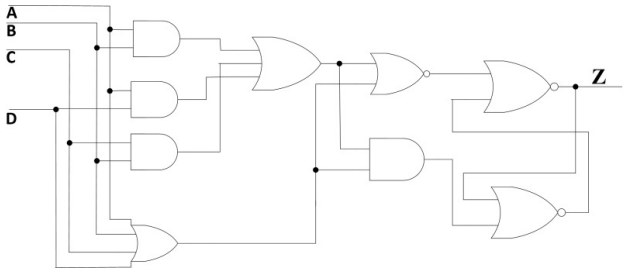

Figure 16. Proposed architecture: THand0 gate.

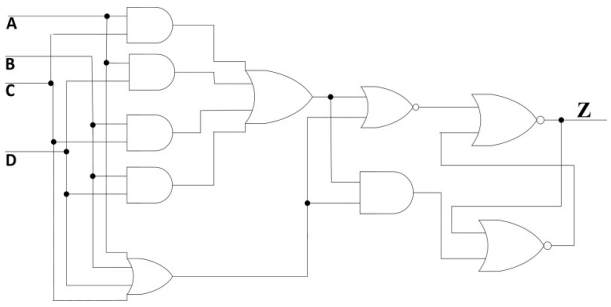

Figure 17. Proposed architecture: TH24comp gate.

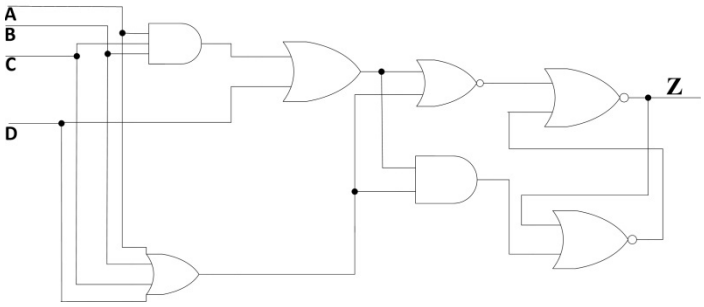

Figure 18. Proposed architecture: TH34w3 gate.

4.2. Timing analysis of proposed NCL gates

Performing the timing analysis in Figure15 circuit, we have that assuming A and B going from 0→1 and C=0, the AND1AB gate goes 0→1, OR3 gate goes 0→1 and NOR4 gate goes 1→0; concurrently the OR2 gate goes 0→1, then AND5 gate goes 0→1 and NOR7 gate 1→0 which the Z output goes 0→1. Immediately, A and B goes from 1→0, so AND1AB goes 1→0, OR3 gate goes 1→0; concurrently OR2 gate goes 1→0 and NOR4 gate goes 0→1 which Z output goes 1→0. For the AND5 gate being QDI, it may be in processing, i.e., still with the value of 1 and consequently, the gate NOR7 with a value of 0, which means that inputs cannot be activated immediately (I/O_M mode). This situation can be measured as shown by inequality 8.

By analyzing (8), we can have glitches if the inequality is not satisfied, for Figure 15 circuit. Since the condition of inequality 8 is robust, i.e., five terms with minimum delay against two maximum delay terms, we can say that it satisfies any DSM-CMOS technology, even if operating at subthreshold voltage, therefore we can accept this gate operating in I/O_M mode as being QDI.

$$2xTp_{MIN\text{-}NOR4} + Tp_{MIN\text{-}NOR6} + Tp_{MIN\text{-}NAND1} + Tp_{MIN\text{-}NOR3} > Tp_{MAX\text{-}AND5} + Tp_{MAX\text{-}NOR7} \quad (8)$$

4.3. Dual-rail NCL Gates

A minimized two-level F function to be implemented as QDI is initially decomposed in basic gates only of fan-in = 2. The basic gates that can be used are: NOT, AND2, OR2, XOR, XNOR, NAND2, NOR2 and AOI4. The seven gates of fan-in = 2 are extended to dual-rail. The dual-rail NOT gate is simply two swapped wires. Each dual-rail basic gate is implemented as NCL gate generating a library of seven dual-rail NCL gates.

The expansion uses the dual-rail code where each signal is encoded in two wires. Figure 19a shows the dual-rail code table for signal a(a1, a0). For a1a0 = 00, it is NULL which means absence of data; for a1a0 = 01 and a1a0 = 10 mean values 0 and 1, respectively. Figure 19b shows the symbol of dual-rail AND4 gate that is implemented from NCL gates knowing that the function F_{AND2} = ab and the inverse function is F'_{AND2} = a'b' + a'b + ab'.

Generating the dual-rail expansion, we have: from F_{AND2}, we obtain $F1_{AND2}$ = a1b1 and from the inverter $F'_{AND}2$, we obtain $F0_{AND2}$ = a0b0 + a0b1 + a1b0. The $F1_{AND2}$ function is mapped to the NCL TH22 gate and the $F0_{AND2}$ function is mapped to NCL THand0 gate. Figure 19c shows the generated THDR-AND2 gate.

Using the same procedure, we can build other THDR-X gates. Figures 20, 21 and 22 show the gates THDR-OR2, THDR-XOR and THDR-AOI4, respectively.

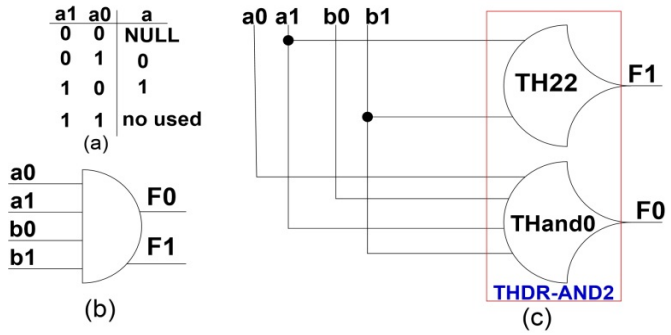

Figure 19. Dual-rail AND Gate: a) Symbol; b) NCL implementation.

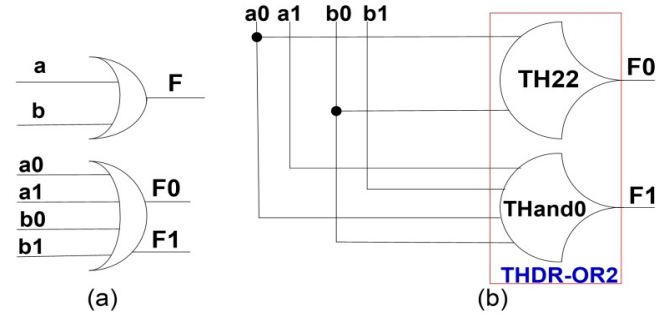

Figure 20. Dual-rail OR gate: a) Symbol; b) NCL implementation.

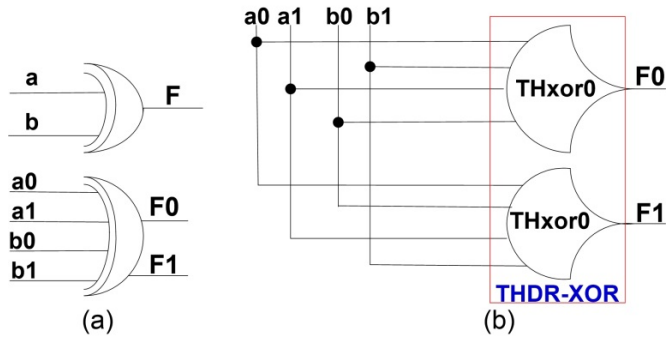

FFigure 21. Dual-rail XOR gate: a) Symbol; b) NCL implementation.

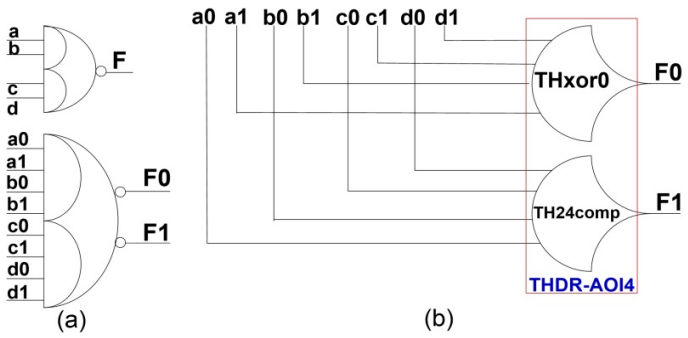

Figure 22. Dual-rail AOI gate: a) Symbol; b) NCL implementation.

Theorem 1. Let the dual-rail NCL gates (THDR-X) synthesized in the proposed approach in section C and implemented in architecture shown in Figure 4. These circuits interact with strong indication.

Proof: Assume all input and output signals are initially in NULL state, since the two functions that make up the THDR-X gate are canonical, then during valid data cycles, every implicant when activated, all input signals acting on the THDR-X must be valid. Since the two TH-X gates contain the reset functions and form the THDR-X gate, then during the NULL cycles all signals that act on the THDR-X gate must go to NULL, therefore the circuit operates with strong indication.

4.4. Proposed Approach for NCL Circuits synthesis

The method starts from a minimized two-level function F_IT (independent of technology) and it follows three steps:

1. Performance of the conventional technology mapping of the $F_{\_IT}$ function using only a basic gates library: The mapping is performed, for example, by the SIS [22] tool in the target library [NOT, AND2, OR2, XOR, XNOR, NAND2, NOR2 and AOI4] and to obtain the $F_{\_DT}$ function (technology dependent).
2. Performance of the dual-rail extension of each gate of the $F_{\_DT}$ function obtaining the $F_{\text{-DT-dual-rail}}$.
3. Performance of the trivial mapping of the $F_{\text{-DT-dual-rail}}$ using a target library of seven dual-rail NCL gates.

To illustrate the approach, we have the minimized function F(A,B,C,D) = A⊕B + CD mapped to a conventional library. The approach performs a mapping that generates for each term of the F function a dual-rail NCL gate and it ends with the NCL dual-rail OR gate. Figure 23 shows mapping to the NCL function and Figure 24 shows mapping of the NCL function to dual-rail NCL. Figure 25 shows implementations in proposed architecture of the NCL gates THxor0, THand0 and TH22, used in the function mapping.

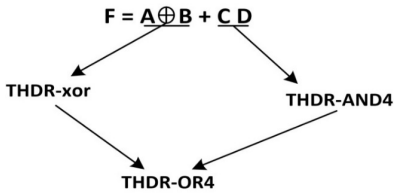

Figure 23. Proposed approach: mapping of NCL gates of F function.

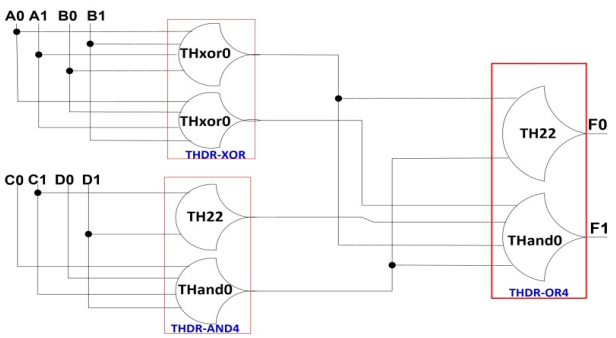

Figure 24. Dual-rail F function: NCL gates.

Theorem 2. Let a dual-rail minimized two-level F function synthesized in the proposed approach of section D with NCL gates THDRmn of section C. This circuit is QDI with constraint of inequality 8 and it interacts with strong indication.

Proof: Assume all the input and output signals of the dual-rail F function are initially in NULL state. The dual-rail F function is free of wire orphan due to isochronic fork assumption. During valid data cycles, the dual-rail F function is free of gate orphan, because of each term of F being associated with a THDR-X gate and there is freedom of gate orphan, with the constraint of inequality 8. As each THDR-X gate operates with strong indication, then the dual-rail function F operates with strong indication, because all terms of the dual-rail F function are activated, either true or false, so all input signals must be valid . For the NULL cycles, the analysis is analogous.

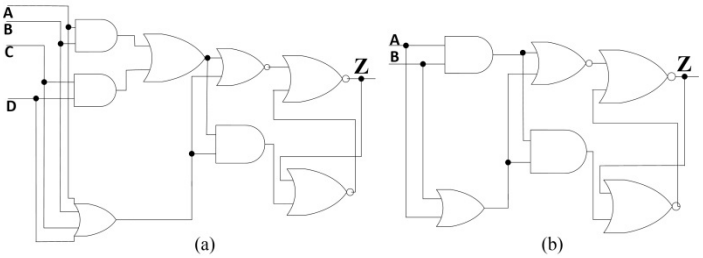

Figure 25. Proposed architectures: a) THxor0 gate; b) TH22 gate.

5. Case Study

In this section we illustrate an approach for the synthesis of NCL circuits. We use an example found in [33] that is a one-bit ALU (Arithmetic Logic Unit) which can be generalized to N bits by using the concept of carry propagation. The ALU is based on the 8-bit ALU of 74181 TTL integrated circuit. Figure 26 shows the table operations with 12 operations being partitioned into three blocks (selection signals M and C0). Figure 27 shows the first step of the approach that is conventional technology mapping generating the multi-level one-bit ALU. The second step transforms the basic gates (single-rail) into dual-rail gates, as shown in Figure 28. The obtained ALU circuit is implemented with XOR, AND2 and OR2 dual-rail gates. The third step performs the trivial mapping of each dual-rail gate into dual-rail NCL gates (THDR-X), as shown in Figure 24, thereby generating the final NCL circuit, as shown in Figure 29.

M=1		M=0	Selection
C_0=0	C_0=1	C_0=X	S_1S_0
A	A plus 1	A	00
$\overline{A}$	$\overline{A}$ plus 1	$\overline{A}$	01
A plus B	A plus B plus 1	A⊕B	10
$\overline{A}$ plus B	$\overline{A}$ plus B plus 1	A⊙B	11

Figure 26. Table of Operations of the ALU presented in [33]

6. Simulation and Results

The design of six benchmarks in two different architectures, in case NCL_D [25], and proposal were synthesized. We also design three NCL gates in four different architectures. These designs were made in structural VHDL, compiled and simulated post-layout in ALTERA tool, Quartus II software, version 9.0, Cyclone III family, in EP3C16F484C6 [34] device.

6.1. Simulations

The simulation post-layout of TH23 NCL gate is shown in Figure 30. Different operations were tested and the waveforms of Figure 30 show its correctness, following the ones shown in operation table of Figure 6a.

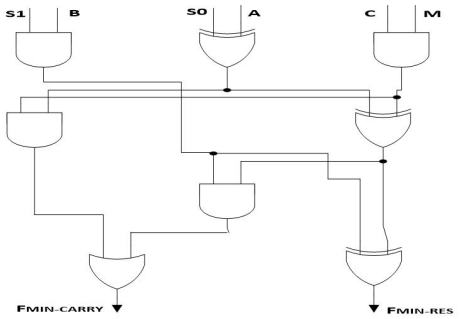

Figure 27. Logic Circuit: Multi-level 1-bit ALU [33].

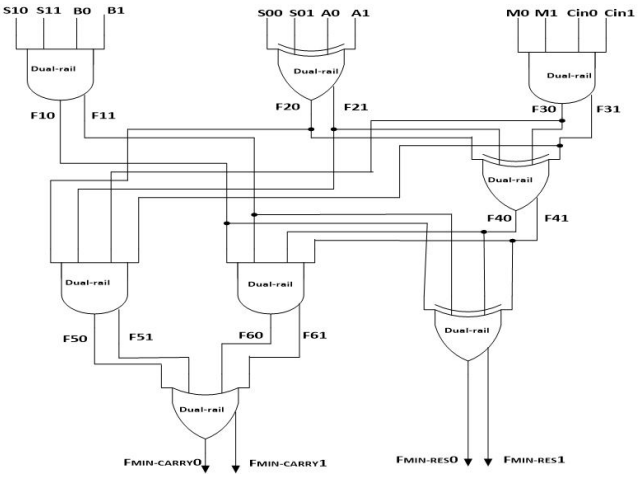

Figure 28. Dual-rail ALU: 1-bit Basic cell.

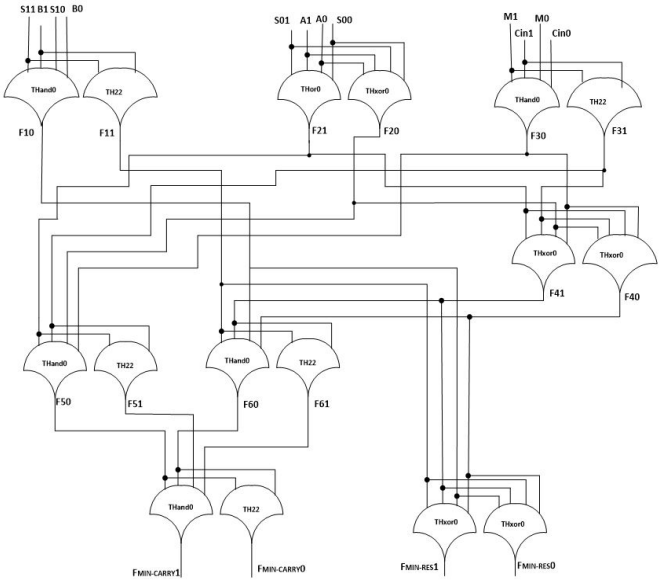

Figure 29. NCL ALU: 1-bit Basic cell.

Figure 31 shows the simulation of NCL ALU. The waveforms show correct results for different tested operations, following the ones shown in operation table of Figure 26. Figure 31 also shows that there are no glitches in the output signal, when compared with the conventional ALU that shows some glitches. The sequence of operations follows the 4-phase handshake protocol, therefore in the timing diagram when all the signals are zero means data absence.

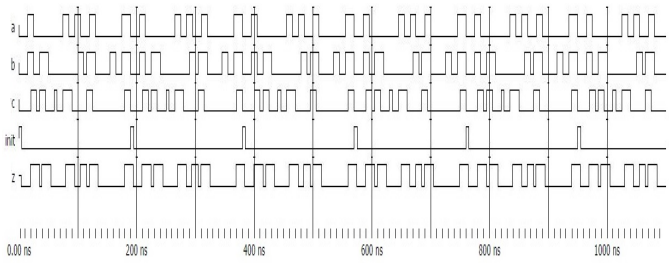

Figure 30. Post-layout simulation: TH23 gate.

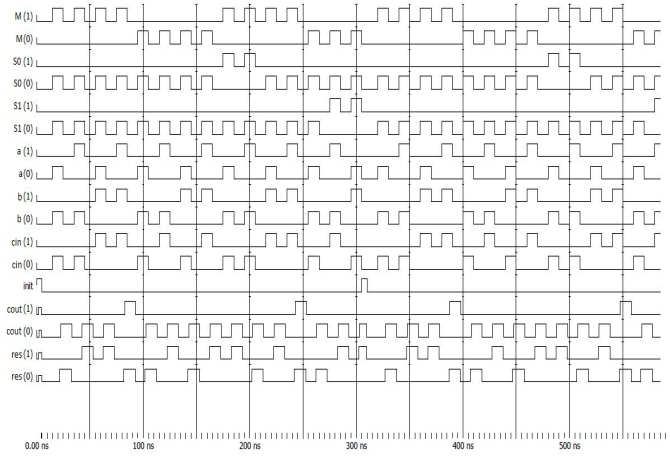

Figure 31. Post-layout simulation: 1 bit ALU.

6.2. Results

Table I shows the results obtained for: area, where only LUTs were used; dynamic power; and latency. Table I is related to the implementation in four architectures of the NCL gate TH23. Analyzing the results of Table I, we have: comparing area in number of LUTs, the proposed architecture, although requiring two LUTs, shows a greater robustness to operate in I/O mode. The proposed architecture obtained an average reduction of 18.6% in latency time when compared with the other three architectures; also obtained an average reduction of 74.0% in dynamic power consumption.

Table II shows the results of six QDI examples design which are: AND of fan-in = 4; detector of prime numbers of 4 bits; detector of odd numbers of 4 bits; full adder of 1 bit; multiplier of 2 bits; ALU of 1 bit of [21]. These examples were synthesized in the NCL_D [25] approach using DIMS components [12] and in the proposed architecture of Figure 4 being both architectures of the type strong indication. The results of six examples in Table II are: number of LUTs; latency time; and the dynamic and static power. Analyzing Table II and comparing the proposal with and NCL_D, we have an average reduction of 13.6% in area (number of LUTs) and 13.7% in static power. There was an average penalty of 4.6% and 32.5% in latency time and dynamic power, respectively.

Table 1. Results of th23 ncl gate in differents architetures

		Time of Latency	Dynamic Power	Number of LUTS
Gate TH23	Figure 7	5.29ns	0.34mw	1
	Figure 10	7.67ns	0.29mw	1
	Figure 12	5.12ns	0.18mw	1
	Figure 15	**4.91ns**	**0.07mw**	2

Table 2. Results of the six examples

	NCL_D architecture				Proposed architecture			
	Nro. LUTs	Latency Time (ns)	Dynamic Power (mw)	Static Power (mw)	Nro. LUTs	Latency Time (ns)	Dynamic Power (mw)	Static Power (mw)
AND4	15	**5.54**	**0.26**	0.051	**12**	5.80	0.36	**0.040**
ODD_4	20	**6.32**	**0.32**	0.067	**16**	7.24	0.45	**0.054**
PRIME_4	65	**7.71**	**1.08**	0.218	**50**	8.38	1.48	**0.168**
ADDER _1 full	27	**6.55**	**0.38**	0.091	**23**	6.63	0.61	**0.077**
ALU_1	43	**8.40**	**1.02**	0.144	**36**	8.83	1.16	**0.121**
MULT_2	95	7.58	**1.49**	0.319	**92**	**7.17**	1.97	**0.309**

7. Conclusions

When comparing the implementation of TH23 NCL gate stated in Table I, our approach clearly shows advantages in terms of latency and power consumption, despite the penalty in area. Therefore, when designs are bounded by achieving the best performance or lower power consumption our approach is advantageous, but for designs bounded by area constraints it is not the best option. Regarding Table II, when it comes to a complete QDI circuit our approach is superior in terms of area.

As a way to increase robustness to FM violation in the NCL gates architectures based in basic gates, it is possible to insert delay elementes in paths that are sensitive to FM mode. This strategy though, has three problems: a) delay elements are not easy to add in FPGAs; b) delay elements degrade the reliability and testability of circuits; c) insertion of delay elements tends to decrease performance and increase power consumption. Thus our approach is more robust because delay elements are not needed.

Due to many different applications requiring robust digital systems in the processing or in data security, an interesting solution shows to be robust components using in their synthesis. In this paper, we present an approach and architecture to synthesize NCL gates on platforms FPGA and standard-cell VLSI. The proposed architecture based on basic gates implements NCL gates that operate in I/O_M mode and they are QDI with restriction of inequality 8 while other architectures based in basic gates generate NCL gates that operate in FM mode, so they are not QDI. Comparing with other approaches [27-31] which need of an additional signal to satisfy the property of indicatability, our approach does not insert any signal. The proposed NCL gates presents other interesting properties such as high robustness to

variations in temperature and to supply voltage, which occurs very often in hostile environments such as in space and in certain areas of military combat. For further works, it is desirable to test the proposed NCL gates considering radiation effects of SEU (Single-Event Upset) in FPGA platform [35, 36].

Conflict of Interest

The authors declare no conflict of interest.

References

[1] D. L. Oliveira, O. Verducci, L. Faria, T. Curtinhas, "A novel null convention logic (NCL) gates architecture based on basic gates" in IEEE XXIV International Conference on Electronics, Electrical Engineering and Computing (INTERCON), Cusco, Peru, 2017. https://doi.org/10.1109/INTERCON.2017.8079680.

[2] B. H. Calhoun, et al., "Digital Circuit Design Challenges and Opportunities in the Era of Nanoscale CMOS," Proc. of the IEEE, Vol. 96, No. 2, pp. 343-365, February 2008. https://doi.org/10.1109/JPROC.2007.911072.

[3] C. J., Myers, "Asynchronous Circuit Design", Wiley & Sons, Inc., 2004, 2a edition.

[4] P. Beerel, R. Ozdag and M. Ferretti, "A Designer's Guide to Asynchronous VLSI". Cambridge University Press, p. 337, 2010.

[5] J. Martin, "Compiling Communication to Delay-Insensitive VLSI Circuits", Distributed Computing, 1(4), pp.226-234, December 1986. https://doi.org/10.1007/BF01660034.

[6] J. Martin, "The Limitations to Delay Insensitive in Asynchronous Circuits," 6th MIT Conference on Advanced Research in VLSI Processes, pp.263-277, 1990. https://doi.org/10.1007/978-1-4612-4476-9_35.

[7] J. Cortadella, A. Kondratyev, L. Lavagno, and C. Sotiriou, "Coping with the variability of combinational logic delays," ICCD, pages 505–508, 2004. https://doi.org/10.1109/ICCD.2004.1347969.

[8] W. Hardt, et. al., "Architecture Level Optimization for Asynchronous IPs", Proc. 13th Annual IEEE Int. Conf. ASIC/SOC, pp.158-162, 2000. https://doi.org/10.1109/ASIC.2000.880694.

[9] L. Spadavecchia, "A Network-based Asynchronous Architecture for Cryptographic Devices," PhD thesis, University of Edinburgh, 2005.

[10] C. L. Seitz, "System Timing," in Introduction to VLSI Systems, Addison-Wesley, pp. 218-262, 1980.

[11] I. David, R. Ginosar, and M. Yoeli, "An Efficient Implementation of Boolean Functions as Self-Timed Circuits," IEEE Transactions on Computers, Vol. 41, No. 1, pp. 2-10,1992. https://doi.org/10.1109/12.123377.

[12] J. Sparsø, J. Staunstrup. "Delay Insensitive Multi Ring Structures", Integration, the VLSI Journal. v15(13), 1993. https://doi.org/10.1016/0167-9260(93)90035-B.

[13] K. M. Fant and S. A. Brandt. "NULL convention logic: a complete and consistent logic for asynchronous digital circuit synthesis". In International Conference on Application Specific Systems, Architectures and Processors, pp. 261-273, 1996. https://doi.org/10.1109/ASAP.1996.542821.

[14] F. A. Parsan and S. C. Smith "CMOS Implementation of Static Threshold Gates with Hysteresis: A New Approach," In Proceedings of the IFIP/IEEE International Conference on VLSI-SoC, Santa Cruz, CA, USA, 7–10, pp. 41-45, October 2012. https://doi.org/10.1109/VLSI-SoC.2012.7332074.

[15] F. A. Parsan and S. C. Smith, "CMOS Implementation Comparison of NCL Gates," In Proceedings of the IEEE International Midwest Symposium on Circuits and Systems, Boise, ID, USA, 5–8 August pp. 394-397, 2012. https://doi.org/10.1109/MWSCAS.2012.6292040.

[16] S. C. Smith, et al., "Optimization of NULL convention self-timed circuits," INTEGRATION, the VLSI journal 37, pp.135–165, 2004. https://doi.org/10.1016/j.vlsi.2003.12.004.

[17] V. Satagopan, et al., "DFT Techniques and Automation for Asynchronous NULL Conventional Logic Circuits," IEEE Trans. on Very Large-Scale Integration (VLSI), vol. 15, no. 10, pp.115-1159, October 2007. https://doi.org/10.1109/TVLSI.2007.903945.

[18] W. K. Al-Assadi and S. Kakarla, "Testing of Asynchronous NULL Conventional Logic (NCL) Circuits in Synchronous-Based Designs," 22nd IEEE International Symposium on Defect and Fault Tolerance in VLSI Systems, pp.215-222, 2007. https://doi.org/10.1109/DFT.2007.40.

[19] W. K. Al-Assadi and S. Kakarla, "Design for Test of Asynchronous NULL Convention Logic (NCL) Circuits," IEEE International Test Conference, pp.1-8, 2008. https://doi.org/10.1109/TEST.2008.4700611

[20] L. Duc Tran, et al., "Null Convention Logic (NCL) based Asynchronous Design – Fundamentals and Recent Advances," International Conference on Recent Advances in Signal Processing, Telecommunications & Computing (SigTelCom), pp.158-163, 2017. https://doi.org/10.1109/SIGTELCOM.2017.7849815.

[21] S. C. Smith, "Design of an FPGA Logic Element for Implementing Asynchronous NULL Convention Logic Circuits," IEEE Transactions on Very Large-Scale Integration (VLSI) Systems, vol. 15, no. 6, pp. 672-683, June 2007. https://doi.org/10.1109/TVLSI.2007.898726.

[22] M. M. Kim, et al., "Design Techniques for NCL-based Asynchronous Circuits on Commercial FPGA," 17th Euromicro Conference on Digital System Design, pp.451-458, 2014. https://doi.org/10.1109/DSD.2014.85.

[23] T. Chelcea, G. Venkataramani, S. C. Goldstein, "Area Optimizations for Dual-Rail Circuits Using Relative-Timing Analysis," 13th IEEE International Symposium on Asynchronous Circuits and Systems (ASYNC'07), pp.1-13, 2007. https://doi.org/10.1109/ASYNC.2007.10.

[24] J. Cheoljoo and S. Nowick. "Technology mapping and cell merger or asynchronous threshold networks," IEEE Trans. on Computer-Aided Design of Integrated Circ. and Systems, Vol. 27(4), pp. 659-672, 2008. https://doi.org/10.1109/TCAD.2007.911339.

[25] M. Ligthart, K. Fant, R. Smith, A. Taubin, A. Kondratyev, "Asynchronous design using commercial HDL synthesis tools", Async'00, pp. 114 – 125, 2000. https://doi.org/10.1109/ASYNC.2000.836983

[26] A. Kondratyev, K. Lwin, "Design of Asynchronous Circuits Using Synchronous CAD Tools", IEEE Design and Test of Computers, vol. 19, no. 4, pp. 107-117, 2002. https://doi.org/10.1109/MDT.2002.1018139.

[27] J. Cortadella, A. Kondratyev, L. Lavagno, and C. Sotiriou, "Coping with the variability of combinational logic delays," ICCD, pages 505–508, 2004. https://doi.org/10.1109/ICCD.2004.1347969.

[28] Zhou, Y., Sokolov, D., Yakovlev, A.: 'Cost-aware synthesis of asynchronous circuits based on partial acknowledgement'. Proc. Int. Conf. Computer-Aided Design, San Jose, USA, November 2006, pp. 158–163. https://doi.org/10.1109/ICCAD.2006.320080.

[29] Fu-Chiung Cheng and Chi Chen, "Can QDI Combinational Circuits be Implemented without C-elements?," IEEE 19th International Symposium on Asynchronous Circuits and Systems, PP.134-141, 2013. https://doi.org/10.1109/ASYNC.2013.13.

[30] P. Balasubramanian, and D.A. Edwards, "Efficient Realization of Strongly Indicating Function Blocks," IEEE Computer Society Annual Symposium on VLSI, ISVLSI '08, pp.429-432, 2008. https://doi.org/10.1109/ISVLSI.2008.103.

[31] P. Balasubramanian, "A Robust Asynchronous Early Output Full Adder," WSEAS Transactions on Circuits and Systems, Issue 7, Volume 10, pp. 221-230, July 2011.

[32] T. Verhoeff, 'Delay-insensitive codes – an overview', Distrib. Comput, 3, (1), pp. 1–8, 1988. https://doi.org/10.1007/BF01788562.

[33] H. Taub, "Circuitos Digitais e Microprocessadores", Portuguese edition, McGraw-Hill, 1982.

[34] Altera Corporation, 2018, www.altera.com.

[35] W. Jang and A. Martin, "SEU-tolerant QDI circuits," in IEEE International Symposium on Asynchronous Circuits and Systems, pp. 156–165, 2005. https://doi.org/10.1109/ASYNC.2005.30.

[36] D. J. Barnhart, et. al. "Radiation Hardening by Design of Asynchronous Logic for Hostile Environments", IEEE Journal of Solid-State Circuits, vol. 44, No. 5, pp.1617-1628, May 2009. https://doi.org/10.1109/JSSC.2009.2017005.

ASTES

Advances in Science, Technology and Engineering Systems Journal
Vol. 3, No. 4, 318-326 (2018)
www.astesj.com
Special Issue on Multidisciplinary Sciences and Engineering

ASTES Journal
ISSN: 2415-6698

A Comparative Analysis of two Controllers for Trajectory Tracking Control: Application to a Biological Process

Abyad Mohamed*, Karama Asma, Khallouq Abdelmounaim

LAEPT-URAC 28, Faculty of Science Semlalia, Cadi Ayyad University, Marrakech, Morocco

ARTICLEINFO

Article history:
Received: 01 June, 2018
Accepted: 04 August, 2018
Online: 20 August, 2018

Keywords:
Bioprocess
Constraints
Fuzzy observer
LMIs
Takagi-Sugeno Model
Trajectory tracking

ABSTRACT

The aim of the present work is to guarantee the trajectory tracking of a nonlinear biological process and compare two control approaches. The main objective of this work is to elaborate a fuzzy model and build a fuzzy controllers for a biological process by using the fuzzy Takagi-Sugeno. Two controllers are synthesized, the parallel distributed compensation control and optimal fuzzy linear quadratic integral control. In both cases, the physical constraints on the manipulated inputs are respected. In addition, the case with and without the observer is presented, where a fuzzy observer based control is used with unmeasurable premise variables. Finally, the performances and the effectiveness of both the modeling and the control are demonstrated via simulations.

1 Introduction

Nowadays, the biological processes become one of the important industrial processes thanks to their advantages, such as the treatment of organic substrates, protein production and the production of ethanol gas etc. However, their modeling and control form a real challenge problem for both control engineers and theorists, where this kind of systems are characterized by strong variations of system parameters and unknown kinetics owing to the time-varying characteristics and multiple interactions generated by the living microorganisms [1, 2]. Therefore, we obtain a highly nonlinear system. The motivation of this work is to linearize the model and benefit from linear theory control and to try to develop a nonlinear control, which is very difficult in this case. Also to use the Takagi-Sugeno (T-S) model, furthermore, the proposed controllers can be applied to the real process. It only needs to identify a T-S model from experimental data. T-S approach has been recognized as an effective tool for handling the previous difficulty.

There are different techniques for controlling the bioprocess using Takagi-Sugeno models, such as optimal fuzzy linear quadratic regulators for discrete-time [3], a fuzzy integral controller to force the switching of a bioprocess between two different metabolic states is treated in [4], an internal model control design strategy is developed for a particular Continuous Stirred-Tank Reactor (CSTR)[5]. A PID and fuzzy controller are proposed in [6] to stabilize the CSTR around the equilibrium point, where the authors consider only one input, which is not the case in practice. Also, the case of uncertain Takagi-Sugeno system is treated in [7], where an observer with unmeasurable premise variables and unknown input is considered for a wastewater treatment plant. In addition, the predictive control based on fuzzy observer is studied for a sludge depollution bioprocess in [8, 9], in this framework one can cite [10, 11, 12]. Furthermore, the modeling and the control of bioprocess based on neural network approach is treated in [13, 14]. In the same spirit, a nonlinear model autoregressive with exogenous input model predictive control is developed in [15] to control the fermentation process. Also, an integral backstepping control law is developed in [16] for controlling the dissolved oxygen level for bacteria fermentation.

The problem treated in this paper is how to model and control the biomass growth process, ensuring the trajectory tracking while taking into account the following constraints:
- The mathematical model is nonlinear and not affine in control.
- The variables control present the physical constraints,

*Corresponding Author: Abyad Mohamed, Faculty of Science Semlalia Marrakech , Morocco, abymedlmp@gmail.com

https://dx.doi.org/10.25046/aj030432

which make the computation of the control gains difficult.
- The full system states are not measurable.

The present paper has two goals, the first is to build a fuzzy model of biological process based on Takagi-Sugeno tool, especially the nonlinearity sector methods. The second is to ensure the tracking trajectory of the desired outputs using two approaches: the Parallel Distributed Compensation (PDC) [17] and the Linear Quadratic Integral (LQI) control. Where the strong physical constraints on the inputs [18] are taking into account. In addition, the proposed controllers are compared. The stability conditions are formed in the Linear Matrix Inequalities (LMIs) terms.

This paper is organized as follows: Section 2 presents the description of the Takagi-Sugeno modeling. Section 3 describes the parallel distributed compensation control. Then, one can address the fuzzy output tracking control problem in section 4 and we show that it can be solved by using two methods: the PDC technique and the optimal linear quadratic control. Section 5 describes the controller design based on fuzzy observer with unmeasurable premise variables. Section 6 introduces the proposed biological process. Finally, the simulation and the discussion of the obtained results are given to compare the proposed controllers.

2 Takagi-Sugeno Fuzzy Model

In order to extend the existing approaches of control and observation for linear to nonlinear system, Takagi and Sugeno have proposed a fuzzy dynamic model to represent this kind of system. The T-S fuzzy model is a set of linear models connecting via membership functions. To build the T-S fuzzy model, three methods exist in the literature [17]: The black box identification, the linearization method and the nonlinearity sector methods. The third method gives an exact T-S representation of nonlinear system without information loss.

Consider the following nonlinear system:

$$\begin{aligned} \dot{x}(t) &= f(x(t)) + g(x(t))u(t) \\ y(t) &= Cx(t) \end{aligned} \tag{1}$$

where $x \in \mathbb{R}^n$ is the state, $u \in \mathbb{R}^m$ is the input vector, $y \in \mathbb{R}^q$ represents the output measurement vectors and $C \in \mathbb{R}^{q*n}$ is the output matrix. In addition, $f(.)$ and $g(.)$ represent the nonlinear functions.

The T-S fuzzy model uses a set of fuzzy if-then rules, which represent local linear input-output relations of a nonlinear system. The i^{th} rule of the T-S model given as follows:

Rule i:

if $z_1(t)$ is $F_1^i(z_1(t))$ **and** $z_2(t)$ is $F_2^i(z_2(t))$ ... **and** $z_p(t)$ is $F_p^i(z_p(t))$

$$\textbf{Then} \begin{cases} \dot{x}(t) = A_i x(t) + B_i u(t) \\ y(t) = C_i x(t) \end{cases} \tag{2}$$

Where F_p^i are the membership functions of fuzzy sets, $i \in \{1, 2, ...r\}$, r is the number of rules, $A_i \in \mathbb{R}^{n*n}$, $B_i \in \mathbb{R}^{n*m}$, $C_i \in \mathbb{R}^{q*n}$ and $z_1(t), ..., z_p(t)$ are the premise variables which can be dependent of the input, the output or the state. The global T-S fuzzy model is given in the following form:

$$\begin{aligned} \dot{x}(t) &= \sum_{i=1}^{r} h_i(z(t))(A_i x(t) + B_i u(t)) \\ y(t) &= Cx(t) \end{aligned} \tag{3}$$

where

$$h_i(z(t)) = \frac{\prod_{j=1}^{p} F_j^i(z_j(t))}{\sum_{i=1}^{r} \prod_{j=1}^{p} F_j^i(z_j(t))} \tag{4}$$

The activation functions $h_i(z(t))$ indicates the activation degree of the i^{th} associated local model, this functions verifies all time the convex sum propriety:

$$\begin{cases} 0 \le h_i(z(t)) \le 1 \\ \sum_{i=1}^{r} h_i(z(t)) = 1, \forall i \in \{1, 2, ..., r\}. \end{cases} \tag{5}$$

3 PDC control approach

3.1 Fuzzy regulator design via PDC

To stabilize the system presented by their T-S fuzzy model, the PDC controller is usually used to design a fuzzy controller. The main idea is to design a local controller for each sub-model based on local control rule, which shares with the fuzzy model the same fuzzy sets. The overall fuzzy controller is represented by:

$$u(t) = -\sum_{i=1}^{r} h_i(z) K_i x(t) \tag{6}$$

Where the K_i represent the local feedback gains. by using (6) in (3) the system in closed-loop becomes:

$$\begin{aligned} \dot{x}(t) &= \sum_{i=1}^{r} \sum_{j=1}^{r} h_i(z) h_j(z)(A_i - B_i K_j) x(t) \\ &= \sum_{i=1}^{r} h_i^2(z) G_{ii} x(t) + 2 \sum_{i<j}^{r} h_i(z) h_j(z) (\tfrac{G_{ij} + G_{ji}}{2}) x(t) \end{aligned} \tag{7}$$

with $G_{ij} = A_i - B_i K_j$, the stability conditions of (7) are given by the following theorem [17].

Theorem 1 *The continuous fuzzy system* (7) *is asymptotically stable, if there exist a common positive matrix* $P \in R^{n \times n}$ *and a common positive semi definite matrix* $Q \in R^{n \times n}$ *and for a number of active rules* s, *where* $1 < s \le r$ *such that:*

$$G_{ii}^T P + P G_{ii} + (s-1)Q < 0 \tag{8}$$

$$(\frac{G_{ij} + G_{ji}}{2})^T P + P(\frac{G_{ij} + G_{ji}}{2}) - Q \le 0, i < j \tag{9}$$

where $s > 1$.

In order to transform the preview conditions into LMIs form, one can consider the following variables: $X = P^{-1}$, $K_i = M_i X^{-1}$, $Q = PYP$, where $X > 0$, $Y \geq 0$ and $M_i (i = 1,...,r)$, then the stabilization conditions become:

$$\begin{aligned} &A_i X - B_i M_i + X A_i^T - M_i^T B_i^T + (s-1)Y < 0 \\ &A_i X - B_i M_j + X A_i^T - M_j^T B_i^T + A_j X - B_j M_i \\ &+ X A_j^T - M_i^T B_j^T - 2Y \leq 0, \qquad i < j \end{aligned} \tag{10}$$

4 Trajectory tracking control

The trajectory tracking control of nonlinear systems is the subject this section. In the tracking loop, we consider the integral of the tracking error $e_I = \int (y_r - y)dt = \int (y_r - Cx)dt$ [19], with y_r is the desired output. If we consider the following augmented state:

$$X_a = \begin{bmatrix} x \\ e_I \end{bmatrix}$$

Then, the following augmented system is obtained:

$$\begin{cases} \dot{X}_a(t) = \sum_{i=1}^{r} h_i(z(t))(\bar{A}_i X_a(t) + \bar{B}_i u(t) + \bar{D} Y_r) \\ y(t) = \bar{C} X_a(t) \end{cases} \tag{11}$$

where: $\bar{A}_i = \begin{bmatrix} A_i & 0 \\ -C & 0 \end{bmatrix}$, $\bar{B}_i = \begin{bmatrix} B_i \\ 0 \end{bmatrix}$, $\bar{C} = \begin{bmatrix} C & 0 \end{bmatrix}$, $\bar{D} = \begin{bmatrix} 0 \\ \mathbb{I} \end{bmatrix}$, $Y_r = \begin{bmatrix} y_{r1} \\ y_{r2} \end{bmatrix}$
with Y_r, denote the desired reference trajectory.

4.1 PDC control

To achieve the output tracking, the state feedback PDC control based on the previous LMIs can be used. The fuzzy controller $u(t)$ has the same form of (6), where x is replaced by the augmented state X_a:

$$u(t) = -\sum_{i=1}^{r} h_i(z) K_i X_a(t) = -\sum_{i=1}^{r} h_i(z)(K_{ix} x + K_{iI} e_I) \tag{12}$$

The feedback gains of the controller $K_i = \begin{bmatrix} K_{ix} & K_{iI} \end{bmatrix}$ are obtained by solving the LMIs (10).

4.2 LQI control

To design the LQI control, the following quadratic cost criterion must be minimized by the control law $u(t)$:

$$J = \int_0^{\infty} (X_a^T(t) Q X_a(t) + u^T(t) R u(t)) dt \tag{13}$$

for this reason, the following candidate quadratic Lyapunov function is considered:

$$V(X_a) = X_a^T P X_a \tag{14}$$

The augmented system (7) is stable if :

$$X_a^T Q X_a + u^T R u + \dot{V}(X_a) < 0 \tag{15}$$

$$(\bar{A}_i + \bar{B}_i K_i)^T P_i + P_i(\bar{A}_i + \bar{B}_i K_i) + Q + K_i^T R K_i < 0 \tag{16}$$

$$(\bar{A}_i X_i + \bar{B}_i Y_i)^T + (\bar{A}_i X_i + \bar{B}_i Y_i) + X_i Q X_i + Y_i^T R Y_i < 0 \tag{17}$$

$$(\bar{A}_i X_i + \bar{B}_i Y_i)^T + (\bar{A}_i X_i + \bar{B}_i Y_i) + Y_i^T R Y_i - X_i(-Q) X_i < 0 \tag{18}$$

by using the Schur complement procedure, the following stability conditions are obtained:

$$\begin{bmatrix} (\bar{A}_i X_i + \bar{B}_i Y_i)^T + (\bar{A}_i X_i + \bar{B}_i Y_i) & X_i & Y_i^T \\ * & -\tilde{Q} & 0 \\ * & * & -\tilde{R} \end{bmatrix} < 0 \tag{19}$$

where: $Q^{-1} = \tilde{Q}$, $R^{-1} = \tilde{R}$, $X_i = P_i^{-1}$, $K_i = Y_i X_i^{-1}$, $i = 1,...,r$
This LMIs will be calculated for each sub-model, here is about the conventional linear quadratic integral control using the fuzzy model. The control law is not based on fuzzy rules.

The control law will be respect the physical constraints on the control input, where this problem is studied in many practical cases [20, 21, 22, 23]. To ensure the stabilization under constraints on the inputs, the conditions given in the following theorem [17] must be verified.

Theorem 2 *For a known initial condition $X_a(0)$, the constraint $\|u(t)\|_2 \leq \eta$ is enforced at all times $t \geq 0$ if the LMIs:*

$$\begin{bmatrix} 1 & X_a(0)^T \\ X_a(0) & X \end{bmatrix} \geq 0 \tag{20}$$

$$\begin{bmatrix} X & M_i^T \\ M_i & \eta^2 I \end{bmatrix} \geq 0 \tag{21}$$

hold

4.3 Observer design

In bioprocess control problems, the state variables are not usually available. By introducing the observer, one can reconstruct partially or all the state variables. This section presents the fuzzy observer design with unmeasurable premise variables $z(t)$ ($h_i(z) \neq h_i(\hat{z})$).
Based on the structure of the fuzzy model (3), the fuzzy observer is given as follows:

$$\begin{cases} \dot{\hat{x}}(t) = \sum_{i=1}^{r} h_i(\hat{z})(A_i \hat{x}(t) + B_i u(t) + L_i(y(t) - \hat{y}(t)) \\ \hat{y}(t) = \sum_{i=1}^{r} h_i(\hat{z}) C_i \hat{x}(t) \end{cases} \tag{22}$$

where $\hat{x}$ denotes the estimated state and L_i the gains of the observer.
In order to compute this gains the following theorem [24] gives the necessary conditions for ensuring the convergence of the state estimation error to zero.

Theorem 3 *If there exist symmetric and definite positive matrices $P \in \mathbb{R}^{n \times n}$, $Q \in \mathbb{R}^{n \times n}$, matrices $Y_i \in \mathbb{R}^{n \times q}$ and a scalar $\alpha > 0$ such that:*

$$A_i^T P + P A_i - C^T Y_i^T - Y_i^T C \leq -Q \tag{23}$$

$$\begin{bmatrix} Q - \alpha^2 \mathbb{I} & P \\ P & \mathbb{I} \end{bmatrix} > 0 \tag{24}$$

then, the estimation error between the T-S fuzzy model (3) *and the fuzzy observer* (22) *is converges asymptotically to zero.*
where: $L_i = P^{-1}Y_i$.

Proof 1 *See Appendix.*

5 Process description

The proposed biological process in this paper is a biomass growth process, which consists to grow the population of microorganisms (biomass) by the consumption of a substrate (glucose), according to the following reaction scheme:

$$k_1 S \xmapsto{\mu(.)} X \tag{25}$$

The dynamic model of this process is established from the mass-balance [25], which describes the evolution of substrate and biomass concentrations in a continuous bioreactor. This model can be represented by a high nonlinear system as follows:

$$\begin{cases} \frac{dX}{dt} = \mu(.)X - DX \\ \frac{dS}{dt} = -k_1\mu(.)X + D(S_{in} - S) \end{cases} \tag{26}$$

The state variables are the biomass X and substrate S concentrations, k_1 denotes the pseudo stoichiometric coefficient and $\mu(.)$ represent the specific growth rate, the "Monod law" characterizes $\mu(.)$ is:

$$\mu(S) = \mu_{max}\frac{S}{K_s + S} \tag{27}$$

where μ_{max} is the maximum specific growth rate; K_s is the Monod or saturation constant. The input variables are the dilution rate $D(t)$ and the influent substrate concentration S_{in}. The parameters of the proposed model are given in the Table 1.

Parameters	Value	Unit
μ_{max}	0.38	h^{-1}
K_s	5	g/l
k_1	1/0.07	
S_{in}^{max}	140	g/l

Table 1: Simulation parameters

5.1 Takagi-Sugeno model design

The model (26) must be transformed into affine in control model like in (1), where the bioprocess models are known belong to the class of affine nonlinear models, this can be easily shown by assuming that:

$$\begin{aligned} D &= D_1 + D_2 \\ S_{in} &= \frac{D_2}{D_1+D_2}S_{in}^{max} \end{aligned} \tag{28}$$

where $D_1(t)$ and $D_2(t)$ are respectively the water and the substrate dilution rate, then one can replace $D(t)$ and $S_{in}(t)$ in (26) by their expressions (28), the following affine model is obtained:

$$\begin{bmatrix} \frac{dX}{dt} \\ \frac{dS}{dt} \end{bmatrix} = \begin{bmatrix} \mu(S)X \\ -k_1\mu(S)X \end{bmatrix} + \begin{bmatrix} -X & -X \\ -S & S_{in}^{max} - S \end{bmatrix}\begin{bmatrix} D_1 \\ D_2 \end{bmatrix} \tag{29}$$

where:

$$f(x) = \begin{bmatrix} \mu(S)X \\ -k_1\mu(S)X \end{bmatrix},\ g(x) = \begin{bmatrix} -X & -X \\ -S & S_{in}^{max} - S \end{bmatrix}$$
$$x(t) = \begin{bmatrix} X \\ S \end{bmatrix} \text{ and } u(t) = \begin{bmatrix} D_1 \\ D_2 \end{bmatrix}$$

To build the T-S model, the following nonlinearities are considered:

$$z_1(x) = \mu(S) \tag{30}$$
$$z_2(x) = X \tag{31}$$
$$z_3(x) = S \tag{32}$$

This leads:
$A(z) = \begin{bmatrix} z_1 & 0 \\ -k_1 z_1 & 0 \end{bmatrix}$ and $B(z) = \begin{bmatrix} -z_2 & -z_2 \\ -z_3 & -z_3 + S_{in}^{max} \end{bmatrix}$
where the number of nonlinearities $n = 3$, the global model can be represented by $r = 2^n = 8$ sub-models. The local membership functions are defined by:

$$F_1^1(z_1) = \frac{z_1 - z_1^{min}}{z_1^{max} - z_1^{min}}, \quad F_1^2(z_1) = \frac{z_1^{max} - z_1}{z_1^{max} - z_1^{min}}$$
$$F_2^1(z_2) = \frac{z_2 - z_2^{min}}{z_2^{max} - z_2^{min}}, \quad F_2^2(z_2) = \frac{z_2^{max} - z_2}{z_2^{max} - z_2^{min}}$$
$$F_3^1(z_3) = \frac{z_3 - z_3^{min}}{z_3^{max} - z_3^{min}}, \quad F_3^2(z_3) = \frac{z_3^{max} - z_3}{z_3^{max} - z_3^{min}}$$

Finally, the activation functions are:

$$h_1(z) = F_1^1(z_1)F_2^1(z_2)F_3^1(z_3), \quad h_2(z) = F_1^1(z_1)F_2^1(z_2)F_3^2(z_3)$$
$$h_3(z) = F_1^1(z_1)F_2^2(z_2)F_3^1(z_3), \quad h_4(z) = F_1^1(z_1)F_2^2(z_2)F_3^2(z_3)$$
$$h_5(z) = F_1^2(z_1)F_2^1(z_2)F_3^1(z_3), \quad h_6(z) = F_1^1(z_1)F_2^1(z_2)F_3^2(z_3)$$
$$h_7(z) = F_1^2(z_1)F_2^2(z_2)F_3^1(z_3), \quad h_8(z) = F_1^2(z_1)F_2^2(z_2)F_3^2(z_3)$$

For the simulation, the parameters given in Table 1 are considered and leads to the following *min* and *max* of premise variables:

$$\begin{aligned} 0.018 &\le \mu(S) \le 0.35 \\ 3.8 &\le X \le 20 \\ 0.6 &\le S \le 140 \end{aligned}$$

the computed matrix A_i and B_i of each sub-model are given as follows:

$$A_1 = A_3 = A_5 = A_7 = \begin{bmatrix} 0.3507 & 0 \\ -5.0106 & 0 \end{bmatrix}$$
$$A_2 = A_4 = A_6 = A_8 = \begin{bmatrix} 0.0179 & 0 \\ -0.2551 & 0 \end{bmatrix}$$

$$B_1 = B_2 = \begin{bmatrix} -20 & -20 \\ -140 & 0 \end{bmatrix}, B_3 = B_4 = \begin{bmatrix} -3.8 & -3.8 \\ -140 & 0 \end{bmatrix}$$
$$B_5 = B_6 = \begin{bmatrix} -20 & -20 \\ -0.6 & 139.4 \end{bmatrix}, B_7 = B_8 = \begin{bmatrix} -3.8 & -3.8 \\ -0.60 & 139.4 \end{bmatrix}$$

6 Simulation and results

In the first case, all the states variables (substrate and biomass concentrations) are supposed measurable (i.e. $C = \begin{bmatrix} 1 & 0 \\ 0 & 1 \end{bmatrix}$).
The desired trajectory (X_r and S_r), which represent respectively of biomass and substrate concentrations are computed by using the following reference model:

$$\begin{aligned} \dot{X}_r &= -0.97X_r + 0.97ref_X \\ \dot{S}_r &= -0.65S_r + 0.65ref_S \end{aligned} \tag{33}$$

where ref_X and ref_S are the setpoints.

6.1 Tracking control based on state feedback

6.1.1 PDC control

The studied bioprocess presents the physical constraints on the control as shown in the Table 2

Variables	Constraints
Dilution rate h^{-1}	$0.01 \leqslant D \leqslant 0.38$
Influent substrate g/l	$60 \leqslant S_{in} \leqslant 140$

Table 2: The control constraints

For a number of active sub-model $s = 5$ and $\eta = 1.55$, the LMIs (10), (20) and (21) are solved by using the solver SeDuMi in MATLAB toolbox YALMIP, gives the following gains:

$$K_1 = \begin{bmatrix} 0.0384 & -0.0044 & -0.0007 & 0.0083 \\ -0.2821 & 0.0064 & 0.0564 & -0.0088 \end{bmatrix}$$

$$K_2 = \begin{bmatrix} 0.0052 & -0.0044 & -0.0007 & 0.0083 \\ -0.2472 & 0.0064 & 0.0563 & -0.0088 \end{bmatrix}$$

$$K_3 = \begin{bmatrix} 0.03470 & -0.0044 & 0.0002 & 0.0083 \\ -0.2963 & 0.0064 & 0.05930 & -0.0088 \end{bmatrix}$$

$$K_4 = \begin{bmatrix} 0.0011 & -0.0044 & 0.0002 & 0.0083 \\ -0.2605 & 0.0064 & 0.05910 & -0.0088 \end{bmatrix}$$

$$K_5 = \begin{bmatrix} -0.2149 & -0.0010 & 0.0572 & 0.0074 \\ -0.0287 & 0.0044 & -0.0014 & -0.0083 \end{bmatrix}$$

$$K_6 = \begin{bmatrix} -0.2480 & -0.0010 & 0.0571 & 0.0074 \\ 0.0060 & 0.0044 & -0.0015 & -0.0083 \end{bmatrix}$$

$$K_7 = \begin{bmatrix} -0.22450 & -0.0009 & 0.0592 & 0.0074 \\ -0.0371 & 0.0044 & 0.0003 & -0.0083 \end{bmatrix}$$

$$K_8 = \begin{bmatrix} -0.25660 & -0.0009 & 0.0590 & 0.0074 \\ -0.0028 & 0.0044 & 0.0003 & -0.0083 \end{bmatrix}$$

$$P = \begin{bmatrix} 0.0059 & -0.0000 & -0.0011 & 0.0000 \\ -0.0000 & 0.0008 & 0.0000 & -0.0002 \\ -0.0011 & 0.0000 & 0.0008 & -0.0000 \\ 0.0000 & -0.0002 & -0.0000 & 0.0008 \end{bmatrix}$$

$$Q = \begin{bmatrix} 7.5254 & 0.0002 & 2.9997 & -0.0011 \\ 0.0002 & 35.5015 & 0.0002 & 0.0002 \\ 2.9997 & 0.0002 & 23.9724 & 0.0013 \\ -0.0011 & 0.0002 & 0.0013 & 26.1931 \end{bmatrix}$$

The initial conditions are $x_0 = (6.6 \quad 5.50)^T$ and the obtained results are shown in Figures 1 and 2, the trajectory tracking is achieved, where the biomass and the substrate concentrations follow the desired outputs. In addition, the constraints on the inputs control $D(t)$ and $S_{in}(t)$ are respected.

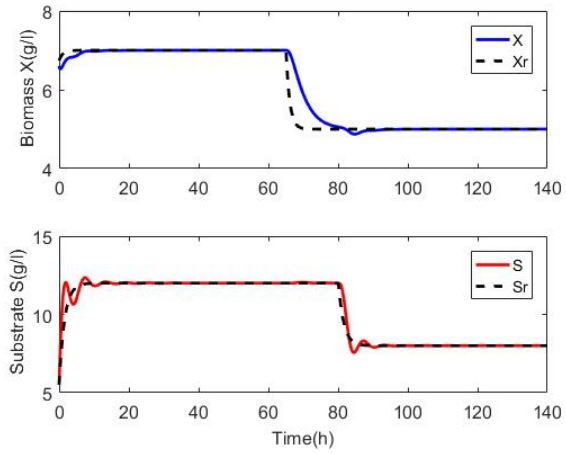

Figure 1: Evolution of the system outputs

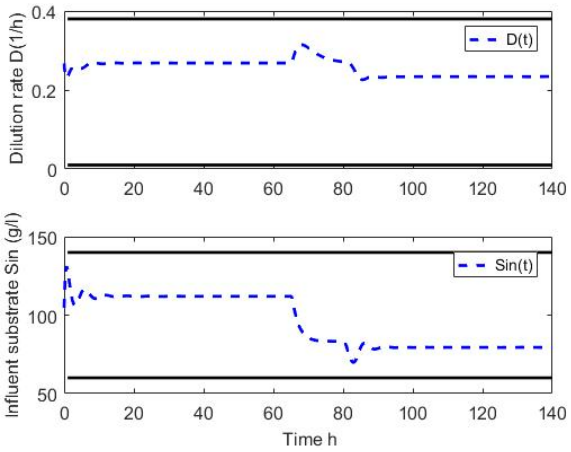

Figure 2: Control inputs $D(t)$ and $S_{in}(t)$

6.1.2 LQI control

Solving the LMIs established in (19), (20) and (21) the obtained weighting matrices are:

$$R = \begin{bmatrix} 0.328 & 0.000 \\ 0.000 & 0.328 \end{bmatrix}.10^{-3}$$

$$Q = \begin{bmatrix} 0.2529 & 0.0025 & -0.0264 & -0.0007 \\ 0.0025 & 0.2252 & -0.0004 & -0.0422 \\ -0.0264 & -0.0004 & 0.1345 & 0.0015 \\ -0.0007 & -0.0422 & 0.0015 & 0.1966 \end{bmatrix}.10^{-3}$$

The controller gains are:

$$K_1 = \begin{bmatrix} 0.0202 & -0.0081 & 0.0044 & 0.0101 \\ -0.0736 & 0.0128 & 0.0098 & -0.0056 \end{bmatrix}$$

$$K_2 = \begin{bmatrix} 0.0010 & -0.0095 & 0.0010 & 0.0105 \\ -0.0368 & 0.0052 & 0.0195 & -0.0030 \end{bmatrix}$$

$$K_3 = \begin{bmatrix} 0.0317 & -0.0095 & 0.0008 & 0.0106 \\ -0.2002 & 0.0039 & 0.0165 & -0.0004 \end{bmatrix}$$

$$K_4 = \begin{bmatrix} 0.0016 & -0.0096 & 0.0002 & 0.0106 \\ -0.1086 & 0.0023 & 0.0271 & -0.0005 \end{bmatrix}$$

$$K_5 = \begin{bmatrix} -0.0247 & -0.0003 & 0.0211 & 0.004 \\ -0.031 & 0.0095 & -0.0006 & -0.009 \end{bmatrix}$$

$$K_6 = \begin{bmatrix} -0.0345 & -0.0050 & 0.0200 & 0.0033 \\ -0.0024 & 0.0096 & 0.0009 & -0.0105 \end{bmatrix}$$

$$K_7 = \begin{bmatrix} -0.1471 & -0.0047 & 0.0211 & 0.0035 \\ -0.0369 & 0.0095 & 0.0003 & -0.0105 \end{bmatrix}$$

$$K_8 = \begin{bmatrix} -0.1064 & -0.0026 & 0.0274 & 0.0009 \\ -0.0023 & 0.0096 & 0.0003 & -0.0107 \end{bmatrix}$$

The Figures 3 and 4 show the simulation results using LQI control, where the controlled outputs variables achieve the desired outputs, also the constraints on control are respected.

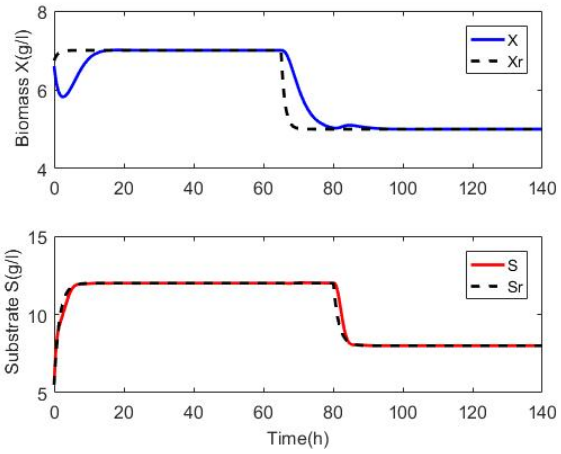

Figure 3: Evolution of the system outputs

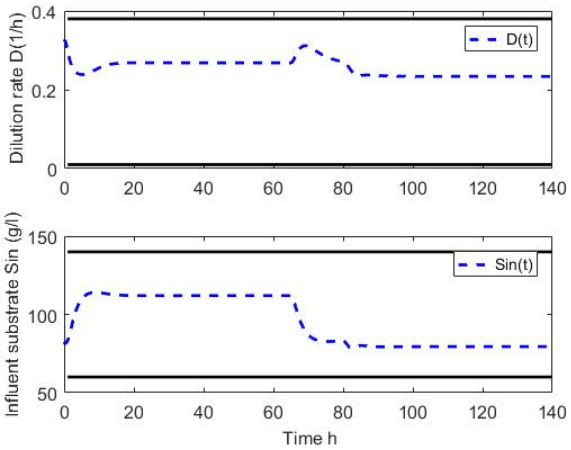

Figure 4: Control inputs $D(t)$ and $S_{in}(t)$

The results obtained are comparable or even better than those obtained using the PDC controller.

6.2 Tracking control based on reconstructed state feedback

In the practical case, only the substrate concentration is measured and the biomass is estimated, then the output matrix in (1) becomes $C = \begin{bmatrix} 0 & 1 \end{bmatrix}$. For the initial conditions of system $x_0 = (4 \quad 8)^T$, the initial conditions of observer $\hat{x}_0 = (5 \quad 7)^T$ and for a scalar $\alpha = 0.5$, the following observer gains are obtained:

$$L_1 = L_3 = L_5 = L_7 = \begin{bmatrix} 5.2458 \\ -1.3202 \end{bmatrix}$$

$$L_2 = L_4 = L_6 = L_8 = \begin{bmatrix} 0.3483 \\ -0.6440 \end{bmatrix}$$

$$Q = \begin{bmatrix} 5.655 & 0.000 & -0.000 \\ 0.000 & 4.4141 & 0.000 \\ -0.00 & 0.000 & 6.2045 \end{bmatrix}$$

$$P = \begin{bmatrix} 0.5985 & 0.0843 & 0.0000 \\ 0.0843 & 0.6103 & 0.0000 \\ 0.0000 & 0.0000 & 0.6103 \end{bmatrix}$$

6.2.1 PDC control

The resolution of the same LMIs in last case gives the following gains.

$$K_1 = \begin{bmatrix} 0.0231 & -0.0043 & 0.0067 \\ -0.1294 & 0.0058 & -0.0037 \end{bmatrix}$$

$$K_2 = \begin{bmatrix} -0.0057 & -0.0044 & 0.0066 \\ -0.1082 & 0.0058 & -0.0033 \end{bmatrix}$$

$$K_3 = \begin{bmatrix} 0.0304 & -0.0044 & 0.0064 \\ -0.1425 & 0.0058 & -0.0027 \end{bmatrix}$$

$$K_4 = \begin{bmatrix} -0.0038 & -0.0045 & 0.0065 \\ -0.1187 & 0.0058 & -0.0031 \end{bmatrix}$$

$$K_5 = \begin{bmatrix} -0.0814 & -0.0015 & 0.0094 \\ -0.0336 & 0.0044 & -0.0065 \end{bmatrix}$$

$$K_6 = \begin{bmatrix} -0.1090 & -0.0015 & 0.0092 \\ -0.0016 & 0.0044 & -0.0064 \end{bmatrix}$$

$$K_7 = \begin{bmatrix} -0.0857 & -0.0018 & 0.0096 \\ -0.0359 & 0.0048 & -0.0065 \end{bmatrix}$$

$$K_8 = \begin{bmatrix} -0.1151 & -0.0015 & 0.0094 \\ -0.0036 & 0.0046 & -0.0064 \end{bmatrix}$$

$$P = \begin{bmatrix} 0.0114 & -0.0001 & -0.0003 \\ -0.0001 & 0.0010 & -0.0002 \\ -0.0003 & -0.0002 & 0.0008 \end{bmatrix}$$

$$Q = \begin{bmatrix} 0.0114 & -0.0001 & -0.0003 \\ -0.0001 & 0.0010 & -0.0002 \\ -0.0003 & -0.0002 & 0.0008 \end{bmatrix}$$

The Figure 5 shows a comparison between the controlled variable S, his estimated $\hat{S}$ and the desired output S_r. The obtained result show that S follows correctly S_r and the observer estimates the states of

system ($\hat{S} = S$) after 4.33 hours. The Figure 6 presents the control inputs $D(t)$ and $S_{in}(t)$, which respect the constraints.

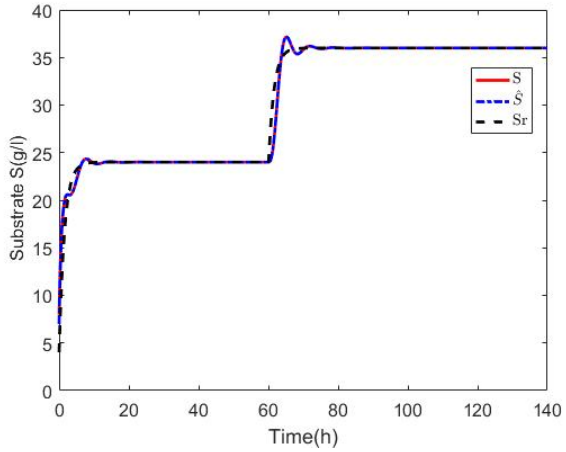

Figure 5: Evolution of the system outputs

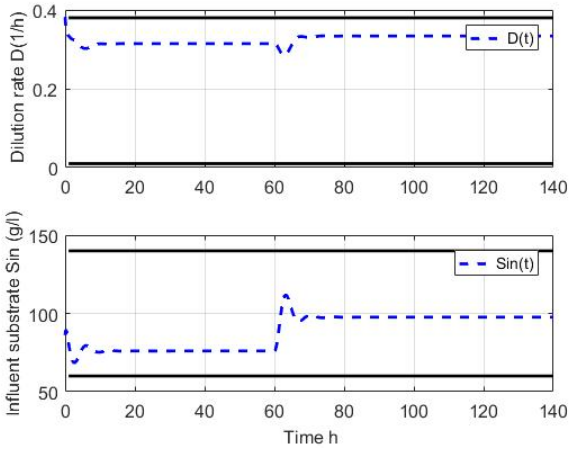

Figure 6: Control inputs $D(t)$ and $S_{in}(t)$

6.2.2 LQI control

In this part, we illustrate the obtained results using LQI control. Solving the LMIs (20), (21), (19) we obtain the following controller gains and weighting matrices:

$$R = \begin{bmatrix} 0.2040 & 0.0002 \\ 0.0002 & 0.2028 \end{bmatrix}.10^{-3}$$

$$Q = \begin{bmatrix} 0.1138 & 0.0012 & -0.0009 \\ 0.0012 & 0.1360 & -0.0196 \\ -0.0009 & -0.0196 & 0.1072 \end{bmatrix}.10^{-3}$$

$$K_1 = \begin{bmatrix} 0.0000 & -0.0043 & 0.0066 \\ -0.0566 & 0.0087 & -0.0035 \end{bmatrix}$$

$$K_2 = \begin{bmatrix} 0.0015 & -0.0076 & 0.0067 \\ -0.0124 & 0.0015 & -0.0001 \end{bmatrix}$$

$$K_3 = \begin{bmatrix} 0.0182 & -0.0072 & 0.0069 \\ -0.1308 & 0.0032 & -0.0003 \end{bmatrix}$$

$$K_4 = \begin{bmatrix} 0.0017 & -0.00760 & 0.0067 \\ -0.0222 & 0.0003 & 0.0002 \end{bmatrix}$$

$$K_5 = \begin{bmatrix} -0.0130 & 0.0005 & 0.0032 \\ -0.0231 & 0.0071 & -0.00560 \end{bmatrix}$$

$$K_6 = \begin{bmatrix} -0.0105 & -0.0017 & 0.0009 \\ -0.0016 & 0.0076 & -0.0067 \end{bmatrix}$$

$$K_7 = \begin{bmatrix} -0.0624 & -0.0034 & 0.0027 \\ -0.0327 & 0.0073 & -0.0062 \end{bmatrix}$$

$$K_8 = \begin{bmatrix} -0.0204 & -0.0009 & 0.0004 \\ -0.0018 & 0.0076 & -0.0067 \end{bmatrix}$$

The Figures 7 and 8 present the same variables in the Figures 5 and 6 using the LQI control. where the obtained results indicate clearly that the desired performances can be achieved more better than the results obtained by PDC control, the Figure 9 shows the state estimation error of the state variables (biomass and substrate concentrations), where this error tends to zero after 4.33 hours.

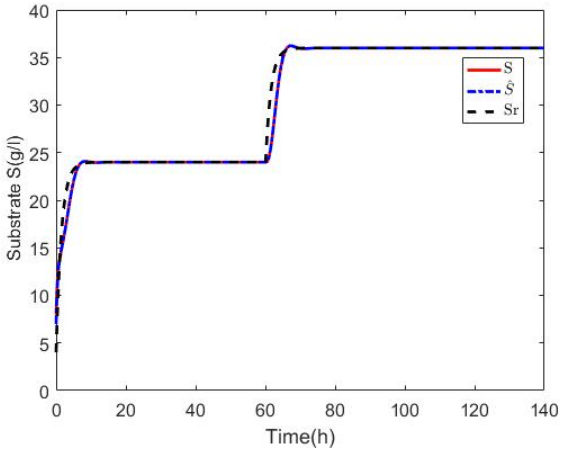

Figure 7: Evolution of the system outputs

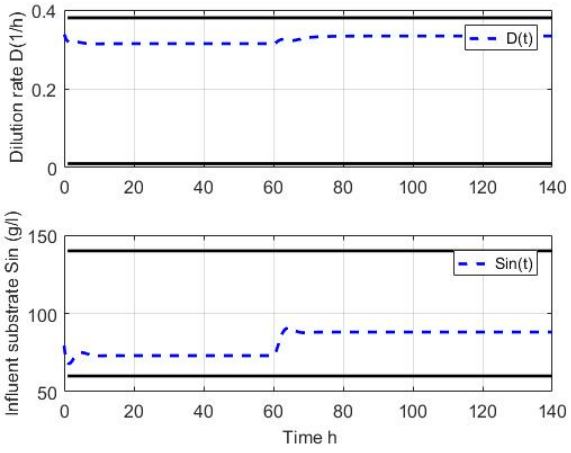

Figure 8: Control inputs $D(t)$ and $S_{in}(t)$

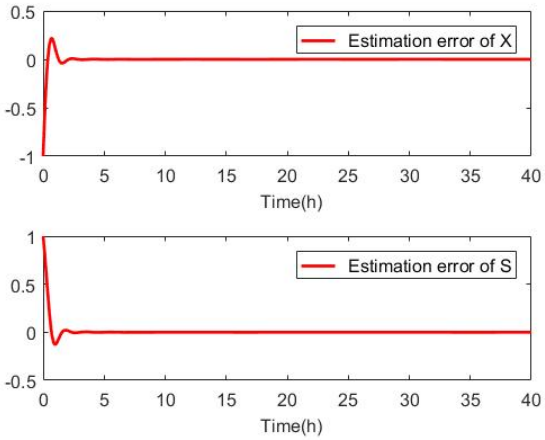

Figure 9: The sate estimation error

6.3 Comparison of both controllers

The outputs behaviors in the Figures 1, 3, 5, 7, show that the PDC controller presents some overshoot compared with LQI controller, where the PDC control requires the stabilization of all the different sub-models cross terms ($h_i(z) \neq h_j(z)$) too, which increases the LMIs need to be solved. Moreover, in terms of speed, the comparison shows clearly that the LQI controller is fast than PDC one. In general, the comparison shows that the LQI controller presents the best performance.

6.4 Comparison with other methods

Another method of bioprocess control based on neural network model has been developed in [13], where the process is controlled via a neural predictive controller in that case the controller doesn't refer to a mathematical model for the process but consider the black box identification. In our case we are based on the mathematical model for the synthesis of the controller, the obtained results are satisfactory regarding the result obtained in [13]. Another work in the same spirit developed by A. Nikfetrat [14], where the study considers a predictive controller applied to a biological feed-batch process without taking into account the constraints on the input variables and shows an important error in tracking reference trajectories, where the present work gave better results.

7 Conclusion

In this paper, the modeling and the control of the biomass growth process are treated. The objective is to control and compare two controllers. The nonlinear model of this process obtained from the mass-balance is transformed to Takagi-Sugeno fuzzy model, which represents exactly the original nonlinear model. Then, a T-S observer is designed to reconstruct the unmeasurable state when the premise variables are not measurable. To ensure the trajectory tracking two controllers are tested. The PDC and the linear quadratic control. The obtained results show that the two controllers are both effective. Finds that the second controller is more stable. In addition, the inputs respect the physical constraints of the process.
In this study, we only focus on the bioprocess control in faulty free case, that is why one interesting future work is to build a fault-tolerant control for this process.

Appendix

The proof of the Theorem 3 is presented here, we consider the following state estimation error:

$$e(t) = x(t) - \hat{x}(t) \tag{34}$$

their dynamic becomes:

$$\dot{e}(t) = \dot{x}(t) - \dot{\hat{x}}(t)$$

we take:

$$\triangle(x, \hat{x}, u) = \left(\sum_{i=1}^{r} h_i(z) - \sum_{i=1}^{r} h_i(\hat{z})\right)(A_i x + B_i u(t)) \tag{35}$$

the error dynamic then becomes:

$$\dot{e} = \sum_{i=1}^{r} h_i(\hat{z})(A_i - L_i C)e(t) + \triangle(x, \hat{x}, u) \tag{36}$$

if we assume that the term $\triangle(x, \hat{x}, u)$ satisfies the condition of Lipschitz as follows:

$$\| \triangle(x, \hat{x}, u)\| \leq \alpha \|x - \hat{x}\| \tag{37}$$

to ensure the convergence of (36) , one can consider the following candidate quadratic Lyapunov function:

$$V(e(t)) = e(t)^T P e(t) \tag{38}$$

leads to:

$$\dot{V}(e(t)) = \sum_{i=1}^{r} h_i(\hat{z}) e(t)^T ((A_i - L_i C)^T P + P(A_i - L_i C)) + \triangle(x, \hat{x}, u)^T P e(t) + e(t)^T P \triangle(x, \hat{x}, u) \tag{39}$$

Lemma 1 *For two real matrices X and Y of appropriate dimensions, the following inequality is verified:*

$$X^T Y + X Y^T < X^T \Omega^{-1} X + Y \Omega Y^T, \Omega > 0$$

Applying the previews lemma to the term:
$\triangle(x, \hat{x}, u)^T P e(t) + e(t)^T P \triangle(x, \hat{x}, u)$, the derivative of (39) is expressed as:

$$\dot{V}(e(t)) \leq e^T (A_i^T P - C^T L_i^T P + P A_i - P L_i C + \alpha^2 \mathbb{I} + P P) e \tag{40}$$

If there exists a symmetric and positive definite matrix $Q = Q^T$ such that:

$$A_i^T P - C^T L_i^T P + P A_i - P L_i C \leq -Q \tag{41}$$

leads to:

$$-Q+\alpha^2\mathbb{I}+PP<0 \tag{42}$$

Finally, we apply the Schur complement to (42) we obtain:

$$\begin{bmatrix} Q-\alpha^2\mathbb{I} & P \\ P & \mathbb{I} \end{bmatrix}>0 \tag{43}$$

Then the proof is completed.

References

[1] V. Vastemans, M. Rooman, P. Bogaerts, "A robust method for the joint estimation of yield coeffcients and kinetic parameters in bioprocess models", Biotechnology Progress 25 (3), 2009, 606–618. doi:10.1002/btpr.89.

[2] A. Karama, O. Bernard, J.-L. Gouzé," Constrained Hybrid Neural Mod- elling of Biotechnological Processes", International Journal of Chemical Re- 70 actor Engineering 8 (1), 2010, 1–15. doi:https://doi.org/10.2202/ 1542-6580.2117.

[3] V. Grisales, A. Gauthier, G. Roux, "Fuzzy Optimal Control Design for Dis- crete Affine Takagi-Sugeno Fuzzy Models: Application to a Biotechnologi- cal Process", 2006 IEEE International Conference on Fuzzy Systems, 2006, 2369–2376, doi:10.1109/FUZZY.2006.1682030.

[4] E. Herrera, B. Castillo, J. Ramrez, E. C. Ferreira, "Takagi-sugeno multiple- model controller for a continuous baking yeast fermentation process", ICINCO 2007 - 4th International Conference on Informatics in Control, Automation and Robotics, Proceedings ICSO, 2007, 436–439. doi:10.5220/0001622704360439.

[5] Min-Sen Chiu, Shan Cui, Qing-Guo Wang. " Internal Model Control Design for Transition Control", AIChE journal, vol 46, 2000

[6] E. J. Herrera-Liopez, B. Castillo-Toledo, R. Femat, "Fuzzy servo controller 65 for CSTB with substrate inhibition kinetics", Journal of Process Control 22 (6) (2012) 959–967. doi:10.1016/j.jprocont.2012.05.003.

[7] A. M. Nagy Kiss, B. Marx, G. Mourot, G. Schutz, J. Ragot, "Observers de- sign for uncertain Takagi-Sugeno systems with unmeasurable premise vari- ables and unknown inputs. Application to a wastewater treatment plant", 30 Journal of Process Control 21 (7), 2011, 1105–1114. doi:10.1016/j. jprocont.2011.05.001.

[8] M. Bouharkat, M. Ramdani," Fuzzy observer based predictive control of an activated sludge depollution bioprocess", 2013 International Conference on Control, Decision and Information Technologies, CoDIT, 2013, 236–241. doi:10.1109/CoDIT.2013.6689550.

[9] E. Herrera, B. Castilloa, J. Ramrezb, E. C. Ferreirac, "Exact fuzzy observer for a baker's yeast fermentation process", IFAC Proceedings Volumes (IFAC- PapersOnline) 10 (1), 2007, 313–318. doi:10.1109/FUZZY.2007.4295502.

[10] S. Aouaouda, M. Chadli, M. T. Khadir, T. Bouarar, "Robust fault tolerant tracking controller design for unknown inputs T-S models with unmeasurable premise variables", Journal of Process Control 22 (5), 2012, 861–872. doi:10.1016/j.jprocont.2012.02.016.

[11] S. Bououden, M. Chadli, H. R. Karimi, "Control of uncertain highly non- linear biological process based on Takagi-Sugeno fuzzy models", Signal Processing 108 (2015) 195–205. doi:10.1016/j.sigpro.2014.09.011.

[12] S. Carlos-Hernandez, E. N. Sanchez, J. F. Béteau, "Fuzzy observers for anaerobic WWTP: Development and implementation", Control Engineering Practice 17 (6), 2009, 690–702. doi:10.1016/j.conengprac.2008.11. 008.

[13] A. Karama, "Contribution à la modélisation et la commande par réseaux de neurones des bioprocédès", thesis, University Cadi Ayyad, Faculty of Science Semlalia Marrakech, 2004.

[14] A. Nikfetrat, A.R. Vali, V. Babaeipour. "Neural Network Modeling and Nonlinear Predictive Control of a Biotechnological Fed-batch Process", IEEE International Conference on Control and Automation Christchurch, New Zealand, December 9–11, 2009.

[15] Mohd N, Aziz N. "Performance and Robustness Evaluation of Nonlinear Autoregressive with Exogenous Input Model Predictive Control in Controlling Industrial Fermentation Process", Journal of Cleaner Production, 2016.

[16] O. Gehan, E. Pigeon, M. Pouliquen, L. Fall, R. Mosrati, "Nonlinear control of dissolved oxygen level for Pseudomonas putida bacterium fermentation", 15 2016 IEEE Conference on Control Applications, CCA 2016 (2016) 1215– 1220 doi:10.1109/CCA.2016.7587972.

[17] K. Tanaka, H. O. Wang, "Fuzzy Control Systems Design and Analysis", John Wiley and Sons, Inc., New York, USA, 2001. doi:10.1002/0471224596.

[18] Saifia, D., Chadli, M., Labiod, S., and Guerra, T. M., " Robust $H\infty$ Static Output Feedback Stabilization of T-S Fuzzy Systems Subject to Actuator Saturation", Int. J. Control Autom. Syst. 10(3), 613–622, 2012

[19] Hassan.K.Khali. "Nonlinear Systems", second edition, Prentice Hall. United States of America, 1996.

[20] Guechi, El-Hadi, Lauber, Jimmy, Dambrine, Michel, et al., "PDC control design for non-holonomic wheeled mobile robots with delayed outputs", J. Intell. Robot. Syst. 60(3-4), 395–414, 2010

[21] Xu, Bin, Wang, Shixing, Gao, Daoxiang, et al., "Command filter based robust nonlinear control of hypersonic aircraft with magnitude constraints on states and actuators", J. Intell. Robot. Syst. 73(1-4), 233–247, 2014

[22] Zhu, Senqiang et Wang, Danwei., " Adversarial ground target tracking using UAVs with input constraints", J. Intell. Robot. Syst. 65(1-4), 521-532, 2012

[23] M. Abyad, A. Karama, A. Khalloq, "Fuzzy Takagi-Sugeno Based Modelling and Control For an Alcoholic Fermentation Process", 3rd International Conference on Electrical and Information Technologies ICEIT, Rabat, Morocco, 2017.

[24] P. Bergsten, R. Palm, D. Driankov, "Fuzzy observers", 10th IEEE International Conference on Fuzzy Systems. (Cat. No.01CH37297) 2, 2001, doi:10.1109/FUZZ.2001.1009051.

[25] Bastin G. and Dochain D. "On-line estimation and adaptive control of bioreactors". Elsevier, Amsterdam, 1990.

ASTES

Advances in Science, Technology and Engineering Systems Journal
Vol. 3, No. 4, 327-340 (2018)
www.astesj.com
Special Issue on Multidisciplinary Sciences and Engineering

ASTES Journal
ISSN: 2415-6698

Minimizing Time Delay of Information Routed Across Dynamic Temporal Sensor Networks

Michael J. Hirsch[*,1], Azar Sadeghnejad[2]

[1]*ISEA TEK, LLC, 32751, U.S.A.*

[2]*Radiation-Oncology Department, University of Texas - Southwestern Medical Center, 75390, U.S.A.*

ARTICLEINFO

Article history:
Received: 13 July, 2018
Accepted: 10 August, 2018
Online: 20 August, 2018

Keywords:
Information Routing
Sensor Network
Communication Topology

ABSTRACT

In this research we address the problem of routing information across dynamic temporal sensor networks. The goal is to determine which information, generated by sensors on resources at various times, is able to be routed to other resources, consumer resources, within the given information time window, while being constrained by temporally dynamic bandwidth limitations across the sensor network, and storage limitations on the resources. A mathematical model of the problem is derived, and used to find solutions to the problem. In addition, a heuristic is developed to efficiently find good quality solutions. Monte-Carlo simulations are performed comparing solutions found by commercial software with the heuristic.

1 Introduction

This paper is an extension of work originally presented at the Military Communications Conference [1]. Wireless sensor networks are a class of networks in which some or all of the sensors or resources collect, analyze, and communicate data acquired from their environment (external or internal) to other nodes in the network [2]. These other nodes could be resources, sensors, or fixed or mobile command posts. Mobile ad-hoc networks (MANETs) are a subset of wireless sensor networks that have an absence of a fixed infrastructure, and exhibit a dynamic communication topology [3]. Resources within transmission range of others communicate directly (depending on bandwidth limitations) and cooperation among intermediate resources is required for resources to communicate with others outside of their direct communication range. More and more networks, in both the military and commercial domain, are relying on wireless sensor networks and MANETs [4, 5, 6].

The ability for data to be collected by manned and unmanned vehicles engaged in military, government, and commercial missions is increasing at an exponential rate [7]. Examples include high-resolution video, telephone intercepts, traffic congestion reports, internal vehicle system states, among others. In commercial telecommunication networks, there are instances where the capacity across the network is in the terabytes per second range [8]. Networks of this type have the ability to transmit all data that is collected without restrictions or delays. However, in times of crisis and disaster, commercial and civil communication networks can be severely degraded [9, 10]. And in military missions, bandwidth is oftentimes severely limited, which results in a reduction in transmission and sharing of information that can be mission-critical. And this will continue to be the case due to the rise of operations performed in anti-access/area denial (A2AD) environments, against near-peer adversaries. In the past, this meant that information collected by vehicles would not be processed, analyzed, and understood until after the vehicle had returned to base and 'uploaded' all of the collections [7, 11].

In performing more of the processing and analysis on-board the vehicles, there has the potential for less bandwidth requirements for vehicles to share information important for mission success. In effect, this can be seen as *pushing the smarts out to the tactical edge*. Each generation of manned and unmanned vehicles is having more and more processing capabilities on-board [11]. Examples include internally monitoring on-board systems, fusing information collected from various on-board sensors, picking out a person of interest from a full motion video, and deciding how much information should be sent over the sensor network and to whom should be the recipient of such information [12]. While some of the collected information can

[*]Michael J. Hirsch, ISEA TEK, 620 N. Wymore Rd., Ste. 260, Maitland, FL 32751 U.S.A., mhirsch@iseatek.com

https://dx.doi.org/10.25046/aj030433

just be generated and stored on a vehicle, and offloaded upon mission completion, other generated information is vital to mission success, and must be transmitted to control station(s) or other resources during mission execution.

To address this, we consider the following problem. There are a set of resources (moving or fixed) that have a set of Information Generation Requests (IGRs) to satisfy over a given time horizon. If a resource executes a task to perform the IGR, then an associated piece of information is generated. We will use the term IGR to denote the information that gets generated. Each IGR can come from one of a fixed set of categories (for an example of information categories, see Table 1). In addition, each IGR has associated with it the following characteristics: an expected time of generation, the set of consumer resources (those resources that would find this information important for their mission), the time by which the information needs to be delivered to the to be of use, the expected original size of the information, and the priority of the information (i.e., a measure of its importance in the mission). We note that the priority of an IGR could be determined *a priori* (e.g., information collected about one kinematic location is deemed very important and therefore is given a high priority) or dynamically on-board the resource at the time of collection, if the resource has the appropriate analytics (e.g., image is given low priority because it does not contain any red cars). By a 'consumer resource' for a particular IGR, we mean that the resource actually performs some processing with that information (e.g., fuses that information with other information [13, 14], makes command and control decisions, etc.).

There is a dynamic sensor network topology in place over the time horizon. This dynamic network has finite, but varying bandwidth limitations between any two resources at any given time, and in many cases there might not be a direct connection between two resources. Each IGR can be sent over the network with different potential granularities (e.g., 100% of original size, 70% of original size, etc.), but there is a minimum size percentage with which the information remains useful to the consumer of the information. As an IGR gets routed from the generating resource to the consumer resource, all resources along this route will need to store this IGR locally for some amount of time. The generating resource will need to store an IGR from the time of generation until the IGR is completely sent to the next resource in the path to the consumer resource(s). Non-consumer resources along this path will need to store the IGR from the time the resource begins receiving the IGR until the time the resource has completely transmitted the IGR to the next resource along the path. And the consumer resource(s) will need to store the IGR form the time they begin receiving it until at least they have finished processing the IGR.

Each resource has a finite storage capacity, and resources can triage information they have stored (e.g., once a piece of information is generated and completely sent to the next resource along the path to the consumer, the generator resource can delete the information from storage). The objective is then to determine which IGRs to route over the network, how to route those IGRs so that they have a minimal time delay (difference between time of consumption and time of generation), from generating resource to consumer resource over the time horizon, while also attempting to maximize the size of granularity of each IGR that is routed. In turn, this produces the higher-level end product of determining which IGRs should be accomplished for mission objectives, given the network topology characteristics.

There has been some prior research into routing schemes for collected data across a dynamic network. In [17], the author considered the problem of sinkholes in a network. A sinkhole node attempts to deceive all the nodes in the network to route network traffic to the sinkhole, by broadcasting false routing information across the network. An approach based upon secondary caching was developed to prevent a sinkhole attack in dynamic source routing sensor networks. In [18], the author consider cellular data networks and the significant increase in data being transmitted over these networks. Their research looked at data traffic management techniques, whereby users and automated approaches 'flag' messages that are of low priority, and an higher-level agent-based scheduling system had the ability to delay scheduling of low priority messages during peak load times. In [19], the authors considered the problem of extending lifetimes of wireless sensor networks. In their view, the sending of redundant data across sensor networks reduced the lifetime of these networks. They looked at providing certain nodes in the network to function as 'data aggregation' nodes, receiving collected data from other nodes in the network, fusing or aggregating the data together to reduce redundant information, and then passing this reduced set of data onwards to a base station. They employed a grid-based routing and aggregator selection scheme to find the minimum number of aggregation points while routing data to the base station ensuring that the network lifetime is maximized.

In addition, there has been some prior research addressing certain aspects of our problem of interest, but none that has addressed the problem completely. In [20], the author considered the problem of routing information across a network, from a workflow perspective, but the network was assumed to be complete and static, and bandwidth was not addressed. In [21], the researchers extended this work to include bandwidth limitations, but still under the assumption on a complete and static network. In [22], the researchers presented a mixed-integer linear programming formulation to model the trajectory of a set of unmanned aerial vehicles, along with routing of information collected from these vehicles back to a base station. They did not consider bandwidth fluctuations in the sensor network, and the resources were not the recipient of any information, just the base station. In addition, all of their information was considered to have the same priority. In [23], the author considered underwater

Table 1: Examples of Information Categories.

Category	Example
Internal System State	Measurements on the engine pressure ratio [15]
External Collection	Photographs of an urban traffic intersection
Situation Assessments	High likelihood that red truck contains person of interest
Command and Control (C2)	Modifying flight plan to conserve battery life [16]

acoustic networks and the long propagation delays and low bandwidths inherent in such networks. A set of nodes was using the same bandwidth channel, and because their problem had bursty data, the solution approach looked at submitting their requests randomly, as demand dictated. A medium access control protocol was in place to minimize the number of collisions among the information flowing across the network. In [24], the researchers investigated ways to enhance the operations of a power grid. One of the ways, taking advantage of the high sampling rates of the measurement data, required a high bandwidth, networked communication system. Their results derived a method to simulate, design, and test the adequacy of a communication system for a particular grid layout.

The rest of this paper is organized as follows. In Section 2, we introduce the parameters and decision variables for our model, and rigorously derive the mathematical program representing our problem. Section 3 develops a heuristic to efficiently find good quality solutions. Section 4 analyzes the results of computational experiments performed on various scenarios, comparing commercial software solving a linearized version of the mathematical program and the solutions found by the heuristic. Section 5 provides some concluding remarks and future research directions.

2 Mathematical Formulation

In this section, we rigorously derive mathematical equations to model the problem of interest. This results in a mixed-integer nonlinear program (MINLP). We note that the time dimension in the model is discretized, over the planning horizon of $\mathcal{K}$ time-steps.

2.1 Parameters

This section lists the parameters for the mathematical programming problem.

$\mathcal{I}$ is the set of resources, $i, i_1, i_2, \in \mathcal{I}$;

$\mathcal{J}$ is the number of Information Generation Requests (IGR)s, $j \in \{1, \ldots, \mathcal{J}\}$;

$\mathcal{K}$ is the number of time-steps in the planning horizon, $k, \hat{k} \in \{1, \ldots, \mathcal{K}\}$;

$\mathcal{P}^{min}$ is the minimum percentage an IGR can be decreased in size and still be considered useful to consumer resource(s);

$\tau_{i,j}$ is the number of time-steps after a consumer receives an IGR before the consumer can delete the IGR, i.e., the number of time-steps it takes resource i (the consumer resource) to 'process' IGR j;

ρ_j is the expected priority of IGR j;

S_j^o is the expected original size of IGR j;

g_j is the expected time of generation of IGR j;

d_j is the time by which IGR j is due to the consumer resource(s) of the IGR;

$$G_{i,j} = \begin{cases} 1 & \text{if resource } i \text{ is tasked with generating IGR } j \\ 0 & \text{o.w.} \end{cases};$$

$$C_{i,j} = \begin{cases} 1 & \text{if resource } i \text{ is a consumer of IGR } j \\ 0 & \text{o.w.} \end{cases};$$

L_i is the storage capacity of resource i;

$b_{i_1,i_2,k}$ is the expected bandwidth capacity from resource i_1 to resource i_2 at time-step k;

$\bar{\rho}$ is the largest expected priority, i.e., $\bar{\rho} = \max_j \left[\rho_j\right]$;

ω_d and ω_s are the weighting coefficients for the priority and size components of the objective function;

$\mathcal{M}$ is a large enough constant, used in Constraints (7).

2.2 Variables

This section lists the decision variables for the mathematical programming problem.

$$x_j = \begin{cases} 1 & \text{if IGR } j \text{ is chosen to be routed} \\ & \text{from the generating resource to} \\ & \text{the consumer resource(s)} \\ 0 & \text{o.w.} \end{cases}, \quad \forall j;$$

s_j = the size of IGR j sent to the consumer resource(s), $\forall j$;

$a_{i_1,i_2,j,k}$ = the amount (size) of IGR j sent from resource i_1 to resource i_2 during time-step k, $\forall i_1, i_2 (\neq i_1), j, k$;

$$\alpha_{i_1,i_2,j,k} = \begin{cases} 1 & \text{if resource } i_1 \text{ sends some of IGR } j \\ & \text{to resource } i_2 \text{ during time-step } k \\ 0 & \text{o.w.} \end{cases},$$

$\forall i_1, i_2 (\neq i_1), j, k$;

$m_{i,j,k}$ = the amount of IGR j being stored on resource i at time-step k, $\forall i,j,k$. **N.B.**: For consistency of the constraints, $m_{i,j,0} = 0 \ \forall i,j$;

$$\phi_{i_1,i_2,j} = \begin{cases} 1 & \text{if resource } i_1 \text{ is assigned to send IGR } j \text{ to resource } i_2 \\ 0 & \text{o.w.} \end{cases},$$

$\forall i_1, i_2 (\neq i_1), j$;

$\beta_{i,j}$ = the amount of time resource i takes in sending IGR j to other resources, i.e., the time between resource i completely receiving or generating IGR j to the time where resource i no longer needs IGR j, $\forall i,j$;

$$t_{i,j,k} = \begin{cases} 1 & \text{if resource } i \text{ cumulatively receives (or generates) } s_j \text{ size units of IGR } j \text{ at time-step } k \\ 0 & \text{o.w.} \end{cases},$$

$\forall i,j,k$;

$T_{i,j}$ = the time-step at which resource i completely receives (or generates) IGR j, $\forall i,j$;

$$d_{i,j,k} = \begin{cases} 1 & \text{if resource } i \text{ deletes IGR } j \text{ from storage at time-step } k \\ 0 & \text{o.w.} \end{cases},$$

$\forall i,j,k$;

$D_{i,j}$ = the time-step at which resource i deletes IGR j from its storage, $\forall i,j$;

$Q_{i,j}$ = the time at which resource i completely consumes (or transmits) IGR j, $\forall i,j$;

$$e_{i,j,k} = \begin{cases} 1 & \text{if resource } i \text{ receives (or generates) IGR } j \text{ by time-step } k \\ 0 & \text{o.w.} \end{cases},$$

$\forall i,j,k$.

N.B.: For consistency of the constraints, it is necessary to set $e_{i,j,0} = 0 \ \forall i,j$. Also, note that $e_{i,j,k} = 1$ implies that $e_{i,j,\ell} = 1$ for each $\ell > k$ and $e_{i,j,k} = 0$ implies that $e_{i,j,\ell} = 0$ for each $\ell < k$.

2.3 Nonlinear Mathematical Formulation

This section presents the mathematical model of the problem described in Section 1, resulting in a mixed-integer nonlinear program (MINLP).

$$\max \ \omega_d \cdot \left(\sum_{j=1}^{\mathcal{J}} \sum_{\substack{i \in \mathcal{I}: \\ C_{i,j}=1}} \frac{\left(\mathcal{K} + g_j\right) \cdot x_j - T_{i,j}}{\mathcal{K}} \right) + \omega_s \cdot \left(\sum_{j=1}^{\mathcal{J}} \frac{s_j}{S_j^o} \right) \quad (1)$$

s.t.

$$s_j \leq S_j^o \cdot x_j \ \ \forall j \quad (2)$$

$$s_j \geq \mathcal{P}^{min} \cdot S_j^o \cdot x_j \ \ \forall j \quad (3)$$

$$\sum_j m_{i,j,k} \leq L_i \ \ \forall i,k \quad (4)$$

$$m_{i,j,k} = m_{i,j,k-1} + \sum_{\substack{i_1 \in \mathcal{I} \\ i_1 \neq i}} a_{i_1,i,j,k} - d_{i,j,k} \cdot s_j + \delta\left[g_j - k\right] \cdot G_{i,j} \cdot s_j \ \ \forall i,j,k \quad (5)$$

$$\sum_{k=1}^{\mathcal{K}} \alpha_{i_1,i_2,j,k} \leq \mathcal{K} \cdot x_j \ \ \forall i_1, i_2, j \quad (6)$$

$$\mathcal{M} \cdot \alpha_{i_1,i_2,j,k} \geq a_{i_1,i_2,j,k} \ \ \forall i_1, i_2, j, k \quad (7)$$

$$\sum_j a_{i_1,i_2,j,k} \leq b_{i_1,i_2,k} \ \ \forall i_1, i_2, k \quad (8)$$

$$\sum_{k=1}^{g_j} a_{i_1,i_2,j,k} = 0 \ \ \forall i_1, i_2, j \quad (9)$$

$$\sum_{k=1}^{\mathcal{K}} a_{i_1,i_2,j,k} \leq s_j \ \ \forall i_1, i_2, j \quad (10)$$

$$e_{i,j,k} > \sum_{\substack{i_1 \in \mathcal{I} \\ i_1 \neq i}} \sum_{\hat{k}=1}^{k} a_{i_1,i,j,\hat{k}} - s_j - \left(1 - x_j\right) \ \ \forall k, \ \forall i,j \text{ s.t. } G_{i,j} = 0 \quad (11)$$

$$e_{i,j,k} \cdot s_j \leq \sum_{\substack{i_1 \in \mathcal{I} \\ i_1 \neq i}} \sum_{\hat{k}=1}^{k} a_{i_1,i,j,\hat{k}} \ \ \forall k, \ \forall i,j \ s.t. \ G_{i,j} = 0 \quad (12)$$

$$t_{i,j,k} \geq e_{i,j,k} - e_{i,j,k-1} \ \ \forall i,j,k \quad (13)$$

$$\sum_{k=1}^{\mathcal{K}} t_{i,j,k} \leq x_j \ \ \forall i,j \quad (14)$$

$$t_{i,j,g_j} = x_j \ \ \forall i,j \ s.t. \ G_{i,j} = 1 \quad (15)$$

$$T_{i,j} = \sum_{k=1}^{\mathcal{K}} k \cdot t_{i,j,k} \ \ \forall i,j \quad (16)$$

$$T_{i,j} \leq d_j \cdot x_j \ \ \forall i,j \quad (17)$$

$$Q_{i,j} = T_{i,j} + \tau_{i,j} \cdot x_j \ \ \forall i,j \ s.t. \ C_{i,j} = 1 \quad (18)$$

$$Q_{i,j} = T_{i,j} + \beta_{i,j} \ \ \forall i,j \ s.t. \ C_{i,j} = 0 \quad (19)$$

$$\beta_{i_1,j} \geq k \cdot \alpha_{i_1,i_2,j,k} - T_{i_1,j} \ \ \forall i_1, i_2, j, k \quad (20)$$

$$D_{i,j} > Q_{i,j} - \left(1 - \sum_{k=1}^{\mathcal{K}} t_{i,j,k}\right) \ \ \forall i,j \quad (21)$$

$$D_{i,j} = \sum_{k=1}^{\mathcal{K}} k \cdot d_{i,j,k} \quad \forall i,j \tag{22}$$

$$\sum_{k=1}^{\mathcal{K}} d_{i,j,k} \leq x_j \quad \forall i,j \tag{23}$$

$$\sum_{\substack{i_1 \in \mathcal{I} \\ i_1 \neq i}} \phi_{i_1,i,j} \leq x_j \quad \forall i,j \tag{24}$$

$$\sum_{k=1}^{\mathcal{K}} \alpha_{i_1,i_2,j,k} \leq \mathcal{K} \cdot \phi_{i_1,i_2,j} \quad \forall i_1,i_2,j \tag{25}$$

$$\sum_{k=1}^{\mathcal{K}} \alpha_{i_1,i_2,j,k} \geq \phi_{i_1,i_2,j} \quad \forall i_1,i_2,j \tag{26}$$

$$\sum_{\substack{i_2 \in \mathcal{I} \\ i_2 \neq i}} \alpha_{i,i_2,j,k} \leq \sum_{\hat{k}=1}^{k-1} t_{i,j,\hat{k}} \quad \forall i,j,k \tag{27}$$

$$s_j = \sum_{k=1}^{\mathcal{K}} \sum_{\substack{i_1 \in \mathcal{I} \\ i_1 \neq c_j}} a_{i_1,c_j,j,k} \quad \forall j \tag{28}$$

$$\sum_{k=1}^{\mathcal{K}} \sum_{i_2 \in \mathcal{I}} \alpha_{c_j,i_2,j,k} = 0 \quad \forall j \tag{29}$$

$$x_j, \alpha_{i_1,i_2,j,k}, \phi_{i_1,i_2,j}, t_{i,j,k}, d_{i,j,k}, e_{i,j,k} \in \{0,1\} \quad \forall i,i_1,i_2,j,k \tag{30}$$

$$s_j, a_{i_1,i_2,j,k}, m_{i,j,k} \in \left[0, S_j^o\right] \quad \forall i,i_1,i_2,j,k \tag{31}$$

$$\beta_{i,j}, D_{i,j}, T_{i,j}, Q_{i,j} \in [0,\mathcal{K}] \cap \mathbb{Z} \quad \forall i,j,k \tag{32}$$

2.4 Interpretation of Nonlinear Mathematical Formulation

In this section, we explain the objective function and each of the constraints that are part of the mathematical formulation.

- The objective function, Equation (1), is a weighted combination of the time delay and size of the IGRs routed across the network.

  The first term in the objective function deals with the time delay of those IGRs chosen to be routed. The sum is over all IGRs j and all resources i that are consumers of IGR j (i.e., those resources such that the parameter $C_{i,j} = 1$). When an IGR j is not chosen to be routed, x_j is set to be 0 and $T_{i,j}$ also ends up as 0, so this term is 0. When an IGR is chosen to be routed, x_j is set to be 1 and $T_{i,j}$ is set to be the time at which resource i completely receives IGR j. The time IGR j is generated is given by the parameter g_j. The maximum value of this term is 1, which occurs when $T_{i,j} = g_j$ (which is an idealistic situation), while the minimum value of this term is $\frac{\mathcal{K}+g_j-d_j}{\mathcal{K}}$, which can be 0 when g_j is 0 and d_j is $\mathcal{K}$.

  The second term of the objective function deals with the size of the IGRs chosen to be routed, looking at the ratio of the actual size of the IGR that gets routed versus the original size.

  Note that that scale of these two terms are the same, i.e., they are both within $[0,1]$, and are unit-less. The first term is weighted by ω_d, while the second term is weighted by ω_s.

- Constraints (2) force s_j to be less than or equal to S_j^o if IGR j is chosen to be routed, and 0 if IGR j is not chosen to be routed;
- Constraints (3) require s_j to be greater than or equal to the minimal amount to be routed for IGR j ($\mathcal{P}^{min} \cdot S_j^o$), if IGR j is chosen to be routed;
- Constraints (4) ensure that at each time-step, the storage capacity for each resource is not exceeded;
- Constraints (5) determine the amount of IGR j stored on resource i at time k as the amount stored at time $k-1$ plus the amount sent to resource i at time-step k minus s_j if IGR j is deleted from resource i's storage at time-step k, plus s_j if IGR j is chosen to be routed by resource i and is generated at time-step k. **N.B.**: The Dirac-Delta impulse function $\delta[q]$ returns 1 when $q = 0$ and returns 0 otherwise [25];
- Constraints (6) only allow $\alpha_{i_1,i_2,j,k}$ to be greater than 0 if IGR j is chosen to be routed;
- Constraints (7) force $a_{i_1,i_2,j,k}$ to be 0 if resource i_1 is not sending IGR j to resource i_2 at time-step k;
- Constraints (8) limit the amount of information traveling from resource i_1 to i_2 at time-step k to be no more that the capacity of this edge, $b_{i_1,i_2,k}$;
- Constraints (9) enforce that no resource can send IGR j before it is generated;
- Constraints (10) enforce that resource i_1 send no more than s_j of IGR j to resource i_2;
- For those resources that do not generate IGR j and IGR j is chosen to be routed, Constraints (11) force $e_{i,j,k}$ to be 1 if all s_j of IGR j reaches resource i at or before time-step k. This constraint allows $e_{i,j,k}$ to be 0 or 1 otherwise;
- For those resources that do not generate IGR j, Constraints (12) force $e_{i,j,k}$ to be 0 while not all s_j of IGR j has reached resource i. This constraint allows $e_{i,j,k}$ to be 0 or 1 otherwise;
- Constraints (13) set $t_{i,j,k}$ to be 1 at the time-step that resource i receives all s_j of IGR j, and to be 0 for all other time-steps;
- Constraints (14) enforce that resource i can receive IGR j at most once;
- Constraints (15) set $t_{i,j,k}$ equal to 1 if IGR j is chosen to be routed, is generated by resource i, and k is the time of generation of IGR j;

- Constraints (16) set $T_{i,j}$ to be the time at which resource i receives IGR j;
- Constraints (17) enforce that any resource that receives IGR j, must do so before its due date/time, if IGR j is chosen to be routed;
- Constraints (18) define the time at which resource i has completely 'processed' IGR j, if resource i is a consumer of IGR j and IGR j is chosen to be routed;
- Constraints (19) define the time at which resource i has completely transmitted IGR j to other resources, if resource i is not a consumer of IGR j and IGR j is chosen to be routed;
- Constraints (20) determine the amount of time it takes resource i to send IGR j to other resources, once resource i receives or generates IGR j;
- Constraints (21) ensure that if IGR j is chosen to be routed, that IGR j cannot be deleted from resource i until resource i is finished with the IGR;
- Constraints (22) determine the time at which resource i deletes IGR j;
- Constraints (23) ensure that resource i can delete IGR j at most once;
- Constraints (24) enforce that at most one resource is assigned to send IGR j to resource i;
- Constraints (25) only allow resource i_1 to send IGR j to resource i_2 if it is assigned to;
- Constraints (26) force i_1 to send IGR j to resource i_2 during at least one time-step, if i_1 is assigned to send IGR j to resource i_2;
- Constraints (27) does not allow resource i to send any portion of IGR j at time-step k if resource i has not completely received (or generated) IGR j by time-step $k-1$;
- Constraints (28) ensure that the consumer resource(s) of IGR j receives all s_j units, if IGR j is chosen to be routed;
- Constraints (29) prohibit resource c_j (the consumer of IGR j) from sending IGR j to other resources;
- Constraints (30) – (32) are domain restriction constraints on the decision variables.

3 Solution Methodologies

The formulation derived in Section 2.3 is a nonlinear mixed-integer programming problem. However, this formulation can be linearized through standard techniques from operations research [26], resulting in a mixed-integer linear program (MILP). As such, in theory the MILP formulation could be solved using a number of commercial software packages (e.g., `CPLEX` [27], `LINDO` [28], etc.). It can be shown that this optimization problem is *NP-Hard*, as a variant of the vehicle routing problem with split deliveries and time windows [29, 30, 31], which necessitate heuristic strategies for finding good-quality solutions efficiently [32, 33] when the problem instances are of sufficient size.

The heuristic developed is split into two phases, an Information Routing phase, and a Storage Management phase. The Information Routing phase attempts to route all of the IGRs, from generating resource to consuming resource(s), without consideration of storage limitations on the individual resources. The only constraints taken into account in the Information Routing phase are the bandwidth limitations across the sensor network. The Storage Management phase of the heuristic then factors in the storage limitations of each resource to reduce the solution to one that is feasible.

Figures 2 and 1 provide pseudo-code for the Information Routing and Storage Management phases, respectively. The Information Routing function is input the set of IGRs (and all information about the IGRs), the initial allocation of bandwidth across the network over time (InitCommBW), the minimum percentage (in size) an IGR is able to be reduced and still be useful (MinSizePercent), and the ratio by which to reduce the size of the IGR in sending over the network, if needed (GranularityRatio). Lines 1 to 5 initialize internal variables. Lines 6 to 32 get executed while there are still IGRs on the list to be routed. For each IGR still on the CurListIGRs list, lines 7 to 25 attempt to determine a route for the IGR that allows for at least the minimum size for the IGR to be routed. Line 8 computes the size of the current IGR and line 9 computes the minimal allowable size of the IGR to be routed. While a feasible route for the current IGR has not been found, and the current size of the IGR is larger then the minimum allowable size, lines 11 to 19 get executed. Line 11 calls the function `ComputeRoute`, given the current size of the IGR and the current allocation of bandwidth across the network. Returned from this function are the route for this IGR from generating resource to consumer resource, as well as the time the IGR will completely reach the consumer resource. If the time by which the consumer completely receives the IGR is less than the due date of the IGR, then a potential route for this IGR is found, and the potential time delay for this IGR is computed. Otherwise, the size of the IGR is reduced by the granularity ratio. If a potential route is not found in lines 11 to 19, then this IGR is moved to the NotRoutedIGRs list and removed from the current list of IGRs (lines 21 and 22). Line 23 also sets this IGR to have a delay time of $+\infty$. After the code in lines 7 to 25 is completed, the heuristic greedily selects the IGR with the current minimal potential delay time (line 26). This IGR is removed from the list of current IGRs, and added to the list of routed IGRs. The potential route computed for this IGR is

```
procedure Storage Management(ResourceList, RoutedIGRs, NotRoutedIGRs, MaxStorageSize)
1     CurrentRL ← ResourceList;
2     while CurrentRL ≠ ∅ do
3           CurR ← Choose(CurrentRL);
4           CurrentRL ← CurrentRL \ CurR;
5           for k = 0 to 𝒦 do
6                 for each IGR_ℓ completely transited through CurR by time-step k do
7                       CurR ← RemoveFromStorage(CurR, IGR_ℓ, k, 𝒦);
8                 end for;
9                 for each IGR_ℓ completely consumed by CurR by time-step k do
10                      CurR ← RemoveFromStorage(CurR, IGR_ℓ, k, 𝒦);
11                end for;
12                if Storage(CurR, k) > MaxStorage then
13                      for each IGR_ℓ generated by CurR and completely transited by time-step k do
14                            CurR ← RemoveFromStorage(CurR, IGR_ℓ, k, 𝒦);
15                      end for;
16                end if;
17                ListIGRs ← GetIGRs(CurR, k);
18                SortIGRs ← Sort(ListIGRs);
19                while Storage(CurR, k) > MaxStorage do
20                      IGR_ℓ ← Choose(SortIGRs);
21                      RemoveFromRouting(IGR_ℓ);
22                      NotRoutedIGRs ← NotRoutedIGRs ∪ {IGR_ℓ};
23                      RoutedIGRs ← RoutedIGRs \ {IGR_ℓ};
24                end while;
25          end for;
26    end while;
27    return(RoutedIGRs, NotRoutedIGRs);
end Storage Management;
```

Figure 1: Pseudo-code for the Storage Management phase of the heuristic.

Table 2: Categories, and values used for the number of resources and density over the numerical experiments.

Category	N	Density
Extra Small	3	
Small	4, 5, 6	1, 0.67, 0.33
Medium	8, 10, 12	
Large	15, 20, 25	

saved into the set IGRRoutes in line 29, and the current bandwidth allocation across the temporal network is updated (due to this IGR having its route finalized) in line 30. This process in lines 6 through 32 continues until the set CurListIGRs is empty. The output from the Information Routing function is the set of IGRs that have been routed (along with all of the necessary details of the routes), as well as the set of IGRs not able to be routed.

The Storage Management function takes as input the list of resources, the list of routed IGRs, the list of IGRs that are not able to be routed, and the maximum storage size for each resource. While not all of the resources have been considered, lines 2 through 26 are executed. Line 3 chooses a resource from those still to be considered. Lines 5 to 25 get executed for each time-step of the time horizon. In lines 6 to 8, each IGR that has completely transited through the current resource by the time-step under consideration, gets removed from the resources' storage, from the time-step under consideration to the end of the time horizon. In lines 9 to 11, each IGR that has been completely consumed by the current resource, by the time-step under consideration, gets removed from the resources' storage, from the time-step under consideration to the end of the time horizon. Now, if the storage for the current resource at the time-step under consideration is above the capacity, in lines 13 to 15 each IGR that was generated by the current resource and has been completely transited through the current resource (i.e., completely sent to the next resource along the path to the consumer resource) by the time-step under consideration gets removed from the resources' storage, from the time-step under consideration to the end of the time horizon. Up to this point, all IGRs that were to be routed (as determined from the Information Routing function) are still valid. Line 17 gets the list of IGRs that are scheduled to be generated by the current resource no later than the time-step under consideration, and line 18 sorts this list. While the storage for the current resource at the time-step under consideration is above the maximum allowed, an IGR from the sorted IGR list is chosen, and it is removed from routing. This continues until the storage constraints are met for the current resource at the time-step under consideration. Output from the Storage Management function is an updated list of IGRs chosen to be routed and IGRs not able to be routed.

```
procedure Information Routing(IGRs, InitCommBW, MinSizePercent, GranularityRatio)
1    CurListIGRs ← IGRs;
2    CurCommBW ← InitCommBW;
3    RoutedIGRs ← ∅;
4    NotRoutedIGRs ← ∅;
5    IGRRoutes ← ∅;
6    while CurListIGRs ≠ ∅ do
7        for IGR_j ∈ CurListIGRs do
8            CurSize ← Size(IGR_j);
9            MinSize ← MinSizePercent · CurSize;
10           FoundRoute ← false;
11           while CurSize > MinSize And FoundRoute = false do
12               [RouteIGR_j, ConsumeTime_j] ← ComputeRoute(IGR_j, CurSize, CurCommBW);
13               if ConsumeTime_j < DueTime(IGR_j) then
14                   FoundRoute ← true;
15                   DelayTime_j ← ConsumeTime_j − g_j;
16               else
17                   CurSize ← GranularityRatio · CurSize;
18               end if;
19           end while;
20           if FoundRoute = false then
21               NotRoutedIGRs ← NotRoutedIGRs ∪ {IGR_j};
22               CurListIGRs ← CurListIGRs \ {IGR_j};
23               DelayTime_j ← +∞;
24           end if;
25       end for;
26       j* ← ArgMin(DelayTime);
27       CurListIGRs ← CurListIGRs \ {IGR_j*};
28       RoutedIGRs ← RoutedIGRs ∪ {IGR_j*};
29       IGRRoutes ← IGRRoutes ∪ {RouteIGR_j*};
30       CurCommBW ← Update(CurCommBW, RouteIGR_j*);
31   end while;
32   return(RoutedIGRs, NotRoutedIGRs);
end Information Routing;
```

Figure 2: Pseudo-code for the Information Routing phase of the heuristic.

4 Computational Experiments

4.1 Test Environment

Java jdk 1.8.0_25 was used to code up the heuristic, the actual exact MILP, and the generation of scenario data. CPLEX Optimization Studio V12.6.3 [27] was called to solve the exact MILP. `Matlab R2011b (7.13.0.564)` [34] was used to generate combinations of input parameters, as well as to analyze the results of all experiments. All experiments were conducted on a Dell Precision Tower 7810 with an Intel(R) Xeon(R) CPU E5-2630 v3 @2.40GHz 2.40 GHz with 32.0 GB memory.

4.2 Experimental Results

The aim of our experiments were to investigate the solution quality found by the heuristic, as compared with commercial software, as well as to determine how close to optimal were the solutions found by the heuristic. We used the commercial software CPLEX [27] to solve the linearized formulation of the mathematical model presented in Section 2. However, as can be seen from the results that follow, for some of the scenarios CPLEX was not able to find solutions significantly close to optimal, within the time-limits to find a solution. Thus, we also ran CPLEX to solve the linearized formulation, providing CPLEX an initial solution found from running the heuristic. These two sets of experiments involving CPLEX are described as ''CPLEX w/o Init. Soln.'' and ''CPLEX w/ Init. Soln.'', respectively. To test the heuristic, as well as CPLEX, we created numerous scenarios, varying the number of resources (N) and the density of the underlying communication network topology, as displayed in Table 2.

The maximum density of the underlying communication network topology is given by Equation (33), where N is the set of nodes, or resources, of the network and E is the set of communication links, or edges, between nodes of the network. So, a maximum density of 0.8 means that 20% of the edges have been deleted from the complete network. We note that deleting these edges has the same effect as enforcing that those edges have a maximum bandwidth of 0 over the time-horizon. Also it is important to point out that this gives the maximum density of the network over any given time. In actuality, based on temporal bandwidth parameters defined ('Bandwidth per Directed Edge per Resource' in Table 3), there exist the potential for two nodes to have 0 available direct bandwidth at a given time-step, even though this edge was not explicitly removed from the network. This can be seen as modeling the possibility for a node to be kinematically out of range of another, and hence not able to communicate, or for a node to be operating in 'radio silence' at that

Table 3: Parameter categories and values used for the numerical experiments. For those parameters with only a minimum value, that is the fixed value for the parameter. For those parameters that have a minimum and maximum value, the distribution listed is the probability distribution through which a specific parameter is determined, via a random draw.

Parameter	Min. Value	Max. Value	Dist.
Number Time-Steps	20		
Bandwidth per Directed Edge per Resource	0	100	Uniform
Number of IGRs in Scenario per Resource	5	10	Uniform
Time Delay Between IGR Generation and Consumption	7	20	Uniform
Resources that Neither Generate nor Consume IGRs	$\lceil 0.2 \cdot N \rceil$		
IGR Size	25	250	Uniform
Storage Capacity per Resource	750	1500	Uniform
Granularity Ratio	0.9		
MinSizePercent	0.8		

Table 4: Solution quality analysis, according to Equation (34), for the mathematical formulation using CPLEX, without and with an initial input solution.

		CPLEX w/o Init. Soln.			CPLEX w/ Init. Soln.	
Num. Resources	Density	% Time Opt. Soln. Found	Mean Soln. GAP	% Time Feasible Soln. Not Found	% Time Opt. Soln. Found	Mean Soln. GAP
3	1	80	0.0012	0	80	0.0012
3	0.67	100		0	100	
3	0.33	100		0	100	
4	1	100		0	100	
4	0.67	90	0.0013	0	90	0.0012
4	0.33	90	0.0001	0	90	0.0001
5	1	80	0.0002	0	90	0.0001
5	0.67	60	0.0029	0	50	0.0027
5	0.33	70	0.0006	0	70	0.0006
6	1	60	0.0207	0	50	0.0035
6	0.67	60	0.0022	0	70	0.0093
6	0.33	100		0	100	
8	1	0	0.0343	0	0	0.0133
8	0.67	0	0.0775	0	10	0.0368
8	0.33	20	0.0109	0	20	0.0115
10	1	0	0.1149	0	0	0.0274
10	0.67	0	0.1031	0	0	0.0240
10	0.33	0	0.0636	0	0	0.0890
12	1	0	0.2145	0	0	0.0390
12	0.67	0	0.1308	0	0	0.0349
12	0.33	0	0.3658	0	0	0.2128
15	1	0	0.4977	0	0	0.0678
15	0.67	0	0.2130	0	0	0.0637
15	0.33	0	0.4390	10	0	0.1810
20	1	0	0.9583	90	0	0.2988
20	0.67	0	0.6205	30	0	0.1122
20	0.33	0	0.2709	10	0	0.2507
25	1	0	1.0000	100	0	0.2614
25	0.67	0	1.0000	100	0	0.3739
25	0.33	0	0.3702	10	0	0.2155

time-step, due to external environmental conditions (e.g., weather, topography, etc). In addition, this can model a node failure [35, 36, 37] if a particular node has 0 available bandwidth at a given time over all edges

Table 5: Average normalized distance, computed according to Equation (35), between the heuristic and CPLEX with/without the initial solution, for those cases where CPLEX found at least a feasible solution. Note: An entry is left blank whenever CPLEX was not able to find a feasible solution for any of the scenarios.

Num. Resources	Density	CPLEX w/out Init Soln	CPLEX w/ Init Soln
3	1	-0.132	-0.132
3	0.67	-0.127	-0.127
3	0.33	-0.115	-0.115
4	1	-0.072	-0.072
4	0.67	-0.174	-0.174
4	0.33	-0.330	-0.330
5	1	-0.098	-0.098
5	0.67	-0.194	-0.194
5	0.33	-0.212	-0.212
6	1	-0.071	-0.089
6	0.67	-0.151	-0.145
6	0.33	-0.481	-0.481
8	1	-0.064	-0.085
8	0.67	-0.079	-0.128
8	0.33	-0.400	-0.400
10	1	0.024	-0.071
10	0.67	-0.013	-0.120
10	0.33	-0.281	-0.254
12	1	0.158	-0.066
12	0.67	0.070	-0.100
12	0.33	0.300	-0.102
15	1	0.779	-0.051
15	0.67	0.090	-0.086
15	0.33	0.491	-0.114
20	1	1.186	-0.037
20	0.67	0.536	-0.066
20	0.33	-0.068	-0.108
25	1		-0.035
25	0.67		-0.036
25	0.33	0.109	-0.104

connecting it to other nodes.

$$\text{Density} = \frac{|E|}{|N| \cdot (|N| - 1)} \tag{33}$$

For each combination of number of resources and density, 10 Monte-Carlo scenarios were created randomly. For each scenario generated, the remaining parameters were derived from the information in Table 3, and then kept fixed for the scenario. In addition, the coefficients of the two terms in the objective function (time-delay and size), ω_d and ω_s, were fixed to 0.7 and 0.3 for all scenarios. Each approach (''CPLEX w/o Init. Soln.'', ''CPLEX w/ Init. Soln.'', and the heuristic) were given 900 seconds to solve each scenario instance. For those cases where CPLEX did not solve the problem to optimality within the 900 seconds, the best solution found by CPLEX is considered. We note that there are cases in the tables to follow where CPLEX was not able to find even a feasible solution by the time-limit, hinting at the limitations of commercial software as the size of the problems get large.

Table 4 examines the results just from the exact approach, using CPLEX (without and with an initial solution). For each combination of number of resources and communication network density, columns 3–5 deal with the solution found by CPLEX without an initial solution, while columns 6–7 are concerned with the solution found by CPLEX with an initial solution provided. Columns 3 and 6 show that as the problem size gets larger, CPLEX has a more difficult time in finding the optimal solution. And for most of the problem sizes, in terms of providing an optimal solution, there is no difference between CPLEX without or with an initial solution. Column 5 shows the percentage of times CPLEX without an initial solution is unable to find a feasible solution to the problem. There is always the trivial feasible solution where no IGRs are routed, so CPLEX unable to find a feasible solution means that CPLEX ran out of memory in the creation of the mathematical model. Again this is as expected; as the problems get larger, more variables and constraints are needed, and eventually memory issues are encountered. Columns 4 and 7 show the mean gap between the upper bound on the solution value computed in CPLEX and the best solution found by CPLEX. For each scenario, this gap is computed as in Equation

Table 6: Mean Time Delay between generation and consumption of IGRs chosen to be routed, for each solution approach. For those cases where CPLEX is not able to find a feasible solution within the time-limit for any scenarios, the entry is left blank. The results are shown as mean:standard deviation.

Num. Resources	Density	CPLEX w/out Init Soln	Heuristic	CPLEX w/ Init Soln
3	1	8.956:0.758	5.070:1.120	8.937:0.738
3	0.67	9.691:1.387	4.968:0.897	9.658:1.389
3	0.33	10.223:0.993	4.651:0.722	10.194:0.960
4	1	9.268:0.954	4.105:0.335	9.278:0.952
4	0.67	9.867:0.734	5.059:0.680	9.856:0.697
4	0.33	10.096:1.153	6.036:1.208	10.128:1.168
5	1	9.004:0.676	3.773:0.327	9.030:0.663
5	0.67	9.762:0.779	5.073:0.433	9.735:0.756
5	0.33	9.588:1.137	5.321:0.700	9.595:1.128
6	1	9.300:0.571	4.021:0.296	9.270:0.582
6	0.67	9.502:0.988	5.257:0.345	9.571:0.953
6	0.33	9.925:1.093	6.361:0.861	9.944:1.050
8	1	9.201:0.700	4.016:0.247	9.186:0.639
8	0.67	9.233:0.558	4.704:0.340	9.426:0.830
8	0.33	10.047:0.665	6.433:0.560	10.099:0.667
10	1	9.010:0.560	3.807:0.321	9.248:0.613
10	0.67	8.504:0.580	4.517:0.316	8.788:0.658
10	0.33	9.460:0.457	6.117:0.519	9.928:0.984
12	1	8.632:0.482	3.846:0.234	9.242:0.494
12	0.67	8.950:0.458	4.684:0.313	9.324:0.497
12	0.33	9.362:0.603	6.194:0.334	11.301:0.979
15	1	7.573:0.398	3.820:0.122	9.599:0.288
15	0.67	8.590:0.698	4.411:0.204	9.197:0.570
15	0.33	9.449:1.149	5.924:0.569	11.035:0.874
20	1	7.633:0.000	3.688:0.148	9.692:0.348
20	0.67	7.586:0.312	4.376:0.068	9.961:0.541
20	0.33	8.684:0.512	5.866:0.269	10.534:1.066
25	1		3.721:0.096	9.629:0.312
25	0.67		4.366:0.211	10.469:0.287
25	0.33	8.471:0.424	5.537:0.139	10.359:1.046

(34), where ub is the upper bound on the solution value and sf is the solution found by CPLEX. We note that when CPLEX finds the optimal solution, $ub = sf$ and the GAP is therefore 0, and when CPLEX is not able to find even a feasible solution, we assigned the trivial solution of $sf = 0$ (the worst feasible solution for the model), resulting in a GAP value of 1.

$$GAP = \frac{ub - sf}{ub} \tag{34}$$

What is apparent from Columns 4 and 7 of Table 4 is that CPLEX with an initial solution performs better most of the time as compared to CPLEX without an initial solution. In most cases, there is a significant decrease in the mean gap. However, there are a few cases that are counter-intuitive. Specifically when the number of resources is 6, 8, or 10 and the densities are 0.67, 0.33, or 0.33 respectively. For these three combinations, CPLEX without an initial solution has a smaller mean gap than does CPLEX with an initial solution. This is because there was one scenario in each of these combinations where the heuristic found a solution not close to the optimal, and CPLEX had a difficult time given the heuristic solution as the initial solution, i.e., the heuristic found a local maximum, and CPLEX had a difficult time finding a solution better than this local maximum.

Table 5 shows the average normalized distances between the heuristic solutions and the CPLEX solutions without and with the initial solution. Each normalized distance is computed according to Equation (35), where $\{x_j^h, s_j^h\}$ is the solution found by the heuristic, $\{x_j^c, s_j^c\}$ is the solution to the linearized formulation using CPLEX, and f is the objective function. Since we have a maximization problem, values of Equation (35) larger than 0 indicate that the heuristic is finding a better solution than is CPLEX, while those less than 0 indicate an heuristic solution worse than that found by CPLEX. First off, as expected, all of the values in the last column of Table 5 are negative, because the worst solution 'CPLEX with initial solution' can find is the same solution as found by the heuristic since this is the solution provided as input to CPLEX. For less than 12 resources, CPLEX without an initial solution

Table 7: Average runtime (in seconds) for each solution approach to find a solution. For those cases where CPLEX is not able to find a feasible solution within the time-limit, the returned time by CPLEX is still used in this computation.

Num. Resources	Density	CPLEX w/out Init Soln	Heuristic	CPLEX w/ Init Soln
3	1	218.705	0.002	224.092
3	0.67	48.794	0.000	132.075
3	0.33	10.150	0.000	12.552
4	1	22.205	0.003	30.301
4	0.67	179.300	0.000	190.852
4	0.33	123.936	0.001	155.227
5	1	388.937	0.000	337.506
5	0.67	433.410	0.002	498.094
5	0.33	465.390	0.001	444.524
6	1	469.135	0.002	634.885
6	0.67	595.497	0.002	502.483
6	0.33	109.626	0.000	161.185
8	1	901.857	0.008	901.757
8	0.67	901.863	0.006	865.321
8	0.33	822.245	0.005	761.825
10	1	904.283	0.006	903.338
10	0.67	905.129	0.005	905.198
10	0.33	903.219	0.002	903.443
12	1	904.817	0.011	905.141
12	0.67	905.752	0.003	906.519
12	0.33	905.980	0.003	904.835
15	1	910.124	0.044	910.081
15	0.67	1310.217	0.005	1071.725
15	0.33	1161.690	0.005	1124.190
20	1	2872.113	0.083	2066.906
20	0.67	1283.765	0.009	994.237
20	0.33	958.069	0.005	1153.269
25	1	4612.964	0.128	2845.093
25	0.67	6458.231	0.006	6317.989
25	0.33	1672.833	0.006	1980.635

is also able to find a better solution on average than is the heuristic. However, after this point, for almost all cases the heuristic is finding a better solution than is CPLEX without an initial solution. Again, this is to be expected, because as the size of the problem grows, commercial software will have more difficulty in solving the larger problems and the heuristic will begin to find better solutions. But in comparing the heuristic with CPLEX with an initial solution, the average normalized distance between solutions is never that large on average, showing that the heuristic is able to find a good-quality solution as compared with commercial software.

$$\frac{f\left(x_j^h, s_j^h\right) - f\left(x_j^c, s_j^c\right)}{f\left(x_j^c, s_j^c\right)} \tag{35}$$

Table 6 presents, for those IGRs chosen to be routed, the mean time delay between IGR generation and IGR consumption. Column 3 of Table 6 shows the mean delay for the CPLEX solution when no initial solution is provided, Column 4 shows the mean delay for the heuristic solution, while Column 5 shows the mean delay for the CPLEX solution when an initial solution is provided. As is clear from this table, for those IGRs routed, the heuristic is able to route them much quicker than is CPLEX. This is regardless of the size of the problem. The rationale for this is that the heuristic is choosing IGRs to route in a greedy way, while CPLEX considers the routing of all IGRs simultanously.

Table 7 presents the average runtime for each of the approaches, in seconds. As is clear, the developed heuristic is quite fast in finding solutions for all of the scenario classes. It is also clear that the heuristic takes longer to run on average when the communication network topology is dense as opposed to sparse. Both of the CPLEX approaches take much longer than does the heuristic. Even when the number of resources is as small as 8, these approaches reach (or almost reach) the time limit of 900 seconds. Hence, to get sightly better solutions (according to the objective function) CPLEX needs much more time than does the heuristic. We note that while CPLEX was given a time limit of 900 seconds, there were cases where CPLEX does take

longer to complete. This is due to CPLEX not being able to 'halt' processing exactly when the time limit is reached.

5 Conclusions and Future Research

In this research, we have examined the problem of routing information amongst a set of resources, when there exists a dynamic communication network topology with limited, time-varying, bandwidth, over a given time horizon. A rigorous mathematical formulation was developed to model the problem, with the objective being to minimize the time delay of the information that can be routed while at the same time maximizing the size of the information routed. This formulation is nonlinear, but a linearized version can be derived through standard techniques of operations research. As the problem is NP-hard, a heuristic has been developed to efficiently find good-quality solutions. Numerous Monte-Carlo simulations were performed on problems with varied resources and communication network topology density. As can be seen in the results, for smaller sized problems commercial software is able to find a better solution on average than is the heuristic. And when the commercial software uses as input the solution found by the heuristic, even better results are obtained. As the size of the problem increases, however, the heuristic begins finding much better solutions compared with the commercial software. And even when the commercial software is provided the heuristic solution as input, the commercial software is not able to improves significantly on this solution. Looking at the metric of the actual time-delay for those IGRs chosen to be routed, it is clear that the heuristic is better able to route those chosen IGRs. When coupled with the time needed for the heuristic to find a good quality solution versus the commercial software, it is clear that the heuristic is outperforming the commercial software.

Future research includes looking at specific network topology structures from realistic military and civil applications, considering the related problem of finding the minimum network temporal connectivity necessary to ensure certain information is able to be routed within time bounds, as well as considering the problem from a decentralized control paradigm, when no resource has knowledge about the network as a whole, but rather must consider only local network knowledge and make independent routing decision. In addition, incorporating the concept of network packet errors will provide added complexity and realism to the problem and scenarios considered.

Conflict of Interest The authors declare no conflict of interest.

Acknowledgment This research was Supported by Office of Naval Research Project N00014-15-C-5163.

References

[1] M. J. Hirsch, A. Sadeghnejad, and H. Ortiz-Pena, "Shortest paths for routing information over temporally dynamic communication networks," in *Proceedings of the IEEE Military Communications Conference*, pp. 587–591, 2017.

[2] I. Akyildiz, W. Su, Y. Sankarasubramaniam, and E. Cayirci, "Wireless sensor networks: A survey," *Computer Networks*, vol. 38, pp. 393–422, 2002.

[3] J. Al-Karaki, , and A. Kamal, "Efficient virtual-backbone routing in mobile ad hoc networks," in *Elsevier Computer Networks*, vol. 52, pp. 327–350, 2008.

[4] E. Huang, W. Hu, J. Crowcroft, and I. Wassell, "Towards commercial mobile ad hoc network applications: a radio dispatch system," *6th ACM International Symposium on Mobile Ad Hoc Networking and Computing*, pp. 355–365, 2005.

[5] "Army 18.1 Small Business Innovation Research (SBIR) Proposal Topic 025: An Adaptively Covert, High Capacity RF Communications / Control Link," tech. rep., 2018.

[6] "Air Force 18.1 Small Business Innovation Research (SBIR) Proposal Topic 019: Novel Battle Damage Assessment Using Snesor Networks," tech. rep., 2018.

[7] C. Howard, "UAV command, control, and communication," *Military and Aerospace Electronics*, vol. 24, 2013.

[8] B. Vignac, F. Vanderbeck, and B. Jaumard, "Reformulation and decomposition approached for traffic routing in optical networks," *Networks*, vol. 67, pp. 277–298, 2016.

[9] J. Brodkin, "Tropical storm Harvey takes out 911 centers, cell towers, and cable networks," *ars Technica*, August 28 2017.

[10] L. K. Comfort and T. W. Haase, "Communication, choerence, and collective action: The impage of Hurrican Katrina on the communication infrastructure," *Public Works Management & Policy*, vol. 11, no. 1, pp. 1–16, 2006.

[11] U.S. Air Force, "USAF Strategic Master Plan," tech. rep., 2015.

[12] "Air Force 17.1 Small Business Innovation Research (SBIR) Proposal Topic 047: Resilient Communication for Contested Autonomous Manned/Unmanned Teaming," tech. rep., 2017.

[13] D. L. Hall and J. Llinas, "An introduction to multisensor data fusion," in *Proceedings of the IEEE*, vol. 85-1, pp. 6–23, 1997.

[14] E. Bosse, J. Roy, and S. Wark, eds., *Concepts, Models, and Tools for Information Fusion*. Artech House, 2007.

[15] F. A. A. U.S. Department of Transportation, "Aviation Maintenance Technician Handbook – Airframe, Volume 2," tech. rep., 2012.

[16] "Navy 17.A Small Business Technology Transfer (STTR) Proposal Topic T029: Multi-Vehicle Collaboration with Minimal Communication and Minimal Energy," tech. rep., 2017.

[17] I. Jebadurai, E. Rajsingh, and G. Paulraj, "Enhanced dynamic source routing protocol for detection and prevention of sinkhole attack in mobile ad hoc networks," *International Journal of Network Science*, vol. 1, pp. 63–79, 2016.

[18] U. Paul, M. Buddhikot, and S. Das, "Opportunistic traffic scheduling in cellular data networks," *IEEE International Symposium on Dynamic Spectrum Access Networks*, pp. 339–349, 2012.

[19] J. Al-Karaki, R. Ul-Mustafa, and A. Kamal, "Data aggregation and routing in wireless sensor networks: Optimal and heuristic algorithms," in *Elsevier Computer Networks*, vol. 53, pp. 945–960, 2009.

[20] M. J. Hirsch, H. Ortiz-Pena, R. Nagi, A. Stotz, and M. Sudit, "On the optimization of information workflow," in *Dynamics of Information Systems: Mathematical Foundations* (A. Sorokin, R. Murphey, M. Thai, and P. Pardalos, eds.), vol. 20, pp. 43–65, Springer, 2012.

[21] M. J. Hirsch and H. Ortiz-Pena, "Information supply chain optimization with bandwidth limitations," *International Transactions in Operational Research*, vol. 24, no. 5, pp. 993–1022, 2017.

[22] E. Grotli and T. Johansen, "Path and data transmission planning for cooperating uavs in delay tolerant network," in *Globecom Workshop*, pp. 1568–1573, IEEE, 2012.

[23] S. Basagni, C. Petrioli, R. Petroccia, and M. Stojanovic, "Optimizing network performance through packet fragmentation in multi-hop underwater communications," in *OCEANS*, pp. 1–7, IEEE, 2010.

[24] P. Kansal and A. Bose, "Bandwidth and latency requirements for smart transmission grid applications," *IEEE Transactions on Smart Grid*, vol. 3, pp. 1344–1352, 2012.

[25] M. Greenberg, *Advanced Engineering Mathematics*. Pearson, 2nd ed., 1998.

[26] L. Wolsey, *Integer Programming*. Wiley, 1998.

[27] I. CPLEX, "http://www-01.ibm.com/software/commerce/optimization/cplex-optimizer/," Accessed January 2017.

[28] LINDO, "http://www.lindo.com/," Accessed July 2016.

[29] J. Lenstra and A. R. Kan, "Complexity of vehicle and scheduling problems," *Networks*, vol. 11, pp. 221–227, 1981.

[30] M. Solomon and J. Desrosiers, "Time window constrained routing and scheduling problem," *Transportation Science*, vol. 22, pp. 1–13, 1988.

[31] M. Dror and P. Trudeau, "Split delivery routing," *Naval Research Logistics*, vol. 37, pp. 383–402, 1990.

[32] G. Ausiello, M. Protasi, A. Marchetti-Spaccamela, G. Gambosi, P. Crescenzi, and V. Kann, *Complexity and Approximation: Combinatorial Optimization Problems and Their Approximability Properties*. Springer-Verlag New York, Inc., 1st ed., 1999.

[33] M. R. Garey and D. S. Johnson, *Computers and Intractability: A Guide to the Theory of NP-Completeness*. New York, NY, USA: W. H. Freeman & Co., 1979.

[34] Matlab, "http://www.mathworks.com/products/matlab/," Accessed January 2017.

[35] B. Szymanski, X. Lin, A. Asztalos, and S. Sreenivasan, "Failure dynamics of the global risk network," *Scientific Reports*, vol. 5, pp. 1–14, 2015.

[36] R. Liu, M. Li, and C. Jia, "Cascading failures in coupled networks: The critical role of node-coupling strength across networks," *Scientific Reports*, vol. 6, pp. 1–6, 2016.

[37] K. Kim, J. Jin, and S. Jin, "Classification between failed nodes and left nodes in mobile asset tracking systems," *Sensors*, vol. 16, pp. 1–18, 2016.

ASTES

Advances in Science, Technology and Engineering Systems Journal Vol. 3, No. 4, 341-346 (2018)

www.astesj.com

ASTESJ

ISSN: 2415-6698

Application of Modularization Idea of Fault Tree in Ship Pilotage Risk Decision Making

Wei Hongbin*

China waterborne transport research institute, shipping technology research center, 100088, China

ARTICLE INFO

Article history:
Received: 27 June, 2018
Accepted: 12 August, 2018
Online: 21 August, 2018

Keywords:
Ship pilotage risk
Dynamic fault trees(DFT)
Binary Decision Diagram (BDD)
Modular Fault Tree (MFT)
Markov models

ABSTRACT

Ship pilotage risk decision-making problems, which is an important issue affecting the safety of navigation. Before the study on the risk decision of ship pilotage, all use direct analysis of fault tree methods. In this paper, through the process analysis of ship pilotage fault tree, the model of fault tree is standardized and simplified. The traditional method solves the fault tree directly, obtains the ship pilotage risk analysis result, in this paper, use modular decomposition fault tree. Combined with the characteristics of no recurrence events in ship pilotage risk fault tree, the Modular Fault Tree (MFT) method is used to decompose the fault tree into static sub module and dynamic sub module. It solves the fault tree for computation reduction difficulty. Solve static fault tree with Binary Decision Diagram (BDD) method, solve dynamic fault tree with Markov Model Method, and make qualitative and quantitative analysis separately. Then synthesize the result, get the critical path and key event that cause the ship pilotage risk. The results can be used in the design of ship pilotage scheme, post training of ship pilots, or be provided recommendations to ship pilotage and maritime safety authorities for risk reduction.

1. Introduction

The piloting of ships is an indispensable part of port security and services, an important part of international shipping, and the first image of a country. With the acceleration of the construction and commissioning of a large number of large-scale berths and the acceleration of large-scale ships, the safety of ship piloting has received increasing attention. Pilotage agencies have formulated the "Navigation Pilot Safety Management System" based on their own operations. The safety precautions for ship pilotage must be internally and externally repaired. While building the internal management system of the piloting organization and improving the pilotage technical level, it is necessary to coordinate and master the changes in the external environment and to prevent the occurrence of the piloting safety accident to the greatest extent possible. The study of ship pilotage risk project has important practical significance and has a strong guiding role in preventing the occurrence of ship pilotage accidents. Risk assessment is the quantitative assessment of the degree of impact or loss brought about by an event or thing. A large number of scholars have already conducted research on the risk assessment of ship pilotage.

1.1. Method

In the application of ship pilotage risk methods, In [1], the author used FMEA Method and DFT analysis of ship pilotage risk. In [2], the author used FTA Method analysis of ship pilotage risk. In [3], the author analysis of ship pilotage risk based on the case of ship pilot accident. The researchers used the FTA method to analysis system failures and risks, and propose solutions based on the results for the corresponding risks [4] [5] [6]. In [7], the author used risk matrix and risk criteria. In [8], the researcher used gray comprehensive evaluation model. In [9], the author used the unknown measure model and the confidence identification criterion. In [10], the presenter used the Bayesian method. In [2], the author established a ship pilotage risk analysis model based on the SHELL model, Li Fen use the A.D. Hall models to do the system analysis [11]. The author uses Synergy-based mode to study the management risk of marine traffic [12] [13]. In [1], the researcher proposed model based on A.D. Hall models. However, the study of the module decomposition method applied to the analysis of ship's piloting risk fault tree is still in the blank.

This paper first simplifies the fault tree construction process. By using the module decomposition method, the complex fault tree is decomposed into independent submodules that can be reduced in dimension, and the appropriate method is used to solve the submodules.

The module decomposition method is used, the top-down or bottom-up combination method is used, MTF method is used to solve the fault-free tree which have no duplicate events. Independent modules can be divided into static modules and dynamic modules. The basic operations of the BDD method are

*Corresponding Author: Wei Hongbin, No.8 Xitucheng Road, Haidian District, Beijing, Email: hrbeuweihongbin@163.com

introduced. The BDD method is used to solve the static fault tree module. Through qualitative and quantitative analysis, the cut set of each static submodule is obtained. The Markov model concept is used, which is used to convert DFT to Markov chain, and the cut set of each dynamic sub-module is obtained through analysis. At last individual modules result is synthesized. Comparing the calculation process and results of module decomposition and non-use, the module decomposition method has high usability and high computing efficiency.

2. FTA Construction Process

The fault tree construction process is shown in the figure. It mainly includes analyzing the event background, determining the top event, determining the basic event, establishing the fault tree, and standardizing and simplifying. For detail, see figure 1.

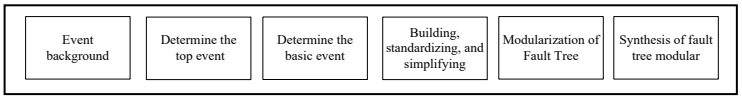

Figure1: Dynamic fault tree construction flow chart

2.1. Event background

Establishing a fault tree first requires a clear structure, condition, purpose, and content. By understanding the background of shipboard piloting risk events and the structure, then environmental conditions of the incidents will be mastered; the impact of subjective and objective factors on the occurrence of the incidents will be identified, the possible transitions between modes and modes of the incidents will be identified, and the failure modes will be identified. Ship pilotage has internal and external risk.

2.2. Determine the top event

A fault tree that meets a variety of different needs is built for different goals. The goals mentioned here are top events. The top event should have a clear definition. When there are many events that are not expected to occur in the system, one or more of the most undesirable events need to be selected as the top event of dynamic fault tree analysis. In the process of establishing the top event, you can use the RPN method to identify the most undesirable events. Collision is as the Ship pilotage risk top event[1].

2.3. Determine the basic event

The basic event is the lowest level cause of the failure of the system, and it is the input parameter of qualitative and quantitative analysis of the system's risk. The granularity of the basic event directly determines the complexity of the dynamic fault tree. Basic events are usually modules that are not easily split in the system, as well as human factors and environmental factors. In the process of establishing a basic event, you can use the FMEA method to identify the lowest event that affects the top event[1]. The Fault tree of Ship pilotage risk has fifteen basic events.

2.4. Building, standardizing, and simplifying

The general method of building trees is divided into two categories: deductive method and computer-aided tree-building method. The second method is that people input relevant basic events and their relationships and are automatically generated by computer programs. The deductive method is the most commonly used method of dynamic fault tree construction, starting from the top event, from top to bottom, following the step-by-step principle until the lowest row of cause events are bottom events. The resulting graph representing these logical relationships is a dynamic fault tree. The specification and simplification are intended to not change the logical functions that they represent, and try to make the fault tree contain only simple typical logic gates for subsequent fault tree solving. The specification and simplified fault tree can be seen from Appendix figure 8. The Fault tree of Ship pilotage risk has been build, and the event can be seen from Appendix table 3[1].

2.5. Modularization of Fault Tree

For complex large fault trees, due to the large scale of their Markov model, the exact processing of Markov chains is almost impossible. Modular thinking applied to dynamic fault tree analysis. Find out the independent static subtrees and dynamic subtrees in the dynamic fault tree [14]. The Fault tree of Ship pilotage risk is decomposed static subtrees and dynamic subtrees.

2.6. Synthesis of fault tree modular

Assume that the bottom event of the dynamic fault tree is, where $\{X_1, X_2, ...X_n\}$ the dynamic fault tree can be expressed as [14] [15]

$$f = f_1(X_1, X_2, ...X_n) \quad (1)$$

The dynamic fault tree is preprocessed and modularized, and it contains the static subtrees are, $S_1, S_2, ...S_n$, and the dynamic subtrees are $D_1, D_2, ...D_n$,then the dynamic fault tree can be written as [14] [15]

$$f = f_1(X_1, X_2, ...X_n, S_1, S_2, ...S_n, D_1, D_2, ...D_n) \quad (2)$$

3. Modularization of Fault Tree

Due to the increase in the complexity of the fault tree, the difficulty of the solution increases during the fault tree computation. Modularity reduces computational complexity. Therefore, we apply the modularization idea to dynamic fault tree analysis to find independent static subtrees and dynamic subtrees in the dynamic fault tree, apply algorithms to the static subtrees, and use the Markov chain for dynamic subtrees. The methods are analyzed separately. Finally, the results of each module are integrated to obtain the results we need. This method is a dynamic fault tree analysis method based on the modular idea.

3.1. The basic idea of MFT method

The MFT method performs depth-first traversal of the fault tree. First, for each intermediate event, decide whether it contains independent modules. If there is a separate module, then it enters the intermediate event traversal, if there is no independent module and the intermediate event itself is independent, the intermediate event is solved using a suitable method according to the characteristics of the module. Then replace the intermediate event with the basic event, and use the failure probability of the intermediate event as the failure probability of the replacement

basic event. Then return to the previous point to traverse again. If each independent module under an intermediate event has been solved and replaced with a basic event, continue to check if the intermediate event is an independent module: If so, based on the current module characteristics of the intermediate event, the appropriate method is used to solve the failure probability. Replace the sub-tree with the intermediate event as the top event with a basic event, and repeat until the top event can be solved.

3.2. Specific operation

Uses the MFT method decompose the fault tree module. In the module decomposition process, dynamic subtrees are no longer subdivided when dynamic logic gates are encountered. Applying the MFT method to the fault tree in Appendix figure 8, we first perform a deep traversal from the top event NO.11; because there is an independent subtree under NO.11, the below flag is true. Then entry node NO.11 continues to traverse and the next check is NO.24, which is in the NO.11 leftmost input. Although there are independent subtrees under NO.24, there are dynamic gates under NO.24.For the dynamic subtree with NO.24 as the top event, use the Markov chain model to solve the problem. It is also replaced by a dynamic independent module M1 whose failure probability is the solution value of the Markov chain model. Although there are independent subtrees under NO.24, there are dynamic gates under NO.24.For the dynamic subtree with NO.24 as the top event, use the Markov chain model to solve the problem. It is also replaced by a dynamic independent module M1 whose failure probability is the solution value of the Markov chain model. Therefore, the below flag is set to false, and then NO.23 is converted to the BDD model. And use the BDD solver to solve. According to the traversal result, the fault tree module is {NO.11, M1, M2, M3}, where {M1, M2} is a dynamic submodule, where {M3} is a static submodule and NO.11 is M1, M2, M3 is the static module M4 of the bottom event. Therefore, the fault tree modules M3 and M4 are solved using the BDD method, and the fault tree modules M1 and M2 are solved using the MARKOV chain method.

4. BDD Based Static Fault Tree (SFT) Analysis

The BDD method is an efficient method for analyzing static fault tree (SFT).BDD transforms a fault tree into a BDD map with only the bottom events. Without the aid of intermediate events, BDD Boolean function expressions can be directly used for qualitative analysis and quantitative analysis. The minimum cut set is obtained by the disjoint expression of the Boolean function. The BDD method has a linear relationship with the amount of BDD graphics. Effectively solve the problem of exponential growth in the computational complexity of the traditional FTA method and the size of the fault tree[14][15].

4.1. Composition method

The basic idea of compositional composition method is "modularization" first. The gate node that has only the bottom event input is represented as a BDD structure. Then regard these gates that have been expressed as BDD as the input of the upper level logic gates. Layer by layer until the top event is expressed by the BDD structure. In the composition method, combination and simplification are based on the following principles. The basic event BDD conversion is relatively simple, as shown in the following figure, the left node is 0, and the right node is 1.for detail see figure 2.

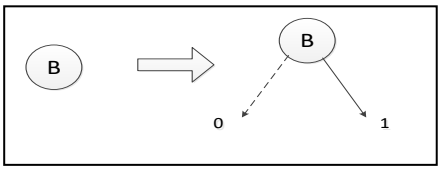

Figure 2: BDD conversion of basic events

For an OR gate in the form of B+C, Assuming B is the top node, C is B left and right nodes. The conversion steps are shown from figure 3.

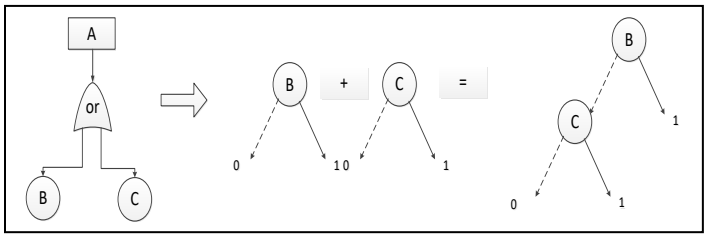

Figure 3: BDD conversion of or door modules

Through qualitative analysis，The cut set of basic events is {B}、{C}.

4.2. Specific operation

The fault tree modules M3 is the static module, for the static module, use BDD method. The conversion steps are shown from figure 4.

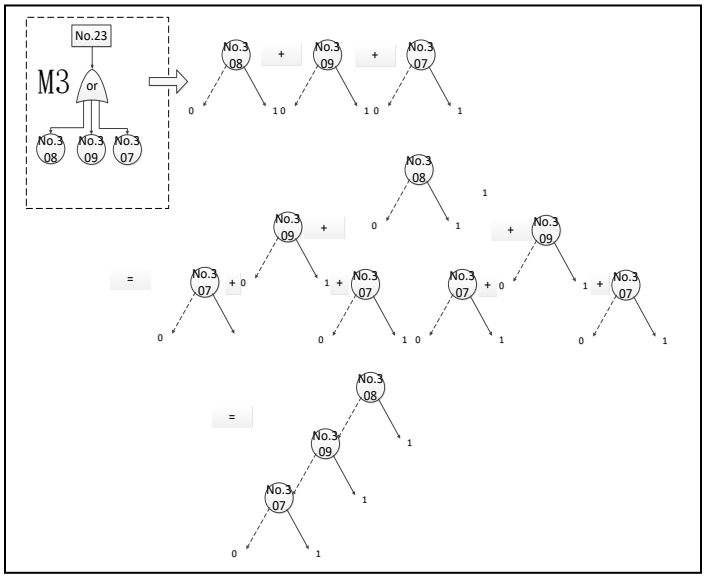

Figure 4: BDD conversion of M3 submodules

Through qualitative analysis，The cut set of basic events is {No.307}、{No.308}、{No.309}.

The fault tree modules M4 is the static module, for the static module, use BDD method. The conversion steps are shown from figure 5.

Through qualitative analysis，The cut set of basic events is {M1}、{M2}、{M3}.

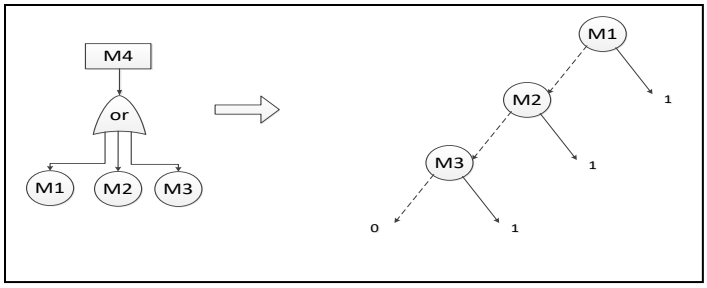

Figure 5: BDD conversion of M4 submodules

5. Markov-based DFT Analysis

The Markov process is a stochastic process. From the current determination of the future behavior of the process, it is the relationship between the "state" and "state" of the system. In a random process, if at a certain moment, the transition probability from one state to another is only related to what state it is now. And it is completely irrelevant to the state it was in before this moment, That is, this transition probability is only related to the current state, and has nothing to do with the state before a finite number of times. This process is called Markov process to analyze the dynamic subtree in the modular fault tree[16][17].

The fault tree modules M1 is the dynamic module, for the dynamic module use Markov model. See figure 6 for detail.

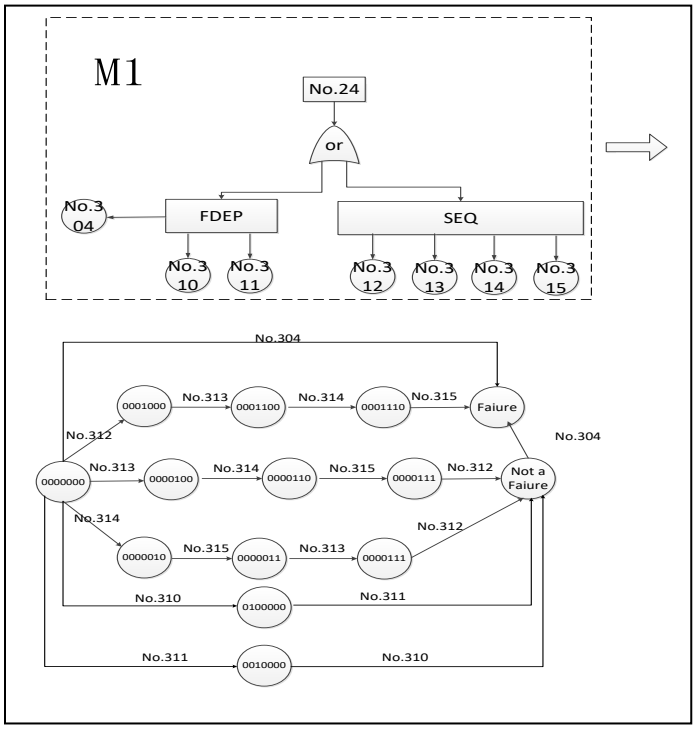

Figure 6: Markov conversion of M1 submodule

Through qualitative analysis，The cut set of basic events is {No.304}、{No.312、No.313、No.314、No.315}.

The fault tree modules M2 is the dynamic module, for the dynamic module use Markov model. See figure 7 for detail.

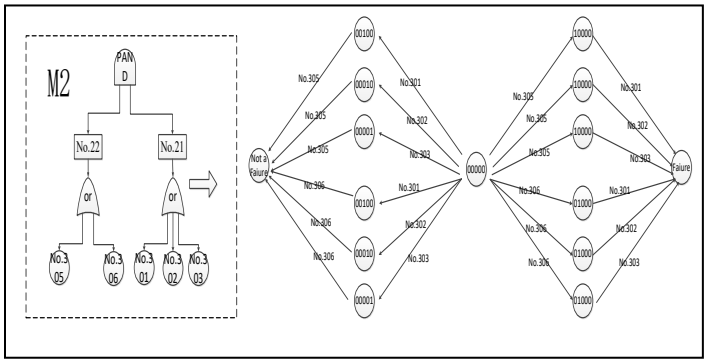

Figure 7: Markov conversion of M2 submodule

Through qualitative analysis，The cut set of basic events is {No.305、No.301}、{No.306、No.301}、{No.305、No.302}、{No.306、No.302}、{No.305、No.303}、{No.306、No.303}.

6. Synthesis of fault tree

Based on SFT and DFT Analysis, the fault tree have four submodules, and every submodule has the cut set of basic events.M4 submodule has the top event.

Table 1. The synthesis sequence cut set of fault tree

The fault tree submodules	The cut set of basic events
M1	{No.304}、{No.312、No.313、No.314、No.315}
M2	{No.305、No.301}、{No.306、No.301}、{No.305、No.302}、{No.306、No.302}、{No.305、No.303}、{No.306、No.303}
M3	{No.307}、{No.308}、{No.309}
M4	{M1}、{M2}、{M3}

From the above results, we can see that the fault tree have four modules and have 14 sequence cut sets, and there are at least 14 ways to lead to the top fault event.in the 14 sequence cut sets, the least one is {No.304}, which contains the least number from the qualitative analysis, and also is the most important structure of bottom events, which should be strengthen security measures to avoid incidents.

7. Comparisons and analysis

The resolution of a DFT is much different than the one of the SFT, because temporal and cross dependencies cannot be modelled and solved through Boolean algebra [17].In these paper the DFT is converted to Markov chain，which can be used to solve the dynamic the sequence cut sets of the fault tree, and the SFT is converted to BDD. Based on SFT and DFT Analysis, the fault tree has four submodules, and the SFT has 3 events.

Table 2. A comparison of the number of dynamic fault tree events

	Direct	After modularization
Number	15	12

From the above results, through modularization, the number of dynamic fault tree events is reduced from 15 to 12. The computation of the DFT has been reduced. Because the events of the dynamic fault tree have sequential dependencies, the numerical combination method cannot be used to solve the problem. In general, Markov model is used to solve the problem. However, the number of states involved in the Markov model is exponentially related to the basic events. The number of basic events of the dynamic fault tree is reduced. This reduces the number of states involved in the Markov model. Thus the computational complexity is reduced.

8. Conclusion

Through the analysis of the fault tree construction process, the fault tree analysis model is simplified and the modular idea is adopted. This simplifies the calculation of the fault number.

Modular decomposition results in mutually independent static submodules and dynamic submodules. BDD method is used to decompose the static fault tree, and the dynamic fault tree is decomposed by Markov model method. Then the results are combined. The computational process shows that compared with the modular decomposition of the fault tree, the analysis efficiency are greatly improved.

The fault tree computation solution process is simplified compared to previous studies. When the fault tree is solved, the static fault tree module is first decomposed and processed from the total fault tree, and the original fault tree consisting of 20 events and 8 gates is decomposed into four independent submodules. Two of them are Static fault tree module, 2 are dynamic fault tree modules, 2 static fault tree submodules contain 6 events and 2 gates, and 2 dynamic fault tree submodules contain 15 events and 6 gates. The dynamic module uses the Markov method to calculate the large-scale process. After the modular decomposition, the fault tree uses the Markov method to reduce the number of incidents from 20 to 15 and from 8 to 6 to reduce the computation. The calculation results are the same as those of the previous study, confirming the availability of the module decomposition method.

9. Results & Discussion.

By using a dynamic fault tree analysis method based on modular thinking, the failure tree analysis of ship pilotage risk is carried out, and the use of a new fault tree analysis method is emphasized, which can effectively reduce the dynamic fault tree analysis calculation. The problem of modular decomposition of fault tree is solved, such as the module decomposition of fault tree, the transformation of static subtree, the combination of dynamic fault tree module and static fault tree module. And the concrete application of ship pilotage risk fault tree is given. This paper compares and analyzes the direct solution of fault tree and module to solve the fault tree, and proves the simplicity and practicability of the new method by the practical calculation of the fault tree of ship pilotage risk.

However, a simplified calculation method is used to solve the dynamic fault tree model (FTM) of ship pilotage risk, the application of complex FTM is still very difficult, in the future, a similar and much simpler analysis would be provided.

Conflict of Interest

The authors declare no conflict of interest.

References

[1] Wei Hongbin, “DFT analysis of Ship pilotage risk based on A.D. Hall models” in 2017 6th International Conference on Transportation and Traffic Engineering, Hong Kong, China, 2017. https://doi.org/10.1051/matecconf/201712404010

[2] Xuan Shaoyong, “FSA and Its Application in Ship Pilotage Safety,” MASTER Thesis, Shanghai Maritime University, 2005.

[3] Xue Yi dong, “Human Errors and Prevention of Accidents in Ship-pilotage,” NAVIGATION OF CHINA, **19**(03), 28-32, 2005. http://dx.chinadoi.cn/10.3969/j.issn.1000-4653.2005.03.007

[4] Lin Tie liang, “Construction of Fault Tree Based on Records of Ship Impact Against Bridges,” JOURNAL OF TONG JI UNIVERSITY(NATURAL SCIENCE), 34(4), 467-471, 2006.http://dx.chinadoi.cn/10.3321/j.issn:0253-74X.2006.04.008.

[5] Bai Xu, “Process Risk Analysis of Lifting Transportation for Offshore Structure Based on FMEA and FTA,”.SHIP BUILDING OF CHINA,0(4), 171-179. 2012. http://dx.chinadoi.cn/ 10.3969/j.issn.1000-4882.2012.04.022.

[6] Zhang Qing, “Failure risk analysis on intelligent brakesbased on FMEA and FTA,” CHINESE JOURNAL OF CONSTRUCTION MACHINERY, 14(2), 109-113,2016. http://dx.chinadoi.cn/10.3969/j.issn.1672-5581.2016.02.004.

[7] FANG Quan-gen. “Application of formal safety assessment to the risk assessment of the ship-pilotage,” Journal of Harbin Engineering University, **27**(03), 329-334, 2006. http://dx.chinadoi.cn/10.3969/j.issn.1006-7043.2006.03.003

[8] Zhou Lili, “Grey assessment model on risk factors of ship pilotage,” Journal of Shanghai Maritime University, 29(02), 21-25, 2008. http://dx.chinadoi.cn/10.3969/j.issn.1672-9498.2008.02.005

[9] XI Yong-tao, “Preliminary Risk Assessment on Pilotage Water Area Based on Unascertained Measure,” SHIP & OCEAN ENGINEERING, 38(01), 56-58, 2009. http://dx.chinadoi.cn/10.3963/j.issn.1671-7953.2009.01.017

[10] Fang Cheng, “Risk Prediction of Ship Pilotage in Harbor,” NAVIGATION OF CHINA, 31(04), 388-391, 2008.http://dx.chinadoi.cn/10.3969/j.issn.1000-4653.2008.04.017

[11] Li Fen, Jichang Ming, Liu Yuan, Kingjian. Research on risk assessment method of a.d.hall system of Water conservancy and hydroelectric project based on analytic hierarchy process [J]. water resources and hydropower engineering,41 (03), 50-52 , 2010.http://dx.chinadoi.cn/ 10.3969/j.issn.1000-0860.2010.03.013

[12] J Zhang, Q Fang, S Hu. Synergic Mode of Grid-based Traffic Risk Control in China’s Coastal Waters. 2010 IEEE International Conference on Industrial Engineering and Engineering Management, Dec, 2010 .https://doi.org/10.1109/ieem.2010.5674148

[13] Q Fang, T Xi, S Hu. Synergic mode for marine traffic risk management based on levels and periods synergic modes. Journal of Shanghai Maritime University. 30(3) , 50-55,2009. http://dx.chinadoi.cn/ 10.3969/j.issn.1672-9498.2009.03.012

[14] Liu dong, Methodologies of Dynamic Fault Tree Analysis, national defense industry press, 2013.

[15] Liu Wenbin, “Research on Dynamic Fault Tree Analysis Method Based on Modular Idea,” MASTER Thesis, Nanjing University of Science and Technology, 2009.

[16] Manno, Gabriele, “MatCarloRe: An integrated FT and Monte Carlo Simulink tool for the reliability assessment of dynamic fault tree,” Expert Systems with Applications, 39(01), 10334–10342 , 2012. https://doi.org/10.1016/j.eswa.2011.12.020

[17] K. Durga Rao, “Dynamic fault tree analysis using Monte Carlo simulation in probabilistic safety assessment,” E Reliability Engineering and System Safety, 94(01), 872–883 , 2009. https://doi.org/10.1016/j.ress.2008.09.007

Appendix

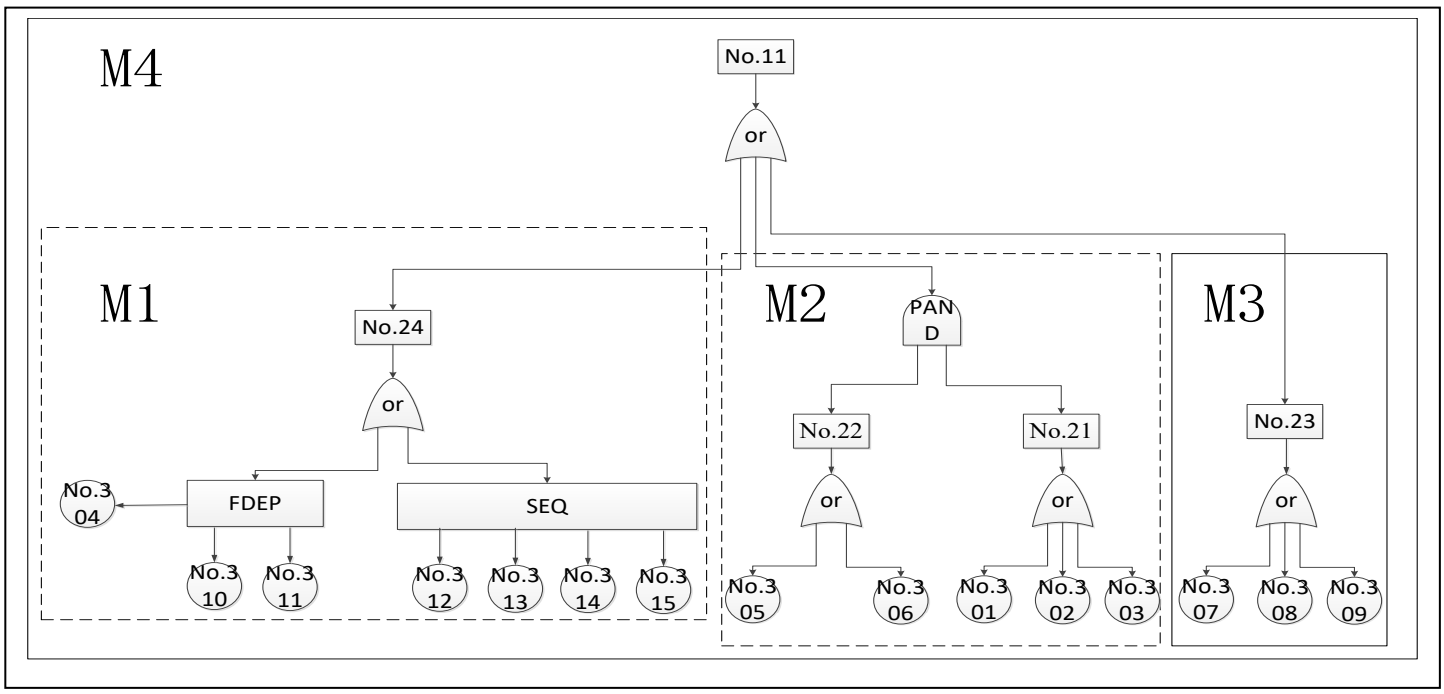

Figure 8: Fault tree figure

Table 3. Fault tree table.

Top event	The first floor	the second floor
No.11 Collision	No.21 software	No.301 Insufficient information exchange with the piloting ship
		No.302 Contact with the other ship failure
		No.303 Contact with tug failure
		No.304 No emergency plan
	No.22 hardware	No.305 Piloting ship - ship fault
		No.306 Passage past ship - ship fault
	No.23 Environment	No.307 Poor visibility
		No.308 Wind
		No.309 Flow
	No.24 Human	No.310 Emergency handling fault
		No.311 Emergency action is not enough
		No.312 Careless alert
		No.313 Collision risk Judgment error
		No.314 Shipping position Control error
		No.315 Collision avoidance action fault

ASTES

Advances in Science, Technology and Engineering Systems Journal Vol. 3, No. 4, 347-353 (2018)

www.astesj.com

Special Issue on Recent Advances in Engineering Systems

ASTESJ

ISSN: 2415-6698

Zebrafish Larvae Classification based on Decision Tree Model: A Comparative Analysis

Bayan AlSaaidah[*,1], Waleed Al-Nuaimy[2], Mohammed Rasoul Al-Hadidi[3], Iain Young[4]

[1]*Department of Electrical Engineering and Electronics, University of Liverpool, Liverpool, L69 3GJ, UK*

[2]*Department of Electrical Engineering and Electronics, University of Liverpool, Liverpool, UK*

[3]*Department of Computer Engineering, Al-Balqa Applied University, Al-Salt, Jordan*

[4]*Institute of Integrative Biology, University of Liverpool, Liverpool, UK*

ARTICLE INFO

Article history:
Received: 18 July, 2018
Revised: 09 August, 2018
Accepted: 21 August, 2018

Keywords:
Classification
CART Model
Feature Extraction
Zebrafish

ABSTRACT

Screening the abnormal development of the zebrafish embryos before and after being hatched for a large number of samples is always carried out manually. The manual process is presented as a tedious work and low-throughput. The single female fish produce hundreds of eggs in every single mating process, the samples of the zebrafish embryos should be studied and analyzed within a short time according to the fast response of their bodies and the ethical regulations. The limited number of the automatic screening systems for aquaculture experiments encourage researchers to find out a high-throughput screening systems with a fast prediction results according to the large number of experimental samples. This work aims to design an automatic segmentation, classification system for zebrafish eggs using two ways for feature extraction and also a classifier. Using the whole image generally with several feature vectors useful for detection process, this way does not depend on the type of the image. The second way focus on specific characteristics of the image which are the colour and the texture features relating to the system purposes. Two different ways for feature extraction integrated by the Classification And Regression Tree (CART) classifier are proposed, analysed, and qualified by comparing the two methods performance and accuracies. The experimental results for zebrafish eggs classification into three distinct classes: live egg, live embryo, dead egg show higher accuracy using the texture and colour feature extraction with an accuracy 97% without any manual intervention. The proposed system results very promising for another type of classification such as the zebrafish larva deformations.

1. Introduction

This paper is an extended work for the published paper in International Conference on Information and Communication Systems (ICICS) [1]. The proposed procedure is a part of an integrated detection, classification, counting system for zebrafish embryo malformations. After adding different chemical substances with different concentration, several deformation types appear on the larva body whether before or after being hatched. The malformations classified depending on the affected part such as the tail curvature, necrosed yolk, and the dead larva. Over the

recent years the zebrafish has become one of the most common animal models. This is due to many factors including a high degree of genetic similarity with humans, short generation times, transparent larval stages, extensively annotated genome and simple husbandry [2][3]. Zebrafish are now widely used in drug development, to measure the impact of environmental changes, of toxins and pollutants and many other applications. However, the use mammals in the biological experiment is expensive and laborious, it also led to an increasing number of

* Bayan AlSaaidah, University of Liverpool, Email: bayan@liv.ac.uk

ethical issues for toxicological research, and that have been limited in large-scale screening efforts [4].

The standard protocols, laws, and regulations for animal protection have been submitted to use zebrafish larvae in the experiment instead of using the adult and also with a specific age depending on the degree of the acuteness of the added materials, as only larvae less than five days after fertilization are exempt from this legislation [5][6]. Screening zebrafish larvae development and evaluating the effects of the chemical compounds is started from the early ages of the samples. This process is carried out manually for a large number of samples. After each mating time, the single female can produce hundreds of eggs [7] that differ depending on their hormones [8].

In [9], the author segmented the embryos from the collected images and classify the sample into live or coagulated using Bayes classifier. However, the image gathering process was carried out using camera over the microscope, this way need to be aware about several factors like illumination and the focal point for high performance capturing process. The capturing process is carried out using different focal points till reach the suitable one. The proposed classification algorithm was Bayes model using colour and shape features. The same dataset of [9] was used by [10] to classify the images into healthy and coagulated eggs. This texture features were extracted using Segmentation-based Fractal Texture Analysis (SFTA) with the rotation forest classifier.

Using video analysis for zebrafish embryos was proposed in [11] to classify if the sample is alive or dead. By detecting the zebrafish embryo heart position and analysing the intensity variation of the heart, if the cyclic motion areas are zero then the sample will be considered as dead embryo.

Despite the rapid growth in the use of zebrafish embryos as an experimental model, there is still a lack of automated classification systems according to several challenges. Screening the zebrafish eggs and larvae abnormalities within one system where the zebrafish embryos grow in a fast way and hatched within few hours. To overcome this limitation global features can be extracted regardless the type of image. The samples may slide to the edges of the petri dish this can affect the detection process. To address this problem a fixed platform is used which is a flatbed scanner with the samples container.

Another challenge is presented by unwanted objects such as the debris or food particles, as these can interfere with the detection process. To avoid this problem pre-processing operations and robust shape with colour thresholding processes are applied. The fast development of the zebrafish embryos lead to have two classes of the live embryos which have different age and different features, one of them is transparent and the other having a completed growing embryo. To address this challenge, robust and consistent different texture and colour features are extracted and used for classification purposes.

The lack of automated capture systems limit the development of a fully automated system. Using the proposed platform which is affordable and easy to use, the images are collected automatically and the biologist only need to place the dish on the scanning area.

2. Experiment and Methodology

The proposed methods aim to identify the status of zebrafish eggs using two different methods of feature extraction. The images are comprised of many features which could be extracted aautomatically or manually. These two types of feature extraction are applied and analysed for the system purposes. The collected images were gathered using a scanner collecting a large number of high resolution images (suitable for biological observation) every scan facilitating high-throughput analysis. The images were classified as: live egg, dead egg or live embryo. The scanning process is always carried out synchronously with the biological experiments. Experiments ran for up to five days post fertilization (after which the embryos become protected) during which time chemical (e.g. application of different chemicals to the holding water) or physical interventions (e.g. temperature) can be applied. The images were prepared and subdivided into three different categories for the software design step.

2.1. Data Collection

The sample images that were used in this work were collected from dish containing a hundreds of zebrafish eggs. The dish images were used in [1] for counting purposes and have been collected by the authors during several biological experiments in the Institute of Integrative Biology laboratories at the University of Liverpool in collaboration with the colleagues in this Institute. The eggs were subjected to a number of chemical substances such as: Dimethyl sulfoxide (DMSO), Alcohol, the waste nitrogenous compounds Ammonia, (Sodium) Nitrite, (Sodium) Nitrate and metals such as Copper (Sulphate) as well as antimicrobial aquarium treatments.

The images were collected using a flatbed document scanner with a high speed scanning for a petri dish of 100mm diameter. The benefit of using a scanner were manifold. The scanner has its own source of illumination and a fixed focal length, therefore, there is no need to consider the exposure or focus on the capturing process. The scanner provides the biologist hundreds of sample images in one scan where the traditional way for collecting images in the proposed systems is always carried on using camera with a microscope which is considered as a time consuming process. Figure 1 shows an example of the collected scanner images. The images that have been used in the proposed classifier were gathered from the dish images.

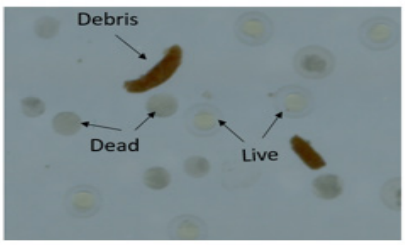

Figure 1: Part of scanner image with hundreds of eggs

Depending on the egg detection process, the samples are cropped using the egg centres and diameters. The egg detection process starts by Canny edge detection function using a threshold produced from a Sobel edge detection function. This process is followed by several morphological operations. Finally, the circles with specific range of radius are extracted from the whole image. The resulting images are collected and have been used to classify them into three classes as resulting from the biological experiments. Figure 2 shows an example from the collected images from the three classes. The live eggs between 0-40 hpf (hours post fertilization) are transparent and looks like a yellow circle. The dead eggs are white and appear dark. The last class which present a bigger embryo with more than 48hpf and before hatching.

Figure 2: Scanner images of three classes :(a) Live egg. (b) Live embryo. (c)Dead egg

2.2. Experiment

In this work, two methods of feature extraction are proposed, analysed, and assessed to develop a high performance classification system. The first method depends up on the image pixel values after splitting each colour image into multiple sub-images, while the second method deals with the sample objects and extracts the most important colour and texture features. With these two different ways the same classifier type with the same parameters is used such as the number of trees of the CART model. These two scenarios are briefly illustrated in the following two sections.

2.3. Colour and Texture Features

Traditionally, feature extraction is one of the most important steps in object recognition. The process of feature extraction uses the most valuable characteristics of the image and converts them into numeric representations. The first proposed method for our system is shown in Figure 3.

2.3.1. Image Pre-Processing

The collected images for the proposed classification system are 1211 images from the three classes live egg, live embryo, and dead egg. Several image processing operations are applied as shown in Figure 4 to segment the sample object from the whole image to make sure that the most important and useful features will be extracted where the image may contain debris and unwanted objects. These operations start with the edge detection process using Canny filter. After detection of the edges, some dilation using a disk mask with two pixels is done. To remove any unwanted objects, the largest object is segmented depending on the object areas. The resulting image is produced from the gray image multiplied by largest object binary image to keep the target object information. The processed images have been used in the next steps to extract the features using two different ways. These features are used to train the classifier how to predict and classify the three classes.

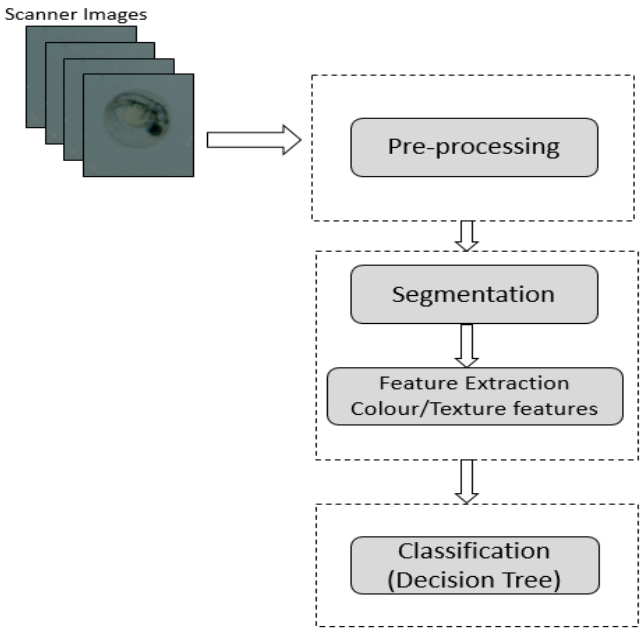

Figure 3: First scenario for classification

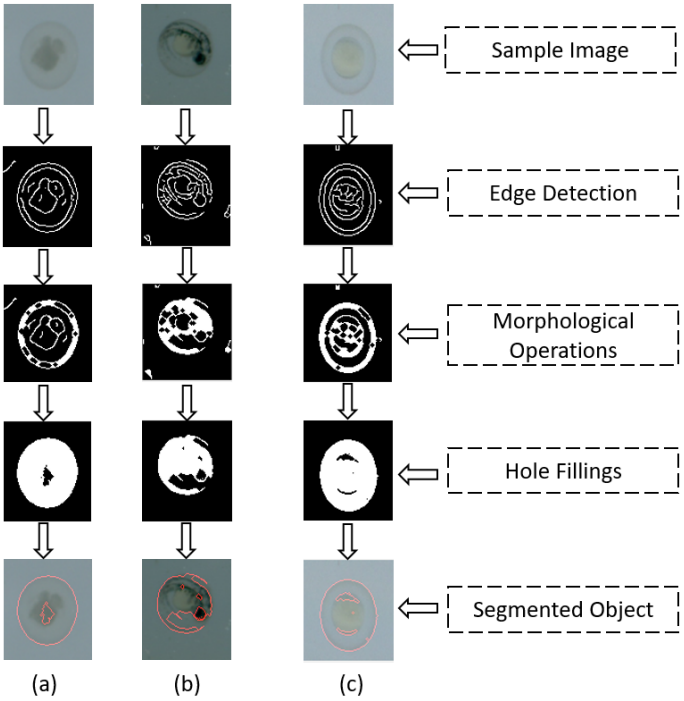

Figure 4: Object segmentation :(a)Dead egg. (b)Live embryo. (c)Live egg

2.3.2. Feature Extraction

The first attempt was done by focusing on two first order colour features of the egg according to the colour variance between the three classes. According to the colour similarity between the dead and the embryo classes, 22 texture features are

extracted from the egg images. The texture features are useful for the classification process when a wide variation of the gray levels are present in the image. Combining first and second order features aims to have robust features for classifier training step. The feature vector consists of 24 features for colour and texture image characteristics. For the image *I* of *n*x*m* in size, the mean and the standard deviation values are calculated as follows:

$$mean = \frac{\sum_{i=1}^{n}\sum_{j=1}^{m} I_{ij}}{mn} \quad (1)$$

$$std = \sqrt{\frac{1}{mn}\sum_{i=1}^{n}\sum_{j=1}^{m}(I_{ij} - mean)^2} \quad (2)$$

The first order features provide a basic information about the gray level distribution. However, the relative positions of these gray levels have not been provided by the first order features. The second order features describe and analyse if the low gray levels are together or mixed with the high gray levels. These features are calculated as proposed and illustrated in [12] [13] [14]. The second order statistics are calculated depending on a matrix $C_{\theta,d}$ (I_{p1},I_{p2}) of the relative frequencies that describes how often the two pixels (I_{p1},I_{p2}) of different or similar gray levels N_g appear as a pair in the image matrix concerning the distance *d* and the direction θ. The value of this parameter *Ng* is 8 levels.

Using the co-occurrence matrix, 22 features are extracted where the smoothness, coarseness, and the image texture information are described and quantified. The image contrast, correlation, cluster shade, cluster prominence, energy, homogeneity, entropy, and variance are measured as following:

1. Auto correlation:

$$f_1 = \sum_i \sum_j (ij)(C(i,j)) \quad (3)$$

2. Contrast:

$$f_2 = \sum_{n=0}^{N_g-1} n^2 \left\{ \sum_{i=1}^{N_g}\sum_{j=1}^{N_g} C(i,j) \middle| |i-j| = n \right| \quad (4)$$

3. Correlation:

$$f_3 = \frac{\sum_i \sum_j (ij) C(i,j) - \mu_x \mu_y}{\sigma_x \sigma_y} \quad (5)$$

Where:

$$\mu_x = \sum_i i\, C_x(i)$$

$$\mu_y = \sum_j j\, C_y(j)$$

$$\sigma_x = \sum_i C_x(i) - \mu_x(i)$$

$$\sigma_y = \sum_j C_y(j) - \mu_y(j)$$

4. Cluster prominence:

$$f_4 = \sum_i \sum_j (i + j - \mu_x - \mu_y)^4\, C(i,j)$$

5. Energy:

$$f_5 = \sum_i \sum_j C(i,j)^2$$

6. Entropy:

$$f_6 = \sum_i \sum_j C(i,j) \log\left(C(i,j)\right)$$

7. Homogeneity:

$$f_7 = \sum_i \sum_j \frac{1}{1 + (i-j)^2}\, C(i,j)$$

The rest of the 15 features are correlated using Matlab functions, cluster shade [13], dissimilarity [13], homogeneity using a Matlab function, maximum probability [13], sum of squares [12], sum average [12], sum variance [12], sum entropy [12], difference variance [12], difference entropy [12], information measure of correlation1 [12], information measure of correlation2 [12], inverse difference [14], inverse difference normalized [14], inverse difference moment normalized [14].

2.3.3. Classification

The idea of the CART classifier model is presented by conditions. In this model, several questions are answered by the trees sequentially like *If-Then* condition statements. These questions depend on the extracted features from the images. Using CART model related to its efficiency and flexibility. The tree model is easy to interpret and modify according to the observed internal work. The classification consists of two main steps, training and testing. The data set is divided for training and testing processes as follows:

Table 1: Data Set Division

Class	Training Set	Testing Set	Total
Dead	322	161	483
Live (Embryo)	14	7	21
Live (Egg)	464	231	695

In the training stage the feature set (predictors) with class labels (responses) are used to train a CART classifier model. The second step is the testing step in which the classifier performance appears as an important indication of its capability. To predict the class of a new sample, the designed model follow the decisions in the tree from the root (beginning) node down to a leaf node. The leaf node contains the response. By repeating the first steps for preparing the image and extracting the 24 features, these features (predictors) are provided to the saved classifier model to predict the class (response).

2.4. Pixel Values Features

This approach based on the basic information of the image and without need for image pre-processing or any calculations for feature extraction. Figure 5 shows the proposed methodology.

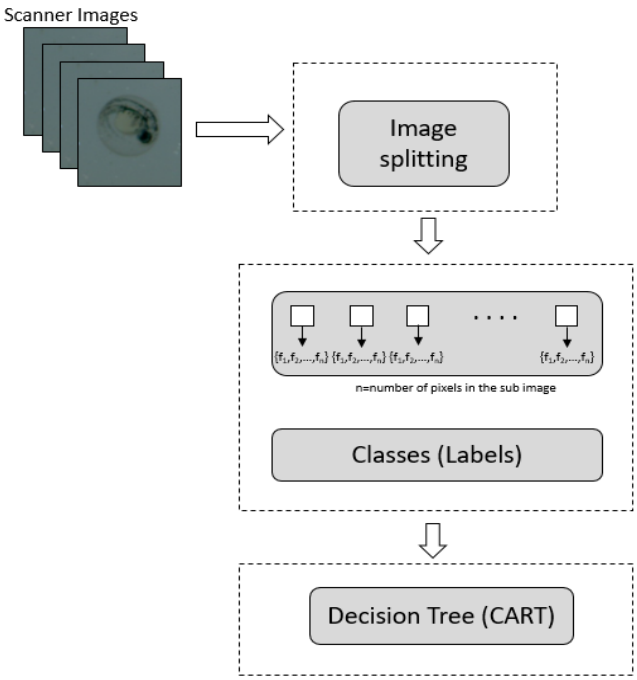

Figure 5: Second scenario of system

2.4.1. *Image Splitting*

The proposed method breaks the sample image down into several sub images. Each sub image presents a part of the whole image with a specific size (10x10) pixels from random positions and locations. The number of these sub images is chosen by trials as a sensitivity test for the process and it appears not to have a strong influence on recognition performance. However, the time complexity rises with increasing the number of extracted sub images. Each sub image is described by a feature vector containing a numerical values which are the pixel values. Using a fixed size for each sub image allows the classifier model to learn using the same size of the feature vectors for these sub images. The positivity of this process in its generalization where it can be applied on any type of images and it does not need for any image processing operations or features calculations.

2.4.2. *Classification*

Based on the ensemble approach in machine learning, a CART classifier model is built for each sub image. Each sub image is labelled according to the original image class then a CART model for each sub image is designed and provided by the feature vectors. According to the large number of features, the learning algorithm should deal with this number efficiently where this is one of the decision tree capabilities. In the training stage, the trees are grown until the model learns perfectly the training sample characteristics and can correctly classifies the training sample classes.

For the testing stage, non-labelled images are used and all the training images are no longer used here. To predict a new image, the image splitting or dividing step is repeated and the resulting vectors are provided to the saved models. Each CART model predict class depending on the sub image features. The most frequent predicted class is considered to be the final decision of the predicted class.

2.5. *Results and Discussion*

Both of the two methods of feature extraction and classification show good results. However, the texture and colour features extraction method has a higher accuracy especially for the live embryos class. This is related to the similarities between the live embryos class and the dead class. The classification algorithm is the same for the two methods where the comparison is done to compare two feature extraction ways. The first method based on the object texture and colour characteristics. The proposed work uses a CART model after extract 24 features as explained earlier. Based on this method, the classification accuracy to classify the sample image into three classes is 97%. This proposed method correctly classify 384 images out of 399 images that were used for testing. Figure 6 shows the confusion matrix for these three classes using this method.

Predicted Class

Actual Class	Dead	Embryo	Live
Dead	96%	0%	4%
Embryo	0%	100%	0%
Live	3%	0%	97%

Figure 6: Confusion matrix of the first method

Depending on the pixel values of the image is the second proposed method in which the most important features are the pixel values regardless the image type. Furthermore, this method does not need for image preparing operation or a various type of calculations for feature extraction. By tuning the number of extracted sub images parameter to different numbers, the training and testing accuracy have not been changed obviously as shown in figure.7. However, the time complexity is affected by this variations directly proportional as shown in Figure 8. In addition, using larger size of the sub images rise the system accuracy as presented in Figure 7.

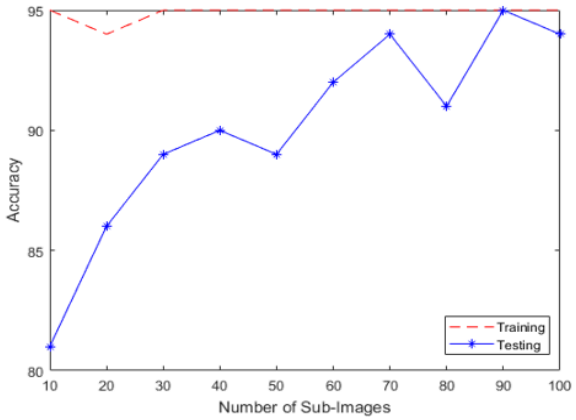

Figure 7: Classifier Performance with parameter tuning

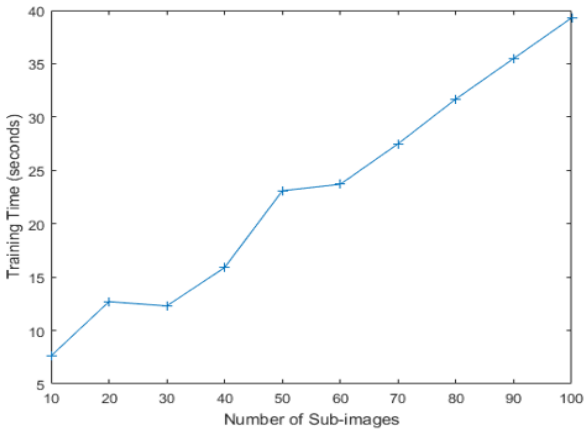

Figure 8: Classifier training time with parameter tuning

All the classification model parameters are the same in the two proposed methods. But, our analysis based on the feature extraction ways. The first one shows satisfactory results using the most important features in the image. The second way use the pixel values of the extracted sub-images to train the classifier model. This method performs well and varies according to the number of the sub-images and the size of each sub-image. The second method can be considered as a robustness and simpleness of the feature extraction calculations.

The first scenario classifier model shows a higher performance comparing with the second one, the complexity time is extremely the same. This classifier model is used to detect, segment, and classify the eggs within the whole dish image. Figure 9 shows examples of small parts of different dishes where the egg samples are detected successfully and classified correctly. The label *L* for the live organism and *D* for the dead ones.

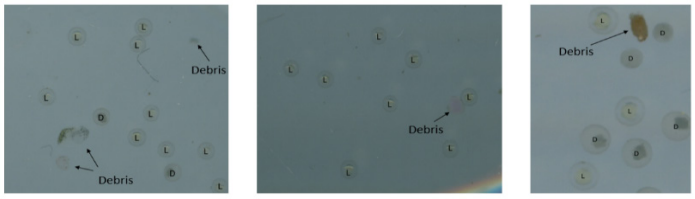

Figure 9: Classification results for the whole dish image

As shown in Figure 9, the debris which is considered as unwanted object is discarded and the target objects are detected, segmented, and classified efficiently. However, in some cases the proposed system fail in detection and classification processes as shown in Figure 10. Some samples are misclassified which can be manipulated either by cross validation for the classifier or reducing the number of extracted features by using a feature selection algorithm.

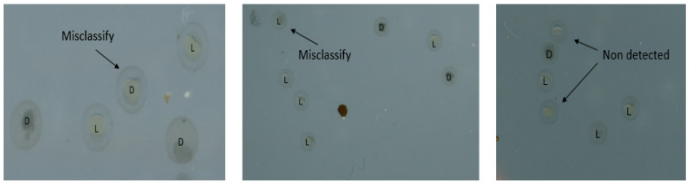

Figure 10: Drawbacks of the classifier

Using the scanner images provide us with a large number of samples of very good quality. However, these images are taken from a bigger image that contains hundreds of eggs. Partitioning process to get every sample and deal with it as a single image distort the sample images in many cases which is considered as a big challenge in this work. Table 2 shows a comparison between the scanner and the tradition way for image gathering process, camera with a microscope which considered as a time-consuming process.

Table 2: Comparison between two imaging tools

Imaging tool	Speed (image/shot)	Illumination	Focal point	Resolution
Flatbed Scanner	Hundreds of images *	Fixed by scanner	Fixed by scanner	High
Microscope & Camera	One	Important and influential (fixed by the expert)	Important and influential (fixed by the expert)	High

*depending on the number of samples, the imaging process is carried out for the whole dish.

3. Conclusion

In this paper, a novel zebrafish egg classification method is proposed using two methods for feature extraction process. Two methods were tested, analysed, and compared to each other and to the ground truth. By extracting the most important features for both colour and texture characteristics of the image, a high performance model is presented and evaluated with 97% testing accuracy to classify the sample image of the zebrafish egg into three classes depending on its status.

Using the flatbed scanner is presented as low cost effective imaging tool that save the consuming time where the one shot provide the system by hundreds of sample images. Furthermore, this tool affordable and easy to use by the biologists with a least imaging problems.

Using the pixel values of the split image parts was considered as a generic method where there is no need for applying any calculations or operations or even image modification. The results of this model is satisfactory and the parameters were tuned to a several values to reach the optimal parameter values and to see to how extent these parameters effect on the system accuracy. The performance of the first method was higher than the second one even though this method is generic and may applied on more than three classes with different characteristics.

Besides the benefits that are provided by using the flatbed scanner for data collection. The proposed system is assessed by the biologists as an effective and time saving process for their experiments. The traditional way for capturing images for the

samples is always carried out individually for hundreds of samples which is a time consuming process. In addition, the biologist need to analyse each sample to decide its status which is also considered as a time consuming process. By using the proposed system the biologist intervention is limited and the experiment time should be shorter than usual. This system present a part from a bigger classification system for detection, classification, and counting system for zebrafish embryo abnormalities using a high-throughput model for both the petri dish and the n-well plates.

4. References

[1] Al-Saaidah, B., Al-Nuaimy, W., Al-Hadidi, M., and Young, I., (2018, April). Automatic Counting System for Zebrafish Eggs using Optical Scanner. The 9th International Conference on Information and Communication Systems, 2018 9th International Conference. IEEE.

[2] Detrich, H. William, Monte Westerfield, and Leonard I. Zon, eds. The zebrafish: Disease models and chemical screens. Vol. 3. Academic Press, 2011.

[3] Yang, Lixin, Nga Yu Ho, Rüdiger Alshut, Jessica Legradi, Carsten Weiss, Markus Reischl, Ralf Mikut, Urban Liebel, Ferenc Müller, and Uwe Strähle. Zebrafish embryos as models for embryotoxic and teratological effects of chemicals. Reproductive Toxicology 28, no. 2 (2009): 245-253.

[4] Bhusnure, O., Mane, J.M., Gholve, S.B., Thonte, S.S. and Giram, P.S., 2015. Drug target screening and its validation by zebrafish as a novel tool. Pharm. Anal. Acta, 6(426), pp.10-4172.

[5] Braunbeck T., Böttcher M., Hollert H., Kosmehl T., Lammer E., Leist E., Rudolf M. and Seitz N., Towards an Alternative for the Acute Fish LC50 Test in Chemical Assessment:The Fish Embryo Toxicity Test Goes Multi-species – an Update. ALTEX - Alternativen zu Tierexperimenten. vol.22, pp. 87–102, (2005).

[6] Al-Jubouri Q., Al-Nuaimy W., Al-Taee M., Luna J., and Sneddon L., An automatic pattern detection method for behavioral analysis of zebrafish larvae, The International Multi-Conference on Systems, Signals and Devices (SSD), Germany, pp. 301-312, (2016).

[7] Chakraborty, Chiranjib, Chi H. Hsu, Zhi Hong Wen, Chang Shing Lin, and Govindasamy Agoramoorthy. Zebrafish: a complete animal model for in vivo drug discovery and development. Current drug metabolism 10, no. 2 (2009): 116-124.

[8] Hisaoka, K.K. and Firlit, C.F., 1962. Ovarian cycle and egg production in the zebrafish, Brachydanio rerio. Copeia, pp.788-792.

[9] Alshut, Rüdiger, Jessica Legradi, Lixin Yang, Uwe Strähle, Ralf Mikut, and Markus Reischl. Robust identification of coagulated zebrafish eggs using image processing and classification techniques. In Proc. of the 19th GMA-FA 5.14" Computational Intelligence" Workshop, pp. 2-4. 2009.

[10] Tharwat, Alaa, Tarek Gaber, Mohamed Mostaf Fouad, Vaclav Snasel, and Aboul Ella Hassanien. "Towards an automated zebrafish-based toxicity test model using machine learning." Procedia Computer Science 65 (2015): 643-651.

[11] Puybareau, É., Genest, D., Barbeau, E., Léonard, M. and Talbot, H., 2017. An automated assay for the assessment of cardiac arrest in fish embryo. Computers in biology and medicine, 81, pp.32-44.

[12] Haralick, R.M. and Shanmugam, K., 1973. Textural features for image classification. IEEE Transactions on systems, man, and cybernetics, (6), pp.610-621.

[13] Soh, L.K. and Tsatsoulis, C., 1999. Texture analysis of SAR sea ice imagery using gray level co-occurrence matrices. IEEE Transactions on geoscience and remote sensing, 37(2), pp.780-795.

[14] Clausi, D.A., 2002. An analysis of co-occurrence texture statistics as a function of grey level quantization. Canadian Journal of remote sensing, 28(1), pp.45-62.

[15] Maree, R., Geurts, P., Piater, J. and Wehenkel, L., 2005, June. Random subwindows for robust image classification. In Computer Vision and Pattern Recognition, 2005. CVPR 2005. IEEE Computer Society Conference on (Vol. 1, pp. 34-40). IEEE.

ASTES

Advances in Science, Technology and Engineering Systems Journal
Vol. 3, No. 4, 354-362 (2018)
www.astesj.com
Special Issue on Multidisciplinary Sciences and Engineering

ASTES Journal
ISSN: 2415-6698

MARWIN: Localization of an Inspection Robot in a Radiation-exposed Environment

Andre Dehne*, Nantwin Möller, Thorsten Hermes

Andre Dehne, hochschule 21 gemeinnützige GmbH, 21614 Buxtehude, Germany

ARTICLEINFO

Article history:
Received: 21 June, 2018
Accepted: 14 August, 2018
Online: 28 August, 2018

Keywords:
Mobile robots
Localization
Radiation detection

ABSTRACT

MARWIN is a mobile autonomous robot platform designed to carry out maintenance and inspection tasks in the European XFEL. The XFEL is an accelerator plant which is operated in Hamburg, Germany. The robot system consists of an four-wheel drive chassis and a scissor lift for easy inspection and maintenance tasks. Through this manipulator and the chassis, the robot system acquires three degrees of freedom. MARWIN is intended for autonomous radiation measurements along the XFEL research facility and thus needs accurate localization. The facility describes a straight tunnel and consists partly of irregular structures and also of sections with almost no obstacles. In the 1000 meter long sections in which MARWIN operates, the robot must approach the facilities to a few centimeters, but must not touch them. For this purpose, different localization methods were tested and checked for accuracy. Furthermore, the influence of radiation on the localization is investigated.

1 Introduction

This paper is an extension of work originally presented in International Conference on Research and Education in Mechatronics (REM) 2017 [1]. Within the research co-operation of the "hochschule 21" and the German Electron Synchrotron (DESY) of the Helmholtz Association a "mobile and autonomous robot for maintenance and inspection" (MARWIN) was developed. For targeted radiation measurement the robot navigates along the new accelerator of the research facility European XFEL. Therefore different systems like localization, drive, charge and lifting are required. After the two-year project, which had to proof that the radiation measurements in accelerator systems can be reliably executed by a robot, which is build of hardware that comes from the consumer sector and is not protected from the radiation, a second robot was build. While the testing phase weaknesses were detected so that improvements could be implemented in the second robot.

1.1 Motivation

The accelerator of the research facility European XFEL is world wide the only one generating 27000 X-ray flashes a second[1]. Compared to other research facilities the XFEL is generating 225 times more X-Ray flashes per second. This improvement grants the enforcement of certain experiments. This results in a high demand for that technology. Therefore it is important to maximize the run-time of the accelerator and thus the effectively usable time for research purposes and experimentations. In return, this means that minimizing the shutdown-time for maintenance is necessary. An automated inspection can help to reduce this time. Through information gathered in advance about certain conditions in the system, maintenance work can be carried out in a targeted manner. In addition, the system must be cleared before it can be entered after a shutdown. This is important to ensures that the radiation generated during operation already is decayed and the accelerator tunnel is safe to enter[2]. An automation of this task, which is otherwise performed manually by employees of the radiation protection department, reduces the burden of these persons and leads to an accurate measurement with a high repeatability.

*Andre Dehne, hochschule 21 gemeinnützige GmbH, Harburger Str. 6, 21614 Buxtehude, Germany, dehne@hs21.de
[1] see https://www.xfel.eu/facility/comparison/index_eng.html
[2] see https://www.xfel.eu/facility/safety_and_environment/index_eng.html

https://dx.doi.org/10.25046/aj030436

1.2 Conditions

A robot system is to be developed that can carry out inspections during accelerator operation. Thus, the availability of the system but also the efficiency of troubleshooting and diagnostics, maintenance and repairs can be increased. The robot should be equipped with a manipulator due to the sometimes tight and difficult to access spatial conditions. This is needed to take measurements on the various components. In addition, a drive system is to be used which enables collision-free movement in the tunnel. The robots are used in the 3.2 *km* long European XFEL tunnel. This is divided into several sections by interlock doors. The robots should measure the radiation in the different sections as autonomously as possible. The current status of the robot systems should always be visible from the monitoring center. In addition, manual intervention by the monitoring center must be possible. The robots will perform two deployment scenarios.

- Scenario 1: For autonomous driving, measuring positions and other data are transmitted by the monitoring center. Based on this configuration, the robot travels the predetermined distance along the accelerator and selectively records radiation measurement values.
- Scenario 2: Manually controlled, the monitoring center can remotely drive the robot to a certain measuring position in order to carry out punctual measurements on the accelerator. In addition, in the unlikely event of autonomous driving failure, the robot is still mobile.

The monitoring center must always be able to switch between scenarios via remote access. The measured radiation values are recorded by a measuring device and then processed by servers outside of the accelerator facility. The individual measurements are linked with the current position data by the robot system.

2 Related work

The application areas of automation and robotics are steadily increasing and more and more solutions are being developed. Nowadays robots can be found in the most diverse areas. For example, at home in the garden for lawn mowing, in the house for vacuuming, in the industry for manufacturing, as transport systems in warehouse logistics or also for support in home care [2, 3, 4].

Another area of responsibility for robots lies in the so-called 4D environments. These environments are characterized by the extreme conditions: Dirty, dull, dangerous or distant conditions. The fourth D is also mentioned for dear conditions where saving money in expensive projects can be achieved through robots[3].

More and more industrial companies prefer the robotics to manual labor, for example in hazardous work environments or in dull tasks [5, 6]. Especially when it comes to keeping people from dangers, developments have been driven forward. They help, for example, with bomb investigations or space exploration [7]. The TRADR project[4] and the Curiosity mission[5] provide important insights in this regard. Another danger arises when dealing with radioactive substances. Here too, first attempts have already been made to use robots in environments with nuclear hazards.

In particle research with accelerator systems, radioactivity also arises. The Large Hadron Collider (LHC) in Geneva also works on mobile solutions to keep dangerous radiation away from humans [8]. At the LHC a rail-based robotic system was installed to perform inspection work in this hazardous environment. It is equipped with various sensors to record local conditions. Since 2016, TIM (Train Inspection Monorail) has been driving through the tunnel hanging on a rail system[6].

Rail-based systems are inherently rigid and can only be used to a limited extent for later additions. The use of freely moving robots in accelerator systems with extended possibilities of use has not yet been sufficiently researched. Localization is an important part of this. It is unclear how a robot must be designed so that it can reliably work freely in such environments.

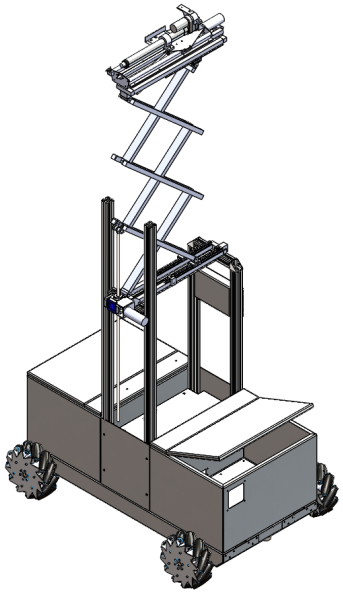

Figure 1: Schematic illustration with mecanum wheel drive in the chassis and scissor lift on top.

[3] see https://www.bernardmarr.com/default.asp?contentID=1195
[4] see http://www.tradr-project.eu
[5] see https://mars.nasa.gov/msl/
[6] see https://home.cern/about/updates/2016/11/meet-tim-lhc-tunnels-robot

3 System overview

Figure 1 shows the developed prototype of a robot system for use in the European XFEL. The robot consists of a mobile drive unit in the lower area and an attached scissor lift for special measuring and inspection tasks.

The drive system of the robot was realized with the mecanum technology [9]. Equipped with four Mecanum wheels, an omnidirectional mobility is achieved. The omnidirectional freedom of movement allows the robot to move better in narrower sections of the XFEL tunnel.

The special feature of a mecanum wheel are the 45 degree angle mounted freewheel rollers, which represent the running surface of the wheel. The size and load capacity of the wheel can be selected according to requirements. There are two different Mecanum wheels. These differ in the arrangement of the freewheel rollers. For the drive with four wheels, two wheels of each type are needed. During assembly, it is important that the pivot of the freewheel rollers points towards the vehicle center.

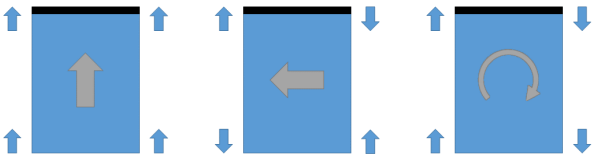

Figure 2: Three examples for the mechanical drive (left: forward; middle: sideways; right: turn on the spot). The arrows indicate the direction of rotation of the wheels.

To illustrate the operation of the mecanum drive, figure 2 shows three different motion scenarios. Driving the wheels in different variations gives corresponding movement patterns. These are enabled by the freewheel rollers. Depending on the direction of rotation of the wheels, movement forces are generated. These can be overlaid or partially canceled out. The resultant force gives the direction of movement. Since there is not much room in the tunnel for turning maneuvers or similar, this property is highly important to avoid possible damage.

For measuring the radiation, as already mentioned, a measuring probe is carried along. This should be guided along the linear accelerator during various measuring runs. There are different scenarios here. One of them is to run along horizontally at a certain height. There are also open structures where the height can vary. For measurement along the accelerator, the probe must be variable in height and positioning. In addition, the robot must not exceed a height of 1.70 m to take his parking position in the charging station.

To meet these requirements, a scissor lift was constructed.With the scissor lift it is possible to reach a big stroke although the basic height is low. For this purpose, three pairs of scissors are used (see figure 1). In order to move the probe horizontally, a platform with a shifting mechanism was set up on top of the scissor lift. This moves the mounted linear actuator up to 30 cm to the outside. The measuring probe is attached to the linear actuator and can thus be moved horizontally by a further 30 cm. To enable the measurement on the irregular structures, a tilt mechanism has been installed. This tilts the platform, mounted on the scissor lift, by up to 30 degrees. The mechanisms are driven by DC gearmotors. For the vertical stroke a spindle-type lifting gear is used to convert the rotary motion of the motor into a lifting movement of the scissor lift. The motor of the displacement mechanism drives a spindle on which a carriage is moved back and forth, depending on the direction of rotation. To move the tilting mechanism, a linear actuator is used.

The robot is a mobile electronic system that is battery powered. Therefore, several charging stations are mounted in the tunnel to charge the battery. Since the robot performs its tasks autonomously, the charging process must also be carried out autonomously. The safety aspect has to be taken into special consideration. Therefore the charging station may only be active when the robot is in the charging station.

In order to ensure safe charging, the two internal contacts of the charging station must be actuated in order to release the charging current at the external charging contacts. For the precise positioning of the robot in the charging station, guide rails were installed on the right and left. These center the robot when driving into the charging station. This ensures that the contacts always lie directly on top of each other.

3.1 Power unit

The power supply of the robot system is realized with a lithium iron phosphate battery (LiFePo4) from the manufacturer ”Super B”. The model ”SB12V100E-ZC” was used[7]. This battery is protected by an external undervoltage protection and was selected due to its high rated capacity of 100 Ah at a nominal voltage of 13.2 V (1320 Wh). The large capacity in relation to the small size and the low weight of the battery is also crucial for the selection of the battery.

The measured current consumption of the entire system is between 15 to 18 A. Thus, the system can be powered up to five hours. That means, that the system can be operated long enough to carry out measuring trips and to get back to a charging station.

3.2 Hardware

The installed IT components are divided as follows:

- Two main computers,
- two single-board computers of the ”Odroid XU4” type with eMMC flash memory,
- one Raspberry Pi 3,

[7] see http://www.super-b.com/en/aviation/utility-avionics-batteries/sb12v100e-zc

- one router,
- one network switch,
- two control units
- six motor driver and
- several sensors and cameras.

The control of the entire system is based on the two main computers, one of which controls the processes and the other idles. The single-board computers are connected to the actuators and sensors. They are used as an interface to the main computers, process sensor signals, control the actuators and output status messages. The control of the lifting system is realized with the Raspberry Pi 3. Router and network switch are required for internal and external communication. With the sensors and cameras, the environment of the robot is observed.

3.3 Sensors

For the localization there are two 2D laser scanners of the type "UST-10LX"[8] manufacturer Hokuyo installed. One in front and one in the back of the robot. Within a range of 270 degree and up to a distance of 10 m, the laser scanner records the surroundings in a single line. This data is also used for the orientation of the robot to the tunnel wall and to prevent collisions. If an object is in the route and is less than 2 m away, a warning is issued. If the object is less than 1 m away, the robot stops to cause no damage. In this case, the monitoring center can intervene manually. For this purpose, eight cameras are installed, which allows complete vision all around the robot. In addition to the camera systems for remote monitoring there is a CCD camera for detecting QR codes, which are installed permanently in the XFEL tunnel. The QR codes contain information about the current location and thus serve the absolute localization of the robot system.

In order to monitor the movement speed of the robot, odometry sensors are used. Hall effect sensors are installed, which incrementally record the rotational movement of the motors. This actual value is processed by a controller to adjust the wheel speed. The regulation of the lifting system is carried out according to the same principle.

3.4 Redundance

With a redundant system a single point of failure should be excluded. Therefore, components such as the main computer are built in duplicate as a master and slave combination. In the event of a fault, the slave can take over the task of the master and restart it. Thus, a total system failure can be avoided and important measurement data will not get lost. If there is a failure of the data transmission, the measured values can be stored on different hard disks and retransmitted later. The redundant design greatly reduces the risk of failure or data loss.

4 Localization

Reliable localization is one of the most important parts of the robot system. On the one hand, it ensures that the measurement results can be correctly assigned and, on the other hand, MARWIN must be able to find its charging station safely. Repeat accuracy also plays a very important role for meaningful measurement results. The localization is based on the measurement data of the laser scanner and on the odometry data of the wheels. The odometry data are determined from the individual speeds of the wheels and from this the resulting motion of the robot.

In general, a distinction is made between global and local localization. The second has already been researched and discussed many times. In local localization, the robot begins by summing the odometry or laser data to determine its current position from the starting position. It estimates its relative position to the start. For absolute positioning, global localization is added. This topic is far more complex, as the robot must be able to record more information about its environment and thus determine an absolute position. At this point, the "kidnapped robot" problem should also be mentioned [10].

The entire IT hardware of the robot is linux-based and builds on the "Robot Operating System" (ROS)[9]. The main components of the software framework of ROS are hardware abstraction, message exchange, packet management and software libraries. The system is divided into the actual basic system ROS and a selection of additional packages which extend the basic system by individual capabilities. ROS is published under the BSD license and is thus open-source. How exactly ROS works and is implemented has already been described several times, see e.g. [11, 12, 13].

4.1 Environmental conditions

The total length of the XFEL tunnel is about four kilometers. The robot-assisted radiation measurements are carried out for two sections each one kilometer long. As shown in Figure 3, the tunnel is straight. The robot moves along a corridor about 1.4 m wide along the tunnel. The charging stations described in section 3 are located underneath the beamline. In order to prevent damage to the research facility when entering the charging station, precise positioning is crucial. The robot must not collide with the system in any situation. As shown in Figure 3, QR codes are mounted along the tunnel on a rail at 10-meter intervals. The absolute position is encoded in the QR codes.

Furthermore occurs during operation of the accelerator facility ionizing radiation. This consists mainly of gamma and neutron radiation. Since the robot is used

[8] see https://www.hokuyo-aut.jp/search/single.php?serial=167

[9] see http://www.ros.org

during operation, it can happen that one bit flip over due to radiation, software errors can occur.

Figure 3: View along the XFEL tunnel

4.2 Solving approaches

It is important for the robot to be able to determine its absolute position in the tunnel because it must travel to exact coordinates for targeted measurements and loading maneuvers. Therefore, global localization is essential. For this reason, a camera was attached to the robot, so QR codes can be scanned by passing. The position information is encoded in the QR code, the edge length is 5 *cm*, and the average distance between QR code and CCD camera is 120 *cm*. The image data of the QR camera are read in and converted to a ROS format. The image is then decoded by the ROS package *zbar_ros*. The result is a string that contains the tunnel position.

Since the QR codes are 10 meters apart on average, further localization is required. There are basically two approaches to this:

- Localization without known map (SLAM)
- Localization with known map

So-called "Simultaneous Localization And Mapping" (SLAM) algorithms work on the principle of adding up the smallest trajectories and thus drawing conclusions about the relative position. There are different sources of information. In the case of MARWIN, a SLAM method was tested and evaluated with the existing sensors.

Likewise, the localization was tested on the basis of an existing map. However, this method requires an already existing as accurate map. These exist theoretically in the blueprints of the XFEL research facility, but there are many details that actually look different (eg mobile pumps, work platforms, smaller implements, tools, etc). For this reason, a map was generated by means of QR codes and SLAM methods. Based on this map a pure map based localization was tested.

4.3 SLAM results

Different ROS packages were used for the SLAM test. During the software research of possible SLAM algorithms, it was found that no software package allows localization correction by external sensors such as the QR camera. The information of the QR codes can therefore not support the localization in the SLAM approach. The condition of supporting laser and odometry data has fulfilled two software packages, *gmapping* by OpenSlam[10] and *hector_slam* by TU-Darmstadt[11]. Both build on so-called particle filter which has been described in several papers [14, 15, 16]. In the application, they differ in that *hector_slam* also works without odometry data. Furthermore, they differ in the generation of the maps. The software *gmapping* starts with a freely definable initial map size. When the robot reaches the limits of the initial map, it is extended by another unknown block. The software *hector_slam* is different here. The map size must already be known at the beginning, as well as the map must be square. It is not dynamically expanded during runtime. If the robot reaches one of the map boundaries, it loses itself and the localization fails in this area.

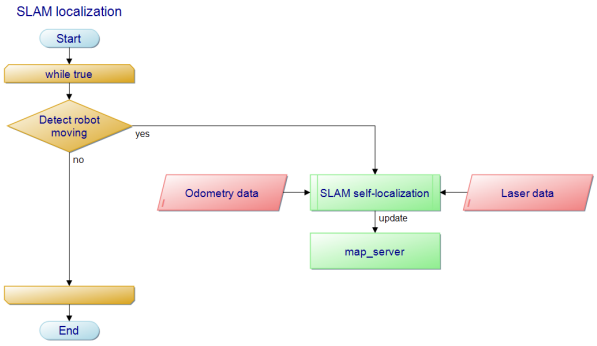

Figure 4: Flow chart of SLAM localization

Figure 4 shows the procedure for the SLAM approach. As the robot moves, this map will be expanded with obstacle information through the SLAM algorithm. The software receives the information from the odometry and laser sensors, weights them and estimates the probable pose.

4.3.1 Using gmapping

First tests with *gmapping* showed that the laser scanners are not arranged with sufficient accuracy (see fig-

[10] see http://wiki.ros.org/gmapping
[11] see http://wiki.ros.org/hector_slam

ure 5). However, this is not a *gmapping* error, but a misalignment of the laser sensors. The resulting map clearly shows a curvature that is not present in reality. The XFEL tunnel is straight.

Figure 5: Incorrectly set laser data lead to curvature of the straight tunnel

Then the test was repeated for a distance of 50 meters and the laser data was recorded. In a simulation a correction factor could be determined over several iterations and thus the arrangement of the laser scanners could be corrected by software. When creating maps with an edge length of 1000 meters and more, a limit was detected. It seems like there is a maximum size of the map, which depends on the chosen resolution. It was found that at a resolution of 20 *cm* per pixel the entire tunnel section (about 1000 *m*) can be mapped. By increasing the resolution to 10 or 5 *cm* per pixel, the dynamic map extension stops after some successful expansion. This has the consequence that *gmapping* is usable in this case only at a maximum resolution of 20 *cm* per pixel. However, the positioning accuracy is worse than expected. The rough map has the consequence that the robot can not approach its measuring positions exactly. Likewise, a precise retraction into the charging station is not possible.

4.3.2 Using hector_slam

As already described, the map size is already defined at program start and is not dynamically expanded during runtime. In addition, the map is necessarily square, since only the edge length of the map can be specified. It has been found that the memory used and the resulting computation cost is significant for a 20000 *px* square map (1000 *m*/0.05 *m* px^{-1}). Therefore the software was adapted and the possibility of a rectangular map implemented. This allowed the map to be reduced to 20000 *px* length and 200 *px* width. It also increased performance and reduced processor load.

Our first test purpose was the reproducibility of the measuring points. Therefore, we let MARWIN perform, for three different distances, 20 times the same test drives autonomously. The first given range was 50 *m*, the second 100 *m* and finally 200 *m*. The tests were always starting from the same point at 280m of the XFEL. The distance travelled in real world was compared against the distance the robot was estimating. Finally, the deviation of the position alongside the tunnel was determined. The results are shown in figures 6. It seems that the localization error is increasing with longer traveled distances.

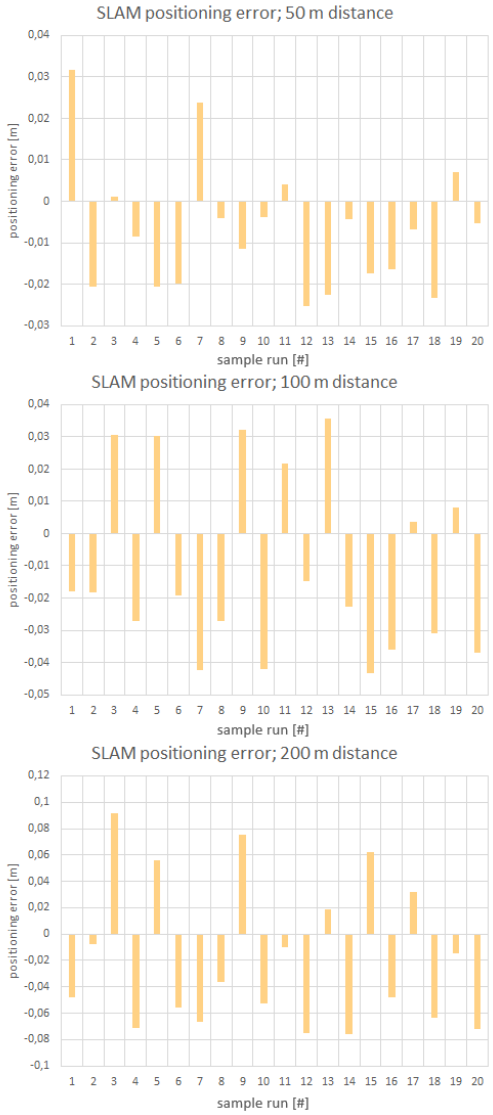

Figure 6: Experimental results of slam test drive (50 to 200 *m*) using hector_slam in the XFEL tunnel

Since the robot has been delivered, the system is constantly being further developed and improved. For a different section in the tunnel (1100 *m* to 2100 *m*) a second robot with the same sensor setup was built. Contrary to expectations, however, the position accuracy has deteriorated considerably here. After a distance of 900 *m* the robot had a positioning error of 9.63 *m*. Some areas in the second tunnel section lead to positioning problems.

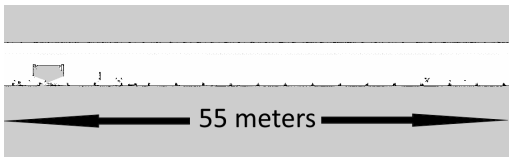

Figure 7: Area with less obstacles in XFEL lead to localization errors

As shown in figure 7 areas were passed with nearly no objects. Within these areas *hector_slam* had problems for determining the travelled distances. For bet-

ter results the covariances of odometry data had to be optimized. The covariances give the odometry data a weighting and thus describe a probability of correctness. The procedure of the optimization can be considered in detail in [17]. As a result the error after travelled distance of 900 *m* could be reduced from 9.63 *m* to 2.43 *m*.

4.4 Static map results

The final map of the SLAM tests described above was taken for static map tests. As described, there is an error of 2.43 *m* after 900 *m* travelled distance, resulting in an error of 0.27 %. The length of the map has been corrected by this value in order to approximate it linearly to reality.

The software for the static map tests is included in ROS as a software package from the navigation stack, called *amcl*[12]. As shown in figure 8, it requires sensor input of 2D-LIDAR data, odometry data and a given static map. Optionally, the position estimation can dynamically be set to a given point in the map. In this way, the QR data are used.

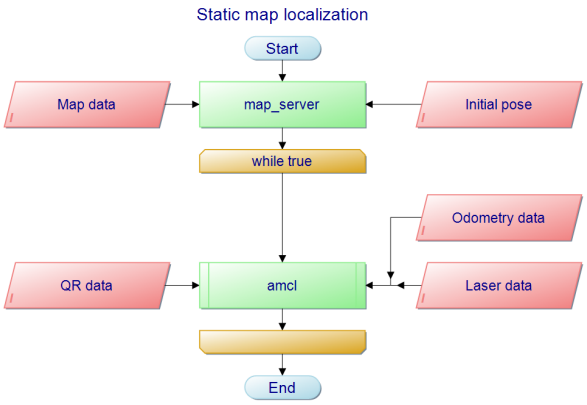

Figure 8: Flow chart of static map localization

Tests for the different distances (50 *m*, 100 *m* and 200 *m*) were repeated as done before in SLAM tests. The results are shown in figure 9. The tolerance in the positioning accuracy is about 5 *cm*.

4.5 Influence of radiation

Due to the redundant structure of the computer units a failure of a unit can be compensated. However, it has been found that the neutron radiation measurably affects the laser sensors. Depending on the intensity of the radiation, it happens that individual measuring points of the laser scanner are falsified. This expresses itself concretely in the fact that the distance in this point is zero.

Due to the fluctuating radiation conditions in the XFEL, it is difficult to carry out targeted radiation tests and to condition the robot system with defined radiation doses. Nevertheless, initial findings were obtained. For this purpose, MARWIN measured weekly the radiation doses of the accelerator system and the number of falsified measuring points. These data were related to each other (see figure 10). The radiation was recorded at a distance of about 80 *cm* from the laser scanners.

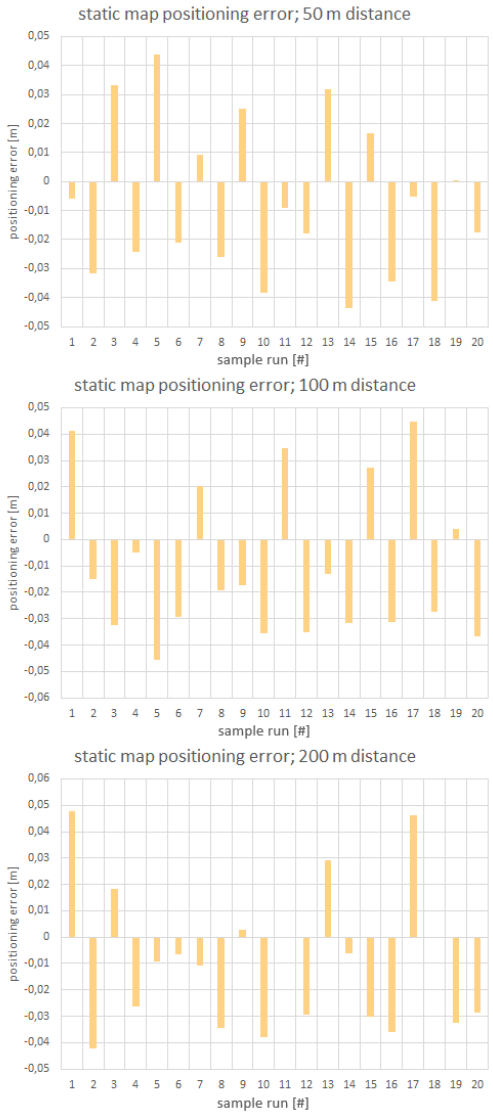

Figure 9: Experimental results of static map test drive (50 to 200 *m*) in the XFEL tunnel

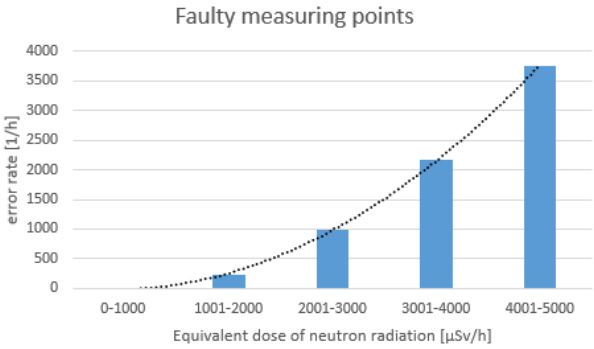

Figure 10: Faulty measurement points for selected groups of neutron radiation doses

[12] see http://wiki.ros.org/amcl

5 Conclusions

The SLAM tests have shown that the positioning error increases with the distance traveled. The SLAM approach with *hector_slam* has great results in map sizes up to 200 m. After that, the accumulated errors become larger, so that the localization error becomes too large for the entire tunnel distance of 1000 m and is therefore not sufficient for the requirements of MARWIN. An unconfigurable relationship between map size and resolution in *gmapping* also leads to insufficient positioning accuracy for MARWIN. In smaller environments, such as the office, these mistakes are not really crucial. However, the accumulation of small localization errors, especially in larger and wide environments, has considerable influence on the positioning accuracy.

The second approach to localization with a static map is a way to move robots in large areas with high positioning accuracy. Due to the positioning tolerance of a maximum of 5 cm, which is related to the resolution of the map, the absolute error is minimal even 1000 m distances traveled. In comparison, the error in the SLAM approach after this distance was 2.43 m.

The combination of creating a map by SLAM method and its linear correction for tunnel-like structures seems to be a good basis for localization methods using static maps.

However, the use of static maps also has the disadvantage that the robot system is no longer able to respond to dynamic changes in the environment. If too many details change in the environment, this can lead to the total loss of localization. This event was detected with tools and mobile equipment left in the XFEL research facility. SLAM approaches are more robust in this scenario.

With the described static map approach the robot system MARWIN is successfully in use. Several times during the operation of the accelerator facility, inspections and autonomous radiation measurements were carried out. For a long-term view of the radiation conditions, a weekly snapshot of the entire research facility is created autonomously by MARWIN.

The influence of neutron radiation on the measurement data of the laser scanner has no noticeable effect on the positioning accuracy. This may be because the number of faulty measurement points per time interval is a fraction of the total number of measurement points. According to the data sheet of the laser scanner used, about 155 million measuring points are recorded per hour, whereas in the dose range of $4001 - 5000\ \mu Sv\ h^{-1}$ only about 3700 incorrect measuring points occur. However, should the radiation dose continue to increase, there could be a significant deterioration on the accuracy of localization due to the tendency of the faulty measurement points.

5.1 Further work

The robot system is constantly being improved and developed further. In the specific case of localization, further approaches could be considered. Currently relatively new but very promising is a new approach called *Cartographer*. This software package is developed by Google and is also based on the SLAM method. Larger environments should be able to be mapped with it [18].

In the long term, further cooperations are to be concluded in order to promote the expansion of other research facilities. It also has a great focus on the development of a manipulator in order to make minor repairs and interventions in the operation of the accelerator system.

References

[1] A. Dehne, N. Möller, and T. Hermes, "Marwin: a mobile autonomous robot for maintenance and inspection in a 4d environment," in *2017 International Conference on Research and Education in Mechatronics (REM)*, Sept 2017, pp. 1–5.

[2] J. H. Zhou, J. Q. Zhou, Y. S. Zheng, and B. Kong, "Research on Path Planning Algorithm of Intelligent Mowing Robot Used in Large Airport Lawn," in *2016 International Conference on Information System and Artificial Intelligence (ISAI)*, June 2016, pp. 375–379.

[3] Y. Zhou, R. Sun, S. Yu, J. Yang, and L. Sun, "An obstacle avoidance method based on non-radial arrangement of distance sensors for vacuum cleaning robot," in *2016 IEEE International Conference on Robotics and Biomimetics (ROBIO)*, Dec 2016, pp. 608–612.

[4] D. Portugal, L. Santos, P. Alvito, J. Dias, G. Samaras, and E. Christodoulou, "SocialRobot: An interactive mobile robot for elderly home care," in *2015 IEEE/SICE International Symposium on System Integration (SII)*, Dec 2015, pp. 811–816.

[5] F. He, Z. Du, X. Liu, and Y. Sun, "Indoor dangerous gas environment detected by mobile robot," in *2009 IEEE International Conference on Robotics and Biomimetics (ROBIO)*, Dec 2009, pp. 396–401.

[6] C.-T. Chiang, "A versatile gas/vision tracking robot for security system applications," in *2012 IEEE Conference on Control, Systems Industrial Informatics*, Sept 2012, pp. 50–53.

[7] I. Kruijff-Korbayov, L. Freda, M. Gianni, V. Ntouskos, V. Hlavac, V. Kubelka, E. Zimmermann, E. Zimmermann, H. Surmann, Dulic, Rottner, and E. Gissi, "Ground and aerial robots in earthquake-response in amatrice, italy: a field report," in *Proceedings of the 2016 IEEE International Symposium on Safety, Security and Rescue Robotics (SSSR)*, Lausanne, Switzerland, October 2016.

[8] K. Kershaw, F. Chapron, A. Coin, F. Delsaux, T. Feniet, J. L. Grenard, and R. Valbuena, "Remote inspection, measurement and handling for lhc," in *2007 IEEE Particle Accelerator Conference (PAC)*, June 2007, pp. 332–334.

[9] B. I. Erland, "Wheels for a course stable selfpropelling vehicle movable in any desired direction on the ground or some other base," Patent US3 876 255, 1975.

[10] I. Bukhori, Z. H. Ismail, and T. Namerikawa, "Detection strategy for kidnapped robot problem in landmark-based map monte carlo localization," in *2015 IEEE International Symposium on Robotics and Intelligent Sensors (IRIS)*, Oct 2015, pp. 75–80.

[11] M. Köseoğlu, O. M. Çelik, and Ö. Pektaş, "Design of an autonomous mobile robot based on ros," in *2017 International Artificial Intelligence and Data Processing Symposium (IDAP)*, Sept 2017, pp. 1–5.

[12] Q. Xu, J. Zhao, C. Zhang, and F. He, "Design and implementation of an ros based autonomous navigation system," in *2015 IEEE International Conference on Mechatronics and Automation (ICMA)*, Aug 2015, pp. 2220–2225.

[13] J. Boren and S. Cousins, "Exponential growth of ros [ros topics]," *IEEE Robotics Automation Magazine*, vol. 18, no. 1, pp. 19–20, March 2011.

[14] G. Grisetti, C. Stachniss, and W. Burgard, "Improved techniques for grid mapping with rao-blackwellized particle filters," *IEEE Transactions on Robotics*, vol. 23, no. 1, pp. 34–46, Feb 2007.

[15] G. Grisetti, C. Stachniss, and W. Burgard, "Improving grid-based slam with rao-blackwellized particle filters by adaptive proposals and selective resampling," in *Proceedings of the 2005 IEEE International Conference on Robotics and Automation*, April 2005, pp. 2432–2437.

[16] S. Kohlbrecher, O. von Stryk, J. Meyer, and U. Klingauf, "A flexible and scalable slam system with full 3d motion estimation," in *2011 IEEE International Symposium on Safety, Security, and Rescue Robotics*, Nov 2011, pp. 155–160.

[17] P. Eberhard and Q. Tang, "Sensor Data Fusion for the Localization and Position Control of One Kind of Omnidirectional Mobile Robots," in *Multibody System Dynamics, Robotics and Control*, pp. 45–73, Springer, Vienna, 2013.

[18] W. Hess, D. Kohler, H. Rapp, and D. Andor, "Real-time loop closure in 2d lidar slam," in *2016 IEEE International Conference on Robotics and Automation (ICRA)*, May 2016, pp. 1271–1278.

ASTES

Advances in Science, Technology and Engineering Systems Journal Vol. 3, No. 4, 363-371 (2018)

www.astesj.com

Special Issue on Multidisciplinary Sciences and Engineering

ASTESJ

ISSN: 2415-6698

Amplitude-Frequency Analysis of Emotional Speech Using Transfer Learning and Classification of Spectrogram Images

Margaret Lech[*,1], Melissa Stolar[1], Robert Bolia[2], Michael Skinner[2]

[1]*School of Engineering, RMIT University, VIC 3000, Australia*

[2]*Defence Science and Technology Group, VIC 3207, Australia*

ARTICLE INFO

Article history:
Received: 06 June, 2018
Accepted: 03 August, 2018
Online: 25 August, 2018

Keywords:
Speech processing
Emotion recognition
Deep neural networks

ABSTRACT

Automatic speech emotion recognition (SER) techniques based on acoustic analysis show high confusion between certain emotional categories. This study used an indirect approach to provide insights into the amplitude-frequency characteristics of different emotions in order to support the development of future, more efficiently differentiating SER methods. The analysis was carried out by transforming short 1-second blocks of speech into RGB or grey-scale images of spectrograms. The images were used to fine-tune a pre-trained image classification network to recognize emotions. Spectrogram representation on four different frequency scales - linear, melodic, equivalent rectangular bandwidth (ERB), and logarithmic - allowed observation of the effects of high, mid-high, mid-low and low frequency characteristics of speech, respectively. Whereas the use of either red (R), green (G) or blue (B) components of RGB images showed the importance of speech components with high, mid and low amplitude levels, respectively. Experiments conducted on the Berlin emotional speech (EMO-DB) data revealed the relative positions of seven emotional categories (anger, boredom, disgust, fear, joy, neutral and sadness) on the amplitude-frequency plane.

1. Introduction

This paper is an extension of work originally presented in the 11th International Conference on Signal Processing and Communication Systems, ICSPCS'2017 [1]. The conference work introduced a new, efficient, real-time speech emotion recognition (SER) methodology. A demo of this application can be found on: (https://www.youtube.com/watch?v=cIsVGiFNJfE&t=41).

In this study, the method proposed in [1] was used for analytical purposes to determine how different emotional categories are coded into the amplitude-frequency characteristics of emotional speech. The underlying assumption was that, the accuracy of detecting a particular emotion depends on how many cues related to this emotion are given by the input speech features. By selecting acoustic speech features representing or emphasizing different frequency and amplitude values, and observing which emotions were best recognised, the study determined links between different emotions and corresponding amplitude-frequency characteristics of speech. In other words, features that lead to higher classification accuracy for a given emotion were thought to be highly representative of this emotion.

The search for the "best" or the most representative acoustic features has been one of the most important themes driving SER, as well as emotional speech synthesis studies [2]. In SER, this knowledge can improve differentiation between emotions, and in speech synthesis, it can lead to more natural sounding emotional speech. Despite extensive research, it is still unclear what the "best" features are, as it is uncertain how different emotions are coded into the time-varying amplitude-frequency characteristics of speech.

The remaining sections of the paper are organised as follows. Section 2 gives a brief review of related studies. Section 3 explains the methodology. The experiments and discussion of results are presented in Section 4, and Section 5 provides the conclusion.

2. Previous Works

Traditionally, the links between speech acoustics and emotions have been investigated by classifying emotional speech samples

[*]Corresponding Author: Margaret Lech, School of Engineering, RMIT University, GPO Box 2476, 3000 VIC, Australia, Contact No: +61 3 99251028, Email: margaret.lech@rmit.edu.au

based on various low-level parameters, or groups of parameters, defined by models of speech production. Examples of low-level parameters include the fundamental frequency (F0) of the glottal wave, formant frequencies of the vocal filter, spectral energy of speech, and speech rate. The low-level features were later enriched by the addition of higher level derivatives and statistical functionals of the low-level parameters. The Munich Versatile and Fast Open-Source Audio Feature Extractor (openSMILE) [3] gives the current software standard, allowing for the calculation of over 6000 low- and high-level acoustic descriptors of speech. In [4] links between acoustic properties of speech and emotional processes in speakers performing a lexical decision task were investigated. Basic parameters such as F0, jitter and shimmer were found to be correlated with emotional intensity. The results indicated that acoustic properties of speech can be used to index emotional processes, and that characteristic differences in emotional intensity may modulate vocal expression of emotion. However, acoustic parameters characterizing different types of emotions were not investigated.

It has been often assumed, especially in earlier studies, that unlike facial expressions that convey qualitative differences between emotions (emotional valence), speech can only communicate emotional intensity (arousal) [5,6]. This assumption was shown to be incorrect by proving that judges are almost as accurate in inferring different emotions from speech as from facial expression [7,8]. As suggested in [6], it is possible that F0, energy, and rate may be most indicative of arousal while qualitative, valence differences may have a stronger impact on source and articulation characteristics. One of the tables presented in [8] showed how selected acoustic speech parameters vary with different emotional categories. Namely, speech intensity, mean, variability and range of F0, sentence contours, high-frequency energy, and articulation rate have been compared across six emotional states (stress, anger/rage, fear/panic, sadness, joy/elation, and boredom). An investigation described in [9] shows links between emotions and prosody features including intonation, speaking rate and signal energy. Correlation between naturally expressed anger and despondency, and various acoustic cues of the speech signal of 64 call centre customers was analysed in [10]. It was found that anger was characterized by a rise of F0 and speech amplitude, whereas despondency by a decreased F0 and syllable rate. Teager energy operator (TEO) parameters [11-13], which simultaneously estimate the instantaneous energy and frequency changes of speech signals, have been shown to be effective in the classification of speech under stress [14,15] and in automatic SER [16]. It was suggested that the high effectiveness of these parameters is due to their sensitivity to the acoustic effects caused by a nonlinear air flow and the formation of vortices in the vicinity of the vocal folds. A discussion of the links between emotions and some of the basic acoustic features including F0, formants, vocal tract cross-section, mel-frequency cepstral coefficients (MFCCs) and TEO features, as well as the intensity of the speech signal and the speech rate can be found in [13]. The high velocity of air moving through the glottis and causing vocal fold vibration was found to be indicative for music-like speech such as joy or surprise while, low velocity was an indicator of harsher styles such as anger or disgust [17]. Identification of the "best" frequency sub-bands of the power spectrum for the classification of different emotions has not been conclusive. A number of studies [18-20] have indicated high importance of the low frequency band ranging from 0 to 1.5 kHz for speech emotions, whereas [21] pointed to the high frequency range (above 1.5 kHz). In He [16] discriminative powers of different frequency bands were examined. It was found that the largest diversity between energy contributions from different emotions occurs in the low frequency range of 0-250 Hz and the high frequency range of 2.5-4 kHz. The middle range of 250 Hz to 2.5 kHz did not show clear differences between emotions. Some of the most often used parameters in speech classification across different databases and languages are the MFCCs [22]. In general, MFCCs are thought to give good representation of the speech signal by considering frequency response characteristics of the human auditory system. However, applications of MFCCs into the SER task have shown relatively poor results [14,16,21,23]. The log-frequency power coefficients (LFPCs) calculated within critical bands of the human auditory system [24] were found to outperform the MFCCs [21]. Experiments presented in [16] examined and ranked 68 different low and high-level features for emotion recognition from natural (non-acted) speech. TEO parameters estimated within perceptual wavelet packet frequency bands (TEO-PWP), as well as the area under the speech energy envelope (AUSEE), have been found to produce the highest performance in both natural emotion and stress recognition.

As shown in the above few examples of the very rich research field, the task of finding links between categorical emotions and acoustic speech parameters has been particularly challenging due to inconsistencies between studies, which include the ways emotions are evoked in speakers (natural, acted, induced), types of emotional labels (different emotional categories or arousal/valence) and types of acoustic speech parameters [8,12,25]. To deal with these difficulties, current trends in automatic speech emotion recognition (SER) are shifting away from learning differences between individual low- or high-level parameters, and moving towards using speech spectrograms that capture the entire time-evolution of emotional acoustics in the form of two-dimensional, time-frequency, spectral magnitude arrays.

Deep neural network structures have been trained to efficiently classify speech spectrograms to recognize different emotional categories [26][33]. Although this methodology is very powerful, the current state-of-the-art results indicate that there is still room for improvement. In particular, the inter-emotional confusion tables show high levels of misclassification between neutral and dysphoric [16], neutral and boredom [34], and joy and anger [16],[34]. Systems designed with prior knowledge of emotional cues have been shown in the past to be particularly effective in increasing the overall SER accuracy. In [35][36] for example, a saliency analysis was applied to speech spectrograms to determine regions of the time-frequency plane that provide the most important emotional cues.

Application of these regions as inputs to a Convolutional Neural Network (CNN) led to high SER accuracy, however, the saliency analysis had a time-varying character and involved very high computational cost. This study offers a more computationally efficient approach to finding what parts of the amplitude-frequency plane carry the most important cues for different emotions. It is expected that the knowledge of the amplitude-frequency

characteristics of individual emotions will facilitate future designs of more efficient SER systems with reduced inter-class confusion.

Table 1: Speech and image data description.

Emotion	No. of speech samples (utterances)	Total duration of speech samples [sec]	No. of generated spectrogram images (RGB or Grey-Scale)
Anger	129	335	27220
Boredom	79	220	18125
Disgust	38	127	11010
Fear	55	123	5463
Joy	58	152	12400
Neutral	78	184	14590
Sadness	53	210	18455
TOTAL	390	1207	111425

3. Method

3.1. Speech Data

The study was based on the EMO-DB database [37] that is routinely used in evaluations of SER systems. It contains speech recordings collected from 10 professional actors (5 male and 5 female) speaking in fluent German. Each actor simulated 7 emotions (anger, joy, sadness, fear, disgust, boredom and neutral speech) while pronouncing 10 different fixed-text utterances consisting of single sentences with linguistically neutral contents. Each actor pronounced each utterance with a different emotion, however in some cases the speakers provided more than one version of the same utterance. Table 1 shows the numbers and total duration of available speech samples (pronounced utterances) for each emotion. The original recordings were validated using listening tests conducted by 10 assessors; details can be found in [37]. Only speech samples that scored recognition rates greater than 80% were used in this study. The sampling rate was 16 kHz, giving 8 kHz speech bandwidth. Despite more recent developments of emotional speech datasets, the EMO-DB remains one of the best and most widely used standards for testing and evaluating SER systems. The important strength of the EMO-DB is that it offers a good representation of gender and emotional classes. The main disadvantage is that the emotions appear to be acted in a strong way, which in some cases may be considered as unnatural.

3.2. SER Using Transfer Learning and Images of Spectrograms

Existing state-of-the-art SER methods apply deep Convolutional Neural Networks (CNNs) trained on spectral magnitude arrays of speech spectrograms [26-29]. To achieve high accuracy, complex CNN structures must be trained on a very large number (in the order of millions) of labelled spectrograms. This method (known as "fresh training") is computationally intense, time consuming and requires large graphic processing units (GPUs).

At present the availability of large datasets of emotionally labelled speech is limited. On the other hand, in many cases, close to the state-of-the-art results can be achieved using a much simpler process of transfer learning. In transfer learning a small, problem-specific data set is used to fine-tune an existing network that has been already pre-trained on a very large amount of more general data.

Table 2: Fine-tuning parameters for AlexNet (Matlab version 2017b)

Parameter	Value
Minibatch size	128
Maximum number of epochs	5
Weight decay	0.0001
Initial learning rate	0.0001
Weight learn rate factor	20
Bias learn rate factor	20

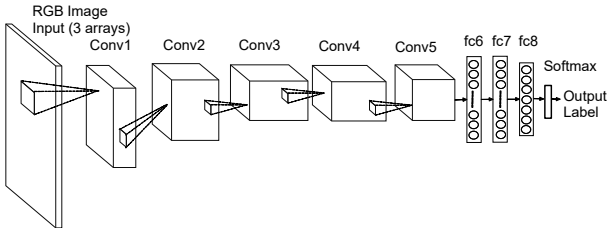

Figure 1. Structure of AlexNet. The input consists of 3 arrays (3 input channels). Feature extraction is performed by 5 convolutional layers (Conv1-5), and classification by 3 fully-connected layers (fc5-8). The output is given in the form of soft labels indicating probability of each class.

The current study applied transfer learning to a pre-trained, general-purpose image classification network known as AlexNet [38], with inputs given as images (not magnitude arrays) of speech spectrograms. AlexNet has been trained on over 1.2 million images from the ImageNet [39] data representing 1000 classes. As shown in Figure 1, AlexNet is a CNN [40] that consists of a 3-channel input layer followed by five convolutional layers (Conv1-Conv5) along with max-pooling and normalization layers, and three fully connected layers (fc6-fc8). The output from the last layer is passed through the normalized exponential Softmax function [41] that maps a vector of real values (that sum to 1) into the range [0, 1]. These values represent the probabilities of each object class. In the experiments described here, the final classification label was given by the most probable class (emotion). The fine tuning of AlexNet was performed within the Matlab (version 2017b) programming framework [42]. The network was optimized using stochastic gradient descent with momentum (SGDM) and L2 regularization factor applied to minimize the cross-entropy loss function. Table 2 provides values of the tuning parameters. Given this choice of parameters, the fine-tuning process changed mostly the final, fully connected (data-dependent) layers of the network leaving the initial (data-independent) layers almost intact.

Despite the fact that in recent years AlexNet has been rivalled by newer, significantly more complex and more data demanding networks, the pre-trained structure is still of great value, as it provides a good compromise between data requirements, network simplicity and high performance. Informal tests on more complex networks such as the residual network ResNet-50, the Oxford Visual Geometry Group networks VGG-16 and VGG-19, and the GoogleLeNet have shown that for a given outcome, the training time needed by the larger networks was significantly longer than for AlexNet. It could also imply that a larger dataset may be needed, but it would have to be confirmed by formal testing.

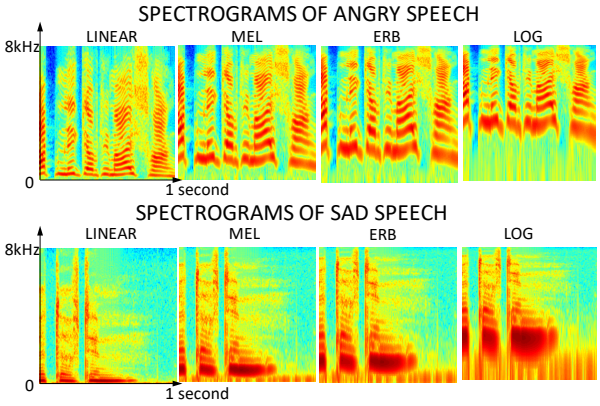

Figure 2. Examples of RGB images of speech spectrograms for the same sentence pronounced with sadness and anger, and depicted on four different frequency scales linear, mel, ERB and log. The linear scale represents the high frequency details, mel scale-the mid-high frequency details, ERB – the mid-low frequency details and log – the low frequency details.

3.3. Generation of Spectrogram Images

The amplitude-frequency analysis of the characteristics of emotional speech was achieved by analyzing the SER results given by different forms of features (i.e. spectrogram images representing speech signals. The SER was performed by applying transfer learning to the pre-trained AlexNet with input arrays given as RGB or grey-scale images depicting speech spectrograms [1] (see Figure 4). To preserve the feasibility of real-time SER [1,26,27], the features were generated on a frame-by-frame basis, and no utterance based parameters were calculated. Since the emotional labels for the EMO-DB data were given for entire utterances, the emotional label for each frame was assumed to be the same as the label of the utterance from which it was extracted. Short-time Fourier transform spectrograms were computed for 1-second blocks of speech waveforms using Hamming window frames of length 25 milliseconds with 12.5 milliseconds of overlap between frames. Short silence intervals occurring within sentences were kept intact. The calculations were performed using the Matlab Voicebox *spgrambw* procedure [43], which generated magnitude spectrogram arrays of size 257 x 259 for the frequency and time dimensions, respectively. The stride between subsequent 1-second blocks was 10 milliseconds. Table 1 shows the numbers of images generated from the available speech data.

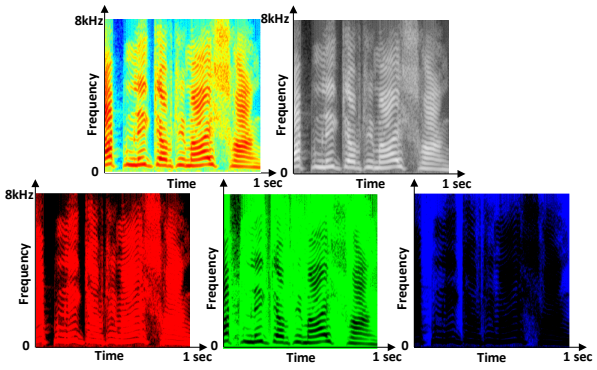

Figure 3. An example of the RGB, grey-scale, R, G and B spectrogram images for the same speech sample of emotionally neutral speech. The R components emphasizes high-amplitude details, the G component – the mid amplitude details and the B component – the low-amplitude details.

The experiments investigated and compared four frequency scales of speech spectrograms: linear, melodic (mel) [44], equivalent rectangular bandwidth (ERB) [45] and logarithmic (log) [46]. While the alternative frequency scales were applied along the vertical axis of the spectrograms from 0 to 8 kHz, the horizontal time scale was in all cases linear spanning the time range of 0 to 1 second. The dynamic range of spectral magnitudes was normalized from -130 dB to -22 dB, representing the respective minimum (Min) and maximum (Max) magnitude values. These values were calculated for magnitude spectrograms over the entire database. The magnitude spectrograms were transformed into RGB or grey-scale images. The RGB images were generated with the Matlab "jet" colormap [47,48] containing 64 default colors. After downsampling to 227 x 227 pixels (using the Matlab *imresize* command), the spectrogram images provided input arrays to AlexNet (Figure 4). More details on the AlexNet input arrangements are given in Section 4.

3.4. Frequency Representation by Different Scales of Spectrogram Images

Four different frequency scales (linear, mel, ERB and log) [49] were applied when generating the spectrogram images in order to visually emphasize different frequency ranges. Figure 2 shows examples of spectrograms for the same sentence pronounced with sad and angry emotion plotted on four different frequency scales: linear, mel, ERB and log [49]. This order of scales corresponds to the process of gradually "zooming into" the lower frequency range features (about 0 to 2 kHz), and at the same time "zooming out" of the higher frequency range features (about 2 kHz to 8 kHz) features. Therefore, the application of different frequency scales effectively provided the network with either more- or less-detailed information about the lower or upper range of the frequency spectrum.

Thus, the linear scale emphasized details of the high-frequency (6-8 kHz) components of speech characterizing unvoiced consonants. The mel and ERB scales provided details of the mid-high (4-6 kHz) and mid-low (2-4 kHz) ranges, respectively (characteristic to both voiced and unvoiced speech), and the log scale provided the most details of the low-frequency (0.02-2 kHz) range (important for vowels and voiced consonants).

3.5. Amplitude Representation by R, G and B Images of Spectrograms

While the RGB images of spectrograms used in the speech classification gave visual representations of the time-frequency decomposition of speech signals, each of the R, G and B color components emphasized a different range of speech spectral amplitude values. As shown in Figure 3, the R component gave greatest intensity of the red color for high spectral amplitude levels, thus emphasizing details of the high-amplitude spectral components of speech (e.g. vowels and voiced consonants). The B component gave greatest intensity of the blue color for lower amplitudes, and therefore it emphasized details of the low-amplitude spectral components of speech (e.g. unvoiced consonants) and gaps between speech. Similarly, the G component emphasized details of the mid-range spectral amplitude components (both voiced and unvoiced).

3.6. Experimental Setup

A 5-fold cross-validation technique was used with 80% of the data distributed for the fine tuning, and 20% for the testing of AlexNet. All experiments were speaker- and gender-independent. The experimental framework is illustrated in Figure 4. Three different experiments, each having different data arrangements for the three input channels of the AlexNet were conducted as follows:

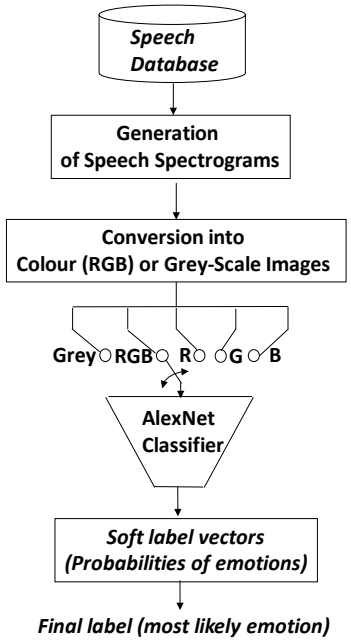

Figure 4. Framework diagram for the amplitude-frequency analysis of emotional speech.

- Experiment 1. To investigate the performance of the color RGB images of spectrograms on average and across emotions.

  AlexNet input: A different color-component array (R, G and B) was given as an input to each of the 3 input channels. The same process was repeated for four different frequency scales of spectrograms.

- Experiment 2. To investigate how the grey-scale image representation of spectrograms performs on average and across emotions.

  AlexNet input: Identical copies of grey-scale image arrays were given as inputs to each of the 3 input channels. It was repeated for four different frequency scales of spectrograms.

- Experiment 3. To investigate how each of the individual color components (R, G or B) performs on average and across emotions.

  AlexNet input: Identical copies of arrays representing the same color component were provided as inputs to each of the 3 input channels. It was repeated for four different frequency scales of spectrograms.

In contrast with the common practice of duplicating the information provided to the network channels [29], the first experiment provided more meaningful and complimentary information to each of the three processing channels of the neural network.

3.7. SER Performance Measures

The emotion classification performance was assessed using standard measures applied in SER tasks. It included accuracy, F-score, precision and recall [50][51] given by (1)-(4) respectively, and calculated separately for each emotion.

$$Accuracy = \frac{t_p+t_n}{t_p+t_n+f_p+f_n} \quad (1)$$

$$F-Score = 2\frac{Precision\ x\ Recall}{Precision+Recall} \quad (2)$$

$$Precision = \frac{t_p}{t_p+f_p} \quad (3)$$

$$Recall = \frac{t_p}{t_p+f_n} \quad (4)$$

Where, t_p and t_n denoted numbers of true positive and true negative classification outcomes, while f_p and f_n denoted numbers of false positive and false negative classification outcomes, respectively.

To reflect the fact that the emotional classes were unbalanced, the weighted average accuracy and F-score were estimated as:

$$Weighted\ Average = \frac{Q_{c_1}|c_1|+\cdots+Q_{c_N}|c_N|}{|c_1|+|c_2|+\ \ldots+\ |c_N|} \quad (5)$$

Where Q_{c_i} denoted either accuracy or F-score for the ith class ($i = 1,2,\ldots,N$) given as (1) or (2) respectively. The values of $|c_i|$ denoted class sizes and N was the number of classes.

4. Results and Discussion

The outcomes of the three SER experiments showed what type of input to AlexNet provided the most efficient training and emotion recognition results. By doing so, indirect insights into the spectral amplitude-frequency characteristics of different emotions were gained. It was achieved through both the application of different frequency scales of spectrograms that visually emphasized details of different frequency ranges, as well as the use of different color components that emphasized different spectral amplitude ranges of speech.

4.1. Comparison between Classification Performance of RGB, Grey-Scale and R, G and B Components

On average, the RGB images outperformed the individual color components and grey-scale images, giving the highest average classification accuracy and F-scores for all frequency scales (Figure 5). Both the RGB and grey-scale images achieved highest performance with the mel frequency scale. The largest difference between RGB and grey-scale images was observed for the ERB and log scales (about 2%). For the other scales, the difference was only about 1% showing that the high frequency details depicted by the ERB and log scales were likely to be clearly depicted by the color RGB images, and to some extend blurred by the grey-scale images.

In addition, Figure 5 shows that the best performing single-color component was green (G) followed by red (R), and the worse performing was blue (B). It indicates that the mid-amplitude

spectral components of speech are likely to be the most important for the differentiation between emotions. The low-amplitude components play a less important role, since they predominantly represent unvoiced speech and gaps of silence between words. For the R color-component, which emphasized high-amplitude speech components, the highest performance was given by the mel scale, which provided a detailed view of the mid-high frequency range. Therefore, the high-amplitude emotional cues appeared to be linked mostly to the mid-high frequency speech components (which amongst other things contain information about the harmonics of the glottal wave fundamental frequency (F0) and the higher formants of the vocal tract).

For the G color-component, the ERB scale, which reveals the mid-low frequency details of speech, was the best performing. This shows that the mid-amplitude emotional cues could be linked to the mid-low-frequency speech components (low harmonics of F0 and low formants). Finally, for the B color-component, the linear scale provided the best performance. This indicates that the low-amplitude emotional cues are predominantly linked to the higher frequency components of speech, such as unvoiced consonants, higher formants and higher harmonics of F0, as well as additional harmonic components generated due to the nonlinear air flow and vortex formation in the vicinity of the glottal folds [14].

4.2. Comparison between RGB, Grey-Scale and R, G and B Components across Different Emotions and Frequency Scales.

To analyze the performance of different spectrogram representations across different emotions, precision-recall graphs shown in Figures 6 and 7 were made. When using this representation, the classification aim was to achieve results that were close to the diagonal line of equal precision and recall values, and as close as possible to the top right corner showing the maximum values of these two parameters. Taking this into account, anger was detected with the highest precision/recall scores by the R-components using the ERB-scale, indicating that the anger cues are most likely to be encoded into the high amplitude and medium-low frequency components of speech.

Disgust was most efficiently detected by the RGB images using the logarithmic frequency scale, which points to the low frequency speech components spanning all amplitude values as carriers of this emotion. Joy was coded the same way as anger into the medium-low frequency and high amplitude components, as it was best detected by the R-image components and the ERB scale.

Boredom showed a distinctly different pattern by being best detected by the mel-scale and G-images. This means that boredom was coded into the medium-high frequencies and medium range amplitudes of speech.

Fear was also distinctly different by being best detected by the mel-frequency scale and grey-scale images. This points to the medium-high frequency range and all amplitude values of speech as carriers of this emotion.

Sadness gave the best performance for the mel-scale and RGB images, showing that like fear, it was coded into mid-high frequencies and all amplitude values of speech.

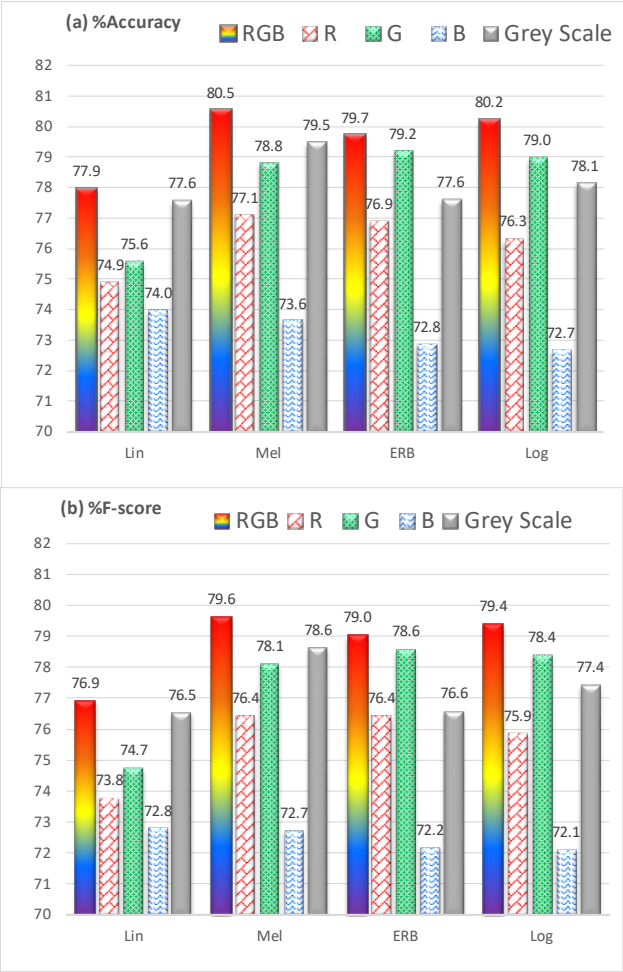

Figure 5. Average weighted classification accuracy (a) and F-score (b) using different frequency scales.

Finally, the emotionally neutral speech was best detected by the ERB scale and RGB images. Therefore, it was likely to be coded into the medium-low frequencies across all amplitudes values of speech. These observations are summarized in Table 3.

4.3. Statistical Significance Analysis

As shown in the above examples, different forms of spectrogram image representation lead to different classification outcomes. To find out which of the observed differences were statistically significant, one-way ANOVA analysis with Bonferroni correction was conducted using the SPSS package. The results comparing the average accuracy values obtained during SER are presented in Table 4. In 5 out of 10 possible pairs of spectrogram image representation, the differences were found to be statistically significant. Namely, the B components were significantly different compared to all other types of images, the R components were different compared to the RGB and B components, and finally the G components were significantly different only when compared to the B components. On average, there was no significant difference between the RGB images and G image-components. The least significant differences were obtained for the grey-scale images compared to the G image-components. This means that, in terms of the classification accuracy, the grey-scale representation appears to be very close to the G images - both

giving good visual information of the mid-amplitude components of speech, which, as previously discussed, were the most important carriers of emotional cues.

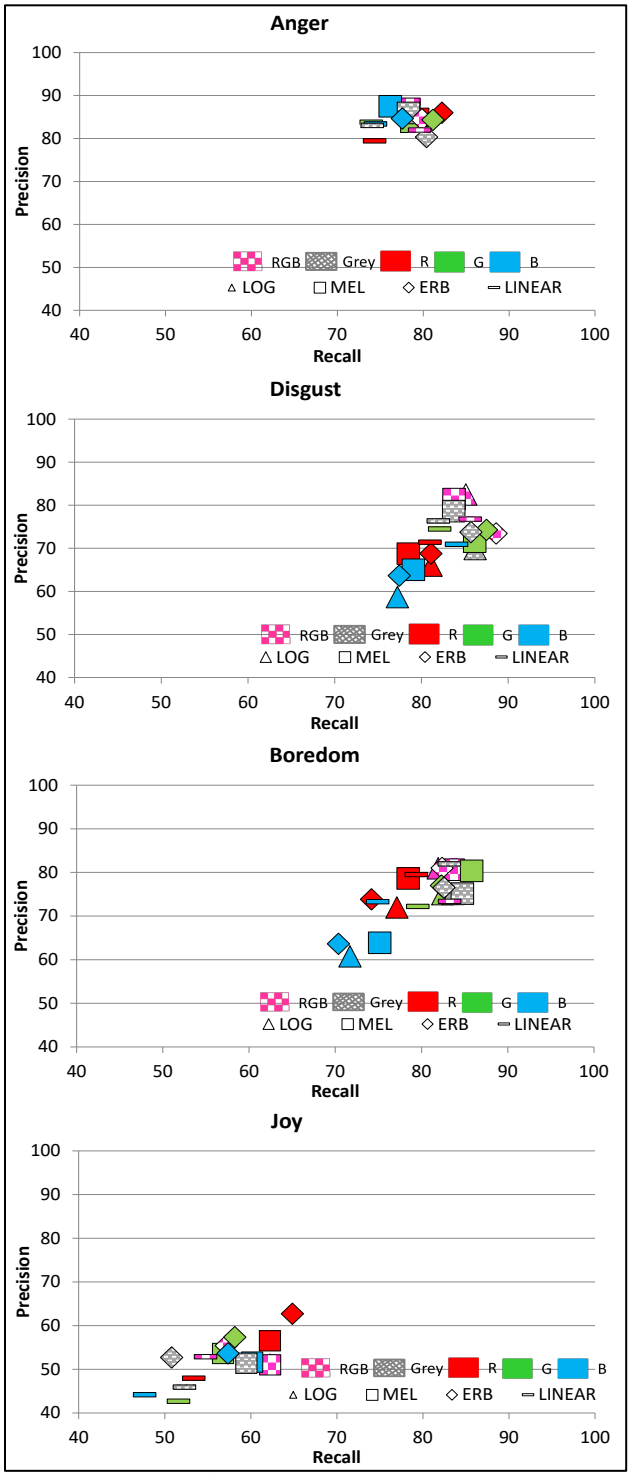

Figure 6. Precision vs. recall using different frequency scales for anger, disgust, joy and boredom. The markers shapes indicate the frequency scale, while their colors indicate types of spectrogram images.

4.4. Distribution of Categorical Emotions on the Amplitude-Frequency Plane

Given the performance analysis of the separate R, G and B images across emotions and frequency scales summarized in Table 3, Figure 8 was made to show the relative positions of seven emotional states of the EMO-DB database on the amplitude-frequency plane. The graph predicts high possibility of confusion in the differentiation between joy and anger, which is consistent with [16,34], as well as, between sadness and fear. Much higher precision/recall scores for anger in Figure 6 suggested that joy was frequently mistaken for anger. Similarly, higher precision/recall scores for sadness in Figure 7 suggested that fear was frequently mistaken for sadness. As expected, neutral speech took central position in relation to other emotions. Both joy and anger were acted in the EMO-DB data by rising the voice level, which is consistent with [10]. Disgust on the other hand, was achieved by variation of the fundamental frequency (F0) and the first formants. Sadness and fear were placed across all amplitudes, but at relatively high frequencies, which could be due to a large number of unvoiced consonants that can be heard when listening to the recordings.

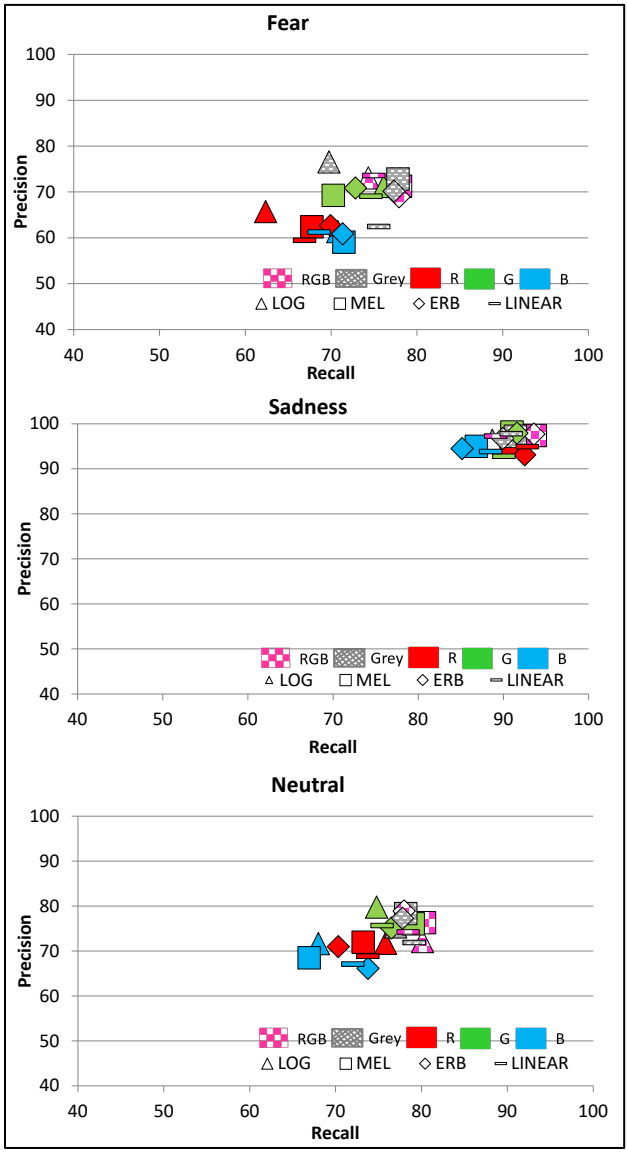

Figure 7. Precision vs. recall using different frequency scales for fear, sadness, and neutral emotional state. The markers shapes indicate the frequency scale, while their colors indicate types of spectrogram images.

Table 3: Amplitude-frequency characteristics of categorical emotions. The total frequency range was 8 kHz, and the total amplitude range was 108 dB.

Emotion	Best Freq. Scale	Best Freq Range	Best CNN Input (3 channels)			Important Amplit. Range
			Ch1	Ch2	Ch3	
Anger	ERB	Medium-Low	R	R	R	High
Disgust	LOG	Low (0.02-2kHz)	R	G	B	All
Joy	ERB	Medium-Low (2-4kHz)	R	R	R	High
Boredom	MEL	Medium-High (4-6kHz)	G	G	G	Medium
Fear	MEL	Medium-High (4-6kHz)	R or Grey scale	G or Grey scale	B or Grey scale	All
Sadness	MEL	Medium-High (4-6kHz)	R	G	B	All
Neutral	ERB	Medium-Low (2-4kHz)	R	G	B	All

Table 4: Statistical significance (p) values obtained when comparing average accuracy of SER based on different types of spectrogram images.

p-values for one-way ANOVA with post-hoc Bonferroni correction, confidence interval: 95%, Bonferroni alpha: 0.05					
	RGB	Grey	R	G	B
RGB	-	0.997	**0.009**	0.868	**0.000**
Grey	0.997	-	0.315	1.000	**0.000**
R	**0.009**	0.315	-	0.367	**0.019**
G	0.868	1.000	0.367	-	**0.000**
B	**0.000**	**0.000**	**0.019**	**0.000**	-

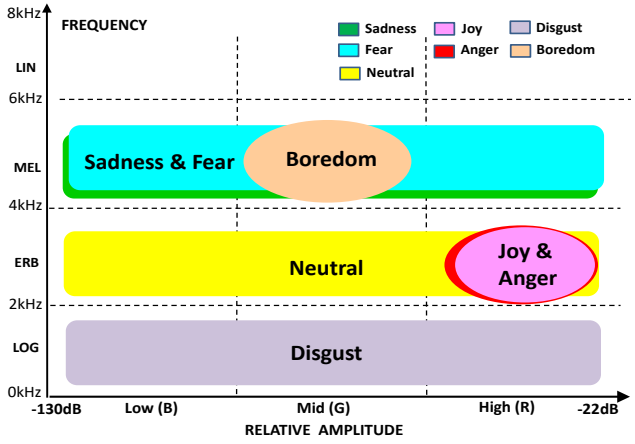

Figure 8. Relative positions of categorical emotions on the amplitude-frequency plane representing acoustic characteristics of emotional speech. These results were obtained using the EMO-DB database

Finally, boredom was localized at mid amplitude levels and high frequencies, which is consistent with very flat, monotonous speech having shallow amplitude modulation. In general, these insights confirmed the expectations, and the fact that they have been generated through machine learning shows that the analysis was valid and consistent with linguistic knowledge. From the perspective of machine learning these insights have direct practical consequences. It is likely that in the future, the SER training process can be enhanced by an adaptive choice of the input features to the network based on optimal configurations given in Table 4.

5. Conclusion

An automatic SER technique based on transfer learning and spectral image classification has been applied to perform an indirect analysis of the amplitude-frequency characteristics of the seven emotional categories represented by the EMO-DB database. Spectrogram images generated on different frequency-scales emphasized different frequency ranges of speech signals, while different color components of the RGB images of spectrograms indicated different values of spectral amplitudes. The analysis provided insights into the amplitude-frequency characteristics of emotional speech. Areas of the amplitude-frequency plane containing cues for different emotions were identified. One of the major limitations of this study is that, the findings apply to acted emotional speech, and only one language (German) was tested. Future works will investigate if the outcomes of the current study are consistent with natural (non-acted) emotional speech, and if they apply across different languages. In addition, factors allowing to efficiently differentiate between highly confused emotions such as for example anger and joy or sadness and fear will be investigated.

Conflict of Interest

The authors declare no conflict of interest.

Acknowledgment

This research was supported by the Defence Science Technology Institute and the Defence Science and Technology Group through its Strategic Research Initiative on Trusted Autonomous Systems, and the Air Force Office of Scientific Research and the Office of Naval Research Global under award number FA2386-17-1-0095.

References

[1] M.N. Stolar, M. Lech, R.S. Bolia, and M. Skinner, "Real Time Speech Emotion Recognition Using RGB Image Classification and Transfer Learning", ICSPCS 2017, 13-16 December 2017, Surfers Paradise, Australia, pp.1-6.

[2] M. Schröder, "Emotional Speech Synthesis: A Review", Seventh European Conference on Speech Communication and Technology, Aalborg, Denmark September 3-7, 2001, pp. 1-4.

[3] F. Eyben, F. Weninger, M. Woellmer, and B. Schuller, "The Munich Versatile and Fast Open-Source Audio Feature Extractor", [Online] Accessed on: Feb 15 2018, Available: https://audeering.com/technology/opensmile/

[4] J.A Bachorovski and M.J. Owren, Vocal expression of emotion: Acoistic properties of speech are associated with emotional intensity and context", Psychological Science, 1995, 6(4), pp. 219-224.

[5] K.R. Scherer, "Non-linguistic indicators of emotion and psychopathology". In: Izard, C.E. (Ed.), Emotions in Personality and Psychopathology. Plenum Press, New York, 1979, pp. 495–529.

[6] K.R. Scherer, 1986. Vocal affect expression: A review and a model for future research. Psychol. Bull. 99 (2), 143–165.

[7] T. Johnstone and K.R. Scherer, 2000. Vocal communication of emotion. In: Lewis, M., Haviland, J. (Eds.), Handbook

[8] K.R. Scherer, "Vocal communication of emotion: A review of research paradigms", Speech Communication 2003, (40), pp. 227–256.

[9] J. Tao, and Y. Kang, "Features importance analysis for emotional speech classification", International Conference on Affective Computing and Intelligent Interaction, ACII 2005: Affective Computing and Intelligent Interaction pp 449-457.
[10] M. Forsell, "Acoustic Correlates of Perceived Emotions in Speech", Master's Thesis in Speech Communication, School of Media Technology, Royal Institute of Technology, Stockholm, Sweden 2007.
[11] Maragos, P., J.F. Kaiser, and T.F. Quatieri, Energy separation in signal modulations with application to speech analysis. Signal Processing, IEEE Transactions on, 1993. 41(10): p. 3024-3051.
[12] D. Ververidis and C. Kotropoulos, Emotional speech recognition: resources, features and methods ", Speech Communication, Volume 48, Issue 9, September 2006, Pages 1162-118.
[13] D. Ververidis, and C. Kotropoulos, Emotional speech recognition: Resources, features, and methods. Speech Communication, 2006. 48(9): p. 1162-1181.
[14] G. J. Zhou, J. H. L. Hansen, and J. F. Kaiser, "Nonlinear feature based classification of speech under stress," IEEE Trans. Speech Audio Process., vol. 9, no. 3, pp. 201–216, Mar. 2001.
[15] L. He, M. Lech, N. Maddage, and N. Allen, "Stress detection using speech spectrograms and sigma-pi neuron units", iCBBE, ICNC'09-FSKD'09, 14-16 August 2009 Tianjin, China, pp. 260-264.
[16] L. He, "Stress and emotion recognition in natural speech in the work and family environments", PhD Thesis, RMIT University, Australia, 2010.
[17] A. Nogueiras, J.B. Marino, A. Moreno, and A. Bonafonte,, 2001. Speech emotion recognition using hidden Markov models. In: Proc. European Conf. on Speech Communication and Technology (Eurospeech 2001), Denmark.
[18] F.J. Tolkmitt and K.R. Scherer, 1986. Effect of experimentally induced stress on vocal parameters. J. Exp. Psychol. [Hum. Percept.] 12 (3), 302–313.
[19] R. Banse and K.R. Scherer, 1996. Acoustic profiles in vocal emotion expression. J. Pers. Soc. Psychol. 70 (3), 614–636.
[20] D.J. France, R.G. Shiavi, S. Silverman, M. Silverman, and M. Wilkes, 2000. Acoustical properties of speech as indicators of depression and suicidal risk. IEEE Trans. Biomed. Eng. 7, 829–837.
[21] T. L. Nwe, S.W. Foo, and L.C. De Silva, 2003. Speech emotion recognition using hidden Markov models. Speech Comm. 41, 603–623.
[22] S.B. Davis and P. Mermelstein (1980), "Comparison of parametric representations for monosyllabic word recognition in continuously spoken sentences." IEEE Transactions on ASSP 28: 357–366.
[23] L. He, M. Lech, and N.B. Allen, "On the Importance of Glottal Flow Spectral Energy for the Recognition", Interspeech 2019, pp. 2346-2349.
[24] B.C.J. Moore and B.R. Glasberg (1983) "Suggested formulae for calculating auditory-filter bandwidths and excitation patterns" The Journal of the Acoustical Society of America (JASA) 1983, 74, pp. 750-753.
[25] R. Cowie, E. Douglas-Cowie, N. Tsapatsoulis, G. Votsis, S. Kollias, W. Fellenz, and J.G. Taylor, "Emotion recognition in human-computer interaction", 2001 IEEE Signal Processing Magazine, 2001, Volume 18, Issue 1, pp. 32-80.
[26] H. Fayek, M. Lech, and L. Cavedon, "Towards real-time speech emotion recognition using deep neural networks", ICSPCS, 14-16 December 2015, Cairns, Australia, pp. 1-6.
[27] H.M. Fayek, M. Lech and L. Cavedon L, "Evaluating deep learning architectures for speech emotion recognition", Neural Networks, March 2017, Special Issue 21, pp. 1-11.
[28] Z. Huang M. Dong, Q. Mao, and Y. Zhan, "Speech emotion recognition using CNN", ACM 2014, November 3-7, 2014, Orlando Florida, USA, pp. 801-804.
[29] W. Lim, D. Jang, and T. Lee, "Speech emotion recognition using convolutional and recurrent neural networks". In Proceedings of the Signal and Information Processing Association Annual Summit and Conference, Jeju, Korea, December 2016, pp. 1–4.
[30] Q. Mao, M Dong, Z.Huang and Y. Zhan, "Learning salient features for speech emotion recognition using convolutional neural networks", IEEE Transactions on Multimedia, 16(8), December 2014, pp. 2203-2213.
[31] S. Prasomphan and K. Mongkut, "Use of neural network classifier for detecting human emotion via speech spectrogram", The 3rd IIAE International Conference on Intelligent Systems and Image Processing 2015, pp. 294-298.
[32] S. Mirsamadi, E. Barsoum, and C. Zhang, "Automatic speech emotion recognition using recurrent neural networks with local attention", Acoustics, Speech and Signal Processing (ICASSP), 2017 IEEE International Conference on, 5-9 March 2017, New Orleans, LA, USA, pp. 2227 - 2231.
[33] A.M. Badshah, J. Ahmad, N. Rahim, and S.W. Baik, "Speech emotion recognition from spectrograms with deep convolutional neural network", Platform Technology and Service (PlatCon), 2017 International Conference on, 13-15 Feb. 2017, Busan, South Korea, pp. 1-5.
[34] M. Stolar, "Acoustic and conversational speech analysis of depressed adolescents and their parents", 2017, PhD Thesis, RMIT University.
[35] Z. Huang M. Dong, Q. Mao, and Y. Zhan, "Speech emotion recognition using CNN", ACM 2014, November 3-7, 2014, Orlando Florida, USA, pp. 801-804.
[36] Q. Mao, M Dong, Z.Huang and Y. Zhan, "Learning salient features for speech emotion recognition using convolutional neural networks", IEEE Transactions on Multimedia, 16(8), December 2014, pp. 2203-2213.
[37] F. Burkhardt, A. Paeschke, M. Rolfes, W. Sendlmeier, and B. Weiss, "A database of German emotional speech", Interspeech 2005, 4-8 September 2005, Lisbon, Portugal pp. 1-4.
[38] A. Krizhevsky, I. Sutskever, and G.E. Hinton, "Imagenet classification with deep convolutional neural networks", Advances in Neural Information Processing Systems, 2012, pp.1097-1105.
[39] IMAGENET, Stanford Vision Lab, Stanford University, Princeton University 2016 Accessed on: Jan 14 2018 [Online], Available: http://www.image-net.org/
[40] Y. LeCun, Y. Bengio, and G. Hinton, "Deep learning", Nature, 2015, 521, pp. 436-444.
[41] C.M. Bishop, "Pattern Recognition and Machine Learning", Springer 2006.
[42] MathWorks documentation: Alexnet, Accessed on: Jan 14 2018, [Online], Available: https://au.mathworks.com/help/nnet/ref/alexnet.html?requestedDomain=true
[43] Voicebox, Description of spgrambw Accessed on: Jan 14 2018, [Online], Available: http://www.ee.ic.ac.uk/hp/staff/dmb/voicebox/doc/voicebox/spgrambw.html
[44] S.S. Stevens and J. Volkman, "The relation of pitch to frequency: A revised scale" The American Journal of Psychology 1940, 53, pp. 329-353.
[45] B.C.J. Moore and B.R. Glasberg (1983) "Suggested formulae for calculating auditory-filter bandwidths and excitation patterns" The Journal of the Acoustical Society of America (JASA) 1983, 74, pp. 750-753.
[46] H. Traunmüller and A. Eriksson, "The perceptual evaluation of F0-excursions in speech as evidenced in liveliness estimations" The Journal of the Acoustical Society of America (JASA), 1995, 97: pp. 1905 - 1915.
[47] MathWorks; Documentation Jet; Jet colormap array, Accessed on: Jan 14 2018, [Online], Available: https://au.mathworks.com/help/matlab/ref/jet.html?requestedDomain=www.mathworks.com
[48] Matlab Documentation Colormaps: Accessed on: Jan 14 2018, [Online], Available: https://au.mathworks.com/help/matlab/colors-1.html
[49] B. Moore, "An Introduction to the Psychology of Hearing", Sixth Edition, Emerald Group Publishing Limited, 2012.
[50] B. Schuller, S. Steidl, and A. Batliner, "The Interspeech 2009 emotion challenge". In Proceedings of Interspeech 2009, pp. 312–315.
[51] B. Schuller, S. Steidl, A. Batliner, F Schiel and J Krajewski, "The Interspeech 2011 speaker state challenge". In Proceedings of Interspeech 2011, August 2011, pp.1-4.

Advances in Science, Technology and Engineering Systems Journal Vol. 3, No. 4, 372-377 (2018)

www.astesj.com

Special Issue on Multidisciplinary Sciences and Engineering

ASTESJ

ISSN: 2415-6698

IR Sensing Embedded System Development for Prototype Mobile Platform and Multisensory Data Fusion for Autonomous Convoy

Hubert Bryan Riley*, David Solomon Raj Kondru, Mehmet Celenk

School of Electrical Engineering and Computer Science, Ohio University, Athens, OH, 45701, USA

ARTICLE INFO

Article history:
Received: 22 May, 2018
Accepted: 10 August, 2018
Online: 25 August, 2018

Keywords:
Autonomous vehicles
Self-driving cars
Embedded systems
IR sensing
Sensor fusion

ABSTRACT

Advanced sensing technologies are providing for greater capabilities to discern and classify details of objects as they appear in actual environments as experienced by nonprofessional drivers. Distinctive geometric configurations of new sensory devices including but not limited to infrared (abbreviated as IR) and LIDAR sensory units are appearing as cost effective data acquisition systems for environment sensing and presenting. Here, we describe a novel IR sensory-based autonomous vehicle guidance and its associated convoy unit. The underlying systems is first presented in a general system model and the experimental test results have been elaborated to demonstrate the usefulness of the presented prototype in futuristic auto industries and its supporting branches, respectively.

1. Introduction

As edge cities continue to emerge, drivers are seeking to increase their productivity during commute time and self-driving vehicles are expected to be facilitating platforms. The Boston Consulting Group and the World Economic Forum have been collaborating for the past several years and forecasting that 14% of residents will ultimately expect safe autonomous vehicles [1]. This paper examines the performance of an infrared (IR) sensing using a prototype mobile platform for autonomous vehicle convoy following. The IR spectrum sensing for autonomous vehicle applications is a compelling approach to detecting objects in the path of vehicle travel. Since cost, reliability, and detection performance are the critical criteria for technology production, the study of performance is the primary interest in this work. Beyond the practical benefits, autonomous cars could contribute $1.3 trillion in annual savings to the US economy alone, with global savings estimated at over $5.6 trillion[2]along with a technology adaptation time line as shown in Figure 1. Design of self-driving or autonomous vehicles with smart sensing systems will positively impact planning decisions for optimal traffic flow, minimize traffic congestions, and alleviate human error leading to personal injuries or property damage. As commuters elevate expectations for their time efficiencies during travels it is expected that technology developers reduce the potential for crashes due to driver fatigue, poor maneuvering decisions, and negligence.[3],[4],[5].

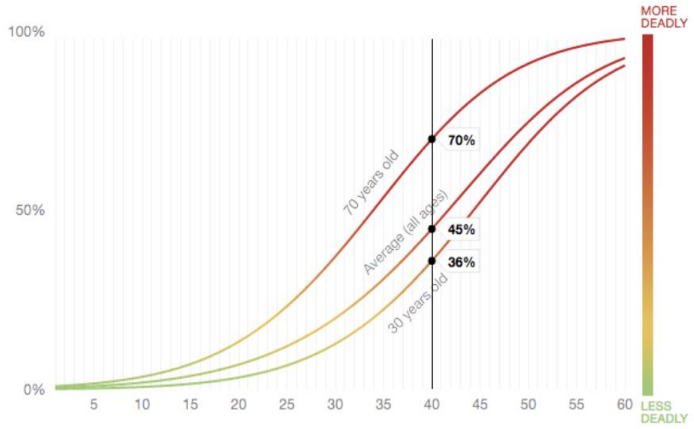

Figure 1. Trends of serious injury vs. vehicle speed in mph.

The curves in Figure 1 is derived comes from typical driving research conducted by AAA Foundation which clearly indicated the probability of getting seriously injured increases with increases in driving speeds. The research also notes these trends depend on several other factors such as size of car, angle of impact, and perhaps age. Autonomous driving systems can aid in reducing or eliminating in the severity of slope in the curves as computed from a small sample size. Cost appears to be a primary driver factor at the onset systems design requirements. To this end, low-cost IR

*Corresponding Author H. Bryan Riley, rileyhbryan@ieee.org

sensing is the motivated attribute to tackle with a vehicle subsystem implementation by noting that IR sensory data acquisition apparatus is capable of sensing surroundings by means of measuring the temperature differences between two vehicles in motion. The vehicle sensor set with field of view (FOV) typically varying from 120º to 150º, and the respective processing software are imperative for safe operation of autonomous vehicles (AVs). Characterizing the performance of sensing to determine the location of the host vehicle relative to other moving vehicles, all in path targets and road lane boundaries are equally important. Human driver sensing reports that approximately 90% of the primary factors behind crashes are due to human errors (see the statistics of the National Highway Traffic Safety Administration (NHTSA) in 2012). [6],[7] AVs with a high performance sensor suite are predicted to reduce crashes and injury rates by upwards of 50% as compared to non-AVs. Vehicle manufactures are motivated to contribute to transformative and highly beneficial technologies to support Intelligent Transportation Systems (ITS) and the future of the mobility industry. The state of the art reports the rationale for selection of IR sensors rather than ultrasonic sensors, RADARs, or cameras to perform the sensing function. This research proceeds with a conceptual design, implementation, testing, and verification of an IR sensor set interfaced to a single board computer. A desired outcome is to follow a vehicle that is remotely controlled. This vehicle is denoted as RC (remote controlled) down scaled-model vehicle. In the literature, Kou et al. employed two low cost sensors using a kinematic model of a car-like mobile robot (CLMR). [8] Chao-Lin Kuok et al., devised to compare two non-linear model-based approaches for autonomous vehicles. [9] Carson et al., and Englund et al. studied safety criteria for driver assisted systems and enabling technologies. [10],[11] Paden et al. investigated a decision-making hierarchy (i.e., route planning, behavioral decision making, motion planning, and vehicle control) for driverless vehicles. This paper is organized as follows. Section II describes the overall system configuration and sensor interfaces to accomplish the autonomous tracking capability. Here, we also present the embedded system design. Section III is devoted to the testing and the IR sensor configuration. We then describe analysis of the measured test results in Section IV. Section V provides a discussion and the conclusion.

2. Formulation of Research Project

This section describes the design and implementation of an embedded system onto the scale of 1/10 of remote controlled (RC) autonomous vehicles. The system design for this embedded system began by conducting tradeoff study between the Arduino and Raspberry Pi single board computers. In view of ease of programming, a large suite software algorithm readily available in the open source domain. Hence, the decision we have chosen the Raspberry Pi Model B+. It is a fully featured very compact computer operating at 700 MHz and uses the Raspbian Operating System (OS). The computer interface circuitry has mainly 7 components; namely,

- 4 Universal Serial Bus (USB) 2.0 slots
- Single storage data card slot
- 24 Pin Header
- Ethernet port
- Customer Support Identifier (CSI) connector for a camera
- High-Definition Multimedia Interface (HDMI) output
- Power from micro-USB Connector

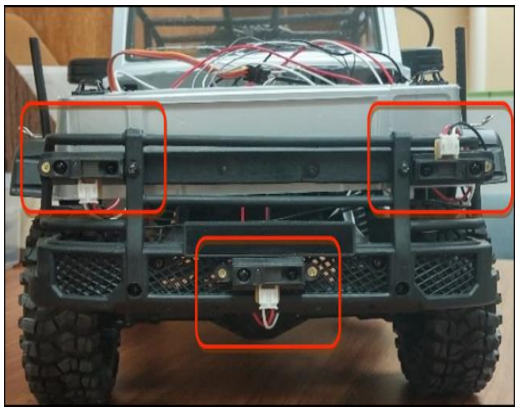

Figure 2. Mounting of IR sensors

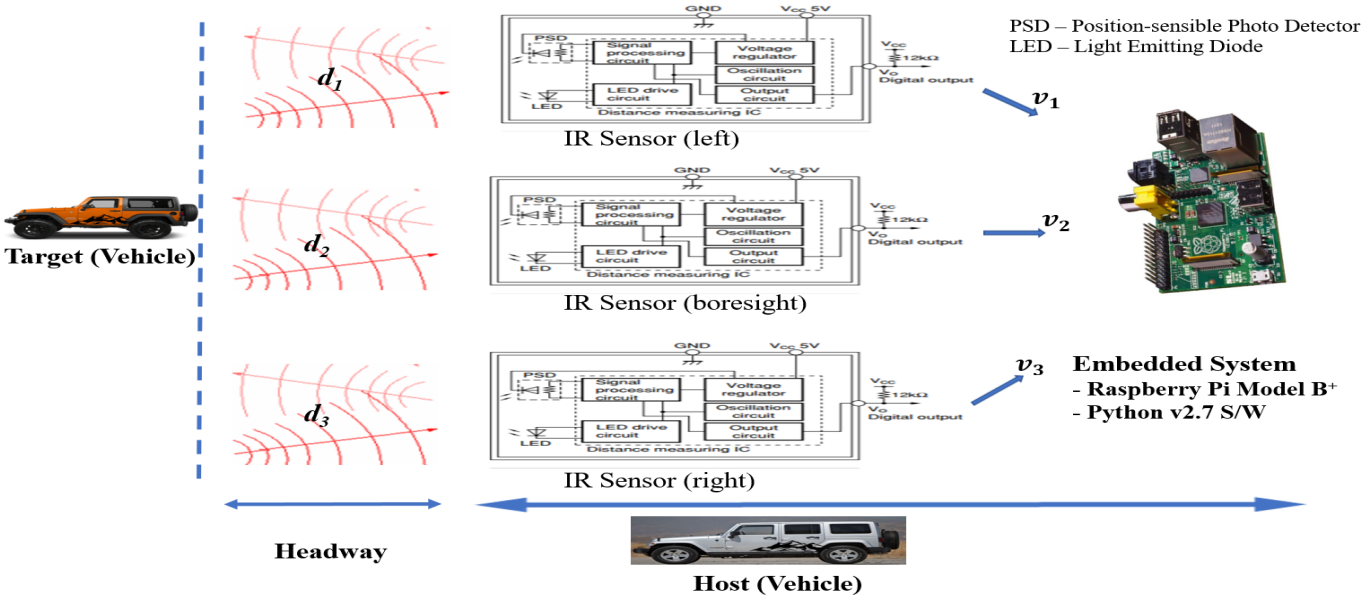

Figure 3. Autonomous convoy embedded system design. [16]

Since cost is always a consideration, an inexpensive SharpGP2YOD21YK IR Sensor operating at the wavelength λ=780 nano-meter (nm) is selected. [12]. The next step is to determine the optimal Field of View (FOV) for forward coverage on the model robotic vehicle. Figure 2. Depicts the mounting of three IR sensors. Specifically, the sensors are mounted in the headlight areas and lower front center of the RC controlled model. Work proceeds to install, calibrate and independently test the sensor in a standalone modes to consume less energy and to operate with nonlinear characteristics [9].

The relationship between the distance d_i and the operating voltage is inversely proportional, and it is given as

$$d_i = k\frac{1}{v_i^a}, \quad i = 1,2,3. \tag{1}$$

with k being the scaling constant and a is the exponent of proportionality. Equation (1) is empirical formula and for the given Sharp GP2YOA21YK IR sensor, it is specified as

$$d = \left(\frac{1}{c * A_{DC} + b}\right) - K \tag{2}$$

where distance d in cm, K is a corrective constant, A_{DC} is the digitized output voltage, b and c are variable constants to be evaluated from trend line equation. Besides proposed equation (2), the governing sensor equation (3) has three variables (b, c, and K) which are evaluated from the measured data.

The embedded Time-Division Multiplexing (TDM) system is implemented by discrete electronic components mounted on a Printed Circuit Board (PCB). The hardware is physically mounted into the body of the robotic model vehicle. Also, it is evident that the data streaming from sensors are converted into a single signal by segmenting the signal with short durations. Figure 3 shows the electrical interface and message traffic block diagram of the Sharp IR sensor in which the digital output V_o is directed to the digital I/O channel of a single board computer (i.e., Raspberry Pi Model B^+) [14][15]. This prototype design minimizes the sensor wiring and power connections.

The Python 2.7 language is employed to write the IR sensing system software illustrated in Figure 3. The algorithm is designed using classical Proportional Integral Derivative (PID) controller techniques. Specifically, the PI algorithm is selected as automatic, greater, and basic [17] to implement. SP is defined as a headway or fixed distance and independent of the measurement sensor PVs are the computed distances, shown in Figure 3. "PIDSYS" a MATLAB R2017A based function is utilized to return the parallel form of a continuous-time PI controller shown in Figure 4.

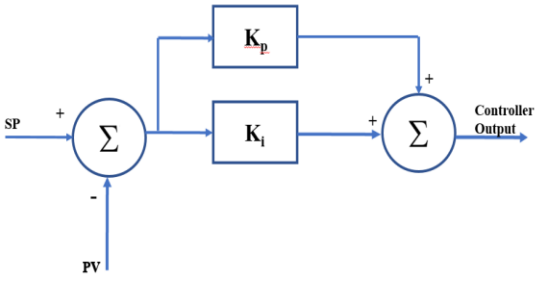

Figure 4. Block Diagram for PI controller.

Here, the instances of error are corrected by proportional term ($\mathbf{K_p}$) corrects and the accumulation of error is corrected by integral term ($\mathbf{K_i}$) corrects the. Based on the rise and fall of error signal {e(t)}, the amount added to the Controller Output (CtrlOut) increases or decreases immediately and proportionately. The CtrlOut is governed by Equation 3 and is given by

$$\text{CtrlOut} = \boldsymbol{K_p}\, e + \boldsymbol{K_i}\int e(\tau)\, d\tau \tag{3}$$

where the range of integration is [0, t], and e is error e = SP-PV required to achieve the controller output. The host vehicle track was based on the sensor voltages and the distances computed, independent of sensor specifications, that occurs per Equation 4.

$$d_1 > (d_2 + d_3) \Rightarrow \text{host tracks target to left} \tag{4a}$$

$$d_1 \simeq d_2 \simeq d_3 \Rightarrow \text{host tracks target straight} \tag{4b}$$

$$d_3 > (d_1 + d_2) \Rightarrow \text{host tracks target to right} \tag{4c}$$

The last stage of this research project formulation is to test the PI algorithm and ensure it is properly tuned or adjusted by starting with low proportional and no integral. The values of K_p and K_i are returned as 1.14 and 0.454, respectively. Figure 5 presents the deviation error of measured PV from SP in response to the computation of step response for this PI controller.

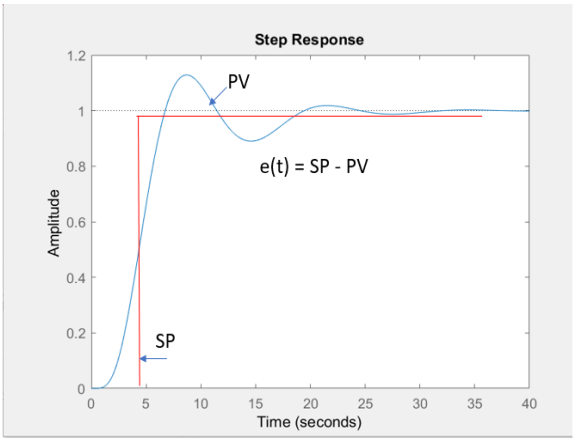

Figure 5. Step response for AV PI controller

3. Analysis of Test Results

After some troubleshooting and software debugging, smooth hallway surfaces are used to perform the initial simulation trials with the embedded system on the host vehicle following a lead vehicle where a smooth following is demonstrated for several test conditions. Figure 6 depicts static photos of the host vehicle chasing the target vehicle in the actual demonstration of this embedded system. The IR sensors are use in individual configurations (i.e., degraded FOV) or by combining that which addresses the redundancy of a given number of sensors

Figure 6. Host tracks target as per equation (4)

4. Data Fusion and Simulation

Sensor fusion is the most important and critical process for autonomous vehicles on the road for increased safety. The short comings of individual sensor can be overcome by fusing the data in such a way that each sensor can complement or augment in the presence of the other sensor failure. The failure or the malfunctioning of the sensors installed could cause by a natural phenomenon or manmade phenomenon [18]. In this parlance, the adaption of the sensor fusion methodology can maintain the essential functions for a required level of safety. With these insights, this section presents the advantage of using Kalman filter-based data fusion over single IR sensor and amid individual sensor failure. Equation 2 is utilized for range tracking and a complete mathematical modeling and simulation based on optimal state estimation theory is presented. With assumed and known values of measurement errors caused by system noises, an optimal estimator computes and processes the measurements for reducing the state error estimate using measurement system dynamics [19].

A. System Dynamic Model

The system dynamic model is a generic representation given by

$$\hat{X}_k(-) = F\hat{X}_{k-1}(+) + Gw_{k-1} \quad (5)$$
$$w_k \sim N(0, Q_k)$$

$$Z_k = H\hat{X}_{k-1}(+) + v_k \quad (6)$$
$$V_k \sim N(0, R_k)$$

where $\hat{X}_{k-1}(+)$ is a priority or the initial estimate of $\hat{X}_k$ taken as [6,1,1] for the purpose of this simulation. F or ϕ is denoted as the state transition matrix for predicting the future states and is given as

$$\phi = \begin{bmatrix} 1 & T & T^2/2 \\ 0 & 1 & T \\ 0 & 0 & 1 \end{bmatrix} \quad (7)$$

Here, the process noise w_k and the measurement noise v_k are modeled as white Gaussian noise with mean of zero and standard deviation of one. The noises in IR sensor and systems are described as statistical fluctuations or distortions in electrical current modeled by various mathematical models as [20]

$$\text{Photovoltaic noises or } \sigma_{\text{noise}} = \sqrt{\text{jn(r)} + \text{sn(r)} + \text{pn(r)}} \quad (8)$$

$$\text{Photoconductive noises or } \sigma_{\text{noise}} = \sqrt{\text{jn(r)} + \text{grn(r)} + \text{pn(r)}} \quad (9)$$

$$\text{where} \quad \text{jn(r)is Johnson noise} = \frac{4kT_dB(R)}{R_d} \quad (10)$$

$$\text{sn(r)is Dark current shot noise} = 2qi_DB(R) \quad (11)$$

$$\text{grn(r)is Generation Recombine noise} = 4qGi_DB(R) \quad (12)$$

$$\text{pn(r) is Photon noise} = \frac{2\eta q^2(P_s+P_b)B\lambda}{hc} \quad (13)$$

For a particular sensor and with its specifications the measurement noise variances can be modeled by using the equations from 12 to 17.

B. Fusion Algorithm

For the purpose of simulation, the sensor and the system are considered as time invariant systems in which all three IR sensors produce measurement at the same time. The method of the fusion process [21] depend on the covariance matrix and its trace operation, given by

$$\hat{x}_k = \sum_{i=1}^{N} a_i z_i(k) \quad (14)$$

where N is the total number of IR sensors mounted on the convoy, z(k) denotes the sensor value from the i^{th} IR sensor for every time interval k, and the quotient a_i is given by

$$a_i = \frac{1/tr((R_i(k))}{\sum_{J=1}^{N} \frac{1}{tr((R_j(K))}} \quad (15)$$

where *tr()* performs the trace operation with mapped measurement covariance $R_i(k)$ of the i^{th} IR sensor at k^{th} *time interval.* The quotient a_i is summed to unity by assumption.

C. Kalman Filter steps

Measurements from each sensor are fused using the below algorithm [21]:

- Perform the state estimate extrapolation expressed as
$$\hat{X}_k(-) = \phi_{k-1}\hat{X}_{k-1}(+) \quad (16)$$
- Perform the error covariance extrapolation given as
$$P_k(-) = \phi_{k-1}P_{k-1}(+){\phi^T}_{k-1} + Q_{k-1} \quad (17)$$
- Update the state estimate observation
$$\hat{X}_k(+) = \hat{X}_k(-) + \bar{K}_k[Z_k - H_k\hat{X}_k(-)] \quad (18)$$
- Calculate the error covariance update
$$P_k(+) = [1 - \bar{K}_k H_k]P_k(-) \quad (19)$$
- Calculate the Kalman Gain Matrix
$$\bar{K}_k = P_k(-){H_k}^T[H_kP_k(-){H_k}^T + R_k]^{-1} \quad (20)$$

The bock diagram describing the system, measurement model, and discrete-time Kalman Filter is shown in Figure 7.

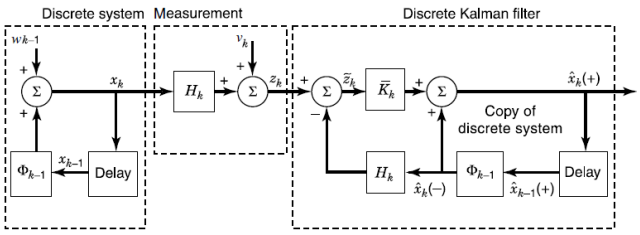

Figure 7. System model and Discrete Kalman filter [22]

The initial values for predicted covariance and state transition matrix are taken as

$$P_{k-1}=\begin{bmatrix}1 & 1 & 1\\ 1 & 1 & 1\\ 1 & 1 & 1\end{bmatrix} \quad (21)$$

Figure 7 presents the iterative recursion process of the Kalman filter and sums up the equations described in 17 to 21. The simulation results shown in the Figures 9 and 10 describe the effectiveness of Kalman filter-based data fusion. These iterative recursive filters are used for continuous time problems and considered as a breakthrough for estimation in linear dynamic systems. The propagation of covariance matrix and the dynamic calculation of the Kalman filter gains make this filter superior. The state vector dimension is 3-by-1 known as one dimensional third order filter tracking with one position or relative distance component, one velocity component and one acceleration component obtained by each individual IR sensor. The measurements from each sensor are fused using the algorithm and the fused measurement is optimally estimated by the filter steps mentioned in equations 17 to 21. Next, using the state estimate and the covariance matrix the propagation of prediction and correction will continue to obtain the smoothed estimate.

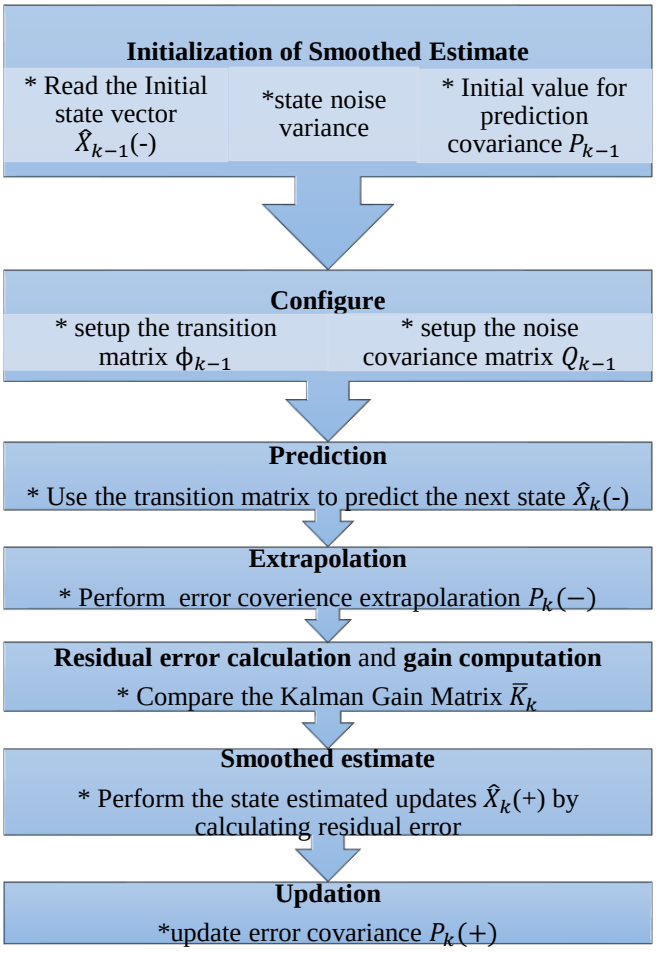

Figure 8. Iteration steps for Kalman filter [23]

Figures 8 presents the MATLAB simulation flowchart. Figure 11 indicates the digitally computed true distance between the target vehicle and the sensor mounted vehicle simulated based on the equation 2. It also shows the measured distances d1, d2 and d3 from each IR sensor and fused distance estimate based on Kalman filter.

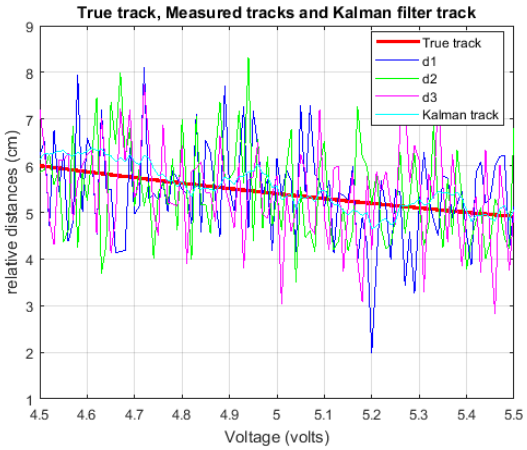

Figure 9. Tracks simulation

The simulation parameters are chosen such as sampling interval of 0.1 sec over the supply voltage values between 4.5 volts to 5.5 volts. The initial values of relative distances d1, d2 and d3 are 6.2, 5.8 and 7.1 cm. These values of relative distances are chosen based on the distance measuring range of the sensor considered in section 2. For each sample the values of d1, d2 and d3 vary between minimum of 4 cm to a maximum of 7 cm. Also, the minimum and the maximum values of true values of track is 4.9 cm to 6cm, and from Figure 10 it is evident that Kalman filter track has the best estimate that follows the true track closely. Table 1 shows the RMS errors and the performance of each sensor and the Kalman filter is analyzed by computing the distance error in relative position between the two vehicles using

$$RMS\ Error_{dist} = \sqrt{\frac{1}{N}\sum_{i=1}^{N}\frac{(x_{true}-x_{esti})^2}{3}} \quad (22)$$

In equation 22, x_{rue} are the true track values and x_{esti} are the individual estimates of each sensor and Kalman filter estimates as well. Therefore, using the equation 22, the RMS error values for each sensor tracks alongside the Kalman filter based fusion tracks are obtained and presented in Table 1.

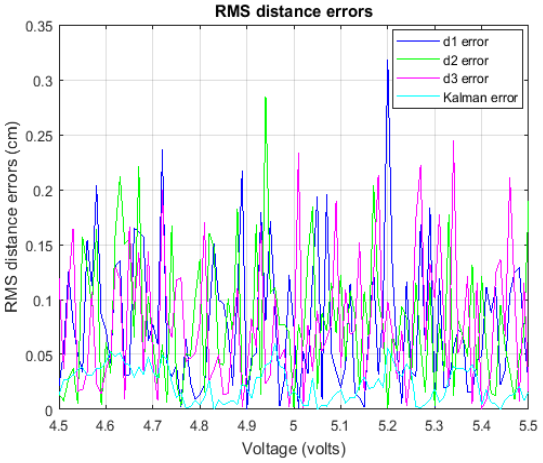

Figure 10. RMS errors in relative distances

From Figure 10 and Table 1, it is evident that Kalman filter based fusion method shows the better performance compared to individual IR sensors and the superiority and the advantage of implementing optimal estimation based fusion process.

Table 1. Average RMS Errors

Estimator	RMS Error (cm)
IR sensor 1	0.0230
IR sensor 2	0.1893
IR sensor 3	0.016
Kalman filter based fusion	**0.015**

Conclusion

This research project resulted in the successful development and implementation of an embedded system design for an autonomous vehicle. The implementation based on theoretical multisensory data fusion is based upon IR sensors and a single board computer. A dynamic demonstration of active following by the host is successful and was accomplished while considering the design constraints of the embedded system. The performance achieved on the 1:10 scaled model indicates positive proof of concept for real-world scaling of OEM (Original Equipment Manufacturer) vehicles. The system architecture provided for sensors from varied range of specifications to be incorporated and demonstrate performance of maintaining a set headway and smoothly following a target vehicle. From the test results, an overall error is found to be less than 5% in following distance and a measurement order of eight seconds resulted in response to steady state. A comparison to other research results reported in the literature confirms similar result where the trade of is use of two sensors (i.e., narrower FOV) whereas this work utilized a configuration of three sensors ((i.e., broader FOV). Also, the incorporation of the fusion applications for the robustness of distance and tracking, could potentially improve the safety considerations. Research results included determination of the system RMS error based on Kalman filter which provides greater accuracy than other computational approaches for error calculations. As error is reduced, AV operational safety will be enhanced. The average RMS error for the lower IR sensor (i.e., centered position and single sensor configuration) is within +/- .001cm. Furthermore, the contextual practical application of the sensor fusion for automotive applications reliability detects in-path targets that aid in collision avoidance. This research maybe be extended by configuring dissimilar sensors such as RADAR, LiDAR in conjunction with IR sensors leading to an Advanced Driver Assistance System (ADAS). These systems are totally dependent on weighting sensor information to make intelligent and safe decisions. Based on the theoretical simulation of sensor fusion presented in the paper, it is believed the paradigm of data fusion can enhance the reliability and robustness of an ADAS for improved safety considerations. The future scope of this research will be demonstrated in the real-world environment amid poor visible conditions to check the accuracy of the proposed methods outlined above. An approach may include resolving distances based on the speed of light by measuring the Time-of-Flight (ToF) between the sensor and the targeted image using a ToF Camera or LIDAR. Motion planning conducted by a low-level feedback controller is also a consideration for additional research since trajectory and path planning are computationally complex and require computing resources well beyond the selected Raspberry Pi Model B^+ single board computer.

References

[1] N. Lang *et al*., "*Making Autonomous Vehicles a Reality: Lessons from Boston and Beyond*., The Boston Consulting Group, Oct. 2017.

[2] A. Jonas *et al.*, "Autonomous Cars: Self-Driving the New Auto Industry Paradigm," *Morgan Stanley Blue Pap.*, pp. 1–109, 2013.

[3] L. Gannes, "Google Introduces New Self Driving Car at the Code Conference," *Re/code*. 2014.

[4] L. Mearian, "Nissan plans to offer affordable self-driving cars by 2020," *Computerworld*. 2013.

[5] D.A. Dickmanns and D. L. Wiesenthal, "Traffic congestion, driver stress, ana driver aggression," Agbressive behavior, pp 409 - 423, 1988.

[6] NHTSA, "U.S. Department of Transportation releases policy on automated vehicle development," *Nhtsa 14-13*, 2013.

[7] C. Pozna and C. Antonya, "Issues about autonomous cars," in *SACI 2016 - 11th IEEE International Symposium on Applied Computational Intelligence and Informatics, Proceedings*, 2016.

[8] C. L. Kuo, N. S. Pai, Y. P. Kuo, and Y. C. Hu, "Following method for a car-like mobile robot using two IR sensors," in *IEEE International Conference on Control and Automation, ICCA*, 2014.

[9] E. Alcal; *et al.*, "Comparison of two non-linear model-based control strategies for autonomous vehicles," *2016 24th Mediterranean Conference on Control and Automation (MED)*. 2016.

[10] O. M. G. Carsten and L. Nilsson, "Safety assessment of driver assistance systems," *Eur. J. Transp. Infrastruct. Res.*, 2001.

[11] C. Englund *et al.*, "Enabling technologies for road vehicle automation," in *Road Vehicle Automation 4*, 2017.

[12] Sharp Corporation, "Distance Measuring Sensor GP2YOA21YK," 2016.

[13] B. Paden et .al, "A Survey of Motion Planning and Control Techniques for Self-driving Urban Vehicles., IEEE Transactions on Intelligent Vehicles, pp. 33-55. Volume: 1, Issue: 1, March 2016.

[14] Raspberry Pi Foundation, "Raspberry Pi - Teach, Learn, and Make with Raspberry Pi," w*ww.raspberrypi.org*, 2012.

[15] E. Upton and H. Gareth, *Raspberry Pi User Guide*. 2014.

[16] D. Gunnarsson, S. Kuntz, G. Farrall, A. Iwai, and R. Ernst, "Trends in Automotive Embedded Systems," in *CASES'12: Proceedings of the 2012 ACM International Conference on Compiliers, Architectures and Synthesis for Embedded Systems, 2012*.

[17] R.-E. Precup, A.-D. Balint, E. M. Petriu, M.-B. Radac, and E.-I. Voisan, "PI and PID controller tuning for an automotive application using backtracking search optimization algorithms," *SACI 2015 - 10th Jubil. IEEE Int. Symp. Appl. Comput. Intell. Informatics, Proc.*, 2015.

[18] Hannes Estl, "Sensor Fusion: A Critical step on the road to autonomous vehicles", Automotive ADAS sector, April 11th 2016.

[19] A. Gelp et al, "*Applied optimal estimation*", Second edition, MIT press, February 1974.

[20] Christopher W. Keefer, "Infrared Target Detection: Signal and Noise Sensitivity Analysis", Master's Thesis, December 1989, School of Engineering of the Air Force Institute of Technology, Wright-Patterson Air Force Base, Ohio.

[21] X. Yu, J. Yihui, Z. Yan, "Several methods of radar data fusion", IEEE 3rd International Symposium on Electromagnetic Compatibility, May 2002, China.

[22] Mohinder S. Grewal and Angus P. Andrews, *Kalman filtering theory and practice using MATLAB*, 2 Edition, Wiley & Sons, Inc.

[23] David Kondru, Mohan Krishna, "Kalman filter based Target Tracking for Track while scan Data Processing", 2015 2nd IEEE International Conference on Electronics and Communication Systems (ICECS), 26-27 Feb. 2015.